NUREG/CR-4166
EPRI NP-4111
WCAP-10375

Analysis of FLECHT-SEASET 163-Rod Blocked Bundle Data Using COBRA-TF

NRC/EPRI/Westinghouse Report No. 15

Westinghouse Electric Corporation

Electric Power Research Institute

Prepared for
U.S. Nuclear Regulatory Commission

FLECHT SEASET Program
NRC/EPRI/Westinghouse Report No. 15
NUREG/CR-4166
EPRI NP-4111
WCAP-10375

ANALYSIS OF FLECHT SEASET 163-ROD BLOCKED BUNDLE DATA USING COBRA-TF

October 1985

C. Y. Paik
L. E. Hochreiter
Westinghouse Electric Corporation

J. M. Kelly
R. J. Kohrt
Battelle Northwest Laboratory

prepared for

United States Nuclear Regulatory Commission
Washington, DC 20555

Electric Power Research Institute
3412 Hillview Avenue
Palo Alto, California 94303

and

Westinghouse Electric Corporation
Nuclear Energy Systems
P. O. Box 355
Pittsburgh, Pennsylvania 15230

by

Westinghouse Electric Corporation

under

Contract No. NRC-04-77-127, EPRI Project No. RP959-1

Program Management Group

NRC - R. Lee
EPRI - A. Singh
Westinghouse - H. B. Rosenblatt

0438X:1b-080385

ABSTRACT

Flow blockage and spacer grid heat transfer models for rod bundle arrays have been developed for a two-phase flow situation characteristic of a PWR reflood. These models have been incorporated into COBRA-TF, which is a three-dimensional, three-field, two-fluid mechanistic two-phase flow subchannel computer code. Comparisons of the predicted flow blockage heat transfer in large rod bundle arrays with test data indicate that the blockage and grid heat transfer models used with the COBRA-TF code agree quite well with the measured data. Bias plots of the predicted and measured temperature rises from different tests indicate that, in general, the computer code calculations tend to underpredict the heat transfer improvement observed to have been caused by grids and blockage in the experiments.

The principal reason for heat transfer improvement due to blockages and grids is the breakup of the entrained liquid droplets in the superheated steam flow above the quench front. The breakup of these entrained drops results in a population of much smaller drops, which are more easily evaporated in the superheated vapor. The enhanced heat transfer observed in and downstream of blockages and grids is also attributable to increased turbulence caused by the droplets in the steam flow.

The resulting computer models and methods of modeling both grids and blockages, which are described in this report, are believed to be applicable to PWR safety analysis. Application of such models is expected to significantly reduce or eliminate the calculated peak clad temperature penalty due to flow blockage for a hypothetical PWR LOCA, using the Appendix K criteria.

ACKNOWLEDGMENTS

The work of the following Westinghouse Nuclear Energy Systems contributors is hereby acknowledged:

TECHNOLOGY PROGRAMS
L. M. Williams

SAFEGUARDS ENGINEERING
M. J. Loftus
M. Y. Young
K. F. McNamee
D. W. Sklarsky
D. P. Kitzmiller
K. S. Chiou

PUBLICATION PROGRAMS
J. G. Nagle

The work of the following members of the Program Management Group, their colleagues, and their consultants is hereby acknowledged:

EPRI - K. H. Sun, R. B. Duffy
NRC-RSR - L. H. Sullivan, R. Lee
NRC-NRR - W. Hodges, G. N. Lauben
EG&G - M. Bolander, D. M. Ogden

NOMENCLATURE

A	flow area
A_H	heat transfer surface area
A_I	intercell friction area
A_I'''	interfacial area per unit volume
A_K	transverse flow area
a	absorption coefficient
b	phase mobility
C_D	drag coefficient
Cp	specific heat capacity
$\underline{\underline{D}}$	deformation tensor
$\underline{\underline{D}}^*$	deleted deformation tensor
D_H	hydraulic diameter
$\underline{\underline{F}}$	turbulence anisotropy tensor
$\underline{F}_I$	intercell drag force
F	gray body factor
f	friction factor
G	mass flux
g	gravitational acceleration
$\underline{g}$	gravitational acceleration vector
g_c	gravitational conversion constant
H	heat transfer coefficient
h	enthalpy
h_{fg}	enthalpy of vaporization
j	superficial velocity
K	loss coefficient

K_I	interfacial friction coefficient
k	thermal conductivity
k_s	equivalent sand roughness
k_σ	mass transfer coefficient
L	transverse coordinate
ℓ_h	energy mixing length
ℓ_M	momentum mixing length
$\underline{M}^d$	interfacial drag force
M_i	mass of heat transfer node i
$\underline{M}^\Gamma$	interfacial momentum exchange due to mass transfer
$\dot{m}$	mass flow rate
N	number density
N_μ	viscosity number
P	pressure
P^T	turbulent pressure
Pr	Prandtl number
Pr^t	turbulent Prandtl number
P_w	wetted perimeter
$\underline{Q}$	conduction heat flux
Q'''_w	wall heat flux per unit fluid volume
$\underline{q}$	fluid-fluid conduction heat flux
q''	surface heat flux
q'''_I	interfacial heat flux per unit volume
$\underline{Q}^T$	turbulent heat flux
R	internode resistance
Re	Reynolds number
r	radius

S	net rate of entrainment
S_{DE}	rate of deentrainment
S_E	rate of entrainment
S_k	gap width of gap k
S_u	entrainment correlation parameter
S_γ	rate of interfacial area concentration change due to phase change
S'_{nk}	orthogonal gap width
S'''	net rate of entrainment per unit volume
$(S'''U)$	momentum exchange due to entrainment
T	temperature
$\underline{\underline{T}}$	stress tensor
$\underline{\underline{T}}^T$	Reynolds stress tensor
t	time
Δt	averaging time interval
$\underline{U}$	fluid velocity
$\underline{U}_{vj}$	drift velocity
u	velocity component in vertical (x) direction
V	volume
v	velocity component in transverse (y) direction
We	Weber number
w	velocity component in transverse (z) direction
x	vertical direction
y	transverse direction
z	transverse direction

Greek letters

α	void fraction
β	thermal expansion coefficient
Γ	net rate of mass transfer per unit volume
Γ'''	net rate of vapor generation per unit volume
$(\Gamma'''U)$	momentum exchange due to vapor generation
δ	film thickness
δ_{ij}	Kronecker delta
ε	thermal diffusivity
ε^T	turbulent thermal diffusivity
η	fraction of vapor generation coming from entrained liquid
η_{NR}	deentrainment efficiency
μ	viscosity
μ^T	turbulent viscosity
ρ	density
$\underline{\underline{\sigma}}$	fluid-fluid stress tensor
σ	surface tension
$\underline{\underline{\tau}}$	viscous stress tensor (stress deviator)
$\underline{\tau}_I'''$	interfacial drag force per unit volume
λ	characteristic wave length
σ_β	Boltzman constant

Subscripts

B	bulk
BR	bubble rise
b	bubble
CHF	critical heat flux
DE	deentrainment

d	drop
E	entrainment
e	entrained field
f	saturated liquid film
g	saturated vapor
I	interfacial
i,j	heat transfer nodes
k	phase k
ℓ	liquid field
MIN	minimum film boiling point
m	mixture
R	relative
SHL	superheated liquid
SCL	subcooled liquid
SHV	superheated vapor
SCV	subcooled vapor
SP	single phase
S	surface
s	drop formation
V	vapor phase (Vapor properties used in heat transfer correlations are evaluated at the film temperature.)
v	vapor field
vℓ	between vapor and liquid fields
ve	between vapor and entrained fields
W-D	wall to drop
W-V	wall to vapor

x,y,z	directions
2ϕ	two phase

Superscripts

i	interfacial surface average
n	old time level
n+1	new time level
s	surface average
T	turbulent
t	transpose

TABLE OF CONTENTS

TABLE OF CONTENTS (cont)

TABLE OF CONTENTS (cont)

TABLE OF CONTENTS (cont)

LIST OF ILLUSTRATIONS

LIST OF ILLUSTRATIONS (cont)

LIST OF TABLES

SECTION 1
INTRODUCTION

1-1. BACKGROUND

Nuclear reactors are conservatively designed using the defense in depth concept. Defense in depth comprises multiple barriers and backup systems which protect the public from the release of fission products. For example, zircaloy fuel cladding provides a barrier to release of fission products into the primary coolant system. The primary coolant system piping and vessel of a PWR prevent release to the containment and release to the atmosphere is prevented by the reactor containment.

One very important subsystem, the emergency core cooling system (ECCS), provides an independent backup to the reactor coolant piping system, ensuring that the failure of the reactor piping will not result in unacceptably high peak clad temperature and fuel failure release of fission products to the containment atmosphere. The ECCS system is designed to mitigate the consequences of the worst postulated pipe break or loss-of-coolant accident (LOCA).

A series of public hearings[1] were conducted in the United States in 1972 and 1973 to evaluate whether sufficient margin was being incorporated into the design of the reactor emergency core cooling systems. The hearings also examined the state of the art of reactor safety analysis, particularly the concern about the possible large uncertainty in reactor transient calculations due to empirical modeling and/or unknown phenomena.

As a result of the hearings, two sets of criteria were released; the Interim Acceptance Criteria (IAC) in 1972,[2] which remained valid for a year, and

---

1. "Interim Acceptance Criteria for Emergency Core Cooling Systems for Light Water Reactors," AEC Regulatory Staff Testimony, January 1972.

2. Rulemaking Hearing, "Acceptance Criteria for Emergency Core Cooling Systems for Light Water Cooled Nuclear Reactors," Opinion of the Commission, CLI-73-39, December 1973.

the Final Acceptance Criteria (FAC),[1] published in 1973 to replace the IAC. The FAC, 10CFR50.46 A1, and Appendix K rule form the basis for current licensing and safety analysis assessment. The analytical models which are used to evaluate ECCS performance against the FAC must employ the many conservative assumptions prescribed in Appendix K.

When the FAC and the Appendix K rule were issued in 1973, both the United States Nuclear Regulatory Commission (USNRC) and the industry recognized that the rule was conservative. That is, the performance of the ECC systems would be conservatively underestimated by the rule, resulting in higher-than-expected predicted peak clad temperatures. However, the extent of the rule's conservatism could not be adequately quantified at that time, because of the lack of experimental data.

Since 1973, the NRC and the nuclear industry have carried out extensive experimental research to identify and quantify the conservatisms in assumptions, models, and requirements of the Appendix K rule. This research has provided a better understanding of the phenomena associated with LOCA and the uncertainty in reactor transient calculations has been significantly reduced.

To date, several areas of significant conservatism have been identified which could justify either a reinterpretation of the Appendix K rule or a relaxation of some of the prescriptive models in the safety analysis calculations.

A joint program was developed by the NRC, the Electric Power Research Institute (EPRI), and Westinghouse to address one of these areas of conservatism, the flow blockage steam cooling rule. The Appendix K rule required that the effects of flow blockage must be considered and that cooling is only by steam when the reactor reflooding rate decreases below 2.54 cm/sec (1 in./sec). The original NRC concern was that, at low flooding rates, the core cooling flow could all be superheated steam and that substantial flow bypass could occur if the fuel rods should swell and burst. The subsequent flow diversion would

---

1. Rulemaking Hearing, "Acceptance Criteria for Emergency Core Cooling Systems for Light Water Cooled Nuclear Reactors," Docket R. M.-50-1, 1973.

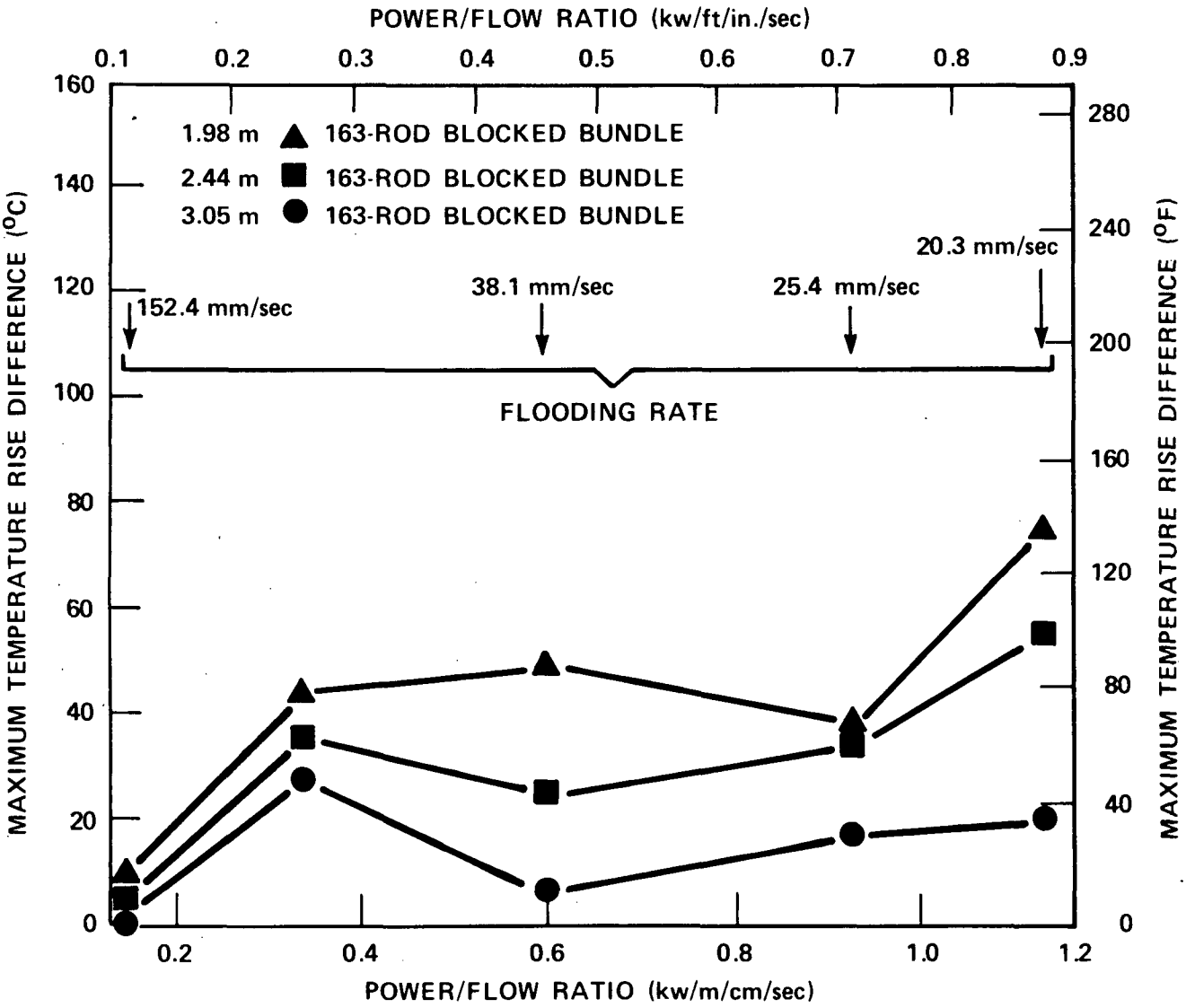

Figure 1-1. Maximum Temperature Rise Difference Between Blocked and Unblocked Bundles as a Function of Flooding Rate and Elevation

decrease the amount of flow going through the blocked assembly, and thus result in reduced cooling and a higher peak clad temperature. Most calculated reactor transients do indicate that for a large-break LOCA, the flooding rate will drop below 2.54 cm/sec (1 in./sec) at some point. A significant amount of research has been performed on flow blockage heat transfer in rod arrays with different blockage shapes and with flow bypass.[1] The research indicates that the heat transfer may even be improved in rod arrays with blockage rather than reduced, as prescribed by Appendix K.

An example of the results is shown in figure 1-1, which quantifies the net effects of flow blockage and bypass.[2] To provide a comprehensive, yet simple, comparison of the flow blockage results, the temperature rise difference ($[T_{max} - T_{initial}]_{unblocked} - [T_{max} - T_{initial}]_{blocked}$) between the FLECHT SEASET blocked 163-rod bundle and the unblocked 161-rod bundle was calculated as a function of elevation and flooding rate. The unblocked and blocked bundle tests which were compared had power-to-flow ratios from 0.16 to 1.124 kw/m (6.3 to 44.25 kw/in.) with inlet flooding rates from 0.15 to 0.020 m/sec (6 to 0.8 in./sec). The elevations selected for these comparisons were 1.98 m (78 in.), which is immediately downstream of the blockage, and 2.44 and 3.05 m (96 and 120 in.), elevations located in the next two grid spans. A positive temperature rise difference indicates improved heat transfer for the tests with flow blockage.

These comparisons generally indicate the following effects:

- As the flooding rate decreases, the temperature rise difference between the unblocked and blocked bundles increases, indicating that the maximum temperature in the blocked bundle decreases because of the improved heat transfer downstream caused by the

1. Erbacher, F. J., et al., "Post-CHF Effects of Spacer Grids and Blockages in Rod Bundles," paper presented at the Post-CHF Heat Transfer Workshop, Salt Lake City, April 1984.

2. Loftus, M. J., and Hochreiter, L. E., "Reflood Heat Transfer in the FLECHT SEASET 163-Rod Bundle With Flow Blockage and Bypass," ASME Paper 83-WA/HT-16, 1983.

blockage. As the power-to-flow ratio increases (flooding rate decreases), the favorable blockage heat transfer effects become even larger.

- As the distance downstream of the blockage increases, the temperature rise difference between the unblocked and blocked bundles decreases, indicating that the maximum temperature in the blocked bundle increases with distance from the blockage. However, the blocked bundle maximum temperature is still less than that for the unblocked bundle. This axial effect downstream of the blockage is similar to a thermal entry region effect for a tube and has been observed downstream of a grid or other blockage.

1-2. PROGRAM OBJECTIVES AND APPROACH

One of the objectives of the FLECHT SEASET program was to develop models of flow blockage which could be used for PWR calculations to assess the influence of flow blockage on rod bundle heat transfer. Although there are several options that could be used to develop models for blockage heat transfer, it was felt that a physically based model used with a state-of-the-art two-phase flow computer code would give the most accurate results.

It was reasoned that such an approach would provide a technically sound basis for PWR analysis with flow blockage, such that the methodology could be extrapolated to other blockage shapes and geometries.

The code selected was the COBRA-TF code,[1] which is a three-dimensional, three-field, two-fluid fluid mechanics and heat transfer model. COBRA-TF was developed specifically to examine hot assembly performance for postulated accidents. The following strategy was used in this program:

- Perform additional code validation with forced reflooding tests using different size bundles without blockage, to reduce uncertainties in the code calculations with new models for grid spacers
- Perform code calculation on small bundles with blockages, to develop blockage models for COBRA-TF

1. Thurgood, M. J., et al., "COBRA/TRAC Manual," Volumes 1-5, PNL-4220, March 1983.

- o Perform calculations with COBRA-TF on large bundle tests with blockage and bypass effects, to assess the code's capability to model the combined effect of both blockage and bypass

The program used data from the Karlsruhe FEBA experiments,[1-3] the FLECHT SEASET 161-, 21-, and 163-rod bundle experiments,[4-6] and the EPRI/UCLA two-phase turbulence enhancement experiments[7] to develop and validate models for COBRA-TF.

1-3. REPORT ORGANIZATION

This evaluation report is organized into several major subsections:

- o First, the COBRA-TF model is explained in detail, along with the modifications which were made to the model.
- o The grid and blockage heat transfer models are explained, as well as how they were installed in COBRA-TF.

1. Ihle, P., and Rust, K., "FEBA - Flooding Experiments With Blocked Arrays, Evaluation Report," KfK 3657, March 1984.
2. Ihle, P., and Rust, K., "FEBA - Flooding Experiments With Blocked Arrays, Data Report 1, Test Series I Through IV," KfK 3658, March 1984.
3. Ihle, P., and Rust, K., "FEBA - Flooding Experiments With Blocked Arrays, Data Report 2, Test Series V Through VII," KfK 3659, March 1984.
4. Lee, N., et al., "PWR FLECHT SEASET Unblocked Bundle Forced and Gravity Reflood Task Data Evaluation and Analysis Report," NRC/EPRI/ Westinghouse-10, September 1981.
5. Loftus, M. J., et al., "PWR FLECHT SEASET 21-Rod Bundle Flow Blockage Task Data and Analysis Report," NRC/EPRI/ Westinghouse-11, September 1982.
6. Loftus, M. J., et al., "PWR FLECHT SEASET 163-Rod Bundle Flow Blockage Task Data Report," NRC/EPRI/Westinghouse-13, September 1983.
7. Drucker, M., and Dhir, V. K., "Studies of Single- and Two-Phase Heat Transfer in a Blocked Four-Rod Bundle," EPRI NP-3485, June 1985.

- Comparisons of the calculated heater rod temperatures and vapor temperatures are presented along with bias plots to assess the overall COBRA-TF agreement with the experimental data.

- The report ends with conclusions and recommendations on how to further reduce the calculated uncertainties observed in this study.

Detailed information on the blockage models is provided in the appendixes.

SECTION 2
COBRA-TF MODEL DESCRIPTION

2-1. INTRODUCTION

The COBRA-TF (COolant Boiling in Rod Arrays - Two-Fluid) computer program[1] was developed at the Pacific Northwest Laboratory under the sponsorship of the United States Nuclear Regulatory Commission to provide best-estimate thermal-hydraulic analyses of a light water reactor (LWR) vessel for design basis accidents and anticipated transients. In particular, COBRA-TF has two major application areas:

- o PWR primary system loss-of-coolant analysis
- o LWR rod bundle accident analysis

To perform LOCA simulations of a PWR primary system, COBRA-TF[1] and TRAC-PD2[2] were combined. The resulting code, COBRA/TRAC, utilizes the flexible noding of COBRA-TF to model the reactor vessel and the one-dimensional component models of TRAC-PD2 for the loop. The COBRA-TF rod bundle analysis effort has concentrated on the reflood phase of a LOCA; it applies best-estimate modeling techniques to evaluation model conditions (for example, rod temperature at initiation of reflood, flooding rate, power decay, and maximum peaking factors).

In cooperation with the FLECHT SEASET program, COBRA-TF was modified to enhance its predictive capability for reflood transients. Models for inter-subchannel thermal radiation, grid spacer effects, and flow blockage heat

---

1. Thurgood, M. J., et al., "COBRA-TRAC: A Thermal-Hydraulic Code for Transient Analysis of Nuclear Reactor Vessels and Primary Coolant Systems," NUREG-CR-3046 (PNL 4385), Volumes 1-5, March 1982.

2. "TRAC-PD2: An Advanced Best-Estimate Computer Program for Pressurized Water Reactor Loss-of-Coolant Accident Analysis," NUREG-CR-2054, 1981.

transfer were added. This section documents the COBRA-TF reflood models and constitutive relations, with the exception of the grid spacer and flow blockage models, which are detailed in sections 3 and 4, respectively.

2-2. TWO-FLUID CONSERVATION EQUATIONS

The two-fluid formulation uses a separate set of conservation equations (mass, energy, and momentum) for each phase. COBRA-TF extends this treatment to three fields: vapor, continuous liquid, and entrained liquid drops. Dividing the liquid phase into two fields is the most convenient and physically reasonable way to handle flows where the liquid coexists in continuous (film, inverted annular) and discrete (droplet) forms. In such flows, the motion of the droplets can be quite different from the motion of the continuous liquid; therefore, a single set of average liquid-phase equations cannot adequately describe the liquid flow or the interaction between liquid and vapor. In addition, COBRA-TF allows for the transport of a noncondensible gas mixture with the vapor field.

This two-fluid, three-field description of two-phase flow results in a set of nine conservation equations. These equations are described in the paragraphs below. More information on the derivation and averaging of these equations may be found in Thurgood, section 2.[1] Similarly, BNWL-2214[2] describes the differencing and semi-implicit solution scheme employed by COBRA-TF.

2-3. Mass Conservation Equations

Four mass conservation equations are required for the vapor, continuous liquid, entrained liquid, and noncondensible gas mixture. In vector form they are, respectively, as follows:

---

1. Thurgood, M. J., et al., "COBRA-TRAC: A Thermal-Hydraulic Code for Transient Analysis of Nuclear Reactor Vessels and Primary Coolant Systems," NUREG-CR-3046 (PNL 4385), Volumes 1-5, March 1982.

2. Stewart, C. W., et al., "COBRA-IV: The Model and the Method," BNWL-2214, 1977.

$$\frac{\partial}{\partial t}\alpha_v\rho_v + \nabla \cdot (\alpha_v\rho_v\vec{U}_v) = \Gamma''' + \nabla \cdot \vec{G}_v^T \quad (2\text{-}1)$$

$$\frac{\partial}{\partial t}\alpha_\ell\rho_\ell + \nabla \cdot (\alpha_\ell\rho_\ell\vec{U}_\ell) = -\Gamma_\ell''' - S''' + \nabla \cdot \vec{G}_\ell^T \quad (2\text{-}2)$$

$$\frac{\partial}{\partial t}\alpha_e\rho_\ell + \nabla \cdot (\alpha_e\rho_\ell\vec{U}_e) = -\Gamma_e''' + S''' \quad (2\text{-}3)$$

$$\frac{\partial}{\partial t}\alpha_g\rho_g + \nabla \cdot (\alpha_g\rho_g\vec{U}_v) = \Gamma_g''' + \nabla \cdot \vec{G}_g^T \quad (2\text{-}4)$$

The individual terms in the equations become

Rate of change of mass	+	Rate of mass gain by convection	=	Rate of mass gain by interfacial transfer or chemical reaction	+	Rate of mass gain by entrainment	+	Rate of mass efflux due to void drift drift

Also, a gas mixture transport equation (for each species of noncondensible gas) is solved explicitly at the end of each time step.

2-4. Energy Equations

Two energy conservation equations, in which the liquid and the entrained liquid are assumed to interact at a rate sufficient to nearly maintain equilibrium, are specified for the vapor-gas mixture and the combined liquid fields:

$$\frac{\partial}{\partial t}(\alpha_v\rho_{vg}h_{vg}) + \nabla \cdot (\alpha_v\rho_{vg}h_{vg}\vec{U_v}) = \Gamma''' h_g + q_{iv} + Q_{vg}''' - \nabla \cdot (\alpha_v \underline{q}_{vg}^T) \quad (2\text{-}5)$$

$$\frac{\partial}{\partial t}\ (\alpha_\ell + \alpha_e)\rho_\ell h_\ell\ + \nabla \cdot (\alpha_\ell \rho_\ell h_\ell \vec{U}_\ell) + \nabla \cdot (\alpha_e \rho_\ell h_\ell \vec{U}_e) = \Gamma'''h_f + q_{i\ell} + Q_L''' - \nabla \cdot (\alpha\, \underline{q}_\ell^T) \qquad (2\text{-}6)$$

The individual terms in the equations become

Time rate of change	+ Convection	= Energy transport due to phase change	+ Interfacial heat transfer	+ Wall heat flux	- Turbulent heat flux

The use of a single energy equation for the combined continuous liquid and liquid droplet fields implies that both fields are at the same temperature. In regions where both liquid droplets and liquid films are present, this assumption can be justified in view of the large rate of mass transfer between the two fields, tending to draw both to the same temperature. The assumption leads to a simplification of the numerical solution, resulting in reduced computing cost.

2-5. Momentum Equations

Three momentum equations are solved in COBRA-TF, allowing the liquid and entrained liquid fields to flow with different velocities relative to the vapor phase. They are as follows:

$$\frac{\partial}{\partial t}\ (\alpha_v \rho_{vg} \vec{U}_v) + \nabla \cdot (\alpha_v \rho_{vg} \vec{U}_v \vec{U}_v) = -\alpha_v \nabla P + \alpha_v \rho_{vg} \vec{g} - \vec{\tau}_{wv}''' - \vec{\tau}_{I_{\ell v}}''' - \vec{\tau}_{I_{ev}}''' + (\Gamma''' \vec{U}) + \nabla \cdot (\alpha_v \underline{\underline{I}}_{vg}^T) \qquad (2\text{-}7)$$

$$\frac{\partial}{\partial t}\ (\alpha_\ell \rho_\ell \vec{U}_\ell) + \nabla \cdot (\alpha_\ell \rho_\ell \vec{U}_\ell \vec{U}_\ell) = -\alpha_\ell \nabla P + \alpha_\ell \rho_\ell \vec{g} - \vec{\tau}_{w\ell}''' + \vec{\tau}_{I_{\ell v}}''' - (\Gamma_\ell''' \vec{U}) - (S''' \vec{U}) + \nabla \cdot (\alpha_\ell \underline{\underline{I}}_\ell^T) \qquad (2\text{-}8)$$

$$\frac{\partial}{\partial t}(\alpha_e \rho_{\ell} \vec{U}_{e\ell}) + \nabla \cdot (\alpha_e \rho_{\ell} \vec{U}_{e\ell} \vec{U}_{e\ell}) = -\alpha_e \nabla P + \alpha_e \rho_{\ell} \vec{g} - \tau''' + \Gamma_{ev}''' (\vec{U}_{ie} - \vec{U}_{e\ell}) + (S''' \vec{U}_{ie}) \quad (2\text{-}9)$$

The individual terms in the equations become

Rate of change of momentum	+	Rate of momentum change by convection	=	Pressure gradient	+	Gravity force	+	Wall shear

+ Interfacial drag between vapor and continuous liquid	+	Interfacial drag between vapor and drops	+	Interfacial momentum exchange	+	Momentum exchange due to entrainment	+	Momentum exchange due to turbulence

COBRA-TF was developed for use with either rectangular Cartesian or subchannel coordinates. This allows a fully three-dimensional treatment in geometries amenable to description in a Cartesian coordinate system. For more complex or irregular geometries, the user may select the subchannel formulation (which neglects some of the momentum flux terms in the above equations) or a mixture of the two. The subchannel approach has been used by Wheeler et al. for bundle thermal-hydraulic analysis by the COBRA series of codes.[1] A comparison of the subchannel and Cartesian momentum equations is given in section 2.3 of the Thurgood report.[2]

2-6. PHYSICAL MODELS

The conservation equations presented in paragraphs 2-2 through 2-5 are solved numerically on a finite-difference mesh consisting of numerous computational cells. Closure of the equation set requires physical models for the mass exchange and momentum exchange among the three fields at the phase interfaces,

---

1. Wheeler, C. L., et al., "COBRA-IV-I: An Interim Version of COBRA for Thermal-Hydraulic Analysis of Rod Bundle Nuclear Fuel Elements and Cores," BNWL-1962, March 1973.

2. Thurgood, M. J., et al., "COBRA-TRAC: A Thermal-Hydraulic Code for Transient Analysis of Nuclear Reactor Vessels and Primary Coolant Systems," NUREG-CR-3046 (PNL 4385), Volumes 1-5, March 1982.

the drag forces at solid boundaries, knowledge of the turbulence terms in the continuous fields, and the entrainment rate. In addition, property relations for water are needed.

The following paragraphs contain descriptions of the physical models used in COBRA-TF for bottom reflood. To facilitate the explanation of the physical models, a brief description of the computational cell structure and variable placement is given in paragraph 2-7. To implement many of these models the code must define the flow regime; paragraph 2-8 describes the flow regime map. The interfacial mass transfer model is explained in paragraph 2-9, and in paragraph 2-10 the interfacial drag force is discussed. Paragraph 2-11 contains the wall drag force model. Paragraph 2-12 describes the entrainment models. The "small drop field," a second drop field added for shattered drops, is described in paragraph 2-13. Paragraph 2-14 details the void-drift turbulence model.

2-7. Computational Cell Structure

A typical finite-difference mesh cell is shown in figure 2-1. The fluid volume is partitioned into a number of computational cells. The equations are solved using a staggered difference scheme in which the velocities are obtained at the mesh cell faces and the state variables such as pressure, density, enthalpy, and void fraction are obtained at the cell center. The mesh cell is characterized by its cross-sectional area, A, its height, ΔX, and the width, S, of its connection with adjacent mesh cells. The cell depicted in figure 2-1 is a mass/energy cell, so named because it is the cell used for solving the scalar continuity and energy equations. The momentum equations are solved on staggered cells that are centered on the scalar mesh cell face. The vertical and transverse momentum cells are shown in figure 2-2.

2-8. Flow Regimes

The flow regime map can be divided into two main parts: (1) the logic used to select physical models in the absence of unwetted hot surfaces (such as fuel rods) and (2) the logic used when hot surfaces are present. The flow regimes described by the first set of logic are referred to as "normal" flow regimes;

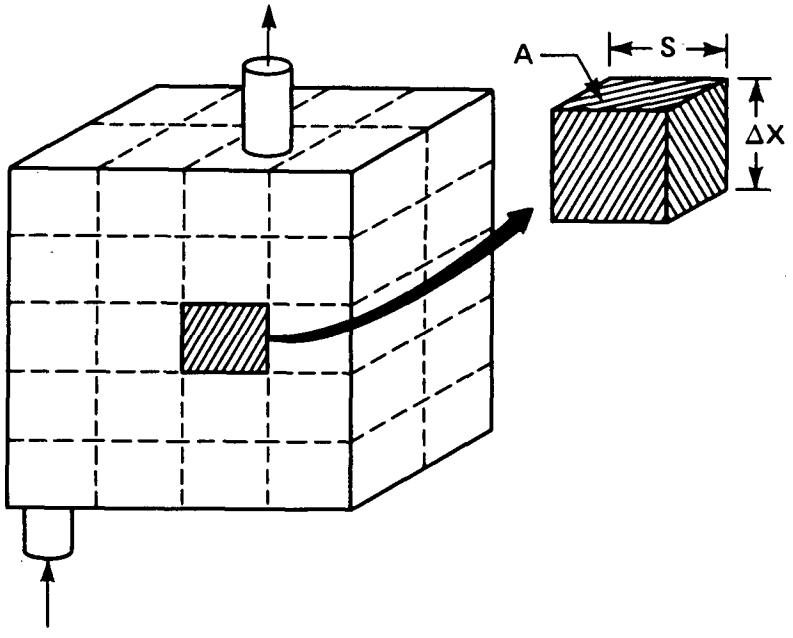

Figure 2-1. Mass/Energy Cell

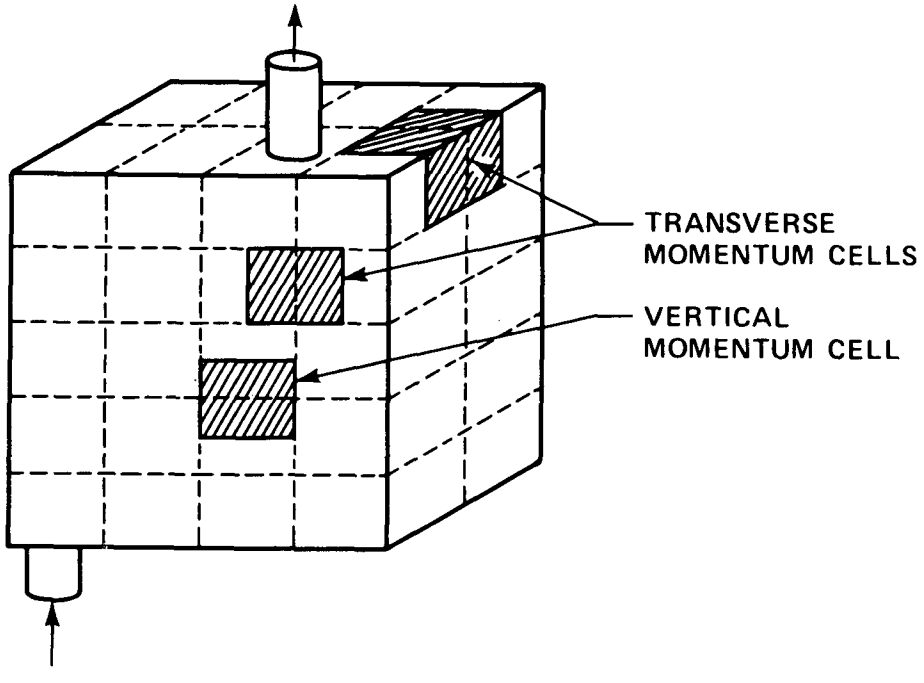

Figure 2-2. Vertical and Transverse Momentum Cells

those described by the second set are called "hot wall" flow regimes. Since COBRA-TF was developed for vertical two-phase flow, horizontal flow regimes are not considered.

The physical models used in the numerical solution must be defined for each mesh cell. Therefore, the flow regime must be determined from fluid properties and flow conditions within each cell or in the immediate surrounding cells. Only the hot wall flow regimes, used in bottom reflood, are discussed below.

Effective cooling of the core is calculated to be lost during the blowdown stage of a loss-of-coolant accident in light water reactors, and the core is subjected to a nearly adiabatic heatup. The steam environment surrounding the rods does not provide sufficient heat transfer from the cladding to remove the heat added from the fuel pellet stored energy and from fission-product decay. This temperature excursion is halted by the injection of emergency core cooling water into the reactor vessel.

As the cooling water enters the core, it contacts the hot rods and begins to reestablish effective cooling of the core. It is during this period that the temperature excursion of the cladding is turned around. Complex hydrodynamic and heat transfer processes take place during this phase of the transient as a result of water contact with the high-temperature cladding. When the cladding temperature is above the surface rewetting temperature, a film boiling heat transfer mechanism will be established. This may correspond to either a dispersed or an inverted annular, two-phase flow regime, depending on the liquid content of the flow and the vapor velocity. As the cladding temperature is reduced because of the cooling provided by film boiling, the cladding will enter a transition boiling and eventually a nucleate boiling regime. The temperature will fall below the surface rewet temperature, and the rods will quench. Heat transfer from the rod will then take place in the form of nucleate boiling or single-phase liquid heat transfer.

High flow rates of superheated vapor result from the steam generated as the rods quench. Vapor velocities are usually high enough to entrain significant

fractions of the ECC liquid in the form of drops. This droplet entrainment is beneficial, since it enhances heat transfer downstream of the quench front by desuperheating the steam and contributing to the total steam flow rate as the drops evaporate.

The hot wall flow regimes are used when a mesh cell contains a solid surface with a temperature greater than T_{sat} + 42°C (75°F). These flow regimes attempt to describe the hydrodynamics of the highly nonhomogeneous, thermal nonequilibrium, two-phase flow encountered during reflood. The hot wall flow regimes include subcooled inverted annular flow, saturated liquid chunk flow, dispersed drop-vapor flow, falling film flow, and top liquid deluge.

The normal direction for reflood is from the bottom of the core, but a top quench front is assumed to exist if the mesh cell above a cell with a hot wall contains no surfaces with a temperature greater than T_{sat} + 42°C (75°F). If the void fraction is greater than 0.8, a falling film flow regime is assumed to exist in the cell containing the top quench front; otherwise a top deluge is assumed. In the deluge regime, the flow is assumed to consist of large liquid chunks having diameters nearly equal to the flow channel hydraulic diameter. Droplet deposition and entrainment is allowed in the falling film regime.

An inverted annular flow regime is assumed during bottom reflood if the continuous liquid phase is subcooled. This regime consists of a liquid core surrounded by a vapor film. If the liquid is saturated, then a liquid chunk flow regime is assumed in which the flow is treated as large liquid drops surrounded by vapor. Entrainment of liquid into the entrained droplet field is allowed in both these flow regimes, permitting a transition to dispersed flow based on the physical models for the entrainment rate and droplet/vapor interfacial drag. The deposition and breakup of droplets on grid spacers is also considered (see section 4). The hot wall flow regimes are illustrated in figure 2-3, and figure 2-4 shows the selection logic.

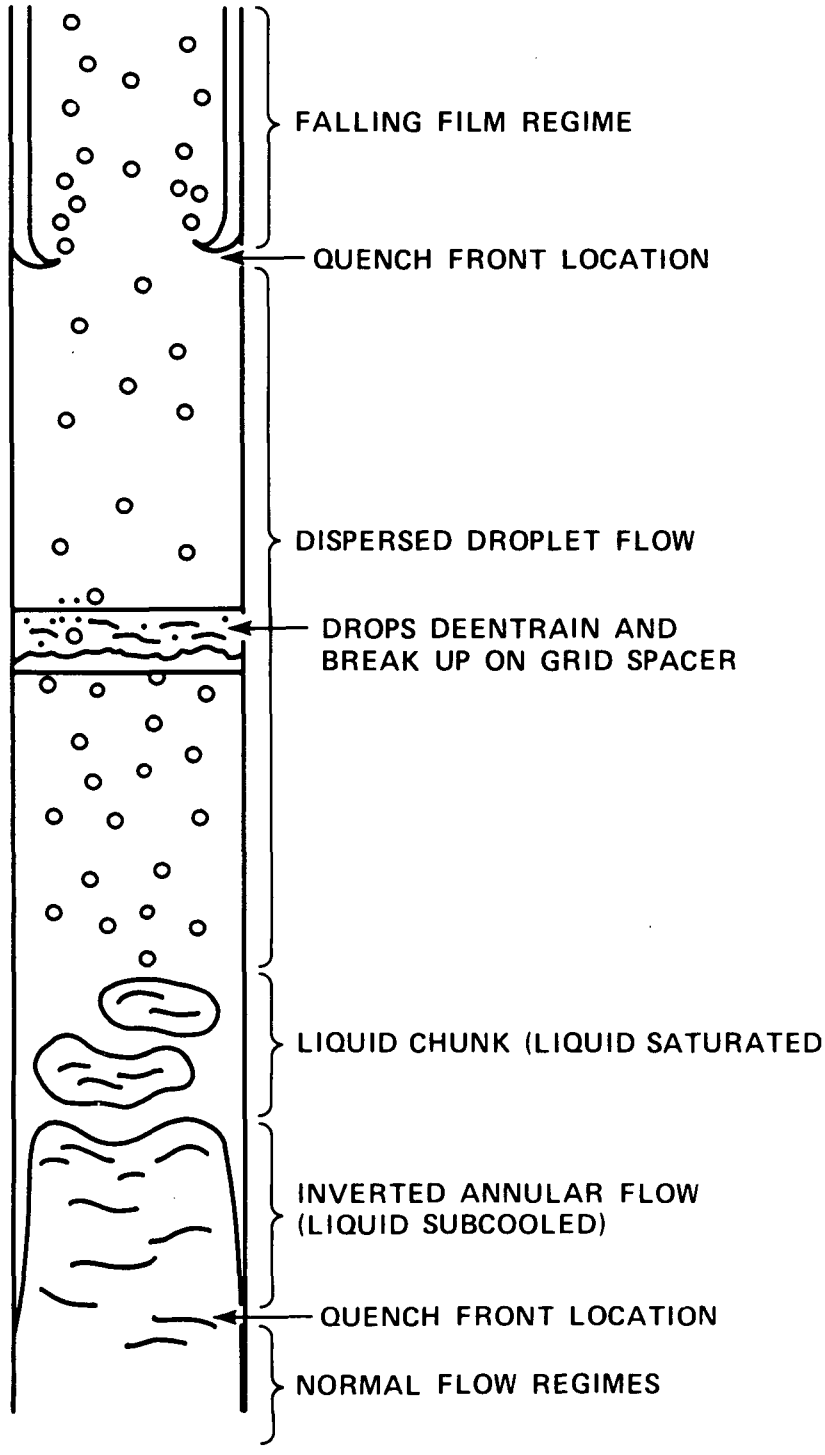

Figure 2-3. Hot Wall Flow Regimes

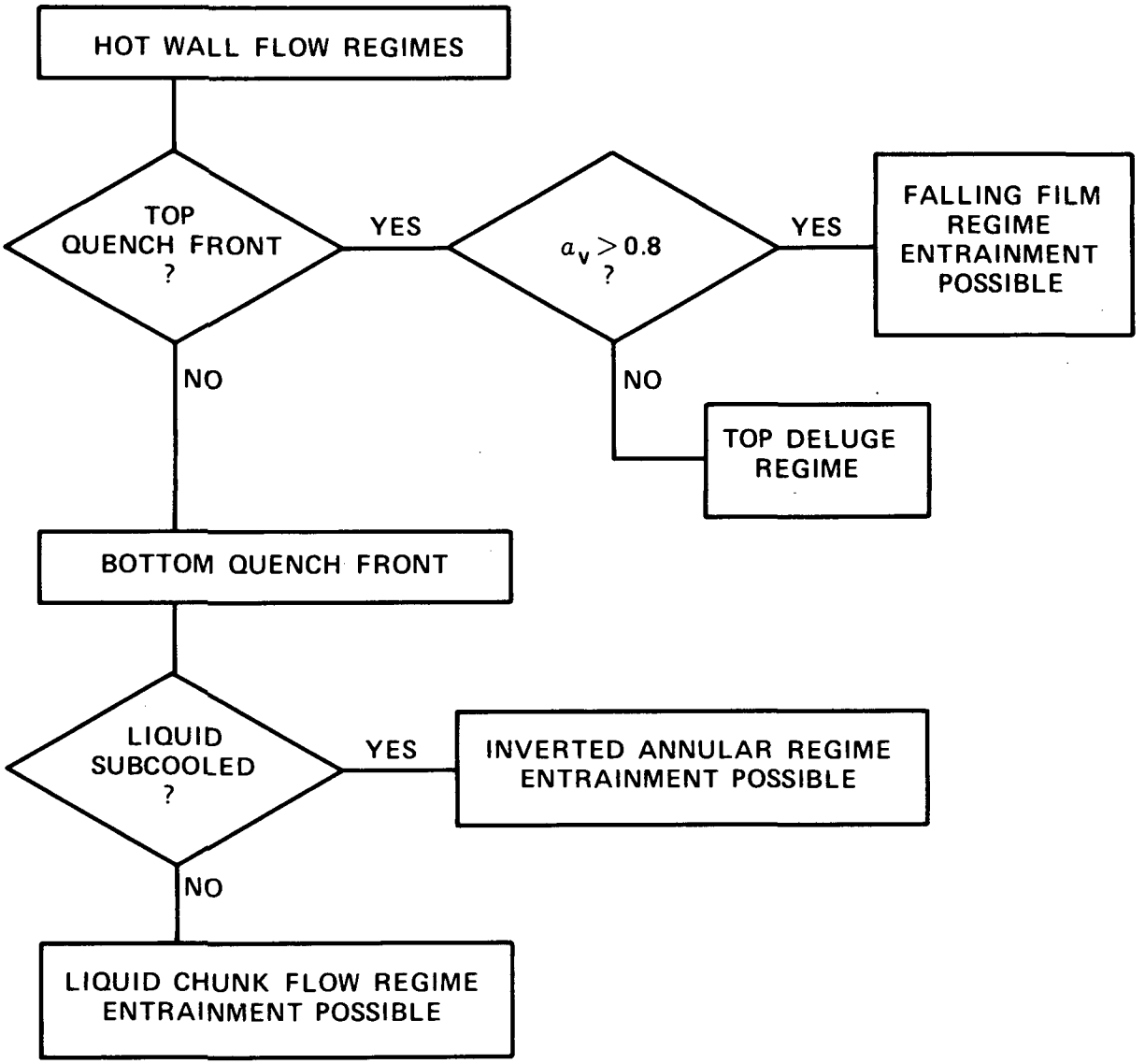

Figure 2-4. Hot Wall Flow Regime Selection Logic

2-9. Interfacial Mass Transfer

The model for interfacial mass transfer is obtained from the energy jump condition by neglecting the mechanical terms and averaging. This yields

$$\Gamma''' = \frac{-q_{I_\ell}''' - q_{I_v}'''}{h_{fg}} \tag{2-10}$$

The interfacial heat transfer, q_I''', for phase k is given by

$$q_{I_k}''' = H A_I''' (T_s - T_k) \tag{2-11}$$

where A_I''' is the average interfacial area per unit volume and H is a surface heat transfer coefficient. It is convenient to divide the vapor generation into four components, two for each phase, depending on whether the phase is superheated or subcooled. The total vapor generation rate is given by the sum of these components. For example, Γ_{SHL}''' the vapor generation per unit volume resulting from superheated liquid, is given by

$$\Gamma_{SHL}''' = \frac{H_{SHL} A_I''' (h_\ell - h_f)}{C_{p\ell} h_{fg}} \tag{2-12}$$

Analogous relations hold for subcooled liquid (SCL) superheated vapor (SHV) and subcooled vapor (SCV). The fraction (η) of total vapor generation coming from the entrained liquid is given by

$$\eta = \min \left[\frac{\alpha_e}{1-\alpha_v}, \left(1.0 - \frac{Q_{w\ell}'''}{\Gamma''' h_{fg}}\right) \right] \tag{2-13}$$

for vaporization and

$$\eta = \left(\frac{\alpha_e}{1-\alpha_v}\right) \tag{2-14}$$

for condensation.

The interfacial area per unit volume, A_I''' is based on flow regime, as are the heat transfer coefficients, H. Correlations for the various heat transfer coefficients are given in table 2-1, and models for interfacial area for each flow regime are given in table 2-2. The various Reynolds numbers used in table 2-1 are defined as follows:

$$Re_v = \frac{D_H \rho_v |\underline{U}_{v\ell}|}{\mu_v} \tag{2-15}$$

$$Re_d = \frac{2r_d \rho_v |\underline{U}_{ve}|}{\mu_v} \tag{2-16}$$

$$Re_f = \frac{D_H \rho_\ell |\underline{U}_\ell|}{\mu_\ell} \tag{2-17}$$

The film friction factor, f_I, is given by Wallis[1]:

$$f_I = 0.005\ (1 + 75\ \alpha_\ell) \tag{2-18}$$

The total interfacial area of drops within a mesh cell is determined by solving an interfacial area concentration transport equation as follows:

$$\frac{\partial A_{I_d}'''}{\partial t} + \nabla \cdot (A_{I_d}'''\ \underline{U}_e) = \frac{3\ S'''}{\rho_\ell r_s} + S_\Gamma \tag{2-19}$$

---

1. Wallis, G. B., One-Dimensional Two-Phase Flow, McGraw-Hill, New York, 1969.

TABLE 2-1

INTERFACIAL HEAT TRANSFER COEFFICIENTS

Mode of Heat Transfer	Correlation (Btu/hr-ft^2-°F)	Flow Regime
H_{SHV}	$\frac{f_I}{2} \rho_v C_{p_v} \lvert U_{v\ell} \rvert Pr_v^{-2/3}$	Film
	$\frac{(2.0 + 0.55\ Re_d^{0.5}\ Pr_v^{1/3})\ \frac{k_v}{2r_d}}{1 + 0.5\ (h_v - h_g)/h_{fg}}$	Drop(a)
	$\frac{(2.0 + 0.55\ Re_v^{0.5}\ Pr_v^{1/3})\ \frac{k_v}{D_H}}{1 + 0.5\ (h_v - h_g)/h_{fg}}$	Liquid chunk, inverted annular
H_{SCV}	1.0×10^4 (b)	All regimes
H_{SHL}	1.0×10^5 (b)	Large bubble, liquid chunk and inverted annular
H_{SHL}	The maximum of $1.925\ \rho_\ell\ C_{p_\ell} \lvert U_\ell \rvert / [Re_f^{2/3}\ Pr_\ell^{2/3}]$ for $Re_f \leq 1000$	Film(c)

a. Rowe, P. N., et al., "Heat Transfer From a Single Sphere in an Extensive Flowing Fluid," Trans. Inst. Chem. Engin. 43, 1965, T14-T31.

b. A constant large value is used to drive toward phase equilibrium.

c. From Colburn analogy using friction factors of Hughmark(e)

TABLE 2-1 (cont)

INTERFACIAL HEAT TRANSFER COEFFICIENTS

Mode of Heat Transfer	Correlation (Btu/hr-ft^2-°F)	Flow Regime
H_{SCL}	$0.2701 \rho_\ell C_{p_\ell} \mid U_\ell \mid / [Re_f^{0.38} Pr_\ell^{2/3}]$ for $1000 \leq Re_f$ and $2.0\ k_\ell/\delta$ $C \frac{\pi^2}{3} \frac{k_\ell}{r_d}$ $(C = 2.7)$	Drop[d]
	$1.925\ \rho_\ell\ C_{p_\ell} \mid U_\ell \mid / [Re_f^{2/3}\ Pr_\ell^{2/3}]$ for $Re_f < 1000$ $0.2701\ \rho_\ell\ C_{p_\ell} \mid U_\ell \mid / [Re_f^{0.38}\ Pr_\ell^{2/3}]$ for $1000 \leq Re_f$	Film[c]
	$C \frac{\pi^2}{3} \frac{k_P}{r_d}$ $(C = 2.7)$	Drop, liquid chunk, inverted annular[d]

d. Andersen, J. G. M., REMI/HEAT COOL, A Model for Evaluation of Core Heatup and Emergency Core Spray Cooling System Performance for Light-Water Cooled Nuclear Power Reactors, "Heat Transfer in a Spherical Droplet," Report 296, Riso National Laboratory, Denmark, September 1973.

e. Hughmark, G. A., "Film Thickness, Entrainment, and Pressure Drop in Upward Annular and Dispersed Flow," J. Amer. Inst. Chem. Engin. 14, 1973, 1062.

TABLE 2-2
INTERFACIAL HEAT TRANSFER AREA PER UNIT VOLUME

Flow Regime	Interfacial Area, A_I'''
Film	$\alpha_v P_w/A$
Liquid chunk	$N_d \pi D_H^2$ (a)
Inverted annular	$\alpha_\ell P_w/A$
Drop	Drop interfacial area transport equation

a. $$N_d = \frac{\alpha_\ell}{\frac{\pi D_H^3}{6}}$$

The individual terms in the equation become

Rate of change of interfacial area concentration	+	Rate of efflux of interfacial area concentration	=	Rate of interfacial area generation due to entrainment and deposition of drops	+	Rate of interfacial area concentration change due to phase change

Once a drop is formed, no aerodynamic breakup is assumed to occur, and the drops change size only as a result of condensation, vaporization, or new drop formation or breakup at a grid spacer or flow blockage. The drop size is easily computed from the interfacial area as

$$r_d = 3\,\alpha_e / A'''_{I_d} \qquad (2\text{-}20)$$

The expression for r_s, the drop formation size, is dependent on the conditions under which the drop is formed, and is discussed with the entrainment model in paragraph 2-12.

The effect of grid spacers on the superheated vapor interfacial heat transfer during reflood is added to the interfacial heat transfer between drops and vapor. Experimental data discussed in section 3 have indicated that grid spacers have a significant effect on desuperheating the vapor flowing through the grid spacer. This effect is important, because the reduced vapor temperature enhances the rod heat transfer in the upper portions of the bundle, resulting in lower peak cladding temperatures. This effect has been accounted for in two ways.

First, as droplets pass through the grid spacer, a certain fraction of them will hit the grid structure. Since the grid has no internal heat generation, the droplets may rewet the grid early in the reflood transient, forming a liquid film on the grid. This wet grid acts as a large area for interfacial heat transfer between the liquid film and the superheated vapor.

The second major effect of grid spacers is that, as the droplets hit the grid, the impact creates a splatter of smaller droplets which rapidly evaporate.

This has been accounted for by generating a second drop field with a Sauter mean diameter representative of the shattered drops downstream of each grid.

Both the grid rewet and droplet breakup models are detailed in section 3, and the second "small" drop field is described in paragraph 2-12.

2-10. Interfacial Drag Force

The average interfacial drag force per unit volume between the vapor and continuous liquid is defined as a function of relative velocity,

$$\underline{\tau}'''_{I_{v\ell}} = K_{I_{v\ell}} \underline{U}_{v\ell} \tag{2-21}$$

The drag force between the vapor and entrained liquid is also a function of the relative velocities of the two fields,

$$\underline{\tau}'''_{I_{ve}} = K_{I_{ve}} \underline{U}_{ve} \tag{2-22}$$

The interfacial friction coefficients, K_I, are dependent on flow regime and are defined as

- o Drop

$$K_{I_{ve}} = 0.375 \frac{C_{D_d}}{r_d} \alpha_e \rho_v |\underline{U}_{ve}| \tag{2-23}$$

- o Film

$$K_{I_{v\ell}} = 2.0 \frac{f_I}{D_H} a_v \rho_v |U_{v\ell}| \tag{2-24}$$

- o Inverted annular

$$K_{I_{v\ell}} = 16 \frac{f_I}{D_H} \alpha_\ell \rho_v |\underline{U}_{v\ell}| \tag{2-25}$$

The viscous regime is assumed for drops, and the drag coefficient has the form

$$C_{D_d} = \frac{24}{Re_D}\left(1 + 0.1\ Re_D^{0.75}\right) \qquad (2\text{-}26)$$

The drop drag coefficient is limited to a minimum value of 0.45.

The friction factor, f_I, for film flow is dependent on whether the film is stable or unstable. It has been observed experimentally that the onset of film instability causes a sudden increase in system pressure drop. This is a result of increased roughness of the liquid film caused by large, unstable waves. Although the film friction factor for unstable film flow in large tubes has been studied, the correlation does not extrapolate to hydraulic diameters typical of LWR fuel bundles. Henstock and Hanratty[1] have correlated a large amount of cocurrent and countercurrent film flow data; however, their correlation does not predict the sudden increase in pressure drop at the onset of instability.

Until further information becomes available, it has been assumed that the film friction factor for stable films is given by the correlation recommended by Wallis, equation (2-18). This expression is also used for unstable films when solving the transverse momentum equations. When solving the vertical momentum equations, the friction factor for unstable films is taken to be the larger of either Henstock and Hanratty's correlation or five times the value of f_I given by the Wallis correlation.

Henstock and Hanratty's correlation is of the form

$$f_I = f_s\left(1 + 1400F\left\{1 - \exp - \left[\frac{1}{G} - \frac{(1 + 1400F)^{3/2}}{13.2F}\right]\right\}\right) \qquad (2\text{-}27)$$

---

1. Henstock, W. H., and Hanratty, T. J., "The Interfacial Drag and the Height of the Wall Layer in Annular Flows," J. Amer. Inst. Chem. Engin. 22 (6), 1976, 990-1000.

where

$$G = \frac{\rho_\ell \, g \, D_H}{\rho_v \, u_v^2 \, f_s} \tag{2-28}$$

$$F = \frac{m^+}{Re_v^{0.9}} \frac{\mu_\ell}{\mu_v} \quad \frac{\rho_v}{\rho_\ell} \tag{2-29}$$

$$m^+ = [(0.707 \, Re_\ell^{0.5})^{2.5} + (0.0379 \, Re_\ell^{0.9})^{2.5}]^{0.40} \tag{2-30}$$

$$f_s = 0.046 \, Re_v^{-0.20} \tag{2-31}$$

The multiplication factor of five was obtained from the observed difference between the pressure drop characteristics for stable films and that for unstable films.[1] This can be replaced by a more appropriate correlation, should one become available.

A thin laminar vapor film is assumed to surround the fuel rods in the inverted annular flow regime. The laminar friction factor is

$$f_L = \frac{64}{Re_v} \tag{2-32}$$

where

$$Re_v = \frac{\rho_v \mid \underline{U}_{vp} \mid \delta}{\mu_v} \tag{2-33}$$

---

1. Dukler, A. E., and Smith, L., "Two-Phase Interactions in Countercurrent Flow Studies of the Flooding Mechanism," NUREG/CR-0617, January 1979.

The vapor film thickness, δ, is calculated from:

$$\delta = (0.313)\ \alpha_v D_R$$

D_R = rod diameter

In addition, an empirical ramp is applied to force the interfacial friction to zero as either phase is depleted and to maintain a liquid interface, as

$$f_I = f_L \times \text{RAMP} \tag{2-34}$$

and

$$\text{RAMP} = \alpha_v^2 \cdot \text{minimum}\ [1,\ (\alpha_L/0.6)^2] \tag{2-35}$$

The above formulation is applied to both the inverted annular and the liquid chunk flow regimes. After a node has quenched, a small amount of vapor may be generated because of the decay heat release. The vapor generation rate is so low that the vapor probably remains near the rod suface and experiences much less interfacial shear than if it were evenly dispersed throughout the subchannel. Therefore, the above thin laminar film friction factor is applied to this regime also and helps to minimize the transition from the hot wall flow regime.

An additional interfacial drag force is calculated for interfaces that occur at mesh cell boundaries. These interfaces are detected by changes in void fraction between adjacent cells, and can occur on either horizontal or vertical cell boundaries. For two cells, i and j, connected to each other by a vertical or transverse connection, an intercell interface is assumed when $\alpha_i < 0.8$ and $\alpha_j > 0.6$, so that cell i is on the vapor side of the interface and cell j is on the liquid side. The drag force is a function of the difference between the vapor velocity in cell i and the liquid velocity in cell j, and is given by

$$F_{I_x} = f_I \frac{1}{2} \rho_v |u_{v_i} - u_{\ell_j}| (u_{v_i} - u_{\ell_j}) A_{I_x} \tag{2-36}$$

for the vertical direction and

$$F_{I_y} = f_I \frac{1}{2} \rho_v |v_{v_i} - v_{\ell_j}| (v_{v_i} - v_{\ell_j}) A_{I_y} \tag{2-37}$$

for the transverse direction. In these equations, A_{I_x} and A_{I_y} are the appropriate intercell areas. A friction factor of 0.08 is assumed and has given good results. The intercell interfacial force is added to the liquid momentum equation in cell j (on the liquid side of the interface) and subtracted from the vapor momentum equation in cell i (on the vapor side).

2-11. Wall Drag Force

The wall drag forces per unit volume on each phase, $\underline{\tau}'''_{w\ell}$, and $\underline{\tau}'''_{wv}$, are defined as functions of the phase velocities

$$\underline{\tau}'''_{w\ell} = - K_\ell \underline{U}_\ell \tag{2-38}$$

$$\underline{\tau}'''_{wv} = - K_v \underline{U}_v \tag{2-39}$$

The drag coefficients, K_ℓ, and K_v, contain both the local form loss and the friction factor, and are defined

$$K_\ell = \left(\frac{f_\ell}{2D_H} + \alpha_\ell \frac{K}{\Delta x} \quad \rho_\ell | \underline{U}_\ell | \right) \tag{2-40}$$

$$K_v = \left(\frac{f_v}{2D_H} + \alpha_v \frac{K}{\Delta x} \quad \rho_v | \underline{U}_v | \right) \tag{2-41}$$

The friction factors for single-phase liquid flow, f_ℓ and single-phase vapor flow, f_v, are computed from laminar or modified Blasius correlations based on the single-phase liquid or vapor Reynolds number:

$$f_k = \begin{cases} 64.0/Re_k & \text{laminar flow} \\ 0.0055 + 0.55\ Re_k^{-1/3} & \text{turbulent flow} \end{cases} \qquad (2\text{-}42)$$

The vapor friction factor, f_v, is set to zero for the bubbly, film, and single-phase liquid flow regimes. The liquid friction factor, f_ℓ, is set to zero for the single-phase vapor, inverted annular, and droplet (no film) flow regimes.

2-12. Entrainment Rate

Entrainment of liquid drops from the continuous liquid phase can occur under a variety of conditions. The physical models used to determine the average net mass rate of entrainment and the drop formation size will be different for each condition. Entrainment mechanisms that may have a significant influence on reactor thermal hydraulics have been addressed in the development of entrainment models. These include entrainment from liquid films, reflood entrainment, entrainment resulting from vapor bubbling through liquid pools, and entrainment resulting from vapor flow across rod structures such as the upper plenum internals of a PWR.

The net mass entrainment rate is defined as

$$S = S''' \cdot (\text{volume of cell}) \qquad (2\text{-}43)$$

The net mass entrainment rate, S, has units of mass per unit time and is the net result of the opposing mechanisms of entrainment, S_E, and deentrainment, S_{DE}. Models for entrainment rate, deentrainment rate, and drop formation size are discussed below for the regimes important in reflood.

2-13. Deentrainment in Film Flow -- During bottom reflood, the top end of the fuel rods is usually wettable because of the axial power shape. Drops entrained at the froth front are deposited on this "cold" surface and form a falling film top quench front.

The deposition of drops on this liquid film occurs as a result of random turbulent motions that impart transverse velocity to the drops, bringing them into contact with the solid surfaces or liquid films within the flow channel. The rate at which this occurs has been correlated by Cousins et al.[1] using a drop concentration gradient diffusion model in which the concentration at the wall is assumed to be zero. Cousins' model is used to determine the deentrainment rate for film flow as

$$S_{DE} = k_\sigma \Delta C \, P_w \, \Delta x \tag{2-44}$$

where ΔC is the concentration gradient as given by

$$\Delta C = \frac{\alpha_e \rho_\ell}{\alpha_e + \alpha_v} \tag{2-45}$$

and k_σ is the mass transfer coefficient. The mass transfer coefficient has been found to be a function of surface tension.[2] This function is reasonably represented by

$$k_s = \max \left(3.0491 \times 10^{12} \, \sigma^{5.3054}, \, 12.491 \, \sigma^{0.8968}\right) \tag{2-46}$$

---

1. Cousins, L. B., et al., "Liquid Mass Transfer in Annular Two-Phase Flow," Paper C4 presented at the Symposium on Two-Phase Flow, Exeter, England, June 1965.

2. Whalley, P. B., "The Calculation of Dryout in a Rod Bundle," Int. J. Multiphase Flow 13, 1977, 501-515.

2-14. Entrainment During Bottom Reflood -- Several mechanisms for the formation of droplets during reflood can be postulated. The droplets may be formed by the breakup of the inverted annular liquid core because of surface instabilities if the liquid is subcooled. If the liquid is saturated, droplets may be formed by bubbles breaking through the surface of the liquid. During top reflood, droplets are formed at the sputtering front as the liquid film is disrupted by the large vaporization rates. A model similar to one proposed for droplet entrainment by vapor bubbling through liquid pools[1] is used for bottom reflood. The entrainment rate is given by

$$S_E = (\alpha_v u_v / u_{crit})^2 \cdot \dot{m}_v \qquad (2\text{-}47)$$

where $\dot{m}_v$ is the vertical vapor mass flow rate and u_{crit} is the vertical vapor velocity required to lift a droplet with radius defined by the critical Weber criterion against gravity. The critical velocity is obtained from a balance between the drag force and gravity force acting on the drop,

$$u_{crit} = \left(\frac{4\ We_d}{3C_D}\right)^{1/4} \left(\frac{\sigma g \Delta\rho}{\rho_g^2}\right)^{1/4} \qquad (2\text{-}48)$$

A Weber number of 2.0 (typical of reflood in the FLECHT tests) and a drag coefficient of 0.45 are used. The use of the vapor flow rate, $\dot{m}_v$, in equation (2-47) reflects the effect of boiling at the quench front on droplet formation. The droplet formation size for bottom reflood is taken as:

$$D_s = \text{minimum}\ (D_H, D_1, D_2) \qquad (2\text{-}49)$$

$$D_1 = 1.13/((\rho_f - \rho_g)/\rho_g)^{0.865} \qquad (2\text{-}50)$$

$$D_2 = 0.3\sigma/\rho_f - \rho_g) \qquad (2\text{-}51)$$

---

1. NRC Steam Generator Workshop, Silver Spring, MD, April 1979.

The drop diameter, D_1, is calculated from the formula:

$$D_1 = \frac{C}{(U_{BR})^b} \tag{2-52}$$

where

U_{BR} = bubble rise velocity
C,b = constants adjusted to fit FLECHT movie data

Similarly, the equation for D_2 was derived by applying a force balance between gravity and interfacial shear. The relative velocity was assumed to be equal to that associated with the critical Weber number for that drop size. Then,

$$D_2 = \frac{3\ We\ \sigma\ C_D}{4(\rho_f - \rho_g)} \tag{2-53}$$

The value of the product, $We*C_D$, was adjusted to match FLECHT data at 0.28 MPa (40 psi).

2-15. Entrainment at a Top Quench Front -- It is assumed that the entrainment rate from a falling film top quench front is equal to the liquid film flow rate, $\dot{m}_\ell$, minus the vapor generation rate at the quench front, Γ'''_q, times the volume of the cell:

$$S_E = \dot{m}_\ell - \Gamma'''_q \text{ (volume of cell)} \tag{2-54}$$

The droplet formation size for top reflood is assumed to be given by a critical Weber number criterion,

$$r_s = 0.5 \cdot \frac{We_d \, \sigma}{\rho_v \, (\underline{u}_{v\ell})^2} \qquad (2\text{-}55)$$

The maximum droplet size for top reflood is limited to r_s = 0.91 mm (0.036 in.). The low value for the Weber number is a result of using the superficial velocity to compute the droplet size. The vapor velocity where the drops are formed is much higher than the superficial velocity as a result of the violent boiling near the quench front.

2-16. Deentrainment on Upper Plenum Structure -- Liquid carried over during bottom reflood may be deentrained in the upper plenum as it flows around the upper plenum structures such as support columns and guide tubes. This liquid may then flow down the structures and form a pool above the upper core plate.

The model used in the code is a simple one, employing deentrainment fractions obtained in the upper plenum deentrainment experiments of Dallman and Kirchner[1]:

$$S_{DE} = \eta_{NR} \, \alpha_e \rho_\ell |V_e| \text{ (transverse flow area)} \qquad (2\text{-}56)$$

The deentrainment fraction, η_{NR}, is input. Following the recommendations of Dallman and Kirchner, the deentrainment fraction for an array of tubes is given by

$$\eta_{NR} = 1 - (1 - \eta_R)^N \qquad (2\text{-}57)$$

$$\eta_R = \eta_I \, (1 + 4.5 \, \beta^2) \qquad (2\text{-}58)$$

1. Dallman, J. C., and Kirchner, W. L., "Deentrainment Phenomena on Vertical Tubes in Droplet Cross Flow," NUREG/CR-1421, April 1980.

where

η_R = deentrainment fraction for a single row of tubes
N = number of rows of tubes
β = diameter-to-pitch ratio of the array
η_I = deentrainment fraction for a single tube
(0.19 for cylindrical tubes and 0.27 for square tubes)

2-17. Deentrainment at Area Changes -- Droplets will deentrain at restrictions in the flow path as a result of drop impingement on solid surfaces. This can be expected to occur as droplets formed during reflood flow through, for example, the upper tie plate. Droplets that strike the solid portions of the tie plate deentrain and provide the initial liquid for the top quench front. This type of deentrainment is accounted for using a simple flow area ratio,

$$S_{DE} = (1 - A_1/A_2)\, \alpha_e \rho_\ell |u_e| A_2 \qquad (2\text{-}59)$$

where A_1 is the flow area in the restriction and A_2 is the flow area before the restriction. Deentrainment is not calculated for cells in the hot wall flow regime.

2-18. Deentrainment on Solid Surfaces and Liquid Pools -- All entrained droplets flowing toward a horizontal solid surface, such as the top of the upper plenum, or towards a liquid pool, are assumed to be deentrained.

2-19. Small Drop Field

An explicit "small drop" field was added to COBRA-TF. This model calculates the enforced vapor generation resulting from the rapid evaporation of microdrops generated by droplet shattering at grid spacers and flow blockages. To simplify the incorporation of this model into COBRA-TF and minimize the additions in computer time, several restrictions were imposed:

- o The small drop field is not implicity coupled with the hydrodynamic solution.
- o It interfaces with the fluid solution only through source/sink terms for the small drop vapor generation rate and the removal of the large drops that were shattered.
- o The model is not operable for negative flow.
- o Lateral transport of small drops between subchannels is assumed to be insignificant.

2-20. Droplet Breakup -- At grid spacers and flow blockages, some fraction of the entrained drop flow may be shattered into microdrops. These drop breakup models are described fully in sections 3 and 4. Both the mass source of small drops and the initial small drop diameter are specified by the grid and blockage models. From the mass source and the initial diameter, a number flux can be calculated:

$$N_{SD} = \frac{S_{SD}}{\frac{\pi}{6} \rho_\ell D_{SD}^3} \qquad (2\text{-}60)$$

where

S_{SD} = mass source of small drops
D_{SD} = diameter of small drops

The drop number flux, N_{SD} (number of drops per second), is assumed to remain constant downstream of the breakup point.

If small drops coexist with the large drop population that is broken up at a grid spacer, these small drops are further shattered. Preexisting small drops are not further shattered by flow blockages.

2-21. Drop Evaporation -- The vapor generation rate from a single drop is

$$\Gamma = h_i \cdot \pi D_{SD}^2 \left(\frac{T_v - T_f}{h_{fg}} \right) \qquad (2\text{-}61)$$

where

Γ = vapor generation rate from one drop (lbm/sec)
h_i = interfacial heat transfer coefficient (Btu/sec-ft^2-°F)
T_v = superheated vapor temperature (°F)
T_f = saturation temperature (°F)
h_{fg} = latent heat of vaporization (Btu/lbm)

The Lee-Ryley correlation[1] is used to evaluate h_i:

$$h_{L\text{-}R} = \frac{k_v}{D_{SD}} (2 + 0.55 \ Re_D \ Pr_v^{1/3}) \qquad (2\text{-}62)$$

where

k_v = thermal conductivity of vapor (Btu/sec-ft-°F)

Re_D = drop Reynolds number $\left(\frac{\rho_v \cdot (V_v - V_{SD}) \cdot D_{SD}}{\mu_v} \right)$

ρ_v = superheated vapor density (lbm/ft^3)
V_v = axial velocity of vapor (ft/sec)
V_{SD} = axial velocity of small drop (ft/sec)
μ_v = vapor viscosity (lbm/ft-sec)
Pr_v = vapor Prandtl number

---

1. Lee, R., and Ryley, D. J., "Evaporation of Water Droplets in Superheated Steam," J. Heat Transfer, November 1968.

In addition, a correction for the effect of vapor leaving the drop surface is applied:

$$h_i = \frac{h_{L-R}}{1 + 0.5 \cdot Cp_v \frac{T_v - T_s}{h_{fg}}} \tag{2-63}$$

where Cp_v = vapor specific heat (Btu/lbm-°F).

Then,

$$\Gamma = \frac{k_v(2 + 0.55\ Re_D\ Pr^{1/3}) \cdot \pi D_{SD}^2 \cdot (T_v - T_f)}{D_{SD}\left[H_{fg} + \frac{1}{2}(H_v - H_g)\right]} \tag{2-64}$$

where

H_v = vapor enthalpy (Btu/lbm)
H_g = saturated vapor enthalpy

This can be rewritten:

$$\Gamma = C_\Gamma \cdot D_{SD} \tag{2-65}$$

where

$$C_\Gamma = \frac{k_v(2 + 0.55\ Re_D\ Pr^{1/3}) \cdot \pi(T_v - T_f)}{H_{fg} + \frac{1}{2}(H_v - H_g)} \tag{2-66}$$

and C_Γ is a function of vapor temperature and drop relative velocity. The mass conservation equation for a drop is then

$$\frac{d\ D_{SD}}{dZ} = \frac{2\ C_\Gamma}{\pi\ \rho_\ell\ D_{SD}\ V_{SD}} \tag{2-67}$$

Then, for any one node, where C_Γ and V_{SD} are assumed constant, the diameter of the drops exiting the node is given by

$$D_{SD_2} = \left[D_{SD_1}^2 - \frac{4\ C_\Gamma}{\pi\ \rho_\ell\ V_{SD}}\ \Delta Z \right]^{1/2} \qquad (2\text{-}68)$$

where

D_{SD_2} = exit drop diameter
D_{SD_1} = inlet drop diameter
ΔZ = node length

The vapor generation rate in node (i) is then:

$$\Gamma_i = N_{SD} \cdot \frac{\pi}{6} \left(D_{SD_2}^3 - D_{SD_1}^3 \right) \cdot \rho_\ell \qquad (2\text{-}69)$$

2-22. Calculation Procedure -- At a grid spacer or flow blockage, a mass source, number flux, and initial diameter for small drops is calculated. The initial velocity is assumed to be one half that of the impacting drop. The diameter and relative velocity at the bottom (1) of the node are used to determine the evaporation constant, C_Γ. Then the drop diameter at the top (2) of the node is determined from

$$D_{SD_2} = \left[D_{SD_1}^2 - \frac{4\ C_\Gamma}{\pi\ \rho_\ell\ V_{SD}}\ \Delta Z \right]^{1/2} \qquad (2\text{-}70)$$

The vapor generation rate is then

$$\Gamma_i = N_{SD} \cdot \frac{\pi}{6} \left(D_{SD_2}^3 - D_{SD_1}^3 \right) \cdot \rho_\ell \qquad (2\text{-}71)$$

The drop velocity at the top of the node is calculated from a simplified momentum equation:

$$V_{SD} \frac{d V_{SD}}{dZ} = 0.75 \frac{C_D \cdot \rho_v \cdot (V_v - V_{SD})^2}{\rho_\ell \cdot D_{SD}} - g \qquad (2\text{-}72)$$

where all quantities are evaluated at the bottom of the node. Then,

$$V_{SD_2} = V_{SD_1} + \left[0.75 \frac{C_D \cdot \rho_v \cdot (V_v - V_{SD_1})^2}{\rho_\ell \cdot D_{SD_1}} - g \right] \frac{\Delta Z}{V_{SD_1}} \qquad (2\text{-}73)$$

The new drop diameter and velocity (D_{SD_2} and V_{SD_2}) are used to calculate the evaporation constant, C_I, for the next node, and so forth. This process continues until all the small drops are evaporated.

2-23. Population Merging -- If all the small drops generated at one grid (i) are not evaporated before the next grid (i + 1), they will be combined with the drops generated at the next grid. From conservation of mass,

$$\left[N_D \cdot D_{SD}^3 \right]'_{i+1} = (N_D \cdot D_{SD}^3)_i + (N_D \cdot D_{SD}^3)_{i+1} \qquad (2\text{-}74)$$

$$\left[N_D \cdot D_{SD}^2 \right]'_{i+1} = (N_D \cdot D_{SD}^2)_i + (N_D \cdot D_{SD}^2)_{i+1} \qquad (2\text{-}75)$$

Then,

$$\left[D_{SD} \right]'_{i+1} = \frac{\left[N_D \, D_{SD}^3 \right]'_{i+1}}{\left[N_D \, D_{SD}^2 \right]'_{i+1}} \qquad (2\text{-}76)$$

and

$$\left[N_D \right]'_{i+1} = \frac{\left[N_D \, D_{SD}^3 \right]'_{i+1}}{\left[D_{SD}^3 \right]'_{i+1}} \qquad (2\text{-}77)$$

Thus, a new drop group formed from two groups is used. This simplification is not considered to seriously compromise the approach because most small drops from one grid are evaporated before encountering the next grid. Drop momentum is also conserved:

$$\left[V_{SD} \right]'_{i+1} = \frac{(N_D \, D_{SD}^3 \, V_{SD})_i + (N_D \, D_{SD}^3 \, V_{SD})_{i+1}}{\left[N_D \, D_{SD}^3 \right]'_{i+1}} \qquad (2\text{-}78)$$

2-24. Void Drift -- Turbulence Model

Turbulent mixing, which causes no net mass transfer, may be important in determining the mass flux and enthalpy distributions within a rod bundle. The effects of mixing are most evident when a severe gradient exists -- for example, the temperature distribution in subchannels near a cold housing and flow recovery downstream of a severe blockage. Single-phase turbulent mixing is modeled in COBRA-TF by means of the traditional intersubchannel mixing coefficient approach.

In two-phase flow, when the liquid is the continuous phase, it has been observed[1,2] that vapor tends to "drift" towards the highest velocity regions. This void drift is believed to be the result of turbulent pressure fluctuations in the liquid driving the relatively massless vapor. A simple formulation, based on the work of Lahey[3] and Kelly[4] is employed.

1. Lahey, R. T., et al., "Mass Flux and Enthalpy Distribution in a Rod Bundle for Single- and Two-Phase Flow Conditions," ASME 70-WA/HT-8, December 1970.
2. Rowe, D. S., "Crossflow Mixing Between Parallel Flow Channels During Boiling," BNWL-371, Part 1, March 1967.
3. Lahey, R. T., and Moody, F. J., The Thermal Hydraulics of a Boiling Water Reactor, ANS Monograph, 1975.
4. Kelly, J. E., and Kazimi, M. S., "Development of the Two-Fluid Multidimensional Code THERMIT for LWR Analysis," AIChE Symposium Series 199, Volume 76, 1980.

2-25. Single-Phase Turbulent Mixing -- Single phase mixing produces no inter-subchannel mass transfer but does result in both energy and momentum transfer. Source terms accounting for these mixing effects are added to both the fluid energy and axial momentum equations. The fluctuating crossflow for gap k, between subchannels i and j, is

$$W'_k = \beta \cdot S_k \cdot \bar{G}_{ij} \qquad (2\text{-}79)$$

where

W' = fluctuating crossflow (lbm/sec ft)
S = intersubchannel gap width (ft)
β = mixing coefficient
$\bar{G}$ = channel averaged mass flux

The energy equation source term (for subchannel i) is then

$$\nabla \cdot q''_i = \sum_{k=1}^{NK} W'_k \cdot (h_j - h_i) \cdot \Delta X \qquad (2\text{-}80)$$

where

NK = number of gaps connected to subchannel i
ΔX = lateral distance between subchannels

Similar source terms appear in the axial momentum equations. If the liquid is in the continuous phase, mixing is calculated for both the liquid and dispersed vapor phases. However, if the continuous phase is vapor, turbulent effects are assumed to be negligible for the dispersed liquid.

2-26. Void Drift Model -- The lateral void drift phenomenon results in the addition of transfer terms to the mass, momentum, and energy equations. The mass conservation equations are as follows:

$$\frac{\partial}{\partial t}(\alpha_v \rho_v) + \nabla \cdot (\alpha_v \rho_v \underline{U}_v) + \nabla \cdot \underline{G}_v^T = \Gamma''' \quad (2\text{-}81)$$

$$\frac{\partial}{\partial t}(\alpha_\ell \rho_\ell) + \nabla \cdot (\alpha_\ell \rho_\ell \underline{U}_\ell) + \nabla \cdot \underline{G}_\ell^T = -\Gamma''' \quad (2\text{-}82)$$

The individual terms in the equation become

Local rate of change of mass	+	Net efflux of mass by convection	+	Net efflux of mass by void drift	=	Rate of change of mass due to vapor generation

The net vapor efflux from channel i due to void drift is written

$$\int\int_{\substack{\text{cell} \\ \text{surface}}} \underline{n} \cdot \underline{G}_v^T \, dS = \sum_{k=1}^{NK} \left(\frac{\varepsilon}{\ell}\right)_k \{[(\alpha_v \ell_v)_i - (\alpha_v \ell_v)_j] - [(\alpha_v \rho_v)_i - (\alpha_v \rho_v)_j]_{EQ}\} \quad (2\text{-}83)$$

Modeling the eddy diffusivity for gap k, ε_k, with the mixing coefficient approach:

$$\left(\frac{\varepsilon}{\ell}\right)_k = S_k \frac{W_k'}{\rho_m} \quad (2\text{-}84)$$

where

ε = eddy diffusivity (ft^2/sec)
ℓ = effective mixing length (ft)
ρ_m = gap-averaged mixture density
S_k = gap distance (ft)

The equilibrium void distribution is assumed as

$$[(\alpha\rho_v)_i - (\alpha\rho_v)_j] = \frac{(G_i - G_j)(\alpha_i + \alpha_j)}{\overline{G_{ij}}} \quad (2\text{-}85)$$

Terms accounting for the momentum and energy transfer associated with the mass transfer are added to the conservation equations. Void drift is only assumed to occur when the liquid is the continuous phase. Also, the void drift model is not applied to the hot wall flow regimes above a quench front.

2-27. HEAT TRANSFER MODELS

The heat transfer models in COBRA-TF determine the material heat release rates and the temperature response of the fuel rods and structural components of a light water reactor during operating and transient conditions. All of the heat transfer calculations are performed at the beginning of each time step before the hydrodynamic solution. Heat transfer coefficients based on old time fluid conditions are used to advance the material conduction solution. The resultant heat release rates are explicitly coupled to the hydrodynamic solution as source terms in the fluid energy equations.

To effectively perform these tasks, a consistent set of heat transfer models was developed. It consists of five components:

o	Conduction model	specifies the conductor geometry and material properties, and solves the conduction equation
o	Heat transfer package	selects and evaluates the appropriate heat transfer correlations
o	Quench front model	a "fine mesh-rezoning" method that calculates quench front propagation due to axial conduction and radial heat transfer
o	Gap conductance model	a dynamic gap conductance model that evaluates fuel pellet-clad conductance for a nuclear fuel rod
o	Radiation model	a subchannel-based radiation model for rod-rod, rod-vapor, and rod-drop radiation heat transfer

2-28. Conduction Model

The "rod" model is designed for nuclear fuel rods, heater rods, tubes, and walls; it contains options for one-dimensional (radial), two-dimensional (radial and axial), and three-dimensional heat conduction. This flexibility allows the user to simulate most of the conduction geometries found in reactor vessels and heat transfer experiments. In addition, an unheated conduction model is provided for structural heat transfer surfaces.

2-29. Rod Conductor Geometry

A nuclear fuel rod model requiring minimal user input is built into the code. Material properties can be specified by input or defaulted to uranium-dioxide and zircaloy. These properties are calculated using correlations taken from MATPRO-11 (Revision 1).[1] The conductor geometry for a nuclear fuel rod is illustrated in figure 2-5. Only cylindrical fuel rods with fluid thermal connections on the rod exterior are considered by this model.

A dynamic gap conductance model based on the GAPCON[2,3] and FRAP[4,5,6] computer codes is available for use with the nuclear fuel rod model. This model is discussed in paragraph 2-44. Alternatively, the user may specify gap

---

1. Hagrman, D. L., et al., "MATPRO-Version 11 (Revision 1): A Handbook of Materials Properties for Use in the Analysis of Light Water Reactor Fuel Rod Behavior," NUREG/CR-0497, TREE-1290, Revision 1, February 1980.

2. Beyer, C. E., et al., "GAPCON-THERMAL-2: A Computer Program for Calculating the Thermal Behavior of an Oxide Fuel Rod," BNWL-1898, November 1975.

3. Lanning, D. D., et al., "GAPCON-THERMAL-3 Code Description," PNL-2434.

(continued on next page)

conductance by input, either as a constant or with axial and temporal variations using input forcing functions. (The gap conductance options are available only with the nuclear fuel rod model.)

Electric heater rods used as fuel pin simulators and other solid cylinders can be modeled with the heater rod option. These rods consist of concentric rings of different material regions, as shown in figure 2-5. In each region, the material type, number of radial nodes, width, and power factor are specified by input. Contact resistances are not calculated between material regions but can be modeled by including a region one node wide with material properties that give it the appropriate thermal resistance.

Conductors, either tube or plate, with thermal connections to channels on either the inner or the outer surface are modeled by the tube and wall models. These geometries, shown in figure 2-6, are similar to the heater rod model except for the interior coolant connections. Concentric and flat plate fuel elements, thermal walls, and simple tubes can be modeled with these options. Each rod may extend through any number of channel-splitting sections, but each heat transfer surface may only be connected to one channel in each section, unless the three-dimensional rod conduction model is used.

2-30. Unheated Conductor Model

Structural heat transfer surfaces can be more efficiently modeled with the unheated conductor model. This option accesses the same conductor geometries as the rod model (except for the nuclear fuel rod geometry), and uses the same heat transfer package. However, to economize computer time and storage, the unheated conductor model is limited in the following ways:

---

4. Dearfen, J. A., et al., "FRAP-S3: A Computer Code for the Steady-State Analysis of Oxide Fuel Rods -- Report I, Analytical Models and Input Manual," TFBP-TR-164, October 1977.

5. Siefken, L. J., et al., "FRAP-T5: A Computer Code for Transient Analysis of Oxide Fuel Rods," NUREG/CR-0840, TREE-1281, June 1979.

6. Berna, G. A., et al., "FRAPCON-1: A Computer Code for the Steady-State Analysis of Oxide Ruel Rods," CDAP-TR-032-R1, November 1978.

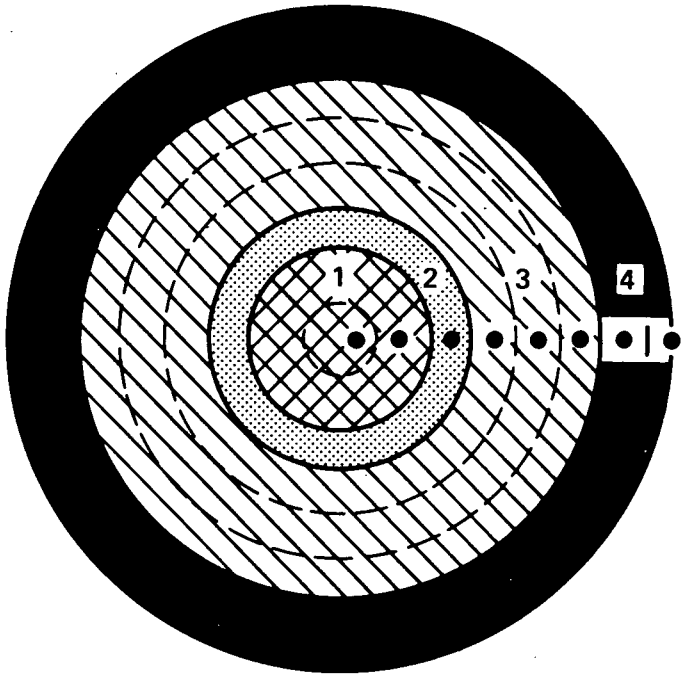

Figure 2-5. Heater Rod Geometry (Fuel Pin Simulator Example)

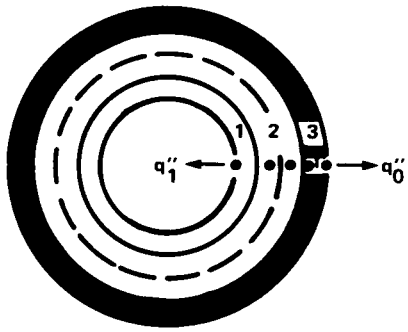

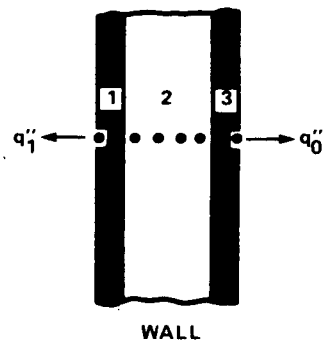

Figure 2-6. Tube and Wall Conductor Geometries

- o No internal heat generation is included.
- o Radial conduction only is used.
- o No fine mesh-rezoning quench front model is included.
- o Unheated conductors do not extend across section boundaries.
- o The fluid solution cannot be forced into the hot wall flow regime.
- o Vapor properties in the convective heat transfer correlations are evaluated at the bulk vapor temperature rather than at the film temperature.
- o The minimum film boiling temperature is set to a constant 500°C (900°F).

These limitations only apply to the unheated conductor model and not to the rod model in general. Unheated conductors should be used to model structural elements for which expected peak temperatures are well below the minimum film boiling point.

2-31. Three-Dimensional Rod Model

The usual assumption of negligible azimuthal temperature gradient is not always suitable. In a small rod bundle during reflood heat transfer tests, for example, significant temperature gradients exist across the outer row of rods near the relatively cold wall. To predict the rod-wall radiation heat transfer without gross errors, the isothermal rod temperature constraint must be relaxed.

The COBRA-TF three-dimensional rod conduction model provides this flexibility. Using this option, a rod may be modeled with up to eight individual circumferential sections. As shown in figure 2-7, each section may have a thermal connection to a different fluid channel. Heat conduction in the azimuthal direction is calculated between each section. The usefulness of this model is limited, however, because each section requires approximately the same computer time and storage as a normal one-section, two-dimensional rod.

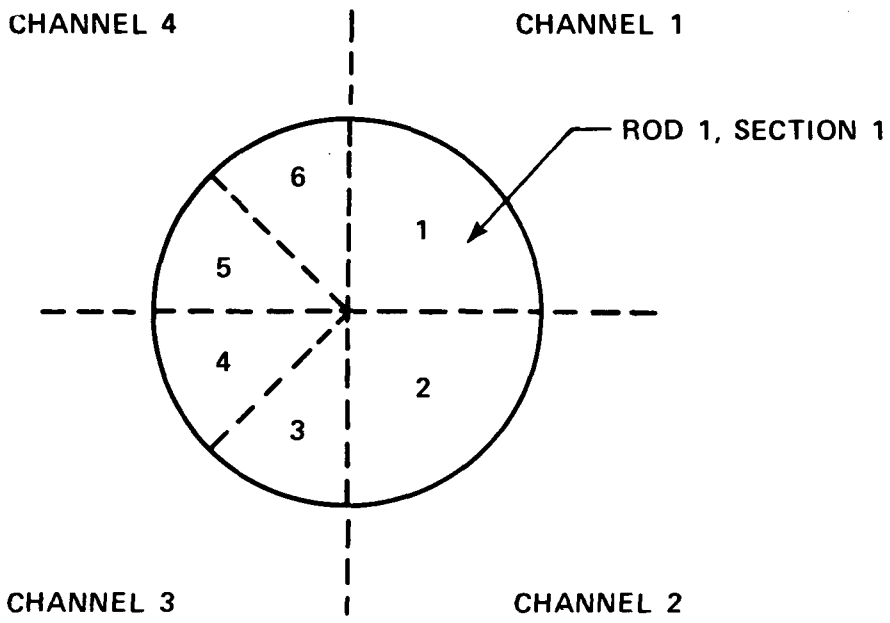

Figure 2-7. Example of Three-Dimensional Rod Model

2-32. HEAT TRANSFER PACKAGE

The heat transfer package consists of a library of heat transfer correlations and a selection logic algorithm. Together these produce a continuous boiling curve that is used to determine the phasic heat fluxes. A schematic diagram of the boiling curve is shown in figure 2-8; figure 2-9 illustrates the heat transfer regime selection logic. The correlations used in each regime are detailed below.

2-33. Single-Phase Vapor

The maximum of the Dittus-Boelter turbulent convection correlation,[1] the FLECHT SEASET 161-rod steam cooling correlation,[2] and a laminar flow Nusselt number is used:

- Dittus-Boelter (steam)[1]

$$HTC = 0.023 \frac{k_v}{D_H} \left(\frac{G_v D_H}{\mu_v} \right)^{0.8} (Pr_v)^{0.4} \qquad (2\text{-}86)$$

- FLECHT SEASET 161-rod bundle[2]

$$HTC = 0.0797 \frac{k_v}{D_H} \left(\frac{G_v D_H}{\mu_v} \right)^{0.6774} (Pr_v)^{0.333} \qquad (2\text{-}87)$$

1./ Dittus, F. W., and Boelter, L. M. K., "Heat Transfer in Automobile Radiators of the Tubular Type," University of California, Berkeley Publ. Eng. 2, 13, 1930, 442-462.

2. Wong, S., and Hochreiter, L. E., "Analysis of the FLECHT SEASET Unblocked Bundle Steam Cooling and Boiloff Tests," NRC/EPRI/ Westinghouse-8, January 1981.

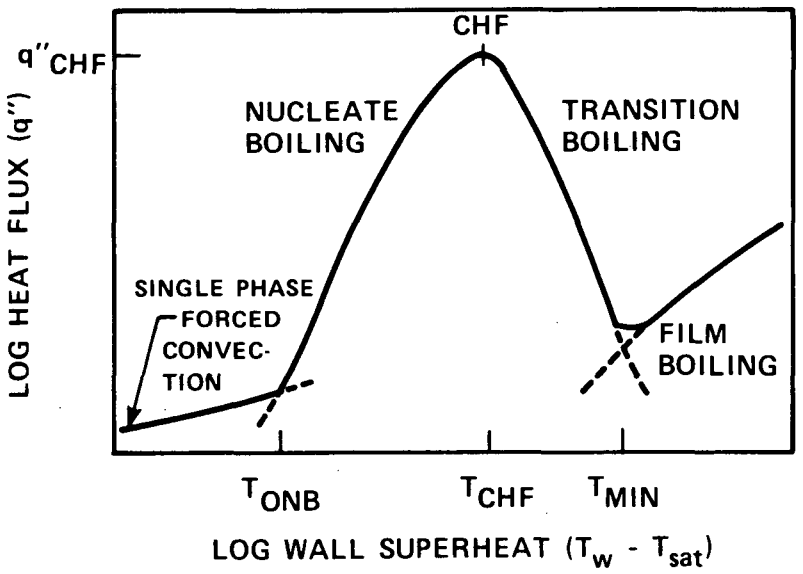

Figure 2-8. Schematic Representation of Boiling Curve

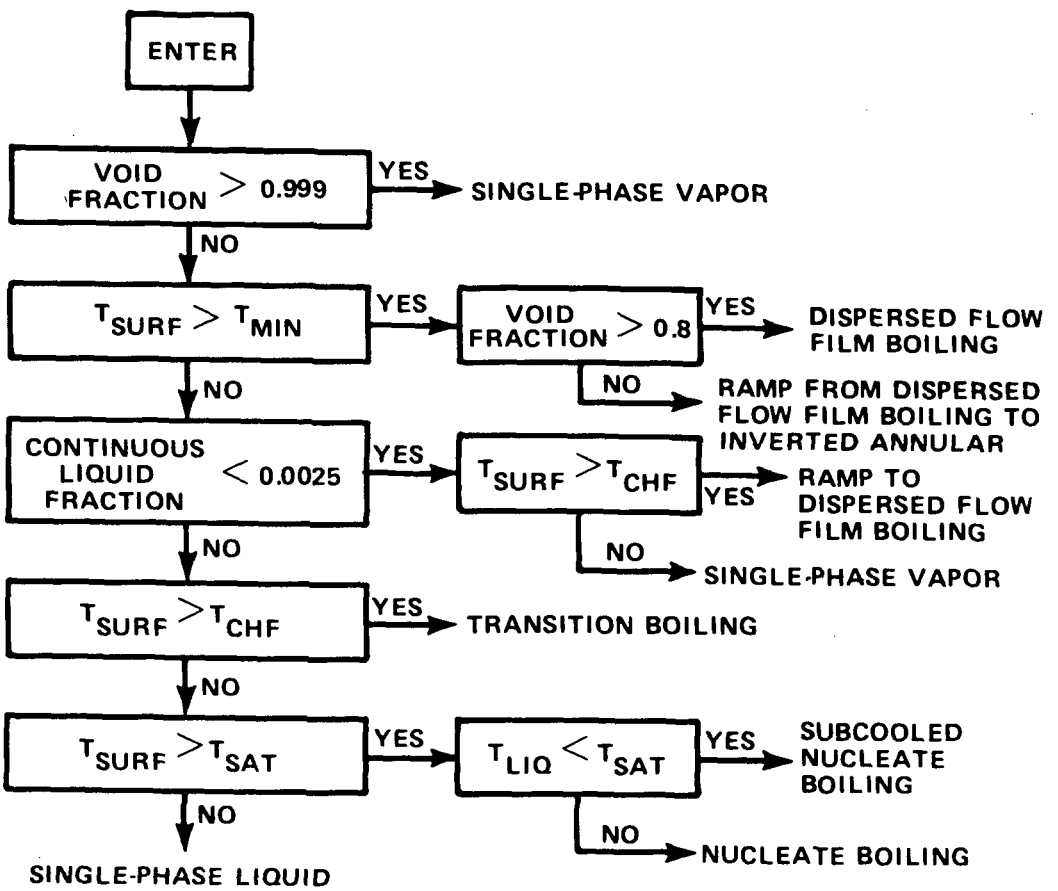

Figure 2-9. Heat Transfer Regime Selection Logic

- Laminar flow

$$HTC = 10\left(\frac{k_v}{D_H}\right) \tag{2-88}$$

For single-phase convection to vapor, all vapor properties[1] are evaluated at the film temperature.

2-34. Single-Phase Liquid

Convection to single-phase liquid is computed as the larger of either the Dittus-Boelter turbulent convection correlation or the laminar flow with a limit Nusselt number equal to 7.86.[2]

- Dittus-Boelter (liquid)

$$HTC = 0.023\,\frac{k_\ell}{D_H}\left(\frac{G_\ell\, D_H}{\mu_\ell}\right)^{0.8}(Pr_\ell)^{0.4} \tag{2-89}$$

- Laminar flow

$$HTC = 7.86\left(\frac{k_\ell}{D_H}\right) \tag{2-90}$$

2-35. Nucleate Boiling

When the wall temperature is greater than saturation but less than the critical heat flux temperature and liquid is present, the Chen nucleate boiling

---

1. Kays, W., Convective Heat and Mass Transfer, McGraw-Hill, New York, 1966.

2. Sparrow, E. M., et al., "Heat Transfer to Longitudinal Laminar Flow Between Cylinders," J. Heat Trans. 83, 1961, 415.

correlation[1] is used. The Chen correlation applies to both the saturated nucleate boiling region and the two-phase forced convection evaporation region. It automatically makes the transition to single-phase convection at low wall superheat and pool boiling at low flow rate. Chen assumes a superposition of a forced-convection correlation (Dittus-Boelter type) and a pool boiling equation (Forster-Zuber). Thus,

$$H_{CHEN} = H_{SPL} + H_{NB} \tag{2-91}$$

where

$$H_{SPL} = 0.023\ F \left(\frac{k_f}{D_H}\right) Re^{0.8}\ Pr^{0.4} \tag{2-92}$$

F = Reynolds number factor (figure 2-10)

Re = Reynolds number = $\dfrac{(1-x)\ G\ D_H}{\mu_f}$

Pr = Prandtl number

$$H_{NB} = 0.00122\ S \left(\frac{k_f^{0.79} Cp_f^{0.45} \rho_f^{0.49} g_c^{0.25}}{\sigma^{0.5} \mu_f^{0.29} h_{fg}^{0.24} \rho_g^{0.24}} \right) (T_w - T_f)^{0.24} (P_w - P)^{0.75} \tag{2-93}$$

S = suppression factor (figure 2-11)

T_w = wall surface temperature

P_w = saturation pressure corresponding to T_w (lbf/ft^2)

All fluid properties are evaluated at saturation conditions. Butterworth developed curve fits for both the Reynolds number factor (F) and the suppression factor[2] (S) as follows:[3]

---

1. Chen, J. C., "A Correlation for Boiling Heat Transfer to Saturated Fluids in Convective Flow," ASME 63-HT-34, 1963.

2. Reynolds number limit modified from original value of 70 to be continuous

3. Collier, J. G., Convective Boiling and Condensation, McGraw-Hill, New York, 1972.

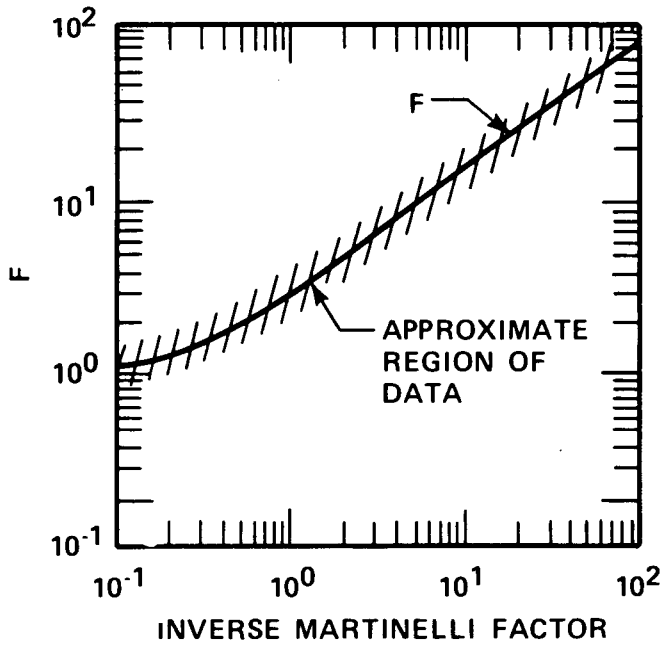

Figure 2-10. Reynolds Number Factor, F, for Chen Correlation

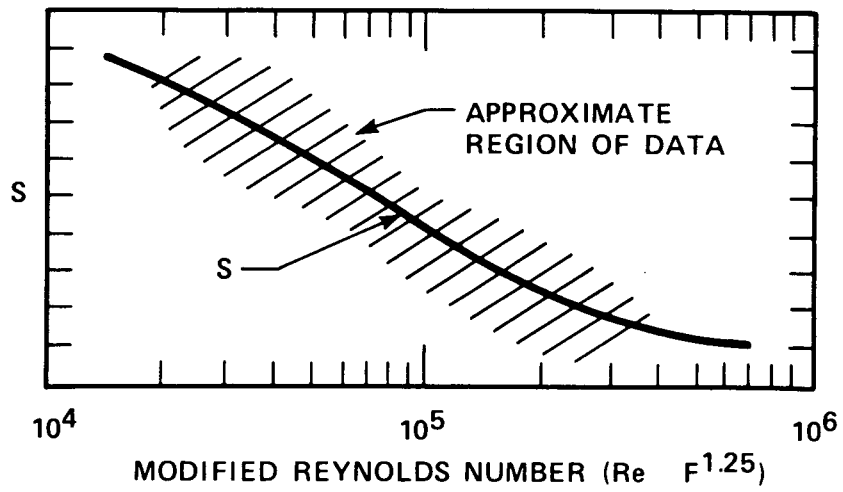

Figure 2-11. Suppression Factor, S, for Chen Correlation

$$F = \begin{cases} 1.0 & ; \ x_{tt}^{-1} < 0.1 \\ 2.34\ (x_{tt}^{-1} + 0.213)^{0.736} & ; \ x_{tt}^{-1} > 0.1 \end{cases} \quad (2\text{-}94)$$

where

x_{tt}^{-1} = inverse Martinelli factor

$$x_{tt}^{-1} = \left(\frac{x}{1-x}\right)^{0.9} \left(\frac{\rho_f}{\rho_g}\right)^{0.5} \left(\frac{\mu_g}{\mu_f}\right)^{0.1} \quad (2\text{-}95)$$

$$S = \begin{cases} [1 + 0.12(Re_{TP}')^{1.14}]^{-1} & ; \ Re_{TP}' < 32.5 \\ [1 + 0.42(Re_{TP}')^{0.78}]^{-1} & ; \ 32.5 < Re_{TP}' < 50.9 \\ 0.1 & ; \ Re_{TP}' > 50.9 \end{cases} \quad (2\text{-}96)$$

where $Re_{TP}' = (1 \times 10^{-4})\ Re\ F^{1.25}$ (2-97)

These factors are illustrated graphically in figures 2-10 and 2-11.

2-36. Subcooled Nucleate Boiling

The Chen correlation, though developed for saturated boiling, may be extended into the subcooled region. As discussed in the saturated boiling section, the Chen correlation superimposes a forced convective and nucleate boiling component. For subcooled boiling,

$$q'' = q''_{FC} + q''_{NB} \quad (2\text{-}98)$$

The nucleate boiling heat flux is evaluated as

$$q''_{NB} = H_{NB}\ (T_w - T_f) \quad (2\text{-}99)$$

where HNB is defined by equation (2-93) above, and the suppression factor, S, is computed from equation (2-96) using the single-phase Reynolds number, $Re = G_\ell D_H/\mu_\ell$. The forced convection heat flux is computed from equation (2-92) using subcooled liquid properties and setting the flow factor, F, to unity, so that

$$q''_{FC} = 0.023 \left(\frac{k_\ell}{D_H} \right) Re^{0.8} \, Pr^{0.4} \, (T_w - T_\ell) \qquad (2\text{-}100)$$

where

$Re = G_\ell D_H/\mu_\ell$
T_ℓ = local bulk fluid temperature

Moles and Shaw[1] compared the Chen correlation to subcooled boiling data for several fluids and reported satisfactory agreement for water at low to moderate subcoolings.

During subcooled boiling, vapor generation occurs and a significant void fraction ($\alpha \sim 0.6$) may exist despite the presence of subcooled water. In this regime, four processes are of interest:

- Forced convection to liquid
- Vapor generation at the wall
- Condensation near the wall
- Bulk condensation (subcooled liquid core)

Condensation occurring because of the presence of vapor in the subcooled liquid core is calculated implicitly during the solution of the energy

1. Moles, F. D., and Shaw, J. F. G., "Boiling Heat Transfer to Subcooled Liquids Under Conditions of Forced Convection," Trans. Inst. Chem. Eng. 50, 1972.

equations and does not affect the determination of phasic heat inputs. Forced convection to liquid is treated using equation (2-100) and the heat input to the liquid energy equation. The nucleate boiling component of the Chen correlation [equation (2-93)] defines the amount of heat available to cause vapor generation at the wall.

The near-wall condensation is estimated using the Hancox-Nicoll correlation[1] for heat flux at the point where all the bubbles generated collapse in the near-wall region:

$$q''_{HN} = 0.4 \left(\frac{C_{p_f} \mu_f}{D_H} \right) \left(\frac{G_\ell D_H}{\mu_f} \right)^{0.662} (T_f - T_\ell) \qquad (2\text{-}101)$$

where

T_f = saturation temperature
T_ℓ = subcooled liquid temperature

The heat flux dissipated in near-wall condensation is calculated as

$$q''_c = \max (0.0, q''_{HN} - q''_{SPL}) \qquad (2\text{-}102)$$

Subtracting the near-wall condensation from the amount available for vapor generation yields

$$Q_\Gamma = (q''_{NB} - q''_c) A_H \qquad (2\text{-}103)$$

---

1. Hancox, W. T., and Nicoll, W. B., "A General Technique for the Prediction of Void Distributions in Nonsteady Two-Phased Forced Convection," Int. J. Heat and Mass Transfer 14, 1971.

However, a fraction of Q_Γ is expended to heat up the subcooled liquid "pumped" into the saturated thermal boundary layer. This fraction is given by the Rouhani model:[1]

$$\varepsilon_p = \frac{(\rho_f/\rho_g)\,(h_f - h_p)}{h_{fg} + (\rho_f/\rho_g)(h_f - h_\ell)} \tag{2-104}$$

and

$$\varepsilon_\Gamma = (1 - \varepsilon_p) = \frac{h_{fg}}{h_{fg} + (\rho_f/\rho_g)(h_f - h_\ell)} \tag{2-105}$$

where

ε_p = fraction of heat to boundary layer
ε_Γ = fraction of heat causing vapor generation

Finally, the amount of vapor generation is

$$Q_\Gamma = (q''_{NB} - q''_c)\,\varepsilon_\Gamma\,A_H \tag{2-106}$$

and, adding all the heat inputs to the liquid,

$$Q_L = (q''_{SPL} + (1-\varepsilon_\Gamma)\,q''_{NB} + \varepsilon_\Gamma\,q''_c)\,A_H \tag{2-107}$$

The heat source term for vapor generation, Q_Γ, enters the liquid energy equation as an explicit vapor generation rate [$\Gamma = Q_\Gamma/(h_q - h_f)$] and will partially condense because of the implicit bulk condensation.

---

1. Rouhani, S. Z., and Axelsson, E., "Calculation of Void Volume Fraction in Subcooled and Quality Boiling Regions," Int. J. Heat and Mass Transfer 13, 1970.

2-37. Critical Heat Flux and Transition Boiling Regime

The intersection of the nucleate boiling and transition boiling heat transfer regimes occurs at the CHF point. To provide for a continuous transition between regimes, the CHF point (q''_{CHF}, T_{CHF}) must be specified.

Three CHF regimes are considered (figure 2-8): pool boiling, forced-convection departure from nucleate boiling (DNB), and annular film dryout. Only the model used for reflood is given below.

2-38. Reflood CHF Model -- During reflood heat transfer, a point on the rod surface traverses the boiling curve in reverse, from film boiling thrugh CHF to nucleate boiling. The Zuber pool boiling CHF correlation[1] is chosen as a reasonable approximation of the maximum heat flux at the quench front:

$$q''_{CHF} = \frac{\pi}{24} h_{fg} \rho_g^{0.5} [g_c g \sigma (\rho_f - \rho_g)]^{0.25} \quad (2\text{-}108)$$

2-39. Critical Heat Flux Temperature -- To define the boiling curve, it is necessary to know the surface temperature at which CHF occurs. An iterative procedure is used to find the wall temperature at which the heat flux from the Chen nucleate boiling correlation[2] is equal to the critical heat flux. Thus,

$$q''_{CHEN}(T_{CHF}) = q''_{CHF} \quad (2\text{-}109)$$

2-40. Minimum Stable Film Boiling Point -- The transition boiling regime is bounded by the CHF point (below which the wall is continuously wetted and

1. Zuber, N., et al., "The Hydrodynamics Crisis in Pool Boiling of Saturated and Subcooled Liquids," Part II, No. 27 in International Developments in Heat Transfer, International Heat Transfer Conference, Boulder, CO, 1961.

2. Chen, J. C., "A Correlation for Boiling Heat Transfer to Saturated Fluids in Convective Flow," ASME 63-HT-34.

nucleate boiling exists) and the minimum stable film boiling point (above which the liquid cannot wet the wall and film boiling exists). It is assumed that the minimum film boiling temperature is the wall temperature that results in an instantaneous contact temperature equal to the homogeneous nucleation temperature, THN. Using a contact temperature correction to include the effects of surface thermal properties, the minimum film boiling temperature is

$$T_{MIN} = T_{HN} + (T_{HN} - T_{\ell}) \frac{(k\rho C_p)_{\ell}}{(k\rho C_p)_w} \quad (2\text{-}110)$$

where the homogeneous nucleation temperature is given as a function of pressure by a simple curve fit:

$$T_{HN} = 705.44 - (4.722E\text{-}2)\ DP + (2.3907E\text{-}5)\ DP^2 - (5.8193E\text{-}9)\ DP^3 \quad (2\text{-}111)$$

where DP = 3203.6 - P.

The minimum film boiling temperature is specified as the larger of either equation (2-110) or that given by Henry's modification of the Berenson correlation:[1]

$$T_{min} = T_B + 0.42\ (T_B - T_{\ell}) \left[\frac{(k\rho C_p)_{\ell}}{(k\rho C_p)_w}\right] \left[\frac{h_{fg}}{C_{pw}(T_B - T_f)}\right]^{0.6} \quad (2\text{-}112)$$

where

$$T_B = T_f + 0.127 \frac{\rho_v\ h_{fg}}{k_v} \left[\frac{g(\rho_f - \rho_g)}{(\rho_f + \rho_g)}\right]^{2/3} \left[\frac{g_c \sigma}{g\ (\rho_f - \rho_g)}\right]^{1/2} \left[\frac{\mu_v}{g\ (\rho_f - \rho_g)}\right]^{1/3} \quad (2\text{-}113)$$

1. Henry, R. E., "A Correlation for the Minimum Film Boiling Temperature," AIChE Symposium Series 70, (138), 1974, 81-90.

In addition, the minimum film boiling temperature is restricted to

$$426°C\ (800°F) \leq T_{min} \leq 650°C\ (1200°F)$$

2-41. Transition Boiling -- At present, there is no consensus on a correlation to use for the transition boiling region. COBRA-TF employs a simple additive scheme for heat transfer beyond the critical heat flux temperature. This method is simple, physically based, and results in a continuous boiling curve.

It is assumed that the transition boiling heat transfer is composed of both liquid contact (wet wall) and film boiling (dry wall) heat transfer, as follows:

$$q''_{TB} = q''_{WET} + q''_{FB} \tag{2-114}$$

The wet wall heat transfer, q''_{WET}, is based on the drop deposition models of Ganic[1] and Hanratty:[2]

$$q''_{WET} = S''_{DE}\, h_{fg}\, \eta \tag{2-115}$$

where S''_{DE} = drop migration rate towards wall (see section 3).

The drop evaporation efficiency, η, is approximated by

$$\eta = \exp\left[1 - (T_w/T_f)^2\right] \tag{2-116}$$

---

1. Ganic, E. N., and Rohsenow, W. M., "Dispersed Flow Heat Transfer," Int. J. Heat and Mass Transfer 20, 1977, 855-866.

2. McCoy, D. D., and Hanratty, T. J., "Rate of Deposition of Droplets in Annular Two-Phase Flow," Int. J. Multiphase Flow 3, 1977, 319-331.

If the rod is below the froth front, the drop deposition rate is modified to force the heat flux towards the Zuber CHF limit such that q''_{WET} is the maximum of equation (2-115) or $\alpha_L \cdot q''_{CHF} \cdot \eta$.

For top quenching, the void fraction can be very large (0.95-0.99) and yet still produce significant quench rates. To model the sputtering front heat transfer, an exponential decay as a function of distance is employed:

$$\xi = \exp(-0.299(\Delta Z - 1.2)) \quad (2\text{-}117)$$

$$\xi = \text{minimum}(1.0, \text{maximum}(\xi, \alpha_L)) \quad (2\text{-}118)$$

where

ξ = exponential modifier

ΔZ = distance below a top quench front (inches)

$$q''_{TB} = \xi \eta q''_{CHF} + q''_{FB} \quad (2\text{-}119)$$

The transition boiling heat flux at a top quench front is not enhanced above the reasonable value of ($\eta q''_{CHF}$); rather, the amount by which it is decreased as a function of void fraction is reduced. The film boiling heat flux is the value obtained by evaluating the appropriate film boiling correlation (see below).

2-42. Dispersed Flow and Inverted Annular Film Boiling

Heat transfer in the film boiling region is assumed to result from one of two mechanisms: dispersed flow film boiling (DFFB) or inverted annular film boiling (IAFB).

Dispersed flow film boiling is selected if the void fraction is greater than 0.9. It is treated by a two-step method where the dominant heat transfer mode is forced convection to superheated steam. The steam superheat is then

determined by the interfacial heat transfer rate to the entrained droplets as part of the hydrodynamic solution. Heat fluxes due to wall-droplet radiation and droplet impingement are superimposed on the vapor convective heat flux. The total heat flux is

$$q''_{DFFB} = q''_{FC} + q''_{R} + q''_{W-D} \tag{2-120}$$

where

q''_{FC} = vapor convection heat flux
q''_{R} = radiation heat flux
q''_{W-D} = drop impingement heat flux

The vapor convective heat flux is given by

$$q''_{FC} = \psi H_{SPV} (T_w - T_v) \tag{2-121}$$

The heat transfer coefficient, H_{SPV}, is calculated using the correlations given in equations (2-86) through (2-88). Some dispersed flow experiments[1,2,3] have shown that interfacial shear between dispersed particles and a continuous phase increases the turbulence level and enhances the convective heat transfer. This two-phase enhancement factor for dispersed flow, ψ, is approximated by an extension of the analogy between wall shear stress and heat transfer,[4] as follows:

1. Spencer, A. C., and Young, M. Y., "A Mechanistic Model for the Best-Estimate Analysis of Reflood Transients (the BART Code)," 19th National Heat Transfer Conference, Orlando, FL, (HTD Vol. 7), 1980

2. Lee, N., et al., "PWR FLECHT SEASET Unblocked Bundle Forced and Gravity Reflood Task Data Evaluation and Analysis Report," NRC/EPRI/Westinghouse-10, September 1981.

3. Drucker, M., and Dhir, V. K., "Studies of Single- and Two-Phase Heat Transfer in a Blocked Four-Rod Bundle," EPRI NP-3485, June 1984.

4. Kays, W., Convective Heat and Mass Transfer, McGraw-Hill, New York, 1966.

$$\tau_w = \frac{1}{2} \rho_v f_w U_v^2 / D_H \tag{2-122}$$

$$\tau_d = \frac{3 \alpha_e \rho_v C_{D_d} (U_v - U_d)^2}{4 D_d} \tag{2-123}$$

$$\tau_{2\phi} = \tau_w + \tau_d \tag{2-124}$$

where

τ_w = vapor-wall shear stress
τ_d = interfacial shear due to droplets
$\tau_{2\phi}$ = total shear stress level for 2ϕ dispersed flow.
f_w = wall friction factor = $0.0791/Re_v^{0.25}$
C_{D_d} = drop drag coefficient
D_d = drop diameter
α_e = volume fraction of entrained drops

From the momentum-heat transfer analogy, the turbulent convection heat transfer coefficient is, to a first-order approximation, proportional to the square root of the shear stress:

$$H_{SPV} \approx \left(\tau_w\right)^{1/2} \tag{2-125}$$

Then,

$$\psi = \frac{H_{2\phi}}{H_{SPV}} = \sqrt{\frac{\tau_{2\phi}}{\tau_w}}$$

$$= \left(1 + \frac{\tau_d}{\tau_w}\right)^{1/2} \tag{2-126}$$

where

$$\frac{\tau_d}{\tau_w} = 1.5\ \alpha_e \left(\frac{D_H}{D_d}\right)\left(\frac{C_{D_d}}{f_w}\right)\left(\frac{U_v - U_d}{U_v}\right)^2 \qquad (2\text{-}127)$$

The instantaneous local values of the variables α_e, D_d, C_{D_d}, f_w, U_v and U_d are used to evaluate equation (2-127). A comparison of the COBRA-TF model and two-phase enhancement inferred from FLECHT reflood tests is shown in figure 2-12. Also shown in figure 2-12 is a correlation for the turbulence enhancement developed from separate air/water tests and from rod bundle tests at UCLA.[1]

Heat transfer due to droplets striking the wall, q''_{W-D}, is evaluated using equation (2-115), where the droplet efficiency is calculated using equation (2-116).

The radiative heat transfer, q''_R, is calculated using the subchannel based model and is discussed in the following paragraphs. A different radiation model would be used for different sized bundles because of the housing effects. Also, if guide tube thimbles were simulated, a different radiation model would be used.

When the void fraction is less than 0.4, inverted annular film boiling is assumed to occur. The heat flux for this regime is computed from the larger of either the value calculated in equation (2-121) for dispersed flow film boiling, or the value from the modified Bromley correlation:[2]

---

1. Drucker, M., and Dhir, V. K., "Studies of Single- and Two-Phase Heat Transfer in a Blocked Four-Rod Bundle," EPRI NP-3485, June 1984.

2. Bromley, L. A., "Heat Transfer in Stable Film Boiling," Chemical Engineering Progress 46 (5), 1950, 221-226.

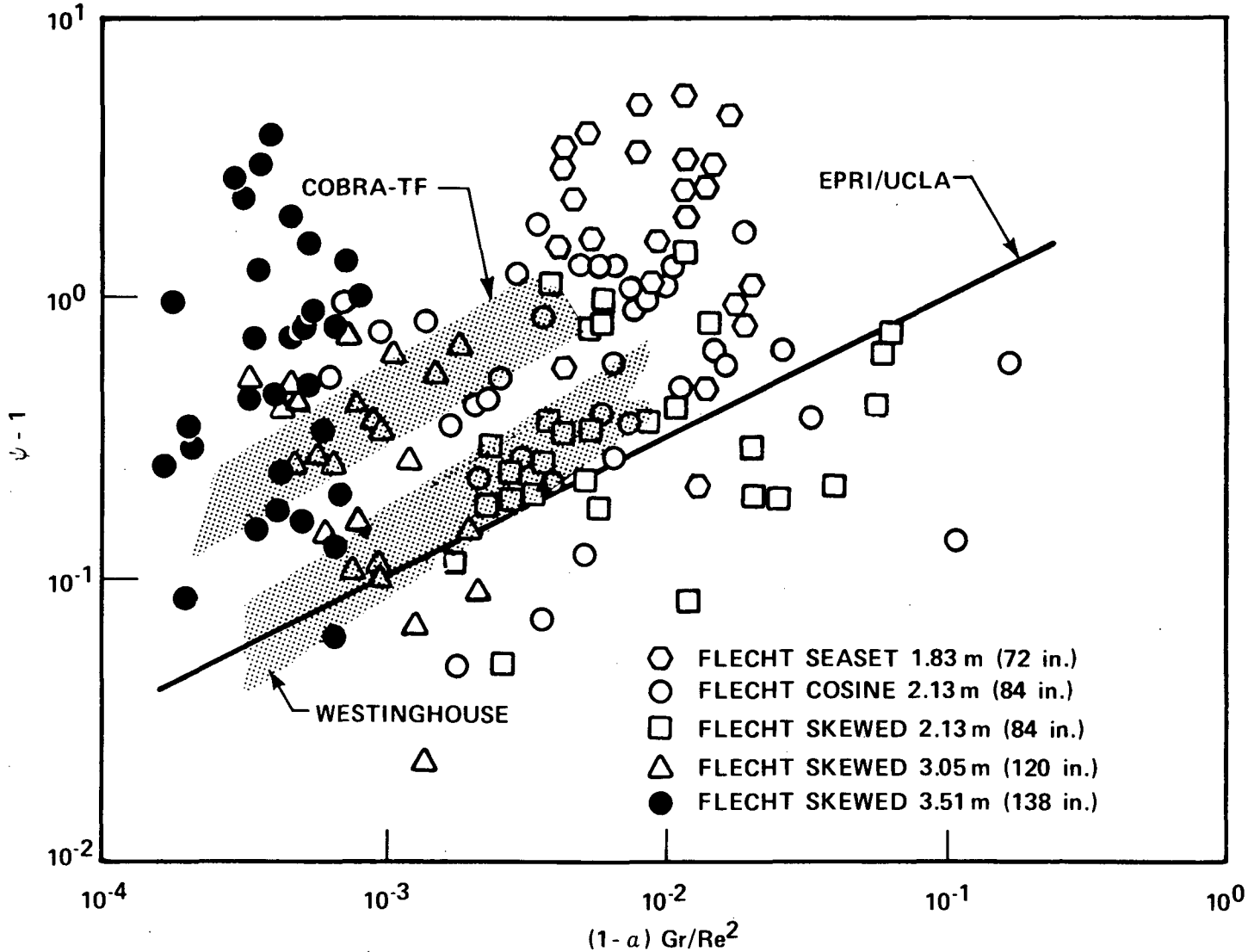

Figure 2-12. Two-Phase Enhancement: Comparison of Models and Reflood Data

$$q''_{BROM} = 0.62 \left(\frac{D_H}{\lambda_c}\right)^{0.172} \left[\frac{k_g^3 \rho_g (\rho_f - \rho_g) h'_{fg} g}{D_H \mu_g (T_w - T_f)}\right]^{1/4} (T_w - T_f) \quad (2\text{-}128)$$

where

$$h'_{fg} = h_{fg} [1.0 + 0.4 C_{pv} (T_w - T_f)/h_{fg}] \quad (2\text{-}129)$$

and

$$\lambda_c = 2 \pi \left[\frac{g_c \sigma}{g (\rho_f - \rho_g)}\right]^{1/2} \quad (2\text{-}130)$$

As before, both radiation and drop contact heat transfer components are added to q''_{BROM}. So, for inverted annular film boiling,

$$q'_{IAFB} = q''_{BROM} + q''_R + q''_{W\text{-}D} \quad (2\text{-}131)$$

At intermediate void fractions ($0.9 > \alpha > 0.4$), the heat flux is linearly interpolated between the values for inverted annular and dispersed flow film boiling with void fraction.

2-43. QUENCH FRONT MODEL

Coupled thermal-hydraulic numerical simulations of rewetting encounter difficulties with large axial computational mesh spacing (typically, 2 feet for a full vessel), which cannot adequately resolve the axial profile of temperature and surface heat flux across the quench front. During quenching, the entire boiling curve, from film boiling through transition boiling and critical heat flux to nucleate boiling, can be encompassed by one hydrodynamic mesh cell. Constraining the entire cell to be in one boiling regime is nonphysical and results in stepwise cell-by-cell quenching, producing flow oscillations that can obscure the correct hydrodynamic solution. Consequently, an integration of the boiling curve shape through the hydrodynamic computational cell must be performed to determine the fluid heat input.

A fine mesh-rezoning technique[1] is employed in COBRA-TF to surmount these difficulties. Fine mesh heat transfer cells with axial and radial conduction are superimposed on the coarse hydrodynamic mesh spacing, and a boiling heat transfer package is applied to each node.

By solving the two-dimensional conduction equation for a variable fine mesh at the quench front, propagation due either to quenching or dryout can be resolved and the surface heat flux integrated to provide the cell-averaged phasic heat inputs for the fluid energy equation. The resulting quench front velocity will be a function of the following:

- Axial conduction
- Boiling curve shape
- Prequench heat transfer
- Internal heat transfer within the rod

Resolution of axial temperature and surface heat flux excursions is achieved by rezoning the heat conductor mesh in their vicinity. Figure 2-13 illustrates the normal axial noding scheme. Both fluid and rod temperatures are calculated at the centers of the fluid continuity cells. Two extra rod nodes are included at the top and bottom of the rod. When axial temperature differences between adjacent axial nodes exceed splitting criteria (user-specified maximum surface temperature differences), an additional row of nodes is inserted halfway between the two original nodes. (This is illustrated in figure 2-14.) The temperatures assigned to these nodes are computed so that energy is conserved. This splitting process continues (over a succession of time steps) until the mesh is fine enough to resolve the surface temperature profile to the desired level of detail.

---

1. Kelly, J. M., "Quench Front Modeling and Reflood Heat Transfer in COBRA-TF," Paper 79-WA/HT-63, ASME Winter Annual Meeting, New York, 1979.

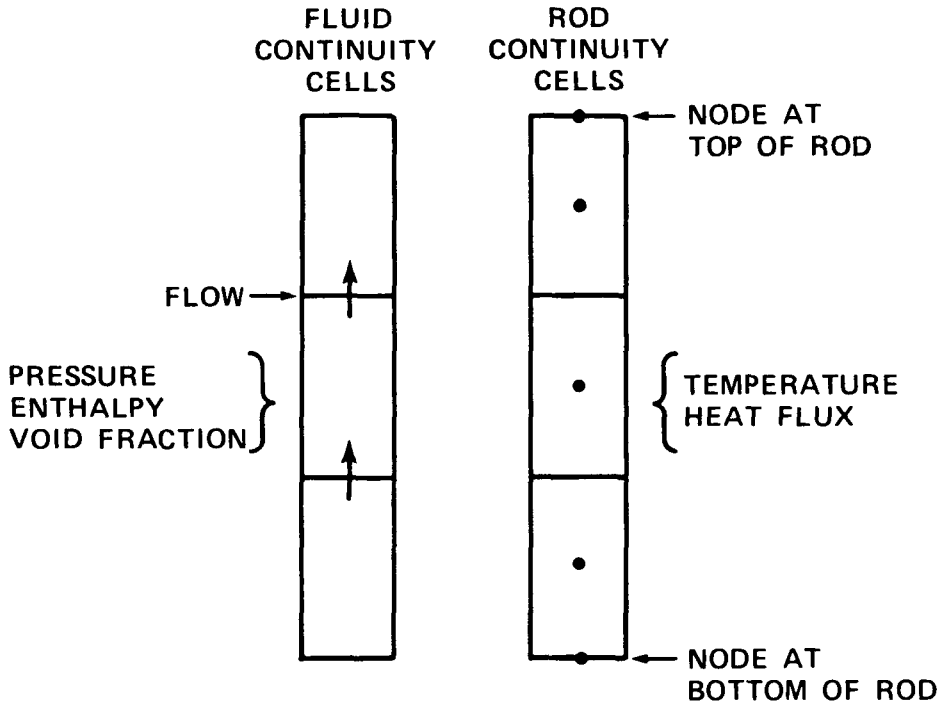

Figure 2-13. Example of COBRA-TF Axial Noding Scheme

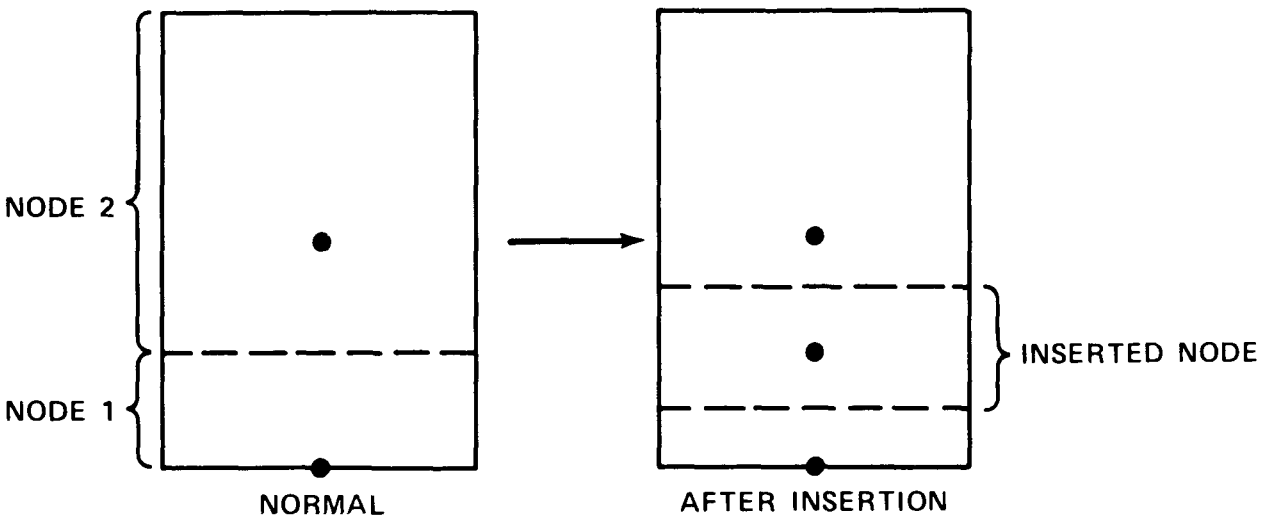

Figure 2-14. Example of Node Insertion

The correct temperature differences to be used as splitting criteria depend on the heat transfer regime. They are further modified by functions of the wall temperature (when the wall temperature is near the critical heat flux temperature) to ensure resolution of the surface heat flux profile in the vicinity of the quench front. The temperatures assigned to the inserted nodes are calculated from an energy balance:

$$Cp_1 (T_1 - T_I) \frac{\Delta X}{2} + Cp_2 (T_2 - T_I) \frac{\Delta X}{2} = 0 \qquad (2\text{-}132)$$

$$T_I = \frac{(CpT)_1 + (CpT)_2}{(Cp_1 + Cp_2)} \qquad (2\text{-}133)$$

where the subscripts I, 1, and 2 represent the inserted and two original nodes, respectively.

Conversely, when a fine mesh has been established, but the disturbance has propagated downstream and the fine mesh is no longer necessary, adjacent nodes are coalesced back down to one node. The decision to merge cells is based on minimum temperature differences between adjacent nodes. Eventually, all the fine mesh nodes in a region will coalesce, and only the original nodes (those coincident with hydrodynamic scalar mesh cell boundaries) will remain.

The fine mesh-rezoning model differs from other reflood models (such as the one employed in RELAP4/MOD6[1]) in that the fine mesh nodes are stationary and do not have a fixed mesh spacing. The fine mesh nodes are split to create a graduated mesh spacing that readjusts itself constantly to the changing axial temperature gradient. This approach permits node sizes small enough [for example, 1.3 mm (0.05 in.)] to resolve axial conduction and the boiling curve shape at the quench front, and yet minimizes the number of nodes required. It ensures conservation of stored energy when cells are added, and

1. "RELAP4/MOD6: A Computer Program for Transient Thermal-Hydraulic Analysis of Nuclear Reactors and Related Systems," PG-R-77-06, March 1977.

simplifies coupling with the hydrodynamic solution. Figures 2-15 and 2-16, taken from a simulation of a FLECHT low forced flooding rate test, illustrate the resolution of the cladding temperature profile and the surface heat flux in the vicinity of the quench front.

2-44. GAP CONDUCTANCE MODEL

The dynamic gap conductance model computes changes in the fuel rod structure and fill gas pressure that affect the gap conductance and fuel temperature during a transient. The method is based primarily on previous work in the GAPCON and FRAP series of fuel performance codes (referenced earlier) but with the mechanics and fill gas pressure models greatly simplified. The material property correlations are taken exclusively from MATPRO-11. For more information, see the COBRA-TRAC reports.

2-45. RADIATION HEAT TRANSFER MODEL

The reflood phase of a LOCA is characterized by a superheated vapor coolant containing dispersed liquid droplets. Heat transfer to the vapor and droplets is poor, resulting in high temperatures at the surface of the fuel rods. Because of the high temperatures, heat transfer by radiation accounts for a significant portion of the heat removed from the fuel rods.

A complete radiation heat transfer solution would include radiation from every infinitesimal solid surface to every other solid surface in an enclosure through a continuously varying medium. To simplify the problem, divide all the solid structures in the enclosure into finite isothermal surfaces. Temperature gradients in the axial direction are small; therefore, radiation in the axial direction can be neglected. Treat all of the surfaces as gray bodies and assume that they are infinite in length, so that Hottel's cross string method[1] can be used to generate geometric configuration factors. Finally, divide the core into regions with the same coolant properties.

---

1. Siegel, R., and Howell, J. R., Thermal Radiation Heat Transfer, McGraw-Hill, New York, 1972.

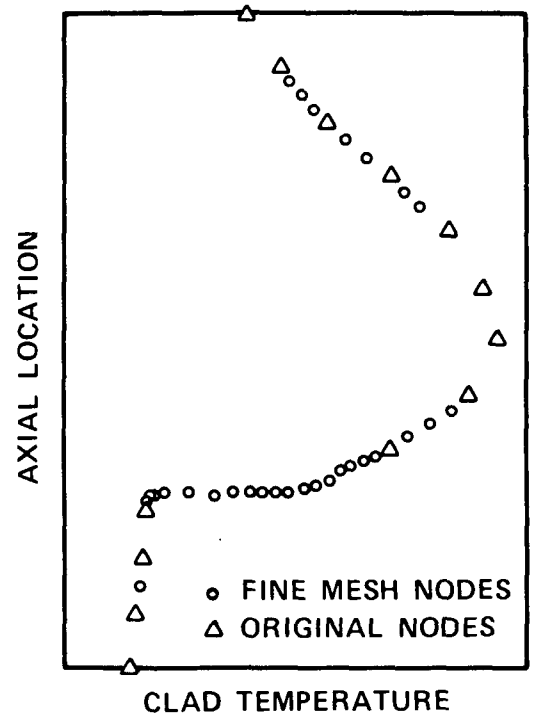

Figure 2-15. Fine Mesh Renoding: Cladding Temperature Profile

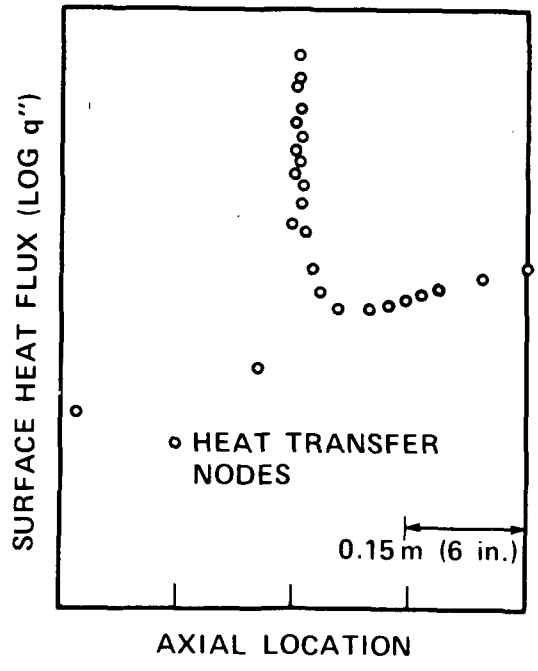

Figure 2-16. Fine Mesh Renoding: Surface Heat Flux

Using these assumptions, a solution of the thermal radiation in a reactor core is possible but still complex and time-consuming. Consider a standard PWR fuel rod assembly with each fuel rod divided into four isothermal surfaces. The solution involves solving more than a thousand equations simultaneously. Even with current state-of-the-art computers, this approach is too expensive for a transient thermal-hydraulic code.

A subchannel-based radiation heat transfer model approximates the complete solution and dramatically reduces storage requirements and computation time. Each subchannel is treated as an enclosure with M surfaces, where M is the total number of isothermal solid surfaces and gaps that define the boundary of the subchannel. An example of one subchannel enclosure is shown in figure 2-17 for an array of fuel rods on a square lattice. Similar enclosures can be drawn for rods in an irregular lattice or for rods adjacent to irregularly shaped structures. Properties of the coolant inside the enclosure must be the same throughout the enclosure. To describe the geometry, a geometric configuration factor and mean beam length must be provided for each pair of surfaces making up the enclosure.

A radiosity equation can be written for solid surface i radiating to all other surfaces j of the enclosure:

$$\sum_{j=1}^{M} C_{ij} B_j = D_i \quad , \; i \leq M_1 \tag{2-134}$$

where

$$C_{ij} = F_{ij} \tau_{ij} \quad , \; i \neq j \tag{2-135}$$

$$C_{ij} = \frac{\varepsilon_i}{1-\varepsilon_i} + 1 - F_{ij} \tau_{ij} \sum_{j=1}^{M} F_{ij} \sigma_{ij} \; , \; i = j \tag{2-136}$$

$$D_i = \frac{\varepsilon_i}{1-\varepsilon_i} E_i + \left(1 - \sum_{j=1}^{M} F_{ij} \tau_{ij} - \sum_{j=1}^{M} F_{ij} \sigma_{ij} \right) \frac{\Omega}{a} \tag{2-137}$$

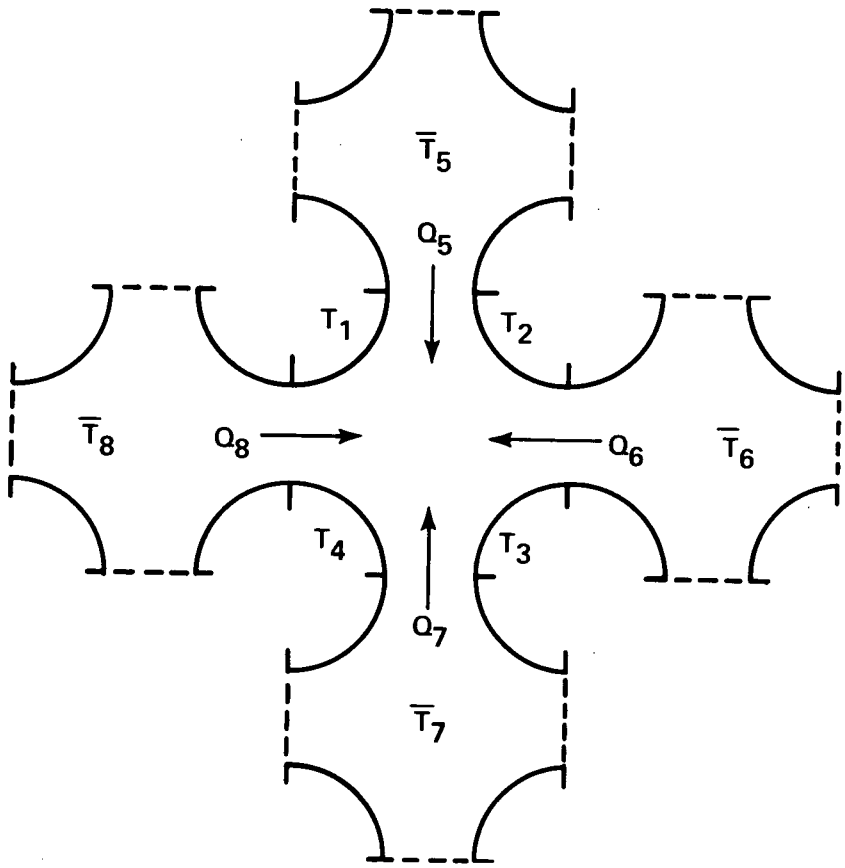

Figure 2-17. Typical Subchannel Enclosure

$$\Omega = a_d E_d + a_g E_g \tag{2-138}$$

B_j = radiosity

F_{ij} = view factor

τ_{ij} = total transmittance

ε_i = emissivity

σ_{ij} = scattering coefficient

a = absorptance

A similar equation can be written for gap i radiating to all other surfaces j of the enclosure:

$$\sum_{j=1}^{M} C_{ij} B_j = D_i \quad , \; i \geq M_1 + 1 \tag{2-139}$$

where

$$C_{ij} = F_{ij} \tau_{ij} \quad , \; i \neq j \tag{2-140}$$

$$C_{ij} = 1 - F_{ij} \tau_{ij} - \sum_{j=1}^{M} F_{ij} \sigma_{ij}, \; i = j \tag{2-141}$$

$$D_i = \frac{Q_i}{A_i} + \left(1 - \sum_{j=1}^{M} F_{ij} \tau_{ij} - \sum_{j=1}^{M} F_{ij} \sigma_{ij} \right) \frac{\Omega}{a} \tag{2-142}$$

Writing one of these two equations for each surface of the enclosure forms a set of M equations. These equations can be solved for the radiosity of the surfaces provided the temperatures of the solid surfaces, the properties of the coolant, and the heat fluxes across the gaps are known.

COBRA-TF supplies temperatures for the solid surfaces, the vapor, and the liquid droplets from the previous time step. The Plank mean absorption coefficient for vapor is used for the vapor absorptance.[1,2] Droplet absorptance is given by the effective absorptance of a liquid droplet.[3]

Heat fluxes through the gaps are the only boundary conditions left to define. The heat flux is determined by considering the subchannels on either side of the gap as cavities. The temperature of the cavity wall is an area-weighted average of the temperatures of the solid surfaces that make up the cavity.

The heat flux across the gap is then

$$\frac{Q_{12}}{A_c} = \left(\frac{\varepsilon_1}{1-\varepsilon_1}\right) \left(\frac{\varepsilon_1 \varepsilon_2}{DET}\right) \left(\frac{1}{\varepsilon_1} - 1\right) F_{12} (\sigma \bar{T}_1^4 - \sigma \bar{T}_2^4) \qquad (2\text{-}143)$$

where

$$DET = \varepsilon_1 \varepsilon_2 \left[1 + \left(\frac{1}{\varepsilon_1} - 1\right) F_{12} + \left(\frac{1}{\varepsilon_2} - 1\right) F_{12}\right] \qquad (2\text{-}144)$$

Properties of the coolant are not used in calculating heat flux through the gaps. Therefore, this approach should not be used in cases where the mean penetration distance of the radiation is short when compared to the mean beam length. In COBRA-TF, the subchannel radiation model is used only in regions of the core where the coolant is primarily vapor with dispersed droplets of liquid. Vapor and dispersed droplets form a medium optically thin enough to allow the subchannel enclosures to be used.

---

1. Abu-Romia, M. M., and Tien, C. L., "Appropriate Mean Absorption Coefficients for Infrared Radiation of Gases," J. Heat Transfer, November 1967, 321-327.

2. Oppenheim, A. K., Radiation Analysis by the Network Method," Trans. Amer. Soc. Mech. Engin., May 1956, 725-735.

3. Harpole, G. M., "Radiative Absorption by Evaporating Droplets," Int. J. Heat and Mass Transfer 23, 1980, 17-26.

Solving equations (2-134) and (2-139) simultaneously provides a radiosity for every surface in the enclosure. Radiosity of a solid surface converts easily to a surface heat flux:

$$\frac{Q_i}{A_i} = \frac{\varepsilon_i}{1-\varepsilon_i} [E_i - B_i] \tag{2-145}$$

Heat that is not transmitted or scattered to another surface of the enclosure is absorbed by the coolant:

$$Q_g = \frac{a_g}{a} \sum_{i=1}^{M} A_i (B_i - E_g) \left[1 - \sum_{j=1}^{M} F_{ij} \tau_{ij} - \sum_{j=1}^{M} F_{ij} \sigma_{ij} \right] \tag{2-146}$$

$$Q_d = \frac{a_d}{a} \sum_{i=1}^{M} A_i (B_i - E_d) \left[1 - \sum_{j=1}^{M} F_{ij} \tau_{ij} - \sum_{j=1}^{M} F_{ij} \sigma_{ij} \right] \tag{2-147}$$

Radiation heat transfer to the solid surfaces and to the coolant is used as an explicit source term in the COBRA-TF solution scheme.

Computation time is reduced further by taking advantage of lumping subchannels together. A single enclosure can be used to model several subchannels in which the geometry, fuel rod temperatures, and coolant conditions are identical. The net heat transfer to the coolant is simply multiplied by the number of subchannels being simulated.

The subchannel radiation approximation is reliable as long as the participating media remain optically thin. During the reflood phase of a loss-of-coolant accident, the coolant is optically thin in the regions of the core where radiation heat transfer is important. A subchannel-based radiation heat transfer model provides a detailed yet economical solution to heat transfer by radiation in an LWR core.

SECTION 3
GRID HEAT TRANSFER MODELS

3-1. INTRODUCTION AND BACKGROUND

Spacer grids are structural members in the reactor core which support the fuel rods at a prescribed rod-to-rod pitch. Examples of simple grids are shown in figure 3-1. All fuel assemblies have grids at the same elevations across the core. Since the grid reduces the fuel assembly flow area, the flow contracts and then expands downstream of each grid. As the flow is accelerated within the grid and then expands downstream, it disrupts and reestablishes the fluid and thermal boundary layers on the fuel rod increasing local heat transfer within and downstream of the grid. Several single-phase experiments[1-8] clearly showed that the continuous phase heat transfer downstream of a spacer

1. Rehme, K., "Pressure Drop Correlations for Fuel Elements Spacers," Nuclear Technology 17, 1973, 15-23.

2. Rehme, K., "Pressure Drop of Spacer Grids in Smooth and Roughened Rod Bundles," Nuclear Technology 31, 1977, 314-317.

3. De Stordeur, A. N., "Drag Coefficients for Fuel Element Spacers," Nucleonics 19, No. 6, 1961, 74-79.

4. de Paz, J. F., "Pressure Drop and Volume Fraction of Grid and Wire Spaced Subassemblies," ANL-AFP-13, 1975.

5. Marek, J., and Rehme, K., "Heat Transfer in Smooth and Roughened Rod Bundles Near Spacer Grids," Fluid Flow and Heat Transfer Over Rod or Tube Bundles, edited by S. Yao and P. Pfund, ASME, 1979, 163-170.

6. Kidd, G. J., and Hoffman, H. W., "The Temperature Structure and Heat Transfer Characteristics of an Electrically Heated Model of a Seven-Rod Cluster Fuel Element," ASME paper 68-WA/HT-33.

7. Krett, V., and Majer, J., "Temperature Fluid Measurement in the Region of Spacing Elements," Report ZJE-114, Skoda Works Nuclear Power Construction Department, Information Centre Pilzen-Czechoslovakia, 1971.

8. Yao, S. C., et al., "Heat-Transfer Augmentation in Rod Bundles Near Grid Spacers," J. Heat Transfer, 104, 1982.

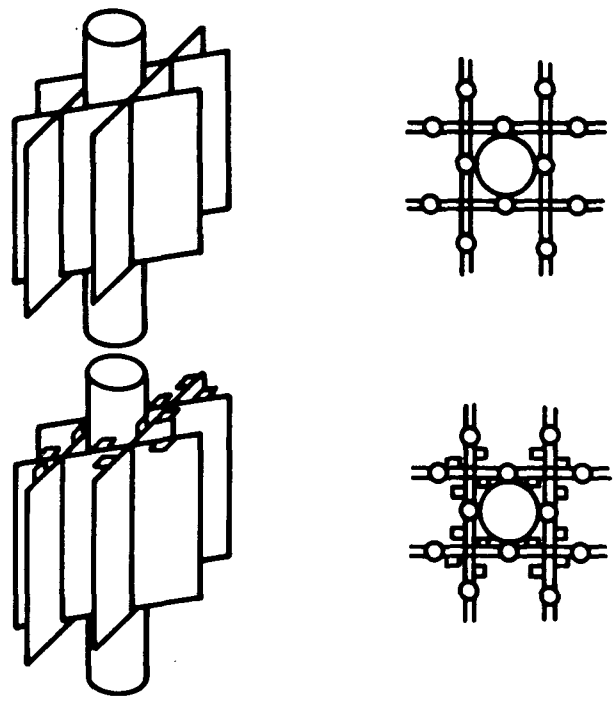

Figure 3-1. Typical Grid Spacers

grid can be modeled as an entrance effect phenomenon, in which the abrupt contraction and expansion result in establishment of a new boundary layer downstream of the grid. This entrance effect heat transfer decays exponentially downstream of the grid, as shown in figure 3-2.

When the flow is a dispersed two-phase droplet flow, characteristic of a low flooding rate PWR reflood, the grids will promote additional heat transfer effects. Since the grids are unpowered, they can quench before the fuel rods. If the grids quench, they create additional liquid surface area, which can help to desuperheat the vapor in the nonequilibrium two-phase droplet flow. A wetted grid will have a higher interfacial heat transfer coefficient than the droplets, since the relative velocity of the vapor flow to the liquid film is larger. In addition to desuperheating the vapor, the liquid film will evaporate, resulting in a higher steam flow and convective heat transfer. The increased interfacial heat transfer between the grid and the vapor flow and the generation of additional saturated vapor from the liquid film on the grid will result in lower vapor temperatures downstream of grids.

In addition to grid rewetting, the grids can also cause shattering of the entrained droplets into smaller, more easily evaporated droplet fragments. The evaporation of the smaller shattered droplets provides an additional steam source, which also increases the convective heat transfer coefficient.

There have been a limited number of experiments which specifically investigated grid heat transfer effects during reflood. The FEBA (Flood Experiments with Blocked Arrays) test series[1,2,3] performed at the Karlsruhe Nuclear Research Center in West Germany examined the difference in heater rod temperatures, vapor temperatures, and rod heat flux when the spacer grid is removed

---

1. Ihle, P., and Rust, L., "FEBA - Flooding Experiments with Blocked Arrays, Evaluation Report," KfK 3657, March 1984.
2. Ihle, P., and Rust, L., "FEBA - Flooding Experiments with Blocked Arrays, Data Report 1, Test Series I through IV," KfK 3658, March 1984.
3. Ihle, P., and Rust, L., "FEBA - Flooding Experiments with Blocked Arrays, Data Report 2, Test Series V through VIII," KfK 3659, March 1984.

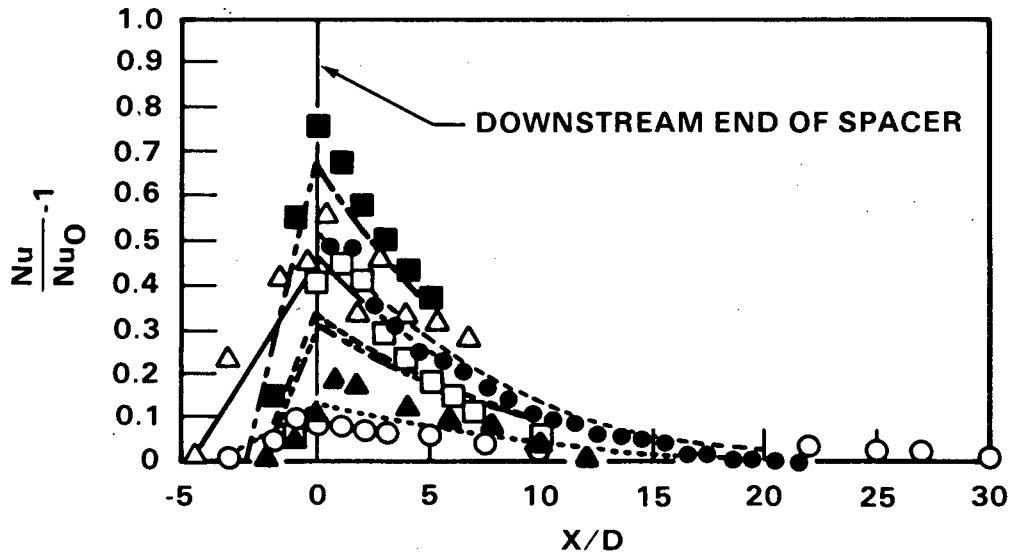

SYMBOL	AUTHOR	TYPE OF GRID REPORTED IN REFERENCE	Re X 10^{-4}	ϵ	CALCULATED $\frac{Nu}{Nu_O}-1 = 5.55\,\epsilon^2$
■	REHME	B.3	12.7	0.348	0.672
△	VELCEK	6 CM	15.5	0.289	0.463
●	KIDD	4.3	5	0.245	0.333
□	KRETT	C	9.5	0.303	0.509
▲	VELCEK	5 MM	12.5	0.237	0.311
○	HUDINA	LB. SMOOTH	1.5 −5	0.156	0.135

Figure 3-2. Heat Transfer Near Straight Spacers at Single-Phase Flow

or inserted at the rod bundle midplane. The ERSEC reflood experiments,[1] performed at Grenoble, France, have examined the heat transfer performance of different grid types during reflooding. In addition, comparable reflood heat transfer tests have been conducted in the FLECHT SEASET 161-rod unblocked bundle[2] to overlap with previously conducted Westinghouse 17x17 G-2 reflood tests. The FLECHT SEASET tests used a simple egg-crate grid; the Westinghouse 17x17 G-2 tests used a Westinghouse production mixing vane grid. The results of these tests are described below.

The FEBA tests were the first reflooding experiments to systematically examine the thermal-hydraulic performance of a grid during reflood. The tests used a 25-rod bundle with a flat chopped cosine power shape and a heated length of 3.9 m. Replicate experiments were performed under similar conditions (as close as experimentally possible), with and without the midplane grid in place. Examples of the axial temperature behavior along the bundle with and without this grid are shown in figure 3-3. The presence of the midplane grid results in improved cooling due to the heat transfer effects of convective enhancement, grid rewetting, and droplet breakup.

Plots of heater rod temperatures, total heat transfer coefficient (referenced to T_{sat}), and vapor temperatures downstream of the midplane grid for tests with and without this grid are shown in figures 3-4 through 3-6. All figures indicate that the grid improves the heat transfer performance, and that the vapor temperature downstream of the grid is reduced.

More recent FEBA tests with flow blockage at the midplane have included thermocouples brazed onto the grids upstream and downstream of the blockage. Examination of the grid upstream of the blockage in figure 3-7 (where there is no blockage effect on the grid) shows whether and how the grid quenches. (Figure

---

1. Clement, P., et al., "Reflooding of a PWR Bundle -- Effect of Inlet Flow Rate Oscillations and Spacer Grids," presented at the European Two-Phase Flow Group Meeting, Paris, June 1982.

2. Loftus, M. J., et al., "PWR FLECHT SEASET Unblocked Bundle Forced and Gravity Reflood Task Data Report," NRC/EPRI/Westinghouse-7, June 1980.

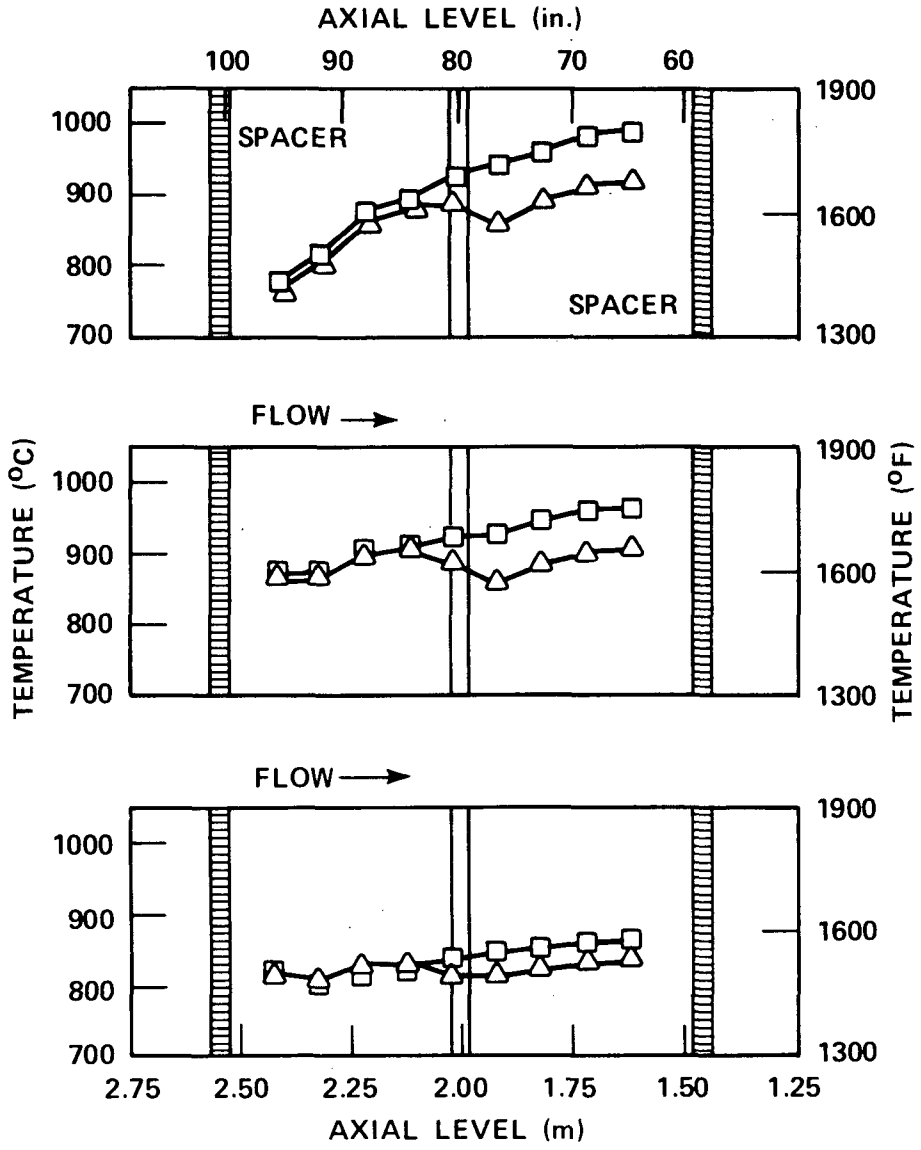

FLOODING RATE = 0.038 m/sec (1.5 in./sec)
SYSTEM PRESSURE = 0.21 MPa (30 psia)

△ TEST 223 (7 GRID SPACERS)

□ TEST 234 (6 GRID SPACERS, WITHOUT SPACER AT BUNDLE MIDPLANE)

Figure 3-3. 5x5 Rod Bundle: Influence of a Grid Spacer on Axial Cladding Temperature Transient With and Without Grid (FEBA Tests)

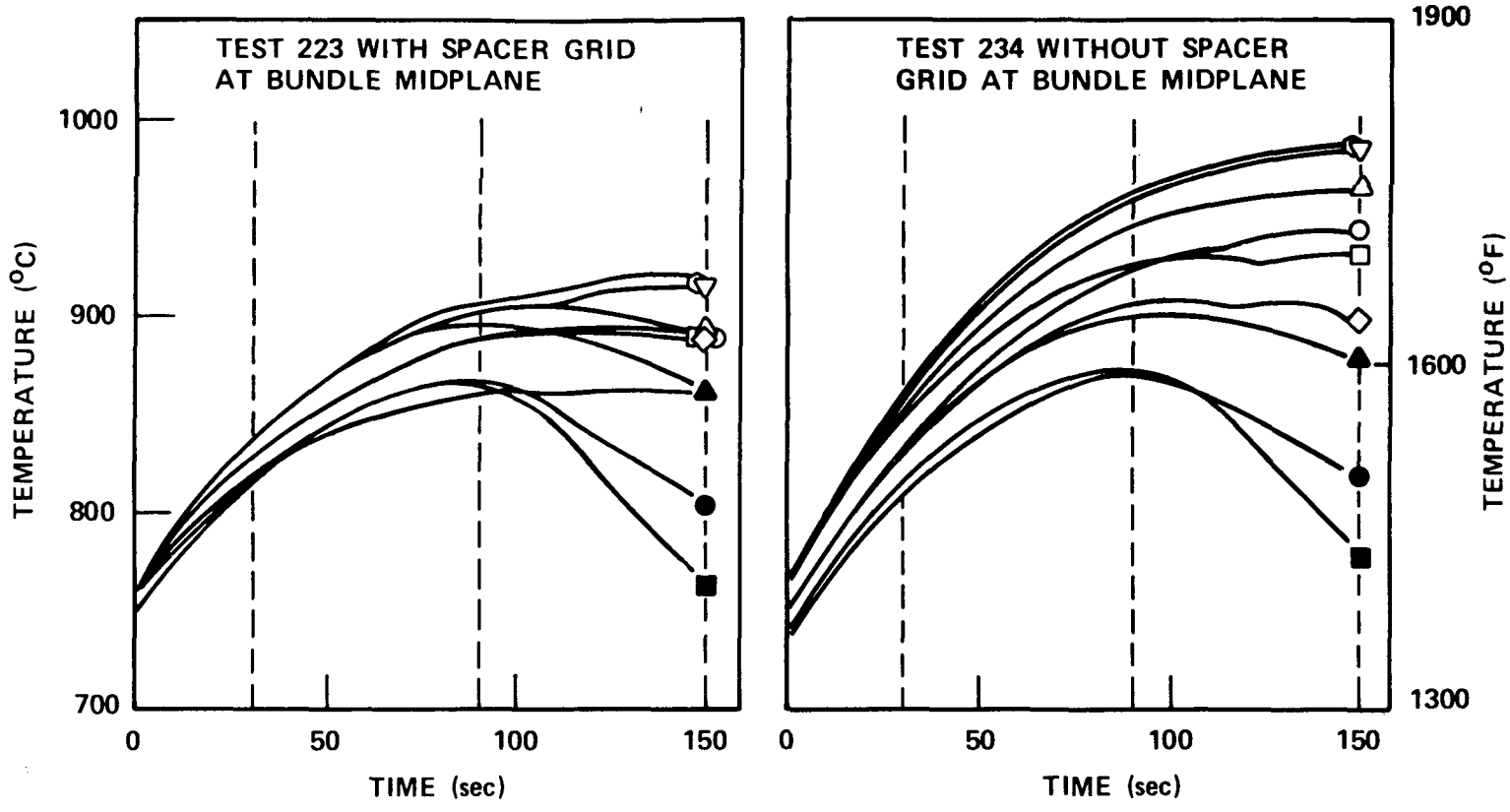

FLOODING RATE = 0.038 m/sec (1.5 in./sec)
SYSTEM PRESSURE = 0.21 MPa (30 psia)

AXIAL LEVEL:

- ○ 1.55 m (61 in.)
- ▽ 1.65 m (65 in.)
- △ 1.75 m (69 in.)
- ○ 1.85 m (73 in.)
- □ 1.95 m (77 in.)
- ◇ 2.05 m (81 in.)
- ▲ 2.15 m (85 in.)
- ● 2.25 m (89 in.)
- ■ 2.35 m (93 in.)

Figure 3-4. Cladding Temperature Transient With and Without Grid Spacer at Bundle Midplane [2.02 m (80 in.) Elevation] (FEBA Tests)

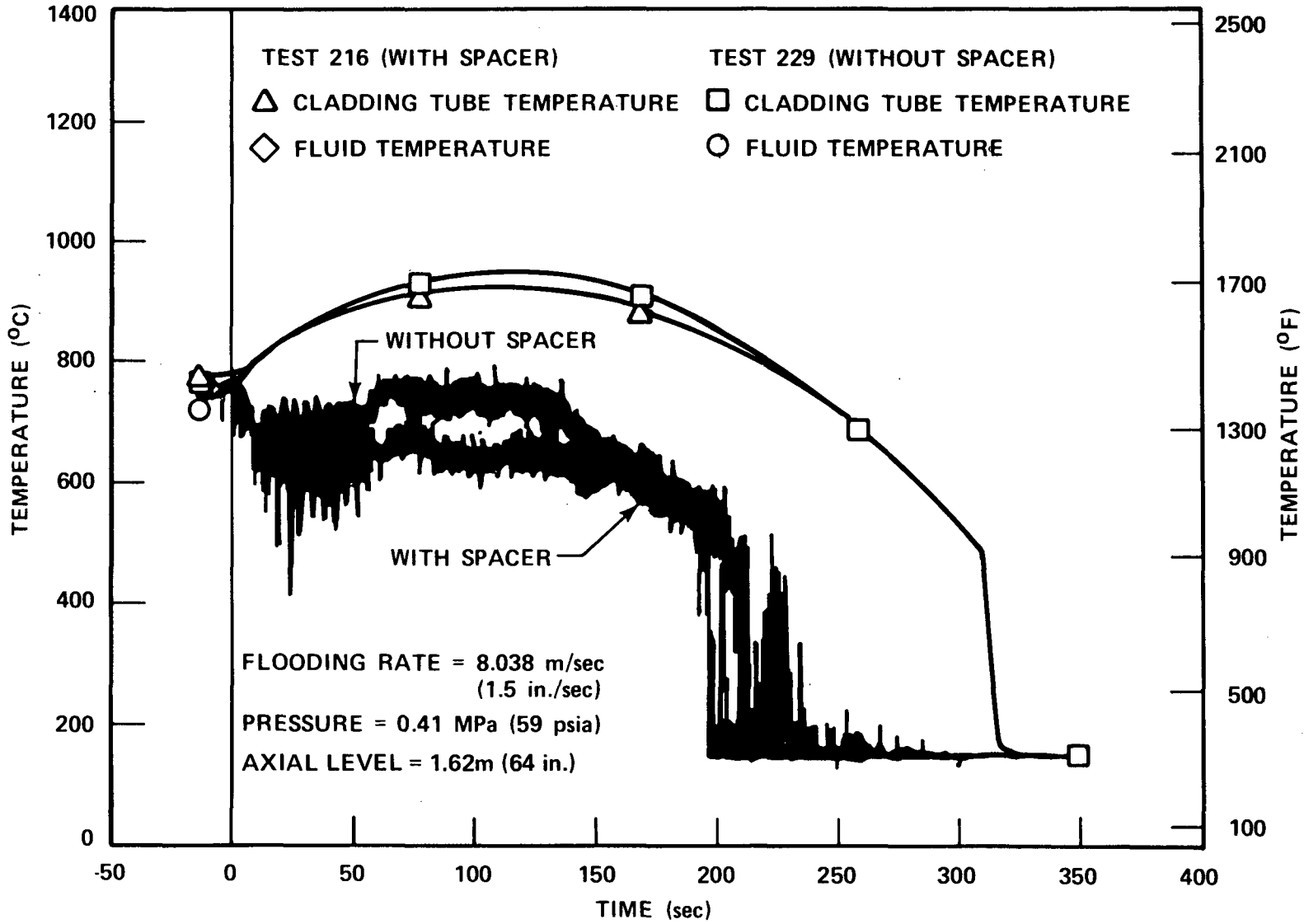

Figure 3-5. FEBA Vapor and Rod Temperatures With and Without Grid

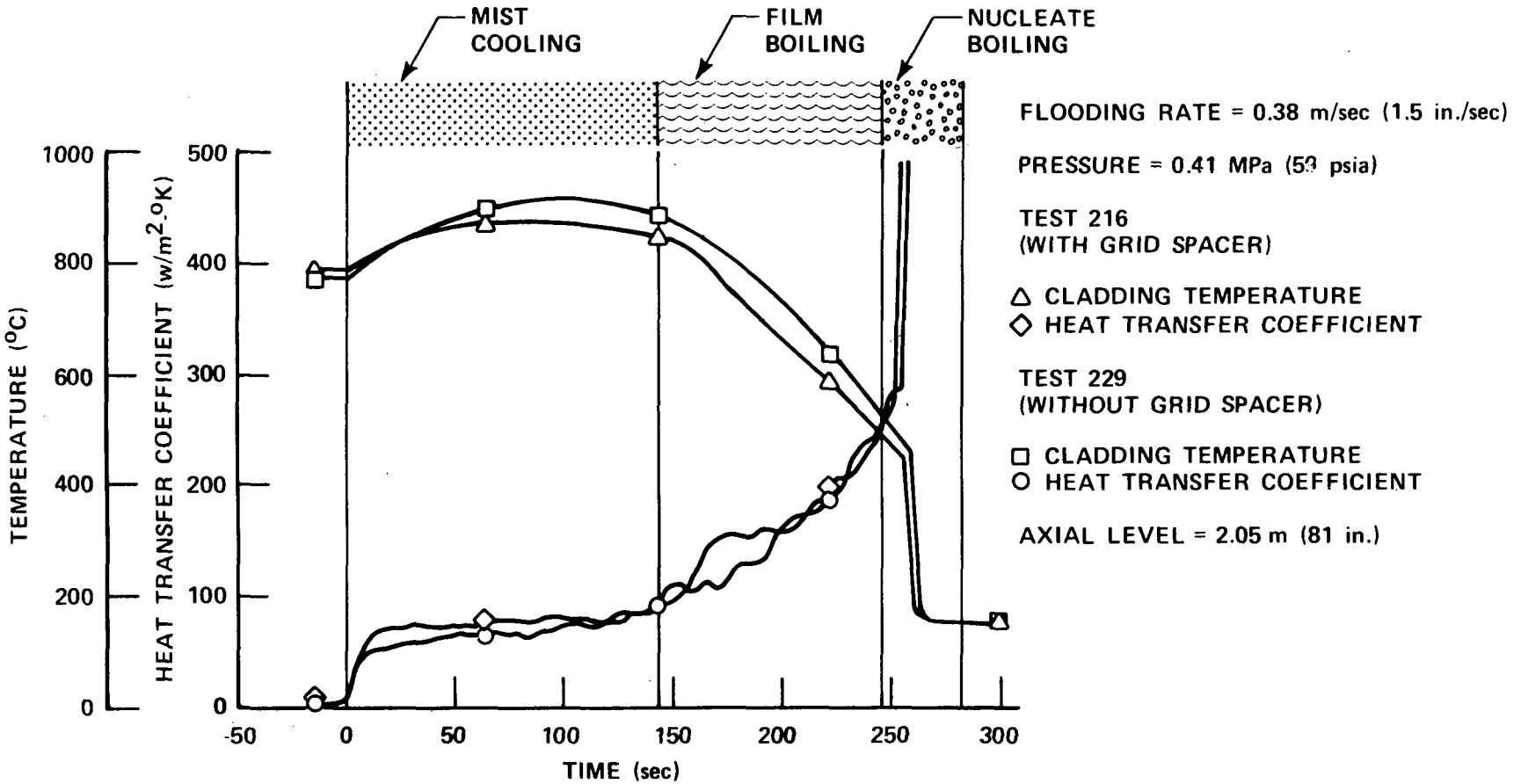

Figure 3-6. Cladding Temperature and Heat Transfer Coefficient Based on Saturation Temperature With and Without Grid Spacer at Bundle Midplane (FEBA Tests)

11509B-21

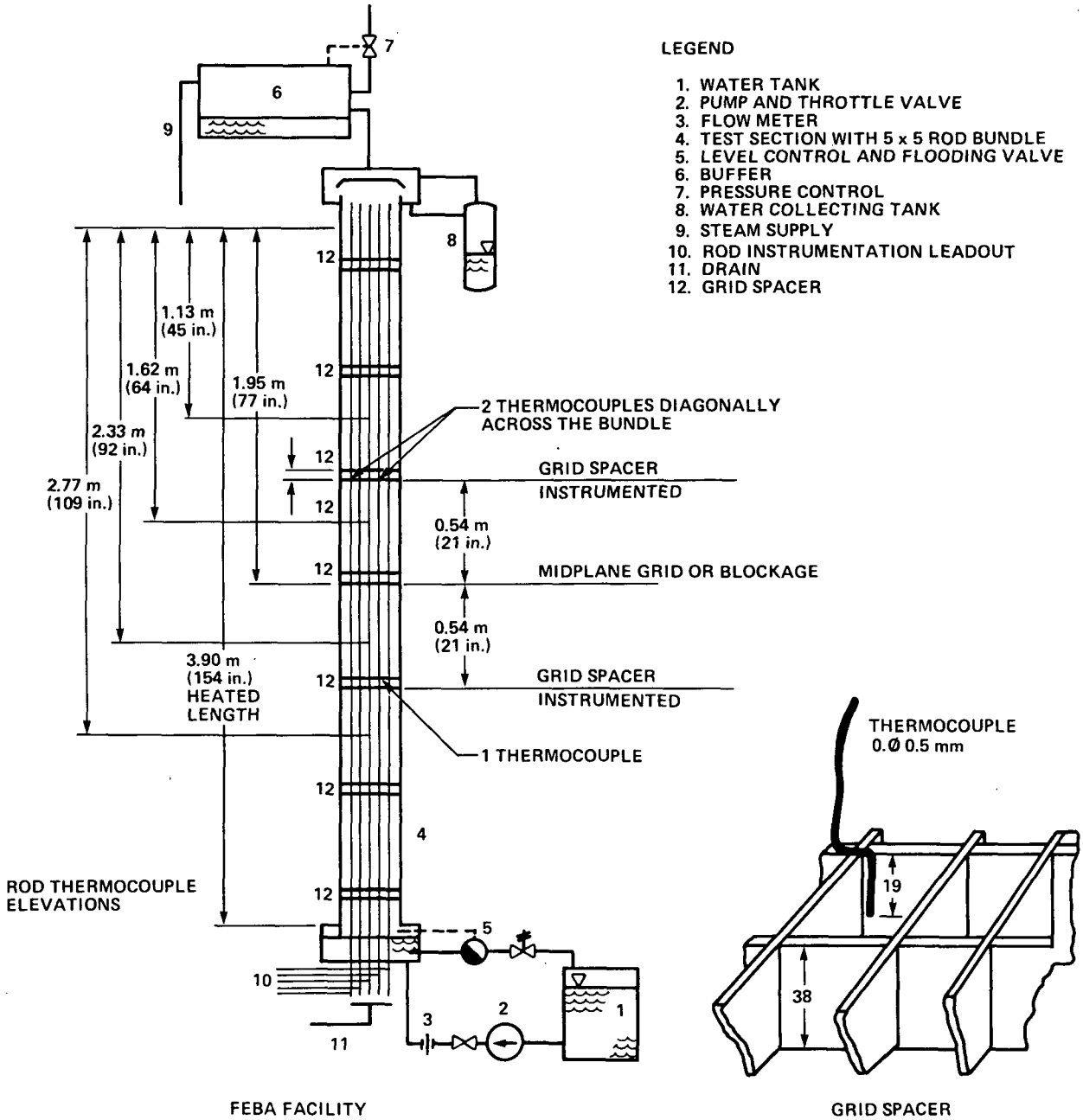

Figure 3-7. FEBA Grid Thermocouple Locations

3-7 also shows the orientation of the thermocouple on the grid -- at half the grid height.) Figure 3-8 shows the grid thermocouple response and heater rod thermocouple response upstream and downstream of the grid. Also shown are the measured vapor superheat temperatures upstream and downstream of the grid.

Prior to the time at which the grid thermocouple indicates quenching (about 150 seconds), the steam probe upstream of the grid quenched, indicating the arrival of the froth front at the elevation. Shortly afterward, the grid quenched and the vapor temperature downstream showed a significant temperature dip. This indicates that the additional interfacial heat transfer between the colder quenched grid and the superheated vapor was reducing the resultant vapor temperature downstream of the grid.

The normalized heat transfer coefficients downstream of the grid (heat transfer coefficient with spacer grid to heat transfer coefficient without spacer grid) indicat the magnitude and the trend of the grid's heat transfer performance. Figure 3-9 shows the normalized heat transfer coefficients versus reflood time for two axial levels, 0.1 and 0.4 m (4 and 16 in.) downstream of the midplane. The heat transfer coefficient ratios are plotted as well as the corresponding linear least-squares fit to the calculated ratio data. This figure shows a clear effect of the grid on the downstream heat transfer, and indicates that the presence of the midplane grid enhances the rod heat transfer downstream. The heat transfer enhancement downstream of a spacer grid is decreasing with increasing distance from the spacer.

Also, the data show that the most pronounced effect of the grid is at early times, when the grid is far from the quench and froth fronts. At these times, the total rod heat transfer is low, such that any incremental increase in heat transfer caused by the grid has a significant effect. The flow is very highly dispersed and nonequilibrium at these times. As the quench front moves toward the grid, the nonequilibrium decreases, and the overall heat transfer rate from the rod increases, such that the incremental grid effects are smaller.

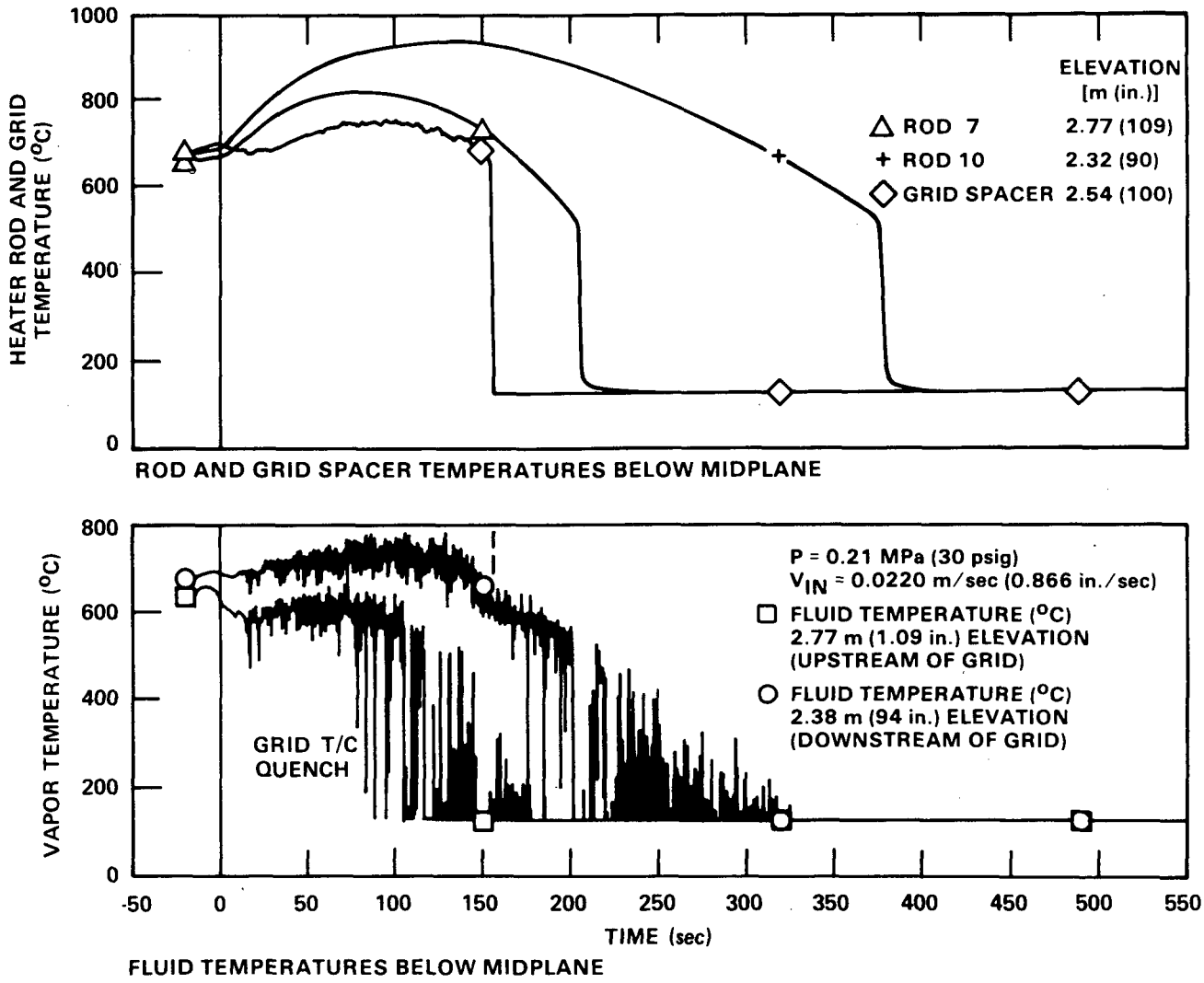

Figure 3-8. FEBA Rod, Grid, and Vapor Temperatures

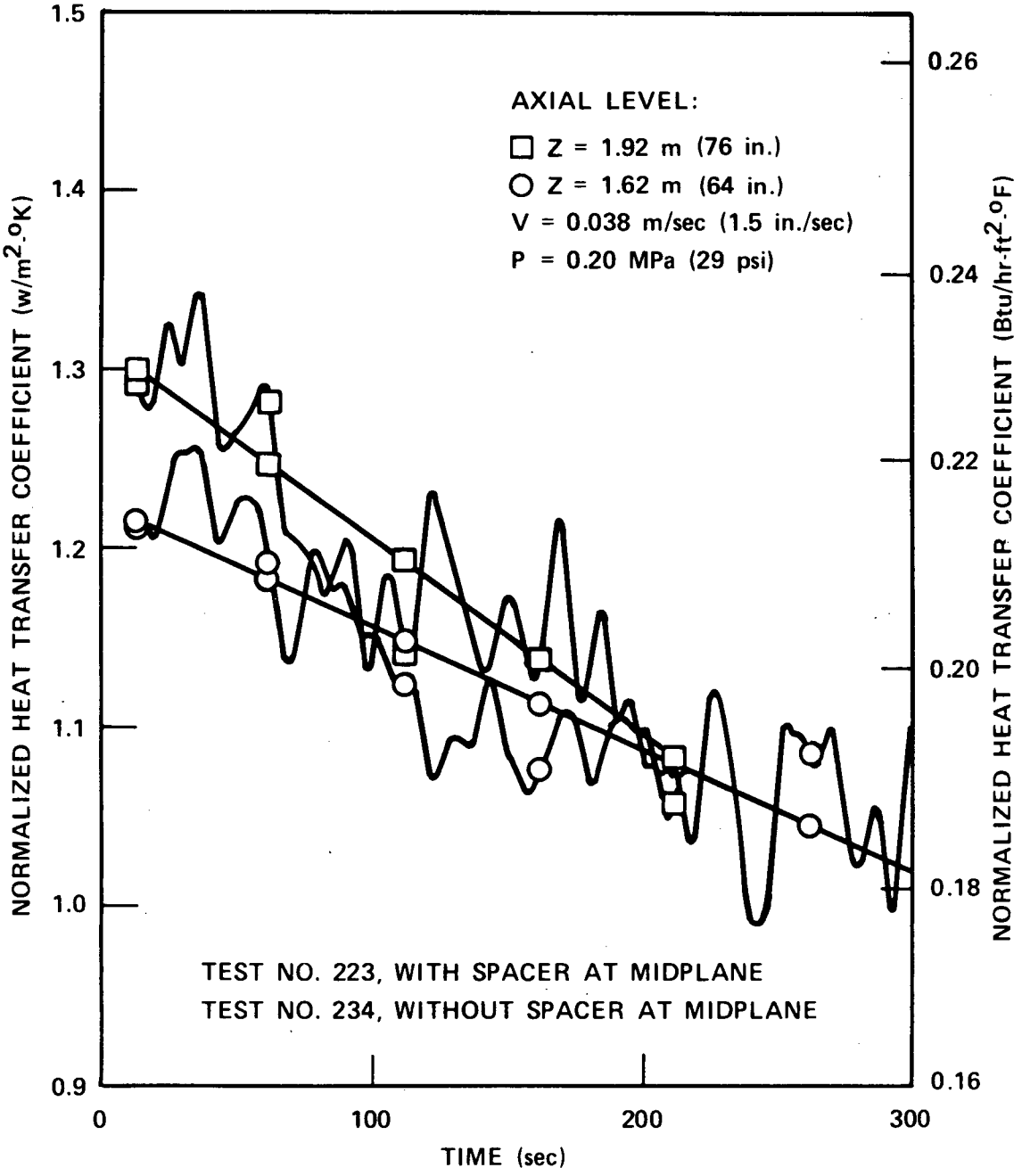

Figure 3-9. Normalized Heat Transfer Coefficients for Two Axial Levels Downstream of Bundle Midplane (FEBA Tests)

The Grenoble ERSEC tests examined the reflood heat transfer effect of three different grid types: a simple low pressure drop grid, a grid similar to a fuel assembly grid without mixing vanes, and a grid with simulated mixing vanes. The rod bundle had 36 full-length heaters of the Westinghouse 17x17 dimensions [9.50 mm (0.374 in.) diameter on a 12.6 mm (0.496 in.) pitch] with a chopped axial cosine power shape similar to that of the FLECHT tests (peak power/average power = 1.65). Figures 3-10 and 3-11 show the heater rod maximum temperature rise at each elevation for each grid type.

The Grenoble simulated mixing vane grids have a larger flow area blockage (because of the vanes) than either the Grenoble grid without vanes or the simple grid. As a result, the droplet breakup and convective enhancement is increased for the simulated mixing vane grid over the other two; this is reflected in the lower heater rod peak clad temperatures shown in figures 3-10 and 3-11.

Two specific tests in the FLECHT SEASET 161-rod bundle reflood program and the Westinghouse G-2 17x17 reflood tests were conducted at nearly identical inlet and initial conditions. Again, the Westinghouse G-2 17x17 reflood tests used production Westinghouse Inconel mixing vane grids; the FLECHT SEASET tests used standard FLECHT egg-crate grids. The Westinghouse production mixing vane grids have a higher projected flow area blockage (approximately 50 percent) than the FLECHT grids (25 percent), and the vanes are especially designed to mix the flow. Comparisons of data from the FLECHT SEASET and Westinghouse G-2 tests are shown in figures 3-12 and 3-13. The quench fronts are similar, but the G-2 data show a higher heat transfer coefficient. This difference, believed to be caused by the use of mixing vane grids rather than the simple FLECHT grids, is consistent with the Grenoble ERSEC results.

The effects of grid heat transfer have also been observed in clad ballooning experiments such as the REBEKA clad ballooning experiments[1] and the most recently completed NRU-MT-3 clad ballooning tests.[2] These experiments showed that, in two-phase dispersed flow, the grids promoted heat transfer downstream of the grid locally depressing the rod temperatures. In the ballooning experiments, the grids so reduced the temperatures downstream of the

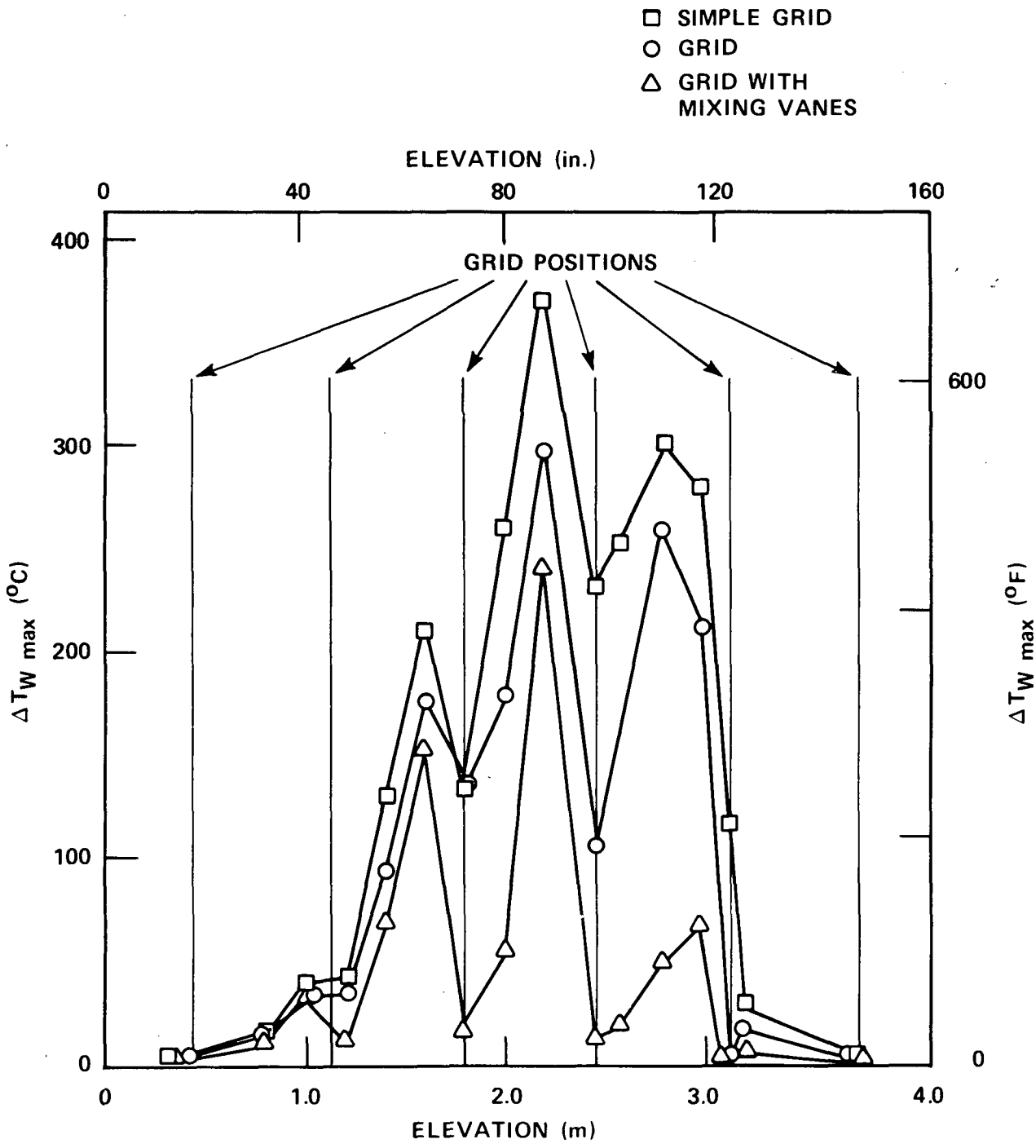

Figure 3-10. Comparison of $\Delta T_{w\ max}$ for Three Kinds of Spacer Grids at High Inlet Mass Velocity (ERSEC Tests)

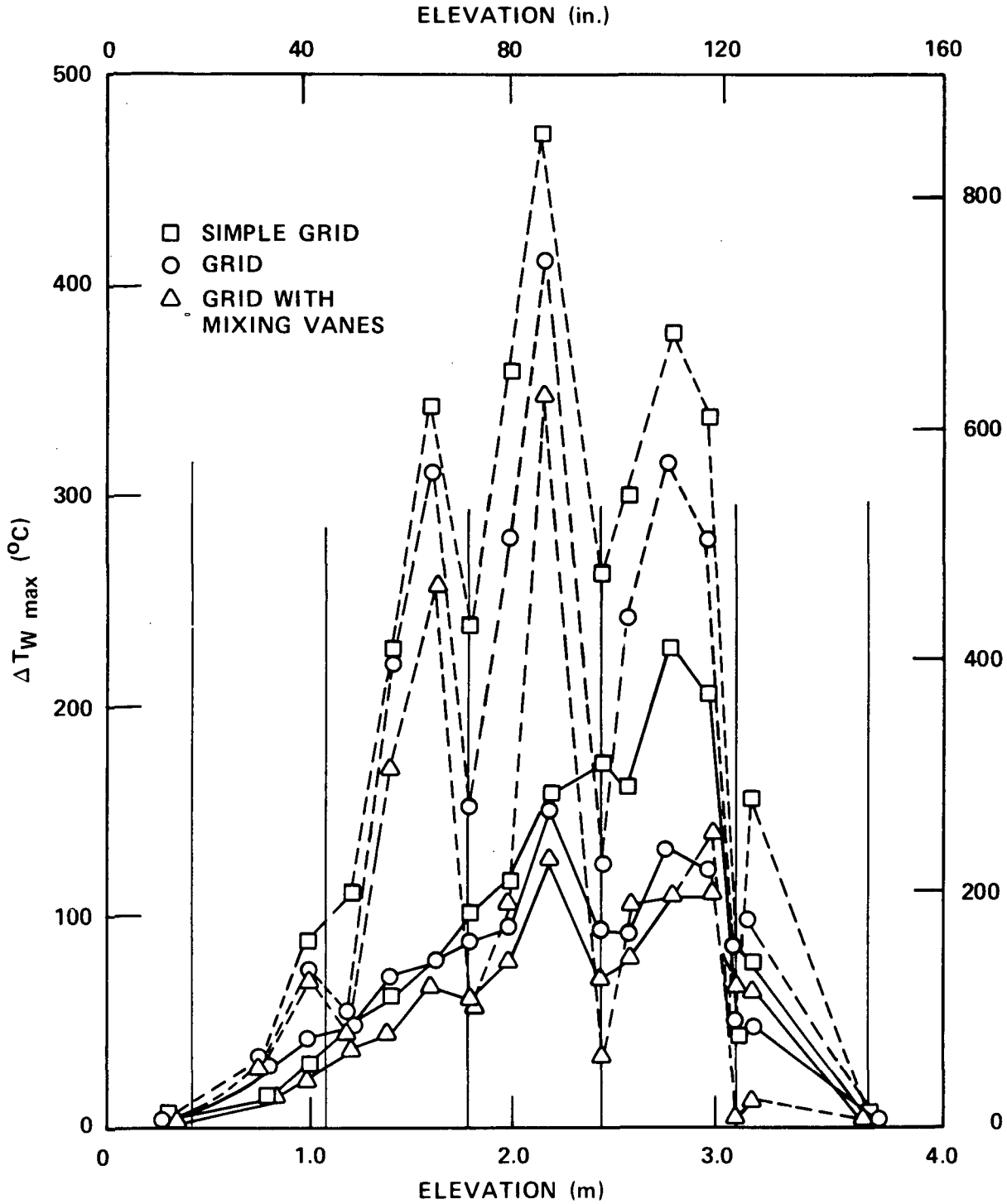

Figure 3-11. Comparison of $\Delta T_{w\ max}$ for Three Kinds of Spacer Grids at P = 0.1 and 0.6 MPa (15 and 87 psia) (ERSEC Tests)

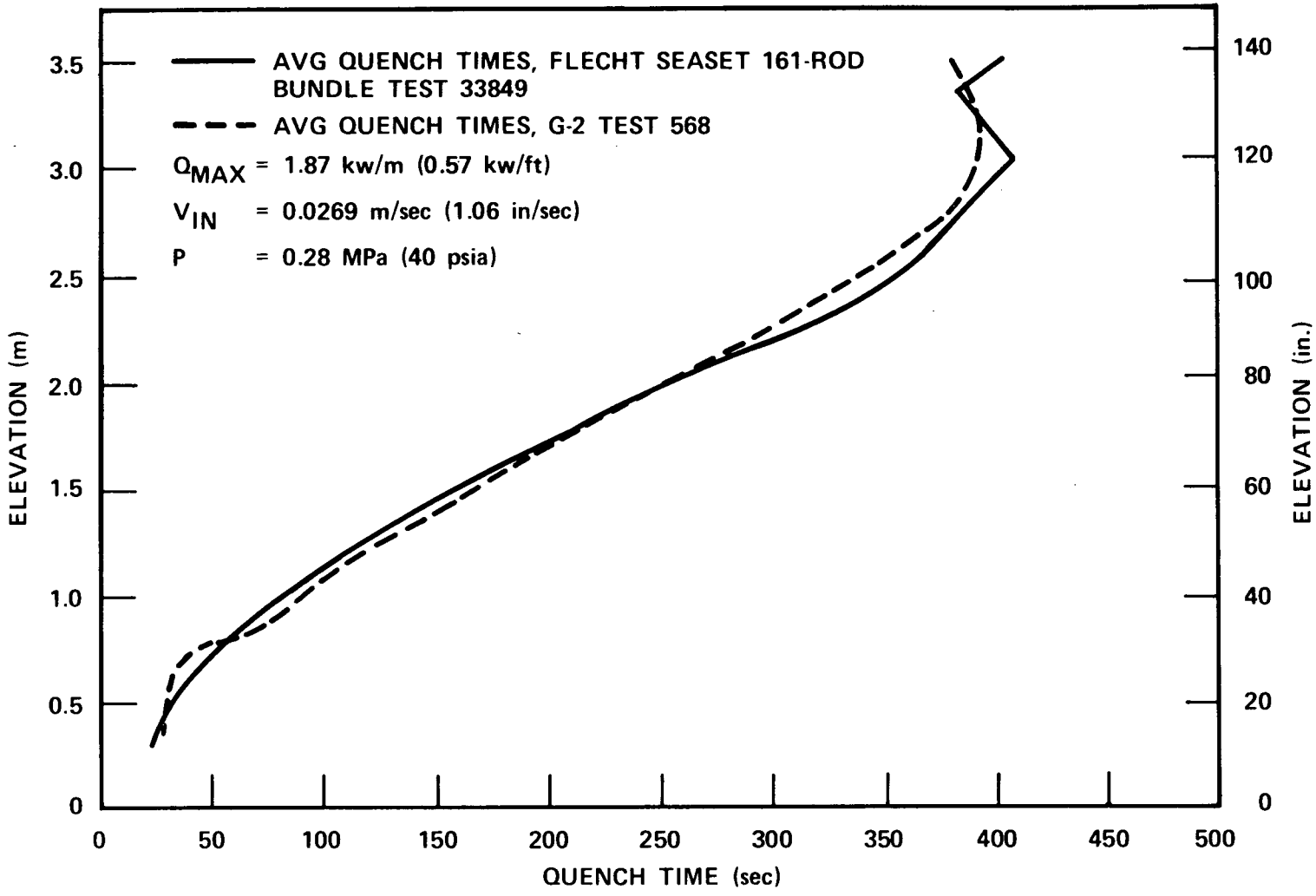

Figure 3-12. Comparison of Westinghouse G-2 and FLECHT SEASET Quench Fronts

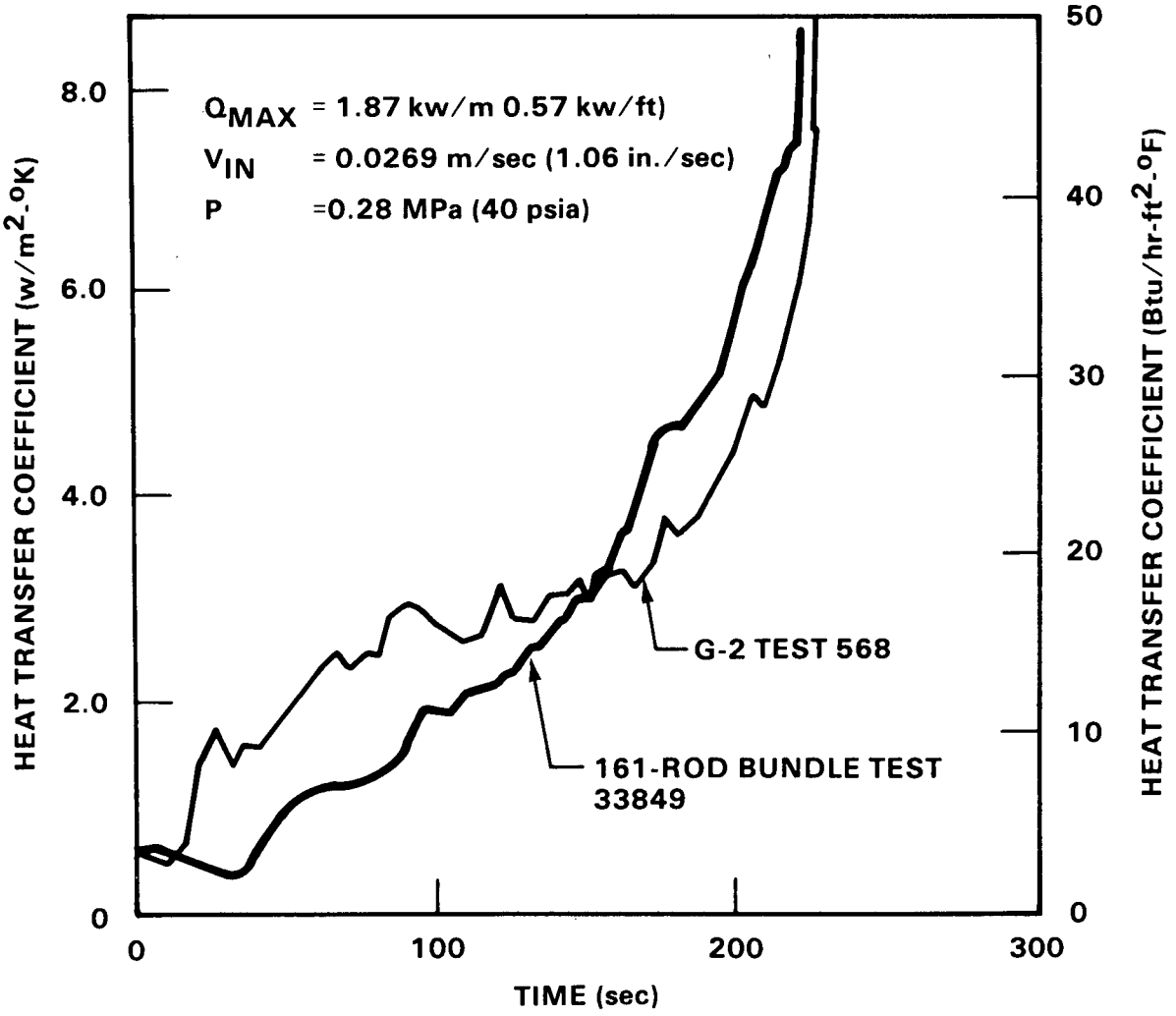

Figure 3-13. Comparison of FLECHT SEASET 161-Rod Bundle Heat Transfer Coefficient and Westinghouse G-2 Heat Transfer Coefficient at Midplane

grid that the strain moved up the rod toward the next higher grid. This axially skewed strain profile was quite apparent in the NRU-MT-3 tests. Therefore, to accurately model two-phase flow situations such as REBEKA and NRU tests, a two-phase grid heat transfer model is necessary.

3-2. GRID HEAT TRANSFER MODELS

The following paragraphs describe the individual grid heat transfer models originally developed for the BART[3] code which have been adapted for COBRA-TF. Three grid heat transfer models have been included:

- o Convective enhancement
- o Grid rewet
- o Droplet breakup

Because of the increased turbulence downstream of a grid, convective enhancement affects the single-phase vapor heat transfer coefficient. The other two grid models, rewet and droplet breakup, locally enhance the interfacial heat transfer between the liquid and superheated vapor. This enhanced interfacial heat transfer removes heat from the vapor and thereby desuperheats the vapor, which results in a source of saturated vapor downstream of the grid. For the upper regions of a rod bundle during a reflood simulation, the vapor and rod temperatures have been overpredicted by COBRA-TF in the past. The inclusion of grid models that decrease the vapor superheat has dramatically improved COBRA-TF temperature predictions for the upper elevations of the rod bundle.

---

1. Erbacher, F., et al., "Interaction Between Thermohydraulics and Fuel Ballooning in a LOCA: Results of REBEKA Multirod Burst Tests With Flooding," presented at Sixth Water Reactor Safety Research Information Meeting, November 6-9, 1978, Gaithersburg, MD.

2. Mohr, C. L., et al., "LOCA Simulation in NRU Material Test 3 Industry Review," presented at NRC-sponsored meeting, Silver Spring, MD, March 3, 1982.

3. Chiou, J., et al., "Models for PWR Reflood Calculations Using the BART Code," WCAP-10062, 1982.

3-3. Single-Phase Heat Transfer Enhancement

The flow acceleration and consequent deceleration as the coolant flows past a grid spacer will cause a local increase in heat transfer rates downstream because of the creation of free steam turbulence and the separation and re-establishment of the boundary layer. Correlations for local Nusselt numbers at and downstream of grids have been published by Hassan and Rehme:[1]

$$\frac{Nu_x}{Nu_o} = K\,(Re,\ a_r)\ \left(\frac{x}{D_h\ Re\ Pr}\right)^{m(Re,\ a_r)} \qquad (3\text{-}1)$$

and by Yao, Hochreiter, and Leech:[2]

$$\frac{Nu_x}{Nu_o} = 1 + 5.55\ a_r^{\,2}\ \exp(-0.13\ x/D_h) \qquad (3\text{-}2)$$

where a_r = the fraction of the subchannel blocked by the grid.

The correlation published by Yao, Hochreiter, and Leech has a relatively simple form for egg-crate grids and was developed for $Re>10^4$, $0.256<a_r<0.348$, and a variety of configurations including single rods.

A comparison has been made between the predictions of these two correlations and data from the FLECHT SEASET 21-rod bundle tests with steam cooling.[1] To minimize uncertainties due to bundle edge effects, the comparison was limited to data from the inner nine rods. A survey of the bundle instrumentation revealed that the comparison could best be made using the thermocouples on

---

1. Hassan, M. A., and Rehme, K., "Heat Transfer Near Spacer Grids in Gas-Cooled Rod Bundles," Nucl. Techn. 52, 1982, 401-414.

2. Yao, S. C., et al., "Heat Transfer Augmentation in Rod Bundles Near Grid Spacers," J. Heat Transfer 104, 1982.

rods 3B and 3D at elevations of 2.02, 2.17, and 2.32 m (79.4, 85.3, and 2.32 m (79.4, 85.3, and 91.4 in.), since a grid is located at a nominal elevation of 2.11 m (83 in.). The heat transfer at these locations was normalized to 1.98 m (78 in.), which is upstream of the grid. The results of this comparison are shown in table 3-1. A grid blockage factor of 0.35 was used which corresponds to the average value for the inner nine rod subchannels. (The blockage area of the grid steam probes is added to that of the grid.)

On the basis of the data available at present it appears that the correlation of Yao, Hochreiter, and Leech provides a better fit to the data. Note that the data do not indicate any dependence on Reynolds number. It should also be noted that there was additional experimental confirmation of this correlation in the original paper.

3-4. GRID REWET MODEL

Experimental data indicate that grid spacers are responsible for significant cooling of the vapor flowing past them during the dispersed flow portion of bottom reflood. The increased interfacial heat transfer that would result from a liquid film on the surface of the grid spacer is one means of desuperheating the vapor.

In contrast to the surrounding heater rods, a grid spacer has no internal heat generation and contains little stored energy. It is likely that impinging droplets would cool the grid and begin to form a film. A grid quench front model is included in COBRA-TF to determine the fraction of the grid covered by such a liquid film.

The quenching of a grid is similar to the classical falling film quench problem. The fine-mesh rezoning quench front model used for heater rods in

---

1. Loftus, M. J., et al., "PWR FLECHT SEASET 21-Rod Bundle Flow Blockage Task Data and Analysis Report," NRC/EPRI/ Westinghouse-11, September 1982.

TABLE 3-1
SINGLE-PHASE STEAM COOLING DATA,
FLECHT SEASET 21-ROD BUNDLE TESTS

Test	Predicted Value		Actual Value	
	Hassen and Rehme	Yao, Hochreiter, and Leech	Rod 3B	Rod 3D
44303A, Re(78") = 14,000				
Nu(84")/Nu(78")	1.26	1.36	1.36	1.30
Nu(90")/Nu(78")	1.10	1.06	1.11	1.09
44401A, Re(78") = 6,100				
Nu(84")/Nu(78")	1.63	1.36	1.36	1.32
Nu(90")/Nu(78")	1.00	1.06	1.09	1.07

COBRA-TF could also be used for the grid spacers, but the cost of calculating a fine-mesh rezoning quench front for each grid spacer is prohibitive. Instead, a simple two-region model is used to determine the fraction of the grid quenched.

Two regions are defined by the location of the quench front on the grid spacer. Below the grid quench front, in the the wet region, the grid spacer and the liquid film are at the saturation temperature. Above the quench front, a dry region exists with the grid temperature close to that of the heater rods. An example of a quench front on a grid spacer with the two-region model is shown in figure 3-14.

3-5. Dry Region Heat Balance -- A heat balance is used to determine the transient temperature response of the dry region:

$$\frac{P_g}{A_c}\left(q''_{rad} - q''_{conv} - q''_{dcht}\right) = \rho Cp \frac{\partial T}{\partial t} \underline{G} \qquad (3\text{-}3)$$

where

T_G = dry grid temperature
A_c = 1/2 $\delta \cdot P_g$ (cross-sectional area/2)
P_g = perimeter of grid strap
δ = grid half thickness
q''_{rad} = radiation heat flux from the heater rods and vapor
q''_{conv} = vapor convective heat flux
q''_{dcht} = heat flux due to drop contact

The radiation heat fluxes include the heat flux from rod to grid and from vapor to grid. A simple enclosure model is used to represent a grid subchannel, as shown in figure 3-15. The geometry of the enclosure is chosen to make the view factors a simple function of rod diameter and pitch:

$$F_{11} = 0,\ F_{12} = 1,\ F_{21} = d1/d2,\ F_{22} = 1 - \frac{d1}{d2} \qquad (3\text{-}4)$$

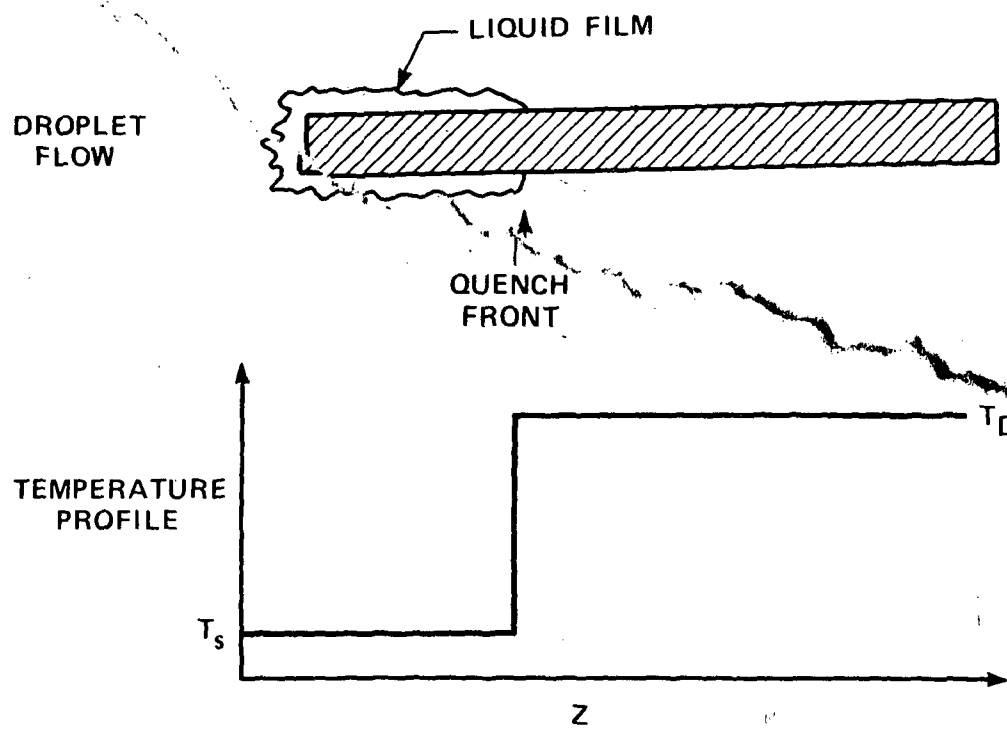

Figure 3-14. Two-Region Grid Quench and Rewet Model

where

D_1 = rod diameter
D_2 = rod pitch

and d_1, d_2 are as shown in figure 3-15.

An expression for the radiant heat flux to the grid can be derived from an equivalent resistance network of the enclosure (figure 3-16):

$$q''_2 = \frac{B_2 - \sigma T_2^4}{A_2 R_{22}} = \frac{B_1 - B_2}{A_2 R_{21}} + \frac{\sigma T_3^4 - B_2}{A_2 R_{23}} \qquad (3\text{-}5)$$

Radiation heat flux to the rod is expressed in the same manner:

$$q''_1 = \frac{B_1 - \sigma T_1^4}{A_1 R_{11}} = \frac{B_2 - B_1}{A_1 R_{12}} + \frac{\sigma T_3^4 - B_1}{A_1 R_{13}} \qquad (3\text{-}6)$$

where

B_1 = black body radiosity of rod (Btu/hr-ft^2)
B_2 = black body radiosity of grid (Btu/hr-ft^2)
A_1 = surface area of rod (ft^2)
A_2 = surface area of grid (ft^2)
T_1 = rod temperature (°R)
T_2 = grid temperature, dry region (°R)
T_3 = vapor temperature (°R)
s = Stefan-Boltzman constant = 0.1714×10^{-8} (Btu/hr-ft^2-°R^4)
$R_{11} = (1-\varepsilon_1)/A_1\varepsilon_1$ (ft^{-2})
$R_{22} = (1-\varepsilon_2)/A_2\varepsilon_2$ (ft^{-2})
$R_{12} = R_{21} = (A_1 F_{12}(1-\varepsilon_3))^{-1}$ (ft^{-2})
$R_{13} = (A_1\varepsilon_3)^{-1}$ (ft^{-2})

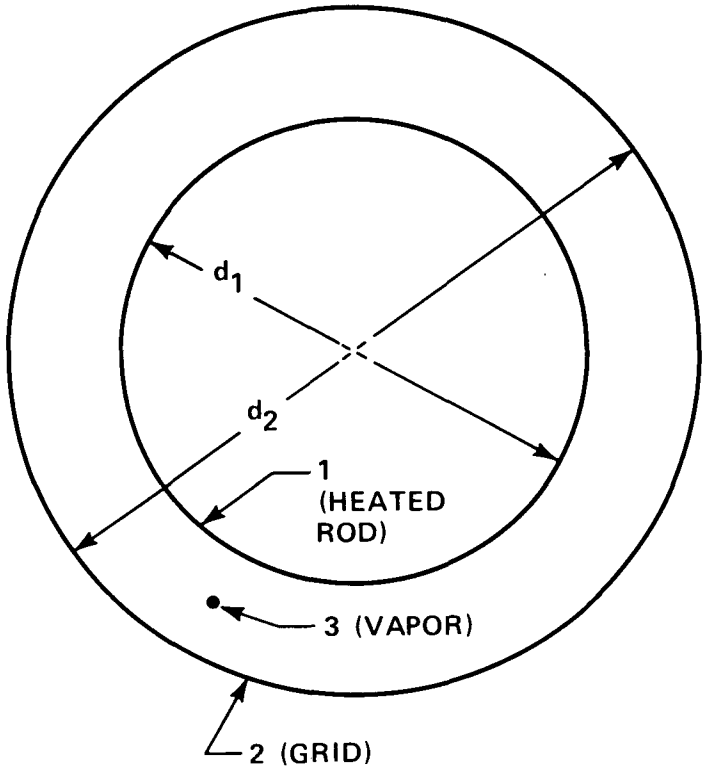

Figure 3-15. Equivalent Radiation Enclosure Model for a Grid Subchannel

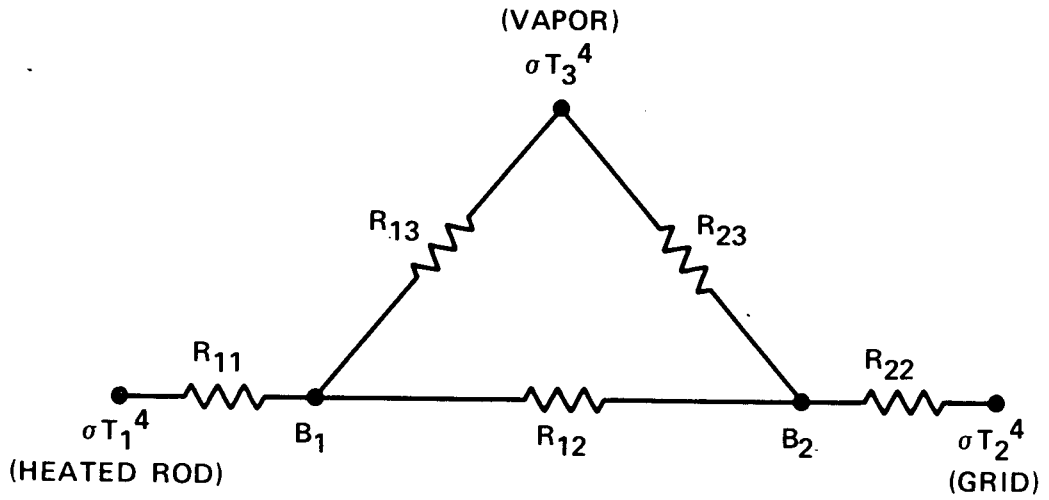

Figure 3-16. Radiation Heat Flux Network

$R_{23} = (A_2\varepsilon_3)^{-1}\ (ft^{-2})$

ε_1 = emissivity of rod = 0.9

ε_2 = emissivity of grid = 0.9

ε_3 = emissivity of vapor

Emissivity of the vapor is calculated using the Plank mean absorption coefficient as reported by Abu-Romia:[1]

$$A_v = 2.146\ e^{[-0.344523221 - (2.96092004\times10^{-3} - 0.444073925\times10^{-6}\ T_v)\ T_v]} \qquad (3\text{-}7)$$

where

A_v = mean absorption coefficient for water vapor $(psi\text{-}ft)^{-1}$

T_v = vapor temperature (°K)

Vapor emissivity is given by

$$E_3 = 1.0 - e^{-A_v \cdot P \cdot L_M} \qquad (3\text{-}8)$$

where

P = pressure (psi)

L_M = mean beam length (ft) = 0.9 • channel hydraulic diameter

To find the radiation heat flux to the grid spacer, equation (3-6) is solved for the black body radiosity of the grid spacer as

$$B_2 = \left(\frac{B_1 - \sigma T_1^4}{A_1\ R_{11}} - \frac{\sigma T_3^4 - B_1}{A_1\ R_{13}} \right) A_1\ R_{12} + B_1 \qquad (3\text{-}9)$$

---

1. Sparrow, E. M., and Cess, R. D., Radiation Heat Transfer, McGraw-Hill, New York, 1977, 231.

Substitution of equation (3-9) for black body radiosity of the grid spacer into equation (3-5) gives the black body radiosity of the rod. After a series of algebraic manipulations, equation (3-5) becomes

$$B_1 = \frac{C_1\ \sigma T_1^4 + C_2\ \sigma T_2^4 + C_3\ \sigma T_3^4}{C_4} \qquad (3\text{-}10)$$

where the coefficients are

$$C_1 = A5\ (A_1R_{12})(A_1R_{13})$$

$$C_2 = (A_1R_{11})(A_1R_{13})(A_2R_{21})(A_2R_{23})$$

$$C_3 = (A_1R_{11})\{(A_1R_{13})(A_2R_{21})(A_2R_{22}) + (A_1R_{12})\ A5\}$$

$$C_4 = (A_1R_{11})(A_1R_{13})(A_2R_{21})[(A_2R_{23} + A_2R_{22})] + (A_1R_{12})[(A_1R_{13})A5 + (A_1R_{11})\ A5]$$

$$A5 = (A_2R_{21})(A_2R_{23}) + (A_2R_{22})(A_2R_{23} + A_2R_{21})$$

The black body radiosity of the rod is now a function of temperature, surface area, and emissivity and can be evaluated. Knowing the black body radiosity of the rod, the black body radiosity of the grid spacer is calculated using equation (3-9). From equation (3-5), the radiation heat flux to the dry region of grid spacer is

$$q''_{rad} = q''_2 = \frac{B_2 - \sigma T_2^4}{A_2\ R_{22}} \qquad (3\text{-}11)$$

The heat transfer coefficient for convection from the rod to the vapor is used to calculate convection from the dry region of the grid spacer to the vapor.

$$q''_{conv} = h\ (T_G - T_v) \qquad (3\text{-}12)$$

where

q''_{conv} = heat transfer from dry region of grid spacer (Btu/hr-ft^2)
h = heat transfer coefficient from rod to vapor (Btu/hr-ft^2-°F)
T_G = temperature of grid dry region (°F)
T_v = vapor temperature (°F)

Each grid spacer is assumed to be at the top of the continuity cell (center of the momentum cell) in which it is located. Therefore the rod convective heat transfer coefficient used is the one at the topmost fine-mesh node in the continuity cell containing the grid spacer.

Lateral migration of drops due to turbulence will cause deposition on the surface of the dry region. The resulting drop contact heat transfer is estimated by

$$q''_{dcht} = S_{DE} \cdot h_{fg} \cdot \eta \qquad (3\text{-}13)$$

where

S_{DE} = lateral deposition rate[1]
η = fraction of droplet evaporated = $\exp [1 - (T_G/T_f)^2]$

The lateral deposition rate can be calculated as

$$S_{DE} = k_D \cdot C \qquad (3\text{-}14)$$

where

k_D = deposition coefficient

$$= 0.102 \left(\frac{\mu_V}{D_H \sigma \rho_\ell}\right)^{1/2} \left(\frac{f}{2}\right)^{1/2} \left(\frac{G_v}{\rho_v}\right) \quad (3\text{-}15)$$

C = droplet concentration

$$= \rho_v \left(\frac{G_d}{G_V}\right) \quad (3\text{-}16)$$

G_d, G_V = droplet and vapor mass flux values

The dry grid temperature is then determined by a balance between radiation [equation (3-11)], convection [equation (3-12)], and drop contact heat transfer [equation (3-13)]. Initially, the grid temperature is set to the average of the surrounding rods surface temperature. During a reflood transient, the dry grid temperature is usually between that of the vapor and heater rods.

3-6. Wet Region Heat Balance -- In a similar manner, a heat balance is calculated for the wet portion of the grid spacer. Water droplets impinging on the grid will be added to the liquid film and may be available to promote further quenching. If, however, the liquid deposition rate is less than the evaporation rate due to radiation and interfacial heat transfer, the liquid film and quench front will recede. All the drops flowing within the projected area of the grid are assumed to be captured. Thus,

$$\dot{m}_{DE} = \left(\frac{A_G}{A_c}\right) \dot{m}_E \quad (3\text{-}17)$$

where

$\dot{m}_{DE}$ = liquid deposition rate

$\dot{m}_E$ = entrained liquid flow rate

A_G = grid projected area

A_c = channel flow area

For the grid quench front to advance, more liquid must be deposited compared to that which is evaporated; that is,

$$\dot{m}_{DE} > \dot{m}_{EVAP} \tag{3-18}$$

where

$\dot{m}_{EVAP}$ = liquid evaporation rate

$$\dot{m}_{EVAP} = (q''_{radw} + q''_I) \cdot P_G \cdot f_q \cdot L_G/h_{fg} \tag{3-19}$$

q''_{radw} = radiant heat flux from rods to wet region of grid

q''_I = interfacial heat transfer from superheated vapor to film

P_G = grid perimeter

f_q = fraction of grid quenched

L_G = grid length

To calculate the radiation heat flux to the wet region of the grid, the saturation temperature is used and it is assumed that the liquid emissivity is equivalent to the emissivity of the grid spacer. Equation (3-10) becomes

$$BW_1 = \frac{C_1\ \sigma T_1^{\,4} + C_2\ \sigma T_2^{\,4} + C_3\ \sigma T_3^{\,4}}{C_4} \tag{3-20}$$

where

T_f = saturation temperature (°R)

BW_1 = black body radiosity of rod for wet region of grid spacer ($Btu/hr\text{-}ft^2$)

The black body radiosity of the wet region of the grid spacer is calculated using equation (3-10) with appropriate changes for the wet region:

$$BW_2 = \left(\frac{BW_1 - \sigma T_{sat}^4}{A_1 R_{11}} - \frac{\sigma T_3^4 - BW_1}{A_1 R_{13}} \right) A_1 R_{12} + BW_1 \qquad (3\text{-}21)$$

Radiation heat flux to the wet region of the grid spacer is simply

$$q''_{radw} = \frac{BW_2 - \sigma T_{sat}^4}{A_2 R_{22}} \qquad (3\text{-}22)$$

The radiation heat flux to or from the grid spacer is only used to determine the maintainability of a liquid film; heat is not transferred to or from the rods.

Interfacial heat transfer between the vapor and the liquid film is expressed

$$q''_I = h_{conv} (T_v - T_f) \qquad (4.18)$$

The vapor convective heat transfer coefficient, h_{conv}, is calculated using the fluid conditions at the top of the continuity cell and the correlations from paragraph 2-9. Both the heat removed from the vapor and the consequent vapor generation are accounted for in the hydrodynamic solution.

3-7. Quench Front Model

If the liquid deposition rate exceeds the evaporation rate in equation (3-18), the grid quench front will advance. The rate of advancement will be limited by both the physics of quench front propagation and the availability of water. Quenching of a thin plate by a liquid film is well described by the two-region analytical conduction solution of Yamanouchi.[1]

1. Yamanouchi, A., "Effect of Core Spray Cooling in Transient State After Loss-of-Cooling Accident," J. Nucl. Science and Technology 5, 11, 1968, 547-558.

The quench front velocity is limited by the heat conduction rate from the dry (hot) region to the wet (cold) region and is given by

$$V_Q = \left\{ \frac{\rho_G \, Cp_G}{2} \left(\frac{\delta}{h_w \, k_g} \right)^{1/2} \left[\left(1 + 2 \, \frac{T_G - T_w}{T_w - T_f} \right)^2 - 1 \right]^{1/2} \right\}^{-1} \quad (3\text{-}24)$$

where

V_Q = grid quench velocity
ρ_G = density of grid material
Cp_G = specific heat of grid material
k_G = thermal conductivity of grid material
δ = grid half thickness
T_G = temperature of dry region
T_w = rewet temperature
h_w = wet region heat transfer coefficient

Equation (3-24) contains two adjustable parameters, h_w and T_w. The heat flux at the quench front, where the temperature is T_w, should be at its maximum value. As a physically reasonable maximum, h_w is set to

$$h_w = \frac{q''_{CHF}}{T_w - T_f} \quad (3\text{-}25)$$

where q''_{CHF} is determined using the Zuber pool boiling critical heat flux correlation.[1] Using the above value for h_w and the rewet temperature recommended by Yamanouchi [260°C (500°F)] has been shown to provide a good prediction of falling film quench data.

The quench front velocity is further constrained by the availability of water to remove the stored energy during quenching. The water remaining after evaporation by radiation and interfacial heat transfer is

1. Zuber, N. et al., "The Hydrodynamic Crisis in Pool Boiling of Saturated and Subcooled Liquids," in International Developments in Heat Transfer, International Heat Transfer Conference, Boulder, CO, 1961, 230-236.

$$\dot{m}_R = \dot{m}_{DE} - (q''_{radw} + q''_I)\, P_G \cdot f_q \cdot L_G / h_{fq} \qquad (3\text{-}26)$$

However, only a fraction of this water can be evaporated at the quench front; the remainder will be blown off the grid surface because of sputtering. The amount that can be evaporated is estimated by

$$\dot{m}_{QF} = \dot{m}_R \cdot \exp\left[1 - \left(\frac{T_G}{T_f}\right)\right]^2 \qquad (3\text{-}27)$$

Therefore, the amount of stored energy removed at the quench front cannot exceed the product of $\dot{m}_{QF}$ and the latent heat, h_{fg}.

This result is used to limit the value of h_w and hence the quench velocity. The stored energy release is limited as

$$\dot{m}_{QF}\, h_{fg} \geq (\rho Cp\ A)_G \cdot V_Q \cdot (T_G - T_f) \qquad (3\text{-}28)$$

or, solving for the quench velocity, V_Q,

$$V_Q \leq \frac{\dot{m}_{QF}\, h_{fg}}{(\rho Cp\ A)_G \cdot (T_G - T_f)} \qquad (3\text{-}29)$$

Substituting equation (3-29) into equation (3-24) indicates that h_w is limited as

$$h_w \leq \left(\frac{\delta}{4k_g}\right)\left(\frac{\dot{m}_{QF}\, h_{fg}}{P_g\, \delta (T_G - T_f)}\right)^2 \left[\left(2\,\frac{T_G - T_w}{T_w - T_f} + 1\right)^2 - 1\right] \qquad (3\text{-}30)$$

The heat transfer coefficient used to determine quench front velocity is the maximum of the coefficient calculated in equation (3-30) and the coefficient calculated by the Zuber correlation for critical heat flux, equation (3-25).

If the froth front rises above the grid spacer, the limit applied by available liquid is removed and the heat transfer coefficient is given by the Zuber correlation.

3-8. Grid Dryout

If the film evaporation rate exceeds the liquid deposition rate [equation (3-18)], the grid will begin to dry out. The quench front regression is modeled by a simple energy balance:

$$(\rho Cp\ A)_G \cdot V_D \cdot (T_G - T_f) = (\dot{m}_{DE} - \dot{m}_{EVAP})h_{fg} \qquad (3\text{-}31)$$

where V_D is the grid dryout velocity.

3-9. Droplet Breakup Model

Experiments conducted by the Central Electricity Generating Board (CEGB) of the United Kingdom,[1] the University of New York at Stony Brook,[2]) and Westinghouse/Carnegie-Mellon University[3] show that significant droplet breakup can occur when a drop impinges on a grid spacer. The preferential evaporation of these microdrops downstream of a grid spacer leads to enhanced rod heat transfer because of the decrease in the vapor superheat. A "small drop" field was added to COBRA-TF (paragraphs 2-19 through 2-23) to calculate

---

1. Adams, J. E., and Clare, A. J., "A Preliminary Study of Droplet Breakup at PWR Spacer Grids," Central Electric Generating Board, PWR/HTWS/P (83) 130 (draft).

2. Lee, S. L., et al., "Reentrainment of Droplets from Grid Spacers in Mist Flow Portion of a LOCA Reflood of a PWR," NUREG-CR-0043, September 1982.

3. Yao, S. C., et al., "Dynamics of Droplets Impacting on Thin Heated Strips," submitted to National Heat Transfer Conference, Denver, 1985.

the evaporation rate of the population of shattered drop fragments. Two quantities are specified as input to this model, the fraction of the incident drop population that is shattered into microdrops and the initial drop diameter that characterizes the new distribution.

3-10. Drop Breakup Efficiency -- High-speed movie observation of drop impingement on a heated grid strap suggests the drop breakup scenario of figure 3-17. The grid strap thickness (about 0.3 mm) is relatively thin compared to the drop diameter (about 1.3 mm). This results in a "slicing" of the impacting drop, with most of the droplet mass remaining in one or two large drops. A binomial droplet distribution is generated with a few large fragments and a large number of very small microdroplets. This shattered fraction of the incident drop is treated by the separate small drop field; the increase of interfacial area due to the large drop fragments is assumed negligible.

The mass source of shattered drops generated by droplet breakup is expressed as a function of the entrained drop flow rate and the grid blockage area.

$$\dot{m}_{DB} = \eta_e \left(\frac{A_G}{A_c} \right) \dot{m}_e \qquad (3\text{-}32)$$

The grid efficiency factor, η_e, represents the portion of the drop within the grid projected area that is shattered into a population of microdroplets. By means of a sensitivity study, employing both FEBA and FLECHT SEASET 21-rod data, the value of η_e was estimated to be 0.6. A value of $\eta_e \approx 0.6$ can also be derived through close examination of high-speed movies of drop impaction on spacer grid straps. If a population of small drops, generated at previous grids or a flow blockage, is also incident upon the grid spacer, they are assumed to break up with the same grid efficiency. The mass source of new microdrops in the next grid span becomes

$$\dot{m}_{DB} = \eta_e \left(\frac{A_G}{A_c} \right) (\dot{m}_e + \dot{m}_{SD}) \qquad (3\text{-}33)$$

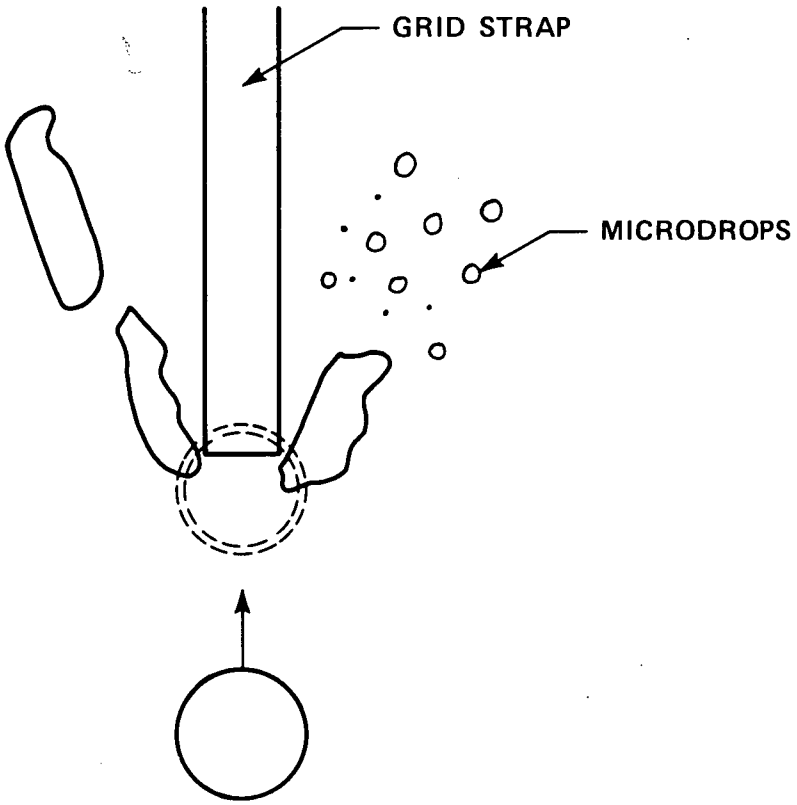

Figure 3-17. Droplet Breakup

...re $\dot{m}_{SD}$ is the mass flowrate of small drops immediately upstream of the grid.

3-11. Initial Drop Diameter -- Figure 3-18 shows the measurable spectrum of drop sizes resulting from the breakup of one large drop. To complete the drop breakup model, an expression which characterizes the diameter of the population of shattered microdrops is needed. Drop breakup data (inferred from high-speed movies) on unquenched, hot, flat plates (Wachters and Takeuchi[1,2,3]) and grid spacers (CEGB, Stony Brook, Westinghouse/Carnegie-Mellon) are plotted in figure 3-19 for different drop size to grid strap thickness ratios (d_o/W) as a function of drop impact Weber number:

$$We_D = \frac{\rho_\ell \, V_{DI}^2 \, D_I}{\sigma} \tag{3-34}$$

where

V_{DI} = velocity of impacting drop normal to surface
D_I = diameter of impacting drop

The shattered microdrop frequency distributions were obtained from the high-speed movies, and the Sauter mean diameters of the microdrops were calculated and correlated as

$$\frac{D_{SD}}{D_I} = 6.167 \, We_D^{-0.53} \tag{3-35}$$

---

1. Wachters, L. H. J., and Westerling, N. A. J., "The Heat Transfer From a Hot Wall to Impinging Water Drops in a Spheroidal State," Chem. Eng. Sci. 21, 1966, 1047-1056

2. Wachters, L. H. J., et al., "The Heat Transfer From a Hot Wall to Impinging Mist Droplets in the Spheroidal State," Chem. Eng. Sci. 21, 1966, 1231-1238.

3. Takeuchi, K., et al., "Experimental Studies on the Behavior of a Small Droplet Impinging Upon a Hot Surface," Proceedings of the Second International Conference on Liquid Atomization and Spray Systems, 1982, 397-404.

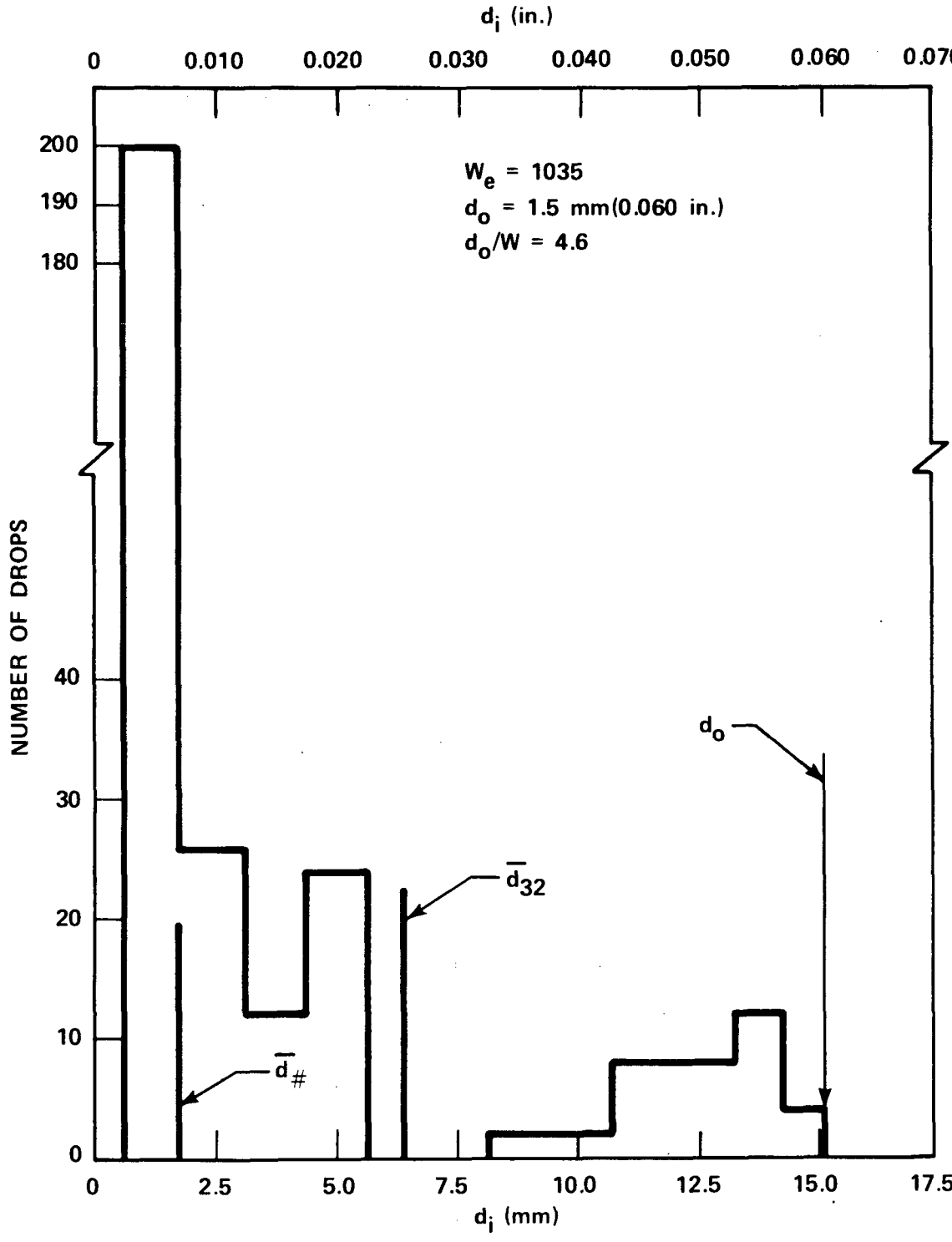

Figure 3-18. Shattered Droplet Spectrum for Initial We = 1035

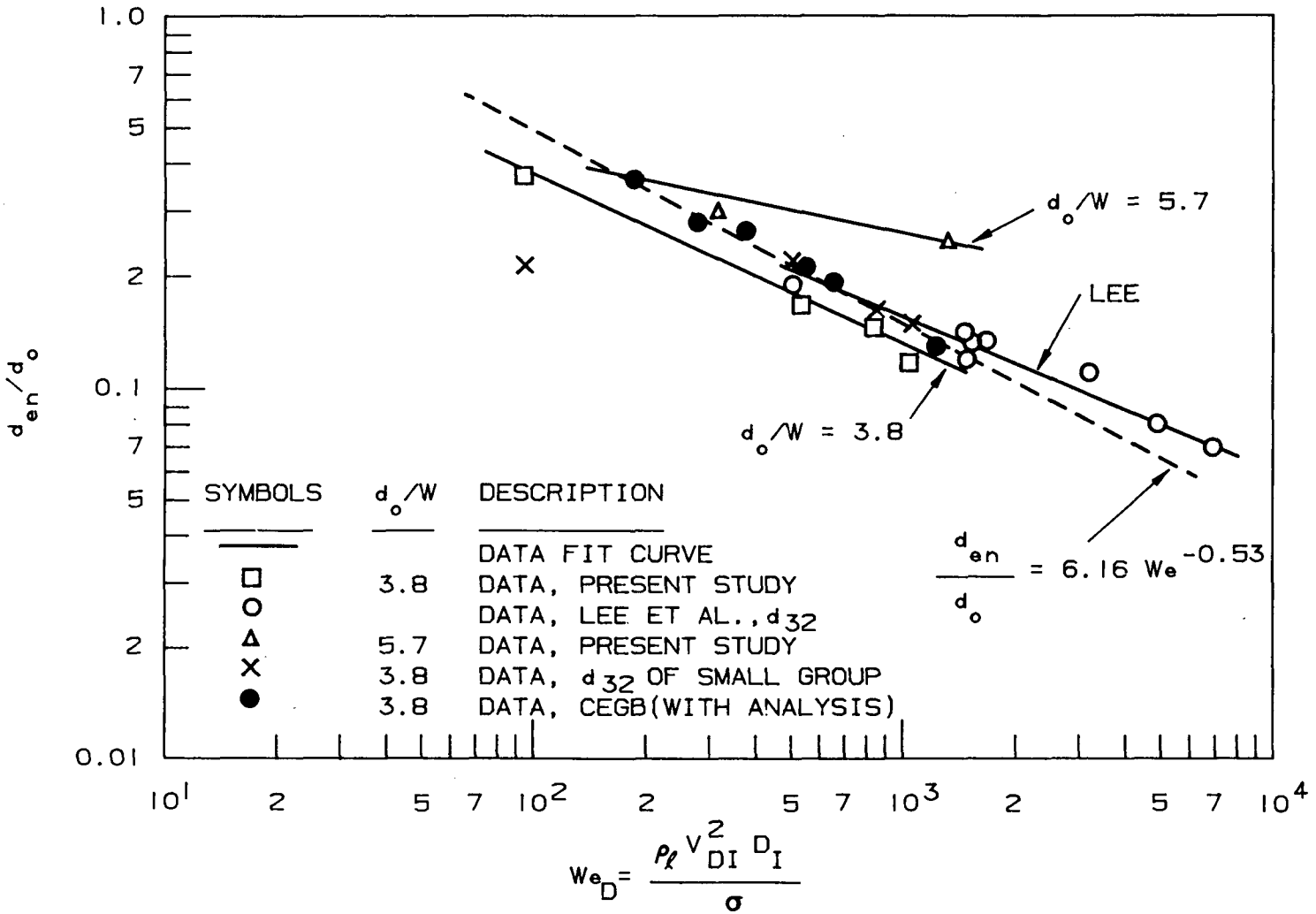

Figure 3-19. Shattered Droplet Size From Heated Grid Straps

This formulation is used to determine the ratio of shattered to incident drop diameter and is limited to $0.05 \leq D_{SD}/D_I \leq 1.0$.

3-12. Implementation Into COBRA-TF -- Incorporating the grid drop breakup model into COBRA-TF was straightforward with two exceptions:

- Low Weber number drop breakup
- Breakup of a preexisting small drop field in addition to that of the normal entrained drops

At low values of drop impact Weber number, equation (3-35) predicts shattered drop diameters of the same order as the incident drop diameter. Rather than considering these large shattered drops in the small drop field, it was more appropriate to treat them by a shift in the characteristic drop size used to represent the spectrum of entrained drops. To accomplish this, the interfacial area created by drop breakup, when $We_D \leq 150$, was added as a source term to the interfacial area conservation equation (paragraphs 2-19 through 2-23).

For drop impact Weber numbers greater than 250, the shattered drops are added to the small drop field in the normal manner. At intermediate values, a linear ramp as a function of drop Weber number is used to in transition between the two different treatments. Thus,

- $We_D < 150$: drop breakup modeled by interfacial area source term in large drop field
- $150 < We_D < 250$: $\xi = \frac{We - 150}{250 - 150}$

  $\xi \cdot \dot{m}_{SD}$ = mass source term for small drop field

  $(1 - \xi)\, \dot{m}_{SD}$ = mass source associated with large drop interfacial area source term
- $We_D > 250$: all shattered drops added to small drop field

At every grid spacer in the dispersed flow region of the bundle, both mass source and initial drop diameter are calculated for the entrained drops that break up. If, in addition to normal entrained drop field, drops in the small drop field are present just upstream of the grid, they are also broken up and the two resulting shattered drop populations are merged. When drop populations are merged, drop mass, interfacial area, and momentum are conserved (paragraphs 2-19 through 2-23).

3-13. COBRA-TF RESULTS WITH GRID MODELS

The series of grid models described above have been programmed into the COBRA-TF code in hopes of improving the correlation between code calculations and experimental data. To verify these models and to assess the agreement of the code with experimental data, three separate experimental forced reflooding test facilities were modeled with COBRA-TF: the FLECHT SEASET 161-rod unblocked facility,[1] the FLECHT SEASET 21-rod facility,[2] and the Karlsruhe 25-rod FEBA facility.[3-5]

The modeled tests were forced flooding reflood experiments in which the flooding rate was a constant or was a stepped flow (two flooding rates), and which

---

1. Loftus, M. J., et al., "PWR FLECHT SEASET Unblocked Bundle Forced and Gravity Reflood Task Data Report," NRC/EPRI/Westinghouse-7, June 1980.

2. Loftus, M. J., et al., "PWR FLECHT SEASET 21-Rod Bundle Flow Blockage Task Data and Analysis Report," NRC/EPRI/ Westinghouse-11, September 1982.

3. Ihle, P., and Rust, K., "FEBA - Flooding Experiments With Blocked Arrays, Evaluation Report," KfK 3657, March 1984.

4. Ihle, P., and Rust, K., "FEBA - Flooding Experiments With Blocked Arrays, Data Report 1, Test Series I Through IV," KfK 3658, March 1984.

5. Ihle, P., and Rust, K., "FEBA - Flooding Experiments With Blocked Arrays, Data Report 2, Test Series V Through VII," KfK 3659, March 1984.

had constant pressure, inlet water temperature, and prescribed power transient. The initial temperatures for these tests were significantly above the Leidenfrost point such that a dispersed two-phase flow cooling would occur for most of the test transient time.

The test conditions examined using COBRA-TF are listed in table 3-2. The COBRA-TF models used to simulate each test facility are described in appendix A, along with the input data required for each simulation.

The COBRA-TF-calculated values and the test data are presented in graph form by test series, as follows:

- o Heater rod temperature versus time at a specified elevation
- o Heater rod temperature versus elevation for selected times
- o Measured vapor temperature versus time at a specified elevation
- o Measured vapor temperature versus elevation at selected times

Also presented are bias plots constructed from the test data and code calculations; these plots show the difference between the data temperature rise and the COBRA-TF temperature rise at specific times for all elevations. That is, the bias plot gives

$$(T_t - T_{t=0})_{data} - (T_t - T_{t=0})_{COBRA\text{-}TF} \qquad (3\text{-}36)$$

plotted against elevation for different times. If the code has perfect agreement with the data, the temperature rise difference is a straight line as a function of elevation through. This plot is an attempt to determine whether COBRA-TF has a bias with elevation in the rod bundle, with test conditions, or with the time after initiation of reflood.

TABLE 3-2
TEST CONDITIONS FOR EXPERIMENTAL DATA
COMPARED WITH COBRA-TF

Test	Flooding Rate [m/sec (in./sec)]	Pressure [MPa (psia)]	Power [kw/m (kw/ft)]	$T_{initial}$ [°C (°F)]
FLECHT SEASET 161-ROD BUNDLE				
31203	0.0399 (1.57)	0.28 (40)	2.3 (0.7)	872 (1601)
31805	0.0206 (0.81)	0.28 (40)	2.3 (0.7)	915 (1679)
32333	0.161 (6.36) 5 sec; 0.021 (0.82) onward	0.28 (40)	2.3 (0.7)	888 (1631)
34209	0.0254 (1.0)	0.14 (20)	2.4 (0.72)	887 (1628)
FEBA 25-ROD BUNDLE				
216	0.0378 (1.49)	0.410 (59.4)	2.3 (0.7)	714 (1317)
223	0.0378 (1.49)	0.220 (31.9)	2.3 (0.7)	767 (1413)
229	0.0378 (1.49)	0.410 (59.4)	2.3 (0.7)	778 (1432)
234	0.0378 (1.49)	0.020 (29.0)	2.3 (0.7)	760 (1400)
FLECHT SEASET 21-ROD BUNDLE				
42606A	0.023 (0.91)	0.273 (39.6)	2.6 (0.78)	872 (1601)
43208A	0.0394 (1.55)	0.280 (40.6)	2.6 (0.78)	873 (1604)
43112A	0.028 (1.1)	0.139 (20.2)	2.6 (0.78)	873 (1604)
42514A	0.161 (6.36) 5 sec; 0.023 (0.89) onward	0.281 (40.8)	2.6 (0.78)	873 (1603)

3-14. FLECHT SEASET 161-Rod Unblocked Bundle Comparisons With COBRA-TF

Four experiments from the FLECHT SEASET 161-rod unblocked bundle test series were simulated using COBRA-TF. The conditions for these tests are given in table 3-2. There were several repeat calculations using COBRA-TF to decide the most appropriate method of modeling the test bundle. Parameters examined included the following:

- o Radial noding
- o Axial noding
- o Location of a grid within a node
- o Size of nodes below the grid
- o Effect of guide tube thimbles in the center region of the bundle

Sample calculations in which the noding was varied in COBRA-TF are shown in appendix B. The conclusion reached is that the code results are not sensitive to the noding used.

The final axial and radial noding chosen for these tests is shown in figures 3-20 and 3-21. A two-node radial representation of the 161-rod bundle with rod-to-thimble radiation was used. The rod-to-thimble radiation would typically reduce the calculated peak temperatures by approximately 25° C (45° F). The inner region of the rod bundle, modeled as node 1, was not directly coupled to the test housing by means of radiation heat transfer, but was insulated from the housing by the outer rows of heater rods. This is consistent with radiation calculations performed in the FLECHT SEASET program.[1] The COBRA-TF code also modeled the housing and calculated its heatup and quench behavior in the same fashion as the fuel rod simulators.

Earlier in the program, attempts were made to read in the housing thermal conditions as a boundary condition -- that is, read in the housing measured wall

1. Loftus, M. J., et al., "PWR FLECHT SEASET 21-Rod Bundle Flow Blockage Task Data and Analysis Report," NRC/EPRI/ Westinghouse-11, September 1982.

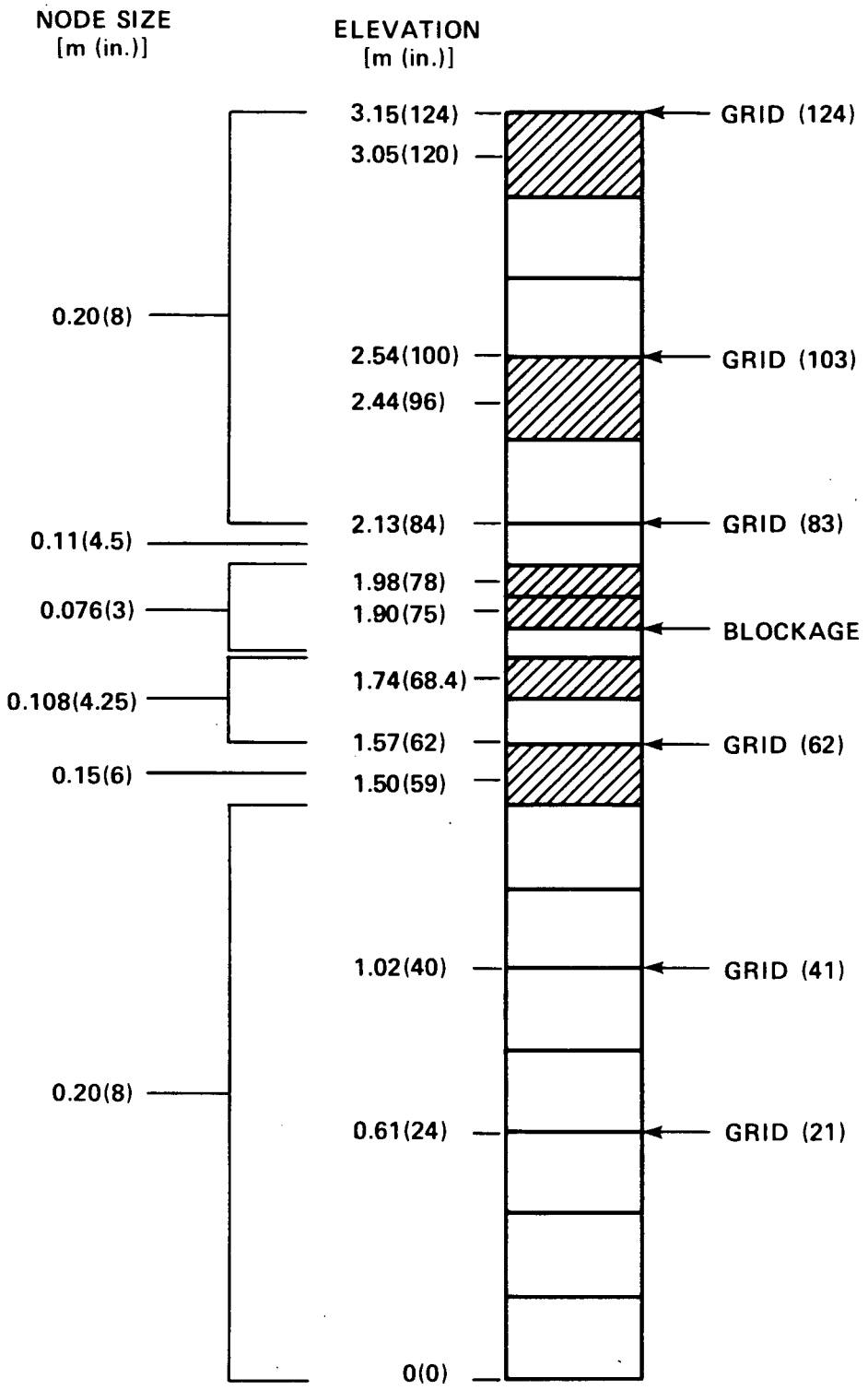

Figure 3-20. Axial Noding for FLECHT SEASET 161-Rod Bundle Test Data Comparisons

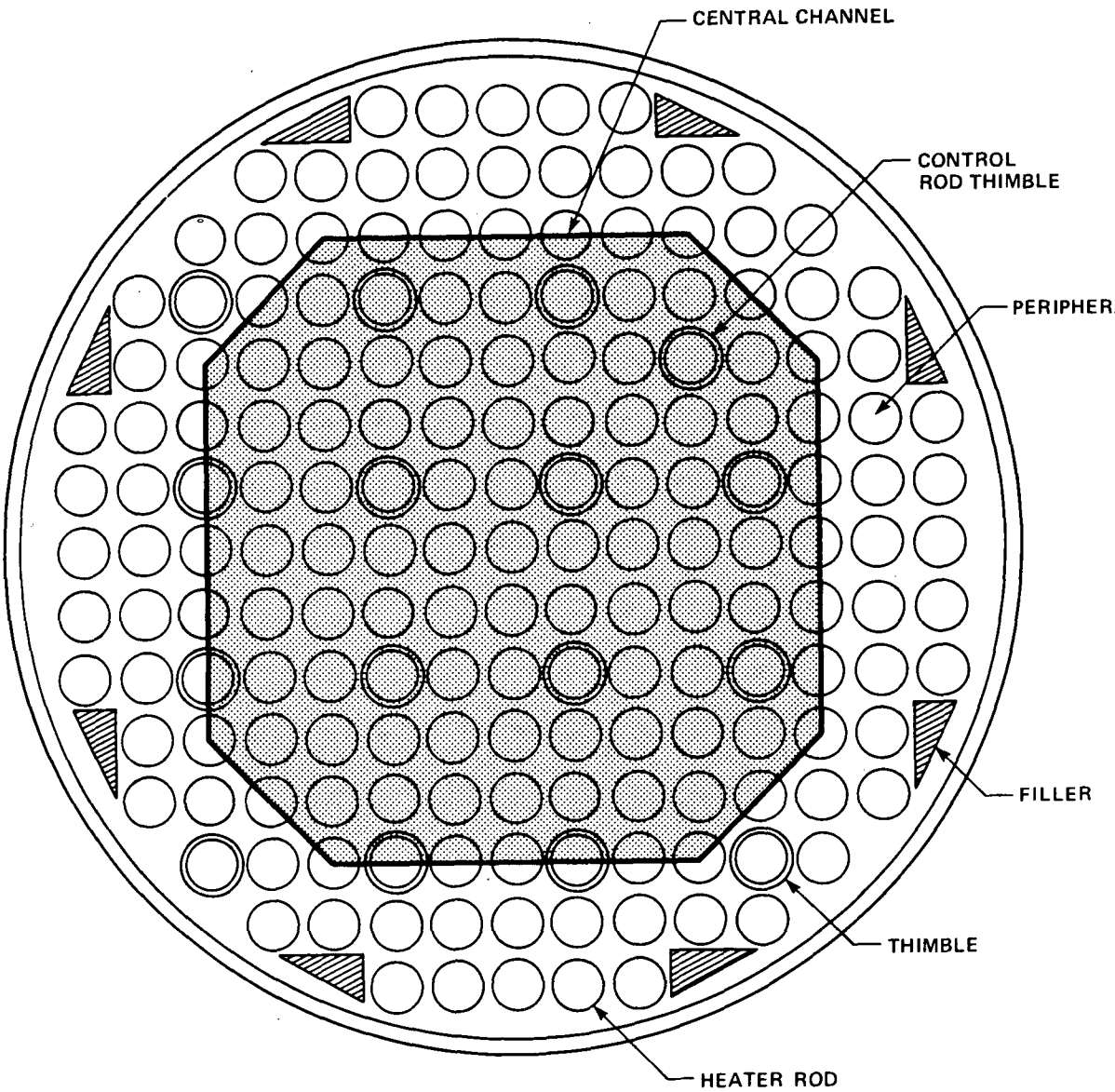

Figure 3-21. Radial Noding for FLECHT SEASET 161-Rod Bundle Test Data Comparisons

temperature and heat release at housing quench, which was calculated from the housing temperature measurements. It was found, however, that the COBRA-TF code would calculate an incorrect heat transfer rate to the housing before housing quench because the housing temperature was decoupled from the code-calculated fluid solution. The code could more accurately predict the housing behavior if the housing was modeled in the code as compared to using the housing data as a boundary condition.

The axial noding used for modeling the 161-rod bundle tests was varied to determine the smallest node sizes which could be used to indicate the grid effects but not penalize the code running time too greatly. Since the grid effects are both local (that is, convective heat transfer enhancement) and global (vapor desuperheating due to wet grids and droplet breakup), the noding scheme chosen attempts to optimize the code predictions for both effects.

The COBRA-TF predictions for the rod bundle center heater rod clad temperature transients for the 161-rod FLECHT SEASET unblocked bundle test 31805 are shown in figures 3-22 through 3-27. The elevation plotted is given on each figure. The data curves represent the data average of the center rods (middle curve) and the data minimum and maximum for the center rods. The data scatter at the quench time reflects the delays in individual rod quenching. The COBRA-TF calculation is the dark line using the star symbol.

Since all rods in the center region of the bundle are modeled as a single rod, the best expectation is that the COBRA-TF-calculated value will fall within the data bands shown on the figures. The variation of the data is caused by individual heater rod resistance differences, local power generation differences, manufacturing tolerances on materials, dimension variations, initial temperature differences,[1] the radial location of a heater rod relative to the unheated guide tube thimbles, and subchannel-to-subchannel flow variations that could exist in the rod bundle.

---

1. There is still a small radial temperature gradient in the rod bundle at the beginning of the test.

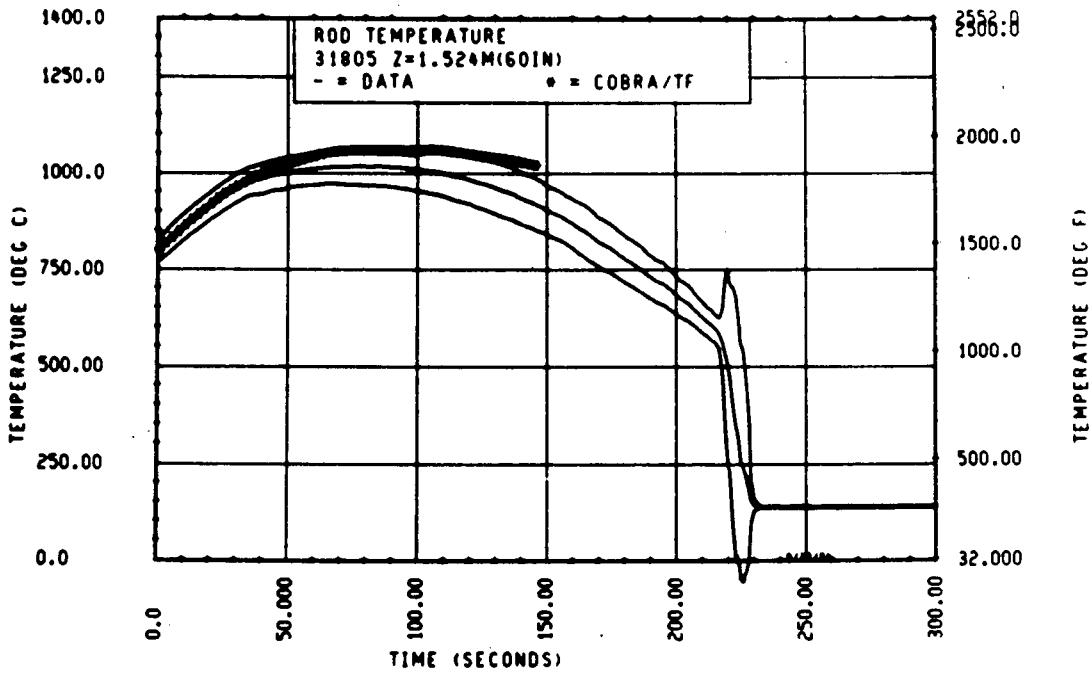

Figure 3-22. Comparison of COBRA-TF-Calculated Heater Rod Temperature Versus Time With FLECHT SEASET 161-Rod Data, Test 31805, 1.52 m (60 in.) Elevation

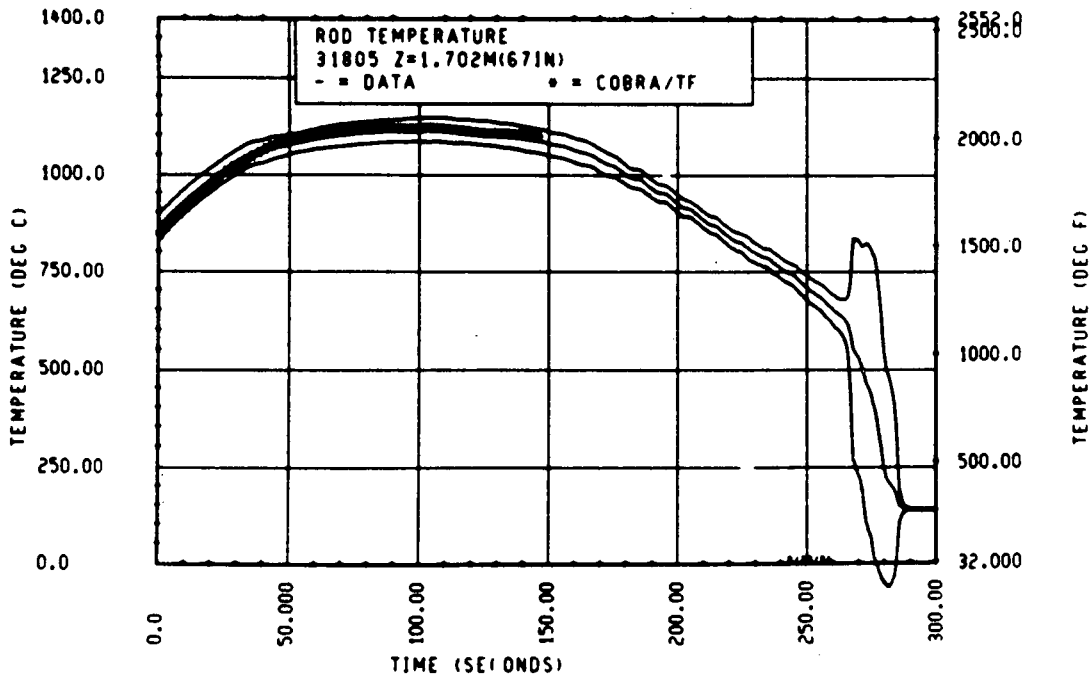

Figure 3-23. Comparison of COBRA-TF-Calculated Heater Rod Temperature Versus Time With FLECHT SEASET 161-Rod Data, Test 31805, 1.70 m (67 in.) Elevation

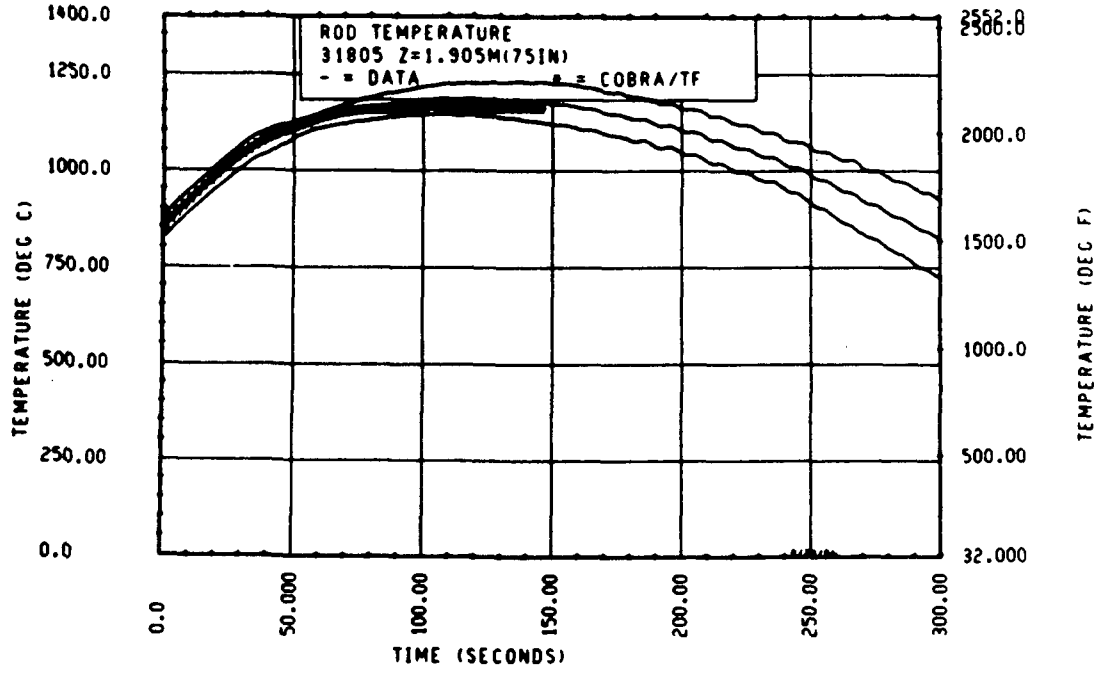

Figure 3-24. Comparison of COBRA-TF-Calculated Heater Rod Temperature Versus Time With FLECHT SEASET 161-Rod Data, Test 31805, 1.90 m (75 in.) Elevation

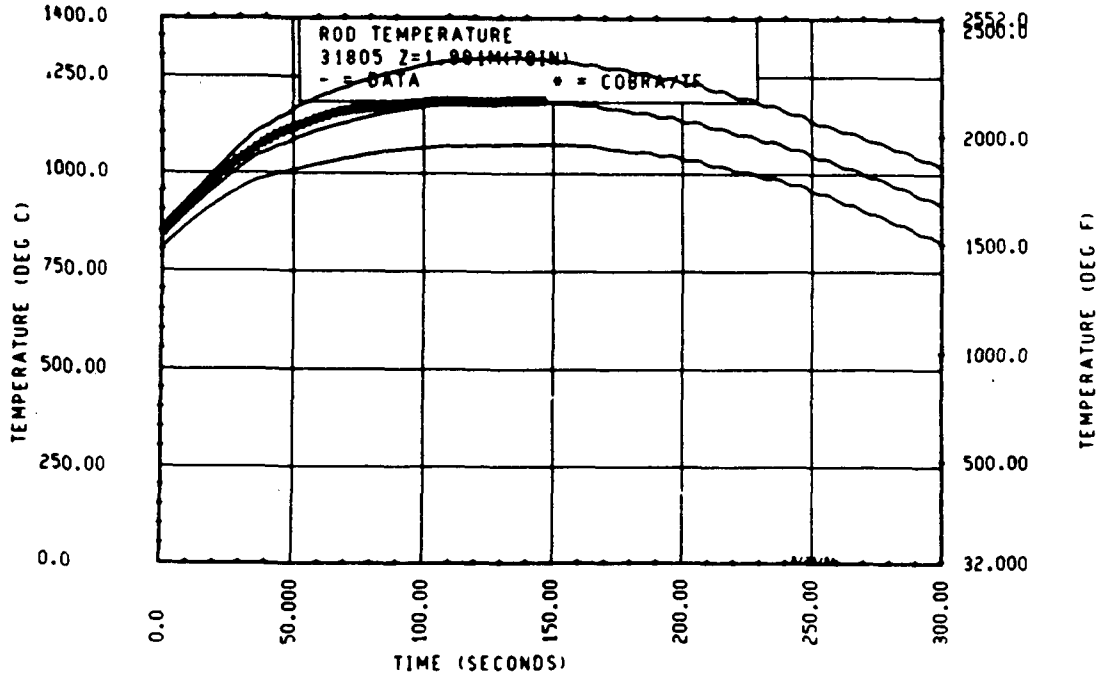

Figure 3-25. Comparison of COBRA-TF-Calculated Heater Rod Temperature Versus Time With FLECHT SEASET 161-Rod Data, Test 31805, 1.98 m (78 in.) Elevation

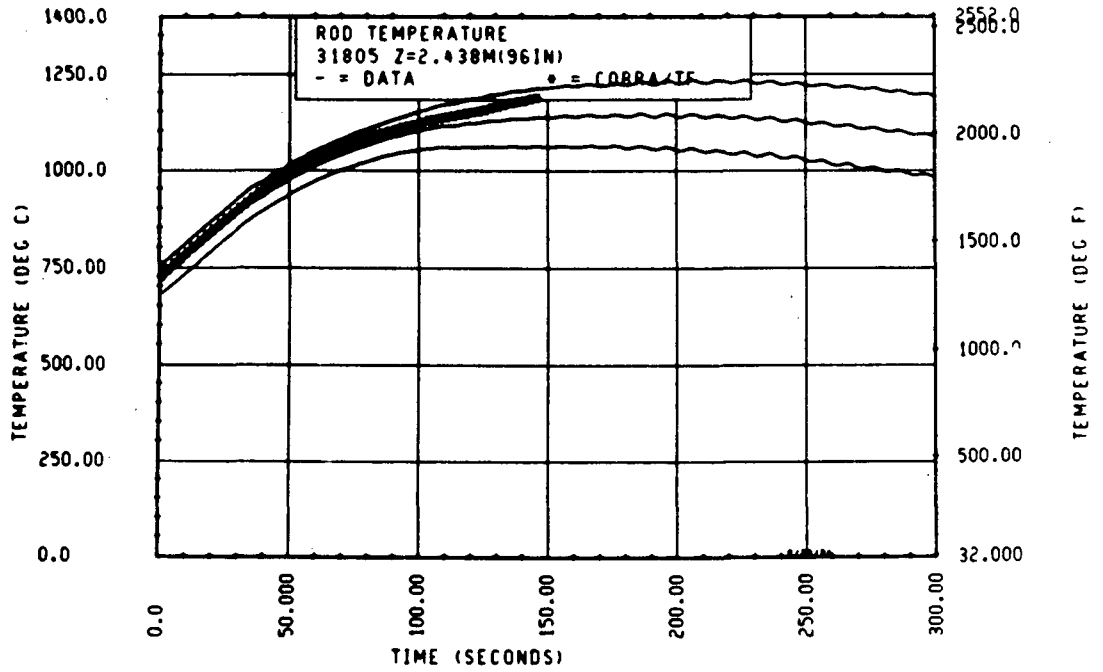

Figure 3-26. Comparison of COBRA-TF-Calculated Heater Rod Temperature Versus Time With FLECHT SEASET 161-Rod Data, Test 31805, 2.44 m (96 in.) Elevation

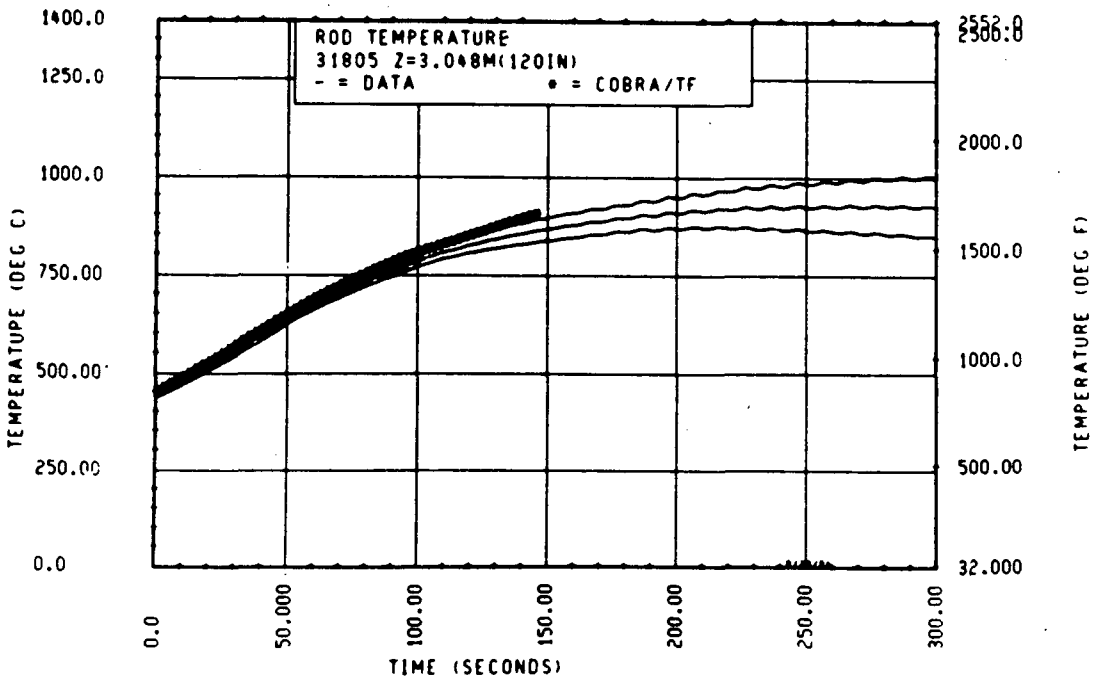

Figure 3-27. Comparison of COBRA-TF-Calculated Heater Rod Temperature Versus Time With FLECHT SEASET 161-Rod Data, Test 31805, 3.05 m (120 in.) Elevation

As figures 3-22 through 3-27 indicate, the COBRA-TF prediction is very good at the bundle midplane and up to the 2.44 m (96 in.) elevation. At the 3.05 m (120 in.) elevation, COBRA-TF tends to overpredict even the maximum value of the data.

The same data and code predictions can be plotted as calculated and measured heater rod temperatures versus elevation for selected times. The advantage of this type of plot is that, if local effects are present due to grids or blockage, an axial plot will show these effects more clearly than a temperature-time plot, since the data upstream of the grid or blockage are shown for comparison.

COBRA-TF-calculated heater rod temperatures versus elevation for several times are compared to the test data for the center rods in the 161-rod bundle in figures 3-28 through 3-34. (Also shown in figure 3-28 is the axial location of the spacer grids.) At 20 seconds, no entrainment is calculated in the COBRA-TF case, and very little entrainment is occurring in the test data. Therefore, the comparison shown in figure 3-28 is almost the same as the initial temperature distribution. As time progresses, the entrainment increases and the local effects of the grids become apparent in both the data and the COBRA-TF calculation. At 80 seconds (figure 3-31), the data clearly show a grid effect at 2.11 m (83 in.); the COBRA-TF calculation shows grid effects at each grid location. [It should be mentioned that the curve which represents the COBRA-TF calculation represents a straight line drawn through the continuity nodes in the code (figure 3-21). The grid locations for the 161-rod bundle are shown in figure 3-28.)]

As time continues to increase, the grid effects are still pronounced because of the increased entrainment (figures 3-33 and 3-34). Also, it should be noted that the quench front prediction of COBRA-TF agrees quite well with the data, as does that for the very steep axial temperature gradient above the quench front. The heater rod temperature changes nearly 1000° C (1800° F) in approximately 0.5 m (20 in.). These figures also show that COBRA-TF begins to

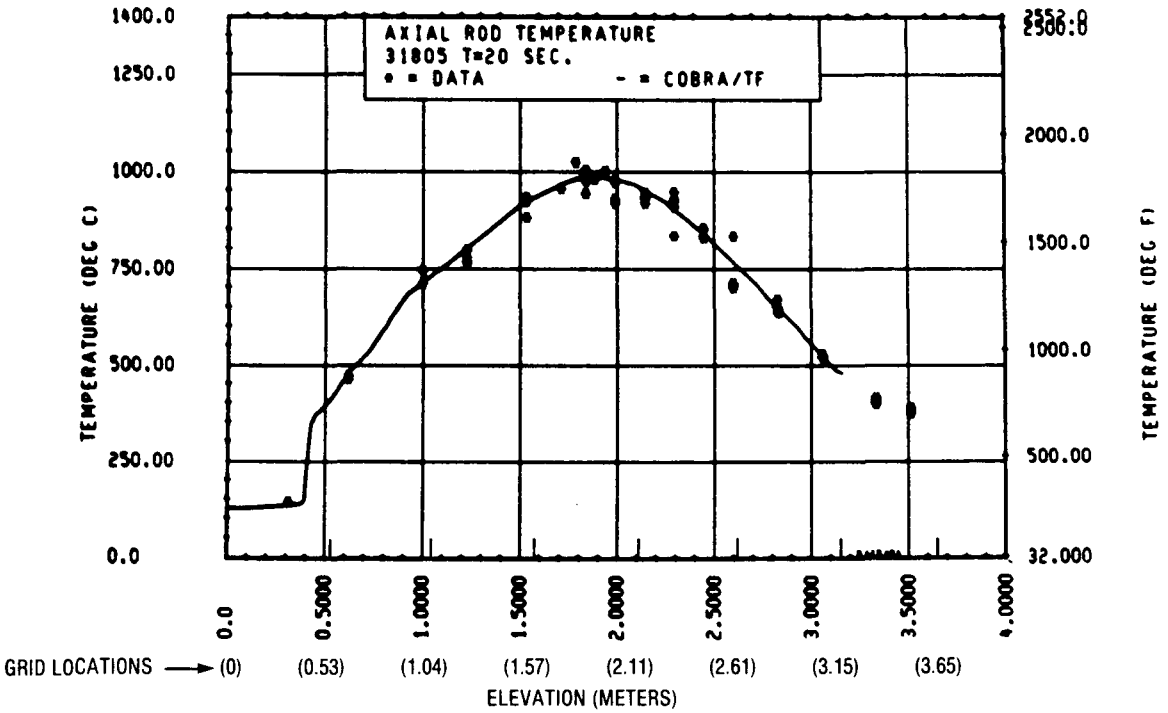

Figure 3-28. Comparison of COBRA-TF-Calculated Heater Rod Temperature Versus Elevation With FLECHT SEASET 161-Rod Data, Test 31805, t = 20 Seconds

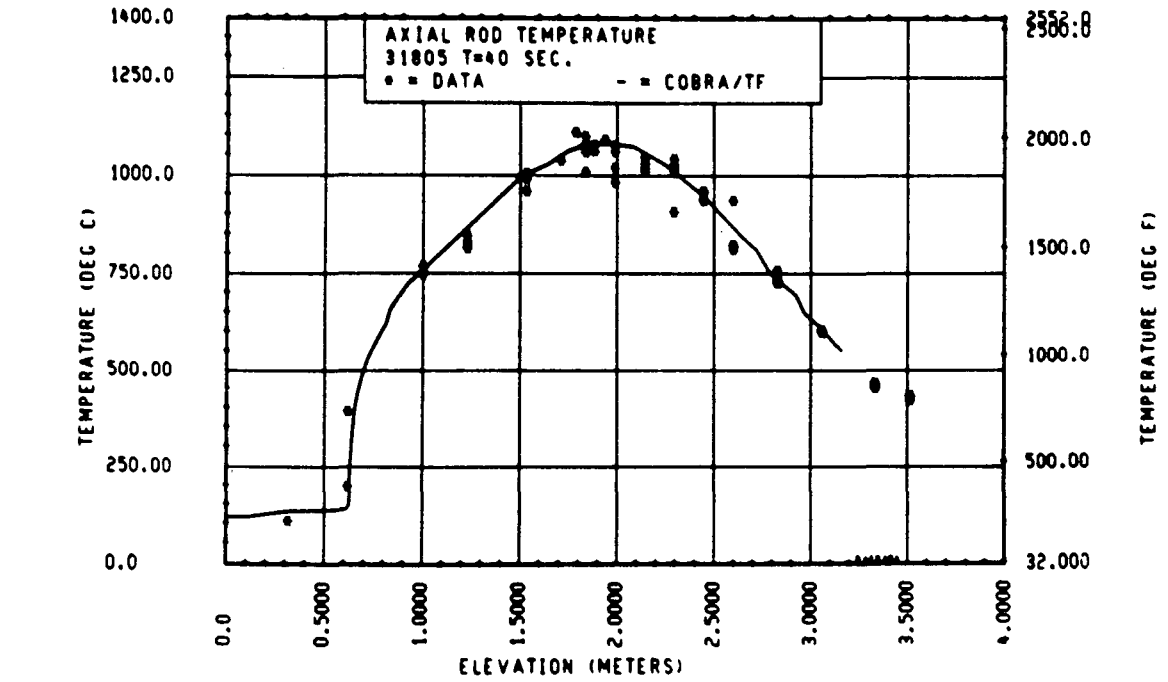

Figure 3-29. Comparison of COBRA-TF-Calculated Heater Rod Temperature Versus Elevation With FLECHT SEASET 161-Rod Data, Test 31805, t = 40 Seconds

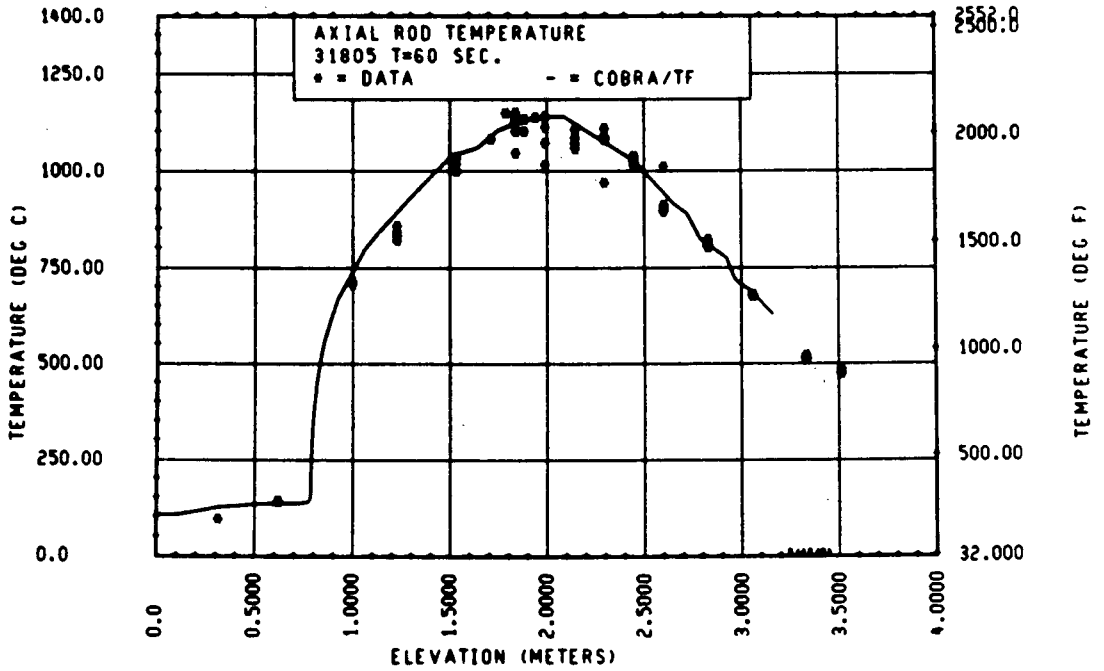

Figure 3-30. Comparison of COBRA-TF-Calculated Heater Rod Temperature Versus Time With FLECHT SEASET 161-Rod Data, Test 31805, t = 60 Seconds

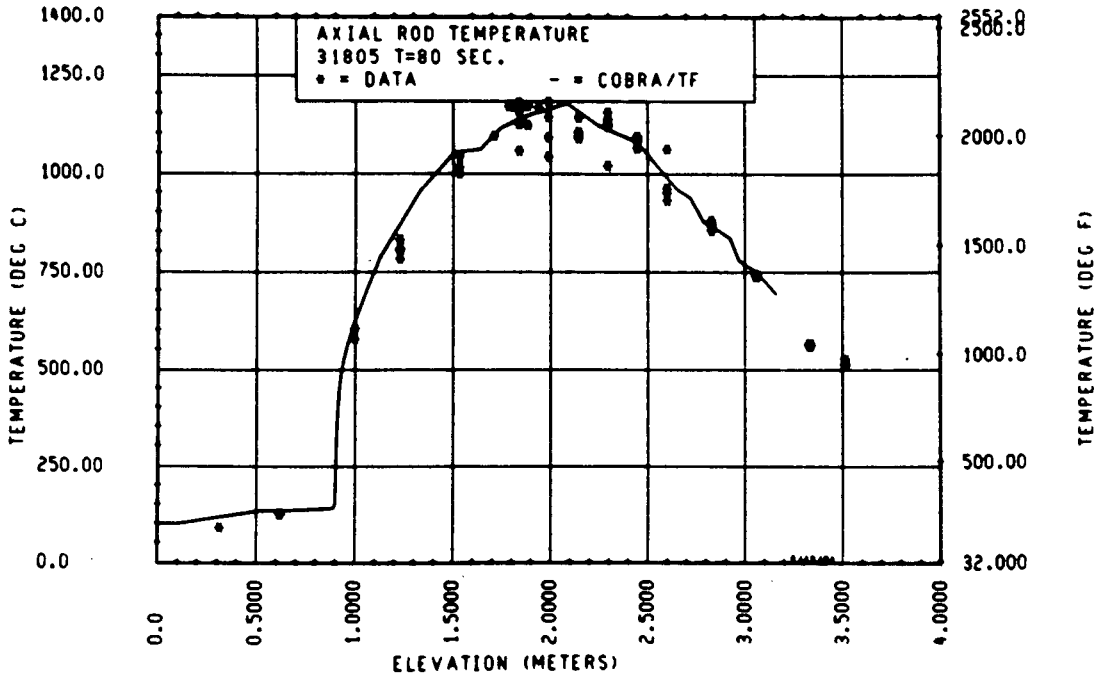

Figure 3-31. Comparison of COBRA-TF-Calculated Heater Rod Temperature Versus Time With FLECHT SEASET 161-Rod Data, Test 31805, t = 80 Seconds

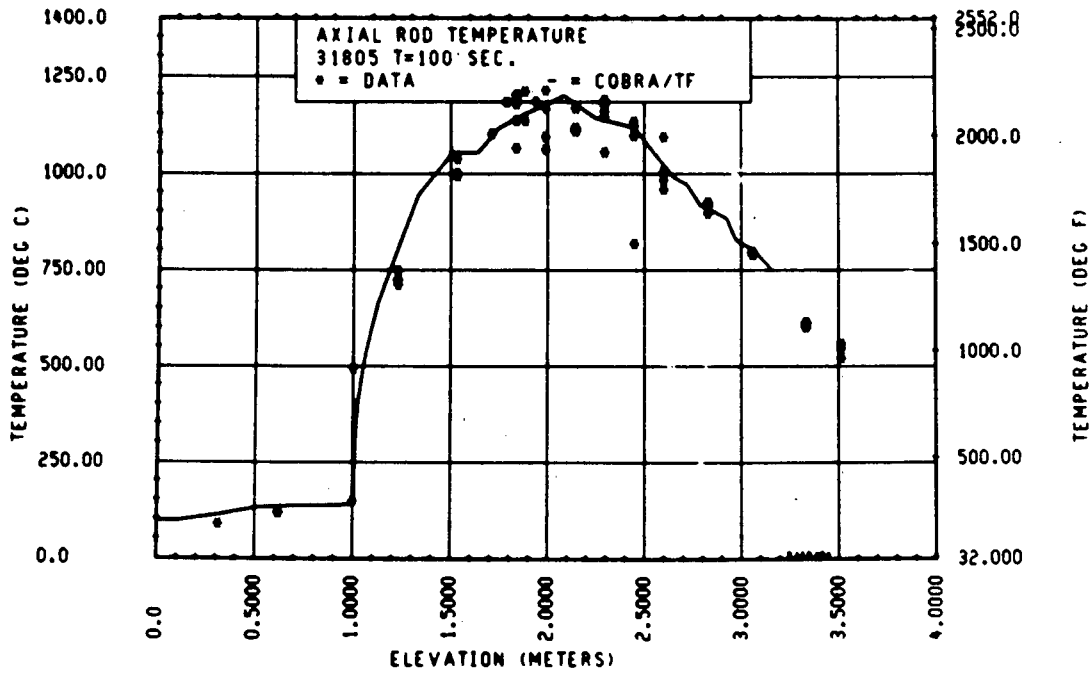

Figure 3-32. Comparison of COBRA-TF-Calculated Heater Rod Temperature Versus Time With FLECHT SEASET 161-Rod Data, Test 31805, t = 100 Seconds

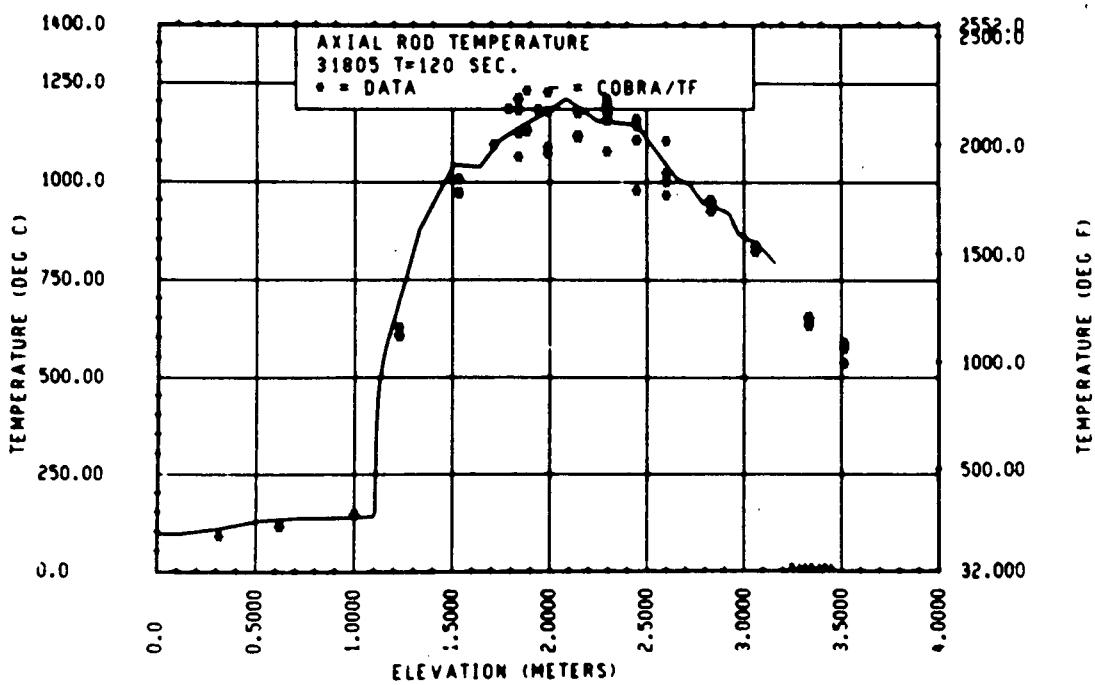

Figure 3-33. Comparison of COBRA-TF-Calculated Heater Rod Temperature Versus Time With FLECHT SEASET 161-Rod Data, Test 31805, t = 120 Seconds

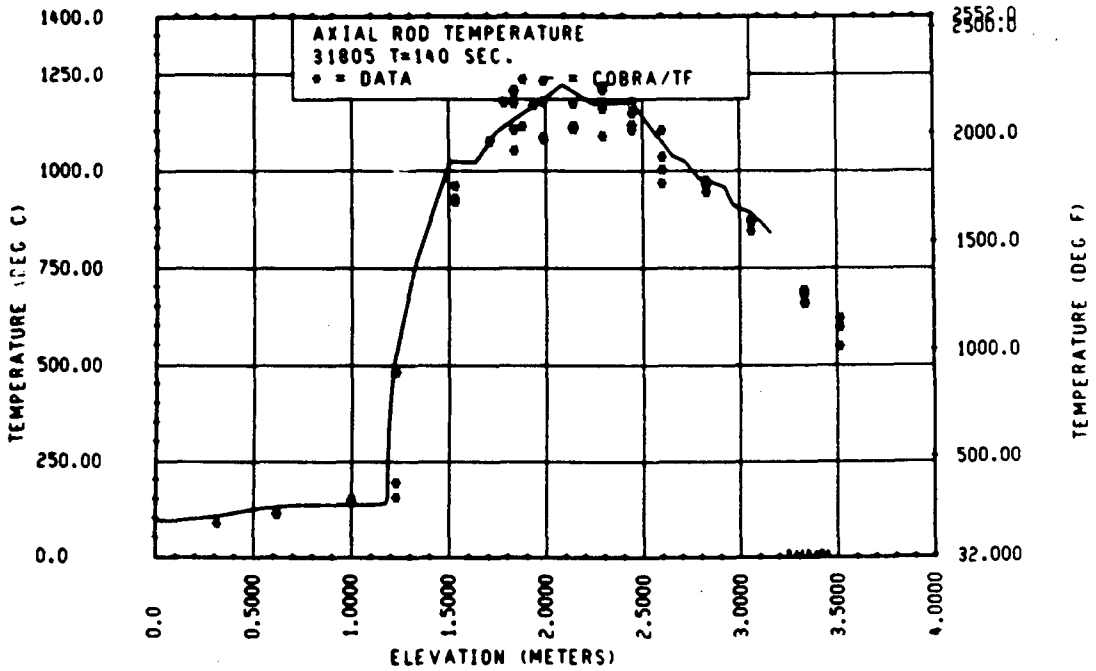

Figure 3-34. Comparison of COBRA-TF-Calculated Heater Rod Temperature Versus Time With FLECHT SEASET 161-Rod Data, Test 31805, t = 140 Seconds

overpredict the heater rod temperature relative to the data at times greater than 100 seconds for the uppermost elevations. However, the COBRA-TF agreement with the heater rod temperature data is excellent for this test.

In addition to comparing the calculated heater rod temperatures to the COBRA-TF prediction, it is also possible to compare the COBRA-TF-predicted vapor temperatures to the measured vapor temperatures obtained by the steam probe thermocouples. The design and operation of the FLECHT SEASET 161-rod bundle steam probes are described in NRC/EPRI/Westinghouse Report No. 7.[1] Also, the guidelines described in this report were used to screen the steam probe data such that only data from those steam probes which exited the top of the bundle were compared to the COBRA-TF predictions.

Vapor temperature versus time plots are shown in figures 3-35 and 3-36 for two elevations. At the 2.44 m (96 in.) elevation, the COBRA-TF calculation lies above the data until sufficient entrainment has occurred at times greater than 65 seconds, such that the calculated vapor temperature rate of change is slowed because of heat transfer to the entrained drops. After 65 seconds, the COBRA-TF and data trends are about the same; this indicates that the two-step thermodynamic nonequilibrium process of superheating the vapor from the heater rod surface, and desuperheating the vapor due to interfacial heat transfer between the entrained drops and the vapor, is predicted correctly by COBRA-TF. At the 3.05 m (120 in.) elevation, the COBRA-TF vapor temperature prediction is above the data for all times. This is consistent with the overprediction of the heater rod temperatures at this elevation.

---

1. Loftus, M. J., et al., "PWR FLECHT SEASET Unblocked Bundle Forced and Gravity Reflood Task Data Report," NRC/EPRI/Westinghouse-7, June 1980.

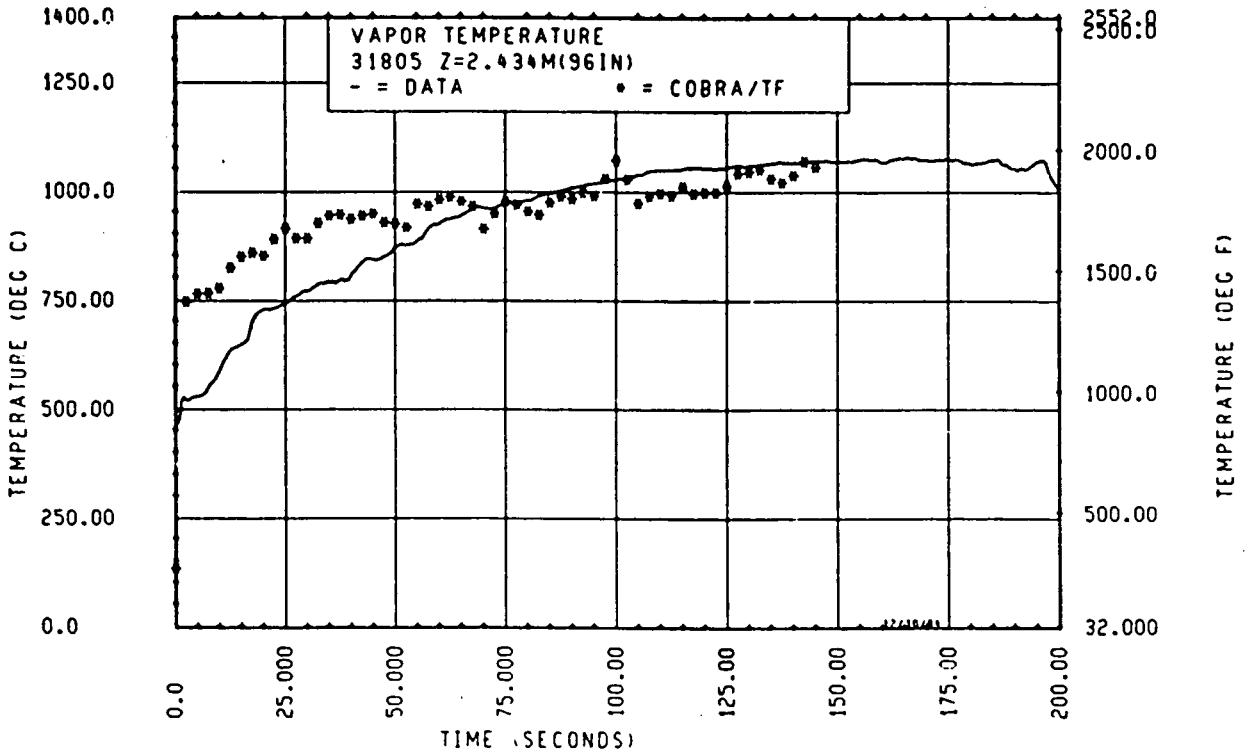

Figure 3-35. Comparison of COBRA-TF-Calculated Vapor Temperature Versus Time With FLECHT SEASET 161-Rod Data, Test 31805, 2.44 m (96 in.) Elevation

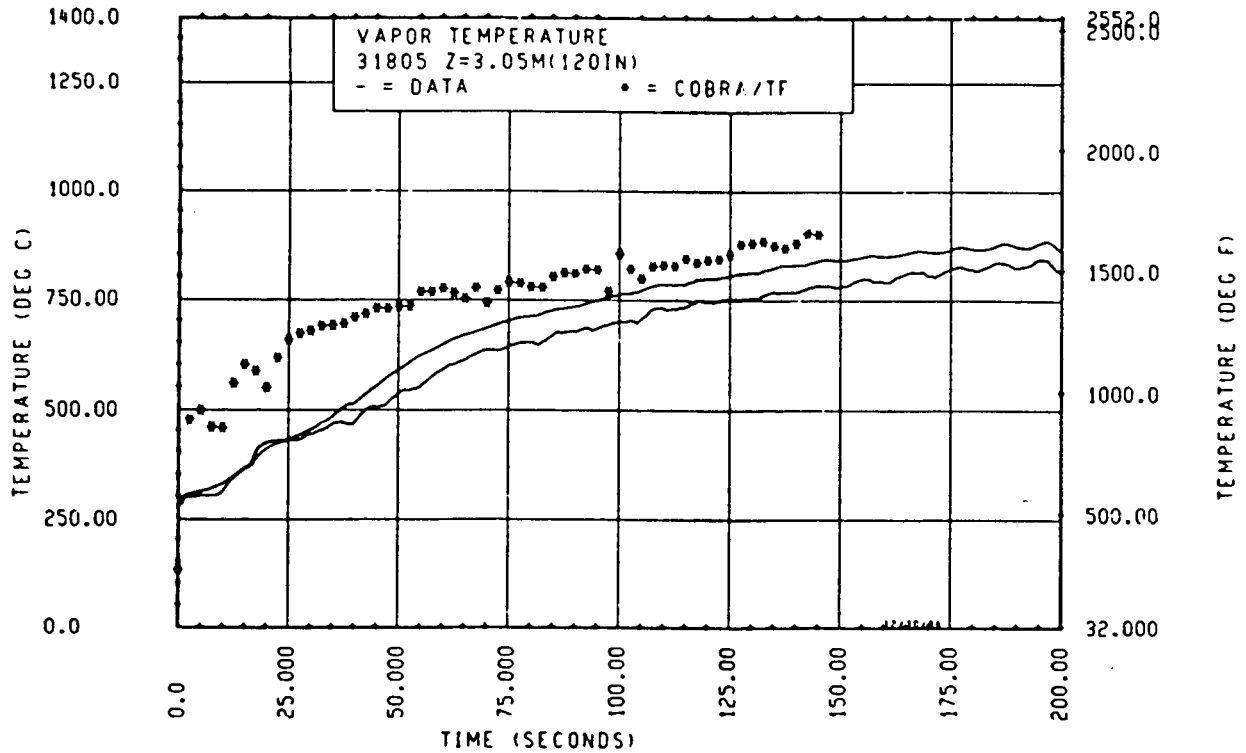

Figure 3-36. Comparison of COBRA-TF-Calculated Vapor Temperature Versus Time With FLECHT SEASET 161-Rod Data, Test 31805, 3.05 m (120 in.) Elevation

The axial plots of the COBRA-TF-predicted vapor temperatures and the measured vapor temperatures at different times are shown in figures 3-37 through 3-43. Generally, the code overpredicts the measured vapor temperature; the agreement improves at later times (times greater than 60 seconds), when sufficient entrainment was predicted to have occurred. It was observed in all the comparisons that COBRA-TF would predict a delay in the entrainment that was not apparent in the experimental data. High-speed movies of the 161- and 163-rod FLECHT SEASET data[1] indicated that droplet entrainment usually occurred within the first 10 seconds after reflood was initiated. It could take almost 40 seconds for entrainment to be calculated to occur in COBRA-TF. The delay in the predicted entrainment will result in excessive vapor super- heating, since the droplet heat sink is missing. Once substantial entrainment is predicted to have occurred, however, the agreement between the COBRA-TF-predicted vapor temperatures and the data is reasonably good, as seen in figures 3-40 through 3-43.

Similar COBRA-TF comparisons to the other three 161-rod FLECHT SEASET unblocked bundle tests listed in table 3-2 are shown in figures 3-44 through 3-75. These comparisons are summarized below.

Plots of the heater rod temperatures versus time are shown in figures 3-44 through 3-49 for test 31203 [0.0399 m/sec (1.57 in./sec) flooding rate]. There is excellent agreement between the COBRA-TF predictions and the heater rod data. As mentioned earlier, there is a delay in the prediction of entrainment, which can be seen in these figures early in time, that is, for times less than 30 seconds. During early times, the COBRA-TF calculation overestimates the heater rod heatup until entrainment begins. Once entrainment begins, the rate of cooling is first overestimated and then agrees reasonably well with the test data.

---

1. Loftus, M. J., et al., "PWR FLECHT SEASET 163-Rod Bundle Flow Blockage Task Data Report," NRC/EPRI/Westinghouse-13, September 1983.

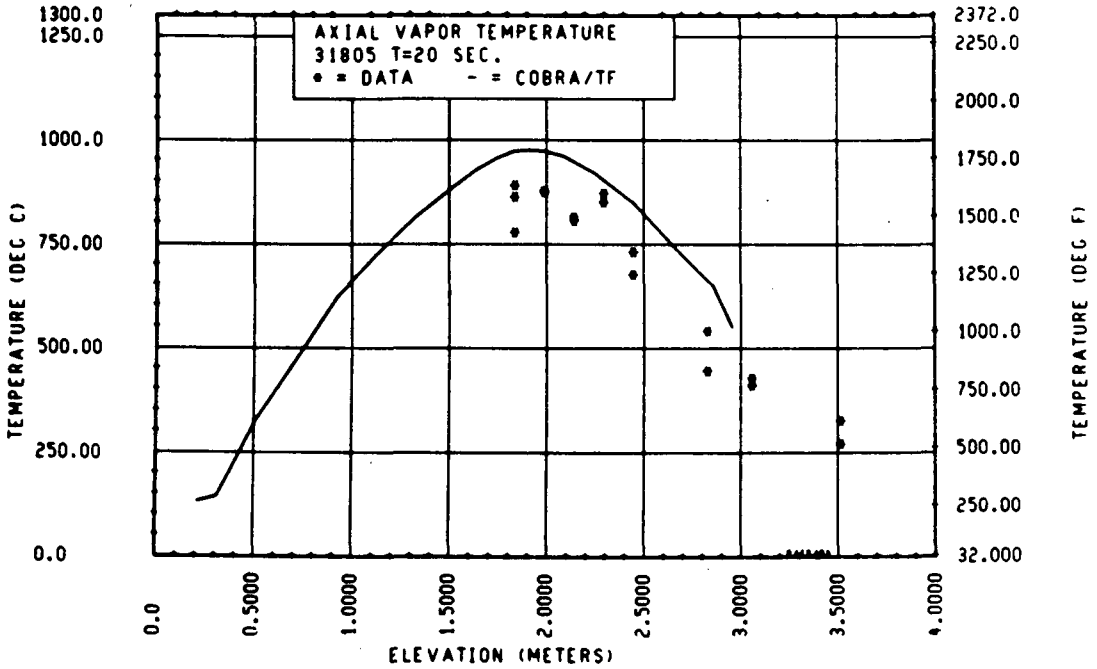

Figure 3-37. Comparison of COBRA-TF-Calculated Vapor Temperature Versus Elevation With FLECHT SEASET 161-Rod Data, Test 31805, t = 20 Seconds

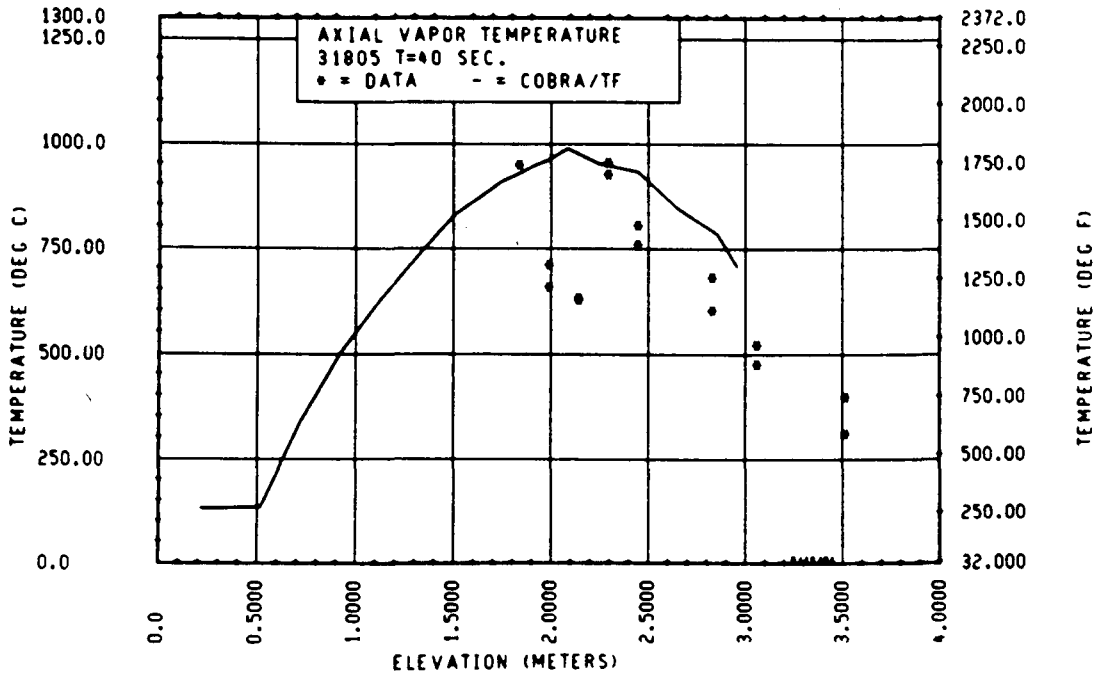

Figure 3-38. Comparison of COBRA-TF-Calculated Vapor Temperature Versus Elevation With FLECHT SEASET 161-Rod Data, Test 31805, t = 40 Seconds

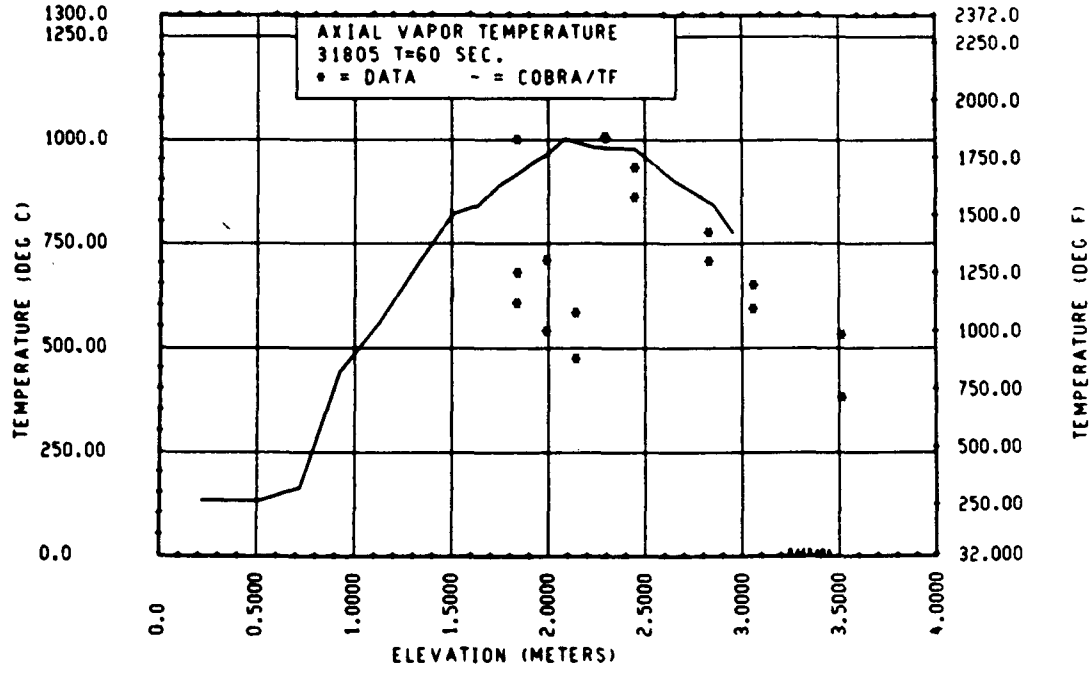

Figure 3-39. Comparison of COBRA-TF-Calculated Vapor Temperature Versus Time With FLECHT SEASET 161-Rod Data, Test 31805, t = 60 Seconds

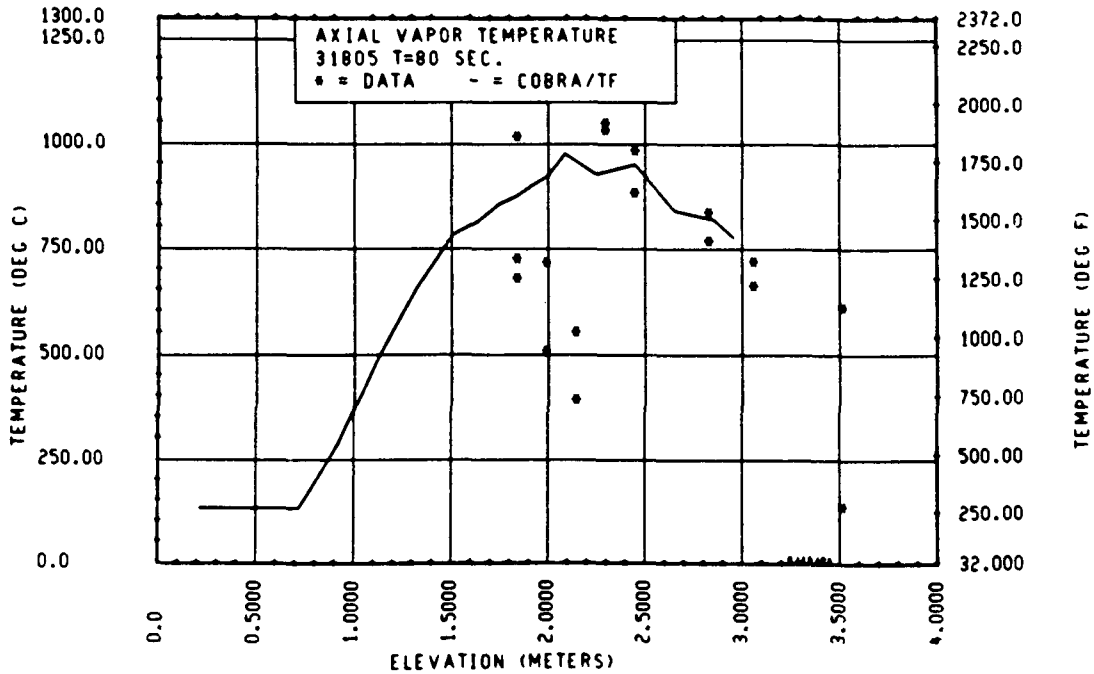

Figure 3-40. Comparison of COBRA-TF-Calculated Vapor Temperature Versus Time With FLECHT SEASET 161-Rod Data, Test 31805, t = 80 Seconds

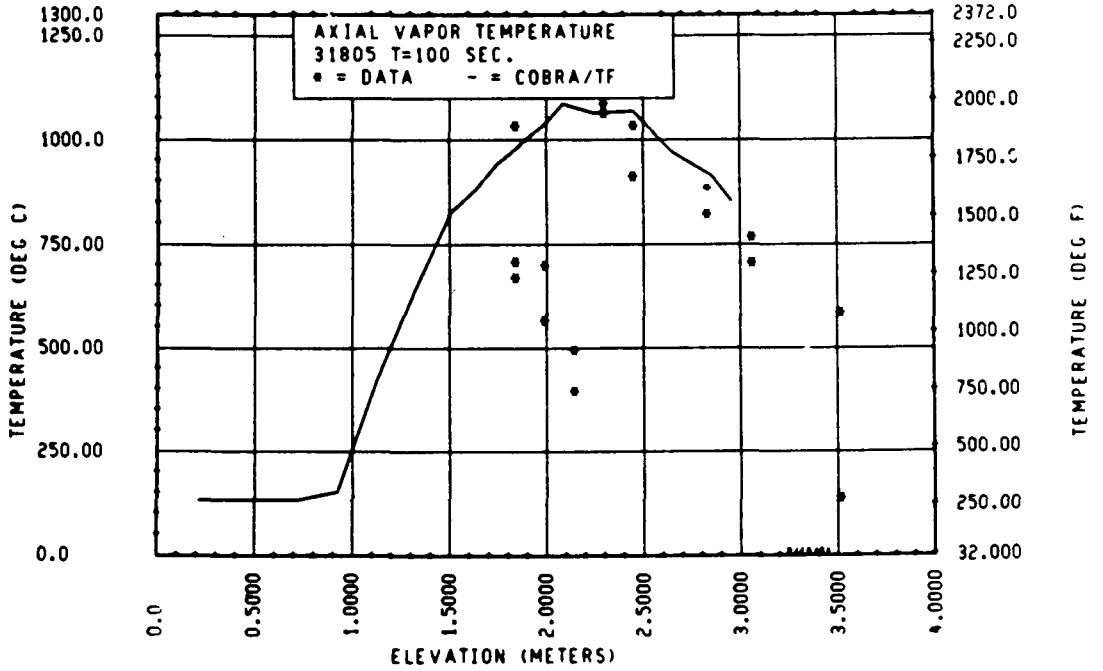

Figure 3-41. Comparison of COBRA-TF-Calculated Vapor Temperature Versus Time With FLECHT SEASET 161-Rod Data, Test 31805, t = 100 Seconds

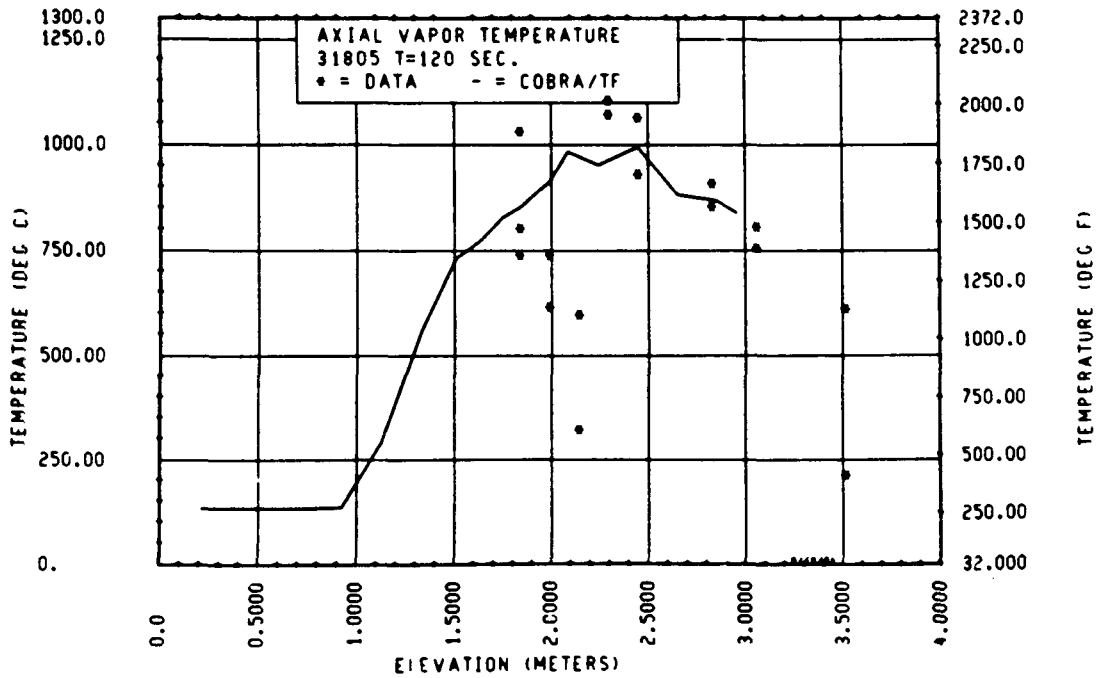

Figure 3-42. Comparison of COBRA-TF-Calculated Vapor Temperature Versus Time With FLECHT SEASET 161-Rod Data, Test 31805, t = 120 Seconds

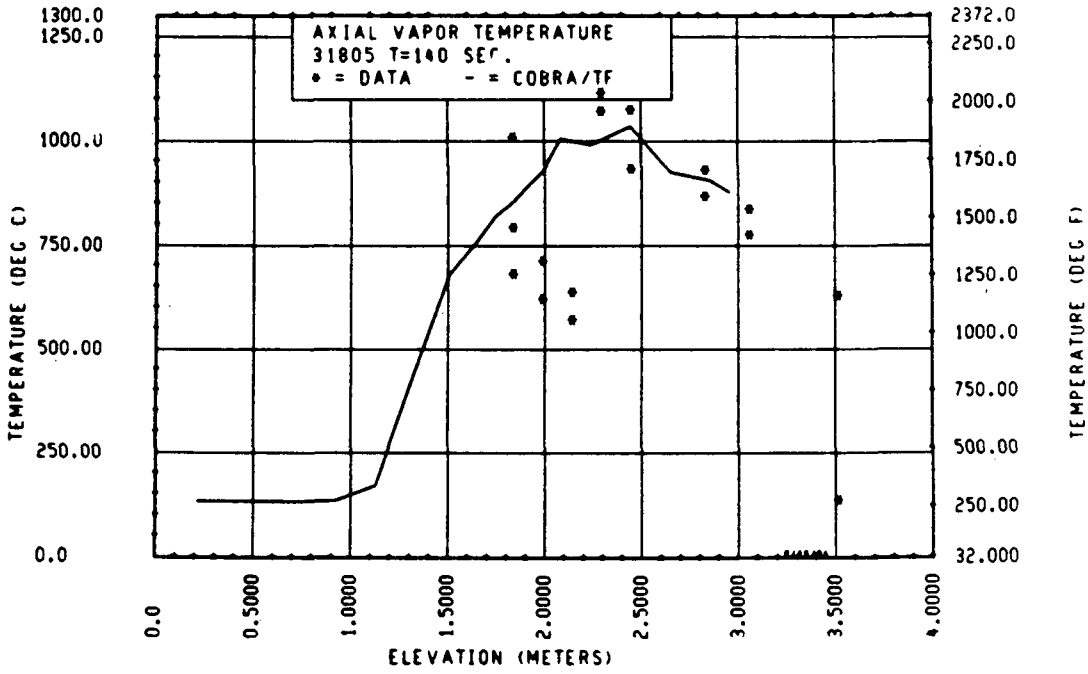

Figure 3-43. Comparison of COBRA-TF-Calculated Vapor Temperature Versus Time With FLECHT SEASET 161-Rod Data, Test 31805, t = 140 Seconds

Comparison of the axial heater rod temperature plots from test 31203 (figures 3-50 through 3-56) again shows excellent comparisons with the test data. (Also shown in figure 3-50 is the axial location of the spacer grids.) Again, once entrainment begins, the local cooling effects due to the grids can be seen in both the test data and the COBRA-TF predictions. The vapor temperature comparisons shown in figures 3-57 and 3-58 indicate that COBRA-TF is predicting the correct degree of nonequilibrium in the flow once entrainment begins, after 40 seconds.

The axial vapor plots (figure 3-59 through 3-65) show similar trends, with COBRA-TF overprediction of the steam probe data at early times and improved predictions after 60 seconds into the reflood transient. There does, however, appear to be a wider scatter in the vapor data for test 31203 than for the previously shown test 31805.

Selected comparisons for FLECHT SEASET test 32333, a 0.28 MPa (40 psia) stepped inlet flooding rate test, are shown in figures 3-66 through 3-71. The agreement between the COBRA-TF calculations and the test data is excellent.

Comparisons between heater rod clad temperatures and COBRA-TF predictions for FLECHT SEASET test 34209 are shown in figures 3-72 through 3-75. Test 34209 was a 0.025 m/sec (1 in./sec) flooding rate test at 0.14 MPa (20 psia). For this test, COBRA-TF overpredicts the cooling once entrainment begins for times greater than 50 seconds.

3-15. FLECHT SEASET 21-Rod Bundle Comparisons With COBRA-TF

The FLECHT SEASET 21-rod bundle tests were small-scale experiments designed to investigate the thermal-hydraulic effects of flow blockage. The 21-rod bundle is a full-length, 3.66 m (144 in.) rod bundle enclosed in a thin-wall tube which serves as a housing and pressure boundary. The COBRA-TF model for the 21-rod unblocked bundle is shown in figures 3-76 and 3-77, which give the radial and axial noding locations. Since the 21-rod bundle had one-eighth symmetry, only this portion of the rod bundle was simulated.

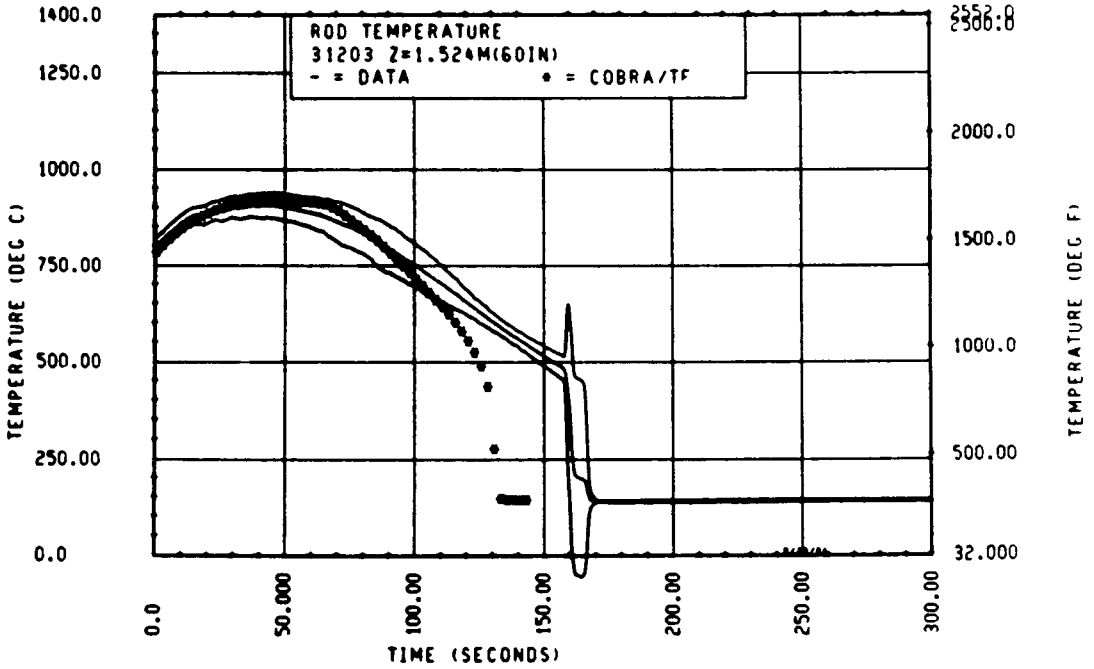

Figure 3-44. Comparison of COBRA-TF-Calculated Heater Rod Temperature Versus Time With FLECHT SEASET 161-Rod Data, Test 31203, 1.52 m (60 in.) Elevation

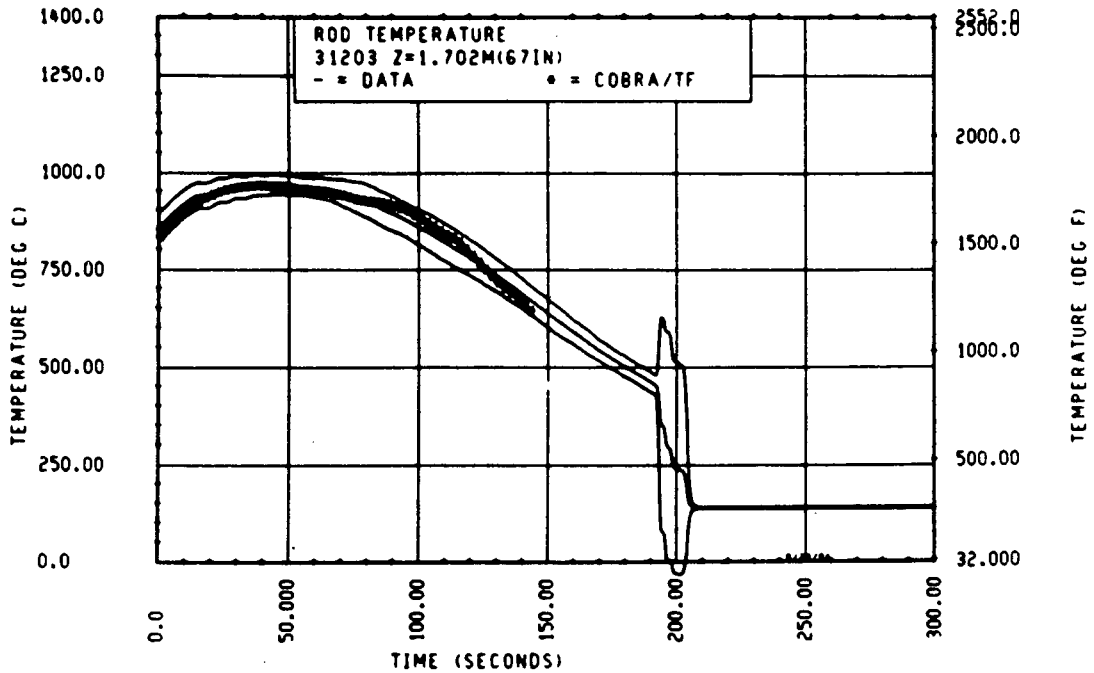

Figure 3-45. Comparison of COBRA-TF-Calculated Heater Rod Temperature Versus Time With FLECHT SEASET 161-Rod Data, Test 31203, 1.70 m (67 in.) Elevation

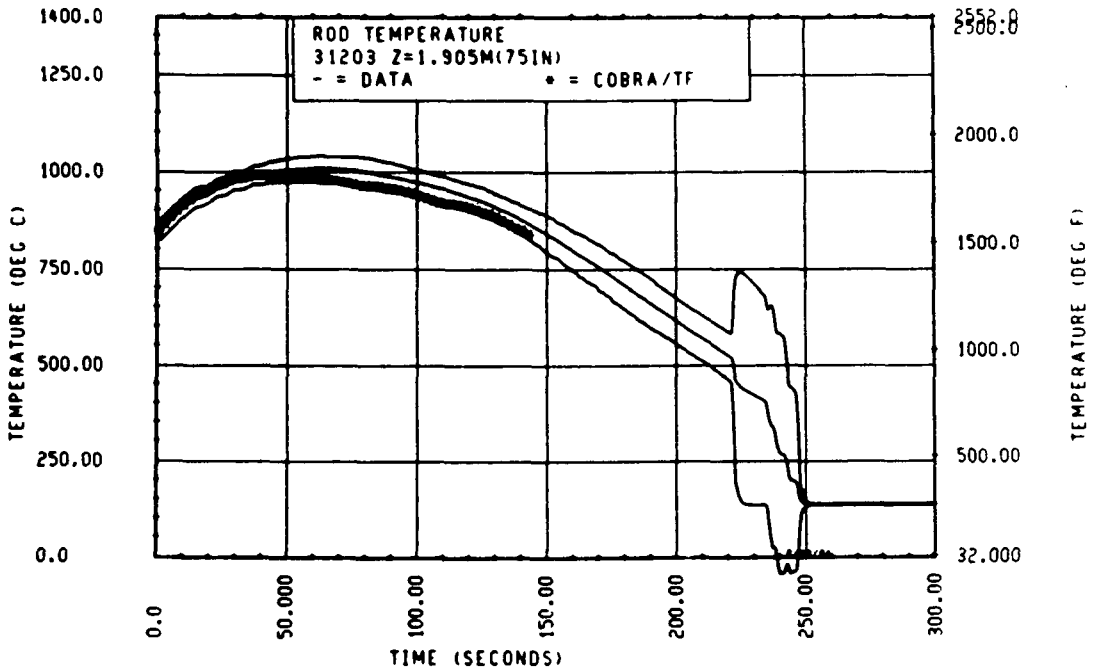

Figure 3-46. Comparison of COBRA-TF-Calculated Heater Rod Temperature Versus Time With FLECHT SEASET 161-Rod Data, Test 31203, 1.90 m (75 in.) Elevation

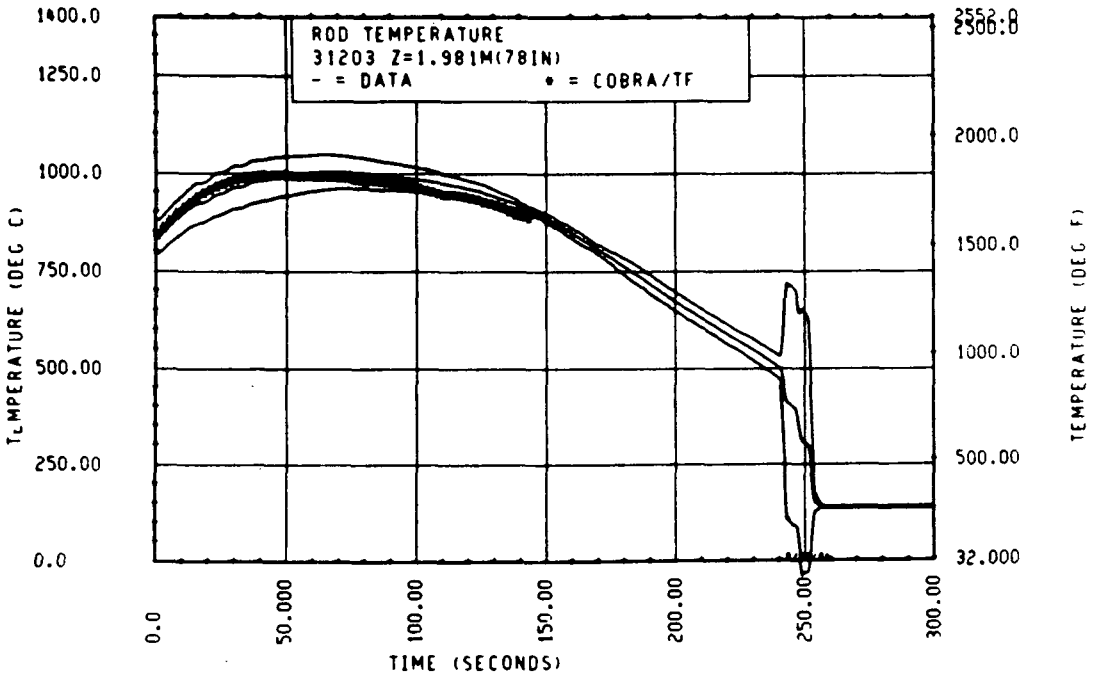

Figure 3-47. Comparison of COBRA-TF-Calculated Heater Rod Temperature Versus Time With FLECHT SEASET 161-Rod Data, Test 31203, 1.98 m (78 in.) Elevation

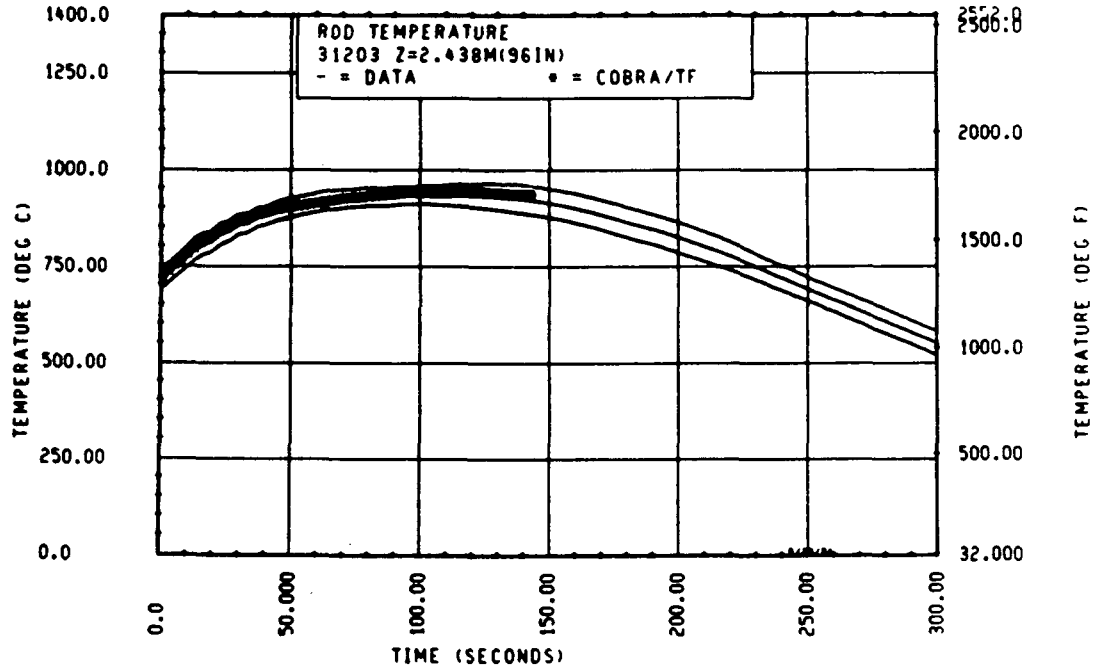

Figure 3-48. Comparison of COBRA-TF-Calculated Heater Rod Temperature Versus Time With FLECHT SEASET 161-Rod Data, Test 31203, 2.44 m (96 in.) Elevation

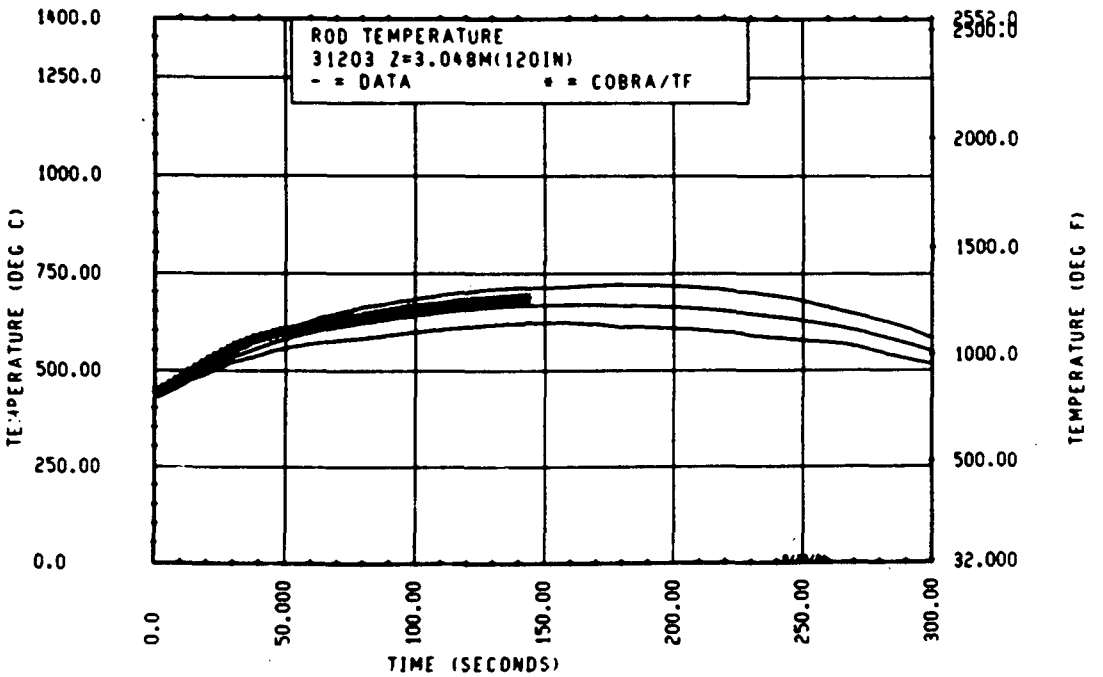

Figure 3-49. Comparison of COBRA-TF-Calculated Heater Rod Temperature Versus Time With FLECHT SEASET 161-Rod Data, Test 31203, 3.05 m (120 in.) Elevation

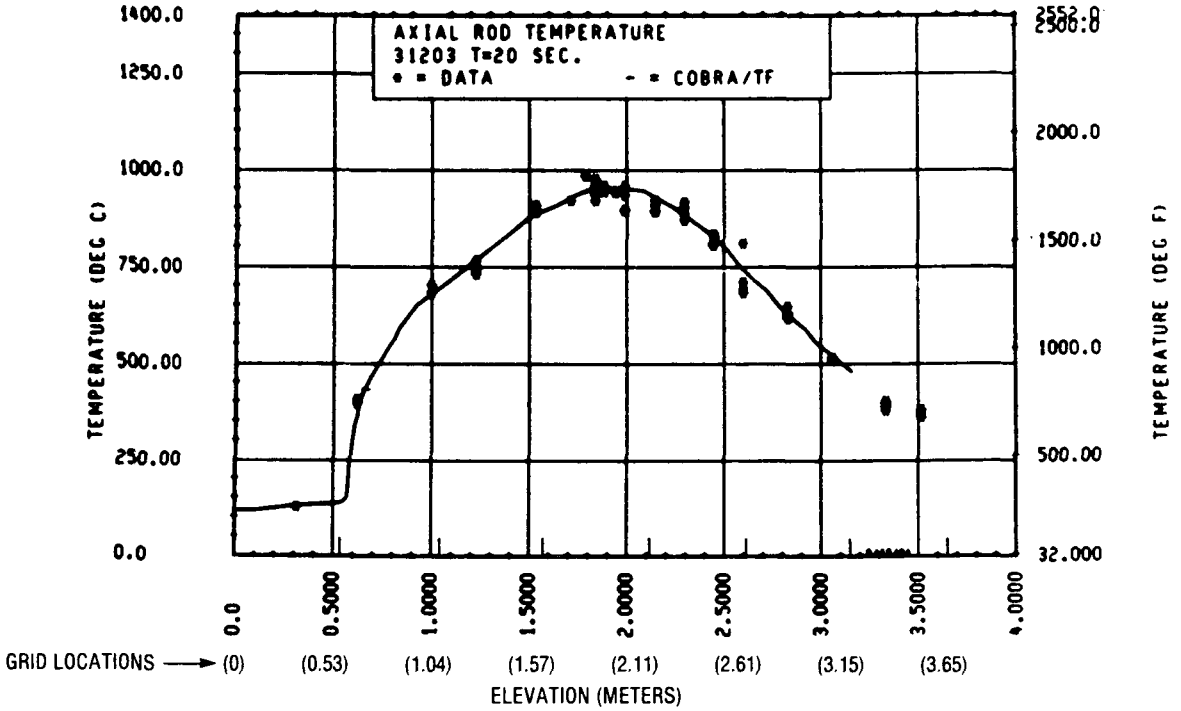

Figure 3-50. Comparison of COBRA-TF-Calculated Heater Rod Temperature Versus Elevation With FLECHT SEASET 161-Rod Data, Test 31203, t = 20 Seconds

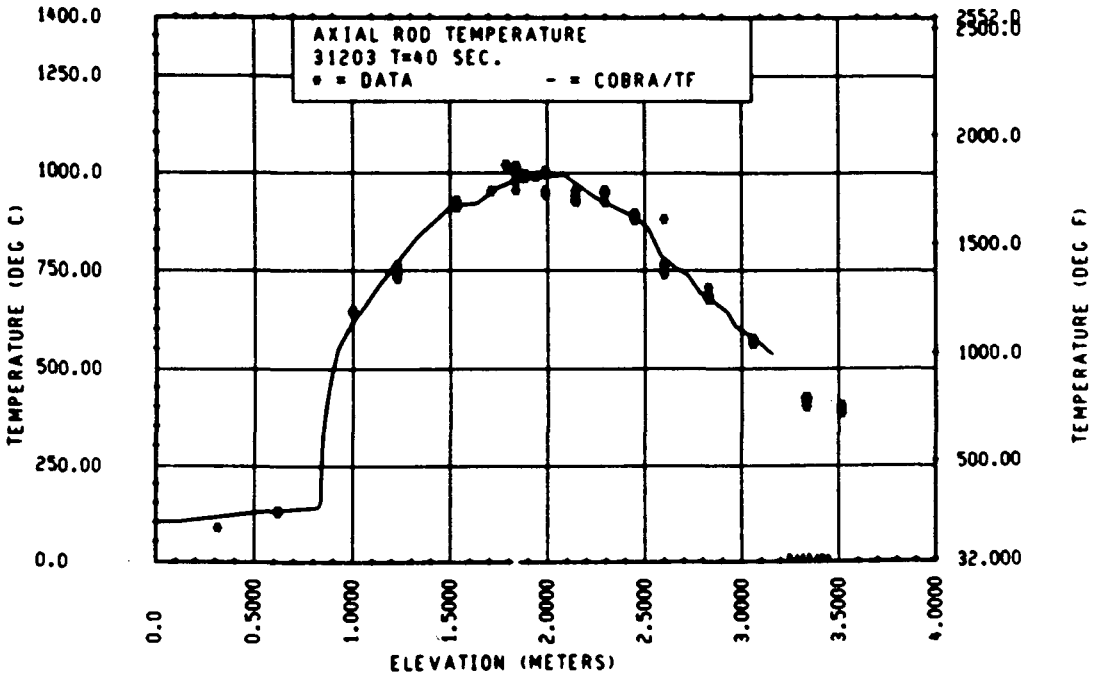

Figure 3-51. Comparison of COBRA-TF-Calculated Heater Rod Temperature Versus Elevation With FLECHT SEASET 161-Rod Data, Test 31203, t = 40 Seconds

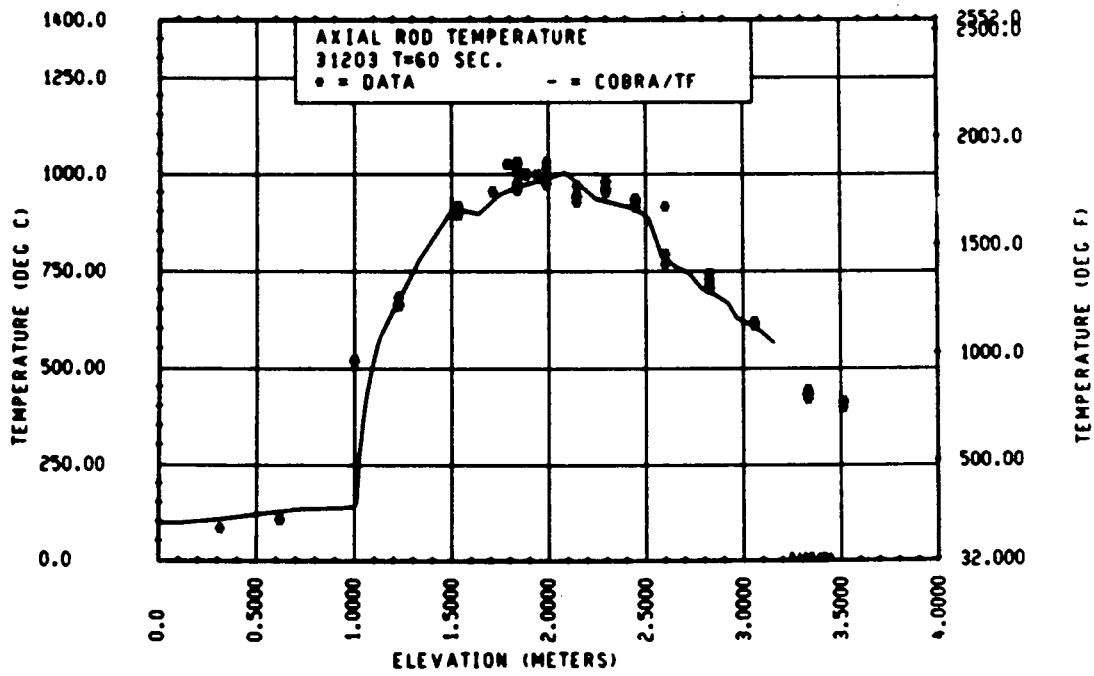

Figure 3-52. Comparison of COBRA-TF-Calculated Heater Rod Temperature Versus Time With FLECHT SEASET 161-Rod Data, Test 31203, t = 60 Seconds

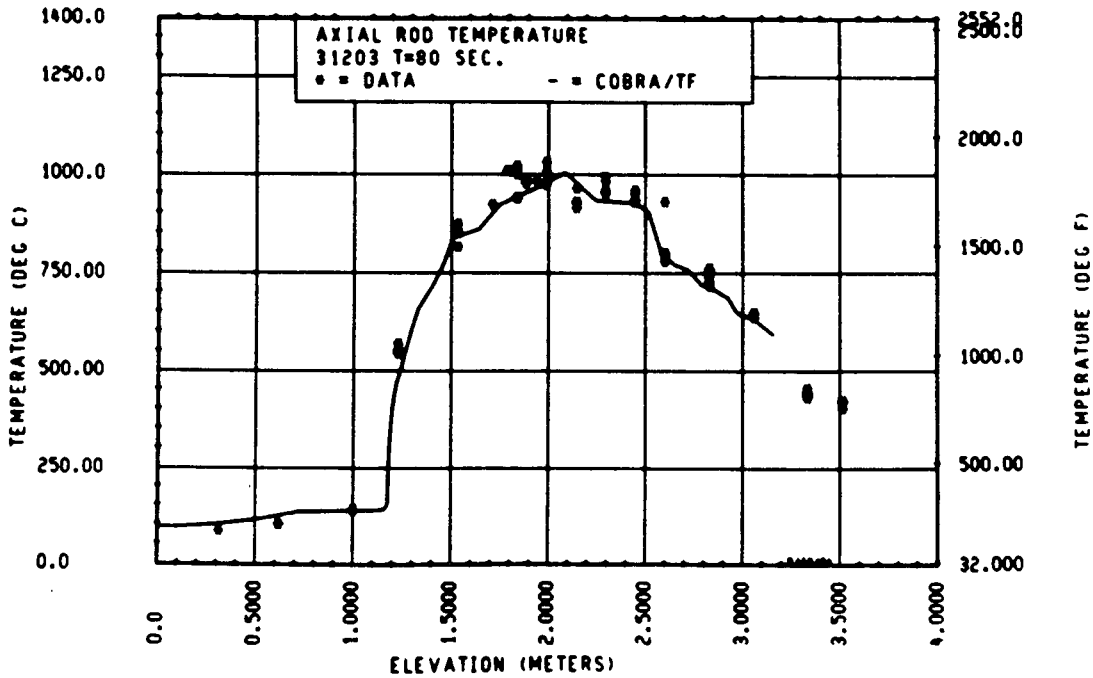

Figure 3-53. Comparison of COBRA-TF-Calculated Heater Rod Temperature Versus Time With FLECHT SEASET 161-Rod Data, Test 31203, t = 80 Seconds

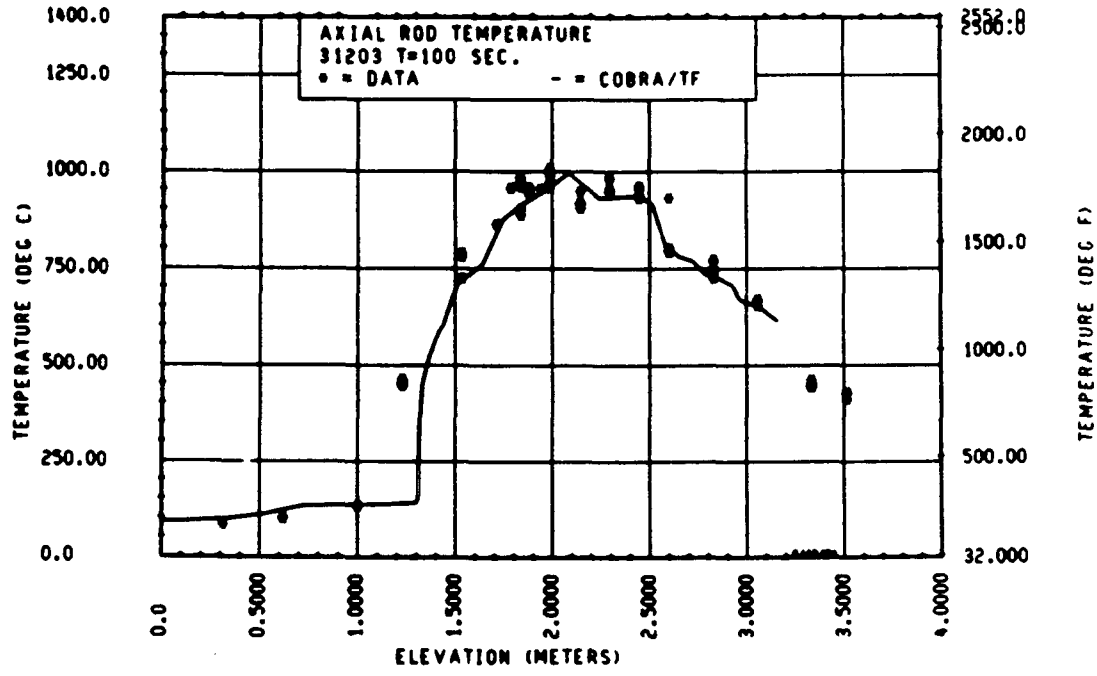

Figure 3-54. Comparison of COBRA-TF-Calculated Heater Rod Temperature Versus Time With FLECHT SEASET 161-Rod Data, Test 31203, t = 100 Seconds

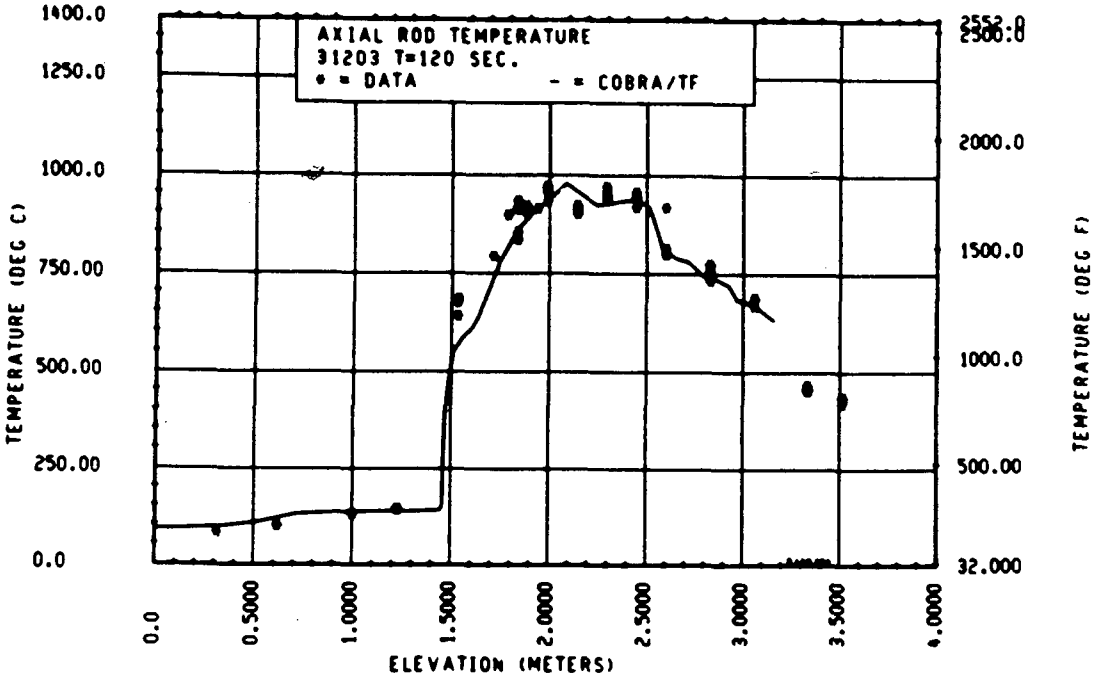

Figure 3-55. Comparison of COBRA-TF-Calculated Heater Rod Temperature Versus Time With FLECHT SEASET 161-Rod Data, Test 31203, t = 120 Seconds

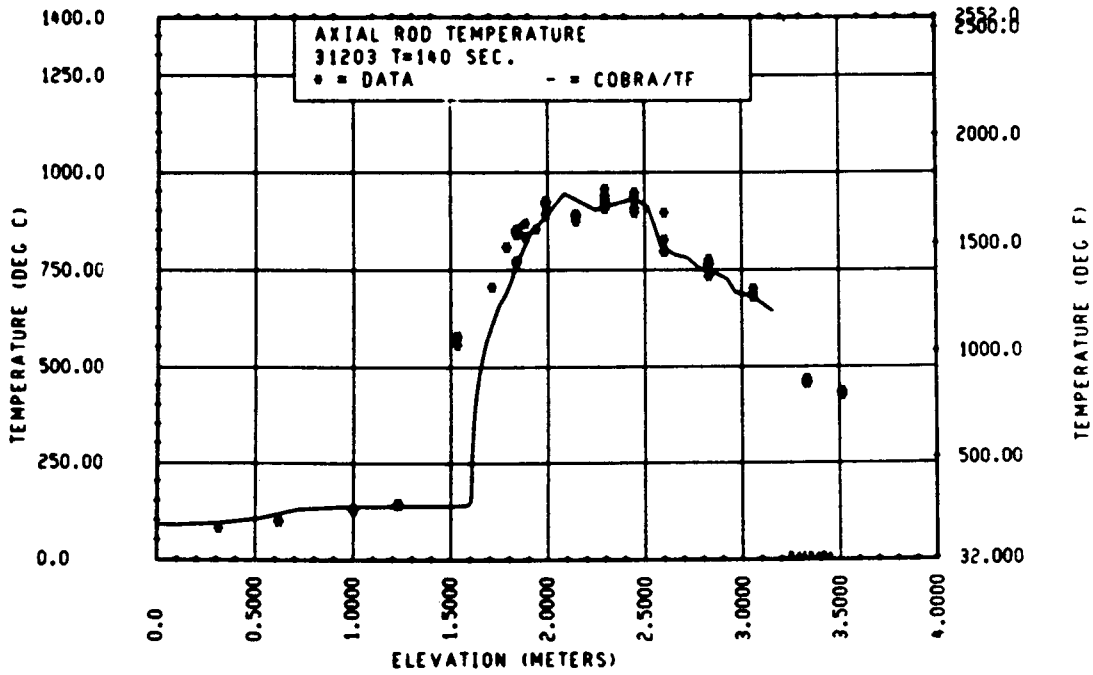

Figure 3-56. Comparison of COBRA-TF-Calculated Heater Rod Temperature Versus Time With FLECHT SEASET 161-Rod Data, Test 31203, t = 140 Seconds

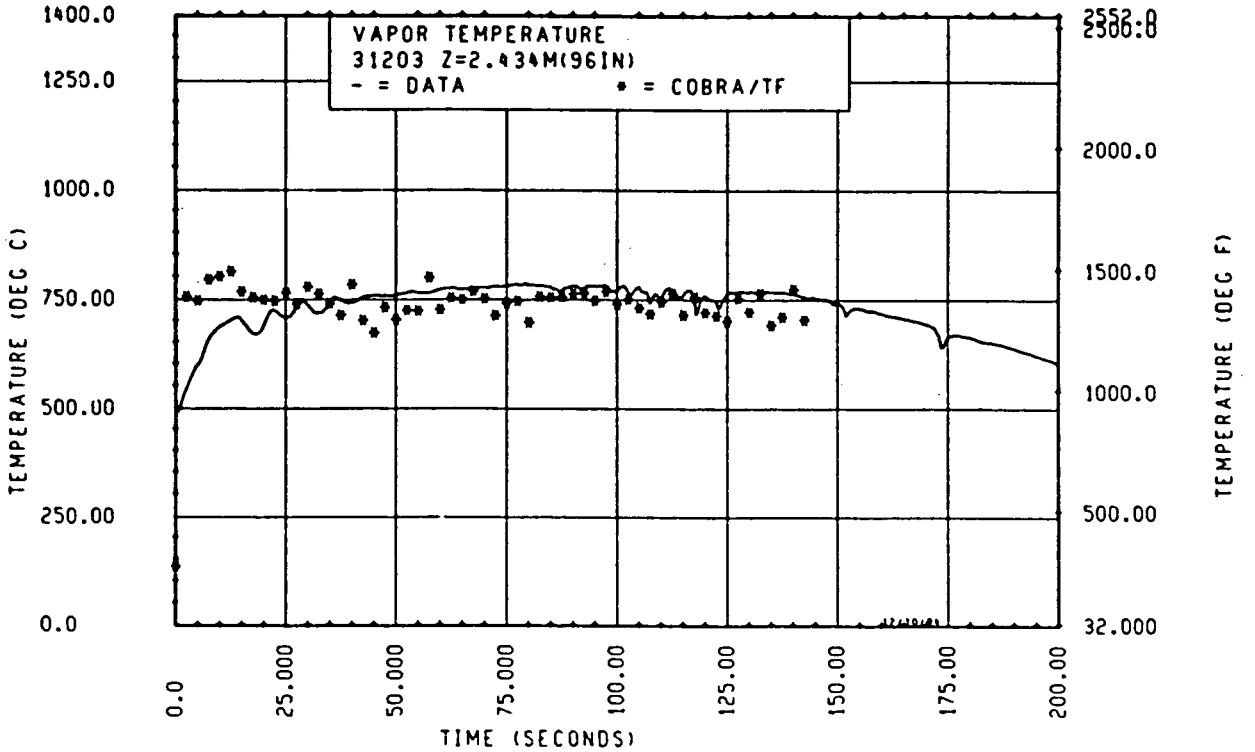

Figure 3-57. Comparison of COBRA-TF-Calculated Vapor Temperature Versus Time With FLECHT SEASET 161-Rod Data, Test 31203, 2.44 m (96 in.) Elevation

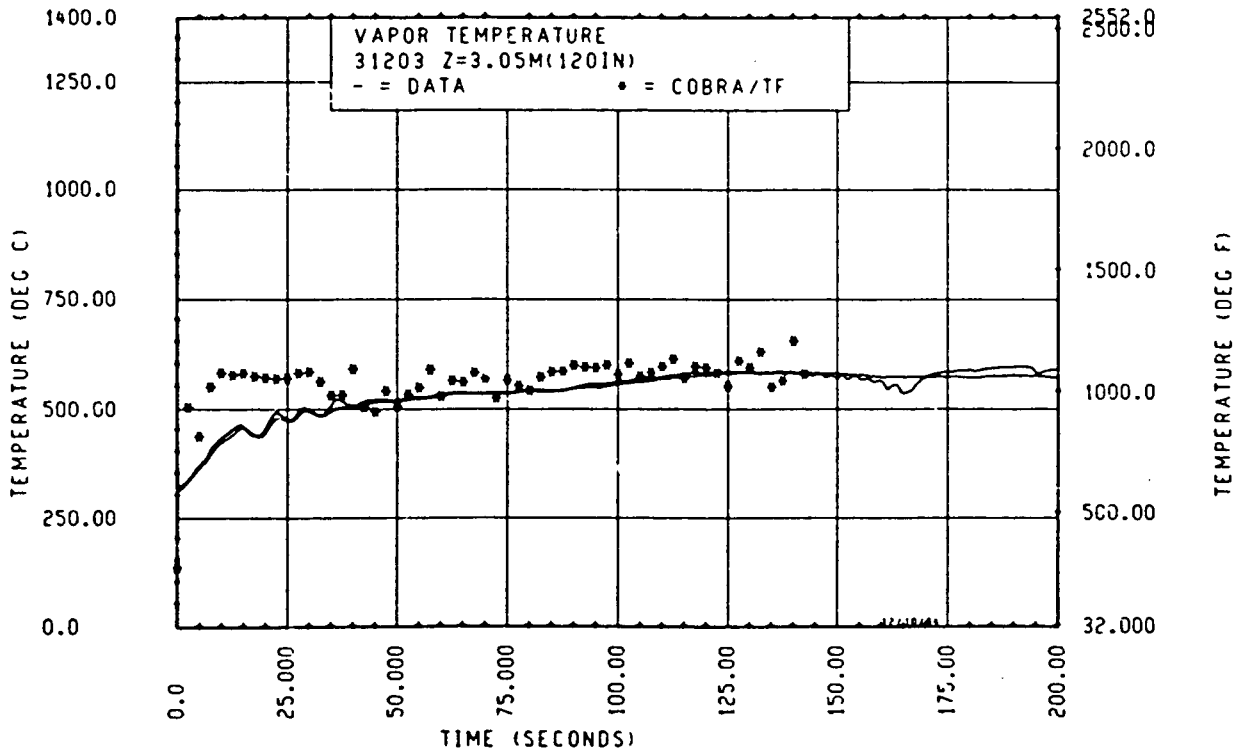

Figure 3-58. Comparison of COBRA-TF-Calculated Vapor Temperature Versus Time With FLECHT SEASET 161-Rod Data, Test 31203, 3.05 m (120 in.) Elevation

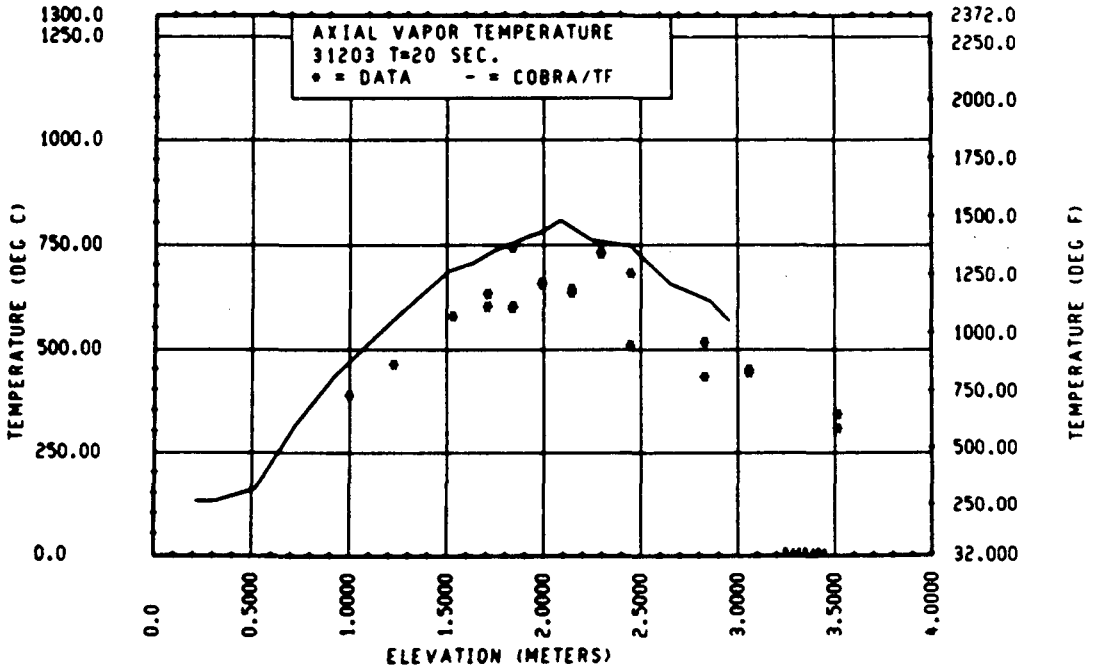

Figure 3-59. Comparison of COBRA-TF-Calculated Vapor Temperature Versus Elevation With FLECHT SEASET 161-Rod Data, Test 31203, t = 20 Seconds

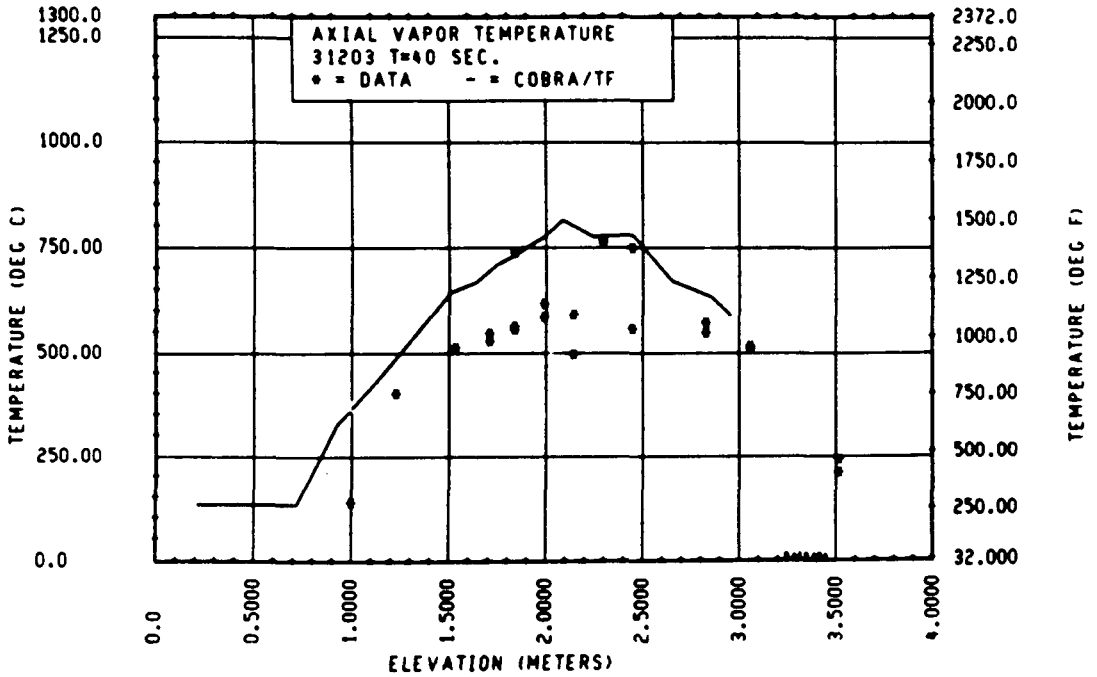

Figure 3-60. Comparison of COBRA-TF-Calculated Vapor Temperature Versus Elevation With FLECHT SEASET 161-Rod Data, Test 31203, t = 40 Seconds

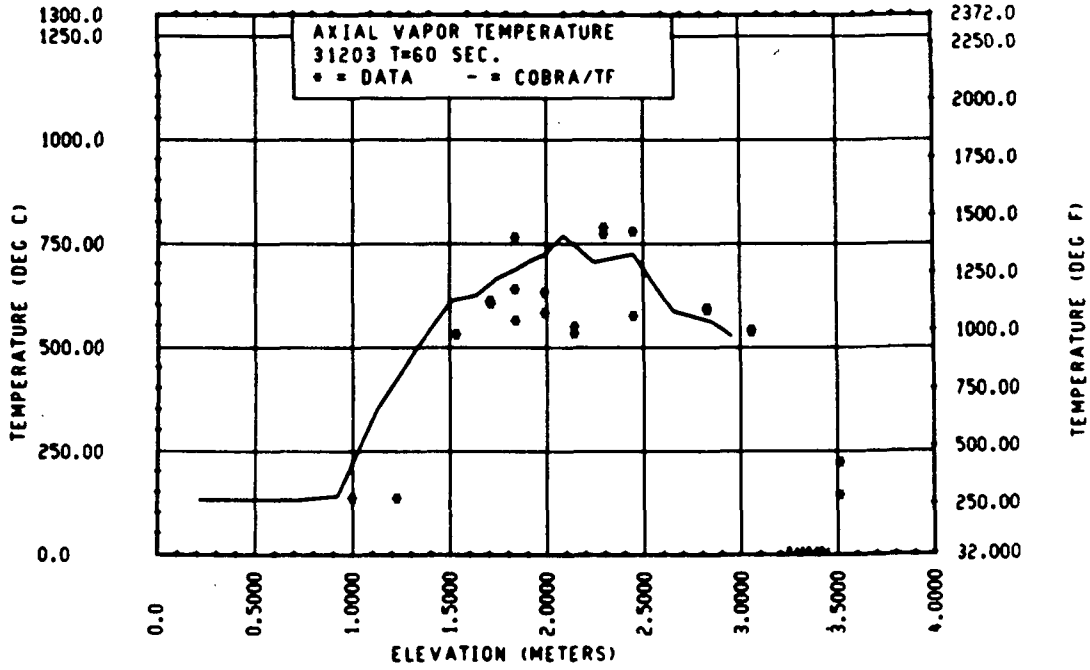

Figure 3-61. Comparison of COBRA-TF-Calculated Vapor Temperature Versus Time With FLECHT SEASET 161-Rod Data, Test 31203, t = 60 Seconds

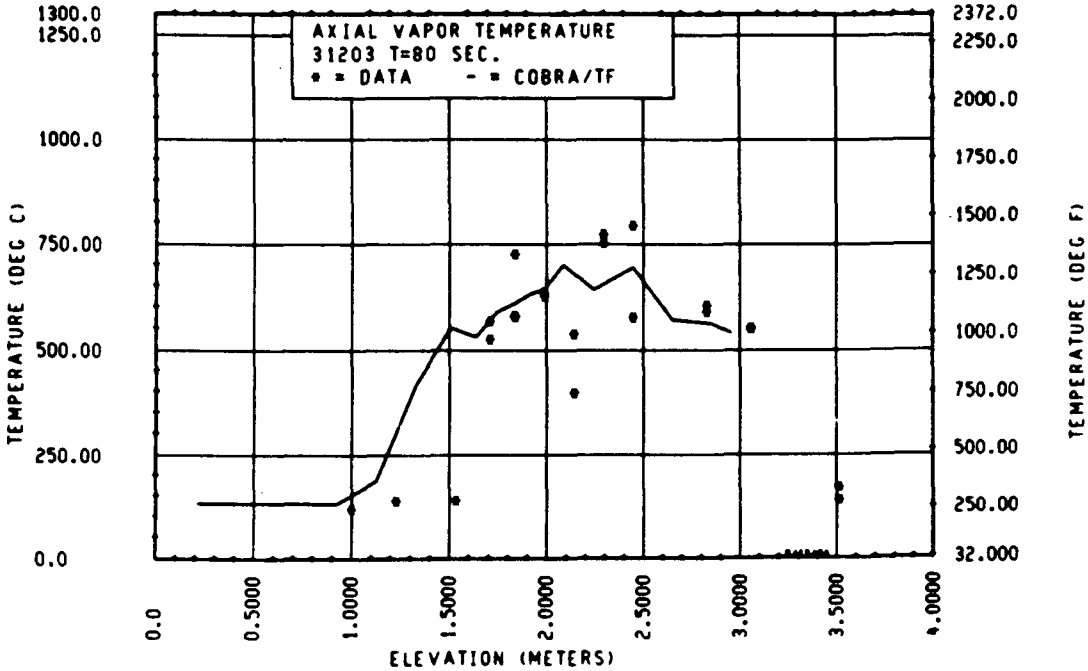

Figure 3-62. Comparison of COBRA-TF-Calculated Vapor Temperature Versus Time With FLECHT SEASET 161-Rod Data, Test 31203, t = 80 Seconds

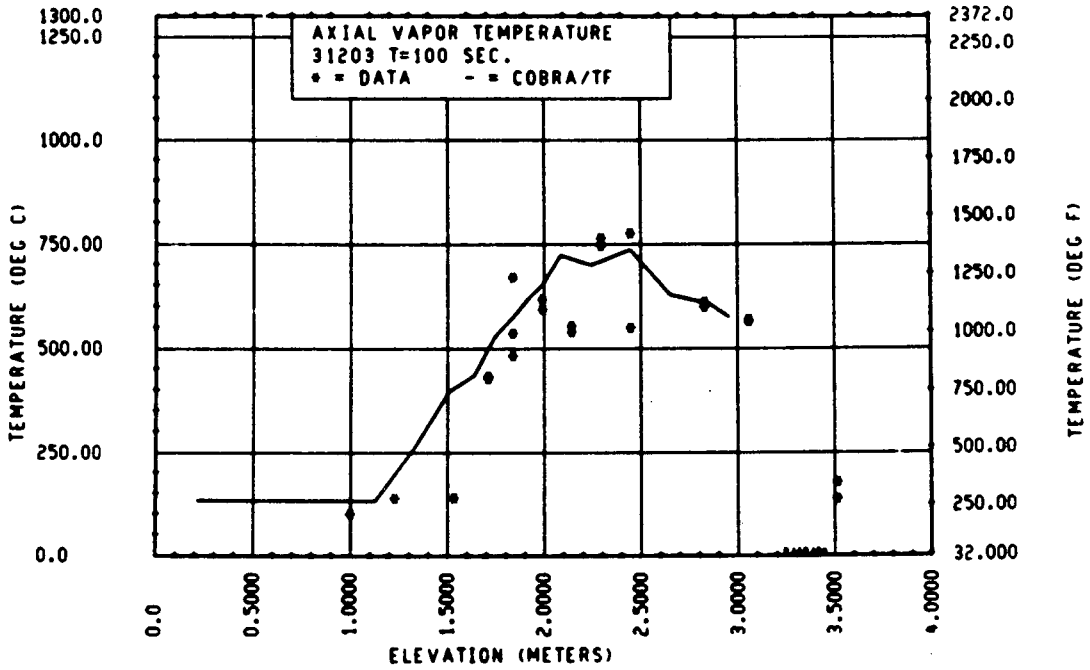

Figure 3-63. Comparison of COBRA-TF-Calculated Vapor Temperature Versus Time With FLECHT SEASET 161-Rod Data, Test 31203, t = 100 Seconds

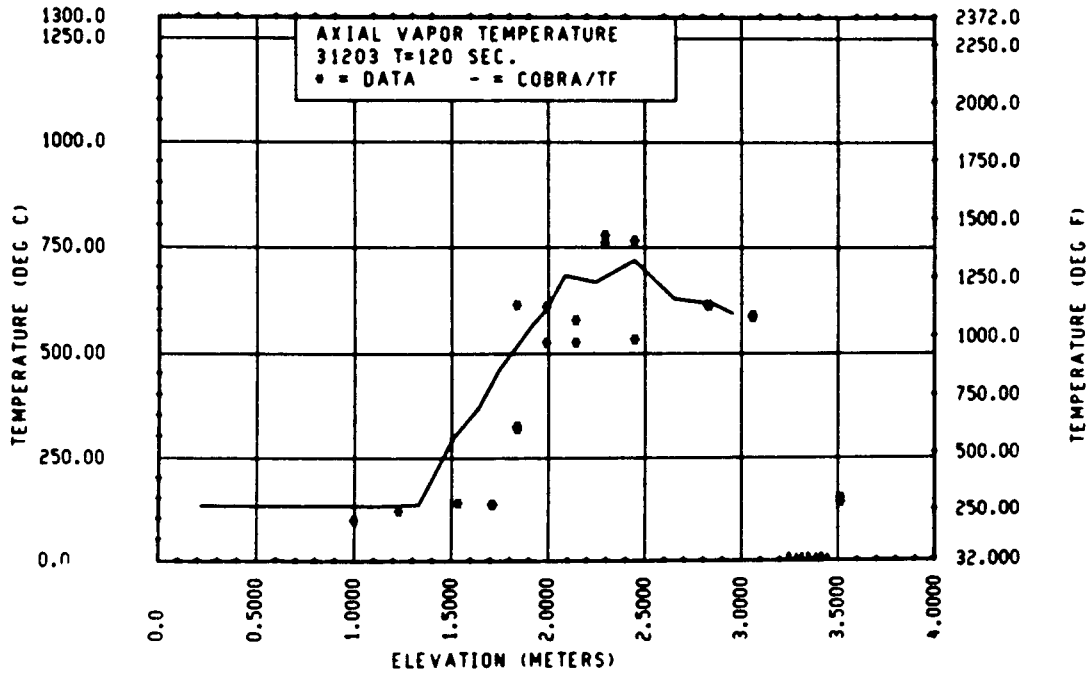

Figure 3-64. Comparison of COBRA-TF-Calculated Vapor Temperature Versus Time With FLECHT SEASET 161-Rod Data, Test 31203, t = 120 Seconds

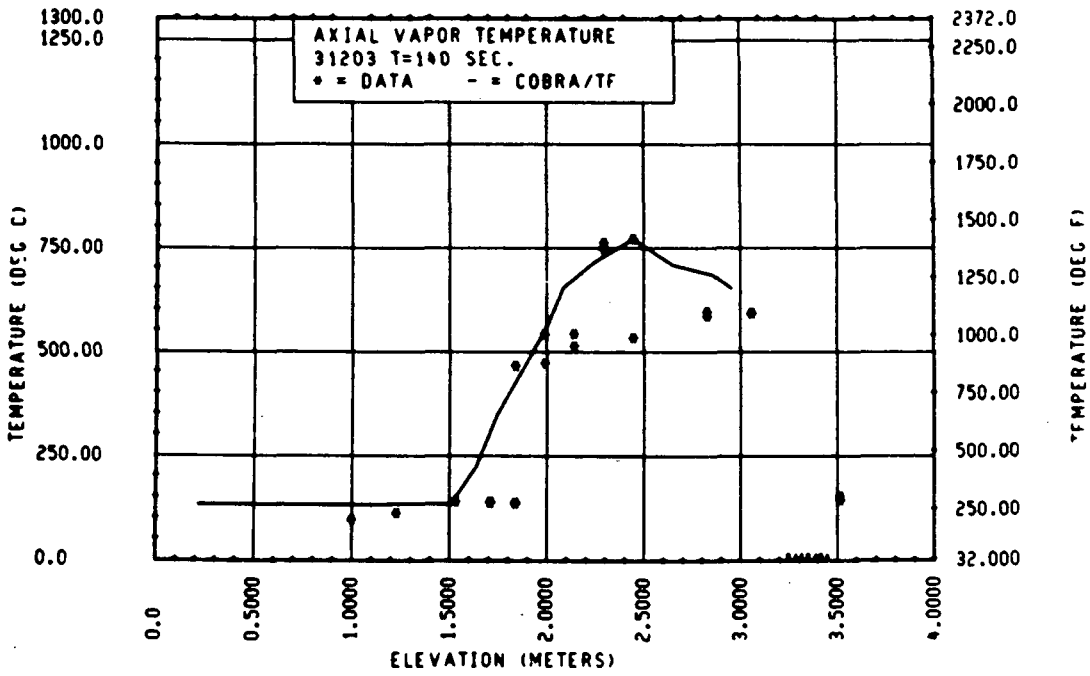

Figure 3-65. Comparison of COBRA-TF-Calculated Vapor Temperature Versus Time With FLECHT SEASET 161-Rod Data, Test 31203, t = 140 Seconds

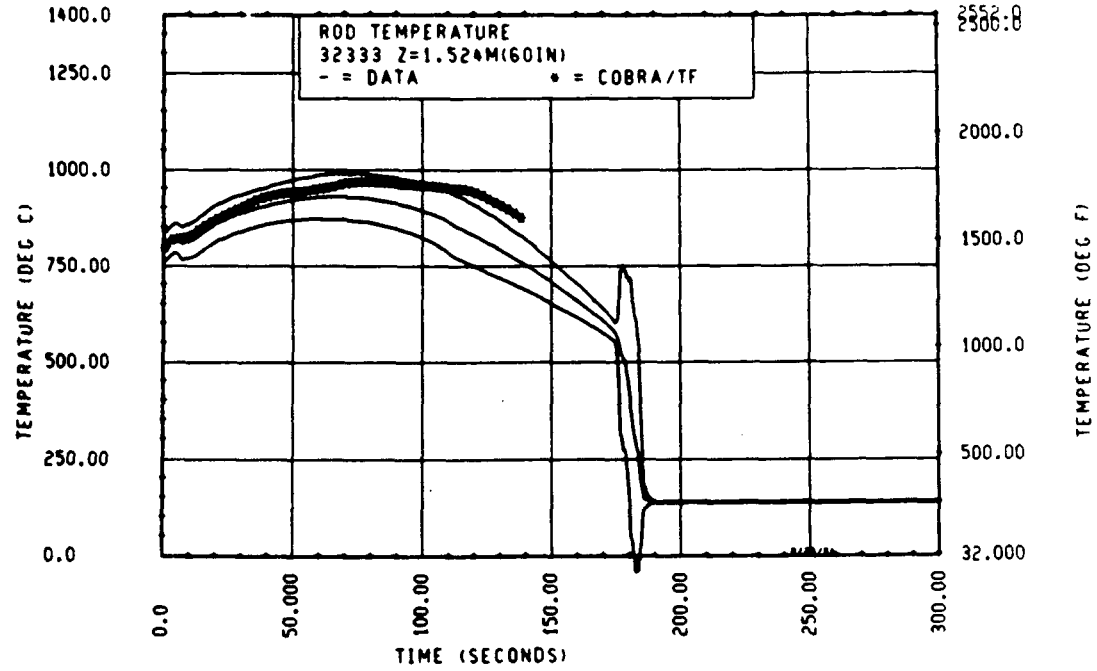

Figure 3-66. Comparison of COBRA-TF-Calculated Heater Rod Temperature Versus Time With FLECHT SEASET 161-Rod Data, Test 32333, 1.52 m (60 in.) Elevation

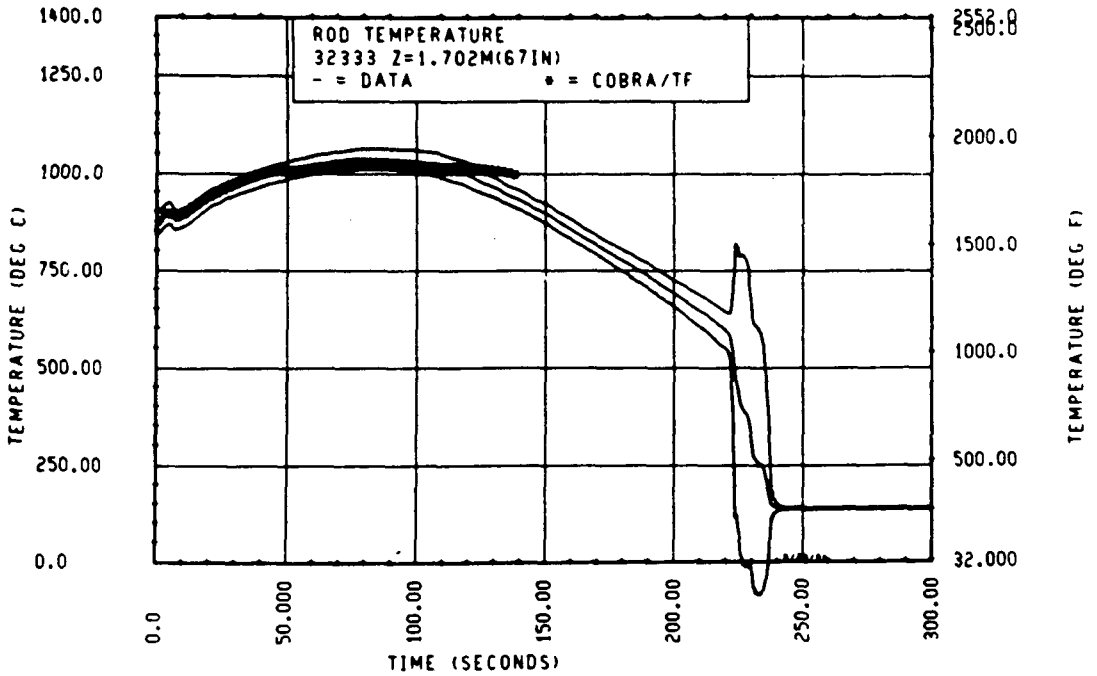

Figure 3-67. Comparison of COBRA-TF-Calculated Heater Rod Temperature Versus Time With FLECHT SEASET 161-Rod Data, Test 32333, 1.70 m (67 in.) Elevation

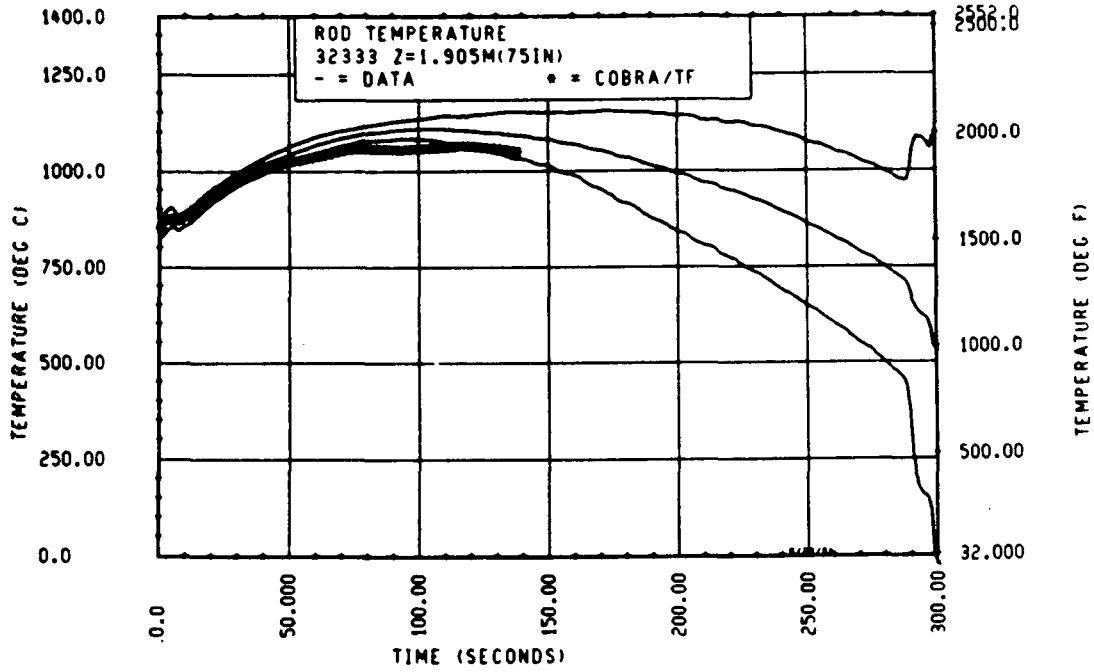

Figure 3-68. Comparison of COBRA-TF-Calculated Heater Rod Temperature Versus Time With FLECHT SEASET 161-Rod Data, Test 32333, 1.90 m (75 in.) Elevation

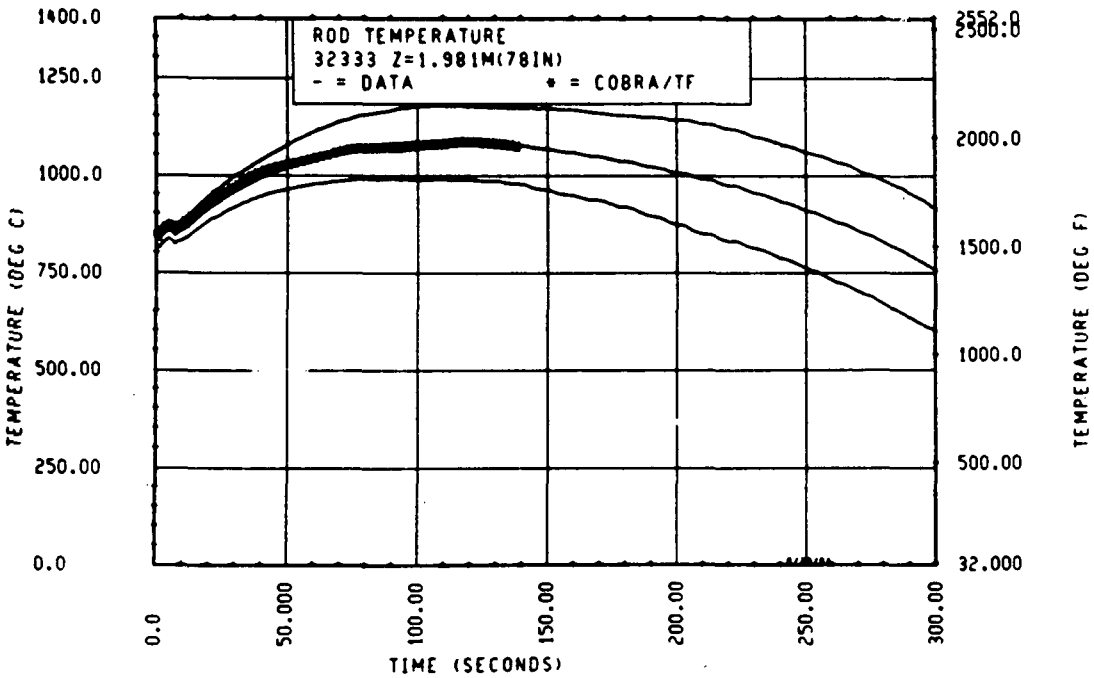

Figure 3-69. Comparison of COBRA-TF-Calculated Heater Rod Temperature Versus Time With FLECHT SEASET 161-Rod Data, Test 32333, 1.98 m (78 in.) Elevation

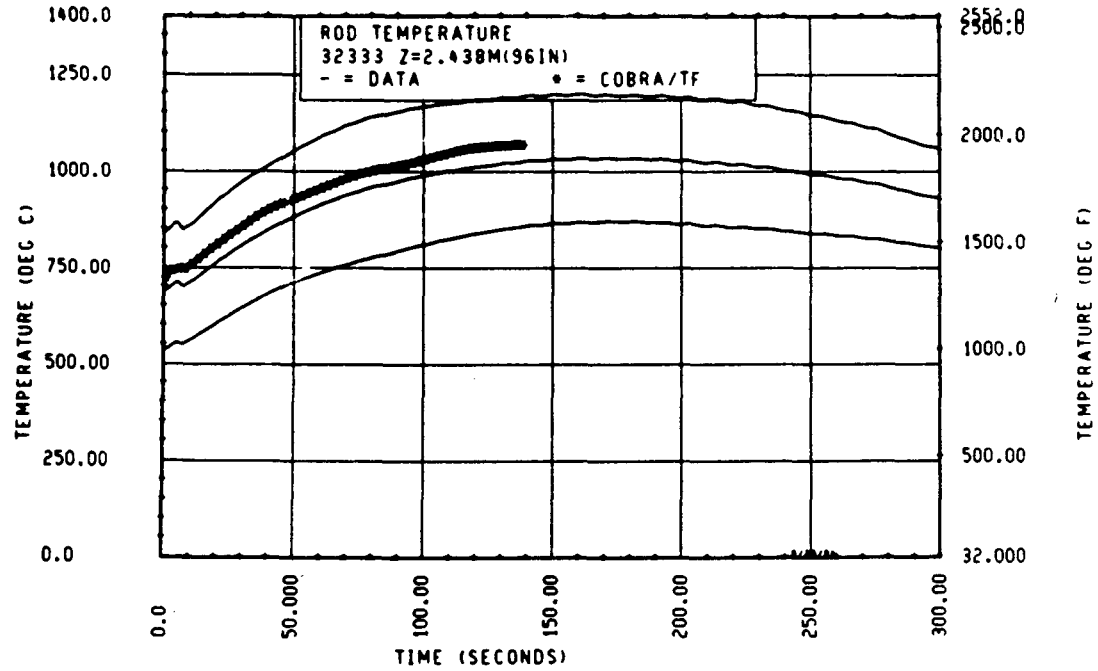

Figure 3-70. Comparison of COBRA-TF-Calculated Heater Rod Temperature Versus Time With FLECHT SEASET 161-Rod Data, Test 32333, 2.44 m (96 in.) Elevation

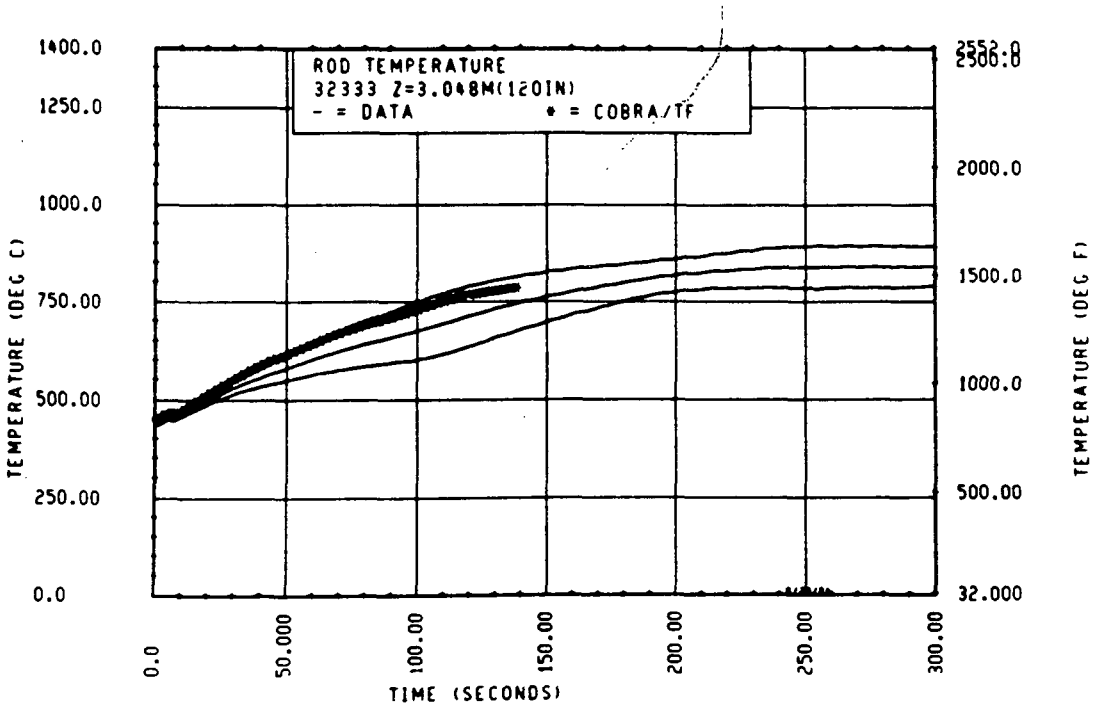

Figure 3-71. Comparison of COBRA-TF-Calculated Heater Rod Temperature Versus Time With FLECHT SEASET 161-Rod Data, Test 32333, 3.05 m (120 in.) Elevation

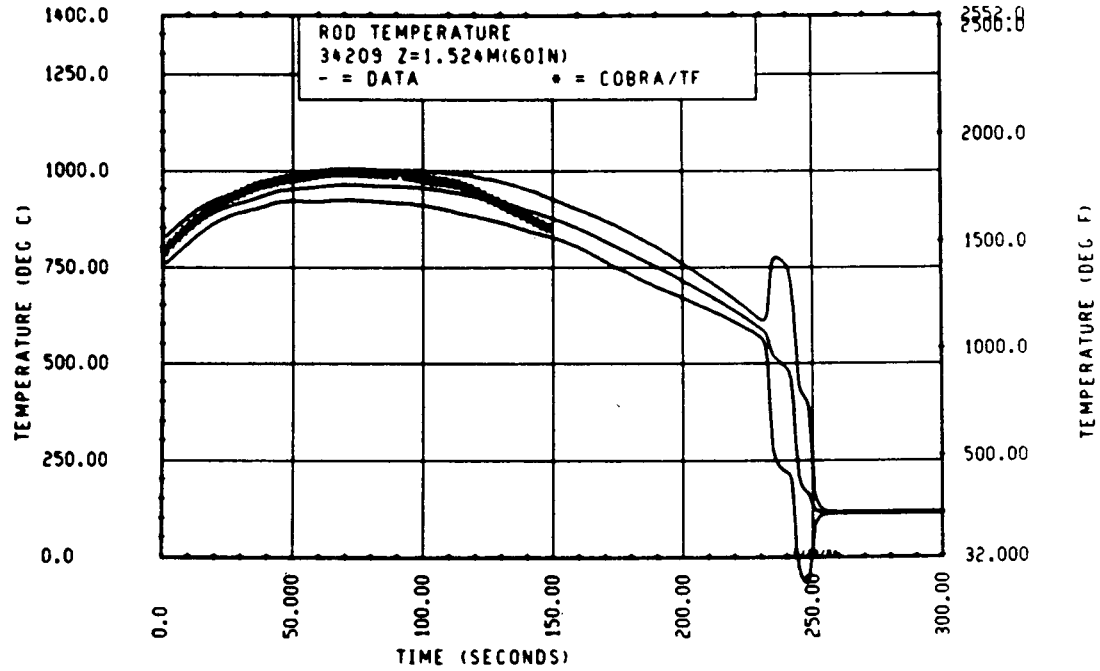

Figure 3-72. Comparison of COBRA-TF-Calculated Heater Rod Temperature Versus Time With FLECHT SEASET 161-Rod Data, Test 34209, 1.52 m (60 in.) Elevation

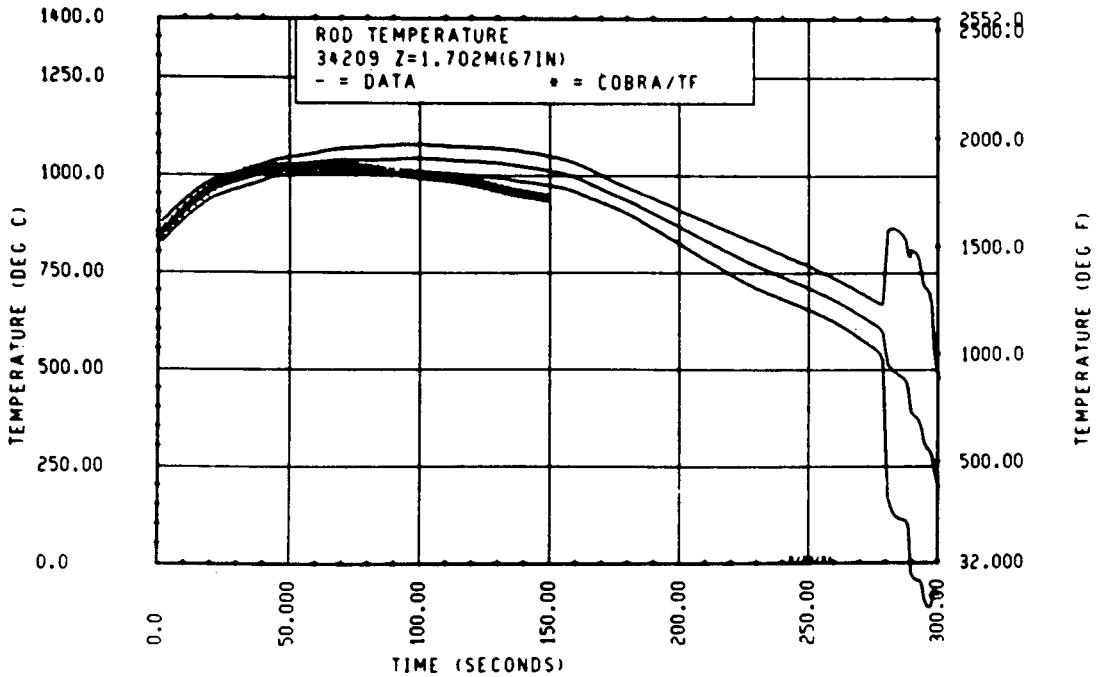

Figure 3-73. Comparison of COBRA-TF-Calculated Heater Rod Temperature Versus Time With FLECHT SEASET 161-Rod Data, Test 34209, 1.70 m (67 in.) Elevation

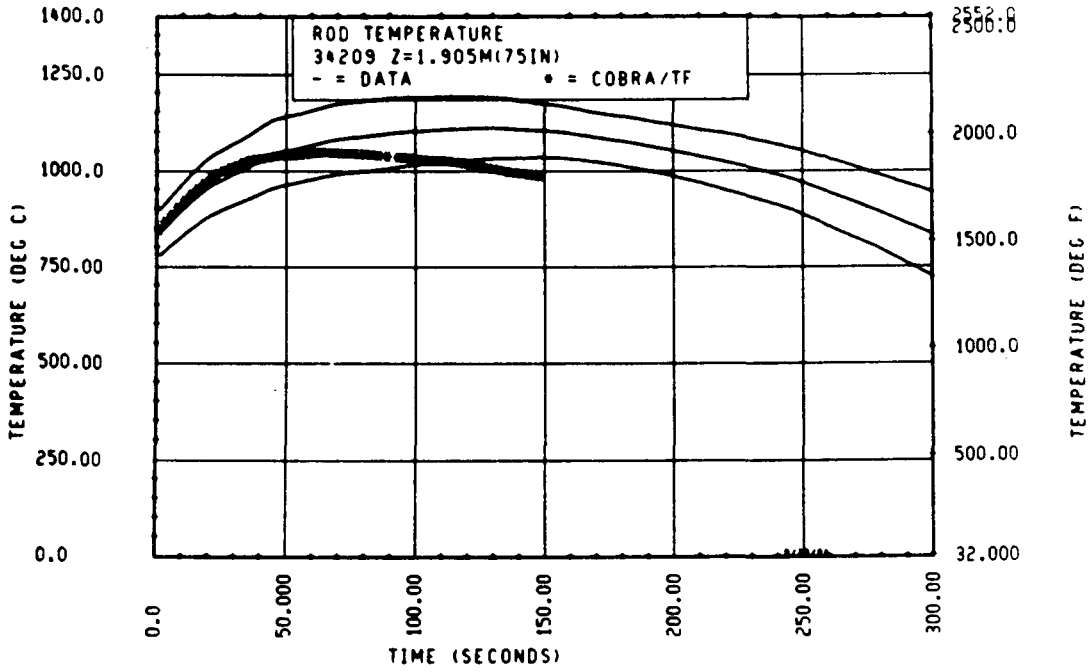

Figure 3-74. Comparison of COBRA-TF-Calculated Heater Rod Temperature Versus Time With FLECHT SEASET 161-Rod Data, Test 34209, 1.90 m (75 in.) Elevation

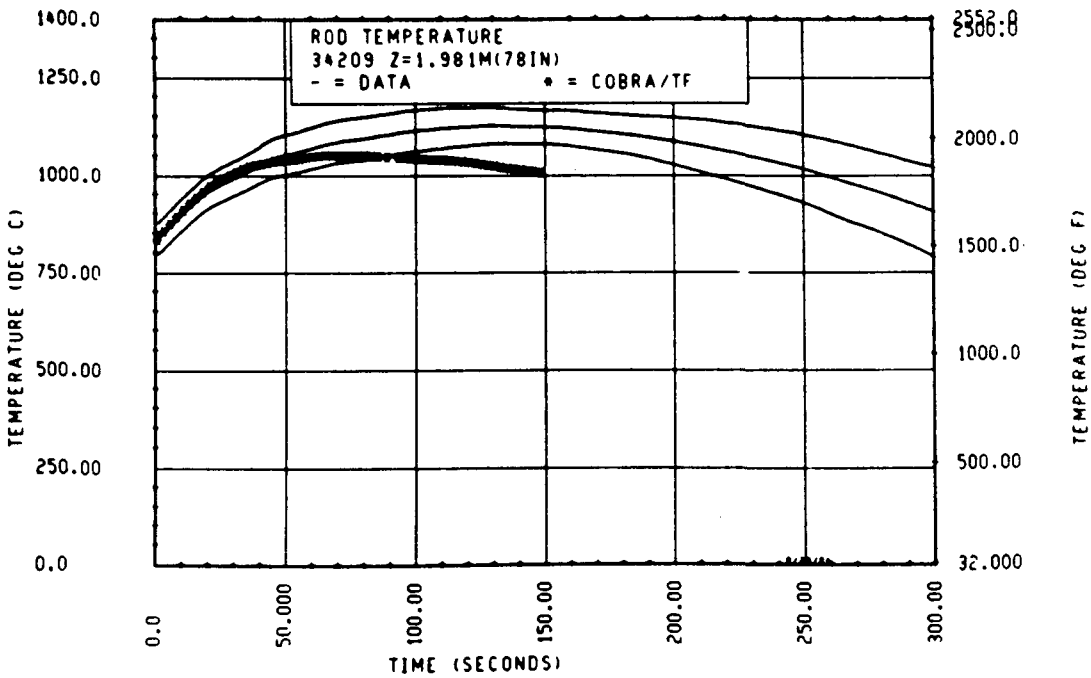

Figure 3-75. Comparison of COBRA-TF-Calculated Heater Rod Temperature Versus Time With FLECHT SEASET 161-Rod Data, Test 34209, 1.98 m (78 in.) Elevation

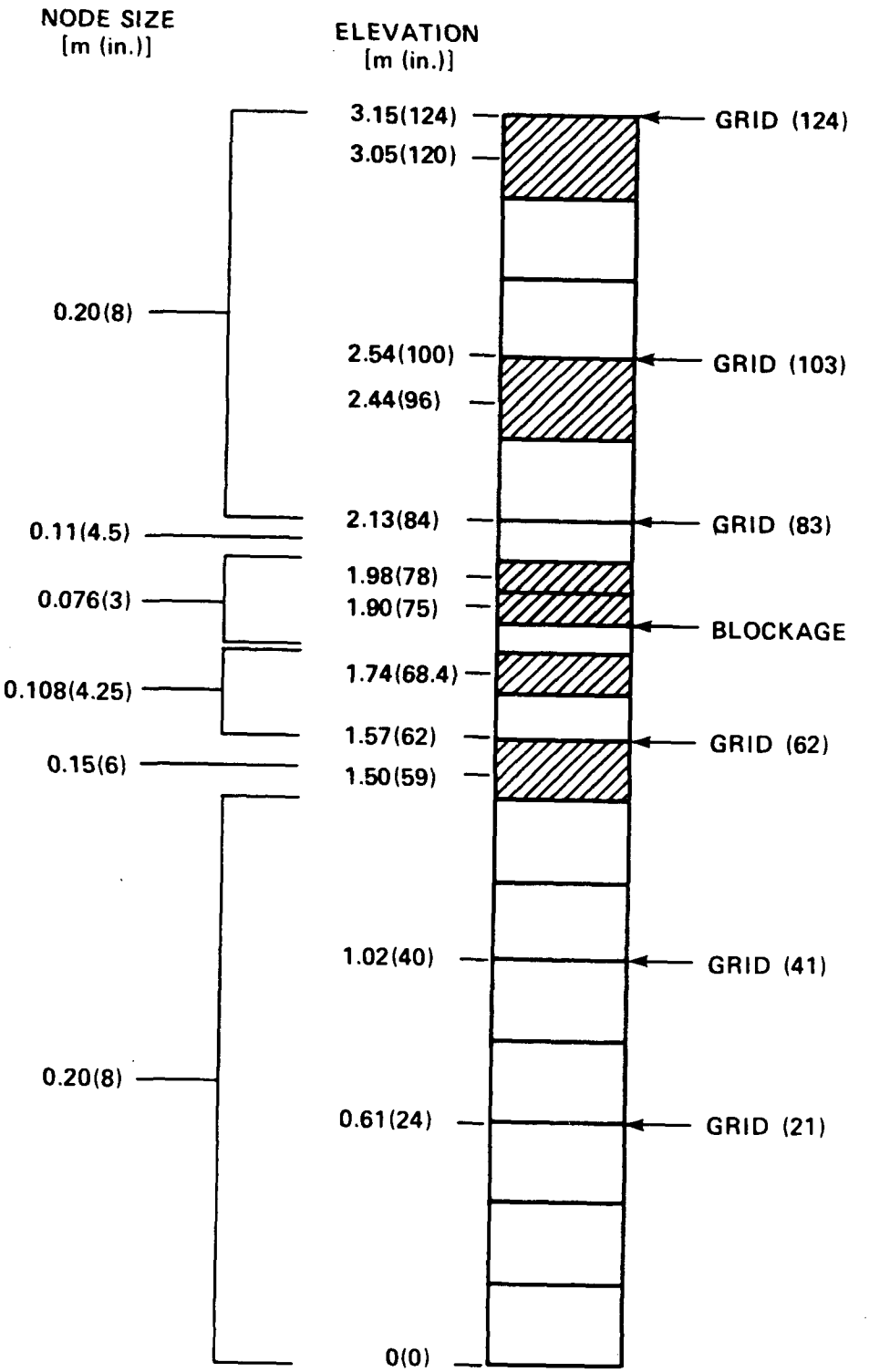

Figure 3-76. Axial Noding for FLECHT SEASET 21-Rod Bundle Test Data Comparisons

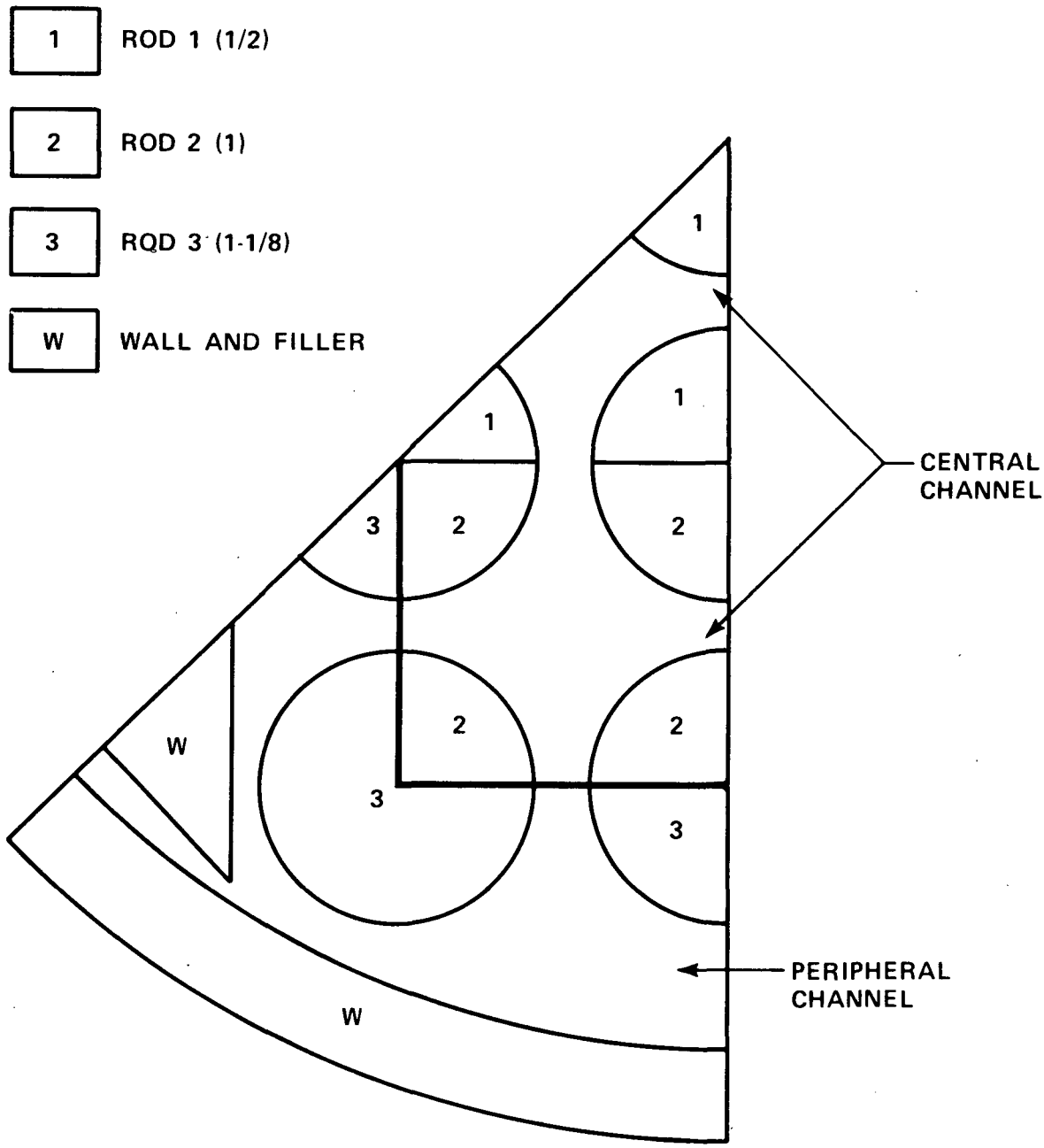

Figure 3-77. Radial Noding for FLECHT SEASET 21-Rod Bundle Test Data Comparisons

The triangular filler rod piece in the rod bundle was modeled thermally as part of the rod bundle housing. Thus, the filler temperature, heat release, and quench time were identical to the housing. This was an approximation made in the modeling to reduce the number of individual rods and thus the code running time. It was observed in experiments that the fillers probably did quench sooner than the housing because of their higher surface area per unit volume. However, the fillers did not quench until the peak heater rod temperatures had turned around.

The 21-rod bundle housing and fillers were modeled as a separate rod in COBRA-TF, similar to the 161-rod unblocked bundle housing. It was observed that when the housing and filler behavior was calculated using COBRA-TF, the bottom quench front was predicted accurately; however, the top-down quench was always underestimated and the housing would quench faster in the experiment than in the COBRA-TF prediction. Since the 21-rod bundle is so small, the effects of quenching the housing is a first-order effect on all the rods, including the centermost rod. The result is improved rod cooling. Therefore, underprediction of the top-down housing quench would result in overprediction of the heater rod temperatures at later times, greater than turnaround times at elevations above 1.98 m (78 in.).

This housing effect was noticed in the data at reflood times greater than 150 seconds, which was usually equal to or later than the peak temperature time. As discussed in the 161-rod bundle results (paragraph 3-14), attempts were made to read in the housing wall temperatures and quench heat flux as a function of time. However, with this scheme, the calculated wall heat flux to the fluid had no thermal-hydraulic feedback (since it was at a prescribed temperature) and the incorrect result was an increased heat flux to the fluid. Therefore, this approach was abandoned and the housing behavior was uniquely modeled in the code.

Since the housing can have a significant radiation heat sink effect, a more elaborate rod-to-rod radiation model was employed in the COBRA-TF 21-rod bundle simulation. The details of this model are given in appendix A for the 21-rod bundle. Choosing the correct representation was somewhat iterative,

and the best radiation model was based on predicting the adiabatic heatup temperature distribution measured in the experiment before reflooding began.

The axial noding for the 21-rod bundle tests (figure 3-77) was specifically chosen to best match the detailed axial thermocouple distribution above the midplane and around the 2.11 m (83 in.) grid. Again, there had to be some compromise between the desired detail and code run time. The axial loss coefficients for the grids were set using the recommended values from the 21-rod bundle report[1] such that COBRA-TF would predict the correct bundle pressure drop.

The 21-rod bundle experiments which were modeled are listed in table 3-2; test conditions were nearly identical to the unblocked bundle tests previously discussed. Repetition of calculations at the same thermal-hydraulic conditions but on a bundle of significantly smaller size, shows how well the COBRA-TF code can handle the scaling effects plus the additional complication of the test model hosing impact on the heater rod performance.

Comparisons of FLECHT SEASET 21-rod unblocked bundle test 42606A with the COBRA-TF predictions are given in figures 3-78 through 3-94. The COBRA-TF calculation was carried out to approximately 100 seconds, which is past hot rod turnaround time and sufficiently long to judge the code agreement with the test data. As mentioned earlier, at longer times COBRA-TF would tend to overpredict the test data. The primary reason for this was the additional cooling effect to the top-down housing quench which was observed in the experiments but not calculated accurately by the code.

---

1. Loftus, M. J., et al., "PWR FLECHT SEASET 21-Rod Bundle Flow Blockage Task Data and Analysis Report," NRC/EPRI/ Westinghouse-11, September 1982.

The heater rod temperature versus time plots are shown in figures 3-78 through 3-83 for different elevations along the rod bundle. The computer code calculation is for a center rod in the 21-rod bundle COBRA-TF model (figure 3-76) and the data are from the same inner rods in the rod bundle. The agreement between the data and the code predictions is excellent, except at the 1.52 m (60 in.) elevation. It is believed that data from this elevation may have been influenced by the filler rod failure which occurred during testing and which moved down the lower filler rod and grid assembly in the rod bundle. There is a FLECHT spacer grid at the 1.57 m (62 in.) elevation which could have slipped down, covering the heater rod thermocouples at the 1.52 m (60 in.) location.

Examination of the heater rod temperature data, the solid lines in figure 3-78, does indicate some influence of the slippage of the 1.57 m (62 in.) grid. The agreement at the other elevations is excellent and as good as or better than the agreement with data from the comparable 161-rod unblocked bundle test, which was performed at the same test conditions.

The heater rod temperature versus elevation plots at different times are shown in figures 3-84 through 3-87, and again indicate excellent comparisons between the data and COBRA-TF predictions. (Also shown in figure 3-84 is the axial location of the spacer grids.) These figures show that, as time progresses, the entrainment increases and the grid effects become more significant, in both the data and the COBRA-TF predictions. Of particular importance are the grids at the 1.57 m (62 in.) and 2.11 m (83 in.) elevations. Figure 3-87 clearly shows the grid effects in the prediction and in the data at this time.

The measured vapor data versus time plots are shown in figures 3-88 through 3-90 for different elevations in the 21-rod bundle. The vapor temperatures were measured in the 21-rod bundle using shielded miniature thermocouples as well as bare thermocouples. The shielded thermocouples were not directly exposed to the radiation heat transfer environment from the heater rods. The bare thermocouples were exposed to direct radiation heat transfer from the

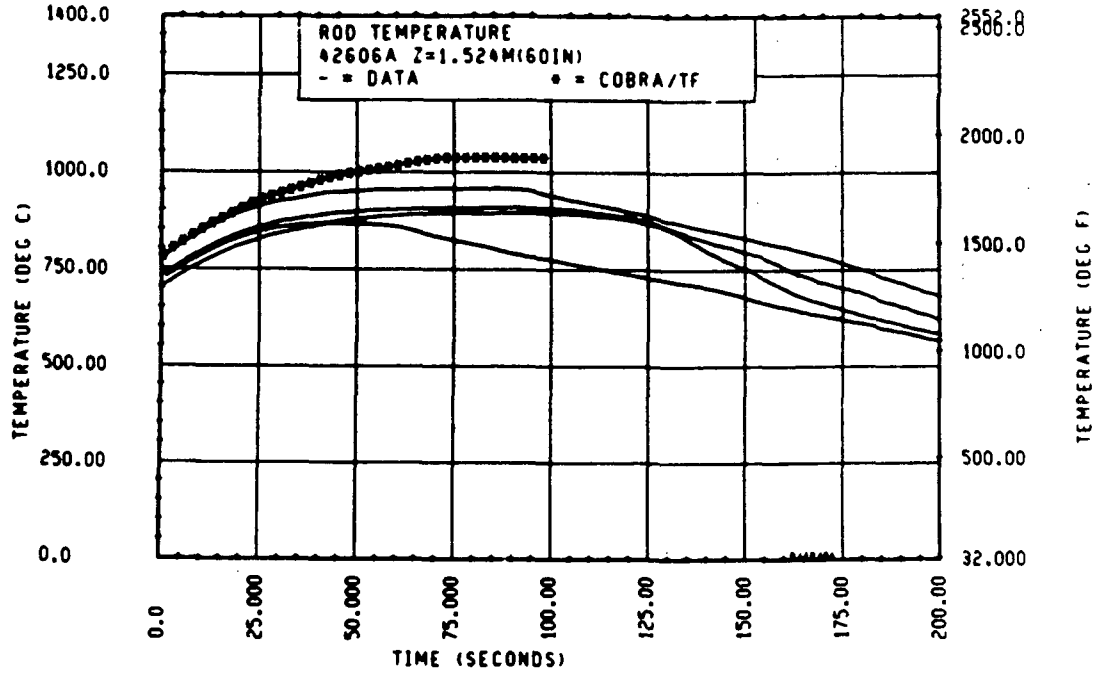

Figure 3-78. Comparison of COBRA-TF-Calculated Heater Rod Temperature Versus Time With FLECHT SEASET 21-Rod Data, Test 42606A, 1.52 m (60 in.) Elevation

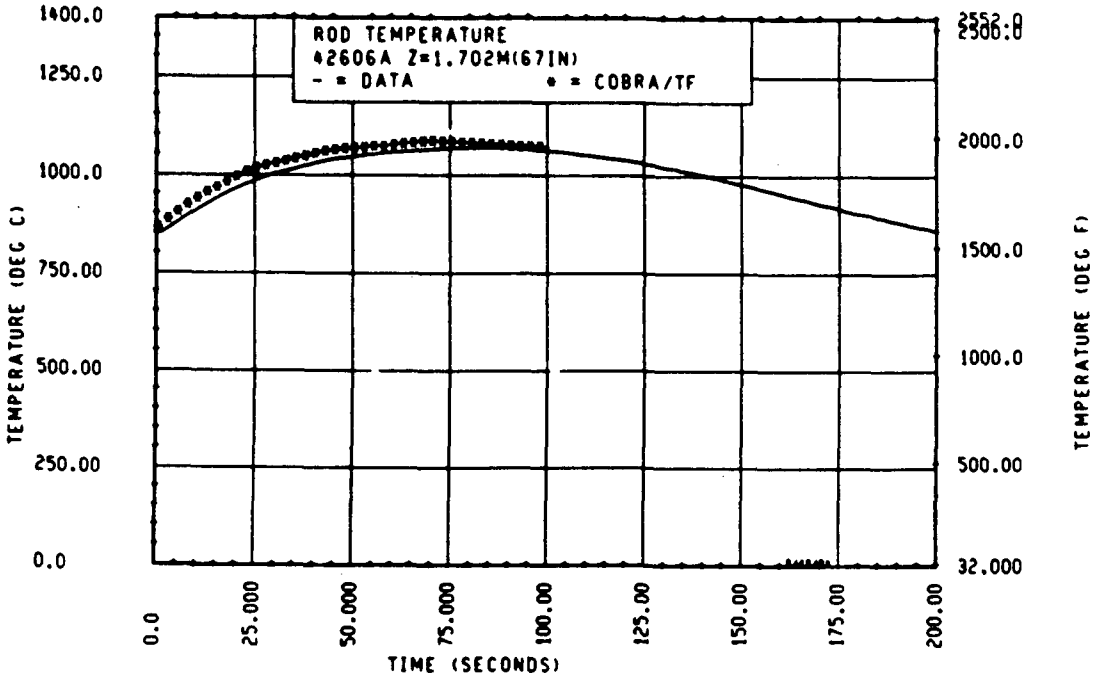

Figure 3-79. Comparison of COBRA-TF-Calculated Heater Rod Temperature Versus Time With FLECHT SEASET 21-Rod Data, Test 42606A, 1.70 m (67 in.) Elevation

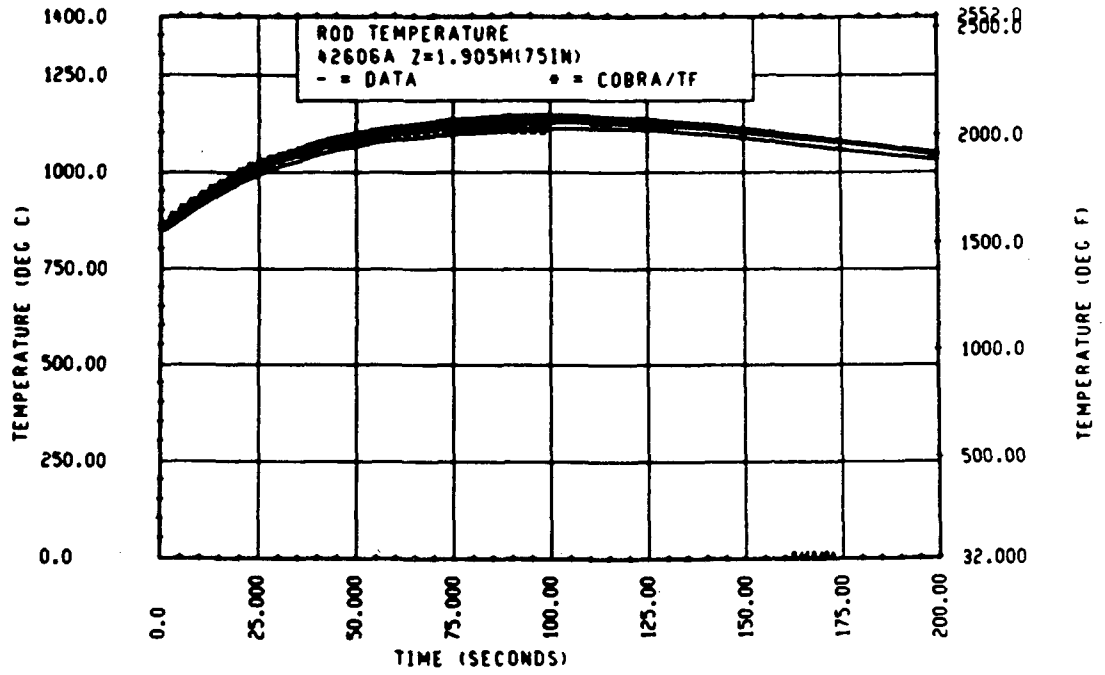

Figure 3-80. Comparison of COBRA-TF-Calculated Heater Rod Temperature Versus Time With FLECHT SEASET 21-Rod Data, Test 42606A, 1.90 m (75 in.) Elevation

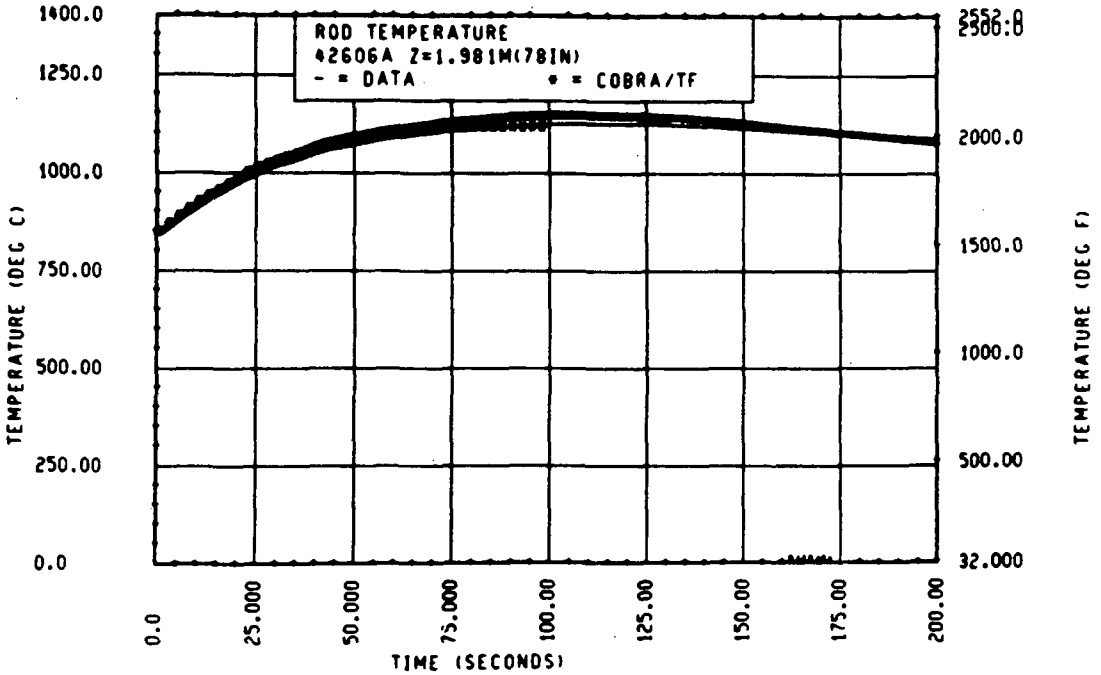

Figure 3-81. Comparison of COBRA-TF-Calculated Heater Rod Temperature Versus Time With FLECHT SEASET 21-Rod Data, Test 42606A, 1.98 m (78 in.) Elevation

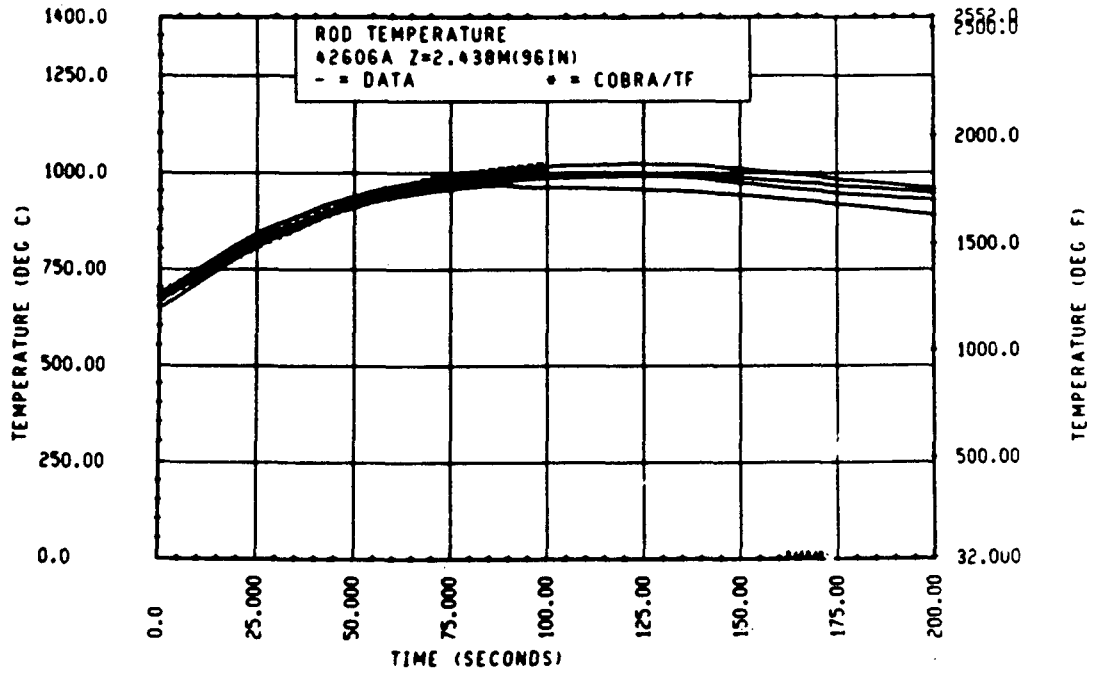

Figure 3-82. Comparison of COBRA-TF-Calculated Heater Rod Temperature Versus Time With FLECHT SEASET 21-Rod Data, Test 42606A, 2.44 m (96 in.) Elevation

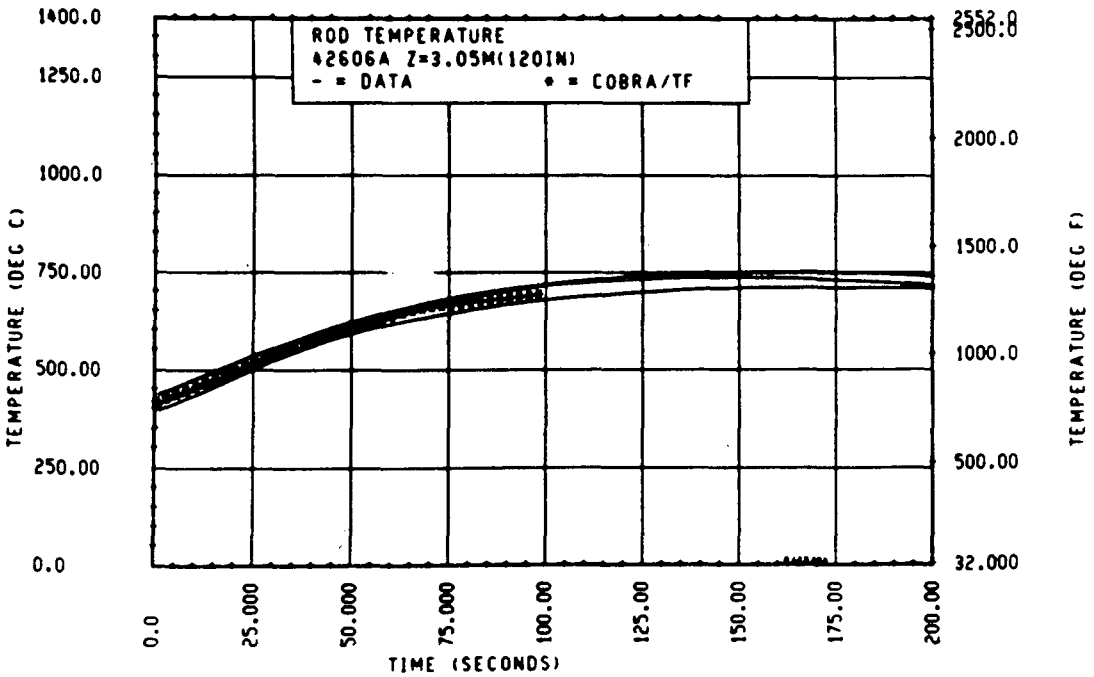

Figure 3-83. Comparison of COBRA-TF-Calculated Heater Rod Temperature Versus Time With FLECHT SEASET 21-Rod Data, Test 42606A, 3.05 m (120 in.) Elevation

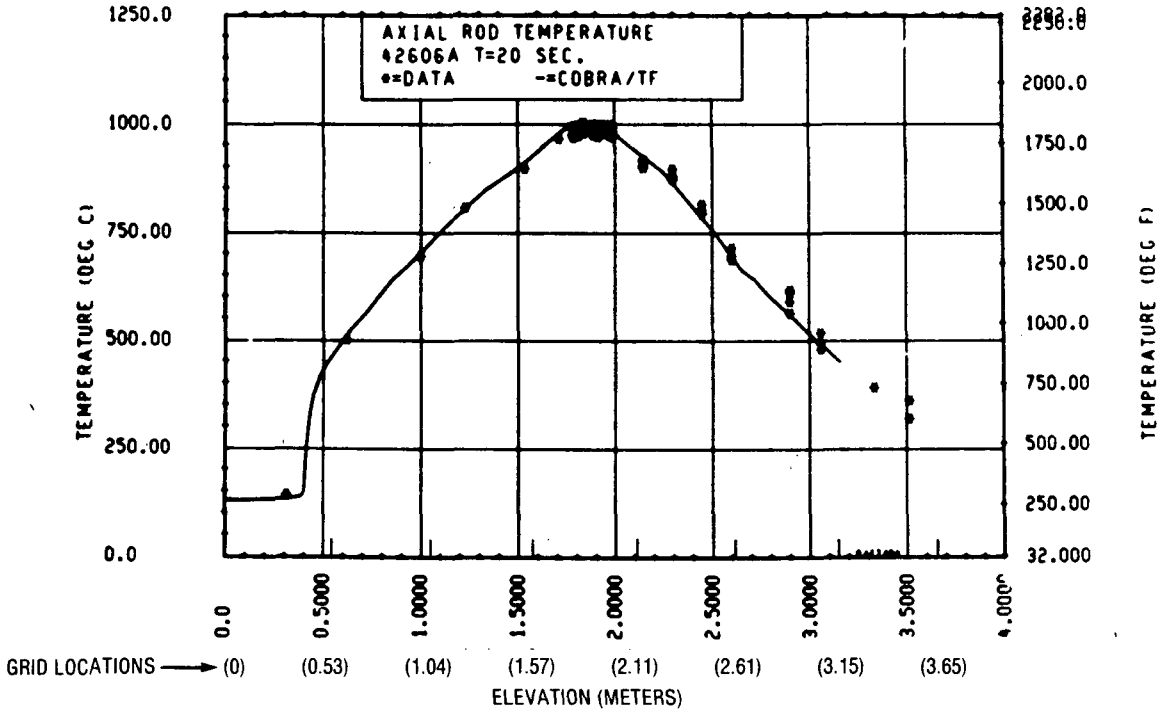

Figure 3-84. Comparison of COBRA-TF-Calculated Axial Rod Temperature Versus Elevation With FLECHT SEASET 21-Rod Data, Test 42606A, t = 20 Seconds

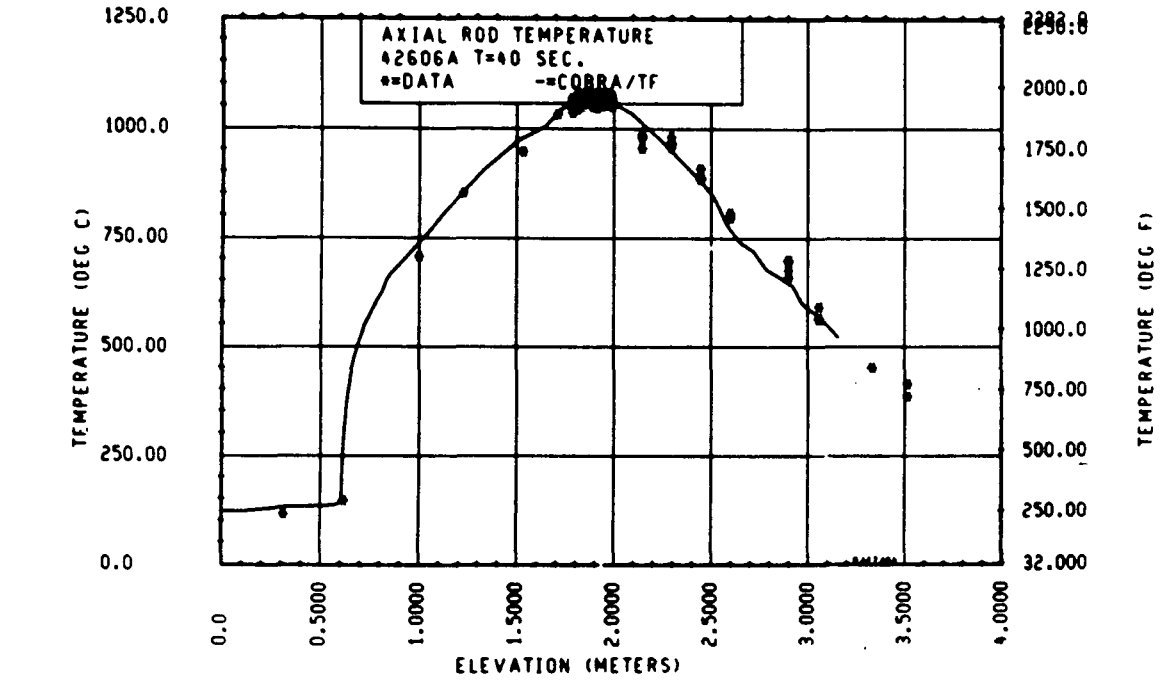

Figure 3-85. Comparison of COBRA-TF-Calculated Axial Rod Temperature Versus Elevation With FLECHT SEASET 21-Rod Data, Test 42606A, t = 40 Seconds

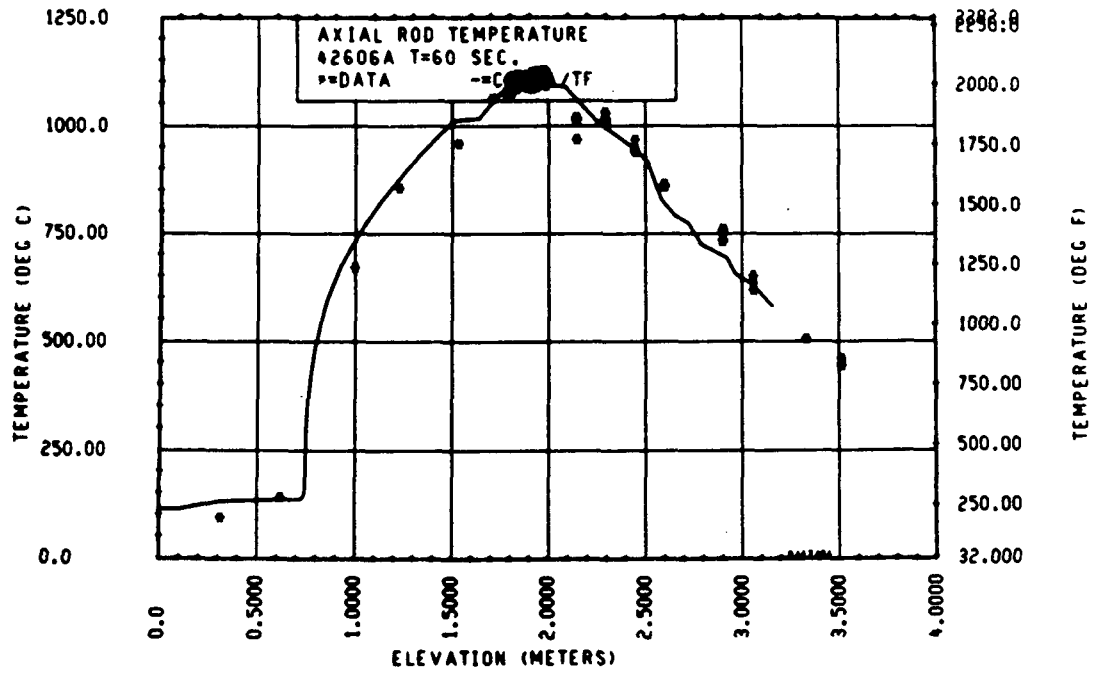

Figure 3-86. Comparison of COBRA-TF-Calculated Axial Rod Temperature Versus Time With FLECHT SEASET 21-Rod Data, Test 42606A, t = 60 Seconds

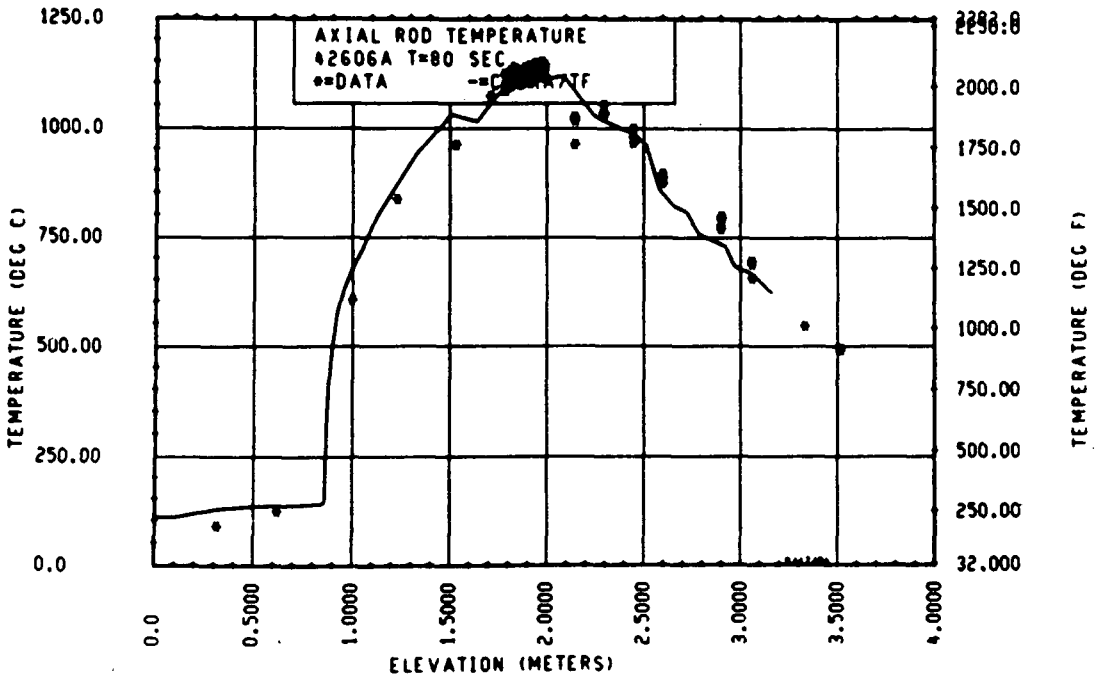

Figure 3-87. Comparison of COBRA-TF-Calculated Axial Rod Temperature Versus Time With FLECHT SEASET 21-Rod Data, Test 42606A, t = 80 Seconds

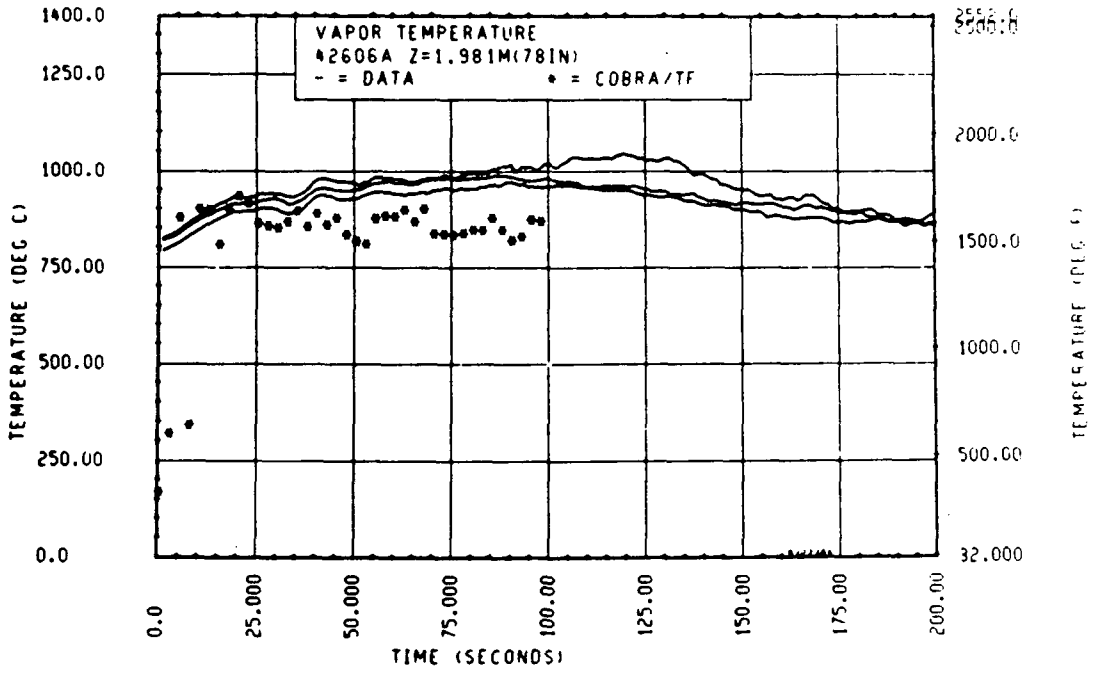

Figure 3-88. Comparison of COBRA-TF-Calculated Vapor Temperature Versus Time With FLECHT SEASET 21-Rod Data, Test 42606A, 1.98 m (78 in.) Elevation

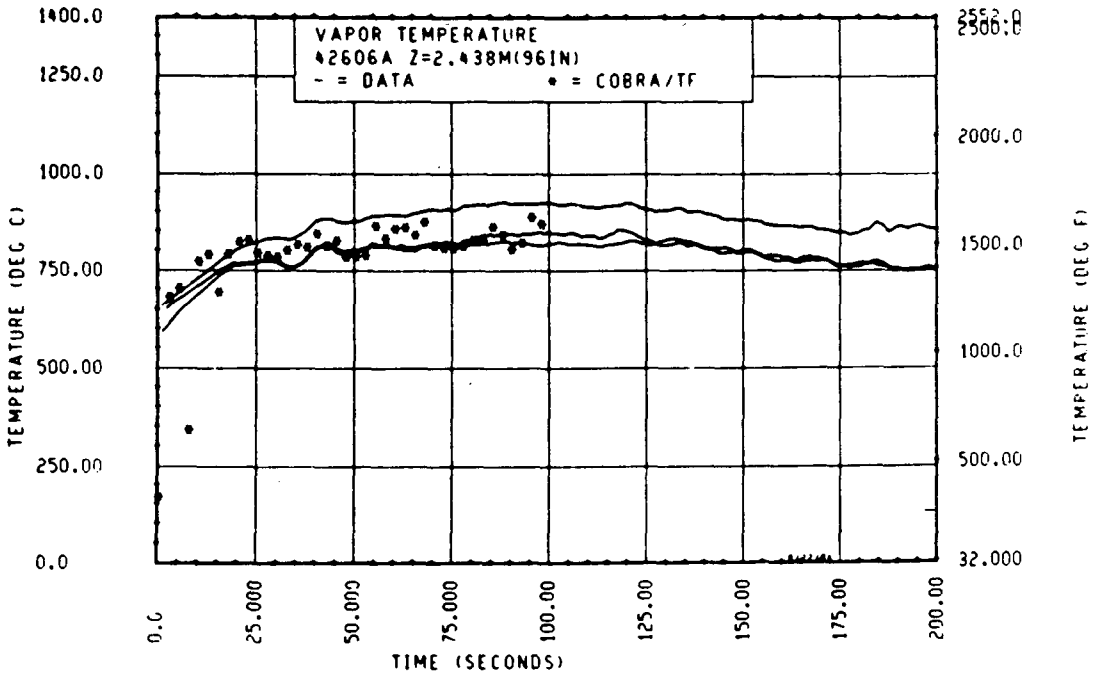

Figure 3-89. Comparison of COBRA-TF-Calculated Vapor Temperature Versus Time With FLECHT SEASET 21-Rod Data, Test 42606A, 2.44 m (96 in.) Elevation

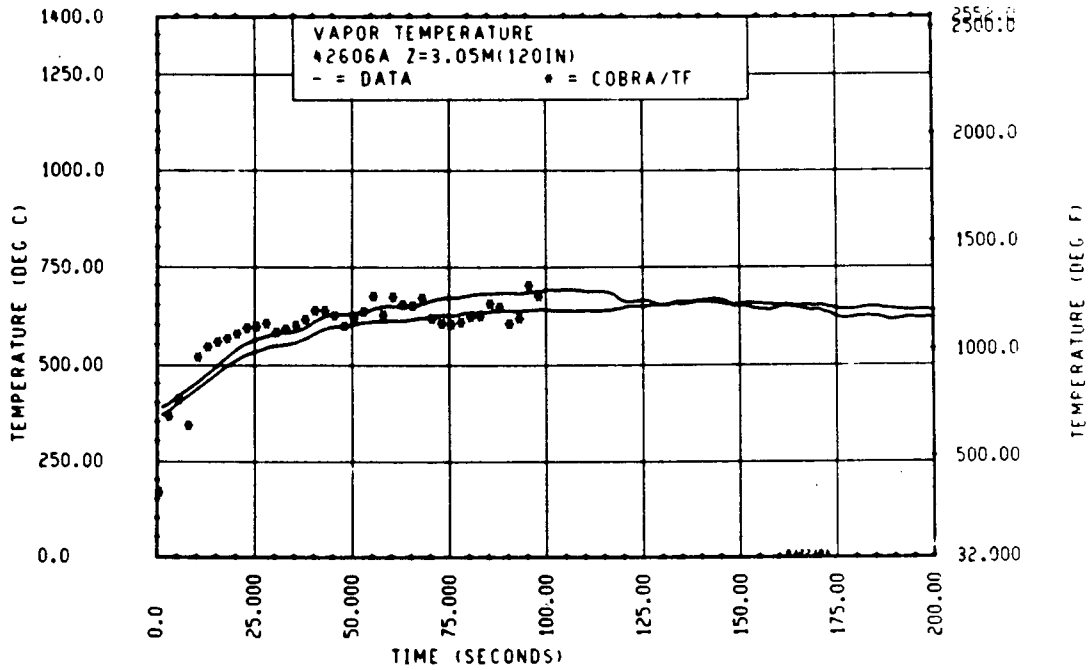

Figure 3-90. Comparison of COBRA-TF-Calculated Vapor Temperature Versus Time With FLECHT SEASET 21-Rod Data, Test 42606A, 3.05 m (120 in.) Elevation

heater rods, which could result in an approximate 20° C (36° F) bias at the 1000° C (1700° F) rod temperature. The different thermocouple design is discussed in the 21-rod bundle report referenced previously as well as in a paper by Loftus et al.[1]

The comparisons between the COBRA-TF-predicted vapor temperature and the measured vapor temperature is quite good, as shown in figures 3-88 through 3-90, even up to the 3.05 m (120 in.) elevation. The axial vapor temperature plots are shown in figures 3-91 through 3-94; again the COBRA-TF prediction agrees reasonably well with the data. The vapor measurements are point measurements within the subchannel, while the COBRA-TF calculation is an average of several subchannels. Detailed calculations of the vapor temperature profile in rod bundles during reflooding have been made by Wong and Hochreiter[2] which show there can be significant vapor temperature gradients within the subchannel. Therefore, perfect agreement between these data and COBRA-TF cannot be expected.

The code does tend to underpredict the vapor temperature at the midplane of the bundle at the 1.98 m (78 in.) elevation. This may be due, in part, to the large effect of the 1.57 m (62 in.) grid, which causes significant desuperheating of the vapor downstream of the grid. The calculated vapor temperature axial profile shows that the slope of the vapor temperature curve almost goes to zero immediately downstream of this grid, then begins to reheat. The data show more vapor reheating compared to code predictions. Conversely, if the calculated vapor temperature axial curve were to be shifted upward in figures 3-93 and 3-94, the agreement with the vapor desuperheating at the 2.29 m (90 in.) elevation would be about correct downstream of the 2.11 m (83 in.) grid. Therefore, it appears that the calculated cooling for the lower 1.57 m (62 in.) grid is too large, whereas the correct amount of cooling is calculated for the 2.11 m (83 in.) grid.

---

1. Loftus, M. J., et al., "Nonequilibrium Vapor Temperature Measurements in Rod Bundles and Steam Generators in Two-Phase Flow," presented at Third OECD Two-Phase Meeting, Pasadena, CA, 1981.
2. Wong, W. and Hochreiter L. E., "A Model For Dispersed Flow Heat Transfer During Reflood," Experimental and Analytical Modeling LWR Safety Experiements, HTD-Vol 7, 19th National Heat Transfer Conference, Orlando, 1980.

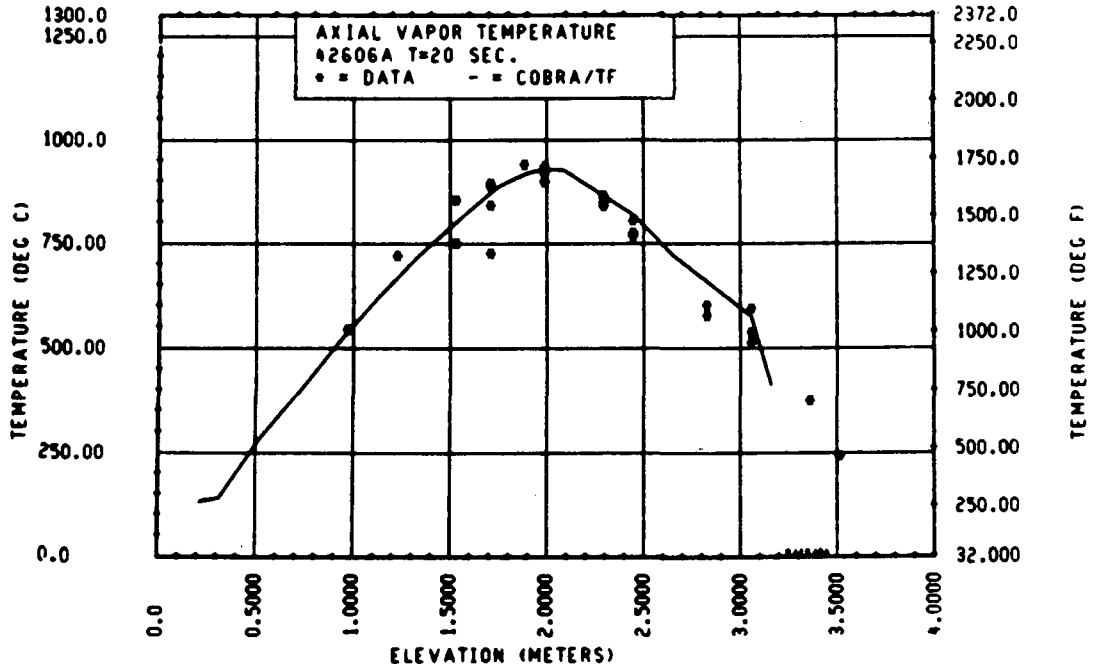

Figure 3-91. Comparison of COBRA-TF-Calculated Axial Vapor Temperature Versus Elevation With FLECHT SEASET 21-Rod Data, Test 42606A, t = 20 Seconds

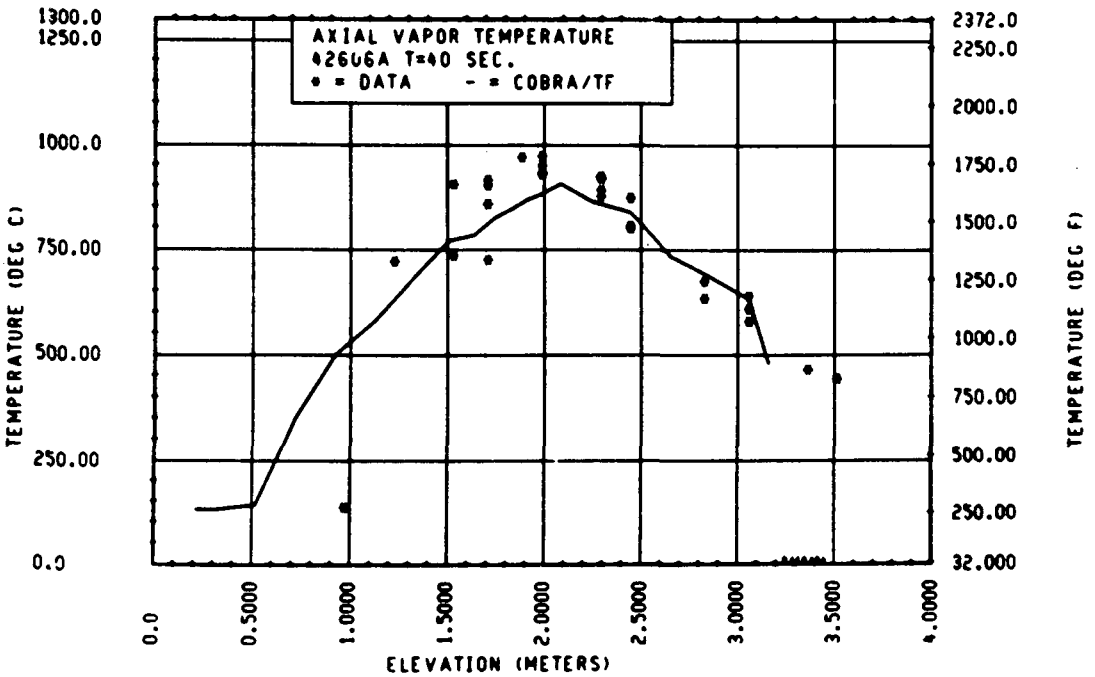

Figure 3-92. Comparison of COBRA-TF-Calculated Axial Vapor Temperature Versus Elevation With FLECHT SEASET 21-Rod Data, Test 42606A, t = 40 Seconds

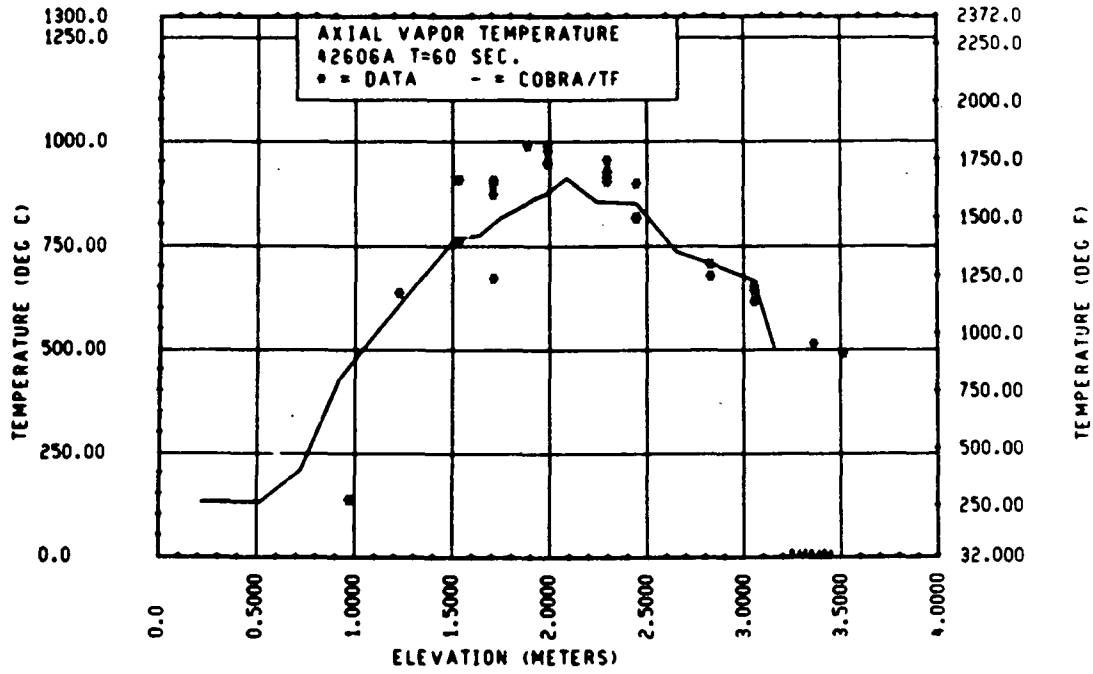

Figure 3-93. Comparison of COBRA-TF-Calculated Axial Vapor Temperature Versus Time With FLECHT SEASET 21-Rod Data, Test 42606A, t = 60 Seconds

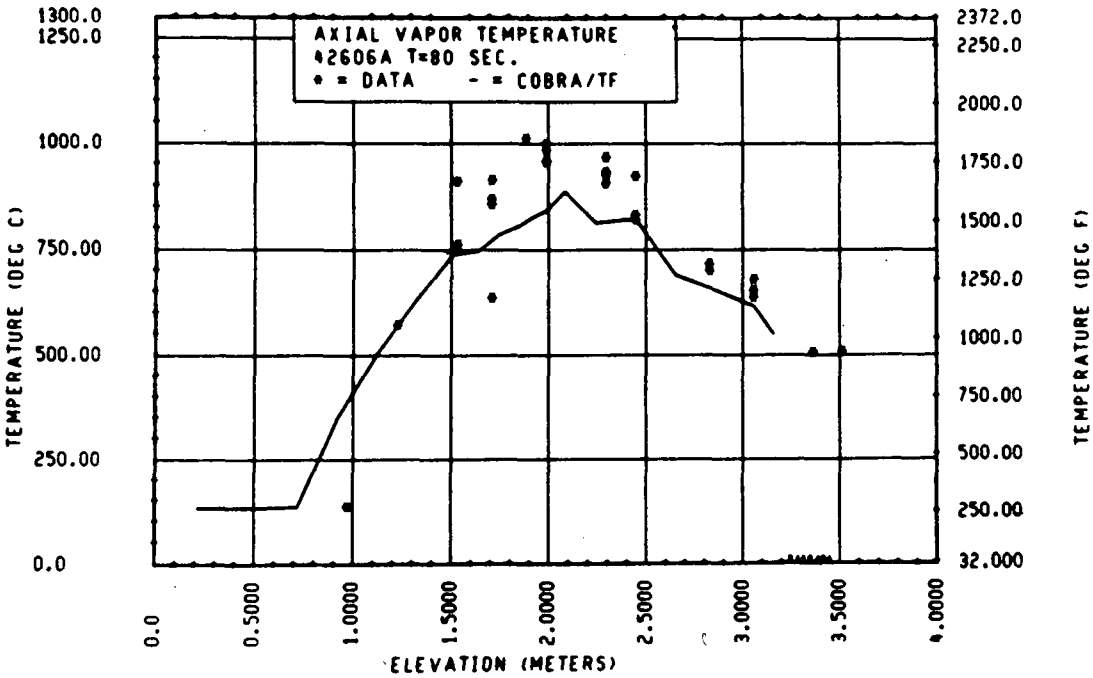

Figure 3-94. Comparison of COBRA-TF-Calculated Axial Vapor Temperature Versus Time With FLECHT SEASET 21-Rod Data, Test 42606A, t = 80 Seconds

The comparisons for 21-rod bundle test 43208A are shown in figures 3-95 through 3-111. This test was conducted at the same conditions as the 161-rod bundle test 31203, that is, 0.038 m/sec (1.5 in./sec) flooding rate and 0.28 MPa (40 psia) system pressure. The heater rod temperature versus time plots are shown in figures 3-95 through 3-100 for this test, with the data for the nine center rods and the COBRA-TF predictions for these rods.

As mentioned in the discussion of test 42606A, the 1.52 m (60 in.) elevation was influenced by the moving down of the filler strips and grid at the 1.57 m (62 in.) elevation. The influence of moving down the grid is evident in the measured heater rod temperatures, as shown in figure 3-95. The other comparisons at the upper elevations in figures 3-96 through 3-100 show very good agreement between the COBRA-TF-calculated temperature response and the heater rod data. At later times at the uppermost elevation, there is an overprediction of the data by the COBRA-TF code. It is believed that the overprediction is caused by the thin-wall test housing quenching by a top-down quench front in the experiment. This top-down quench front was not calculated by COBRA-TF to progress down into the heated region of the bundle as rapidly as it did in the experiment. Thus the test would have improved cooling relative to the calculation.

The axial heater rod temperature profiles are shown in figures 3-101 through 3-104 with the COBRA-TF predictions, at selected times. (Also shown in figure 3-101 is the axial location of the spacer grids.) These figures indicate that, as time progresses and the entrained liquid flow increases, the effects of the spacer grids become more pronounced, both in the COBRA-TF prediction and in the test data. The axial plots indicate that the 1.57 m (62 in.) grid is perhaps giving too much cooling in the COBRA-TF calculation, whereas the 2.11 m (83 in.) grid gives a little less cooling than the data. However, the overall agreement is quite good.

The comparisons of the measured vapor temperature and the predicted COBRA-TF vapor temperature are shown at selected elevations for different times (figures 3-105 through 3-107). In general, the agreement is quite good with the

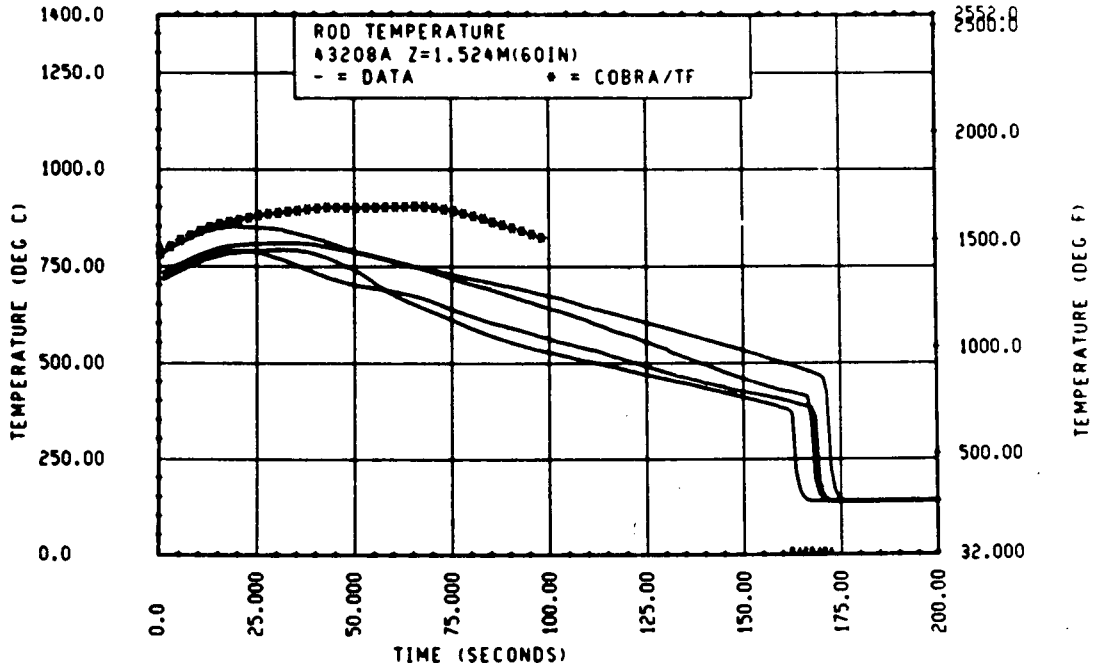

Figure 3-95. Comparison of COBRA-TF-Calculated Heater Rod Temperature Versus Time With FLECHT SEASET 21-Rod Data, Test 43208A, 1.52 m (60 in.) Elevation

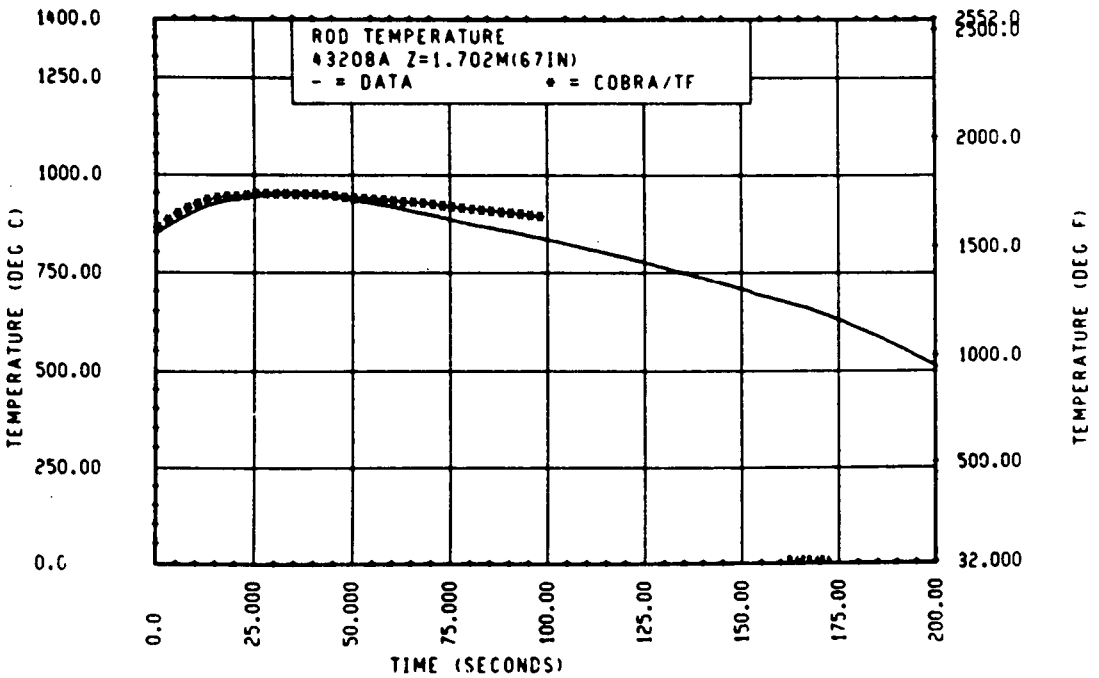

Figure 3-96. Comparison of COBRA-TF-Calculated Heater Rod Temperature Versus Time With FLECHT SEASET 21-Rod Data, Test 43208A, 1.70 m (67 in.) Elevation

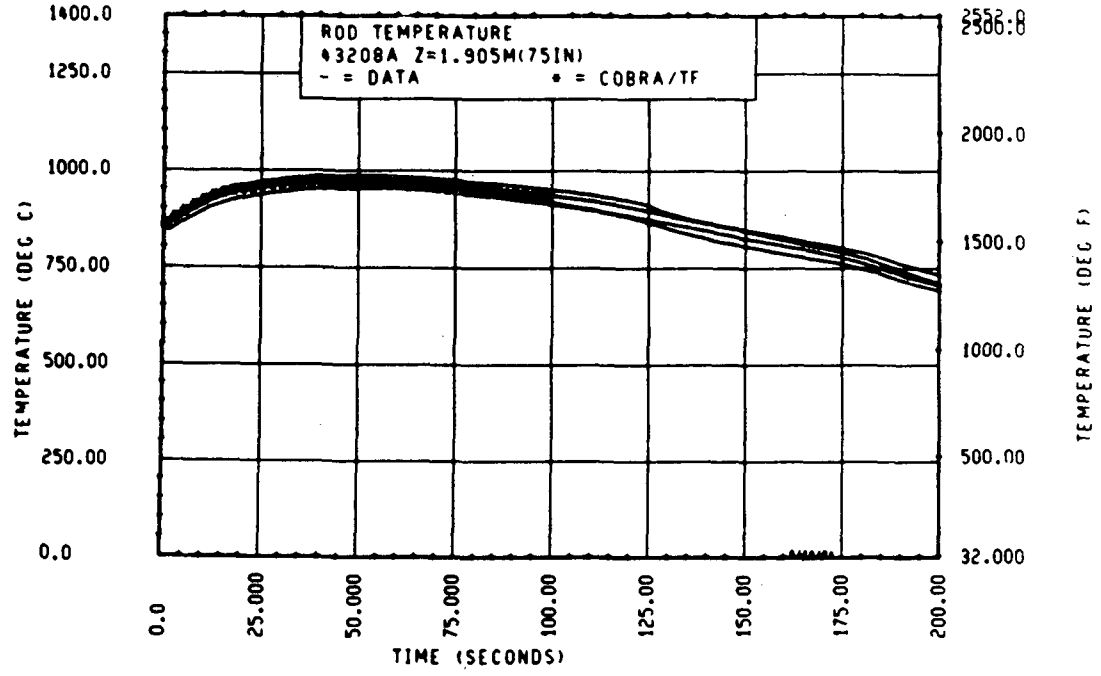

Figure 3-97. Comparison of COBRA-TF-Calculated Heater Rod Temperature Versus Time With FLECHT SEASET 21-Rod Data, Test 43208A, 1.90 m (75 in.) Elevation

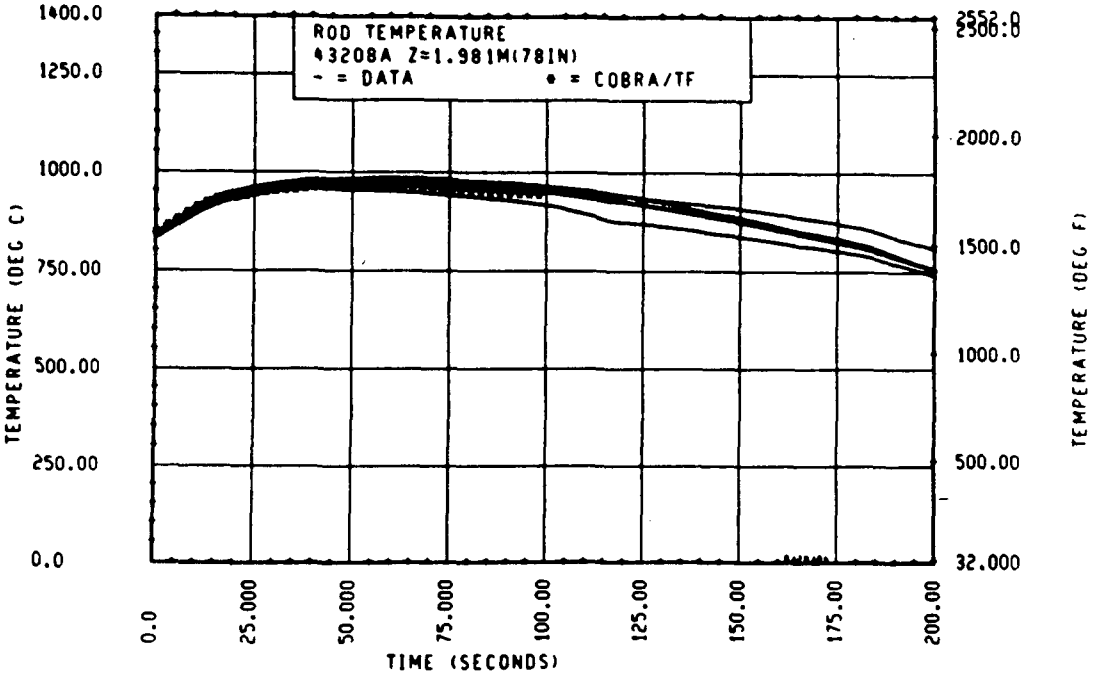

Figure 3-98. Comparison of COBRA-TF-Calculated Heater Rod Temperature Versus Time With FLECHT SEASET 21-Rod Data, Test 43208A, 1.98 m (78 in.) Elevation

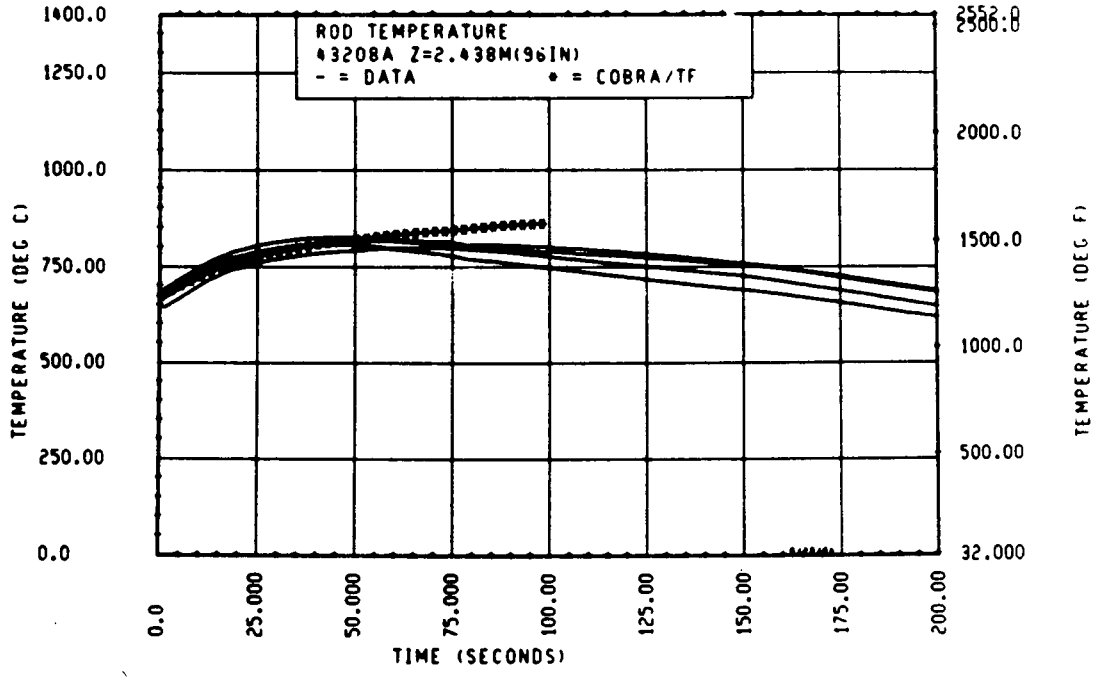

Figure 3-99. Comparison of COBRA-TF-Calculated Heater Rod Temperature Versus Time With FLECHT SEASET 21-Rod Data, Test 43208A, 2.44 m (96 in.) Elevation

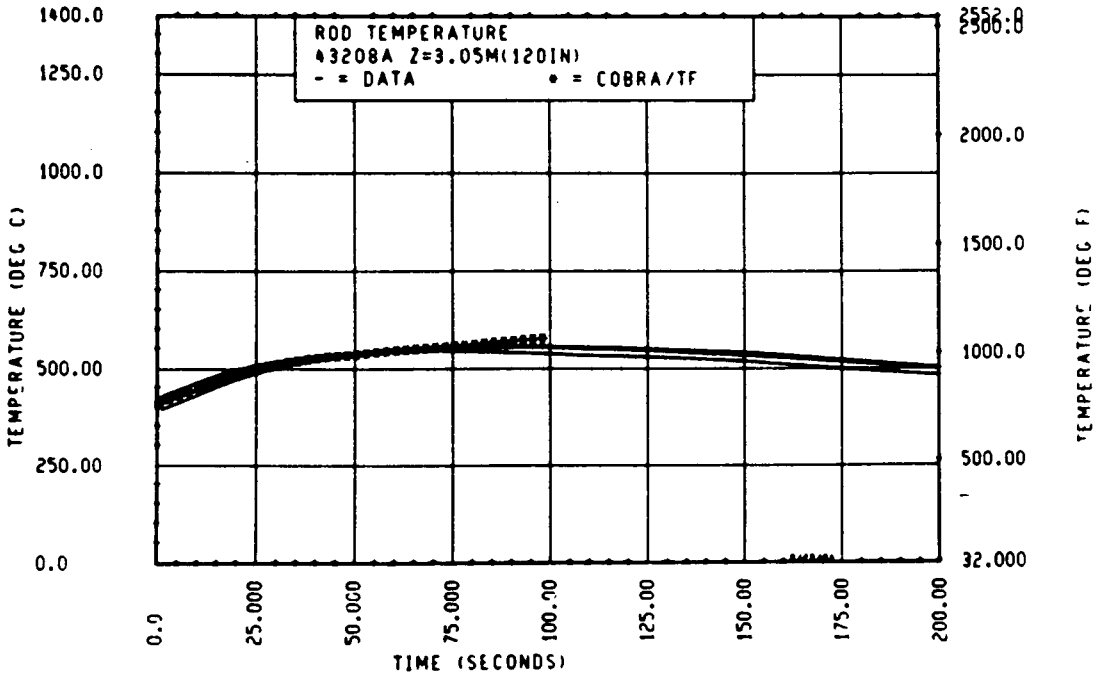

Figure 3-100. Comparison of COBRA-TF-Calculated Heater Rod Temperature Versus Time With FLECHT SEASET 21-Rod Data, Test 43208A, 3.05 m (120 in.) Elevation

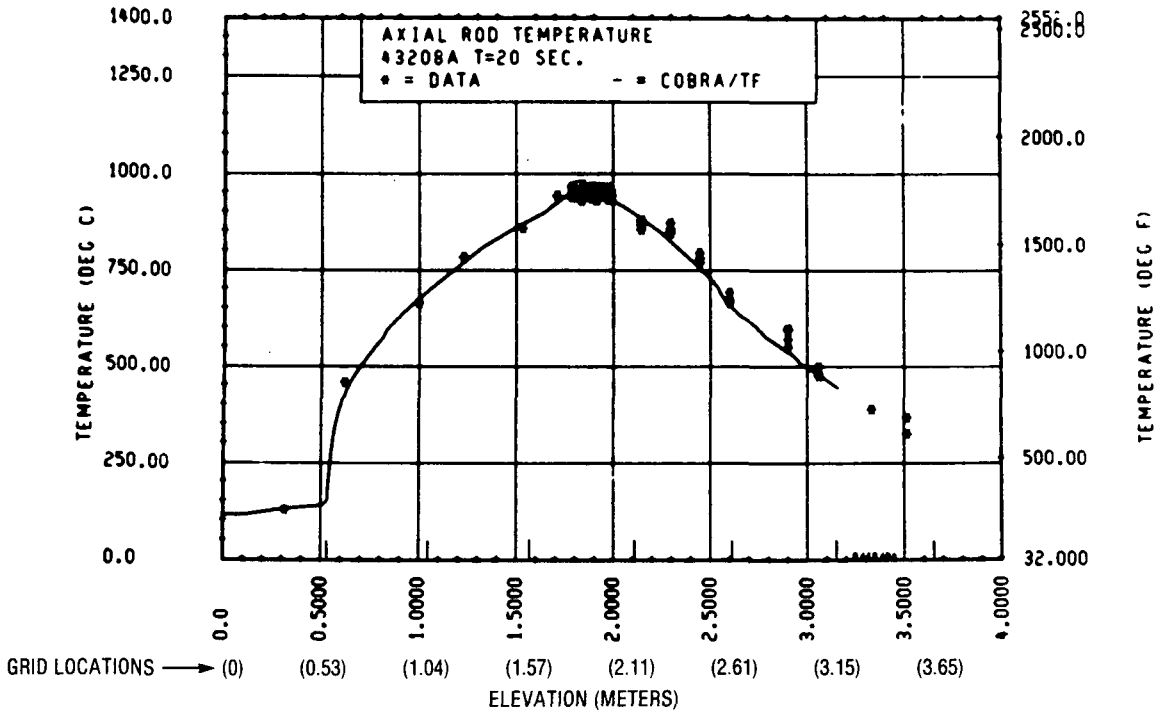

Figure 3-101. Comparison of COBRA-TF-Calculated Axial Rod Temperature Versus Elevation With FLECHT SEASET 21-Rod Data, Test 43208A, t = 20 Seconds

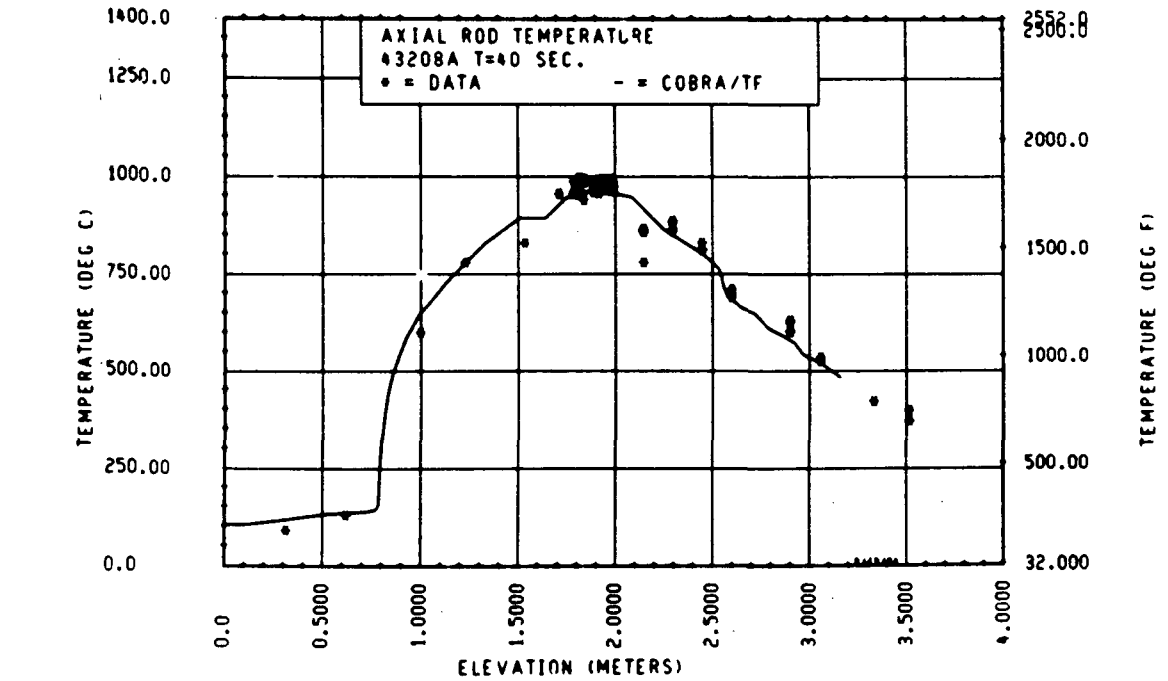

Figure 3-102. Comparison of COBRA-TF-Calculated Axial Rod Temperature Versus Elevation With FLECHT SEASET 21-Rod Data, Test 43208A, t = 40 Seconds

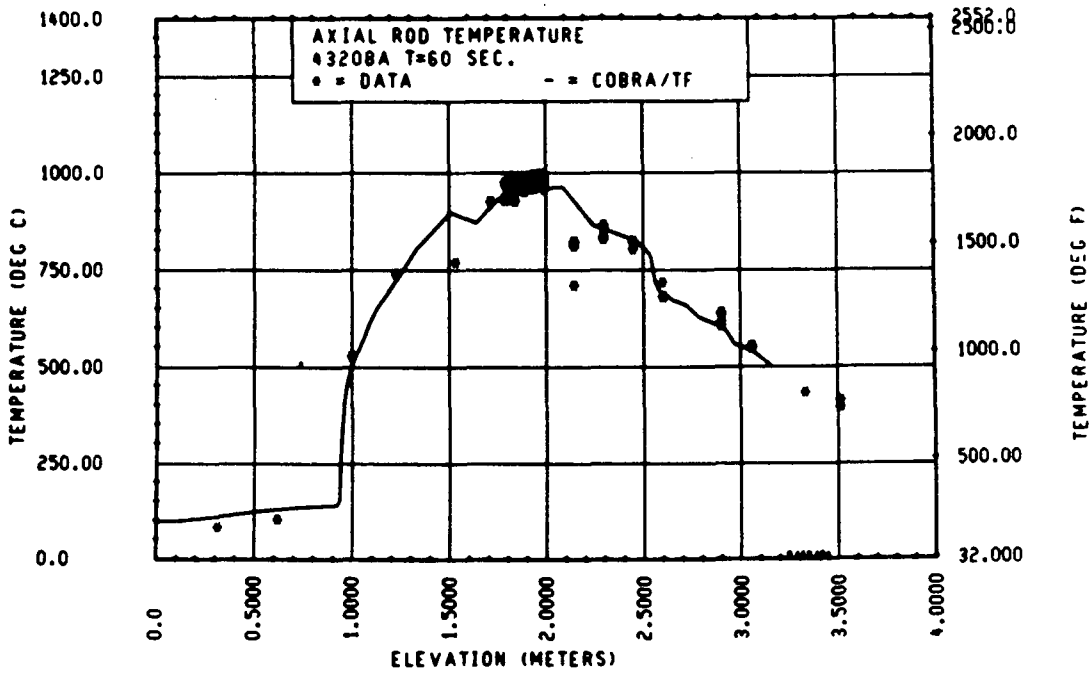

Figure 3-103. Comparison of COBRA-TF-Calculated Axial Rod Temperature Versus Time With FLECHT SEASET 21-Rod Data, Test 43208A, t = 60 Seconds

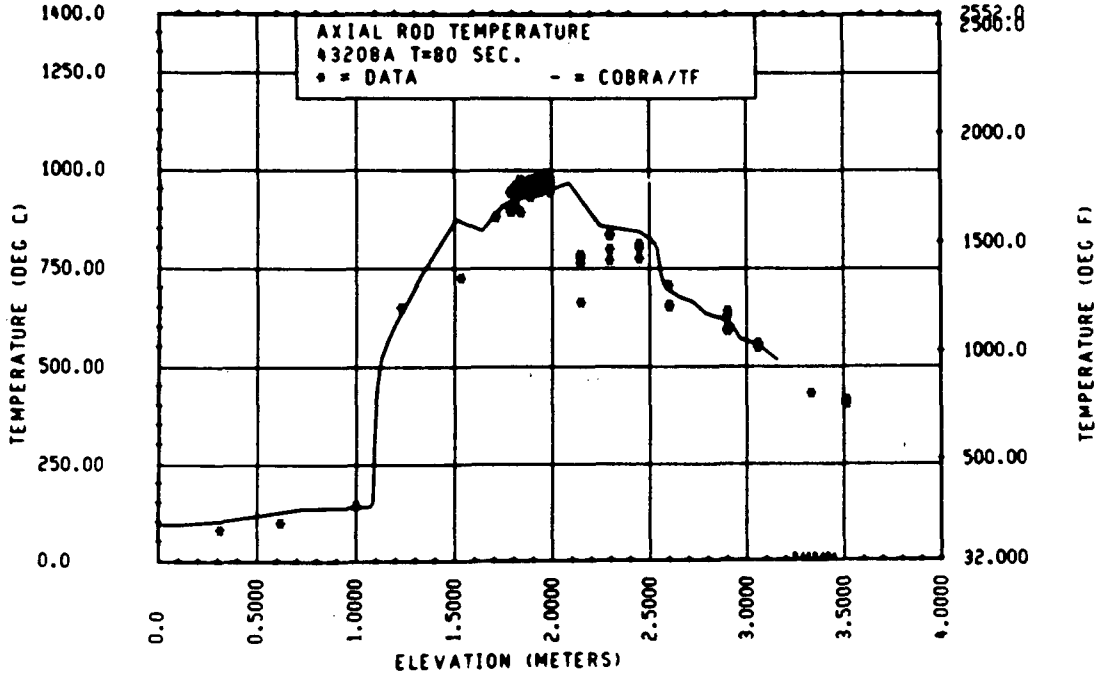

Figure 3-104. Comparison of COBRA-TF-Calculated Axial Rod Temperature Versus Time With FLECHT SEASET 21-Rod Data, Test 43208A, t = 80 Seconds

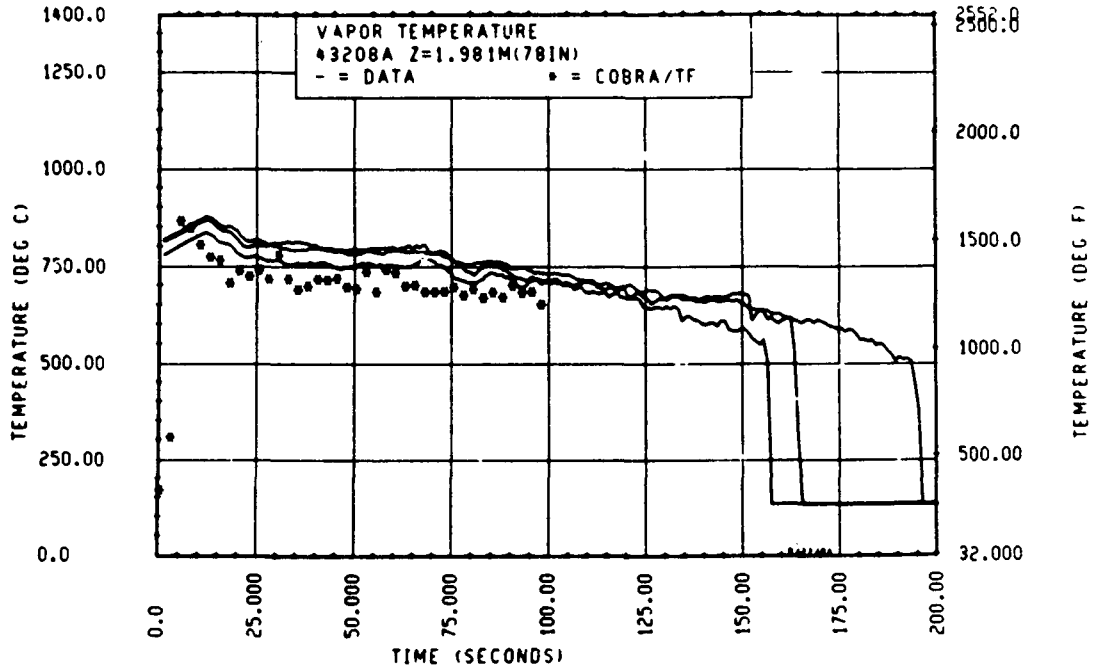

Figure 3-105. Comparison of COBRA-TF-Calculated Vapor Temperature Versus Time With FLECHT SEASET 21-Rod Data, Test 43208A, 1.98 m (78 in.) Elevation

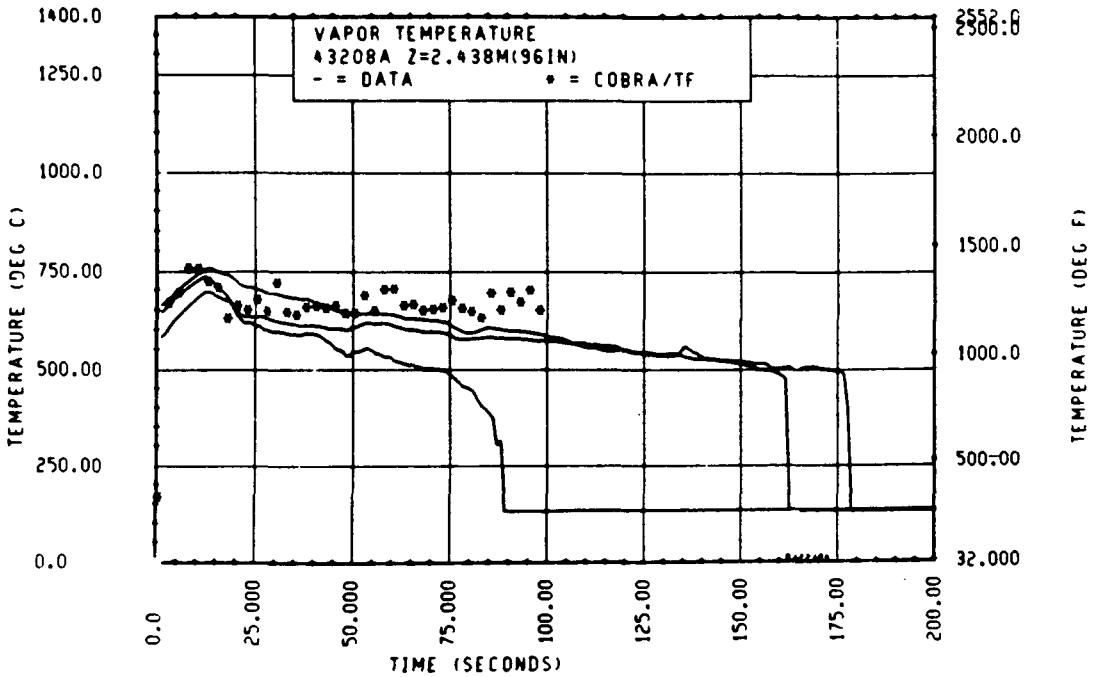

Figure 3-106. Comparison of COBRA-TF-Calculated Vapor Temperature Versus Time With FLECHT SEASET 21-Rod Data, Test 43208A, 2.44 m (96 in.) Elevation

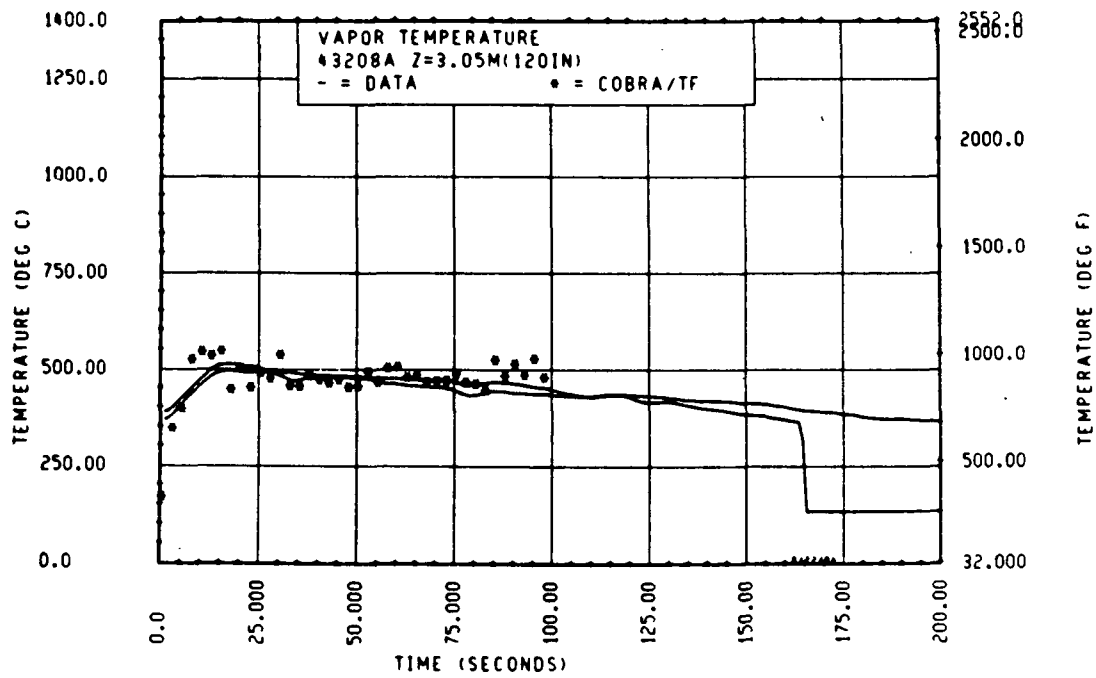

Figure 3-107. Comparison of COBRA-TF-Calculated Vapor Temperature Versus Time With FLECHT SEASET 21-Rod Data, Test 43208A, 3.05 m (120 in.) Elevation

exception that, at later times, the COBRA-TF-predicted vapor temperature exceeds that of the data at the upper elevations. Again, it is believed that the overprediction can be attributed to the housing quenching due to a top-down quench in the experiment, an effect which was not calculated to occur as quickly by COBRA-TF. The axial vapor temperature plots and predictions (figures 3-108 through 3-111) again show very good agreement.

e bare thermocouples and the shielded steam probes were arranged with two orientations: some facing the flow (pointing downward) and some pointing upward. All the steam probes were attached to the spacer grids and the thermocouple leads were lead out through the filler strips. It was found that those thermocouples which pointed upward quenched prematurely relative to similar thermocouples pointed downward. The quenching effect of the thermocouples was ignored in the COBRA-TF model; it is another source of additional cooling in the test which is not modeled in the COBRA-TF code. A quenched thermocouple would act as a radiation heat sink as well as a desuperheating surface. The quenched thermocouple data for the upward-facing steam probes has been removed from figures 3-108 through 3-111 to prevent confusion; this is the reason for the changing number of data points in these figures.

As in test 42606A, the calculated overcooling effect of the 1.57 m (62 in.) grid is apparent in the slope of the COBRA-TF prediction. It appears that the cooling effect of the 2.11 m (83 in.) grid is underestimated. However, the agreement is still quite good.

In addition to the two 21-rod bundle tests described above, there were two other tests (43112A and 42514A) which matched previously analyzed 161-rod blocked bundle test conditions. Test 43112A was a 0.14 MPa (20 psia), 0.025 m/sec (1 in./sec) flooding rate experiment. The comparison of the COBRA-TF predictions with the heater rod temperature versus time data is shown in figures 3-112 through 3-117. In this test, the COBRA-TF calculations lie below the data once entrainment begins, particularly at the lower elevations. At the upper elevations, agreement is actually improved compared to previous tests.

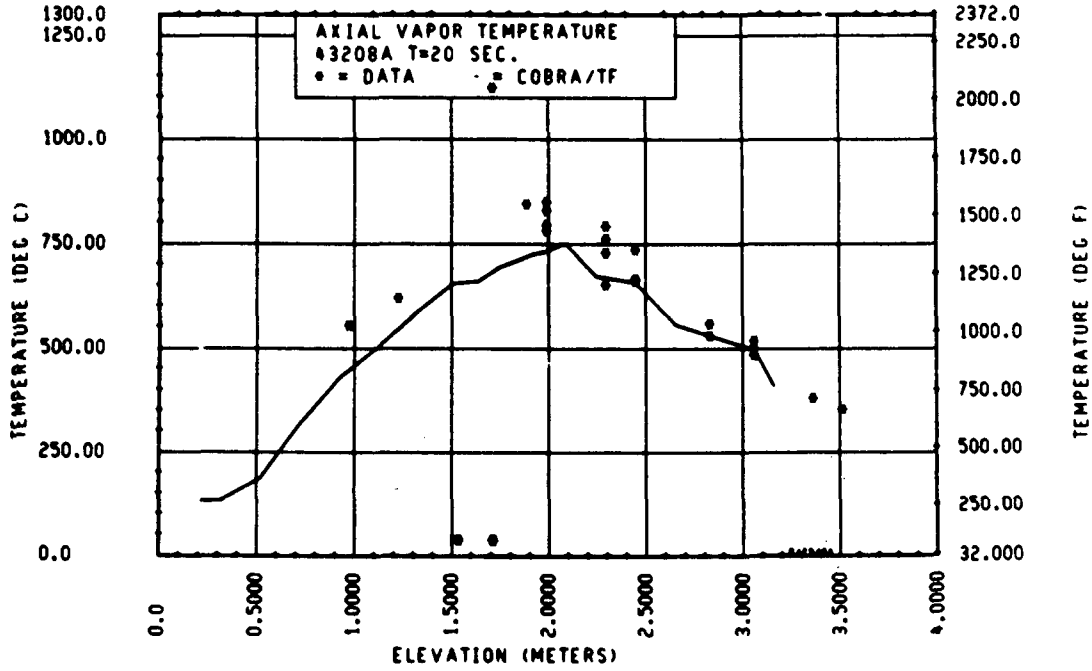

Figure 3-108. Comparison of COBRA-TF-Calculated Axial Vapor Temperature Versus Elevation With FLECHT SEASET 21-Rod Data, Test 43208A, t = 20 Seconds

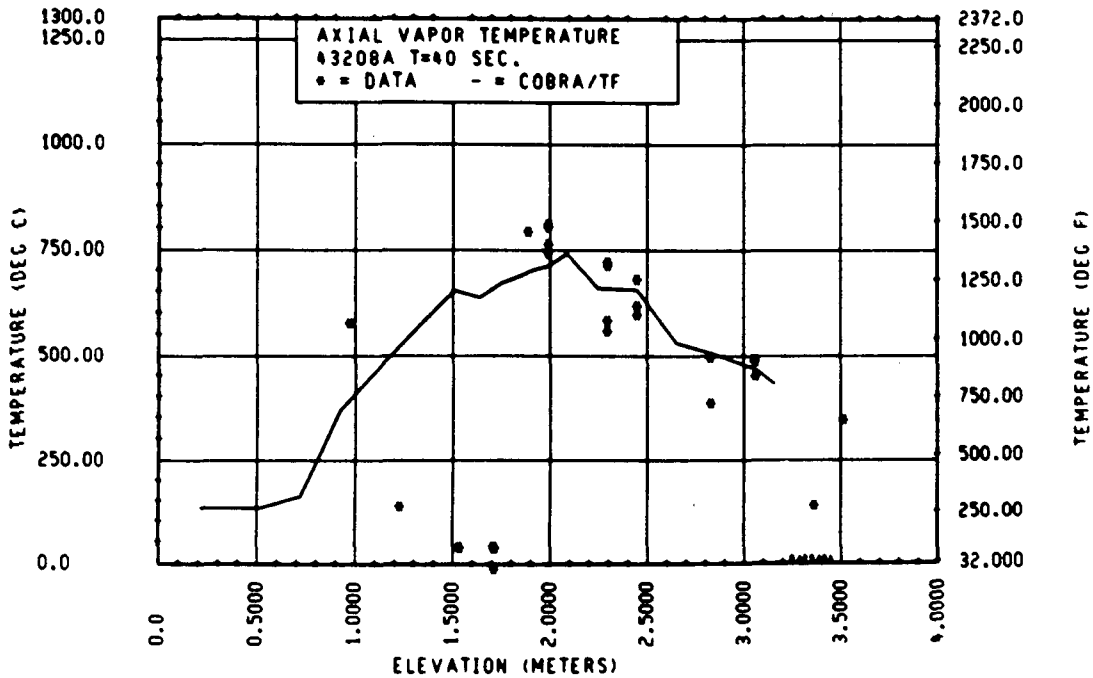

Figure 3-109. Comparison of COBRA-TF-Calculated Axial Vapor Temperature Versus Elevation With FLECHT SEASET 21-Rod Data, Test 43208A, t = 40 Seconds

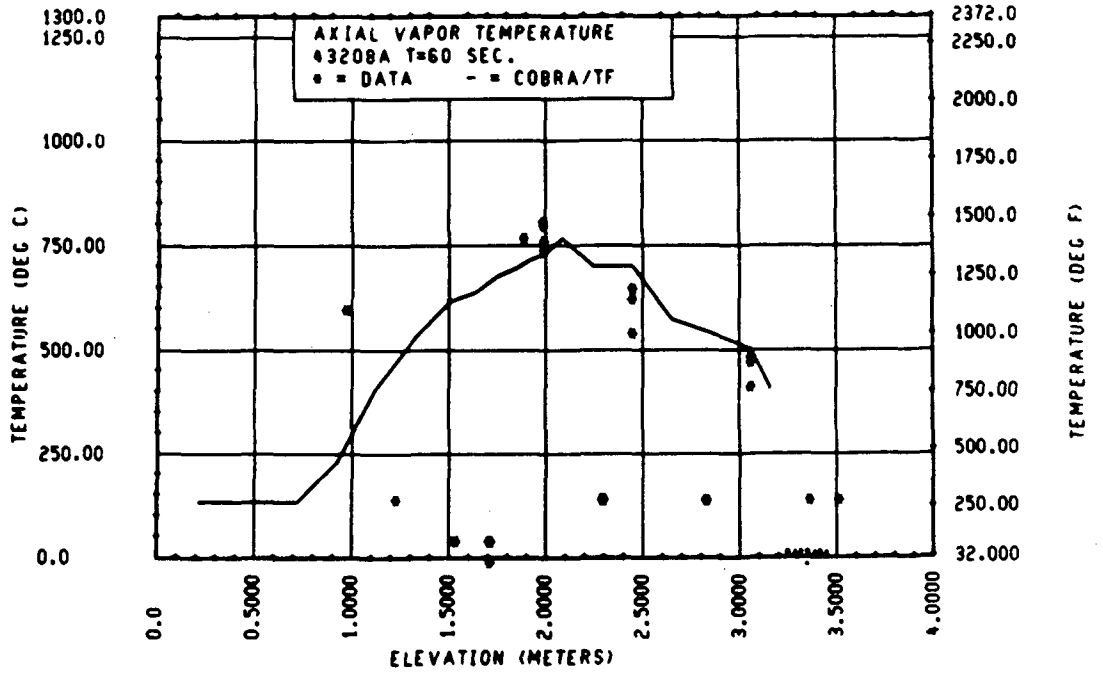

Figure 3-110. Comparison of COBRA-TF-Calculated Axial Vapor Temperature Versus Time With FLECHT SEASET 21-Rod Data, Test 43208A, t = 60 Seconds

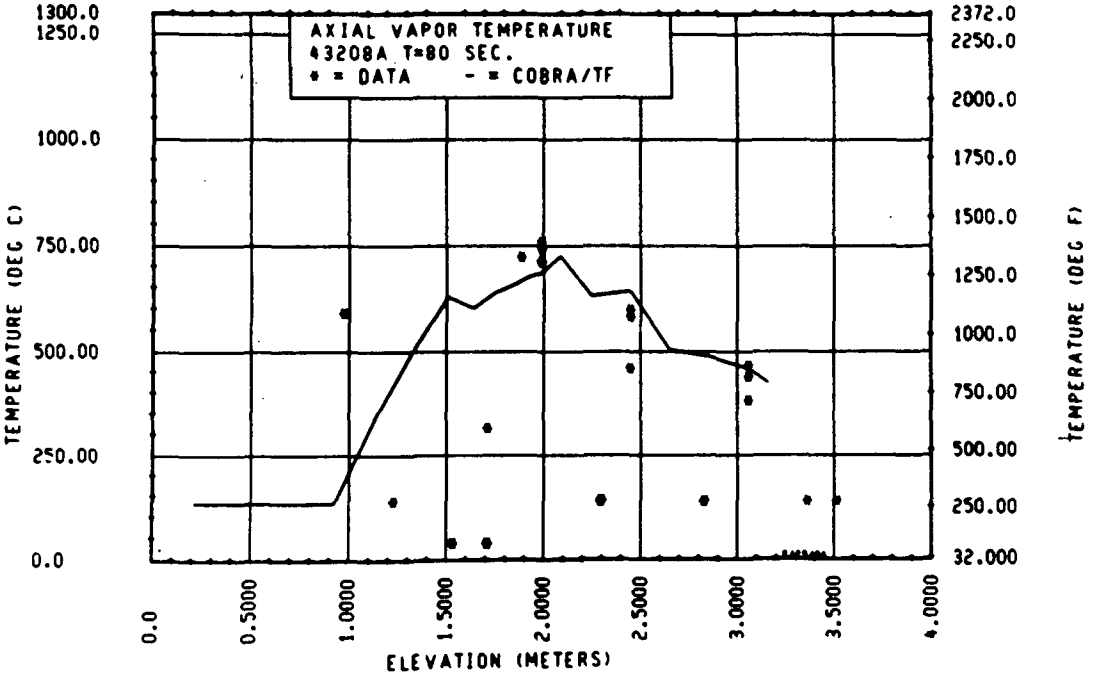

Figure 3-111. Comparison of COBRA-TF-Calculated Axial Vapor Temperature Versus Time With FLECHT SEASET 21-Rod Data, Test 43208A, t = 80 Seconds

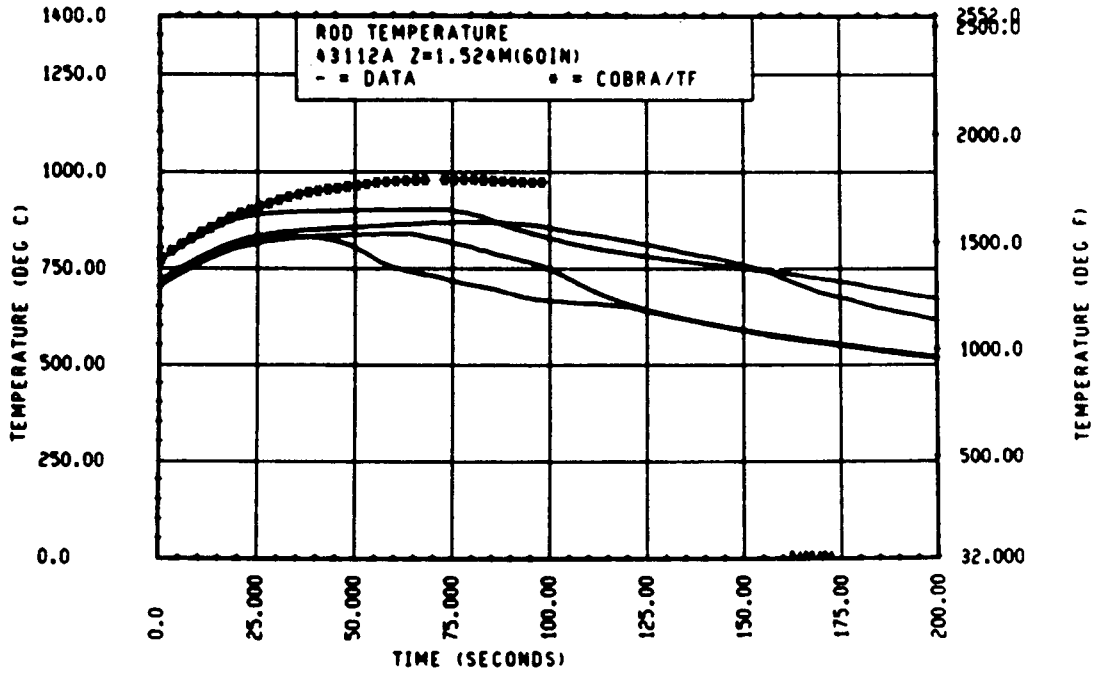

Figure 3-112. Comparison of COBRA-TF-Calculated Heater Rod Temperature Versus Time With FLECHT SEASET 21-Rod Data, Test 43112A, 1.52 m (60 in.) Elevation

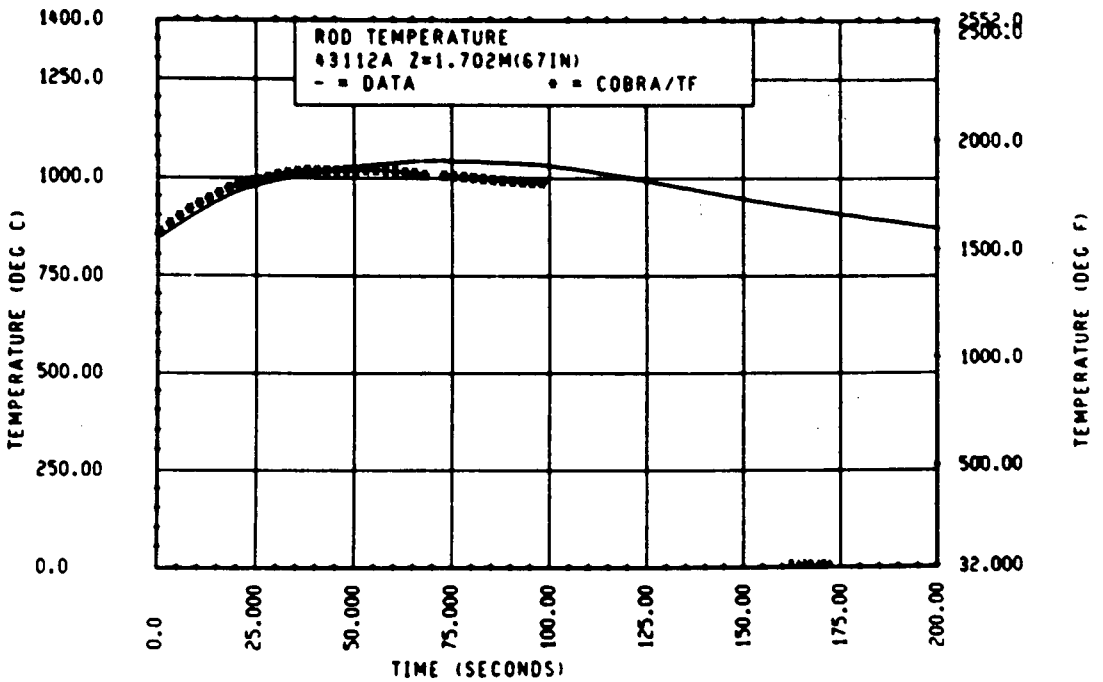

Figure 3-113. Comparison of COBRA-TF-Calculated Heater Rod Temperature Versus Time With FLECHT SEASET 21-Rod Data, Test 43112A, 1.70 m (67 in.) Elevation

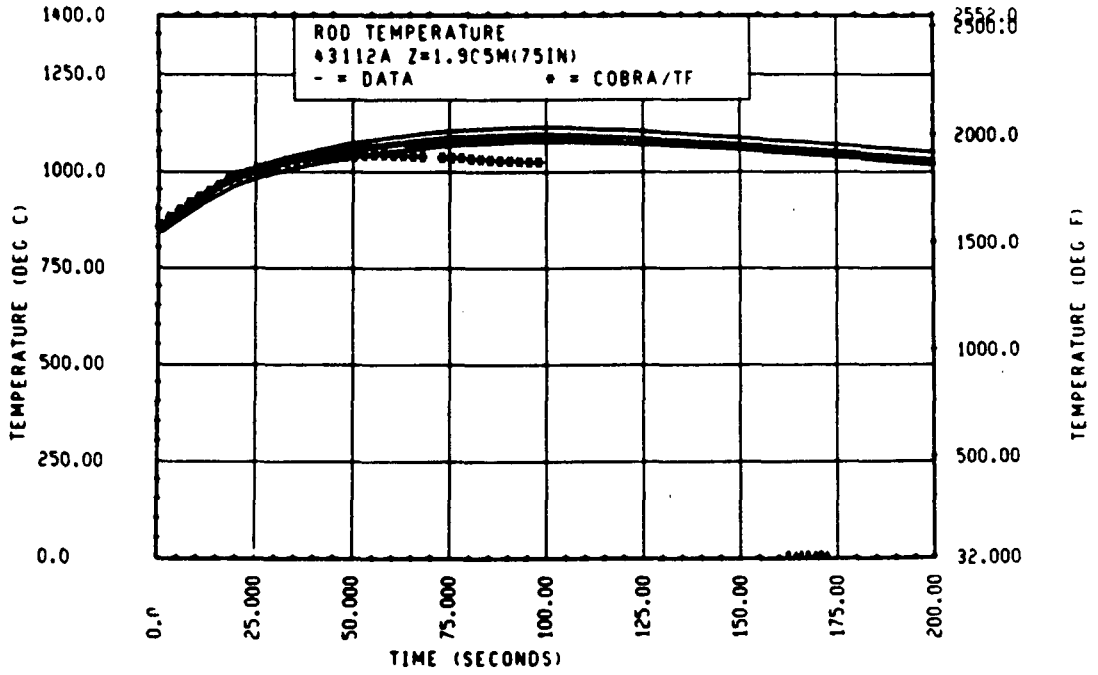

Figure 3-114. Comparison of COBRA-TF-Calculated Heater Rod Temperature Versus Time With FLECHT SEASET 21-Rod Data, Test 43112A, 1.90 m (75 in.) Elevation

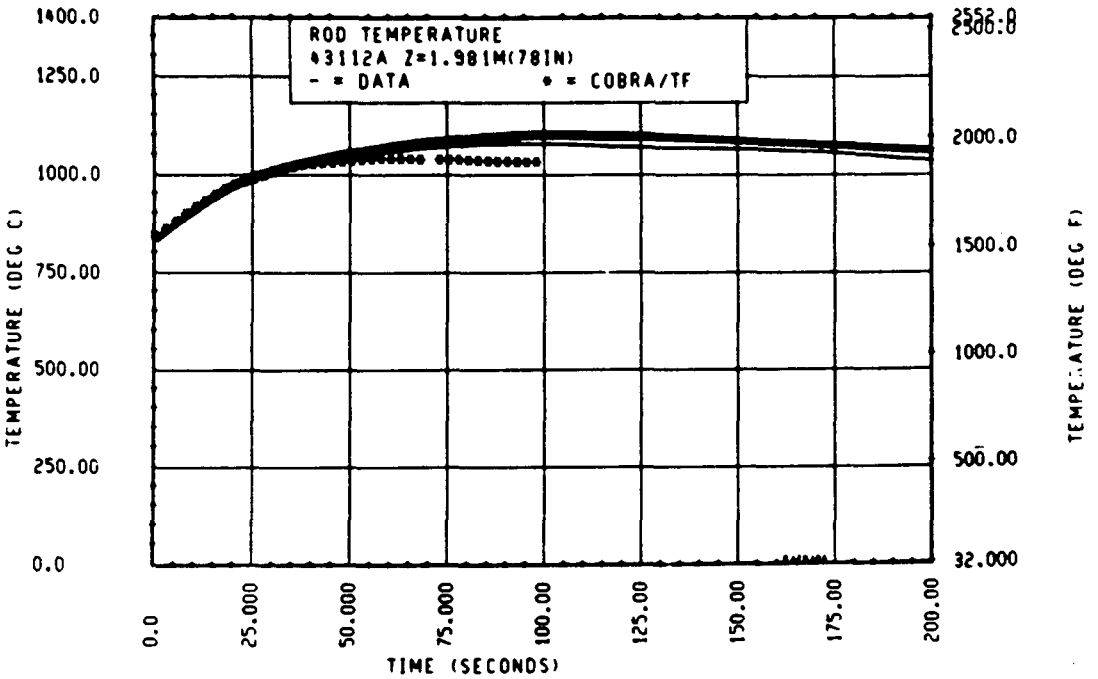

Figure 3-115. Comparison of COBRA-TF-Calculated Heater Rod Temperature Versus Time With FLECHT SEASET 21-Rod Data, Test 43112A, 1.98 m (78 in.) Elevation

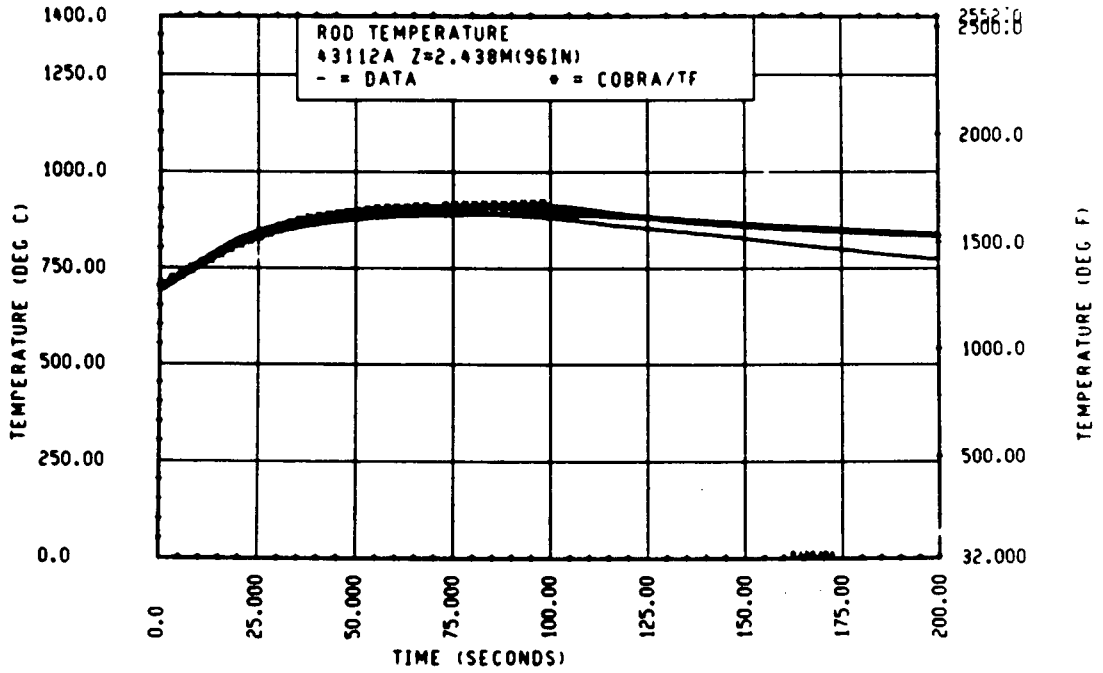

Figure 3-116. Comparison of COBRA-TF-Calculated Heater Rod Temperature Versus Time With FLECHT SEASET 21-Rod Data, Test 43112A, 2.44 m (96 in.) Elevation

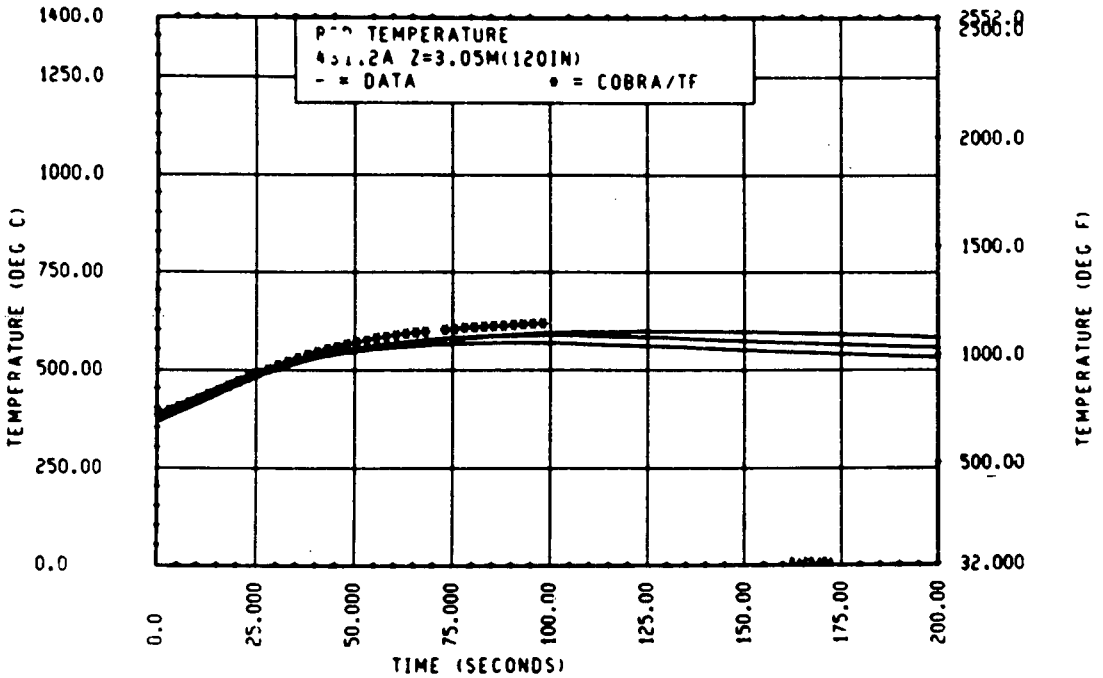

Figure 3-117. Comparison of COBRA-TF-Calculated Heater Rod Temperature Versus Time With FLECHT SEASET 21-Rod Data, Test 43112A, 3.05 m (120 in.) Elevation

The axial heater rod temperature plots with the COBRA-TF calculations are shown in figures 3-118 through 3-121. (Also shown in figure 3-118 is the axial location of the spacer grids.) These plots also show the underprediction of the measured heater rod temperature data at and just below the bundle midplane; the upper elevations look quite good. The underprediction at the bundle midplane is believed to be caused by the strong cooling effect of the 1.57 m (62 in.) grid, which significantly improves the heat transfer downstream of this location and thus causes lower calculated midplane heater rod temperatures. The cooling effect of the 2.11 m (83 in.) grid is smaller than that observed in the data, as shown in figure 3-121.

Test 42514A was a stepped flooding rate test (table 3-2). The heater rod temperature versus time plots in figures 3-122 through 3-127 show reasonable agreement until later times, when COBRA-TF begins to overpredict the heater rod data. The heater rod axial plots (figures 3-128 through 3-131) indicate better agreement than the temperature-time plots; however, there does appear to be a slight overprediction of the temperatures up to the 1.98 m (78 in.) elevation. (Also shown in figure 3-128 is the axial location of the spacer grids.) The overpredictions of the heater rod temperatures at later times is again believed to be due to the more rapid housing quench as well as the steam probes which pointed upward and also quenched early. These effects produced additional cooling in the experiment which was not present in the COBRA-TF calculation. However, the COBRA-TF overprediction is small.

3-16. FEBA Test Comparisons With COBRA-TF

The third test analyzed using COBRA-TF to assess the code and the grid models which were added to it was the FEBA 25-rod bundle reflood test series (referenced previously). Two sets of two tests each were analyzed to assess the grid models. The tests were matched pairs with the boundary and initial conditions replicated as closely as possible; one test had a midplane grid (total of seven grids) and the replicate test was conducted without the midplane grid (total of six grids).

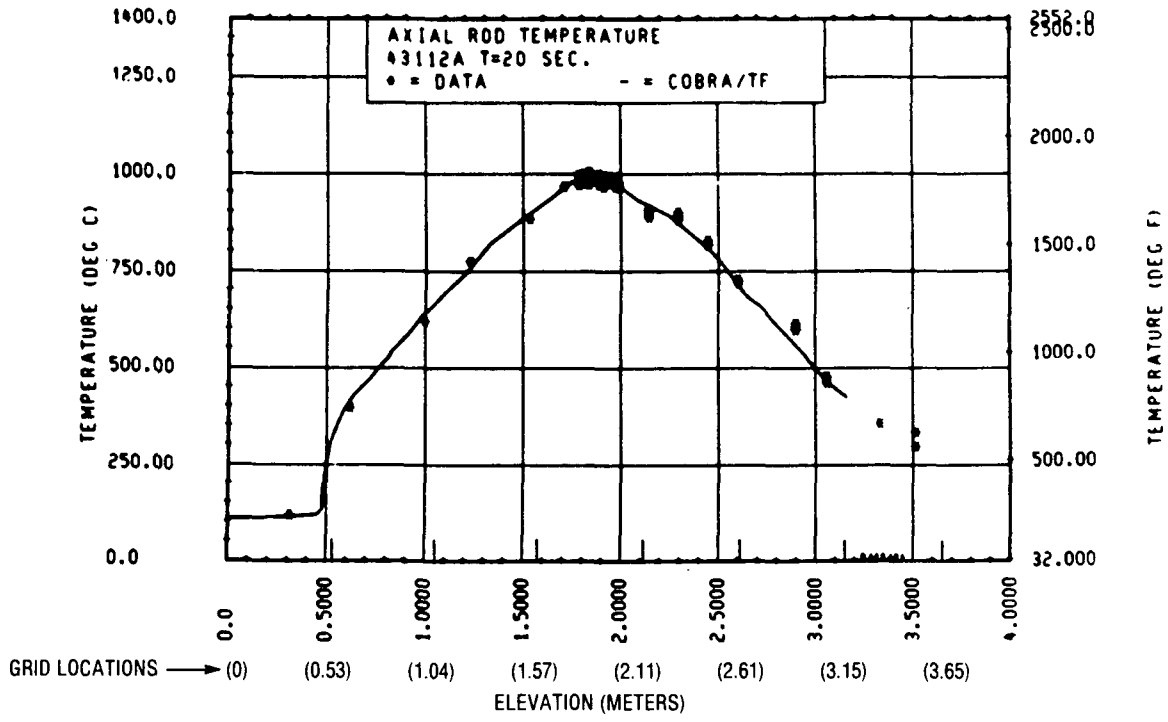

Figure 3-118. Comparison of COBRA-TF-Calculated Axial Rod Temperature Versus Elevation With FLECHT SEASET 21-Rod Data, Test 43112A, t = 20 Seconds

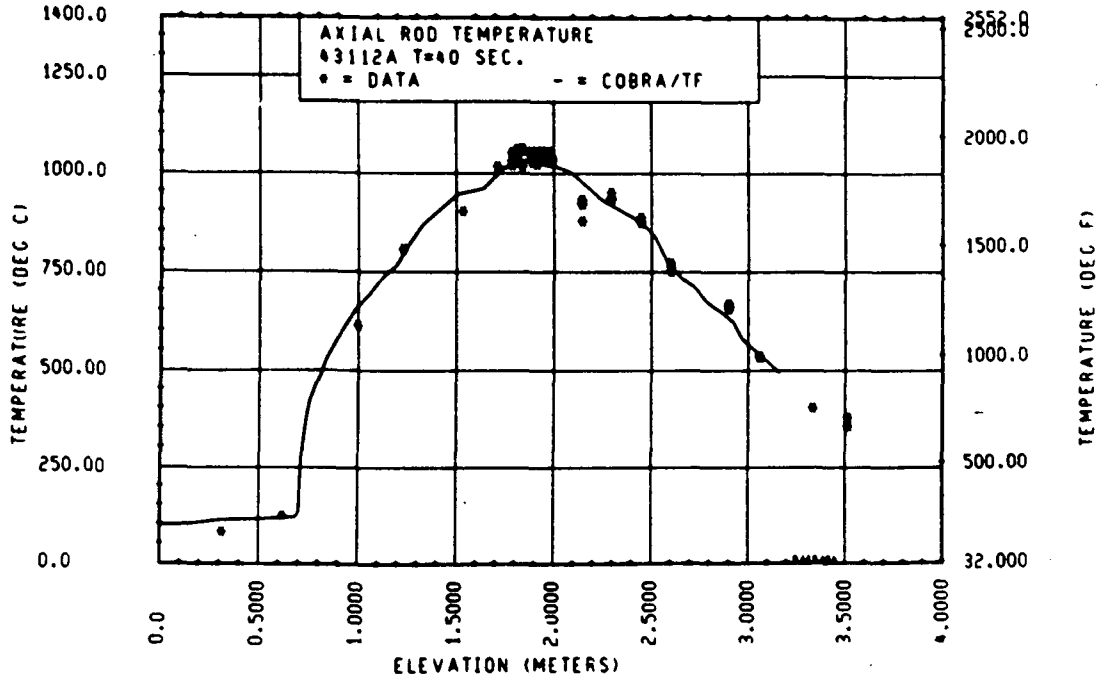

Figure 3-119. Comparison of COBRA-TF-Calculated Axial Rod Temperature Versus Elevation With FLECHT SEASET 21-Rod Data, Test 43112A, t = 40 Seconds

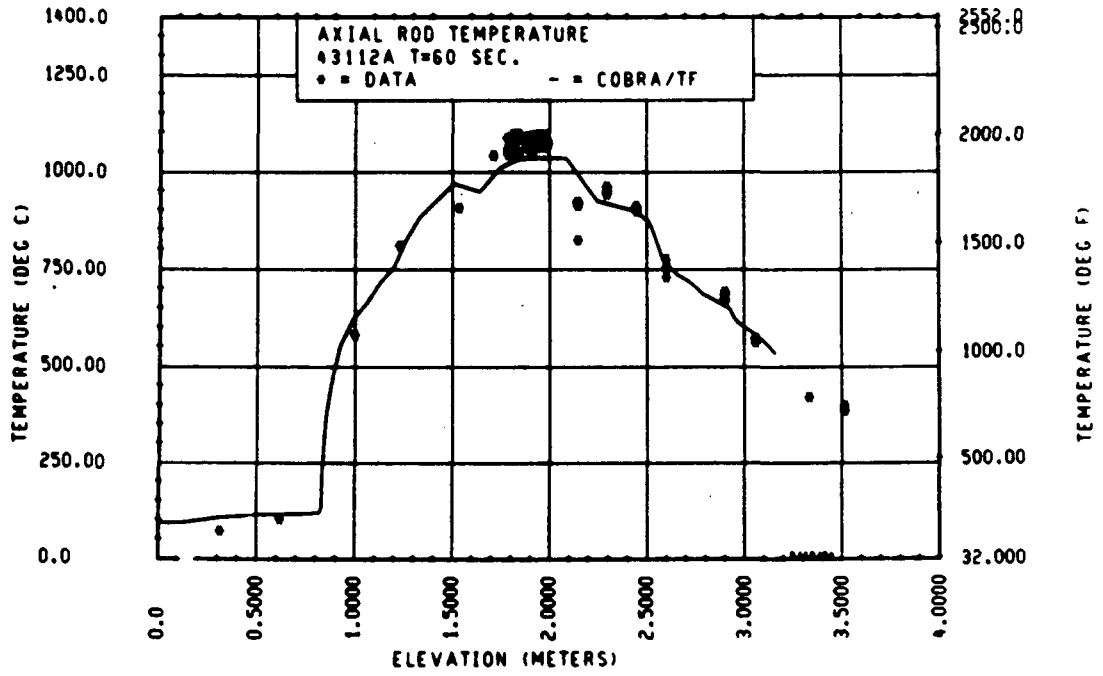

Figure 3-120. Comparison of COBRA-TF-Calculated Axial Rod Temperature Versus Elevation With FLECHT SEASET 21-Rod Data, Test 43112A, t = 60 Seconds

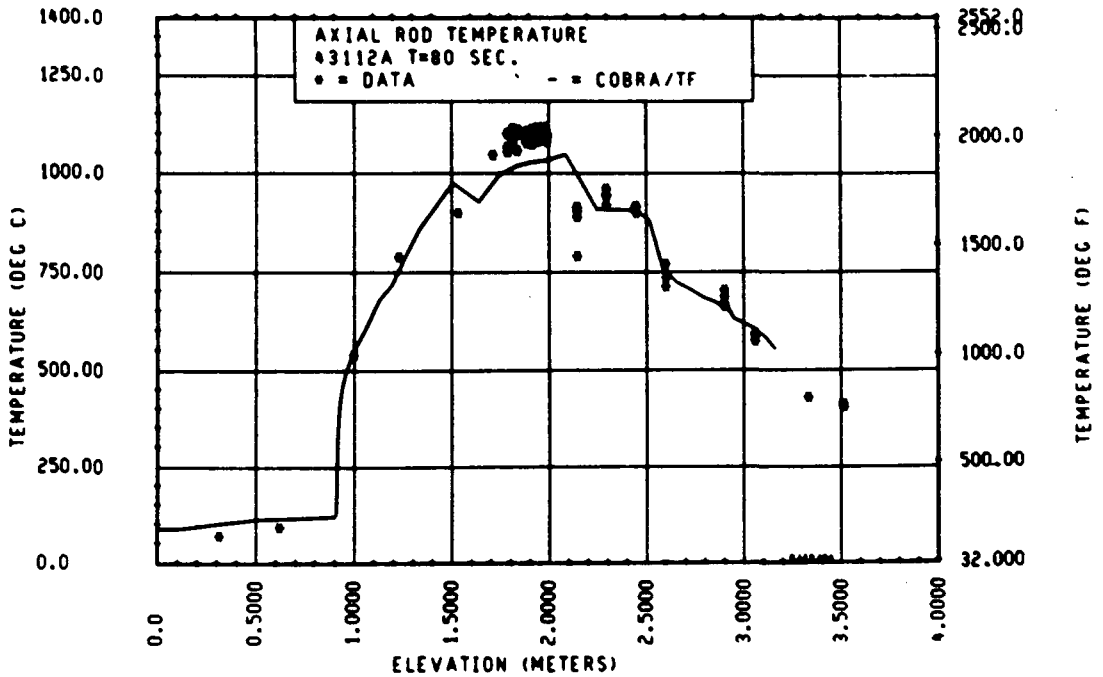

Figure 3-121. Comparison of COBRA-TF-Calculated Axial Rod Temperature Versus Time With FLECHT SEASET 21-Rod Data, Test 43112A, t = 80 Seconds

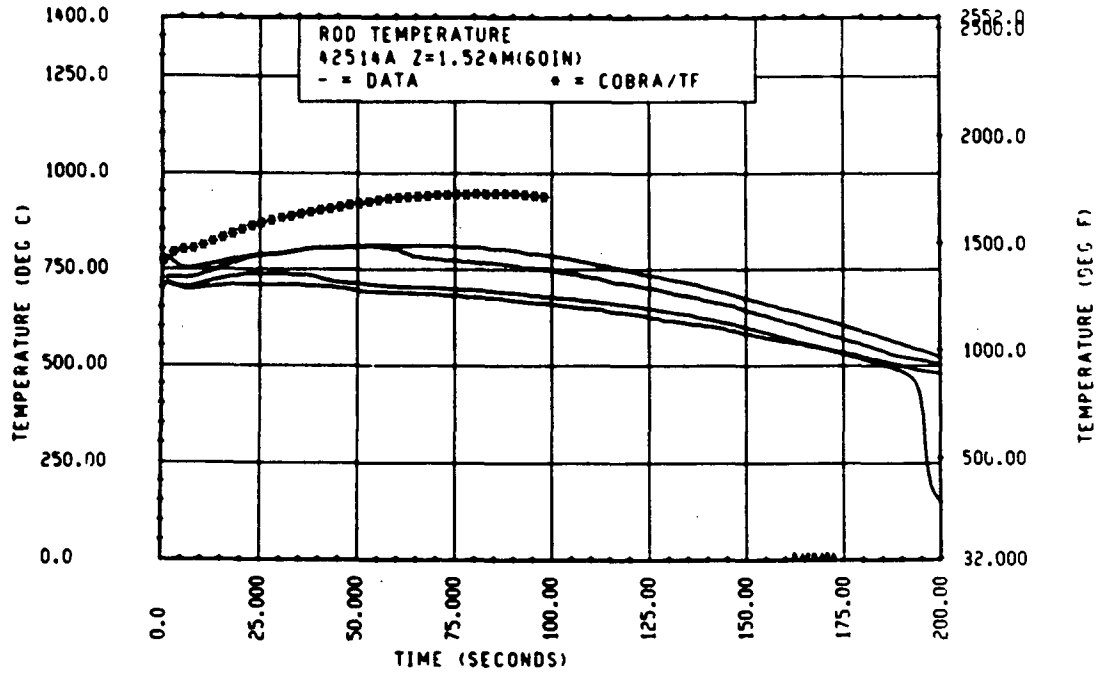

Figure 3-122. Comparison of COBRA-TF-Calculated Heater Rod Temperature Versus Time With FLECHT SEASET 21-Rod Data, Test 42514A, 1.52 m (60 in.) Elevation

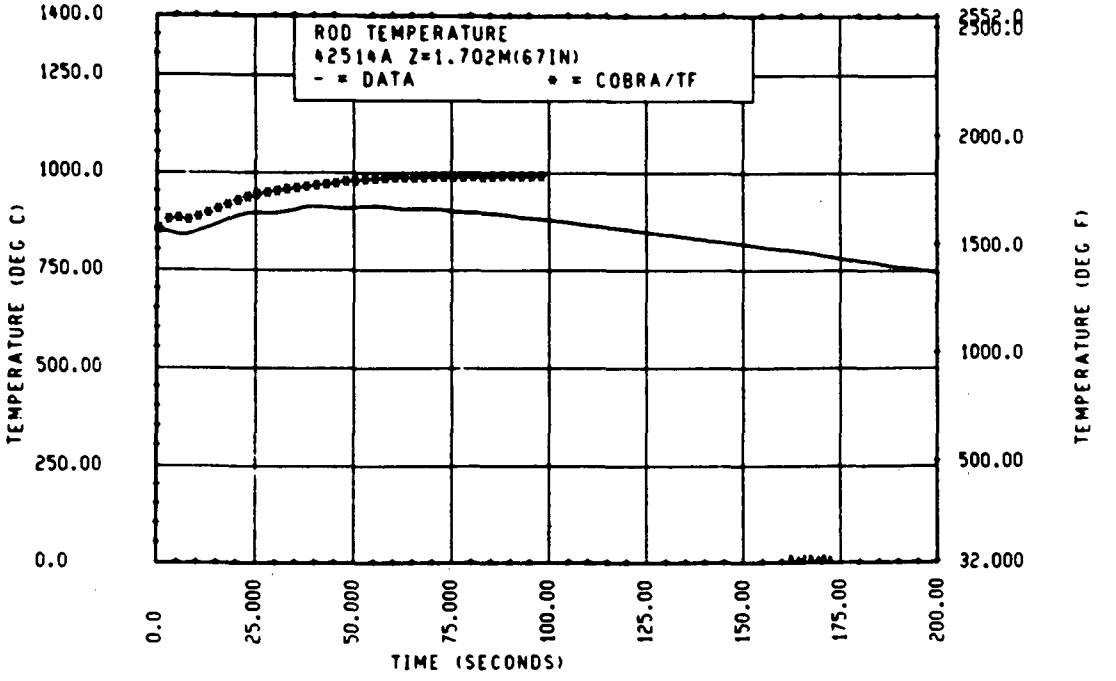

Figure 3-123. Comparison of COBRA-TF-Calculated Heater Rod Temperature Versus Time With FLECHT SEASET 21-Rod Data, Test 42514A, 1.70 m (67 in.) Elevation

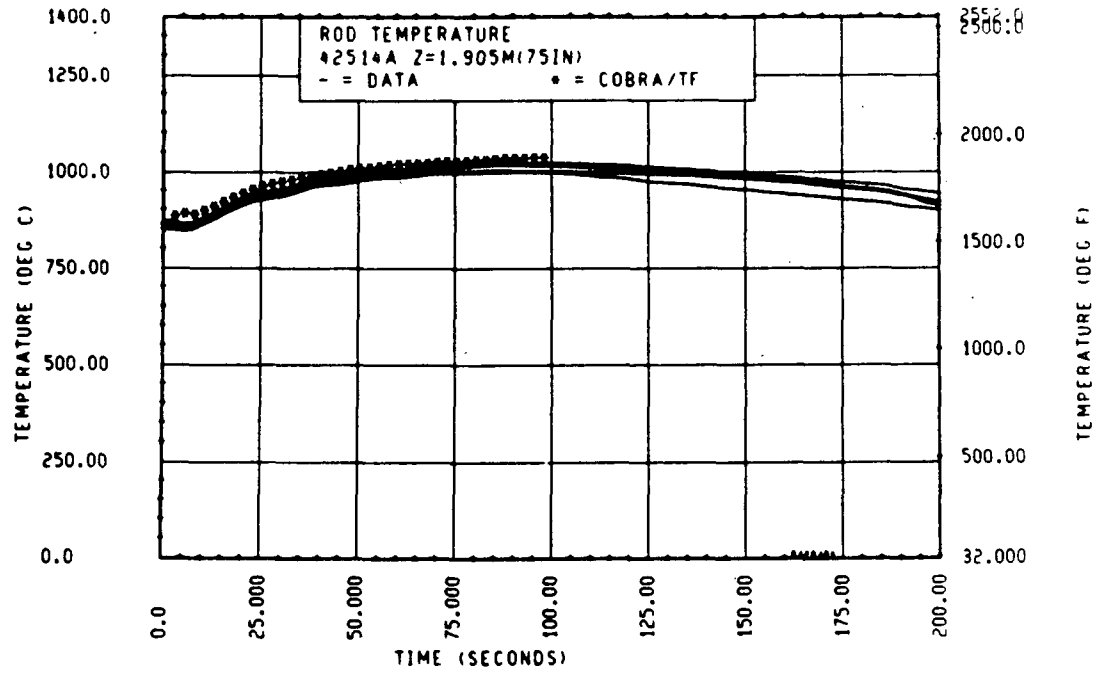

Figure 3-124. Comparison of COBRA-TF-Calculated Heater Rod Temperature Versus Time With FLECHT SEASET 21-Rod Data, Test 42514A, 1.90 m (75 in.) Elevation

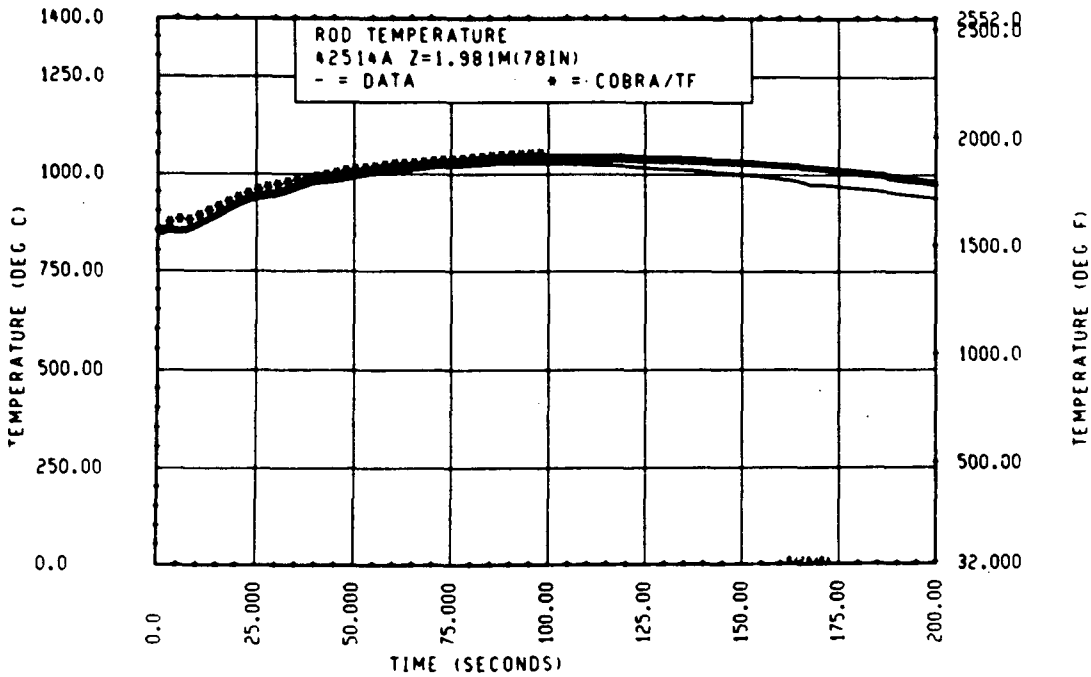

Figure 3-125. Comparison of COBRA-TF-Calculated Heater Rod Temperature Versus Time With FLECHT SEASET 21-Rod Data, Test 42514A, 1.98 m (78 in.) Elevation

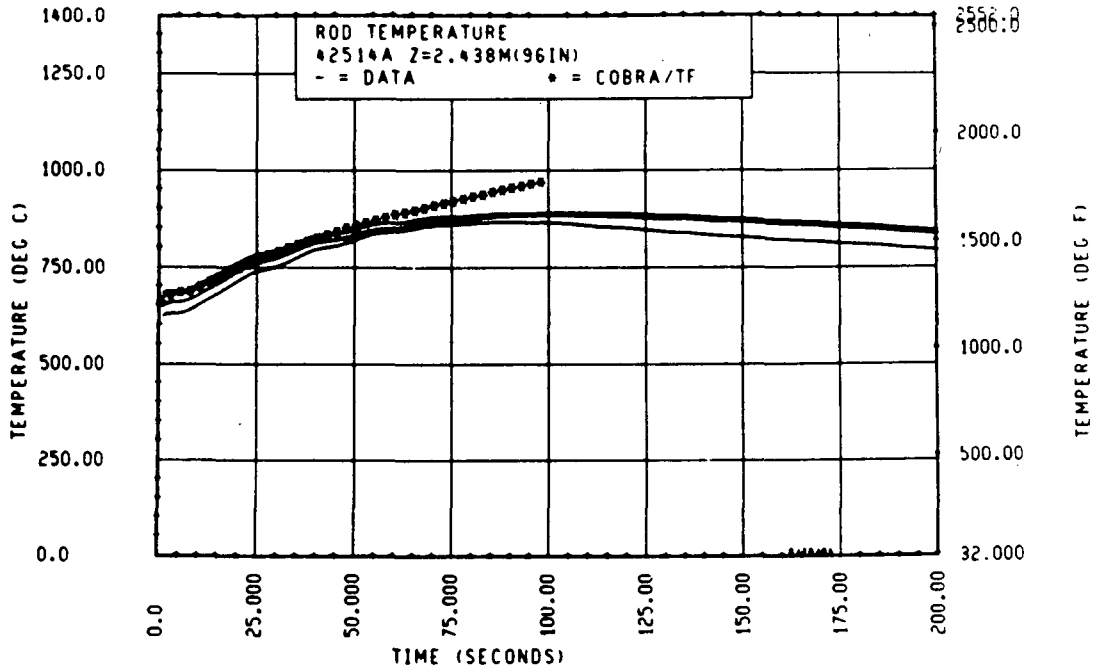

Figure 3-126. Comparison of COBRA-TF-Calculated Heater Rod Temperature Versus Time With FLECHT SEASET 21-Rod Data, Test 43112A, 2.44 m (96 in.) Elevation

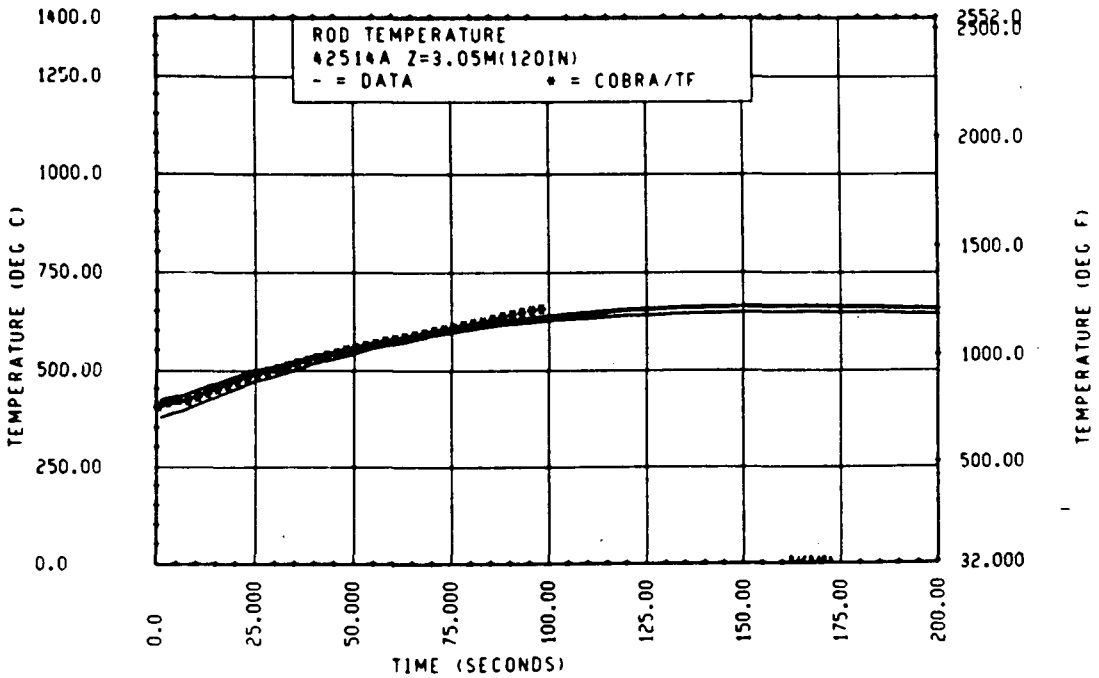

Figure 3-127. Comparison of COBRA-TF-Calculated Heater Rod Temperature Versus Time With FLECHT SEASET 21-Rod Data, Test 43112A, 3.05 m (120 in.) Elevation

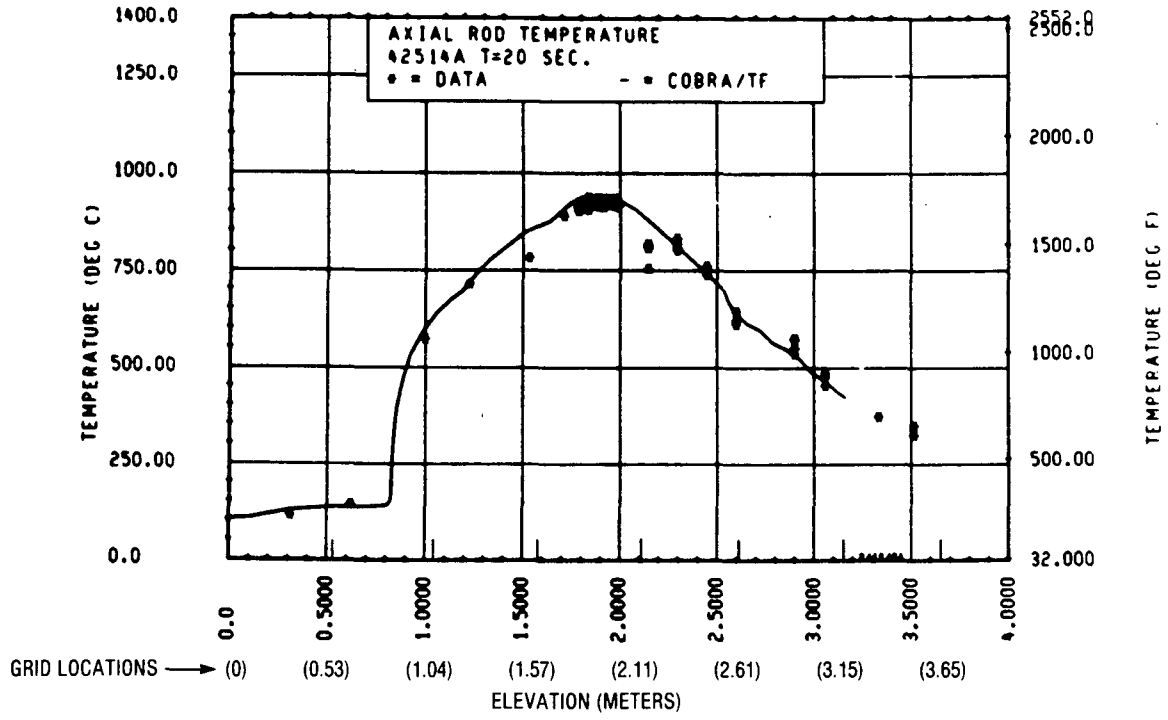

Figure 3-128. Comparison of COBRA-TF-Calculated Axial Rod Temperature Versus Elevation With FLECHT SEASET 21-Rod Data, Test 43112A, t = 20 Seconds

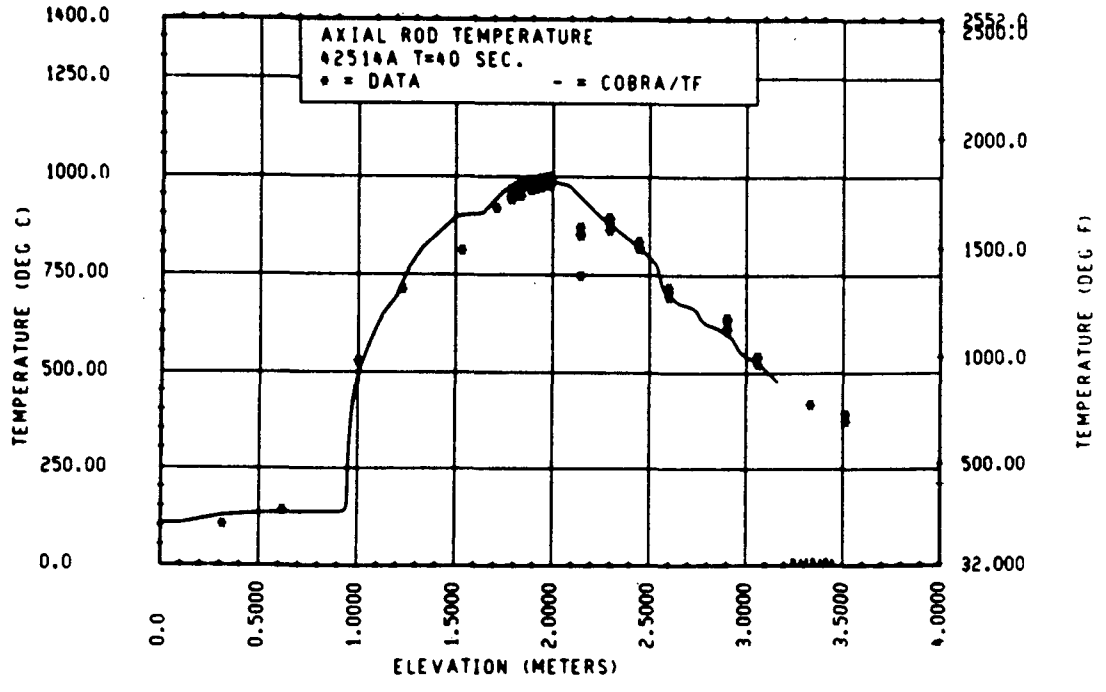

Figure 3-129. Comparison of COBRA-TF-Calculated Axial Rod Temperature Versus Elevation With FLECHT SEASET 21-Rod Data, Test 43112A, t = 40 Seconds

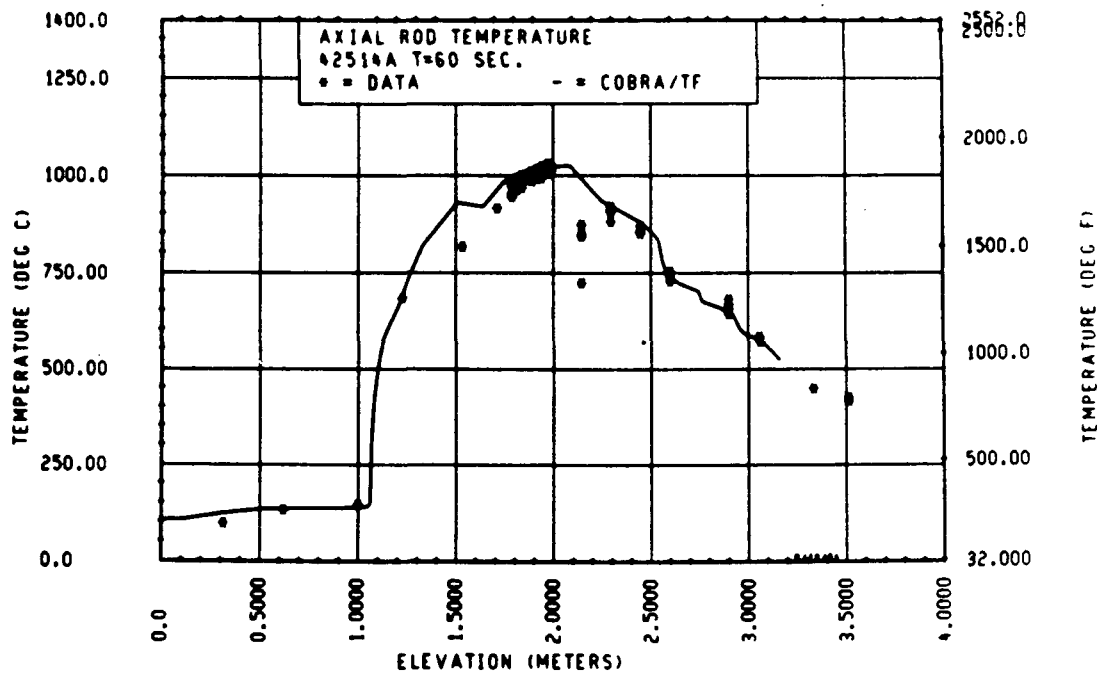

Figure 3-130. Comparison of COBRA-TF-Calculated Axial Rod Temperature Versus Elevation With FLECHT SEASET 21-Rod Data, Test 43112A, t = 60 Seconds

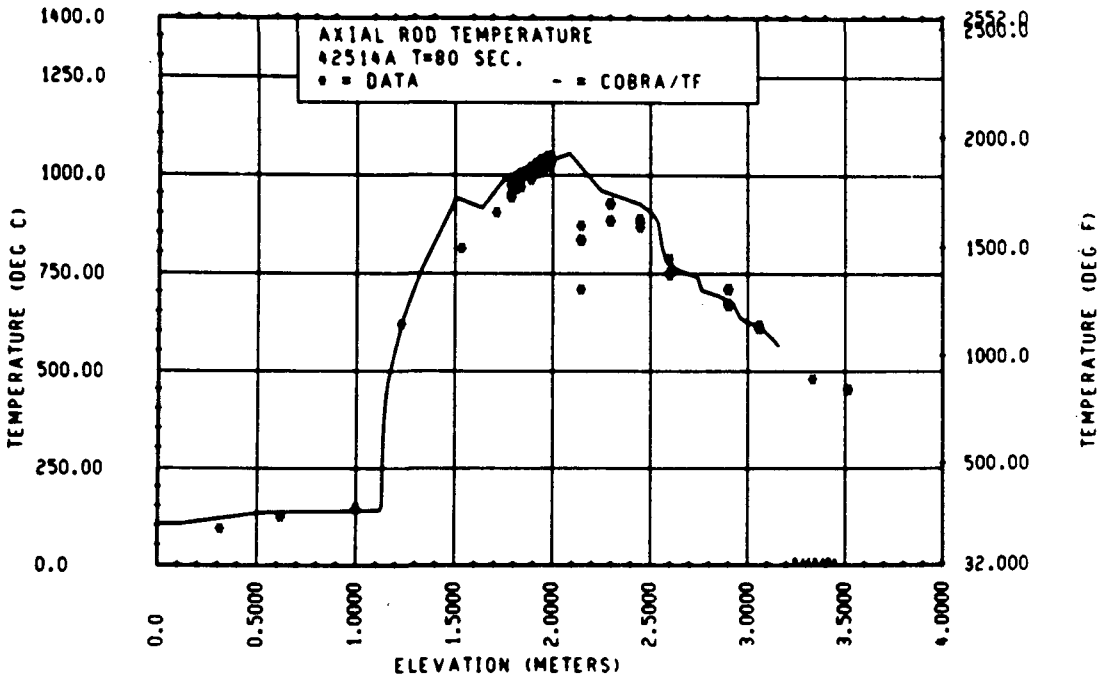

Figure 3-131. Comparison of COBRA-TF-Calculated Axial Rod Temperature Versus Time With FLECHT SEASET 21-Rod Data, Test 43112A, t = 80 Seconds

The FEBA test conditions (table 3-2) overlap those of the FLECHT SEASET experiments previously discussed; however, there are some significant differences, as shown in table 3-3. Because of these differences, the FEBA data provide a unique opportunity to verify the COBRA-TF code.

The axial noding and radial noding used for the FEBA tests is shown in figures 3-132 and 3-133. FEBA was modeled in the same fashion as the 21-rod bundle, with a one-eighth section to take advantage of symmetry in the rod bundle. The axial noding was also specifically designed to show the effect of the presence or absence of the midplane spacer grid. The grid locations are shown in figure 3-133. The details of the FEBA modeling and input are given in appendix A.

The first two tests examined were FEBA test 216, with seven grids, and FEBA test 229, with six grids. Both tests had 0.40 MPa (60 psia) pressure and 0.0378 m/sec (1.49 in./sec) constant flooding rate. The heater rod temperature-time curves with the COBRA-TF calculations are shown in figures 3-134 through 3-139. The data are from the inner nine rods for the test, assuming symmetry, and the COBRA-TF calculation is from the center rod. The agreement between the calculation and the data is excellent, with the possible exception of a slight overprediction at the uppermost elevations.

One possible shortcoming in the FEBA comparisons is the lack of several instrumented rods at the same elevation, such that an estimate of data scatter or variation can be made. Since the FEBA bundle is small (25 rods), there will be a housing heat sink effect that will result in a radial temperature profile in the experiment. COBRA-TF accounts for a possible radial temperature effect due to the housing by the detailed rod-to-rod radiation model. However, there is an insufficient number of heater rod thermocouples at different elevations to assess these effects in detail. Examination of the FEBA data indicates that there could be approximately 20°C (45°F) variation in rod temperatures from the innermost rods to the next row of rods, because of rod-to-rod variation.

The axial heater rod temperature plots are shown in figures 3-140 through 3-143 for different time periods. (Also shown in figure 3-140 is the axial

TABLE 3-3
FLECHT SEASET AND FEBA TEST COMPARISONS

Parameter	FLECHT SEASET 21- and 161-Rod Bundles	FEBA Bundle
Number of rods	21, 161	25
Rod diameter [m (in.)]	0.0950 (3.74)	0.0107 (0.422)
Rod pitch (m (in.)]	0.0126 (0.496)	0.0143 (0.563)
Pitch-to-diameter ratio	1.326	1.334
Axial profile	1.66 chopped cosine	1.19 chopped cosine
Housing effect	21-rod: heated 161-rod: unheated	Heated
Grid type	FLECHT egg-crate grids	KWU support grids
Grid characteristics		
Blockage (%)	23	25
Strap thickness [mm (in.)]	0.38 (0.015)	0.43 (0.017)
Material	304 stainless steel	Inconel 600
Strap height [mm (in.)]	44.4 (1.75)	39.9 (1.57)

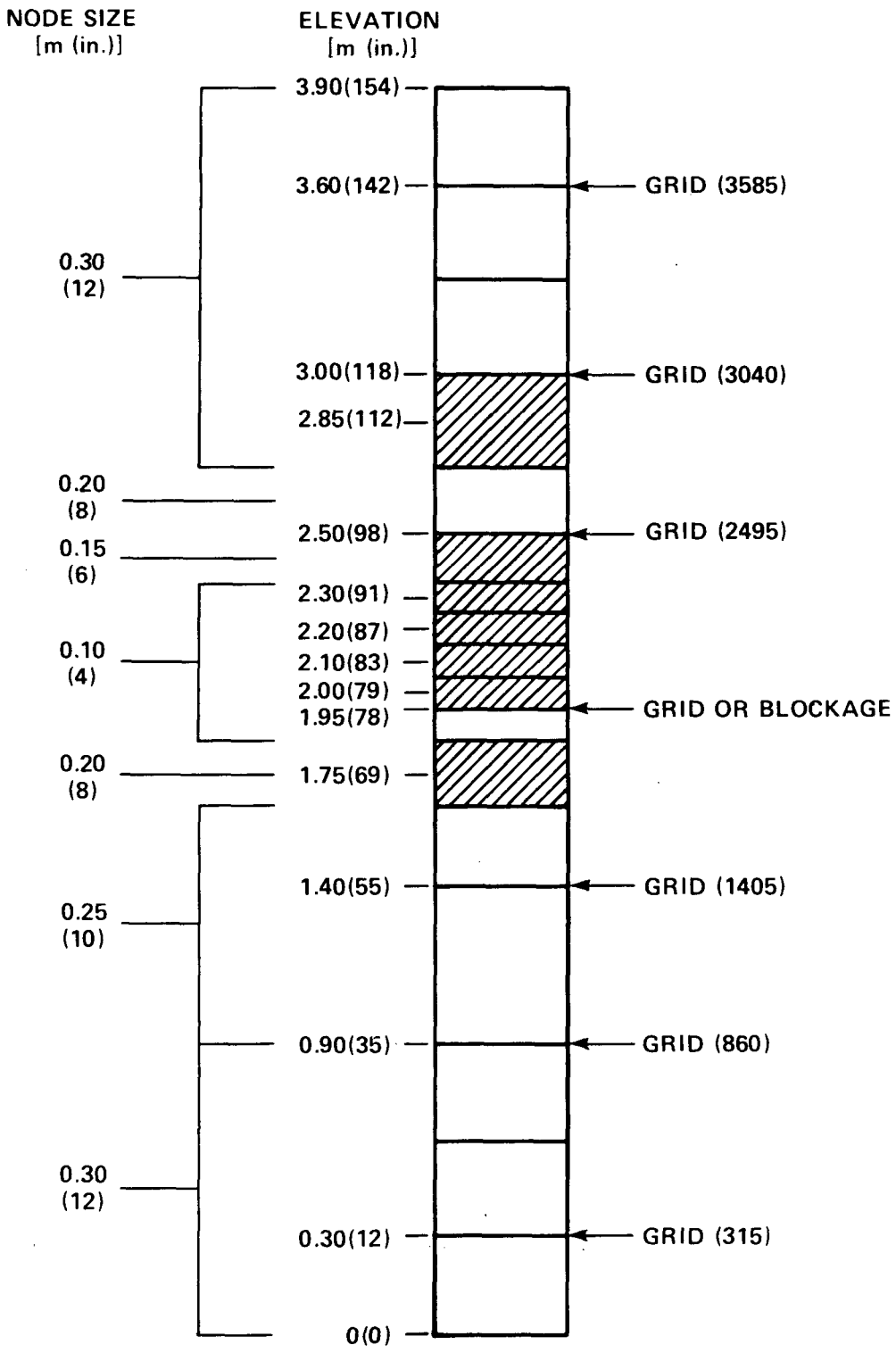

Figure 3-132. Axial Noding for FEBA Test Data Comparisons

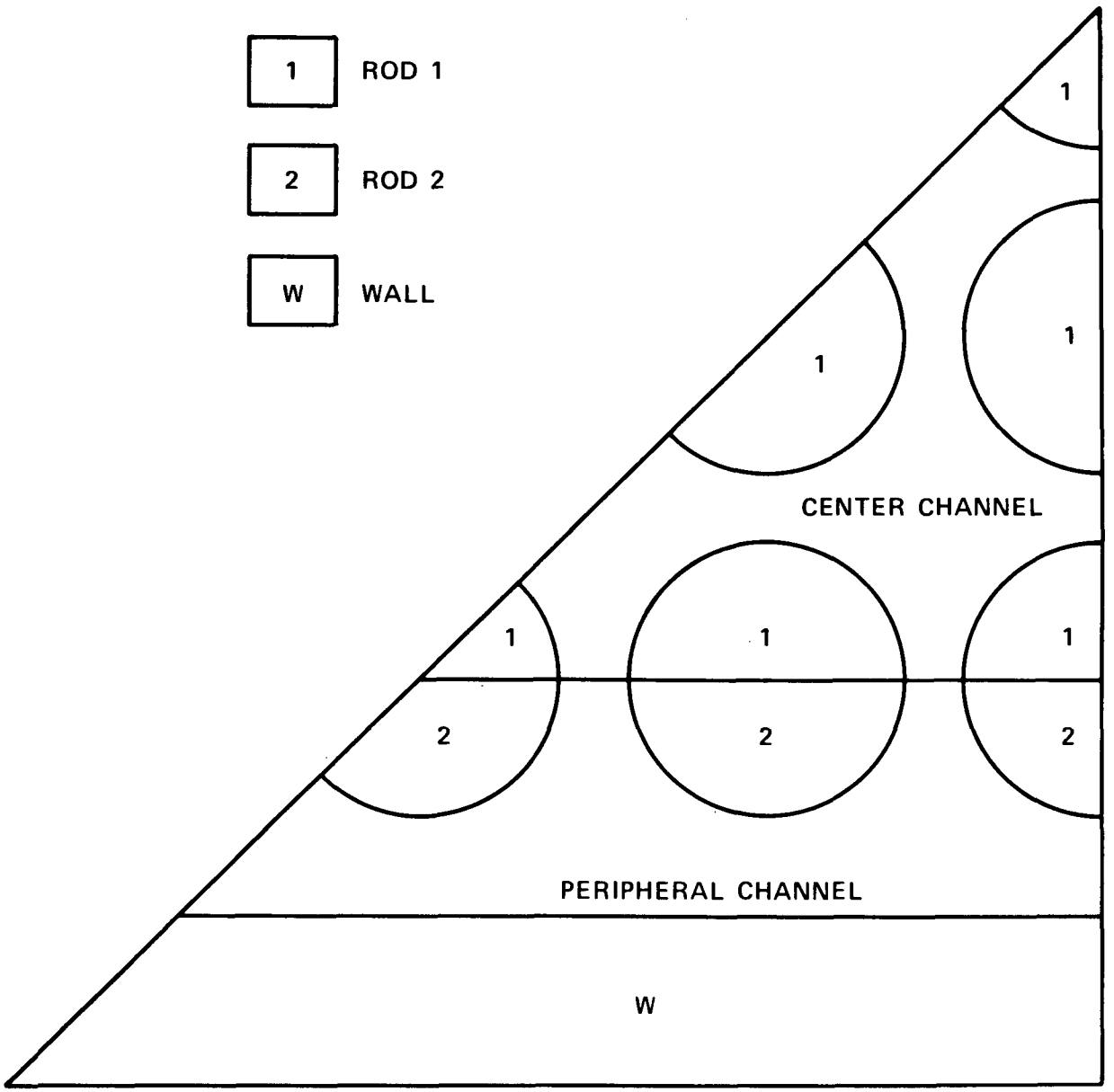

Figure 3-133. Radial Noding for FEBA Test Data Comparisons

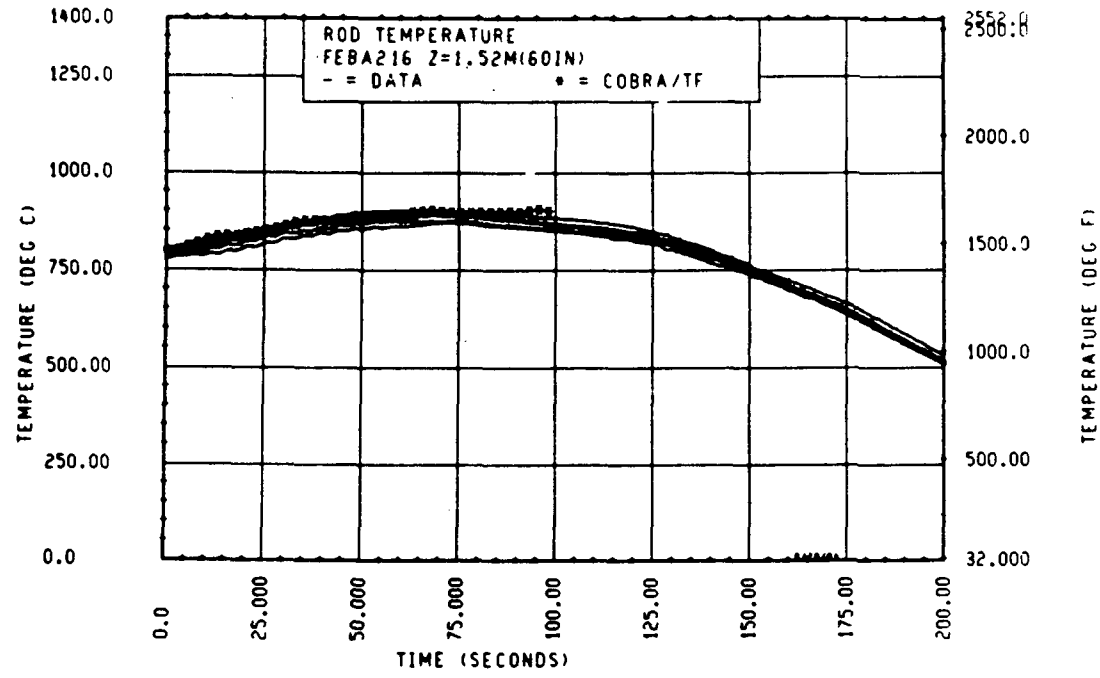

Figure 3-134. Comparison of COBRA-TF-Calculated Heater Rod Temperature Versus Time With FEBA Data, Test 216, 1.52 m (60 in.) Elevation

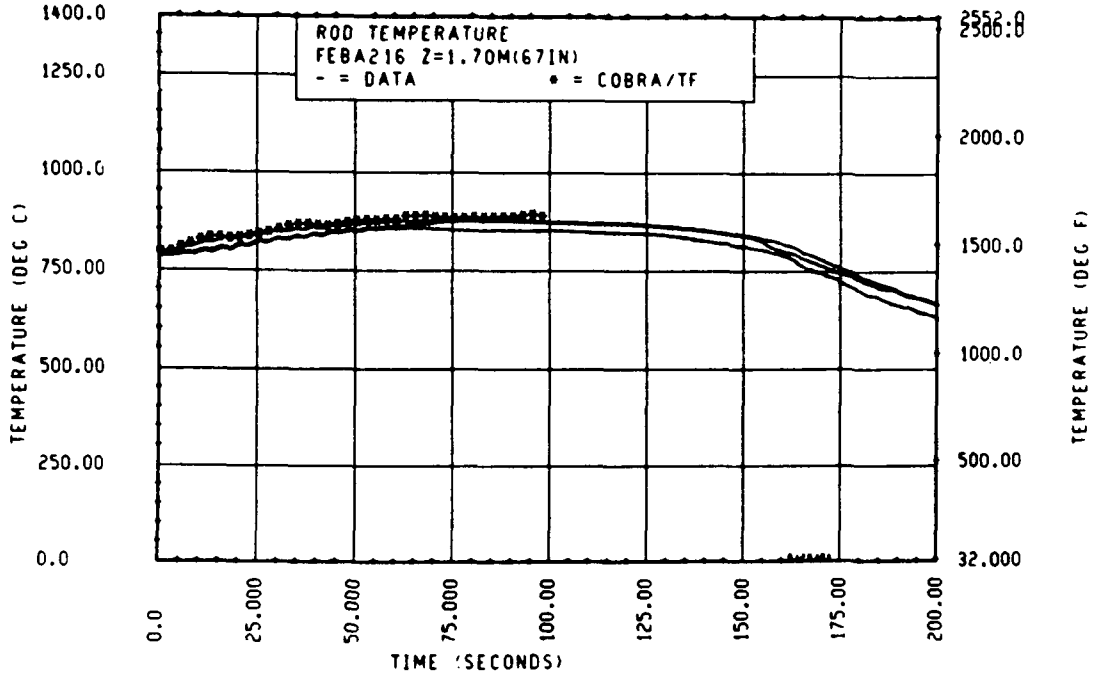

Figure 3-135. Comparison of COBRA-TF-Calculated Heater Rod Temperature Versus Time With FEBA Data, Test 216, 1.70 m (67 in.) Elevation

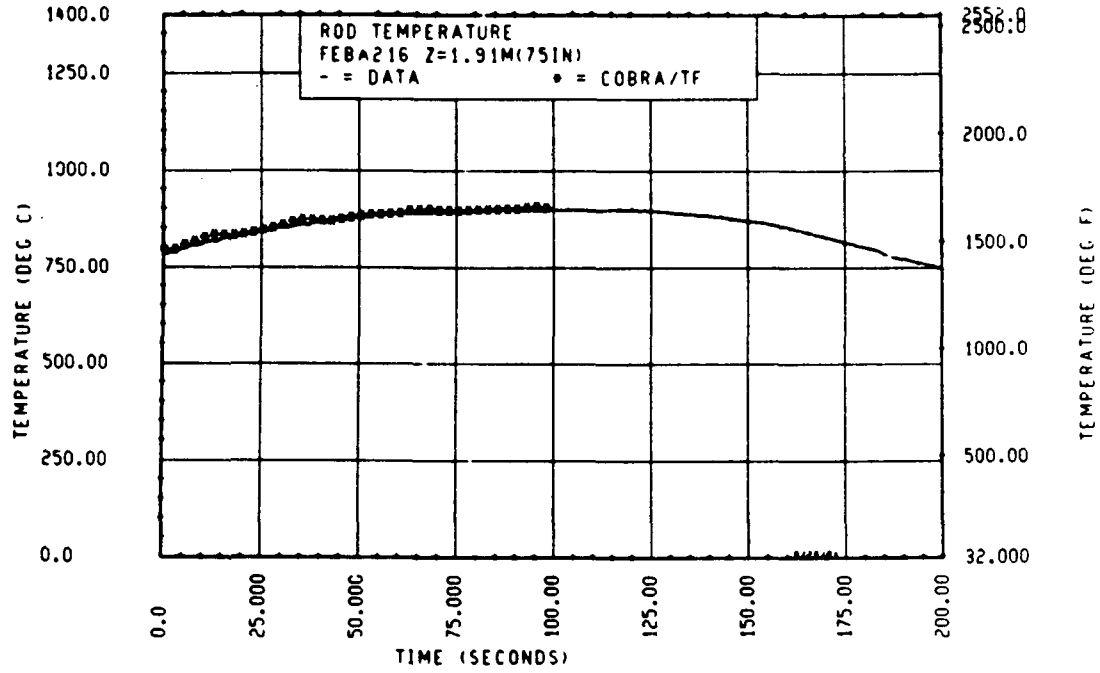

Figure 3-136. Comparison of COBRA-TF-Calculated Heater Rod Temperature Versus Time With FEBA Data, Test 216, 1.91 m (75 in.) Elevation

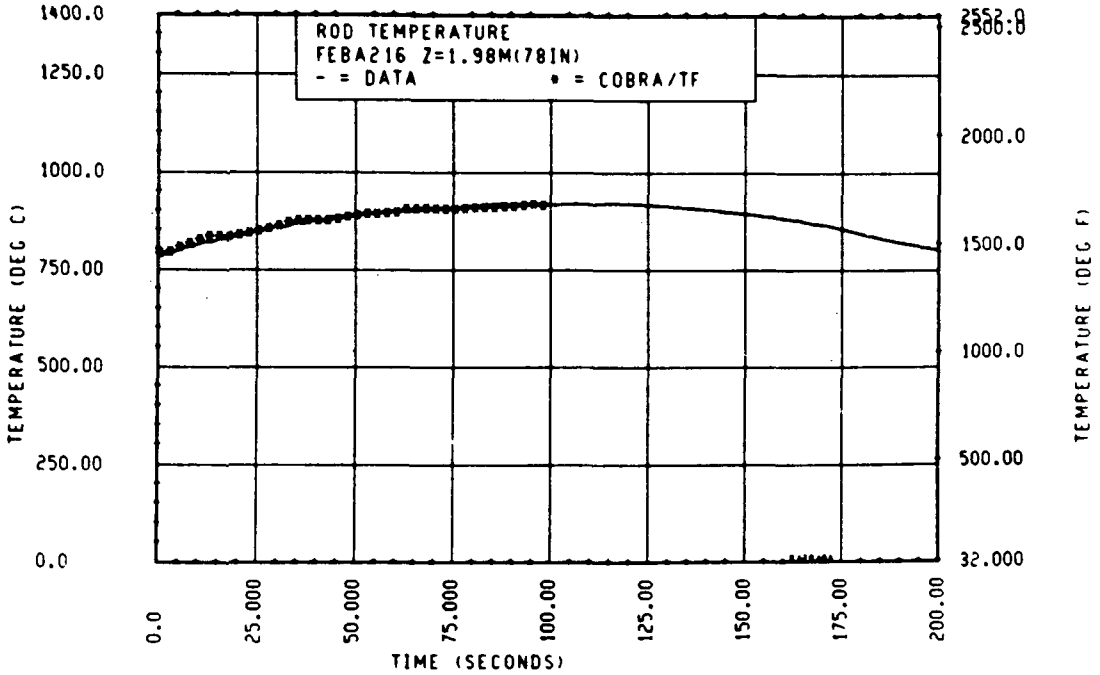

Figure 3-137. Comparison of COBRA-TF-Calculated Heater Rod Temperature Versus Time With FEBA Data, Test 216, 1.98 m (78 in.) Elevation

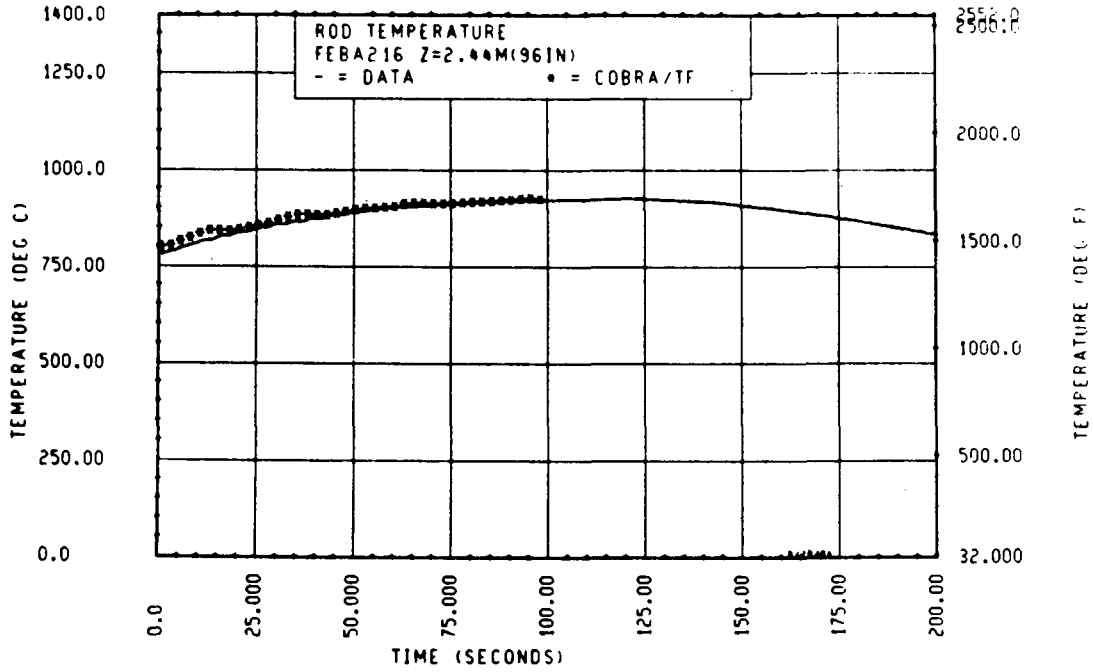

Figure 3-138. Comparison of COBRA-TF-Calculated Heater Rod Temperature Versus Time With FEBA Data, Test 216, 2.44 m (96 in.) Elevation

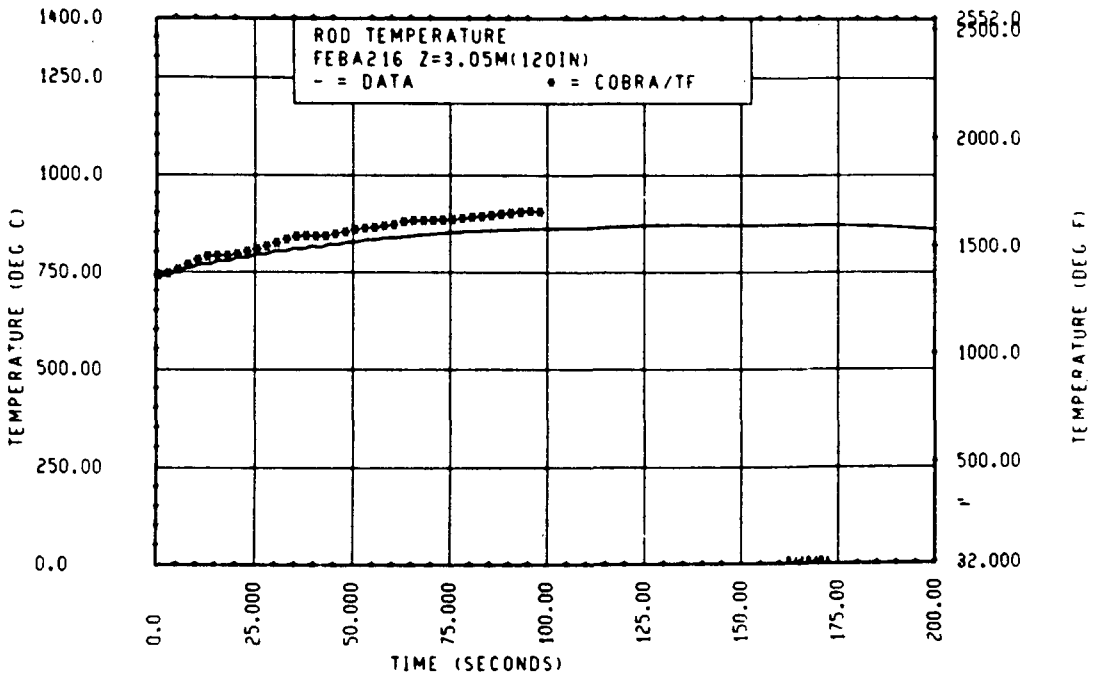

Figure 3-139. Comparison of COBRA-TF-Calculated Heater Rod Temperature Versus Time With FEBA Data, Test 216, 3.05 m (120 in.) Elevation

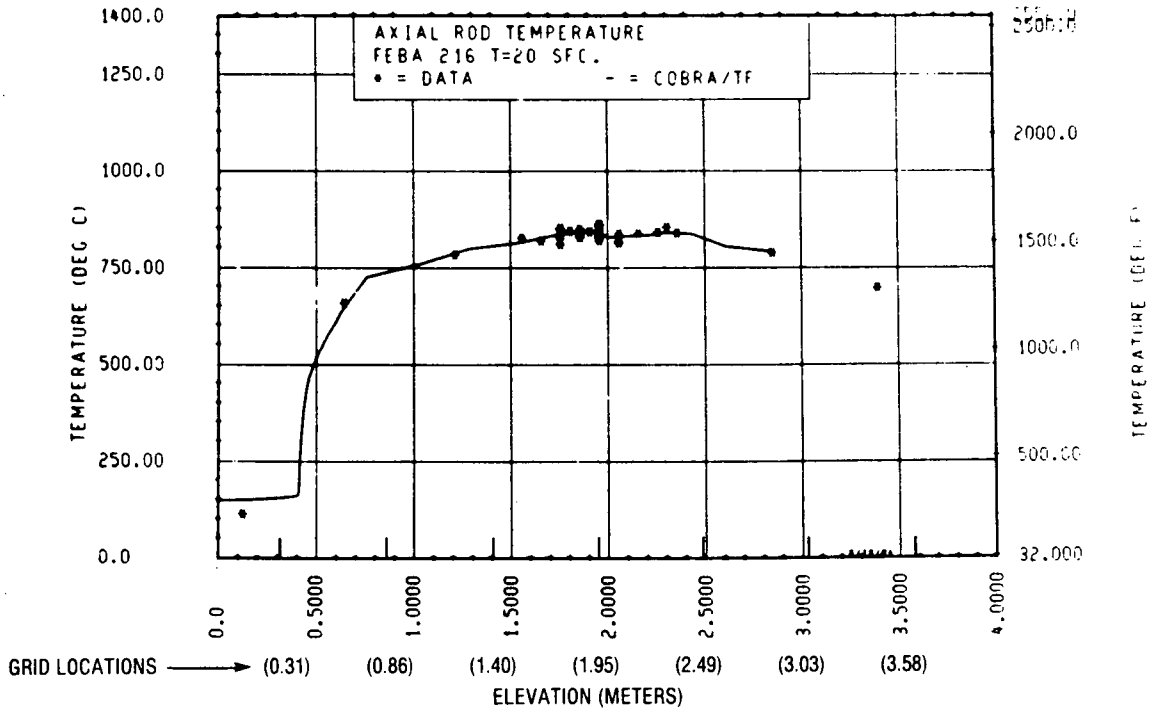

Figure 3-140. Comparison of COBRA-TF-Calculated Axial Rod Temperature Versus Elevation With FEBA Data, Test 216, t = 20 Seconds

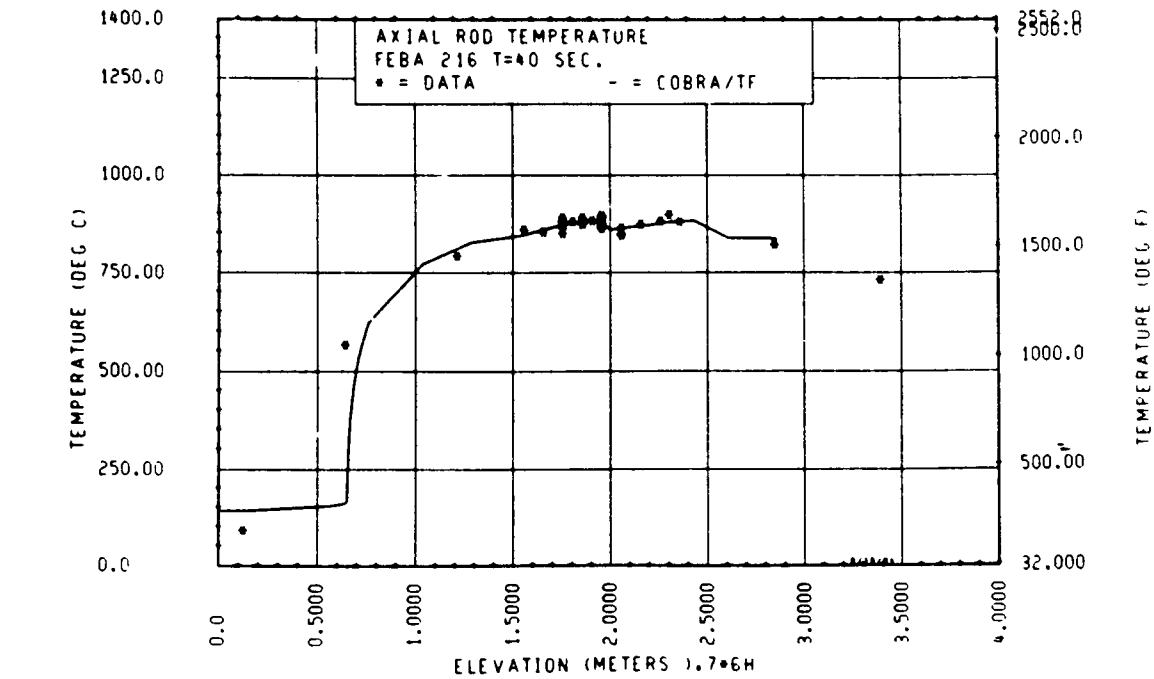

Figure 3-141. Comparison of COBRA-TF-Calculated Axial Rod Temperature Versus Elevation With FEBA Data, Test 216, t = 40 Seconds

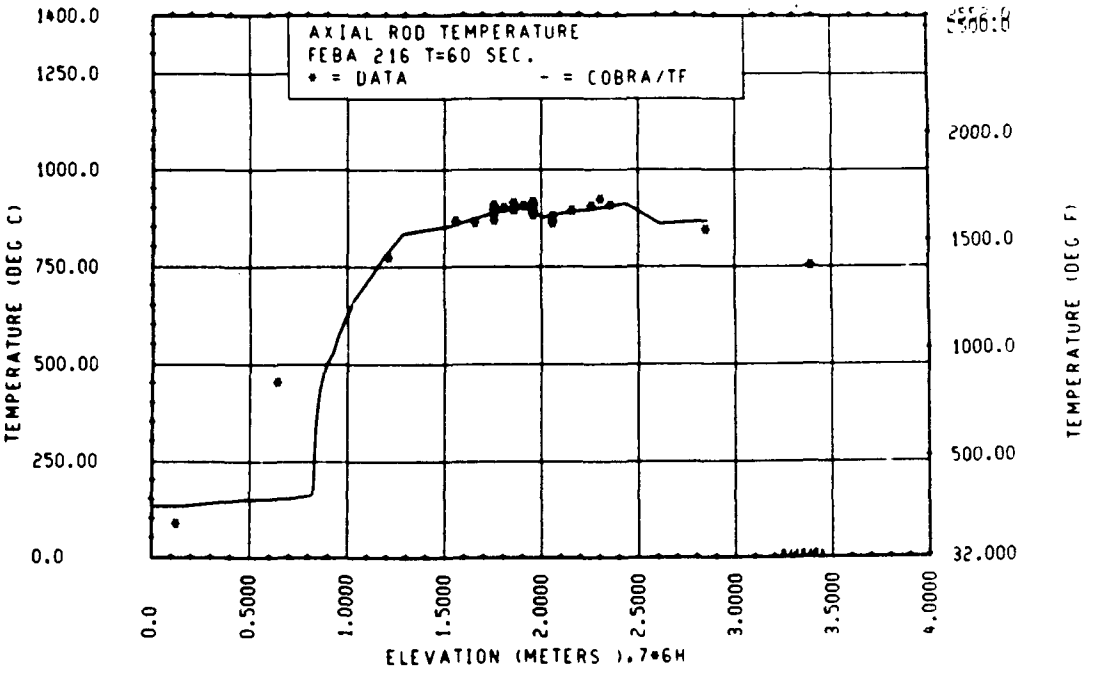

Figure 3-142. Comparison of COBRA-TF-Calculated Axial Rod Temperature Versus Time With FEBA Data, Test 216, t = 60 Seconds

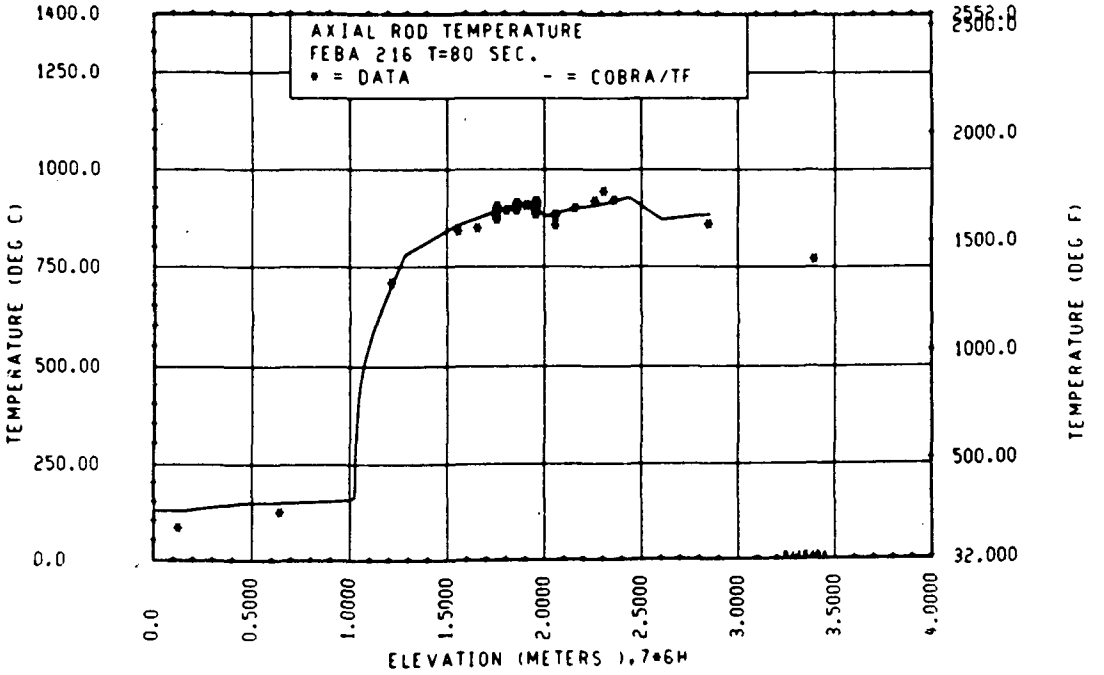

Figure 3-143. Comparison of COBRA-TF-Calculated Axial Rod Temperature Versus Time With FEBA Data, Test 216, t = 80 Seconds

location of the spacer grids.) These figures again indicate excellent agreement of COBRA-TF with the FEBA data, and also show that the code predicts the correct quench rate progression of the rod bundle. The much flatter axial cosine power shape for the FEBA tests (1.19 peak to average) results in a correspondingly flat temperature behavior for reflood. The grid effects, particularly at the 1.95 m (76.8 in.) location, are apparent at later times (60 to 80 seconds), once reflood entrainment is developed.

A similar package of COBRA-TF predictions and FEBA data plots is contained in figures 3-144 through 3-153 for FEBA test 229, which had nearly the same thermal-hydraulic boundary conditions as FEBA test 216 except that the 1.95 m (76.8 in.) grid was removed. Again, the heater rod temperature-time plots show very good agreement between the COBRA-TF prediction and the data.

The axial heater rod temperature plots, figures 3-150 through 3-153, also show good agreement between the COBRA-TF predictions and the FEBA data. (Also shown in figure 3-150 is the axial location of the spacer grids.) There are, however, two points to be noted concerning the axial plots. First, there is no calculated COBRA-TF temperature dip at 1.95 m (76.8 in.) because there was no grid present. These plots should be compared to figures 3-140 through 3-143 for FEBA test 216, which does show this grid behavior. Note also that the grid effect is observed in the test data. Second, it should be noted (figures 3-150 through 3-153) that the grid at 1.40 m (55.3 in.) appears to have a slightly stronger effect in FEBA test 229 than in test 216, such that there is a slight underprediction of the upper elevation axial test data [2 to 2.4 m (79 to 94 in.)] by COBRA-TF for test 229. No explanation can be offered for this difference, since the same model was used in both calculations and the as-run test conditions were also used.

The magnitude of the grid temperature difference predicted by the grid models in COBRA-TF appears to underestimate the grid performance at the 1.95 m (76.8 in.) elevation, as shown in figures 3-142 and 3-143 for FEBA test 216. Part of this difference may be the smearing effect that occurs in the COBRA-TF noding and tends to smooth out local heat transfer effects. On the average over the next 0.5 m (20 in.) downstream of the 1.95 m (76.8 in.) grid, the COBRA-TF-predicted temperature response is correct.

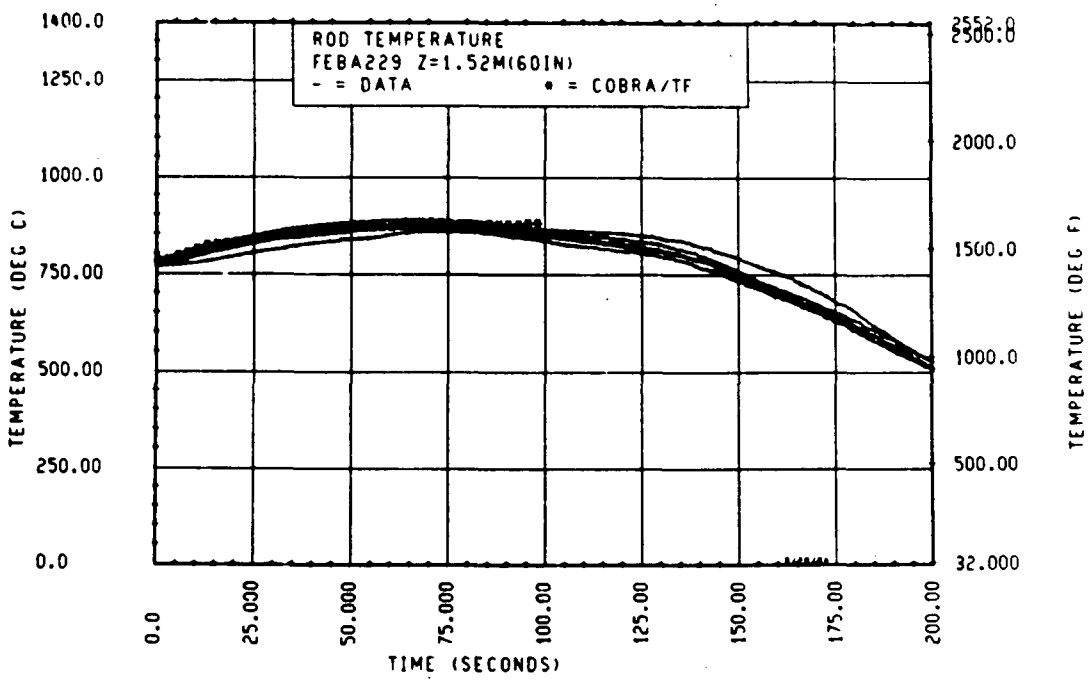

Figure 3-144. Comparison of COBRA-TF-Calculated Heater Rod Temperature Versus Time With FEBA Data, Test 229, 1.52 m (60 in.) Elevation

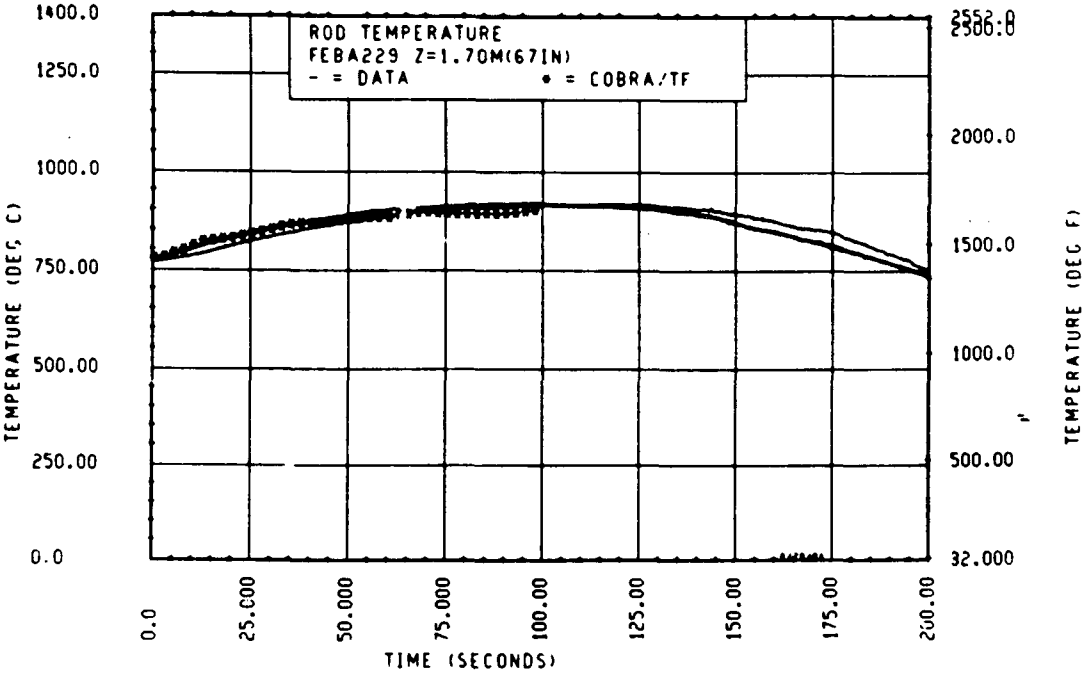

Figure 3-145. Comparison of COBRA-TF-Calculated Heater Rod Temperature Versus Time With FEBA Data, Test 229, 1.70 m (67 in.) Elevation

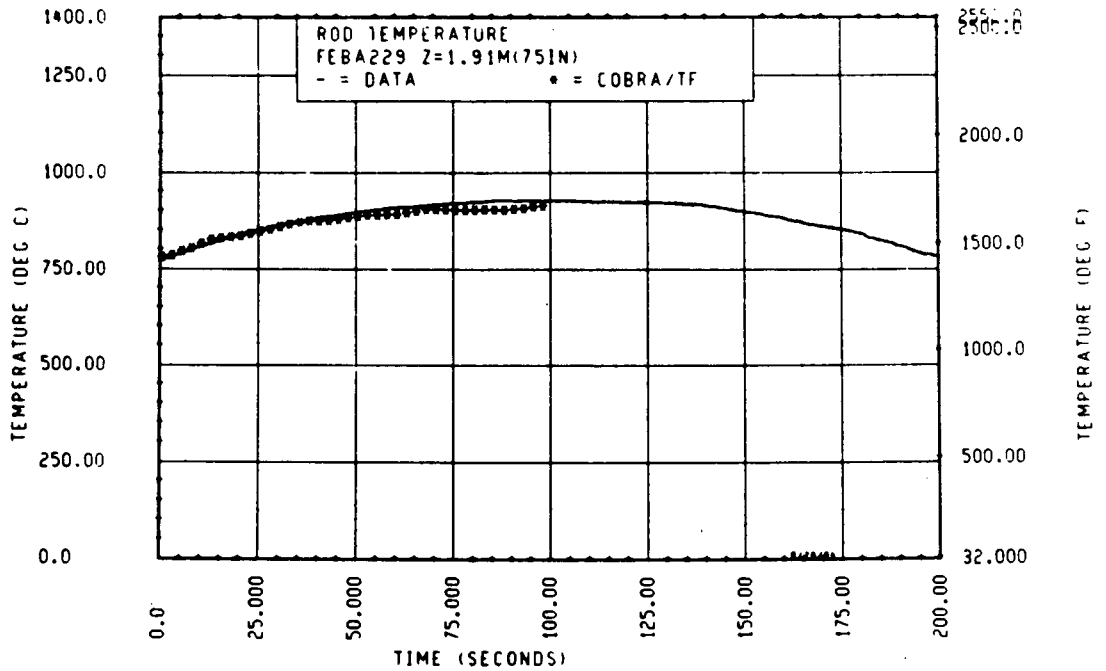

Figure 3-146. Comparison of COBRA-TF-Calculated Heater Rod Temperature Versus Time With FEBA Data, Test 229, 1.91 m (75 in.) Elevation

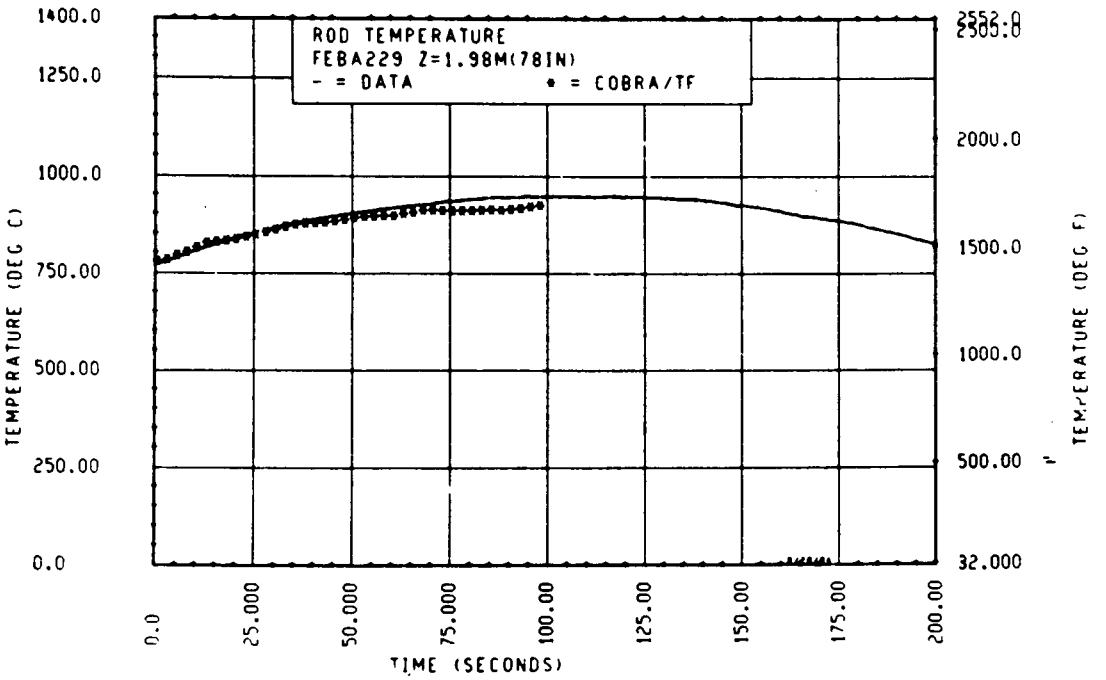

Figure 3-147. Comparison of COBRA-TF-Calculated Heater Rod Temperature Versus Time With FEBA Data, Test 229, 1.98 m (78 in.) Elevation

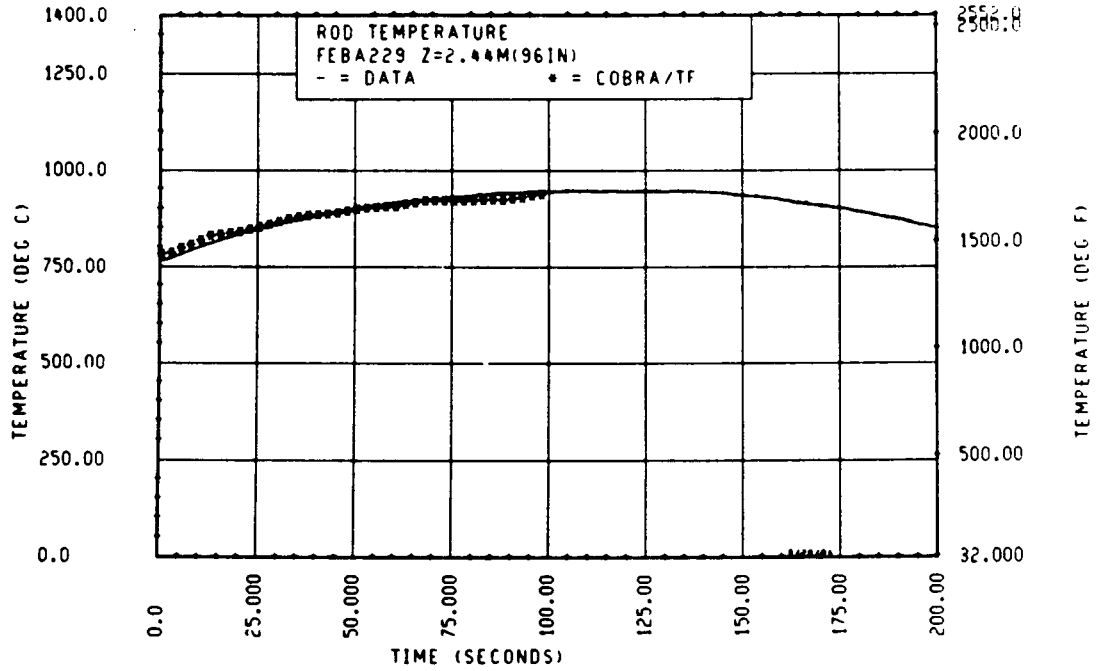

Figure 3-148. Comparison of COBRA-TF-Calculated Heater Rod Temperature Versus Time With FEBA Data, Test 229, 2.44 m (96 in.) Elevation

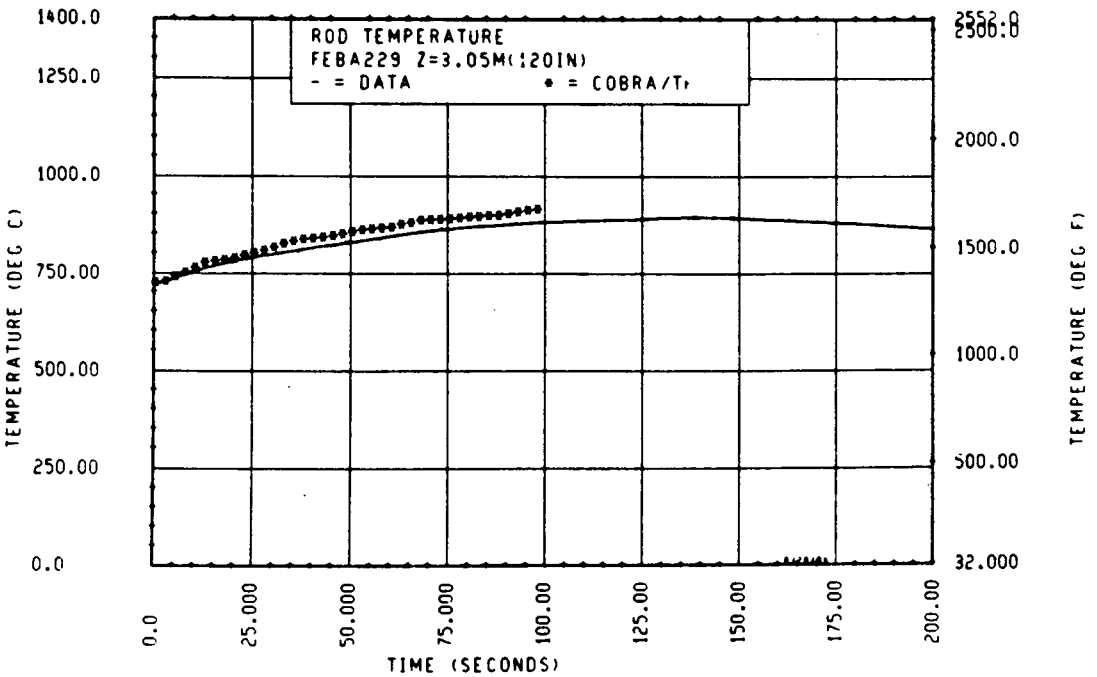

Figure 3-149. Comparison of COBRA-TF-Calculated Heater Rod Temperature Versus Time With FEBA Data, Test 229, 3.05 m (120 in.) Elevation

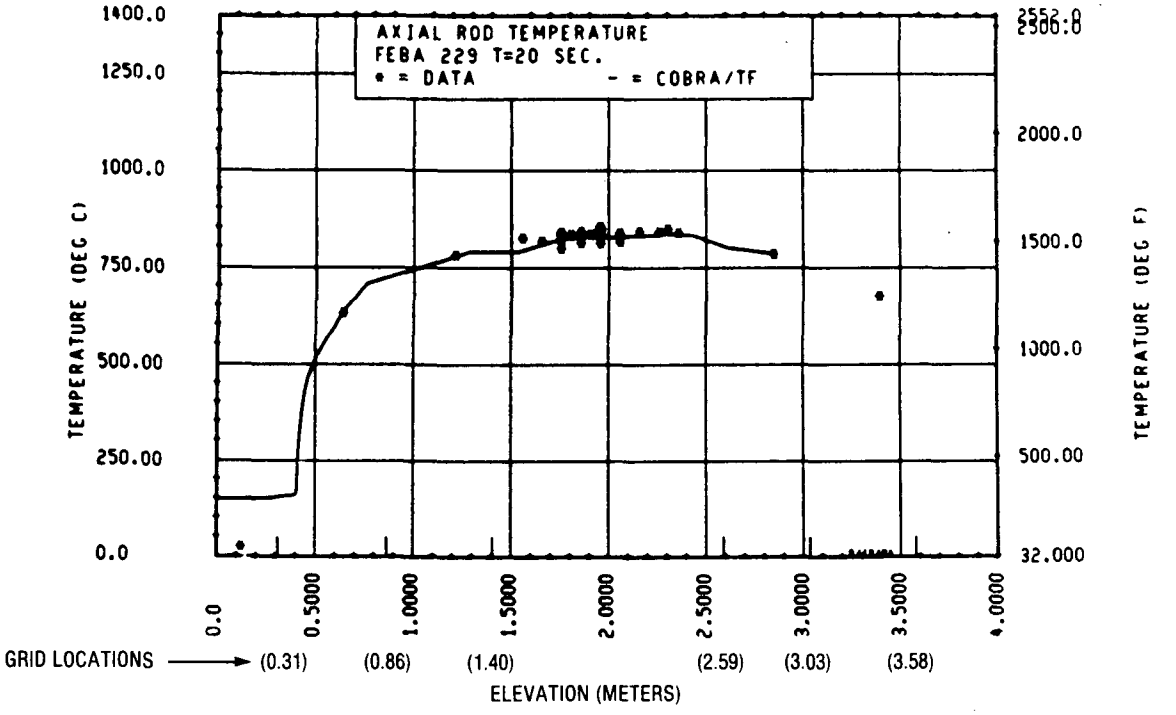

Figure 3-150. Comparison of COBRA-TF-Calculated Axial Rod Temperature Versus Elevation With FEBA Data, Test 229, t = 20 Seconds

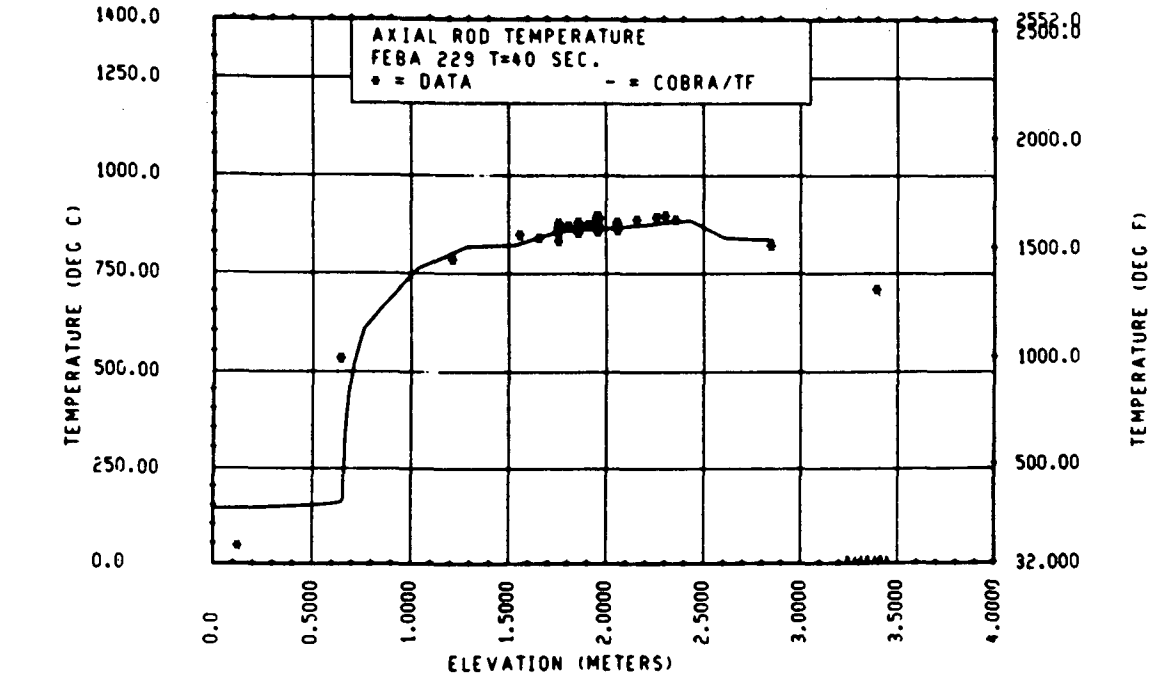

Figure 3-151. Comparison of COBRA-TF-Calculated Axial Rod Temperature Versus Elevation With FEBA Data, Test 229, t = 40 Seconds

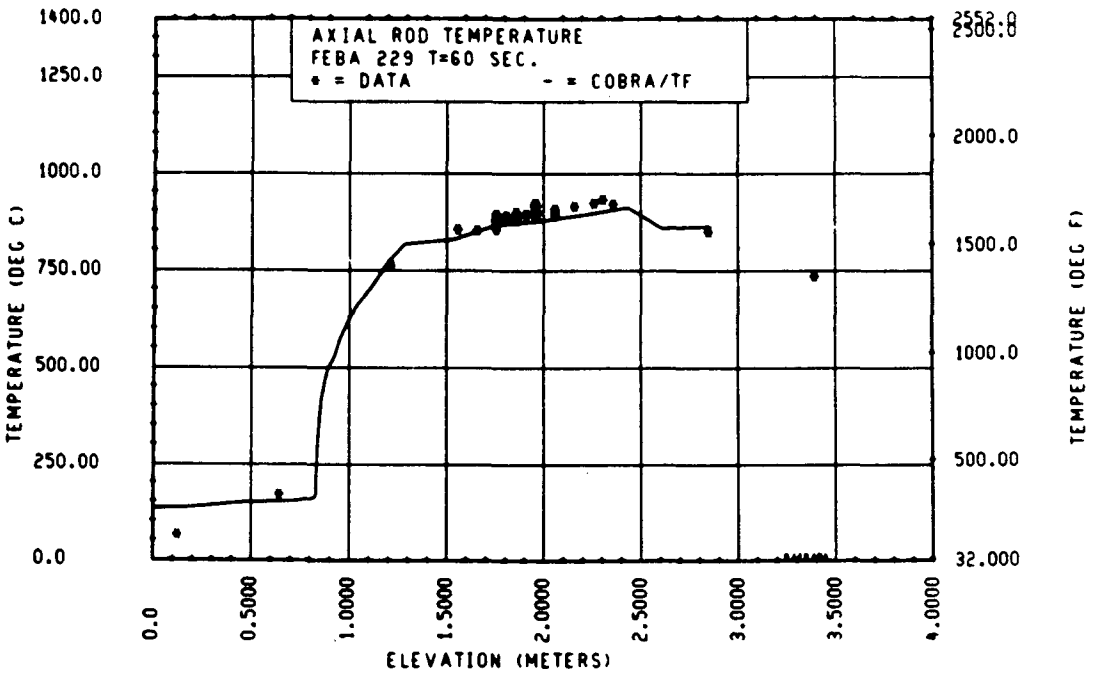

Figure 3-152. Comparison of COBRA-TF-Calculated Axial Rod Temperature Versus Time With FEBA Data, Test 229, t = 60 Seconds

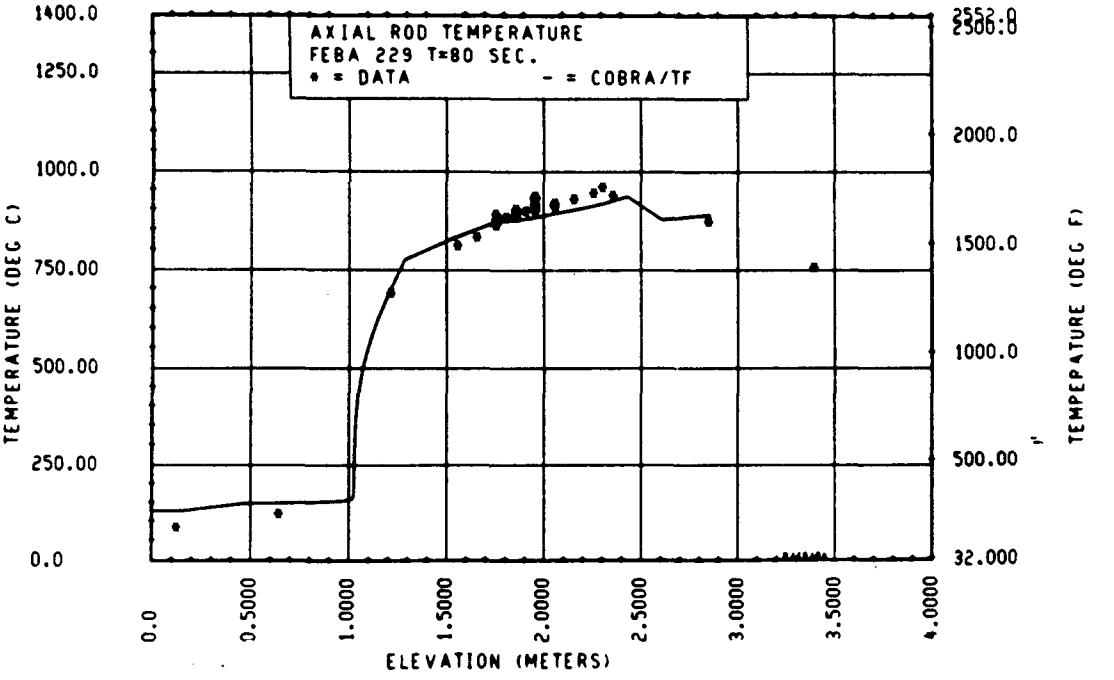

Figure 3-153. Comparison of COBRA-TF-Calculated Axial Rod Temperature Versus Time With FEBA Data, Test 229, t = 80 Seconds

A similar set of FEBA comparisons has been made by comparing FEBA test 223 with the 1.95 m (76.8 in.) grid and FEBA test 234 without this grid. These tests were conducted at 0.20 MPa (29 psia) pressure and 0.0399 m/sec (1.57 in./sec) flooding rate. The comparisons for FEBA test 223 are shown in figures 3-154 through 3-163. The heater rod temperature versus time plots in figures 3-154 through 3-159 show that COBRA-TF predicts the FEBA inner rod (nine center rods) temperature response quite well except for the uppermost elevation, where there is a slight overprediction of the temperature (figure 3-159).

The axial heater rod temperature plots (3-160 through 3-163) clearly show the effect of the COBRA-TF grid models at the 1.95 m (76.8 in.) elevation, both in the data and in the COBRA-TF predictions. (Also shown in figure 3-160 is the axial location of the spacer grids.) Again, the grid models used in the COBRA-TF calculations underpredict the local grid effects at the 1.95 m (76.8 in.) elevation; however, the models do predict the correct grid effects at the 1.40 m (55.3 in.) elevation. The overall agreement between the code and the data is excellent.

A similar set of comparisons has been made for FEBA test 234, which has the same (nearly identical) thermal-hydraulic boundary and initial conditions as FEBA test 223 but does not have the 1.95 m (76.8 in.) grid in the bundle. Figures 3-164 through 3-173 show both the heater rod temperature-time plots and the axial heater rod temperature plots at different times. (Figure 3-160 shows the axial location of the spacer grids.) Again, the comparisons between the COBRA-TF-calculated temperature transients and the FEBA data are excellent.

3-17. Discussion of COBRA-TF Predictions and Data Comparisons

Comparisons of the COBRA-TF code with three independent sets of reflood data have been presented in paragraphs 3-14 through 3-16. The overall comparisons are quite good and the accuracy of the COBRA-TF code has been enhanced with the addition of the grid heat transfer models and other code modifications discussed in section 2. The following paragraphs deal with some details of

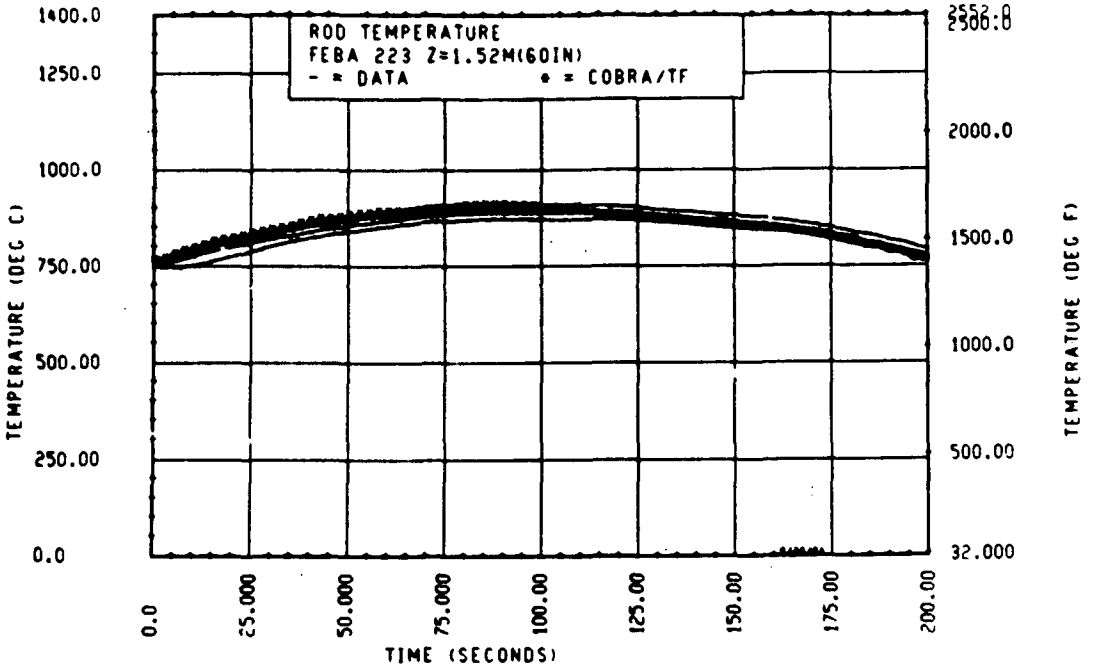

Figure 3-154. Comparison of COBRA-TF-Calculated Heater Rod Temperature Versus Time With FEBA Data, Test 223, 1.52 m (60 in.) Elevation

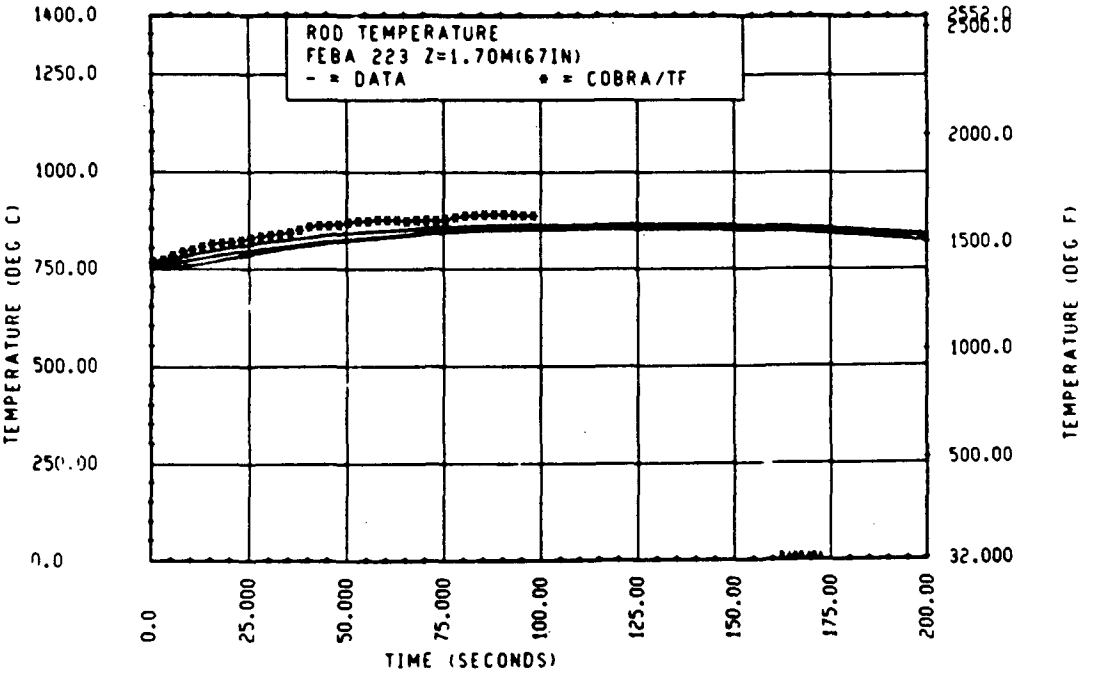

Figure 3-155. Comparison of COBRA-TF-Calculated Heater Rod Temperature Versus Time With FEBA Data, Test 223, 1.70 m (67 in.) Elevation

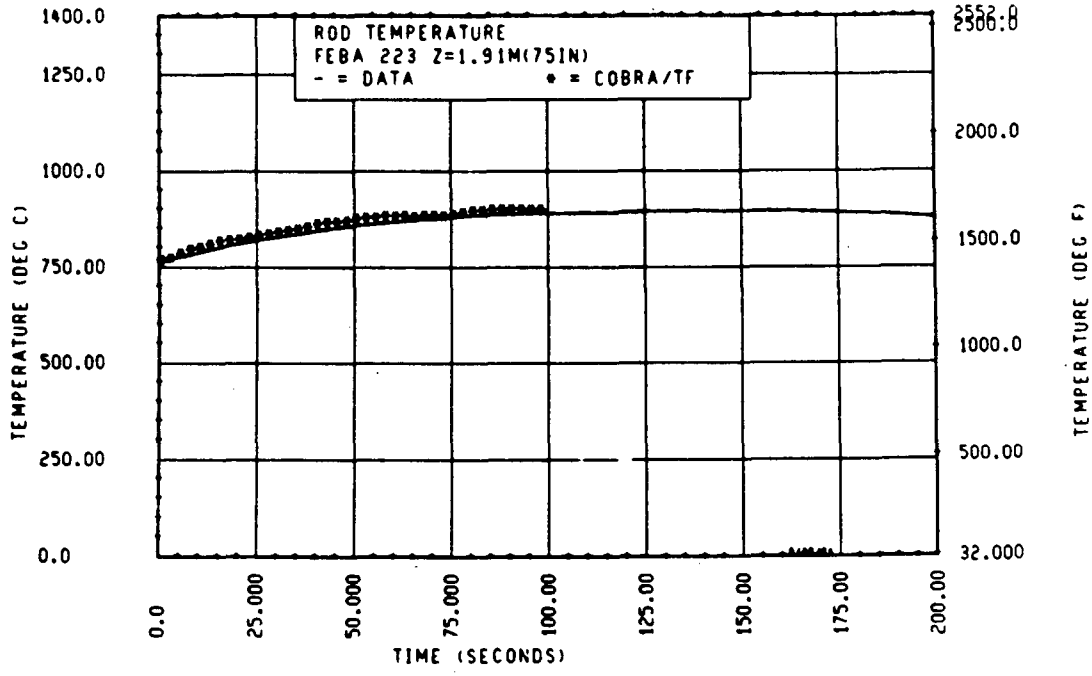

Figure 3-156. Comparison of COBRA-TF-Calculated Heater Rod Temperature Versus Time With FEBA Data, Test 223, 1.91 m (75 in.) Elevation

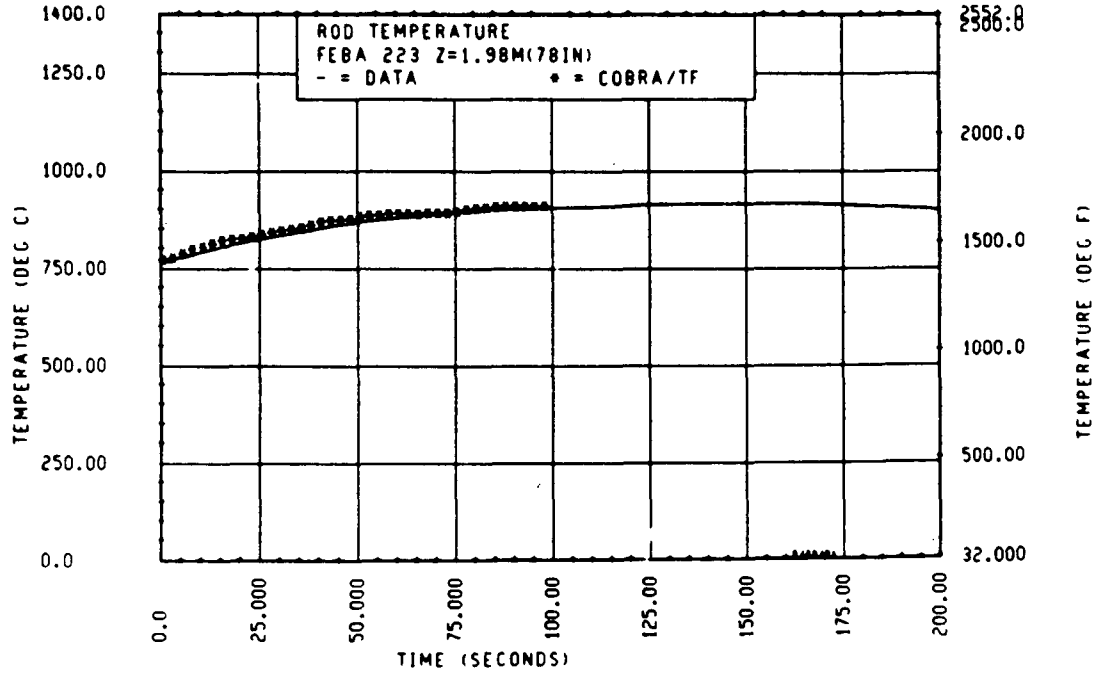

Figure 3-157. Comparison of COBRA-TF-Calculated Heater Rod Temperature Versus Time With FEBA Data, Test 223, 1.98 m (78 in.) Elevation

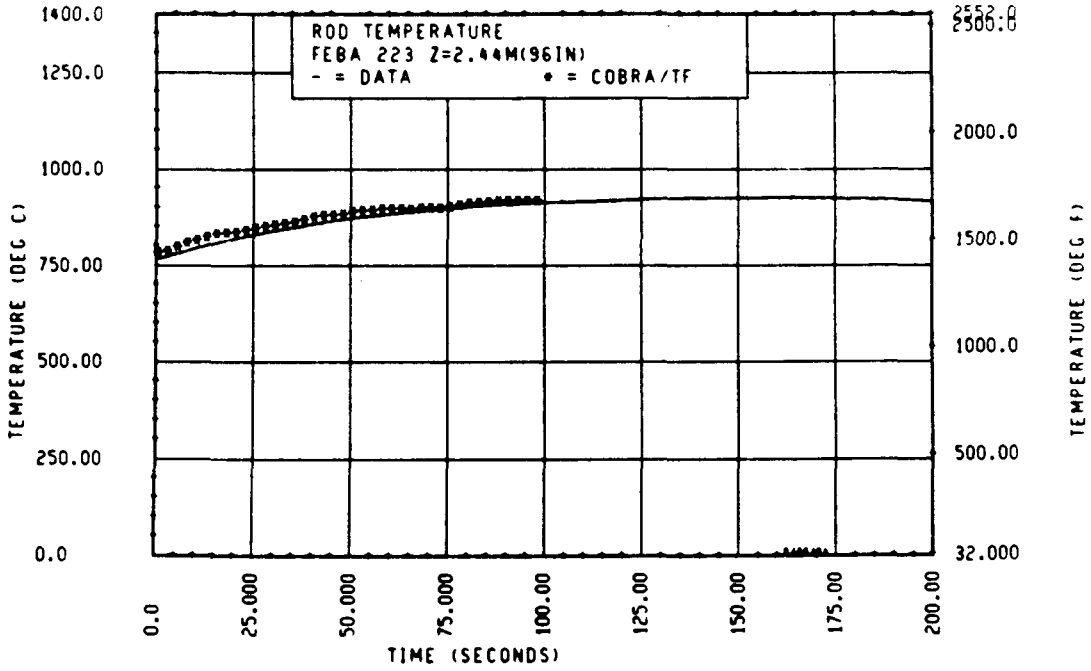

Figure 3-158. Comparison of COBRA-TF-Calculated Heater Rod Temperature Versus Time With FEBA Data, Test 223, 2.44 m (96 in.) Elevation

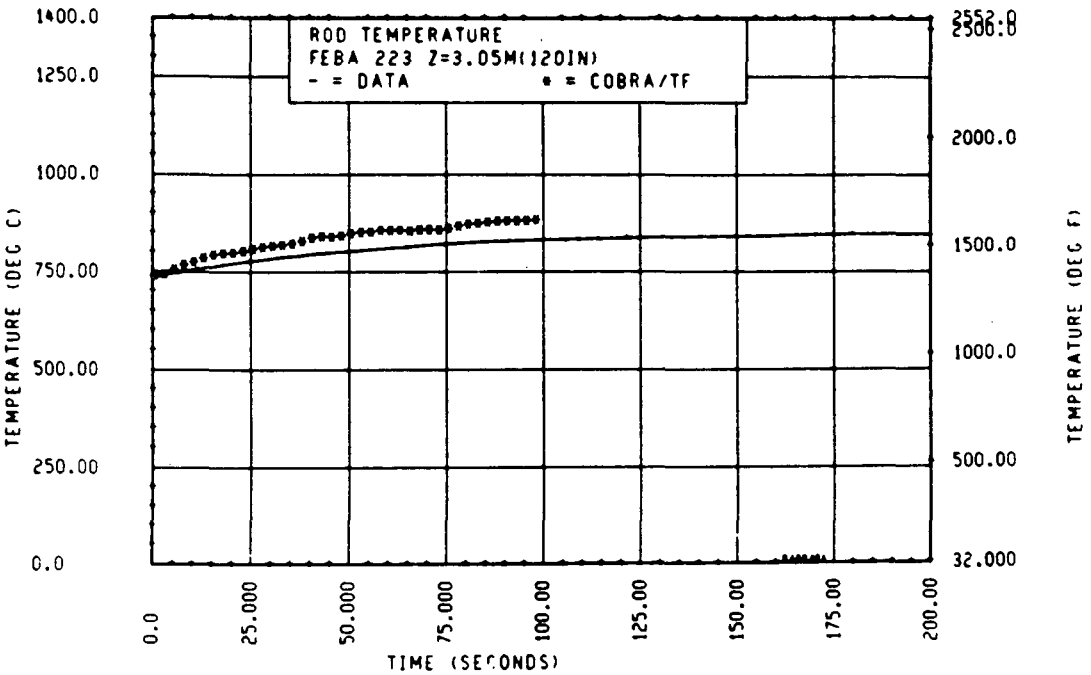

Figure 3-159. Comparison of COBRA-TF-Calculated Heater Rod Temperature Versus Time With FEBA Data, Test 223, 3.05 m (120 in.) Elevation

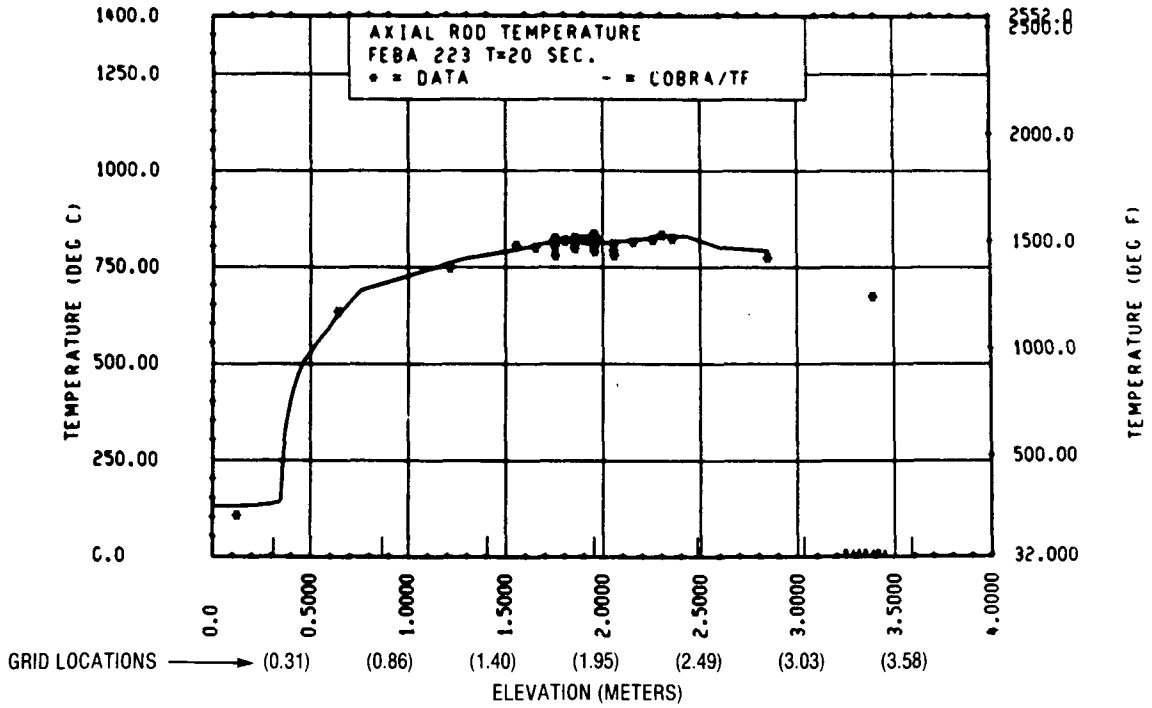

Figure 3-160. Comparison of COBRA-TF-Calculated Axial Rod Temperature Versus Elevation With FEBA Data, Test 223, t = 20 Seconds

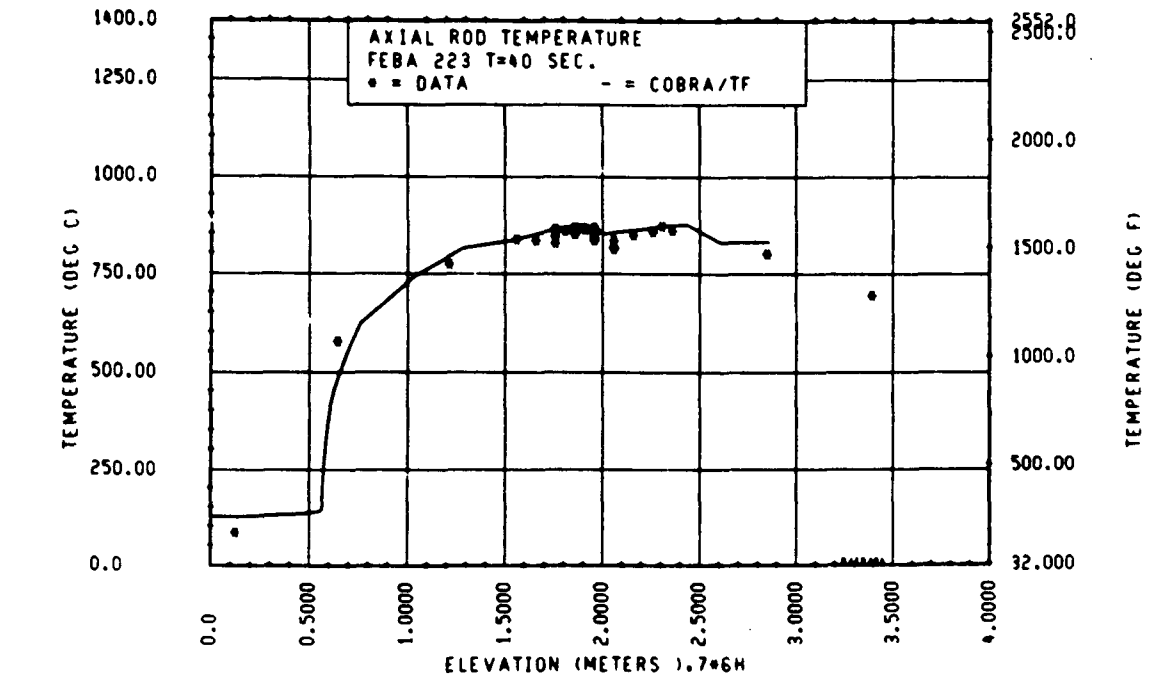

Figure 3-161. Comparison of COBRA-TF-Calculated Axial Rod Temperature Versus Elevation With FEBA Data, Test 223, t = 40 Seconds

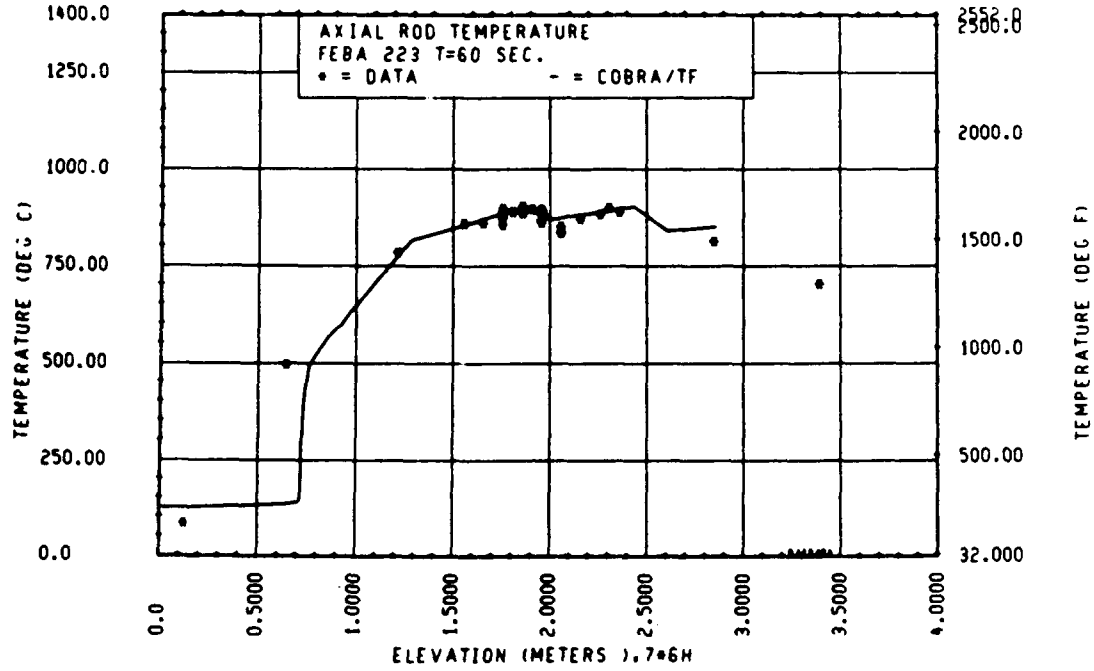

Figure 3-162. Comparison of COBRA-TF-Calculated Axial Rod Temperature Versus Elevation With FEBA Data, Test 223, t = 60 Seconds

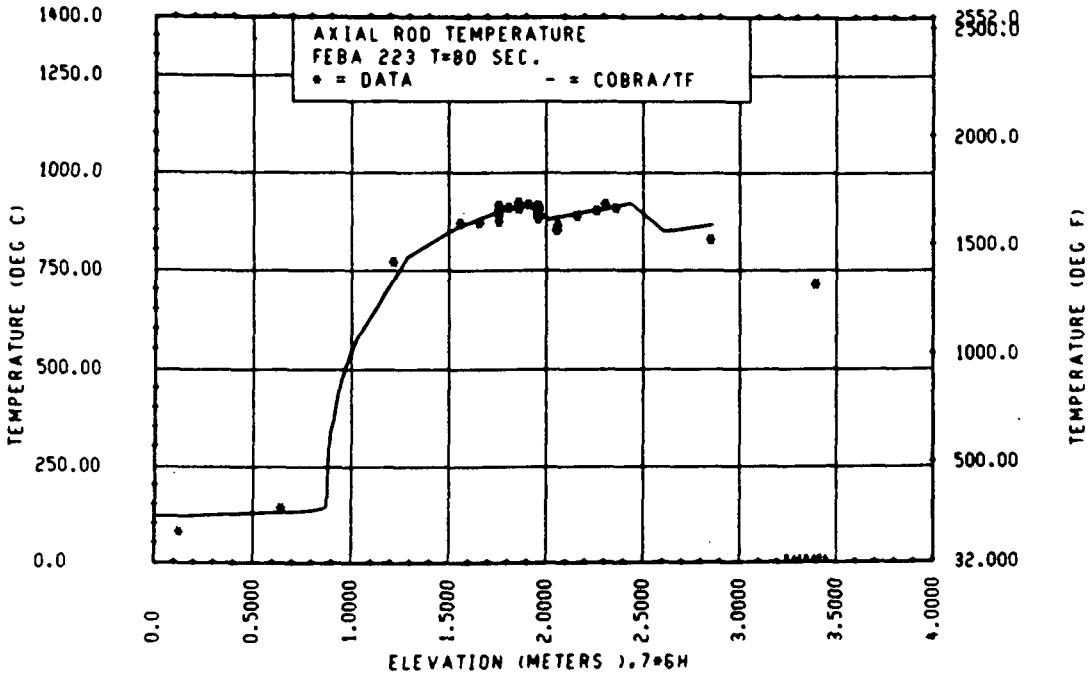

Figure 3-163. Comparison of COBRA-TF-Calculated Axial Rod Temperature Versus Time With FEBA Data, Test 223, t = 80 Seconds

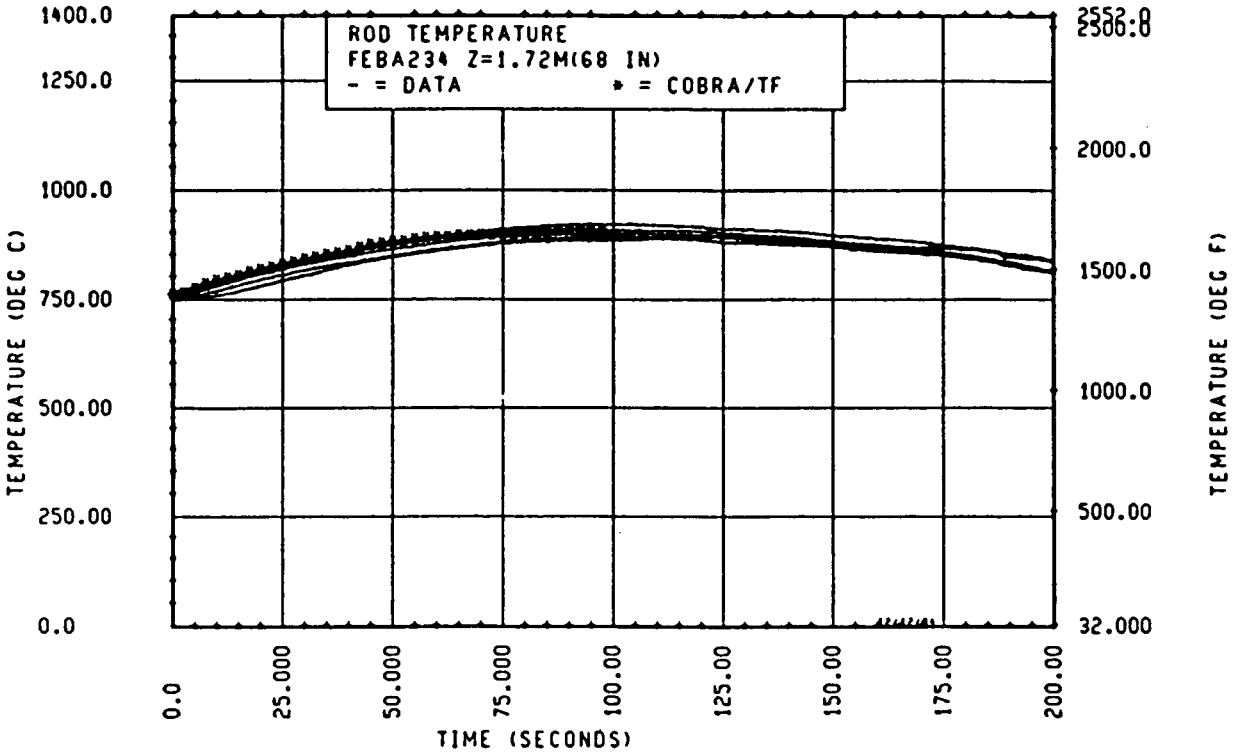

Figure 3-164. Comparison of COBRA-TF-Calculated Heater Rod Temperature Versus Time With FEBA Data, Test 234, 1.72 m (68 in.) Elevation

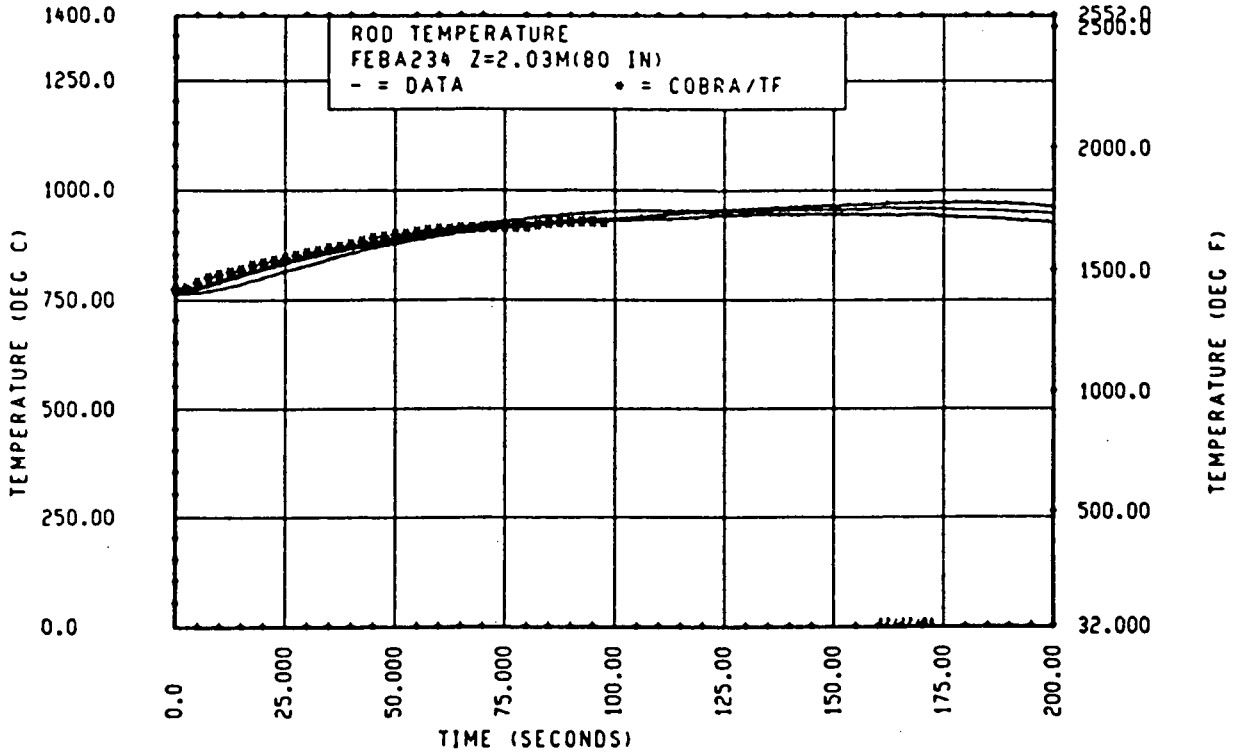

Figure 3-165. Comparison of COBRA-TF-Calculated Heater Rod Temperature Versus Time With FEBA Data, Test 234, 2.03 m (80 in.) Elevation

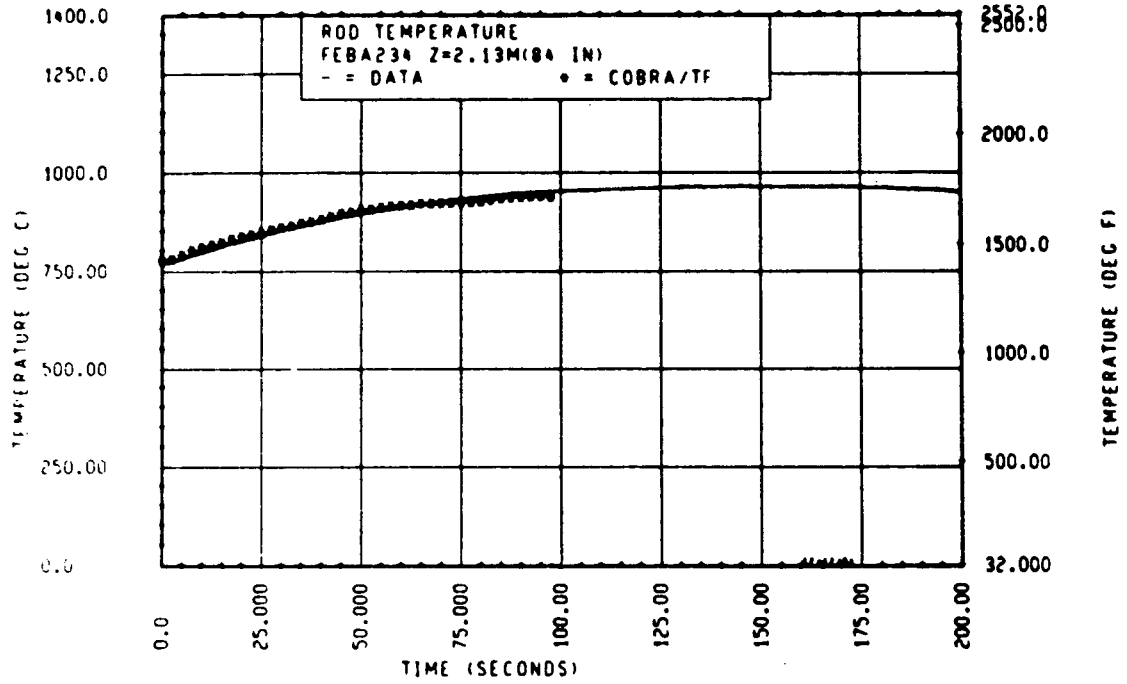

Figure 3-166. Comparison of COBRA-TF-Calculated Heater Rod Temperature Versus Time With FEBA Data, Test 234, 2.13 m (84 in.) Elevation

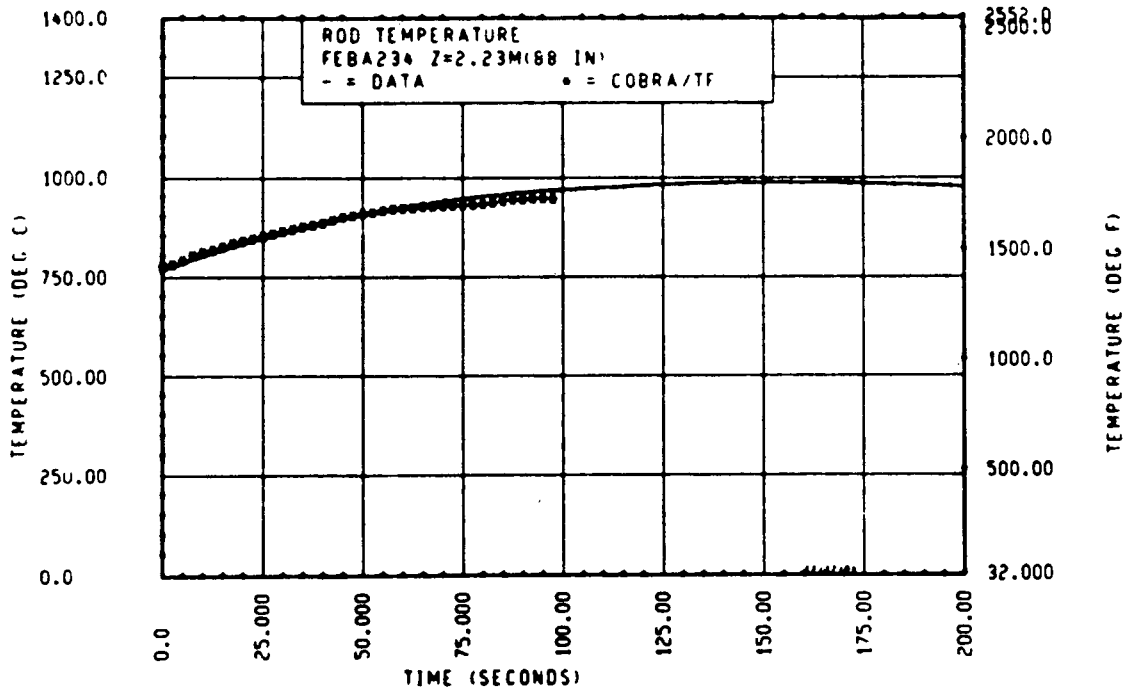

Figure 3-167. Comparison of COBRA-TF-Calculated Heater Rod Temperature Versus Time With FEBA Data, Test 234, 2.23 m (88 in.) Elevation

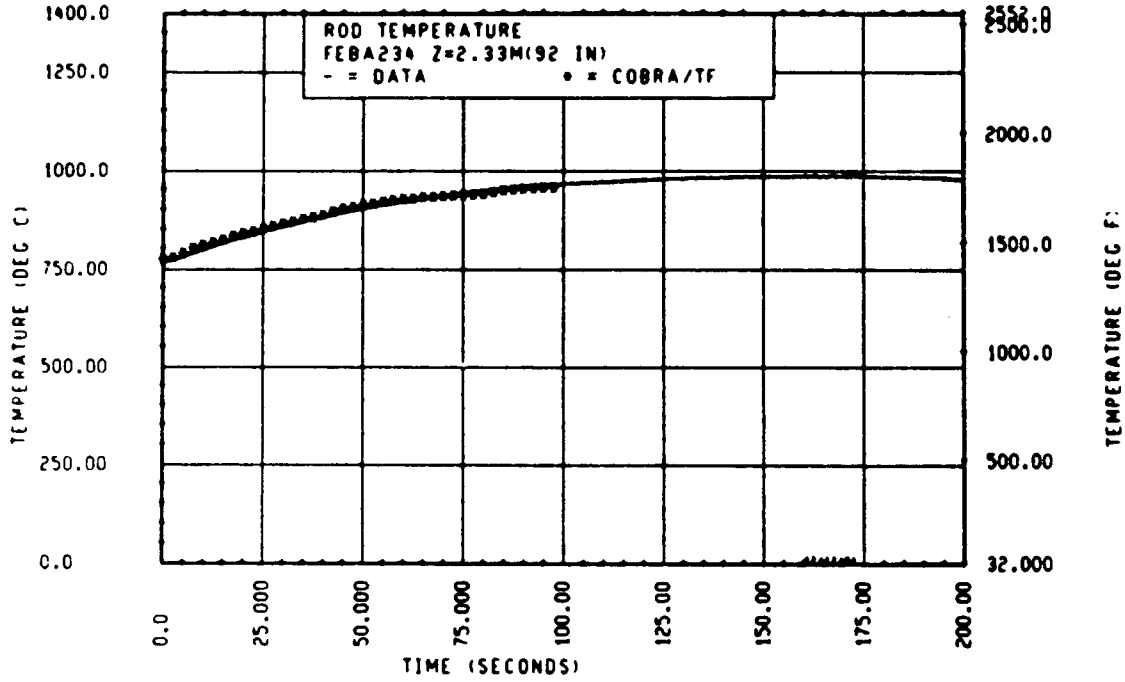

Figure 3-168. Comparison of COBRA-TF-Calculated Heater Rod Temperature Versus Time With FEBA Data, Test 234, 2.33 m (92 in.) Elevation

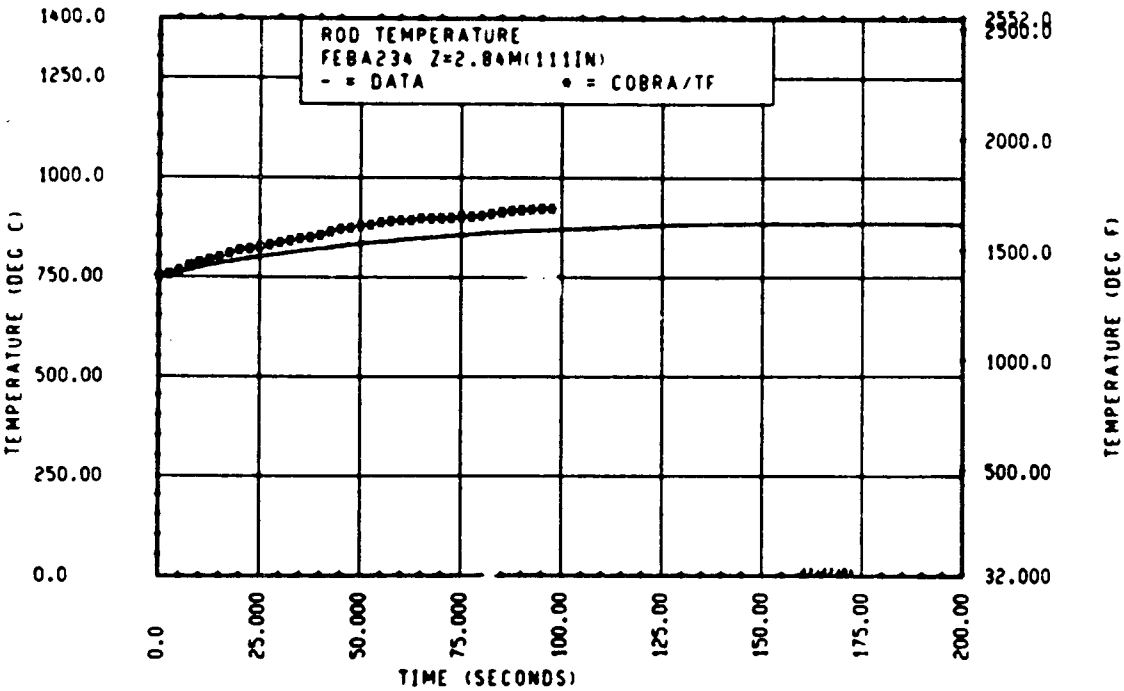

Figure 3-169. Comparison of COBRA-TF-Calculated Heater Rod Temperature Versus Time With FEBA Data, Test 234, 2.84 m (112 in.) Elevation

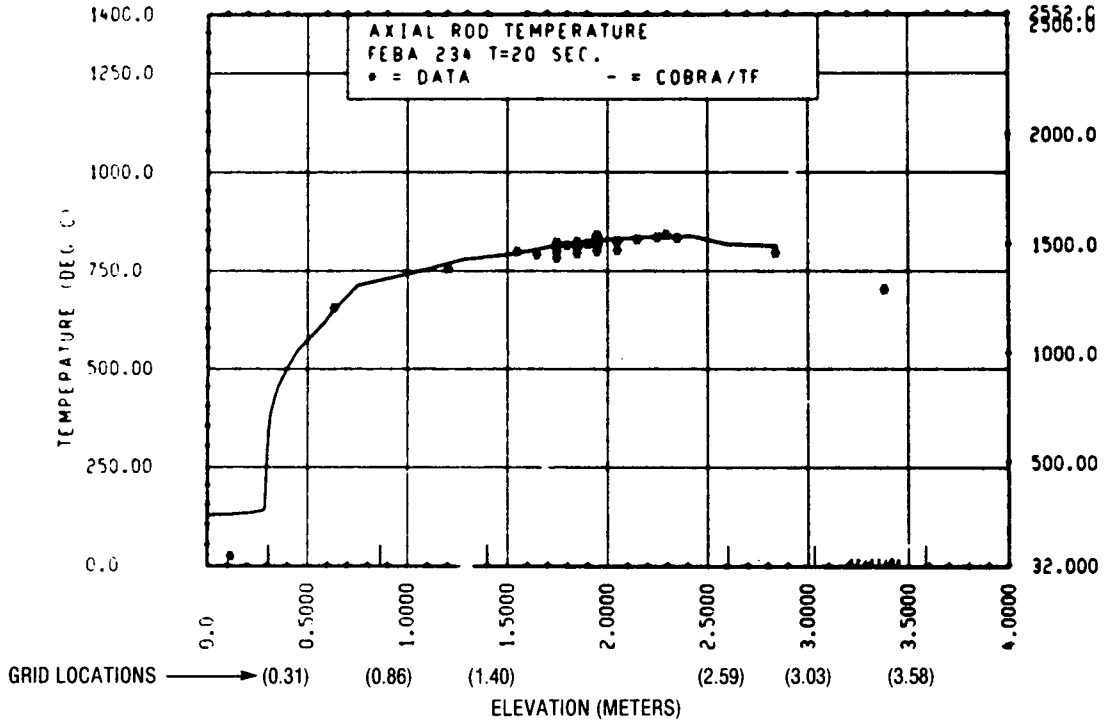

Figure 3-170. Comparison of COBRA-TF-Calculated Axial Rod Temperature Versus Elevation With FEBA Data, Test 234, t = 20 Seconds

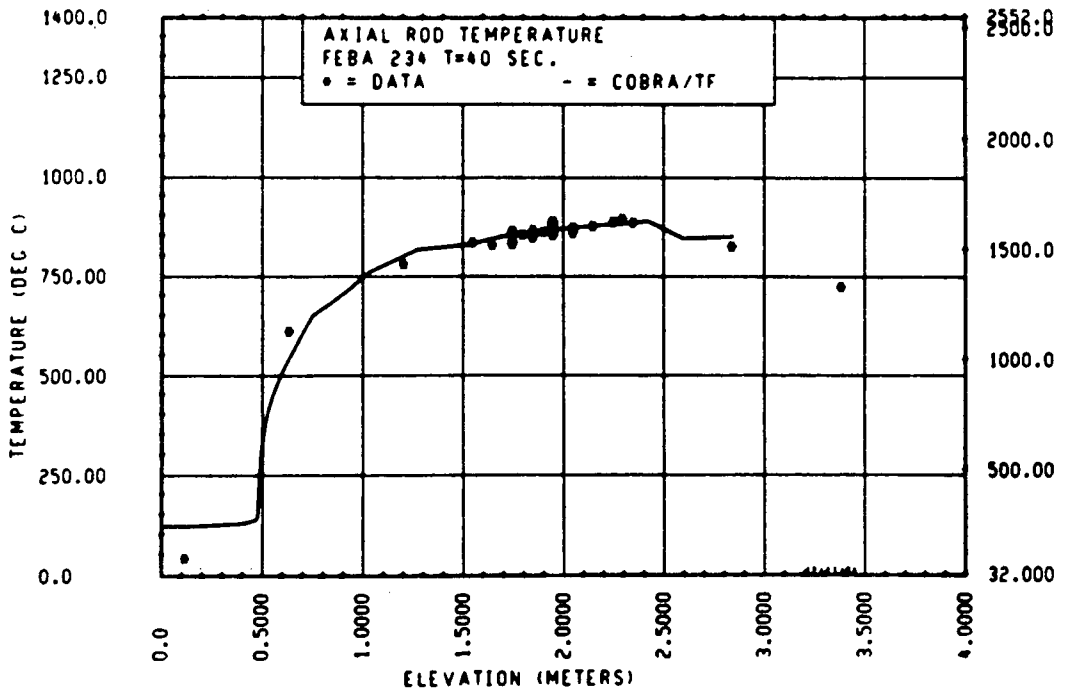

Figure 3-171. Comparison of COBRA-TF-Calculated Axial Rod Temperature Versus Elevation With FEBA Data, Test 234, t = 40 Seconds

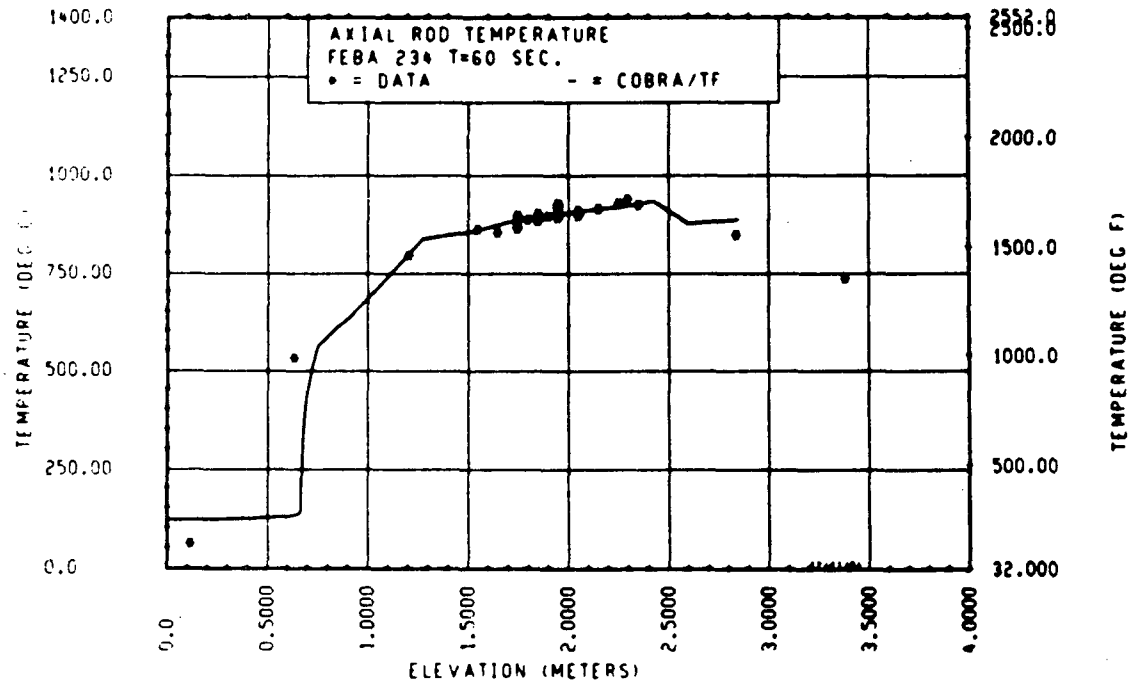

Figure 3-172. Comparison of COBRA-TF-Calculated Axial Rod Temperature Versus Elevation With FEBA Data, Test 234, t = 60 Seconds

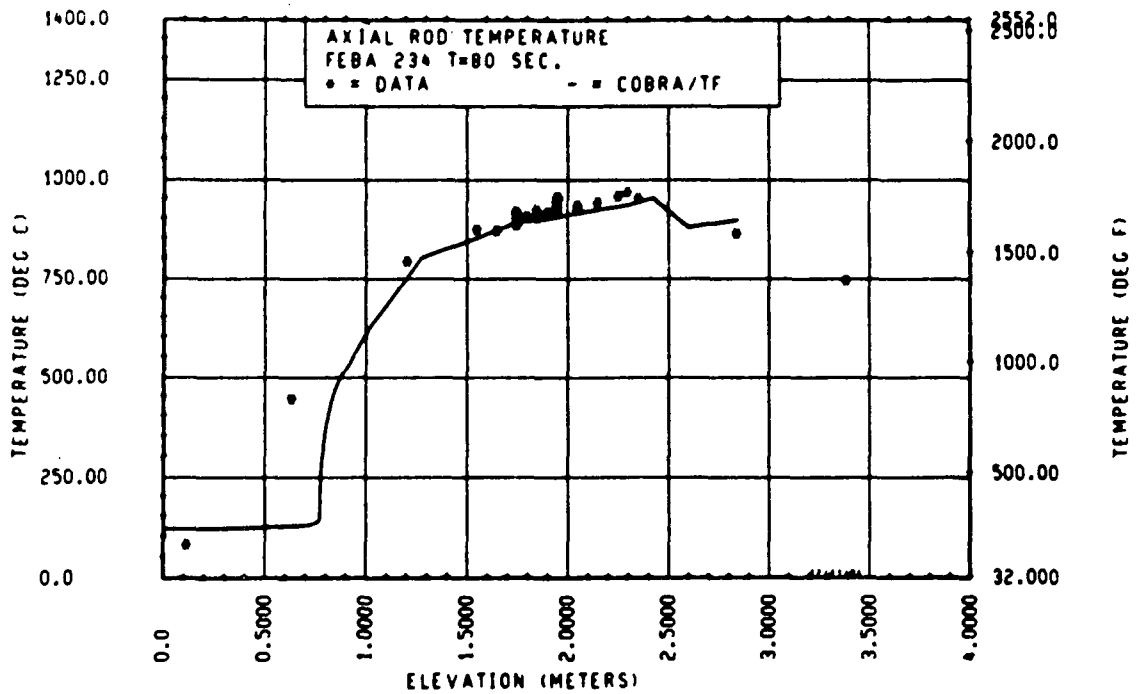

Figure 3-173. Comparison of COBRA-TF-Calculated Axial Rod Temperature Versus Time With FEBA Data, Test 234, t = 80 Seconds

the grid model calculations and results of two tests, FLECHT SEASET 161-rod unblocked bundle test 31805 and FEBA test 223. Also discussed are the relative importance of the grid models and any possible bias of the COBRA-TF code relative to the test data. A "goodness of fit" criterion is developed using bias comparisons with test data and code predictions.

FEBA test 223 was examined in detail at the 1.95 m (76.8 in.) elevation to determine the relative effects of each of the grid models. Axial plots of the COBRA-TF center region heater rod temperature response with each of the grid models selectively turned on and off are shown in figures 3-174 through 3-177 for different time periods. There are six curves on these figures:

- The unlabeled curve has all grid models turned on (as the code was used in the previous data comparisons).
- Curve O has all grid models turned off.
- Curve D has the droplet breakup model off.
- Curve R has the rewet model off.
- Curve V has the convective vapor heat transfer enhancement due to the grids off.
- Curve RW has the rewet model set at 100 percent such that the entire grid is wetted.

Comparison of the unlabeled curve and curve O, with all grid models off, allows observation of the total benefit of the grid models described in section 2. Immediately downstream of the grid, for this test, the effect of the grid models is approximately 50° C (90° F) at 2 m (79 in.), and increases to 100° C (180° F) at 2.6 m (102 in.). Therefore, if the grid models were not included in the COBRA-TF calculations, the code would overpredict the measured heater rod temperature data by a significant amount at and above the bundle midplane.

Next, comparing curve R, with the grid rewet model off, to the unlabeled curve with all grid models on shows that differences between the curves are small; however, turning the rewet model off results in a lower grid temperature. This puzzling result is due to the increased heat transfer to the vapor from the dry part of the grid, which has been heated by rod-to-grid radiation such

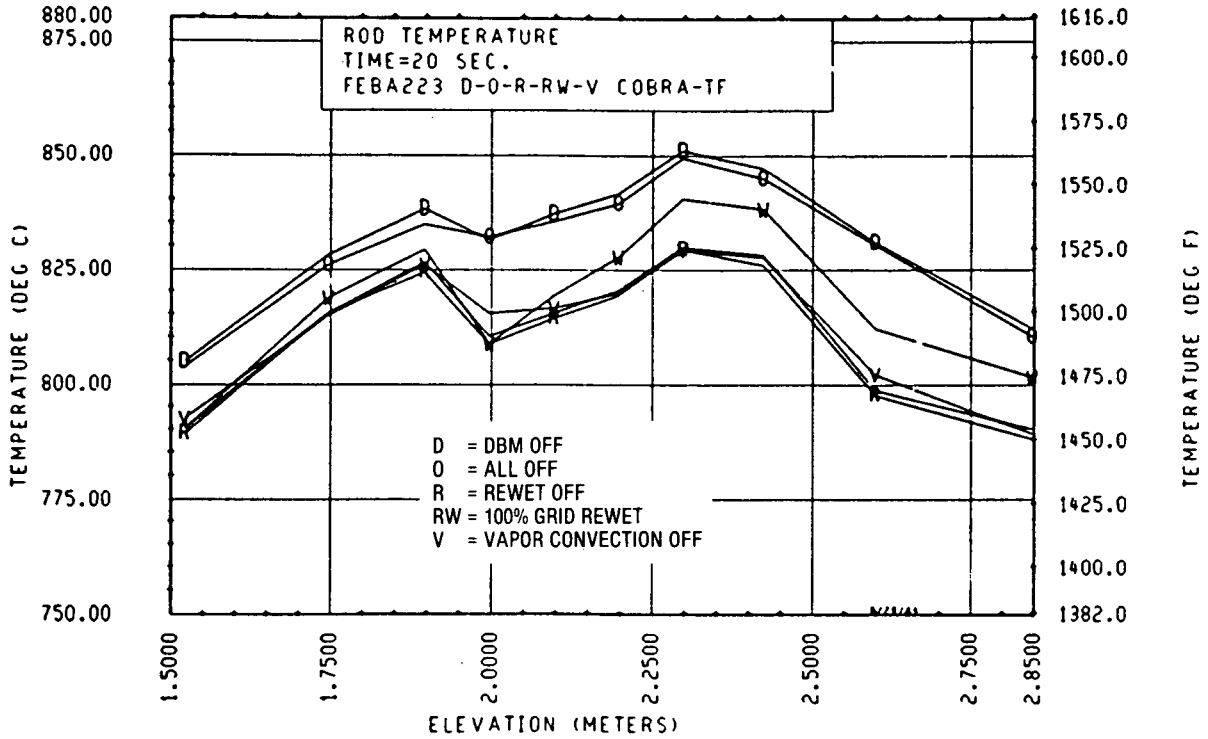

Figure 3-174. Relative Effects of Grid Models on COBRA-TF Predictions (FEBA Test 223, 1.95 m (76.8 in.) Elevation, t = 20 Seconds)

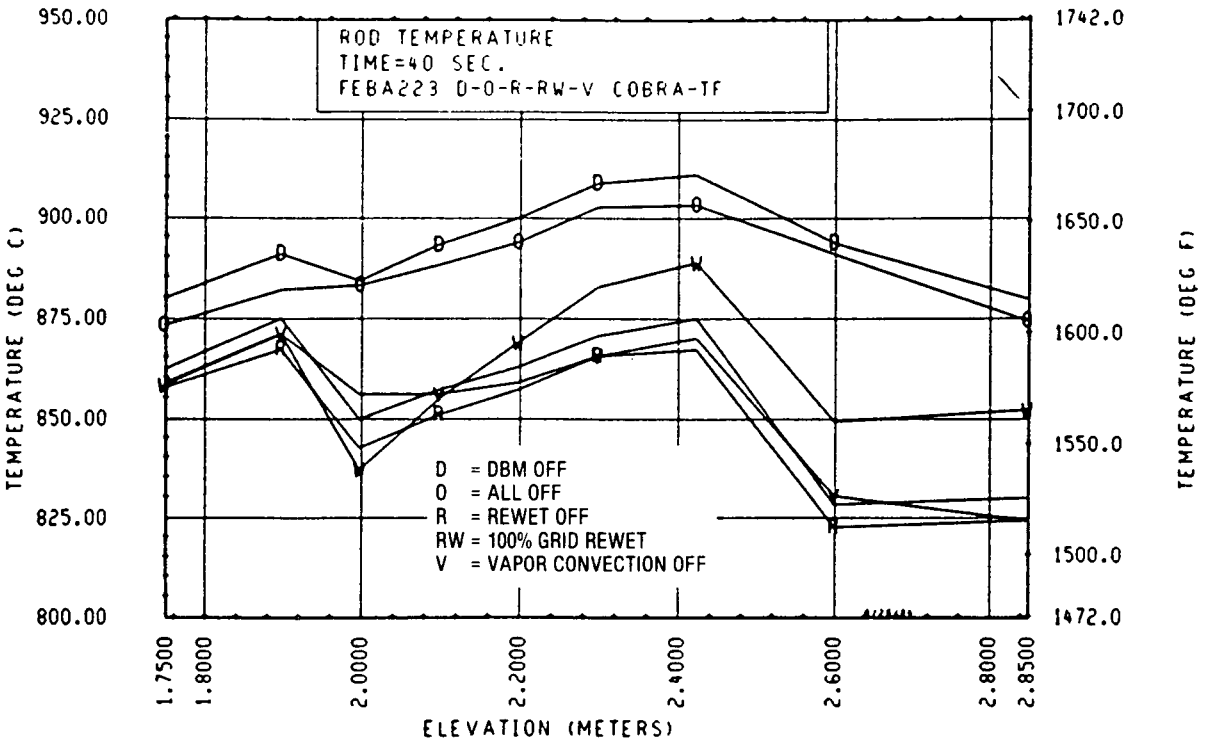

Figure 3-175. Relative Effects of Grid Models on COBRA-TF Predictions (FEBA Test 223, 1.95 m (76.8 in.) Elevation, t = 40 Seconds)

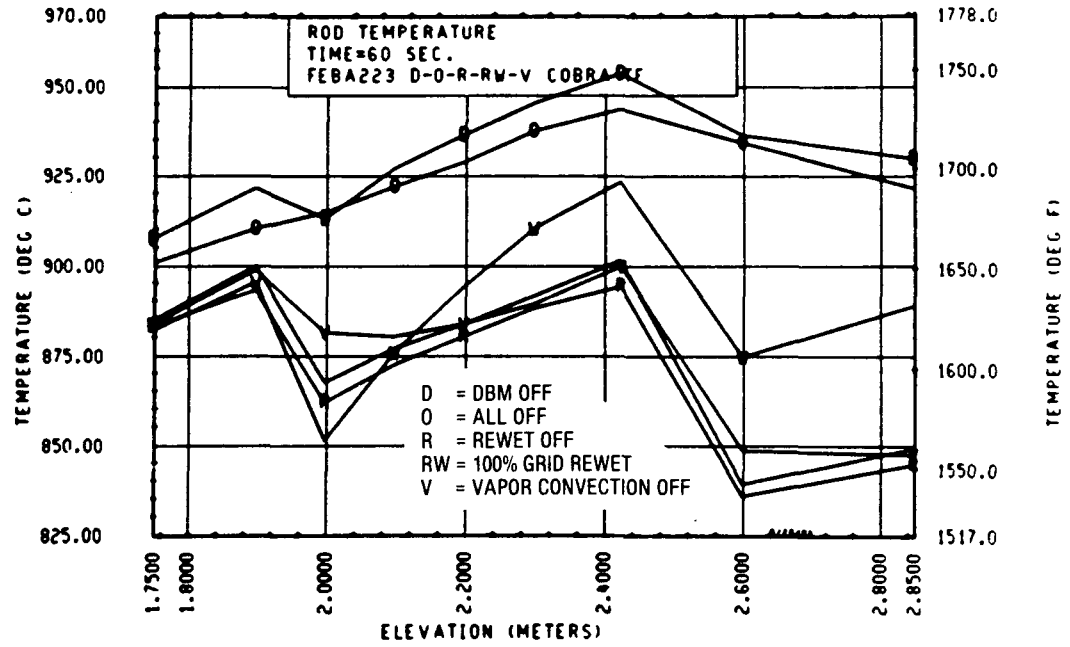

Figure 3-176. Relative Effects of Grid Models on COBRA-TF Predictions (FEBA Test 223, 1.95 m (76.8 in.) Elevation, t = 60 Seconds)

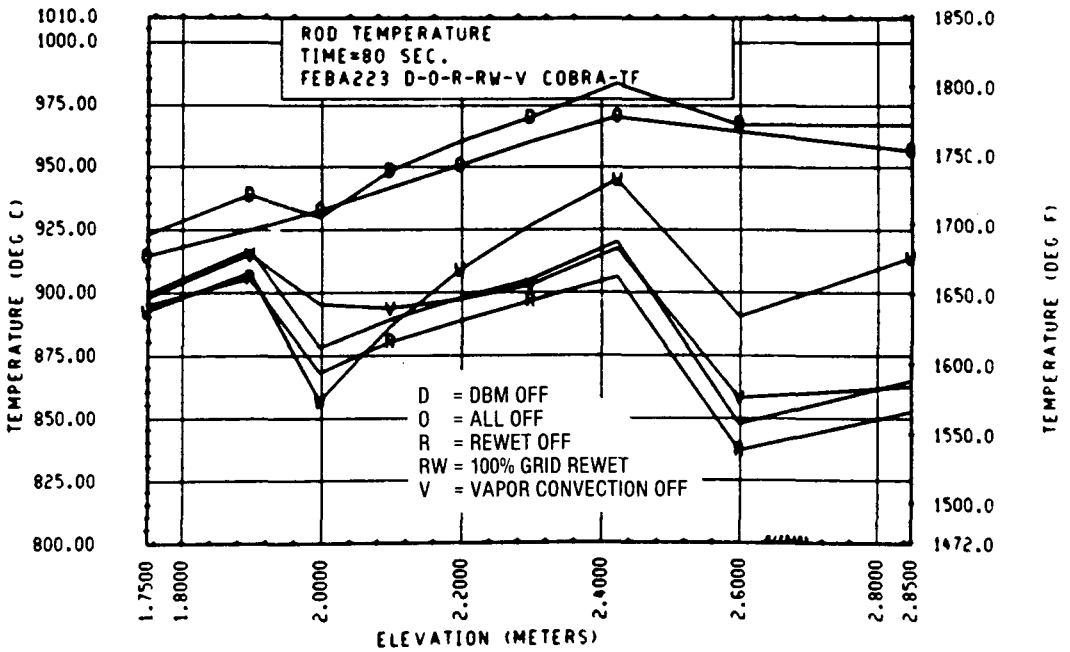

Figure 3-177. Relative Effects of Grid Models on COBRA-TF Predictions (FEBA Test 223, 1.95 m (76.8 in.) Elevation, t = 80 Seconds)

that the dry grid strap is actually hotter than the vapor. Therefore, with the grid rewet model deleted, this additional convective heat transfer to the grid is not present and the resulting rod and vapor temperatures are lower by approximately 10°C (18° F). Another point of interest is shown by comparison of curve R to curve O with no grid models: grid rewet heat transfer is not the dominant heat transfer mechanism in decrease of the calculated heater rod temperature.

Comparing curve V to the unlabeled curve shows that with the single-phase convective vapor heat transfer improvement turned off, there is a decrease in the cooling immediately downstream of the grid. Immediately downstream of the 1.95 m (76.8 in.) grid, curve V shows a 15°C (27° F) temperature increase. Since curve V and the curve with all grid models turned on are nearly identical, the single-phase convective enhancement heat transfer effect is (like grid rewet heat transfer) not the most significant grid heat transfer mechanism.

Comparison of curve D with the unlabeled curve shows the effect of turning off the grid droplet breakup model. Adding curve O to this comparison shows that the droplet breakup mechanism is the dominant heat transfer effect for this grid, for this particular test.

Also, it is noted that when the droplet breakup model is turned off, higher temperatures are predicted than when all grid models are off (comparing curve D to curve O). The reason for this difference is that, with the droplet breakup model off (curve D), there can be additional vapor superheating caused by the dry grid heat transfer and the grid convective heat transfer enhancement, both of which increase the calculated vapor temperature and thus the calculated heater rod temperature.

Last, curve RW represents a case in which the 1.95 m (76.8 in.) grid was forced to be 100 percent wetted with all other models turned off. Comparison of curve RW to curve O shows that a completely wet grid has a significant local effect [approximately 75° C (135° F) at 1.95 m (76.8 in.)]. However, immediately downstream of the grid, the calculated heater rod temperatures quickly increase. The increased heatup is due to the significantly larger

heat flux which is calculated to occur between the heater rod and the vapor immediately downstream of the grid. The heat flows first to the vapor phase, then to the droplets by means of interfacial heat transfer. Since there is no longer a population of small droplets in the case shown by curve RW, to increase the interfacial heat transfer area, the vapor temperature downstream of the grid rapidly superheats and the heater rod temperature correspondingly increases.

The conclusions to be drawn from this evaluation for this test are that apparently the droplet breakup mechanism is the dominant heat transfer effect as long as the grid is mostly dry. Once the grid rewets, the grid rewetting and droplet breakup heat transfer effects are comparable, although the downstream heater rod temperature response can change, depending on which heat transfer mechanism dominates.

FLECHT SEASET 161-rod unblocked bundle test 31805 was also examined in detail, to investigate how the grid models behave during a reflood transient. Figure 3-178 shows the COBRA-TF-calculated dry grid temperatures for the different grids in the FLECHT SEASET 161-rod bundle. As the figure indicates, the grids quickly heat up and reach temperatures typically more than halfway between the vapor temperature and the heater rod temperature. As the transient progresses, the convective heat flux from the grid increases because of the lower vapor temperature; the dry grid temperature decreases and eventually quenches. The percentage of grid quench for each grid is shown in figure 3-179 for FLECHT SEASET 161-rod unblocked bundle test 31805. As this figure indicates, the grids remain almost 100 percent dry until the two-phase mixture level approaches the grid location. A comparable set of grid temperature and percent-quenched curves is shown in figures 3-180 and 3-181 for FLECHT SEASET 161-rod unblocked bundle test 31203, which had a higher flooding rate than test 31805. The trends are similar in both sets of curves, except that the high flooding rate case results in lower grid temperatures and a more rapid grid rewet, as expected.

Calculated droplet Weber numbers upstream of the 1.57 m (62 in.) and 2.11 m (83 in.) grids are shown in figure 3-182 as a function of time for test 31805.

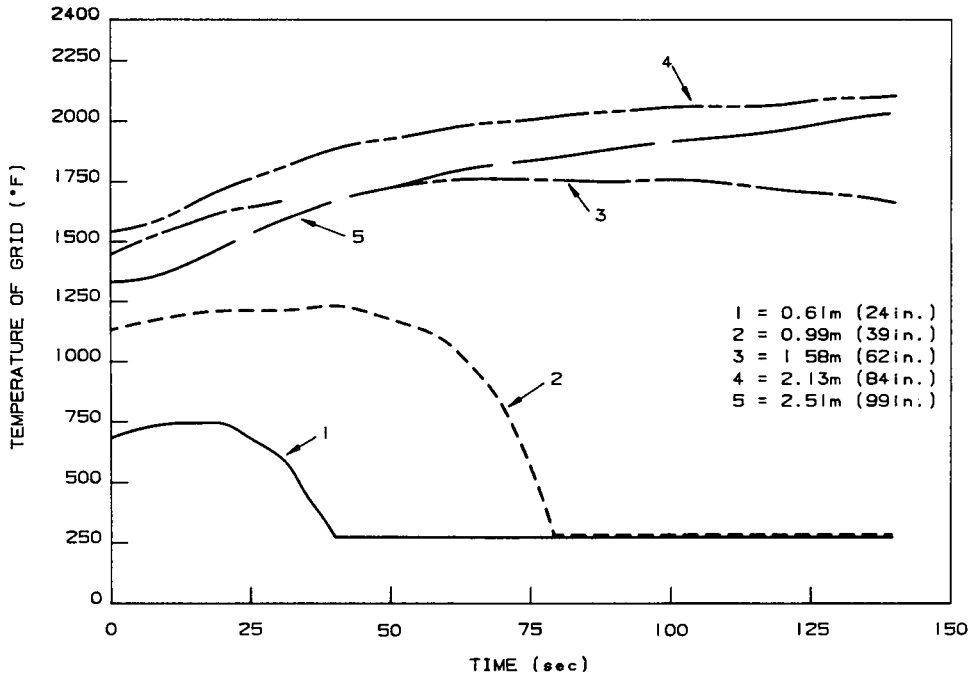

Figure 3-178. COBRA-TF-Calculated Dry Grid Temperatures, FLECHT SEASET 161-Rod Bundle Test 31805

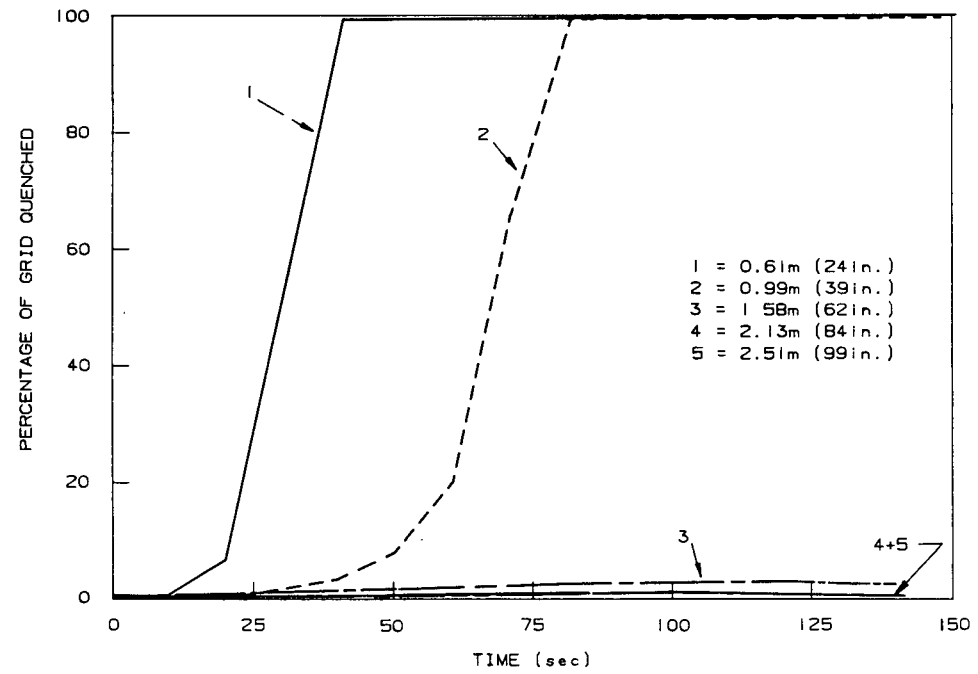

Figure 3-179. Grid Quench Progression, FLECHT SEASET 161-Rod Bundle Test 31805

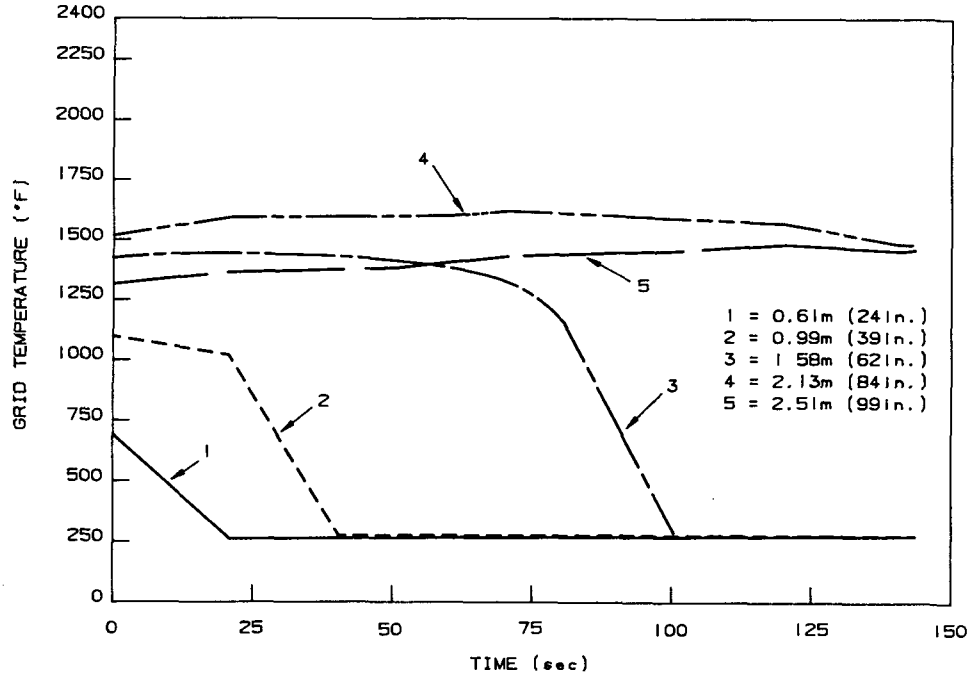

Figure 3-180. COBRA-TF-Calculated Dry Grid Temperatures, FLECHT SEASET 161-Rod Bundle Test 31203

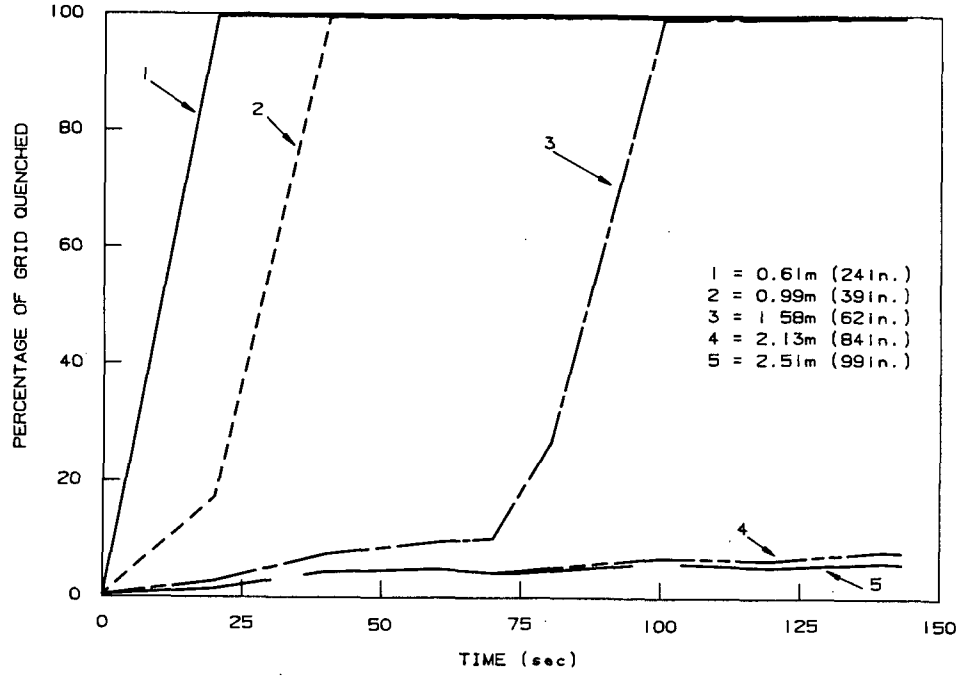

Figure 3-181. Grid Quench Progression, FLECHT SEASET 161-Rod Bundle Test 31203

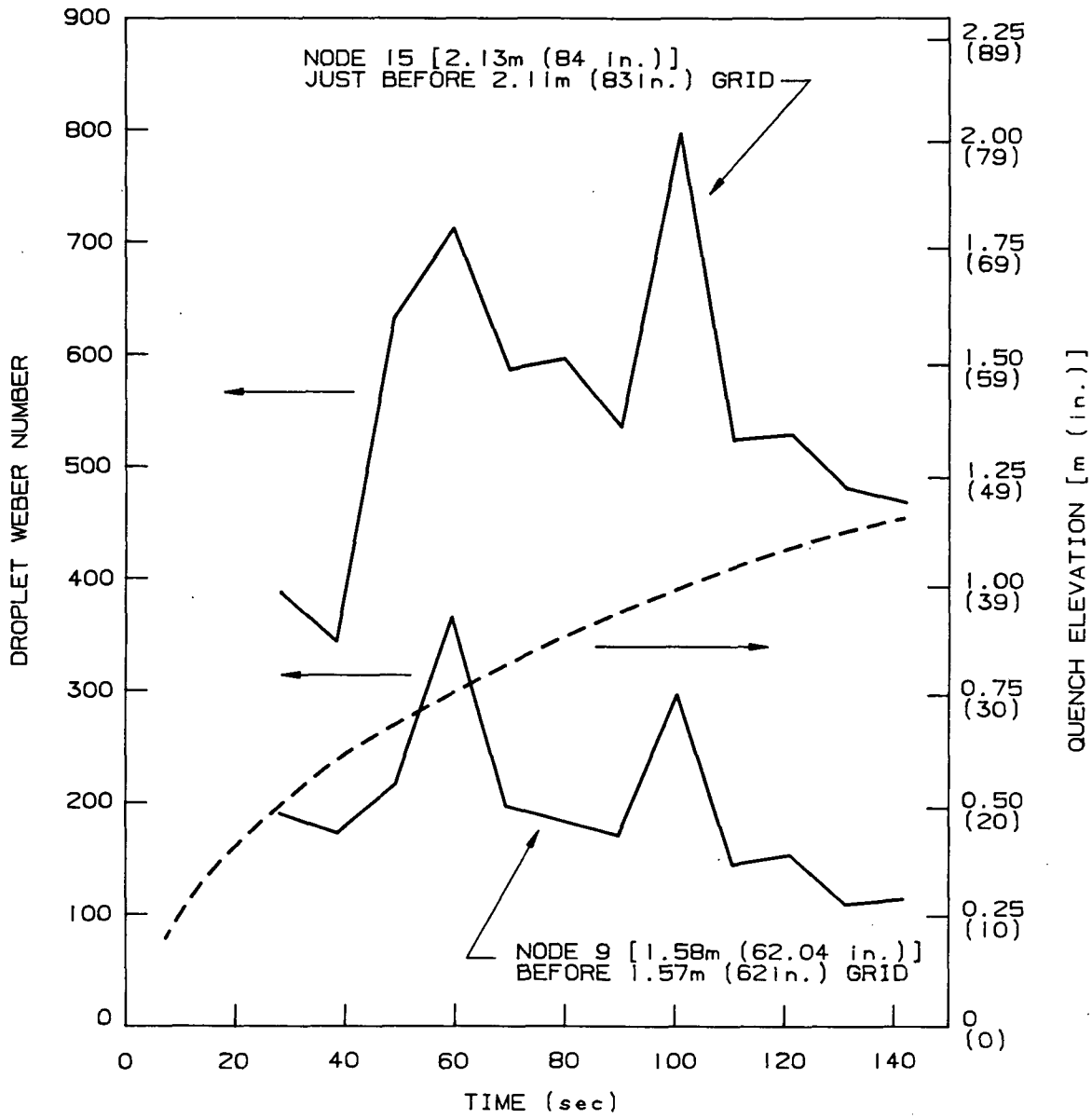

Figure 3-182. COBRA-TF-Calculated Weber Numbers Versus Time, FLECHT SEASET 161-Rod Bundle Test 31805

Also shown is the calculated quench front location. This plot indicates that the calculated droplet Weber number first increases and then decreases as the quench front approaches. This behavior is due to the rate of steam generation and the degree of superheat in the steam above the quench front. Early in reflood time, when the quench front is far from the grids at the bundle mid-plane, the steam is quickly superheated to very high temperatures. This results in a high steam velocity. As the quench front progresses, the steam generation rate increases somewhat because of the steam generation below the quench front; however, the superheat decreases, resulting in a lower vapor velocity. Since the calculated steam velocity determines the droplet acceleration and velocity, it significantly influences the droplet Weber number. If one recalls the droplet shattering curve in figure 3-19, it is apparent that at early times with high droplet Weber numbers, the microdrops generated by impact on the grids will be very small. As the quench front approaches, the droplet Weber number decreases and the microdrop size increases. This decreases the interfacial heat transfer area, and reduces the cooling effects of the grids..

The microdrop size increase as the quench front approaches is somewhat compensated for by the increased liquid fraction in the entrained flow. However, the overall result is a decrease in interfacial heat transfer. The grid droplet breakup heat transfer effect decreases and eventually goes to zero as the quench front approaches a grid. Therefore, for the grid models, as the quench front approaches a grid, the droplet breakup heat transfer mechanism decreases but the grid rewet heat transfer mechanism increases.

Figure 3-183 shows the shattered drop and initial drop sizes calculated by COBRA-TF for FLECHT SEASET test 31805 as a function of elevation at 60 seconds. The microdrops are smaller in diameter by at least an order of magnitude than the original drops, and change by a factor of 6 or more over the bundle length. The diameter of the larger drops changes by only 20 percent. Therefore, the smaller drops preferentially evaporate, creating saturated vapor which results in improved cooling downstream.

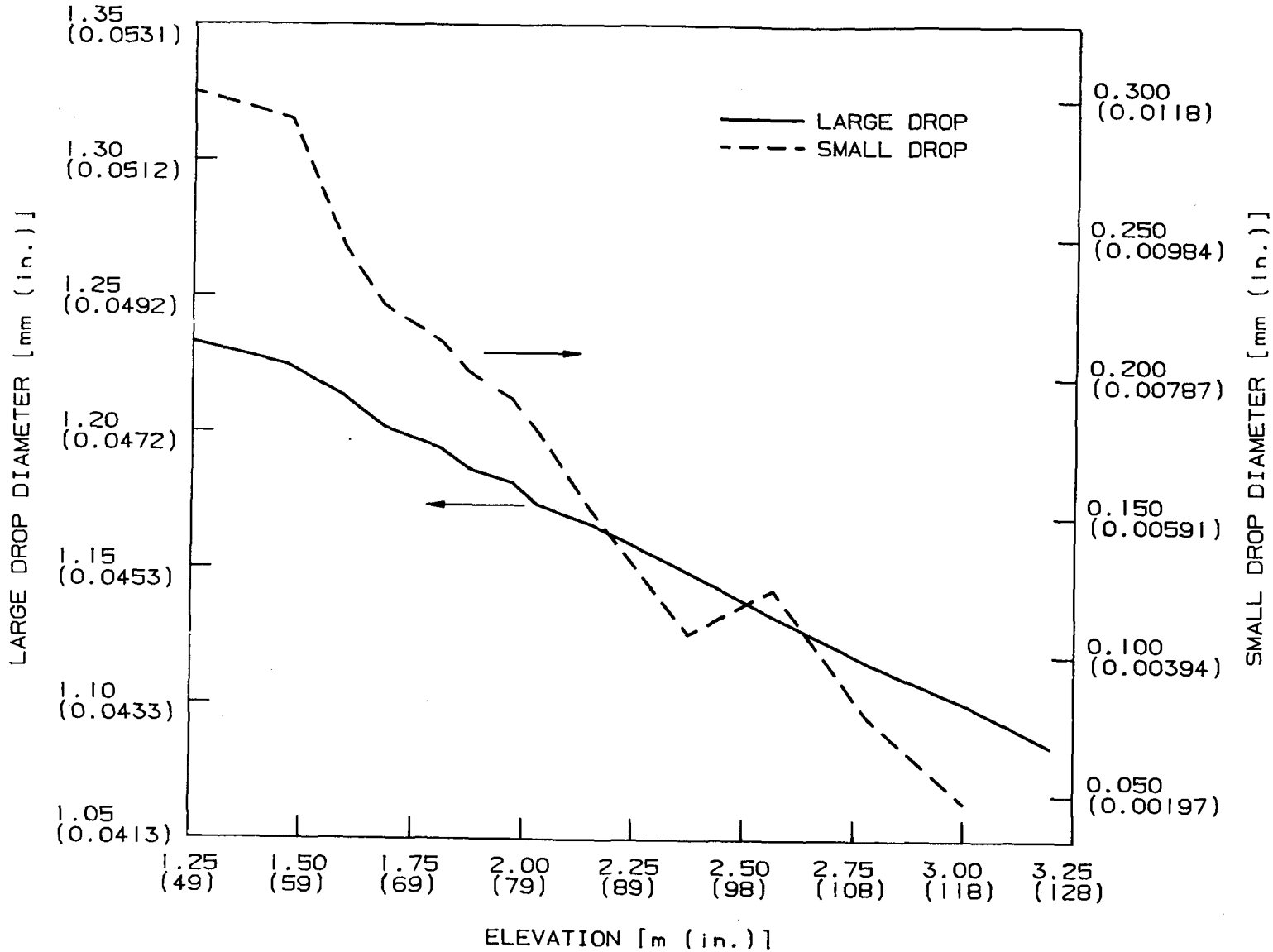

Figure 3-183. COBRA-TF-Calculated Droplet Sizes at 60 Seconds Into Reflood for FLECHT SEASET Test 31805

An attempt has been made to quantify the "goodness of fit" of the resulting COBRA-TF calculations with the three sets of rod bundle reflood data studied. The method chosen was comparison of the difference between the calculated temperature rise at a given elevation and time and that measured in the experiment:

$$\Delta T = (T_{x_1,\ t} - T_{x_1,\ t=0})_{data} - (T_{x_1,\ t} - T_{x_1,\ t=0})_{COBRA\text{-}TF}$$

This parameter, ΔT, is used to compare the fit of the calculation to the test data at each elevation for different times into the transient. If the value of this parameter were zero, the code would agree perfectly with the data. The goodness of fit parameter is plotted in figures 3-184 through 3-193 for nearly all the experiments covered in this section. A negative value for ΔT implies that the code overpredicts the temperature rise of the test; a positive value implies the opposite.

This parameter was plotted against elevation up the rod bundle, since it was expected that there might be a bias in the code calculation that would lead to a characteristic overprediction at the upper elevations of the rod bundle. Examination of these figures indicates only a few clear quantitative trends:

- COBRA-TF does tend to overpredict the temperature rise at the uppermost elevations [3.05 m (120 in.)].
- There is a slight trend toward underpredicting the temperature rise for lower pressure tests compared to higher pressure tests.

The first of these trends is a characteristic of the COBRA-TF code which has been noted in the past. The overprediction at the 3.05 m (120 in.) elevation reflects the integral effect of all the two-phase flow models in the code and their interaction to give the correct fluid side flow and heat transfer conditions. Although there is still a slight overprediction of the temperature rise at the top of the bundle, this version of COBRA-TF is significantly improved.

The low pressure trend toward underpredicting the test temperature rise (too large a heat transfer) may be due, in part, to the initial entrained droplet size used in COBRA-TF as well as the initiation of two-phase entrainment. The

entrained droplet size used in COBRA-TF is based on a model for relative velocity and very little data for smaller droplet sizes at lower pressure. The smaller droplet sizes for the same mass entrained results in a larger surface area for interfacial heat transfer and thus reduced calculated temperature rise values. There is insufficient experimental data at present to indicate what the dependency of pressure on entrained droplet size should be. This remains an open issue.

In an attempt to quantify the data given in figures 3-184 through 3-193, average ΔT rise values were calculated for each series of tests for each elevation for all times, and then combined for all tests and all elevations. If the delta temperature variations at each elevation are averaged for different times and then the elevations are averaged for each test, a measure of agreement can be obtained for each test. The variations for each test ranged from 16.15° C to 19.6° C (29.07° F to 35.27° F). This implies a very good fit of the COBRA-TF calculations to the data, since the rod-to-rod variation for the FLECHT SEASET test were approximately 60° C (100° F).

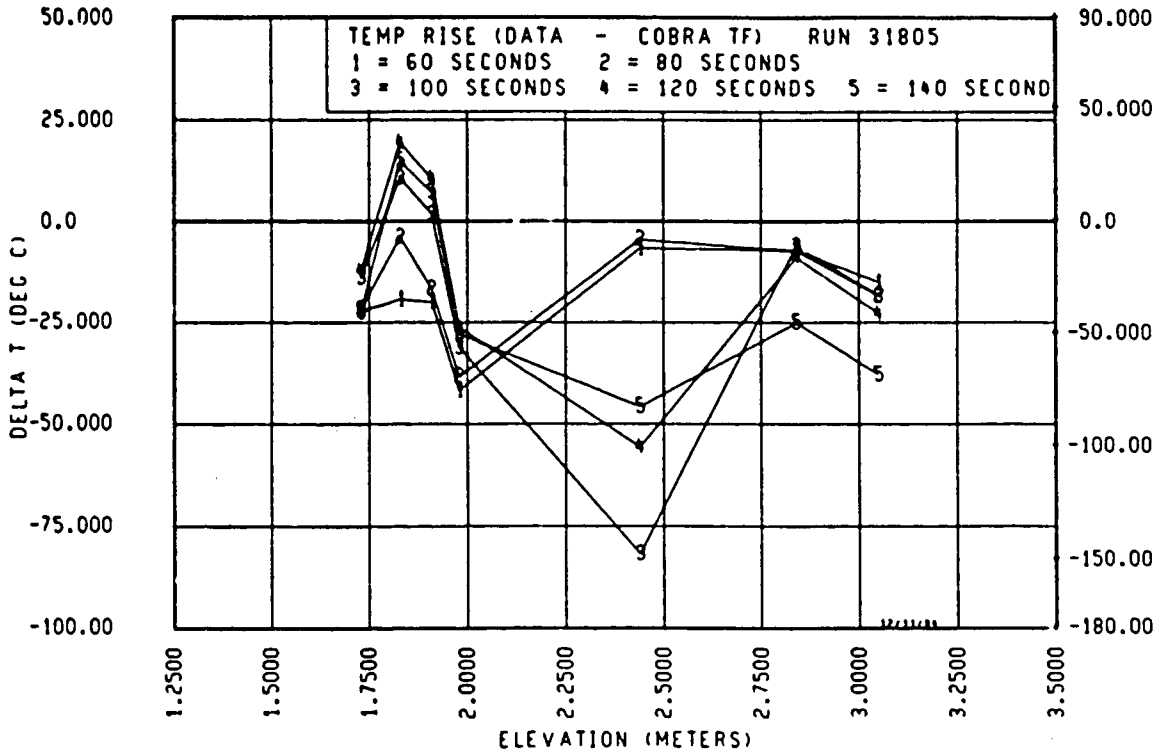

Figure 3-184. Temperature Differential Versus Time, FLECHT SEASET 161-Rod Bundle Test 31805

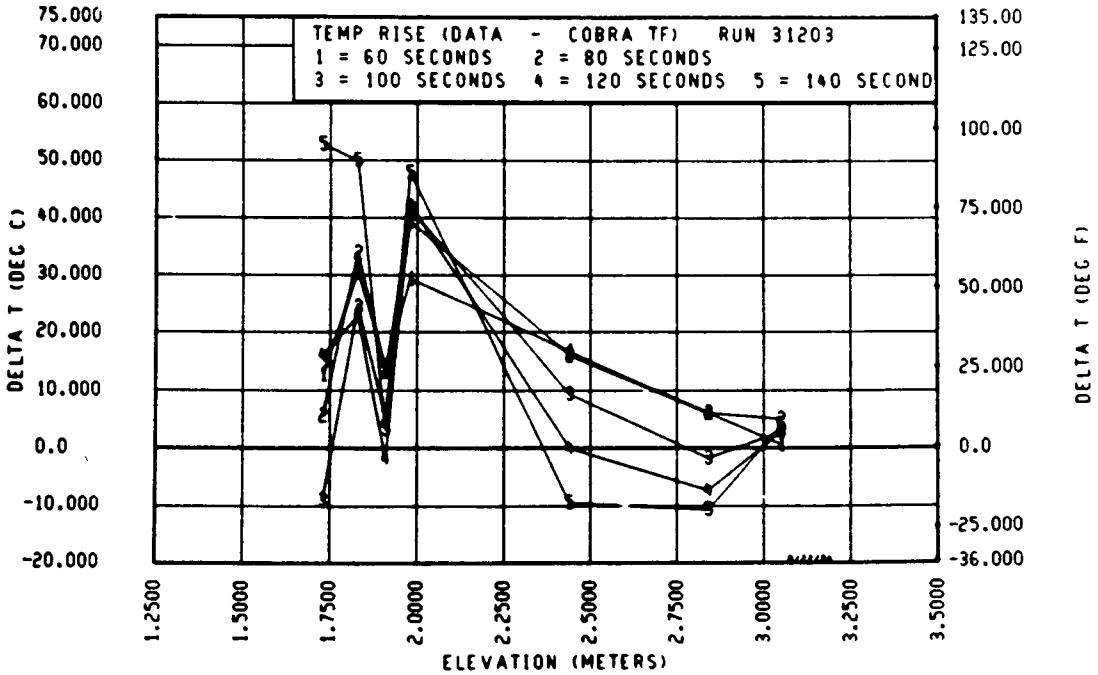

Figure 3-185. Temperature Differential Versus Time, FLECHT SEASET 161-Rod Bundle Test 31203

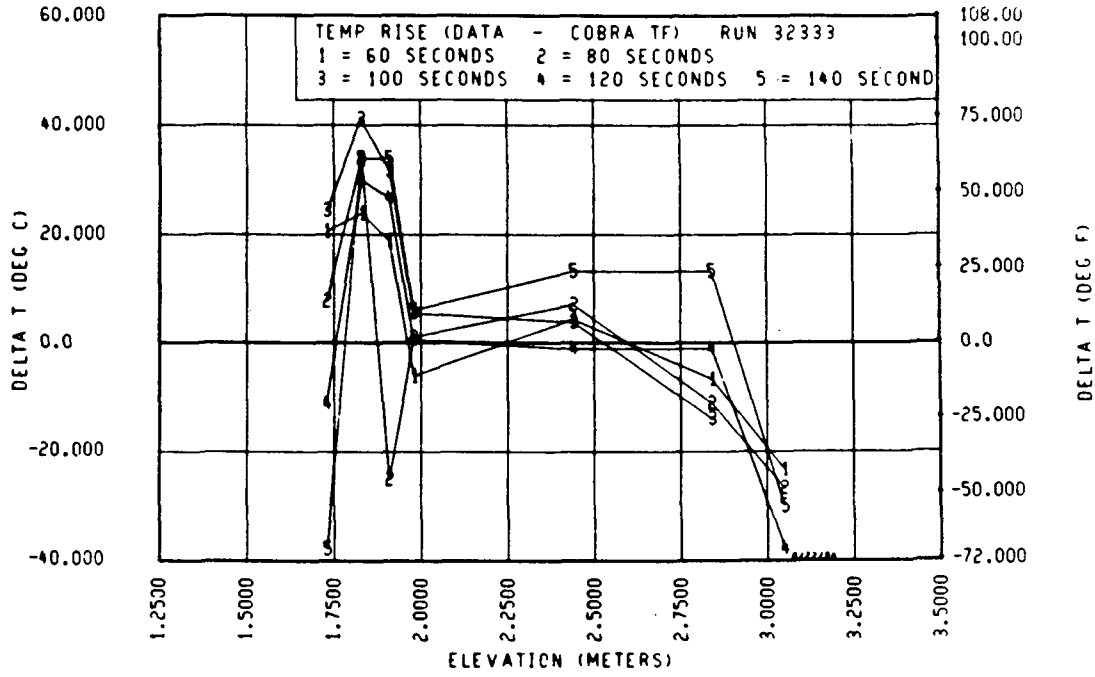

Figure 3-186. Temperature Differential Versus Time, FLECHT SEASET 161-Rod Bundle Test 32333

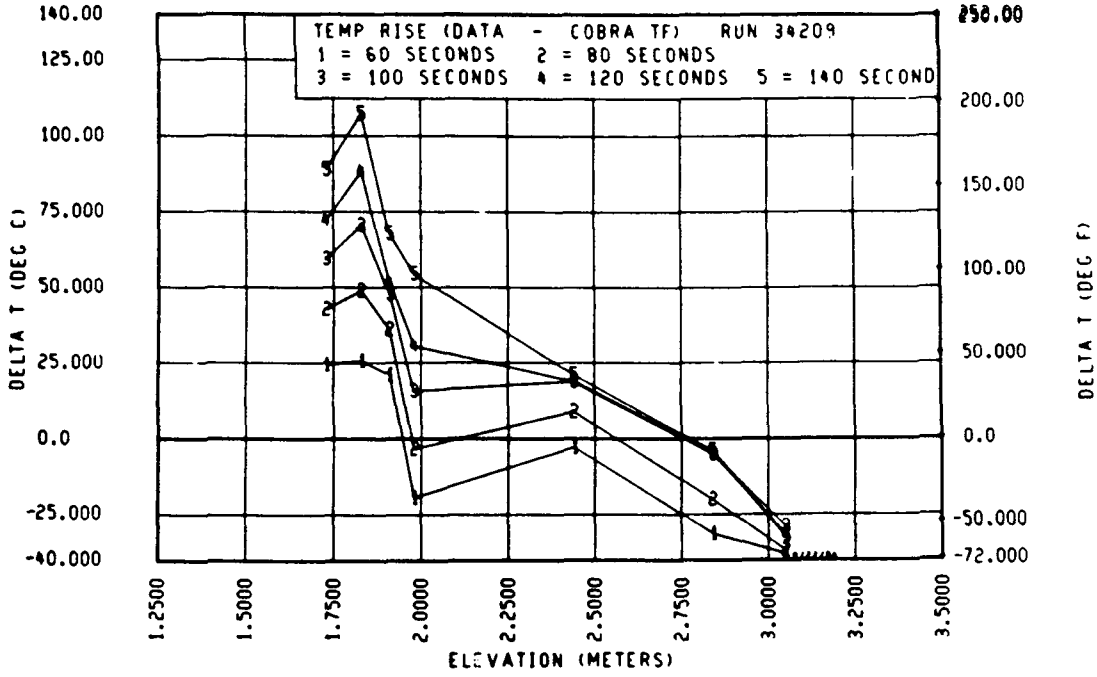

Figure 3-187. Temperature Differential Versus Time, FLECHT SEASET 161-Rod Bundle Test 34209

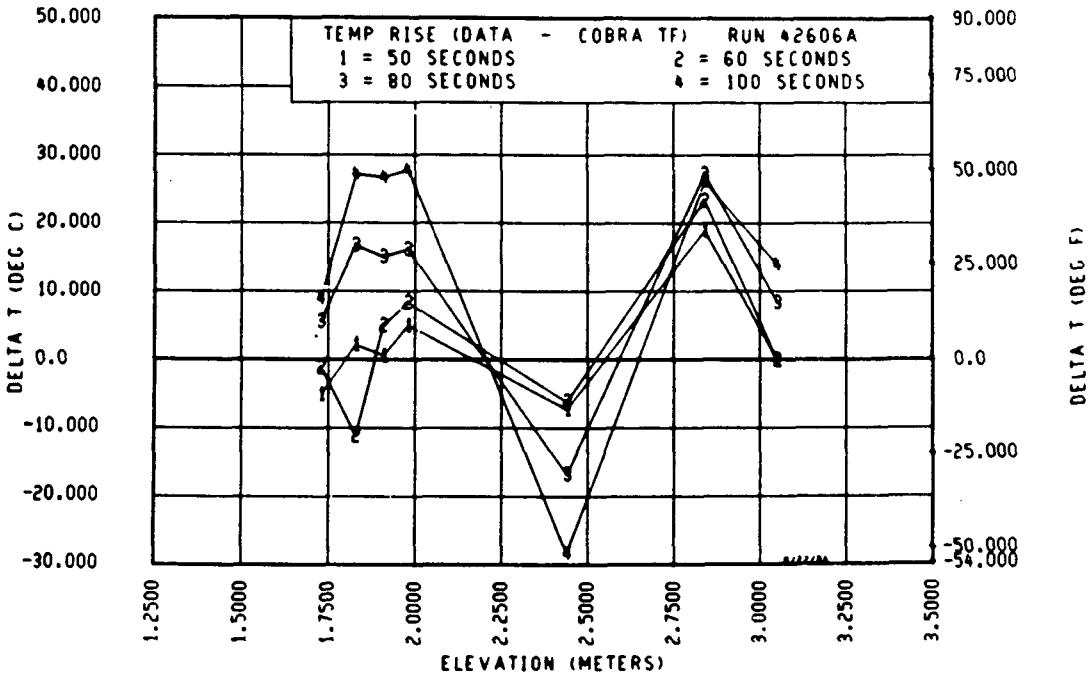

Figure 3-188. Temperature Differential Versus Time, FLECHT SEASET 21-Rod Bundle Test 42606A

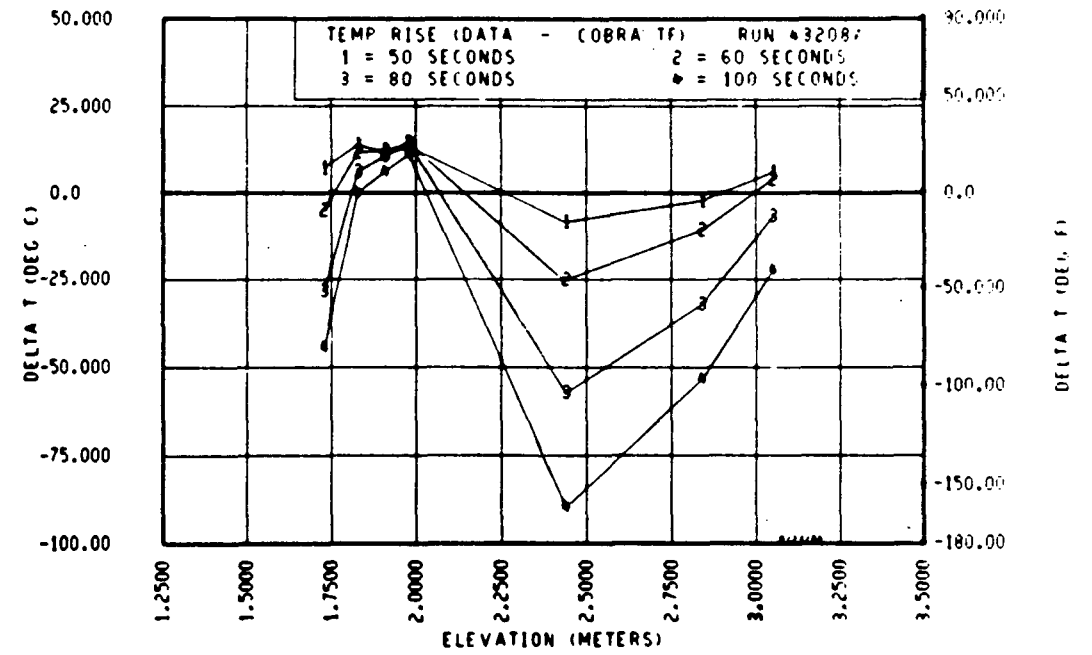

Figure 3-189. Temperature Differential Versus Time, FLECHT SEASET 21-Rod Bundle Test 43208A

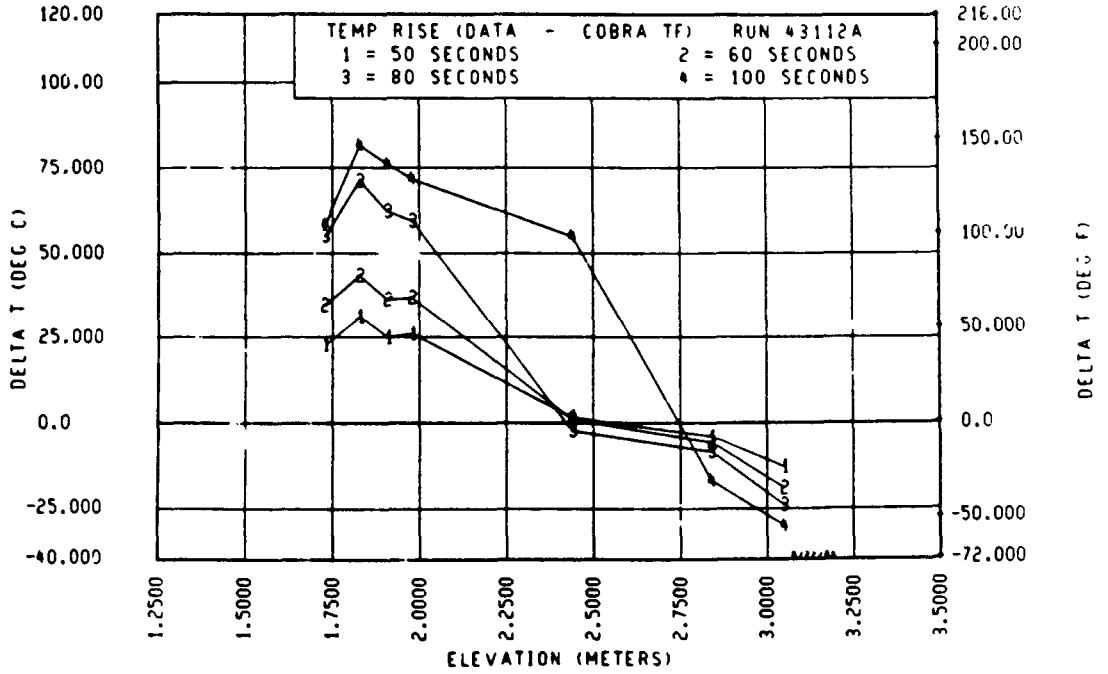

Figure 3-190. Temperature Differential Versus Time, FLECHT SEASET 21-Rod Bundle Test 43112A

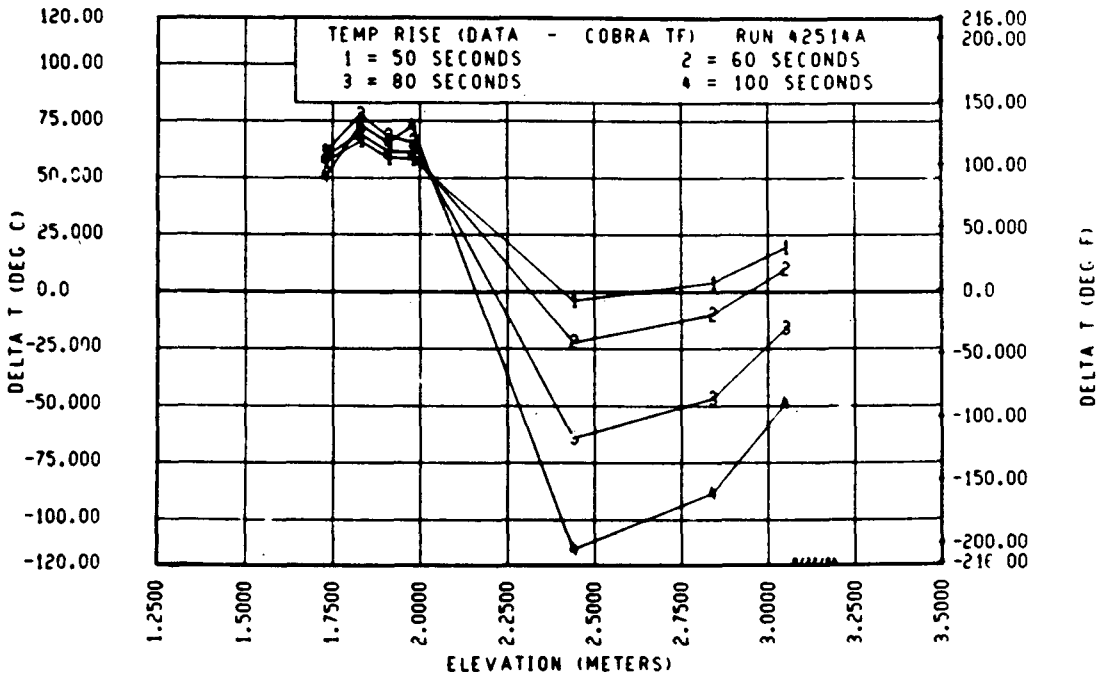

Figure 3-191. Temperature Differential Versus Time, FLECHT SEASET 21-Rod Bundle Test 42514A

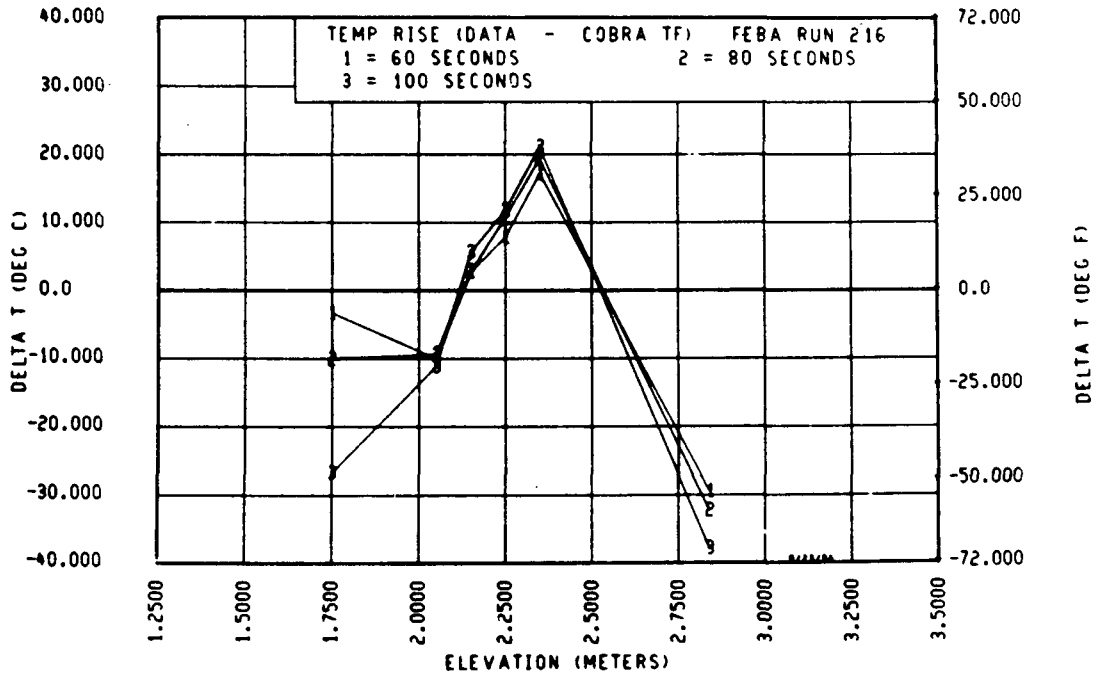

Figure 3-192. Temperature Differential Versus Time, FEBA Test 216

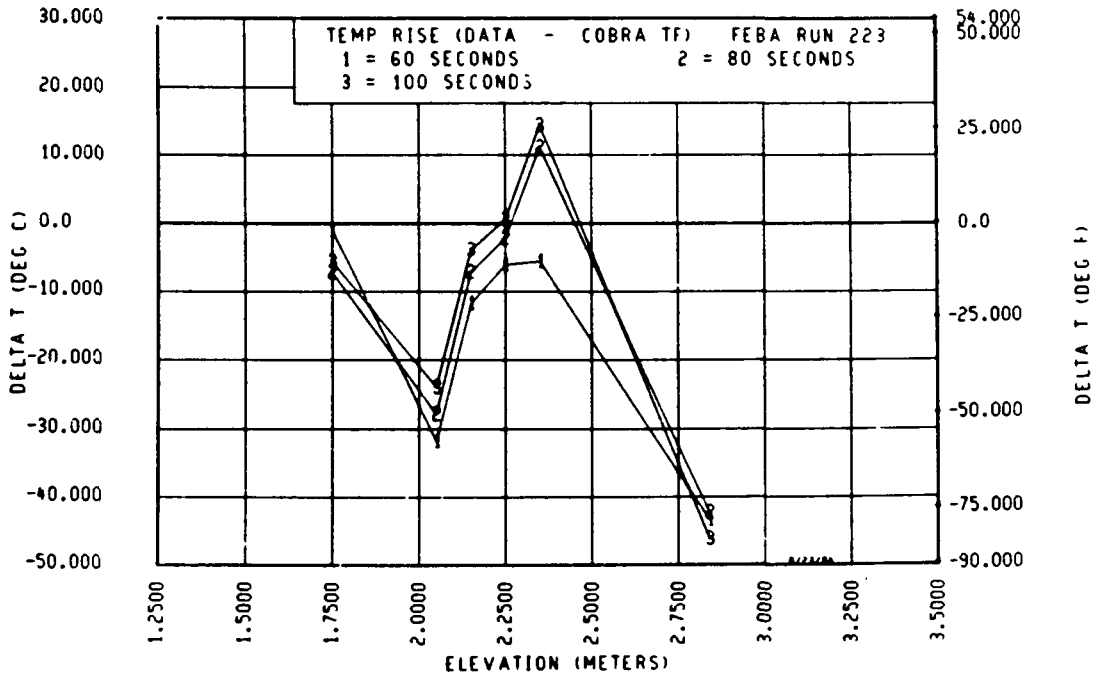

Figure 3-193. Temperature Differential Versus Time, FEBA Test 223

SECTION 4
FLOW BLOCKAGE MODELS

4-1. INTRODUCTION AND BACKGROUND

During the calculated refill and reflood phases of a postulated LOCA in a PWR, Zircaloy-clad fuel rods may reach temperature levels sufficient to swell and burst because of internal overpressure. Such local clad swelling restricts the fuel assembly coolant channels and is referred to as a flow blockage.

Several reflood experiments have been conducted to examine the heat transfer and hydraulic effects of blocked rod arrays with the blockages simulated by either sleeves or a flat plate.[1-6] Of the above experiments, the NRC/EPRI/Westinghouse FLECHT SEASET flow blockage program and the FEBA (Flooding Experiments in Blocked Arrays) experimental program are discussed in detail below.

The FLECHT SEASET and FEBA flow blockage tests were designed to complement each other; the FEBA tests concentrate on coplanar blockage effects and FLECHT

---

1. Ihle, P., and Rust, L., "FEBA - Flooding Experiments with Blocked Arrays, Evaluation Report," KfK 3657, March 1984.

2. Ihle, P., and Rust, L., "FEBA - Flooding Experiments with Blocked Arrays, Data Report 1, Test Series I through IV," KfK 3658, March 1984.

3. Ihle, P., and Rust, L., "FEBA - Flooding Experiments with Blocked Arrays, Data Report 2, Test Series V through VIII," KfK 3659, March 1984.

4. Loftus, M. J., et al., "PWR FLECHT SEASET 21-Rod Bundle Flow Blockage Task Data and Analysis Report," NRC/EPRI/Westinghouse-11, September 1982.

5. Pearson, K. G., et al., "Reflooding Experiments on a 49-Rod Cluster Containing a Long 90-Percent Blockage," AEEW-R-1591, January 1983.

6. Loftus, M. J., and Hochreiter, L. E., "Reflood Heat Transfer in the FLECHT SEASET 163-Rod Bundle With Flow Blockage and Bypass," ASME Paper 83-WA/HT-16, 1983.

SEASET has concentrated on noncoplanar blockage effects. Coplanar blockage is defined as the situation in which the peak strain points on all swollen rods are aligned in a single plane perpendicular to the axial flow direction. Any misalignment of the peak strains is regarded as noncoplanar blockage. In coplanar blockage, the flow is one-dimensional in the axial direction with no intersubchannel exchange if all rods are blocked. In noncoplanar blockage, even if the strains are slightly misaligned, there is flow exchange between the subchannels if all rods are blocked.

4-2. FLECHT SEASET Flow Blockage Results

The FLECHT SEASET reflood experiments were conducted in a 21-rod bundle to examine flow blockage shape and distribution effects, and in a 163-rod bundle to examine flow blockage and bypass effects.

The 21-rod bundle test section consisted of 21 full-length [3.04 m (120 in.) heated length] electrically heated fuel rod simulators with a 1.66 peak-to-average chopped cosine axial power shape. The 9.5 mm (0.374 in.) diameter heater rods were arranged in a 12.6 mm (0.496 in.) square pitch with four solid triangular filler rods at the corners of the 5 x 5 matrix, as shown in figure 4-1.

Two blockage shapes were selected for simulation in the 21-rod bundle: a short, concentric shape, representing high-temperature swelling, and a long, nonconcentric shape, representing low-temperature swelling. These two shapes are shown in figure 4-2.

For the nonconcentric shape, the most representative strain values were found to be approximately 36 and 44 percent. To provide a meaningful comparison between the two shapes, the strain of the concentric shape was selected to provide the same maximum subchannel flow blockage as the 36 percent nonconcentric shape. This provides a strain of 32.5 percent for the short, concentric shape.

The blockage sleeves were placed on the heater rods in both coplanar and noncoplanar distributions. The coplanar distribution, with all the sleeves

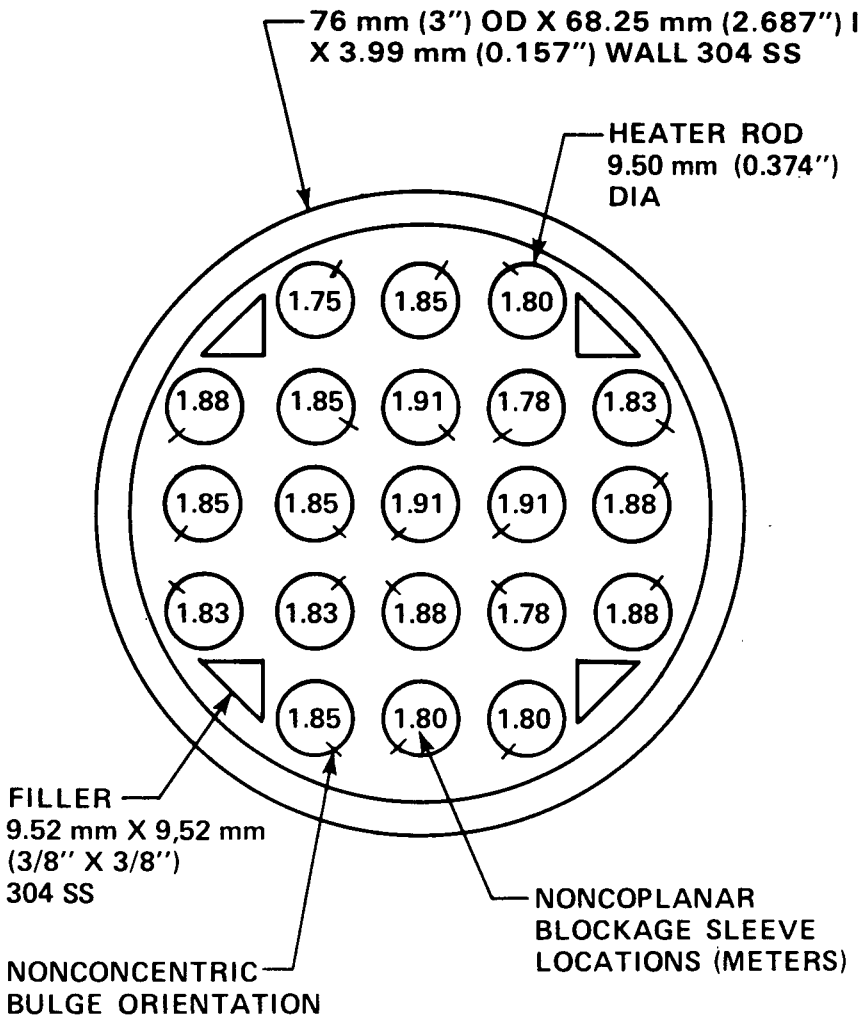

Figure 4-1. FLECHT SEASET 21-Rod Bundle Cross Section

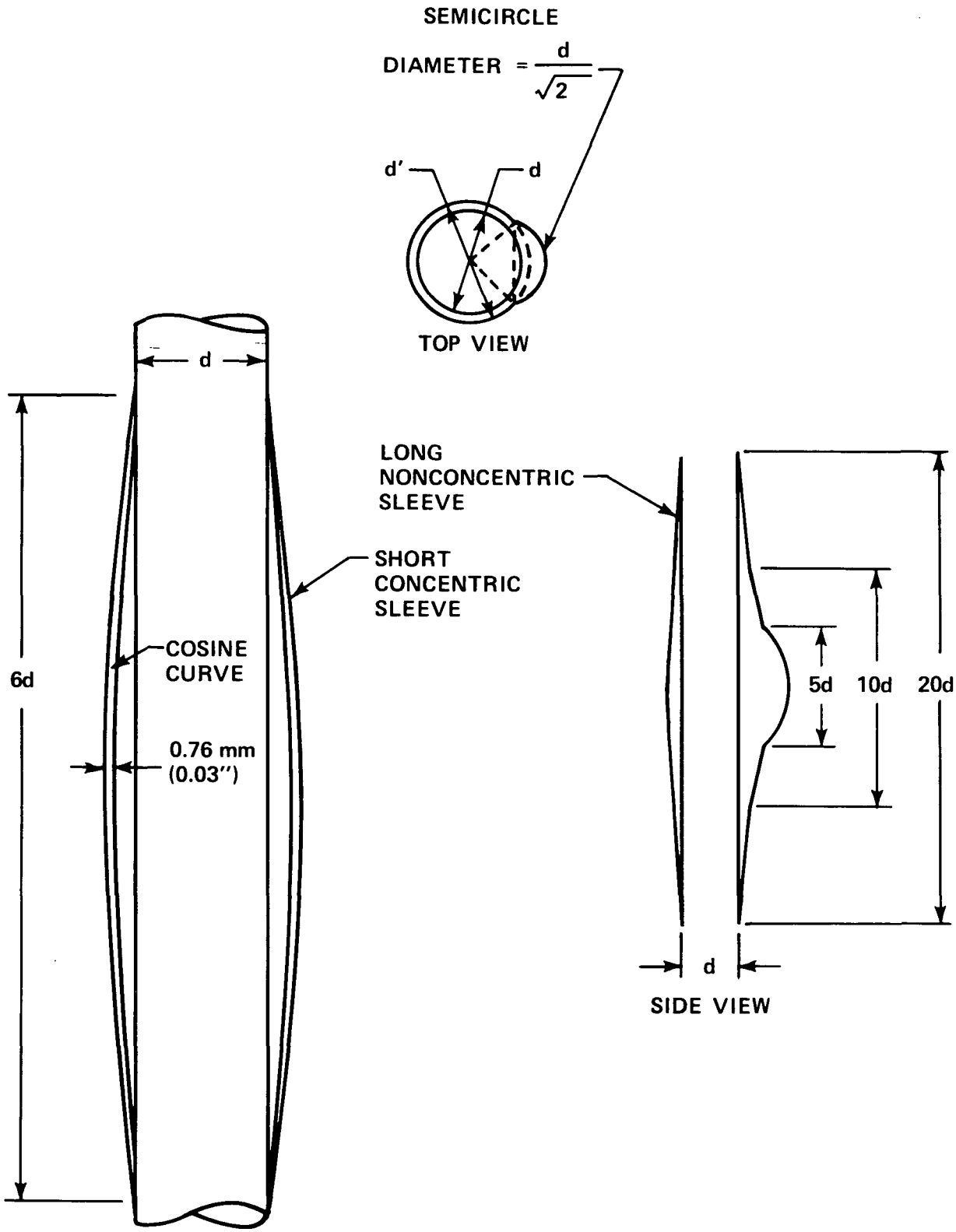

Figure 4-2. FLECHT SEASET 21-Rod Bundle Blockage Sleeve Shapes

centered at the 1.85 m (73 in.) elevation, was selected for the relative simplicity of its data analysis. With the short concentric sleeves in a coplanar distribution, the sleeves on adjacent heater rods just touch and provide a 62-percent flow area blockage.

For noncoplanar blockage, the sleeves were distributed at varous elevations on the heater rods such that the statistics of the sleeve locations coincided with the calculated hot spot location of a PWR. The method developed by Burman and Olson[1] was employed to determine the statistics of the hot spot locations, which were then assumed to be the burst locations in the bundle. The axial distribution of the blockage is shown in figure 4-3 for both the short concentric sleeve and the long nonconcentric sleeve.

4-3. Coplanar Blockage Effects -- Coplanar blockage, centered at 1.85 m (73 in.), was present in the FLECHT SEASET 21-rod bundle tests, configuration B (with flow bypass) and configuration C (without flow bypass). The measured rod temperature transients for rod 3C (in the center of the blockage region) at the 1.93 m (76.1 in.) elevation for the unblocked and both coplanar blockage configurations are shown in figure 4-4. The thermocouple in the blockage configurations is 0.048 m (1.9 in.) downstream of the trailing edge of the blockage. Figure 4-4 shows the early, nearly adiabatic heatup period of approximately 15 seconds when there was very little flow through the bundle and only small temperature differences between blocked and unblocked configurations. When the steam flow increased and liquid entrainment began, the rate of rod temperature rise decreased. Once entrained drops were present in the steam flow, a significant difference is observed between the blocked data and the unblocked data.

This figure also clearly indicates the reduction in the measured rod temperature relative to the unblocked configuration immediately downstream of the coplanar blockage and also the difference between configurations with and

1. Burman, D. L., and Olsen, C. A., "Temperature and Cladding Burst Distribution in a PWR Core During LOCA," Specialists' Meeting on Behavior of Water Reactor Fuel Elements Under Accident Conditions, September 1976.

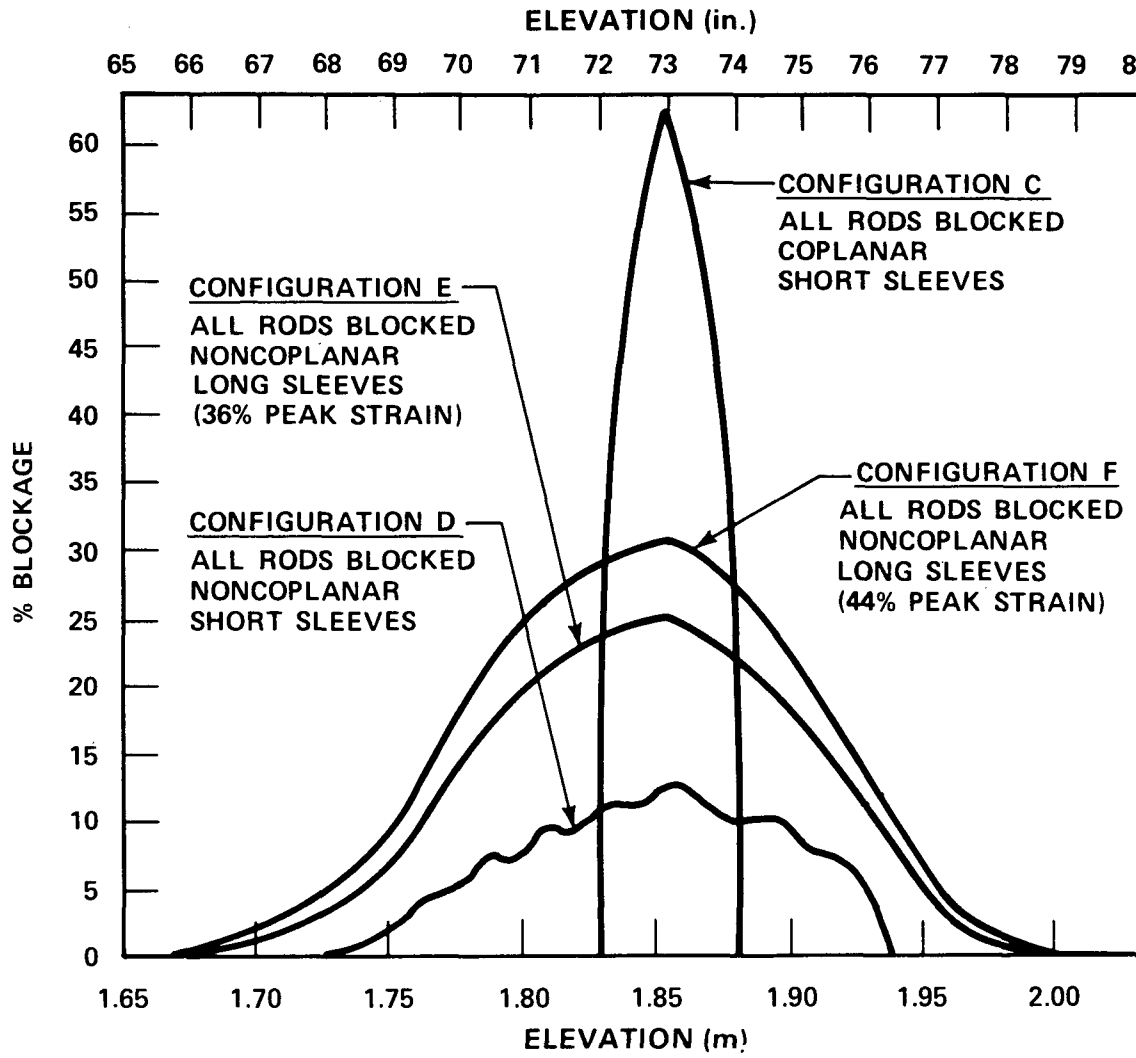

Figure 4-3. Bundle-Wide Flow Blockage as a Function of Elevation, FLECHT SEASET 21-Rod Bundle Tests

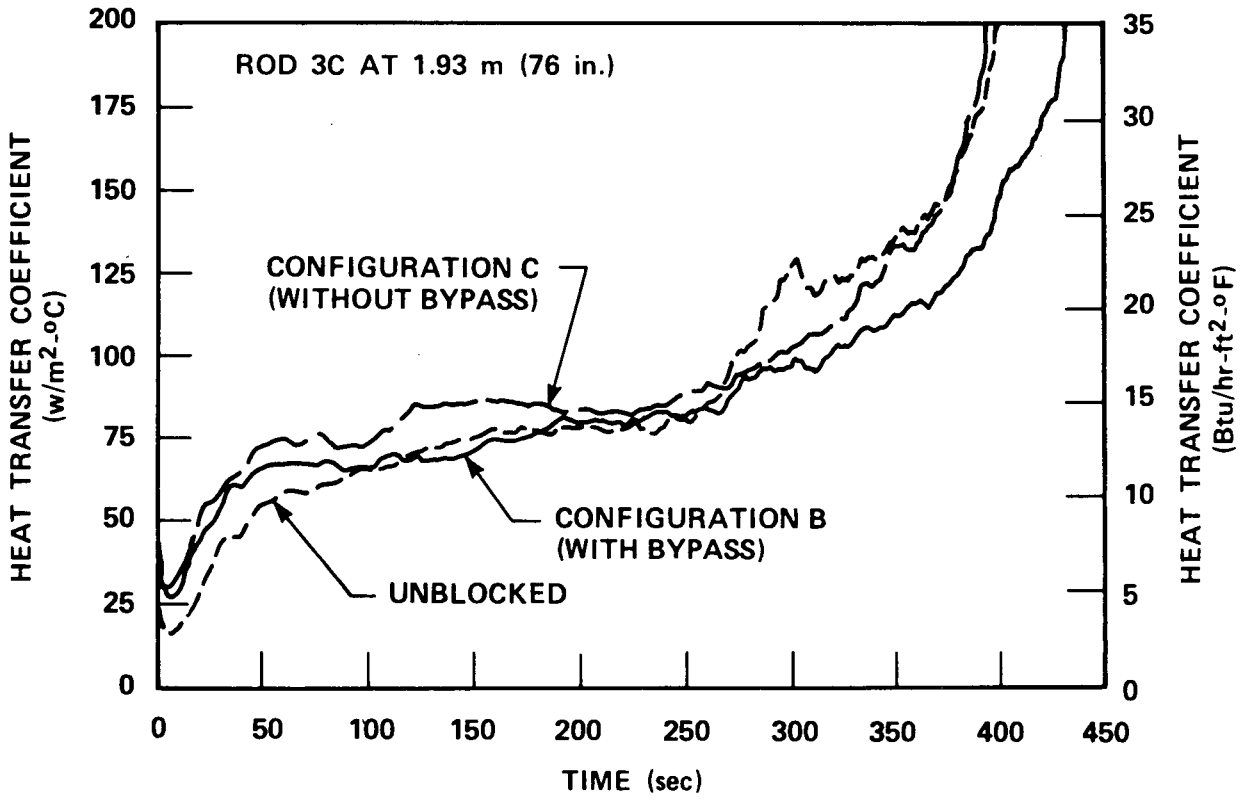

Figure 4-4. Center Rod Temperature for Unblocked Bundle and Two Coplanar Blockage Configurations, FLECHT SEASET Tests

without flow bypass. The fact that the greatest temperature reduction occurs in the blockage configuration without flow bypass is understandable, since the droplets and all the steam flow must pass through the blockage region where the droplets are broken up and the steam flow is accelerated. In the blockage configuration with flow bypass, some of the steam flow is redistributed around the blockage; therefore, the temperature reduction is smaller. These results are fairly typical of all rod thermocouples downstream of the coplanar blockage, and are consistent with the results of the FEBA experiments.

The heat transfer coefficient (relative to T_{sat}) was obtained utilizing the calculated rod surface temperature (from an inverse heat conduction calculation), the measured rod bundle power, and the saturation temperature at the measured system pressure. An example of the heat transfer coefficient as a function of time is shown in figure 4-5 for rod 3C immediately downstream of the blockage, at 1.93 m (76.1 in.), for configurations with and without flow bypass, and the corresponding unblocked bundle data.

The increased heat transfer for the blocked configurations in the first 15 seconds is attributed to the steam flow, which is accelerated through the blockage region. The rapid increase in heat transfer after 15 seconds is due to the onset of two-phase dispersed flow. It is believed that, in the two-phase dispersed flow regime, some fraction of the entrained drops are shattered into much smaller droplet sizes by the blockage desuperheating the steam and resulting in greater heat transfer at and downstream of the blockage zone. As shown by figure 4-5, the heat transfer for blockage without flow bypass is greater than that with bypass or unblocked for the entire transient. The heat transfer for blockage with flow bypass is equal to or less than the unblocked after 100 seconds. The improvement in the blocked heat transfer decreases with time because of the decrease in the steam velocity and corresponding decrease in droplet velocity and breakup as the quench front approaches.

The heat transfer as a function of elevation from the coplanar blockage with and without flow bypass for the center rod (rod 3C) is shown in figure 4-6 for various times after flood. Figure 4-6 shows that the improvement in heat

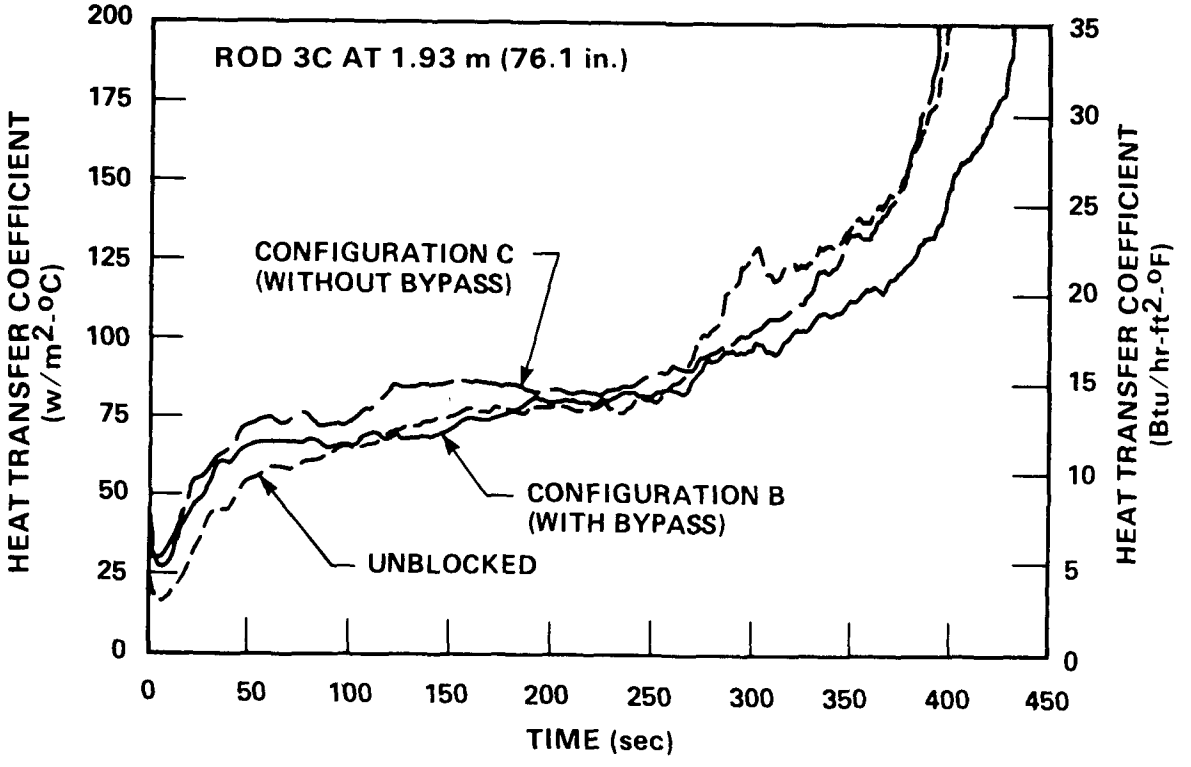

Figure 4-5. Heat Transfer Coefficient for Unblocked Bundle and Two Coplanar Blockage Configurations, FLECHT SEASET Tests

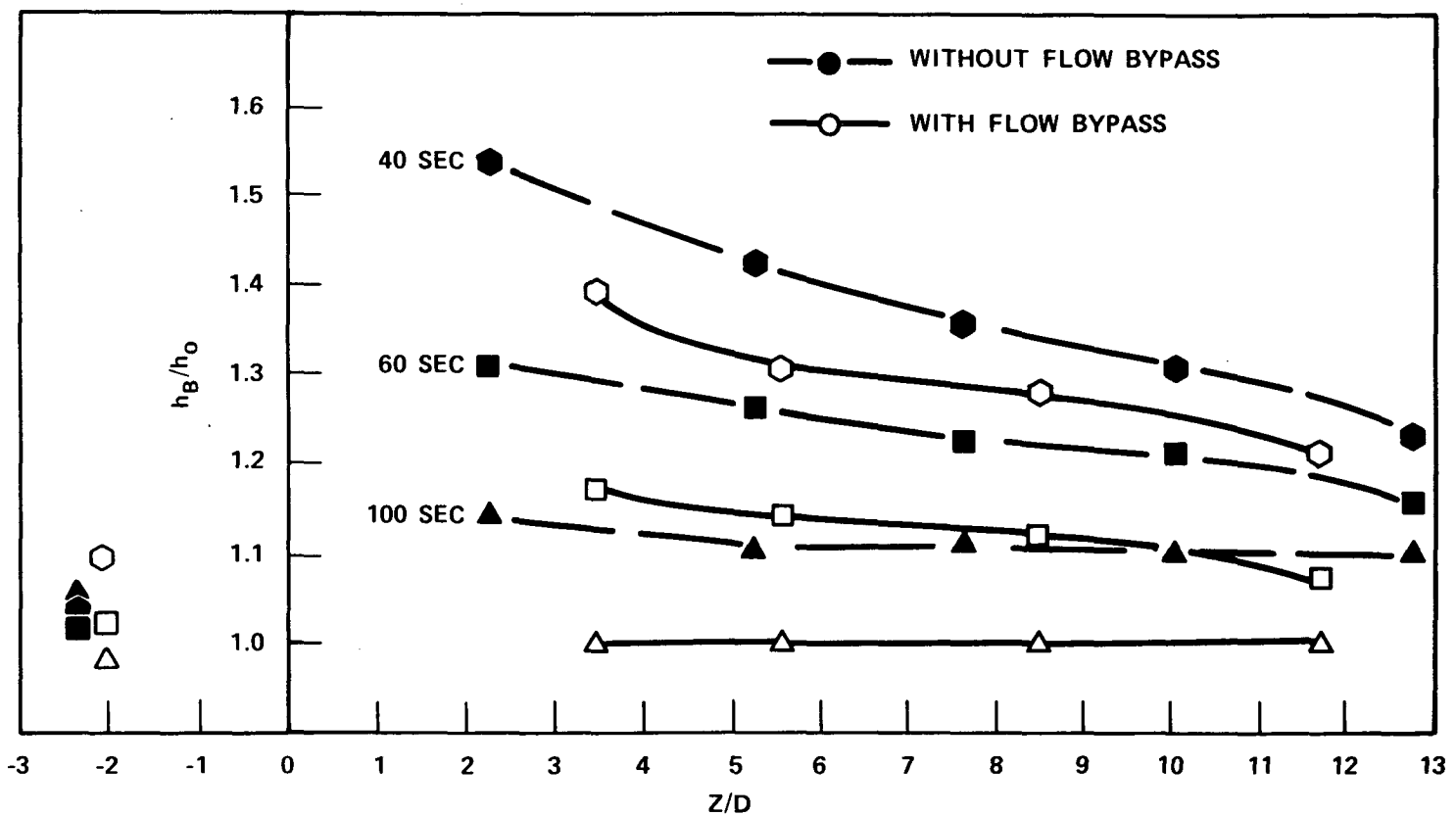

Figure 4-6. Normalized Heat Transfer Coefficient for Two Coplanar Blockage Configurations, FLECHT SEASET Tests

transfer decreases both as the distance increases downstream of the blockage and as the time increases after flood initiation. The reduction in the blocked heat transfer as a function of time is due in part to the relative increase in the absolute level of bundle heat transfer with respect to time. Early in the transient, the heat transfer is small; therefore, any improvement in heat transfer would be significant. Also, as the quench front (and, more important, the transition front) moves up the bundle, the steam velocity at the elevation of blockage zone decreases with a subsequent decrease in the velocity of the entrained droplets. This reduction in the droplet Weber number decreases the droplet breakup, and therefore decreases the heat transfer within and downstream of the blockage. The effect is the same as that of the behavior of droplets impacting the grid straps, noted in section 3.

4-4. Noncoplanar Blockage Effects -- The results of the 21-rod noncoplanar blockage test with the short concentric sleeve (bundle D) have been reported and discussed herein.[1] In these tests it was clear that crossflow effects, caused by the noncoplanar blockage distribution, resulted in the observed improved cooling.

With the long nonconcentric blockage sleeves distributed in a noncoplanar distribution and centered at the same elevations as the short sleeves, there was a large amount of overlap between the sleeves on adjacent rods. The temperature as a function of time for rod 4C at 1.99 m (78.45 in.) for configurations E (36-percent maximum strain sleeve) and F (44-percent maximum strain sleeve), which is approximately 25 mm (1 in.) downstream of the sleeve, is shown in figure 4-7. Also shown in this plot is the corresponding unblocked rod temperature. These data indicate that the effect of increasing blockage sleeve strain without flow bypass was to reduce the rod temperature and vapor temperature significantly over the entire transient. The substantial reduction in the measured rod temperature in configuration F is believed to be due to the increased breakup and evaporation of the droplets as a result of the increased

1. Loftus, M. J., et al., "PWR FLECHT SEASET 21-Rod Bundle Flow Blockage Task Data and Analysis Report," NRC/EPRI/ Westinghouse-11, September 1982.

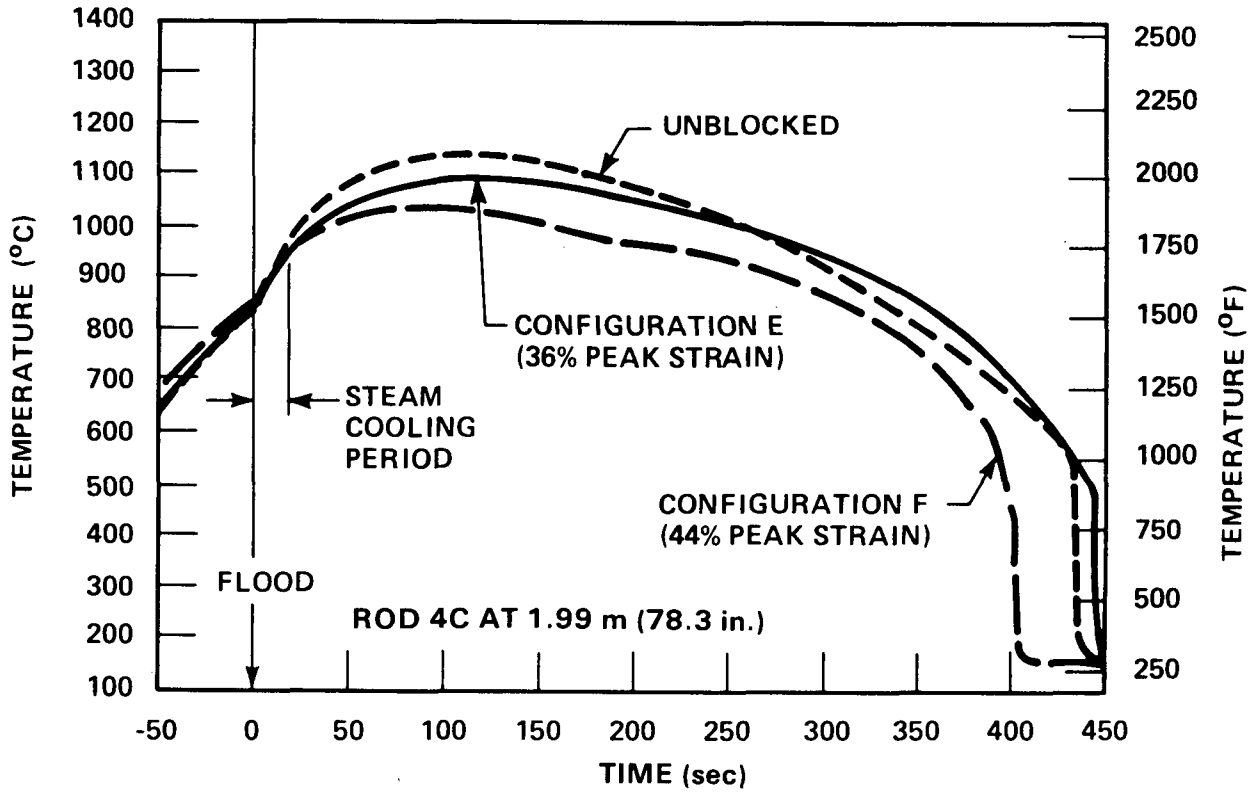

Figure 4-7. Heat Transfer Coefficients for Unblocked Bundle and Two Noncoplanar Blockage (Long Sleeves) Configurations, FLECHT SEASET Tests

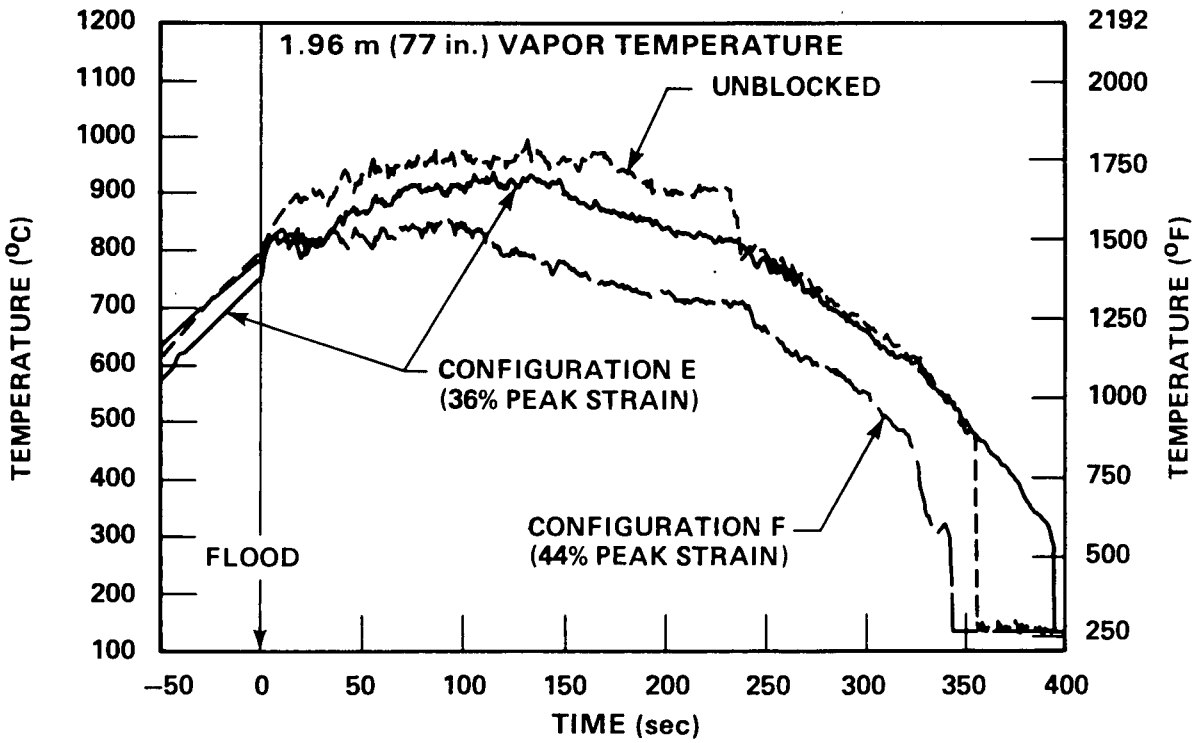

Figure 4-8. Vapor Temperatures for Unblocked Bundle and Two Noncoplanar Blockage (Long Sleeves) Configurations, FLECHT SEASET Tests

blockage, as indicated by figure 4-8, which shows a corresponding decrease in vapor temperature.

The heat transfer coefficient history for rod 4C at 1.99 m (78.45 in.) for configurations E and F, as well as for the corresponding unblocked rod, is shown in figure 4-9. This thermocouple was located immediately downstream of the subchannel with the maximum flow blockage of 93 percent. Again, the large flow blockage provides for increased droplet breakup and improved local heat transfer.

The ratio of exit liquid flow to total flow for configurations A, E, and F (figure 4-10) indicates that a much smaller quantity of the water droplets exit the bundle for configuration F. This observation is consistent with the FEBA liquid carryover results (discussed in paragraphs 4-5 through 4-8). It implies that the droplets of entrained liquid are being shattered and are evaporating, resulting in the improved heat transfer in the test.

Analysis of the 21-rod bundle data led to the conclusion that the long, nonconcentric shape should provide the least favorable heat transfer characteristics in the 163-rod bundle. Therefore, the long, nonconcentric sleeve was used in the 163-rod bundle tests, which are discussed in section 5.

4-5. FEBA Flow Blockage Results

The FEBA 5x5-rod tests used 25 heater rods of 10.7 mm (0.423 in.) diameter on a square pitch of 14.3 mm (0.563 in.) with a heated length of 3.90 m (154 in.). The axial power shape was a chopped cosine with a peaking factor of 1.19. The housing was heated prior to the tests to reduce radiation losses from the rods. The FEBA bundle and heater rod axial power level are shown in figure 4-11, and the configurations tested are shown in figure 4-12.

A total of eight FEBA 5x5 configurations were tested: two to examine grid behavior (series I and II, discussed in section 3) and six to examine blockage effects (series III to VIII). Test conditions were repeated from one series to the next to isolate the effect of the blockage configuration. For those

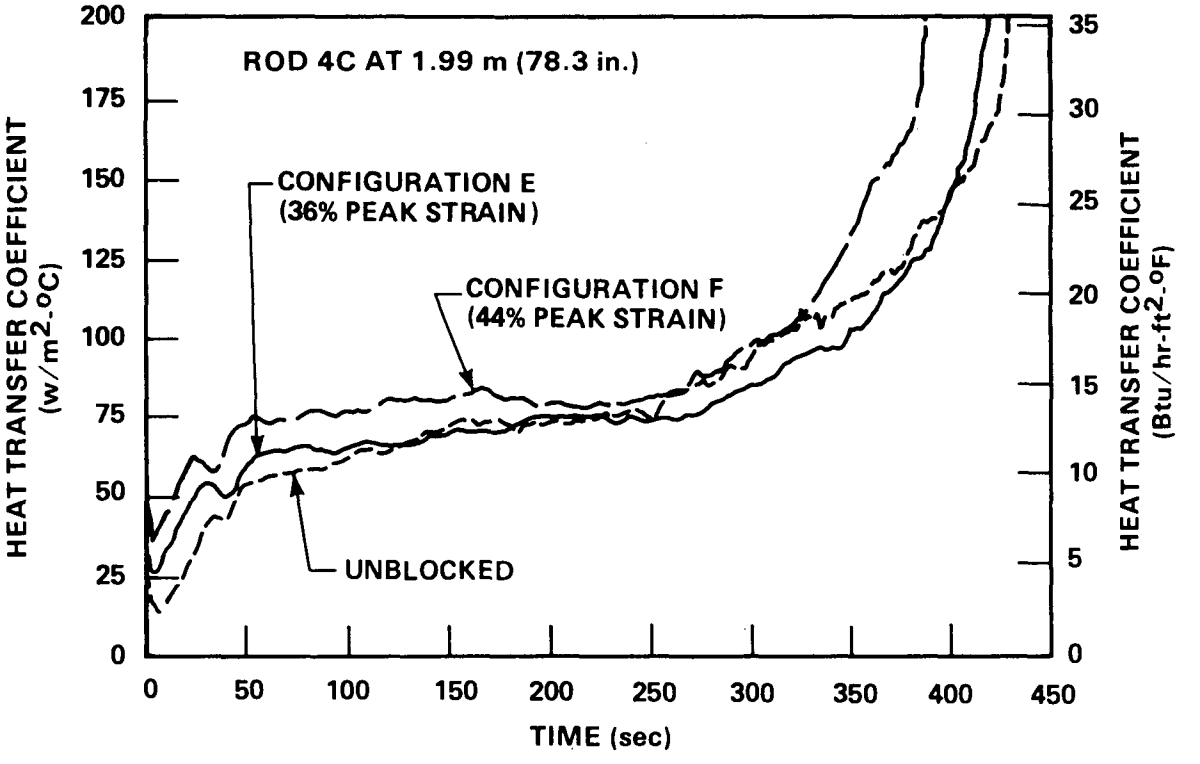

Figure 4-9. Rod Temperatures for Unblocked Bundle and Two Noncoplanar Blockage (Long Sleeves) Configurations, FLECHT SEASET Tests

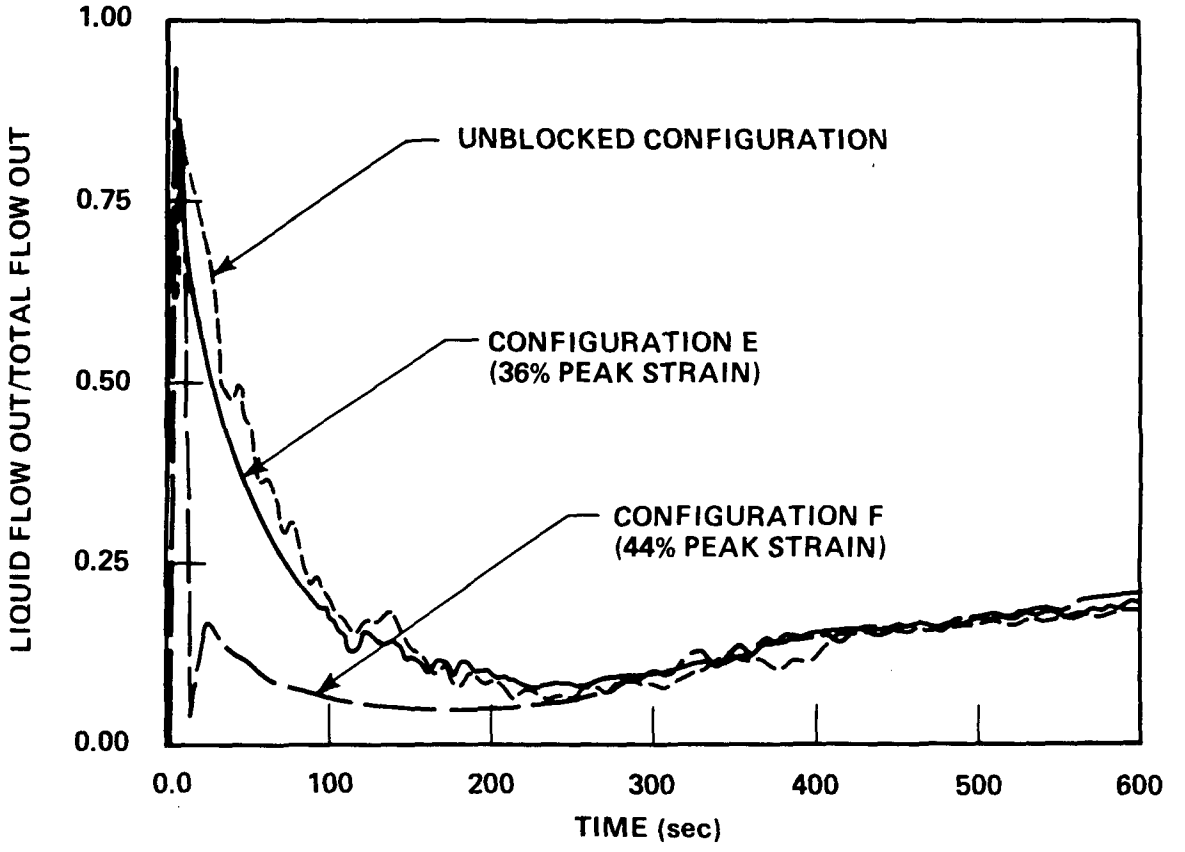

Figure 4-10. Ratio of Liquid Flow to Total Flow, Unblocked Bundle and Two Noncoplanar Blockage (Long Sleeves) Configuration, FLECHT SEASET Tests

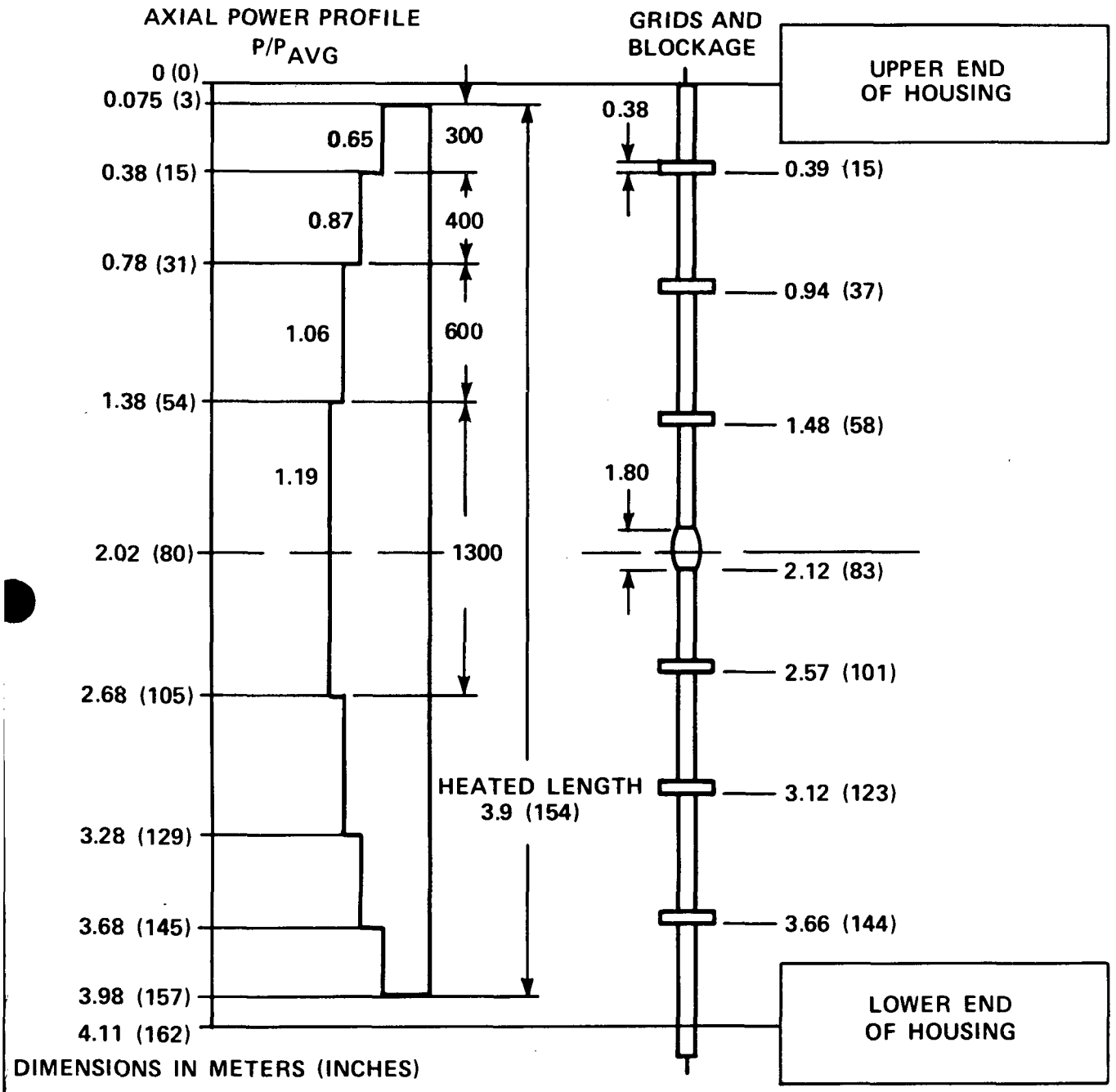

Figure 4-11. Heater Rod and Axial Power Profile Used in FEBA Tests

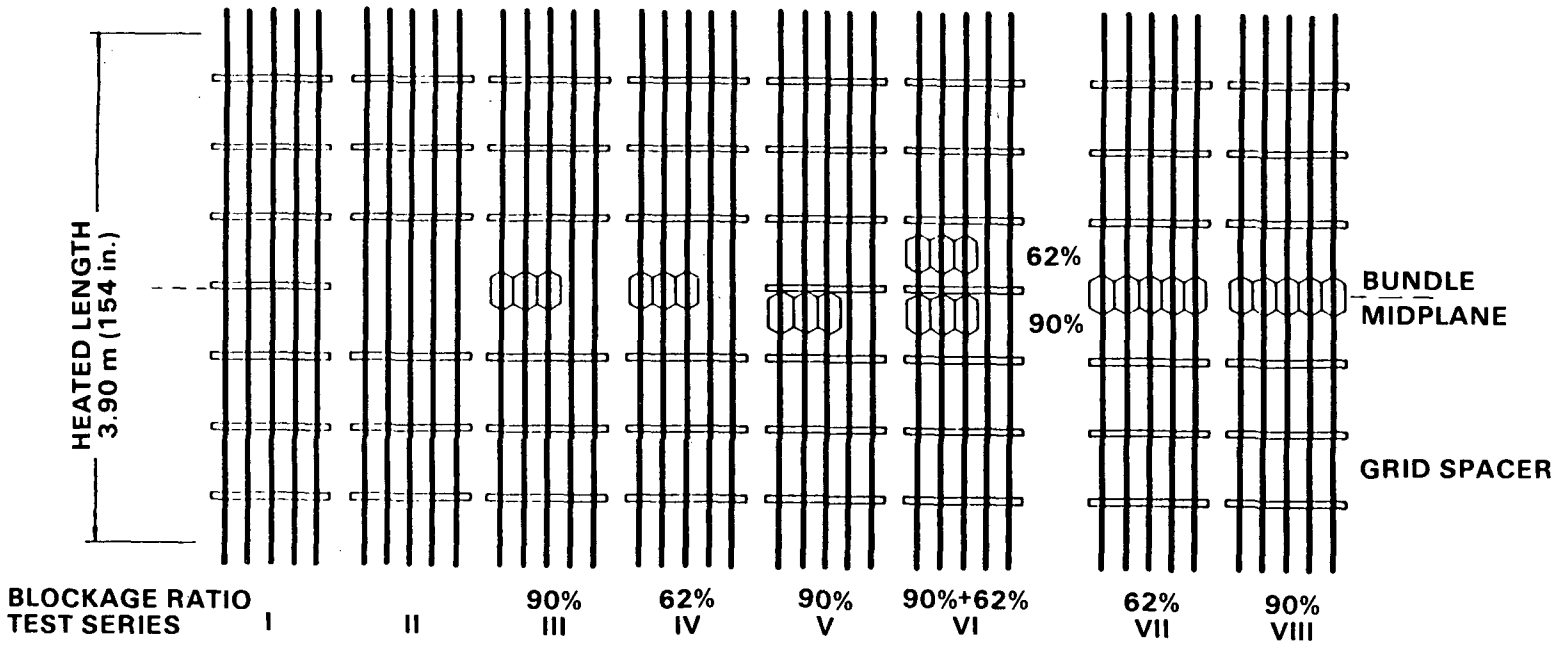

Figure 4-12. Axial Arrangements of Grid Spacers and Sleeve Blockages Used in FEBA Tests

configurations without the midplane grid, the blockage effect is shown by comparison of series III, IV, VII, and VIII with Series II. For those configurations with the midplane grid (series V and VI), the proper unblocked bundle comparison is series I. In the following paragraphs, each test series is briefly discussed and comparisons are made to the proper unblocked configuration, for assessment of the blockage effect. Most of the discussion of the FEBA data has been taken from the published reports [1-3] and from personal communication with these authors.

4-6. Flow Blockage With Bypass -- The first series of tests discussed is series III, the 90-percent blocked tests. The measured rod temperature transients in the region of the blockage are plotted in figure 4-13 for one of the tests. Figure 4-13 includes data from heater rods in the 3x3 blockage zone, data from rods in the bypass zone, and data from a comparable series II unblocked bundle test at the same conditions.

Upstream of the blockage [at 2.12 m (83 in.)], the maximum temperatures and quench times of the blocked rod cluster are almost the same as those of the bypass rod and unblocked bundle test. For these flooding conditions [0.038 m/sec, 0.4 MPa (1.5 in./sec, 58 psia)], a slight improvement of the cooling upstream of the blockage occurs, probably because of drop deentrainment and breakup at the leading edge of the blockage. At the midplane of the blockage [at 2.02 m (80 in.)], the temperature transient measured in the bypass is lower than that of an unblocked bundle at the same elevation under identical flooding conditions. This can be seen through comparison with a data from a series II test rod.

---

1. Ihle, P., and Rust, L., "FEBA - Flooding Experiments with Blocked Arrays, Evaluation Report," KfK 3657, March 1984.

2. Ihle, P., and Rust, L., "FEBA - Flooding Experiments with Blocked Arrays, Data Report 1, Test Series I through IV," KfK 3658, March 1984.

3. Ihle, P., and Rust, L., "FEBA - Flooding Experiments with Blocked Arrays, Data Report 2, Test Series V through VIII," KfK 3659, March 1984.

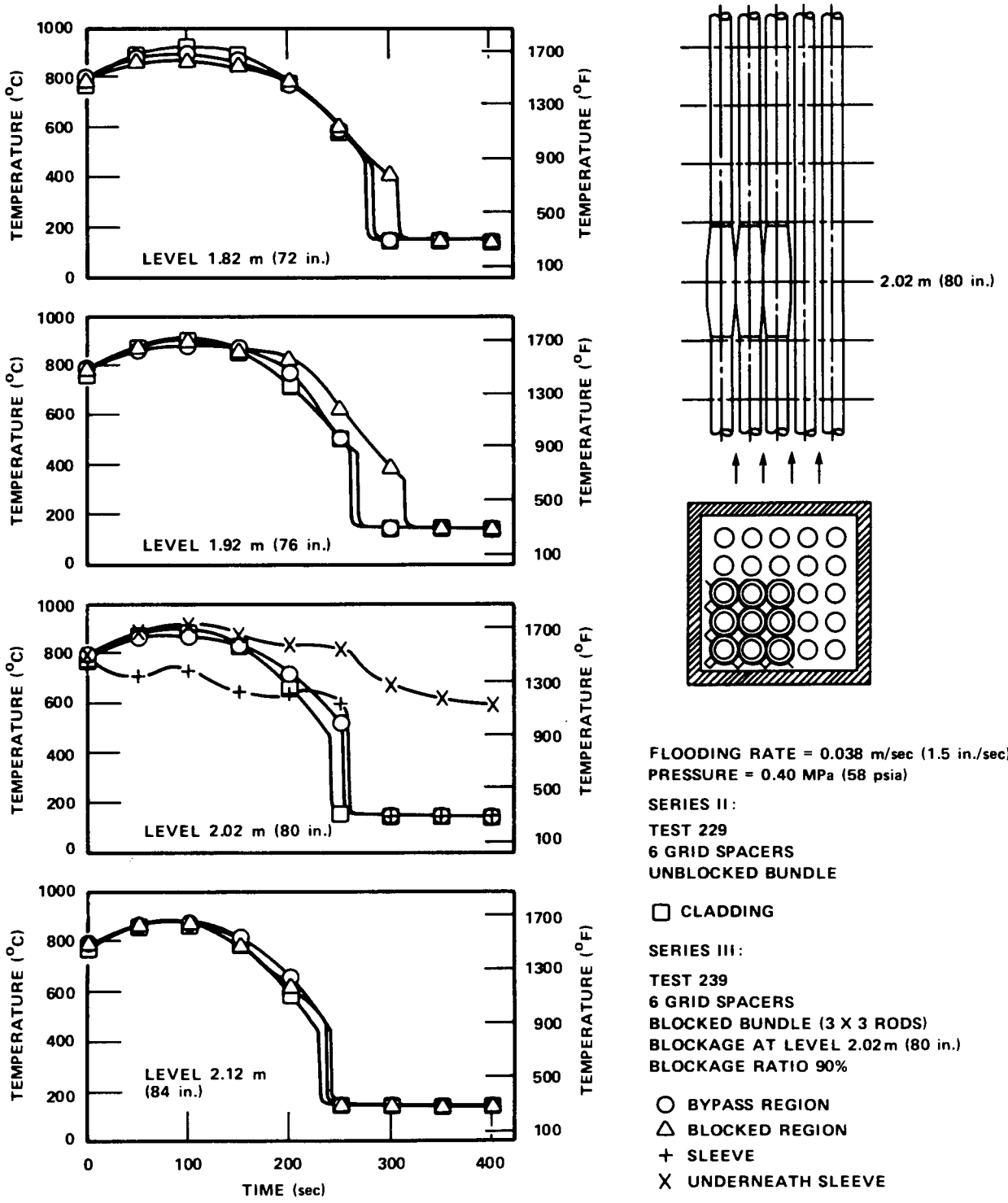

Figure 4-13. Cladding Temperature Results, FEBA Test Series III

The temperatures of the sleeves exposed to the reduced coolant mass flux in the constricted subchannels are lower than those of the rods in the bypass. However, the heater rod temperatures underneath the sleeves remain high throughout the whole period. Downstream of the blockage [at 1.92 m (76 in.)], both the maximum temperature and the quench time of the blocked rod cluster are affected by the blockage. The maximum temperature in the blocked rod cluster is lower than in the unblocked bundle. This comparison indicates that 90-percent blockage with bypass gives better heat transfer in the first half of the reflood period, where the peak temperature occurs, than the comparable unblocked bundle. This improved heat transfer is evident in all of the series III tests.

Further downstream of the blockage, the lower temperature rise of the blocked array (compared to that of the unblocked test) continues in spite of the close coplanar blockage arrangement and the high blockage ratio of 90 percent over an axial length of 0.065 m (2.6 in.). The bypass rod in the blocked bundle also shows a heat transfer benefit of the blockage compared to the unblocked bundle test.

The most dramatic difference between the temperature transients so compared occurs during the second half of the reflood period. After turnaround, the blocked rod temperatures decrease more slowly than the temperatures of the unblocked rods. There are believed to be at least three explanations for this behavior.

The first reason for the delayed decrease of the cladding temperature downstream of the blockage is that a new quench front has to be initiated. When the top end of the sleeves is quenched, the portion of the rod which is covered by the sleeves remains hot. The axial propagation of the quench front due to heat conduction within the rod is interrupted by the sleeve. Therefore, precursory cooling downstream of the blockage has to bring the cladding to a lower temperature level than usually measured. [Compare temperature transients plotted for the 1.92 m (76 in.) level in figure 4-13.] The quench front initiated downstream of the blockage proceeds slower than the quench front in the bypass rod cluster until they are farther downstream.

The second possible explanation is that the blockage accelerates the flow and forces it to remain as a dispersed flow regime instead of becoming a transitional flow regime as in the unblocked bundle. As a result, the period of precursory cooling as droplet flow is longer in the blocked bundle than the unblocked bundle, hence, longer quench times are observed.

The third possible explanation is similar to that given in the report on the UKASA Thetis 90-percent blocked bundle tests.[1] As the quench front approaches the blockage, the steam velocity decreases because of reduced temperature (increased steam density) and reduced steam generation due to lower decay powers. As the steam velocity decreases, the ability of the steam to entrain and accelerate water droplets through the blockage is reduced, such that the entrained liquid flow through the blockage is less than in an unblocked bundle. This reduced entrainment results in a slower heater rod cooldown rate.

FEBA series IV had a 62-percent blockage of a 3x3 rod cluster in a corner of a 5x5 rod bundle. The temperature transients plotted in figure 4-14 are from a test conducted with the same flooding conditions as those in figure 4-13. A comparable unblocked bundle test from series II is also shown. The most significant differences observed are the sleeve temperature and cladding temperature transients downstream of the blockage. The sleeves are quenched earlier than the cladding of the rods in the bypass. A new quench front is initiated downstream of the blockage before the main bundle quench front reaches the blockage level. The portion of the rod which is covered by a sleeve stays hot, indicating delayed heat removal from the blocked portion of the bundle. As figure 4-14 indicates, the 62-percent blockage test with bypass had lower temperature rises in both the blockage zone and the bypass rod zone compared to the unblocked bundle test from series II.

Therefore, it is concluded that coolant channel blockages of 62 percent and even 90 percent with bypass cause a decrease in cladding temperature rise compared to unblocked channel data under the same flooding conditions.

---

1. Pearson, K. G., et al., "Reflooding Experiments on a 49-Rod Cluster Containing a Long 90-Percent Blockage," AEEW-R-1591, January 1983.

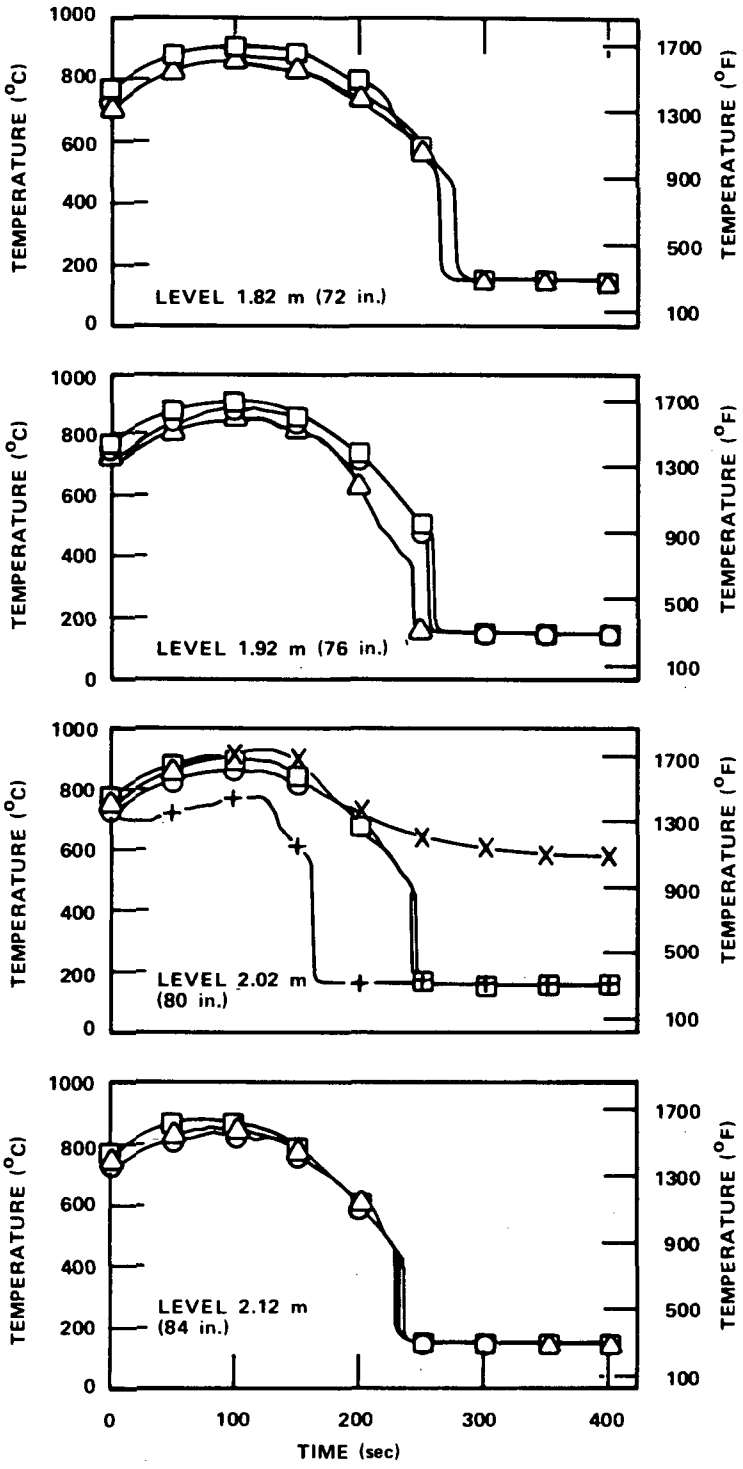

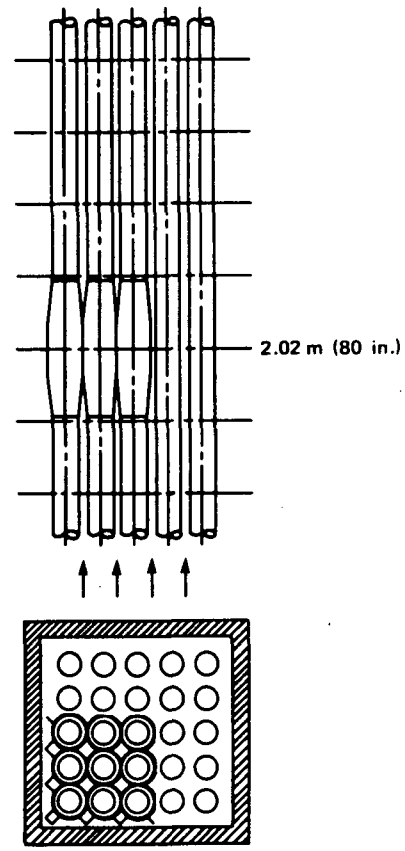

FLOODING RATE = 0.038 m/sec (1.5 in./sec)
PRESSURE = 0.40 MPa (58 psia)

SERIES II:

TEST 229
6 GRID SPACERS
UNBLOCKED BUNDLE

□ CLADDING

SERIES IV:

TEST 263
6 GRID SPACERS
BLOCKED BUNDLE (3 x 3 RODS)
BLOCKAGE AT LEVEL 2.02 m (80 in.)
BLOCKAGE RATIO 62%

○ BYPASS REGION
△ BLOCKED REGION
\+ SLEEVE
X UNDERNEATH SLEEVE

Figure 4-14. Cladding Temperature Results, FEBA Test Series IV

4-7. Flow Blockage and Grid Spacer Interaction

FEBA test series V and VI were designed to provide information about the combined effects of mass flux diversion and redistribution due to blockages and grids. For example, does the cross flow downstream of a 90-percent blockage lead to a reduction in the temperature increase downstream of the grid blockage? Therefore, a grid spacer was placed immediately downstream of a 90-percent blockage in series V. Although the grid spacer hinders cross flow over a certain rod length, it improves cooling downstream for a given mass flux.

A similar question arises if coplanar blockages are assumed to develop simultaneously at two different axial elevations in a rod cluster. Will the main coolant mass flux bypass both blockages and thus cause a hot region between the two blockage elevations? To address this question, the series VI array was tested in FEBA.

The results of one series V test are compared with the results obtained from series I, to investigate the blockage effect (figure 4-15). In series V and series VI, the 90-percent blockage was placed 0.10 m (4 in.) below the bundle midplane. The grid spacer placed downstream of the top end of the blockage reduces the maximum temperature compared to the unblocked bundle test from series I. The bypass rods show more cooling, because of the higher mass flow passing through the spacer compared to the unblocked bundle.

The cooling situation in the blockage region for a blockage followed by a grid spacer is essentially the same as that for an identical blockage not followed by a grid spacer. In the blockage region, up to the leading edge of the midplane grid spacer for series VI, a similar observation can be made.

However, for series VI, the grid spacer effect leads to much lower temperatures at the 1.92 m (76 in.) level upstream of the 62-percent blockage, as shown in figure 4-16. The temperature transients measured at and downstream of the 62-percent blockage are shown in figure 4-17. The sleeve temperatures in the 62-percent blockage and the cladding temperatures downstream are lower

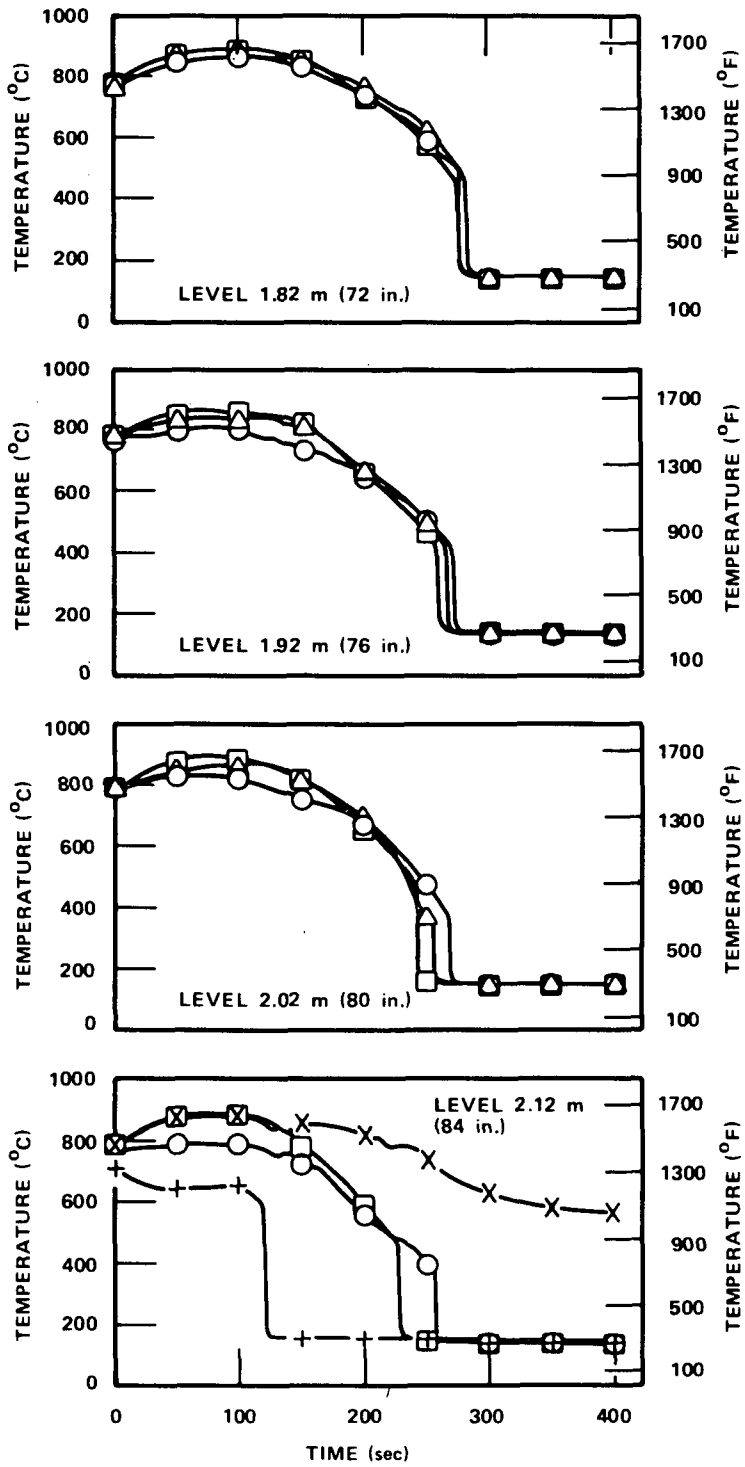

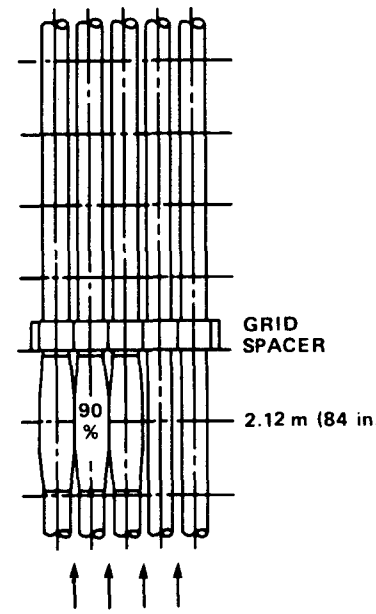

FLOODING RATE = 0.038 m/sec (1.5 in./sec)
PRESSURE = 0.40 MPa (58 psia)

SERIES I:
TEST 216
7 GRID SPACERS
UNBLOCKED BUNDLE

□ CLADDING

SERIES V:
TEST 282
7 GRID SPACERS
BLOCKED BUNDLE (3 X 3 RODS)
BLOCKAGE AT LEVEL 2.12 m (84 in.)
BLOCKAGE RATIO 90%

○ BYPASS REGION
△ BLOCKED REGION
\+ SLEEVE
X UNDERNEATH SLEEVE

Figure 4-15. Cladding Temperature Results, FEBA Test Series V

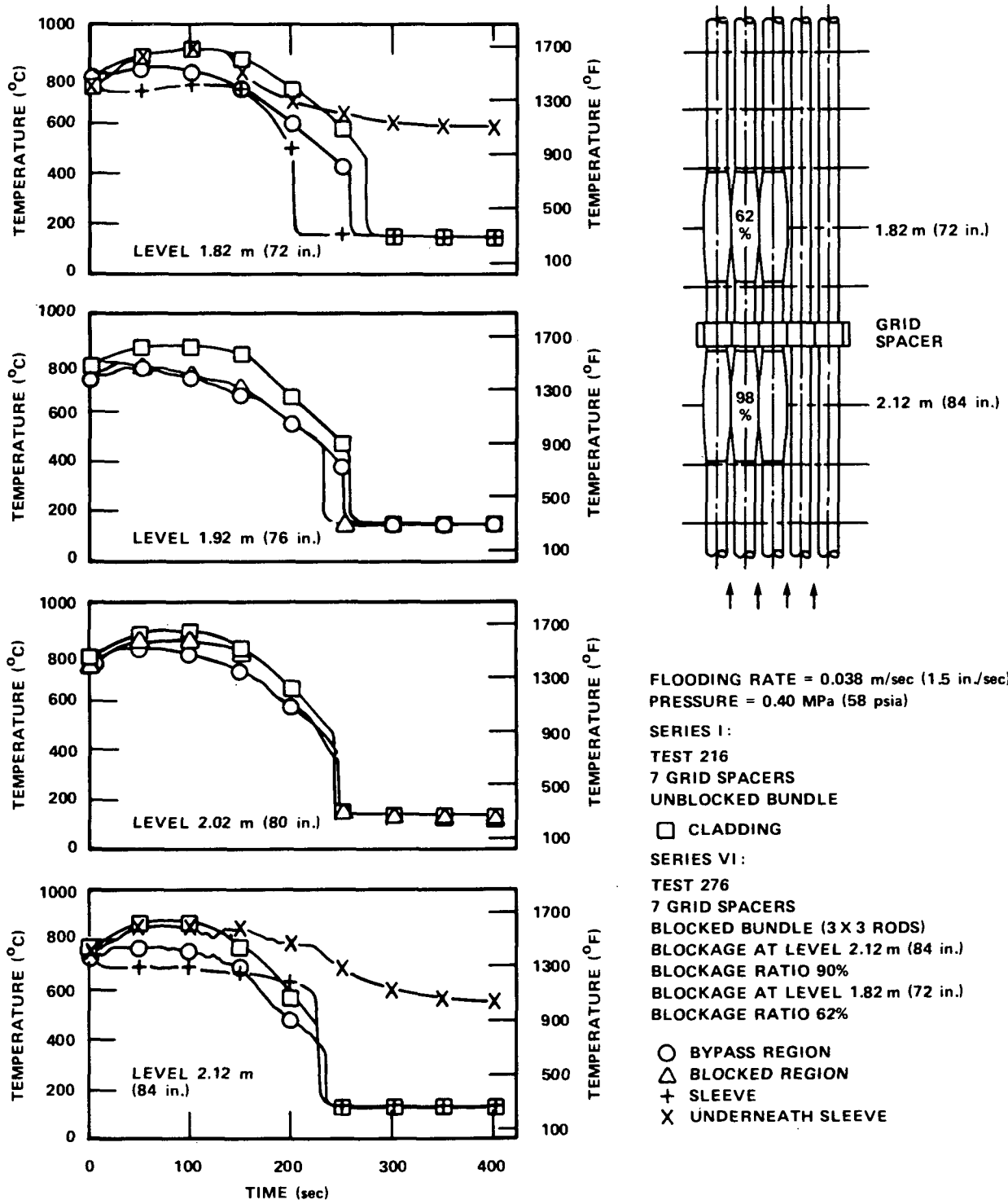

Figure 4-16. Cladding Temperature Results, FEBA Test Series VI

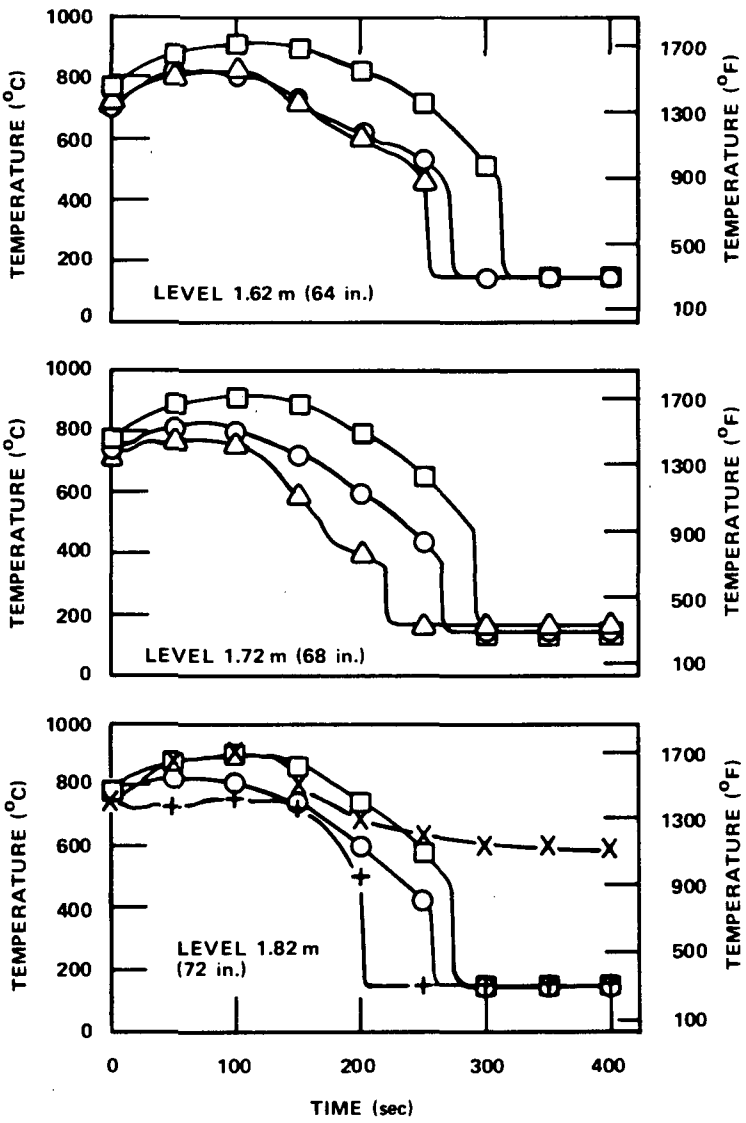

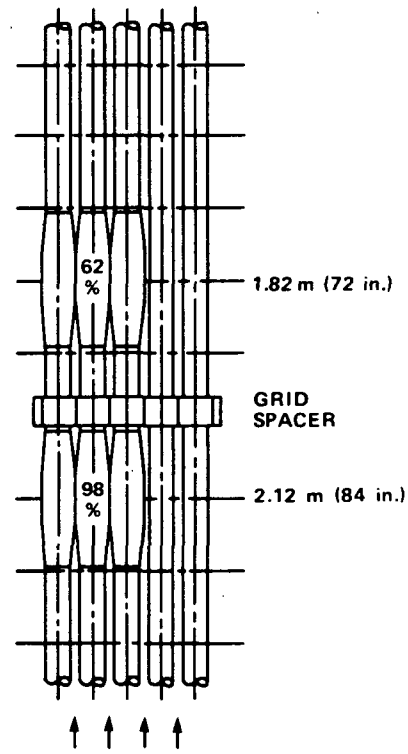

FLOODING RATE = 0.038 m/sec (1.5 in./sec)
PRESSURE = 0.40 MPa (58 psia)

SERIES I:

TEST 216
7 GRID SPACERS
UNBLOCKED BUNDLE

□ CLADDING

SERIES VI:

TEST 276
7 GRID SPACERS
BLOCKED BUNDLE (3 X 3 RODS)
BLOCKAGE AT LEVEL 2.12 m (84 in.)
BLOCKAGE RATIO 90%
BLOCKAGE AT LEVEL 1.82 m (72 in.)
BLOCKAGE RATIO 62%

○ BYPASS REGION
△ BLOCKED REGION
\+ SLEEVE
X UNDERNEATH SLEEVE

Figure 4-17. Cladding Temperature Results, FEBA Test Series VI

than the cladding temperatures in the bypass region and in the comparable unblocked series I test. This result is qualitatively consistent with the effects found in series IV. However, the mass flux through the 62-percent blockage, placed downstream of the 90-percent blockage, must have been reduced as compared with those in the bypass and in the unblocked series I test. A second region of higher cladding temperatures can be found far downstream of the upper blockage, out of the peak temperature zone.

4-8. Flow Blockage Without Bypass

For the blockage configurations with bypass, the coolant mass flux through the constricted subchannels is not readily discernible. This is not the case for series VII and VIII. At the bundle midplane, all subchannels are blocked by identical sleeves of the same design as the blockage arrays presented above. The mass flux transients for the constricted subchannels correspond then to those for the totally unblocked bundle. Strictly speaking, this is not representative of a reactor safety analysis, since it is calculated that unblocked bundles would exist, creating a bypass region. The tests were performed for series VII and VIII with blockage ratios of 62 percent and 90 percent, respectively, with all rods blocked (no flow bypass).

For blockages without bypass, the coolant mass flux through the constricted subchannels is increased significantly compared to that of the constricted subchannels of identical blockages with bypass. The cooling condition within the blockage was improved with all the rods blocked. Figure 4-18 shows temperature transients from a test of series VII [at the base case flooding conditions, flooding rate 0.038 m/sec and 0.4 MPa (1.5 in./sec and 58 psia)]. The cooling conditions within the blockage are similar for series VII and series IV. However, downstream of the blockage, the cooling enhancement increases significantly for the blockage without bypass. The downstream cooling effect is even larger for the 90-percent blockage (series VIII), as shown in figure 4-19. The results of test series VII and VIII allow quantitative analyses of the blockage effects on a basis similar to that used to analyze for the grid spacer effect.

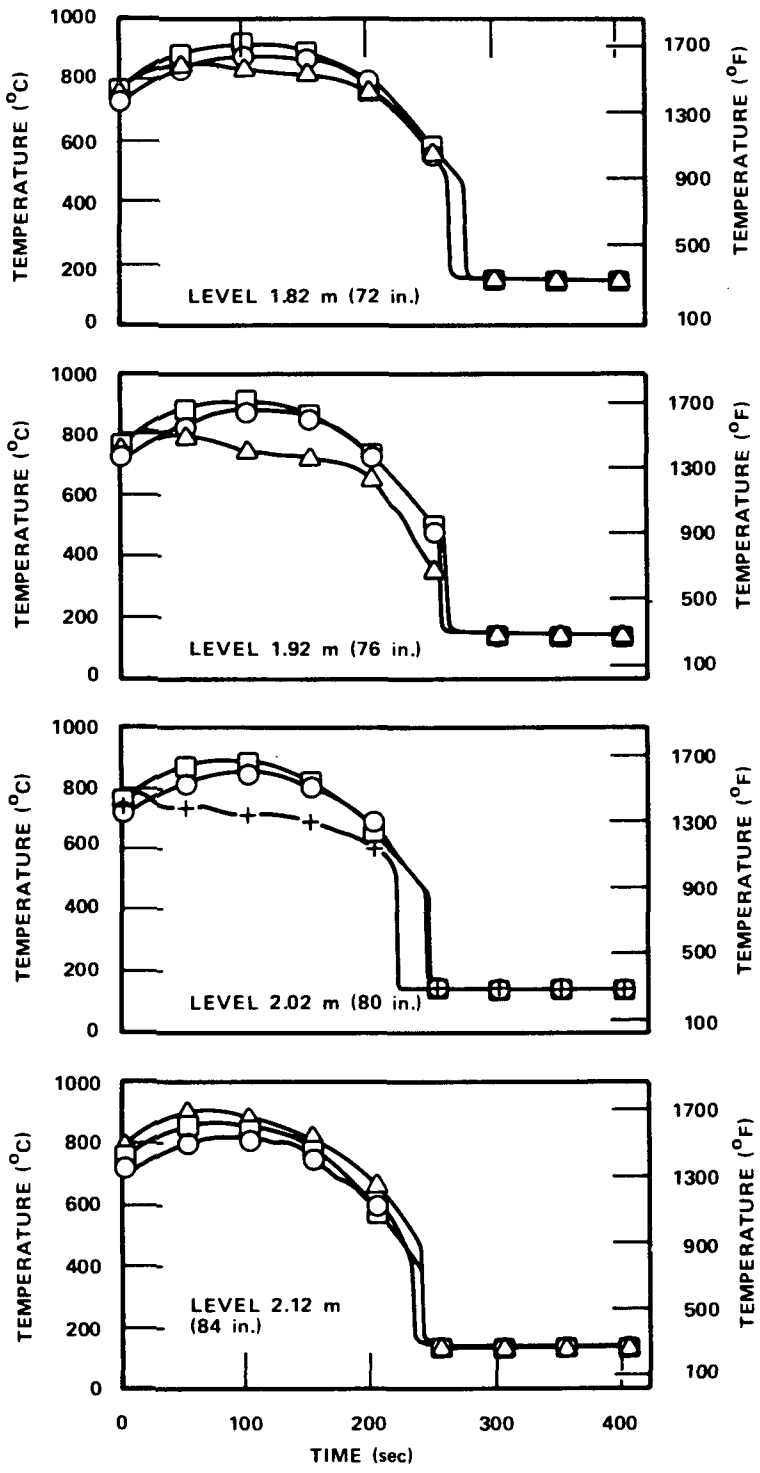

FLOODING RATE = 0.038 m/sec (1.5 in./sec)
PRESSURE = 0.40 MPa (58 psia)

TEST SERIES II:
TEST 229
6 GRID SPACERS
UNBLOCKED BUNDLE

□ CLADDING

SERIES IV:
TEST 263
6 GRID SPACERS
BLOCKED BUNDLE (3 X 3 RODS)
BLOCKAGE AT LEVEL 2.02 m (80 in.)
BLOCKAGE RATIO 62%

○ BYPASS REGION

SERIES VII:
TEST 324
6 GRID SPACERS
BLOCKED BUNDLE (5 X 5 RODS)
BLOCKAGE AT LEVEL 2.02 m (80 in.)
BLOCKAGE RATIO 62%

△ CLADDING
+ SLEEVE

Figure 4-18. Cladding Temperature Results, FEBA Test Series II + IV + VII

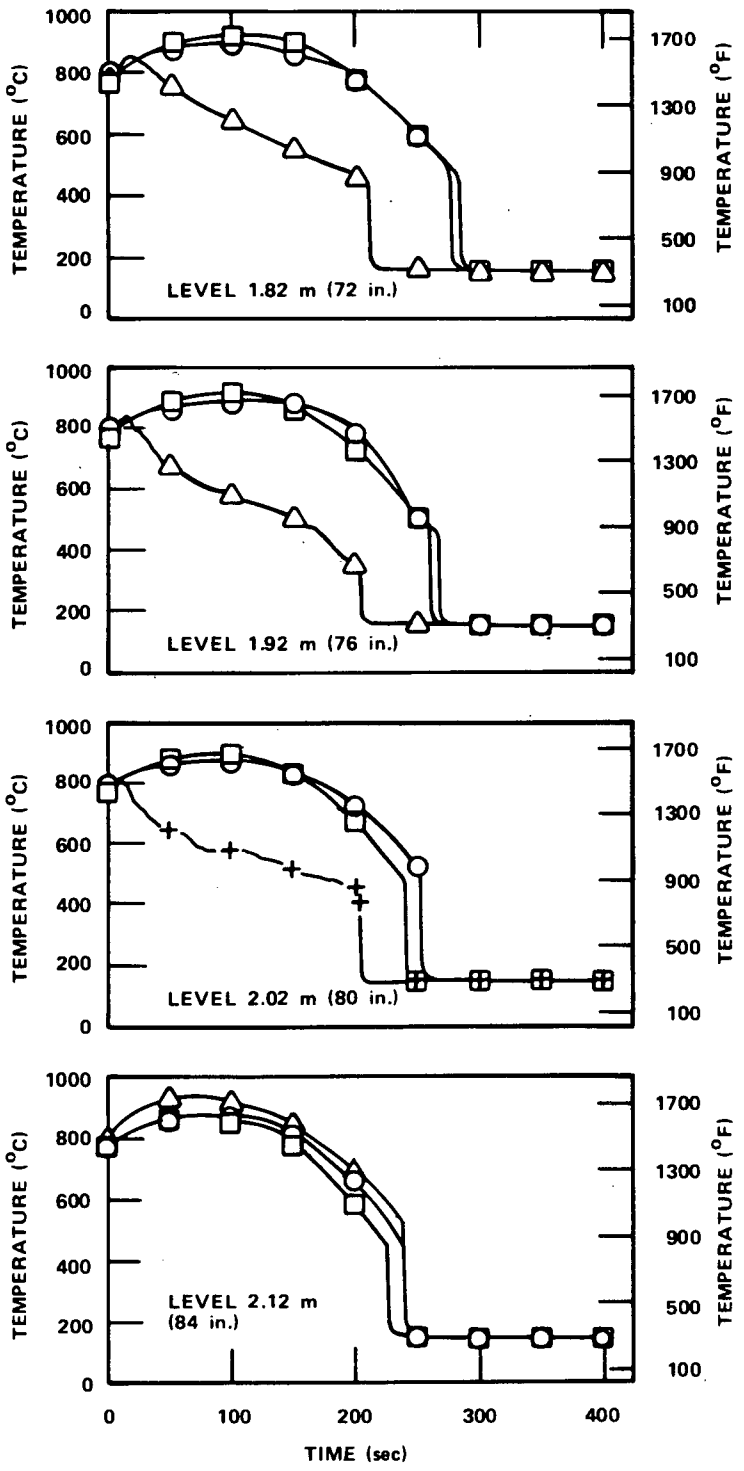

Figure 4-19. Cladding Temperature Results, FEBA Test Series II + III + VIII

The blockage effects seem to be smaller for single-phase flows than for dispersed two-phase flows. It is believed that the main reason for this is the improved effectiveness of the water content of the two-phase flow on the heat removal from the bundle. Normally, water entrained in the lower portion of the bundle is carried by the steam flow through the bundle without removing much heat along the way. With increasing number and/or size of flow obstacles, the amount of water carryover decreases and the overall heat removal increases. Entrained droplets can be dispersed and broken up at each flow obstacle, leading to an increase in the population of smaller droplets and hence enhanced cooling. The increased droplet evaporation due to blockages can be investigated quantitatively by comparing the water carryover for the different blockage arrays.

The water carryover measured from four tests performed with identical flooding conditions (pressure and flooding velocity) but different blockage geometries is presented in figure 4-20. About 30 percent of the water fed into the lower plenum has exited through the upper end of the bundle by the time of midplane quench for the tests of series IV. However, only 22 percent is carried over at the same time in the comparable test of series V with seven grid spacers and a 90-percent blockage array. For test series VI, with seven grid spacers and stacked 90-percent and 62-percent blockage arrays, only 14 percent of the water injected leaves the bundle within a time span of about 250 seconds. In this bundle, it is believed that the droplets hit the flow obstacles, shatter, and contribute to an enhanced evaporation, especially in the blocked rod cluster. Therefore, far downstream of the upper blockage, this drop depletion causes increased heating of the coolant as compared with the bypass. Just downstream of the upper blockage, cladding temperatures are lower than in the bypass region, but 0.200 m (8 in.) downstream, the situation reverses with the bypass rods being cooler.

From the data of test series VIII (all subchannels blocked, blockage ratio 90 percent), it can be concluded that nearly all the water content of the flow passing through the blockage is evaporated inside and downstream of the blockage. Consequently, no water carryover is measurable during the early portion of the reflood phase, as shown in figure 4-20. The high evaporation rate

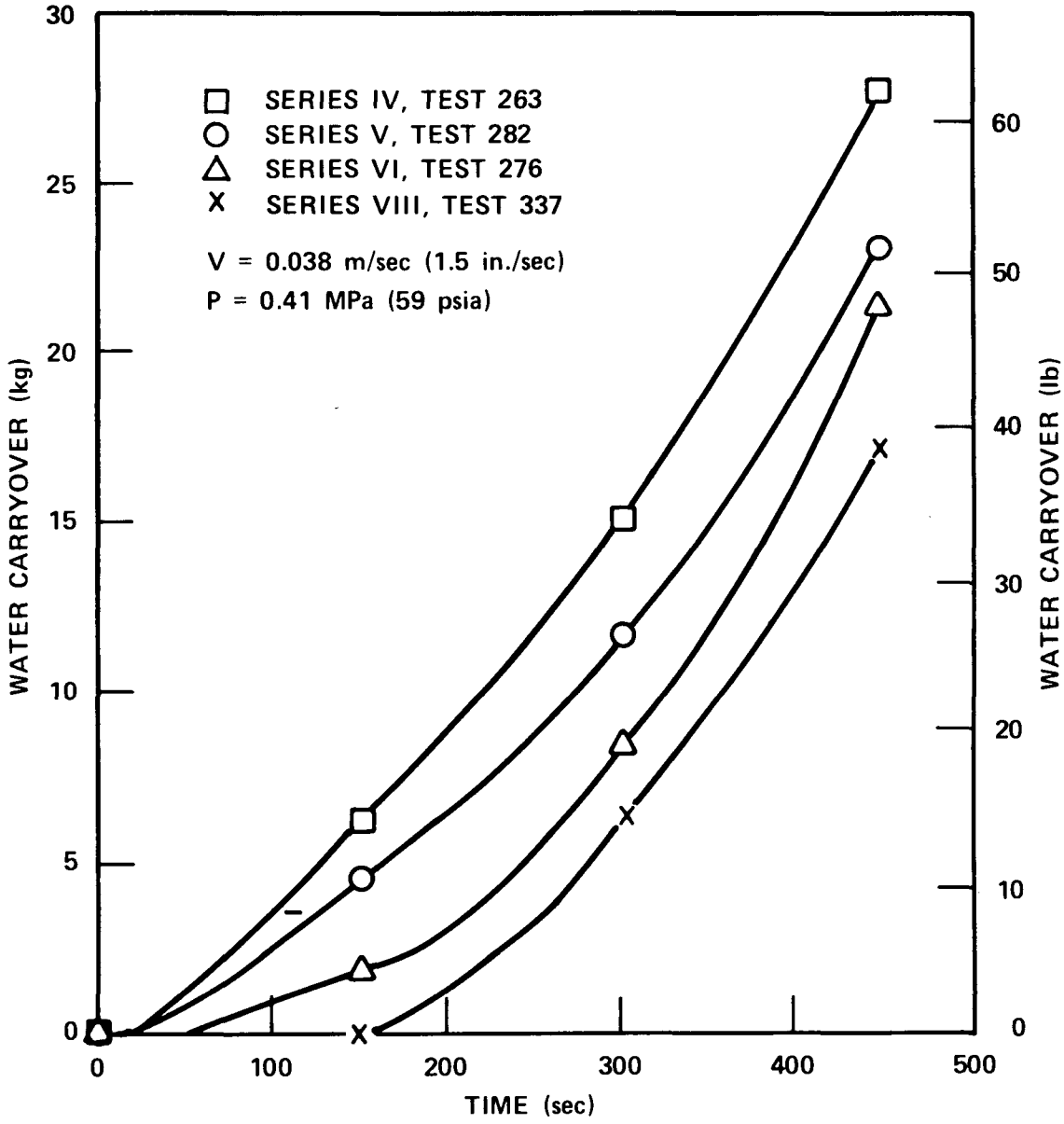

Figure 4-20. Influence of Water Carryover on Flow Blockage in FEBA Tests

inside and downstream of the blockage is believed to be responsible for the significantly higher observed heat transfer rates.

4-9. BLOCKAGE HEAT TRANSFER EFFECTS AND MODELS

Reviews of the FLECHT SEASET and FEBA flow blockage data suggest four heat transfer effects which need to be considered in blocked rod arrays during reflood:

- Flow redistribution effects due to blockage and their effect on the enthalpy rise of the steam behind the blockage. Bypass of steam flow could result in increased superheating of the remaining steam flow behind the blockage region. The higher the downstream steam temperature, the lower the rod heat flux and resulting heat transfer behind the blockage.

- Effect of blockage downstream of the blockage zone and the resulting steam mixing and droplet breakup behind the blockage. The breakup of the entrained water droplets will increase the liquid surface area so that the drops will become a more effective heat sink for the steam. The breakup should desuperheat the steam; this would result in greater rod heat transfer behind the blockage zone in the wake of the blockage.

- The heat transfer effects in the immediate blockage zone due to droplet impact, breakup, mixing, and cooling because of increased slip, and the increased steam velocity due to the blockage flow area changes. The droplet breakup is a localized effect primarily caused by the blockage geometry; it will influence the amount of steam generation which can occur farther downstream of the blockage.

- Effect of blockage on the upstream region of the blockage zone due to steam bypass, droplet velocities, and sizes

In summary, the flow blockage heat transfer effects are a combination of two key thermal-hydraulic phenomena:

- A flow bypass effect, which reduces the mass flow in the blocked region and consequently tends to decrease the heat transfer

- A single- and two-phase flow blockage heat transfer effect, which can cause flow acceleration, droplet breakup, improved mixing, steam desuperheating, and establishment of new boundary layers, and consequently tends to increase the heat transfer

These two effects, which are dependent on blockage geometry and distribution, counteract each other such that it is not evident which effect dominates over a range of flow conditions.

The flow blockage heat transfer effects described in paragraphs 4-2 through 4-8 can be separated into three individual effects:

- o Single-phase convective enhancement
- o Droplet breakup
- o Droplet impact heat transfer on the entrance region of the blockage

The following paragraphs describe the flow blockage models which have been incorporated into COBRA-TF.

4-10. Single-Phase Convective Enhancement

The distortion of a fuel channel by clad swelling will influence local heat transfer rates by changing the resistance to coolant flow and by disturbing the boundary layer on the clad surface. A model has been derived for the convective heat transfer enhancement due to boundary layer separation and reattachment.[1]

Calculation of the convective heat transfer enhancement can be divided into four parts:

- o A test for flow separation and its location
- o The location of the point of maximum heat transfer downstream of the flow separation point (the reattachment point)
- o The magnitude of the maximum Nusselt number
- o The axial distribution of the Nusselt number as it relaxes to its undisturbed value

1. Chiou, J. S., et al., "Models for PWR Reflood Calculations Using the BART Code," WCAP-10062, March 1982.

Each of these items is discussed below, for turbulent flow.

4-11. Flow Separation Point -- The separation point is determined using the criterion published by the Engineering Sciences Data Unit.[1] This criterion (figure 4-21) is a function of two nondimensional quantities, outlet area/inlet area and diffuser length/inlet radius, and is applicable to constant-angle diffusing sections and fully turbulent flow. The criterion has been simplified to the following equation:

$$\log y = 0.114 + 0.203 \log x + 0.04614 (\log x)^2 - 0.01995 (\log x)^3 \quad (4\text{-}1)$$

where

$$x = \frac{L_\chi}{R_1} = \text{nondimensional distance from diffuser inlet}$$

The following iterative procedure is employed to determine if and where the flow separates:

- Choose downstream location, L_χ (figure 4-22).
- Determine local flow area, A_χ, at L_χ.
- Calculate Y from equation (4-1).
- If A_χ/A_1, the ratio of local flow area to diffuser inlet area necessary for separation to occur, equal to or greater than y, separation occurs.
- Iterate until A_χ/A_1 is equal to y. The current value of L_χ is the separation point.

This procedure is not calculated by COBRA-TF; the user must determine the flow separation point separately and then specify it as input.

---

1. "Performance of Conical Diffusers in Incompressive Flow," ESDU Item No. 73024, Engineering Sciences Data Unit, London, pp. 251-259.

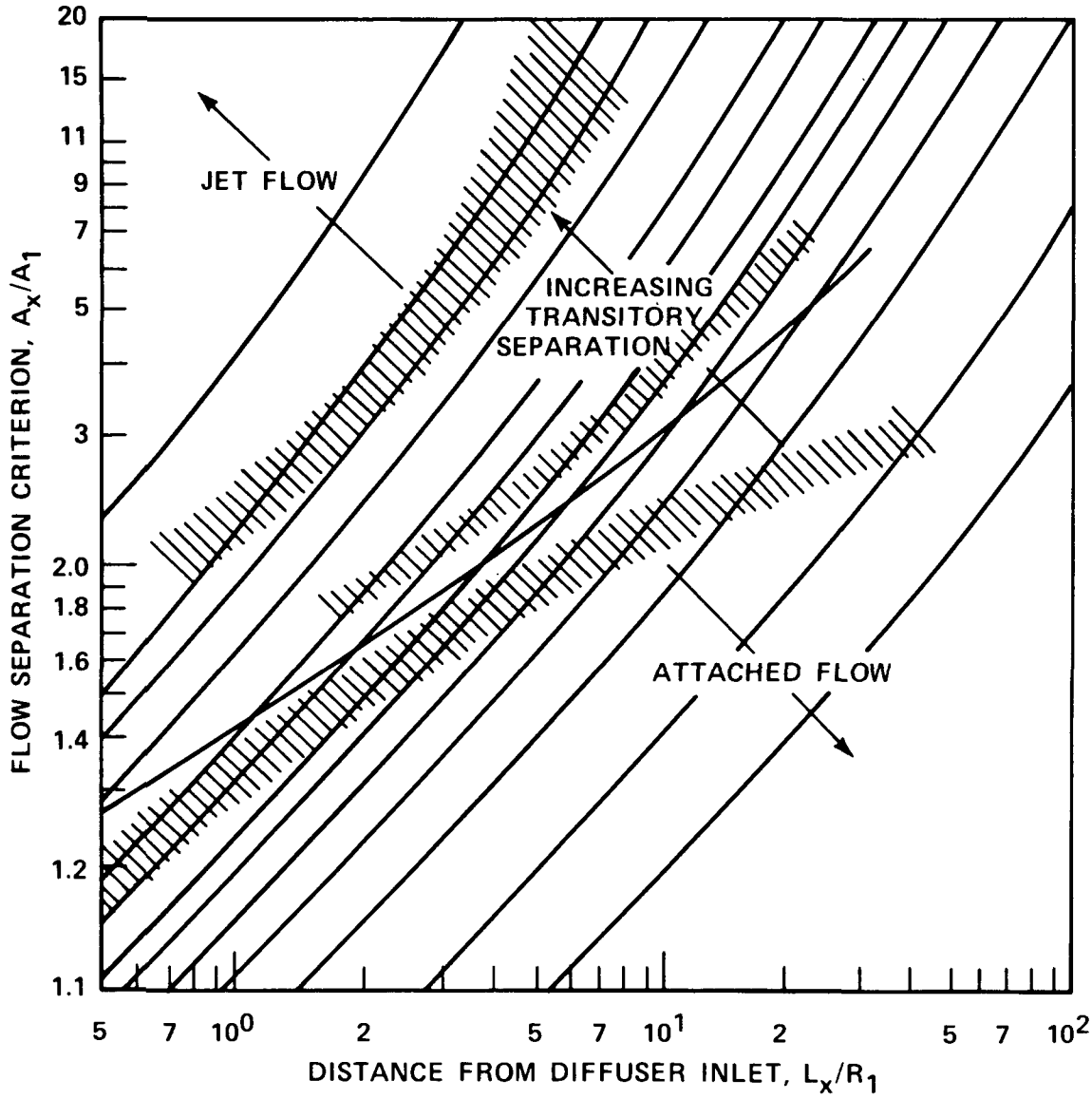

Figure 4-21. ESDU Flow Separation Criterion

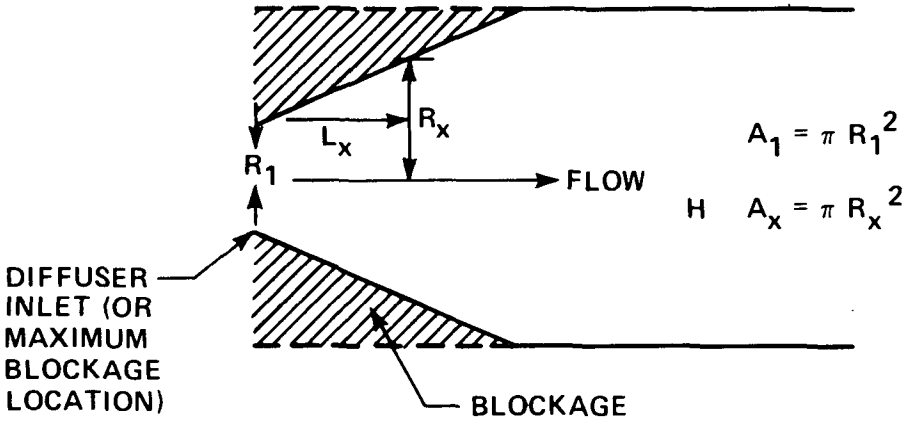

Figure 4-22. Single-Tube Diffuser

This criterion indicates that flow separation will occur at the end of the FLECHT short cosine sleeve, near the end of the FEBA 62-percent blockage, and near the beginning of the exit region of the FEBA 90-percent blockage.

4-12. Maximum Nusselt Number Location -- Calculation of the reattachment point and the enhancement decay to the undisturbed value is based on abrupt expansion tube data. The assumption is made that convective enhancement due to flow separation in a diffuser can be represented by an equivalent abrupt expansion.

Zemanick and Dougall[1] collected data from a variety of abrupt expansion tests and have related the location of the maximum Nusselt number to the step height of the expansion, $(D_o - D_{sep})/2$, where

D_o = diameter of undisturbed tube
D_{sep} = diameter at separation point

The data indicate that the point of maximum Nusselt number occurs six to ten step heights past the separation point. Because there is no obvious dependency on Reynolds number, a constant value of eight step heights was chosen.

4-13. Maximum Nusselt Number -- Zemanick and Dougall correlated their data from abrupt expansion experiments (D_a/D_o = 0.43 - 0.82) with air and found

$$Nu_{max} = 0.2\ Re_{D_a}^{2/3} \qquad (4\text{-}2)$$

where

D_a = diameter immediately upstream of the expansion; for the blockage case, $D_a = D_{sep}$, for orifice, $D_a = D_{orifice}$

D_o = diameter of undisturbed tube

1. Zemanick, P. P., and Dougall, R. S., "Local Heat Transfer Downstream of an Abrupt Circular Channel Expansion," J. Heat Transfer, February 1970, 53-60.

Re_{D_a} = Reynolds number based on the fluid condition and diameter immediately upstream of the expansion

Krall and Sparrow[1] derived a similar correlation from water tests using an orifice plate in a pipe (D_a/D_o = 1/4 ~ 2/3).

The above correlation for Nu_{max} can be expressed in the form of an enhancement factor by dividing by the correlation for fully developed flow. If the 161-rod bundle steam cooling correlation[2] is used, then

$$\frac{Nu_{max}}{Nu_o} = \frac{0.2\ Re_{D_{sep}}^{2/3}}{0.0797\ Re_{D_o}^{0.6774}} \cong 2.5/\left(\frac{D_o}{D_{sep}}\right)^{2/3} \qquad (4\text{-}3)$$

Equation (4-3) illustrates that the enhancement factor, like the maximum Nusselt number location, is essentially independent of Reynolds number. This expression for local enhancement is only used after the flow separation criterion has been met.

Equation (4-3) has been compared with data from the single-phase REFLEX tests,[3] several FLECHT SEASET 21-rod bundle steam cooling tests,[2] and measurements reported by Emerson[4] [a 1.6 mm (1/16 in.) high rib in a 76 mm (3 in.) diameter tube]. The comparison is of Nu_{max}/Nu_o is shown in figure 4-23, where the enhancement factor has been plotted as a function of the

---

1. Krall, K. M., and Sparrow, E. M., "Turbulent Heat Transfer in the Separated, Reattached, and Redevelopment Regions of a Circular Tube," J. Heat Transfer, February 1966, 131-136.

2. Loftus, M. J., et al., "PWR FLECHT SEASET 21-Rod Bundle Flow Blockage Task Data and Analysis Report," NRC/EPRI/ Westinghouse-11, September 1982.

3. Chiou, J. S., et al., "Models for PWR Reflood Calculations Using the BART Code," WCAP-10062, March 1982.

4. Emerson, W. H., "Heat Transfer in a Duct in Regions of Separated Flow," NEL Report 256, 1966.

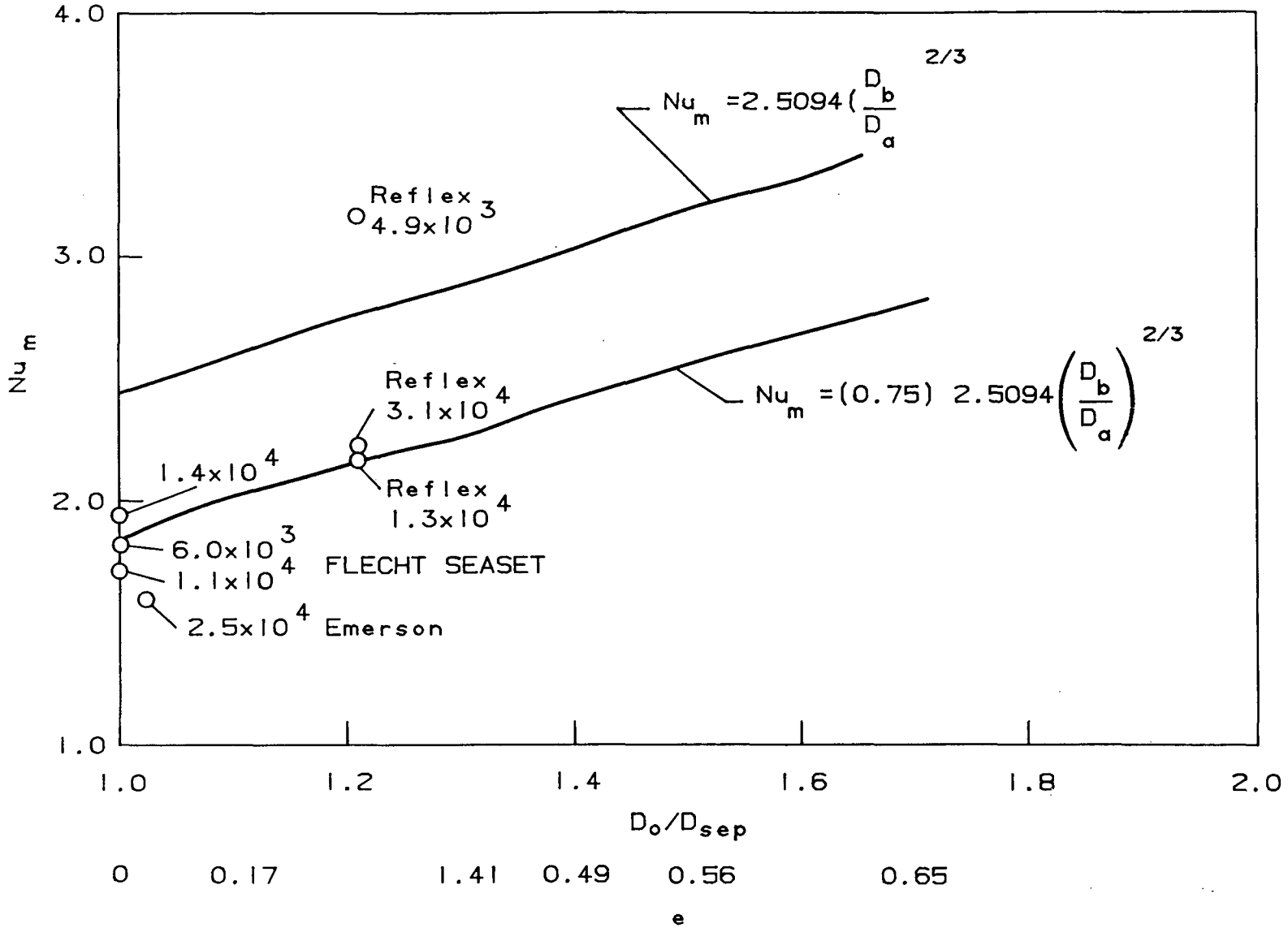

Figure 4-23. Maximum Nusselt Number Enhancement Versus Diameter Ratio (D_b/D_a)

diameter ratio. It can be seen that the REFLEX and FLECHT SEASET data fall below the values predicted by equation (4-3). This is not surprising and can be interpreted as indicative of the difference between an abrupt expansion and separation, and of a smoother contraction and expansion more typical of a blocked channel. From inspection, the maximum value of the Nusselt number after separation should be reduced by a factor of 0.75. Thus,

$$\frac{Nu_{max}}{Nu_o} = 1.88 \left(\frac{D_o}{D_{sep}} \right)^{2/3} \tag{4-4}$$

and

$$Nu_{max} = 0.15 \, Re_{D_{sep}}^{2/3} \tag{4-5}$$

The Nusselt number in the separation region will be calculated by linear interpolation between the separation point ($Nu_z/Nu_o = 1$) and the location of the maximum Nusselt number.

4-14. Axial Decay of Enhancement Factor

The Nusselt number will return to its fully developed value as the reattached boundary layer develops and the free stream turbulence decays. The data of Krall and Sparrow were analyzed and found to exhibit an exponential decay with distance from the Nu_{max} location with no significant dependence on Reynolds number ($10^4 < Re < 1.3 \times 10^5$). The decay for a Reynolds number of 1×10^4 is plotted as a function of the diameter ratio (D_o/D_a) in figure 4-24. The data are approximated by the straight-line equation

$$C = 0.6 - 0.45 \frac{D_a}{D_o}$$

and the axial decay of the enhancement is described by

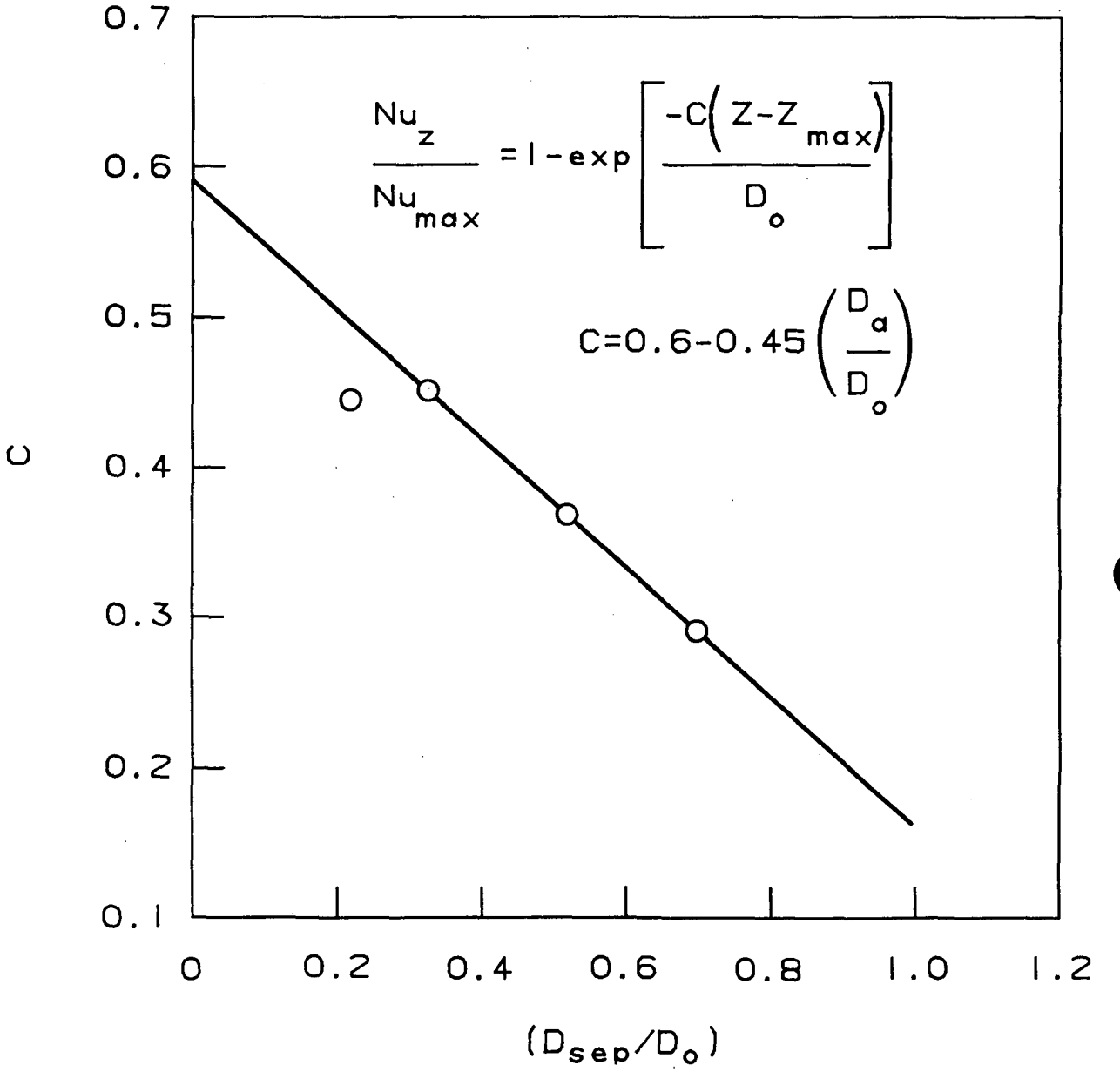

Figure 4-24. Variation of Exponential Decay Constant With Diameter Ratio (D_b/D_a)

$$\frac{Nu_z}{Nu_{max}} = 1 - \exp - \left[0.6 - \left(0.45 \frac{D_{sep}}{D_o}\right) \left(\frac{Z - Z_{max}}{D_o} \right) \right] \quad . \qquad (4\text{-}6)$$

In summary, the heat transfer enhancement for the flow downstream of a reattachment point is

$$\frac{Nu_z}{Nu_o} = \frac{Nu_{max}}{Nu_o} \left\{ 1 - \exp \left[-\left(0.6 - 0.45 \frac{D_{sep}}{D_o}\right) \left(\frac{Z - Z_{max}}{D_o} \right) \right] \right\} \qquad (4\text{-}7)$$

where

$$\frac{Nu_{max}}{Nu_o} = 1.88 \left(\frac{D_o}{D_{sep}} \right)^{2/3}$$

The above equations were derived from single-tube experiments. For application to blocked rod bundles, D_o and D_{sep} in equations (4-4), (4-6), and (4-7) were calculated based on the actual subchannel flow area, as

$$D = \left(\frac{4(\text{flow area})}{\pi} \right)^{1/2}$$

In COBRA-TF, the enhancement factor, Nu_z/Nu_o, is integrated over each axial node. The resulting averaged enhancement factor for each node is multiplied by the undisturbed Nusselt number (based on the hydraulic diameter $D_{o,hyd}$) to get the local Nusselt number.

The heat transfer model given in equation (4-7), which is based on the abrupt expansion tube data, has been compared with the data obtained downstream from the blockage in the single-phase tube flow REFLEX tests and also the single-phase FLECHT SEASET 21-rod bundle tests, in which all rods had flow area short cosine balloons with 62-percent coplanar blockage. The comparisons are shown in figures 4-25 and 4-26. Agreement between the experimental data and the model is considered satisfactory.

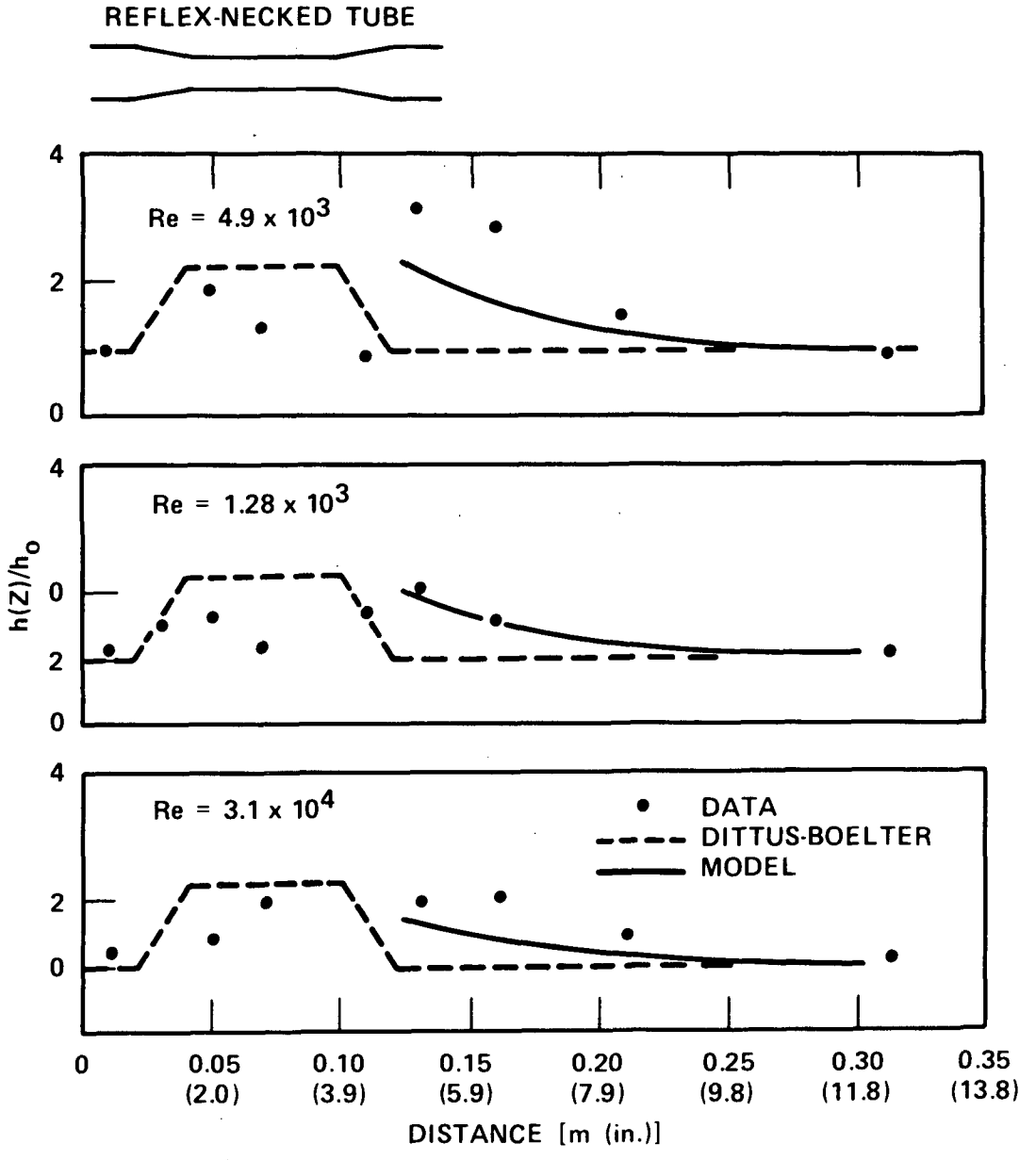

Figure 4-25. Comparison of COBRA-TF Predictions and REFLEX Heat Transfer Data

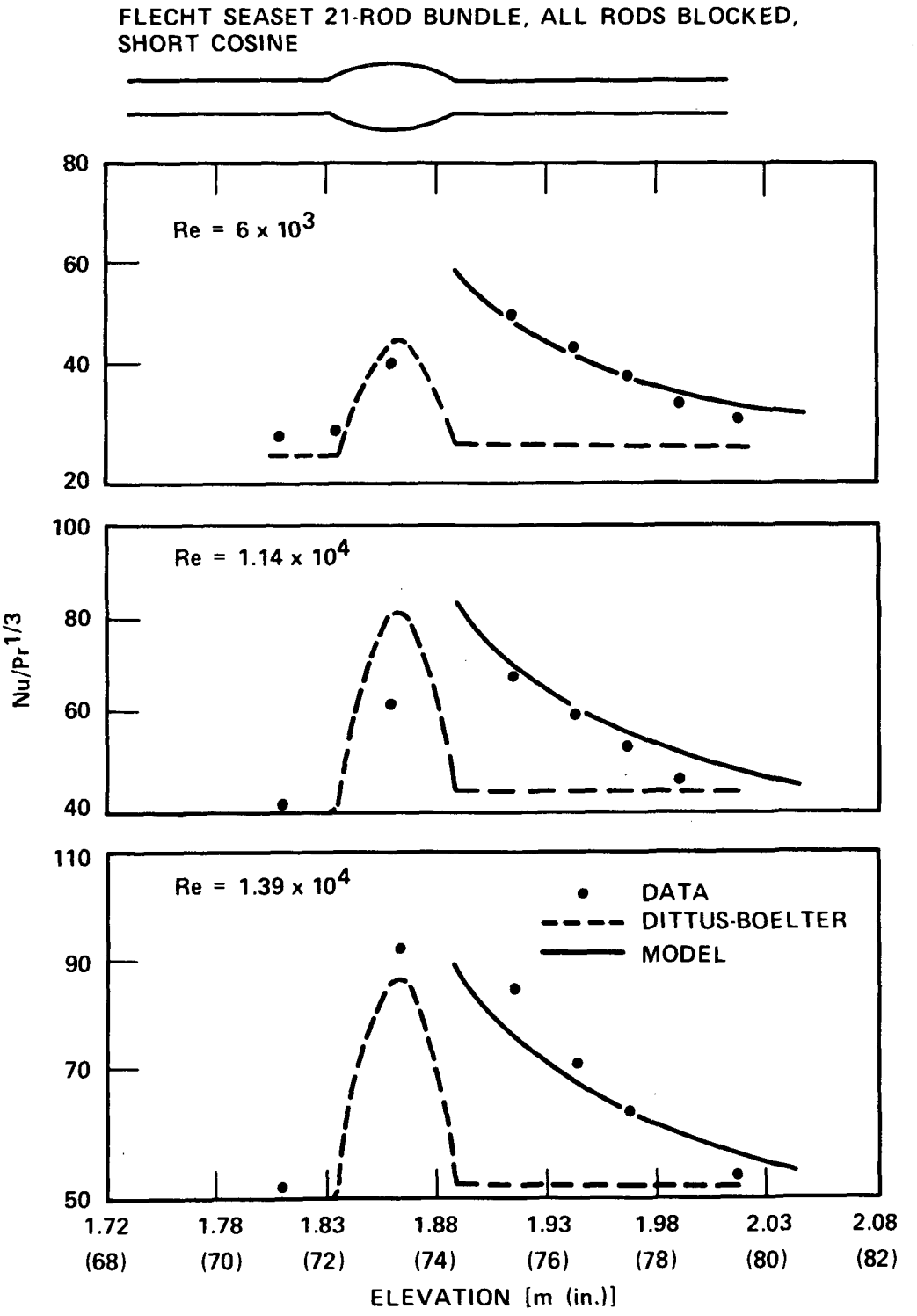

Figure 4-26. Comparison of COBRA-TF Predictions and FLECHT SEASET 21-Rod Bundle Heat Transfer Data

4-15. Blockage Droplet Breakup Model

Droplets impacting on a flat plate heated above the Leidenfrost point undergo a process of deformation, flattening, and reformulation.[1,2] As the drop velocity component normal to the plate increases, the droplet spreads into a liquid sheet so thin that surface tension forces cannot reform the drop and shattering occurs. For droplet shattering to occur the impact Weber number, We_D, must be greater than 30, where

$$We_D = \frac{\rho V_d^2 D_d}{g_c \sigma}$$

where V_d is the normal component of the drop velocity.

The concentric sleeve geometries employed in the FLECHT SEASET and FEBA tests have an incident angle of approximately 3 degrees in the converging section of the blockage, such that the normal component of the droplet velocity is quite small. Clearly, unrealistically high drop axial velocities would be required to exceed the impact Weber number shattering criterion. However, an examination of the converging sections reveals an area in the gap region where incident drops would be "captured" and constrained to lose most of their axial momentum. In effect, this small region would appear to act as a flat plate normal to the droplet flow for entrained drops traveling at high velocities. The drops would be captured an shattered into a population of small microdrops in the blockage.

A droplet breakup model, similar to that employed for grid spacers, was formulated to account for the breakup in this "flat plate" region. The mass source

---

1. Wachters, L. H. J., and Westerling, N. A. J., "The Heat Transfer From a Hot Wall to Impinging Water Drops in a Spheroidal State," Chem. Eng. Sci. 21, 1966, 1047-1056.

2. Wachters, L. H. J., et al., "The Heat Transfer From a Hot Wall to Impinging Mist Droplets in the Spheroidal State," Chem. Eng. Sci. 21, 1966, 1231-1238.

of microdrops generated is expressed as a function of the entrained drop flow rate and the blockage drop breakup area:

$$\dot{m}_{DB} = \eta \cdot \left(\frac{A_{DB}}{A_C} \right) \cdot \dot{m}_e \qquad (4\text{-}8)$$

The drop breakup area, A_{DB}, is the projected area of the portion of the blockage that appears as a flat plate. Figure 4-27 shows the drop breakup area fraction as a function of blockage fraction and appendix C presents the methodology employed to calculate this area. The blockage efficiency factor, η, represents the portion of the drop within this projected area that is shattered into microdrops. By means of a sensitivity study, employing both FEBA and FLECHT SEASET 21-rod data, the value of η was estimated to be 0.25. If a population of small drops, generated by shattering at an upstream grid spacer, is also incident upon the blockage, they are assumed to divert around the flat plate area and not experience further breakup. The basis for this assumption is the three-dimensional converging channel formed by the blockage sleeves. The smaller microdrops generated at an upstream grid would have less inertia and could more easily follow the streamlines in the flow generated by the blockage geometry.

To complete the drop breakup model, the shattered drop size must be specified in addition to the mass source term. The shattered drop size was derived from the unquenched flat plate data of Wachters[1,2] and Takeuchi[3] and is

---

1. Wachters, L. H. J., and Westerling, N. A. J., "The Heat Transfer From a Hot Wall to Impinging Water Drops in a Spheroidal State," Chem. Eng. Sci. 21, 1966, 1047-1056.

2. Wachters, L. H. J., et al., "The Heat Transfer From a Hot Wall to Impinging Mist Droplets in the Spheroidal State," Chem. Eng. Sci. 21, 1966, 1231-1238.

3. Takeuchi, K., et al., "Experimental Studies on the Behavior of a Small Droplet Impinging Upon a Hot Surface," Proceedings of the Second International Conference on Liquid Atomization and Spray Systems, 1982, 397-404.

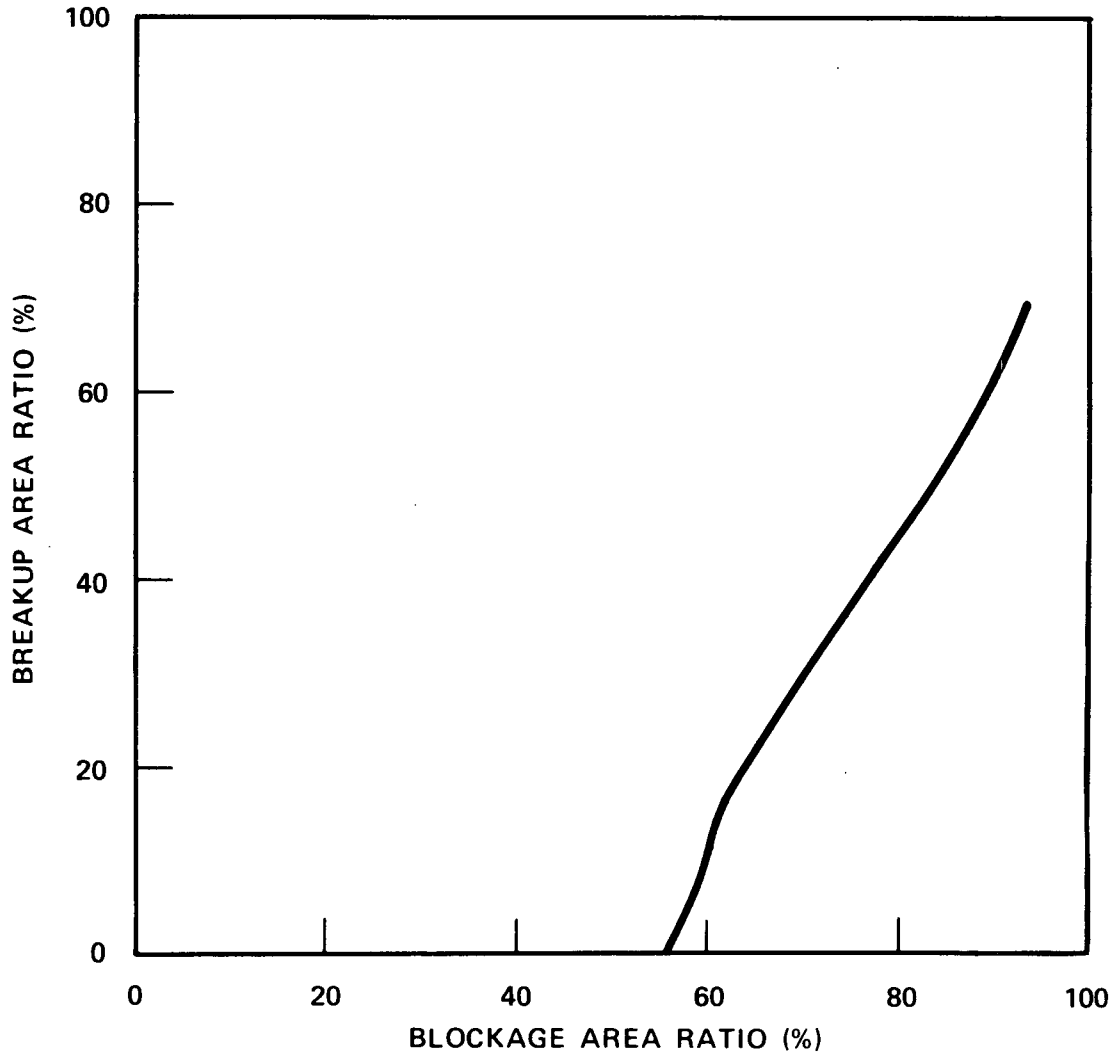

Figure 4-27. Breakup Area Ratio as a Function of Blockage Area Ratio

expressed as a function of impact Weber number similar to the grid droplet breakup correlation given in section 3:

$$\frac{D_{SD}}{D_I} = \exp\left[-\frac{(We_D - 30)}{124}\right] \qquad (4\text{-}9)$$

The ratio of shattered to incident drop diameter is constrained to be greater than 0.05. The methods used in COBRA-TF to handle the small drop field are discussed in section 3.

4-16. Drop Impact Heat Transfer

Iloeje[1] observed that direct liquid contact between droplets and a wall was negligible at high wall superheats. However, droplets can penetrate into the region near the wall, causing additional vaporization and improving the heat transfer. Kendell and Rohsenow[2] have developed a droplet impact model to predict the heat transfer efficiency of an individual droplet impacting a superheated surface. The drop contact heat transfer efficiency is defined as a percentage of the impacting drop evaporated. The heat removed due to drop impact at the blockage inlet is

$$Q = \dot{m}_e \left(\frac{\text{A projected blockage area normal to the flow}}{\text{a normal flow area}}\right) h_{fg}\, \varepsilon \qquad (4\text{-}10)$$

where

$\dot{m}_e$ = total liquid entrainment flow rate

h_{fg} = latent heat of vaporization

ε = droplet contact heat transfer efficiency

The Kendall/Rohsenow model predicts that the drop will spread into a liquid sheet separated from the heated surface by a thin vapor film. The total heat

---

1. Iloeje, O. C., et al., "Three-Step Model of Dispersed Flow Heat Transfer (Post-CHF Vertical Flow)," ASME Paper 75-WA/TH-1, 1978.

2. Kendell, G. E., and Rohsenow, W. M., "Heat Transfer to Impacting Drops and Post-Critical Heat Flux in Dispersed Flow," MIT Report 85694-100, 1978.

transfer to the drop includes the additional evaporation of the drop on the side facing the heated surface as the drop moves toward the wall. Photographs taken by Wachters (referenced previously) indicate that the drop undergoes a process of deformation, flattening, and reformulation due to the liquid surface tension, as described above. The model developed by Kendall and Rohsenow predicts this droplet behavior and the resulting evaporation efficiency. In this model, the main parameter was found to be the velocity of the drop normal to the heated surface.

The equation for droplet heat transfer effectiveness from the Kendell/Rohsenow model is given as

$$\varepsilon = 2.6 \left(\frac{\rho_v}{\rho_\ell}\right)^{1/2} \left(\frac{R}{D}\right) \left(\frac{\rho_\ell V_p^2 D}{\sigma g_c}\right)^{1/8} \cdot \left[\frac{\beta_2 k_v (T_w - T_s)}{h_{fg} (\rho_v \sigma g_c D)}\right]^{1/2} \cdot \left[I_2 \frac{\mu_v h_{fg}}{\beta_2 k_v (T_w - T_s)} + I_1\right]^{-1/4} \quad (4\text{-}11)$$

I_1 and I_2 are constants with values of 0.225 and 1.5 respectively. R is the average drop extension radius over the impact period.

$$\bar{R} = \frac{R_{max} + 0.43\, D}{2} \quad (4\text{-}12)$$

R_{max} is the maximum extension radius, derived by equating the initial kinetic energy of the drop to the surface tension energy in the drop when it has come completely to rest:

$$\frac{R_{max}^2}{D^2} = \frac{2}{3}\left(1 + \frac{We_p}{12}\right) \cos^2\left[\frac{1}{3}\left\{\arccos\left[\frac{-1.225}{\left(1 + \frac{We_p}{12}\right)^{3/2}}\right]\right\}\right] \quad (4\text{-}13)$$

The Weber number used in this equation, We_p, is defined using the initial inertia of the drop perpendicular to the wall, which is the same Weber number for either grid or droplet breakup:

$$We_p = \frac{\rho_\ell V_p^2 D}{\sigma g_c} \tag{4-14}$$

The maximum extension radius calculated by equation (4-12) is limited to $We_p > 1.74$. This limitation arises from the assumption that the drop is a circular cylinder. Before deformation, the sphere and cylinder surface energies are not equal if the volumes are assumed equal; an initial amount of kinetic energy is required to account for the difference. For We_p less than 1.74, it is assumed that $R_{max} = 0.43\ D$, which is consistent with equations (4-11) and (4-12). The factor β_2 accounts for the nonlinear temperature profile beneath the droplet:

$$\beta_2 = \frac{1}{1 + 0.3 \frac{C_p (T_w - T_s)}{h_{fg}}} \tag{4-15}$$

Equations (4-12) through (4-15) can be combined to calculate the drop impact heat transfer efficiency, ε. Then, from equation (4-10), the wall to droplet heat flux can be calculated.

For ordinary parallel flow channels, the drop impact heat transfer is negligible because of low values of We_p. Even for flow blockages where the channels are converging with a slight angle (3 to 5 degrees), We_p will be small so that the effect of drop impact heat transfer is small. For FLECHT SEASET short cosine blockage sleeve and long nonconcentric sleeve, the converging angle is less than 3 degrees.

Then,

$$We_p \sim (V_p^2) = (V^2 \sin^2 3°) = 0.00274\ V$$

where

V_p = perpendicular velocity
V = normal droplet velocity in Z direction
We_p = perpendicular Weber number

Thus, the effect of drop impact heat transfer for FLECHT SEASET blockage is very small compared to the other two-phase blockage heat transfer mechanisms.

4-17. NONCOPLANAR BLOCKAGE MODELING

A three-dimensional drawing of the blockage sleeve distribution is given in figure 4-28 for the FLECHT SEASET 21-rod bundle configuration D. This same noncoplanar distribution was employed for the 21-rod bundle configuration F and the 163-rod bundle blockage islands. This geometry constrains the fluid to follow a serpentine path through the blockage region. Locally significant diversion cross flows exist, resulting in large channel-to-channel variations. This behavior is illustrated in figure 4-29, a plot of the single-phase vapor heat transfer enhancement from steam cooling test 40901F.

An extremely fine discretization is required to reproduce this complicated flow pattern computationally. Both the radial (every subchannel) and axial ($\Delta Z \leq 25$ mm) noding requirements would be excessive. Furthermore, during a transient, the COBRA-TF time step is limited by the Courant condition, which is inversely proportional to the axial node size. Consequently, it is impractical to attempt to model this sinuous flow path in detail.

To gain an insight into how to model a noncoplanar blockage, the two-phase reflooding heat transfer results from a noncoplanar blockage (configuration F) were compared to those of a coplanar blockage (configuration C). Figures 4-30 and 4-31 compare the heat transfer coefficients at 20 seconds for tests with 0.023 and 0.038 m/sec (0.91 and 1.5 in./sec) flooding rates, respectively. The noncoplanar data are given for each thermocouple; an envelope represents

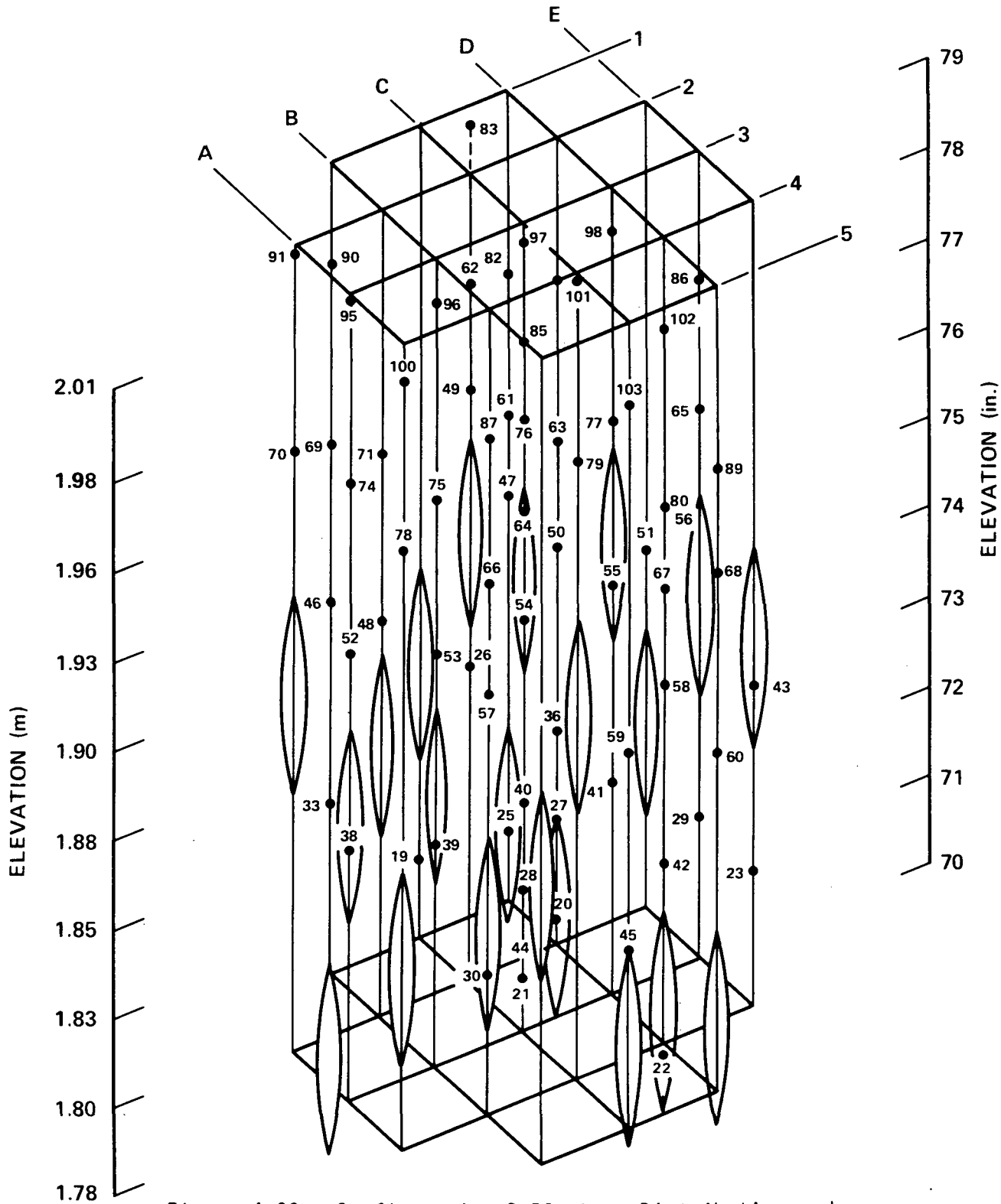

Figure 4-28. Configuration D Blockage Distribution and Instrumentation

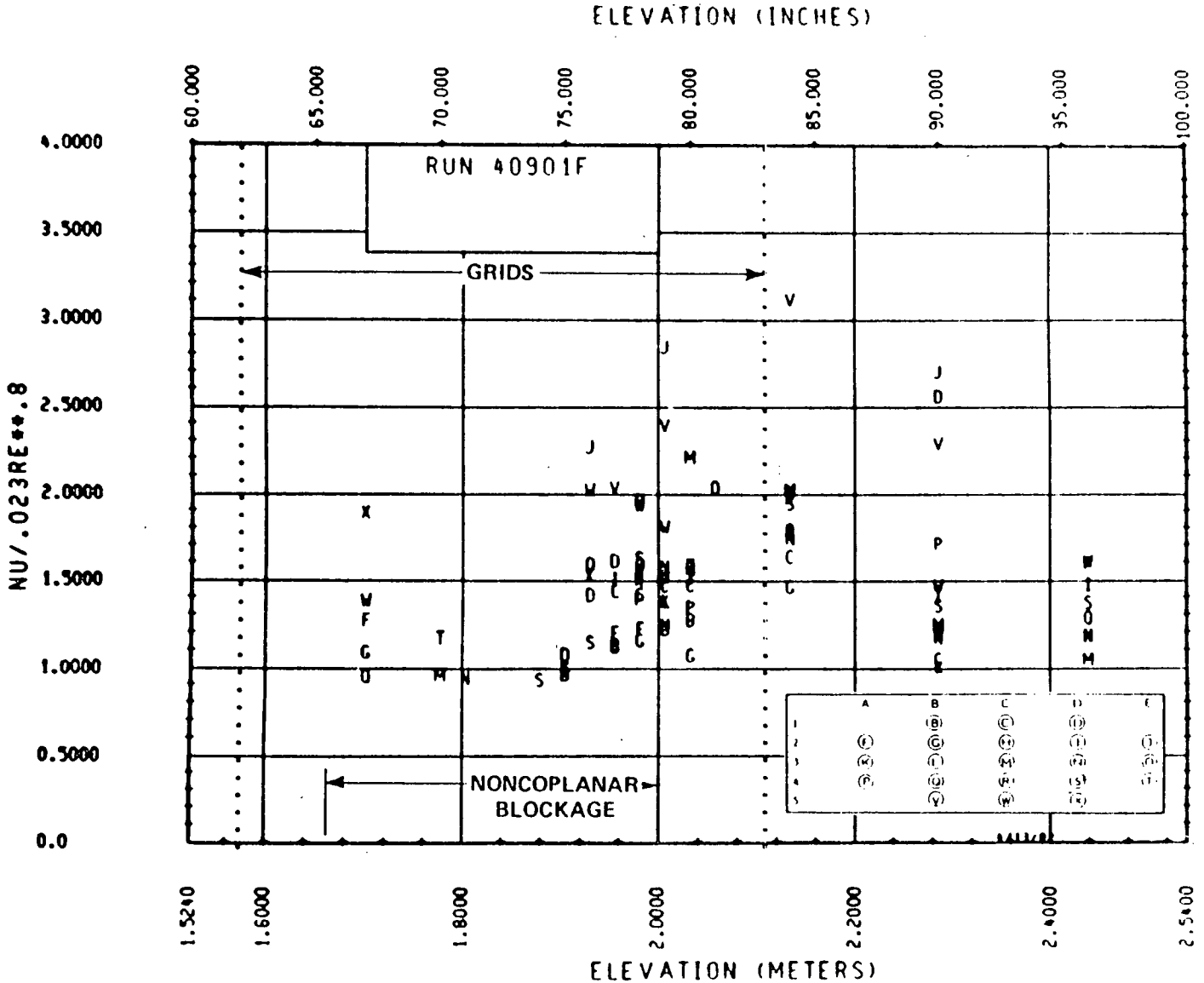

Figure 4-29. Steam Cooling Heat Transfer for FLECHT SEASET 21-Rod Noncoplanar Blocked Bundle With 44-Percent Strain Sleeve

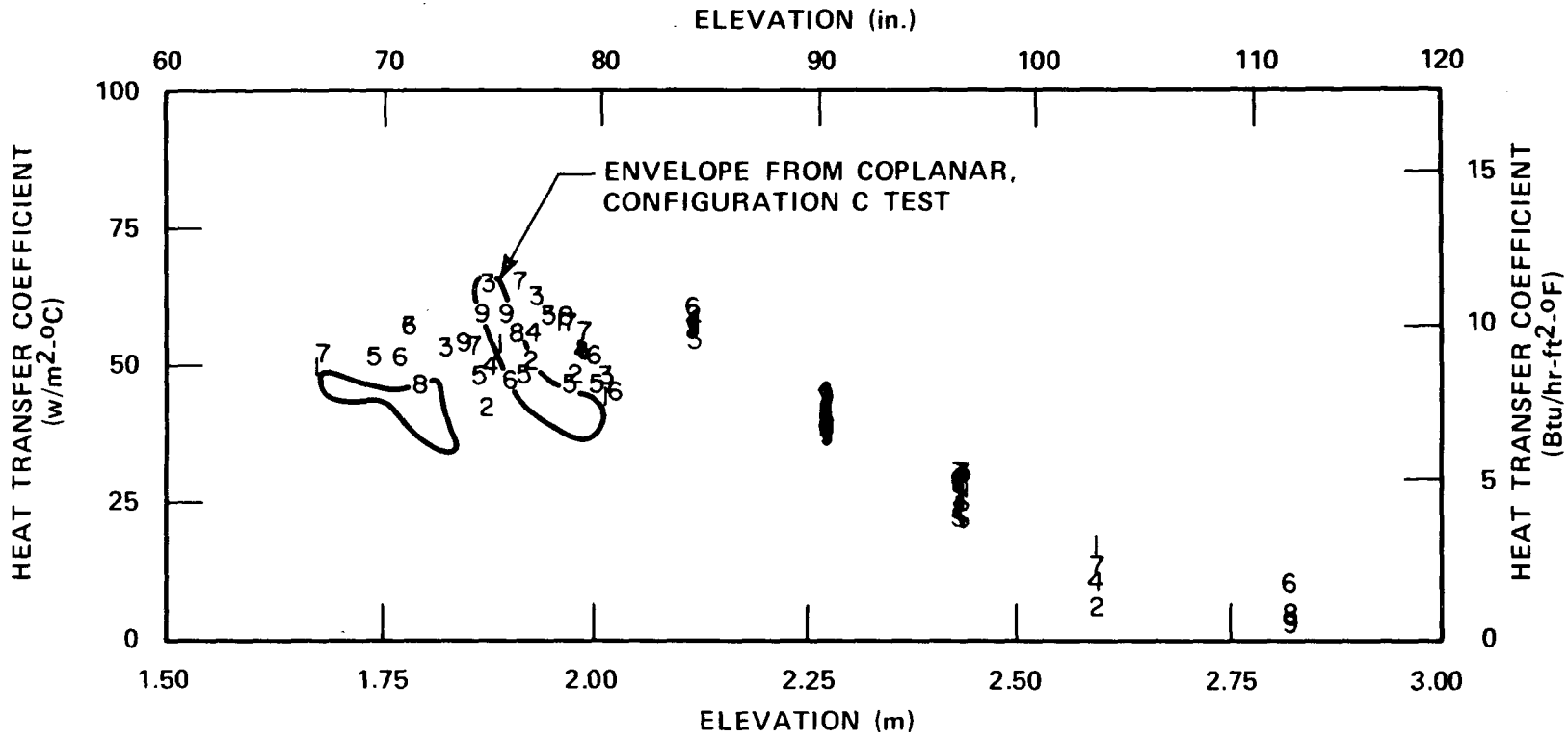

Figure 4-30. Comparison of Heat Transfer Coefficient Data Between FLECHT SEASET Tests 42006F (Noncoplanar Blockage) and 42506C (Coplanar Blockage), t = 20 Seconds

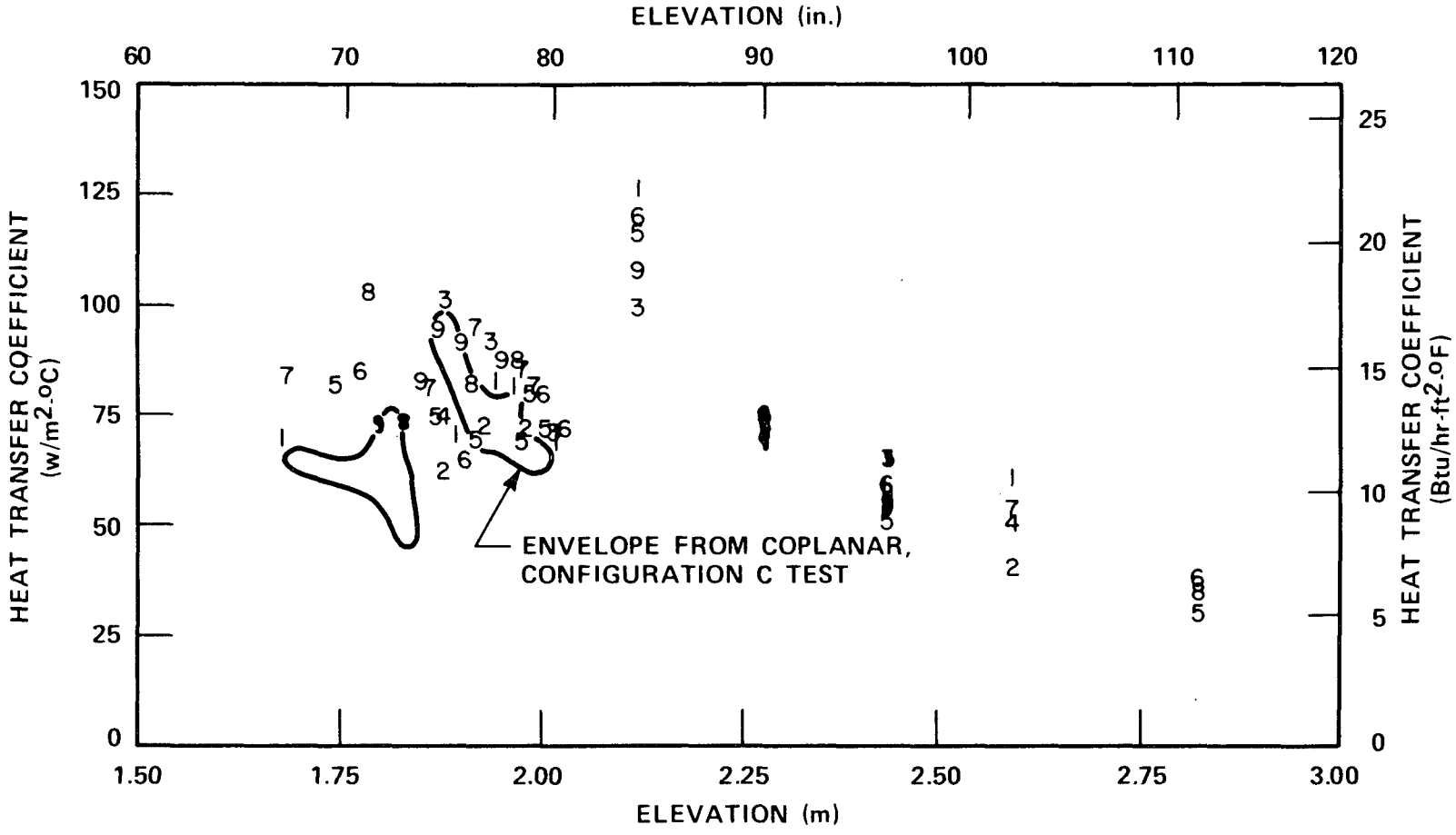

Figure 4-31. Comparison of Heat Transfer Coefficient Data Between FLECHT SEASET Tests 41608F (Noncoplanar Blockage) and 42008C (Coplanar Blockage), t = 20 Seconds

the spread of the coplanar data. Early in time, the flow is essentially single-phase steam, and the configuration F results show large local variations (similar to the steam cooling results). Relative to the noncoplanar data, the coplanar results are quite cohesive.

Later in time, however, the reflood process is well under way and the flow is now two-phase, with droplets dispersed in superheated steam. Figures 4-32 through 4-35 give the heat transfer comparisons at 100 and 140 seconds for the same tests. In this regime, the noncoplanar results display approximately the same degree of cohesiveness as the coplanar results. Apparently, the interaction of the two-phase mixture with the blockage produces fairly homogeneous heat transfer conditions in and downstream of the blockage.

Consequently, it appears that, if the flow is dispersed, a noncoplanar blockage can be simulated by an equivalent coplanar blockage. Fortunately, the single-phase portion of the reflood transient is of short duration (20 to 30 seconds). Then, the lumped subchannel and axially coarse noding (Δ = 75 mm) employed by COBRA-TF is suitable for the noncoplanar blockage. The process by which a noncoplanar blockage is metamorphosed into an "equivalent" coplanar blockage is described in more detail in appendix D.

4-18. FLOW BLOCKAGE MODEL RESULTS

The results of the FLECHT SEASET 21-rod bundle and FEBA 25-rod bundle flow blockage tests that were simulated are shown in tables 4-1 and 4-2 with their initial conditions. The comparisons include heater rod temperature versus time comparisons, heater rod temperature versus axial position comparisons, and vapor temperature comparisons. In addition, a detailed comparison of the test data and COBRA-TF predictions is made in and downstream of the blockage zone to compare the calculated and measured heater rod temperature rise values at different times. Using the temperature rise value ($T_t - T_{initial}$) at an axial position for different times is a more severe test of the ability of the blockage model to predict the data. Also, an overall temperature rise comparison at all elevations was made, similar to the grid model comparisons, to evaluate the fit of the blockage models in COBRA-TF to the test data.

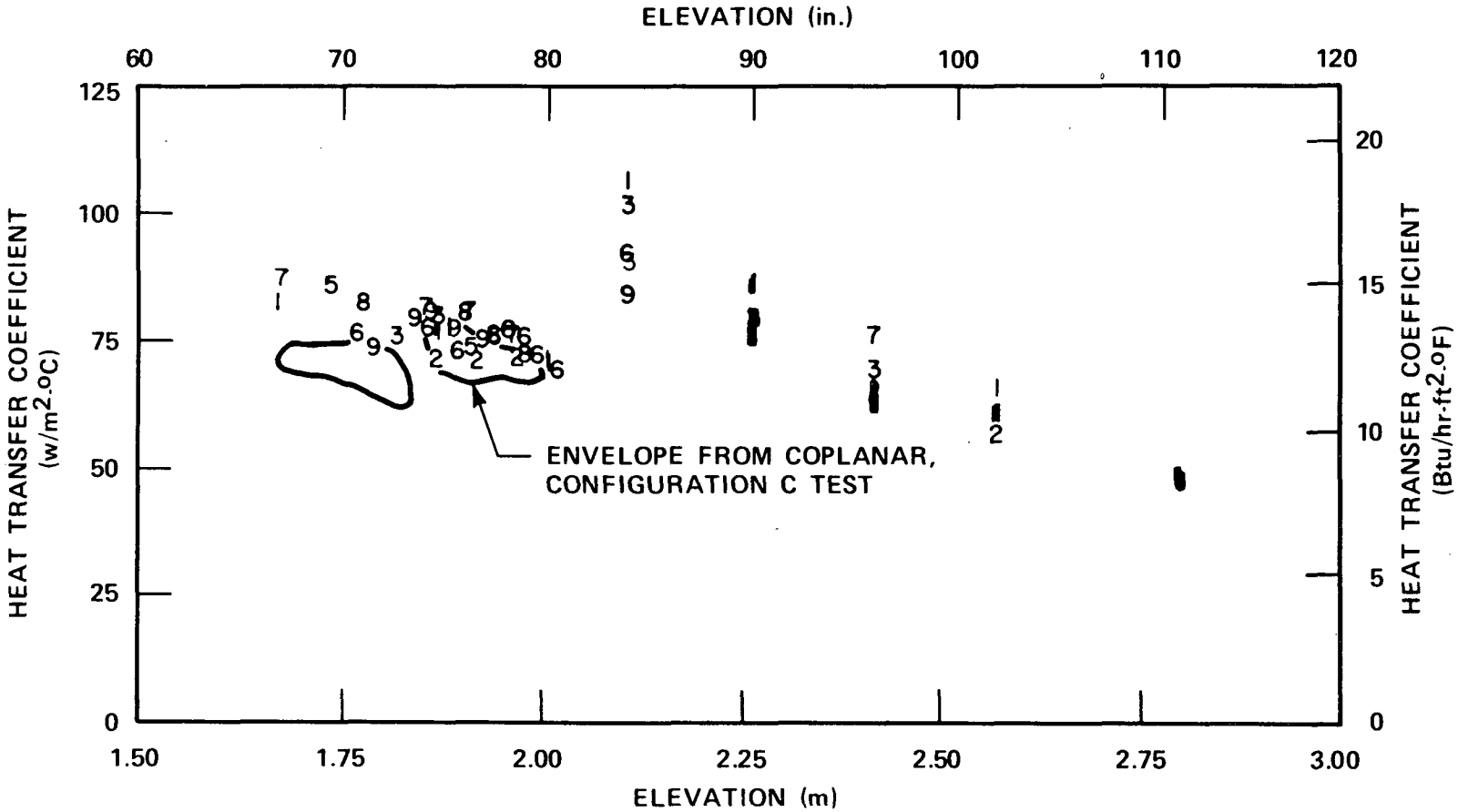

Figure 4-32. Comparison of Heat Transfer Coefficient Data Between FLECHT SEASET Tests 42006F (Noncoplanar Blockage) and 42506C (Coplanar Blockage), t = 100 Seconds

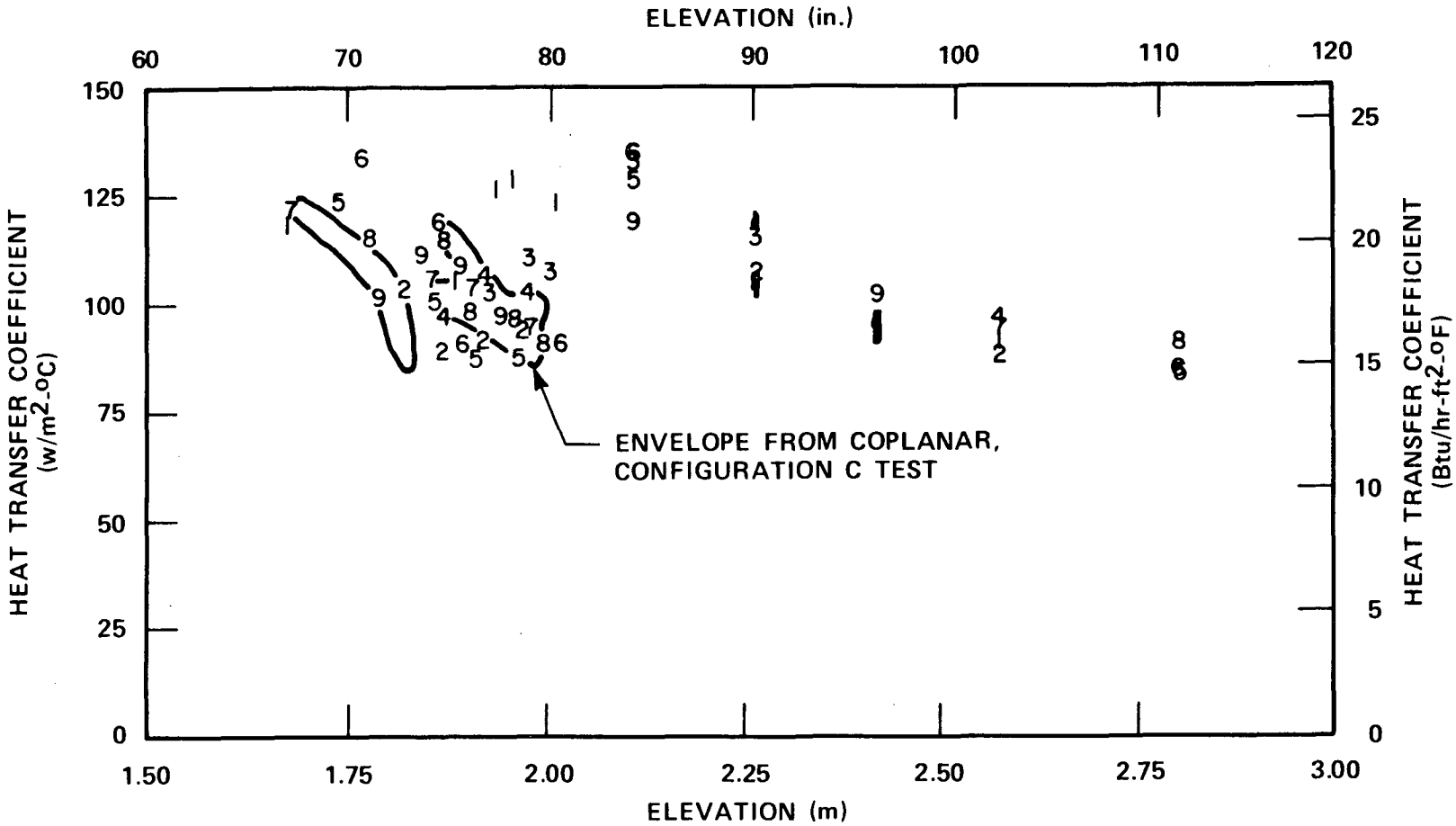

Figure 4-33. Comparison of Heat Transfer Coefficient Data Between FLECHT SEASET Tests 41608F (Noncoplanar Blockage) and 42008C (Coplanar Blockage), t = 100 Seconds

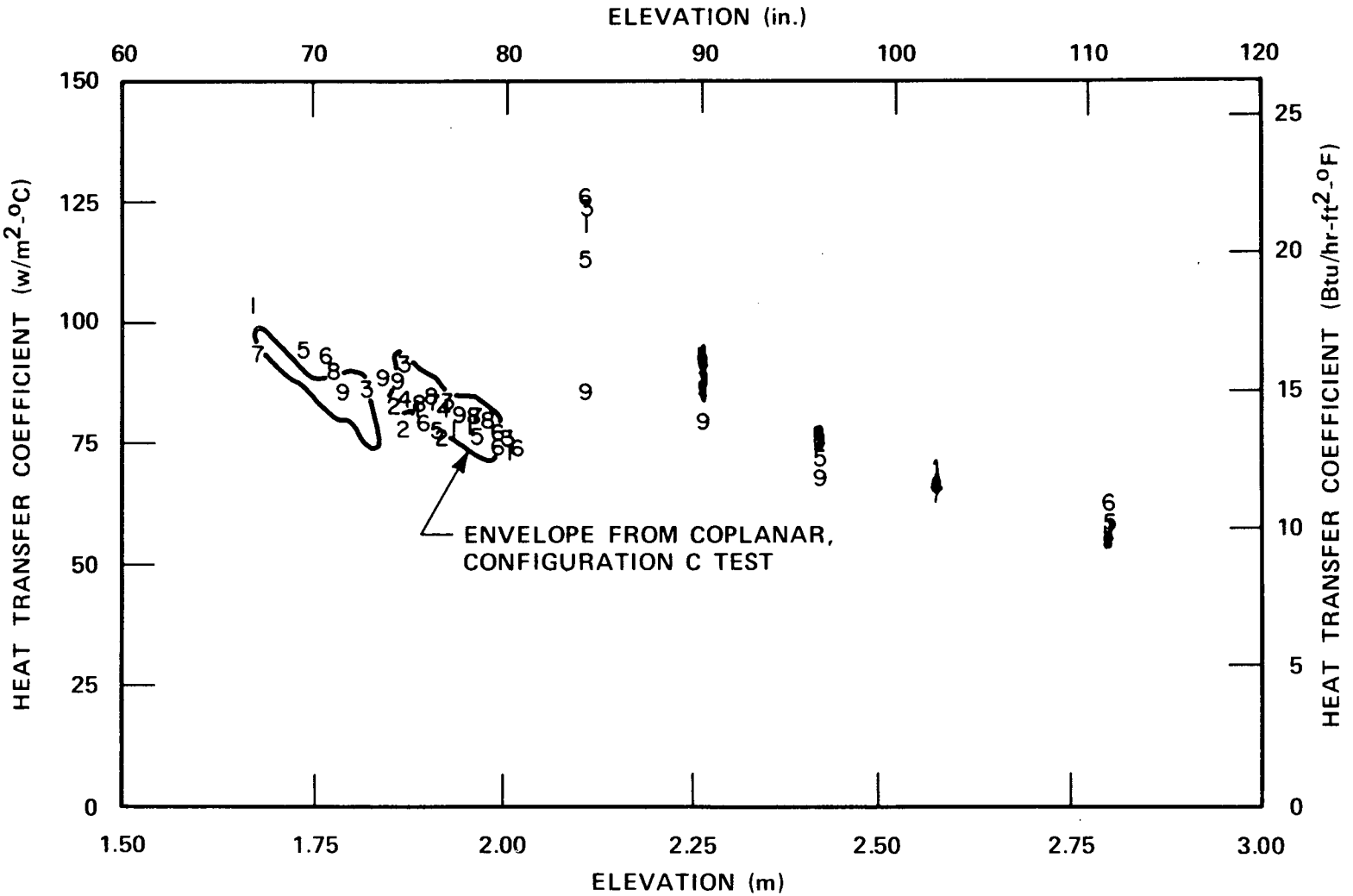

Figure 4-34. Comparison of Heat Transfer Coefficient Data Between FLECHT SEASET Tests 42006F (Noncoplanar Blockage) and 42506C (Coplanar Blockage), t = 140 Seconds

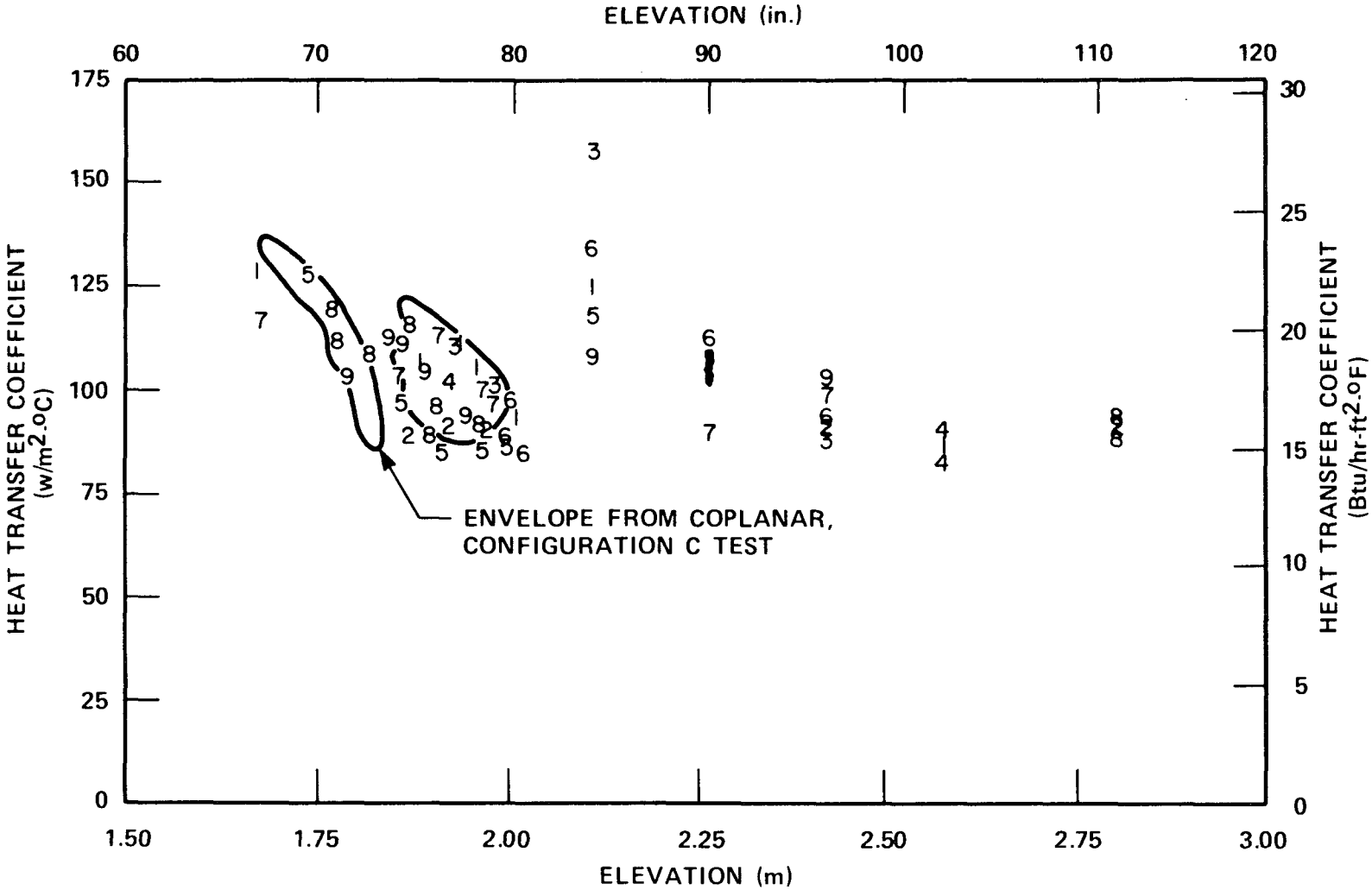

Figure 4-35. Comparison of Heat Transfer Coefficient Data Between FLECHT SEASET Tests 41608F (Noncoplanar Blockage) and 42008C (Coplanar Blockage), t = 140 Seconds

TABLE 4-1

FLECHT SEASET 21-ROD BUNDLE TEST RESULTS SIMULATED

Test	Flooding Rate [m/sec (in./sec)]	Pressure [MPa (psia)]	Power [kw/m (kw/ft)]	$T_{initial}$ [°C (°F)]
Configuration C				
42506C	0.023 (0.91)	0.268 (38.9)	2.6 (0.78)	874 (1606)
42008C	0.0378 (1.49)	0.275 (39.9)	2.3 (0.69)	882 (1619)
42912C	0.0279 (1.10)	0.137 (19.9)	2.6 (0.78)	878 (1613)
42314C	0.153 (6.01) for 5 seconds, 0.022 (0.87) onward	0.274 (39.8)	2.6 (0.78)	876 (1609)
Configuration F				
42006F	0.023 (0.90)	0.278 (40.3)	2.6 (0.78)	875 (1607)
41608F	0.0381 (1.50)	0.279 (40.4)	2.3 (0.69)	875 (1607)
42612F	0.0279 (1.10)	0.139 (20.2)	2.6 (0.78)	877 (1610)
41914F	0.143 (5.64) for 5 seconds; 0.024 (0.95) onward	0.278 (40.3)	2.6 (0.78)	872 (1602)

TABLE 4-2

FEBA 25-ROD BUNDLE TEST RESULTS SIMULATED

Test	Flooding Rate [m/sec (in./sec)]	Pressure [MPa (psia)]	Peak Power [kw/m (kw/ft)]	$T_{initial}$ [°C (°F)]	Inlet Subcooling [°C (°F)]
324[a]	0.038 (1.5)	0.41 (59)	2.3 (0.7)	782 (1440)	42 (76)
337[b]	0.038 (1.5)	0.40 (58)	2.3 (0.7)	795 (1463)	42 (76)

a. 62% blockage all rods

b. 90% blockage all rods; modeled with and without aerodynamic droplet breakup

4-19. COBRA-TF Comparisons With FLECHT SEASET 21-Rod Bundle Blockage Data

The 21-rod bundle experiments that were analyzed with COBRA-TF are listed in table 4-1; test conditions for these experiments were the same as those of the 21-rod bundle experiments described in section 3. The letter designation after the test number denotes the blockage configuration, that is, the combination of sleeve shape and distribution employed in the test series. The letter C represents a configuration of coplanar, short concentric sleeve blockage with a subchannel blockage of 62 percent.

The heater rod temperature versus time plots for FLECHT SEASET 21-rod bundle test 42506C with coplanar blockage on all rods entered at the 1.85 m (73 in.) elevation are shown in figures 4-36 through 4-41 at different axial positions. The COBRA-TF model for this bundle is similar to that for the previous 21-rod bundle configurations, as discussed in section 3. The detailed description of the model is given in appendix A. The COBRA-TF calculation plotted in figures 4-36 through 4-41 is for the center rod in the model; the test data represent the inner nine heater rods. The figures show that the agreement between the code and data is quite good. There is still the observed overprediction of the heater rod temperature before entrainment begins and the resulting underprediction at the 1.9 m (75 in.) elevation after significant entrainment has begun. Since the two-phase blockage impact and droplet breakup models are a function of the calculated entrainment, an overprediction of entrainment will yield higher cooling. However, the agreement at upper elevations is quite good.

The poorer agreement observed at the 1.52 m (60 in.) elevation is believed to be due to the downward shifting of the 1.57 m (62 in.) grid, as discussed in section 3. The shifting of the grid promotes good heat transfer at this lower location, which was not modeled with a grid in COBRA-TF. The grid in COBRA-TF was kept at the 1.57 m (62 in.) location for all the 21-rod bundle studies.

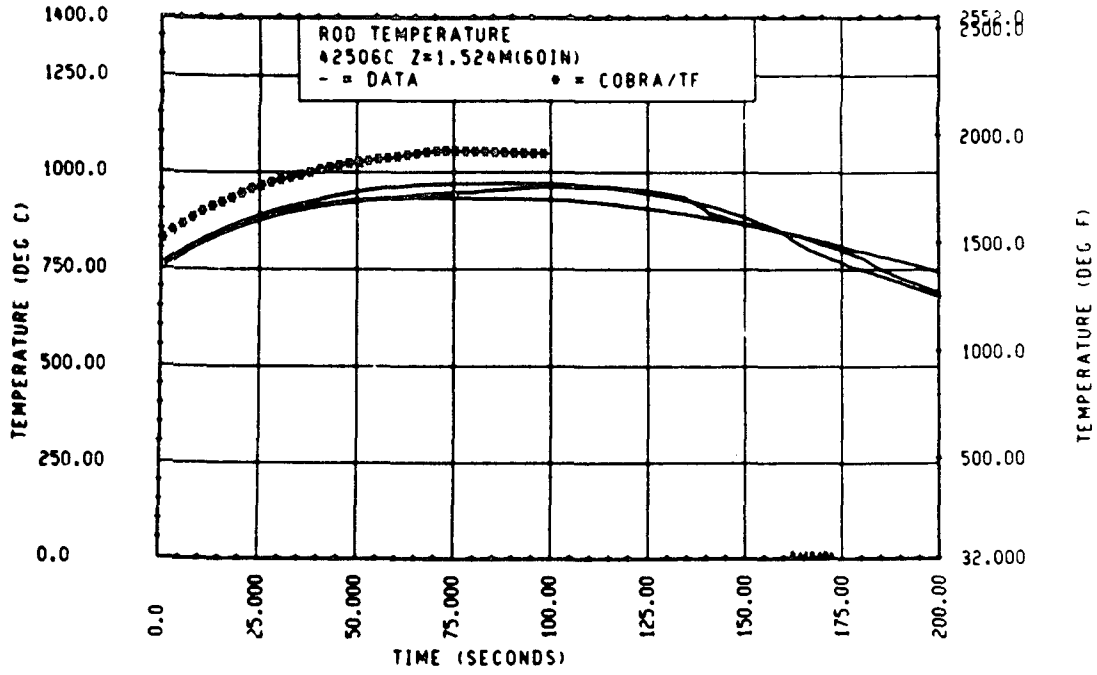

Figure 4-36. Comparison of COBRA-TF-Calculated Heater Rod Temperature Versus Time With FLECHT SEASET 21-Rod Data, Test 42506C, 1.52 m (60 in.) Elevation

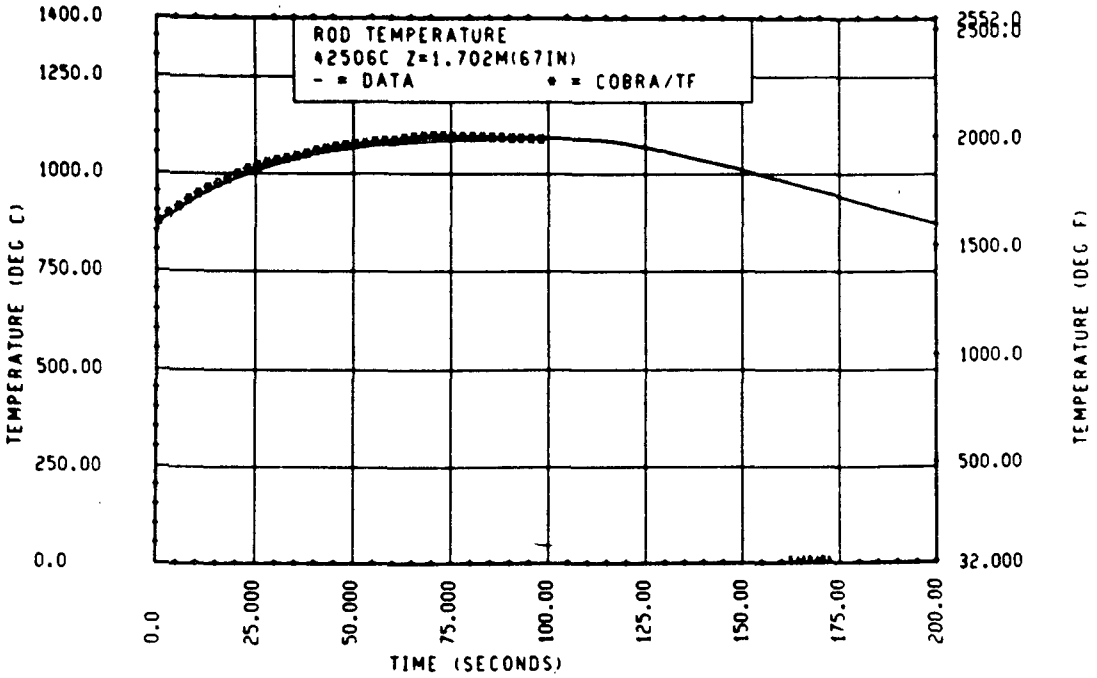

Figure 4-37. Comparison of COBRA-TF-Calculated Heater Rod Temperature Versus Time With FLECHT SEASET 21-Rod Data, Test 42506C, 1.70 m (67 in.) Elevation

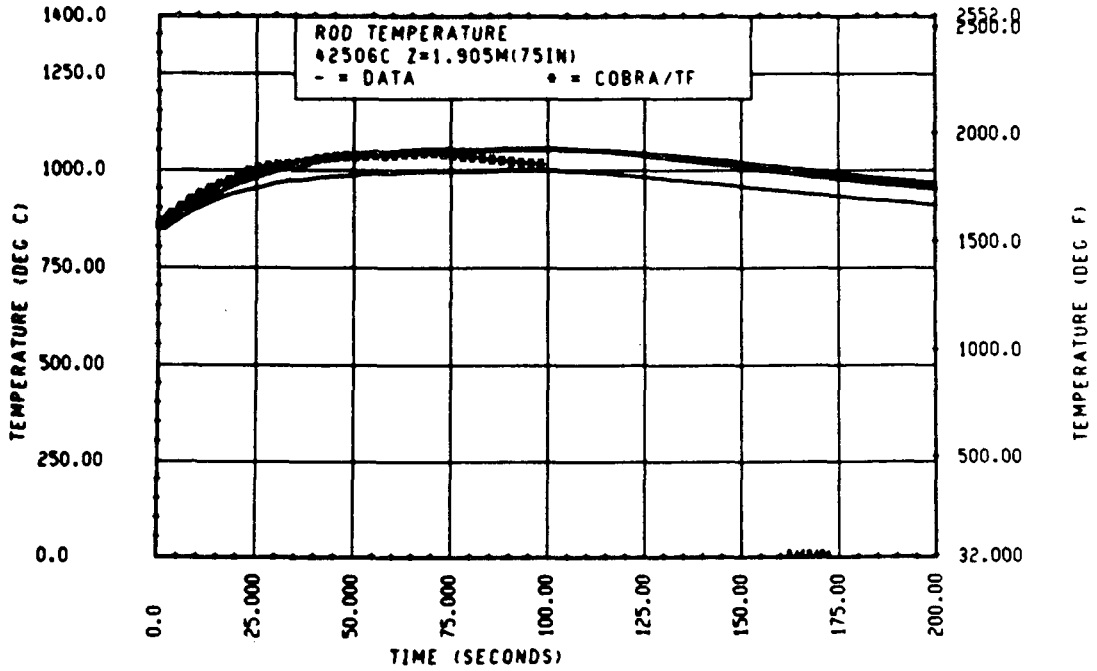

Figure 4-38. Comparison of COBRA-TF-Calculated Heater Rod Temperature Versus Time With FLECHT SEASET 21-Rod Data, Test 42506C, 1.90 m (75 in.) Elevation

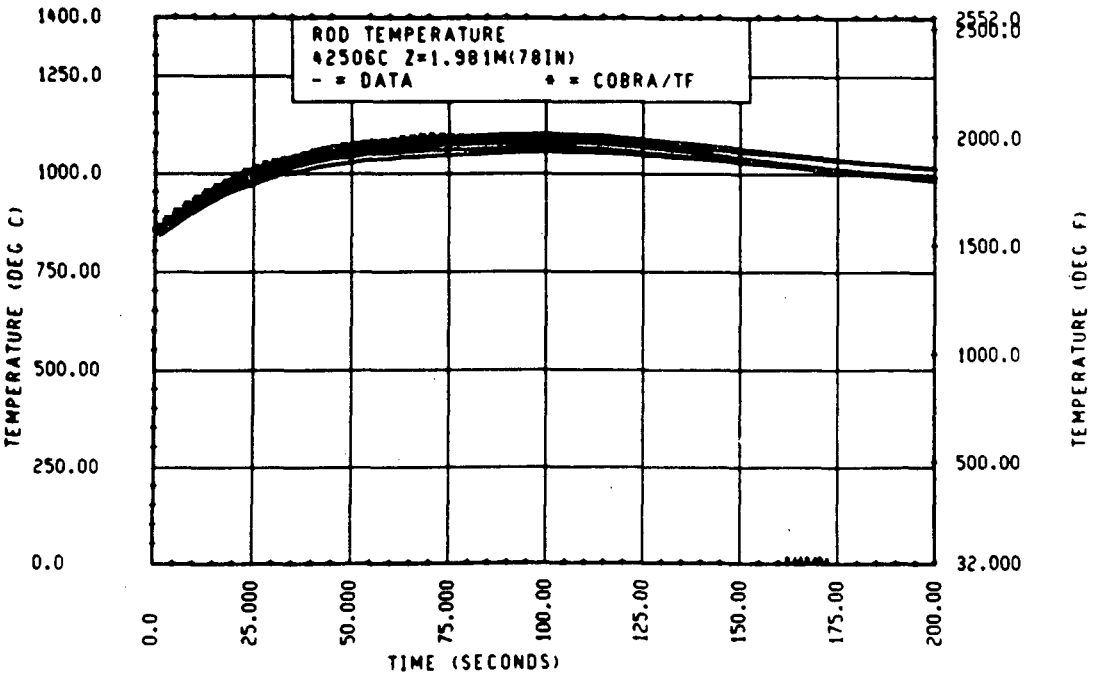

Figure 4-39. Comparison of COBRA-TF-Calculated Heater Rod Temperature Versus Time With FLECHT SEASET 21-Rod Data, Test 42506C, 1.98 m (78 in.) Elevation

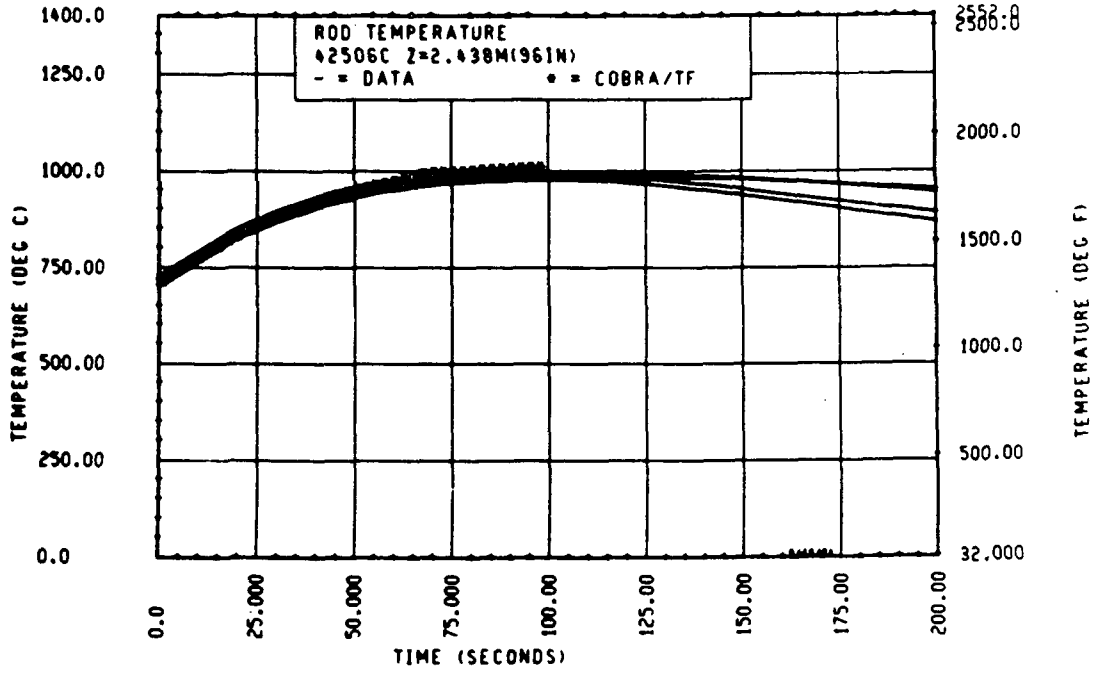

Figure 4-40. Comparison of COBRA-TF-Calculated Heater Rod Temperature Versus Time With FLECHT SEASET 21-Rod Data, Test 42506C, 2.44 m (96 in.) Elevation

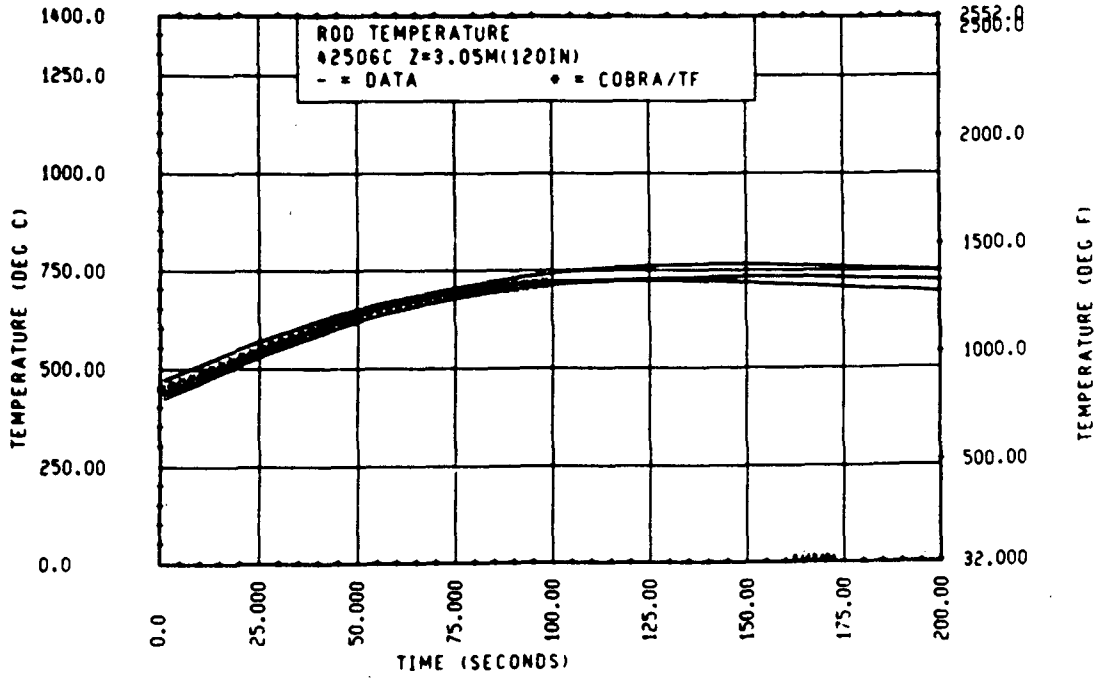

Figure 4-41. Comparison of COBRA-TF-Calculated Heater Rod Temperature Versus Time With FLECHT SEASET 21-Rod Data, Test 42506C, 3.05 m (120 in.) Elevation

The heater rod temperature axial comparison plots at different times are shown in figures 4-42 through 4-45 for test 42506C, where again COBRA-TF is the solid line and the data points are the stars. (Also shown in figure 4-42 is the axial location of the spacer grids and the blockage zone.) These figures show the significantly improved heat transfer, and hence heater rod temperature decrease, downstream of the blockage. The effects of the grid can also be seen at later times (figure 4-45) as the entrainment increases. The COBRA-TF code also predicts the quench front propagation up along the rod bundle.

The comparisons between the measured vapor temperatures and the calculated COBRA-TF vapor temperatures are shown in figures 4-46 through 4-49 as plots of vapor temperature versus axial position for different time periods. Again as was noted in Section 3, the vapor temperature measurements are point measurements within the subchannel and the COBRA-TF calculation is a subchannel average vapor temperature. Therefore, there will be differences. The comparisons are quite good at elevations above 2 m (79 in.), but not as good in the bundle midplane region, before and immediately after the blockage.

Examination of figures 4-47 through 4-49 does show the strong influence of the grid upstream of the blockage zone, which leads to a too-low vapor temperature prediction upstream of the blockage. This effect is noted in the discussion of grid model effects in section 3. Other vapor temperature comparisons for other tests (shown subsequently) do show improved agreement with the test data.

Comparisons of the COBRA-TF calculations with FLECHT SEASET test 42008C are shown in figures 4-50 through 4-63. The conditions for this 21-rod bundle test, given in table 4-1, indicate that it is a replicate of a previously discussed 21-rod bundle test without blockage (test 40008A). Again, the blockage used in test 42008C was coplanar blockage with short concentric sleeves and a subchannel blockage of 62 percent. This is the same configuration as test 42506C, discussed above. The heater rod temperature versus time plots (figures 4-50 through 4-55) show very good agreement with the test data.

The axial heater rod temperature plots shown in figures 4-56 through 4-59 more clearly show the grid and blockage effects as the transient progresses. (Also shown in figure 4-56 is the axial location of the spacer grids and the blockage zone.) The COBRA-TF calculation is underestimating the cooling effects

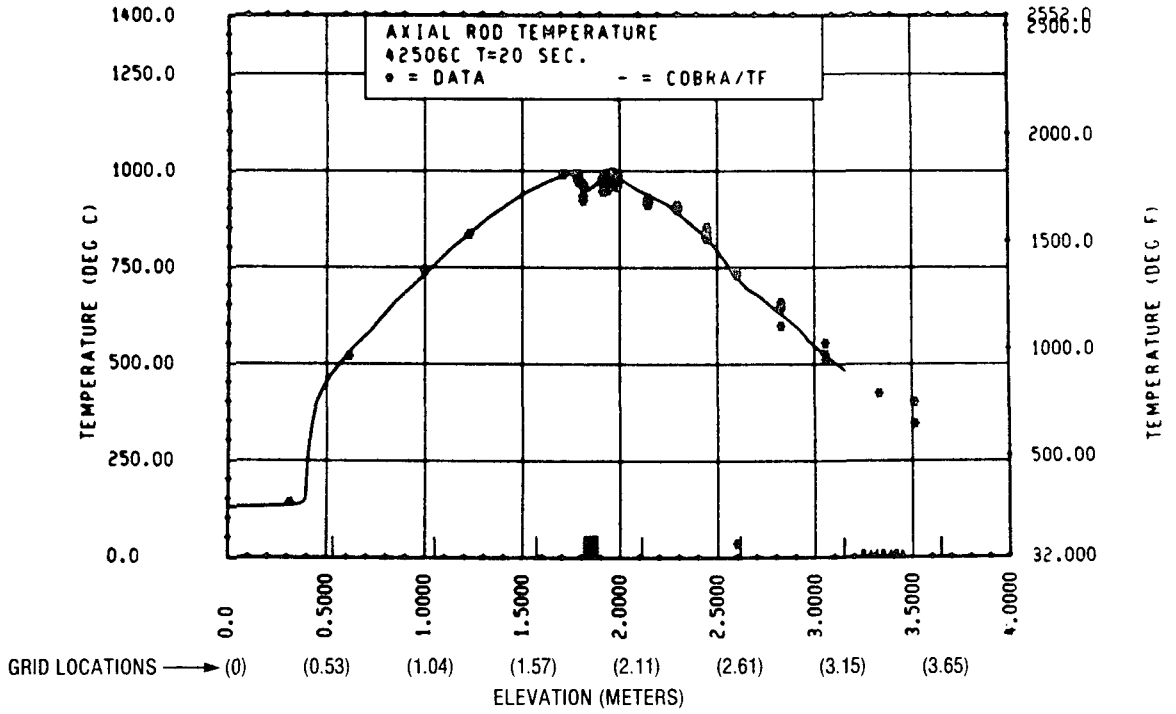

Figure 4-42. Comparison of COBRA-TF-Calculated Axial Rod Temperature Versus Elevation With FLECHT SEASET 21-Rod Data, Test 42506C, t = 20 Seconds

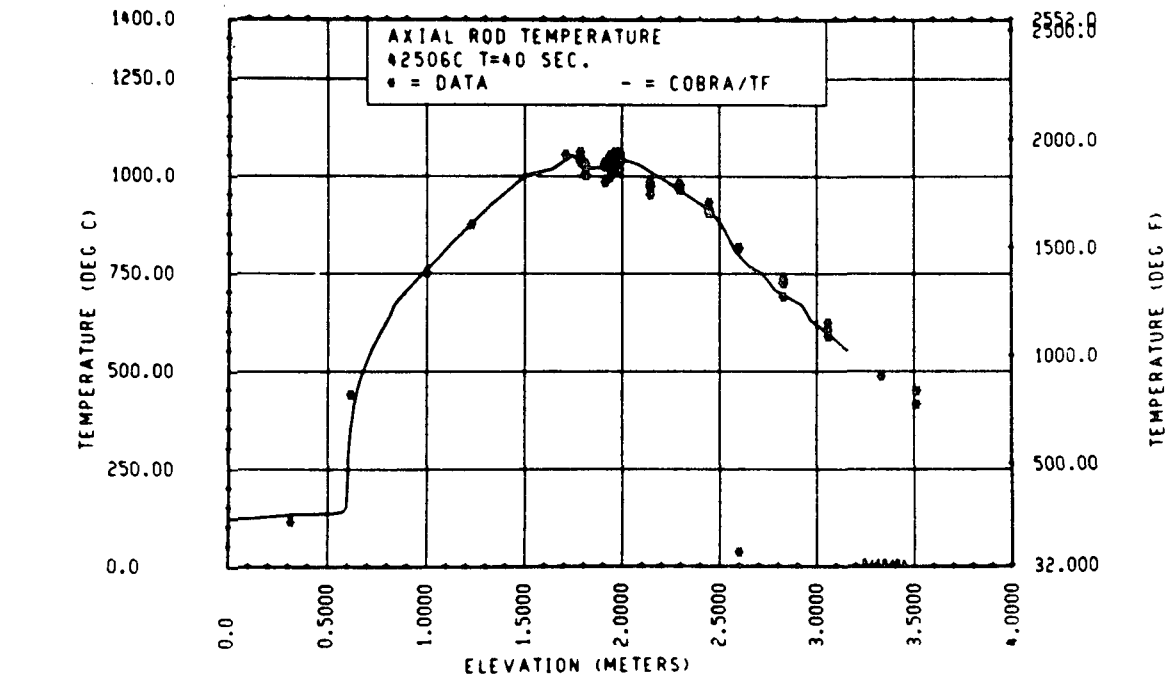

Figure 4-43. Comparison of COBRA-TF-Calculated Axial Rod Temperature Versus Elevation With FLECHT SEASET 21-Rod Data, Test 42506C, t = 40 Seconds

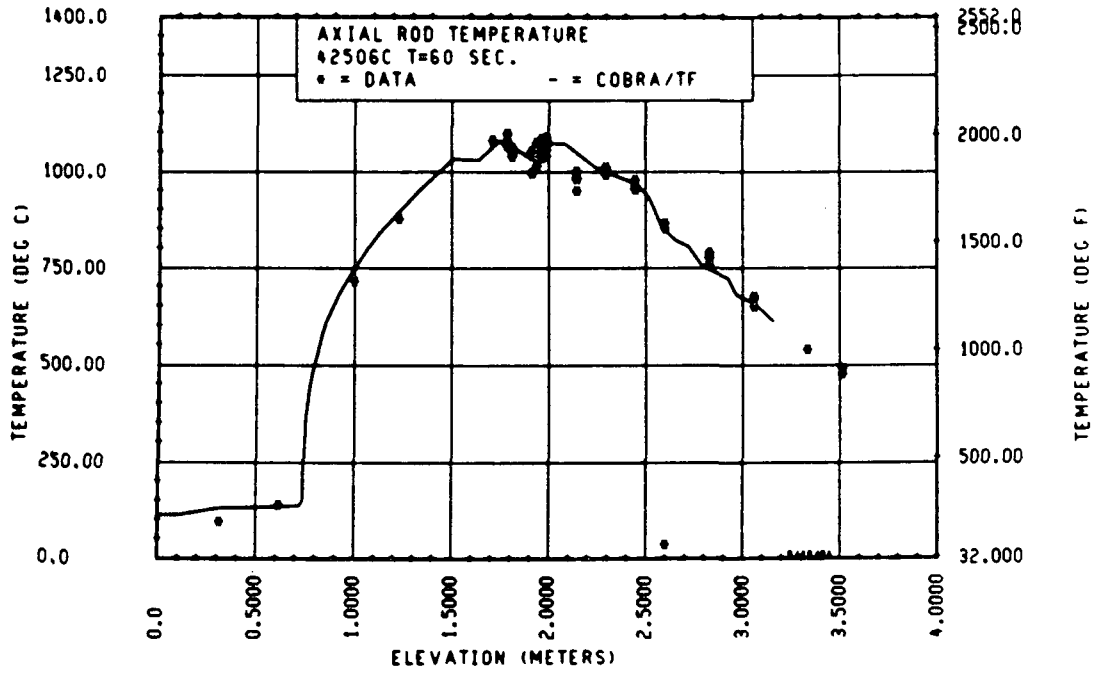

Figure 4-44. Comparison of COBRA-TF-Calculated Axial Rod Temperature Versus Elevation With FLECHT SEASET 21-Rod Data, Test 42506C, t = 60 Seconds

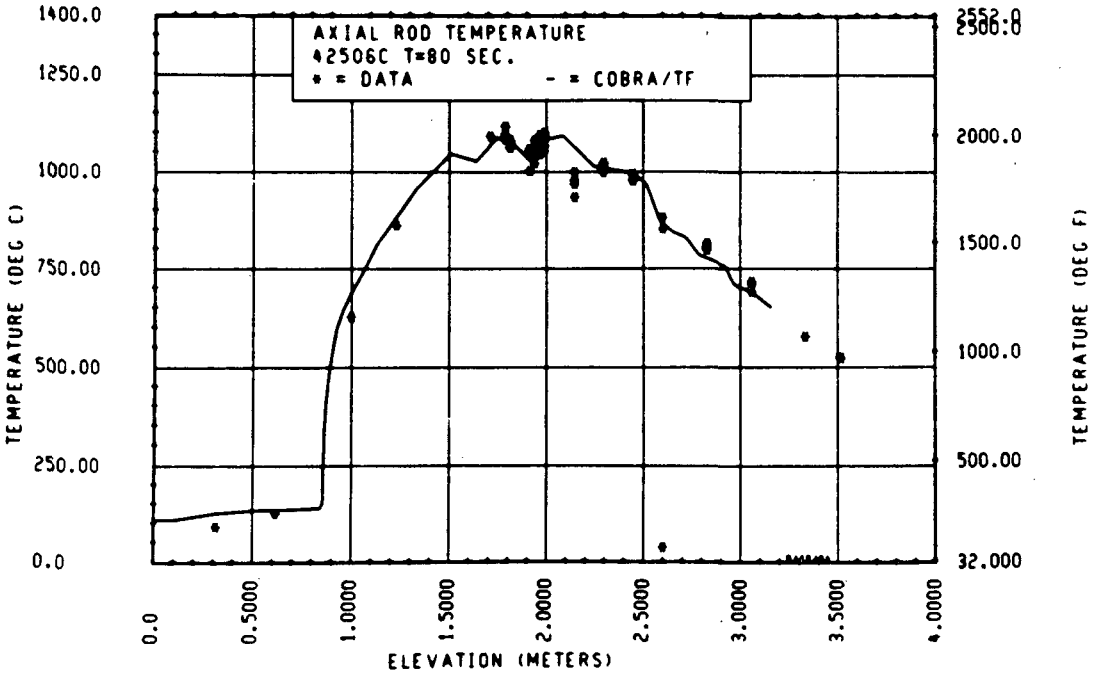

Figure 4-45. Comparison of COBRA-TF-Calculated Axial Rod Temperature Versus Elevation With FLECHT SEASET 21-Rod Data, Test 42506C, t = 80 Seconds

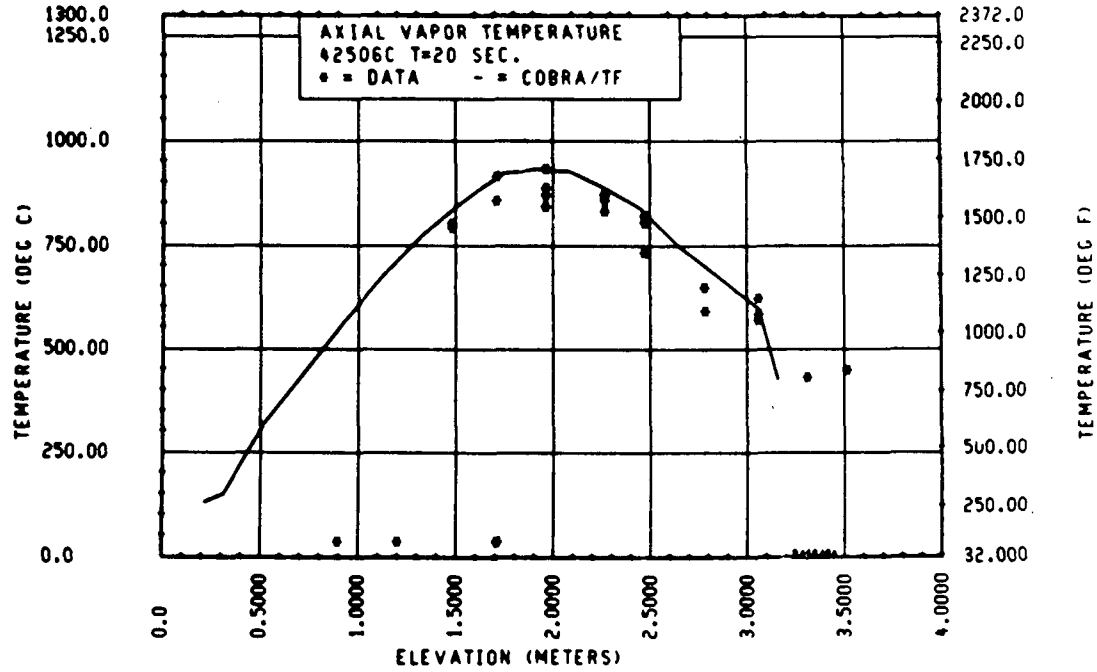

Figure 4-46. Comparison of COBRA-TF-Calculated Axial Vapor Temperature Versus Elevation With FLECHT SEASET 21-Rod Data, Test 42506C, t = 20 Seconds

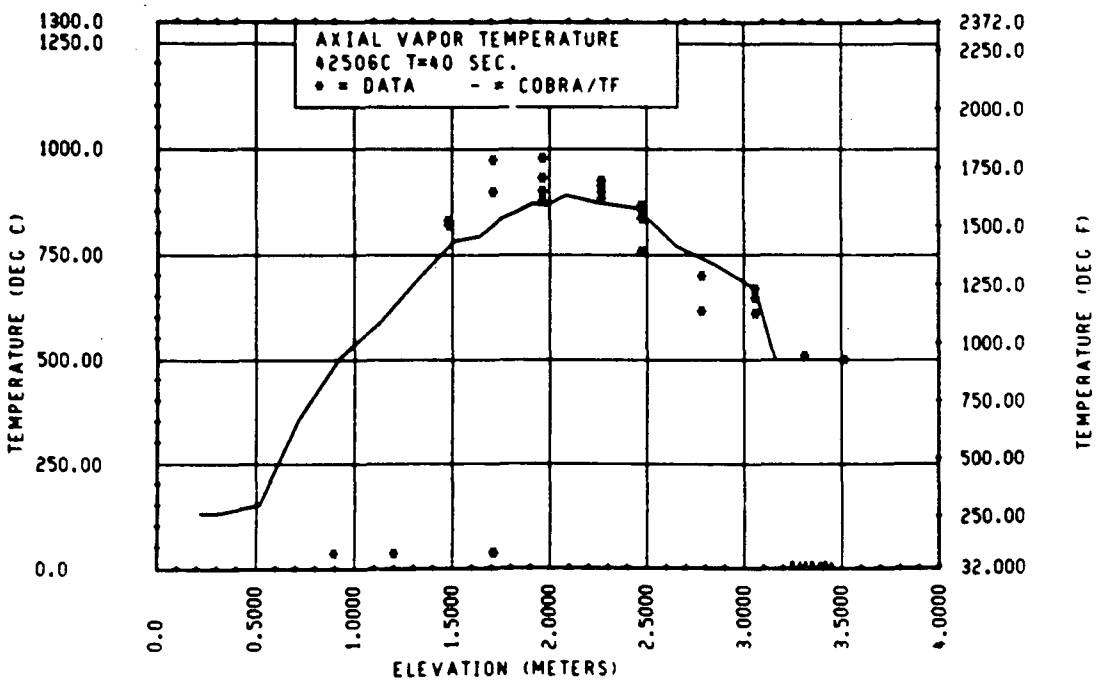

Figure 4-47. Comparison of COBRA-TF-Calculated Axial Vapor Temperature Versus Elevation With FLECHT SEASET 21-Rod Data, Test 42506C, t = 40 Seconds

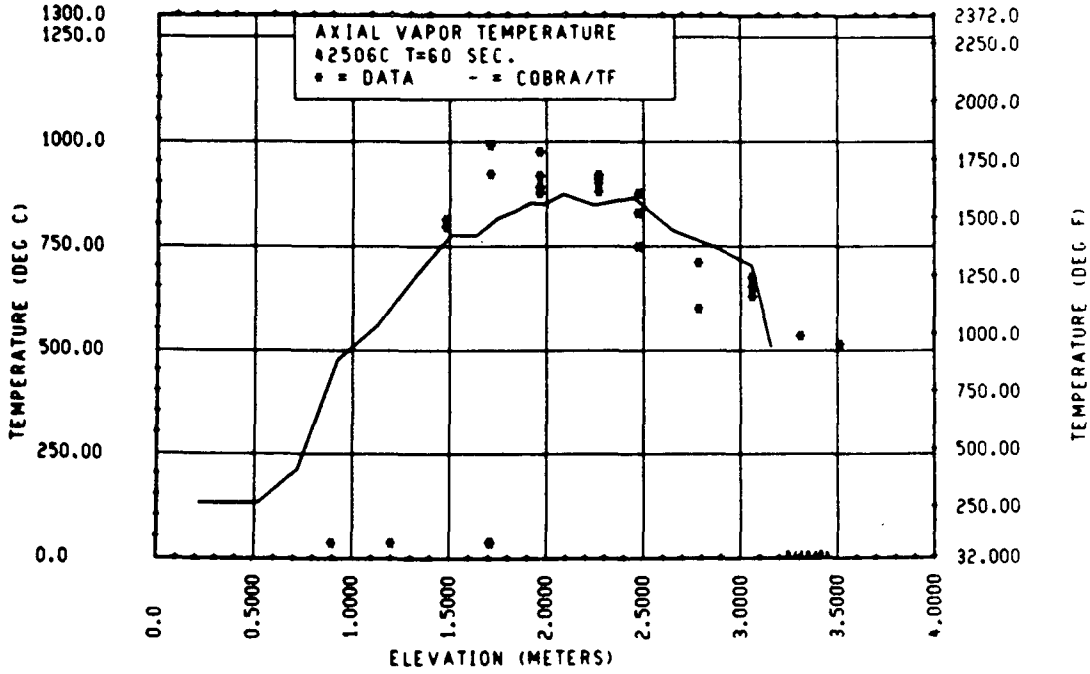

Figure 4-48. Comparison of COBRA-TF-Calculated Axial Vapor Temperature Versus Elevation With FLECHT SEASET 21-Rod Data, Test 42506C, t = 60 Seconds

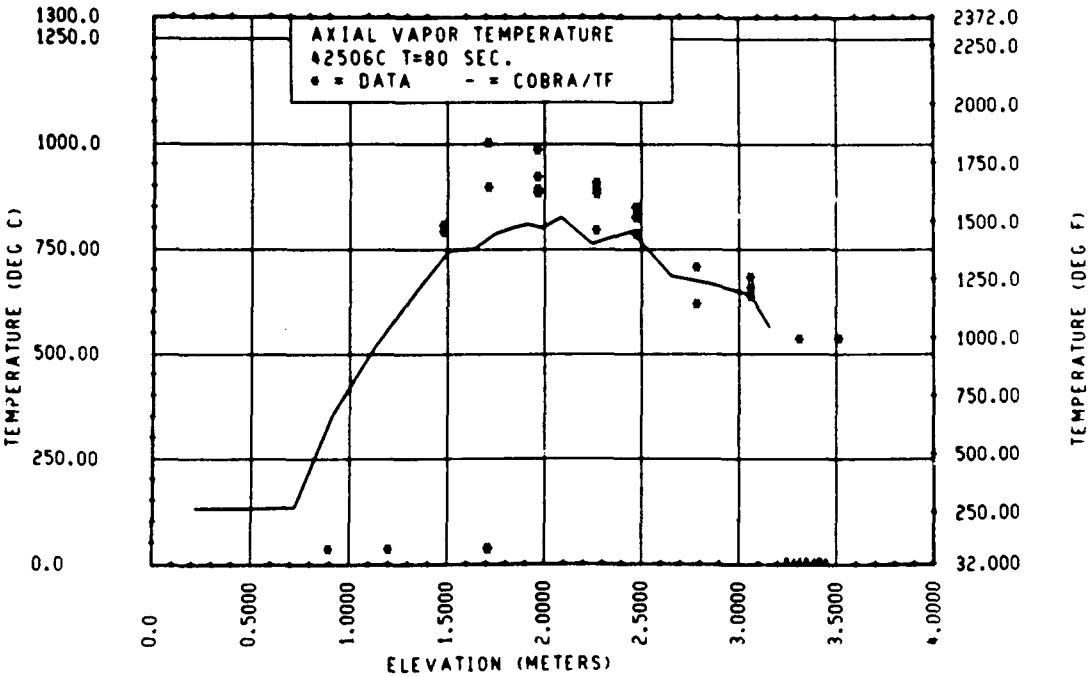

Figure 4-49. Comparison of COBRA-TF-Calculated Axial Vapor Temperature Versus Elevation With FLECHT SEASET 21-Rod Data, Test 42506C, t = 80 Seconds

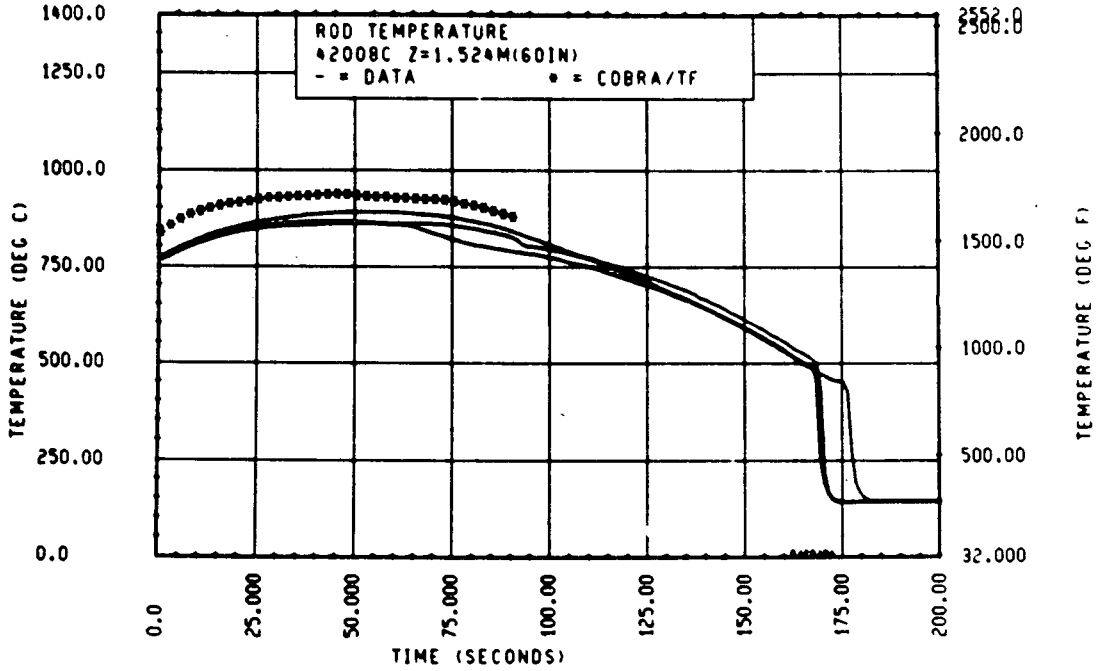

Figure 4-50. Comparison of COBRA-TF-Calculated Heater Rod Temperature Versus Time With FLECHT SEASET 21-Rod Data, Test 42008C, 1.52 m (60 in.) Elevation

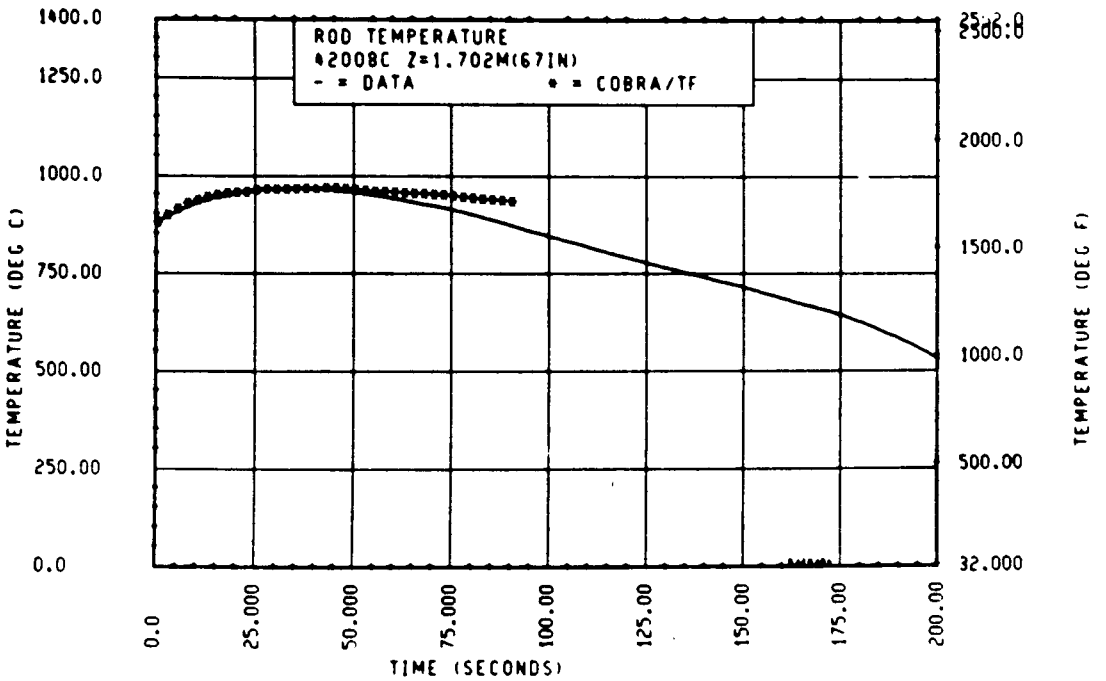

Figure 4-51. Comparison of COBRA-TF-Calculated Heater Rod Temperature Versus Time With FLECHT SEASET 21-Rod Data, Test 42008C, 1.70 m (67 in.) Elevation

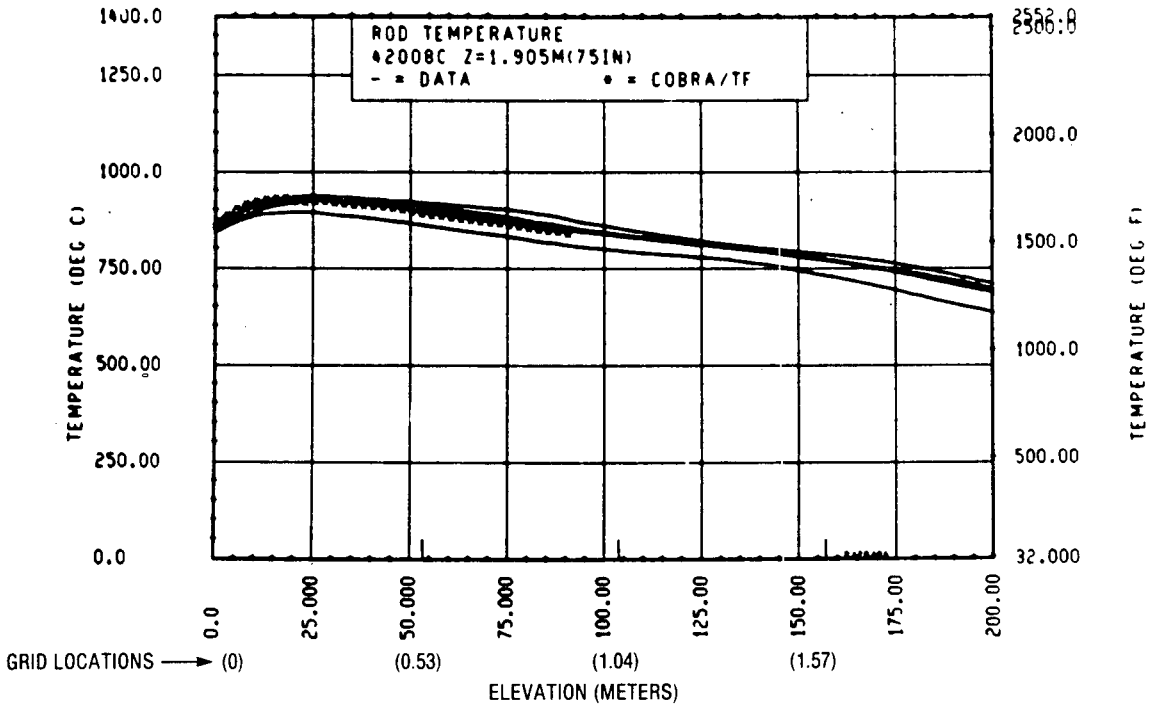

Figure 4-52. Comparison of COBRA-TF-Calculated Heater Rod Temperature Versus Time With FLECHT SEASET 21-Rod Data, Test 42008C, 1.90 m (75 in.) Elevation

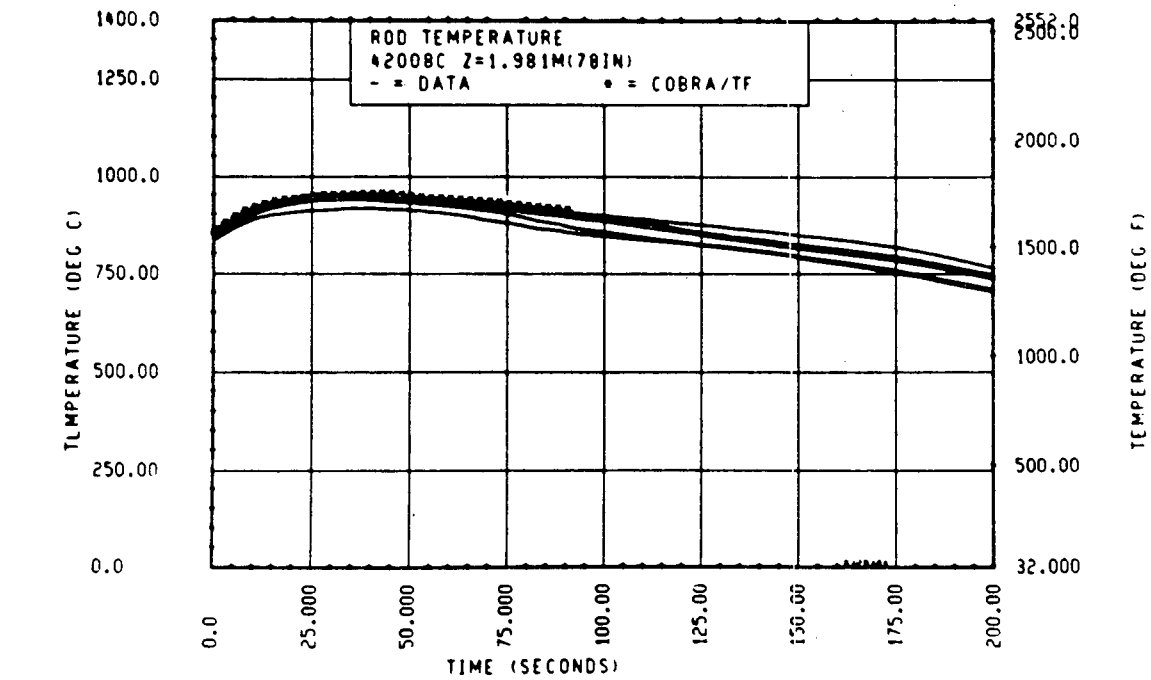

Figure 4-53. Comparison of COBRA-TF-Calculated Heater Rod Temperature Versus Time With FLECHT SEASET 21-Rod Data, Test 42008C, 1.98 m (78 in.) Elevation

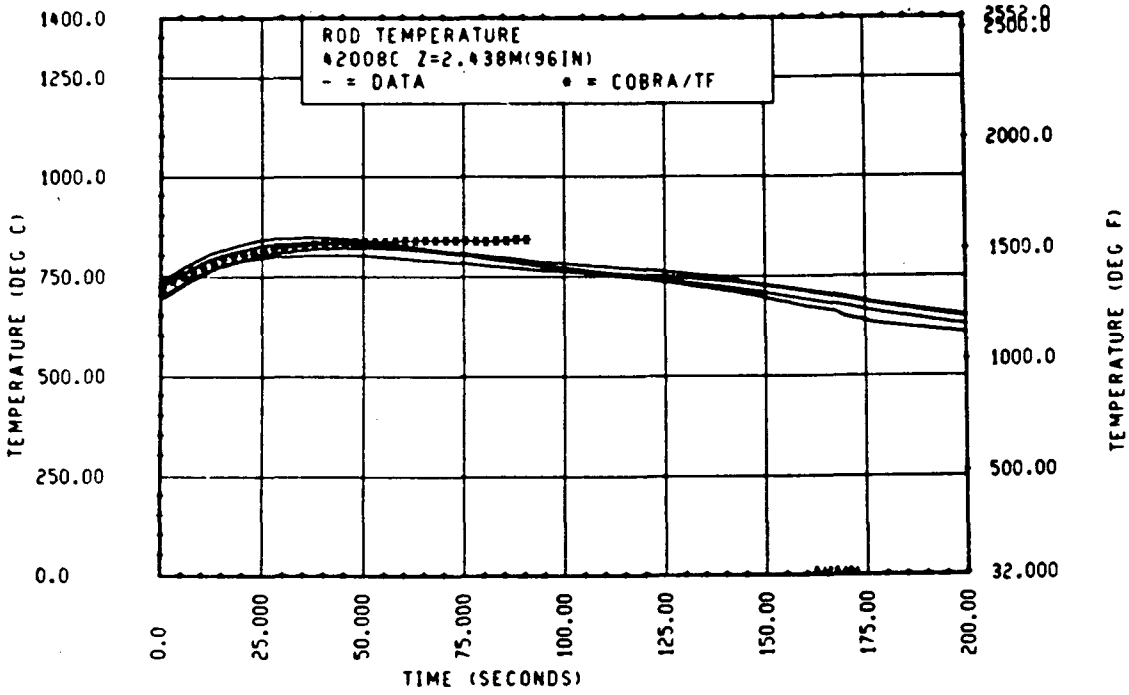

Figure 4-54. Comparison of COBRA-TF-Calculated Heater Rod Temperature Versus Time With FLECHT SEASET 21-Rod Data, Test 42008C, 2.44 m (96 in.) Elevation

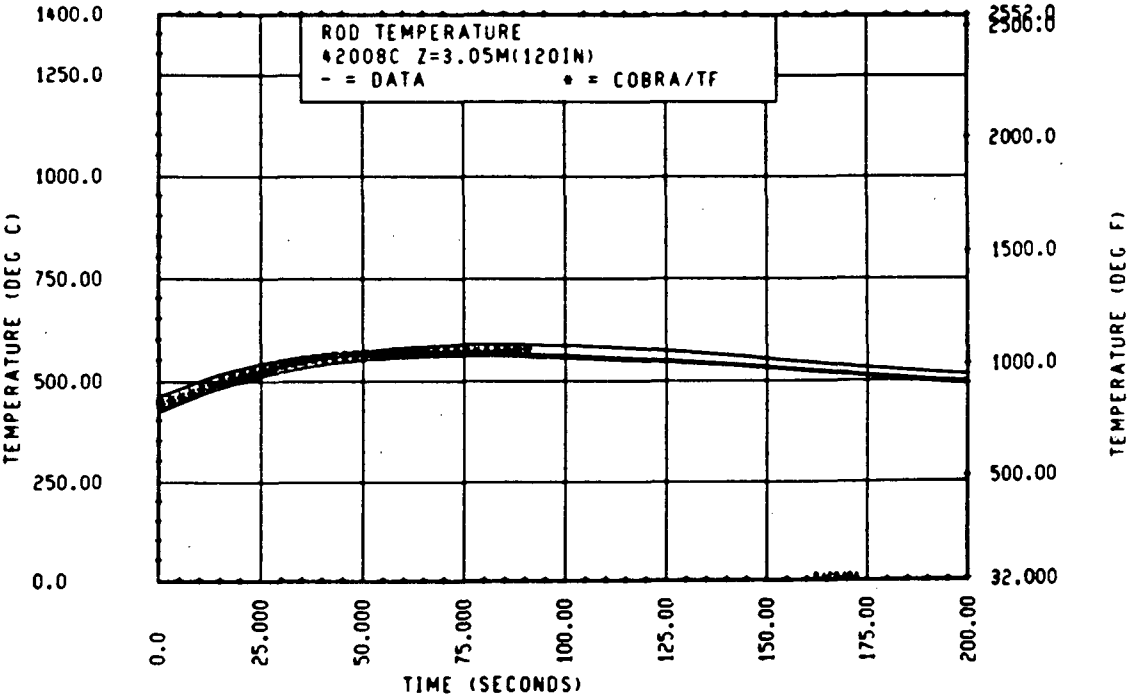

Figure 4-55. Comparison of COBRA-TF-Calculated Heater Rod Temperature Versus Time With FLECHT SEASET 21-Rod Data, Test 42008C, 3.05 m (120 in.) Elevation

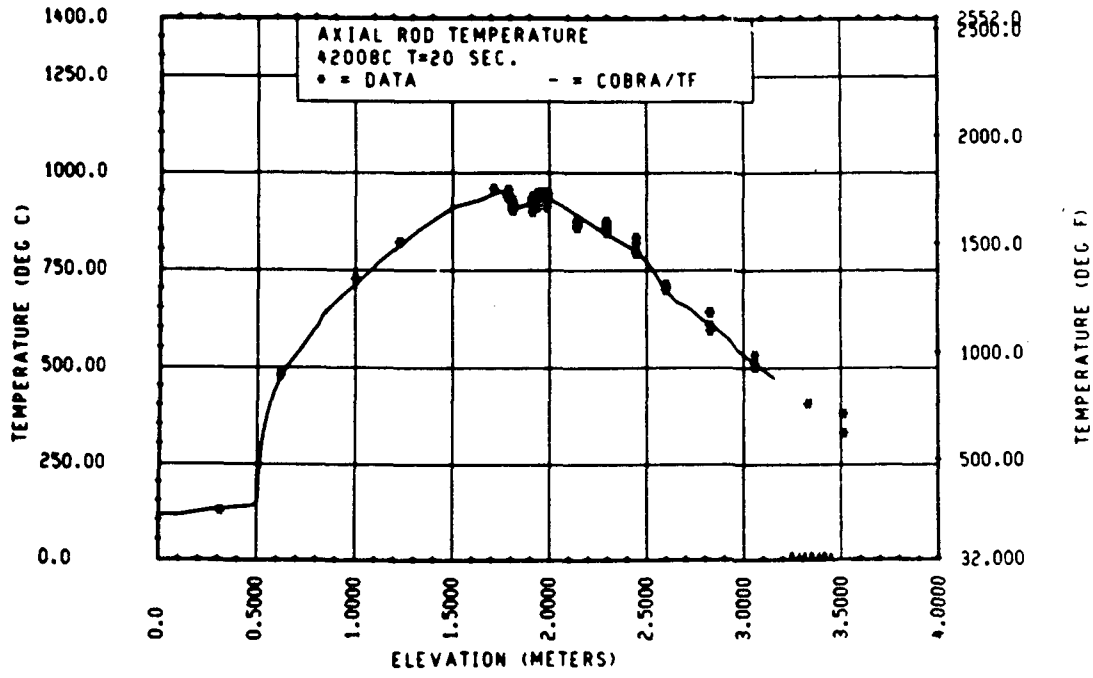

Figure 4-56. Comparison of COBRA-TF-Calculated Axial Rod Temperature Versus Elevation With FLECHT SEASET 21-Rod Data, Test 42008C, t = 20 Seconds

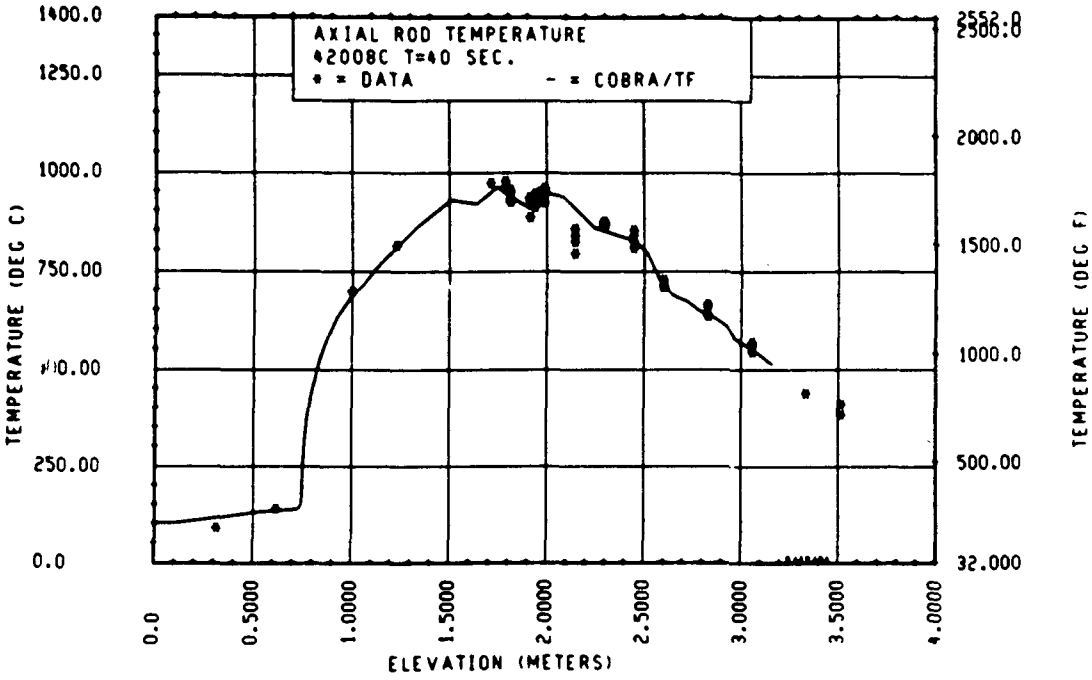

Figure 4-57. Comparison of COBRA-TF-Calculated Axial Rod Temperature Versus Elevation With FLECHT SEASET 21-Rod Data, Test 42008C, t = 40 Seconds

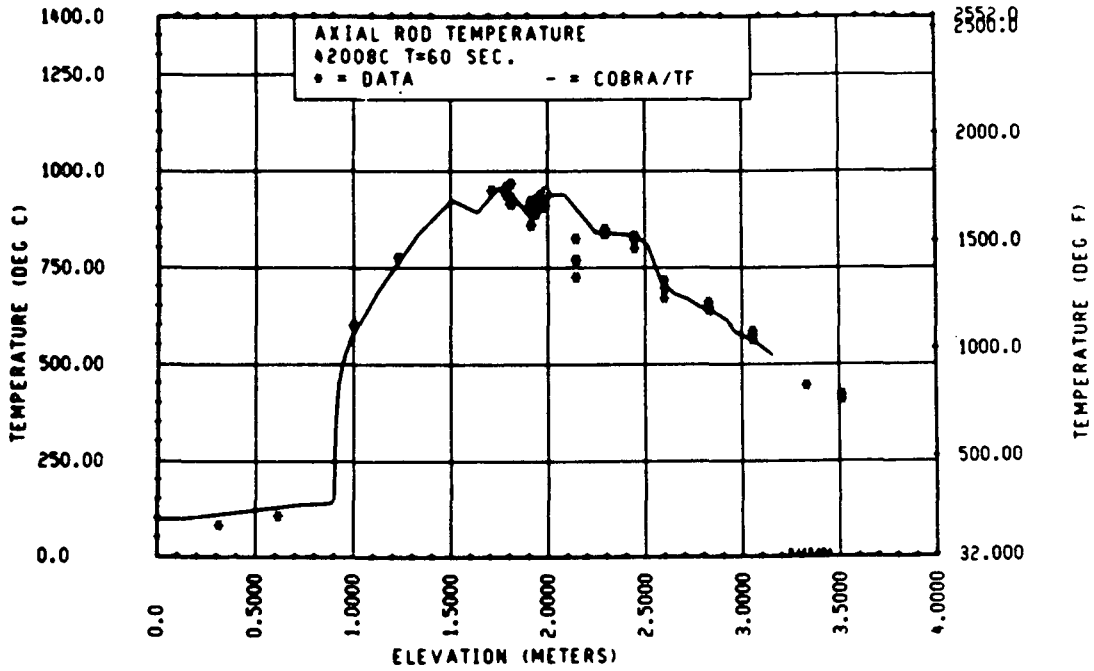

Figure 4-58. Comparison of COBRA-TF-Calculated Axial Rod Temperature Versus Time With FLECHT SEASET 21-Rod Data, Test 42008C, t = 60 Seconds

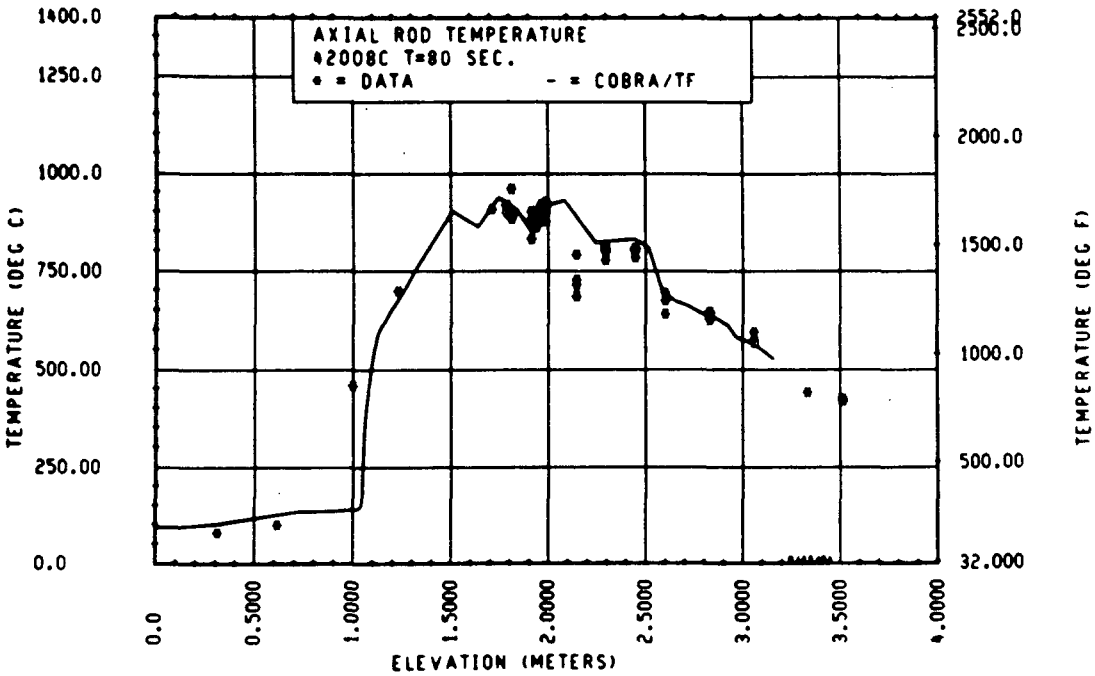

Figure 4-59. Comparison of COBRA-TF-Calculated Axial Rod Temperature Versus Time With FLECHT SEASET 21-Rod Data, Test 42008C, t = 80 Seconds

observed in the experiment downstream of the 2.11 m (83 in.) grid. This is consistent with the unblocked 21-rod bundle data comparisons shown in section 3 for these test conditions. COBRA-TF is predicting about the correct cooling in and downstream of the blockage zone, as illustrated in the figures; the agreement between code and data is quite good.

The COBRA-TF comparisons with the measured vapor temperature are shown in figures 4-60 through 4-63. There is better agreement between calculated and measured vapor temperatures than for the previous test, 42506C. Only the data from steam probes which remained at a superheated condition were compared, since premature quenching of the steam probes which faced downstream was due to the installation method.

Two other 21-rod bundle coplanar flow blockage tests were compared with the COBRA-TF model. Test 42912C was a 0.025 m/sec (1 in./sec), 0.13 MPa (20 psia) reflood test; test 42314 was a stepped flow reflood test. The exact test conditions are given in table 4-1. Heater rod temperatures are plotted versus time in figures 4-64 through 4-75. In general, there is good agreement at each elevation; some heater rod overprediction occurs in test 42314C. The lower-pressure test, 42912C, does show a higher calculated heat transfer and hence lower heater rod temperature immediately downstream of the blockage at 1.90 m (75 in.) compared to the data. At the 1.98 m (78 in.) elevation, the agreement is better; at 3.05 m (120 in.), there is a slight overprediction of the heater rod temperatures. The trends observed in this test are consistent with those of the lower-pressure unblocked 21-rod bundle test 43112A and are more a result of the pressure effect on the entrainment and droplet size than of the blockage models which were used (as detailed in section 3).

In addition to the 21-rod bundle experiments discussed above, there were other comparisons with 21-rod bundle experiments which are not presented herein. These included experiments with only the center nine rods blocked in a coplanar configuration with the short concentric sleeve. These comparisons, performed with earlier versions of the COBRA-TF code, were not rerun with the final version. The agreement in these cases was comparable to that found with the 21-rod bundle configuration C results described above.

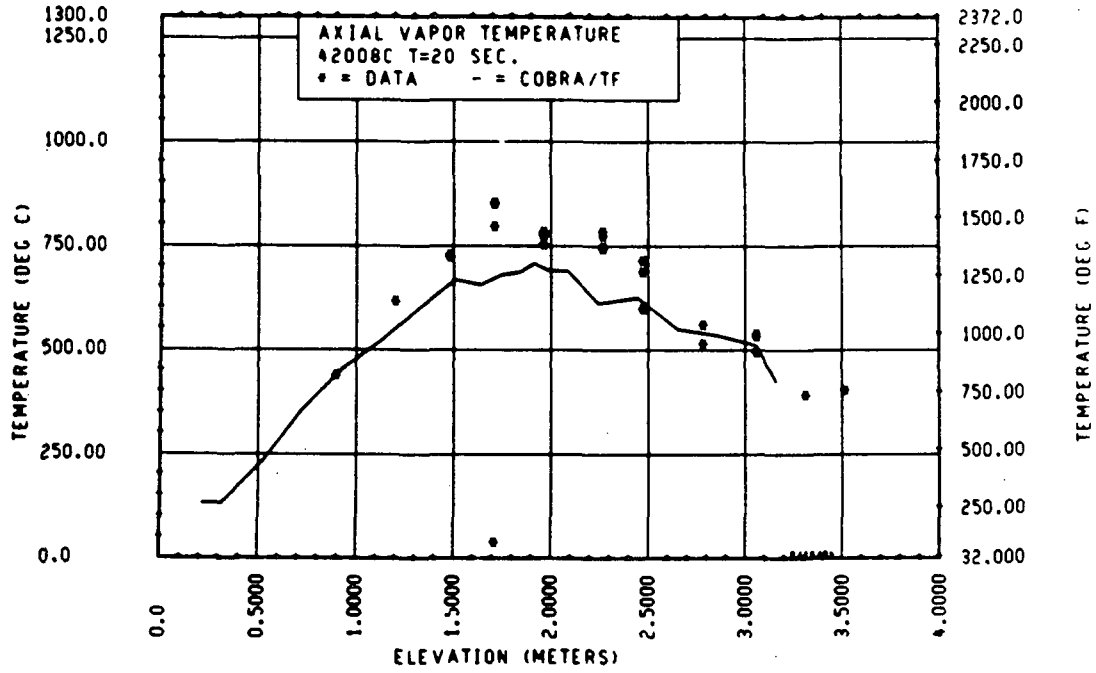

Figure 4-60. Comparison of COBRA-TF-Calculated Axial Vapor Temperature Versus Elevation With FLECHT SEASET 21-Rod Data, Test 42008C, t = 20 Seconds

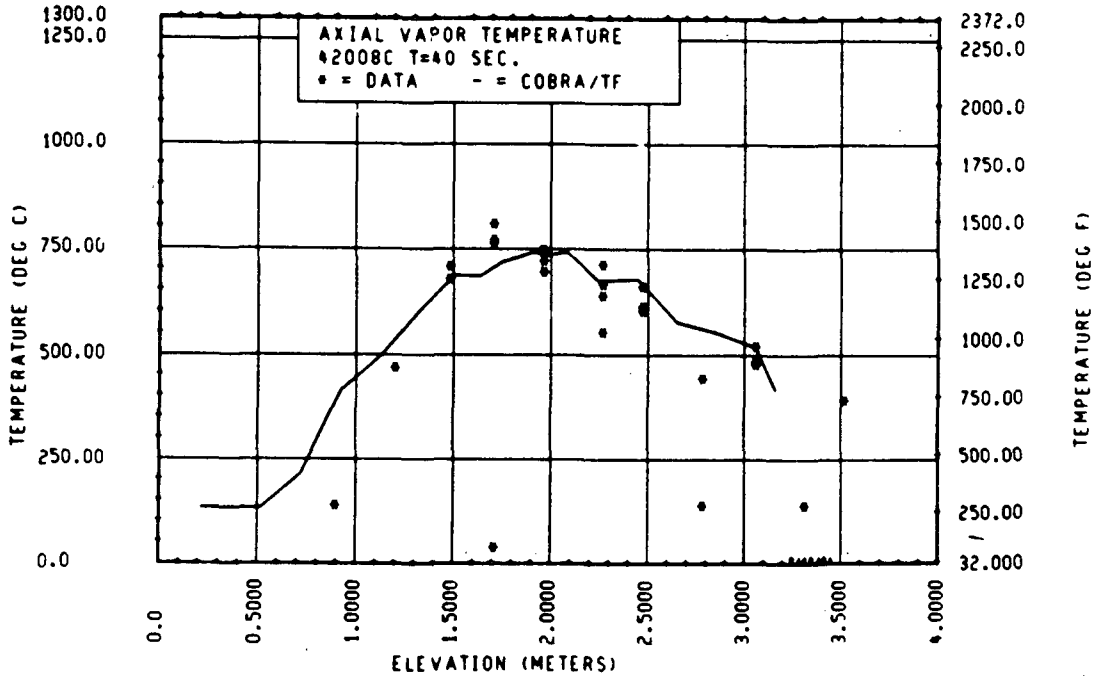

Figure 4-61. Comparison of COBRA-TF-Calculated Axial Vapor Temperature Versus Elevation With FLECHT SEASET 21-Rod Data, Test 42008C, t = 40 Seconds

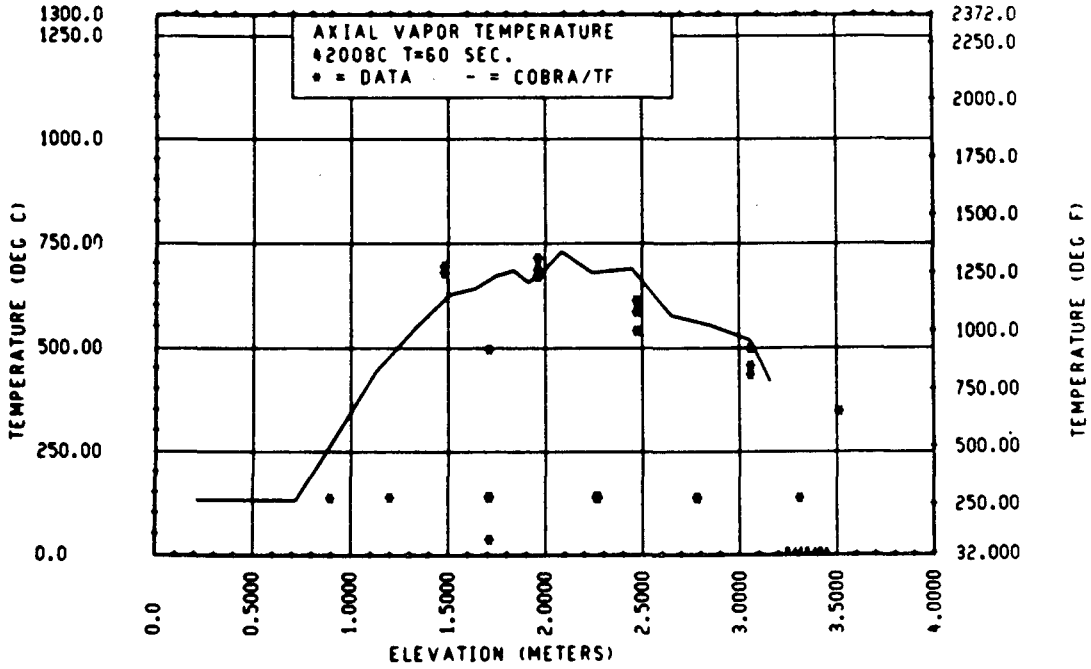

Figure 4-62. Comparison of COBRA-TF-Calculated Axial Vapor Temperature Versus Elevation With FLECHT SEASET 21-Rod Data, Test 42008C, t = 60 Seconds

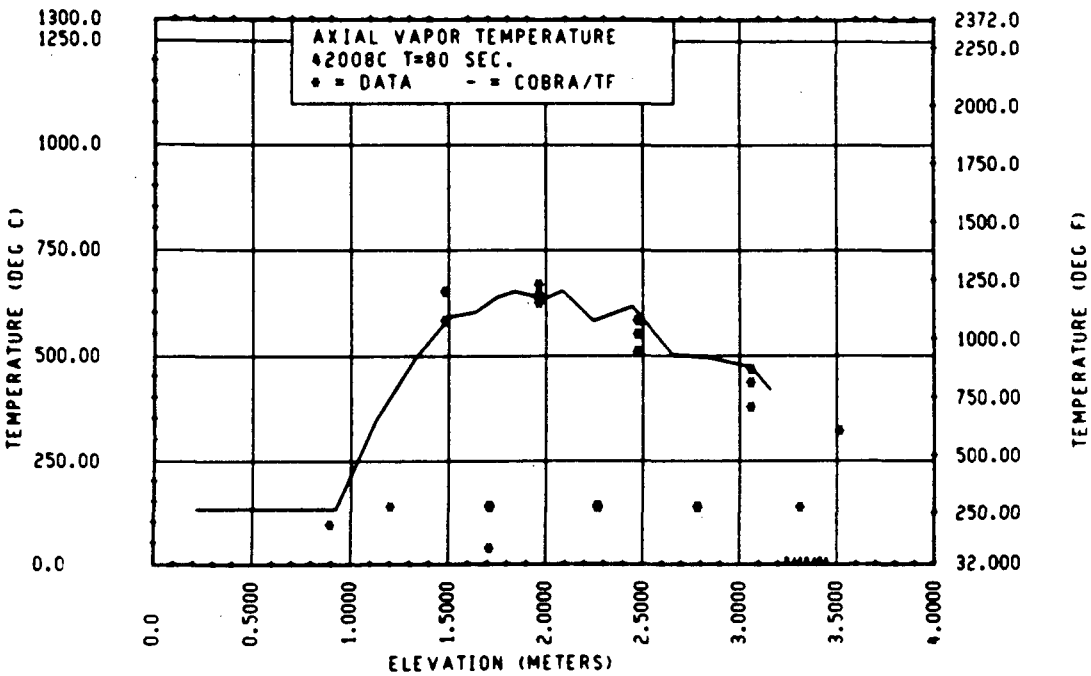

Figure 4-63. Comparison of COBRA-TF-Calculated Axial Vapor Temperature Versus Elevation With FLECHT SEASET 21-Rod Data, Test 42008C, t = 80 Seconds

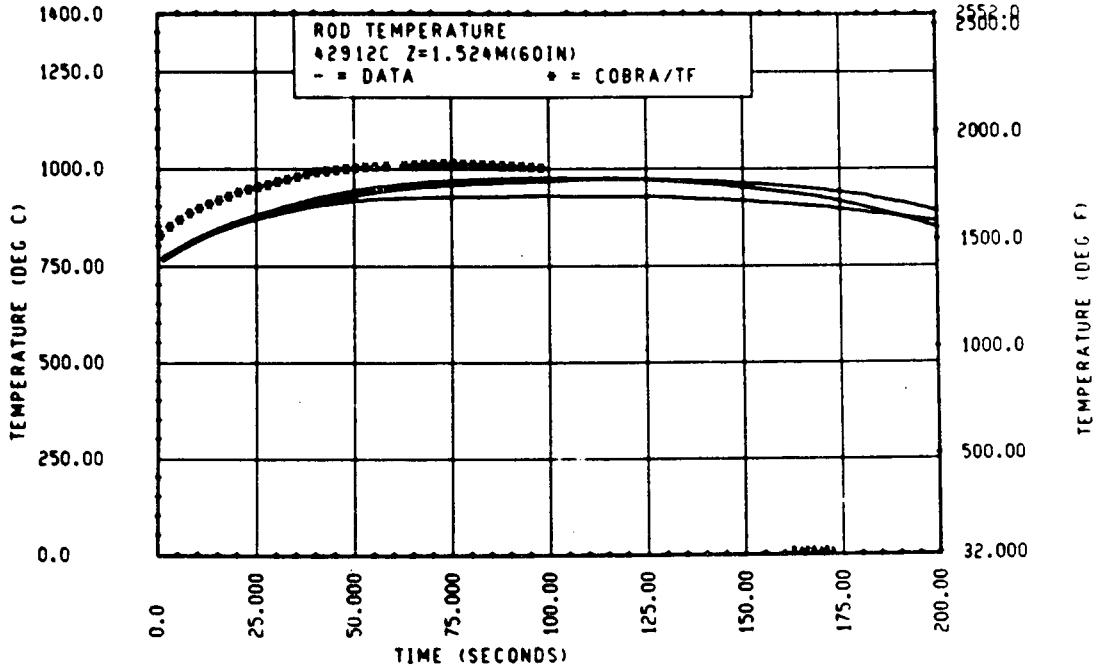

Figure 4-64. Comparison of COBRA-TF-Calculated Heater Rod Temperature Versus Time With FLECHT SEASET 21-Rod Data, Test 42912C, 1.52 m (60 in.) Elevation

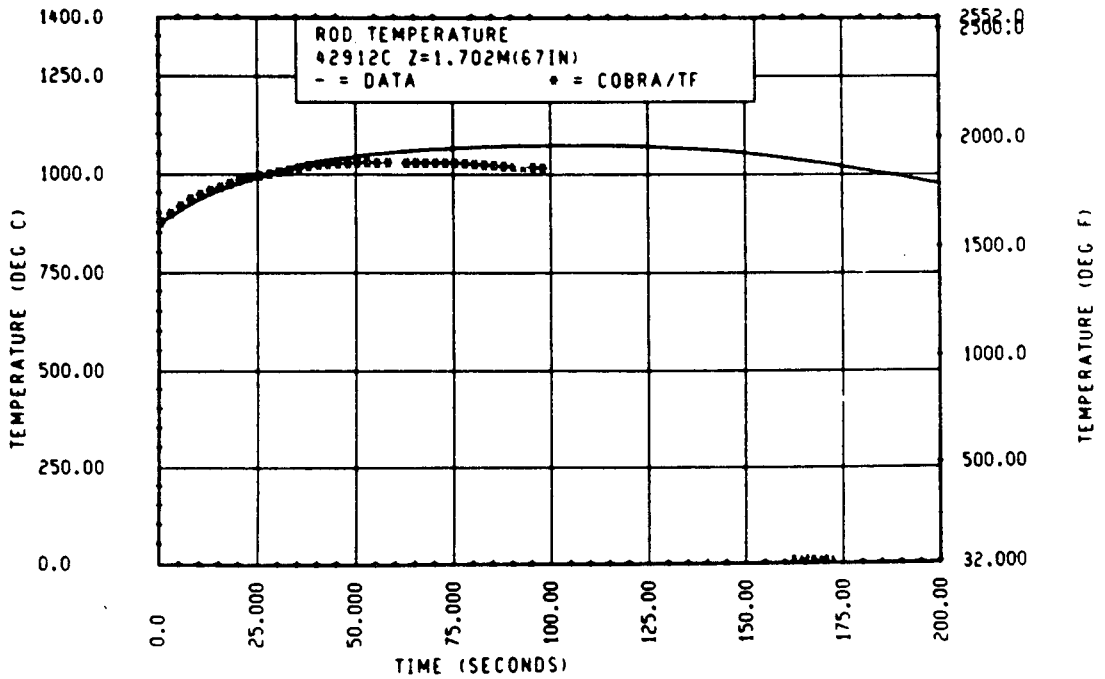

Figure 4-65. Comparison of COBRA-TF-Calculated Heater Rod Temperature Versus Time With FLECHT SEASET 21-Rod Data, Test 42912C, 1.70 m (67 in.) Elevation

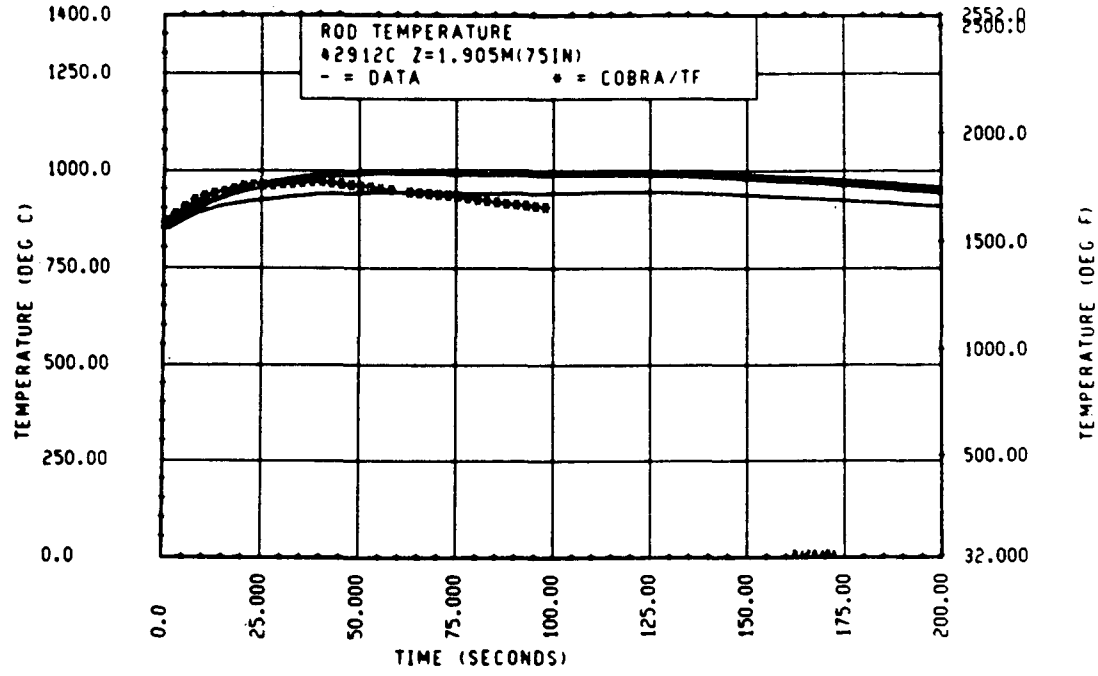

Figure 4-66. Comparison of COBRA-TF-Calculated Heater Rod Temperature Versus Time With FLECHT SEASET 21-Rod Data, Test 42912C, 1.90 m (75 in.) Elevation

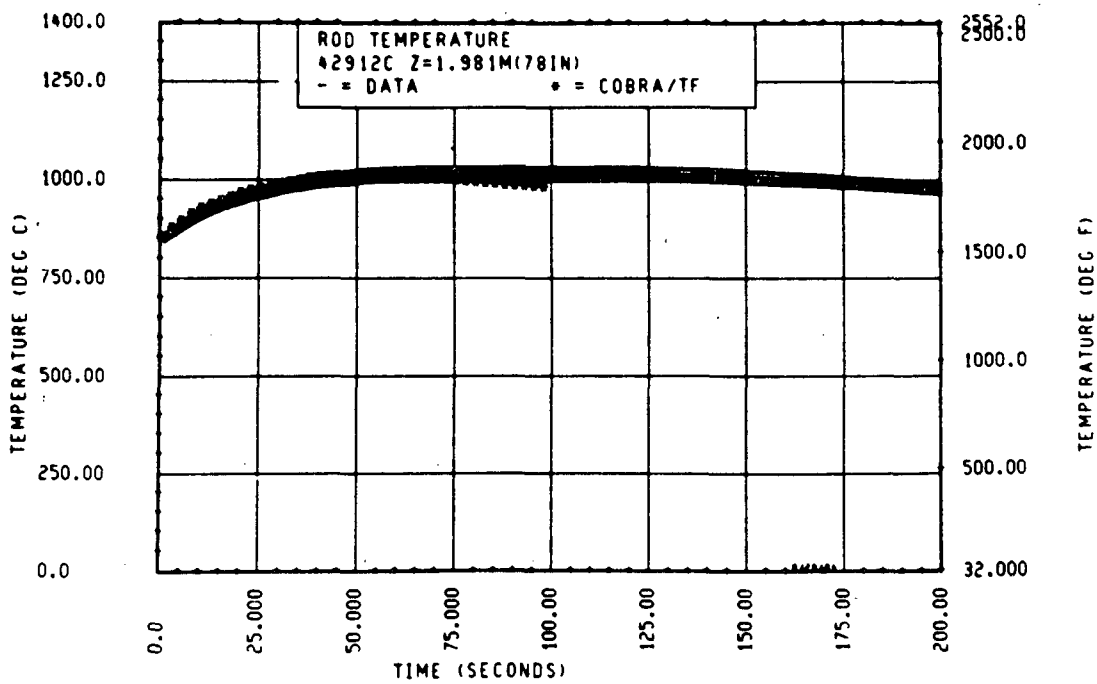

Figure 4-67. Comparison of COBRA-TF-Calculated Heater Rod Temperature Versus Time With FLECHT SEASET 21-Rod Data, Test 42912C, 1.98 m (78 in.) Elevation

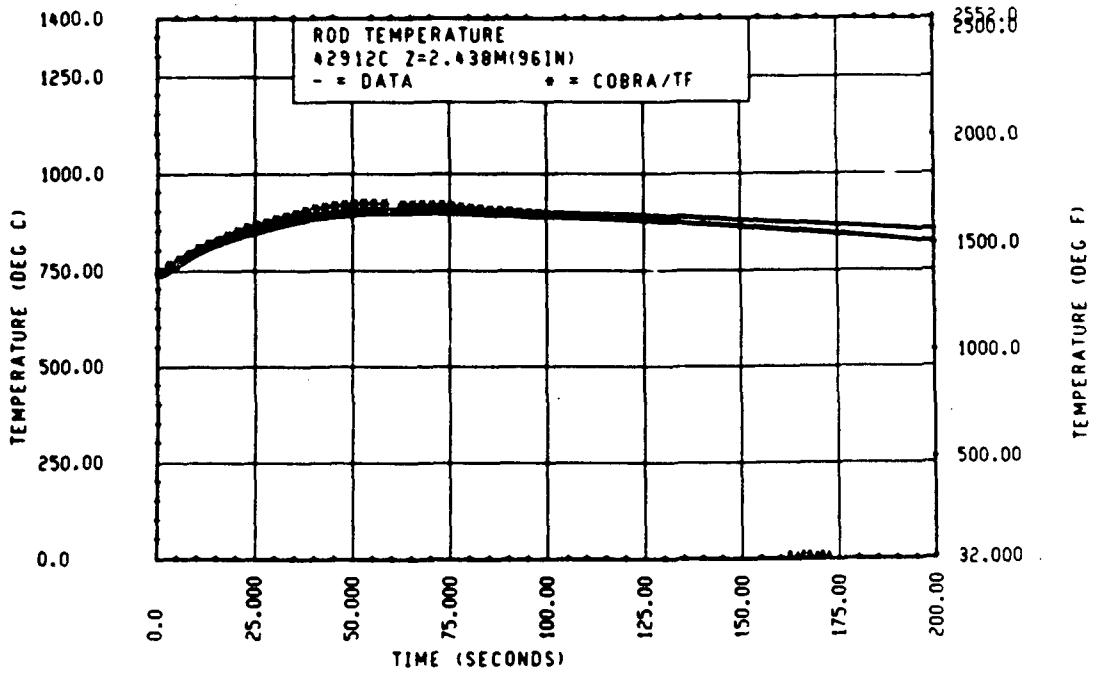

Figure 4-68. Comparison of COBRA-TF-Calculated Heater Rod Temperature Versus Time With FLECHT SEASET 21-Rod Data, Test 42912C, 2.44 m (96 in.) Elevation

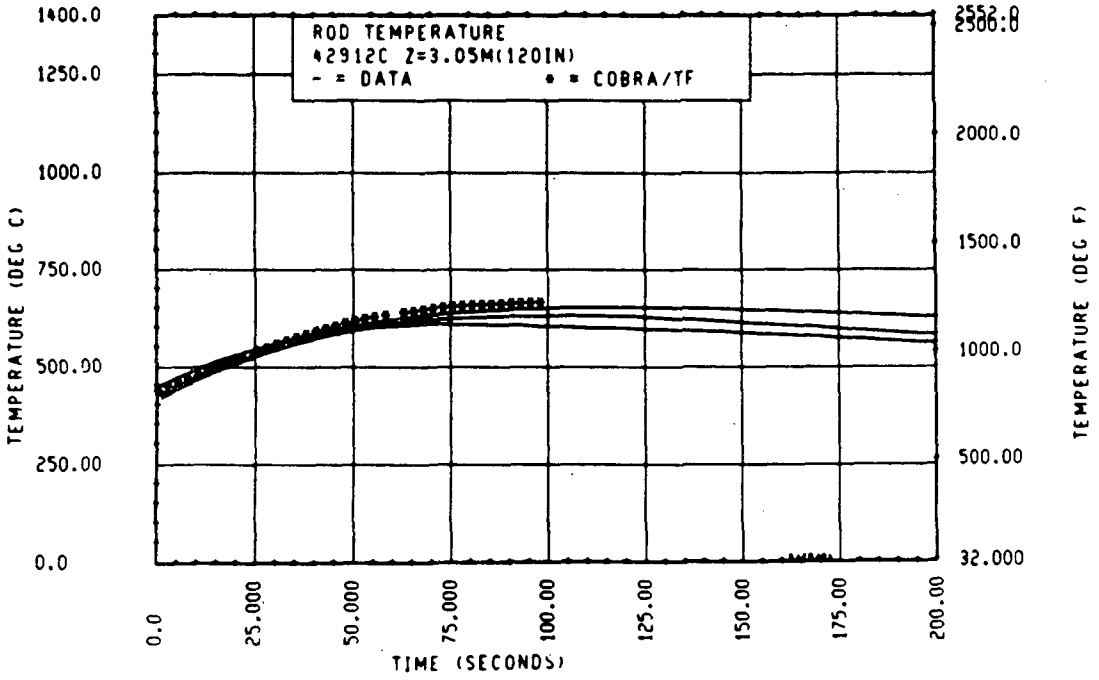

Figure 4-69. Comparison of COBRA-TF-Calculated Heater Rod Temperature Versus Time With FLECHT SEASET 21-Rod Data, Test 42912C, 3.05 m (120 in.) Elevation

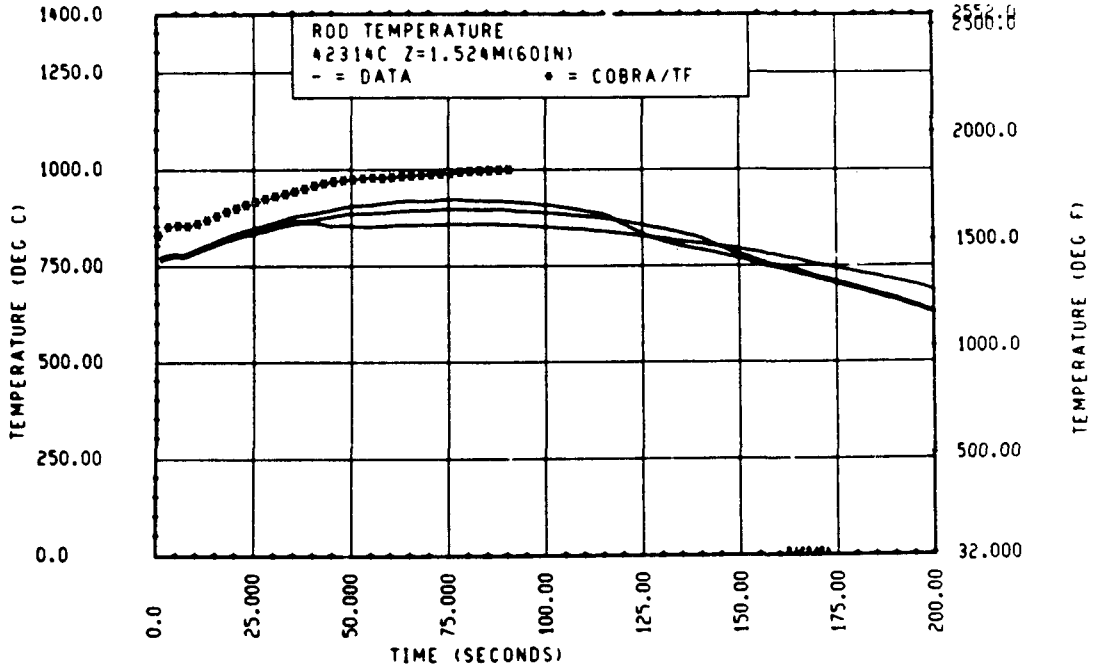

Figure 4-70. Comparison of COBRA-TF-Calculated Heater Rod Temperature Versus Time With FLECHT SEASET 21-Rod Data, Test 42314C, 1.52 m (60 in.) Elevation

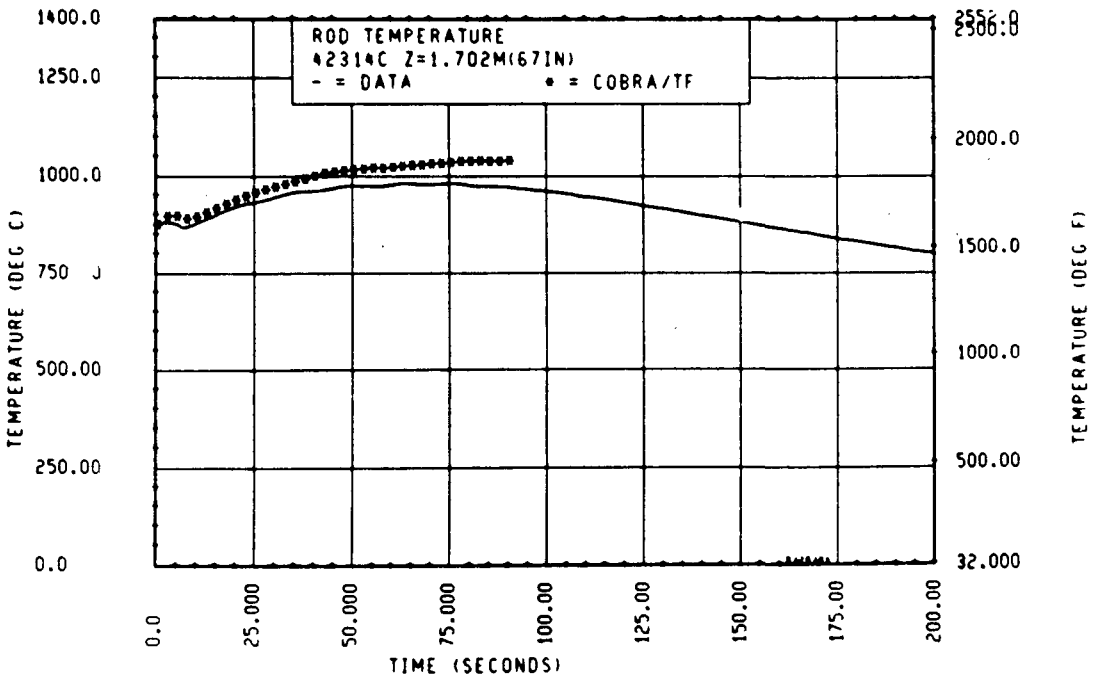

Figure 4-71. Comparison of COBRA-TF-Calculated Heater Rod Temperature Versus Time With FLECHT SEASET 21-Rod Data, Test 42314C, 1.70 m (67 in.) Elevation

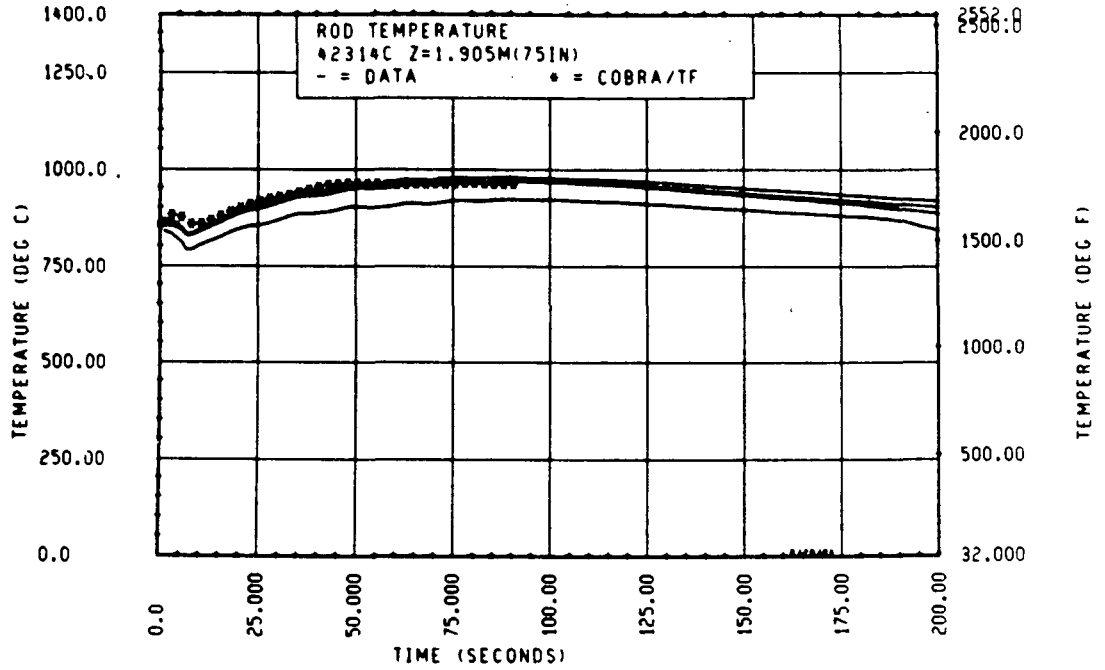

Figure 4-72. Comparison of COBRA-TF-Calculated Heater Rod Temperature Versus Time With FLECHT SEASET 21-Rod Data, Test 42314C, 1.90 m (75 in.) Elevation

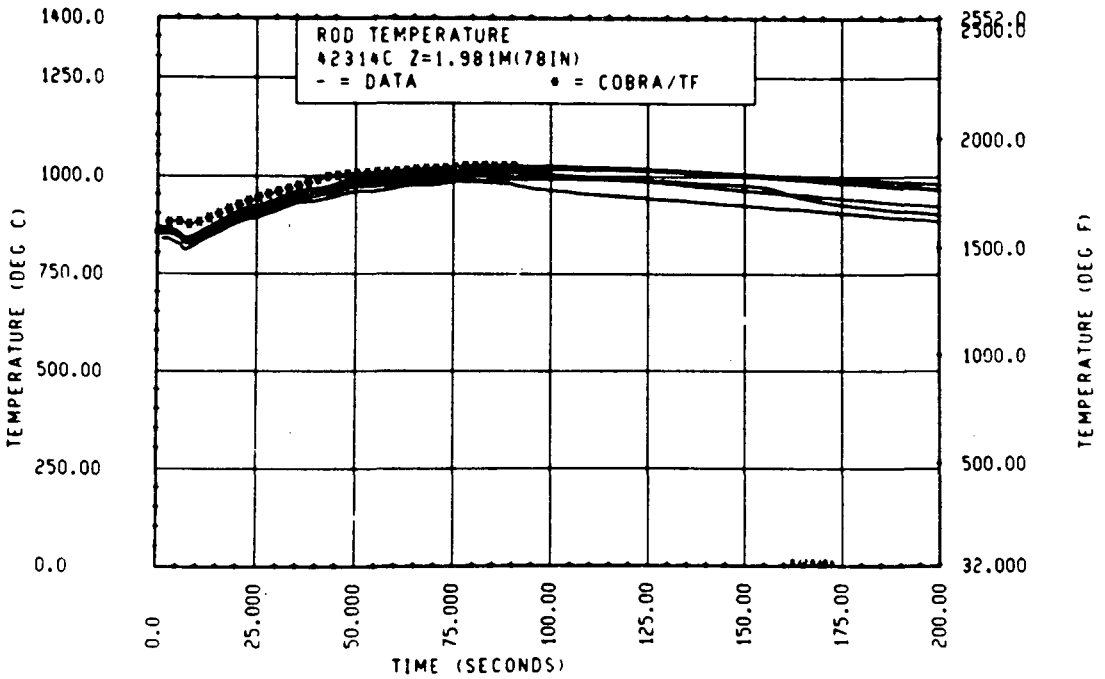

Figure 4-73. Comparison of COBRA-TF-Calculated Heater Rod Temperature Versus Time With FLECHT SEASET 21-Rod Data, Test 42314C, 1.98 m (78 in.) Elevation

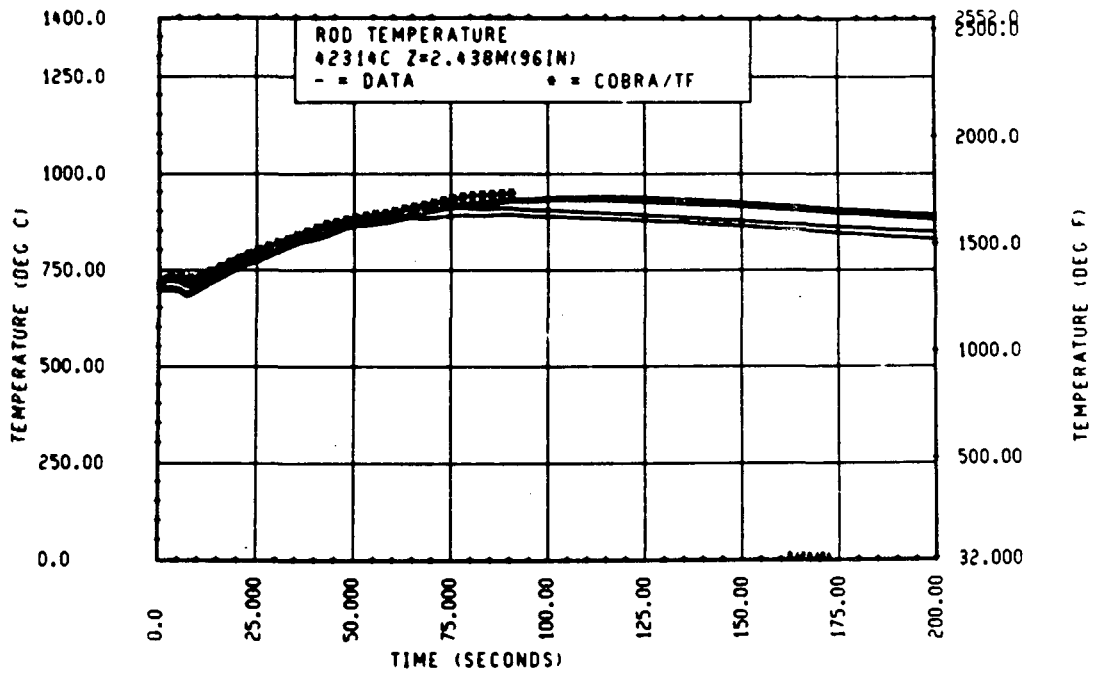

Figure 4-74. Comparison of COBRA-TF-Calculated Heater Rod Temperature Versus Time With FLECHT SEASET 21-Rod Data, Test 42314C, 2.44 m (96 in.) Elevation

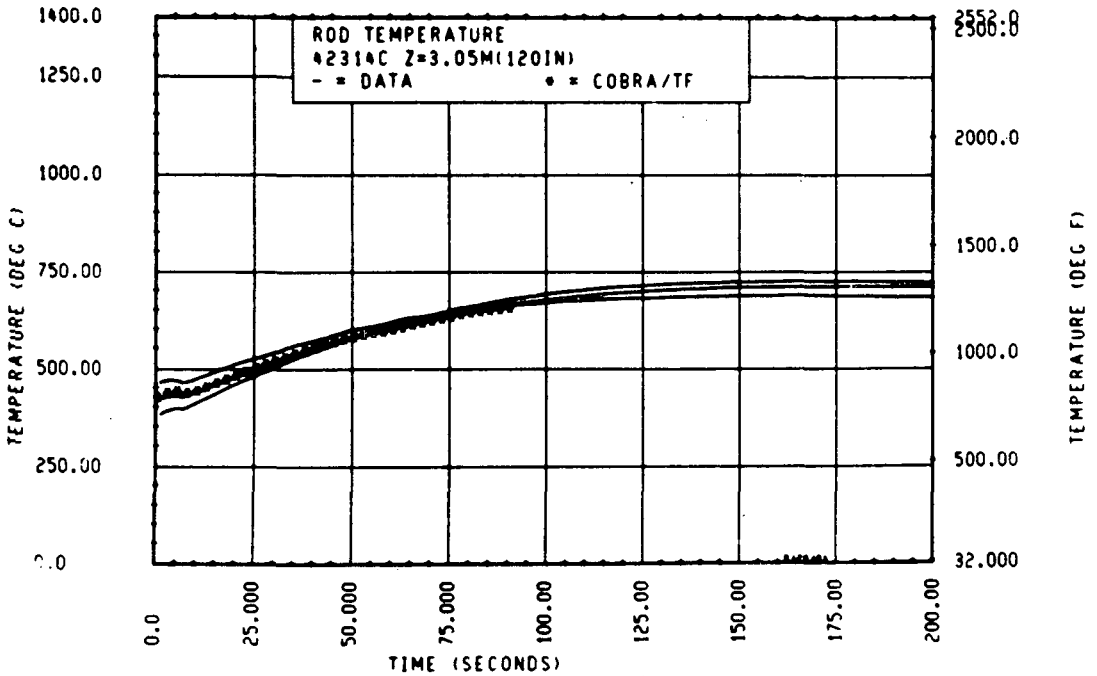

Figure 4-75. Comparison of COBRA-TF-Calculated Heater Rod Temperature Versus Time With FLECHT SEASET 21-Rod Data, Test 42314C, 3.05 m (120 in.) Elevation

The noncoplanar blockage sleeve distributions and shapes tested in the FLECHT SEASET 21-rod bundle configuration F were also modeled with COBRA-TF. The blockage shape used in configuration F is shown in figure 4-2 and the axial distribution of the blockage is shown in figure 4-3. The blockage sleeves were distributed on the heater rods as described earlier in this section to give a noncoplanar blockage distribution. The 21-rod bundle configuration F heat transfer data indicated that, once the two-phase dispersed flow was developed, the noncoplanar blockage data showed the same amount of scatter as the coplanar blockage data; this indicates that good radial mixing was occurring in the tests. Therefore, the noncoplanar blockage distribution was modeled as three regions of coplanar blockage, as described in appendix D.

The key parameter in the modeling is the method used to calculate the droplet breakup area. As shown below, the most important blockage model is the droplet breakup model. The method used for modeling the 21-rod bundle tests is given in appendix C.

The same four test conditions were repeated for the 21-rod bundle configuration F, with the long sleeve, noncoplanar blockage, as for configuration C with the short concentric sleeve coplanar blockage. All rods were blocked in the configuration F tests; however, because the blockage was noncoplanar, the flow field was locally three-dimensional as the flow shifted from one subchannel to another because of local subchannel blockage variation.

The COBRA-TF code with the blockage and grid models is compared with the nonconcentric, noncoplanar blockage data from the FLECHT SEASET 21-rod bundle test 42006F in figures 4-76 through 4-89. It is important to note that the blockage models described earlier in this section were <u>not</u> changed to handle this significantly different blockage shape and distribution. What was changed was the manner in which the blockage was modeled in COBRA-TF as a series of coplanar regions (appendix D).

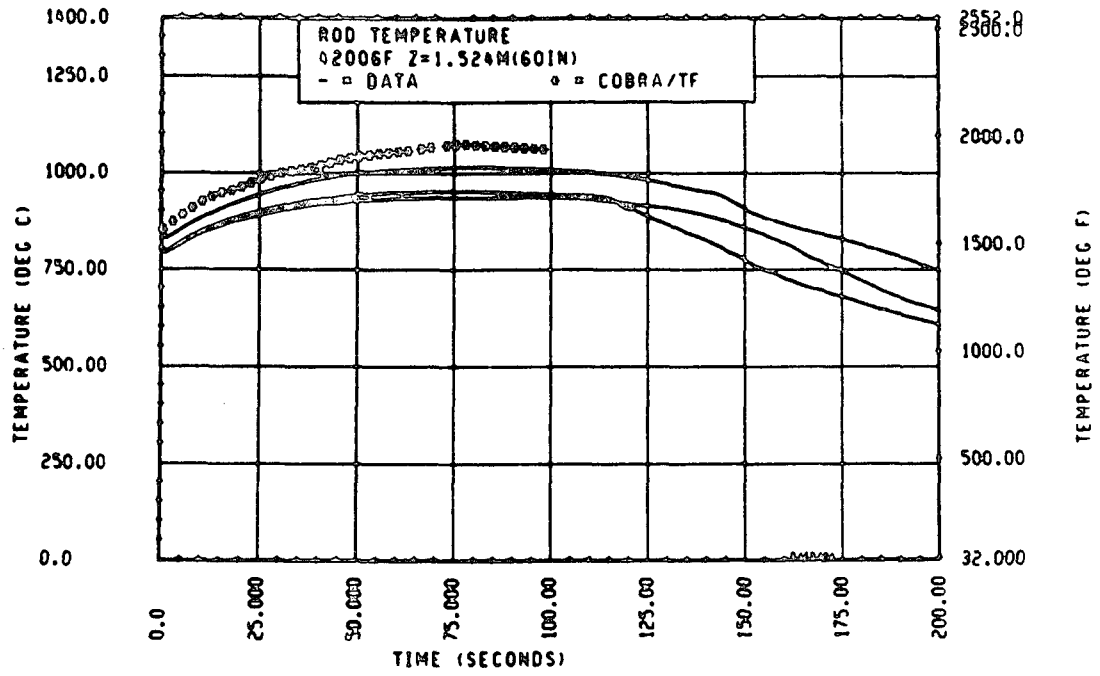

Figure 4-76. Comparison of COBRA-TF-Calculated Heater Rod Temperature Versus Time With FLECHT SEASET 21-Rod Data, Test 42006F, 1.52 m (60 in.) Elevation

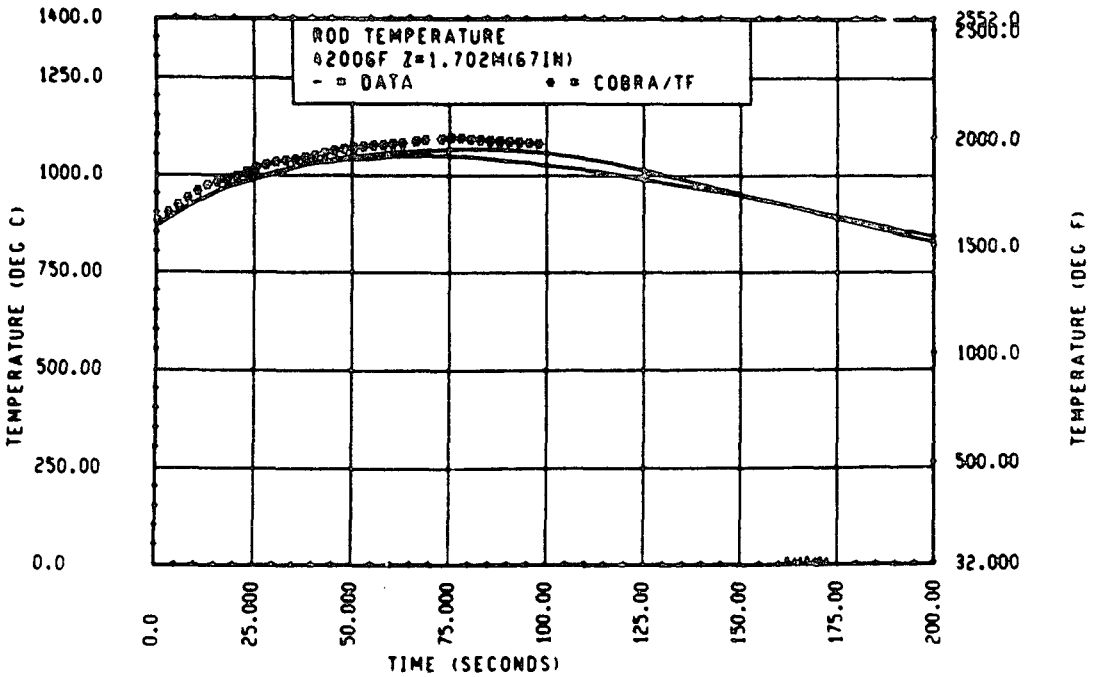

Figure 4-77. Comparison of COBRA-TF-Calculated Heater Rod Temperature Versus Time With FLECHT SEASET 21-Rod Data, Test 42006F, 1.70 m (67 in.) Elevation

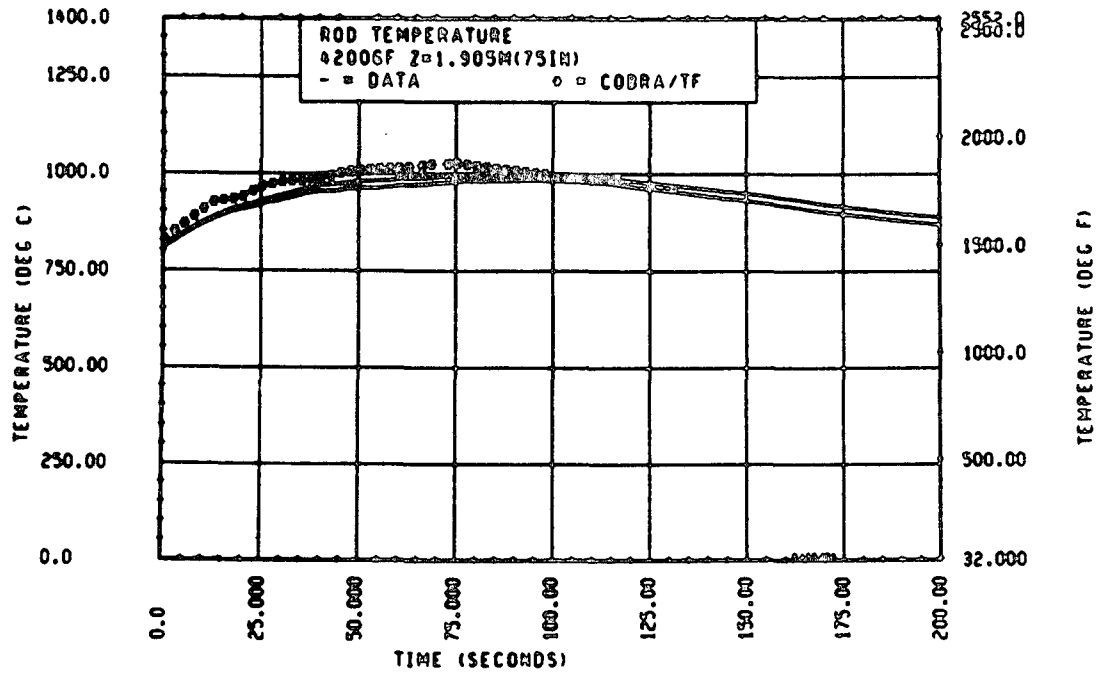

Figure 4-78. Comparison of COBRA-TF-Calculated Heater Rod Temperature Versus Time With FLECHT SEASET 21-Rod Data, Test 42006F, 1.90 m (75 in.) Elevation

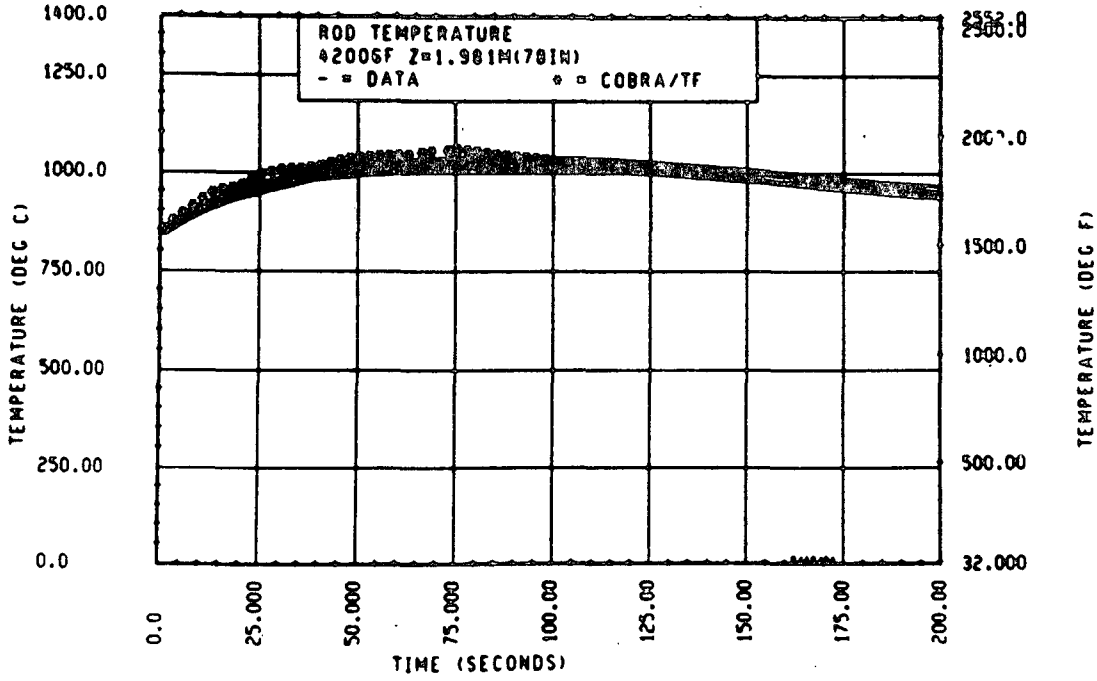

Figure 4-79. Comparison of COBRA-TF-Calculated Heater Rod Temperature Versus Time With FLECHT SEASET 21-Rod Data, Test 42006F, 1.98 m (78 in.) Elevation

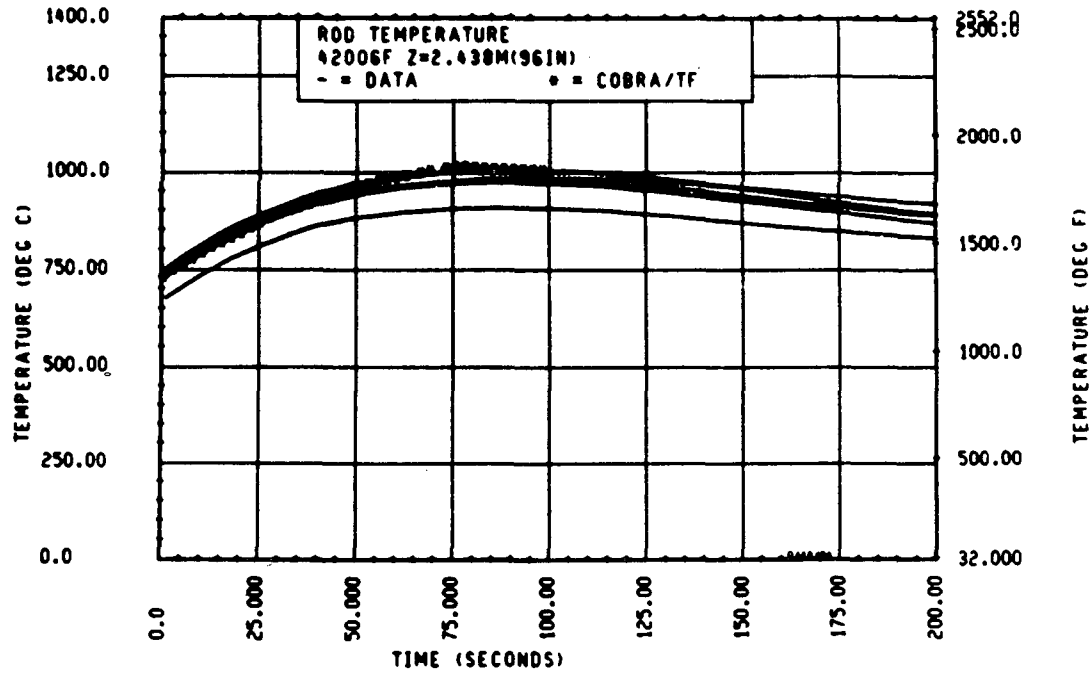

Figure 4-80. Comparison of COBRA-TF-Calculated Heater Rod Temperature Versus Time With FLECHT SEASET 21-Rod Data, Test 42006F, 2.44 m (96 in.) Elevation

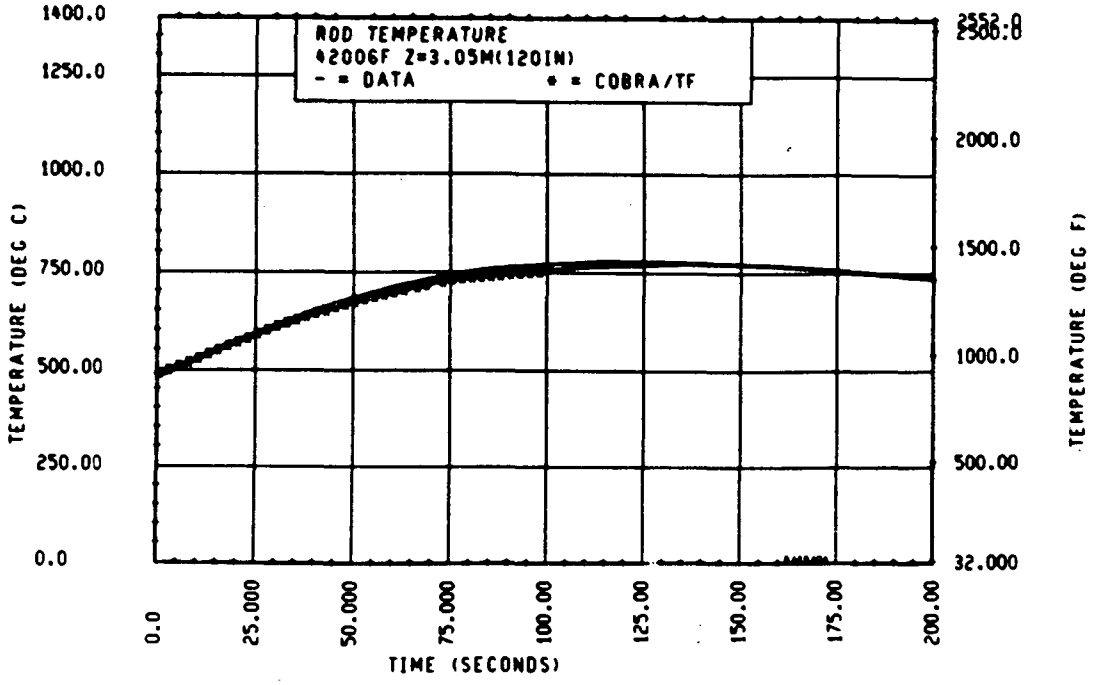

Figure 4-81. Comparison of COBRA-TF-Calculated Heater Rod Temperature Versus Time With FLECHT SEASET 21-Rod Data, Test 42006F, 3.05 m (120 in.) Elevation

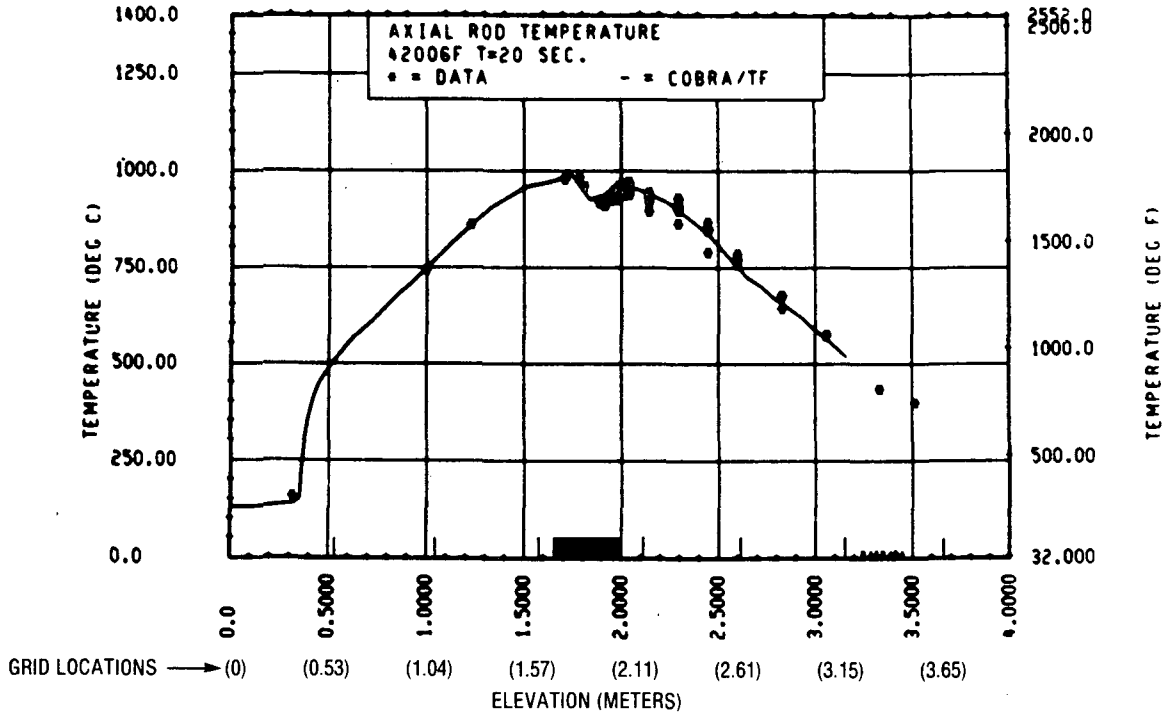

Figure 4-82. Comparison of COBRA-TF-Calculated Axial Rod Temperature Versus Elevation With FLECHT SEASET 21-Rod Data, Test 42006F, t = 20 Seconds

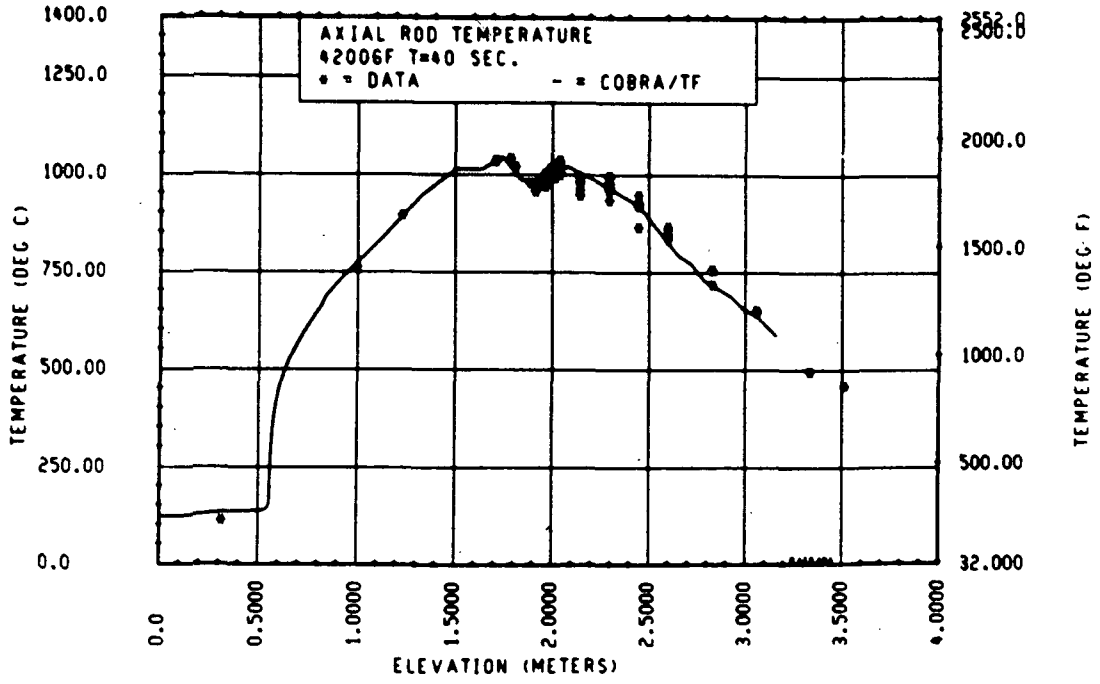

Figure 4-83. Comparison of COBRA-TF-Calculated Axial Rod Temperature Versus Elevation With FLECHT SEASET 21-Rod Data, Test 42006F, t = 40 Seconds

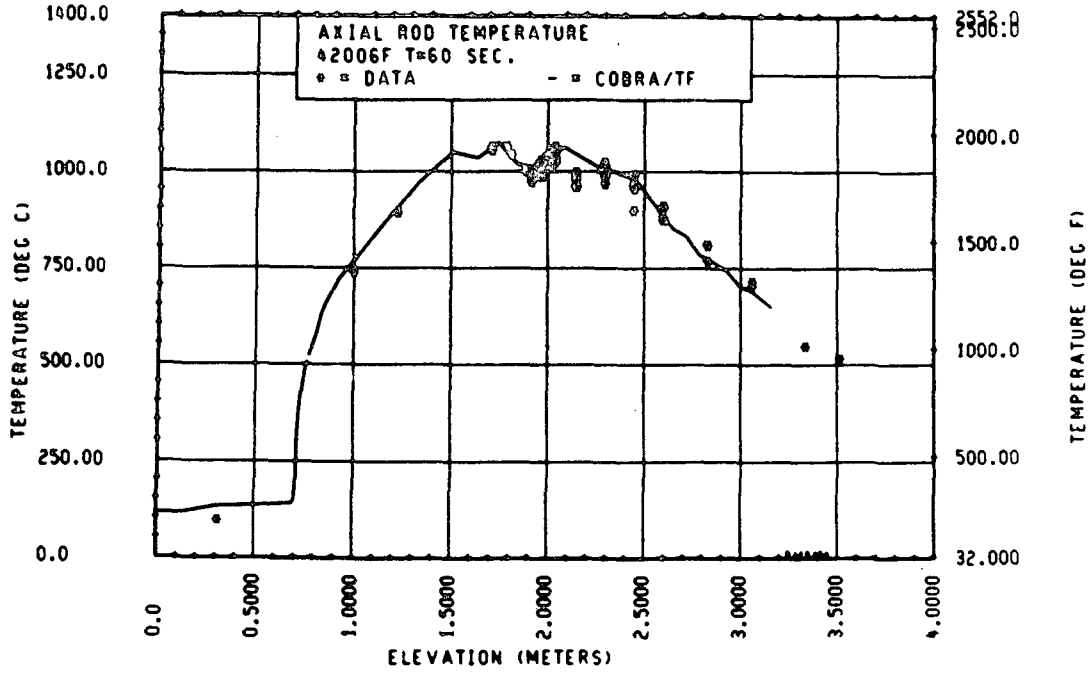

Figure 4-84. Comparison of COBRA-TF-Calculated Axial Rod Temperature Versus Elevation With FLECHT SEASET 21-Rod Data, Test 42006F, t = 60 Seconds

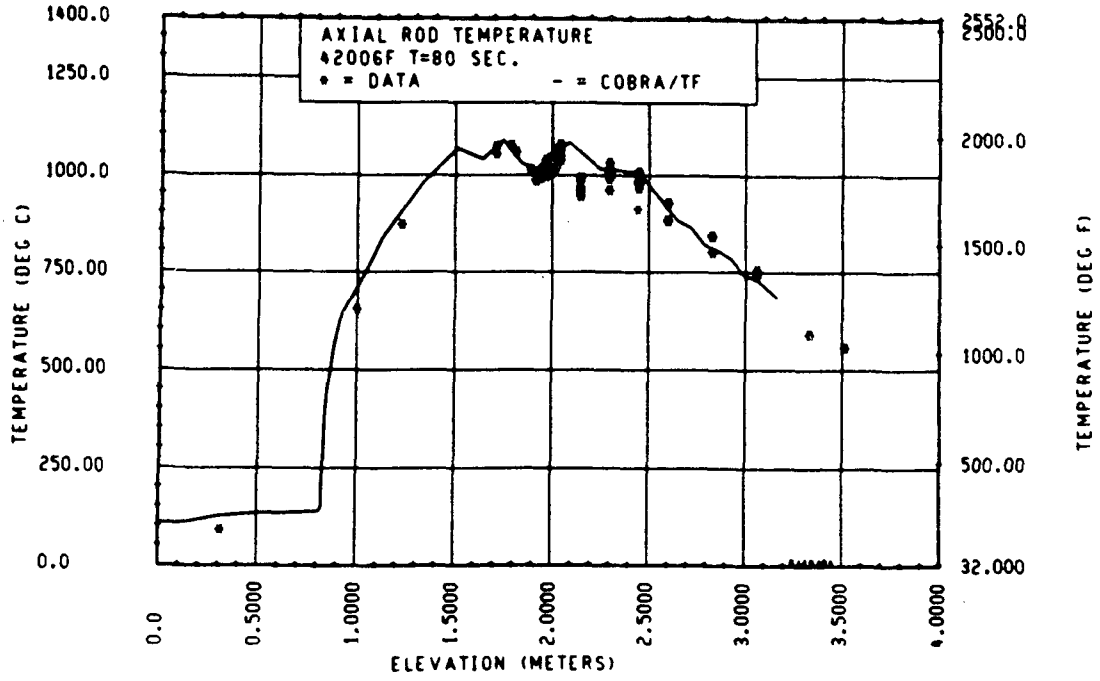

Figure 4-85. Comparison of COBRA-TF-Calculated Axial Rod Temperature Versus Elevation With FLECHT SEASET 21-Rod Data, Test 42006F, t = 80 Seconds

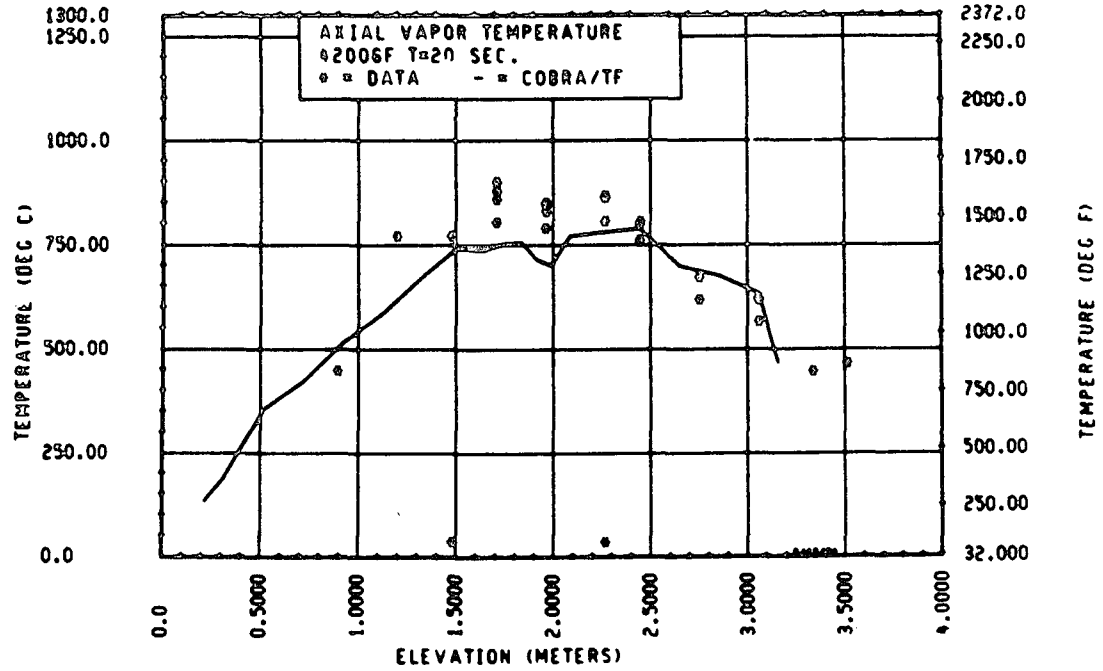

Figure 4-86. Comparison of COBRA-TF-Calculated Axial Vapor Temperature Versus Elevation With FLECHT SEASET 21-Rod Data, Test 42006F, t = 20 Seconds

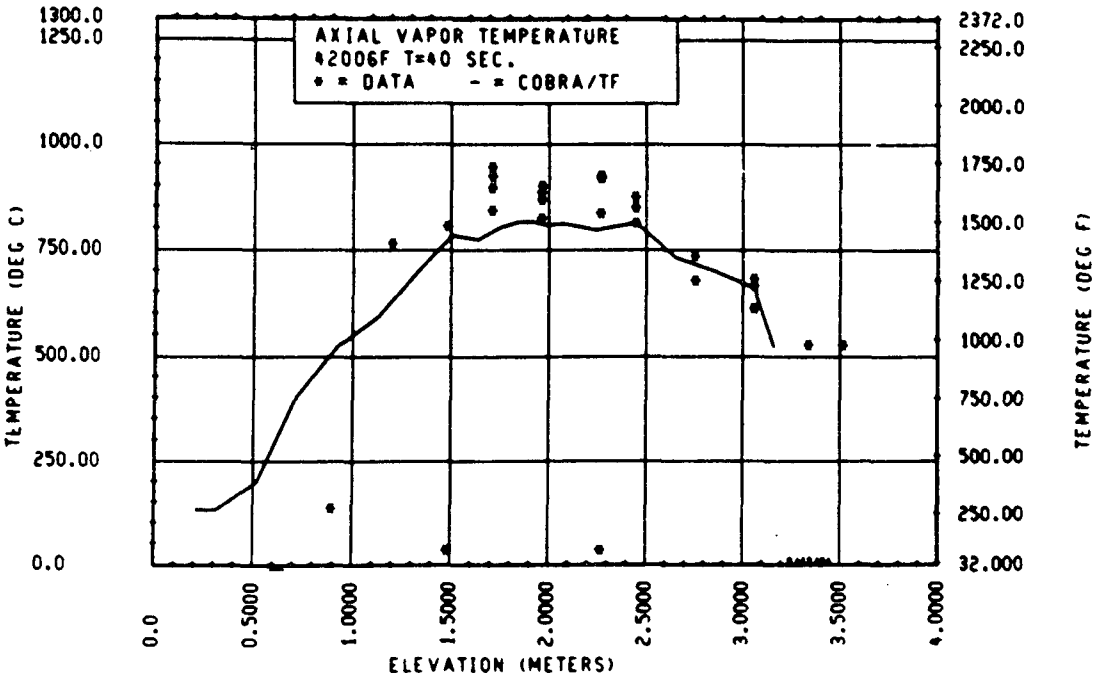

Figure 4-87. Comparison of COBRA-TF-Calculated Axial Vapor Temperature Versus Elevation With FLECHT SEASET 21-Rod Data, Test 42006F, t = 40 Seconds

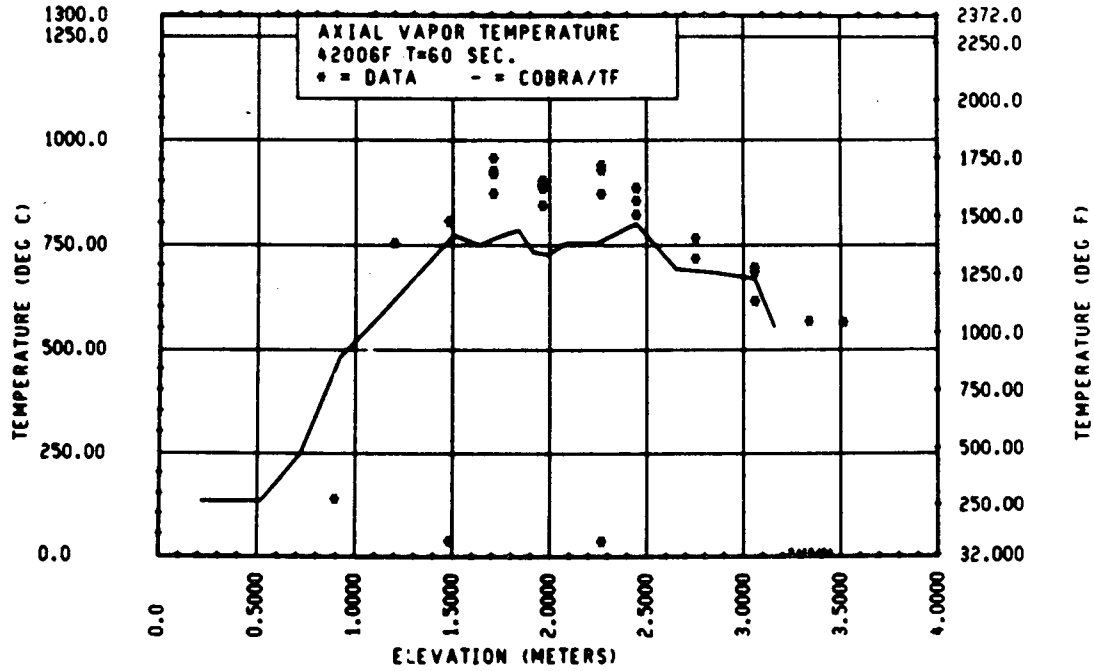

Figure 4-88. Comparison of COBRA-TF-Calculated Axial Vapor Temperature Versus Elevation With FLECHT SEASET 21-Rod Data, Test 42006F, t = 60 Seconds

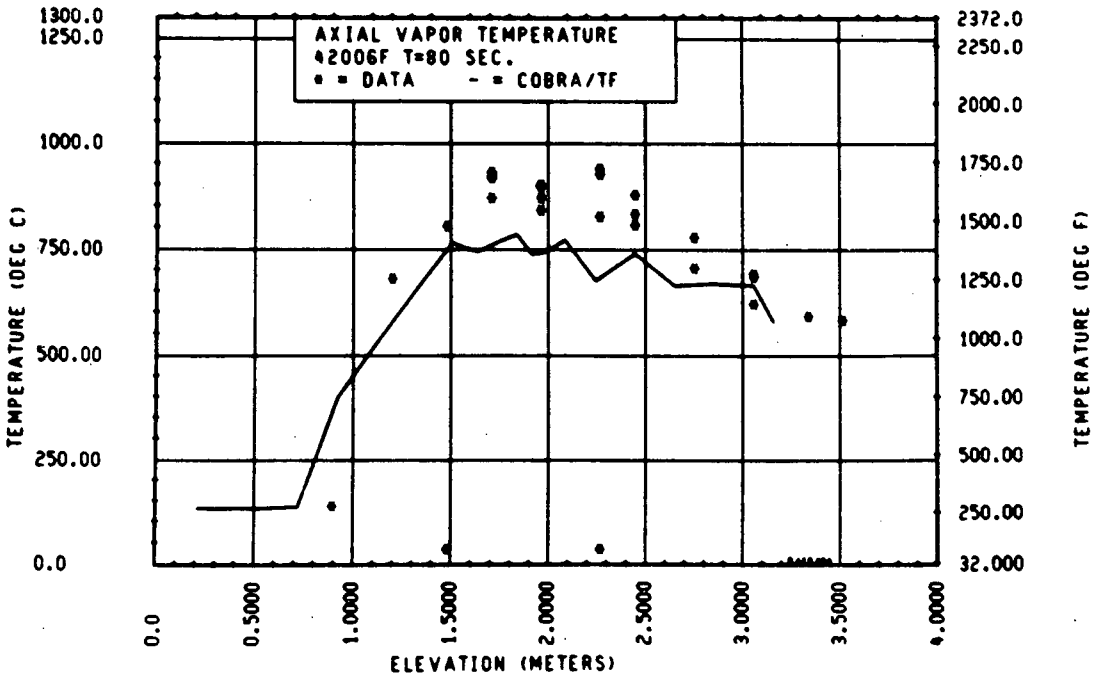

Figure 4-89. Comparison of COBRA-TF-Calculated Axial Vapor Temperature Versus Elevation With FLECHT SEASET 21-Rod Data, Test 42006F, t = 80 Seconds

The heater rod temperature versus time comparisons (figures 4-76 through 4-81) generally show good agreement. However, there appears to be some overprediction at most elevations. The axial heater rod temperature plots (figures 4-82 through 4-85) show improved agreement. (Also shown in figure 4-82 is the axial location of the spacer grids and the blockage zone.) As observed earlier on previous 21-rod bundle configuration, the heat transfer is improved downstream of the 2.11 m (83 in.) grid location. The clad temperature axial distribution through and downstream of the blockage region appears to be predicted quite well by the COBRA-TF code, indicating that both the blockage models used and the method of modeling the blockage in the code give the correct behavior.

The COBRA-TF-predicted vapor temperatures for 21-rod bundle test 42006F are shown in figures 4-86 through 4-89. As observed for other 21-rod bundle tests with these conditions, the COBRA-TF calculations tend to predict lower vapor temperatures than were measured in the experiments. As also noted previously, the effect of the 1.57 m (62 in.) grid is overpredicted, resulting in lower vapor temperatures in the midplane region of the bundle.

A similar series of comparison plots for FLECHT SEASET 21-rod bundle test 41608F, a 0.038 m/sec (1.5 in./sec) flooding rate experiment, are shown in figures 4-90 through 4-103. The heater rod temperature versus time plots (figures 4-90 through 4-95) show a little better agreement than those of test 42006F. The COBRA-TF calculation is usually within or at the upper data curve, such that there is a smaller overprediction. There is an overprediction of the heater rod temperature at the 1.90 m (75 in.) elevation, which is within the blockage zone. This overprediction could be a consequence of the method used to model the blockage, where some simplification had to be made.

The axial heater rod temperature plots shown in figures 4-96 through 4-99 again show very good agreement between the COBRA-TF prediction and the blockage data. (Also shown in figure 4-96 is the axial location of the spacer grids and the blockage zone.) There is a slight overprediction of the heater rod temperatures at the bundle midplane at later times for this test. The comparison of the axial vapor temperatures in this experiment is quite good

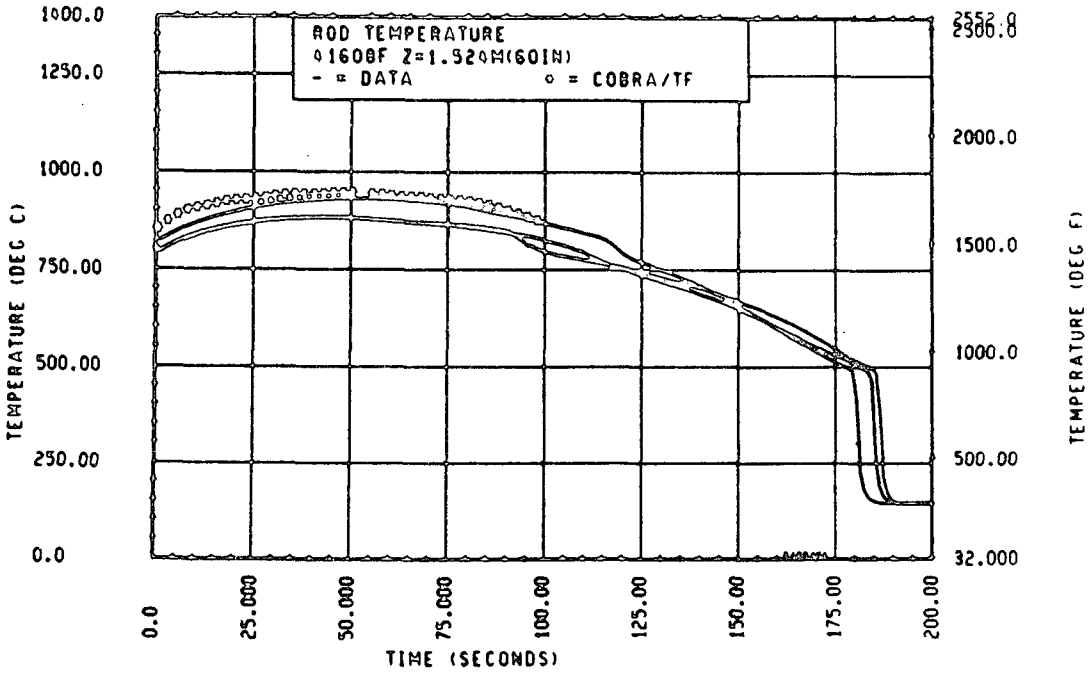

Figure 4-90. Comparison of COBRA-TF-Calculated Heater Rod Temperature Versus Time With FLECHT SEASET 21-Rod Data, Test 41608F, 1.52 m (60 in.) Elevation

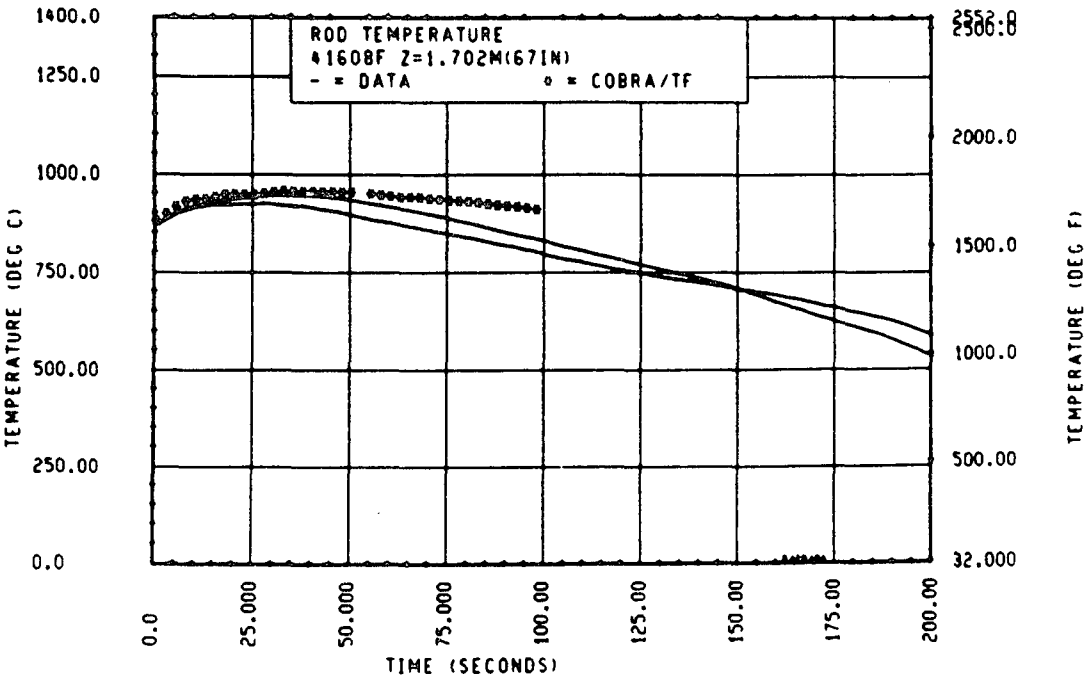

Figure 4-91. Comparison of COBRA-TF-Calculated Heater Rod Temperature Versus Time With FLECHT SEASET 21-Rod Data, Test 41608F, 1.70 m (67 in.) Elevation

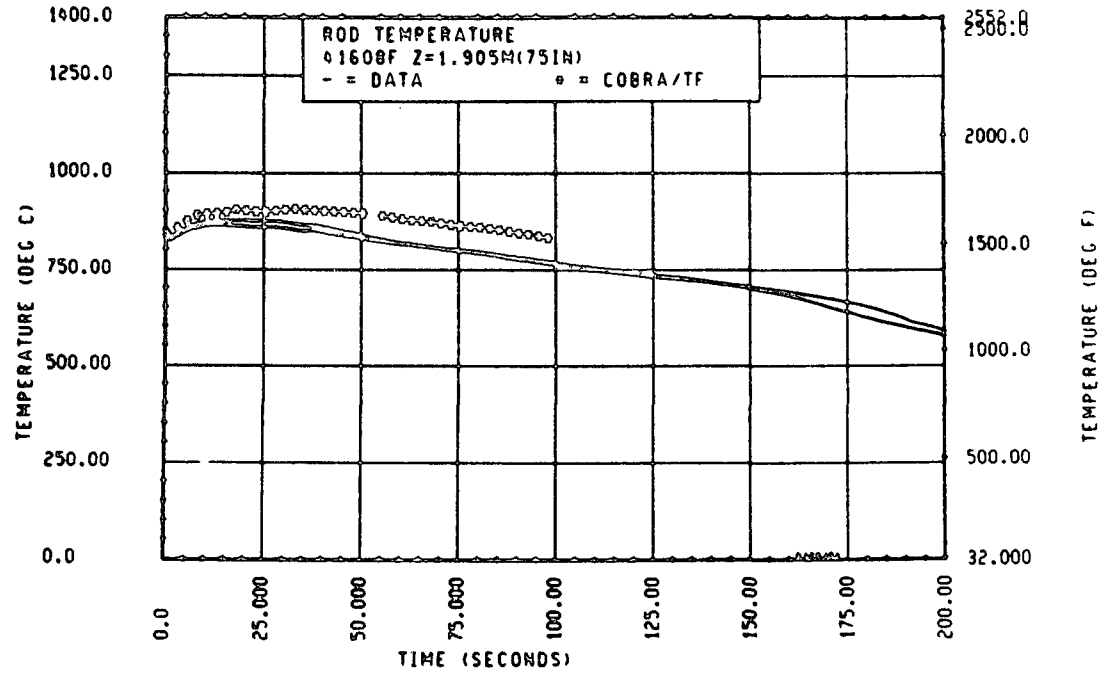

Figure 4-92. Comparison of COBRA-TF-Calculated Heater Rod Temperature Versus Time With FLECHT SEASET 21-Rod Data, Test 41608F, 1.90 m (75 in.) Elevation

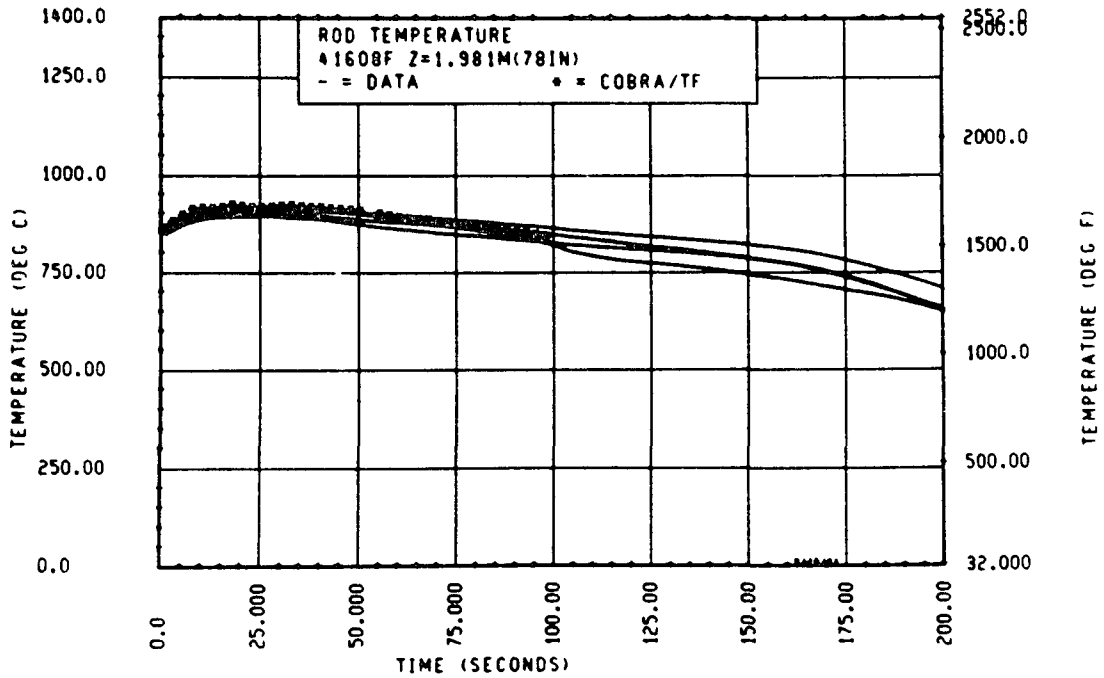

Figure 4-93. Comparison of COBRA-TF-Calculated Heater Rod Temperature Versus Time With FLECHT SEASET 21-Rod Data, Test 41608F, 1.98 m (78 in.) Elevation

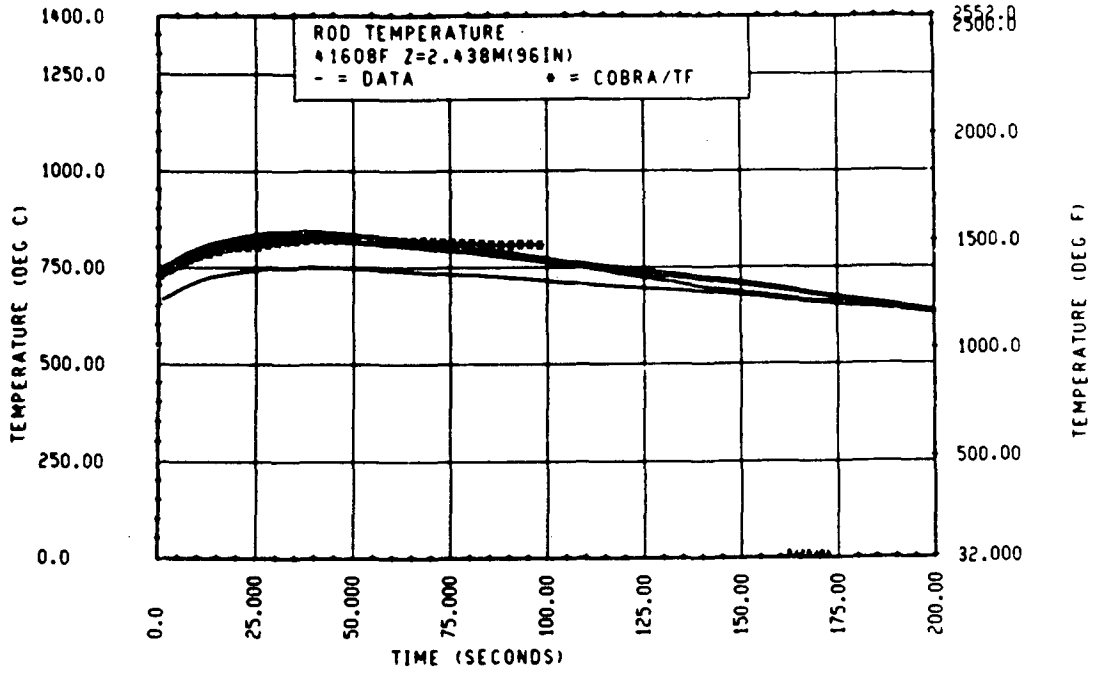

Figure 4-94. Comparison of COBRA-TF-Calculated Heater Rod Temperature Versus Time With FLECHT SEASET 21-Rod Data, Test 41608F, 2.44 m (96 in.) Elevation

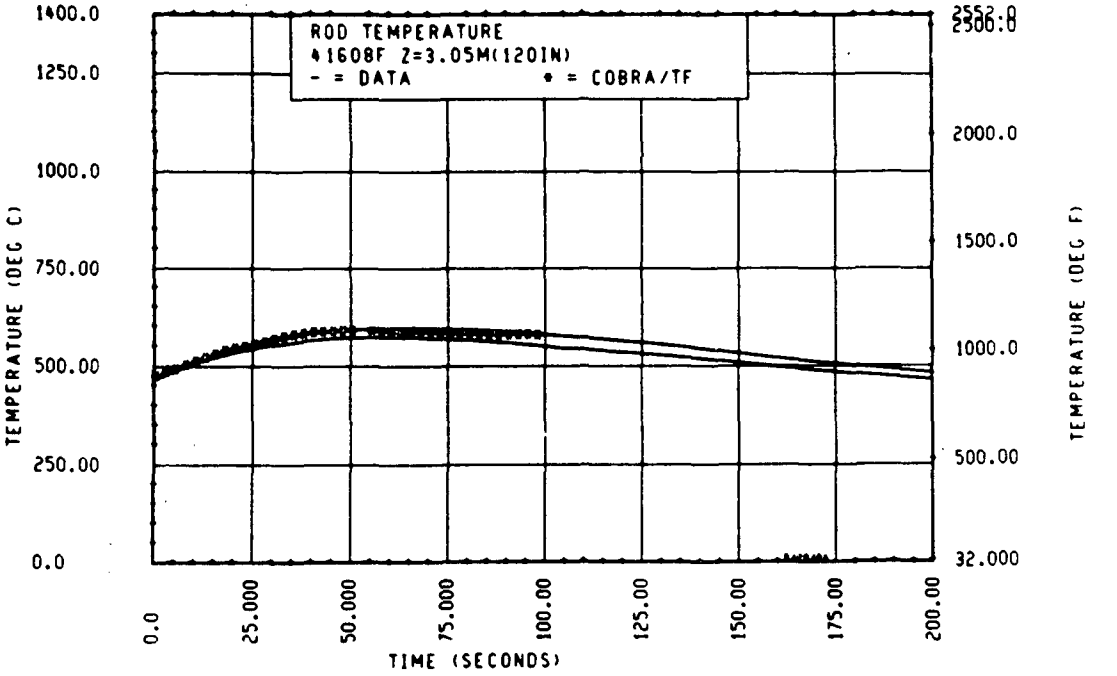

Figure 4-95. Comparison of COBRA-TF-Calculated Heater Rod Temperature Versus Time With FLECHT SEASET 21-Rod Data, Test 41608F, 3.05 m (120 in.) Elevation

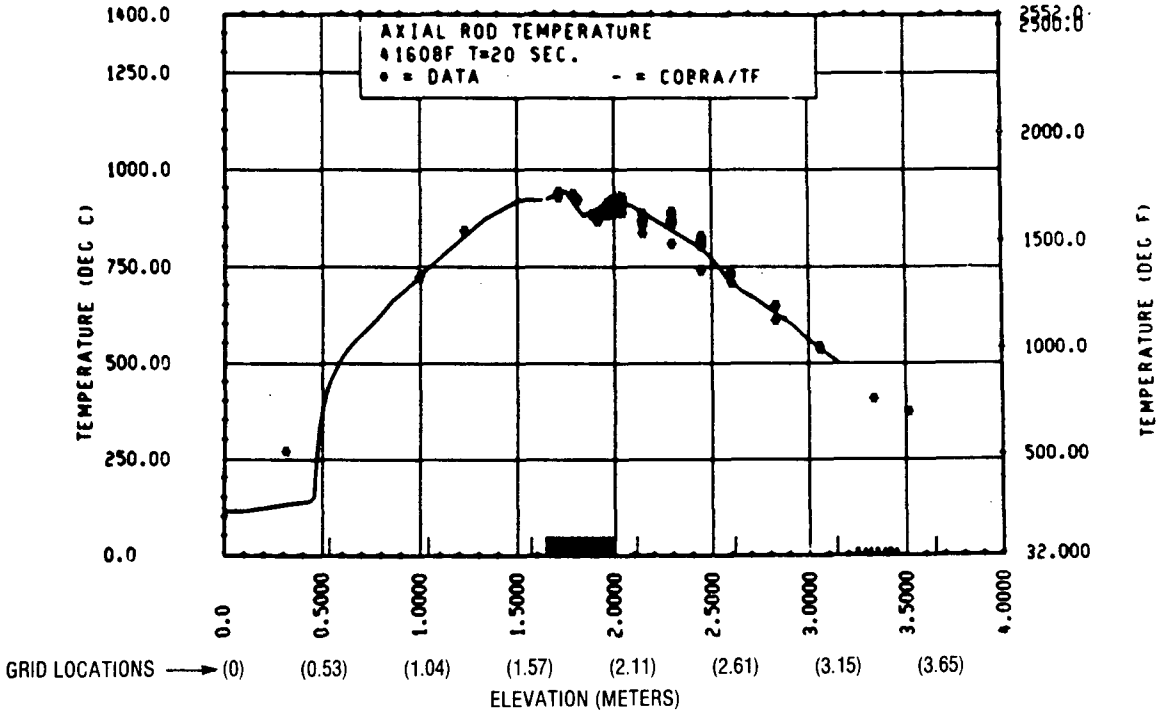

Figure 4-96. Comparison of COBRA-TF-Calculated Axial Rod Temperature Versus Elevation With FLECHT SEASET 21-Rod Data, Test 41608F, t = 20 Seconds

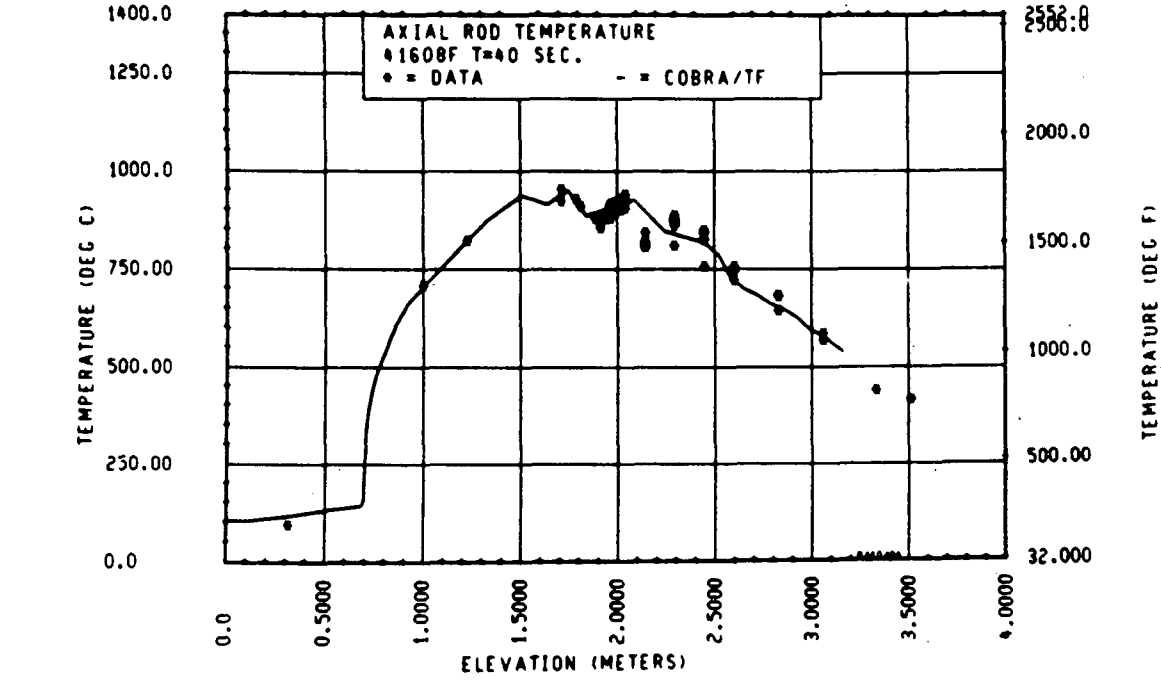

Figure 4-97. Comparison of COBRA-TF-Calculated Axial Rod Temperature Versus Elevation With FLECHT SEASET 21-Rod Data, Test 41608F, t = 40 Seconds

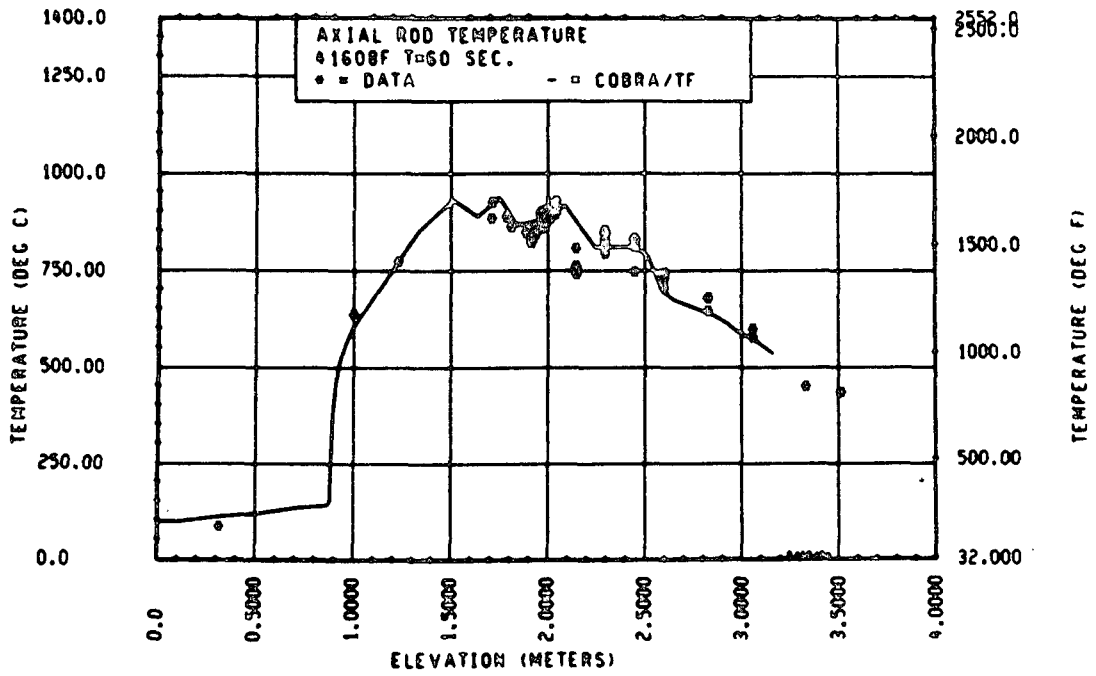

Figure 4-98. Comparison of COBRA-TF-Calculated Axial Rod Temperature Versus Elevation With FLECHT SEASET 21-Rod Data, Test 41608F, t = 60 Seconds

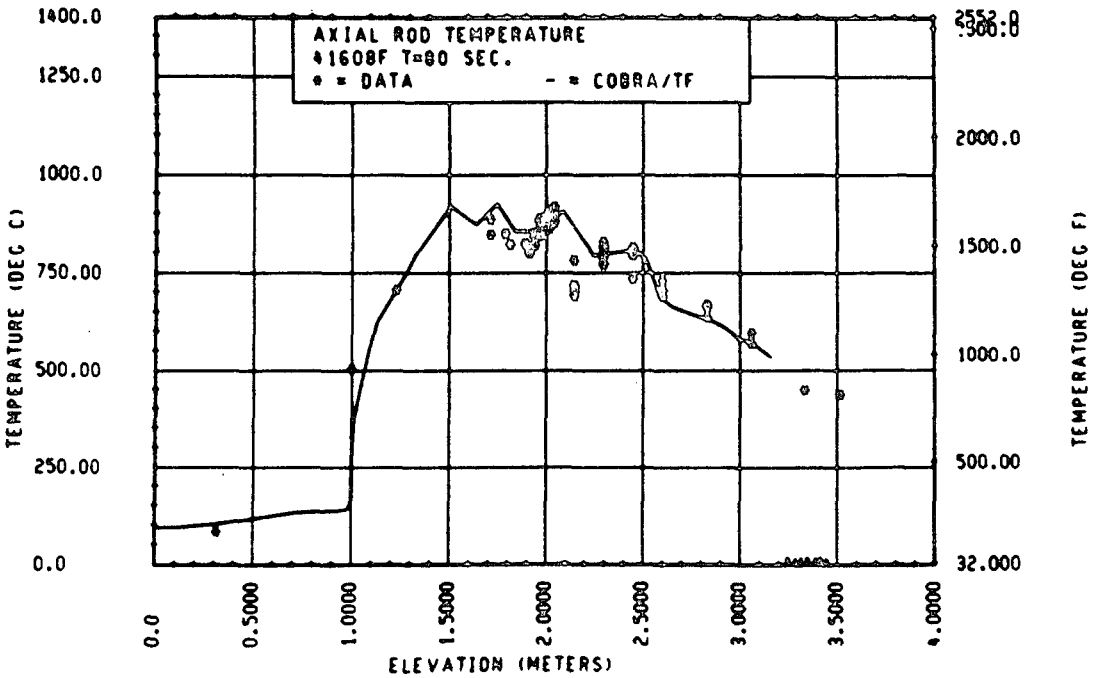

Figure 4-99. Comparison of COBRA-TF-Calculated Axial Rod Temperature Versus Elevation With FLECHT SEASET 21-Rod Data, Test 41608F, t = 80 Seconds

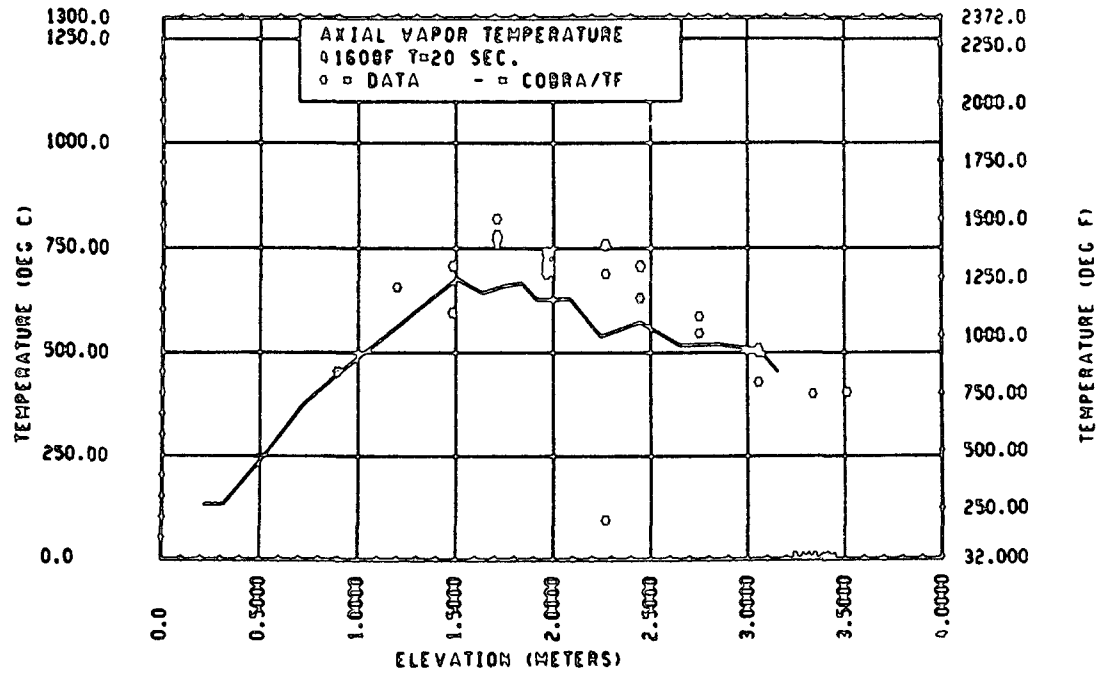

Figure 4-100. Comparison of COBRA-TF-Calculated Axial Vapor Temperature Versus Elevation With FLECHT SEASET 21-Rod Data, Test 41608F, t = 20 Seconds

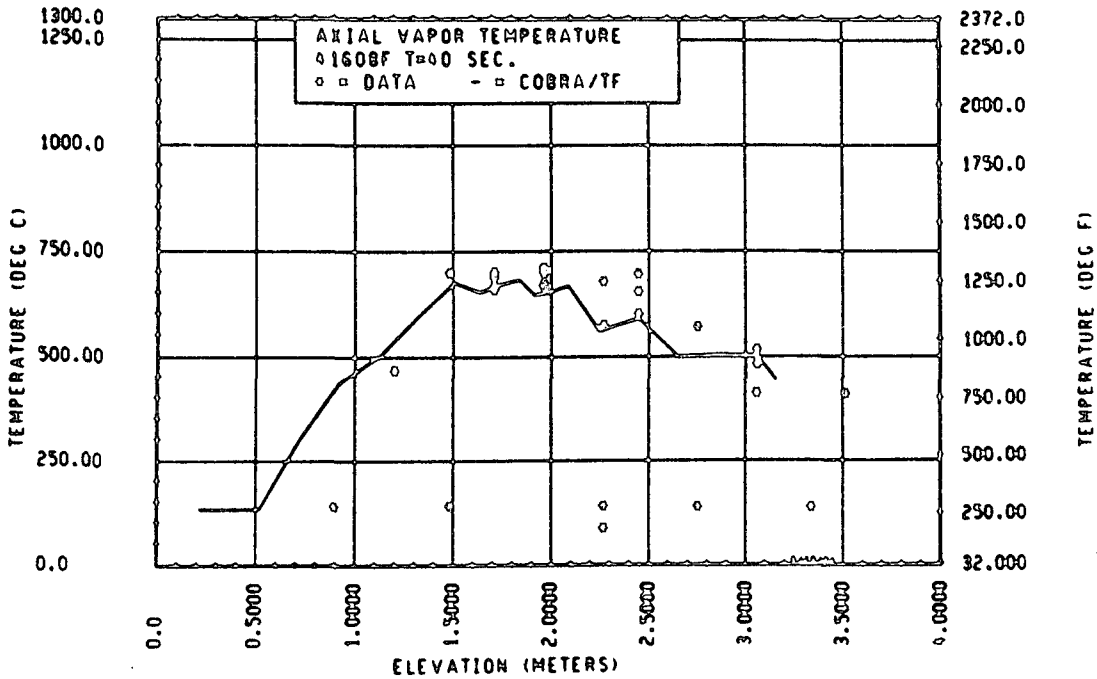

Figure 4-101. Comparison of COBRA-TF-Calculated Axial Vapor Temperature Versus Elevation With FLECHT SEASET 21-Rod Data, Test 41608F, t = 40 Seconds

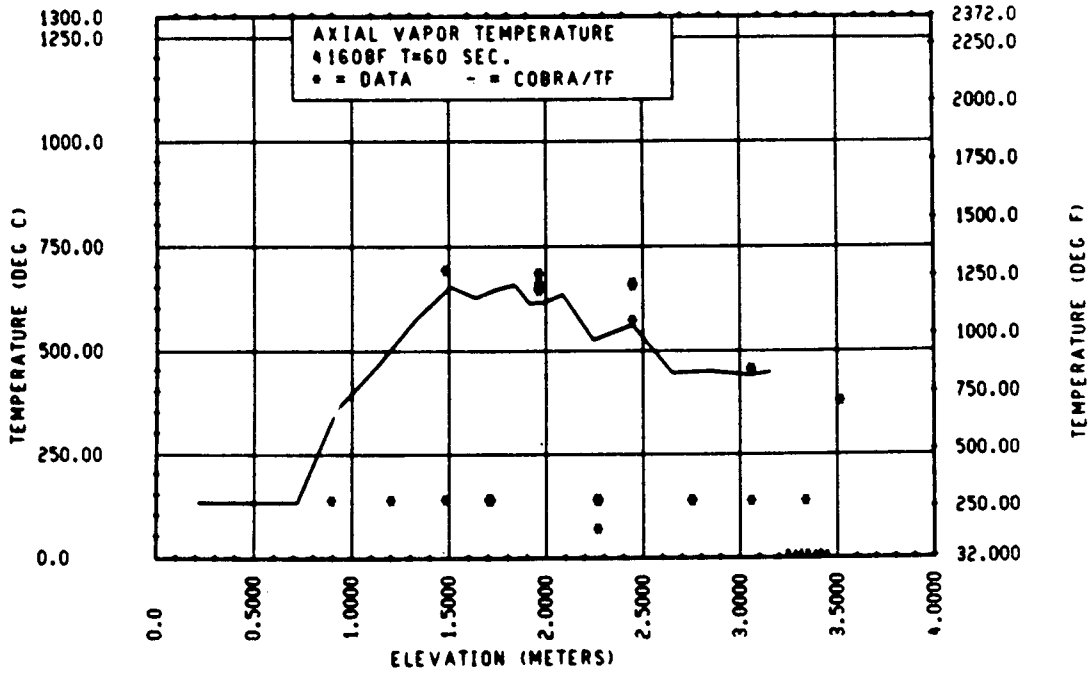

Figure 4-102. Comparison of COBRA-TF-Calculated Axial Vapor Temperature Versus Time With FLECHT SEASET 21-Rod Data, Test 41608F, t = 60 Seconds

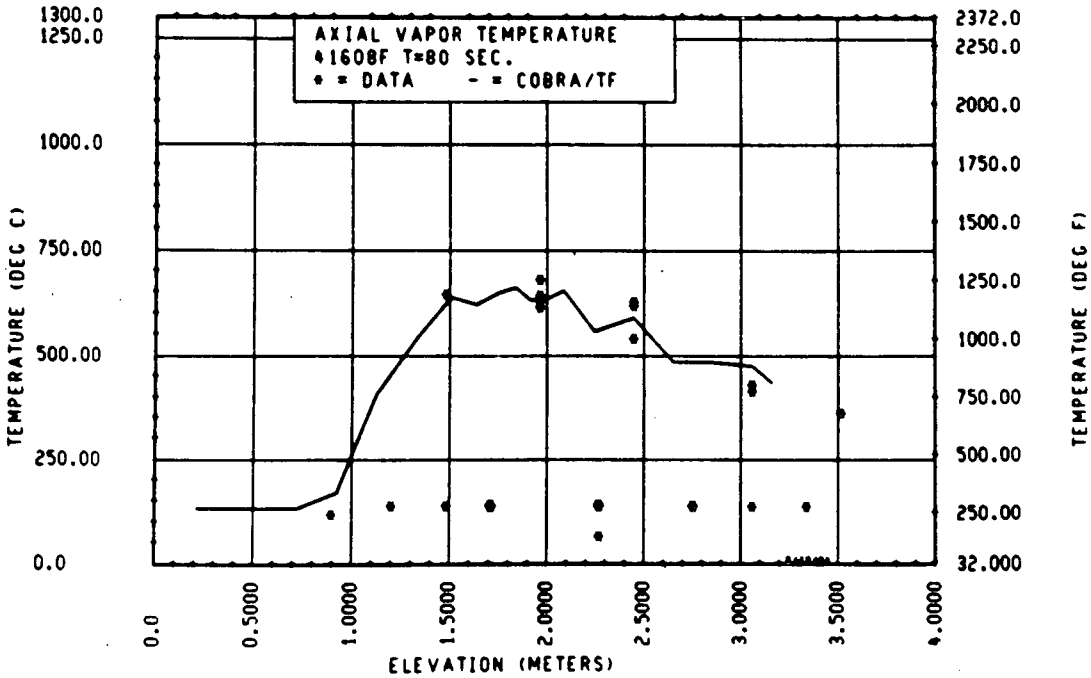

Figure 4-103. Comparison of COBRA-TF-Calculated Axial Vapor Temperature Versus Time With FLECHT SEASET 21-Rod Data, Test 41608F, t = 80 Seconds

and is characteristic of the FLECHT SEASET 21-rod bundle tests with this flooding rate.

Two other 21-rod bundle configuration F tests were compared with the COBRA-TF predictions. Test 42612F was a 0.025 m/sec (1 in./sec), 0.13 MPa (20 psia) reflood test and test 41914F was a stepped flow reflood test. The COBRA-TF comparisons with heater rod test data for test 42612F (figures 4-104 through 4-109) show reasonably good agreement. The COBRA-TF transient tends to over-predict the heater rod temperatures somewhat, and the initial delay in the calculated entrainment is more clearly seen in these comparisons (figures 4-106 and 4-107 at approximately 15 seconds).

The comparisons with test 41914F are not good. It is apparent that the heat transfer effects with the stepped flow both upstream and downstream are being underestimated with COBRA-TF. There is no explanation for this poor agreement, particularly since the other stepped flow tests showed good agreement.

4-20. COBRA-TF Comparisons With FEBA Test Data

Experiments from the FEBA test program series VII and VIII were also simulated with COBRA-TF to test the blockage models developed from the FLECHT SEASET 21-rod bundle test program. These FEBA experiments had all rods blocked with either 62 or 90 percent subchannel blockage. The FEBA blockage sleeves (figure 4-110) were different from those used for the FLECHT SEASET tests. Test conditions for the FEBA experiments modeled with COBRA-TF are given in table 4-2. Other FEBA experiments were modeled earlier in the FLECHT SEASET program; however, only those presented herein were run with the final version of the COBRA-TF code.

FEBA test 324 was modeled with the COBRA-TF configuration described in appendix A. All rods had blockage on them, and a detailed axial noding was used downstream of the blockage. The comparisons of the measured heater rod data and the COBRA-TF prediction for the center region of the FEBA bundle is shown in figures 4-111 through 4-120. The heater rod temperature versus time plots (figures 4-111 through 4-116) show a bias in the COBRA-TF calculation to over-predict the clad temperatures, particularly at the higher elevations.

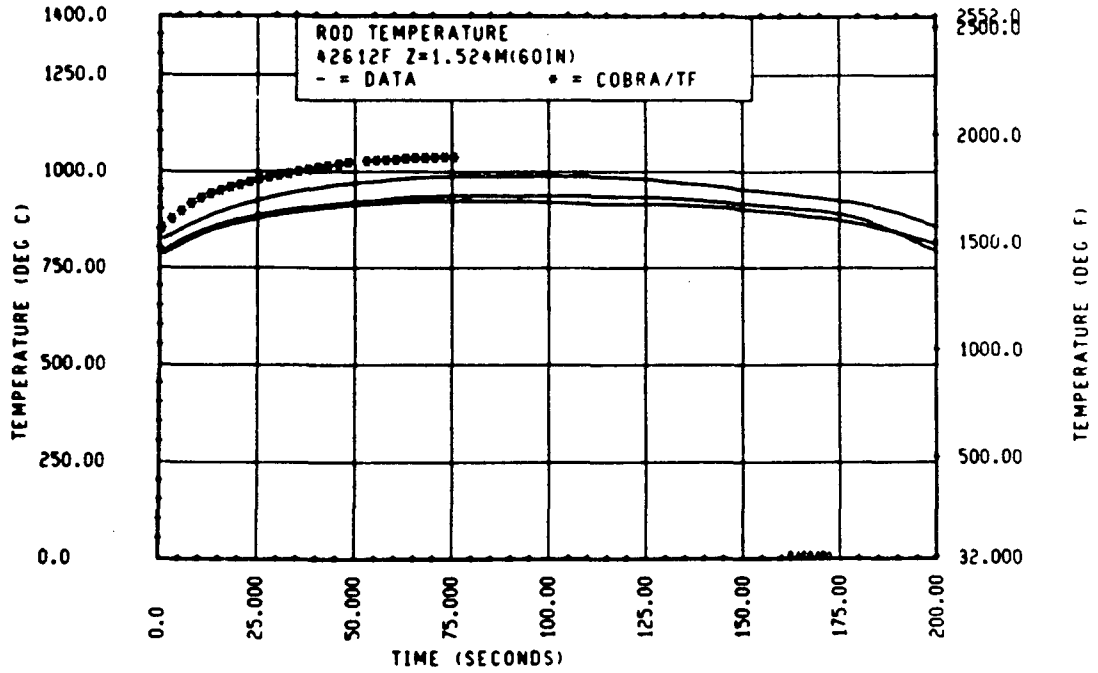

Figure 4-104. Comparison of COBRA-TF-Calculated Heater Rod Temperature Versus Elevation With FLECHT SEASET 21-Rod Data, Test 42612F, 1.52 m (60 in.) Elevation

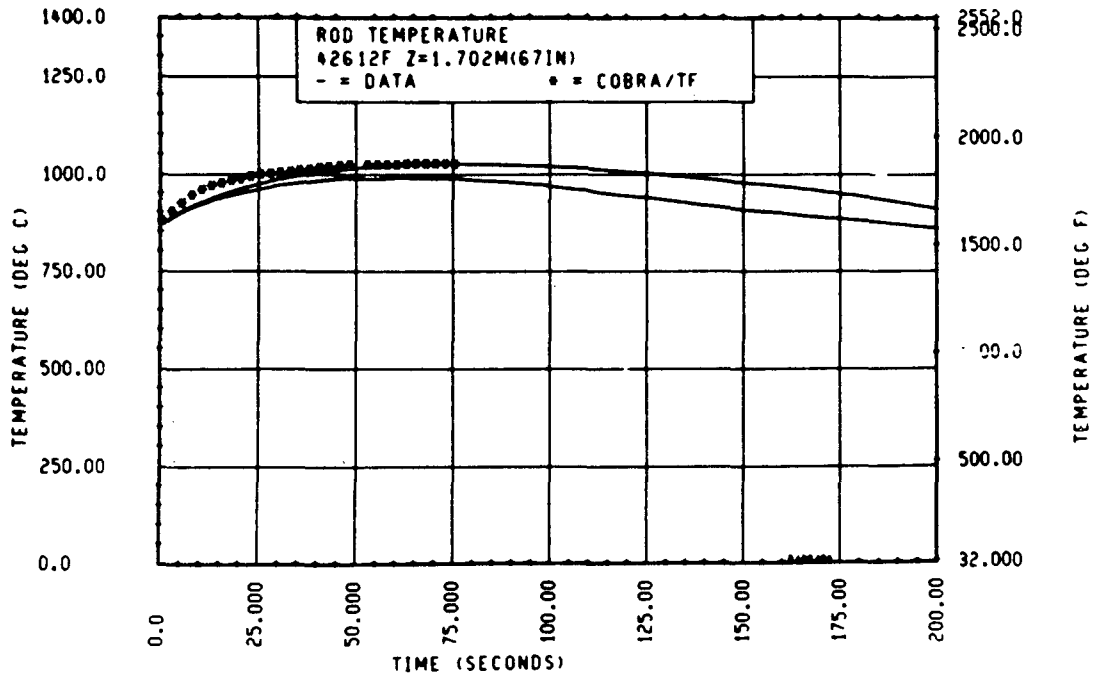

Figure 4-105. Comparison of COBRA-TF-Calculated Heater Rod Temperature Versus Time With FLECHT SEASET 21-Rod Data, Test 42612F, 1.70 m (67 in.) Elevation

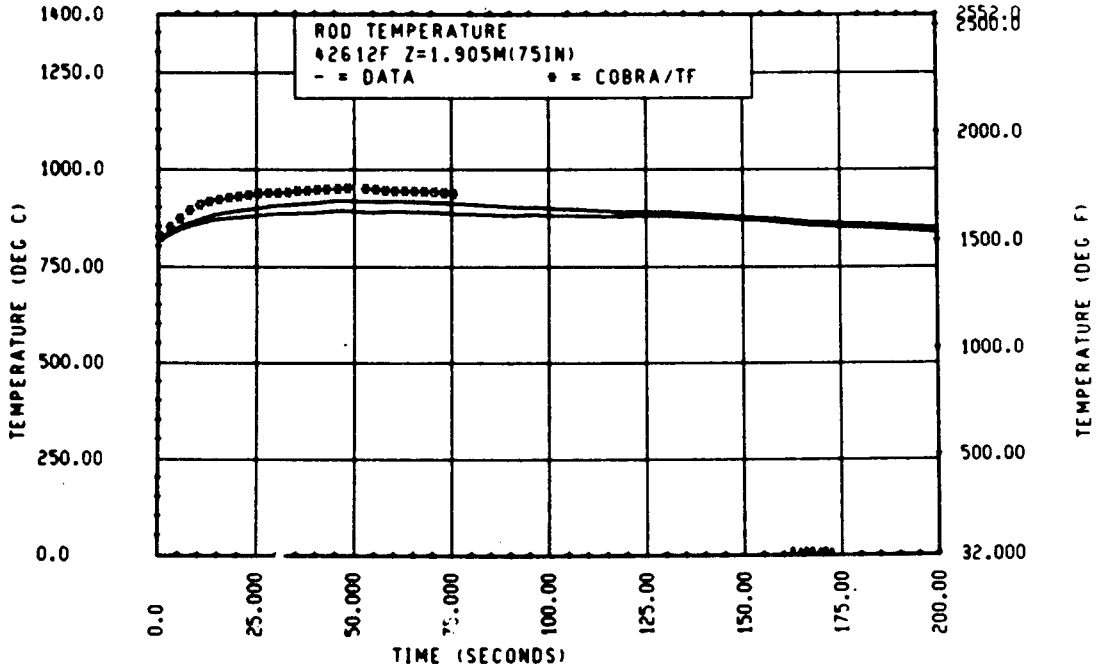

Figure 4-106. Comparison of COBRA-TF-Calculated Heater Rod Temperature Versus Time With FLECHT SEASET 21-Rod Data, Test 42612F, 1.90 m (75 in.) Elevation

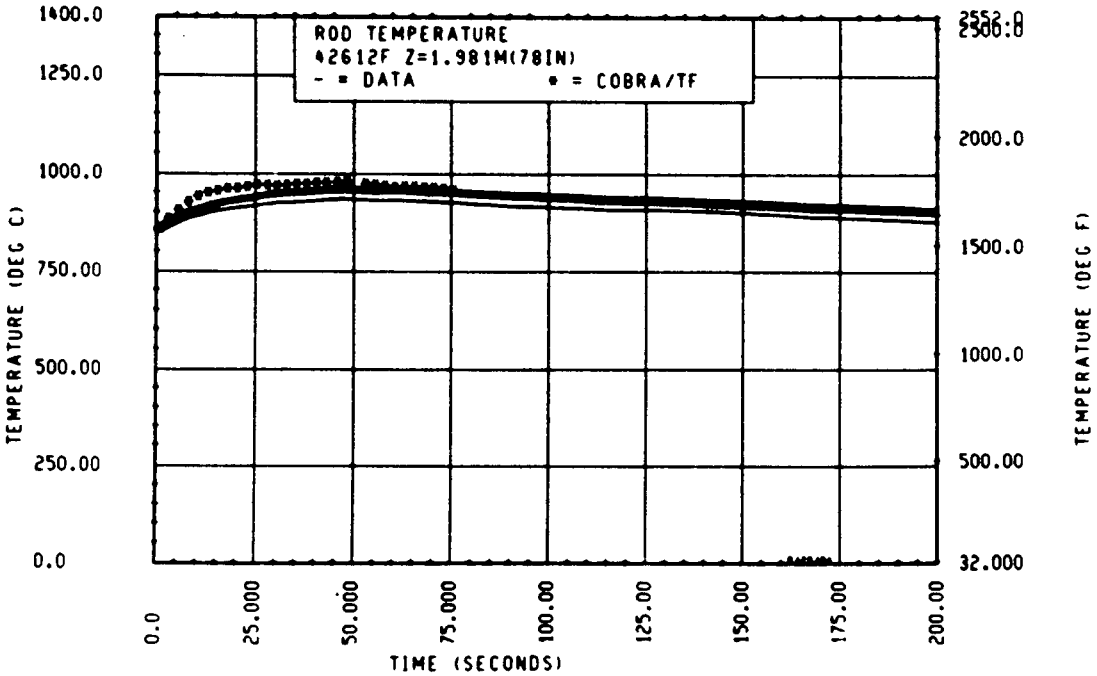

Figure 4-107. Comparison of COBRA-TF-Calculated Heater Rod Temperature Versus Time With FLECHT SEASET 21-Rod Data, Test 42612F, 1.98 m (78 in.) Elevation

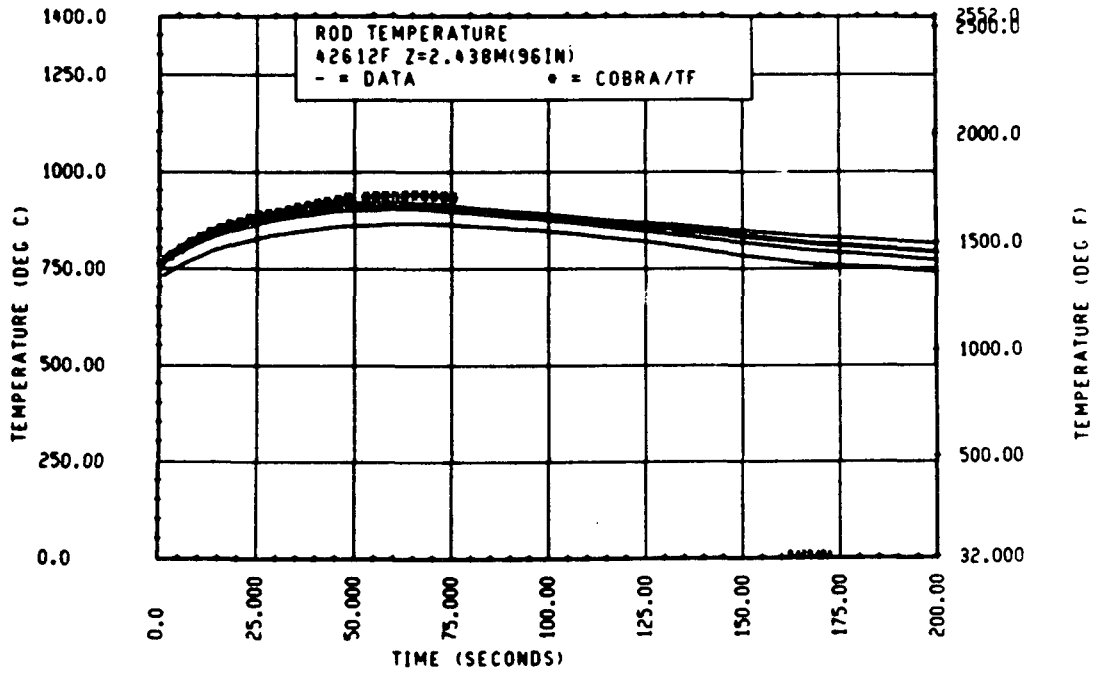

Figure 4-108. Comparison of COBRA-TF-Calculated Heater Rod Temperature Versus Time With FLECHT SEASET 21-Rod Data, Test 42612F, 2.44 m (96 in.) Elevation

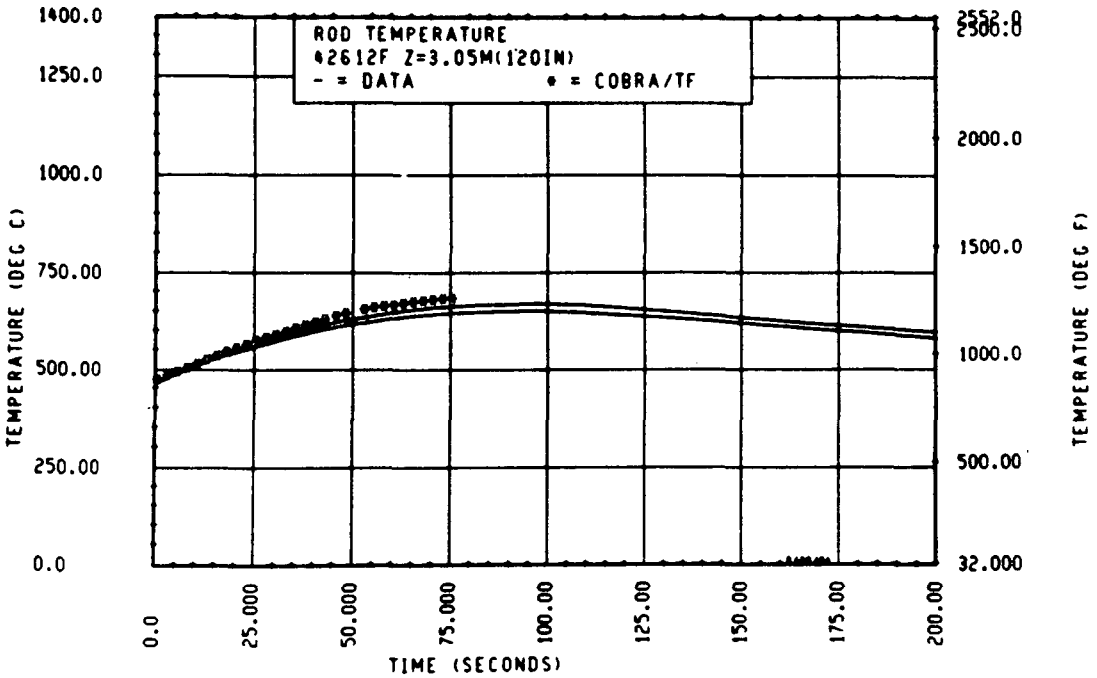

Figure 4-109. Comparison of COBRA-TF-Calculated Heater Rod Temperature Versus Time With FLECHT SEASET 21-Rod Data, Test 42612F, 3.05 m (120 in.) Elevation

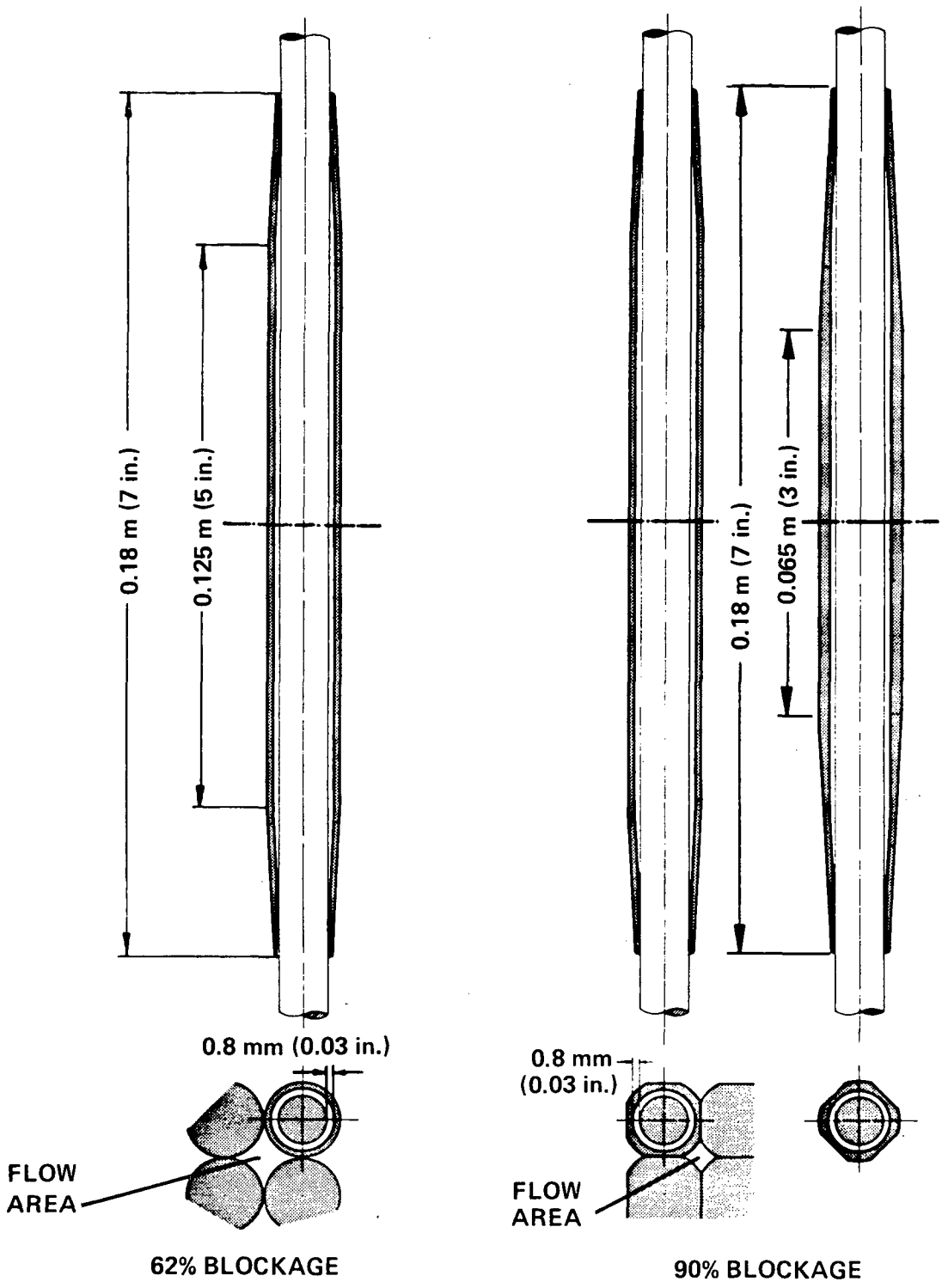

Figure 4-110. FEBA Blockage Sleeve Shapes

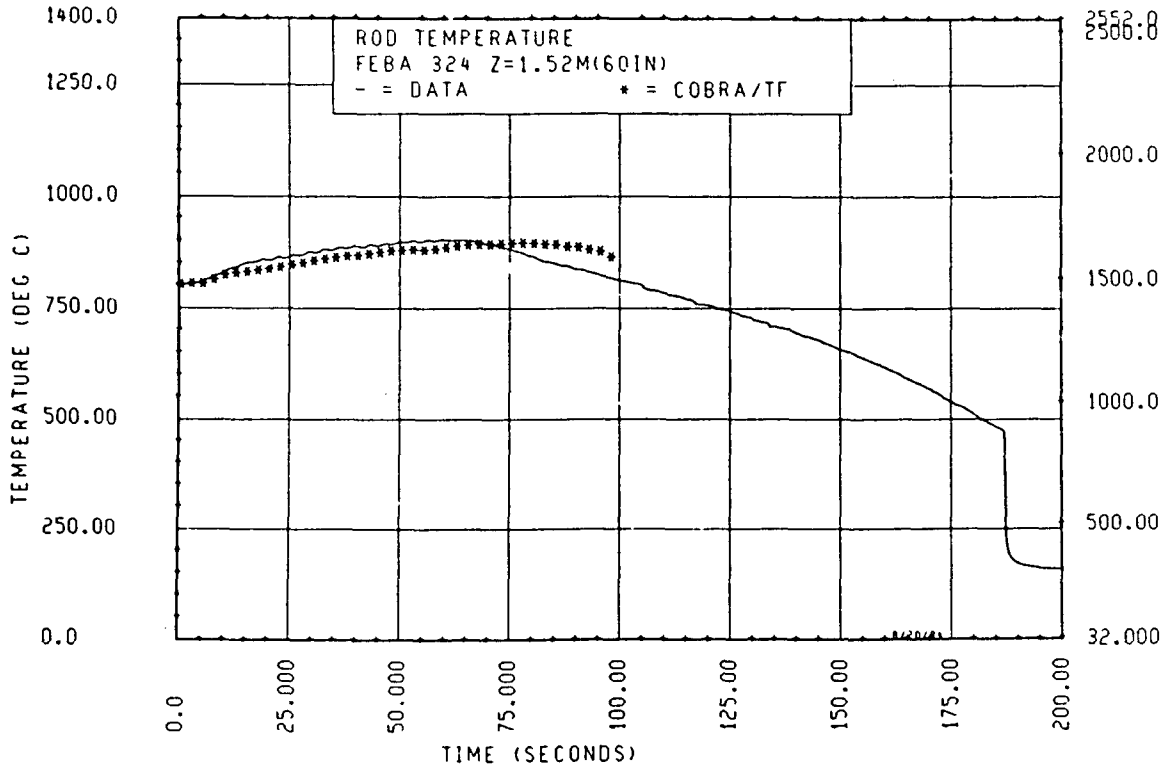

Figure 4-111. Comparison of COBRA-TF-Calculated Heater Rod Temperature Versus Time With FEBA Data, Test 324, 1.52 m (60 in.) Elevation

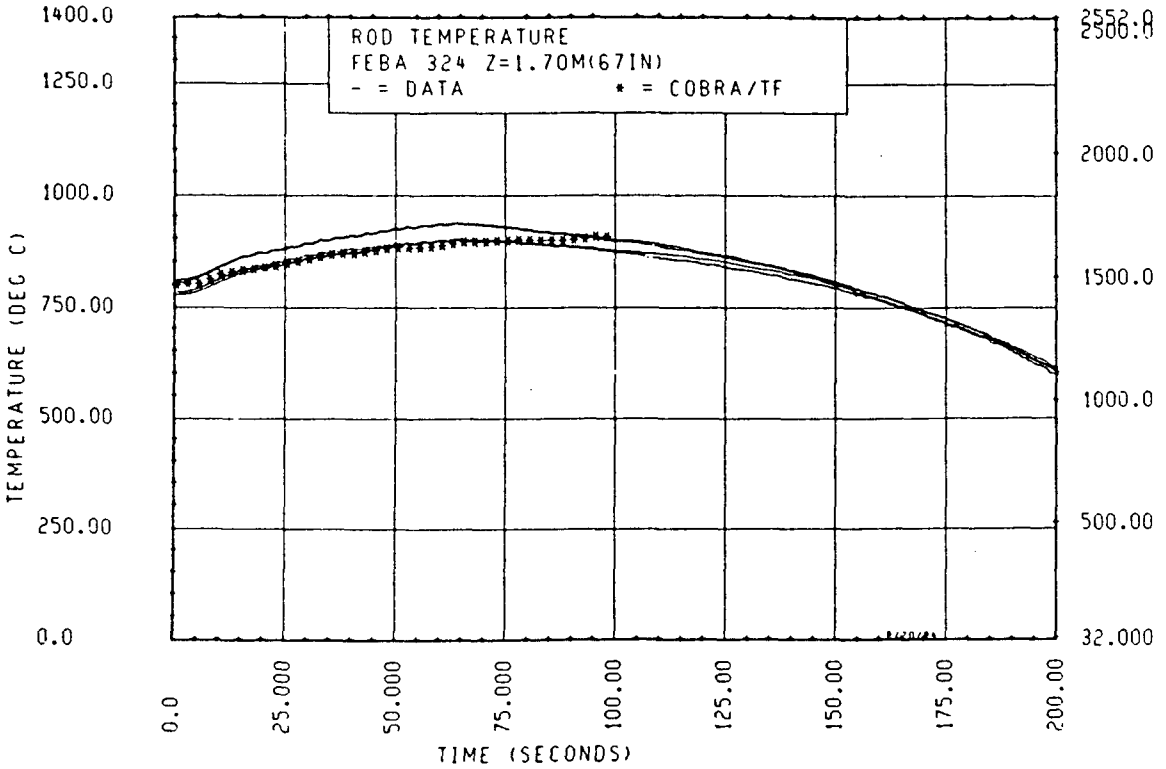

Figure 4-112. Comparison of COBRA-TF-Calculated Heater Rod Temperature Versus Time With FEBA Data, Test 324, 1.70 m (67 in.) Elevation

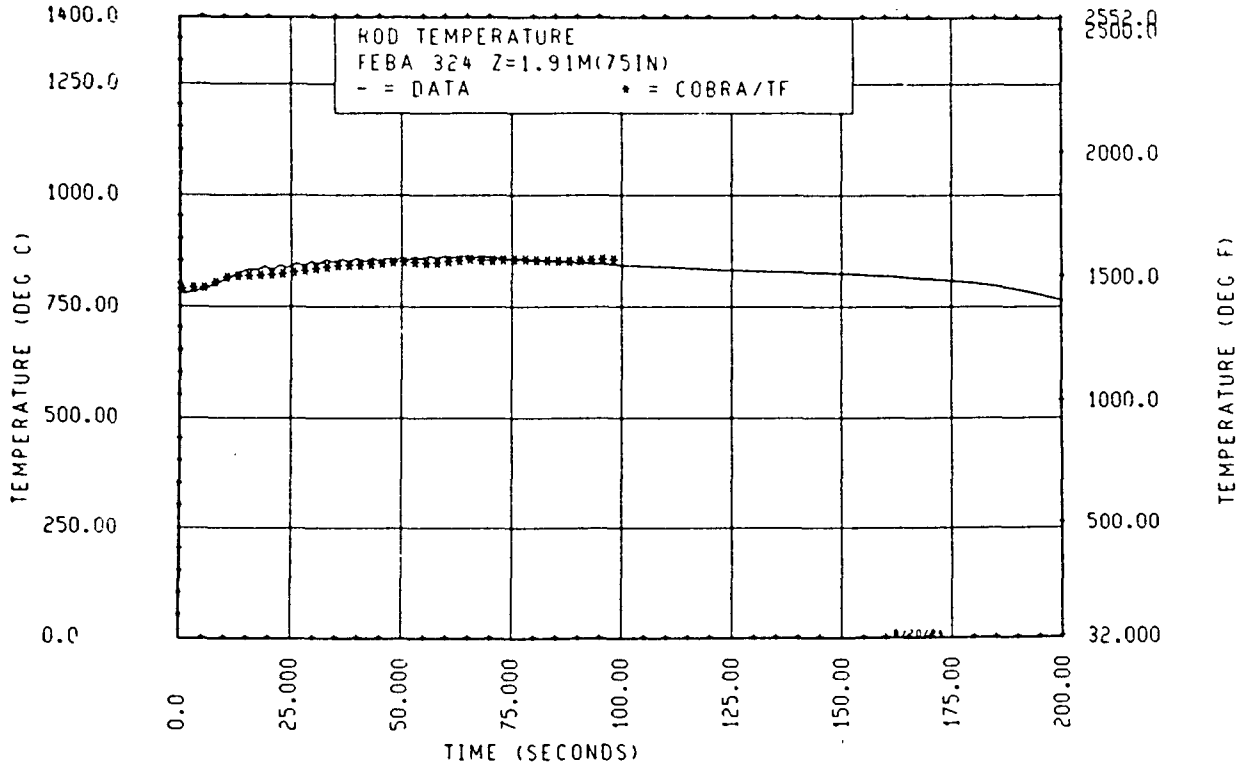

Figure 4-113. Comparison of COBRA-TF-Calculated Heater Rod Temperature Versus Time With FEBA Data, Test 324, 1.91 m (75 in.) Elevation

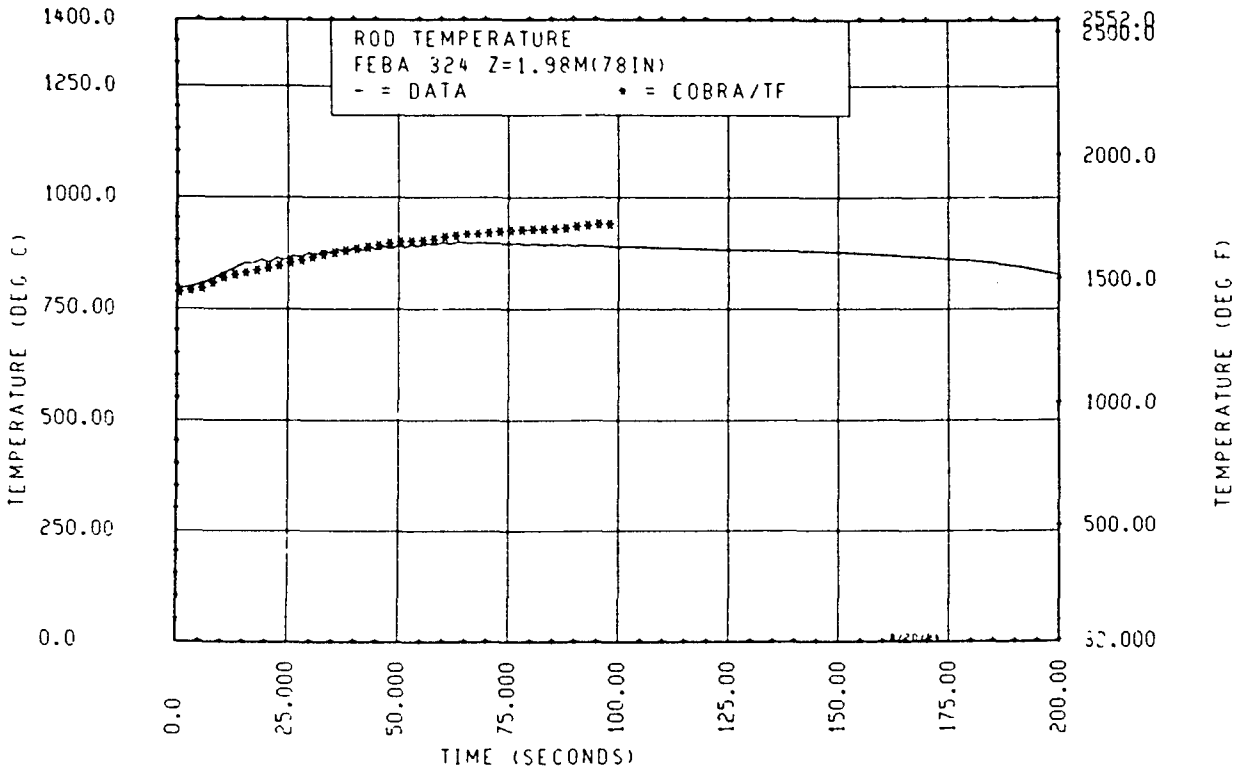

Figure 4-114. Comparison of COBRA-TF-Calculated Heater Rod Temperature Versus Time With FEBA Data, Test 324, 1.98 m (78 in.) Elevation

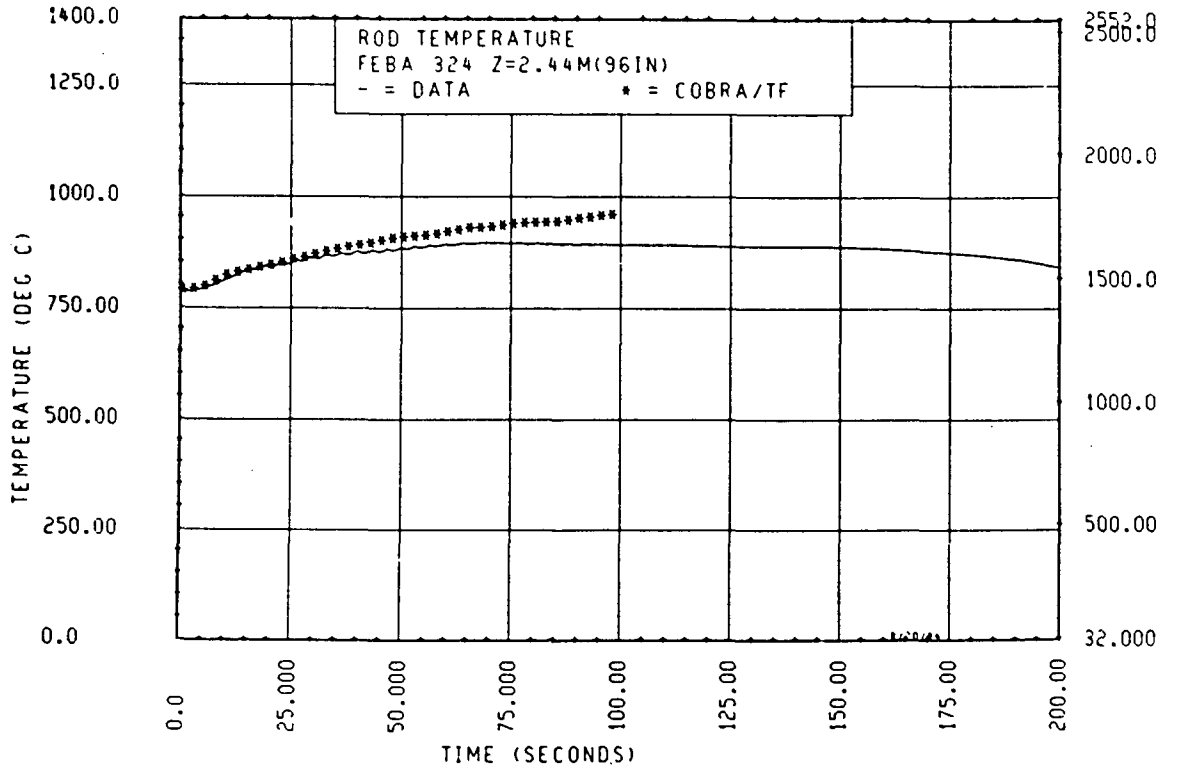

Figure 4-115. Comparison of COBRA-TF-Calculated Heater Rod Temperature Versus Time With FEBA Data, Test 324, 2.44 m (96 in.) Elevation

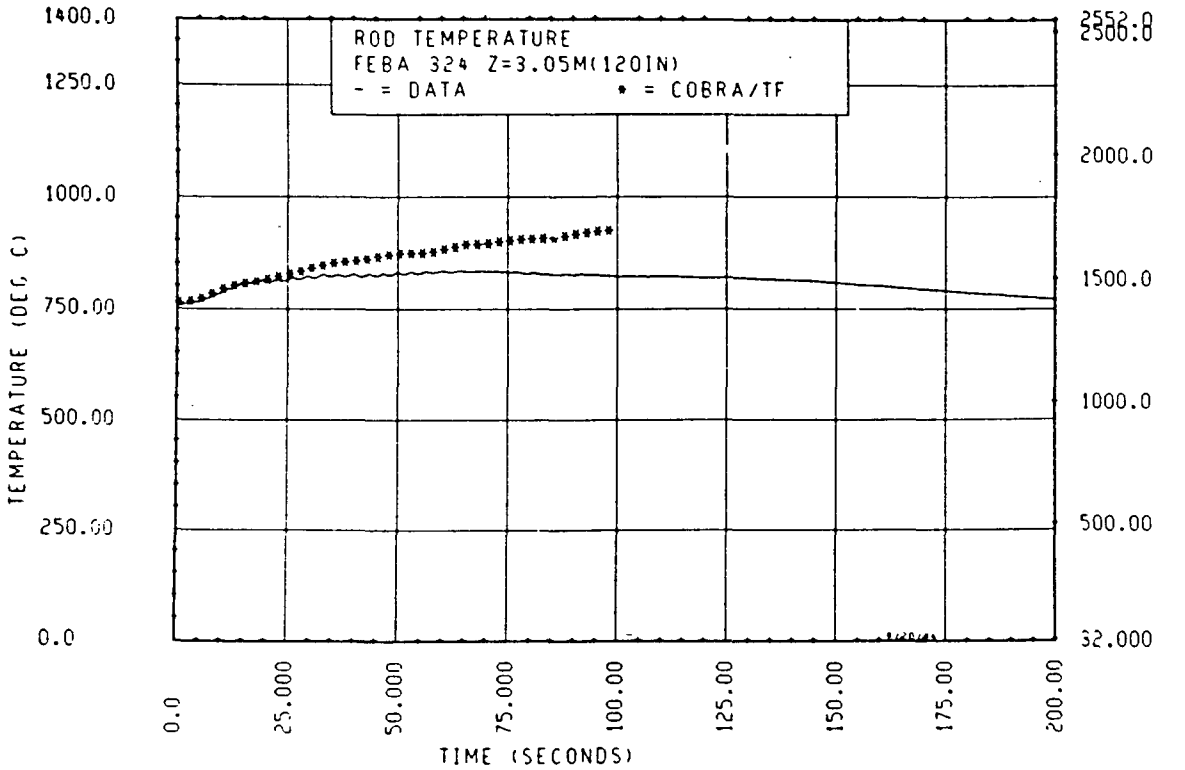

Figure 4-116. Comparison of COBRA-TF-Calculated Heater Rod Temperature Versus Time With FEBA Data, Test 324, 3.05 m (120 in.) Elevation

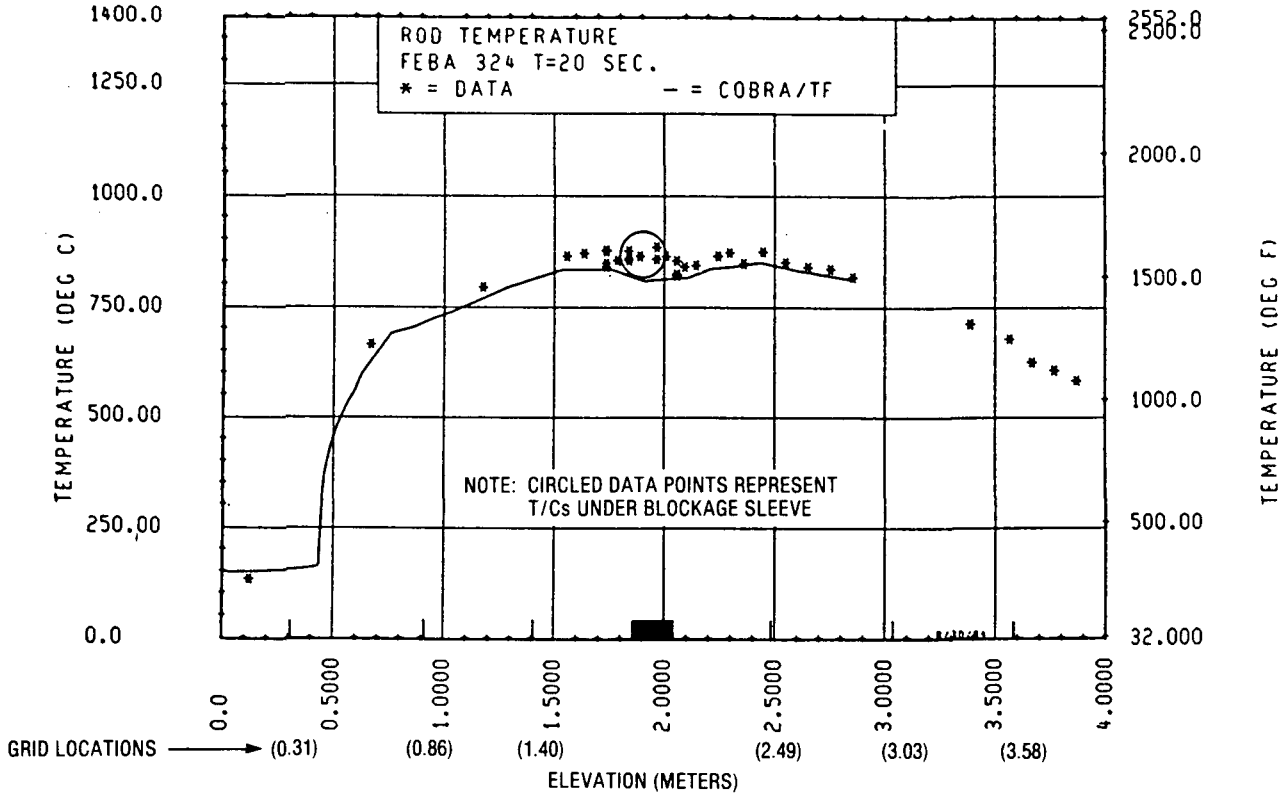

Figure 4-117. Comparison of COBRA-TF-Calculated Axial Rod Temperature Versus Elevation With FEBA Data, Test 324, t = 20 Seconds

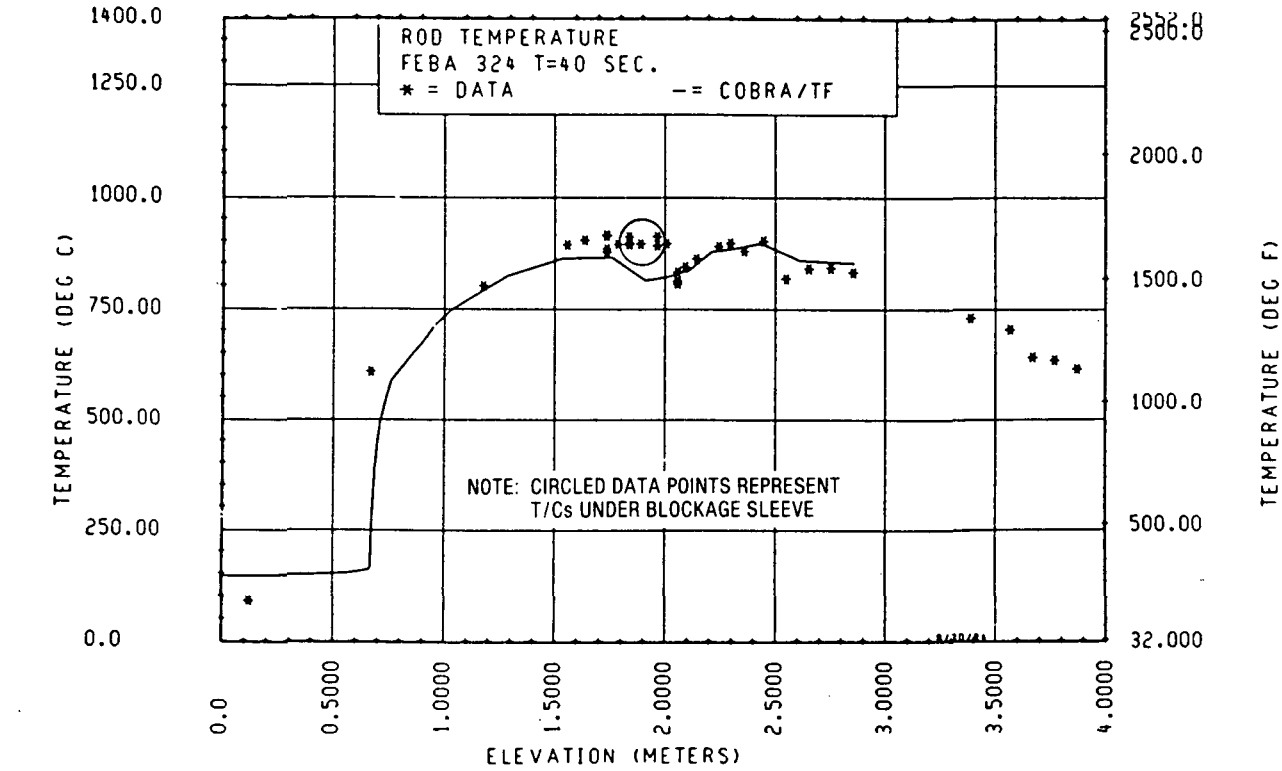

Figure 4-118. Comparison of COBRA-TF-Calculated Axial Rod Temperature Versus Elevation With FEBA Data, Test 324, t = 40 Seconds

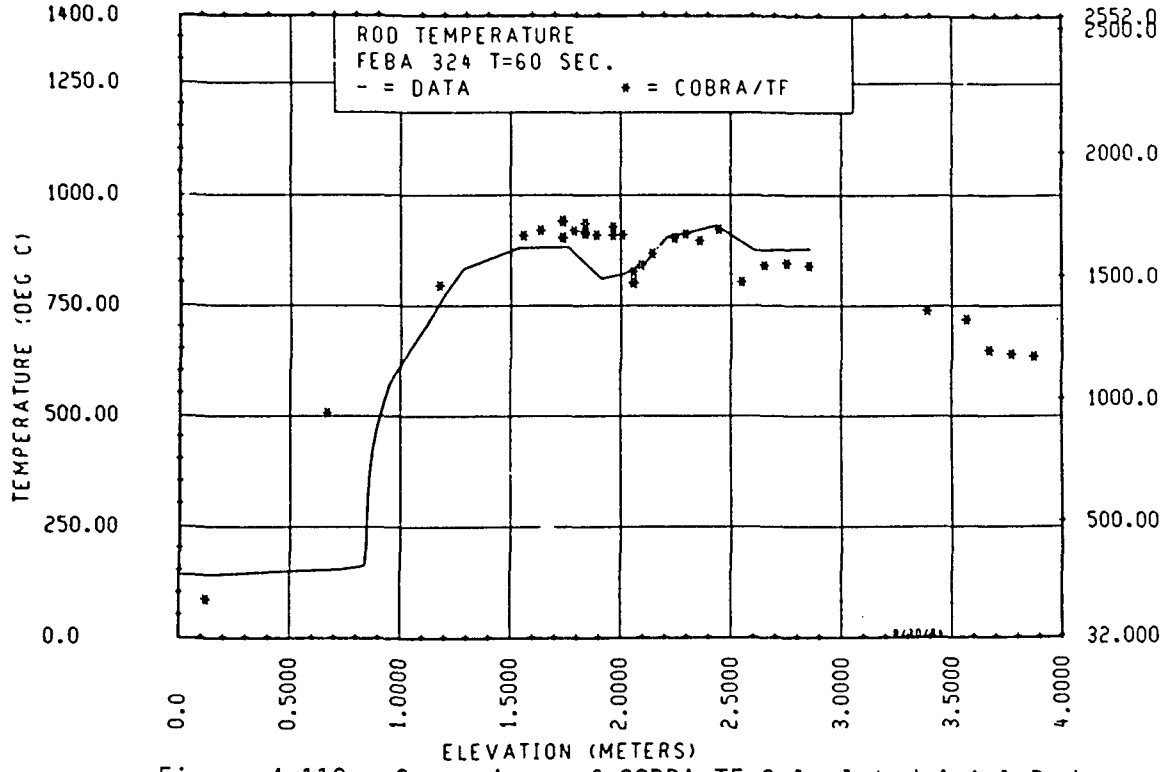

Figure 4-119. Comparison of COBRA-TF-Calculated Axial Rod Temperature Versus Elevation With FEBA Data, Test 324, t = 60 Seconds

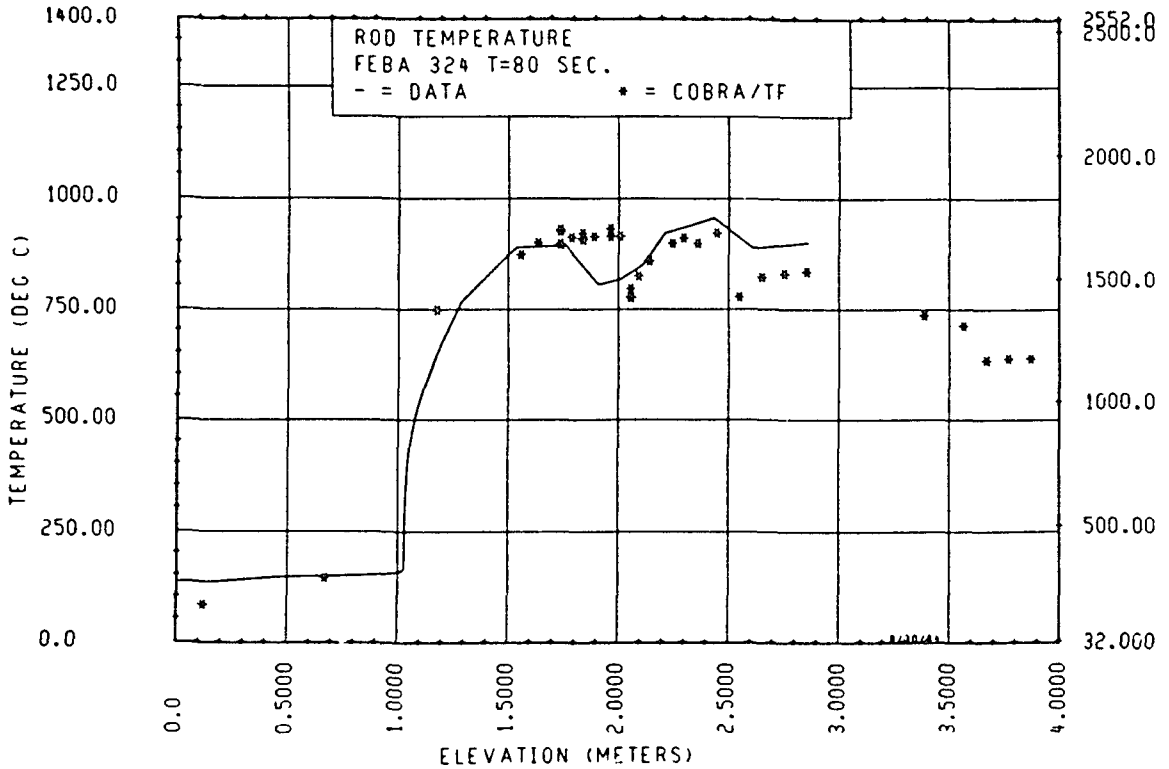

Figure 4-120. Comparison of COBRA-TF-Calculated Axial Rod Temperature Versus Elevation With FEBA Data, Test 324, t = 80 Seconds

This behavior was observed only at the uppermost elevation for FEBA test 229, which had no blockage and six grids (figure 3-153). Comparison of figures 4-114 through 4-116 with their counterparts for test 229, figures 3-147 through 3-149, shows more evidence in the test data of an effect of the blockage at these elevations than in the COBRA-TF calculation. This indicates that the droplet breakup model or calculation is not generating as large a number of smaller drops as the data apparently indicate. The blockage model for the FEBA 62-percent blockage case was the same as that used for the FLECHT SEASET 21-rod bundle configuration C cases, since the projected area for droplet breakup was the same. Although the single-phase heat transfer model was different for FEBA from that for the FLECHT SEASET 21-rod bundle, as discussed earlier in this section, it is expected that this effect would be small. The major effect should be the entrained droplet breakup by the blockage. In terms of peak clad temperature, the COBRA-TF prediction does show reasonable agreement.

The axial plots of the heater rod clad temperatures are shown in figures 4-117 through 4-120; these plots illustrate the higher predicted clad temperatures at the upper elevations compared to the data. (Also shown in figure 4-117 is the axial location of the spacer grids and the blockage zone.) The COBRA-TF calculation is the solid line on these figures and is drawn between the axial nodes used in the calculation. Hence, there are sharp changes in the slopes of the lines.

The droplet breakup is calculated to occur at the entrance of the blockage, such that the population of the microdrops is swept through the blockage throat where the steam flow is the highest. This results in the drop in the predicted COBRA-TF calculation at the 2 m (79 in.) elevation.

The FEBA thermocouple data shown on these figures between the 1.86 and 2.0 m (73 and 79 in.) elevations are from heater rod thermocouples under blockage sleeves, which are insulated somewhat from the flow effects in the subchannel. Thus the data represent temperatures on the inside surface of the sleeve, while the COBRA-TF calculation represents the outer surface of the sleeve. The line which represents the COBRA-TF calculation is smoothing the blockage

effect over the nodes which are equal to the blockage length [0.180 m (7.09 in.)] upstream of the blockage. The difference between the data upstream and that downstream of the blockage is slightly larger than the difference produced by the COBRA-TF calculation; this indicates that the blockage models are not giving as much local heat transfer benefit as observed in the test. A more accurate examination of these differences is made in subsequent figures.

Similar comparisons between COBRA-TF and FEBA test 337, which had all rods blocked 90 percent, were also made (figures 4-121 through 4-126). The heater rod temperature versus time plots showed that once entrainment began (at about 25 seconds), there was significantly more cooling in these experiments than the blockage model in COBRA-TF was calculating. The droplet breakup model used in these calculations does account for the increased subchannel blockage such that the area available to shatter drops in the 90-percent-blocked case is significantly larger than that in the 62-percent-blocked case (appendix C). However, even with this additional area, the COBRA-TF-calculated blockage heat transfer effect is still smaller than that observed in the data. Examination of the COBRA-TF results, particularly in the throat of 90-percent blockage, indicates that restriction of the total mass flow to only 10 percent of the normal flow area results in calculated steam velocities of approximately 100 m/sec (300 ft/sec). The droplet aerodynamic Weber numbers, defined in terms of the relative velocity difference, that is,

$$We_A = \frac{\rho_g (V_g - V_d)^2 d_o}{g_c \sigma}$$

is of the order of 200 or more. Data on drop atomization for drop shattering from liquid jets or continuous liquid sheets in a gas flow indicate that the shear stress due to the relative velocity difference will result in droplet breakup at values of We_A of approximately 12 to 14.[1] Since the calculated drop aerodynamic Weber numbers are significantly greater than 13, it is postulated that the drops will be shattered because of aerodynamic atomization

1. Wallis, G. B., One-Dimensional Two-Phase Flow, McGraw-Hill, New York, 1969, 376-378.

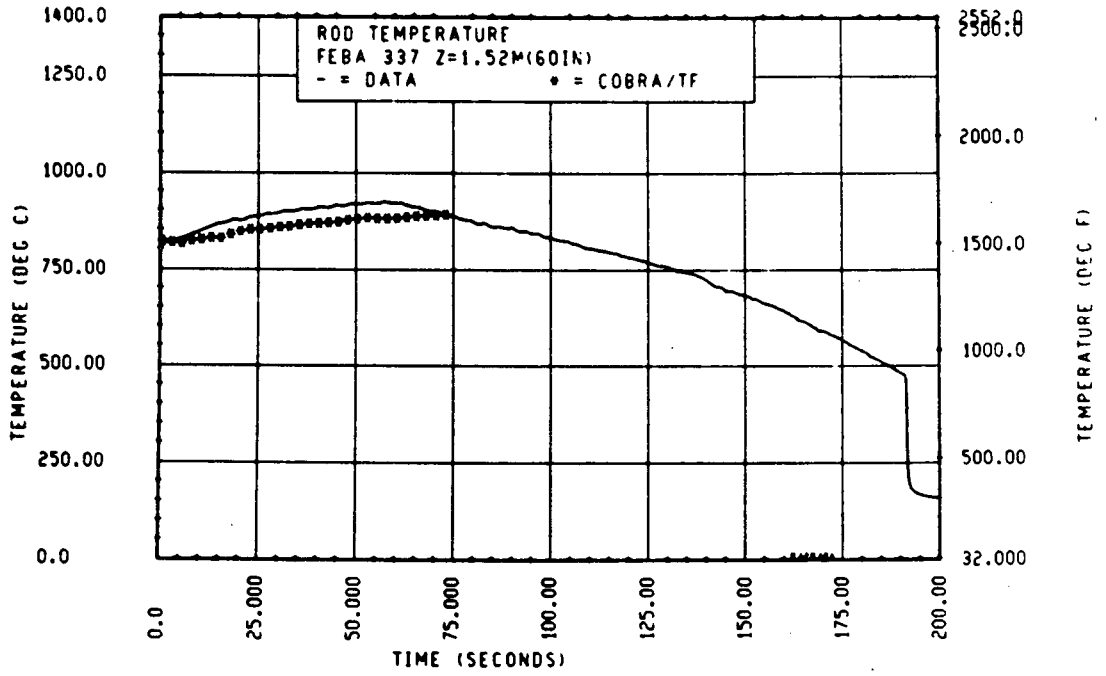

Figure 4-121. Comparison of COBRA-TF-Calculated Heater Rod Temperature Versus Time With FEBA Data, Test 337, 1.52 m (60 in.) Elevation

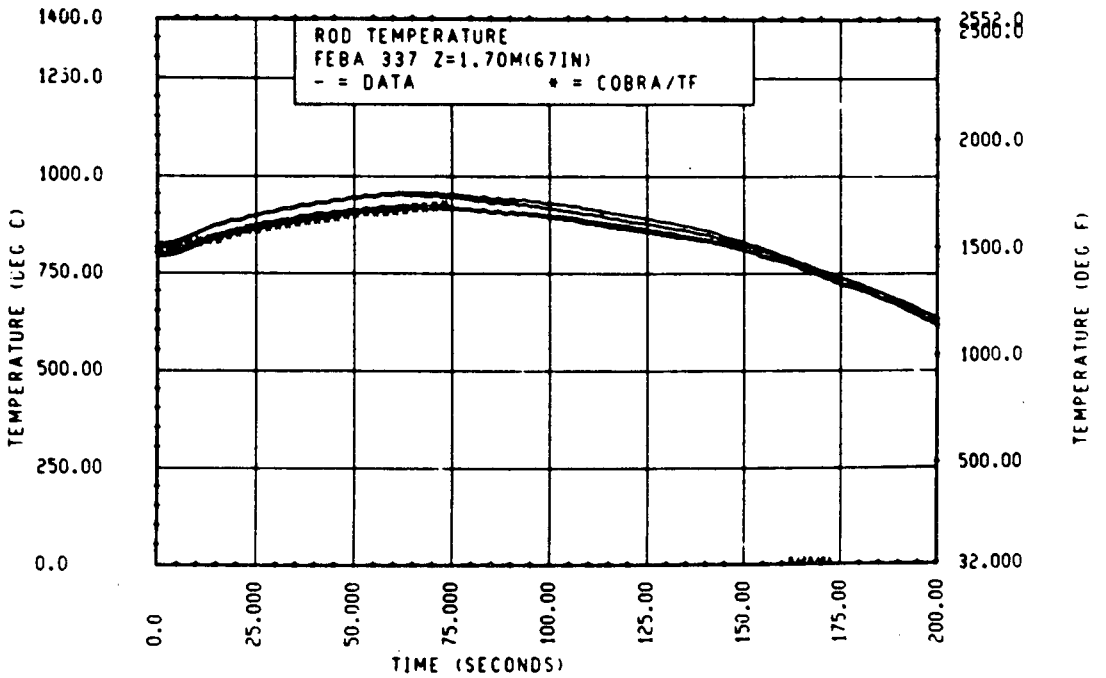

Figure 4-122. Comparison of COBRA-TF-Calculated Heater Rod Temperature Versus Time With FEBA Data, Test 337, 1.70 m (67 in.) Elevation

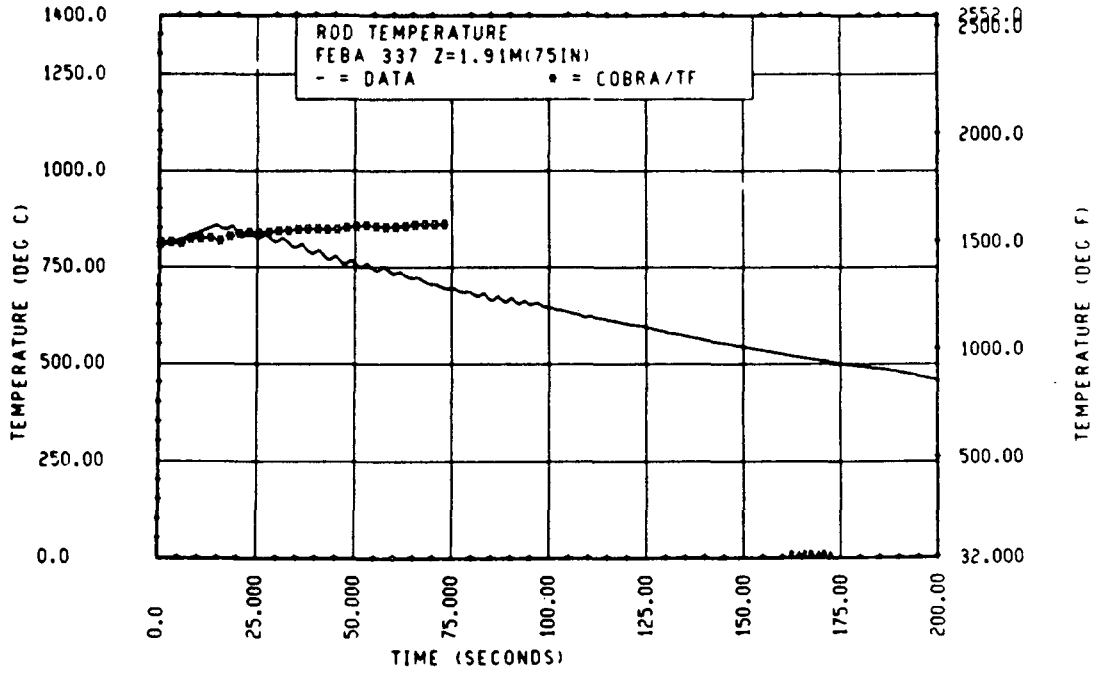

Figure 4-123. Comparison of COBRA-TF-Calculated Heater Rod Temperature Versus Time With FEBA Data, Test 337, 1.91 m (75 in.) Elevation

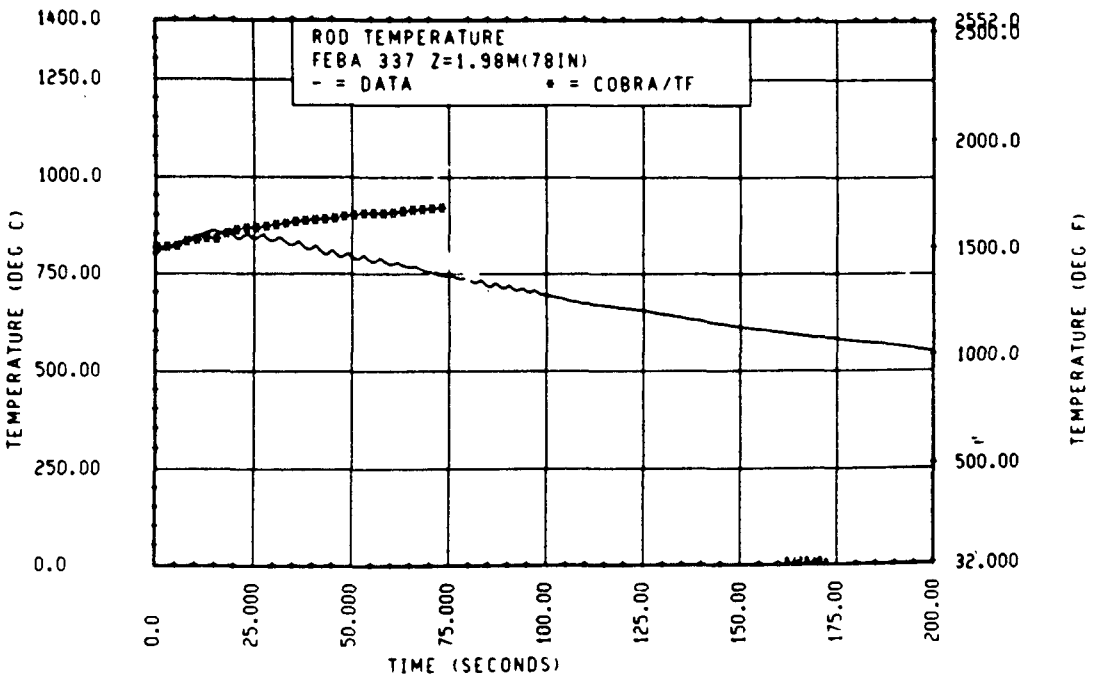

Figure 4-124. Comparison of COBRA-TF-Calculated Heater Rod Temperature Versus Time With FEBA Data, Test 337, 1.98 m (78 in.) Elevation

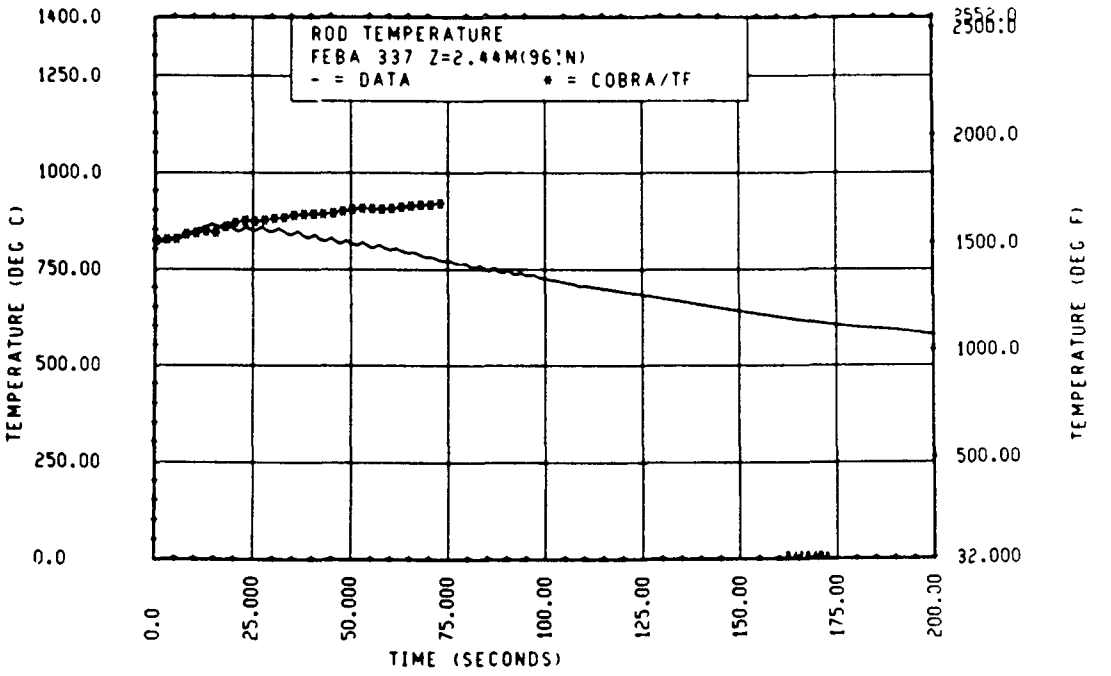

Figure 4-125. Comparison of COBRA-TF-Calculated Heater Rod Temperature Versus Time With FEBA Data, Test 337, 2.44 m (96 in.) Elevation

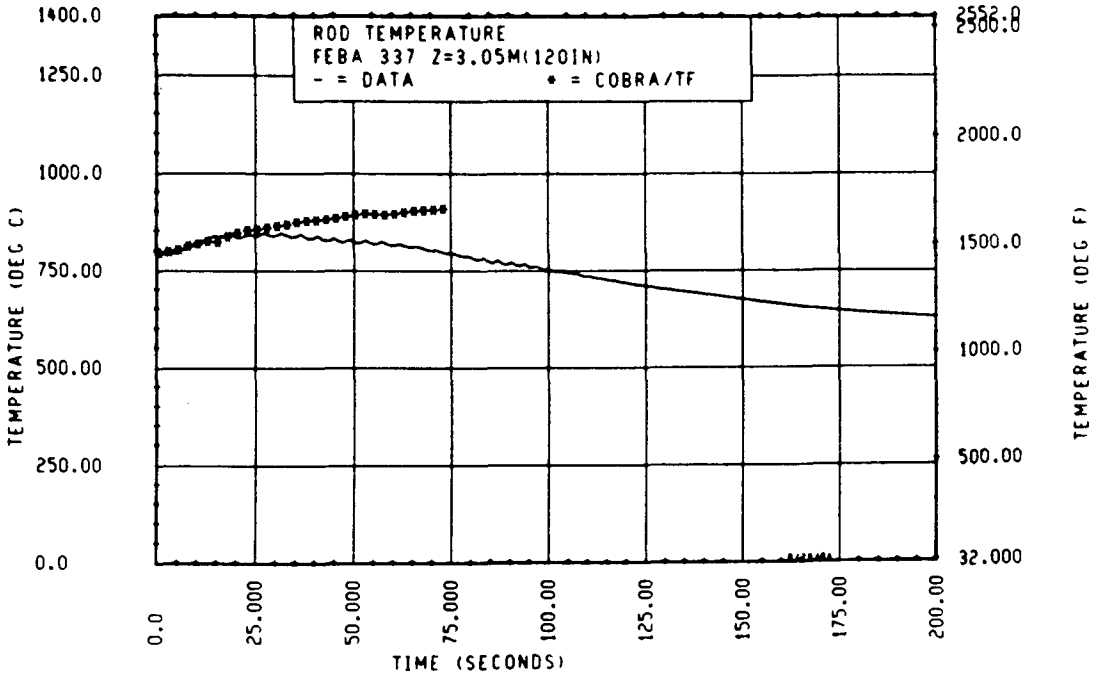

Figure 4-126. Comparison of COBRA-TF-Calculated Heater Rod Temperature Versus Time With FEBA Data, Test 337, 3.05 m (120 in.) Elevation

as well as by any mechanical droplet breakup which occurs as a result of hitting the blockage sleeves. The other FEBA cases with 62-percent blockage were also examined, and it was observed that the calculated aerodynamic Weber number was significantly less than 13, such that no additional droplet breakup would occur. Also, in the FEBA experiments with only 9 of the 25 rods blocked 90 percent, modeled earlier with COBRA-TF, the aerodynamic droplet Weber number was less than 13 in the blocked zone because of the large amount of flow bypass.

A simple droplet criterion was added to COBRA-TF to reflect the aerodynamic droplet breakup. The criterion provides that when the calculated droplet aerodynamic Weber number exceeds 13, the drop is split into two equal volumes and the droplet number is recalculated. The COBRA-TF predictions for FEBA test 337 with this criterion added are compared to the FEBA data in figures 4-127 through 4-132. (Also shown in figure 4-127 is the axial location of the spacer grids and the blockage zone.) Comparison of these calculations to the COBRA-TF calculations without the aerodynamic droplet breakup mechanism clearly shows an improved agreement.

Also, in the calculations shown in figures 4-127 through 4-132, the drops are so small that they are nearly all evaporated within the bundle, resulting in larger steam generation rates and lower steam temperatures. As a result, excellent cooling was calculated downstream of the blockage zones for this test. The larger amount of evaporation was also observed in the FEBA test data (figure 4-20), which showed that the liquid entrainment exiting the test bundle was significantly delayed because of the more rapid evaporation of the droplets. Since only this particular test configuration resulted in aerodynamic droplet breakup, which was a larger effect than the blockage models, no additional comparisons of COBRA-TF with the all-rods-blocked-90-percent FEBA data were made. However, it would be expected that, if there were large islands of blockages on the order of 90 percent, such that not much flow redistribution would occur, the aerodynamic droplet effect could be significant.

4-21. DISCUSSION AND ASSESSMENT OF BLOCKAGE MODEL RESULTS

A series of sensitivity studies were performed to determine the relative performance of each of the blockage models and thus identify the dominant heat

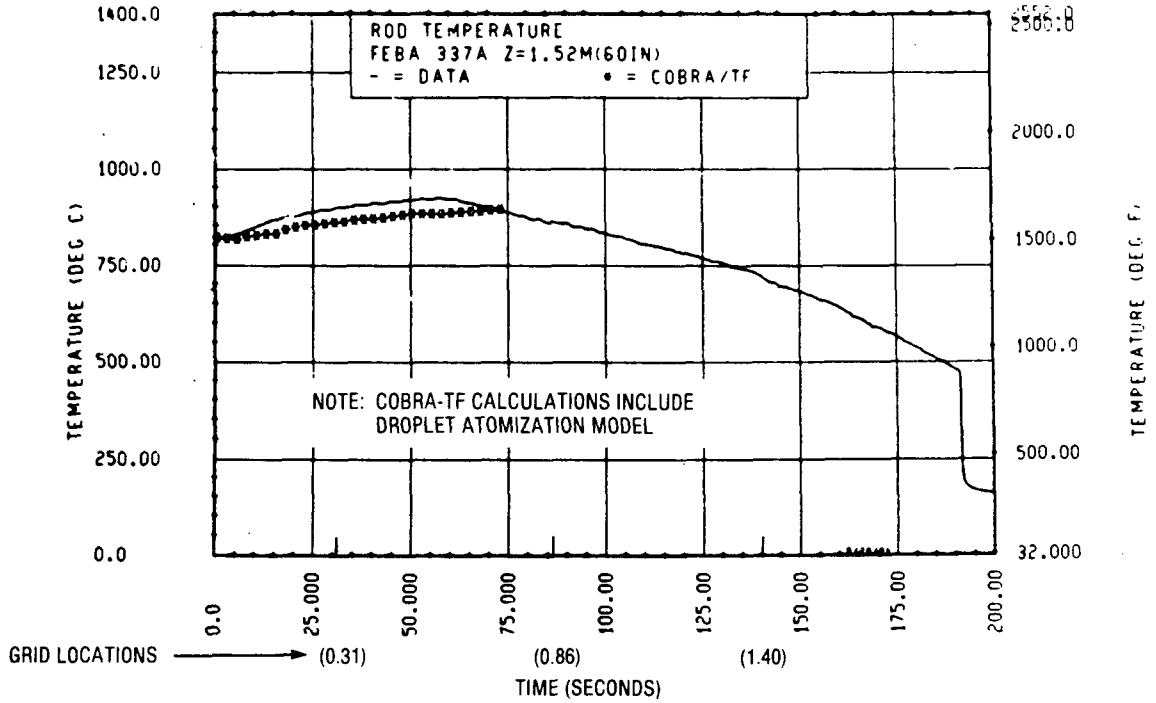

Figure 4-127. Comparison of COBRA-TF-Calculated Heater Rod Temperature Versus Time With FEBA Data, Test 337, 1.52 m (60 in.) Elevation (With Aerodynamic Droplet Breakup Model)

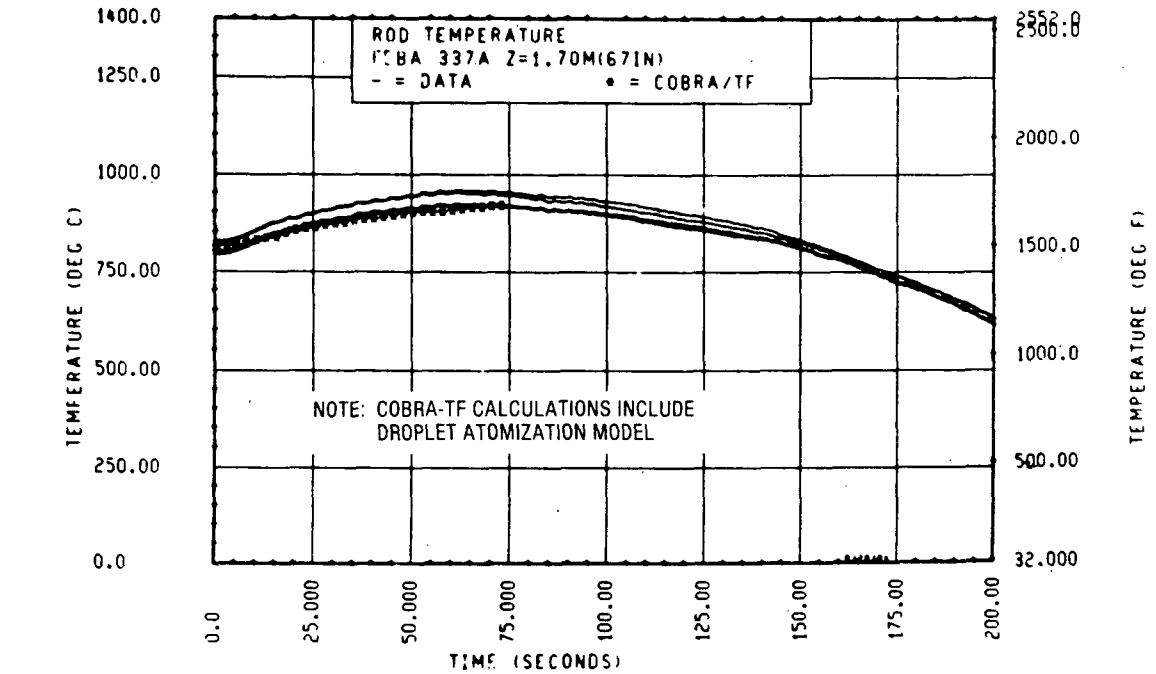

Figure 4-128. Comparison of COBRA-TF-Calculated Heater Rod Temperature Versus Time With FEBA Data, Test 337, 1.70 m (67 in.) Elevation (With Aerodynamic Droplet Breakup Model)

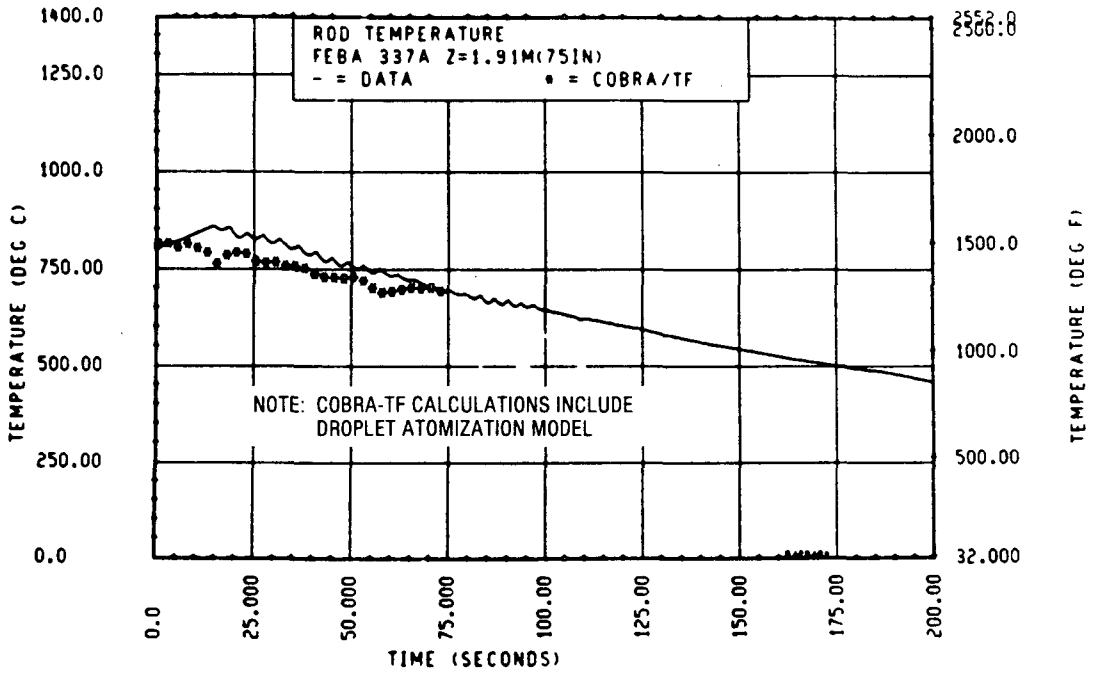

Figure 4-129. Comparison of COBRA-TF-Calculated Heater Rod Temperature Versus Time With FEBA Data, Test 337, 1.91 m (75 in.) Elevation (With Aerodynamic Droplet Breakup Model)

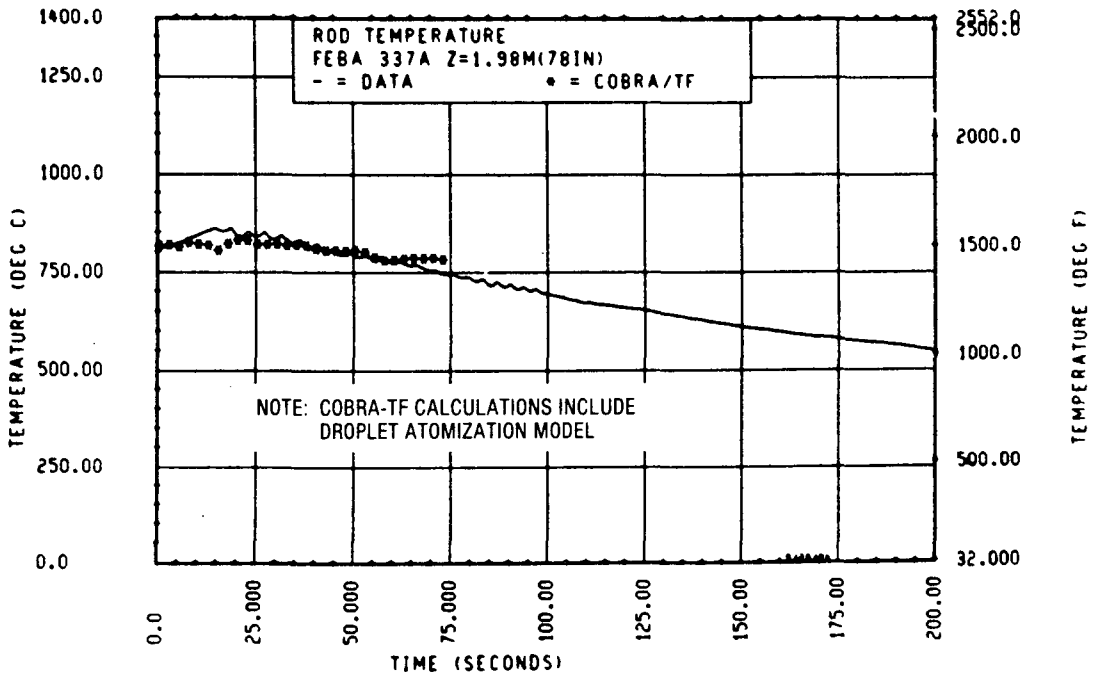

Figure 4-130. Comparison of COBRA-TF-Calculated Heater Rod Temperature Versus Time With FEBA Data, Test 337, 1.98 m (78 in.) Elevation (With Aerodynamic Droplet Breakup Model)

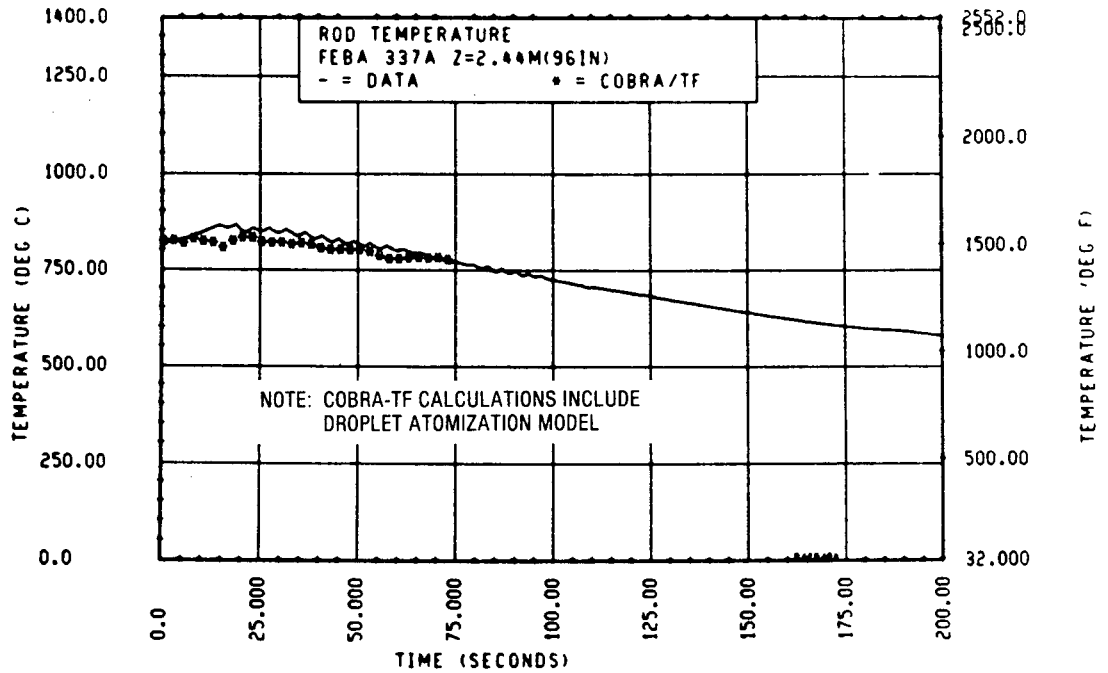

Figure 4-131. Comparison of COBRA-TF-Calculated Heater Rod Temperature Versus Time With FEBA Data, Test 337, 2.44 m (96 in.) Elevation (With Aerodynamic Droplet Breakup Model)

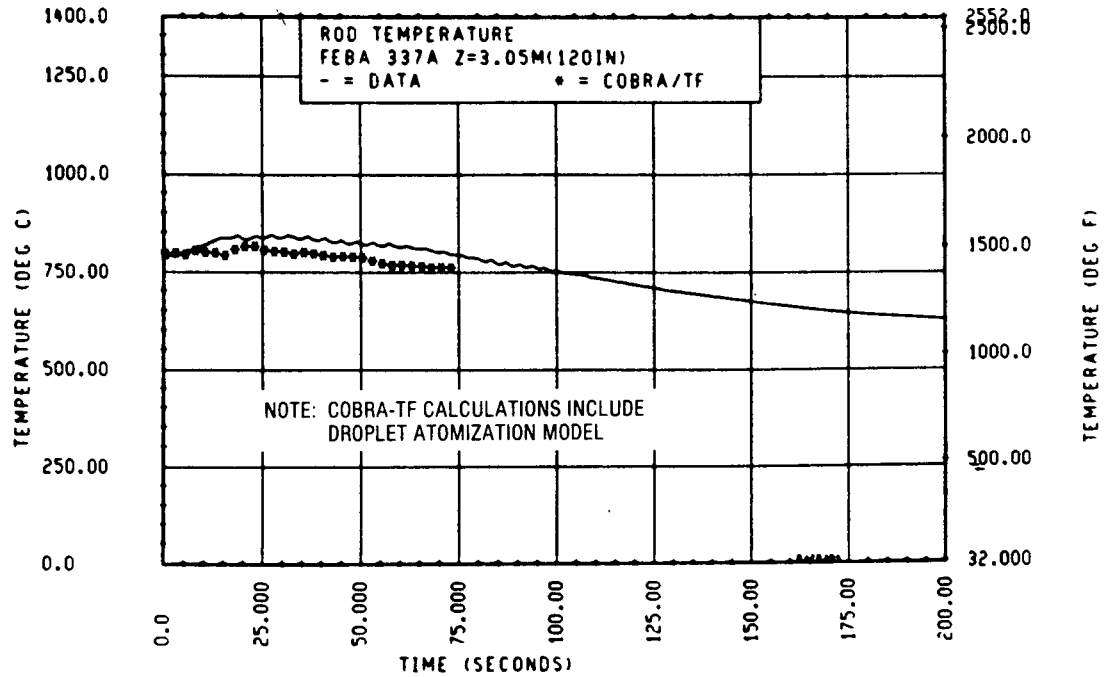

Figure 4-132. Comparison of COBRA-TF-Calculated Heater Rod Temperature Versus Time With FEBA Data, Test 337, 3.05 m (120 in.) Elevation (With Aerodynamic Droplet Breakup Model)

transfer mechanism. FLECHT SEASET 21-rod bundle test 42506C was analyzed with each of the blockage models selectively deleted. That is, there was a calculation with all heat transfer models and a calculation with no models but still with the blockage area reduction. Then the individual blockage heat transfer models were deleted one at a time to demonstrate their relative effects. These calculations are shown in figures 4-133 through 4-136, plotted as calculated axial temperature versus elevation for different times. A more detailed scale was used in and downstream of the blockage zone. All grid models discussed in section 3 were incorporated in these calculations.

The calculations at 80 seconds (figure 4-136) provide the clearest illustration, since the two-phase dispersed flow is fully developed and 80 seconds is about the peak temperature turnaround time. The difference between curve 0, with all models turned off, and the lowest curve which is superimposed with curve I indicates the total blockage model effect on the calculated heater rod temperature. This total effect is approximately 75° C (135° F) immediately downstream of the blockage. It should also be noted that there is a residual effect on the clad temperature at upper elevations [2.2 m (87 in.)] of approximately 25° C (45° F). The heat transfer benefit generated at the blockage zone favorably impacts the heater rod temperatures further downstream. Comparison of the calculations with and without the droplet impact (curve I and the heavier line) indicates no difference. This means that the contribution of droplet impact heat transfer for this blockage shape is negligible, because of the extremely slight angle of the blockage (approximately 3 degrees).

Comparison of the calculation with the blockage convective heat transfer deleted, curve V, with the heavier curve with curve I superimposed on it shows that the addition of the blockage convective heat transfere is worth approximately two-thirds of the total blockage heat transfer benefit immediately downstream of the blockage. The difference with and without the blockage convective heat transfer model is effective only immediately downstream of the blockage [approximately 0.2 m (8 in.)]. Curve D, the calculation with the droplet breakup at the blockage deleted shows that this model is worth approximately one-third of the blockage model benefit immediately downstream of the

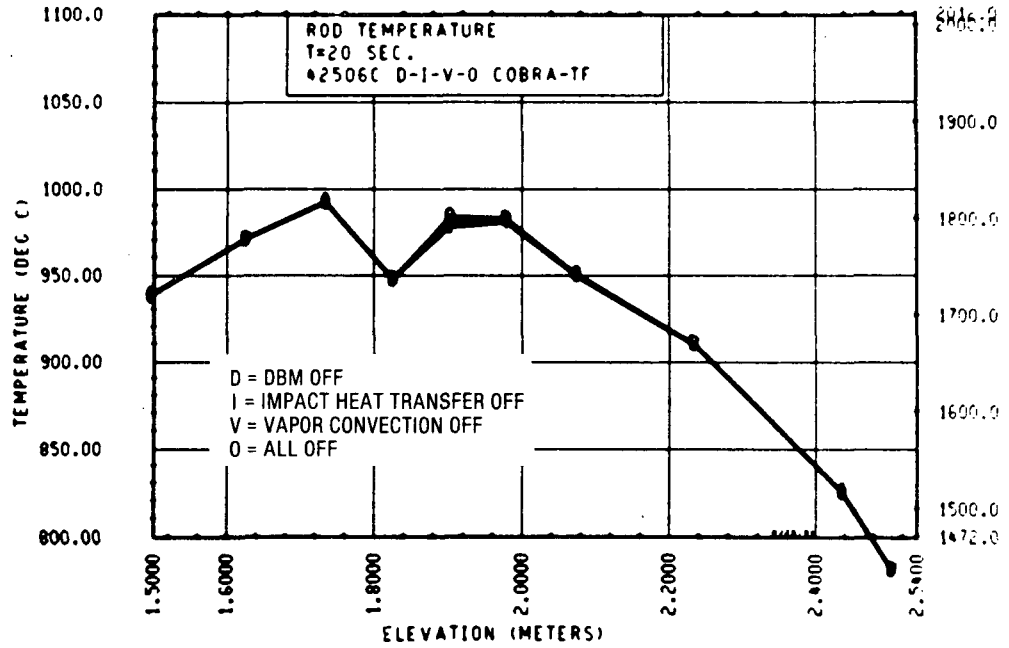

Figure 4-133. Relative Effects of Grid Models on COBRA-TF Predictions (FLECHT SEASET Test 42506C, t = 20 Seconds)

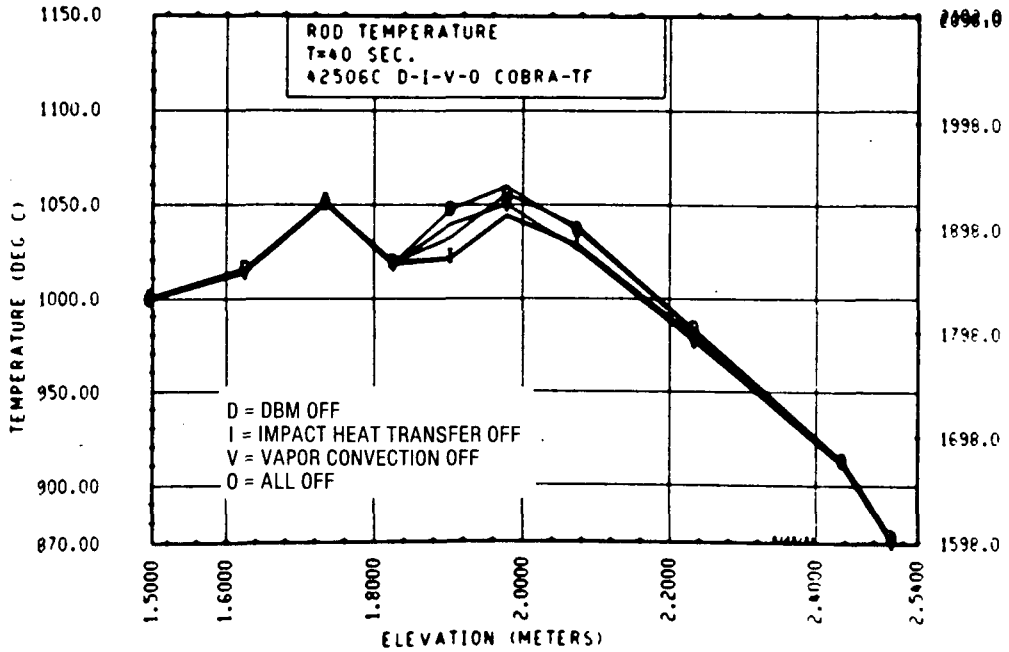

Figure 4-134. Relative Effects of Grid Models on COBRA-TF Predictions (FLECHT SEASET Test 42506C, t = 40 Seconds)

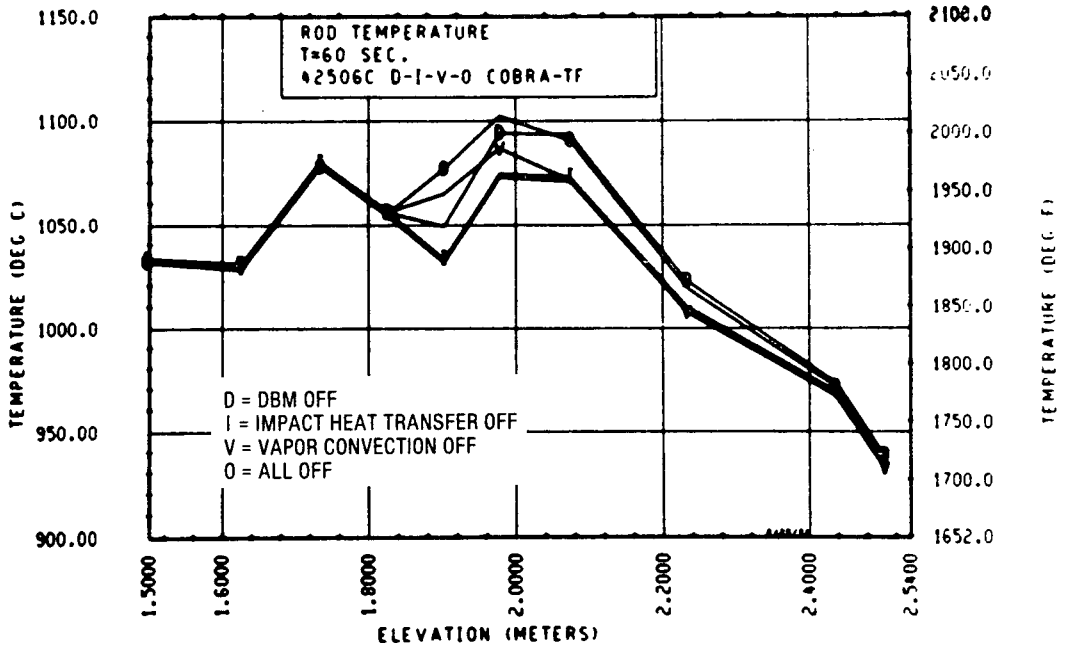

Figure 4-135. Relative Effects of Grid Models on COBRA-TF Predictions (FLECHT SEASET Test 42506C, t = 60 Seconds)

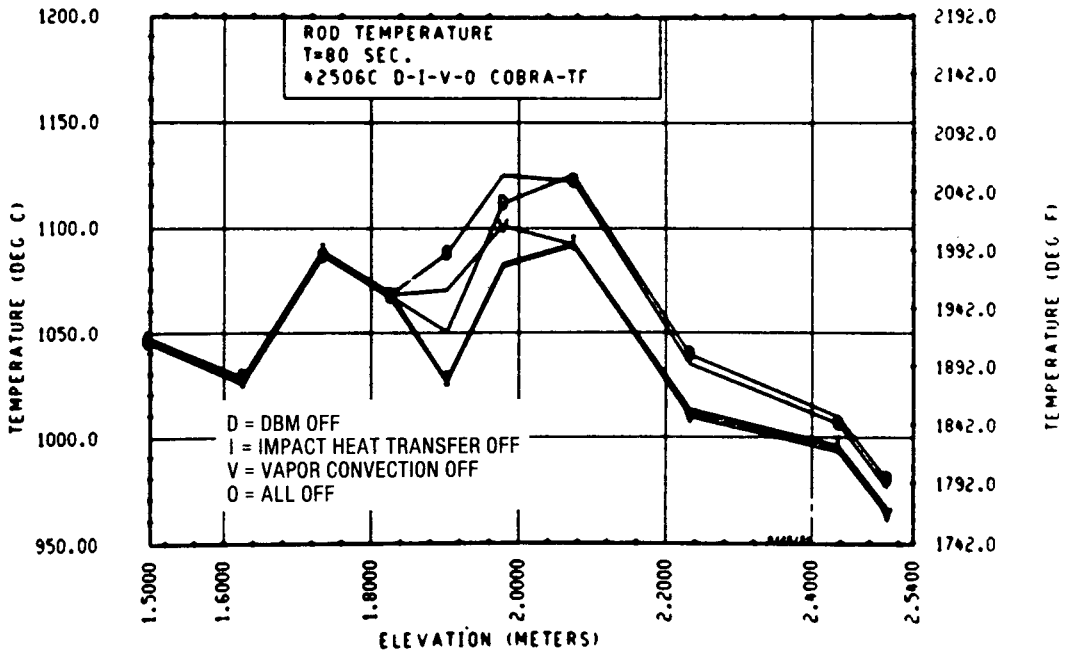

Figure 4-136. Relative Effects of Grid Models on COBRA-TF Predictions (FLECHT SEASET Test 42506C, t = 80 Seconds)

blockage. However, without the droplet breakup model, the calculated temperature increases up to the values calculated with no blockage models at all (curve 0). Therefore, although the droplet breakup model is not as significant for this particular case, it does affect the downstream heat transfer significantly. Droplet breakup in the blockage must be accounted for to accurately predict the entire rod temperature profile.

One method of assessing how well the COBRA-TF calculations using the blockage model fit the test data is to develop a bias plot similar to that constructed for the grid model assessment. The COBRA-calculated temperature rise is compared to the data-calculated temperature rise as

$$(T_t - T_{initial})_{data} - (T_t - T_{initial})_{COBRA\text{-}TF}$$

This value is plotted against elevation for different transient times. The objective of these plots is the discovery of a simple bias (if any) with time, elevation, or test conditions, for which the calculations and the data show significant differences. A positive temperature rise delta implies that the temperature rise observed in the experiment was larger than the COBRA-calculated temperature rise value. If there were perfect agreement between the predictions and the data temperature rise values, the resulting plot would constitute a straight line through zero.

Figures 4-137 through 4-140 show no consistent trend with test conditions for these comparisons. In fact, the trends are divergent in some cases (figures 4-139 and 4-140). Most comparisons do show an underprediction of the temperature rise just before the blockage zone, relative to the test data. The temperature rise predictions downstream of the blockage zone are larger in COBRA-TF relative to the data, such that the delta temperature is negative [at about 2 m (79 in.)].

Similar comparisons for the 21-rod bundle configuration F (long nonconcentric, noncoplanar blockage), shown in figures 4-141 through 4-144, evidence an even larger overprediction of the temperature rise values in COBRA-TF relative to

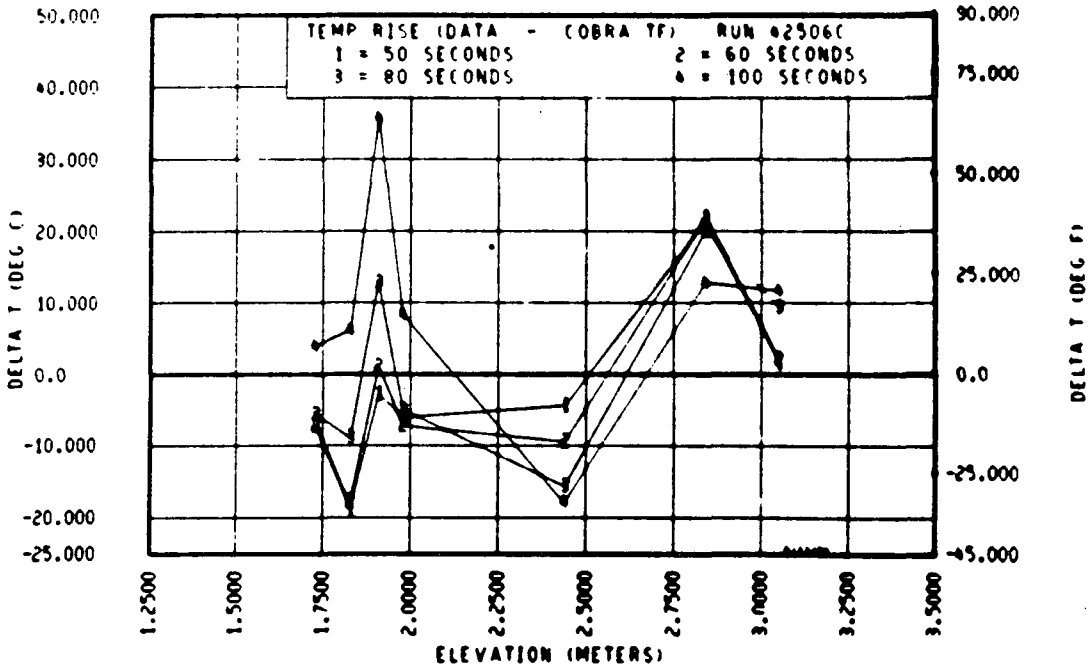

Figure 4-137. Temperature Rise Versus Elevation, FLECHT SEASET Test 42506C

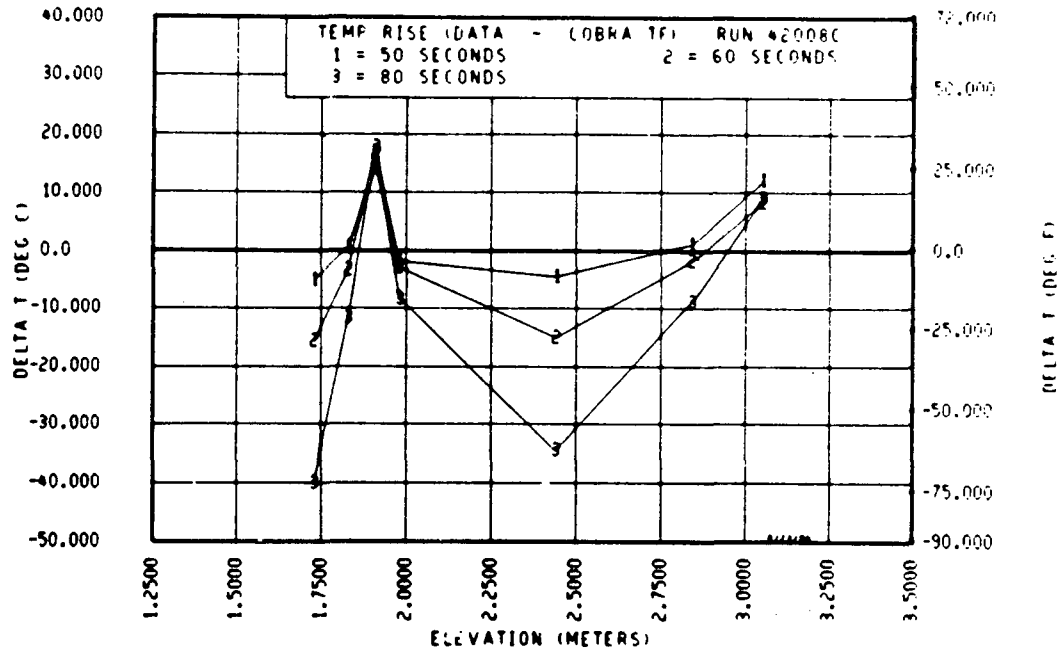

Figure 4-138. Temperature Rise Versus Elevation, FLECHT SEASET Test 42008C

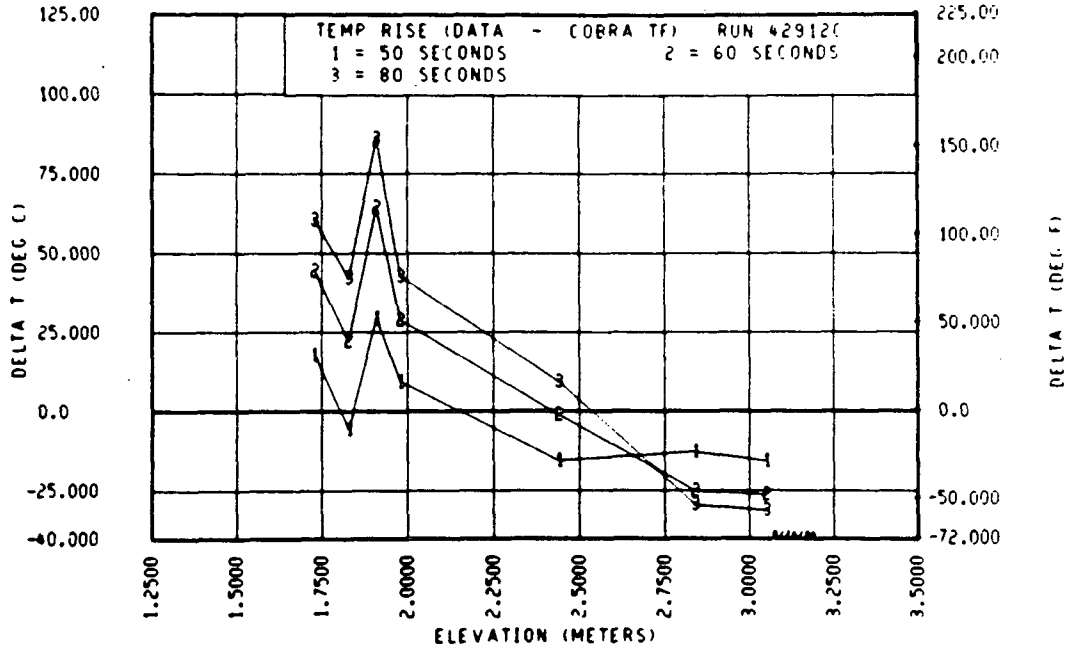

Figure 4-139. Temperature Rise Versus Elevation, FLECHT SEASET Test 42912C

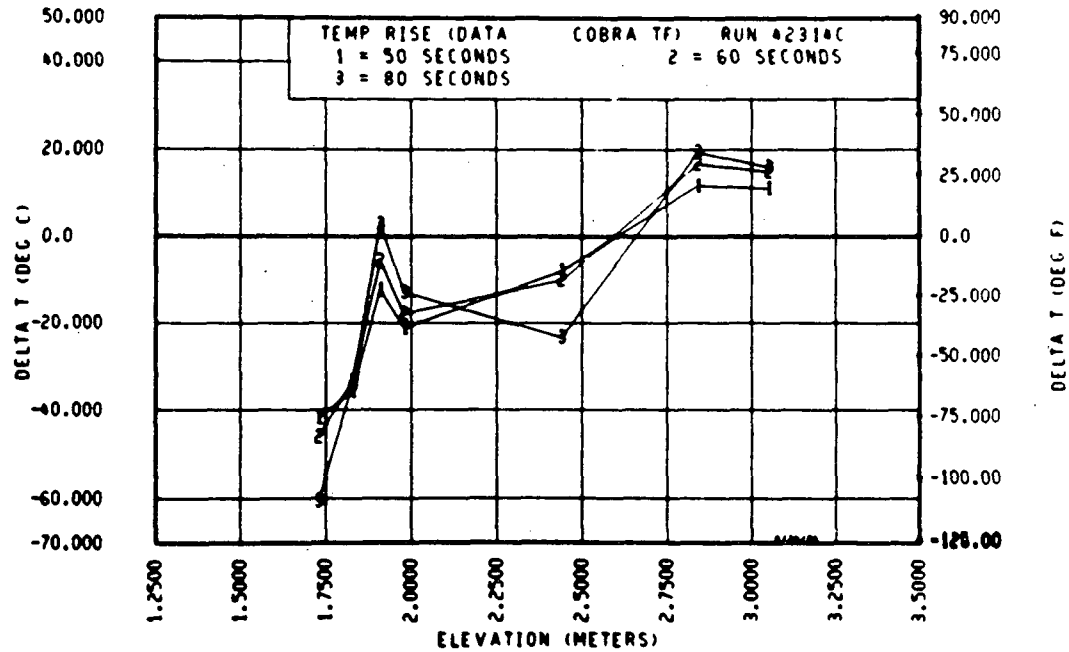

Figure 4-140. Temperature Rise Versus Elevation, FLECHT SEASET Test 42314C

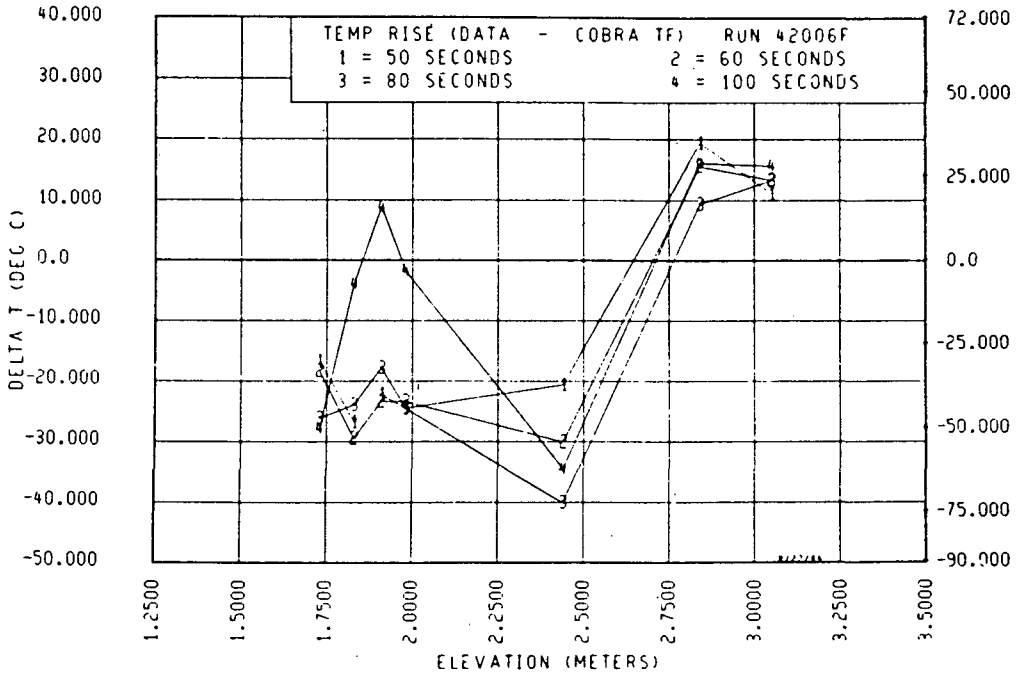

Figure 4-141. Temperature Rise Versus Elevation, FLECHT SEASET Test 42006F

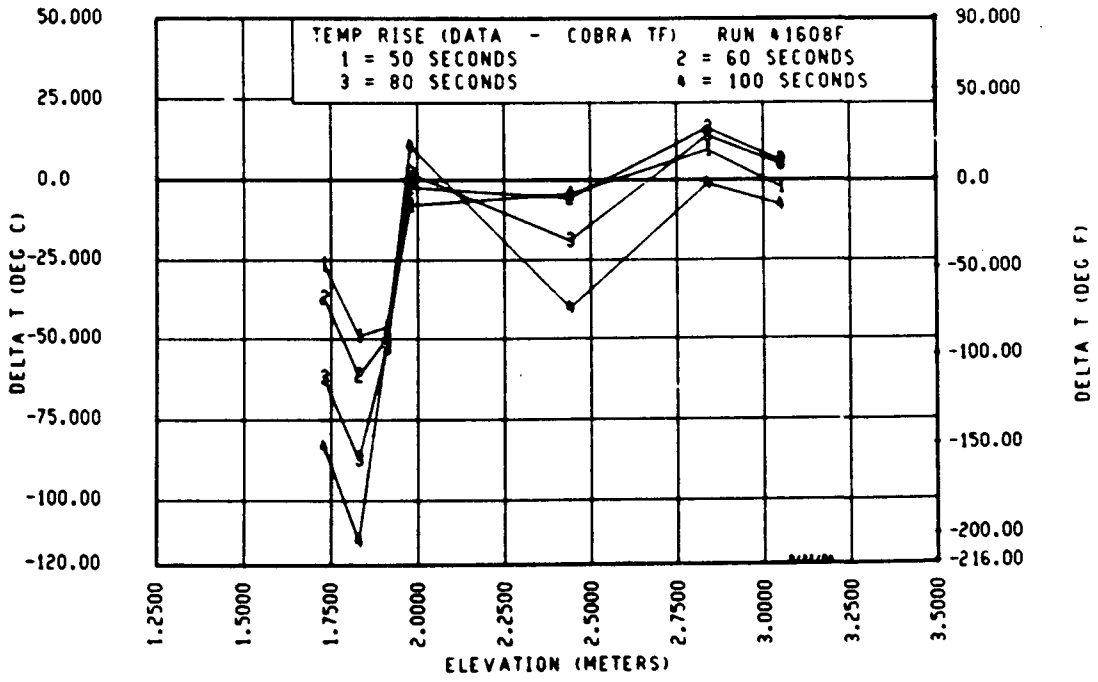

Figure 4-142. Temperature Rise Versus Elevation, FLECHT SEASET Test 41608F

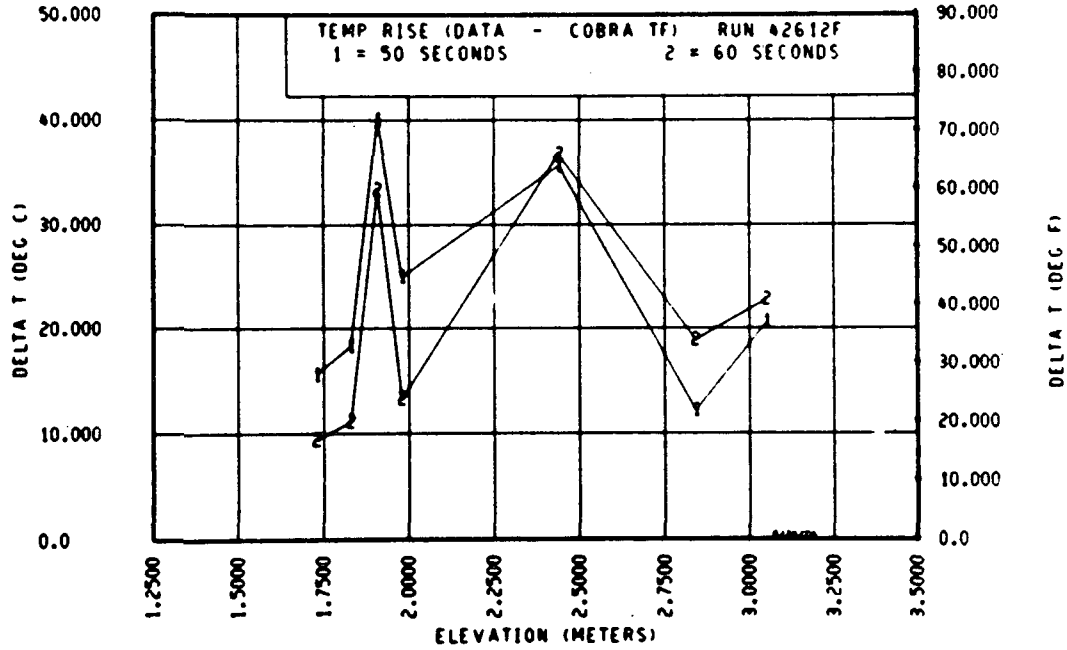

Figure 4-143. Temperature Rise Versus Elevation, FLECHT SEASET Test 42612F

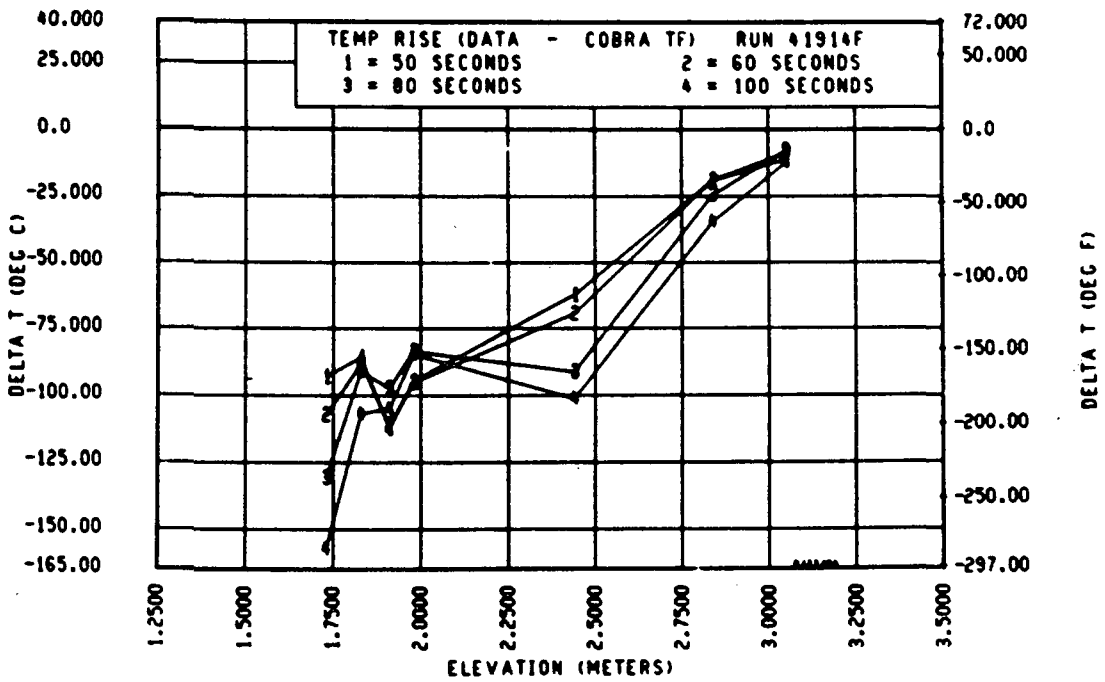

Figure 4-144. Temperature Rise Versus Elevation, FLECHT SEASET Test 41914F

the test data (with the exception of one test). It is believed that the simplification used to model the complex noncoplanar, nonconcentric blockage results in a reduction of the local heat transfer benefits that the blockage can promote. Consequently, the predicted COBRA-TF temperature rise reflects the lower calculated heat transfer in the blockage zone and results in a larger temperature rise than that observed in the experiment.

One method of quantifying the agreement of the COBRA-TF predictions with the experimental data from these temperature rise plots involves obtaining the average of the difference between the test data and the predicted temperature rise values for each elevation for all tests and times up to turnaround time. The temperature rise differences at 50, 60, and 80 seconds were averaged for each elevation for each test, as shown in table 4-3, and a grand average was obtained. In calculation of these averages, the plus and minus delta temperature rises were allowed to cancel one another so that a truer average relative to a delta temperature of zero (perfect agreement) could be obtained. Table 4-3 shows that COBRA-TF can predict the temperature rise values relative to the data within 12.3° C (22.1° F) at the bundle midplane.

In addition to the comparison of COBRA-TF predictions with a single set of test data, another method was used which isolated the blockage effect. In this case, the data from an unblocked test were compared to the results of the blocked bundle test to determine the blockage effect. That is, 21-rod bundle test 42006F was compared to test 42606A. The difference between test 42606A and 42006F at different elevations and different times gave the experimentally observed blockage effect. A similar comparison can be made with the two COBRA-TF calculations for these two tests to indicate the calculated blockage effect. Comparison of these to ΔT values shows whether the blockage effect predicted by the code is approximately correct. The ΔT $rise_{data}$ values from the test data were calculated by referencing the blocked bundle test to the unblocked bundle test conducted at the same conditions. That is, FLECHT SEASET test 42606A (unblocked 21-rod bundle test) was compared to test 42506C (blocked bundle test). A similar set of comparisons was made using the COBRA-TF calculations for each set of experiments.

TABLE 4-3
EVALUATION OF FIT BETWEEN COBRA-TF PREDICTIONS
AND FLECHT SEASET 21-ROD BUNDLE DATA

	Difference Between Test Data and COBRA-TF Prediction for Indicated Configuration [°C (°F)]		
Elevation [m (in.)]	21-Rod Configuration C	21-Rod Configuration F	Grand Average
1.75 (69)	- 8.16 (-14.7)	-38.75 (-69.75)	-23.45 (-42.22)
1.95 (77)	0.42 (0.75)	-25.04 (-45.08)	-12.32 (-22.17)
2.40 (94)	-10.17 (-18.3)	-16.63 (-29.93)	13.39 (24.11)
2.85 (112)	2.75 (4.95)	6.0 (10.8)	4.37 (7.87)
3.05 (120)	1.08 (1.95)	7.17 (12.9)	4.12 (7.42)

The temperature rise effects in this series are different from those shown in figures 4-137 through 4-144 because the reference is an unblocked bundle test or calculation temperature rise, not just the initial temperature.

The results of the temperature rise calculations and the test data are plotted against elevation for different times after reflood. Comparisons of this nature are a severe test of the models, since the differences between temperatures calculated by the model and the data are easy to see.

Figures 4-145 through 4-148 compare the COBRA-calculated temperature rise and the data temperature rise results for FLECHT SEASET 21-rod bundle tests 42606A and 42506C. The solid dots are the data temperature rise values; the solid line shows the values calculated with COBRA-TF. The length of the line for COBRA-TF indicates the node size used in these calculations. The blockage and grid locations are also shown in the figures. A positive delta temperature means that unblocked temperature rise is larger than the blocked bundle temperature rise for the same conditions at the same time after the beginning of reflood; that is, blockage is a heat transfer benefit.

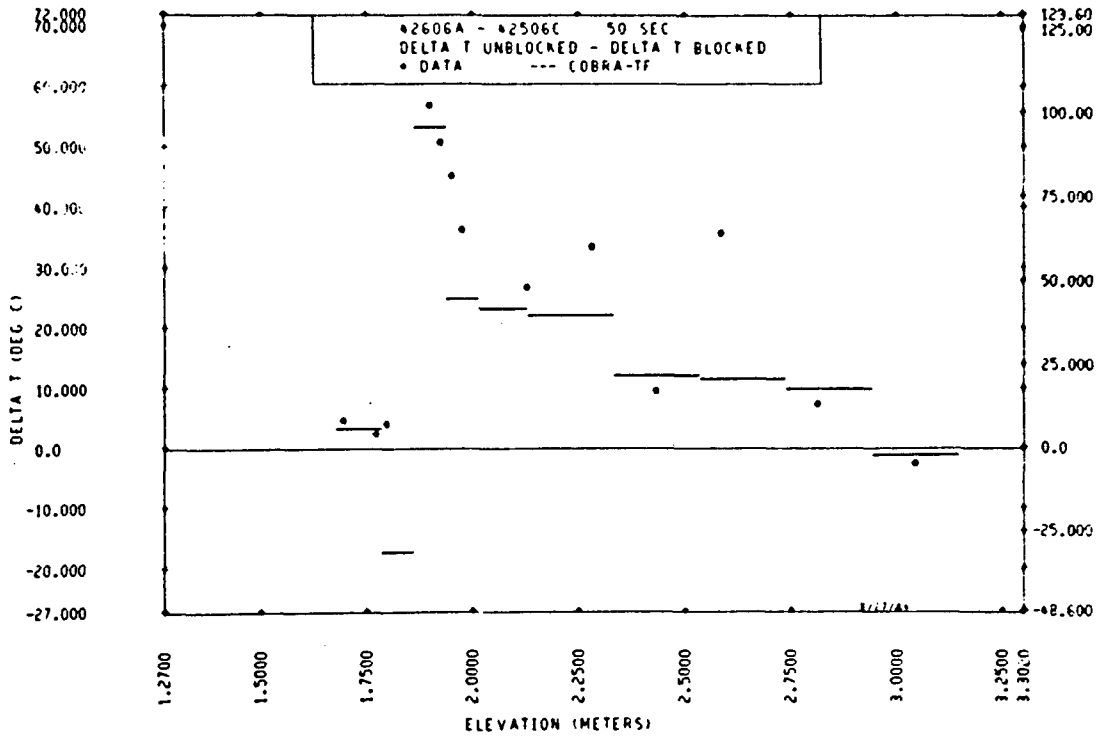

Figure 4-145. Blockage Effect Temperature Rise Versus Elevation, FLECHT SEASET Tests 42606A and 42506C, t = 50 Seconds

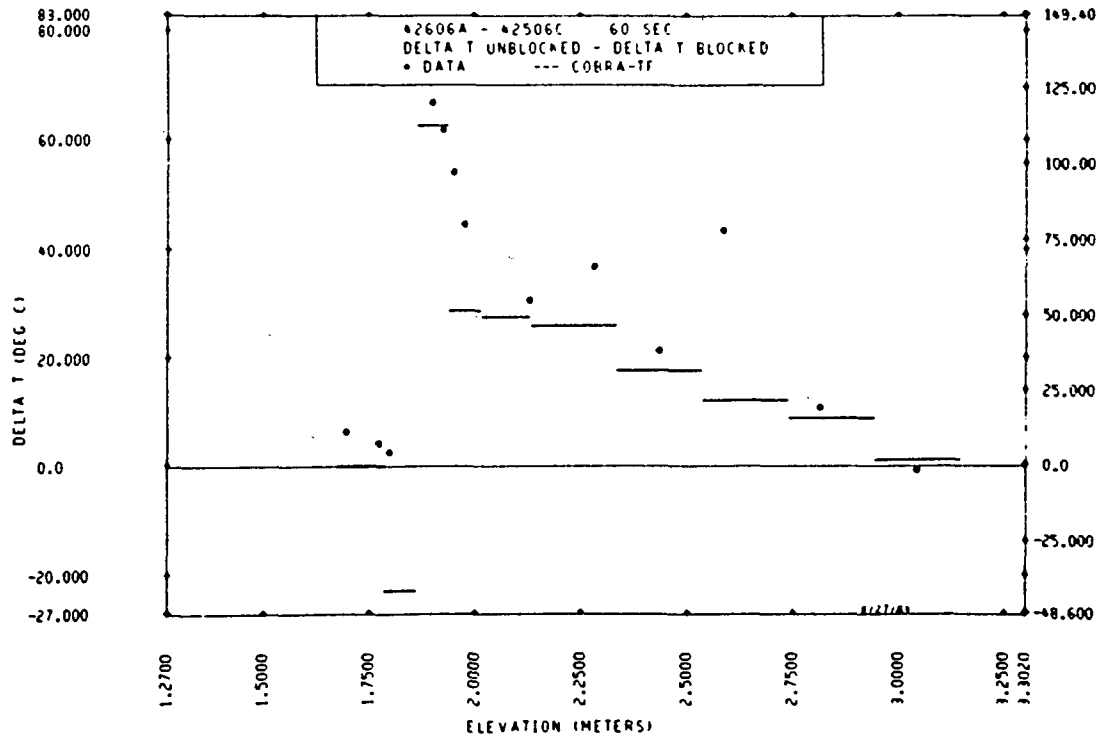

Figure 4-146. Blockage Effect Temperature Rise Versus Elevation, FLECHT SEASET Tests 42606A and 42506C, t = 60 Seconds

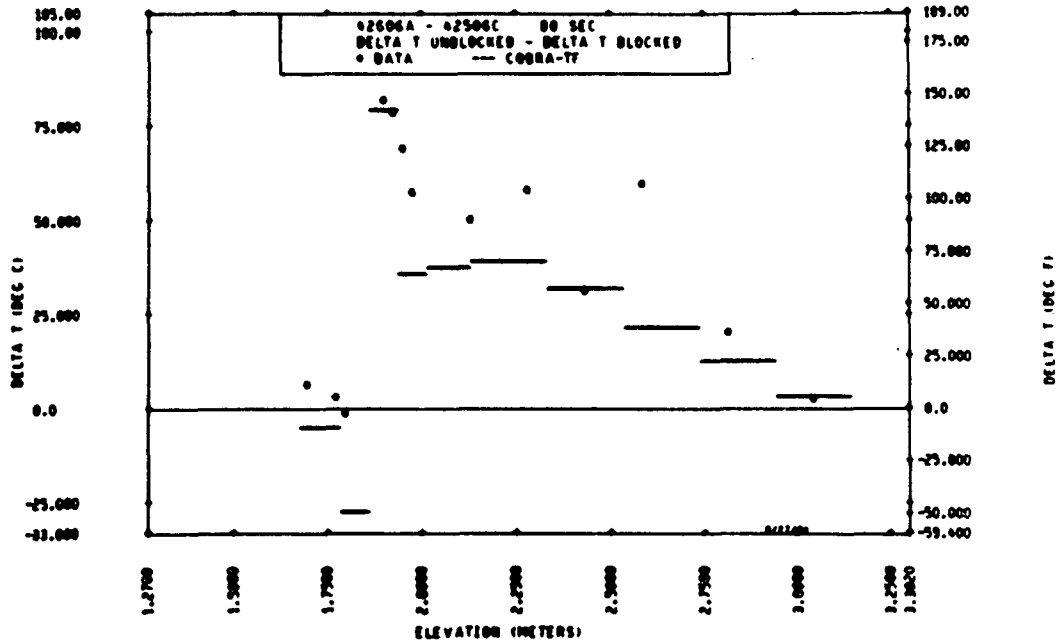

Figure 4-147. Blockage Effect Temperature Rise Versus Elevation, FLECHT SEASET Tests 42606A and 42506C, t = 80 Seconds

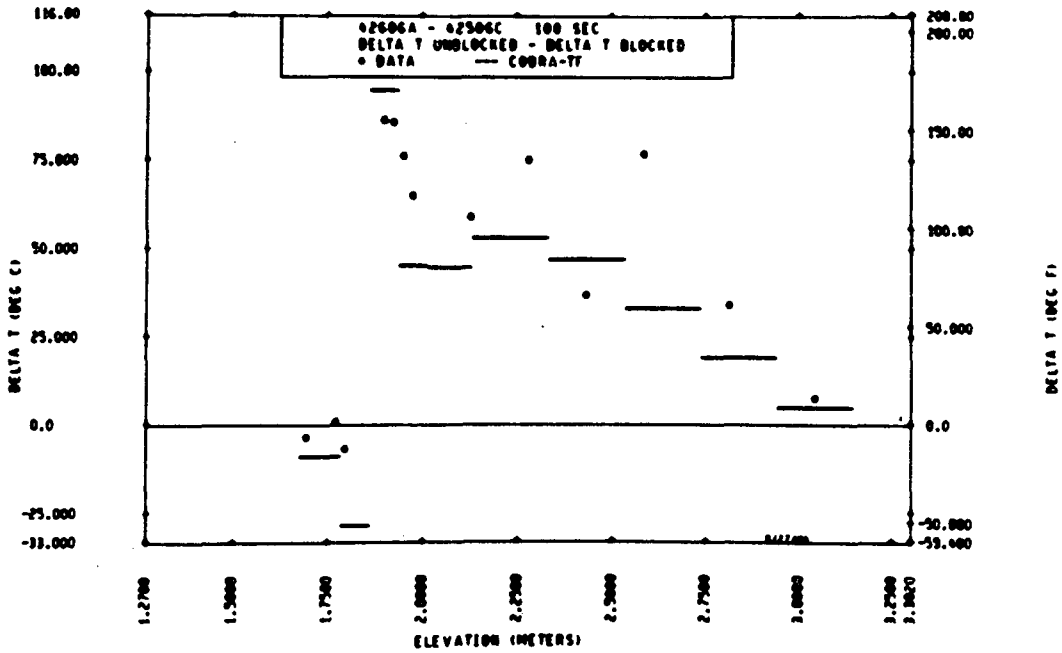

Figure 4-148. Blockage Effect Temperature Rise Versus Elevation, FLECHT SEASET Tests 42606A and 42506C, t = 100 Seconds

The temperature rise results in these figures show that use of the blockage and grid models results in a reasonably good comparison. The data comparisons do indicate a larger delta temperature than that calculated by COBRA-TF; the unblocked bundle temperature rise may not be predicted as accurately as desired. The comparisons in figures 4-145 through 4-148 do require an accurate COBRA-TF prediction of two experiments (the unblocked and the blocked) to calculate the blockage effect. The data trends are predicted correctly and, in many cases, the COBRA-TF prediction of the blockage effects agrees with the data. Generally, however, the COBRA-predicted blockage effect is smaller than that observed in the data.

Figures 4-149 through 4-157 show the same comparisons for the other three coplanar 21-rod bundle blockage tests. Although the correct trend is generally predicted by COBRA-TF, the code tends to underestimate the blockage effect, particularly for tests 42514A-42314C. These plots show that the temperature rise difference between a blocked configuration and an unblocked reference is 70 to 120° C (126 to 216° F), depending on test conditions.

A similar set of comparisions is shown in figures 4-158 through 4-171 for FLECHT SEASET 21-rod bundle configuration F, with the long noncoplanar, nonconcentric blockage. Although the blockage temperature rise trends are predicted reasonably well, the COBRA-TF blockage model underestimates the blockage heat transfer effects observed in the experiments such that the predicted temperature rise delta is too small (the blocked calculation is closer to the unblocked calculation) relative to the test data. In addition, the calculated peak value of the blockage heat transfer is lower than that observed in the experiments; the predicted temperature rise difference between the unblocked bundle and the blocked bundle is only about 60 percent of that observed in the test data.

Table 4-3 indicates that the COBRA-TF code can predict the blockage heat transfer rise within approximately 12° C (22° F) on the average, whereas the blockage effect itself is approximately 70 to 100° C (126 to 216° F). Therefore, the models in COBRA-TF are sufficiently accurate to predict the blockage effects observed in these experiments. As shown in the figures, COBRA-TF tends to underpredict the heat transfer.

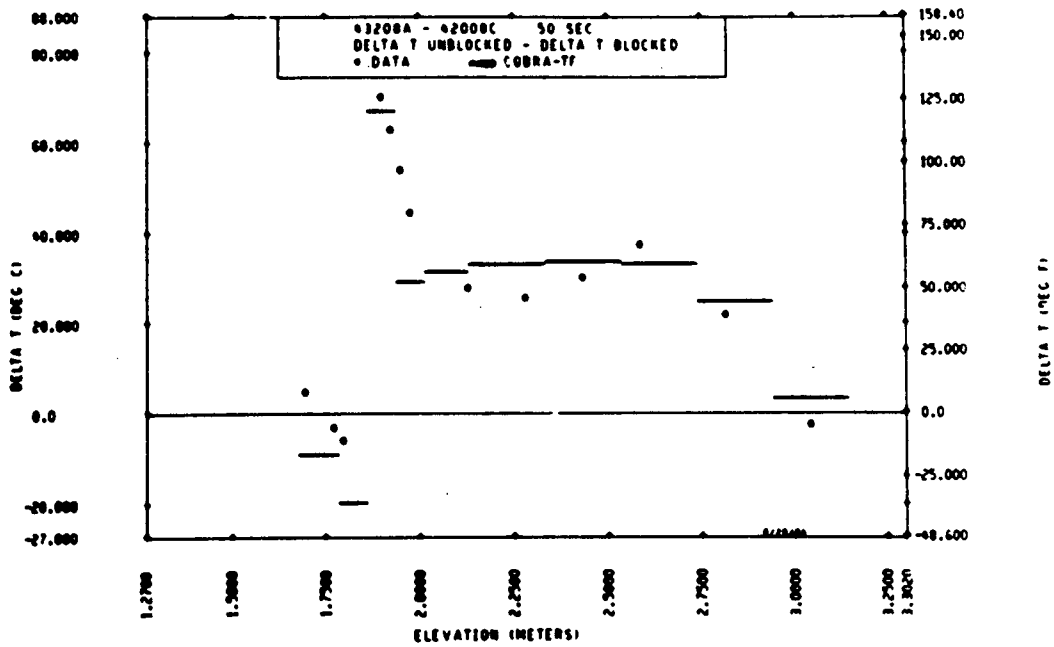

Figure 4-149. Blockage Effect Temperature Rise Versus Elevation, FLECHT SEASET Tests 43208A and 42008C, t = 50 Seconds

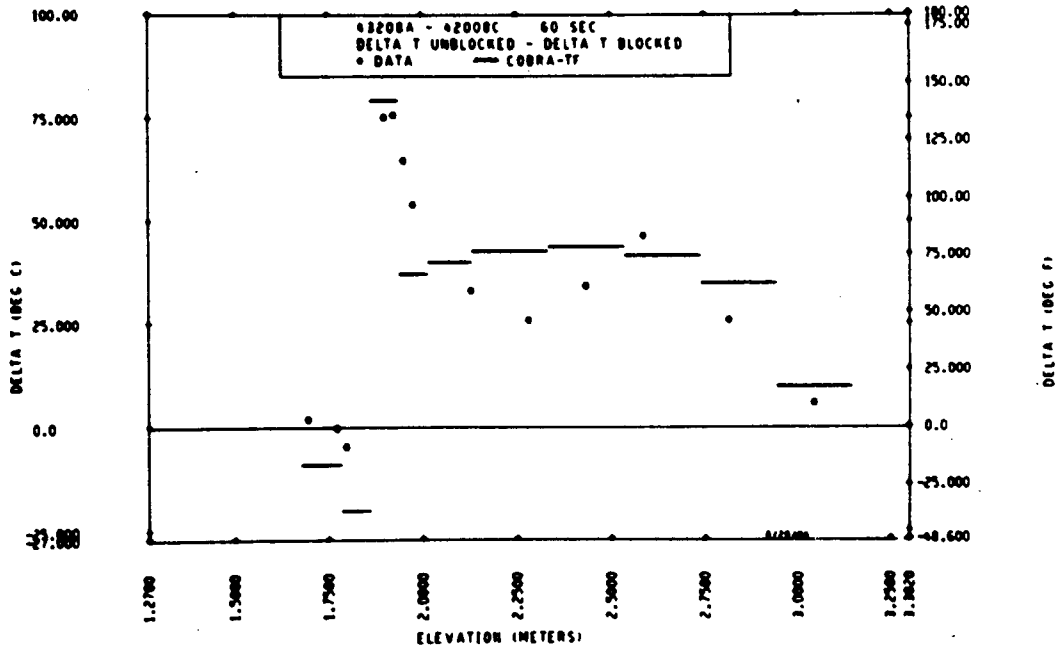

Figure 4-150. Blockage Effect Temperature Rise Versus Elevation, FLECHT SEASET Tests 43208A and 42008C, t = 60 Seconds

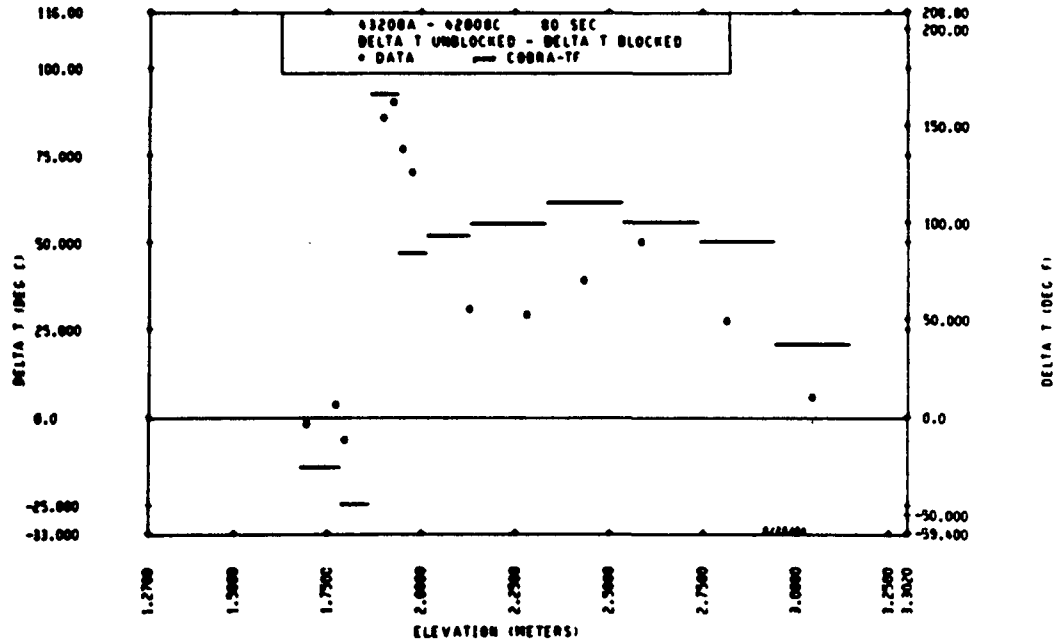

Figure 4-151. Blockage Effect Temperature Rise Versus Elevation, FLECHT SEASET Tests 43208A and 42008C, t = 80 Seconds

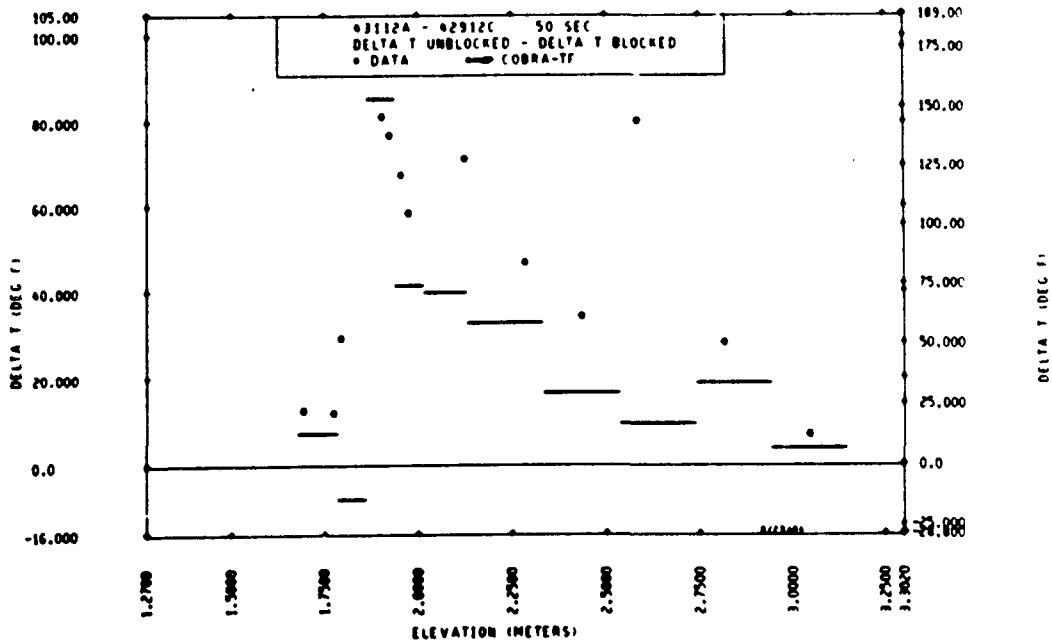

Figure 4-152. Blockage Effect Temperature Rise Versus Elevation, FLECHT SEASET Tests 43112A and 42912C, t = 50 Seconds

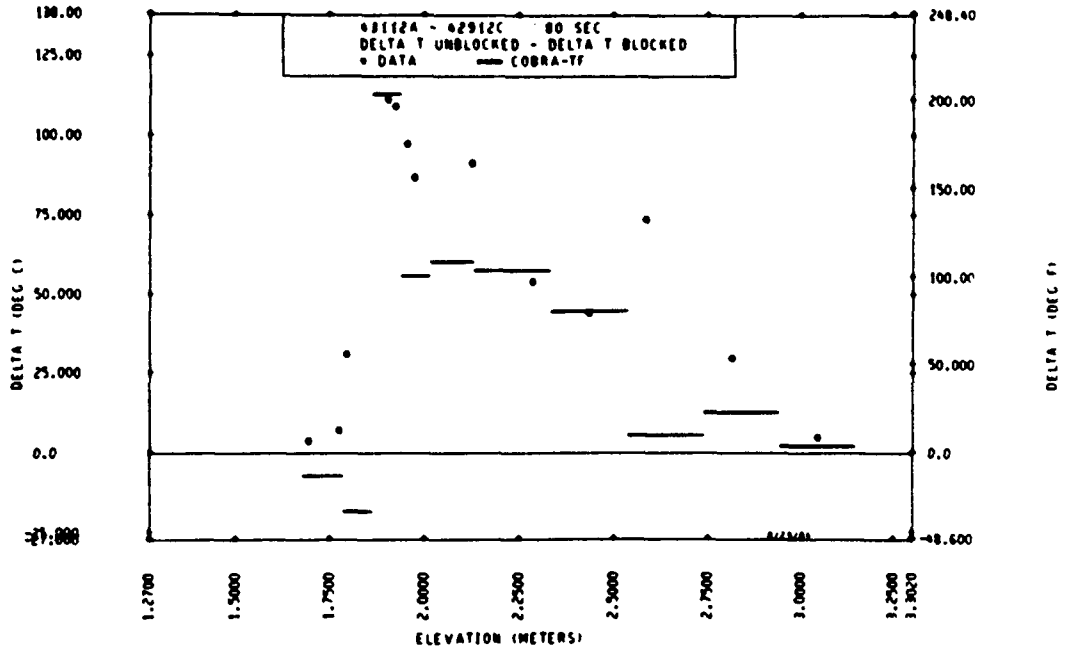

Figure 4-153. Blockage Effect Temperature Rise Versus Elevation, FLECHT SEASET Tests 43112A and 42912C, t = 80 Seconds

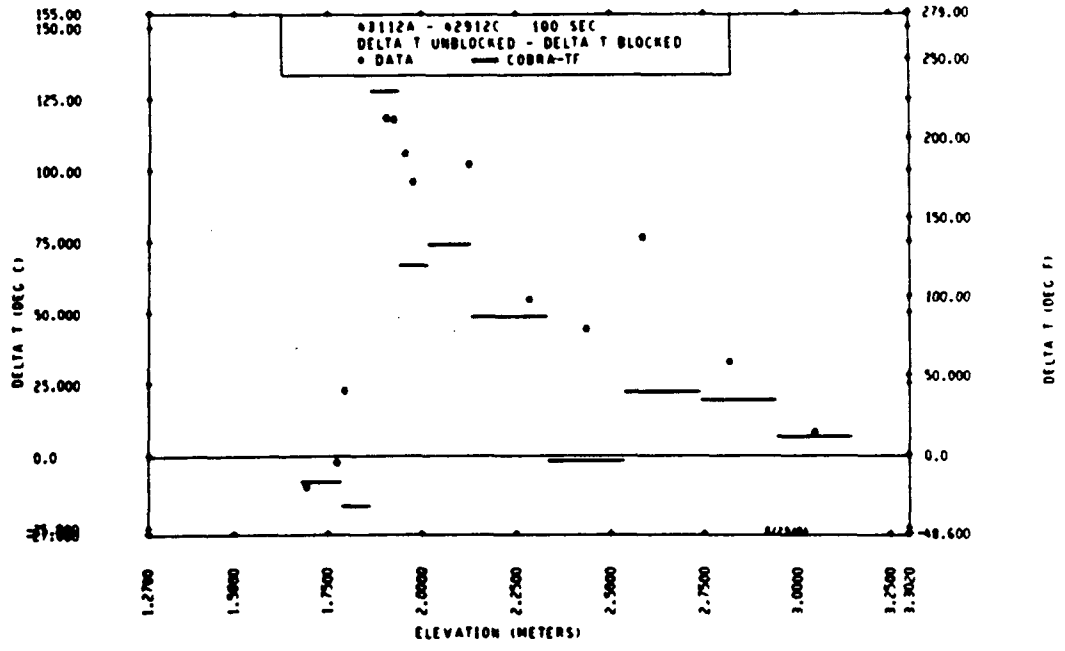

Figure 4-154. Blockage Effect Temperature Rise Versus Elevation, FLECHT SEASET Tests 43112A and 42912C, t = 100 Seconds

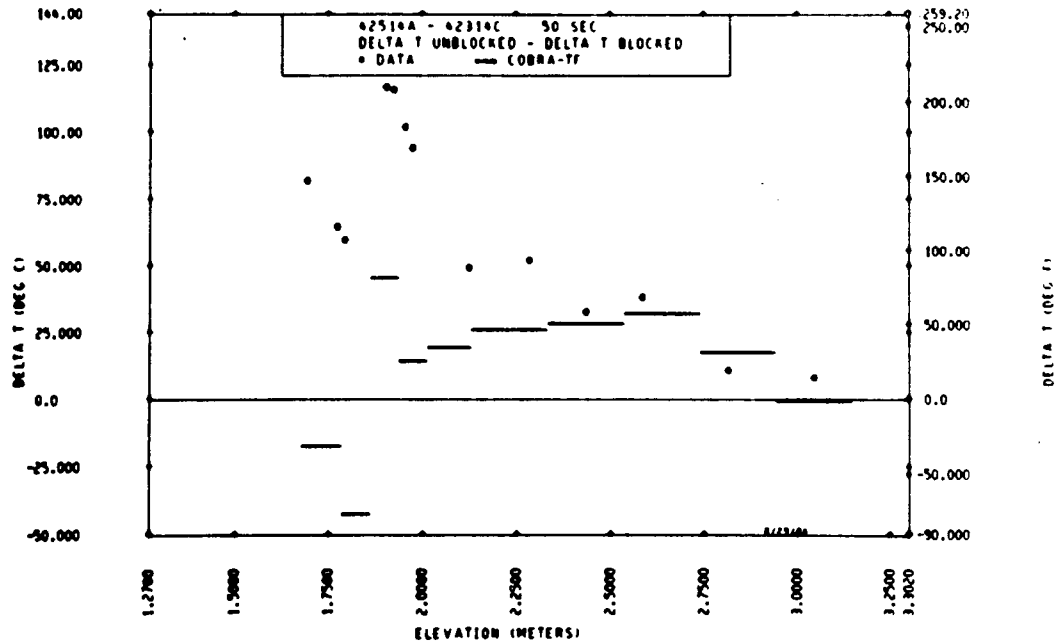

Figure 4-155. Blockage Effect Temperature Rise Versus Elevation, FLECHT SEASET Tests 42514A and 42314C, t = 50 Seconds

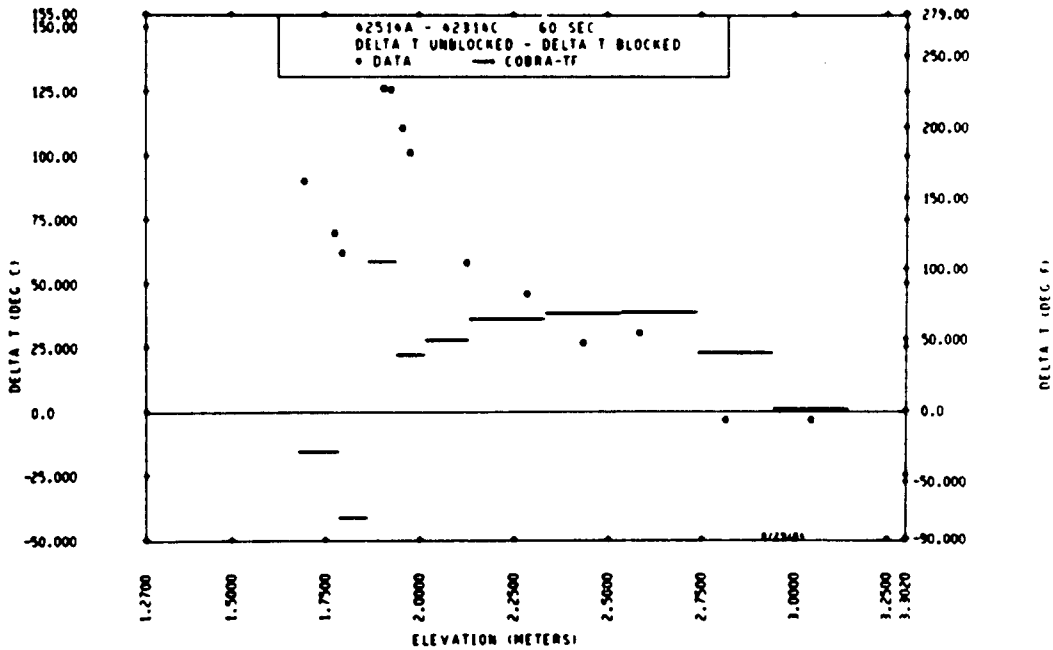

Figure 4-156. Blockage Effect Temperature Rise Versus Elevation, FLECHT SEASET Tests 42514A and 42314C, t = 60 Seconds

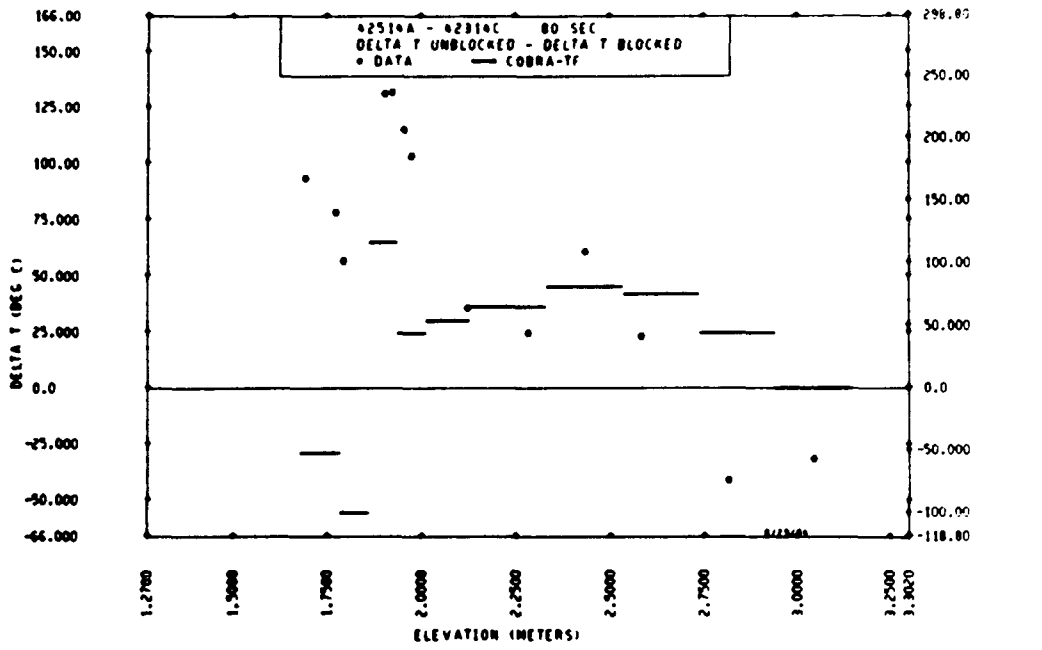

Figure 4-157. Blockage Effect Temperature Rise Versus Elevation, FLECHT SEASET Tests 42514A and 42314C, t = 80 Seconds

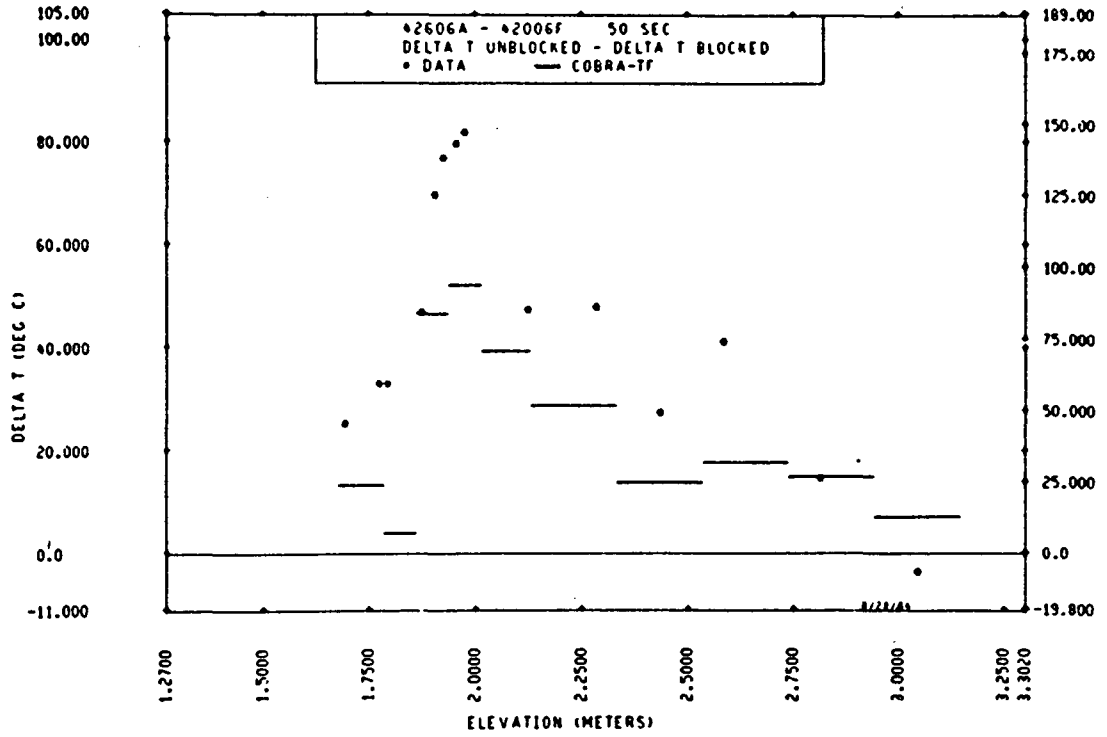

Figure 4-158. Blockage Effect Temperature Rise Versus Elevation, FLECHT SEASET Tests 42606A and 42006F, t = 50 Seconds

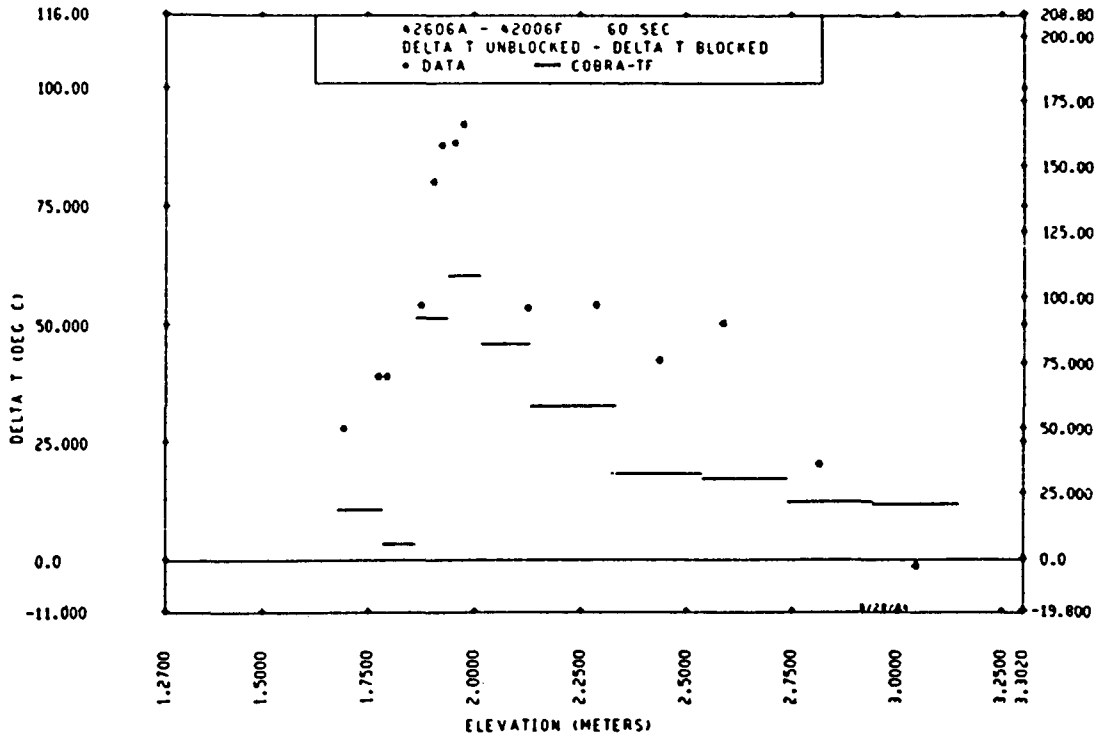

Figure 4-159. Blockage Effect Temperature Rise Versus Elevation, FLECHT SEASET Tests 42606A and 42006F, t = 60 Seconds

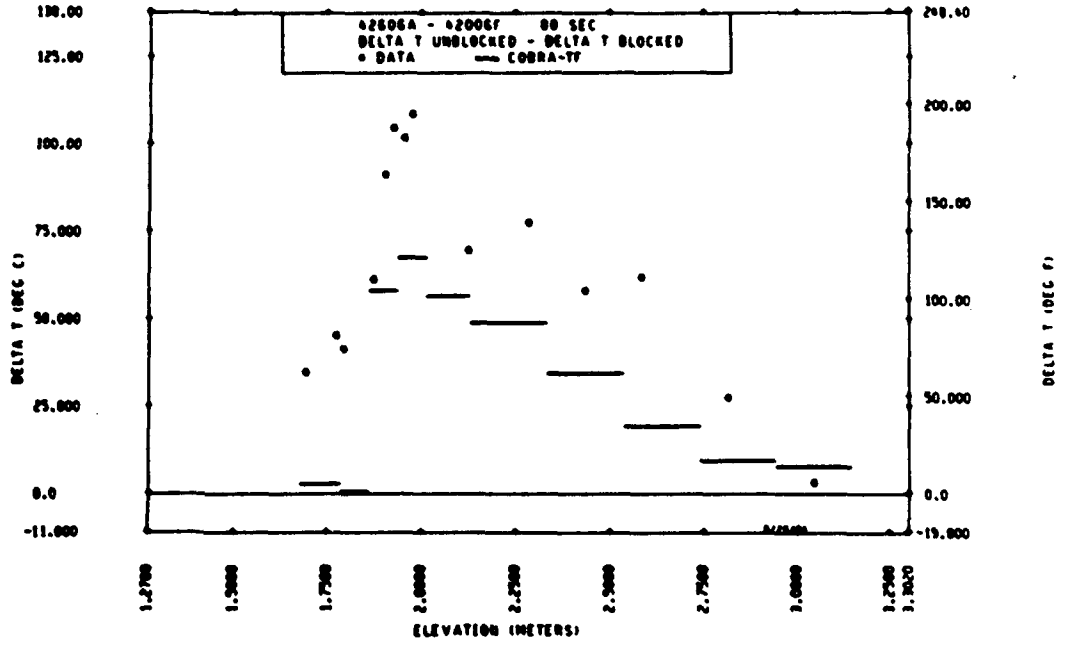

Figure 4-160. Blockage Effect Temperature Rise Versus Elevation, FLECHT SEASET Tests 42606A and 42006F, t = 80 Seconds

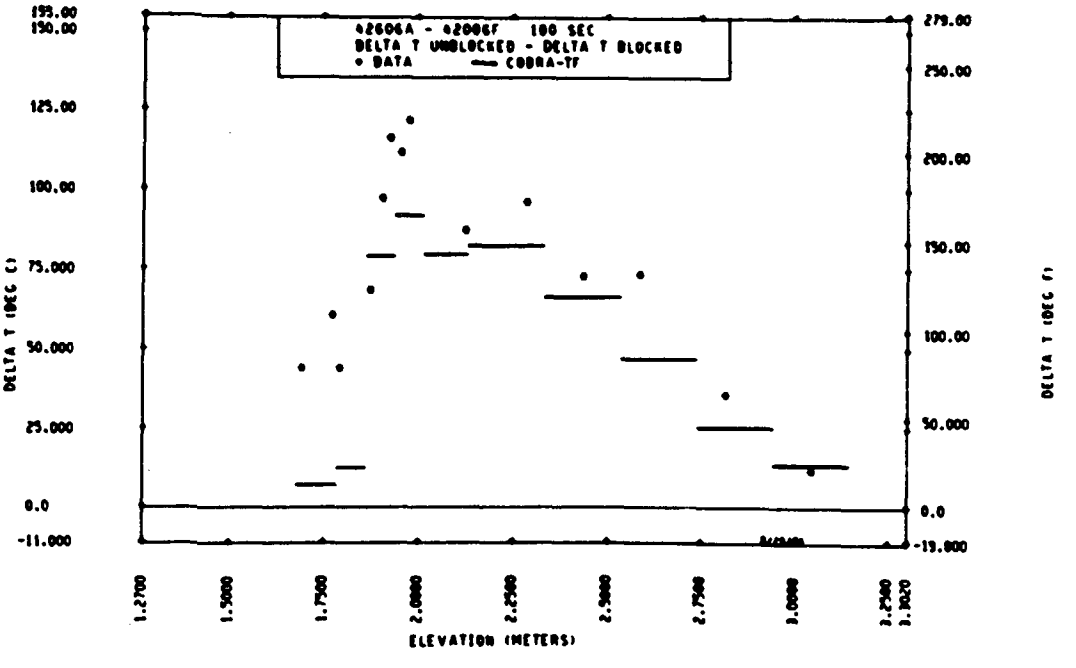

Figure 4-161. Blockage Effect Temperature Rise Versus Elevation, FLECHT SEASET Tests 42606A and 42006F, t = 100 Seconds

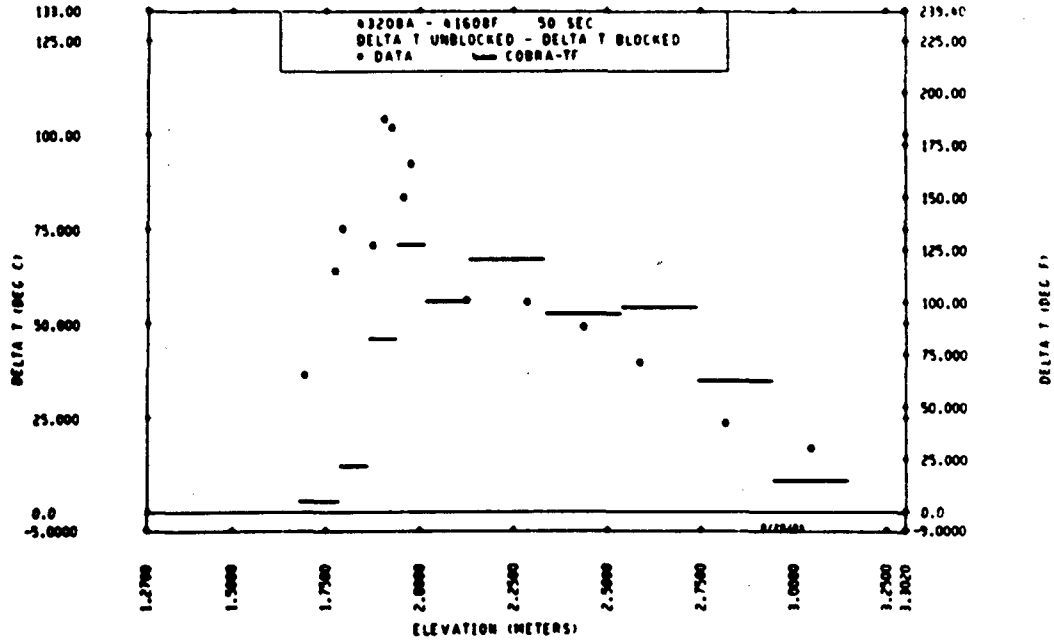

Figure 4-162. Blockage Effect Temperature Rise Versus Elevation, FLECHT SEASET Tests 43206A and 41608F, t = 50 Seconds

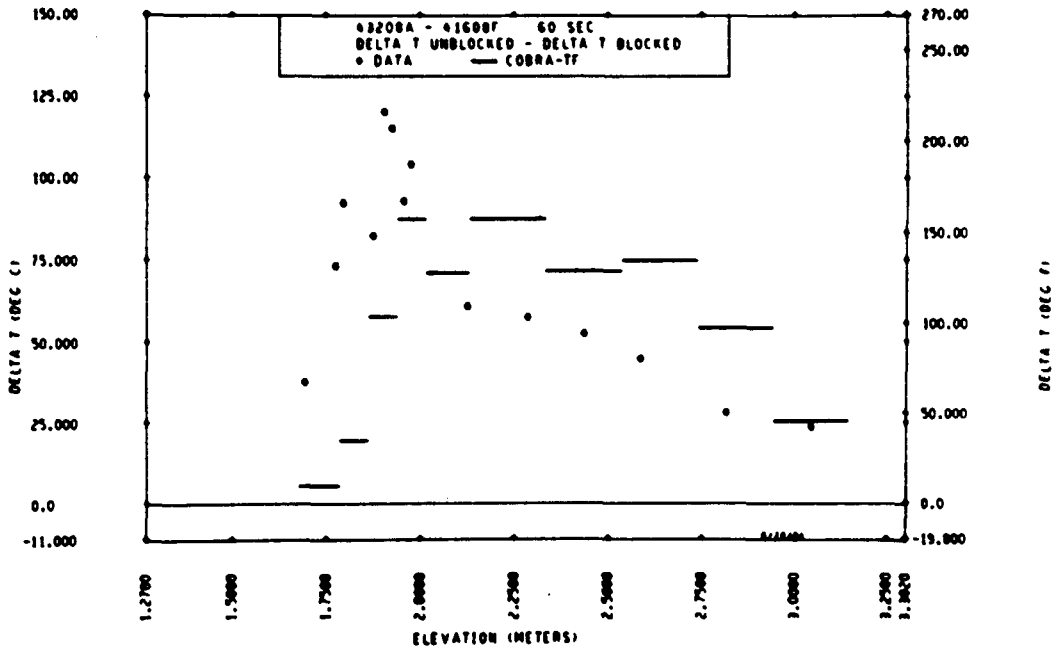

Figure 4-163. Blockage Effect Temperature Rise Versus Elevation, FLECHT SEASET Tests 43206A and 41608F, t = 60 Seconds

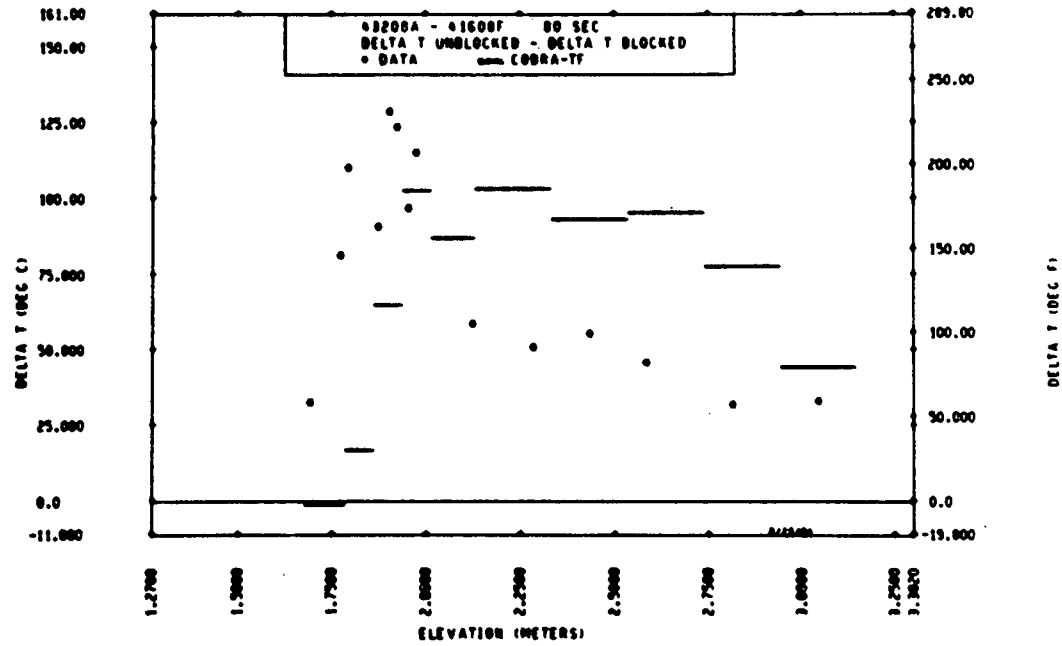

Figure 4-164. Blockage Effect Temperature Rise Versus Elevation, FLECHT SEASET Tests 43206A and 41608F, t = 80 Seconds

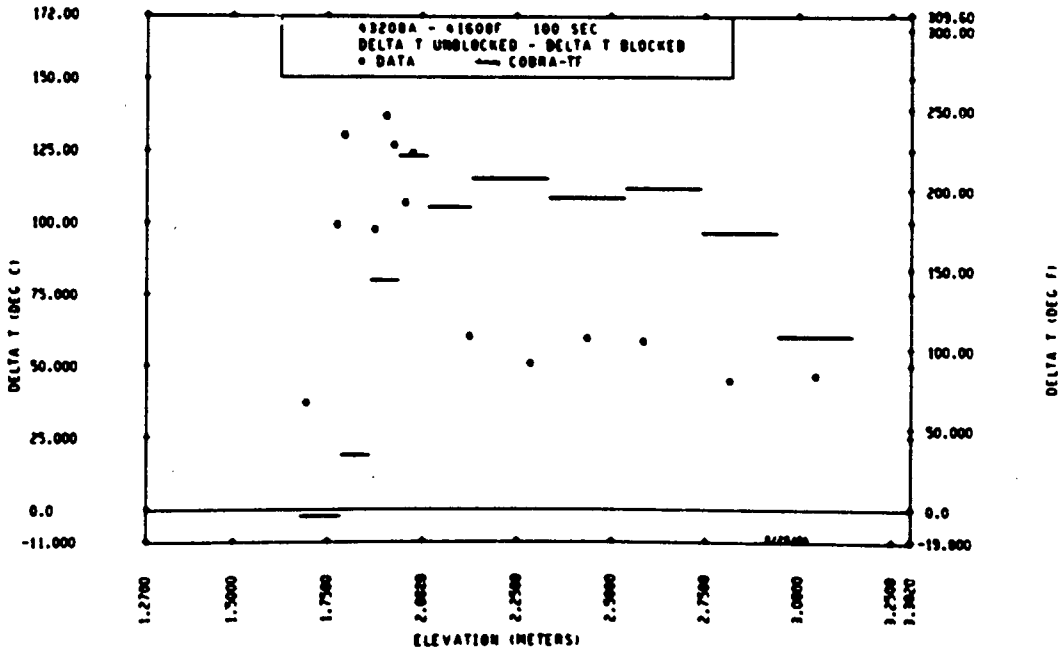

Figure 4-165. Blockage Effect Temperature Rise Versus Elevation, FLECHT SEASET Tests 43206A and 41608F, t = 100 Seconds

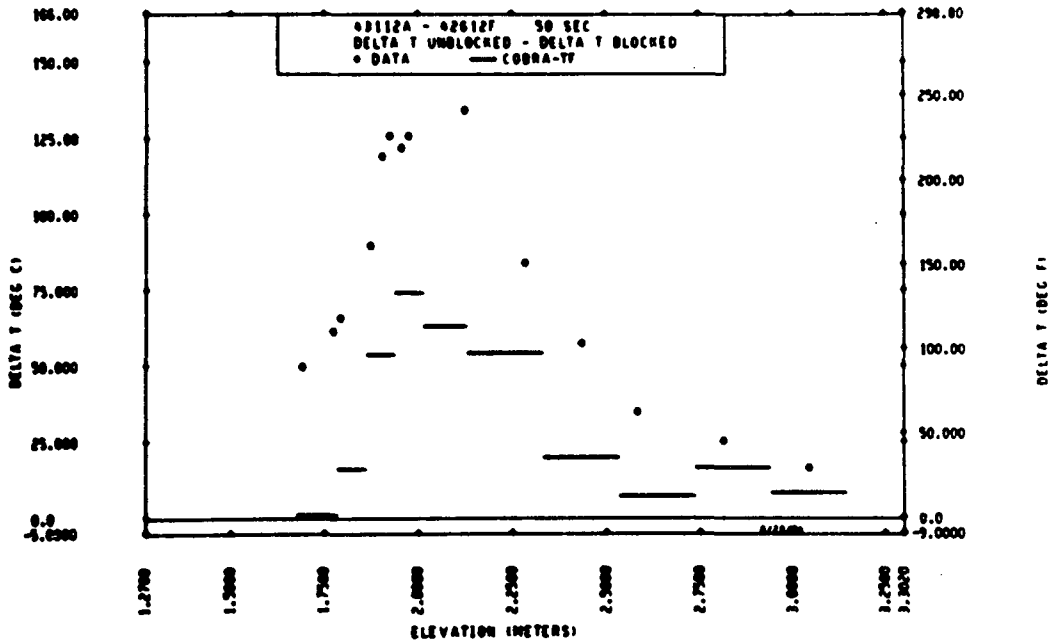

Figure 4-166. Blockage Effect Temperature Rise Versus Elevation, FLECHT SEASET Tests 43112A and 42612F, t = 50 Seconds

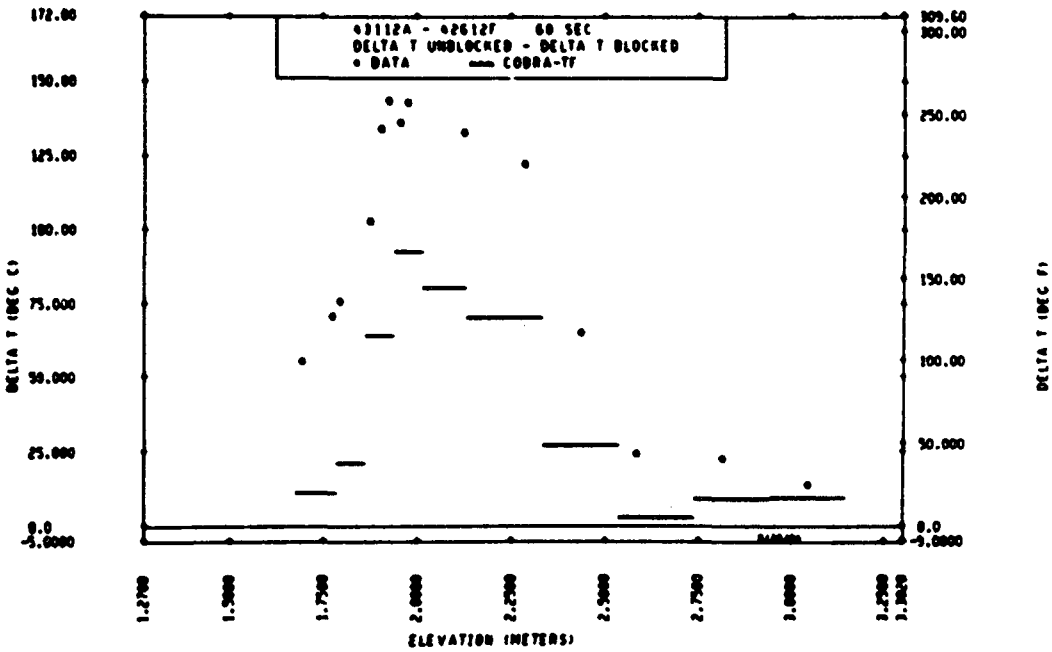

Figure 4-167. Blockage Effect Temperature Rise Versus Elevation, FLECHT SEASET Tests 43112A and 43612F, t = 60 Seconds

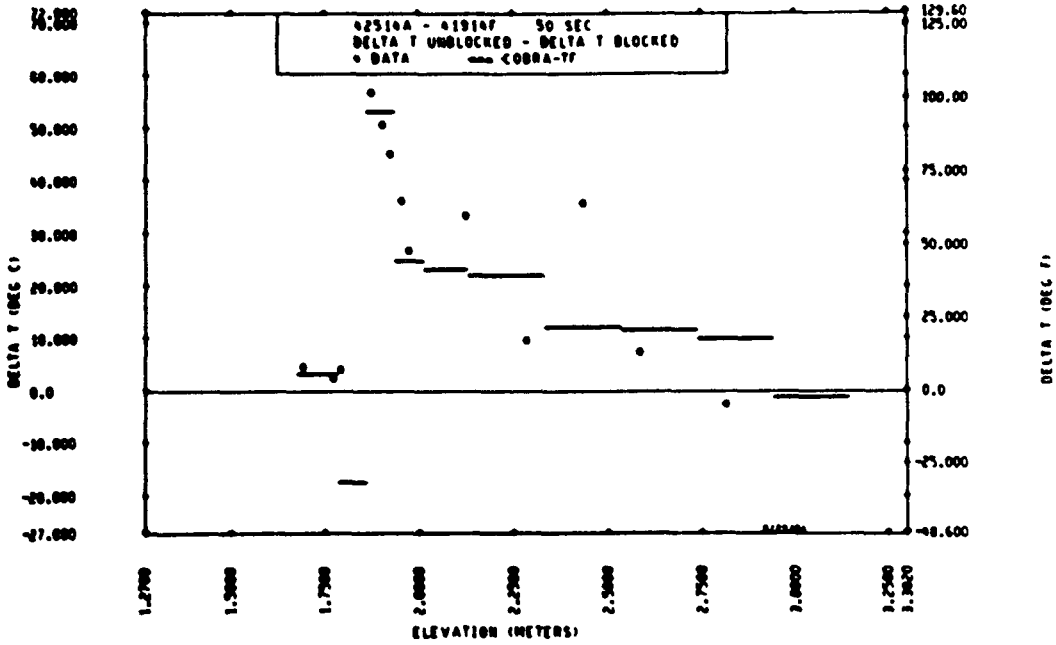

Figure 4-168. Blockage Effect Temperature Rise Versus Elevation, FLECHT SEASET Tests 42514A and 41914F, t = 50 Seconds

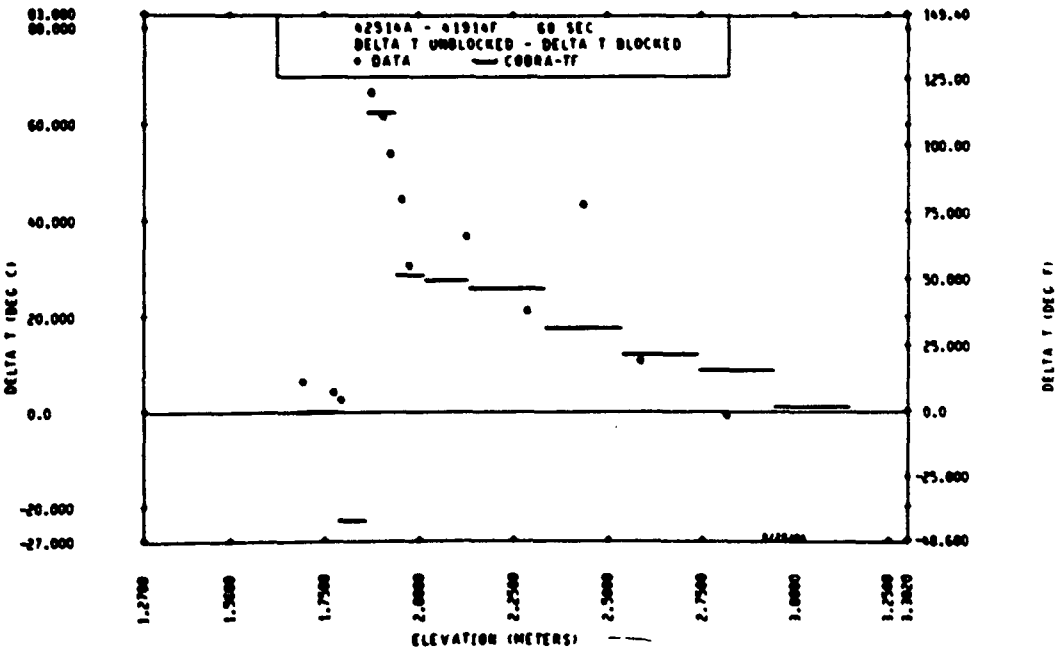

Figure 4-169. Blockage Effect Temperature Rise Versus Elevation, FLECHT SEASET Tests 42514A and 41914F, t = 60 Seconds

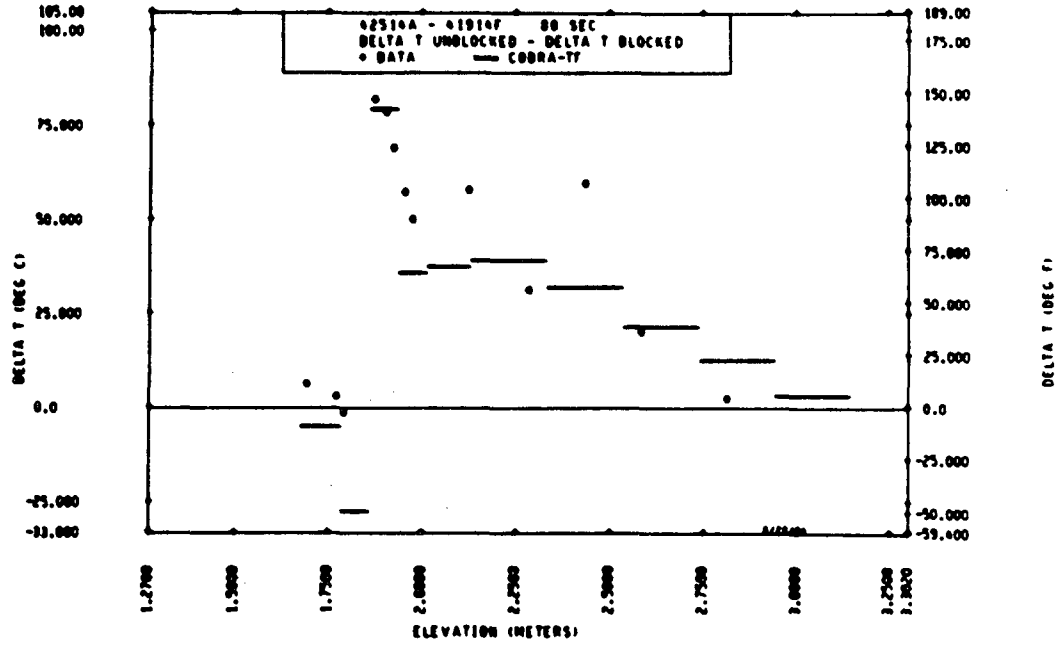

Figure 4-170. Blockage Effect Temperature Rise Versus Elevation, FLECHT SEASET Tests 42514A and 41914F, t = 80 Seconds

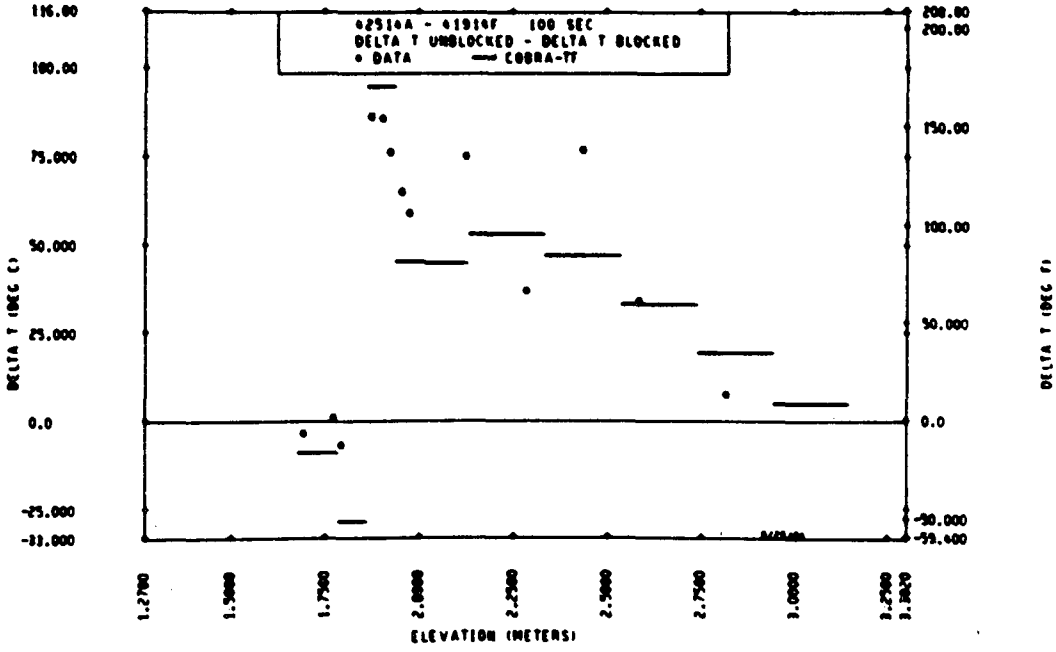

Figure 4-171. Blockage Effect Temperature Rise Versus Elevation, FLECHT SEASET Tests 42514A and 41914F, t = 100 Seconds

SECTION 5
FLOW BLOCKAGE MODEL VERIFICATION WITH 163-ROD BUNDLE DATA

5-1. INTRODUCTION

The strategy in the FLECHT SEASET flow blockage program was to use small rod bundle experiments, single-tube data, and other data in the literature to develop mechanistic heat transfer models for flow blockage in rod bundles, and then to verify these models by comparisons with large rod bundle experiments with flow blockage.

Section 5 describes the blockage models and the comparisons with the small-scale rod bundle experiments. In this section, results from the larger 163-rod bundle with blockage are compared with the blockage models in COBRA-TF to verify that models developed from the small-scale experiments can predict behavior in the larger bundle without any adjustment. (The results presented in this section reflect no adjustment of the blockage models.) This section also discusses the 163-rod bundle experimental results as well as the COBRA-TF predictions.

5-2. TEST FACILITY DESCRIPTION

The test section consisted of 163 full length [3.05 m (144 in.) heated length] electrical fuel rod simulators which were internally heated with a 1.66 peak-to-average chopped cosine axial power shape. The 9.5 mm (0.374 in.) diameter heater rods were arranged in a 12.6 mm (0.496 in.) square pitch with eight solid triangular filler rods and fourteen thimbles (figure 5-1). The eight filler rods were utilized to maintain the axial spacing for the eight FLECHT-type support grids and to minimize the excess flow area in the cylindrical low-mass housing.

The tests were conducted by flooding the steam-filled test section when the rod temperature was 871°C (1600°F) with water at various flooding rates, pressures, peak powers, and fluid temperatures. The power was decayed according to the 1971 ANS + 20 percent curve at the initiation of flood. Tests were also conducted in a gravity-driven reflood mode.

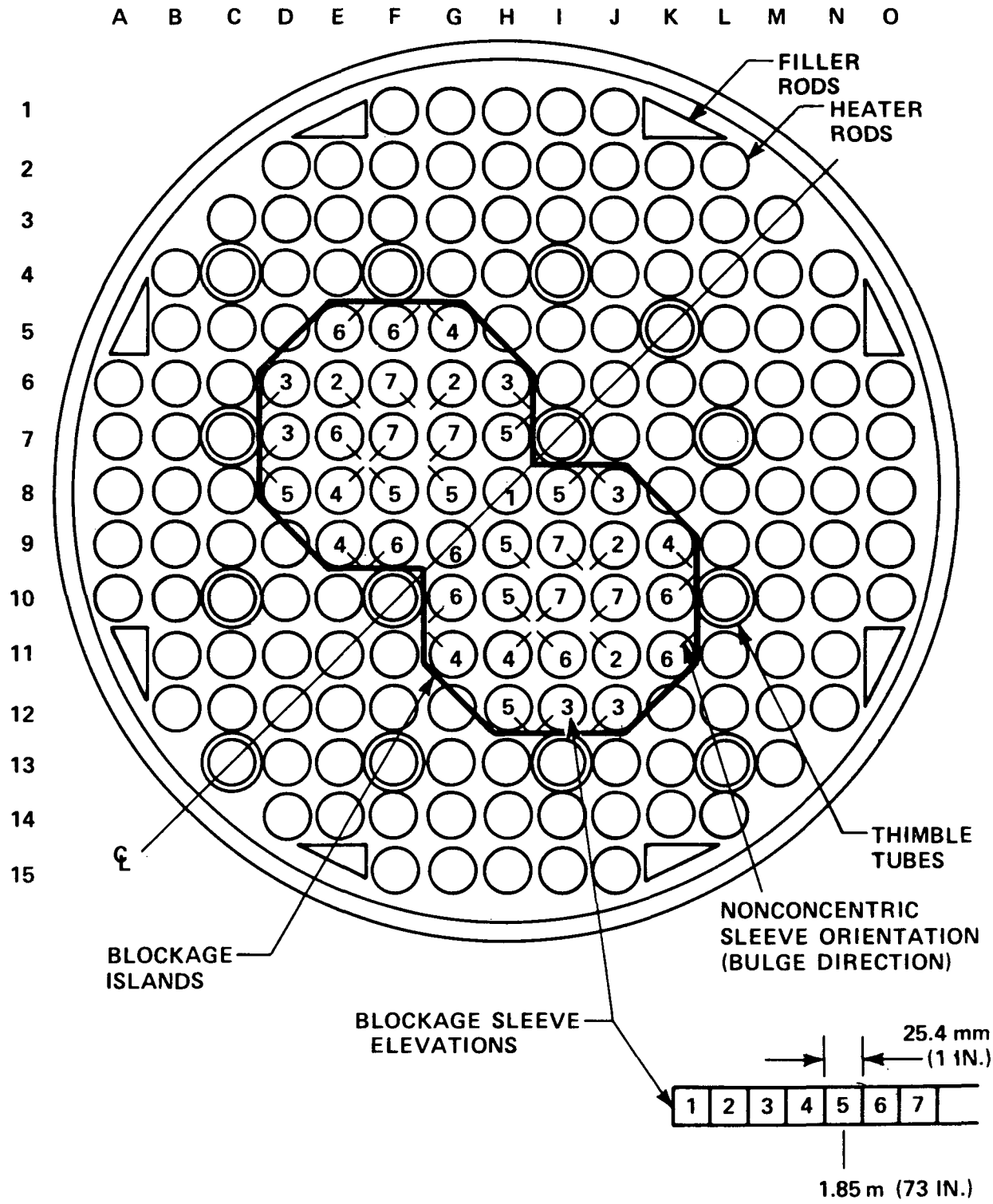

Figure 5-1. 163-Rod Bundle Cross Section

In the reflood tests, the water and steam phases were separated and measured downstream of the test section such that a system mass balance could be calculated to verify the accuracy of the loop instrumentation. Sixty-two of the 163 heater rods were instrumented with eight thermocouples attached to the inside surface of the cladding. Vapor temperatures were measured at various axial and radial locations within the rod bundle utilizing unshielded thermocouples, self-aspirating steam probes,[1] and thimble-tube aspirating steam probes. The housing and thimbles were also instrumented with thermocouples to determine their respective thermal responses.

Two blockage shapes were simulated in the FLECHT SEASET 21-rod bundle test series, representing low- and high-temperature swelling: a short, concentric shape (high-temperature) and a long, nonconcentric shape (low-temperature). These shapes are illustrated and discussed in section 4. An analysis of the 21-rod bundle data led to the conclusion that the long, nonconcentric shape provided the least favorable heat transfer characteristics; therefore the long, concentric sleeve was utilized in the 163-rod bundle, as shown in figure 5-2. For simplicity in installation and data analysis, the nonconcentric bulge was directed into the subchannel and toward a thimble (opposite side of the burst). The azimuthal orientation of the nonconcentric bulges is shown in figure 5-1.

The blockage sleeves were placed on the heater rods in a noncoplanar distribution in the same fashion as the blockage sleeves in configuration F in the 21-rod bundle test series.

---

1. Loftus, M. J., et al., "PWR FLECHT SEASET 21-Rod Bundle Flow Blockage Task Data and Analysis Report," NRC/EPRI/ Westinghouse-11, September 1982.

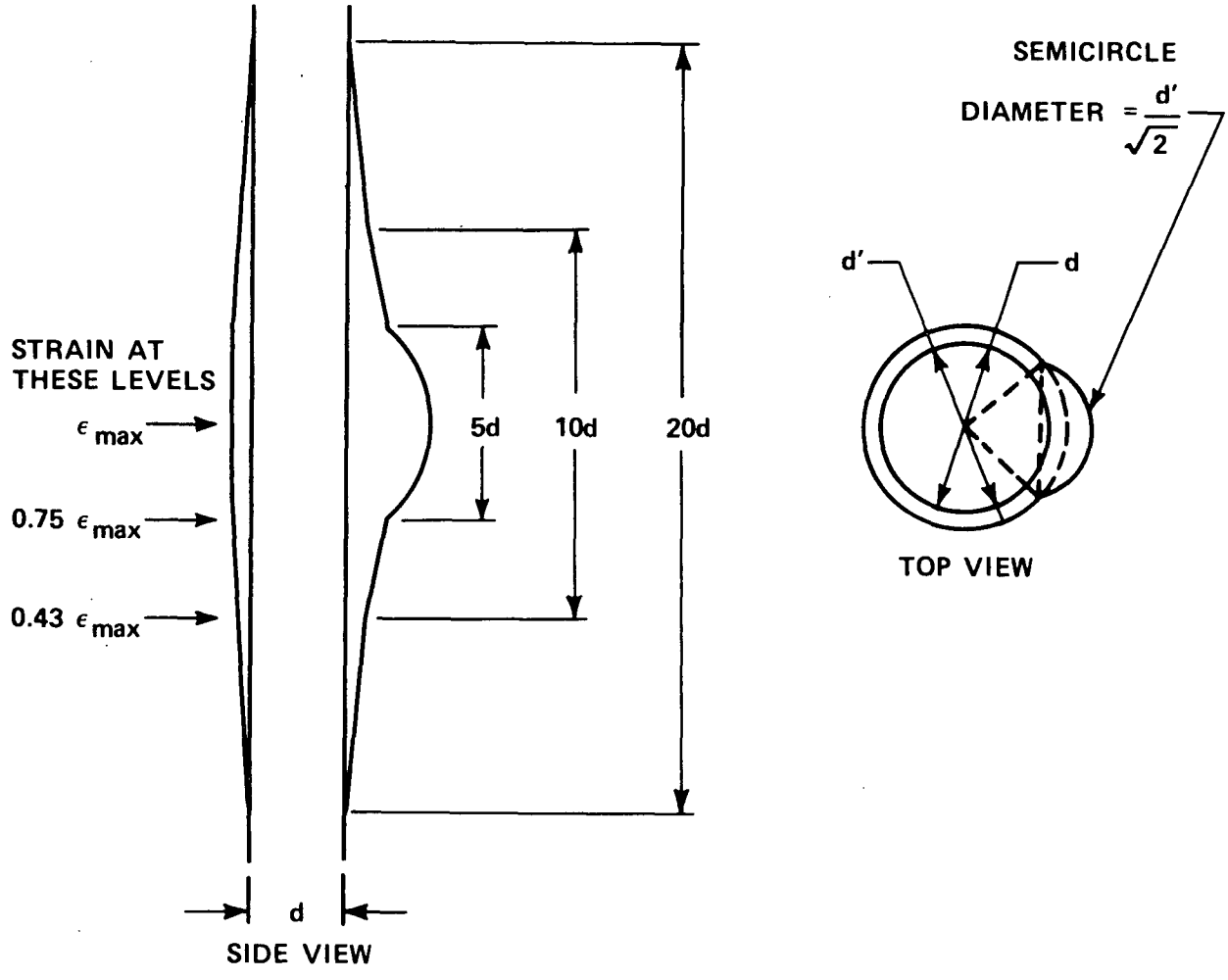

Figure 5-2. Long, Nonconcentric Blockage Shape

5-3. EXPERIMENTAL RESULTS

In the 163-rod blocked bundle test program, 17 forced reflood and two gravity reflood tests were conducted to investigate effects of the following parametric variations:

- o Flooding rate: 0.0152 - 0.152 m/sec (0.6 - 6 in./sec)
- o Pressure: 0.14 - 0.42 MPa (20 - 60 psia)
- o Inlet fluid temperature: 53° C - 123° C (127° F - 252° F)
- o Initial peak linear power: 1.3 - 3.3 kw/m (0.4 - 1.0 kw/ft)
- o Initial clad temperature: 260° C - 871° C (500° F - 1600° F)

There were also three tests conducted at the same forced reflood conditions [0.038 m/sec (1.5 in./sec) flooding rate] at approximately equal intervals, to evaluate data repeatability. Data repeatability reflects the reliability with which the test initial and boundary conditions can be repeated on a consistent basis. The test philosophy was to conduct tests at the same conditions as used in the previously conducted 161-rod unblocked bundle test series, so that the blockage shape would be the only difference between the two bundles. It was felt that bundle-to-bundle comparisons would represent the blockage effect more accurately than comparison of an unblocked rod to a blocked rod in the 163-rod blocked bundle, since the blockage could also affect the heat transfer on an unblocked rod in the blocked bundle relative to that on an unblocked rod in an unblocked bundle.

Great care was taken to ensure that each test met the specified initial and boundary conditions, so that direct data comparisons could be performed between the blocked and the unblocked bundle data. The rod temperature transients and quench front progression were generally the same for the respective blocked and unblocked bundle tests; therefore direct data comparisons can be made.

The radial temperature distribution in the blocked bundle showed an effect of the blockage islands. The rods in the two blockage islands at the midplane had a lower initial temperature than the rods in the bypass region. These

lower initial temperatures are attributed to the cooling effect of the blockage sleeves, which increased the radiation heat transfer between the sleeves and the hotter rods, as well as the increased heat capacity which also reduced the blocked rod temperature. A comparison of the initial measured radial temperature distribution for blocked bundles [at 1.90 m (75 in.)] and unblocked bundles [at 1.83 m (72 in.)] are shown in figure 5-3. Although the radial temperature distributions are significantly different between the two bundles, the average initial temperature was approximately the same. The blockage sleeves caused a very localized effect across the length of the blockage region [1.78 m (70 in.) to 1.96 m (77 in)].

The radial rod temperature distribution as a function of time immediately downstream of the blockage [1.98 m (78 in.)] is shown in figure 5-4. The temperature transients shown in figure 5-4 represent a rod in the center of the blockage (10H), a rod on the edge of the blockage (9K), a rod on the edge of the bypass (9L), and a rod in the bypass (8N). The data show a significant temperature difference between the blockage rod (10H) and the bypass rod (8N) for the entire transient. Initially, the blockage rod is much cooler than the bypass rod; later in the transient, the blockage rod is hotter than the bypass rod.

The radial distribution of vapor temperatures immediately downstream of the blockage zone [at 1.98 m (78 in.)] as a function of time are shown in figure 5-5. The plot clearly shows the desuperheating of the vapor downstream of the blockage relative to measured vapor temperature in the bypass zone.

The radial vapor temperature measurements upstream of the blockage and far downstream of the blockage (at 2.44 m (96 in.) and 3.05 m (120 in.)] do not exhibit this same behavior because the vapor desuperheating due to the droplet breakup is a very localized effect. However, the vapor temperature late in the transient in the blockage islands immediately downstream of the blockage were measured to be greater than the vapor temperature in the bypass zone, as also shown in figure 5-5. This radial effect in the vapor temperature late in the transient is attributed to the bypass of steam flow around the blockage.

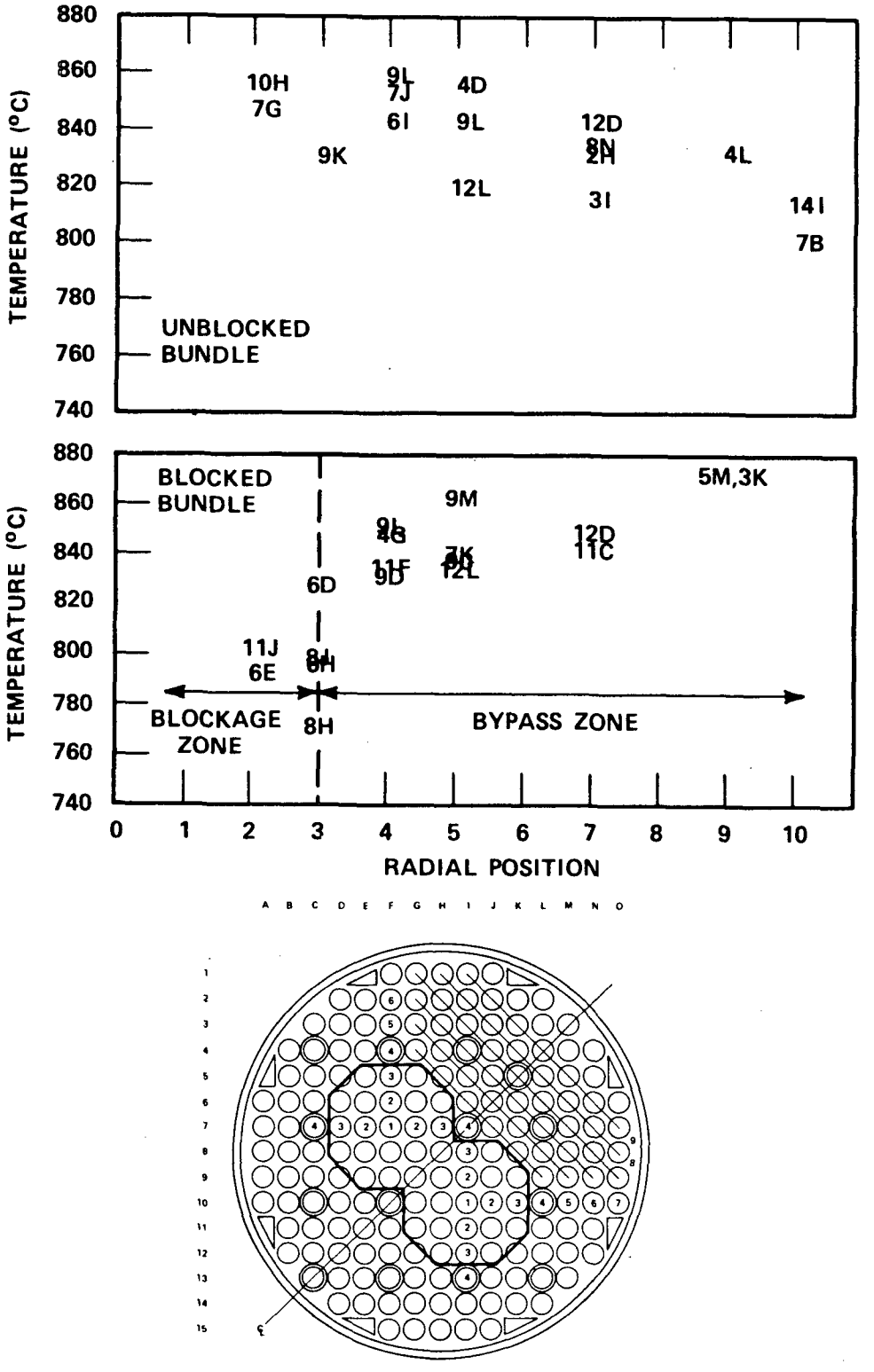

Figure 5-3. Initial Midplane Radial Temperature Distribution for Blocked and Unblocked Bundle Rods

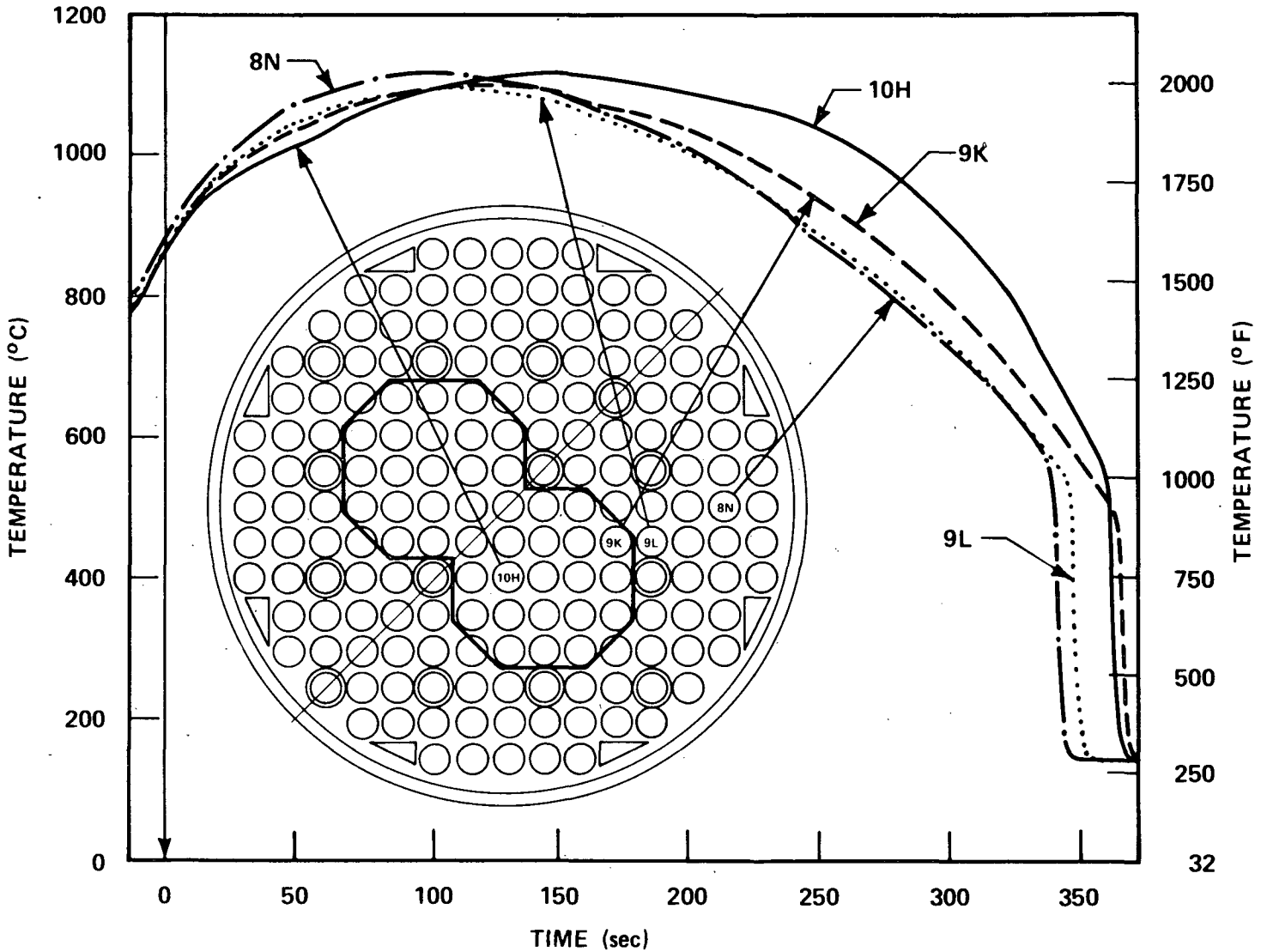

Figure 5-4. Rod Radial Temperature Distribution as a Function of Time

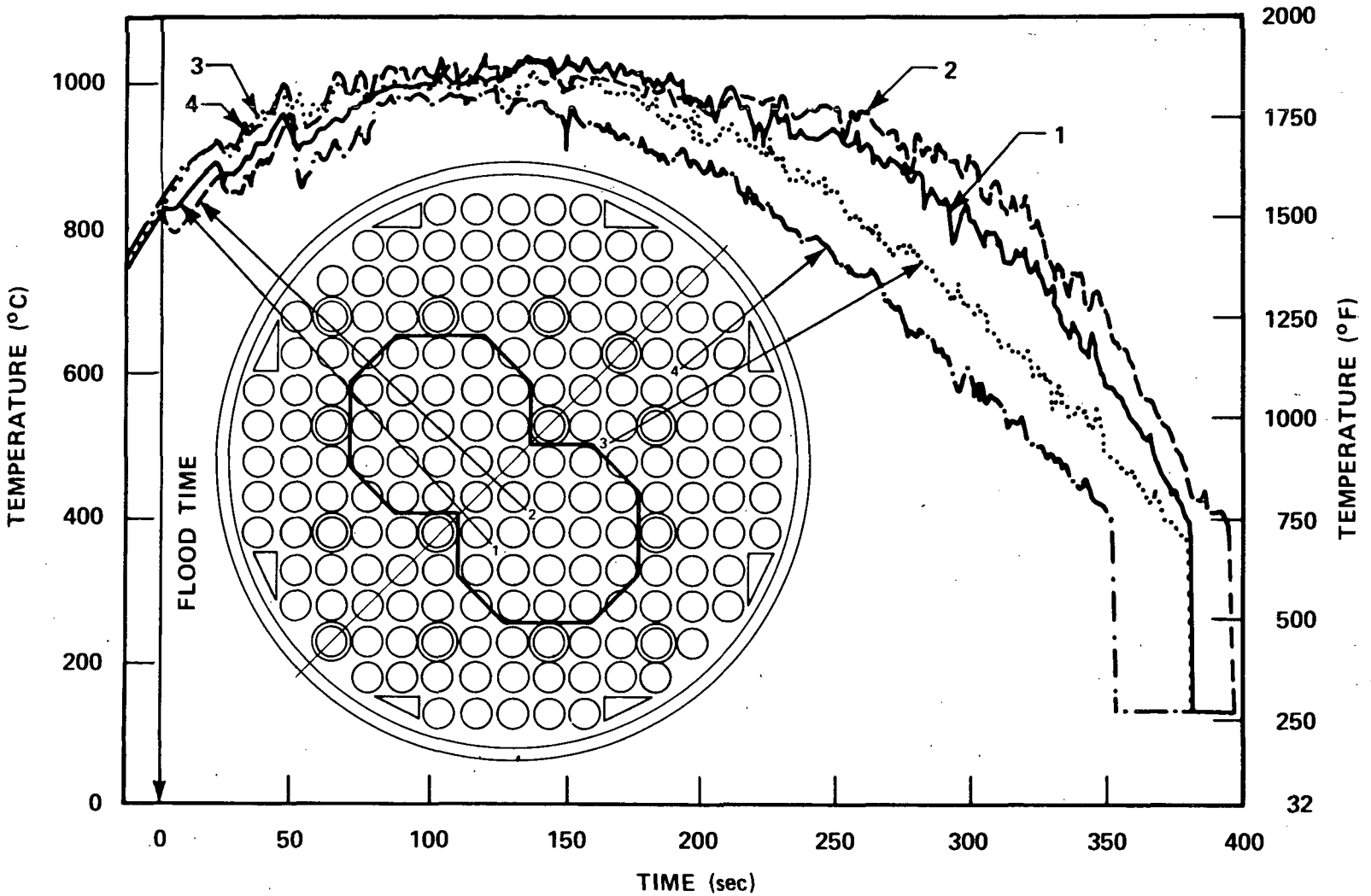

Figure 5-5. Vapor Radial Temperature Distribution as a Function of Time

5318-12

The vapor velocity in the blockage island rods was reduced late in the transient; therefore, the vapor temperature was higher in the blockage islands than in the bypass region.

As the quench front continued to move up the bundle, the vapor generation below the blockage was reduced as well as the steam temperature (and density). Both effects reduced the steam velocity such that the velocity of the entrained droplets was decreased. The reduction in velocity subsequently reduced the droplet breakup, resulting in a decrease of the heat transfer in the blocked bundle similar to or less than that in the unblocked bundle. However, these effects occurred later in the transient, after the temperature had peaked.

The heat flux at each heater rod thermocouple location was calculated for the forced reflood tests using an inverse heat conduction method. The FLECHT SEASET heat transfer coefficient was subsequently determined by dividing the rod heat flux by the difference between the calculated rod surface temperature and the saturation temperature. The FLECHT SEASET heat transfer coefficient is a combination of radiation to the droplets, the vapor, and the cold surfaces, as well as forced convection to steam and film boiling.

Since the blocked and unblocked bundle tests were replicate tests with good repeatability of the initial and boundary conditions, the heat transfer data can be compared on a one-to-one basis. Comparisons of the blocked to unblocked bundle data for two reflood tests are shown in figures 5-6 through 5-11 for elevations within and immediately downstream of the blockage. The heat transfer improvement immediately downstream of the blockage was observed to decrease as a function of time after flood initiation. For all cases, the heat transfer is greater prior to turnaround time for the blocked bundle than for the unblocked bundle, and is less for the blocked bundle late in the transient.

The ratio of the blocked bundle heat transfer to the unblocked bundle heat transfer as a function of time for the 1.88 m (74 in.) elevation is shown in figure 5-12. Both the blockage zone and the bypass zone are shown for the

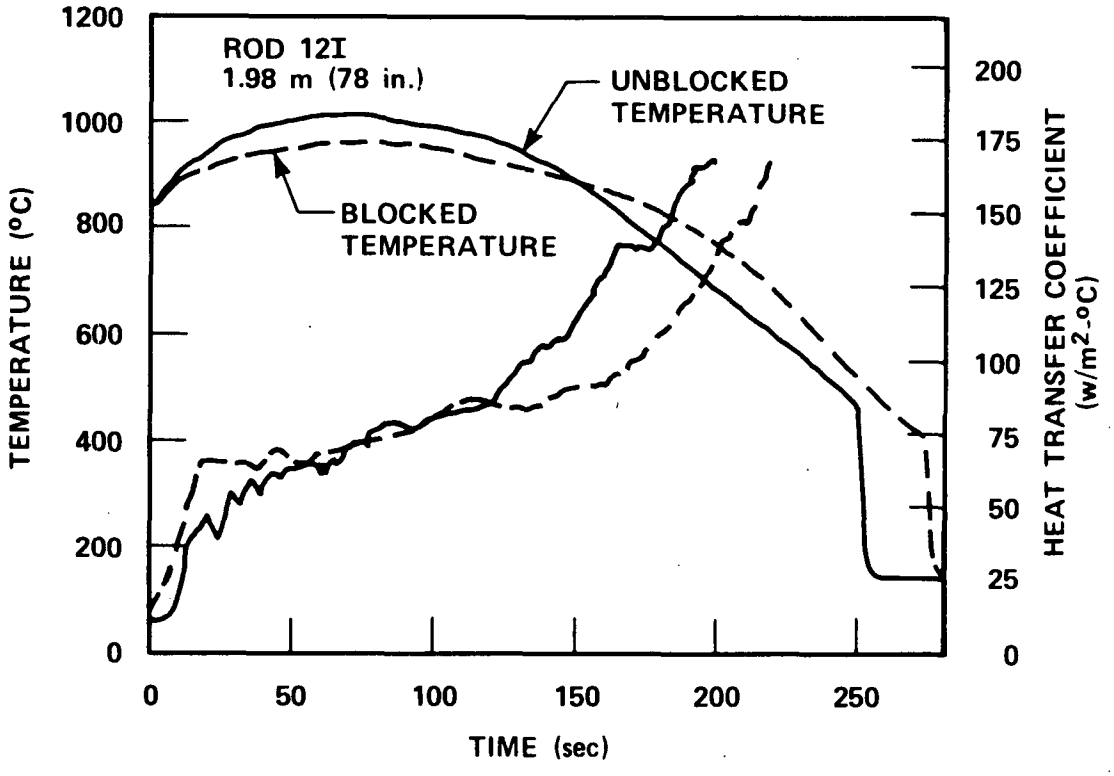

Figure 5-6. Rod Temperature and Heat Transfer for Blocked and Unblocked Bundles at 0.038 m/sec (1.5 in./sec) Flooding Rate and 1.98 m (78 in.) Elevation

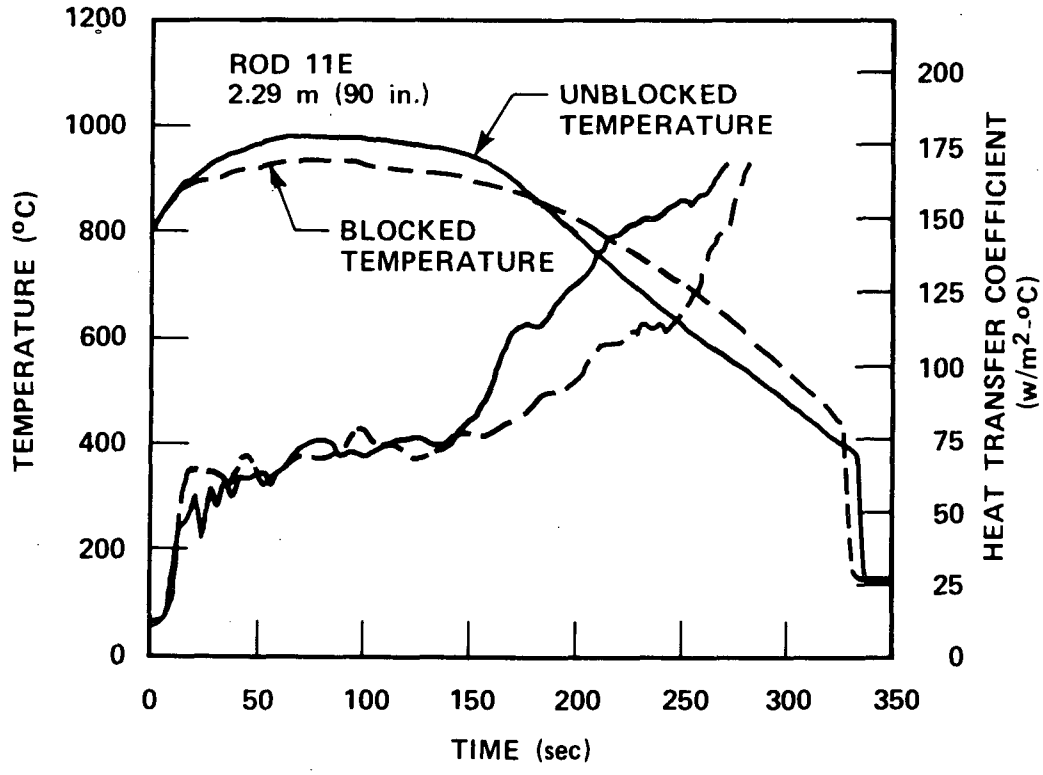

Figure 5-7. Rod Temperature and Heat Transfer for Blocked and Unblocked Bundles at 0.038 m/sec (1.5 in./sec) Flooding Rate and 2.29 m (90 in.) Elevation

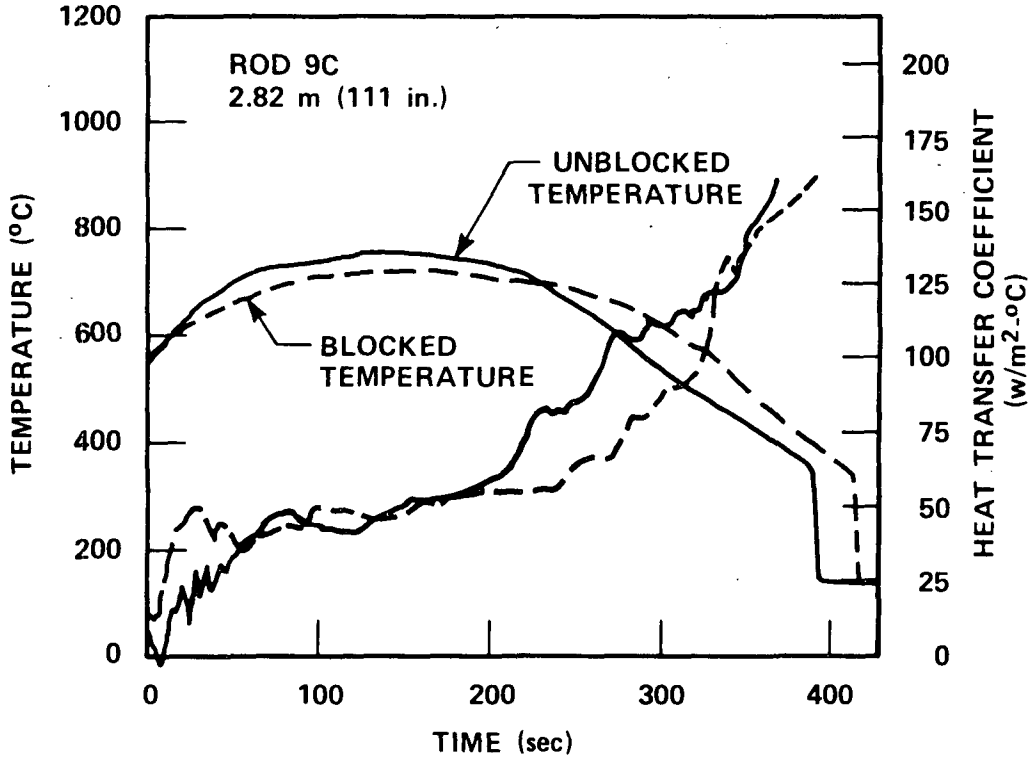

Figure 5-8. Rod Temperature and Heat Transfer for Blocked and Unblocked Bundles at 0.038 m/sec (1.5 in./sec) Flooding Rate and 2.82 m (111 in.) Elevation

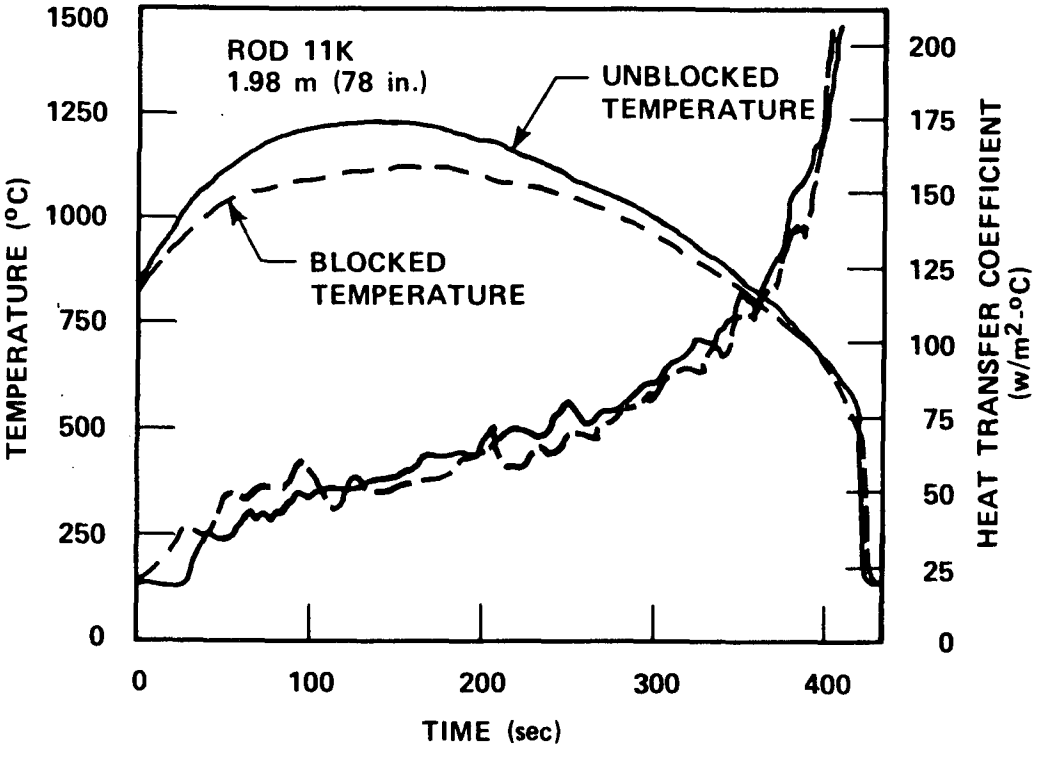

Figure 5-9. Rod Temperature and Heat Transfer for Blocked and Unblocked Bundles at 0.020 m/sec (0.8 in./sec) Flooding Rate and 1.98 m (78 in.) Elevation

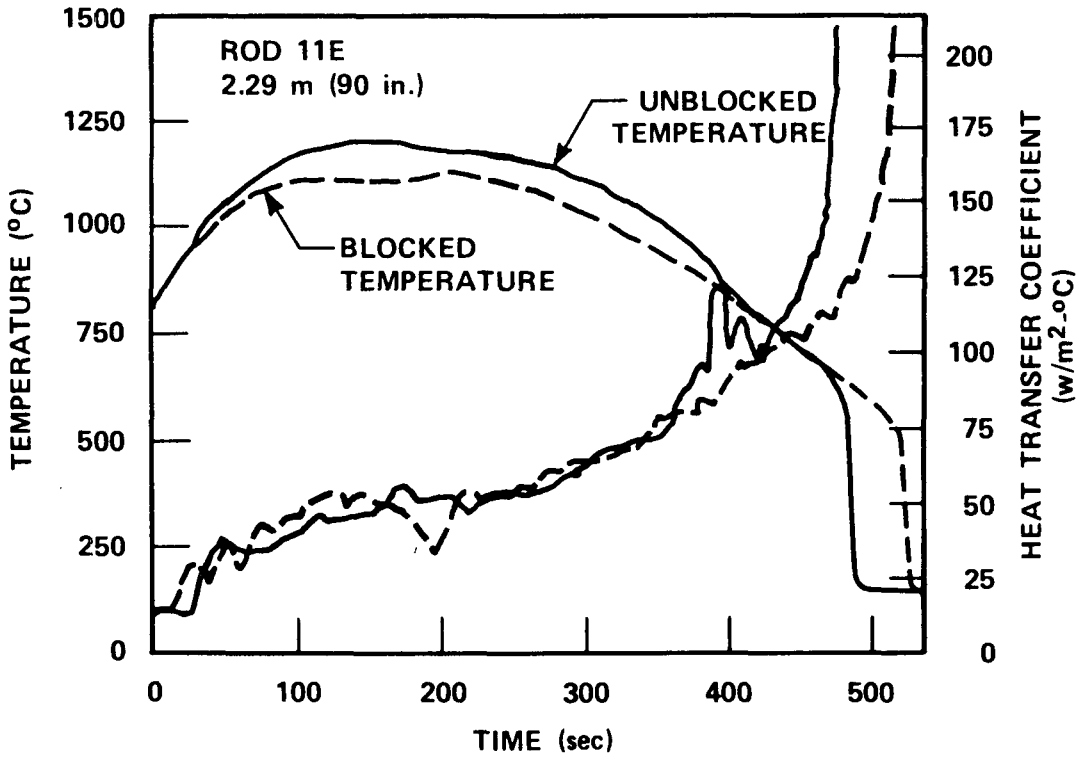

Figure 5-10. Rod Temperature and Heat Transfer for Blocked and Unblocked Bundles at 0.020 m/sec (0.8 in./sec) Flooding Rate and 2.29 m (90 in.) Elevation

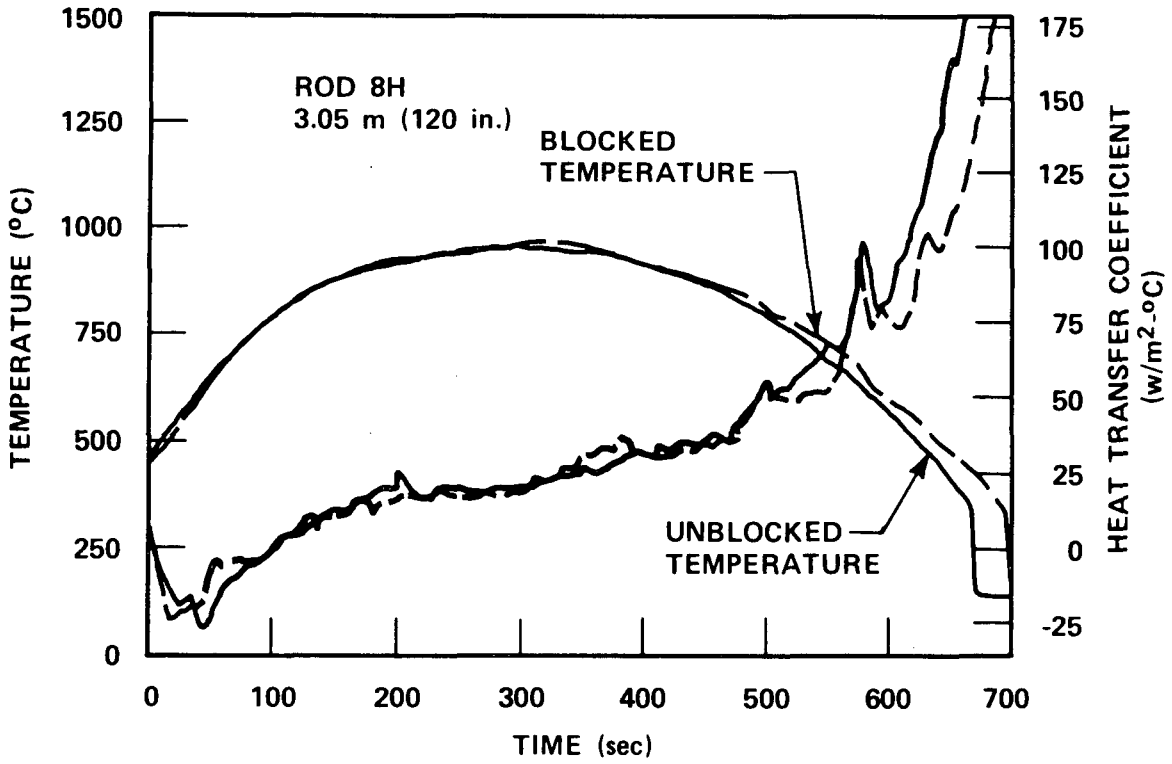

Figure 5-11. Rod Temperature and Heat Transfer for Blocked and Unblocked Bundles at 0.020 m/sec (0.8 in./sec) Flooding Rate and 3.05 m (120 in.) Elevation

test with the highest power-to-flow ratio [0.020 m/sec (0.8 in./sec)]. Figure 5-12 shows that the heat transfer ratio is initially much greater than 1.0, but decreases with time for both the blockage zone and the bypass zone.

To provide a comprehensive, yet simple, comparison of the flow blockage results to quantify the effects of flow bypass, the temperature rise difference between the 163-rod blocked and 161-rod unblocked bundles was calculated as a function of elevation and flooding rate. The temperature rise reflects the integrated heat transfer effect of the flow blockage and bypass. The unblocked to blocked temperature rise difference, defined as

$$(\Delta T_{rise})_{unblocked} - (\Delta T_{rise})_{blocked} \qquad (5\text{-}1)$$

or

$$(T_{max} - T_{init})_{unblocked} - (T_{max} - T_{init})_{blocked} \qquad (5\text{-}2)$$

is obtained from the test data.

If the initial clad temperatures were the same in the two bundles, the above relationships would simply reduce to the difference between the respective maximum or turnaround temperatures,

$$(T_{max})_{unblocked} - (T_{max})_{blocked} \qquad (5\text{-}3)$$

The unblocked and blocked bundle tests which were compared had peak power-to-flow ratios (flooding rates) of 0.12 to 0.87. The elevations selected for these comparisons were 1.98 m (78 in.), which is immediately downstream of the blockage, and 2.44 and 3.05 m (96 and 120 in.), which are located in the next two grid spans. To provide the most appropriate comparisons between the 21-rod bundle and the 163-rod/161-rod bundles, only the heater rods in the two 21-rod blockage islands of the 163-rod bundle were utilized. (No bypass rod data were utilized.)

The results of these calculations (figure 5-13) generally indicate the following effects:

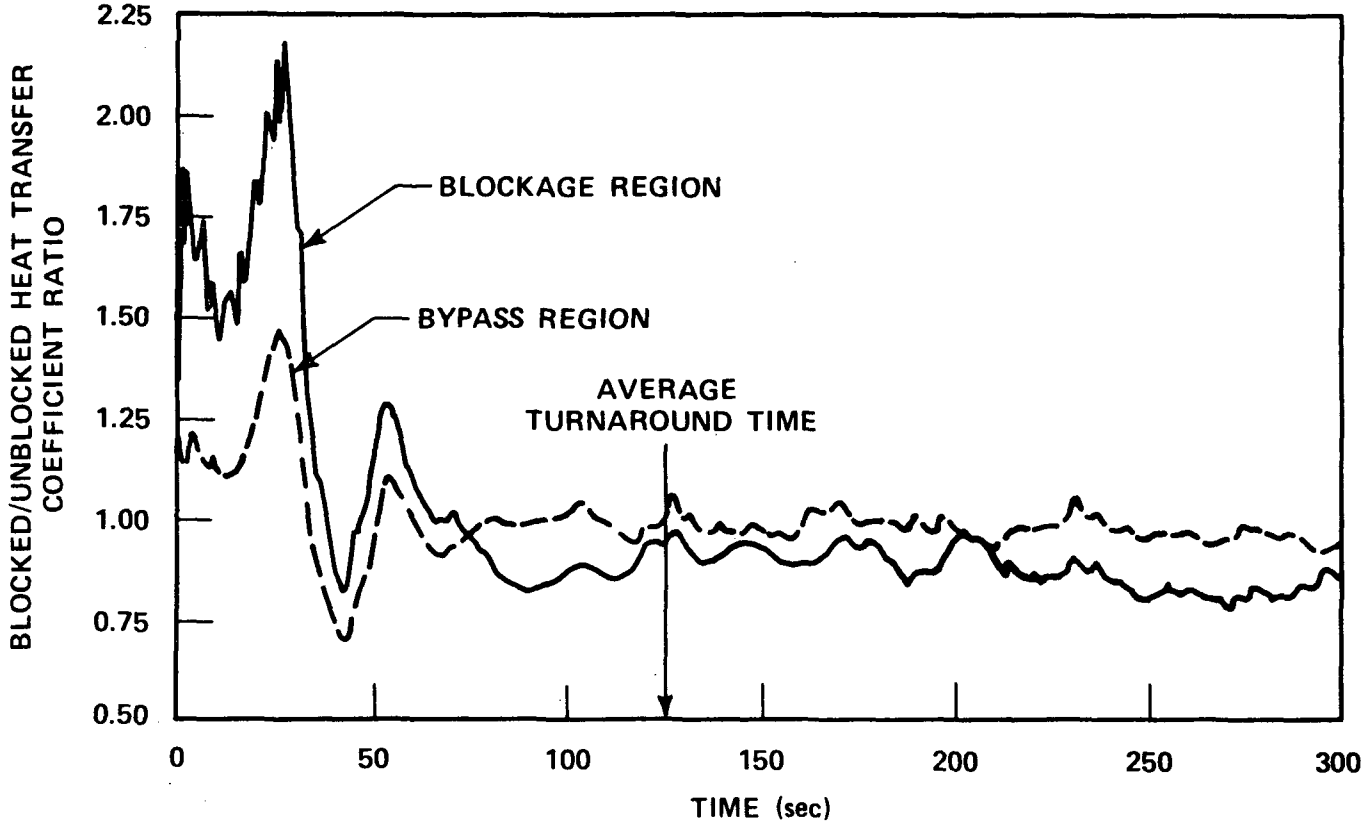

Figure 5-12. Ratio of Blocked to Unblocked Bundle Heat Transfer for Blockage and Bypass Zones at 1.88 m (74 in.)

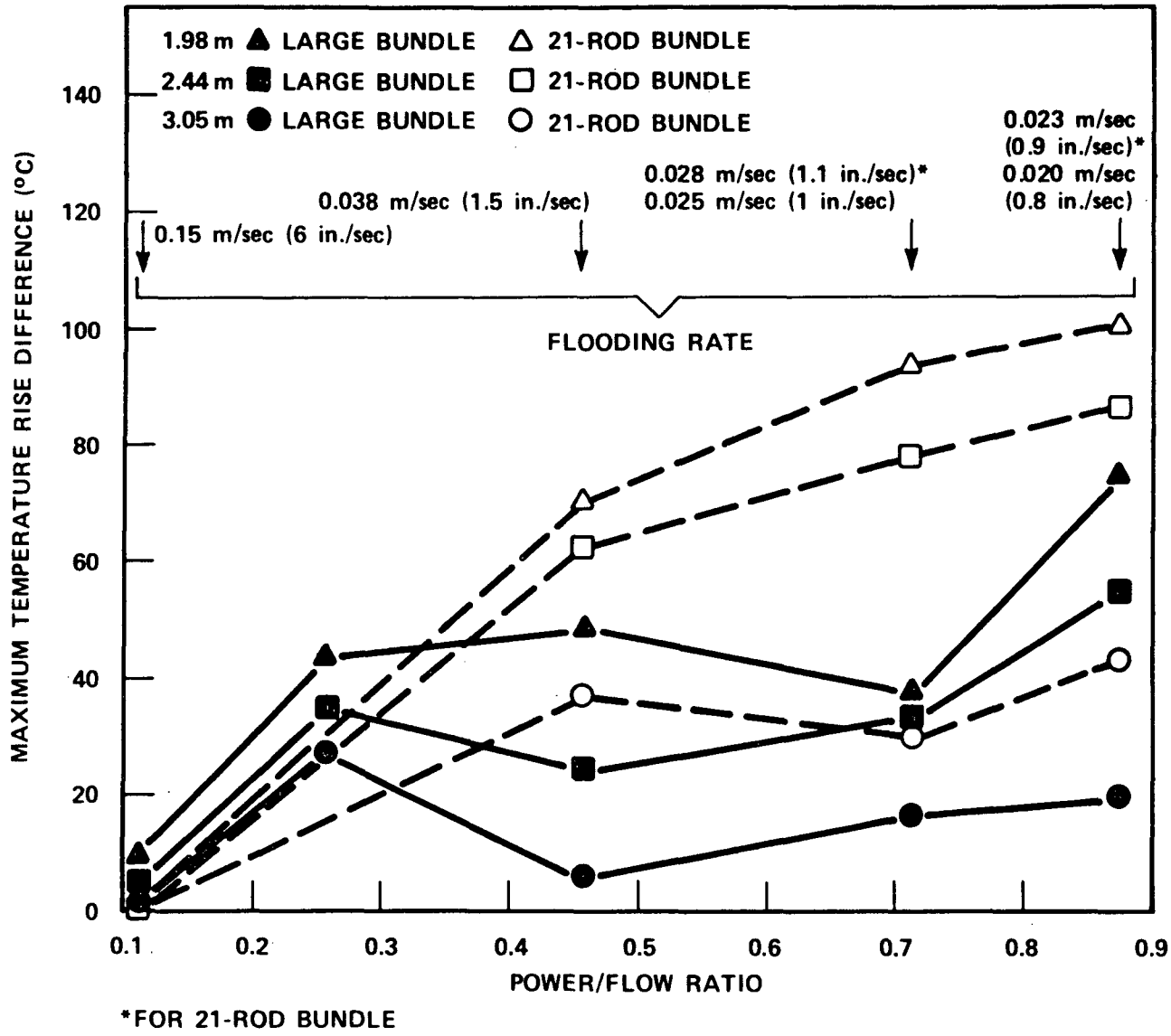

Figure 5-13. Maximum Temperature Rise Difference Between Blocked and Unblocked Bundles as a Function of Flooding Rate and Elevation

- The temperature rise difference is greater for the 21-rod bundle than for the large blocked bundle. This is attributed to the flow bypass effect in the large bundle, which decreases the flow through the blockage region. However, even with the flow bypass effect, the blocked bundle maximum temperature is less than that for the unblocked bundle.

- As the flooding rate decreases, the temperature rise difference between the unblocked and blocked bundles increases. This increase indicates that the maximum temperature in the blocked bundle decreases. The maximum temperature in the blocked bundle decreases because of the improved heat transfer downstream of the blockage. The amount of the heat transfer improvement is affected by the absolute level of the heat transfer. As the flooding rate decreases, the overall heat transfer level decreases; therefore any improvement in the heat transfer significantly affects the measured rod temperature. Also, with reduced flooding rate, the period of two-phase dispersed flow is increased with respect to time, which means that the droplet breakup effect is increased.

- As the distance downstream of the blockage increases, the temperature rise difference between the unblocked and blocked bundles decreases. This decrease indicates that the maximum temperature in the blocked bundle increases with distance from the blockage. However, the blocked bundle maximum temperature is still less than that for the unblocked bundle. This axial effect downstream of the blockage, similar to that in a thermal entry region of a tube, has been observed downstream of a grid and other blockages. as previously discussed.

The temperature rise difference as a function of time is shown in figure 5-14 for the tests with the highest power-to-flow ratio (0.87) at the 1.98 m (78 in.) elevation. The bundle without the flow bypass had a much larger difference in temperature rise between the unblocked and blocked bundles than the bundle with the flow bypass throughout the intire reflood transient.

5-4. COBRA-TF PREDICTIONS OF FLECHT SEASET 163-ROD BLOCKED BUNDLE DATA

The 163-rod blocked bundle experiments which were modeled with COBRA-TF are listed in table 5-1, along with the matching 161-rod unblocked bundle tests. Since the 163-rod bundle tests were replicas of the 161-rod bundle tests, and

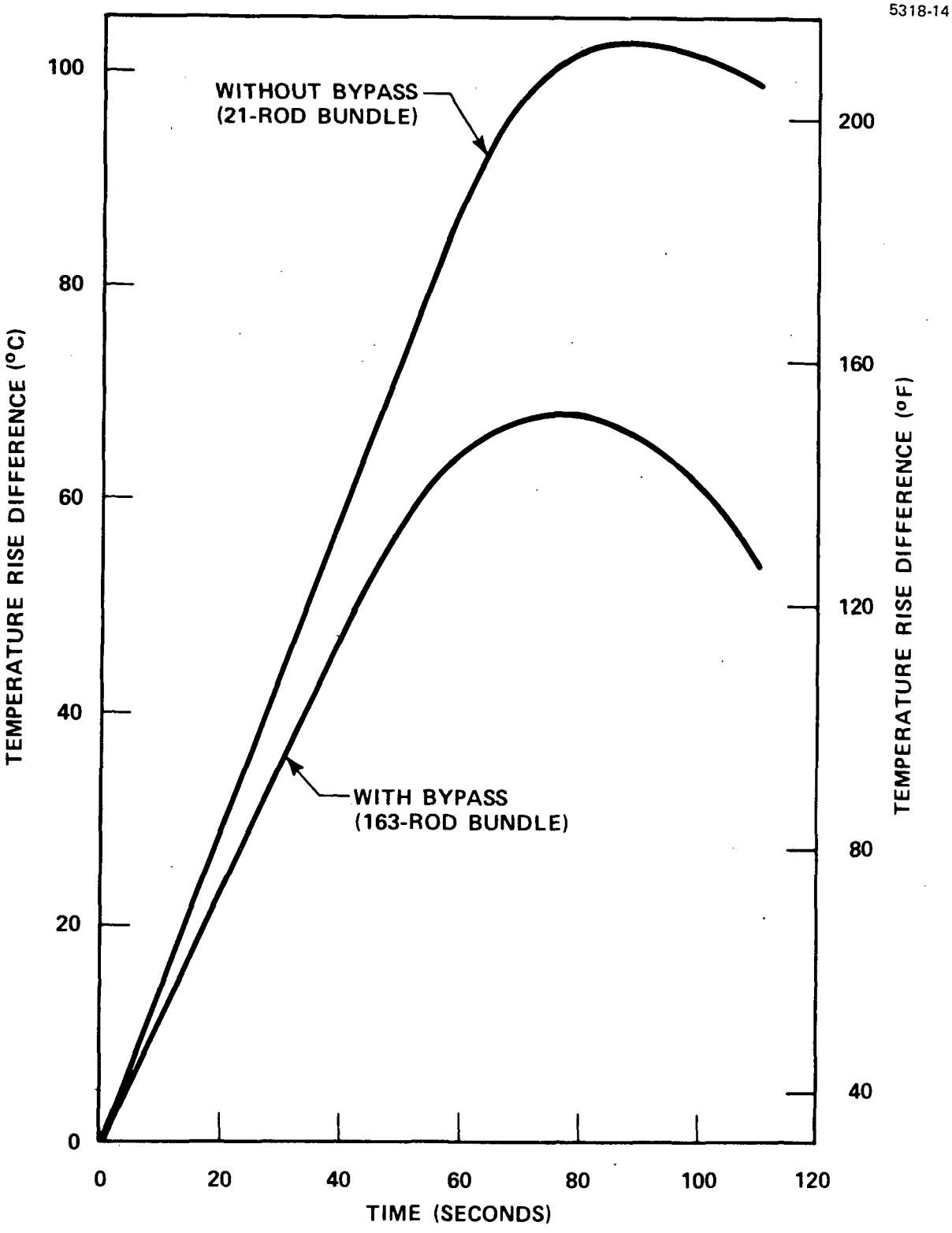

Figure 5-14. Temperature Rise Difference Between Blocked and Unblocked Bundles as a Function of Time at the 1.98 m (78 in.) Elevation

TABLE 5-1
FLECHT SEASET TESTS MODELED WITH COBRA-TF

163-Rod Blocked Bundle Test	Flooding Rate [m/sec (in./sec)]	Pressure [MPa (psia)]	Power [kw/m (kw/ft)]	$T_{initial}$ [(°C (°F)]	Matching 161-Rod Bundle Test
61005	0.0386 (1.52)	0.271 (39.3)	2.3 (0.7)	871.5 (1600.9)	31203
61509	0.0269 (1.06)	0.139 (20.1)	2.2 (0.72)	876.4 (1609.7)	34209
61607	0.0206 (0.81)	0.276 (40.1)	2.3 (0.7)	877.6 (1611.9)	31805
61916	0.15 (6.07) 7 sec, 0.523 (20.6) onward	0.277 (40.2)	2.3 (0.7)	877.0 (1610.8)	32333

COBRA-TF calculations had previously been performed for the 161-rod unblocked bundle, several comparisons were possible between tests and analyses to assess the blockage effects. The COBRA-TF model used for the 163-rod bundle (figure 5-15) had three radial nodes. The axial nodal locations are also shown in figure 5-15.

The first attempt to model the 163-rod bundle used five radial nodes (figure 5-16). However, it was found that the method of calculating the entrainment would lead to overcooling of some channels and undercooling of others. Since the dominant blockage model is the droplet breakup effect, it is most sensitive to the amount of calculated entrainment. Therefore, with the more detailed radial noding, it was found that channels which had droplet breakup area assigned to them were cooler than was expected. On the other hand, the subchannel without droplet breakup area was hotter. A review of the 21-rod bundle data indicated that there was still excellent radial mixing downstream of the blocked zone, such that a coarser noding for the blockage island (where the droplet breakup area was smeared) was justified.

Another way of looking at this problem is that the subchannels for the more detailed radial noding would not isolate single rods or a row of rods in the blocked islands, as shown in figure 5-16. In reality, heater rods would be located on the boundaries between nodes such that the rod thermal response would average the heat transfer effects between these two subchannels. The base case used for the comparisons employed the three-radial-node model.

Comparisons with the 163-rod blocked bundle data are shown in the same fashion as for the FLECHT SEASET 21-rod and 161-rod bundle data comparisons. The heater rod temperature and time plots at different elevations are compared; next, the axial heater rod temperatures at different times are compared. The measured vapor temperatures are also compared, both as a function of time at particular elevations and as a function of elevation for different times.

Figures 5-17 through 5-22 (FLECHT SEASET test 61607) compare the heater rod temperatures in the blockage islands, which correspond to rod 1 (radial node

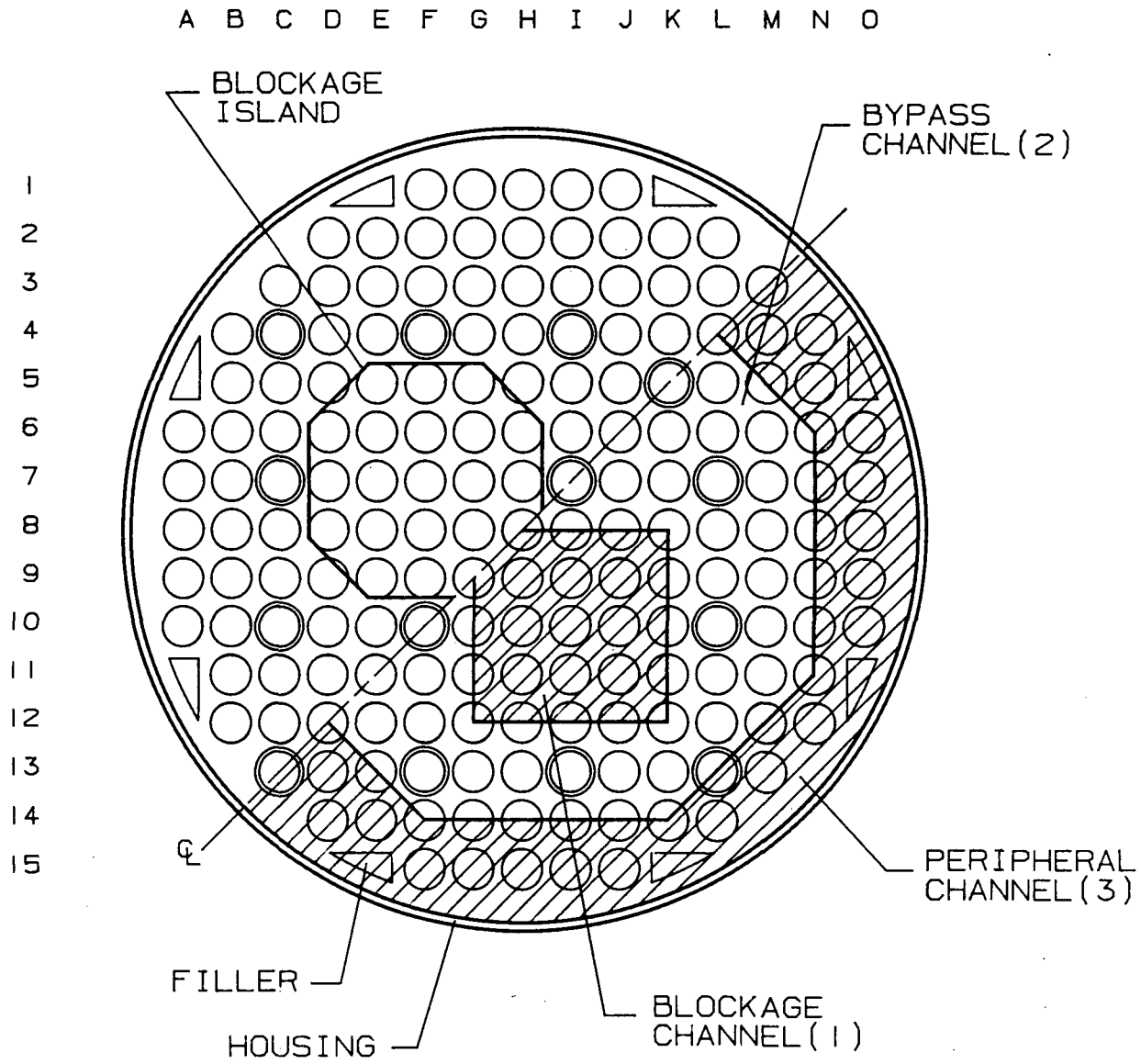

Figure 5-15. 163-Rod Bundle Noding Scheme, Three Radial Rings

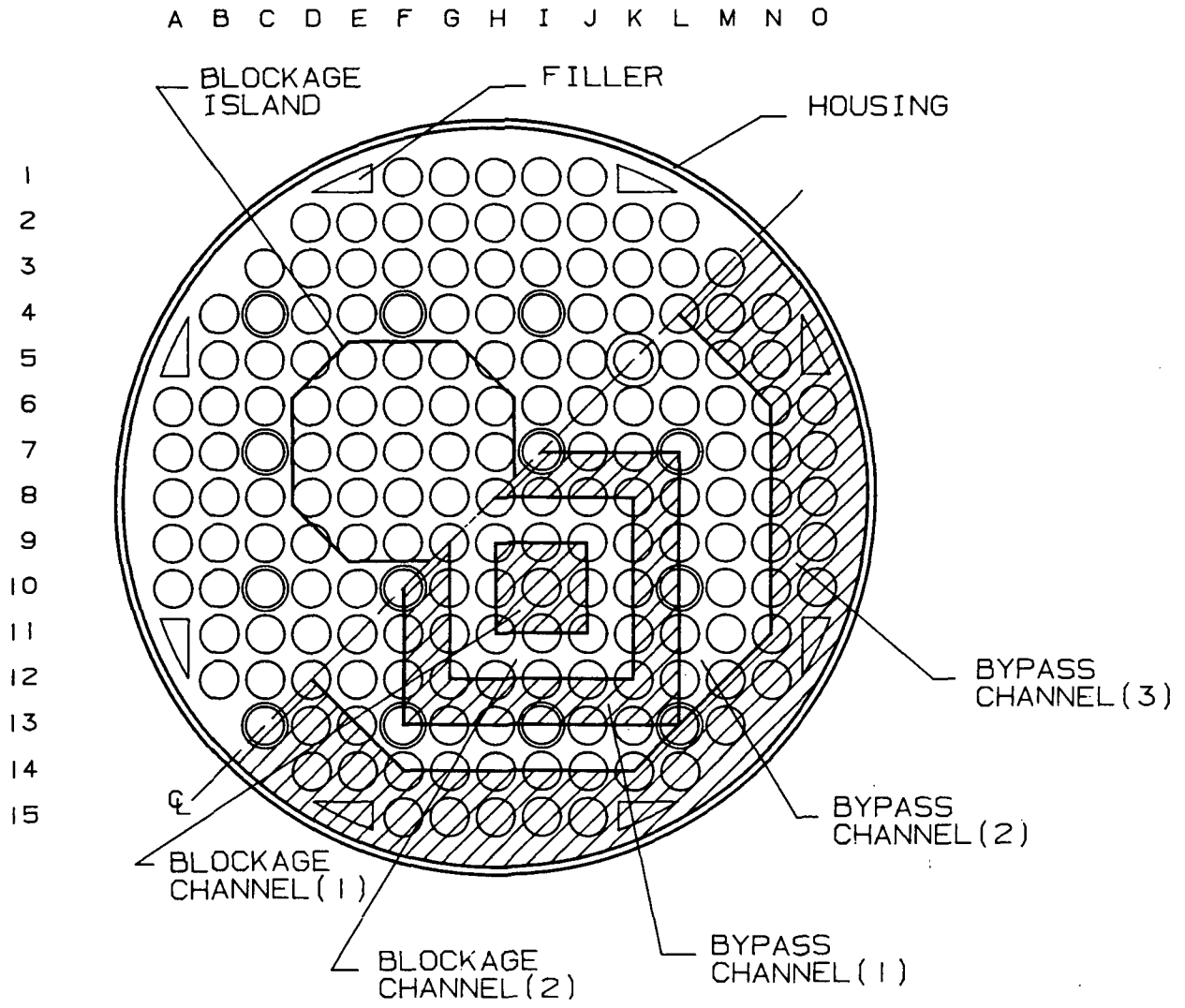

Figure 5-16. 163-Rod Bundle Noding Scheme, Five Radial Rings

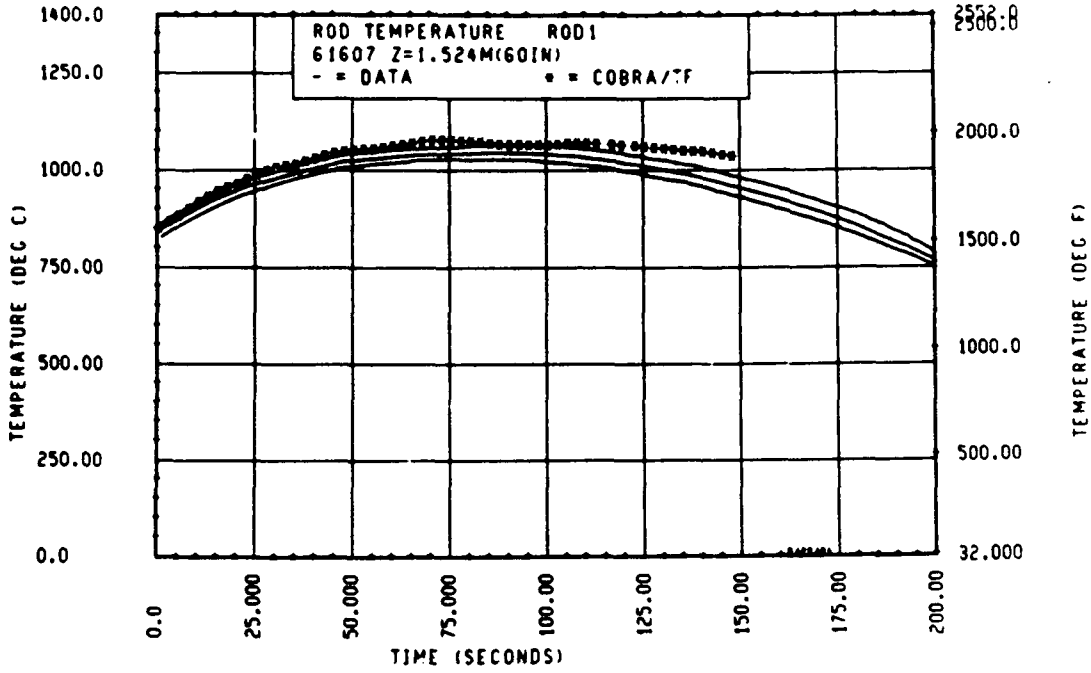

Figure 5-17. Comparison of COBRA-TF-Calculated Heater Rod Temperature Versus Time With FLECHT SEASET 163-Rod Data, Test 61607, 1.52 m (60 in.) Elevation, Rod 1

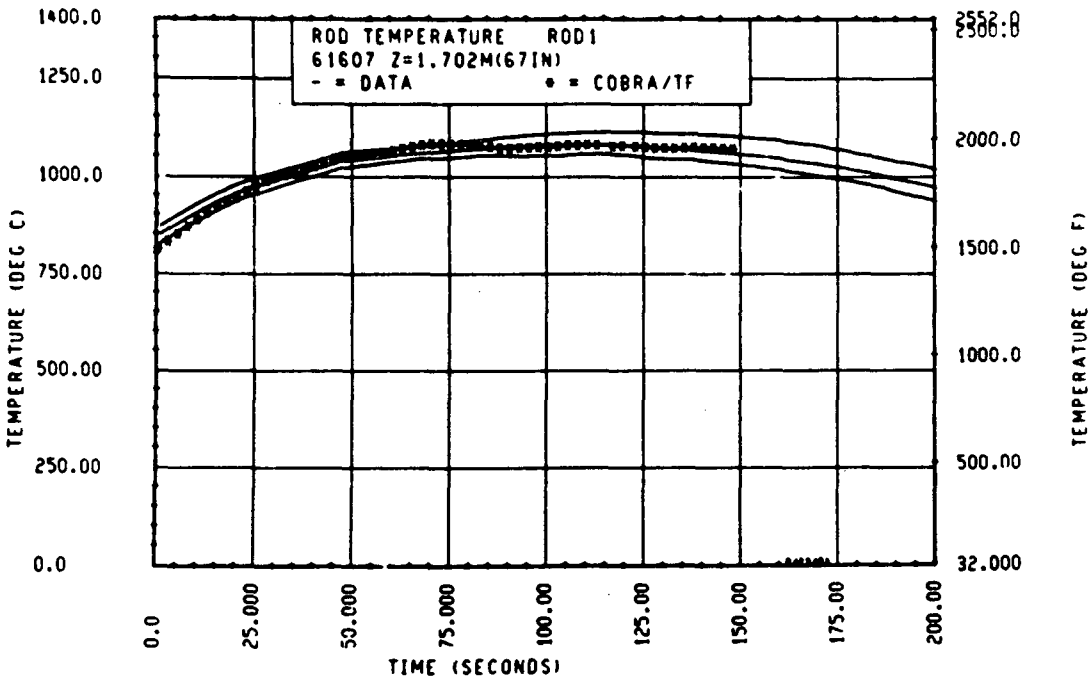

Figure 5-18. Comparison of COBRA-TF-Calculated Heater Rod Temperature Versus Time With FLECHT SEASET 163-Rod Data, Test 61607, 1.70 m (67 in.) Elevation, Rod 1

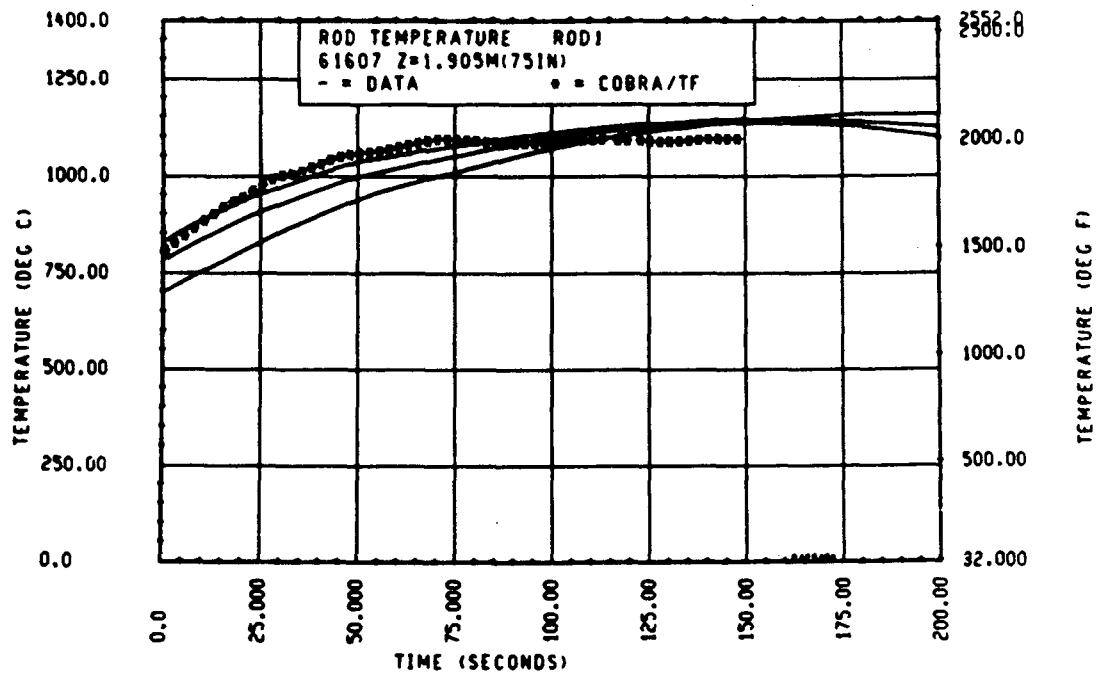

Figure 5-19. Comparison of COBRA-TF-Calculated Heater Rod Temperature Versus Time With FLECHT SEASET 163-Rod Data, Test 61607, 1.90 m (75 in.) Elevation, Rod 1

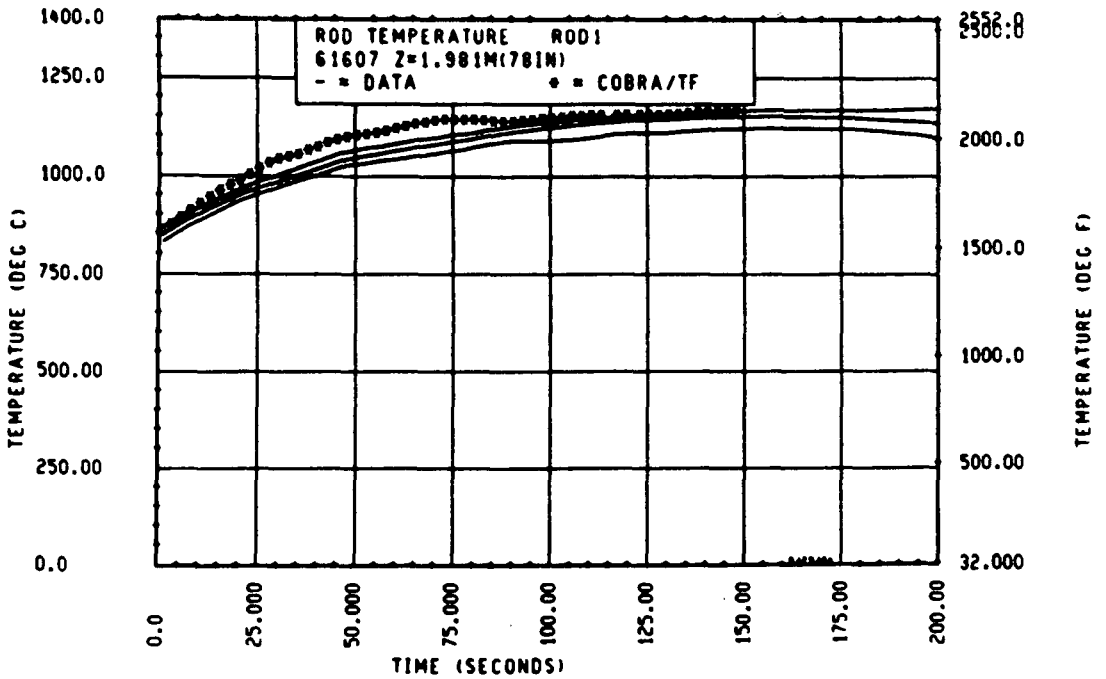

Figure 5-20. Comparison of COBRA-TF-Calculated Heater Rod Temperature Versus Time With FLECHT SEASET 163-Rod Data, Test 61607, 1.98 m (78 in.) Elevation, Rod 1

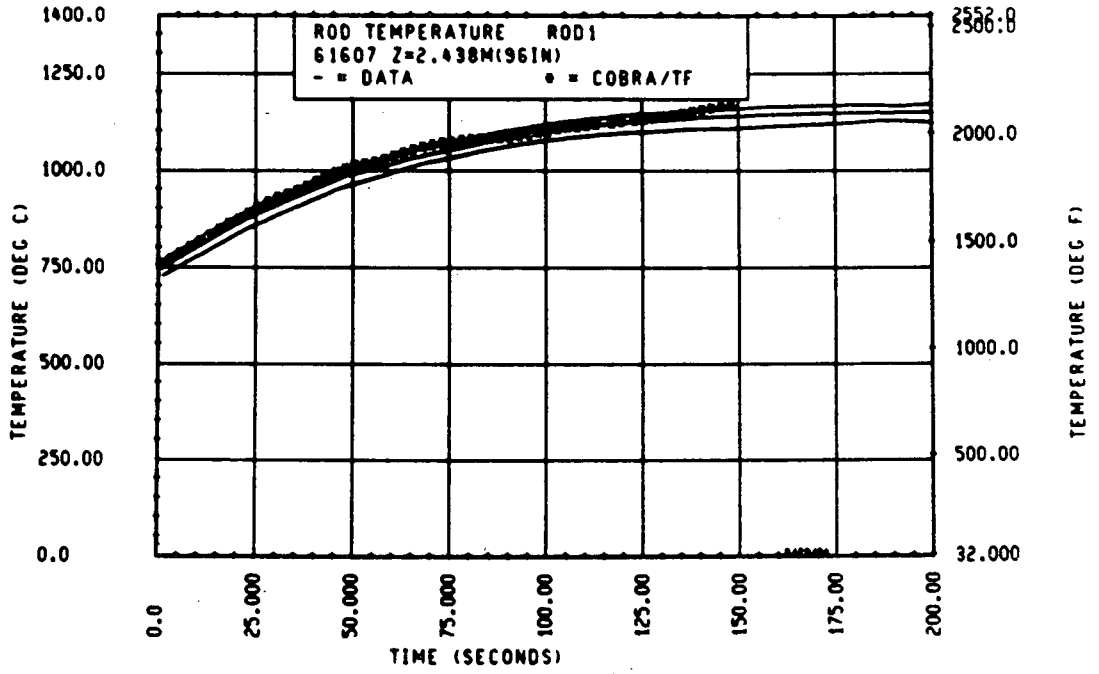

Figure 5-21. Comparison of COBRA-TF-Calculated Heater Rod Temperature Versus Time With FLECHT SEASET 163-Rod Data, Test 61607, 2.44 m (96 in.) Elevation, Rod 1

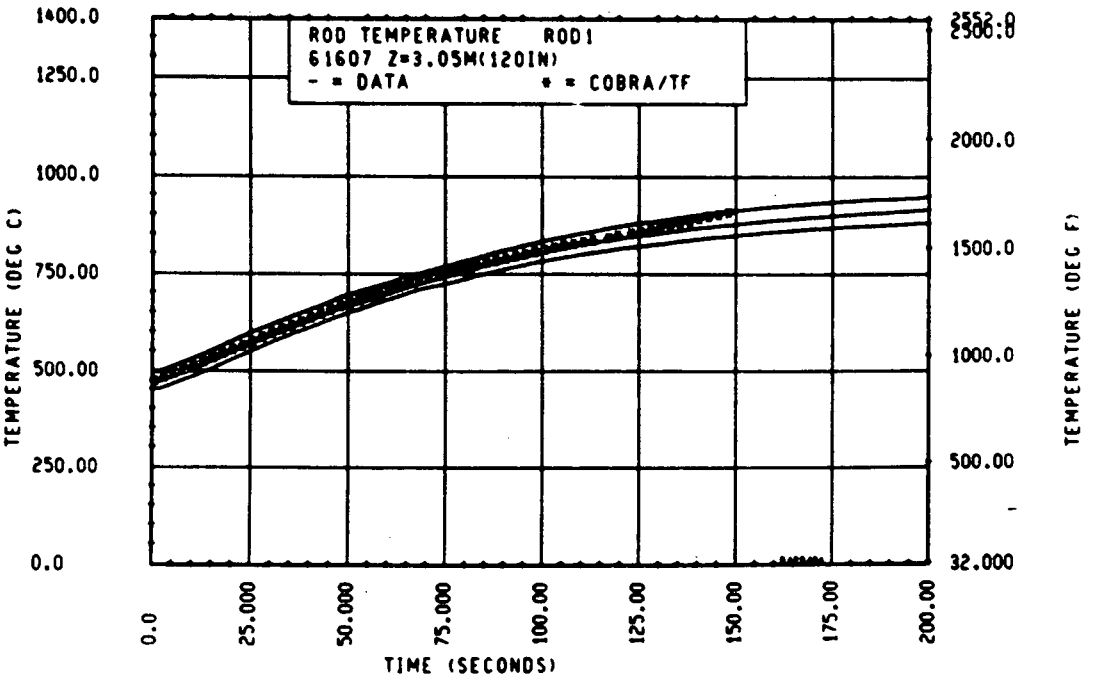

Figure 5-22. Comparison of COBRA-TF-Calculated Heater Rod Temperature Versus Time With FLECHT SEASET 163-Rod Data, Test 61607, 3.05 m (120 in.) Elevation, Rod 1

1) for the three-radial-node COBRA-TF model. The three curves for the heater rod data represent minimum, maximum, and average response of the rods within the node 1 region. The test conditions for test 61607 are given in table 5-1 and compared to test 31805, which had the highest power-to-flow ratio and, generally, the highest heater rod temperatures.

These figures show that the COBRA-TF code predicts the heater rod temperature rise very well at all elevations except the two elevations in the blockage zone. In these cases, the COBRA-TF calculation underestimates the blockage effects locally for the first 100 seconds into reflood. Once significant entrainment begins, the blockage heat transfer effect increases and the prediction crosses the data. The rate of heat release from the rods is underestimated at the beginning of the transient, and then overestimated after about 100 seconds. However, examination of the upper elevations shows that the correct amound of heat is removed in the blockage region, since the agreement between the the data and the COBRA-TF prediction is quite good.

A similar set of comparisons for COBRA-TF radial node 2 is shown in figures 5-23 through 5-28. Rod 2 (radial node 2) represents the bypass region between the blockage islands and the rows of heater rods adjacent to the housing. The comparisons in these figures indicate a general overprediction of the experimental data by COBRA-TF, particularly just upstream of the blockage zone [1.70 m (67 in.)] and in the blockage zone. At the upper elevations, the agreement is improved.

The comparisons between the COBRA-TF predictions and the heater rod data for the blockage islands on axial temperature profile plots are shown in figures 5-29 through 5-35. (Also shown in figure 5-29 is the axial location of the spacer grids and the blockage zone.) As mentioned above, the overall agreement is quite good, with an overprediction of the heater rod temperatures in the blockage zone early in the transient and a slight underprediction of the heater rod temperatures in the blocked zone later in the transient. A closer examination of figures 5-33 through 5-35 indicates that the lower heater rod temperatures in the blockage region could be casued by the strong heat transfer effect of the spacer grid at the 1.57 m (62 in.) elevation. The calculated heater rod temperature downstream of this grid is lower than that observed

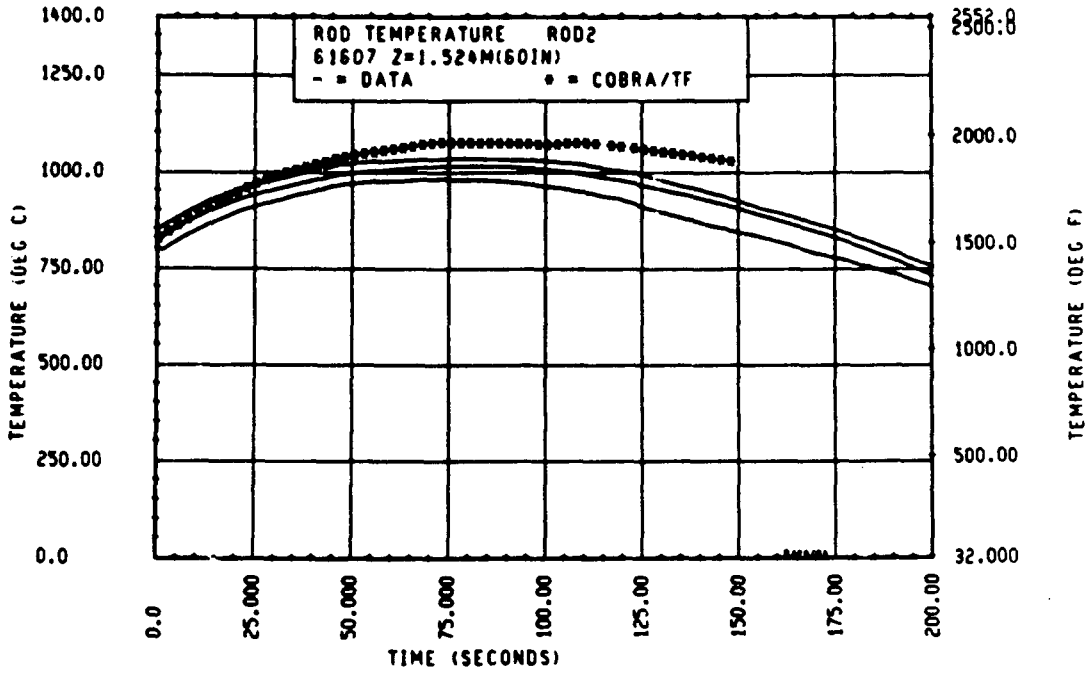

Figure 5-23. Comparison of COBRA-TF-Calculated Heater Rod Temperature Versus Time With FLECHT SEASET 163-Rod Data, Test 61607, 1.52 m (60 in.) Elevation, Rod 2

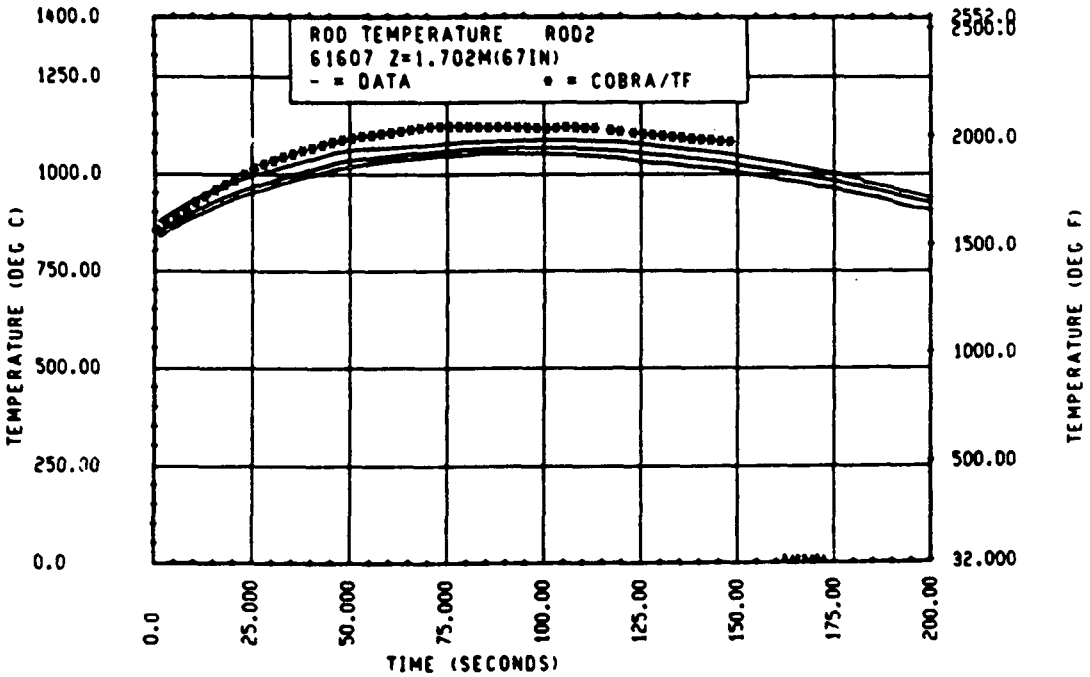

Figure 5-24. Comparison of COBRA-TF-Calculated Heater Rod Temperature Versus Time With FLECHT SEASET 163-Rod Data, Test 61607, 1.70 m (67 in.) Elevation, Rod 2

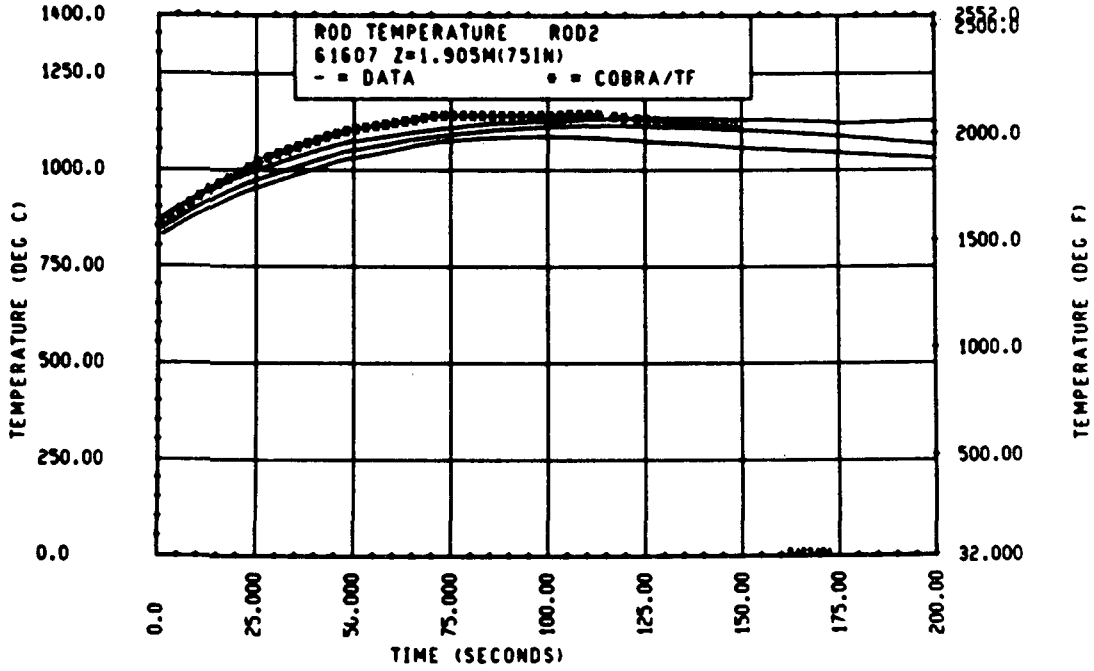

Figure 5-25. Comparison of COBRA-TF-Calculated Heater Rod Temperature Versus Time With FLECHT SEASET 163-Rod Data, Test 61607, 1.90 m (75 in.) Elevation, Rod 2

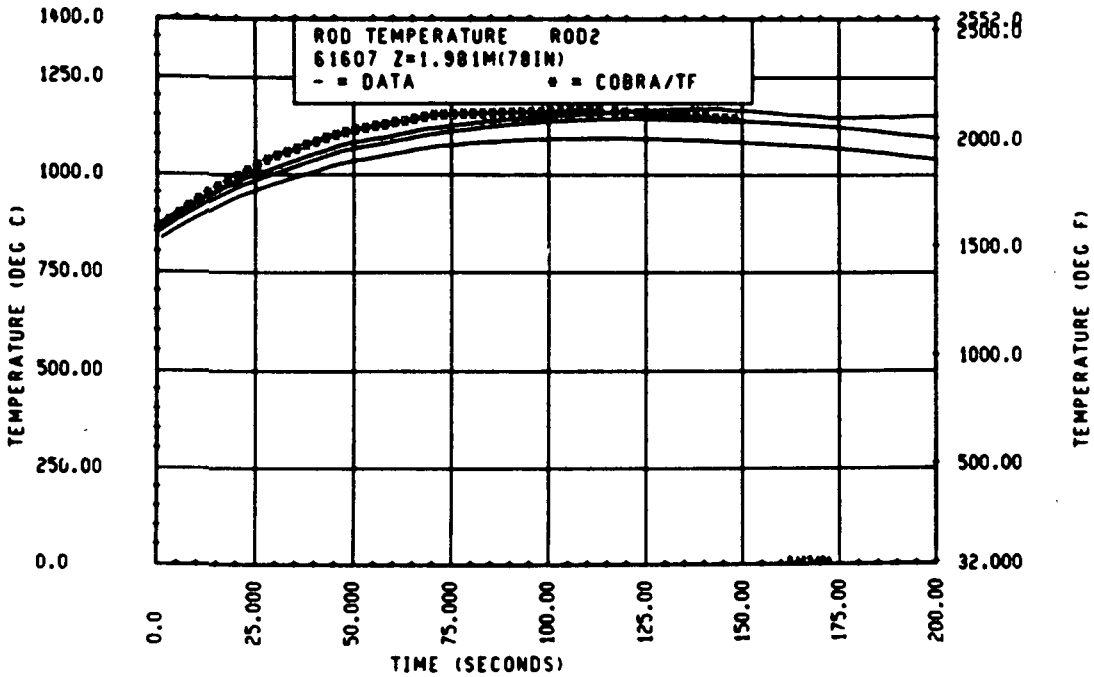

Figure 5-26. Comparison of COBRA-TF-Calculated Heater Rod Temperature Versus Time With FLECHT SEASET 163-Rod Data, Test 61607, 1.98 m (78 in.) Elevation, Rod 2

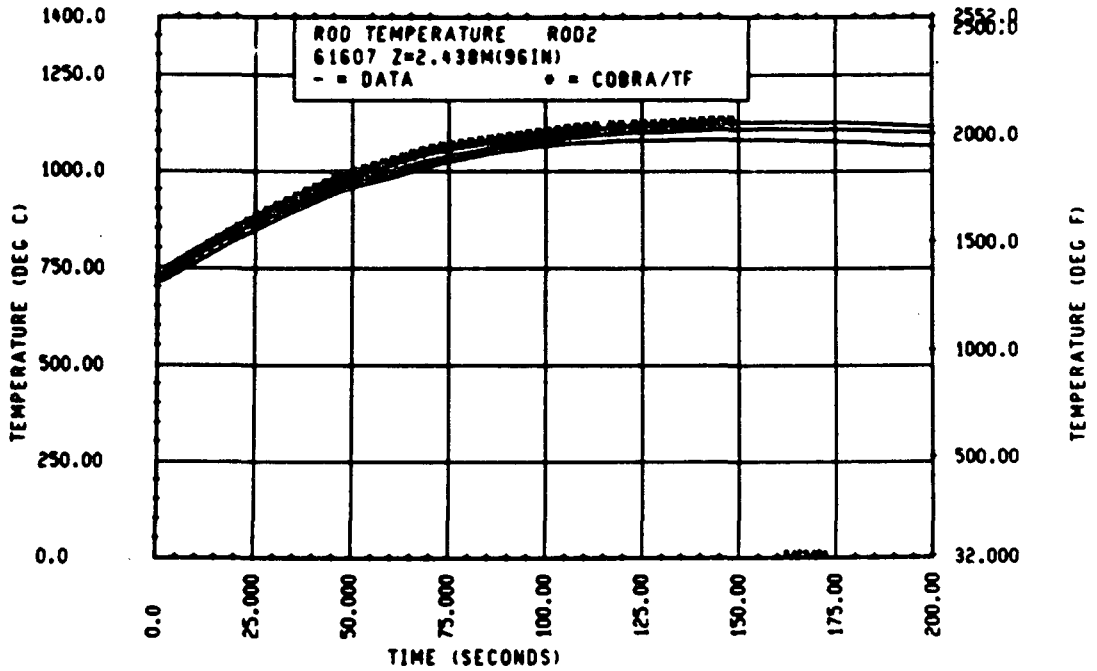

Figure 5-27. Comparison of COBRA-TF-Calculated Heater Rod Temperature Versus Time With FLECHT SEASET 163-Rod Data, Test 61607, 2.44 m (96 in.) Elevation, Rod 2

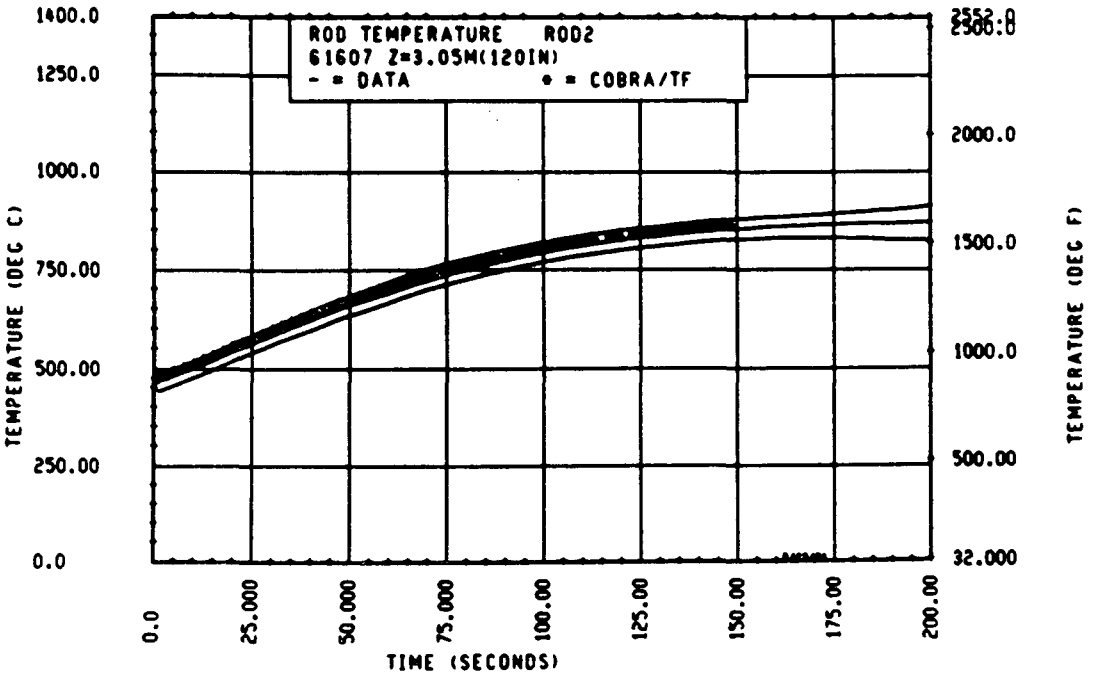

Figure 5-28. Comparison of COBRA-TF-Calculated Heater Rod Temperature Versus Time With FLECHT SEASET 163-Rod Data, Test 61607, 3.05 m (120 in.) Elevation, Rod 2

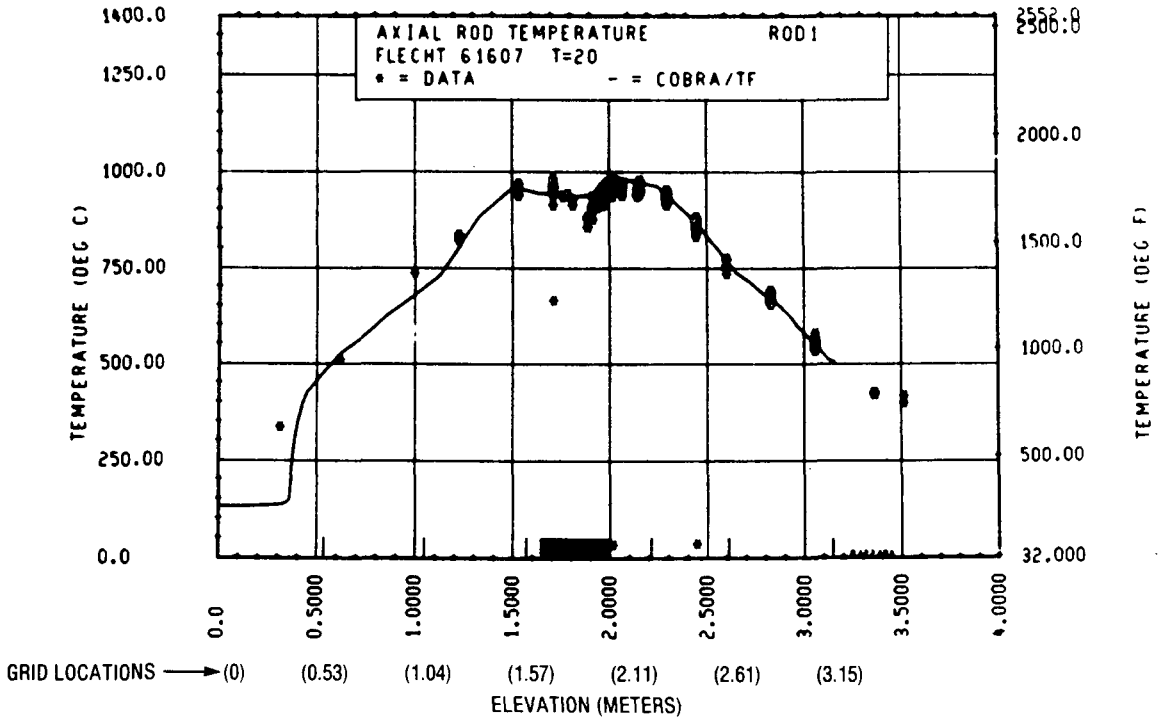

Figure 5-29. Comparison of COBRA-TF-Calculated Axial Rod Temperature Versus Elevation With FLECHT SEASET 163-Rod Data, Test 61607, t = 20 Seconds, Rod 1

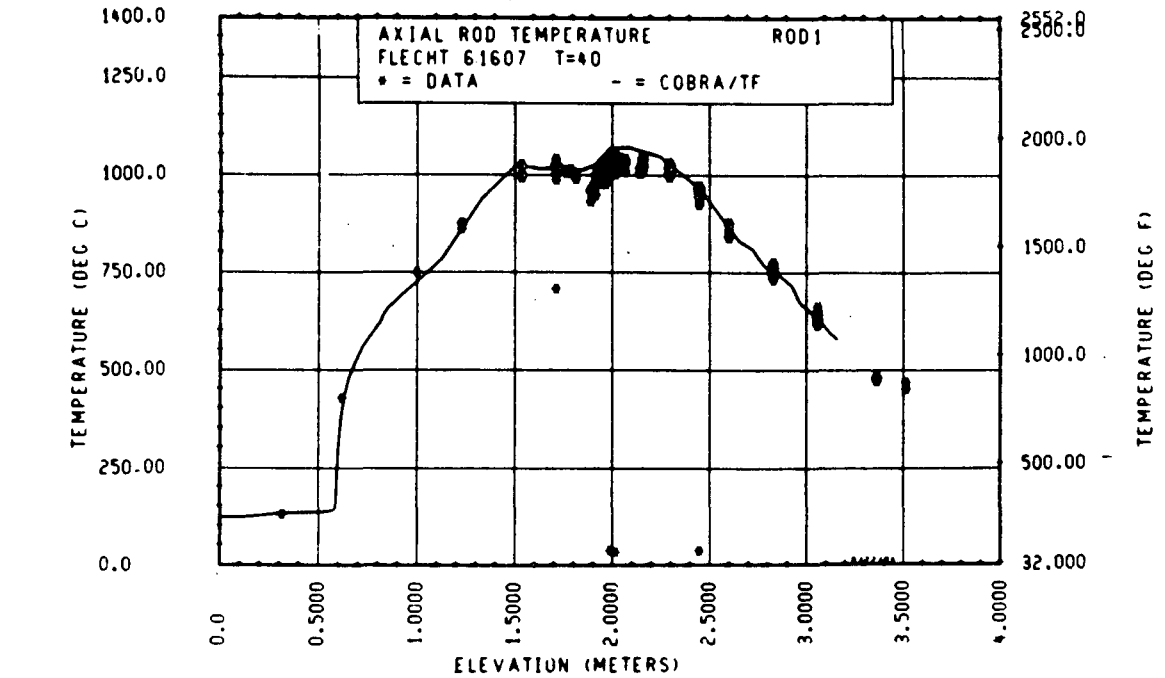

Figure 5-30. Comparison of COBRA-TF-Calculated Axial Rod Temperature Versus Elevation With FLECHT SEASET 163-Rod Data, Test 61607, t = 40 Seconds, Rod 1

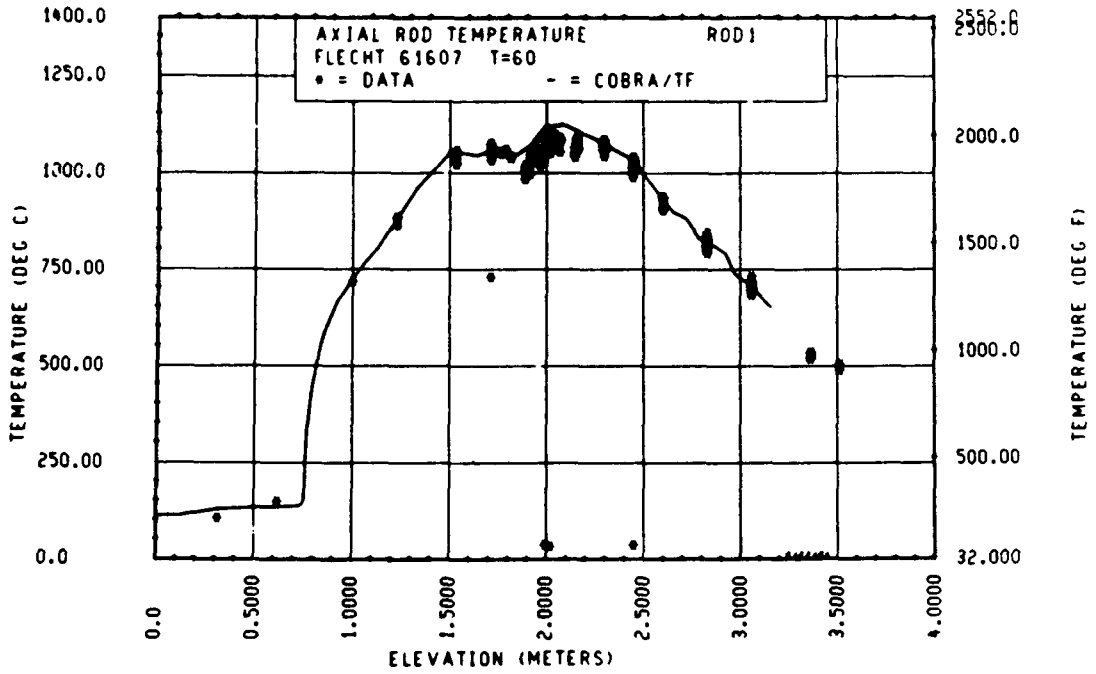

Figure 5-31. Comparison of COBRA-TF-Calculated Axial Rod Temperature Versus Elevation With FLECHT SEASET 163-Rod Data, Test 61607, t = 60 Seconds, Rod 1

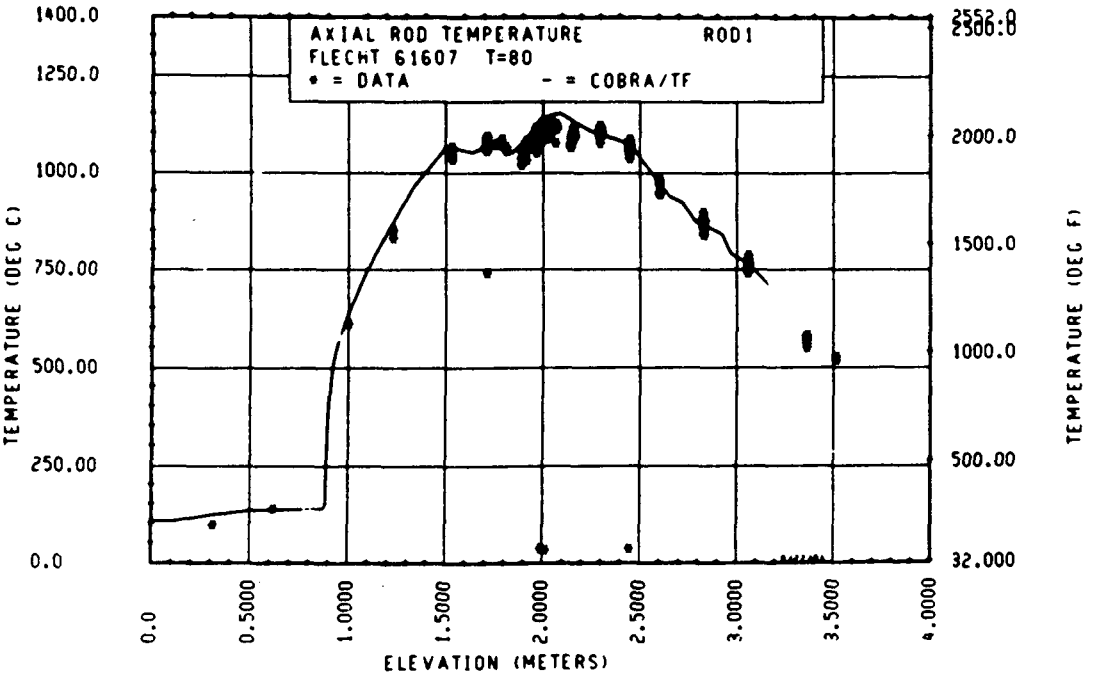

Figure 5-32. Comparison of COBRA-TF-Calculated Axial Rod Temperature Versus Elevation With FLECHT SEASET 163-Rod Data, Test 61607, t = 80 Seconds, Rod 1

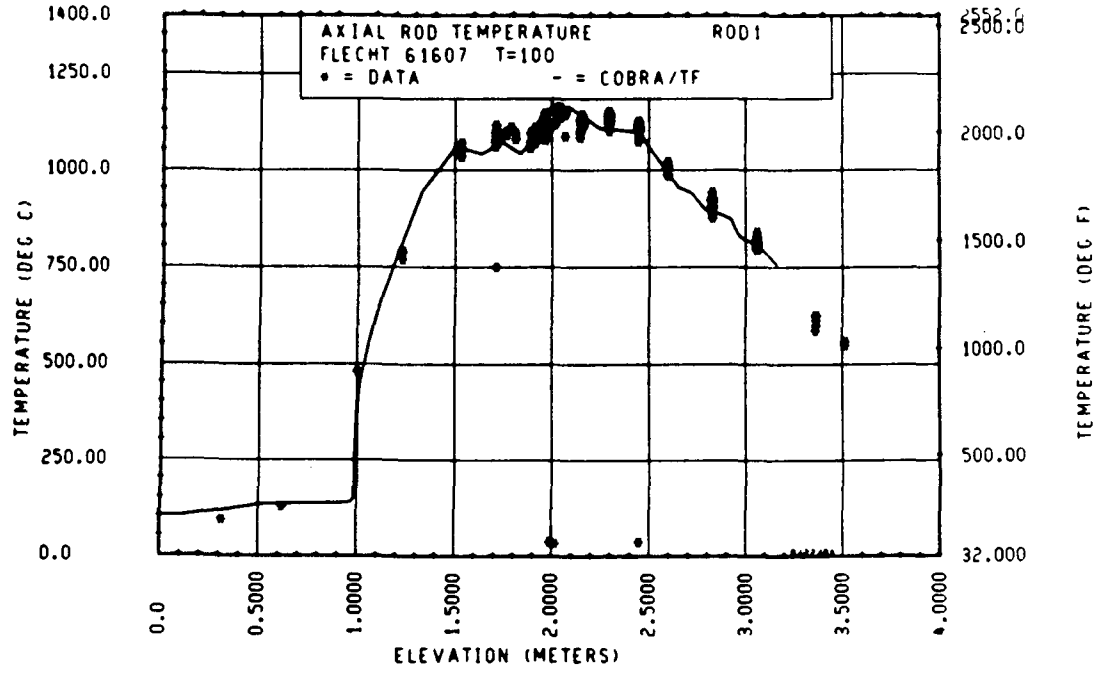

Figure 5-33. Comparison of COBRA-TF-Calculated Axial Rod Temperature Versus Elevation With FLECHT SEASET 163-Rod Data, Test 61607, t = 100 Seconds, Rod 1

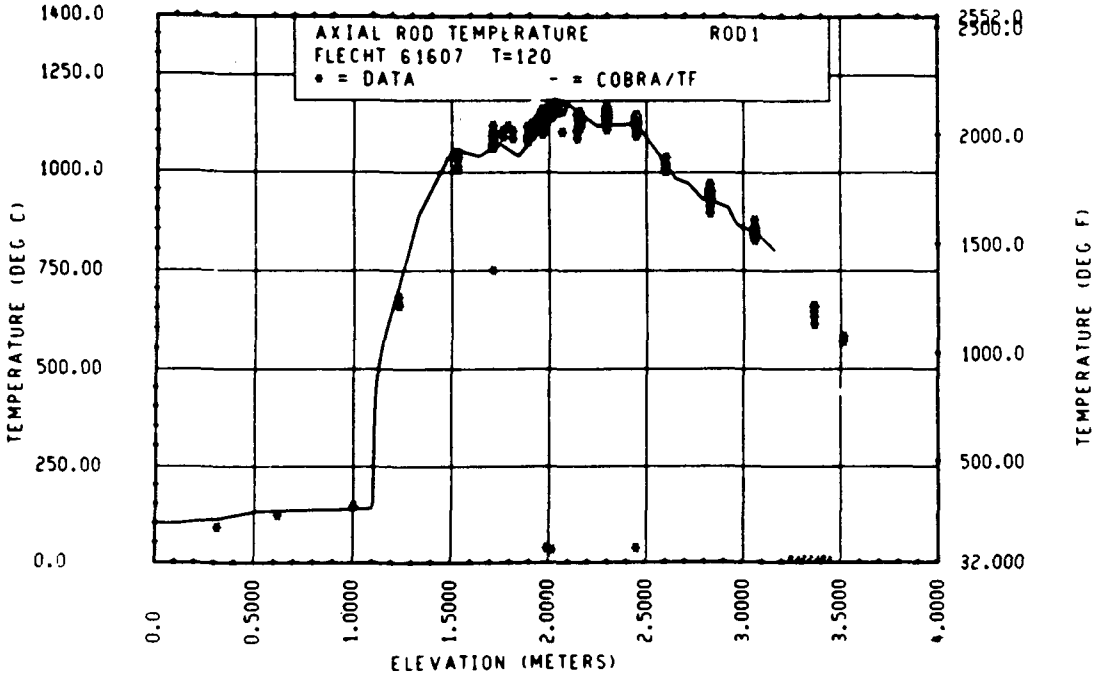

Figure 5-34. Comparison of COBRA-TF-Calculated Axial Rod Temperature Versus Elevation With FLECHT SEASET 163-Rod Data, Test 61607, t = 120 Seconds, Rod 1

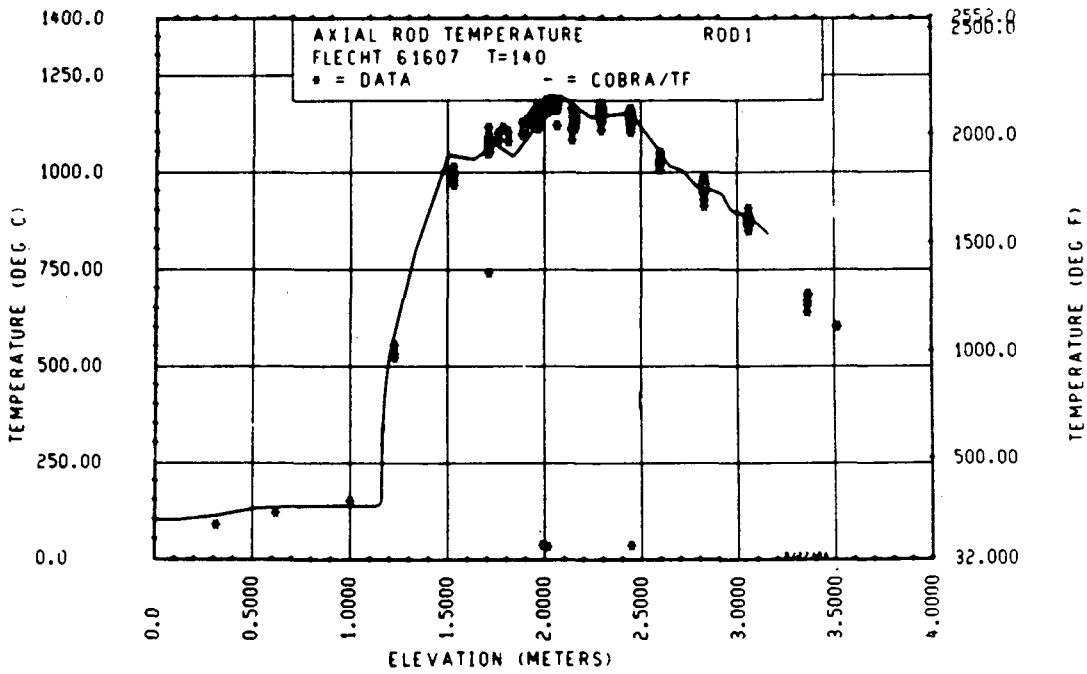

Figure 5-35. Comparison of COBRA-TF-Calculated Axial Rod Temperature Versus Elevation With FLECHT SEASET 163-Rod Data, Test 61607, t = 140 Seconds, Rod 1

in the data. This results in a lower-than-expected temperature as predicted by COBRA-TF coming into the blockage zone. As a result, the COBRA-TF-calculated heater rod temperature in the blockage zone is slightly below the experimental data. The other elevations agree quite well. The dips in the clad temperatures at different elevations are due to the grid and blockage effects, as shown in these figures.

A similar series of comparisons are shown in figures 5-36 through 5-42. Again, a general overprediction is evidenced, particularly in the bundle midplane for early times. At later times, the agreement is improved and the 1.57 m (62 in.) grid effect becomes apparent. For all axial plots, the agreement with the quench propagation and temperatures before the quench are quite good.

The vapor temperature measurement locations are shown in appendix E for the 163-rod bundle, along with the COBRA-TF noding scheme for different elevations. Three types of vapor temperature measurements were used: thimble aspirating steam probes, bare miniature thermocouples, and self-aspirating steam probes. The performance of these probes is discussed in the 163-rod bundle data report.[1] Figures 5-43 through 5-45 show the measured vapor temperature and COBRA-TF-calculated vapor temperature as a function of time for COBRA-TF node 1 (rod 1), which represents the blockage island in the 163-rod bundle.

The data are from the bare and self-aspirating steam probes located in and downstream of the blockage islands, as shown in appendix E. The lines on the figures are the data, one from each probe; the points are the COBRA-TF calculations. The agreement is reasonable; however, the predicted temperatures at the 1.98 m (78 in.) elevation are lower than the data after 75 seconds. The other elevations provide improved comparisons. The data are quite tight, with

1. Loftus, M. J., et al., "PWR FLECHT SEASET 163-Rod Bundle Flow Blockage Task Data Report," NRC/EPRI/Westinghouse-13, October 1983.

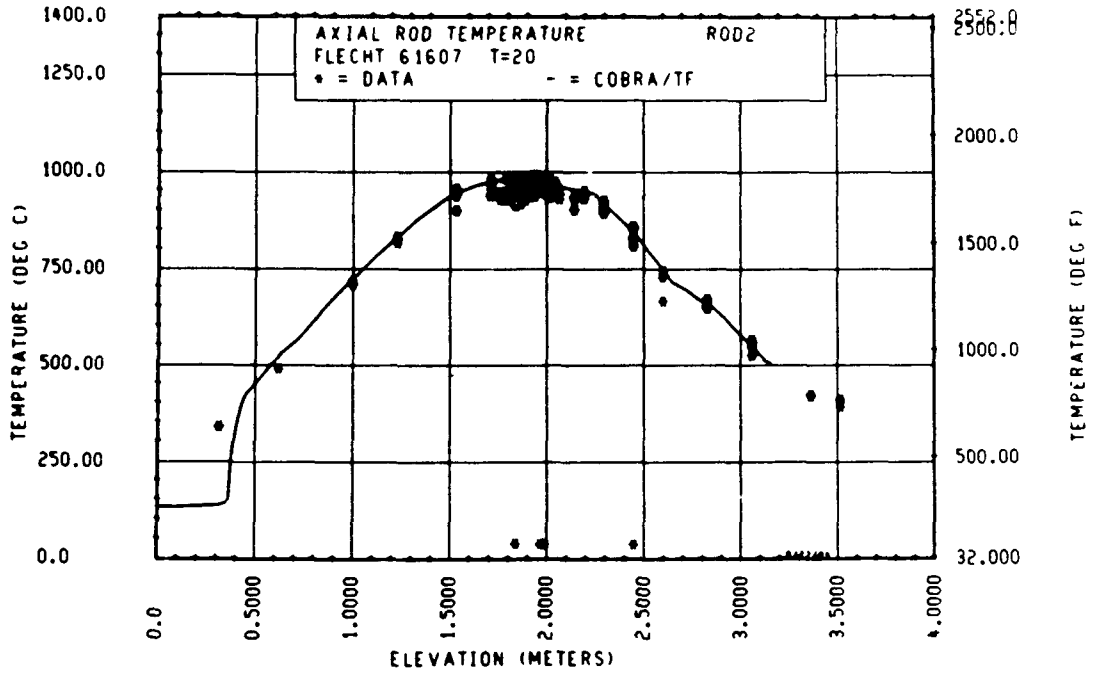

Figure 5-36. Comparison of COBRA-TF-Calculated Axial Rod Temperature Versus Elevation With FLECHT SEASET 163-Rod Data, Test 61607, t = 20 Seconds, Rod 2

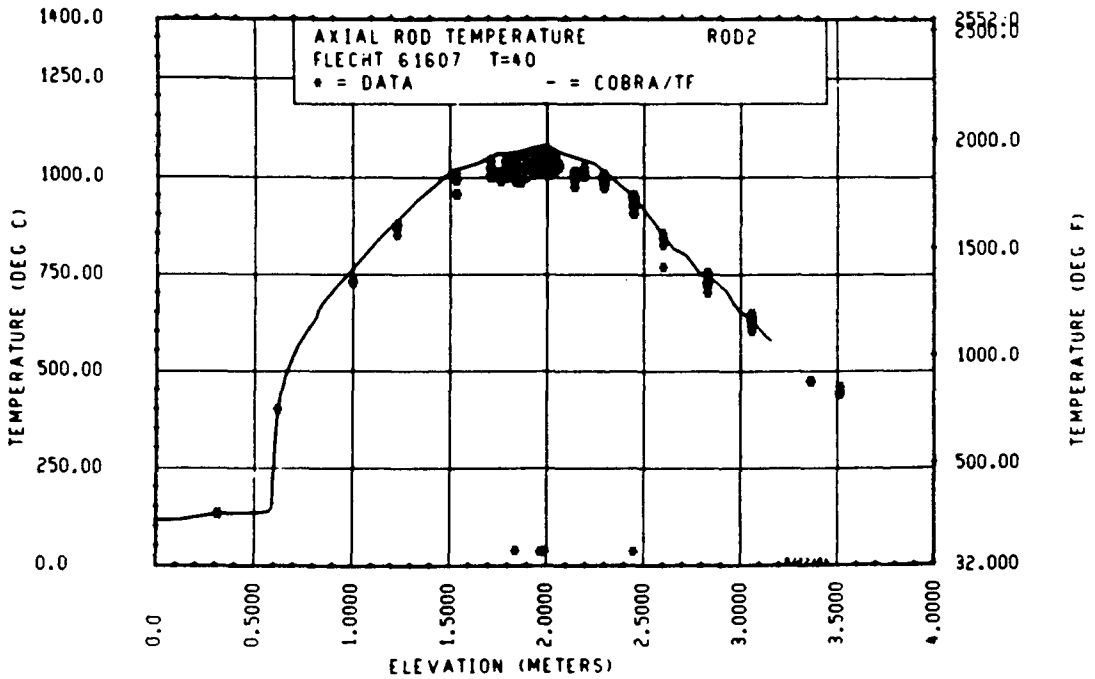

Figure 5-37. Comparison of COBRA-TF-Calculated Axial Rod Temperature Versus Elevation With FLECHT SEASET 163-Rod Data, Test 61607, t = 40 Seconds, Rod 2

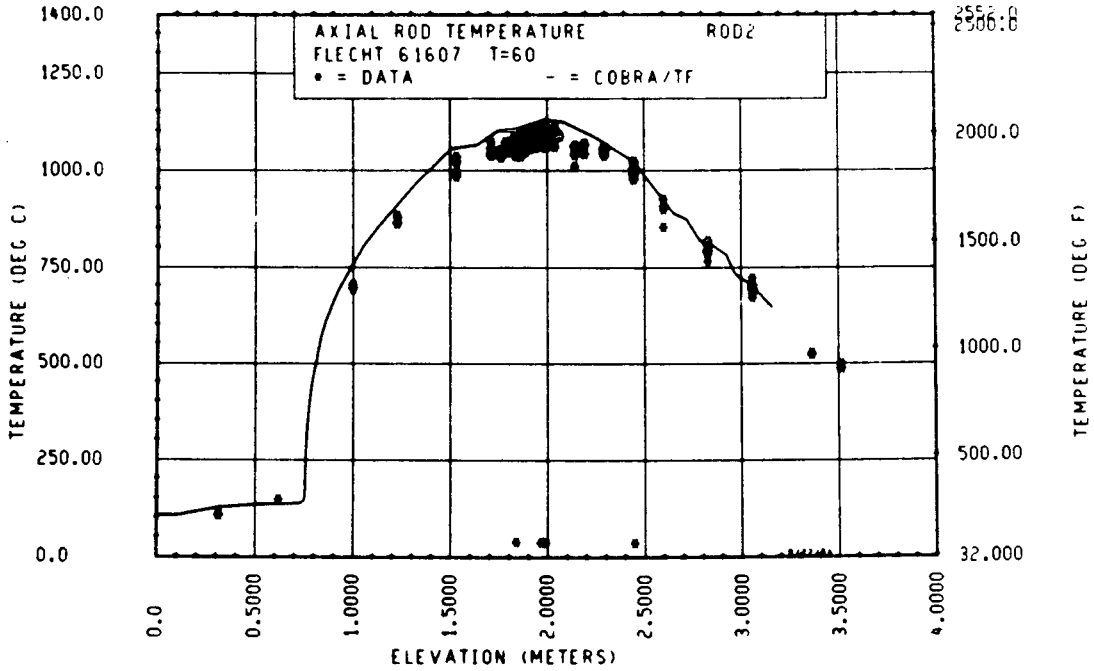

Figure 5-38. Comparison of COBRA-TF-Calculated Axial Rod Temperature Versus Elevation With FLECHT SEASET 163-Rod Data, Test 61607, t = 60 Seconds, Rod 2

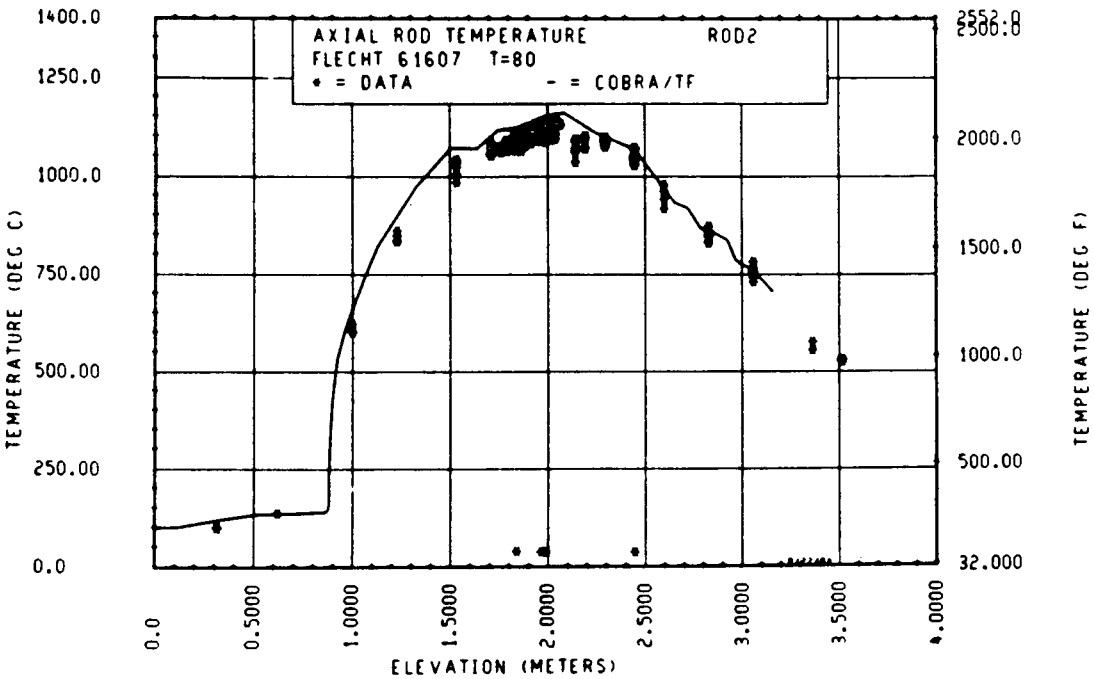

Figure 5-39. Comparison of COBRA-TF-Calculated Axial Rod Temperature Versus Elevation With FLECHT SEASET 163-Rod Data, Test 61607, t = 80 Seconds, Rod 2

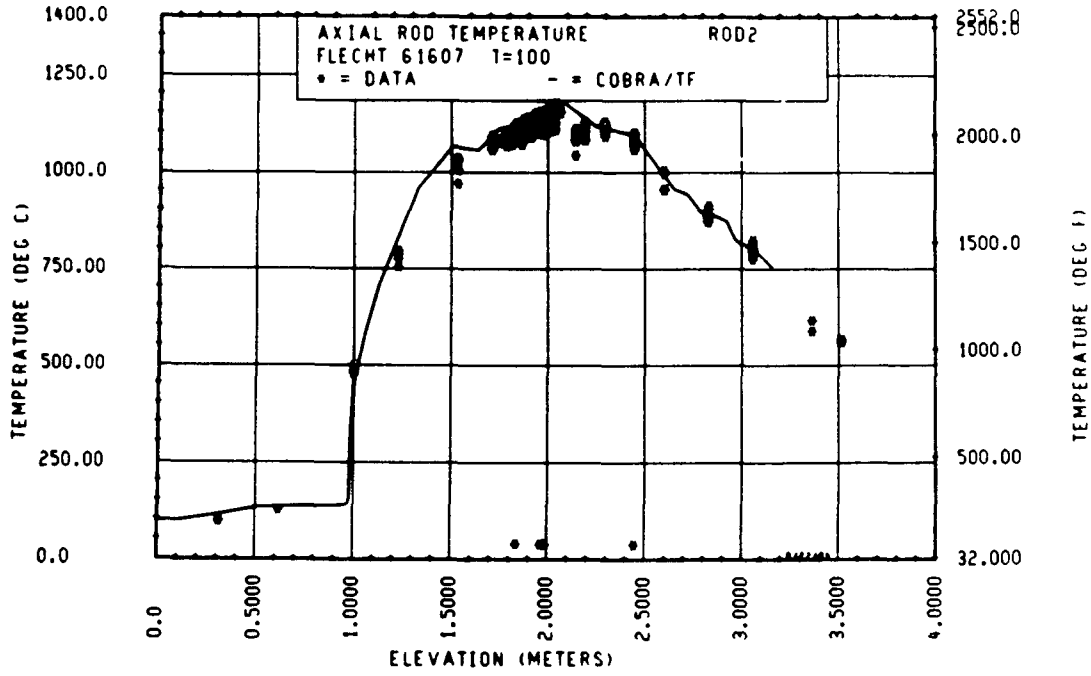

Figure 5-40. Comparison of COBRA-TF-Calculated Axial Rod Temperature Versus Elevation With FLECHT SEASET 163-Rod Data, Test 61607, t = 100 Seconds, Rod 2

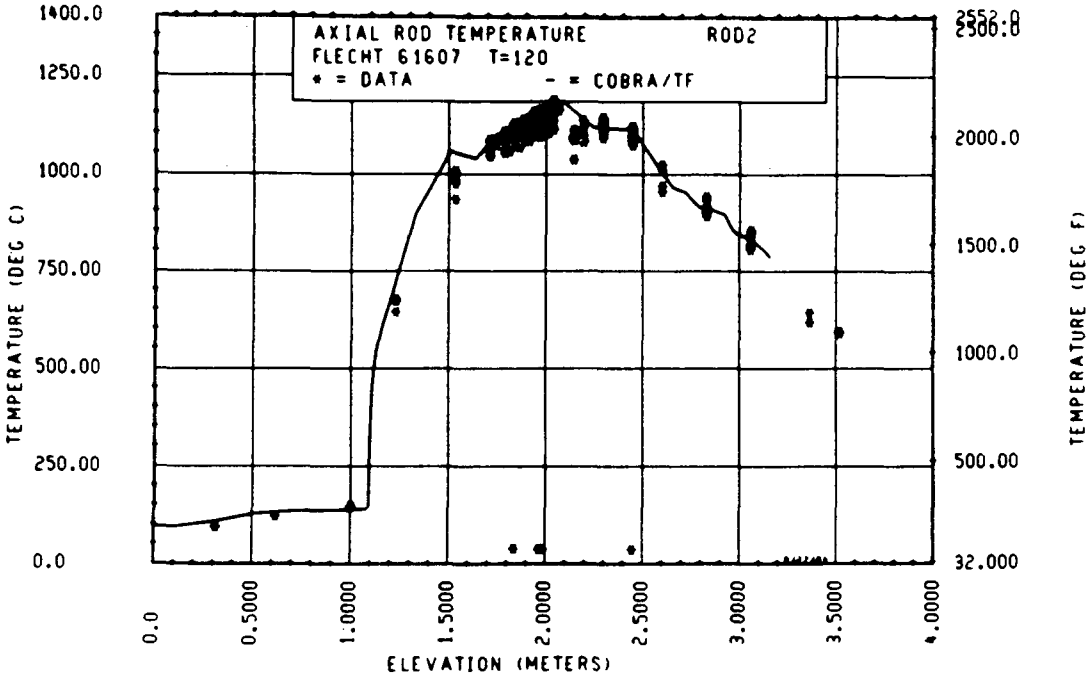

Figure 5-41. Comparison of COBRA-TF-Calculated Axial Rod Temperature Versus Elevation With FLECHT SEASET 163-Rod Data, Test 61607, t = 120 Seconds, Rod 2

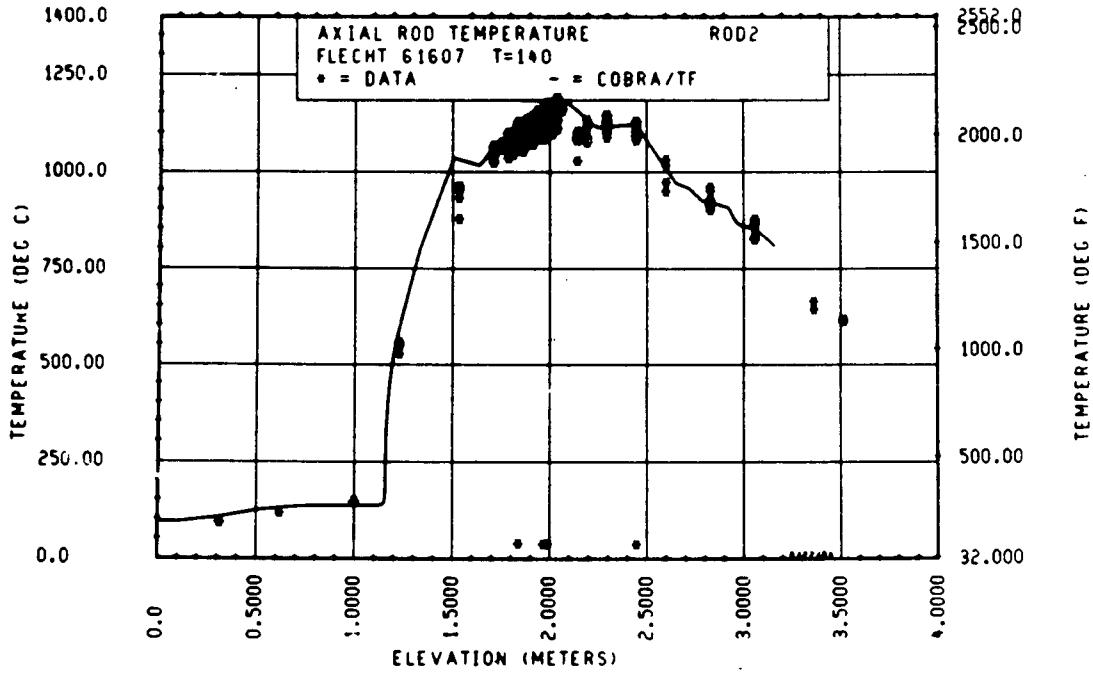

Figure 5-42. Comparison of COBRA-TF-Calculated Axial Rod Temperature Versus Elevation With FLECHT SEASET 163-Rod Data, Test 61607, t = 140 Seconds, Rod 2

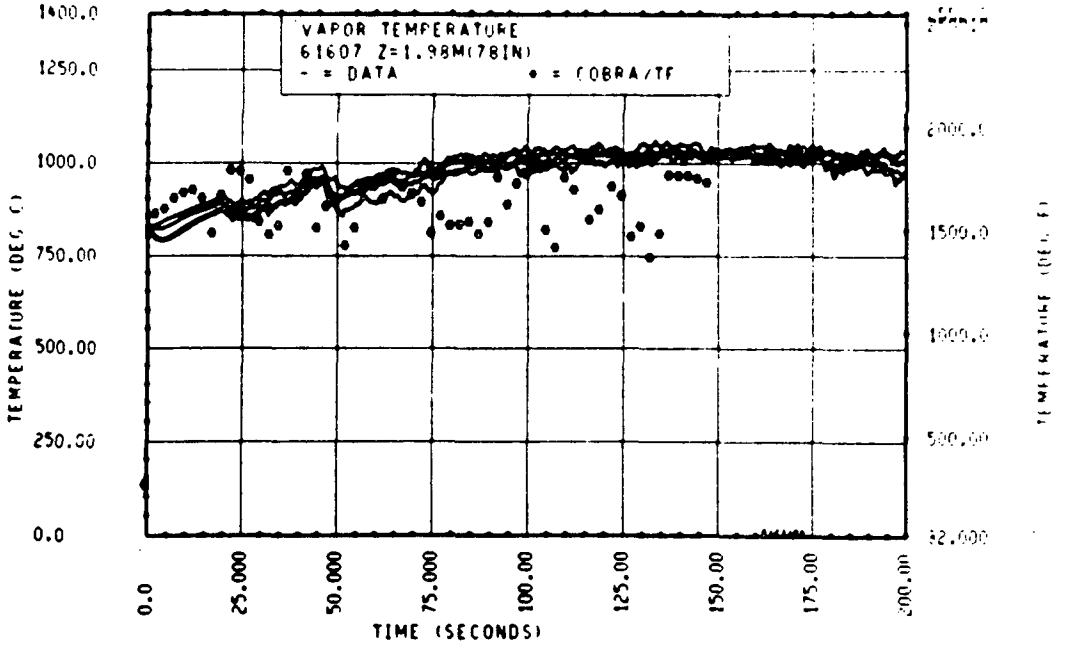

Figure 5-43. Comparison of COBRA-TF-Calculated Vapor Temperature Versus Time With FLECHT SEASET 163-Rod Data, Test 61607, 1.98 m (78 in.) Elevation

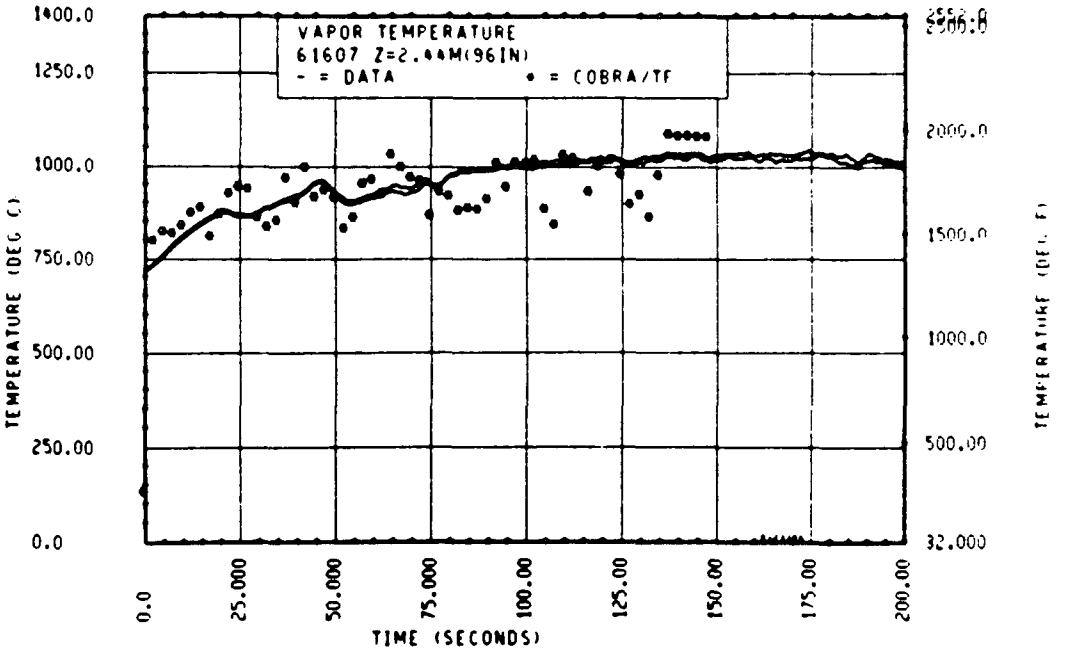

Figure 5-44. Comparison of COBRA-TF-Calculated Vapor Temperature Versus Time With FLECHT SEASET 163-Rod Data, Test 61607, 2.44 m (96 in.) Elevation

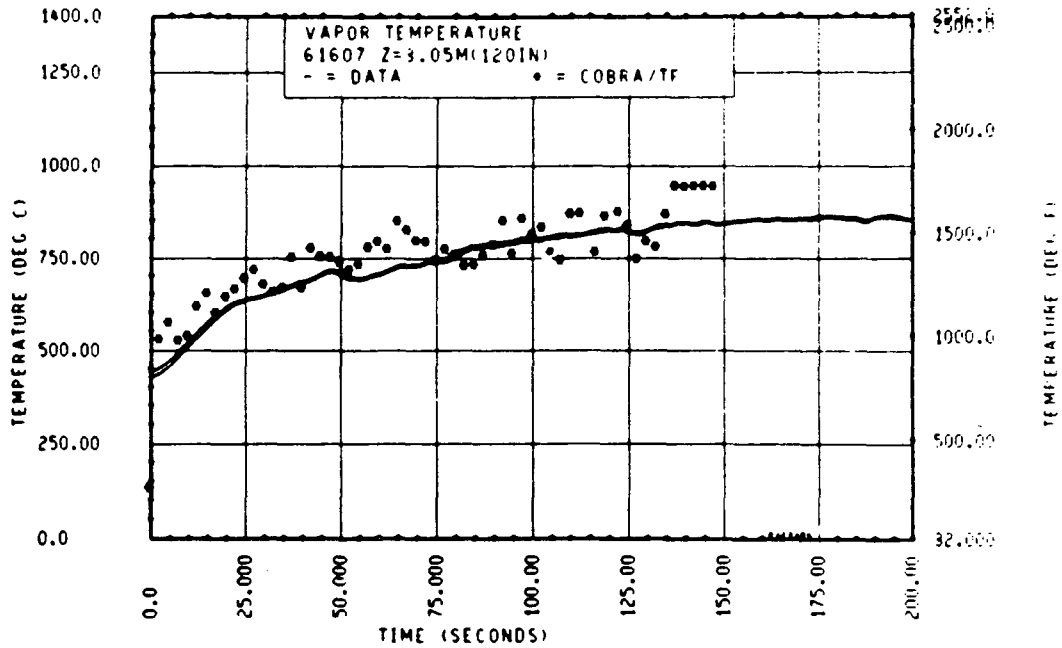

Figure 5-45. Comparison of COBRA-TF-Calculated Vapor Temperature Versus Time With FLECHT SEASET 163-Rod Data, Test 61607, 3.05 m (120 in.) Elevation

only a small radial variation between the probes. This indicates good radial mixing and again supports use of a COBRA-TF model with coarser radial noding for the 163-rod bundle data.

The COBRA-TF-calculated vapor temperature for the blockage regions is plotted against elevation for different times in figures 5-46 through 5-52 with all the measured vapor temperature data. The solid line is for the calculated vapor temperature in the blockage zone. If only the data points for the vapor temperature in the blockage zone are compared to the COBRA-TF calculation, the comparison is quite good as shown in figures 5-53 to 5-59. The axial distribution of the calculated vapor temperature before the blockage agrees quite well with the data; this agreement indicates that the calculated rapid vapor superheating immediately downstream of the quench front is correct.

Comparisons between the COBRA-TF predictions and the other 163-rod blocked bundle tests is discussed only briefly herein. A complete set of figures for each COBRA-TF comparison is presented so that a reviewer can judge for himself how well the code and its blockage models reflect the actual rod bundle response. The comparisons for FLECHT SEASET 163-rod bundle test 61005 are shown in figures 5-60 through 5-95. The predicted and measured temperature-time curves for both the blocked region (rod 1) and bypass region (rod 2) agree very well with the data. There is a slight tendency for overprediction of the temperature data for rod 1 at the uppermost elevations [2.44 and 3.05 m (96 and 120 in.)]. The rod 2 comparisons look much the same at these upper elevations (figures 5-66 through 5-71).

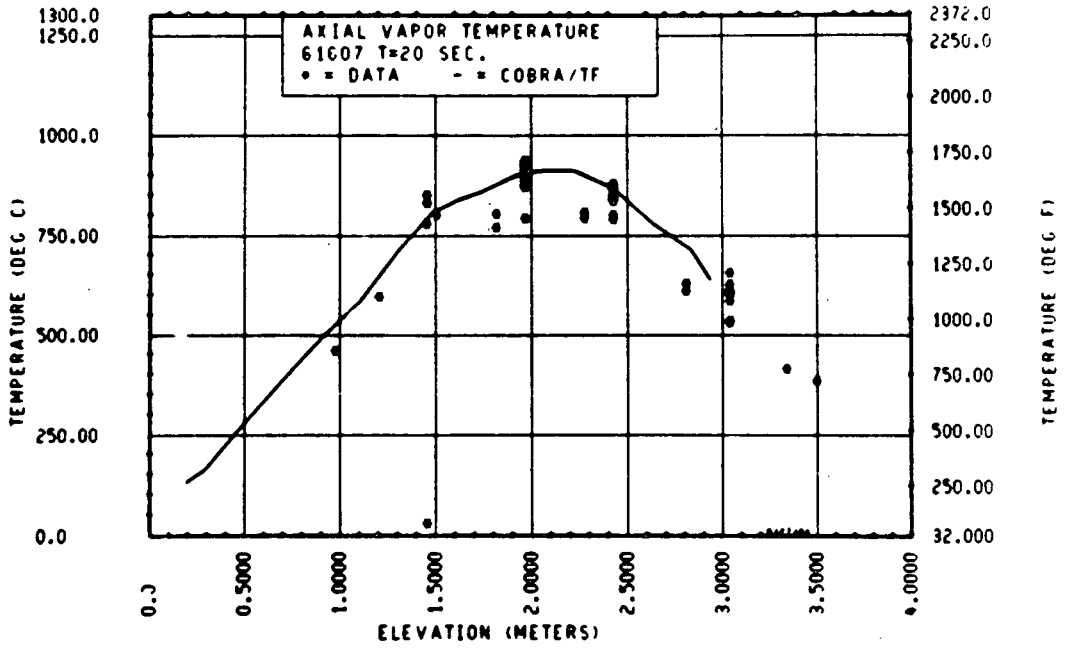

Figure 5-46. Comparison of COBRA-TF-Calculated Axial Vapor Temperature Versus Elevation With FLECHT SEASET 163-Rod Data, Test 61607, t = 20 Seconds

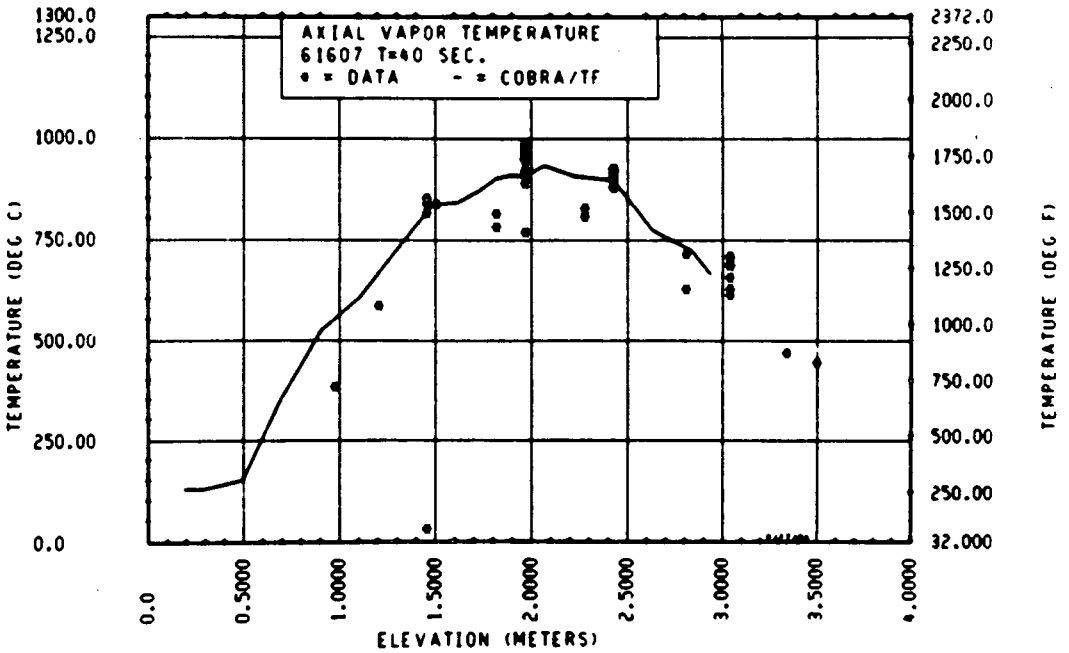

Figure 5-47. Comparison of COBRA-TF-Calculated Axial Vapor Temperature Versus Elevation With FLECHT SEASET 163-Rod Data, Test 61607, t = 40 Seconds

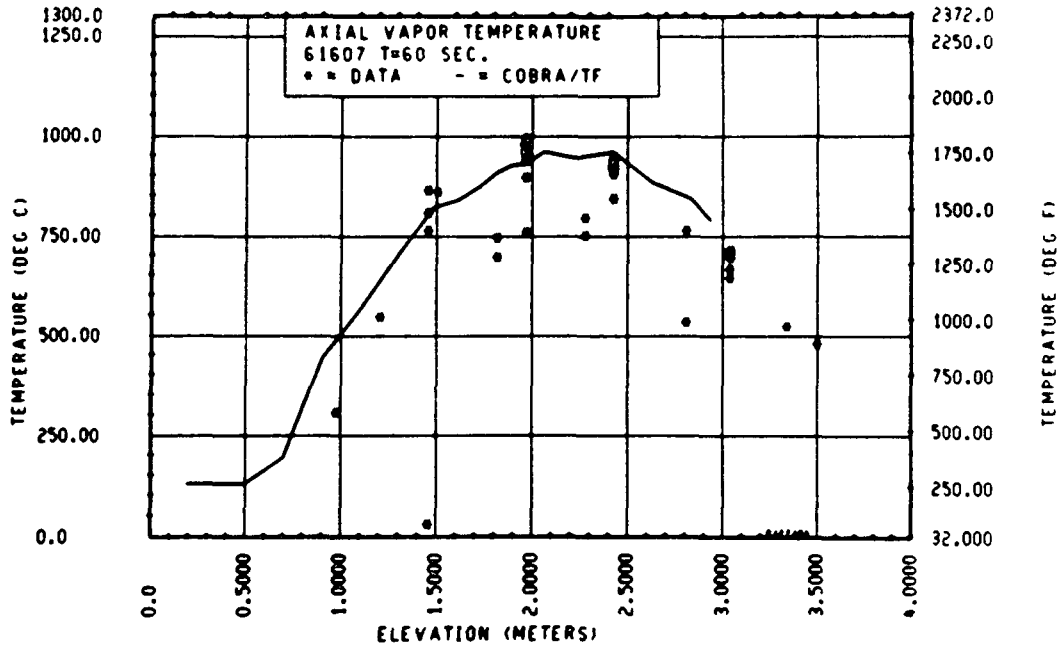

Figure 5-48. Comparison of COBRA-TF-Calculated Axial Vapor Temperature Versus Time With FLECHT SEASET 163-Rod Data, Test 61607, t = 60 Seconds

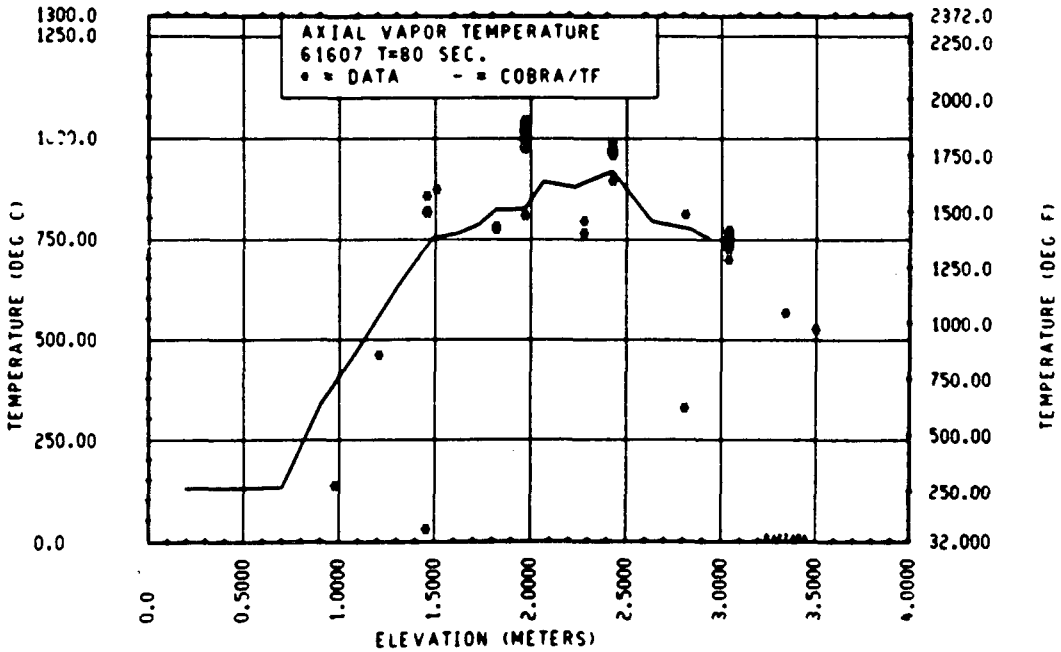

Figure 5-49. Comparison of COBRA-TF-Calculated Axial Vapor Temperature Versus Time With FLECHT SEASET 163-Rod Data, Test 61607, t = 80 Seconds

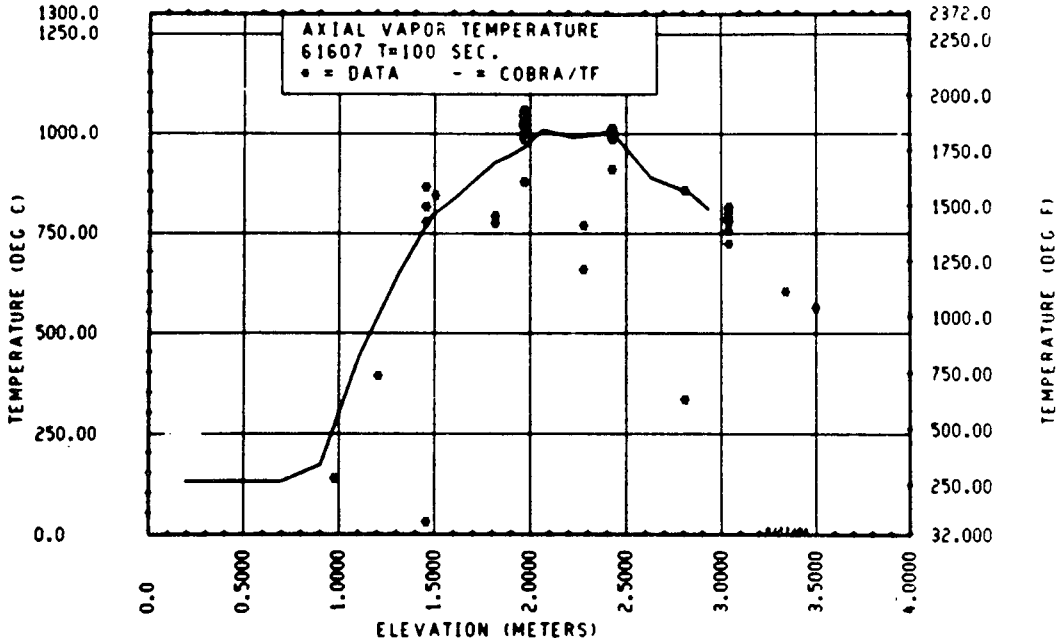

Figure 5-50. Comparison of COBRA-TF-Calculated Axial Vapor Temperature Versus Elevation With FLECHT SEASET 163-Rod Data, Test 61607, t = 100 Seconds

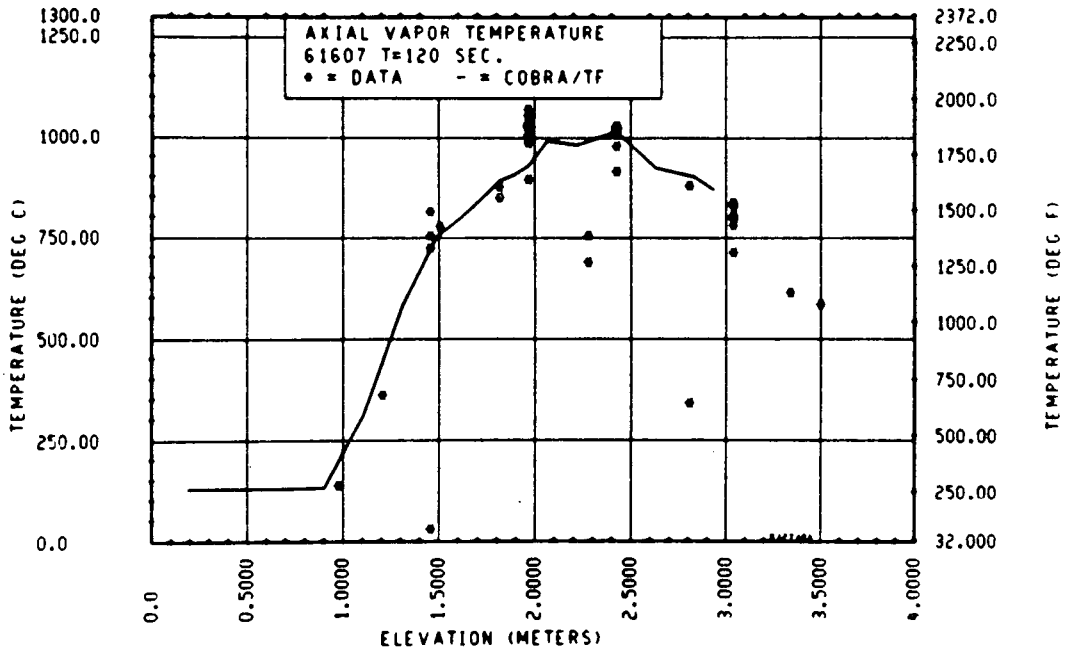

Figure 5-51. Comparison of COBRA-TF-Calculated Axial Vapor Temperature Versus Elevation With FLECHT SEASET 163-Rod Data, Test 61607, t = 120 Seconds

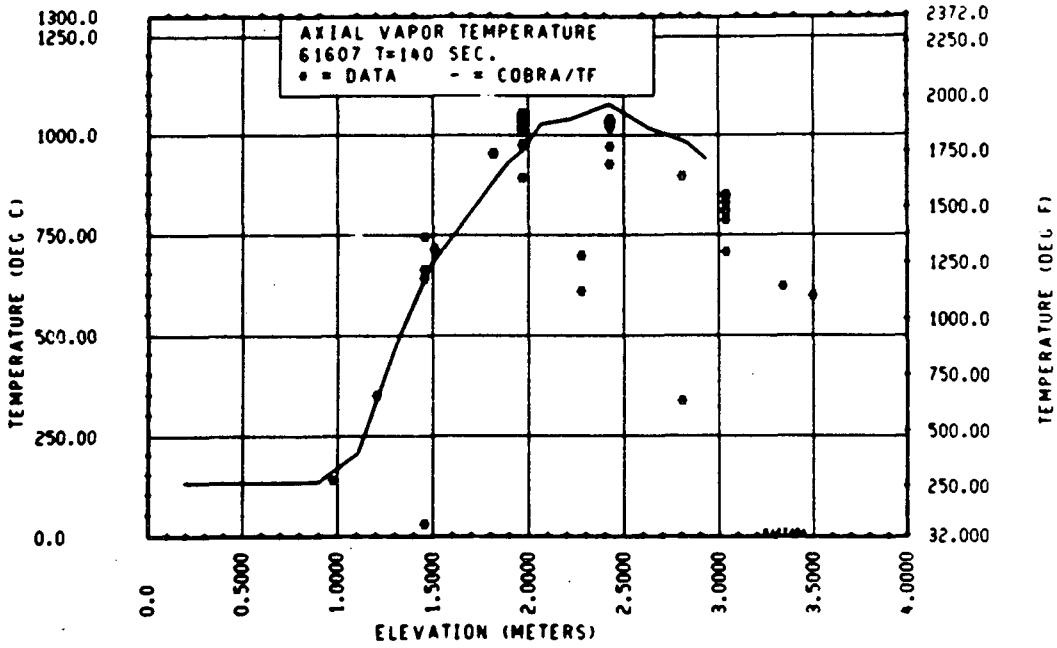

Figure 5-52. Comparison of COBRA-TF-Calculated Axial Vapor Temperature Versus Time With FLECHT SEASET 163-Rod Data, Test 61607, t = 140 Seconds

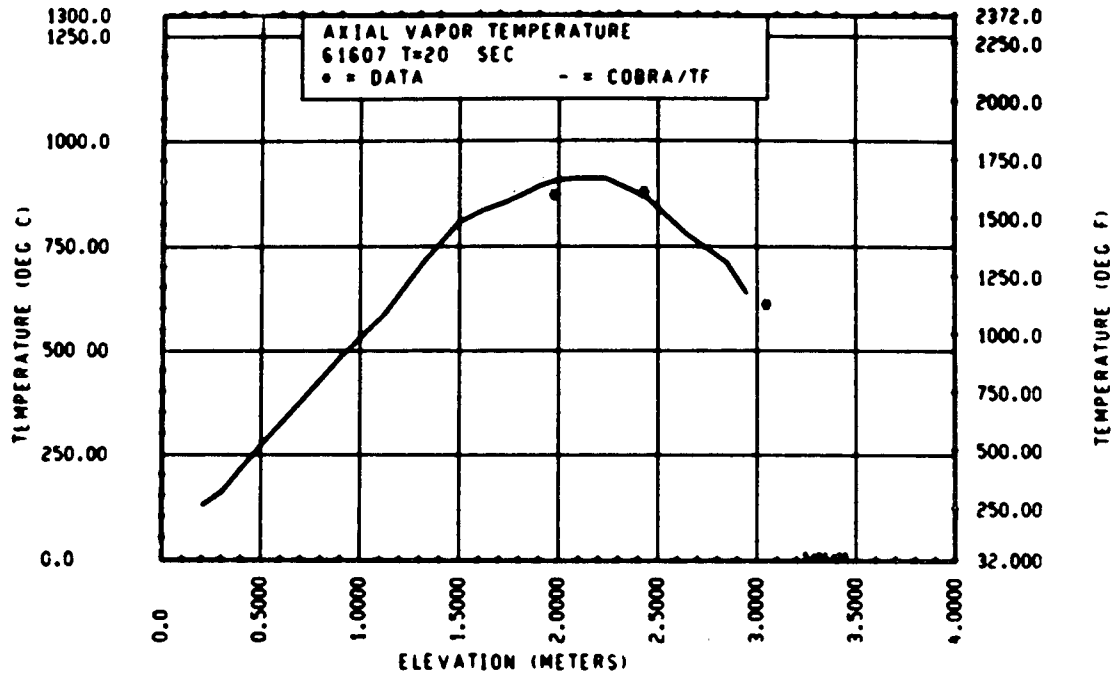

Figure 5-53. Comparison of COBRA-TF-Calculated Vapor Temperature Data Points Versus Blockage Zone Data Points, Test 61607, t = 20 Seconds

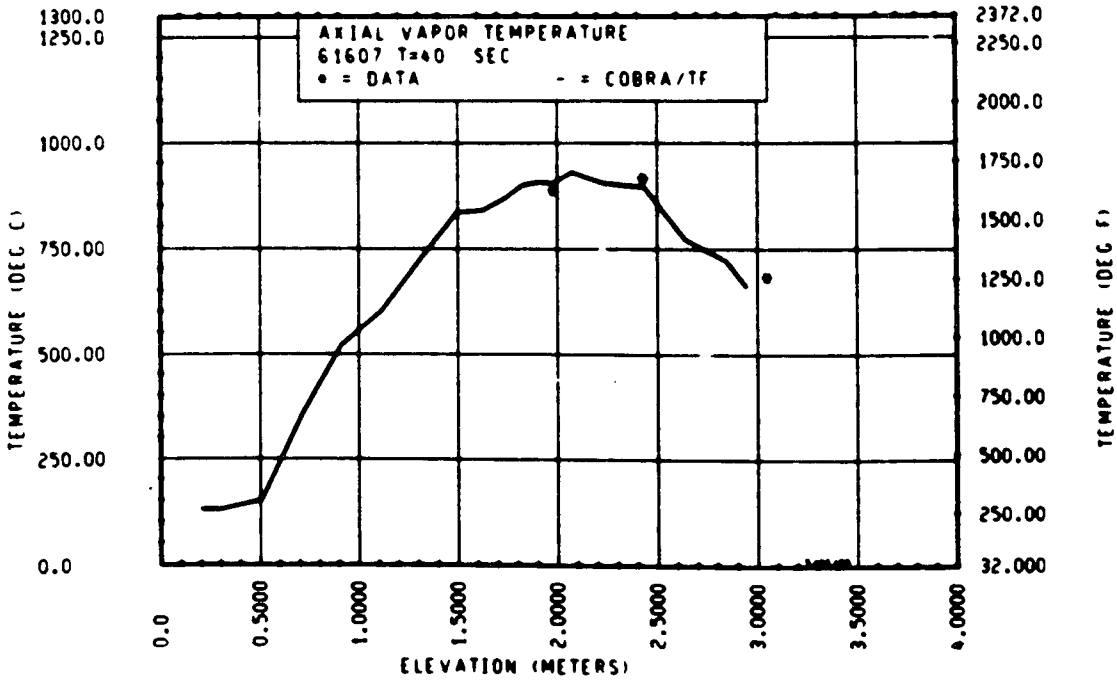

Figure 5-54. Comparison of COBRA-TF-Calculated Vapor Temperature Data Points Versus Blockage Zone Data Points, Test 61607, t = 40 Seconds

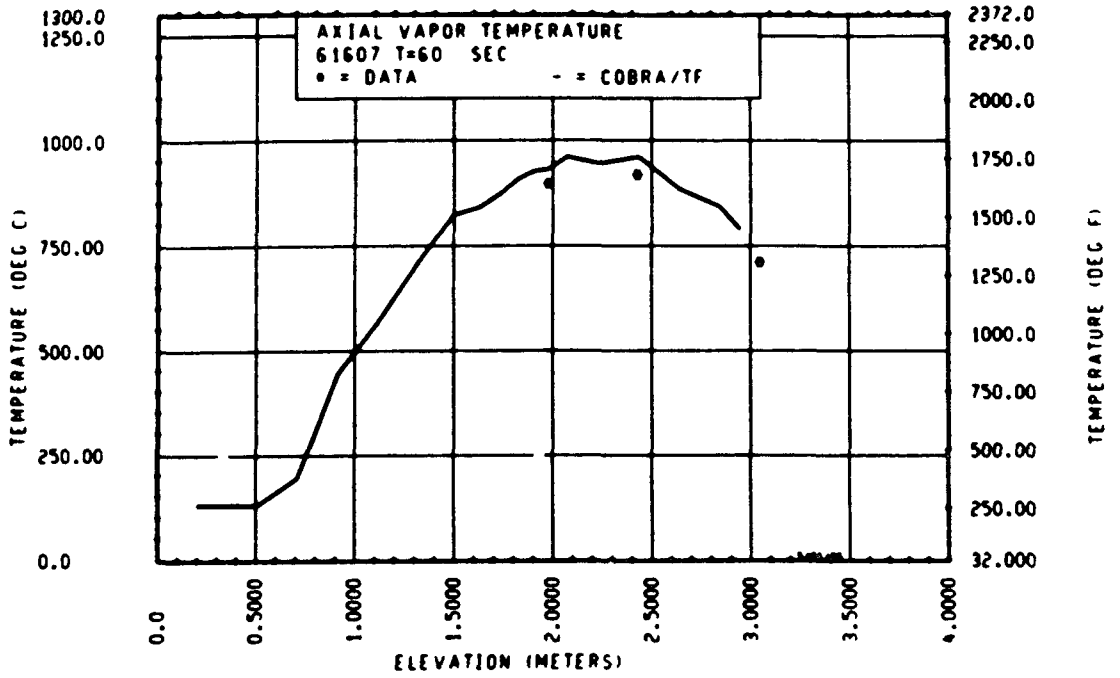

Figure 5-55. Comparison of COBRA-TF-Calculated Vapor Temperature Data Points Versus Blockage Zone Data Points, Test 61607, t = 60 Seconds

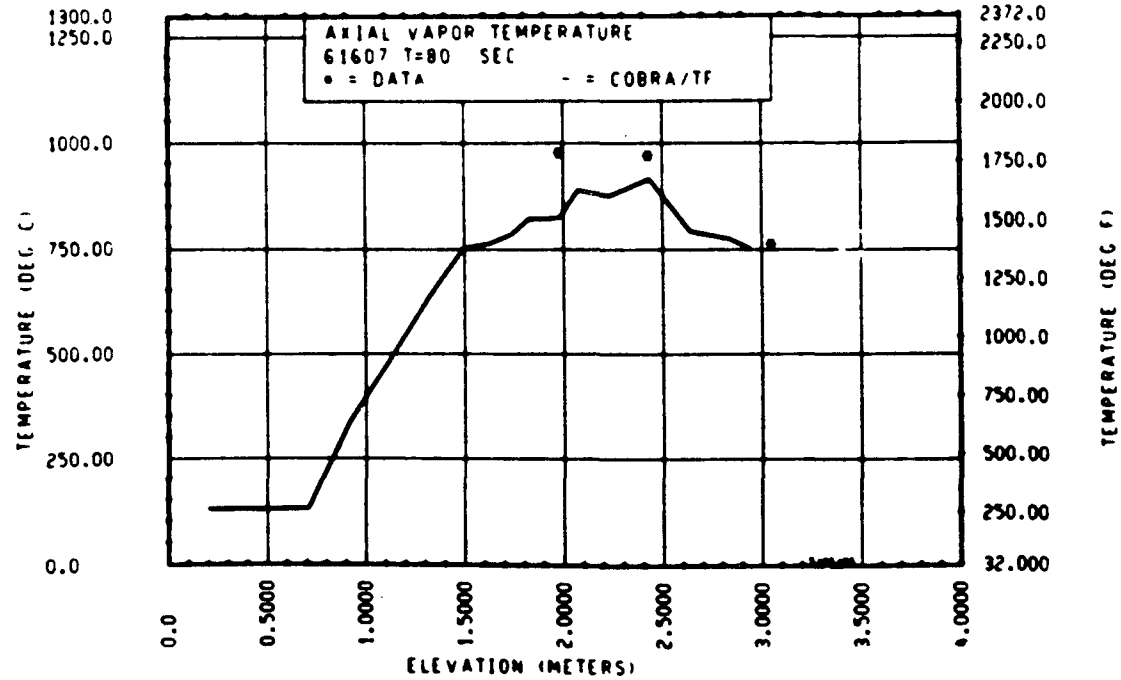

Figure 5-56. Comparison of COBRA-TF-Calculated Vapor Temperature Data Points Versus Blockage Zone Data Points, Test 61607, t = 80 seconds

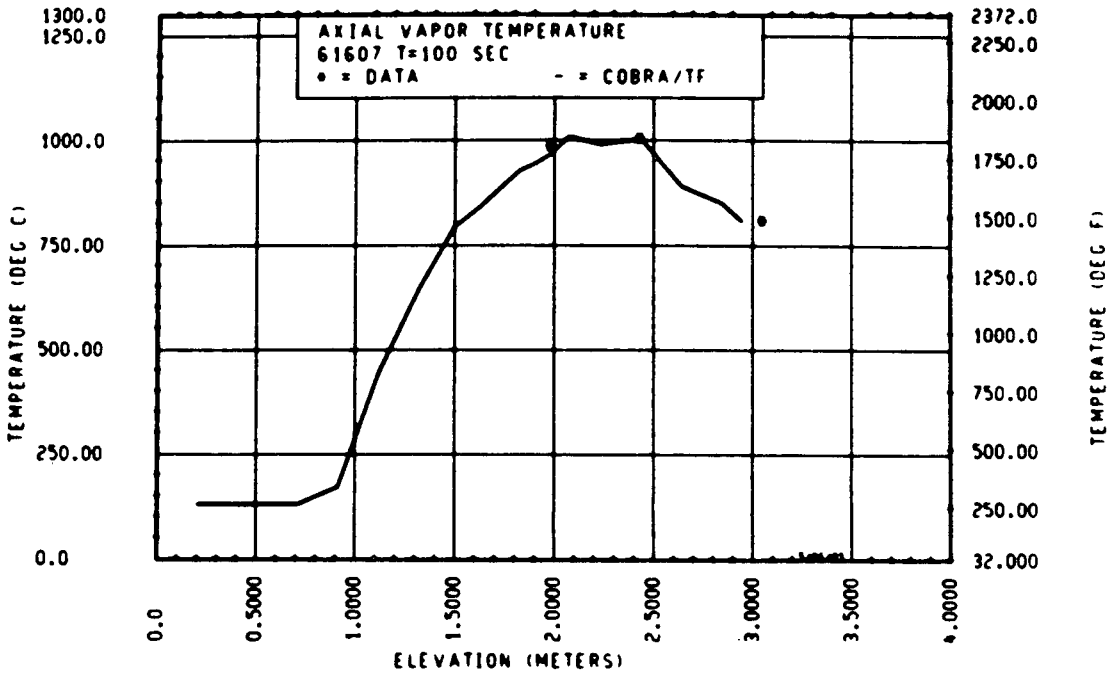

Figure 5-57. Comparison of COBRA-TF-Calculated Vapor Temperature Data Points Versus Blockage Zone Data Points, Test 61607, t = 100 Seconds

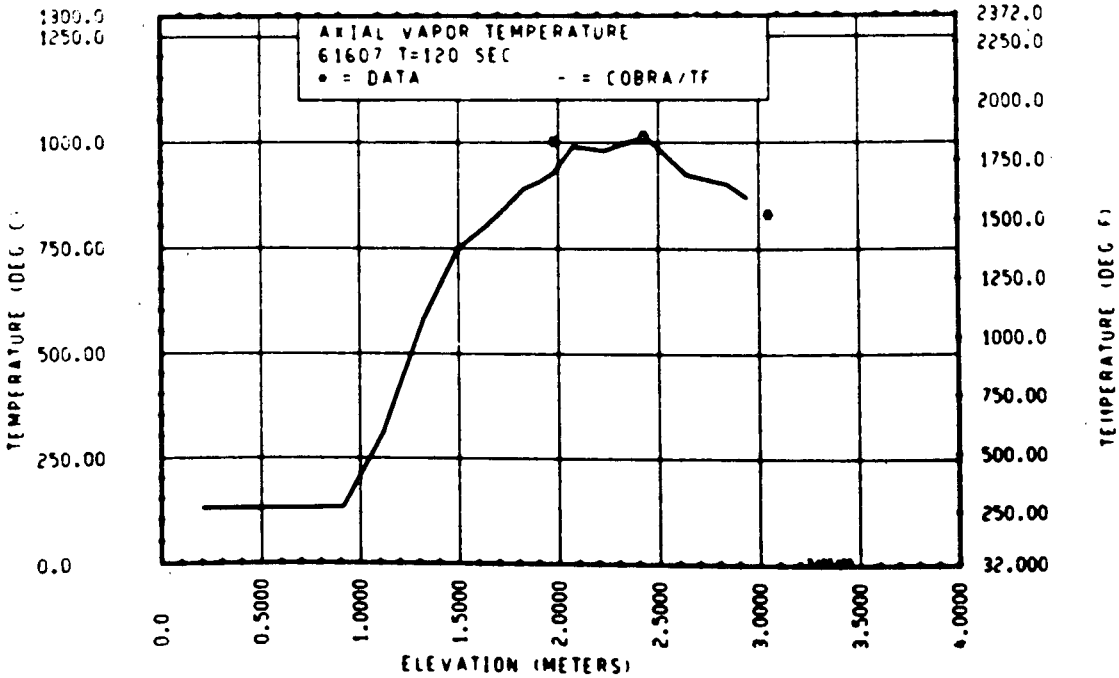

Figure 5-58. Comparison of COBRA-TF-Calculated Vapor Temperature Data Points Versus Blockage Zone Data Points, Test 61607, t = 120 Seconds

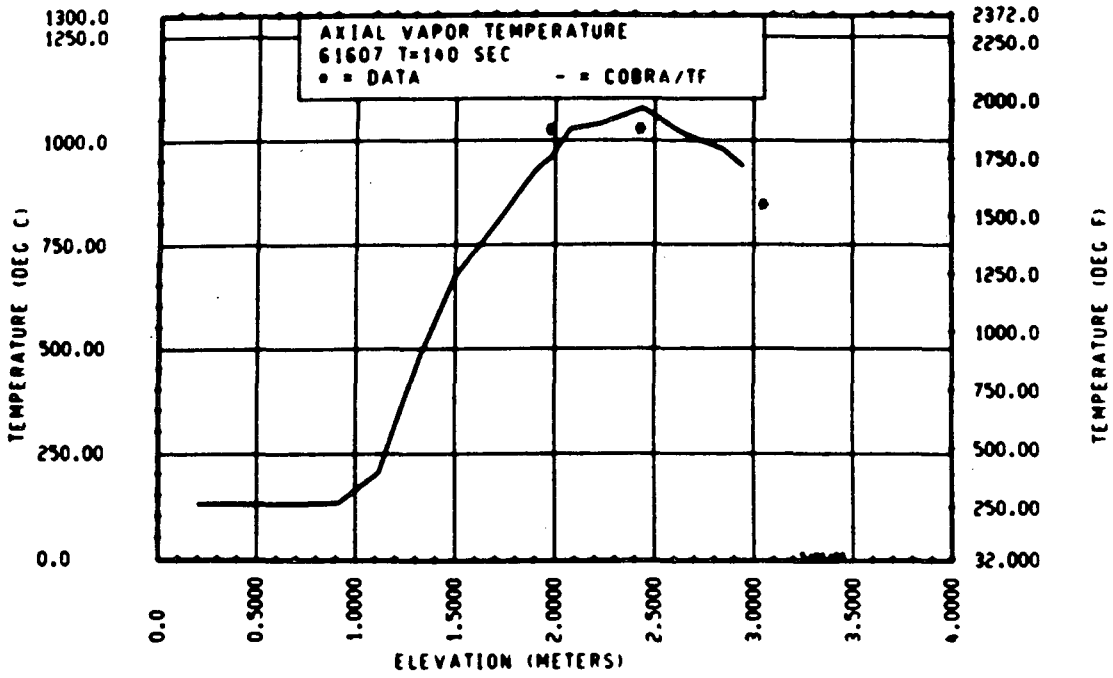

Figure 5-59. Comparison of COBRA-TF-Calculated Vapor Temperature Data Points Versus Blockage Zone Data Points, Test 61607, t = 140 Seconds

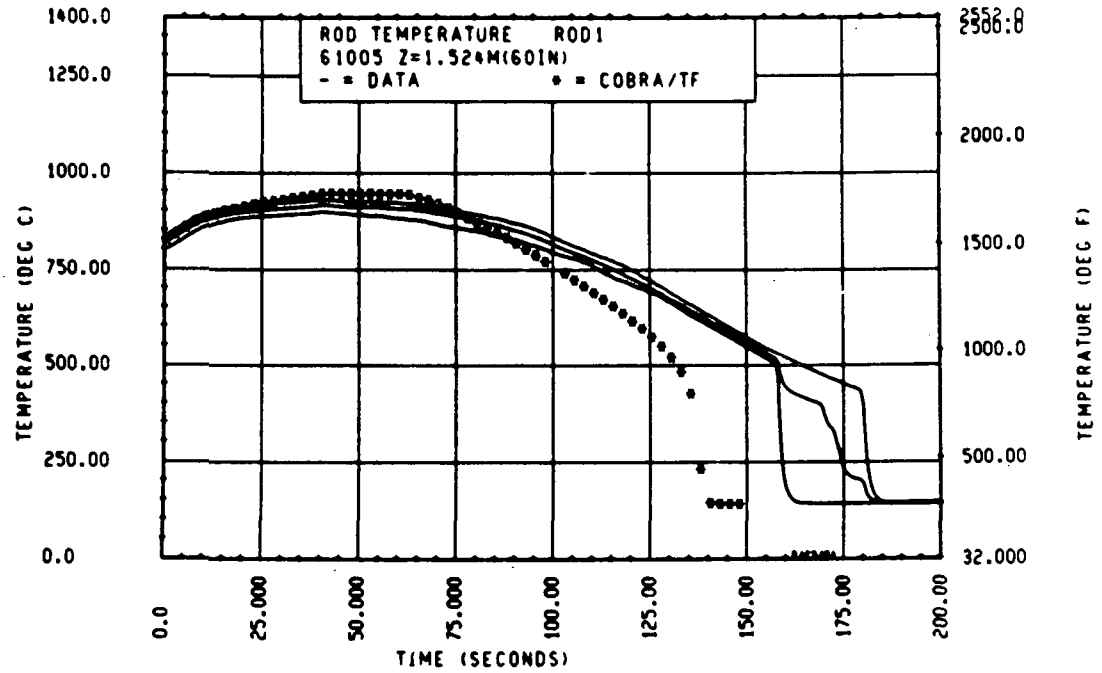

Figure 5-60. Comparison of COBRA-TF-Calculated Heater Rod Temperature Versus Time With FLECHT SEASET 163-Rod Data, Test 61005, 1.52 m (60 in.) Elevation, Rod 1

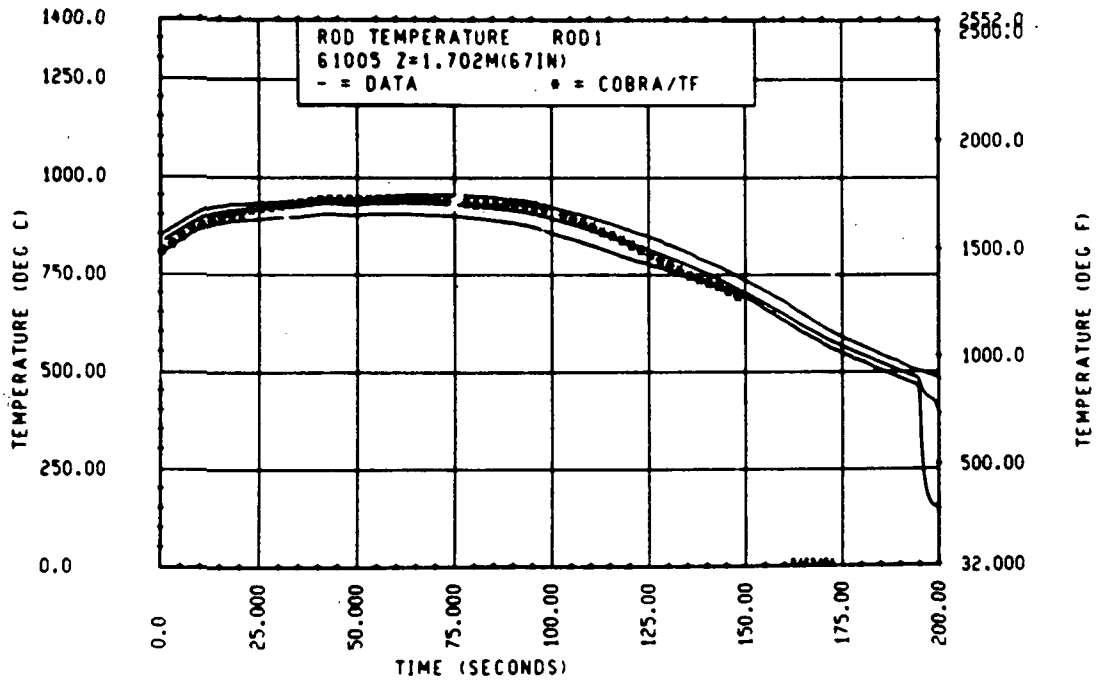

Figure 5-61. Comparison of COBRA-TF-Calculated Heater Rod Temperature Versus Time With FLECHT SEASET 163-Rod Data, Test 61005, 1.70 m (67 in.) Elevation, Rod 1

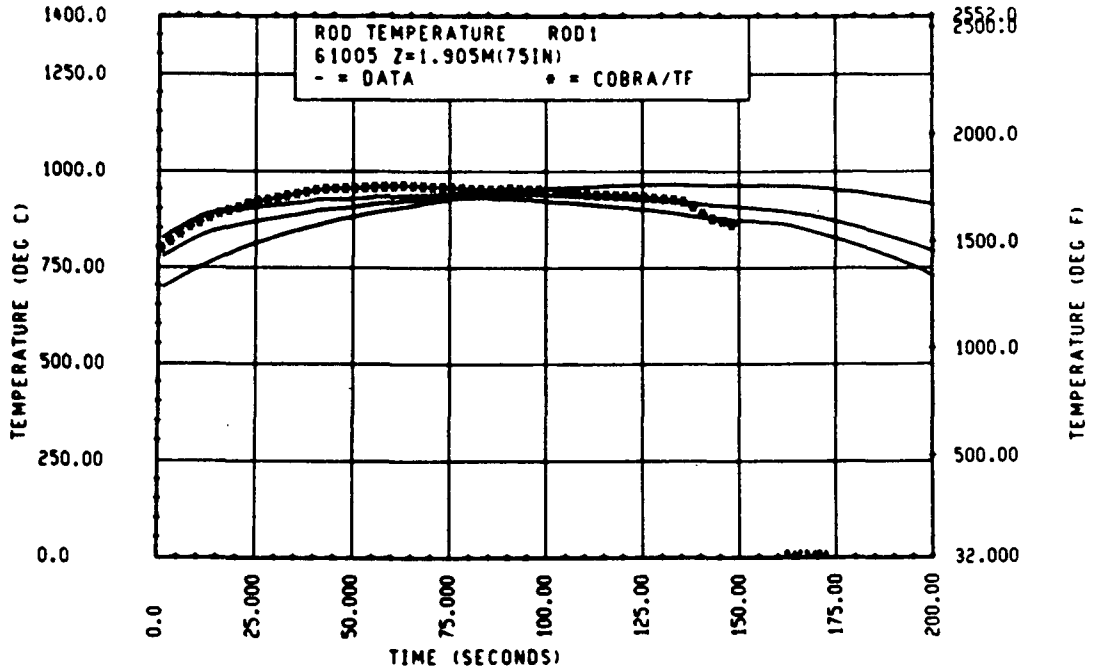

Figure 5-62. Comparison of COBRA-TF-Calculated Heater Rod Temperature Versus Time With FLECHT SEASET 163-Rod Data, Test 61005, 1.90 m (75 in.) Elevation, Rod 1

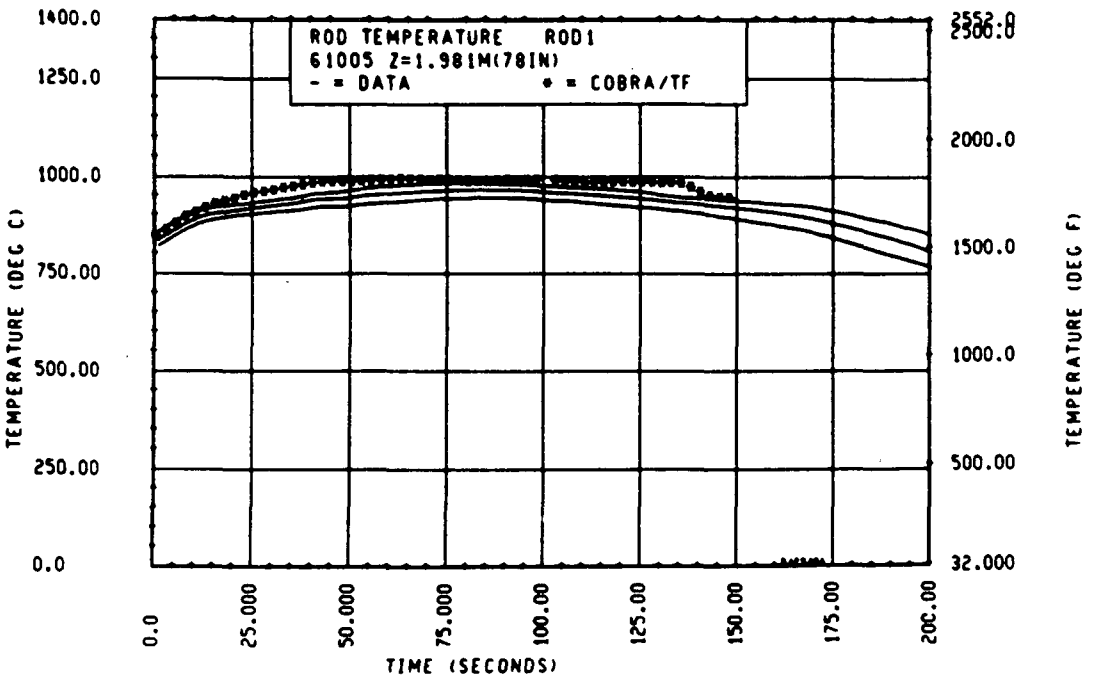

Figure 5-63. Comparison of COBRA-TF-Calculated Heater Rod Temperature Versus Time With FLECHT SEASET 163-Rod Data, Test 61005, 1.98 m (78 in.) Elevation, Rod 1

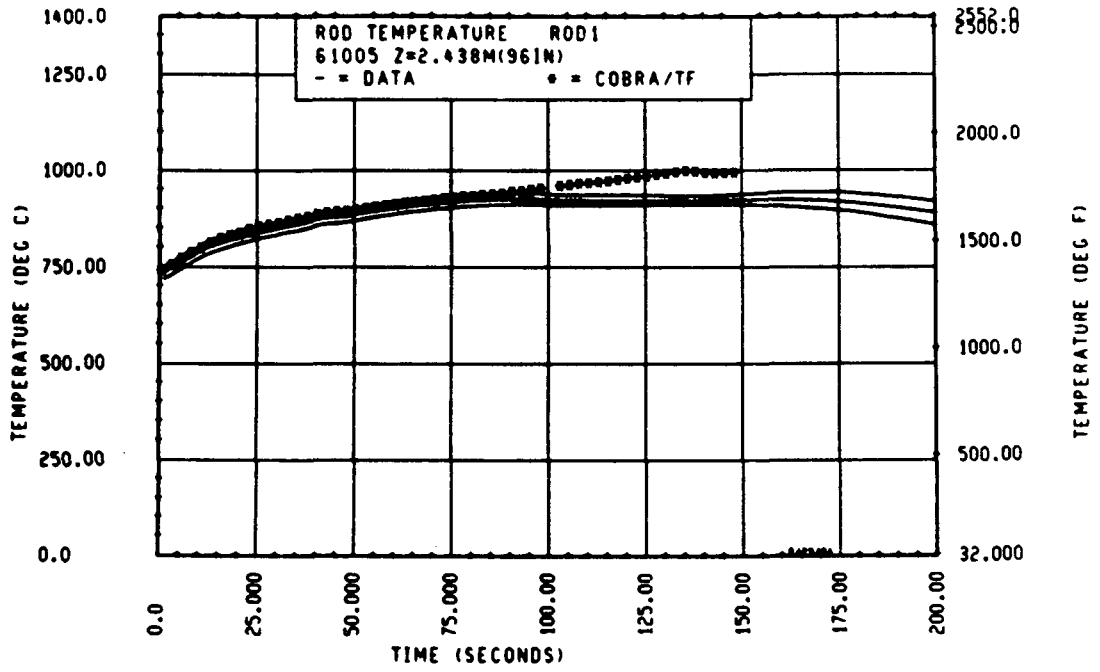

Figure 5-64. Comparison of COBRA-TF-Calculated Heater Rod Temperature Versus Time With FLECHT SEASET 163-Rod Data, Test 61005, 2.44 m (96 in.) Elevation, Rod 1

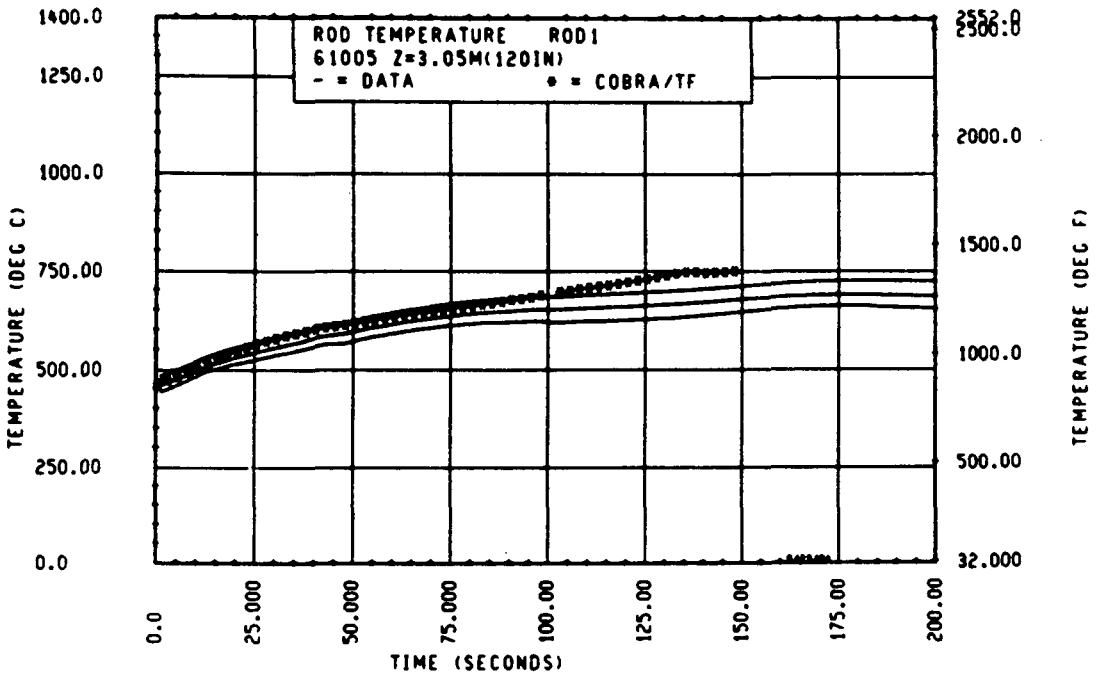

Figure 5-65. Comparison of COBRA-TF-Calculated Heater Rod Temperature Versus Time With FLECHT SEASET 163-Rod Data, Test 61005, 3.05 m (120 in.) Elevation, Rod 1

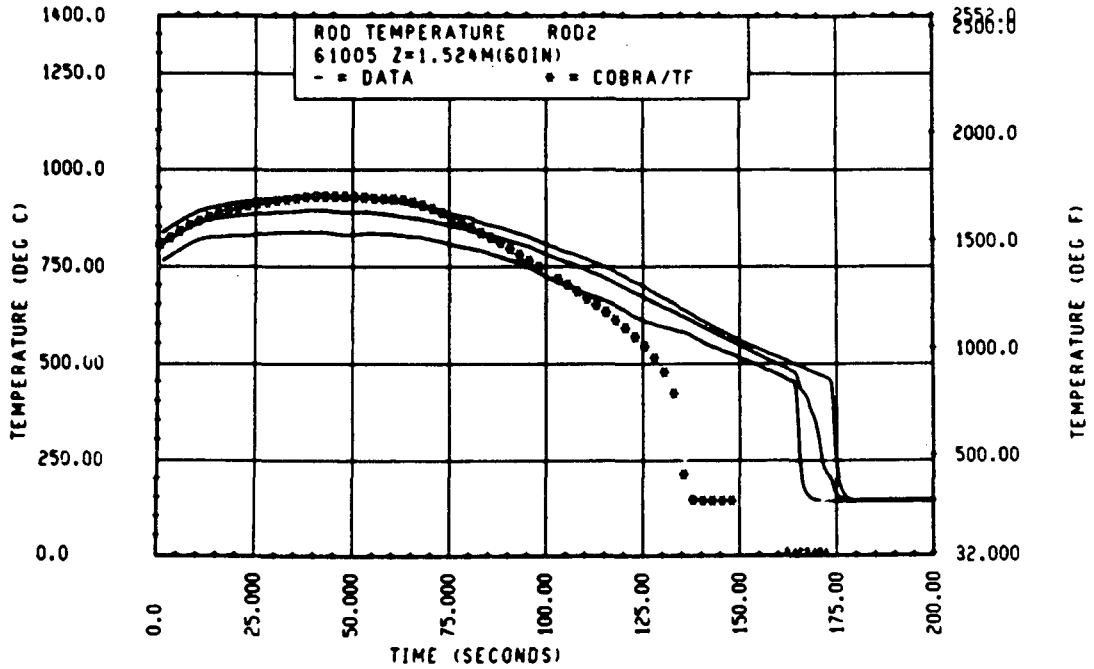

Figure 5-66. Comparison of COBRA-TF-Calculated Heater Rod Temperature Versus Time With FLECHT SEASET 163-Rod Data, Test 61005, 1.52 m (60 in.) Elevation, Rod 2

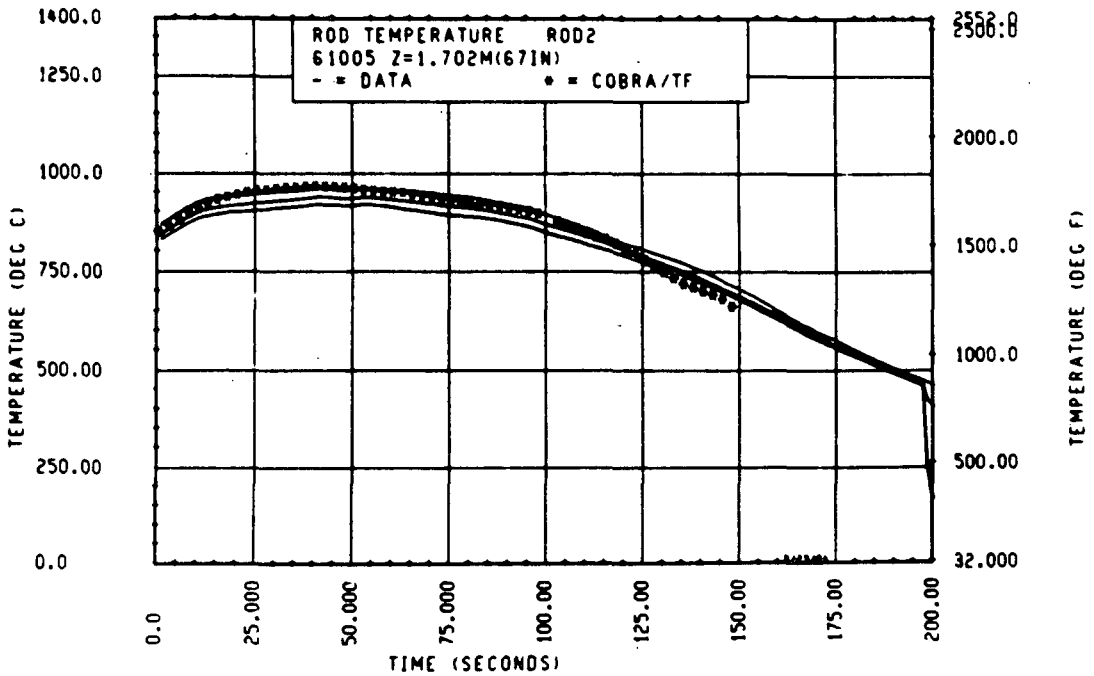

Figure 5-67. Comparison of COBRA-TF-Calculated Heater Rod Temperature Versus Time With FLECHT SEASET 163-Rod Data, Test 61005, 1.70 m (67 in.) Elevation, Rod 2

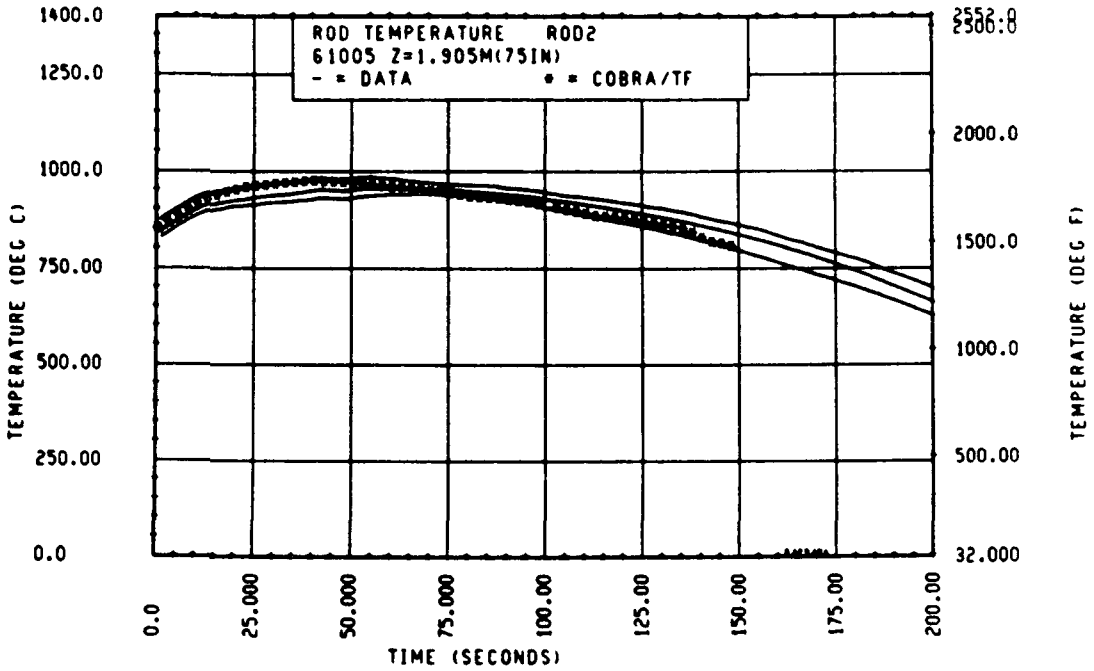

Figure 5-68. Comparison of COBRA-TF-Calculated Heater Rod Temperature Versus Time With FLECHT SEASET 163-Rod Data, Test 61005, 1.90 m (75 in.) Elevation, Rod 2

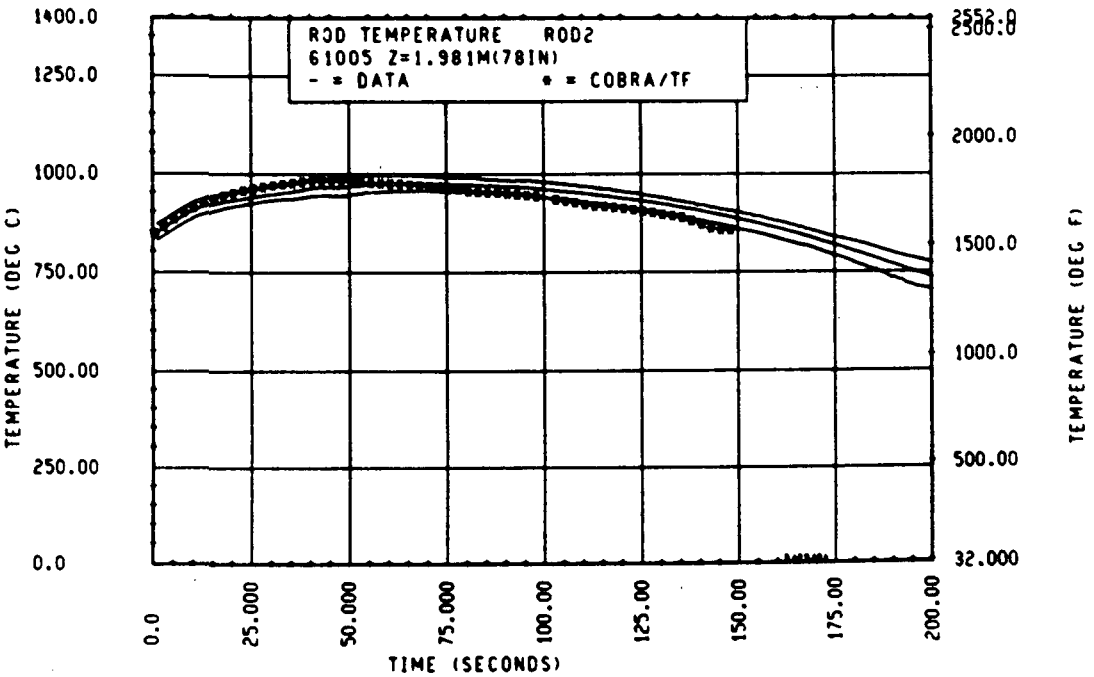

Figure 5-69. Comparison of COBRA-TF-Calculated Heater Rod Temperature Versus Time With FLECHT SEASET 163-Rod Data, Test 61005, 1.98 m (78 in.) Elevation, Rod 2

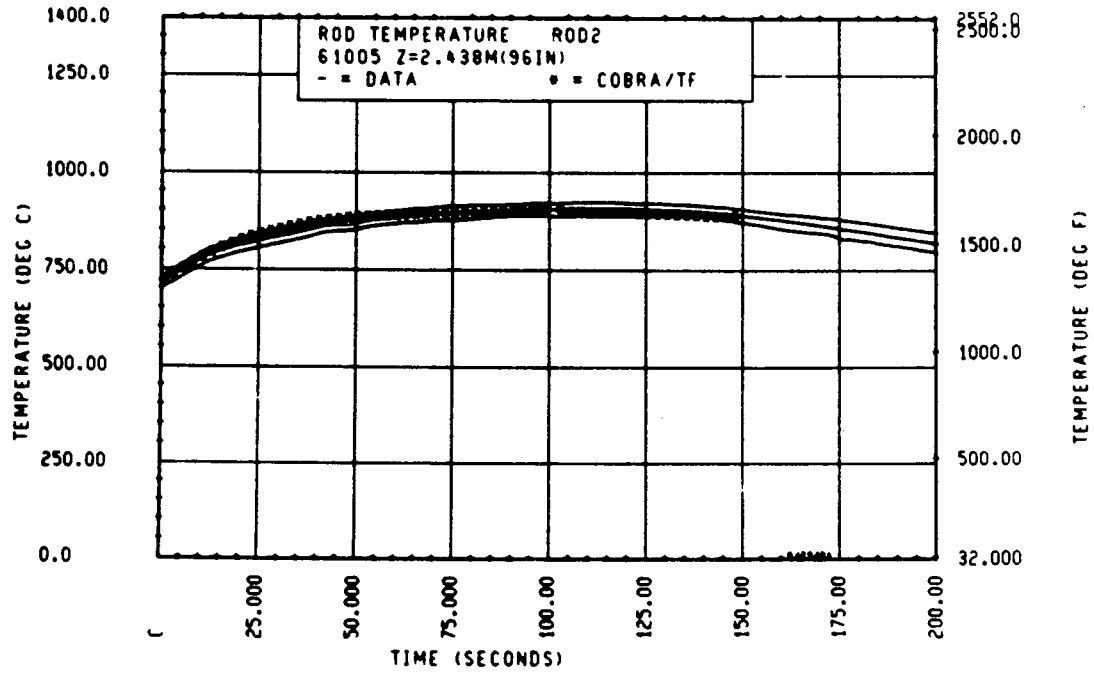

Figure 5-70. Comparison of COBRA-TF-Calculated Heater Rod Temperature Versus Time With FLECHT SEASET 163-Rod Data, Test 61005, 2.44 m (96 in.) Elevation, Rod 2

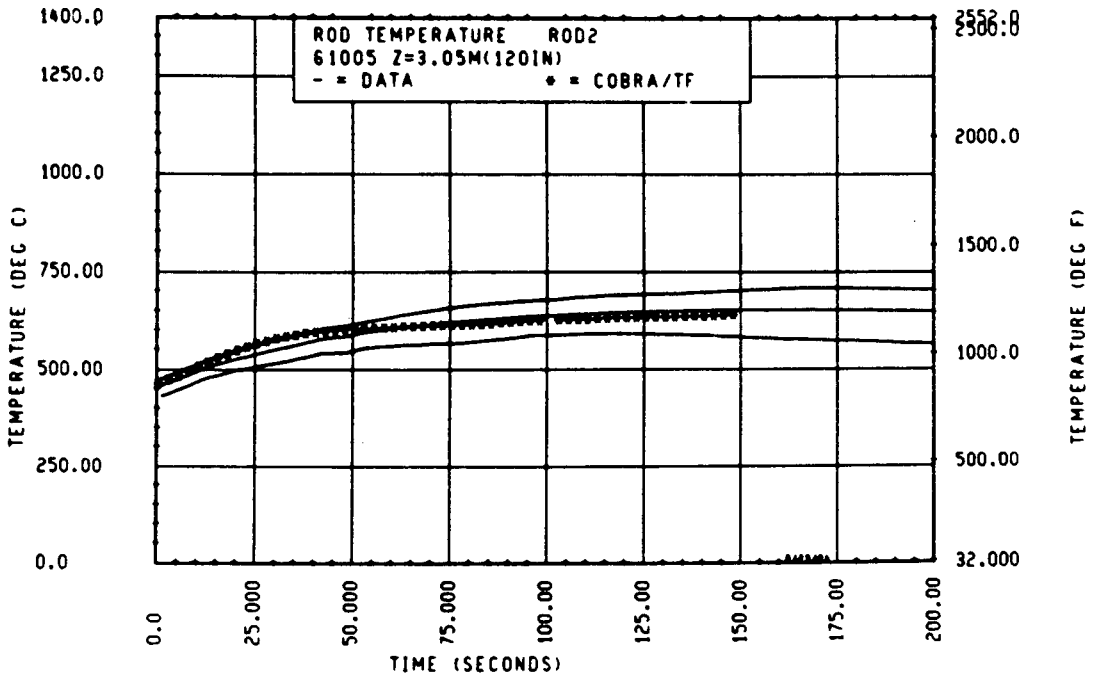

Figure 5-71. Comparison of COBRA-TF-Calculated Heater Rod Temperature Versus Time With FLECHT SEASET 163-Rod Data, Test 61005, 3.05 m (120 in.) Elevation, Rod 2

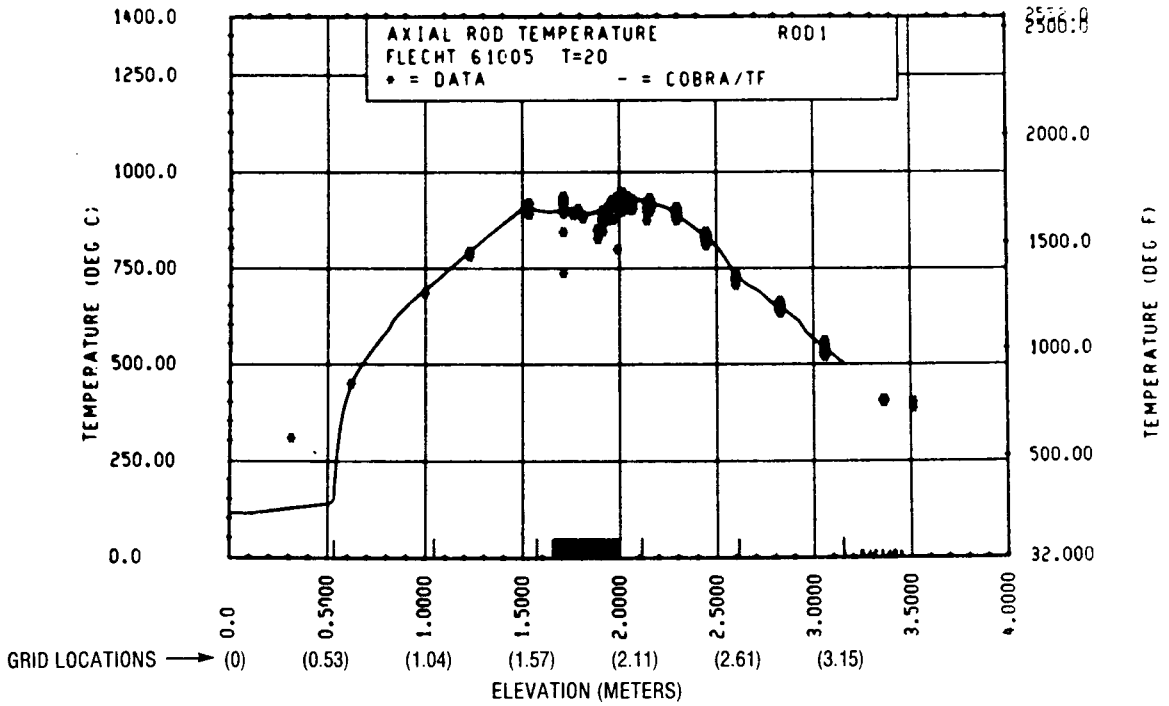

Figure 5-72. Comparison of COBRA-TF-Calculated Axial Rod Temperature Versus Elevation With FLECHT SEASET 163-Rod Data, Test 61005, t = 20 Seconds, Rod 1

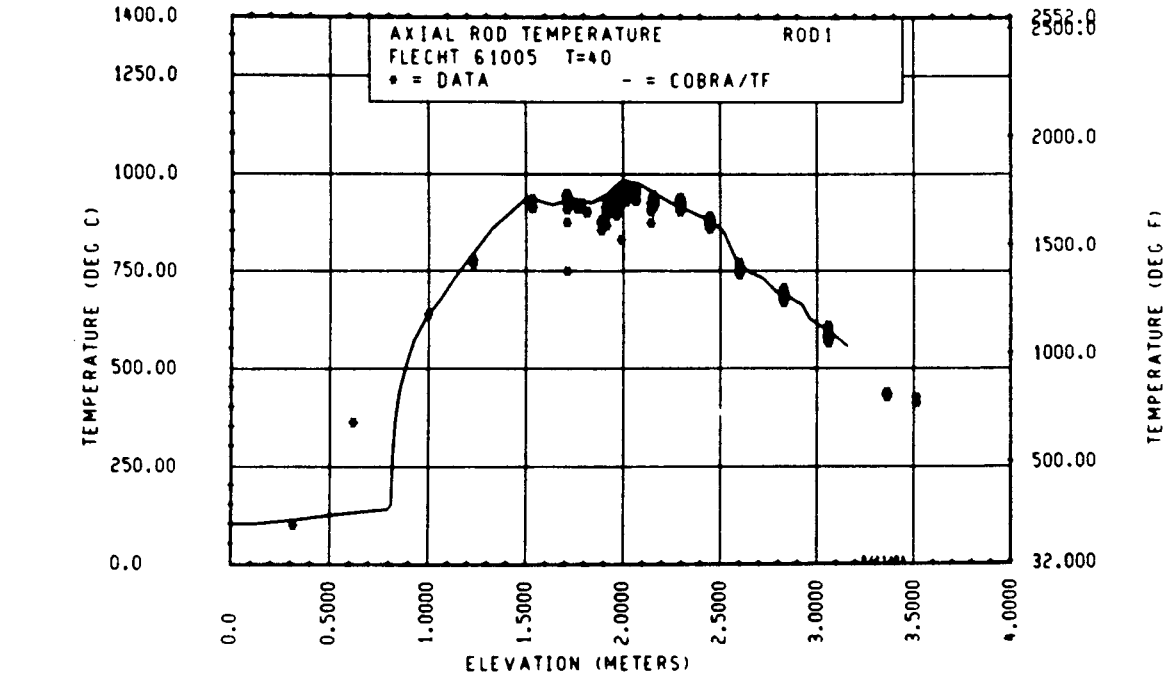

Figure 5-73. Comparison of COBRA-TF-Calculated Axial Rod Temperature Versus Elevation With FLECHT SEASET 163-Rod Data, Test 61005, t = 40 Seconds, Rod 1

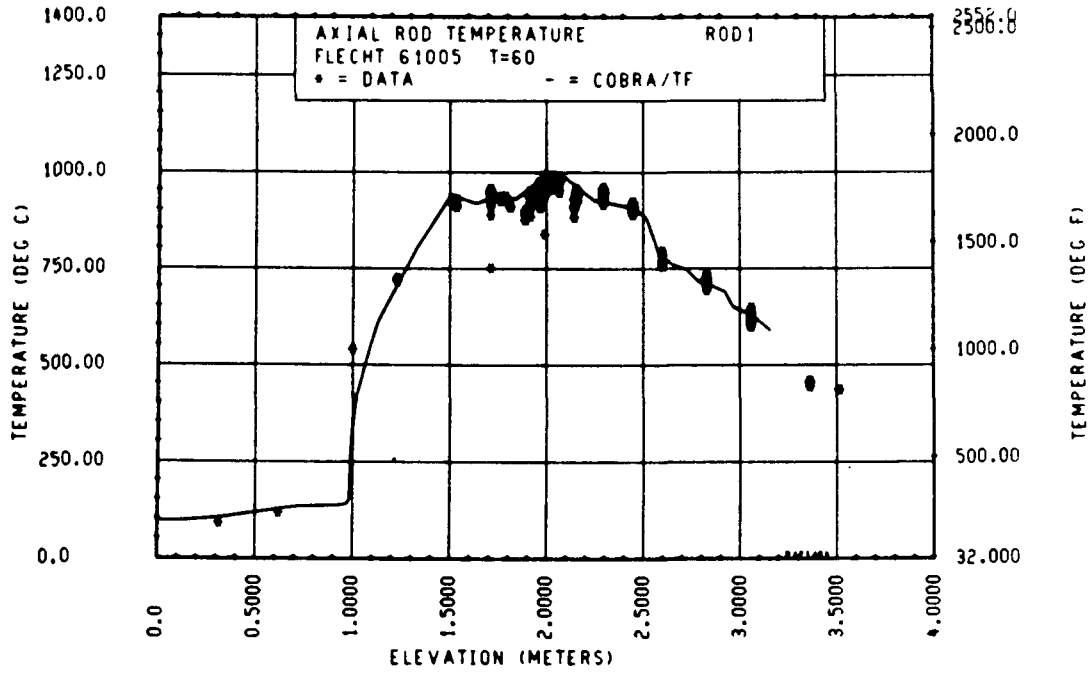

Figure 5-74. Comparison of COBRA-TF-Calculated Axial Rod Temperature Versus Elevation With FLECHT SEASET 163-Rod Data, Test 61005, t = 60 Seconds, Rod 1

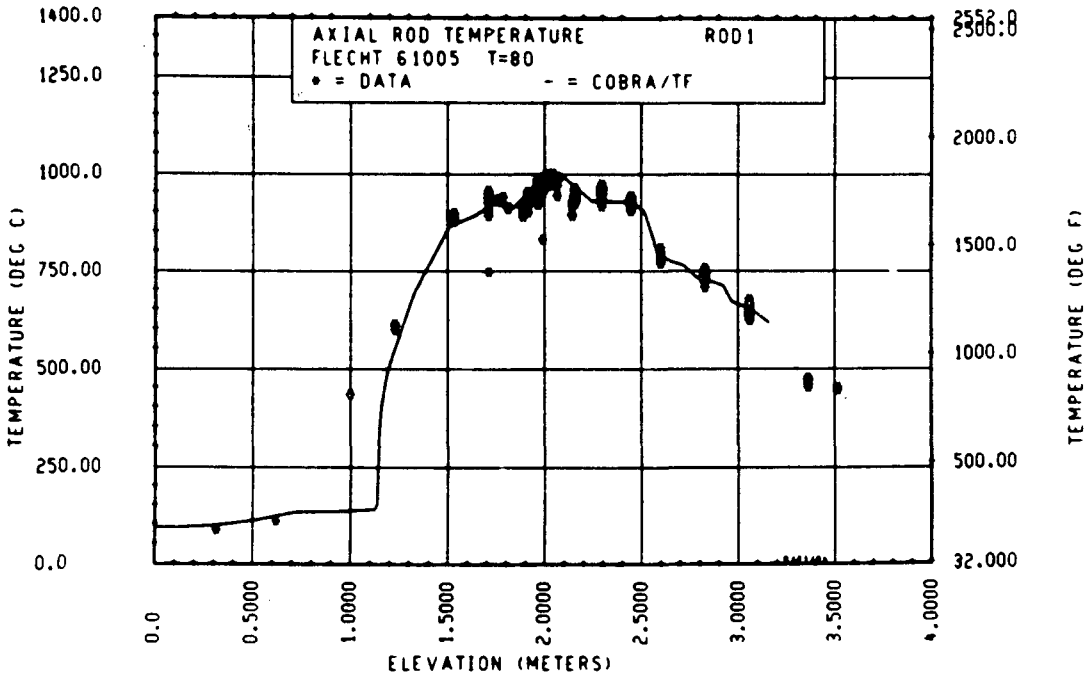

Figure 5-75. Comparison of COBRA-TF-Calculated Axial Rod Temperature Versus Elevation With FLECHT SEASET 163-Rod Data, Test 61005, t = 80 Seconds, Rod 1

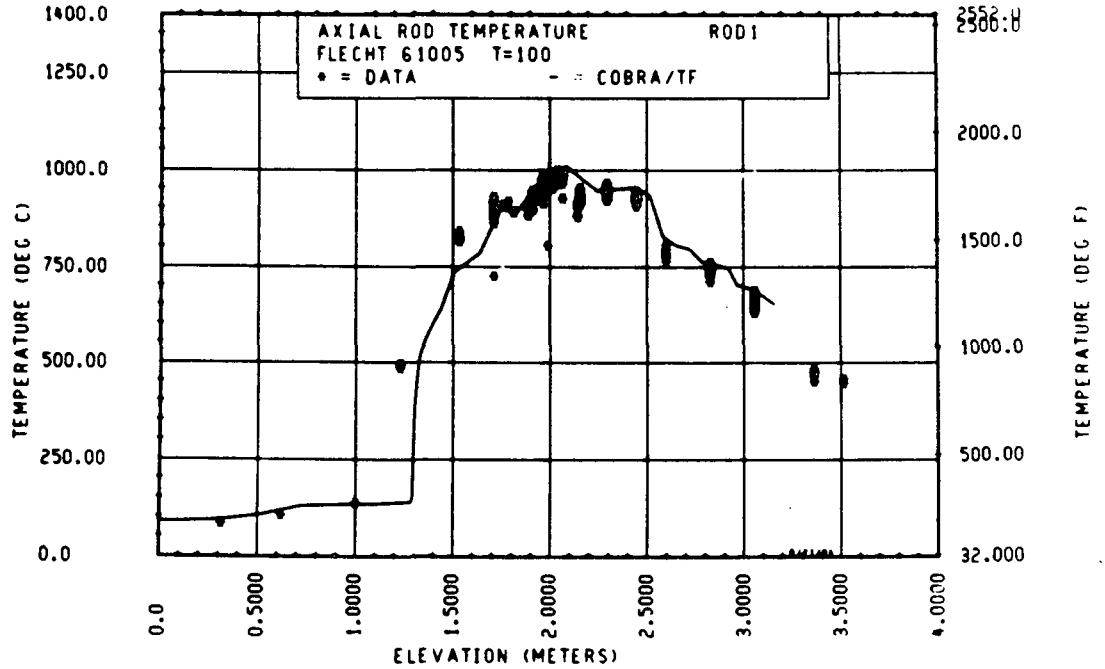

Figure 5-76. Comparison of COBRA-TF-Calculated Axial Rod Temperature Versus Elevation With FLECHT SEASET 163-Rod Data, Test 61005, t = 100 Seconds, Rod 1

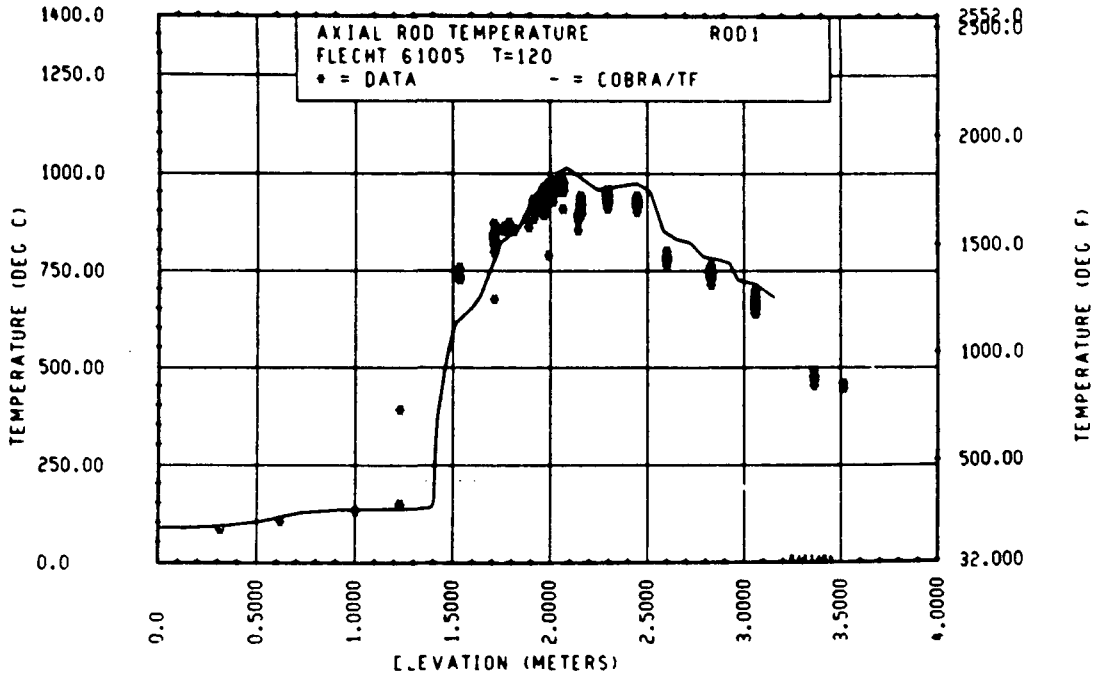

Figure 5-77. Comparison of COBRA-TF-Calculated Axial Rod Temperature Versus Elevation With FLECHT SEASET 163-Rod Data, Test 61005, t = 120 Seconds, Rod 1

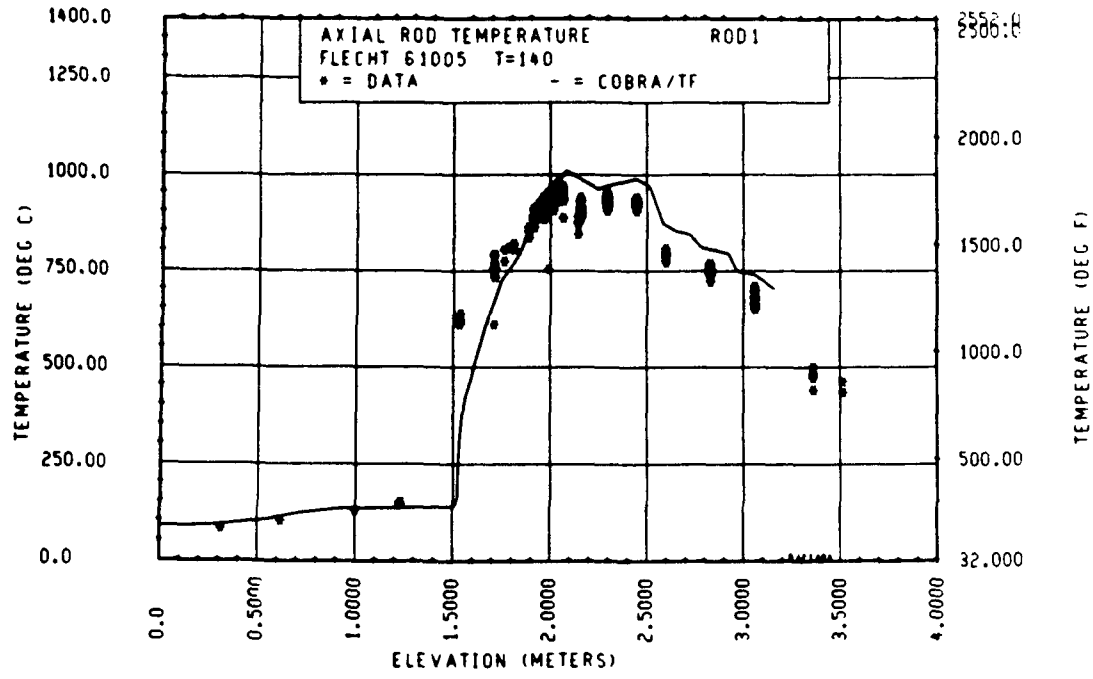

Figure 5-78. Comparison of COBRA-TF-Calculated Axial Rod Temperature Versus Elevation With FLECHT SEASET 163-Rod Data, Test 61005, t = 140 Seconds, Rod 1

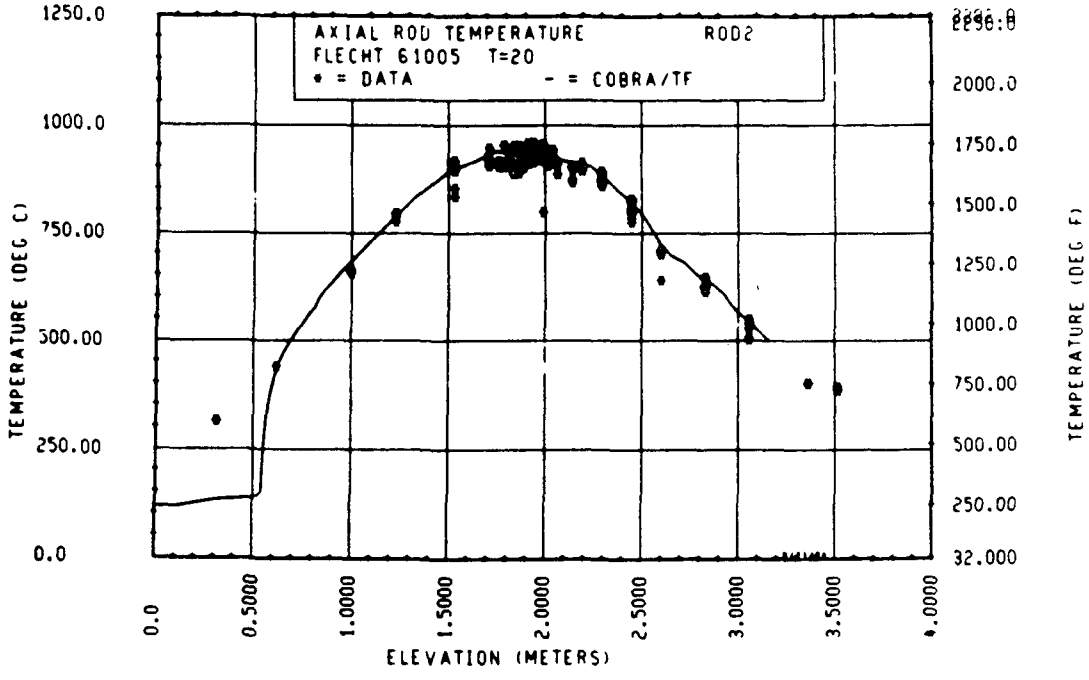

Figure 5-79. Comparison of COBRA-TF-Calculated Axial Rod Temperature Versus Elevation With FLECHT SEASET 163-Rod Data, Test 61005, t = 20 Seconds, Rod 2

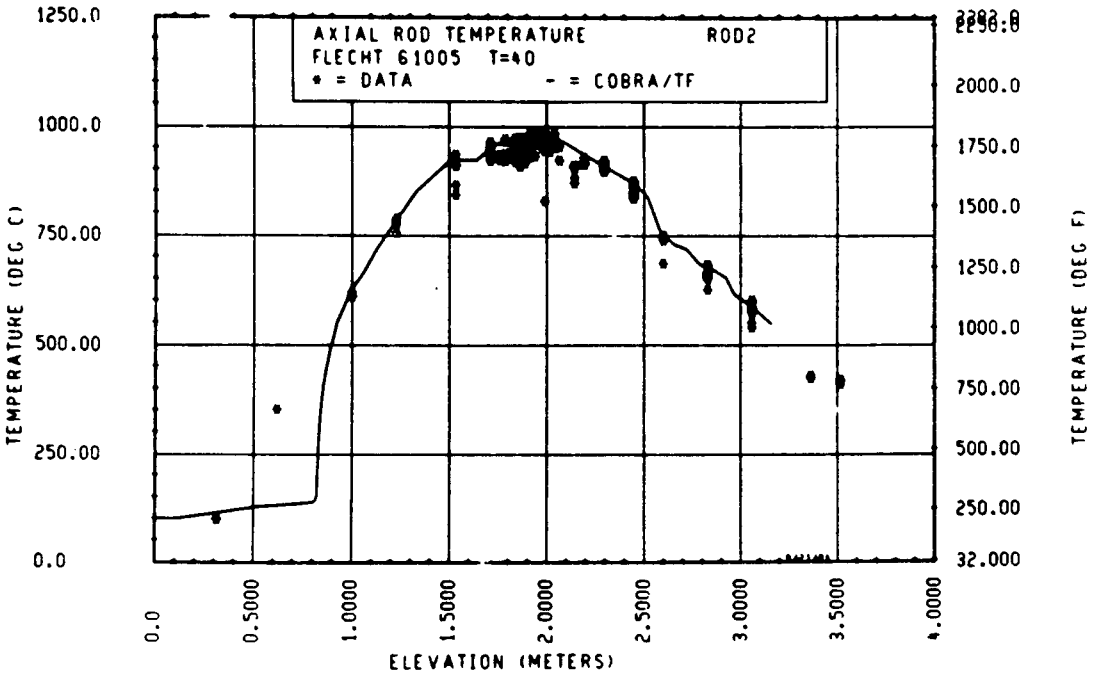

Figure 5-80. Comparison of COBRA-TF-Calculated Axial Rod Temperature Versus Elevation With FLECHT SEASET 163-Rod Data, Test 61005, t = 40 Seconds, Rod 2

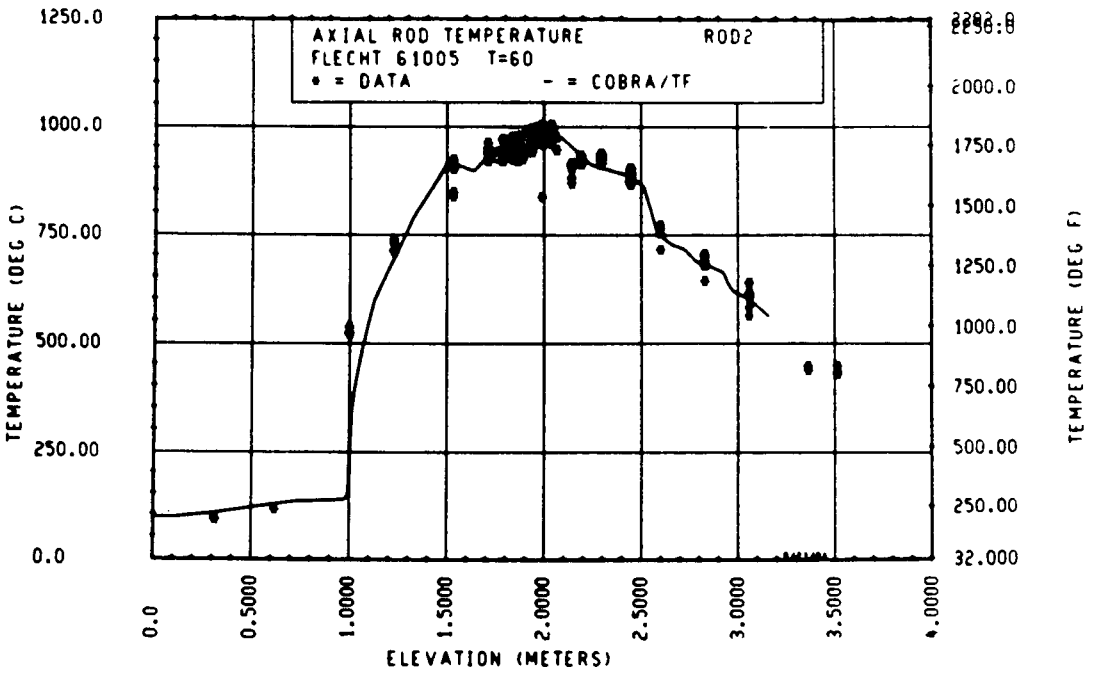

Figure 5-81. Comparison of COBRA-TF-Calculated Axial Rod Temperature Versus Elevation With FLECHT SEASET 163-Rod Data, Test 61005, t = 60 Seconds, Rod 2

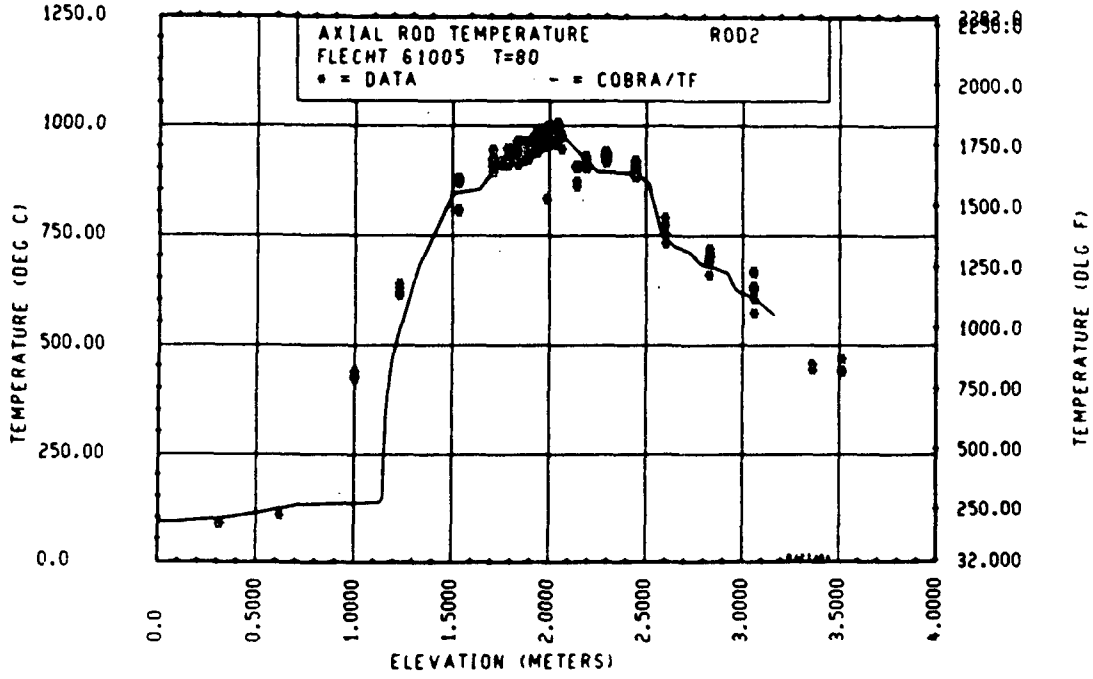

Figure 5-82. Comparison of COBRA-TF-Calculated Axial Rod Temperature Versus Elevation With FLECHT SEASET 163-Rod Data, Test 61005, t = 80 Seconds, Rod 2

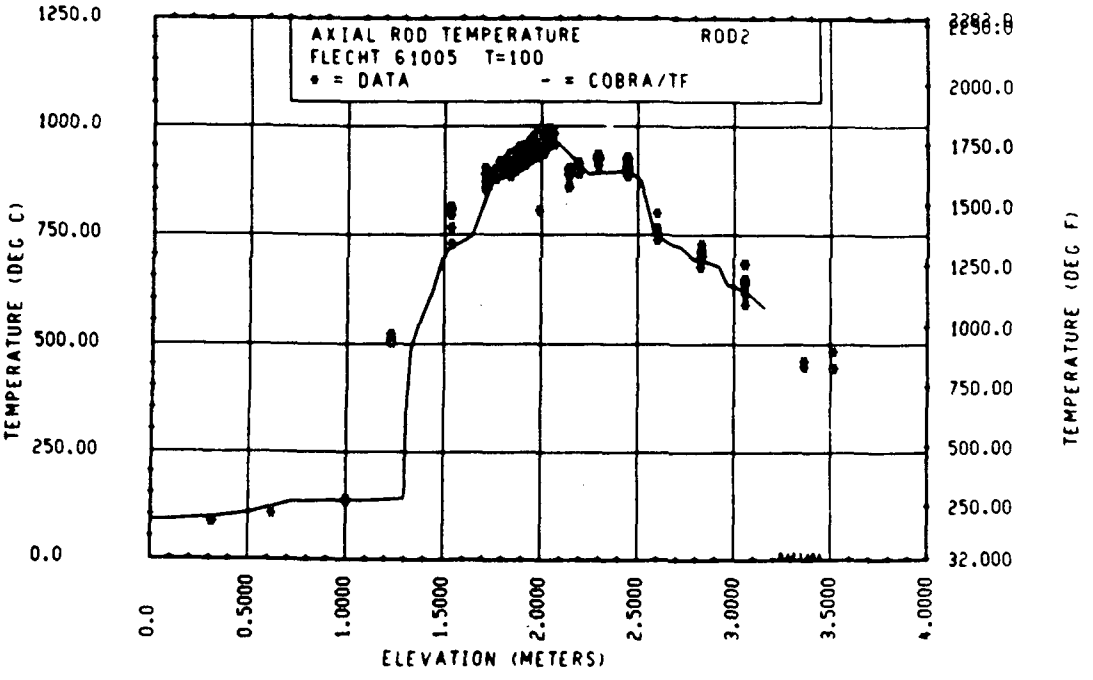

Figure 5-83. Comparison of COBRA-TF-Calculated Axial Rod Temperature Versus Elevation With FLECHT SEASET 163-Rod Data, Test 61005, t = 100 Seconds, Rod 2

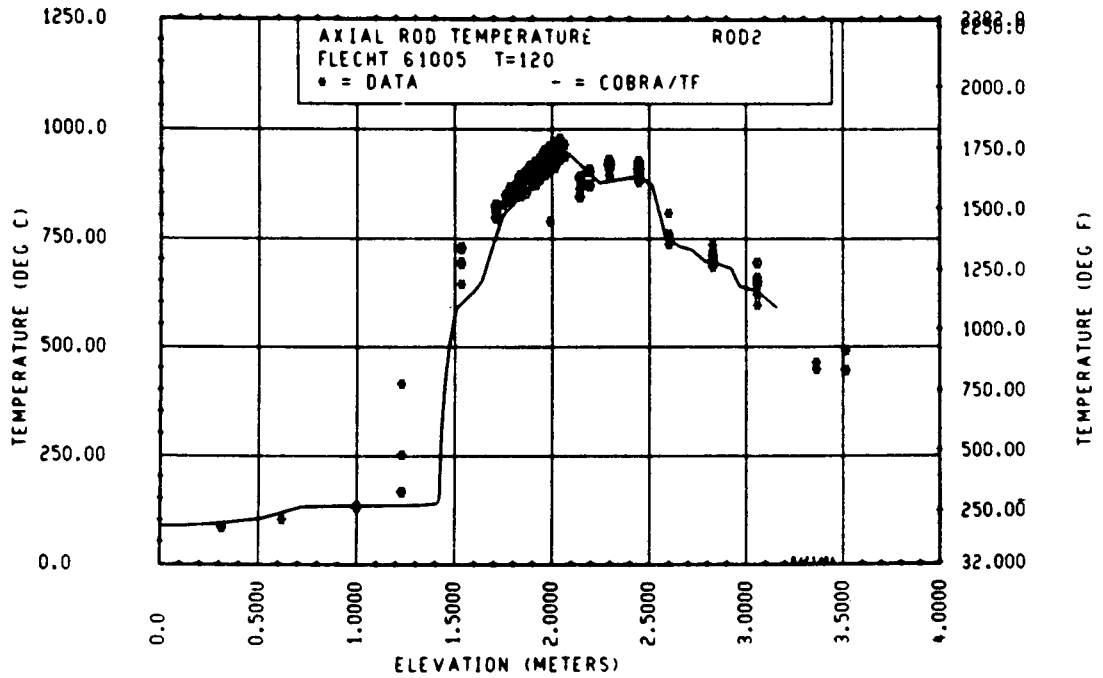

Figure 5-84. Comparison of COBRA-TF-Calculated Axial Rod Temperature Versus Elevation With FLECHT SEASET 163-Rod Data, Test 61005, t = 120 Seconds, Rod 2

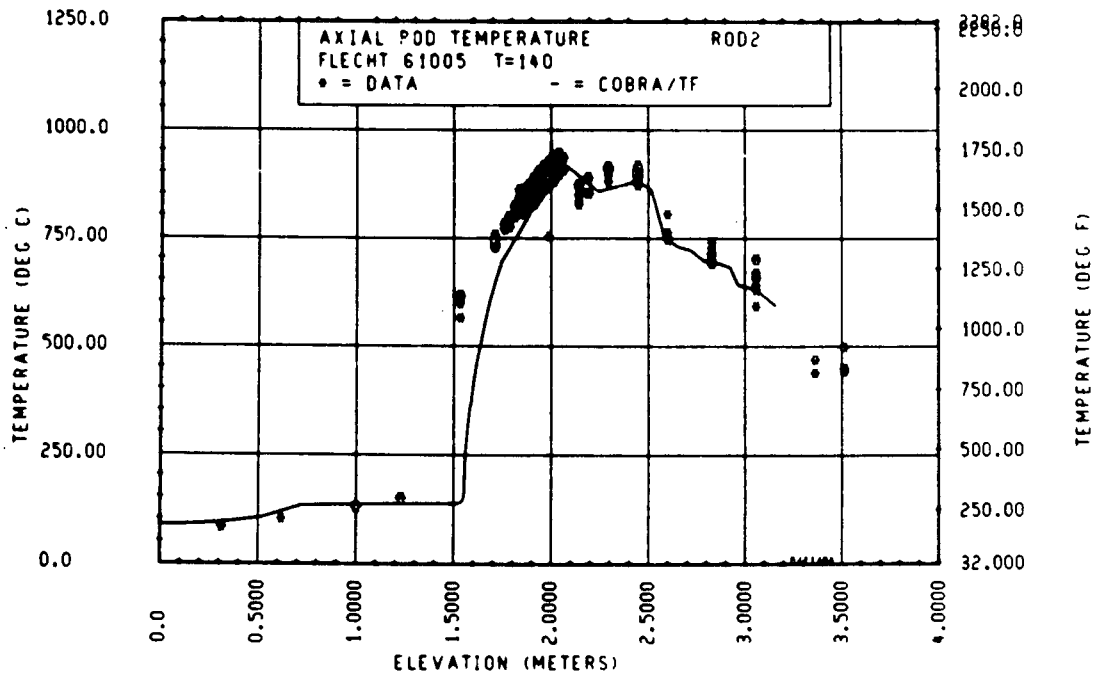

Figure 5-85. Comparison of COBRA-TF-Calculated Axial Rod Temperature Versus Elevation With FLECHT SEASET 163-Rod Data, Test 61005, t = 140 Seconds, Rod 2

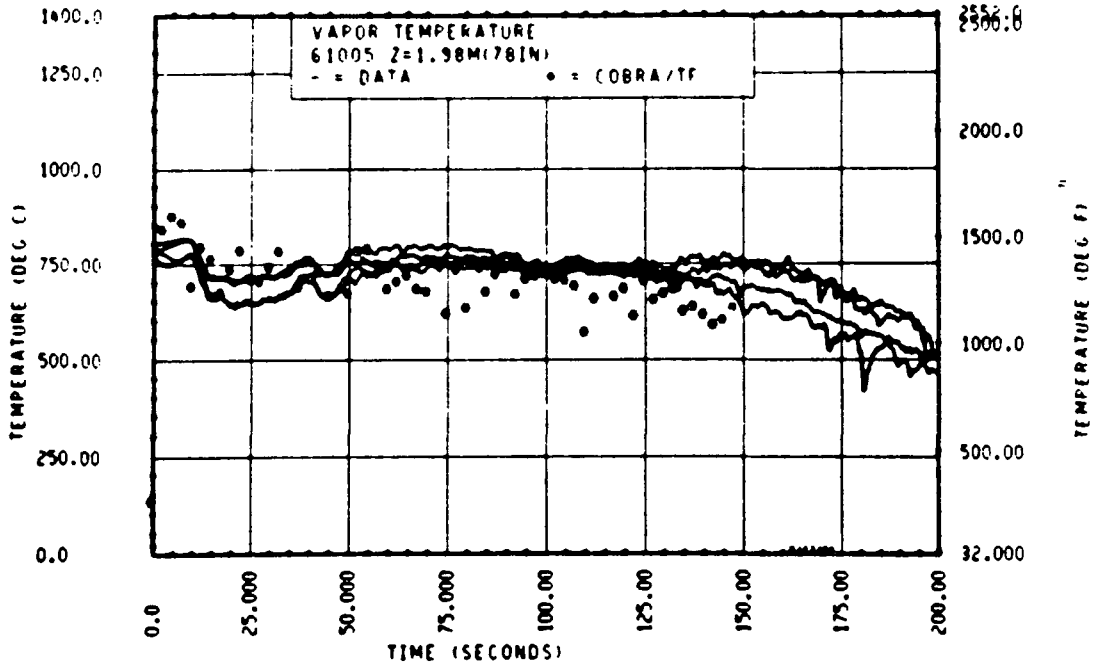

Figure 5-86. Comparison of COBRA-TF-Calculated Vapor Temperature Versus Time With FLECHT SEASET 163-Rod Data, Test 61005, 1.98 m (78 in.) Elevation

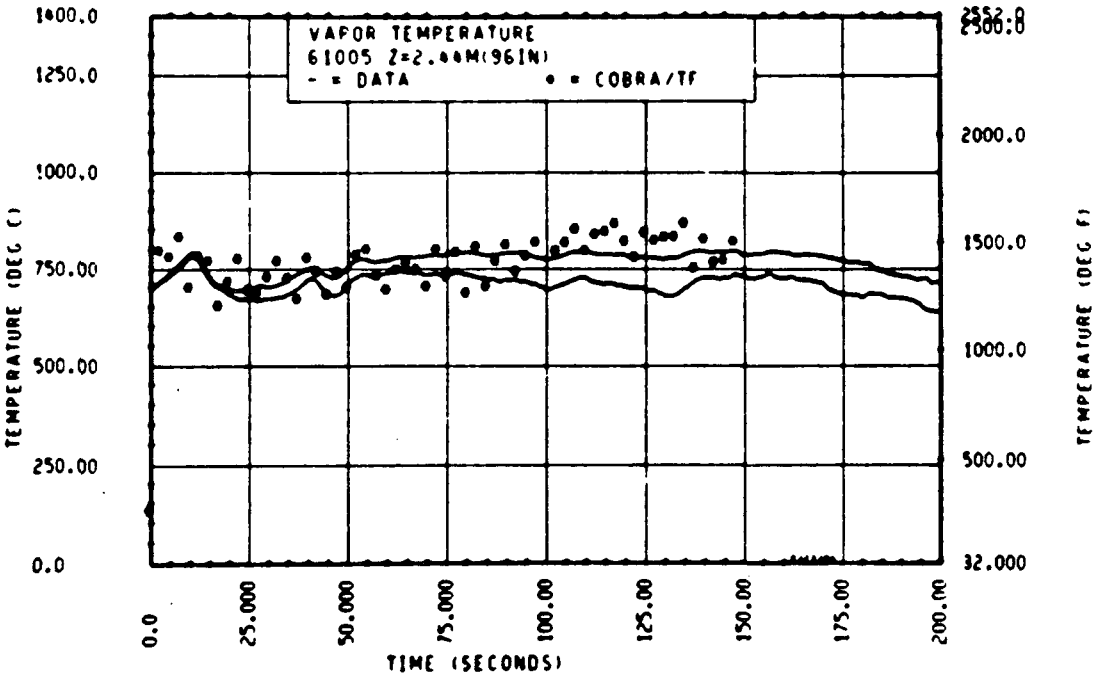

Figure 5-87. Comparison of COBRA-TF-Calculated Vapor Temperature Versus Time With FLECHT SEASET 163-Rod Data, Test 61005, 2.44 m (96 in.) Elevation

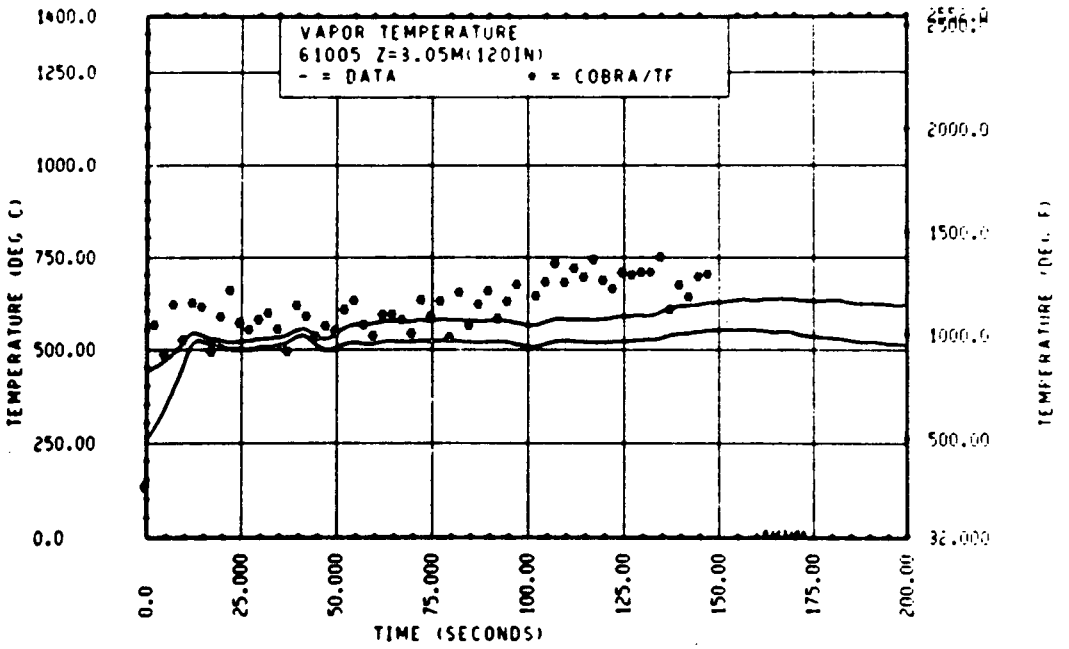

Figure 5-88. Comparison of COBRA-TF-Calculated Vapor Temperature Versus Time With FLECHT SEASET 163-Rod Data, Test 61005, 3.05 m (120 in.) Elevation

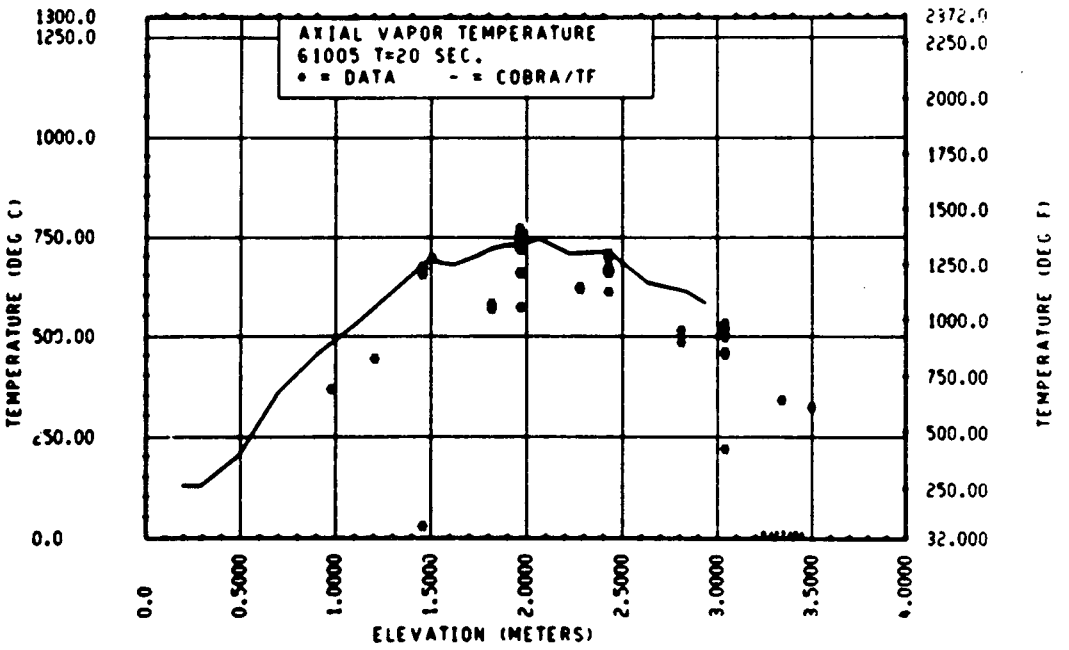

Figure 5-89. Comparison of COBRA-TF-Calculated Axial Vapor Temperature Versus Elevation With FLECHT SEASET 163-Rod Data, Test 61005, t = 20 Seconds

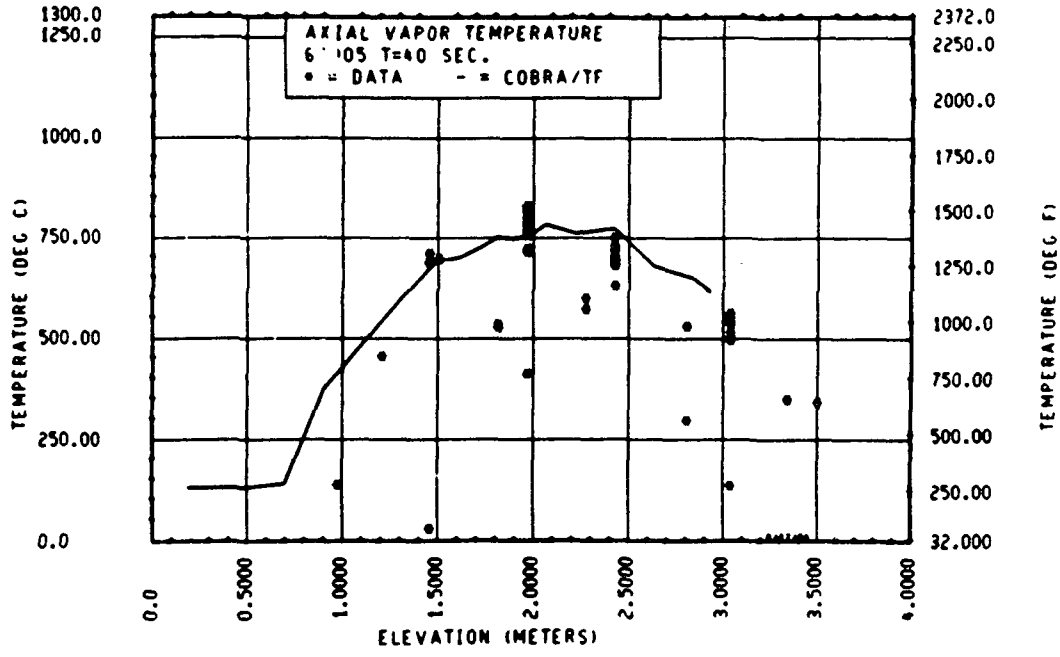

Figure 5-90. Comparison of COBRA-TF-Calculated Axial Vapor Temperature Versus Elevation With FLECHT SEASET 163-Rod Data, Test 61005, t = 40 Seconds

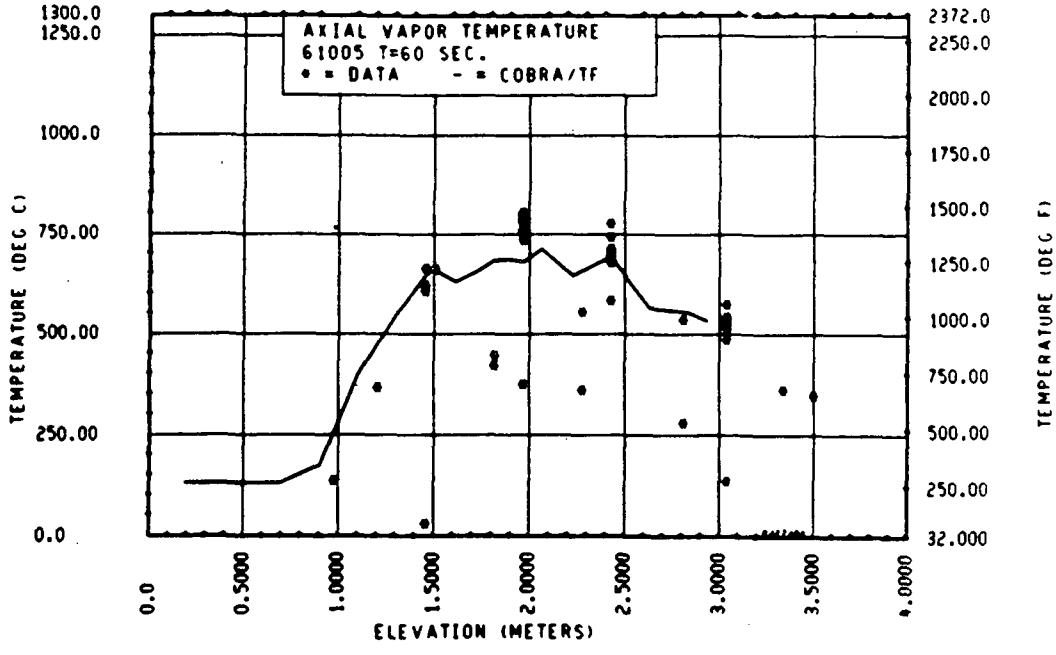

Figure 5-91. Comparison of COBRA-TF-Calculated Axial Vapor Temperature Versus Time With FLECHT SEASET 163-Rod Data, Test 61005, t = 60 Seconds

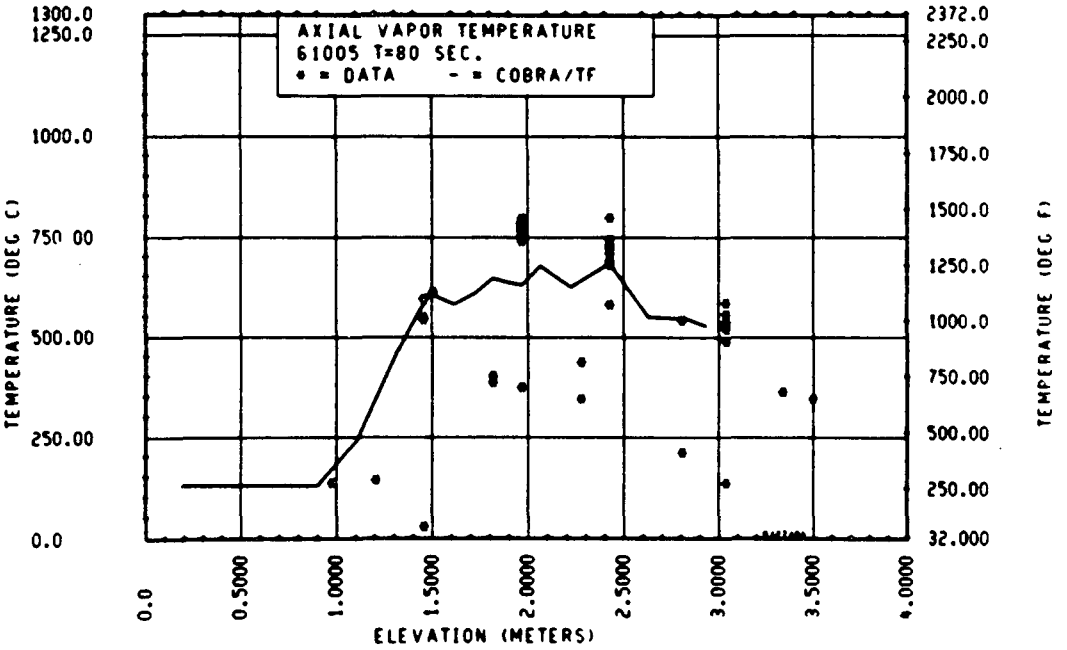

Figure 5-92. Comparison of COBRA-TF-Calculated Axial Vapor Temperature Versus Time With FLECHT SEASET 163-Rod Data, Test 61005, t = 80 Seconds

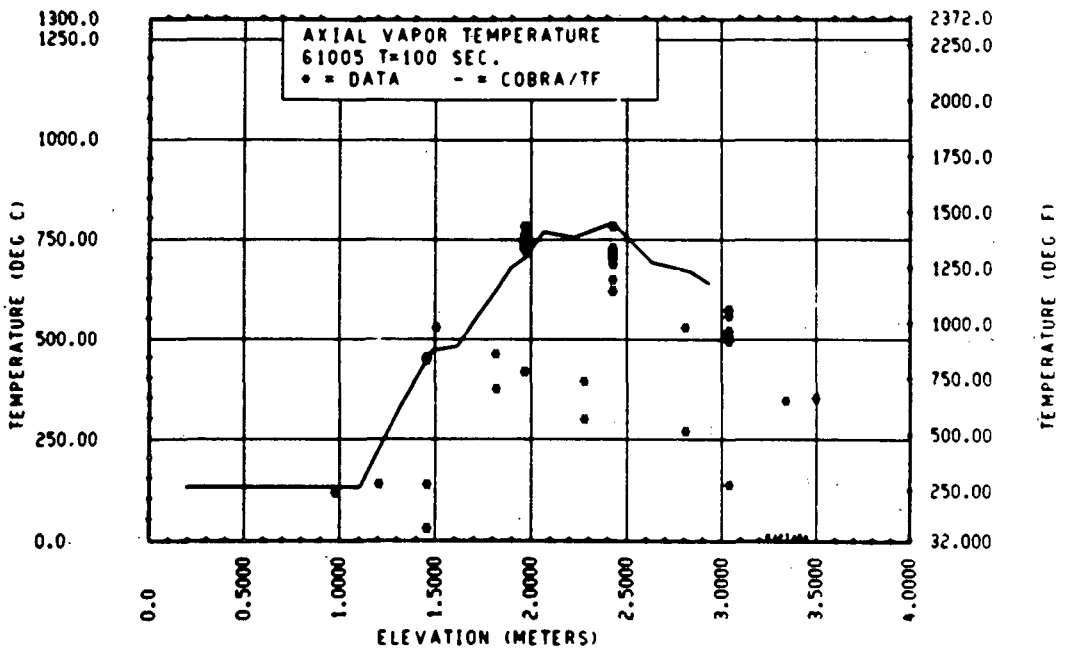

Figure 5-93. Comparison of COBRA-TF-Calculated Axial Vapor Temperature Versus Elevation With FLECHT SEASET 163-Rod Data, Test 61005, t = 100 Seconds

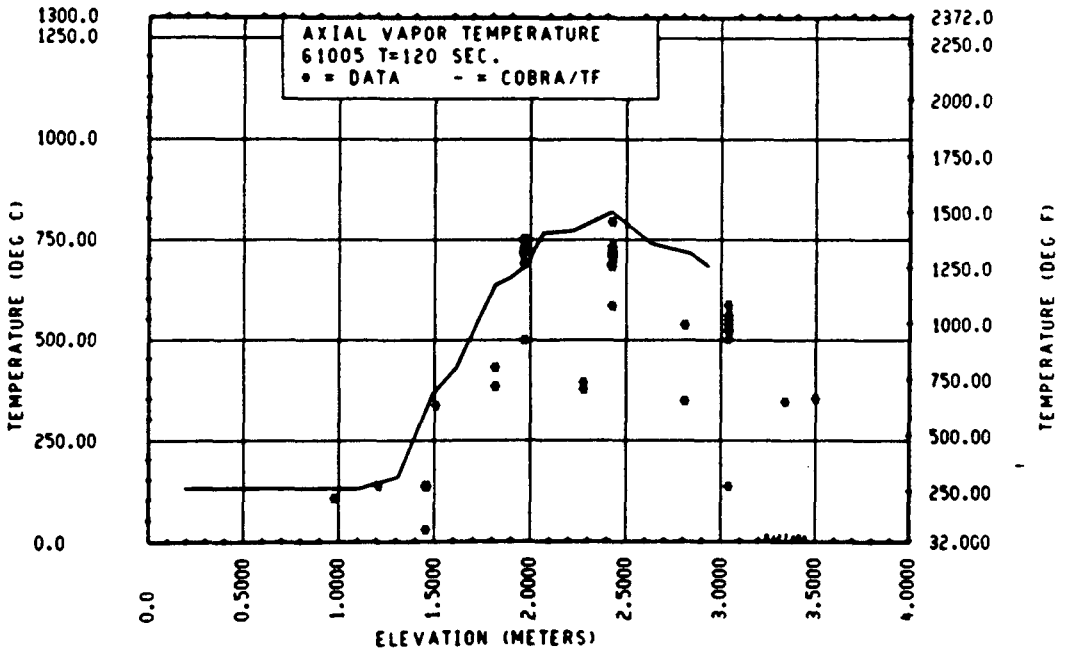

Figure 5-94. Comparison of COBRA-TF-Calculated Axial Vapor Temperature Versus Elevation With FLECHT SEASET 163-Rod Data, Test 61005, t = 120 Seconds

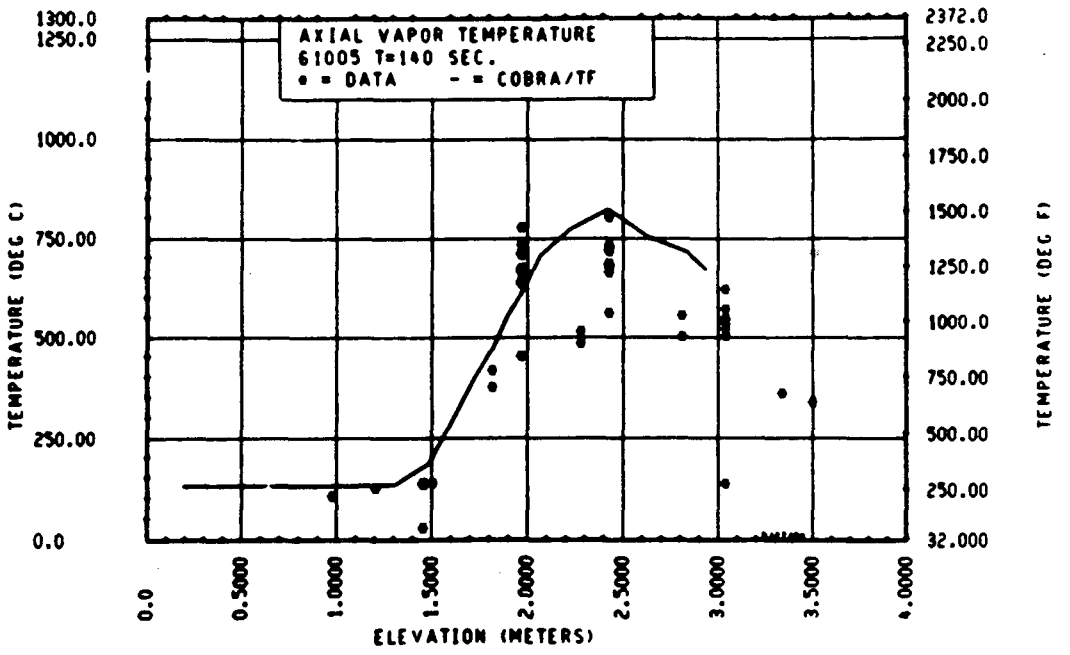

Figure 5-95. Comparison of COBRA-TF-Calculated Axial Vapor Temperature Versus Time With FLECHT SEASET 163-Rod Data, Test 61005, t = 140 Seconds

The axial temperature plots shown in figures 5-72 through 5-78 for rod 1 and figures 5-79 through 5-85 for rod 2 also confirm that the upper elevations are overpredicted in COBRA-TF for rod 1, but that the agreement is improved for rod 2. (Also shown in figure 5-72 is the axial location of the spacer grids and the blockage zone.) The rod 1 comparisons are quite good for these test conditions, and do not show the strong grid effect at the 1.57 m (62 in.) elevation early in time. Later in time (after 100 seconds), there is an effect, which results in lower predicted heater rod temperatures coming into the blockage zone. Similar results are shown for rod 2.

The measured vapor temperatures for the blockage zone are shown in figures 5-86 through 5-88. Generally, the agreement between the COBRA-TF calculation and the data is quite good, with a slight tendency to overpredict the vapor temperature at the 3.05 m (120 in.) elevation. This overprediction is consistent with the heater rod temperature overprediction at this elevation. There is more spread in the data for this test than for the test previously discussed. The axial plots of all the vapor temperature measurements compared to the predicted COBRA-TF vapor temperature for the blocked radial node are shown in figures 5-89 through 5-95. The comparison of the vapor temperature data in the blocked zone and the calculated vapor temperature axial distribution in the blocked zone is shown in figures 5-96 through 5-102. The agreement between the predicted COBRA-TF vapor temperature and data from thermocouples in the blocked region is reasonably good.

A similar package of comparisons is shown in figures 5-103 through 5-128 for FLECHT SEASET 163-rod bundle test 61509, which was a 0.14 MPa (20 psia) test at 0.025 m/sec (1 in./sec) flooding rate. (Figure 5-101 shows the axial location of the spacer grids and the blockage zone.) Both rod 1 and rod 2 tend to overpredict the heat transfer at times greater than 75 seconds after flood. The prediction cuts across the data for these comparisons after these times. The axial plots show more clearly that the calculated heater rod temperatures are too low after 100 seconds for rod 1 and 120 seconds for rod 2. Again, part of the problem could be the overcooling effect predicted for the 1.57 m (62 in.) grid. However, these lower backpressure comparisons are quite good.

Figures 5-129 through 5-154 show the comparison to FLECHT SEASET 163-rod bundle test 61916, which was a stepped flooding rate experiment. (Figure

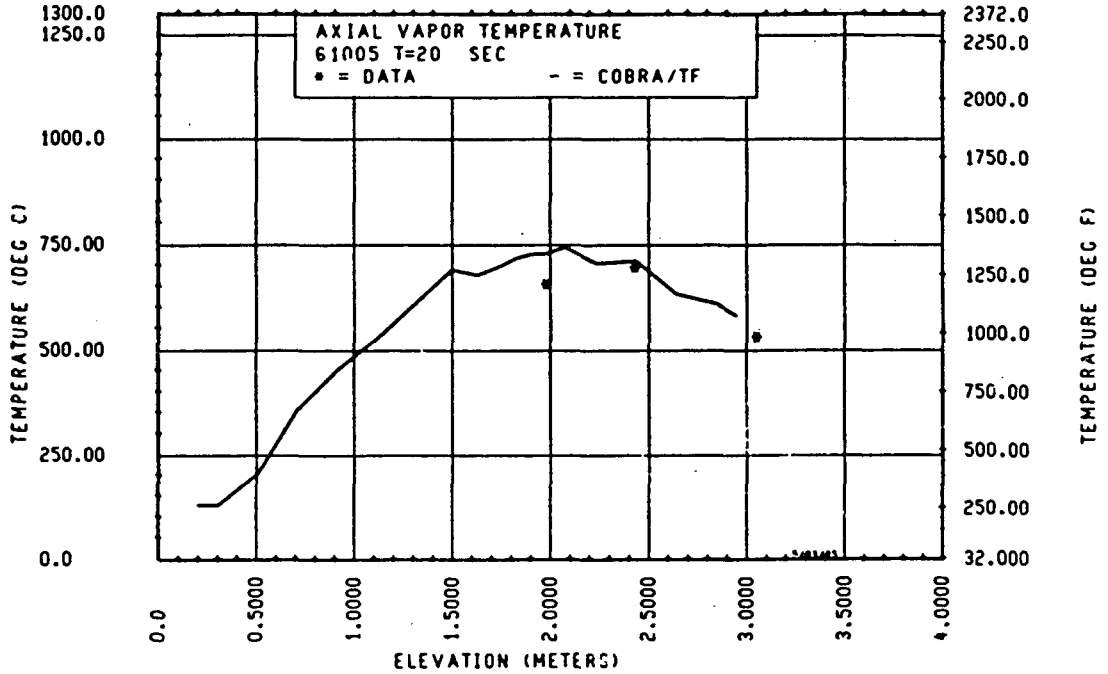

Figure 5-96. Comparison of COBRA-TF-Calculated Vapor Temperature Data in Blocked Zone Versus Calculated Vapor Temperature Axial Distribution in Blocked Zone, Test 61005, t = 20 Seconds

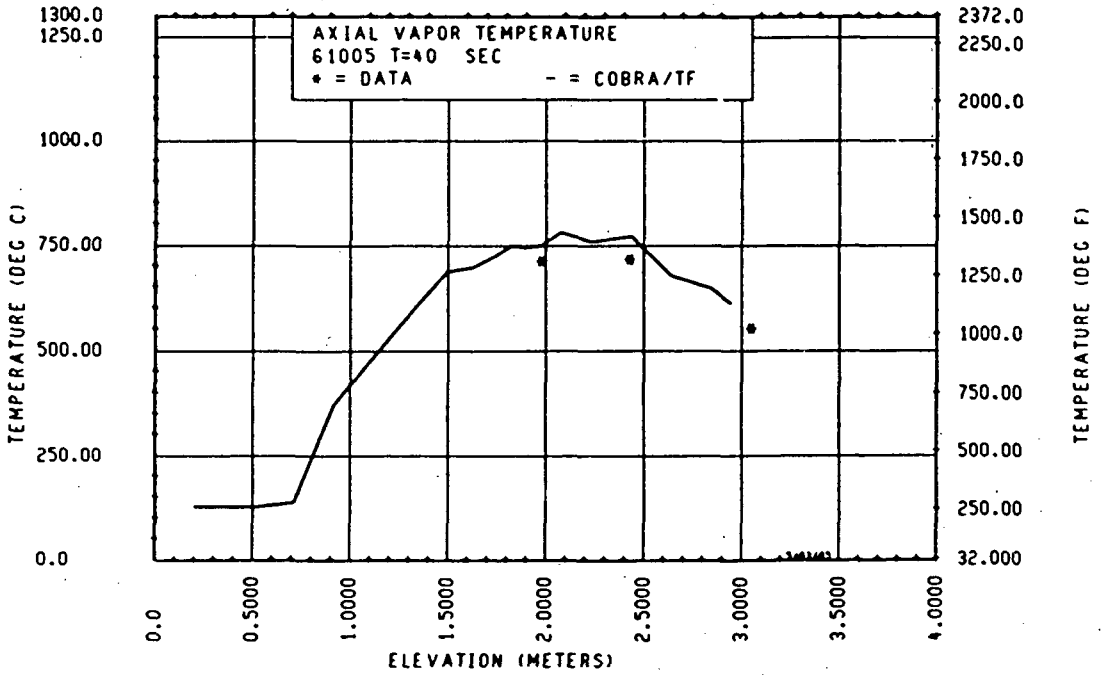

Figure 5-97. Comparison of COBRA-TF-Calculated Vapor Temperature Data in Blocked Zone Versus Calculated Vapor Temperature Axial Distribution in Blocked Zone, Test 61005, t = 40 Seconds

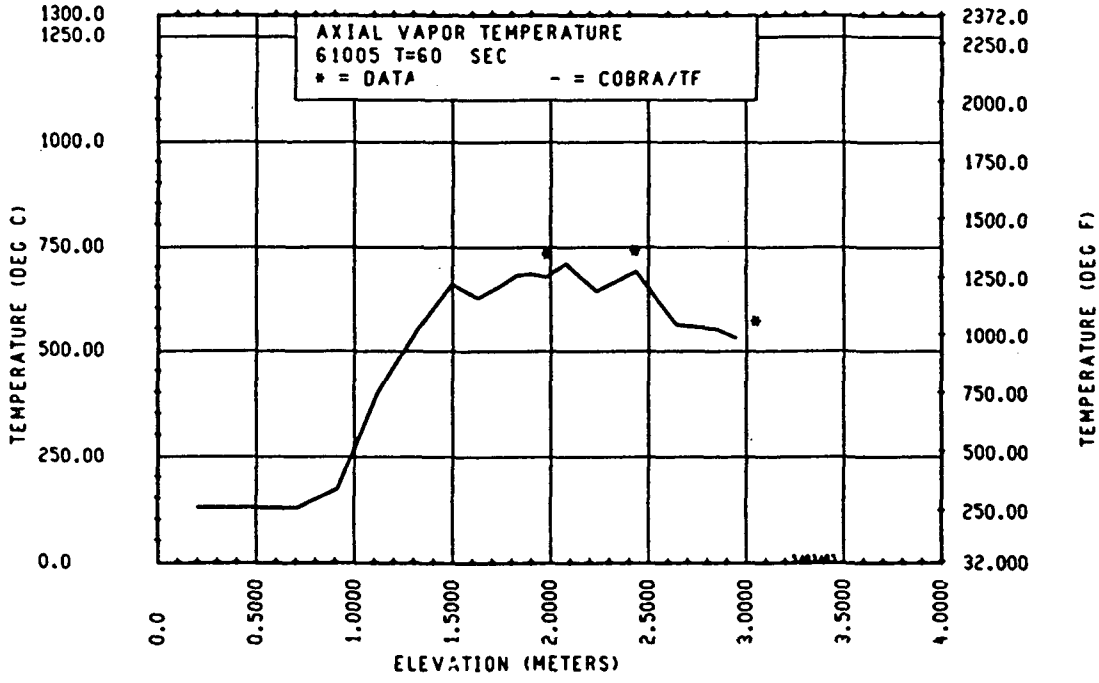

Figure 5-98. Comparison of COBRA-TF-Calculated Vapor Temperature Data in Blocked Zone Versus Calculated Vapor Temperature Axial Distribution in Blocked Zone, Test 61005, t = 60 Seconds

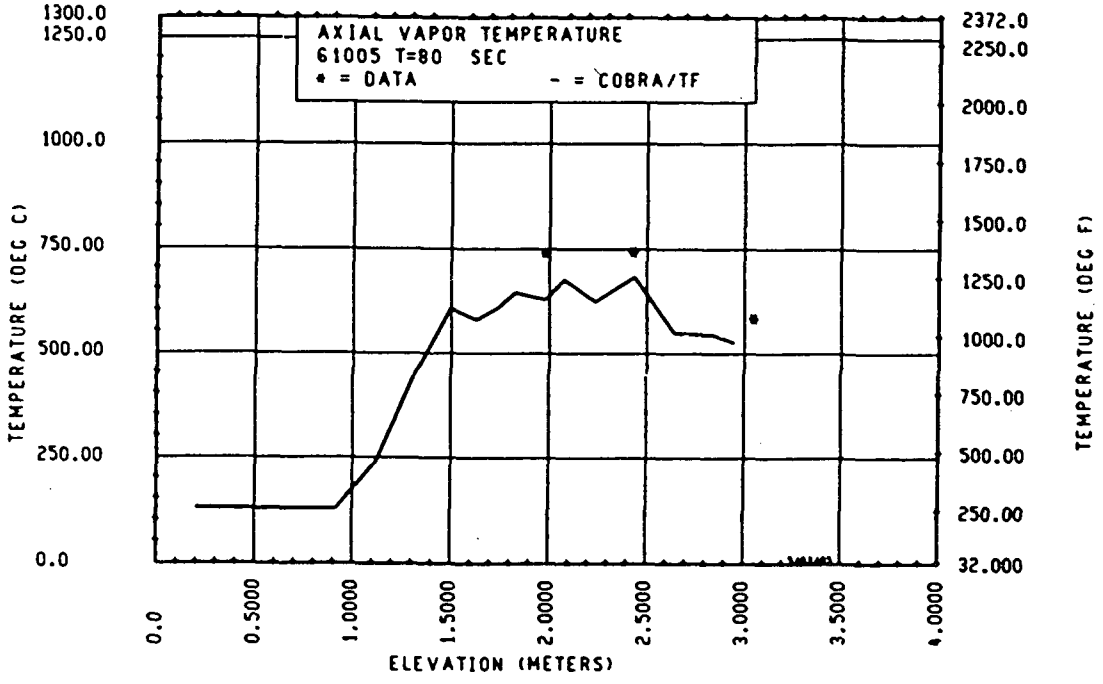

Figure 5-99. Comparison of COBRA-TF-Calculated Vapor Temperature Data in Blocked Zone Versus Calculated Vapor Temperature Axial Distribution in Blocked Zone, Test 61005, t = 80 Seconds

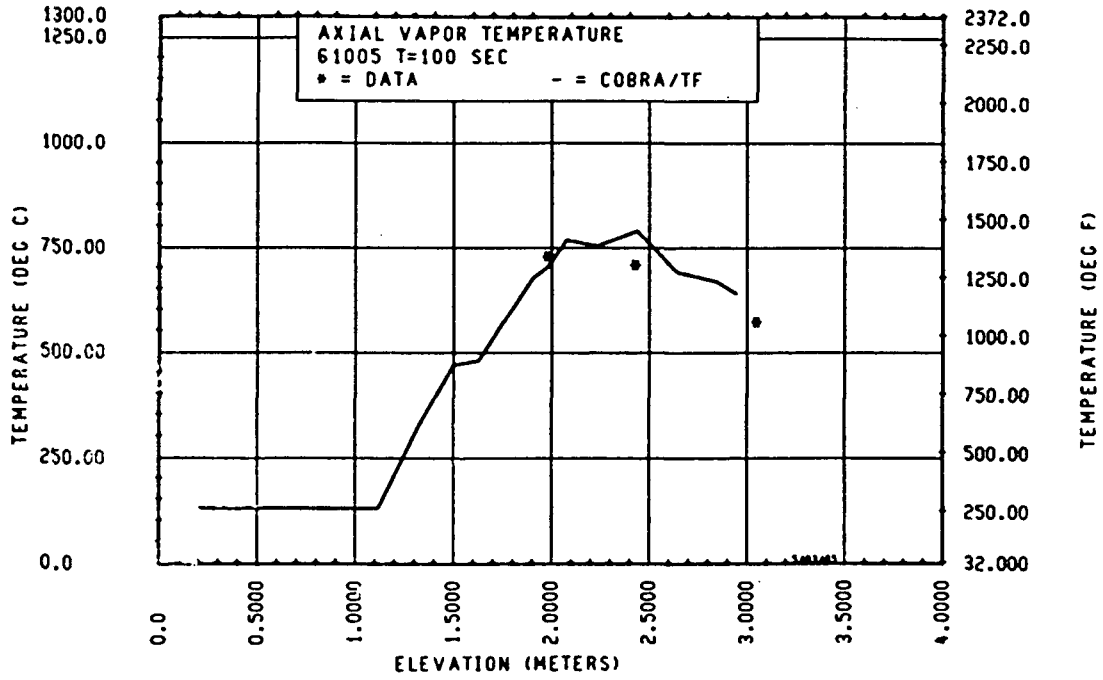

Figure 5-100. Comparison of COBRA-TF-Calculated Vapor Temperature Data in Blocked Zone Versus Calculated Vapor Temperature Axial Distribution in Blocked Zone, Test 61005, t = 100 Seconds

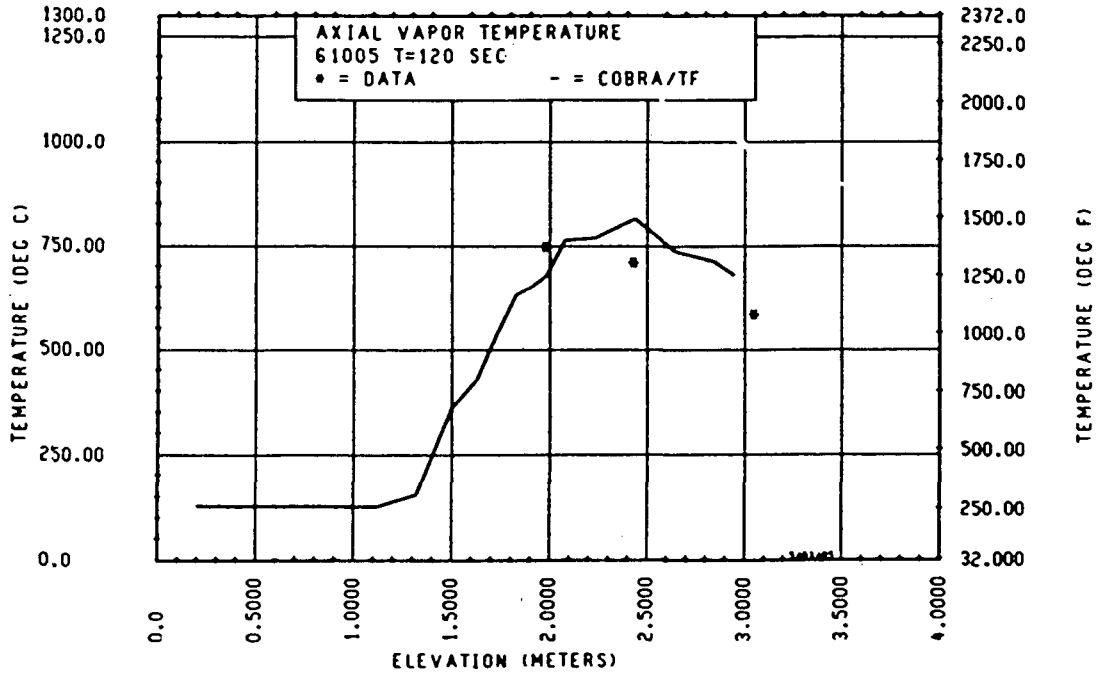

Figure 5-101. Comparison of COBRA-TF-Calculated Vapor Temperature Data in Blocked Zone Versus Calculated Vapor Temperature Axial Distribution in Blocked Zone, Test 61005, t = 120 Seconds

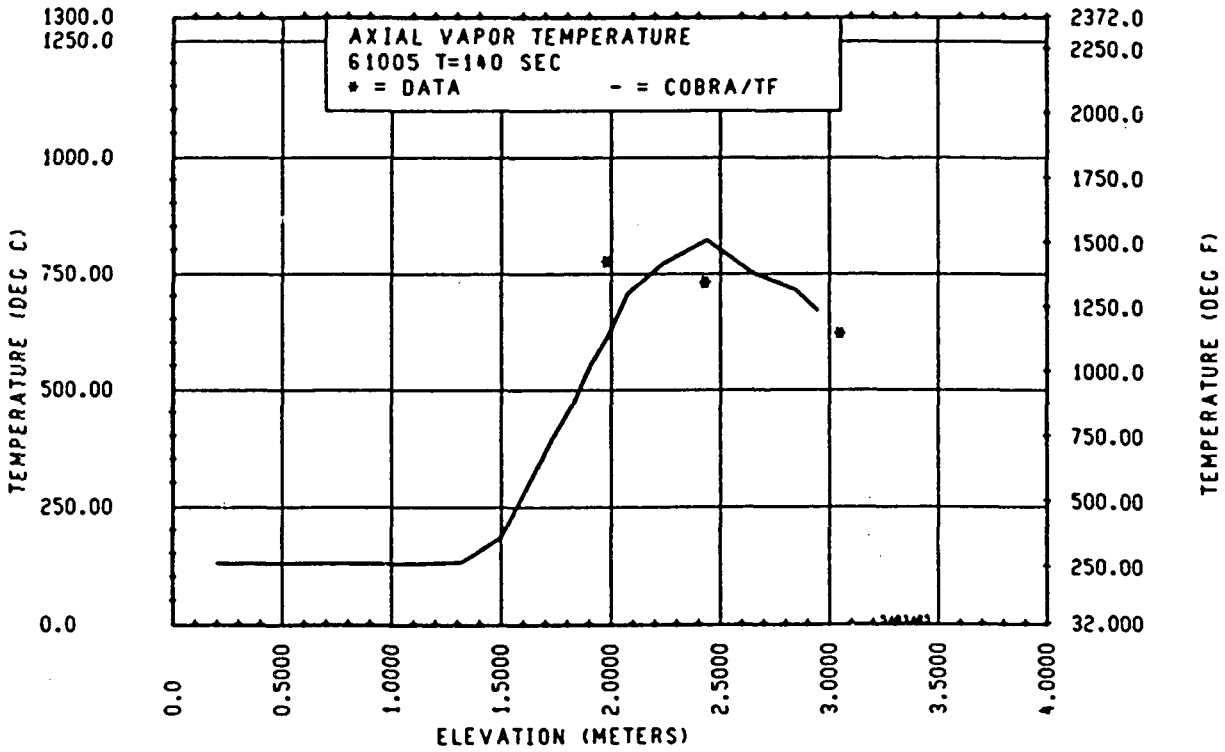

Figure 5-102. Comparison of COBRA-TF-Calculated Vapor Temperature Data in Blocked Zone Versus Calculated Vapor Temperature Axial Distribution in Blocked Zone, Test 61005, t = 140 Seconds

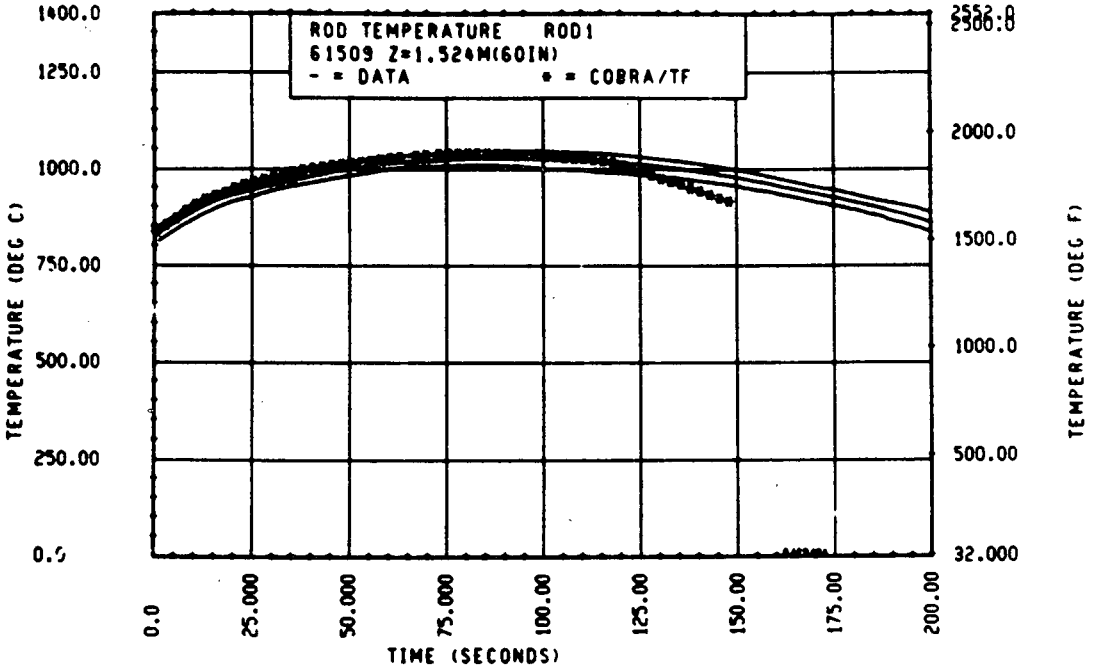

Figure 5-103. Comparison of COBRA-TF-Calculated Heater Rod Temperature Versus Time With FLECHT SEASET 163-Rod Data, Test 61509, 1.52 m (60 in.) Elevation, Rod 1

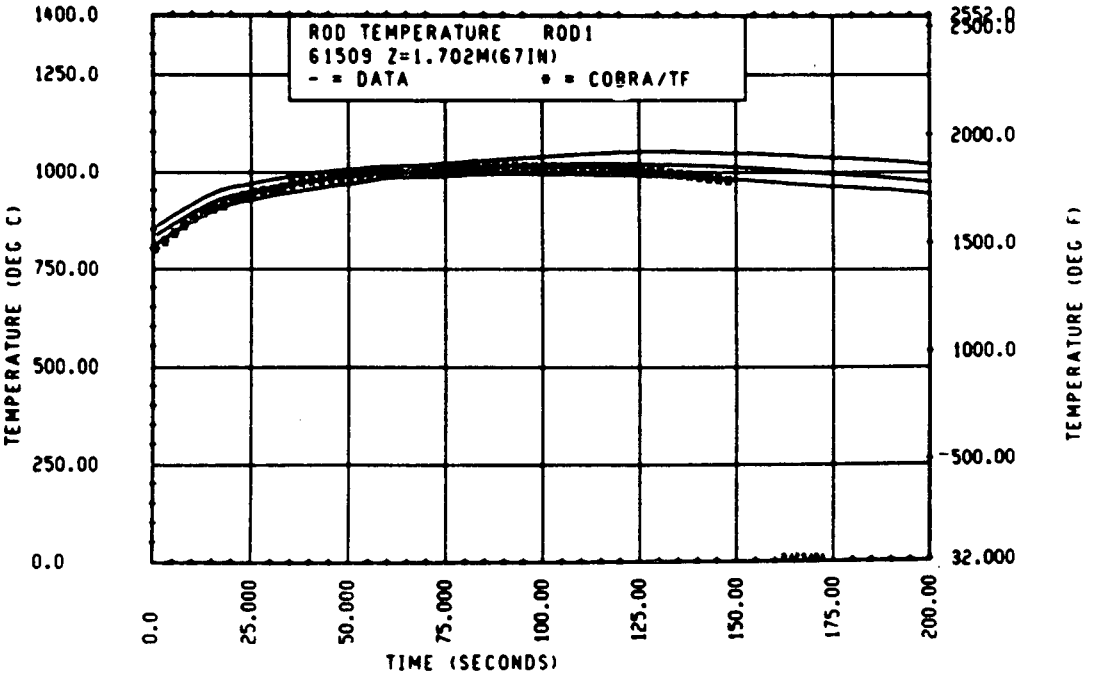

Figure 5-104. Comparison of COBRA-TF-Calculated Heater Rod Temperature Versus Time With FLECHT SEASET 163-Rod Data, Test 61509, 1.70 m (67 in.) Elevation, Rod 1

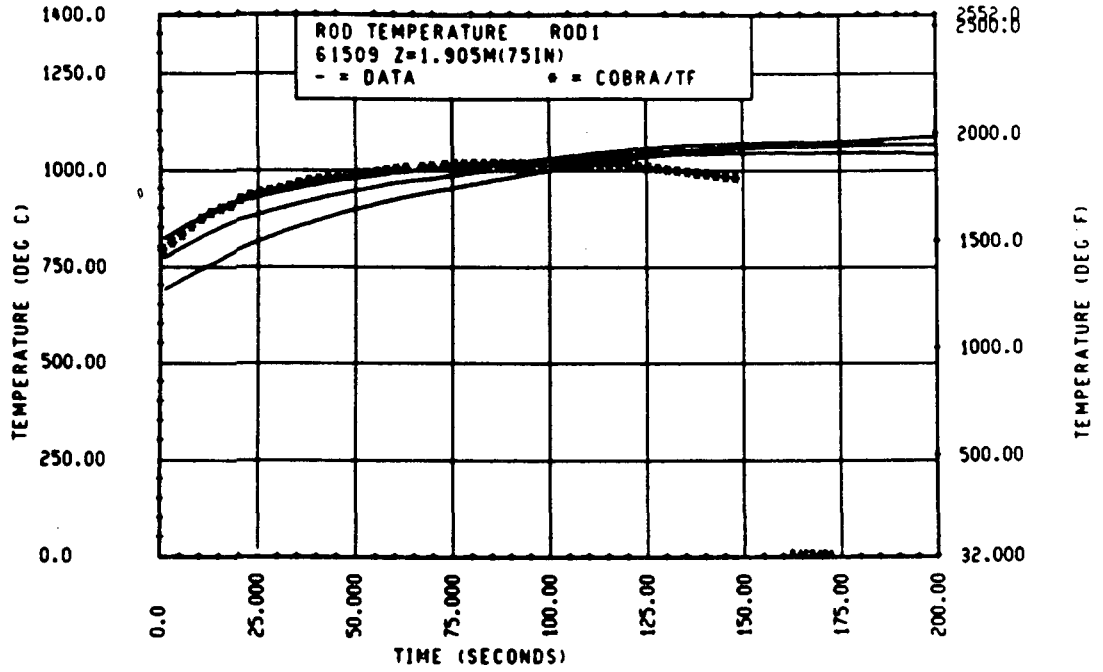

Figure 5-105. Comparison of COBRA-TF-Calculated Heater Rod Temperature Versus Time With FLECHT SEASET 163-Rod Data, Test 61509, 1.90 m (75 in.) Elevation, Rod 1

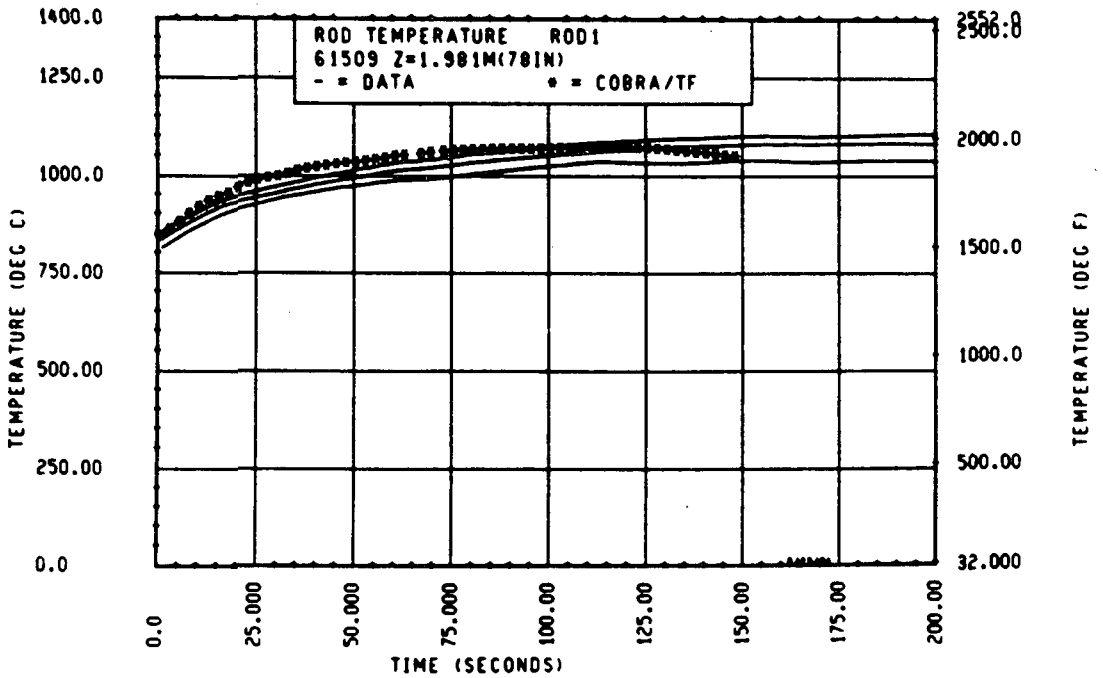

Figure 5-106. Comparison of COBRA-TF-Calculated Heater Rod Temperature Versus Time With FLECHT SEASET 163-Rod Data, Test 61509, 1.98 m (78 in.) Elevation, Rod 1

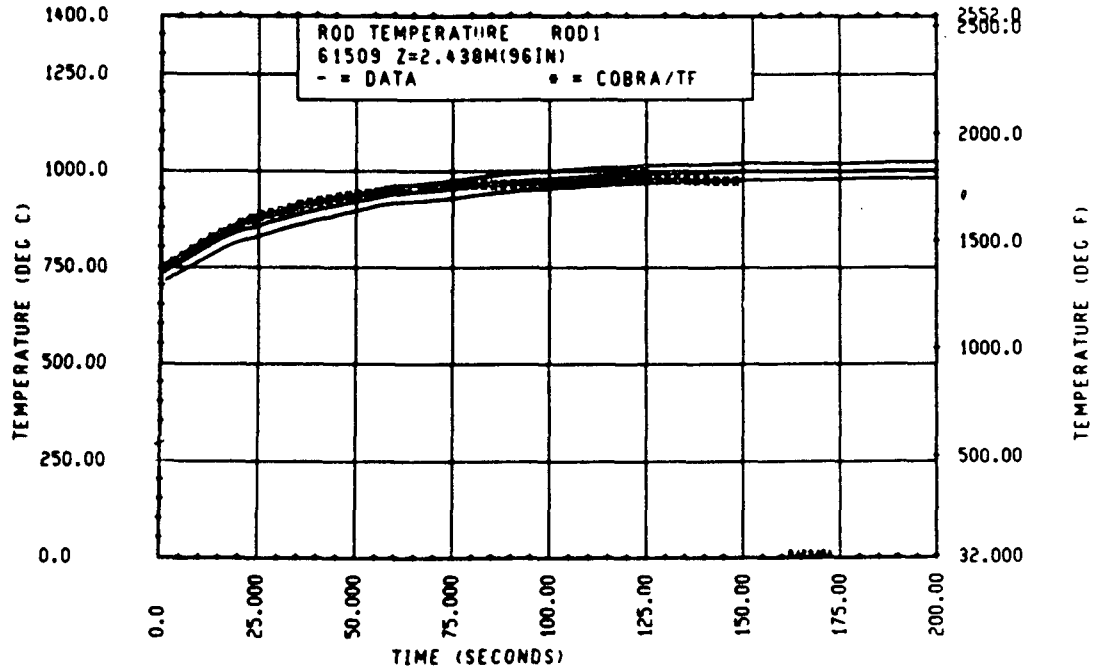

Figure 5-107. Comparison of COBRA-TF-Calculated Heater Rod Temperature Versus Time With FLECHT SEASET 163-Rod Data, Test 61509, 2.44 m (96 in.) Elevation, Rod 1

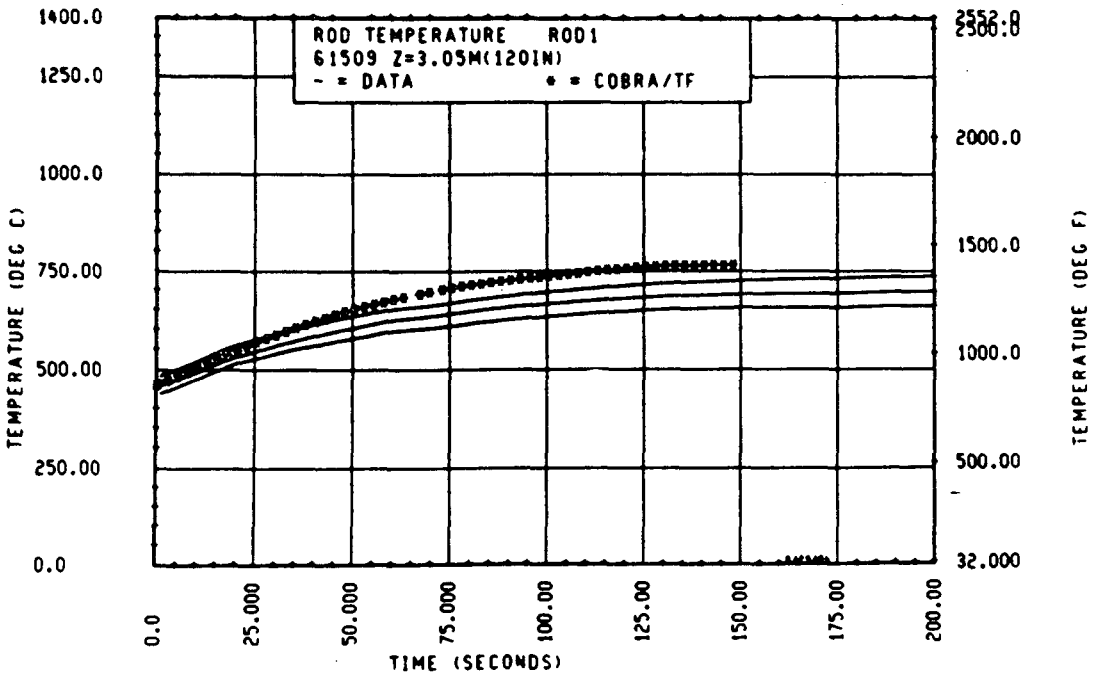

Figure 5-108. Comparison of COBRA-TF-Calculated Heater Rod Temperature Versus Time With FLECHT SEASET 163-Rod Data, Test 61509, 3.05 m (120 in.) Elevation, Rod 1

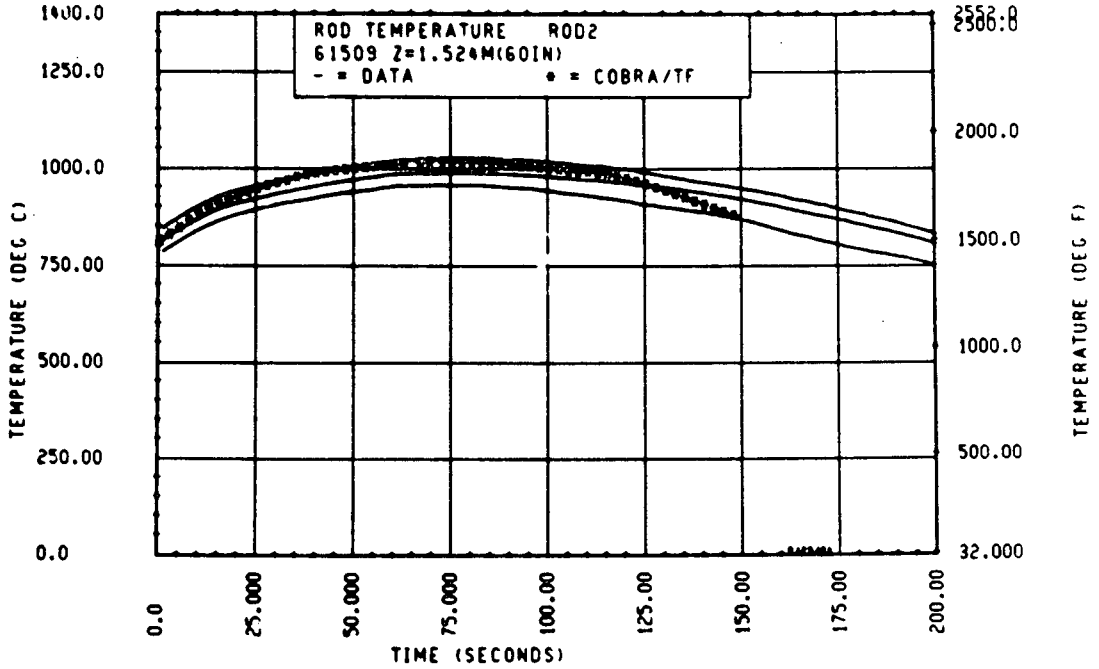

Figure 5-109. Comparison of COBRA-TF-Calculated Heater Rod Temperature Versus Time With FLECHT SEASET 163-Rod Data, Test 61509, 1.52 m (60 in.) Elevation, Rod 2

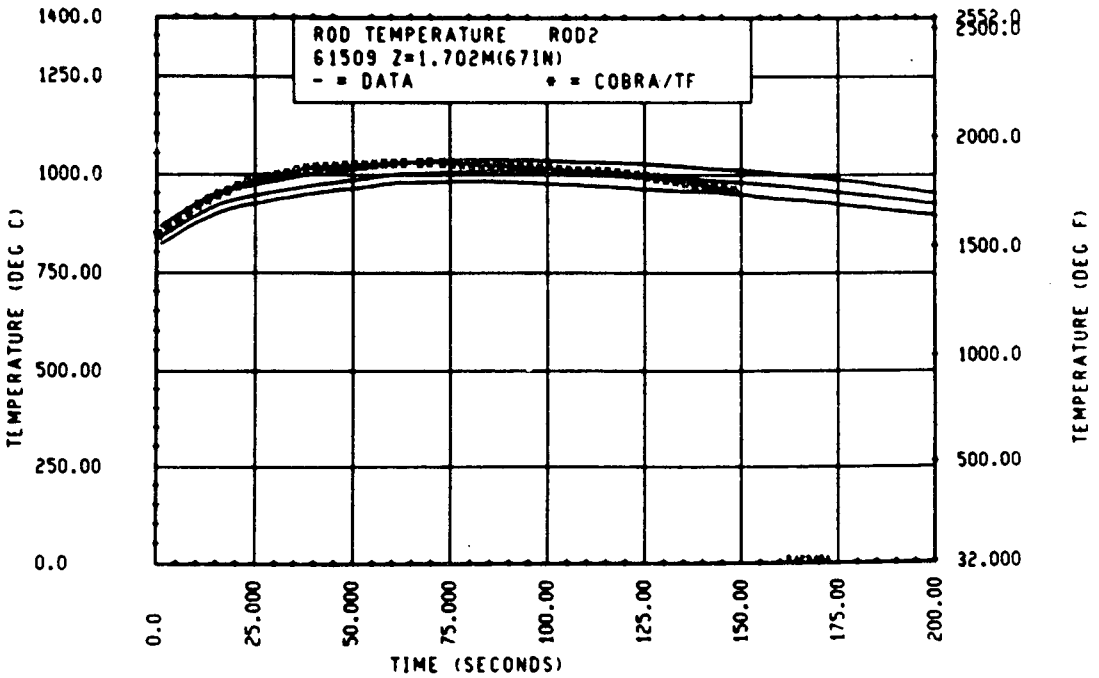

Figure 5-110. Comparison of COBRA-TF-Calculated Heater Rod Temperature Versus Time With FLECHT SEASET 163-Rod Data, Test 61509, 1.70 m (67 in.) Elevation, Rod 2

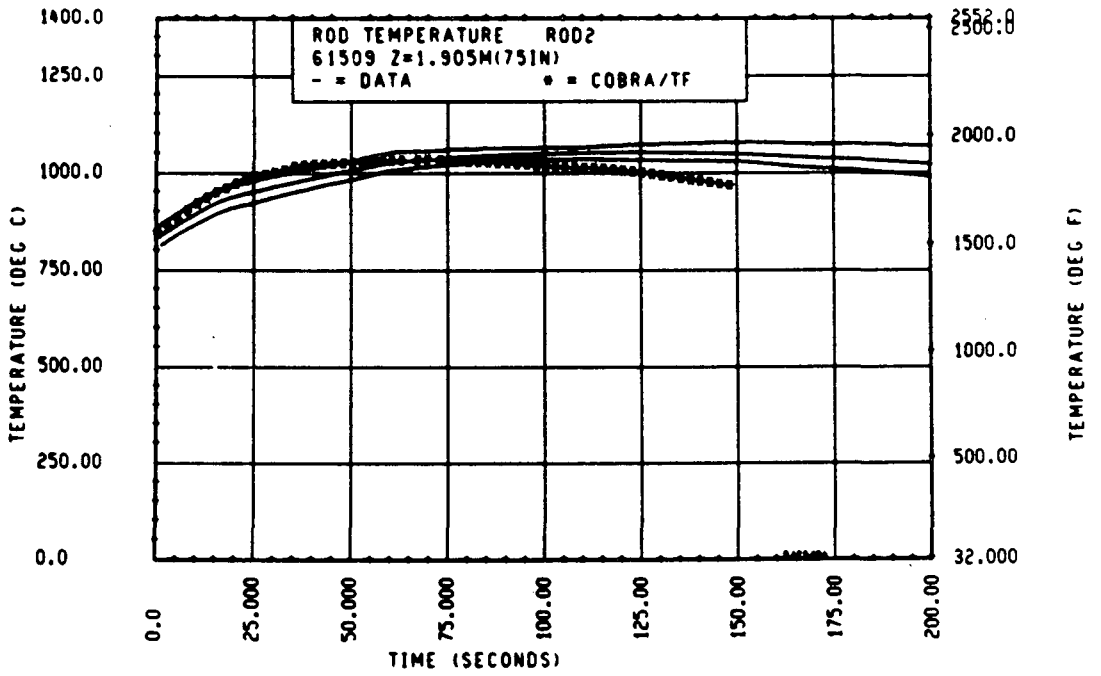

Figure 5-111. Comparison of COBRA-TF-Calculated Heater Rod Temperature Versus Time With FLECHT SEASET 163-Rod Data, Test 61509, 1.90 m (75 in.) Elevation, Rod 2

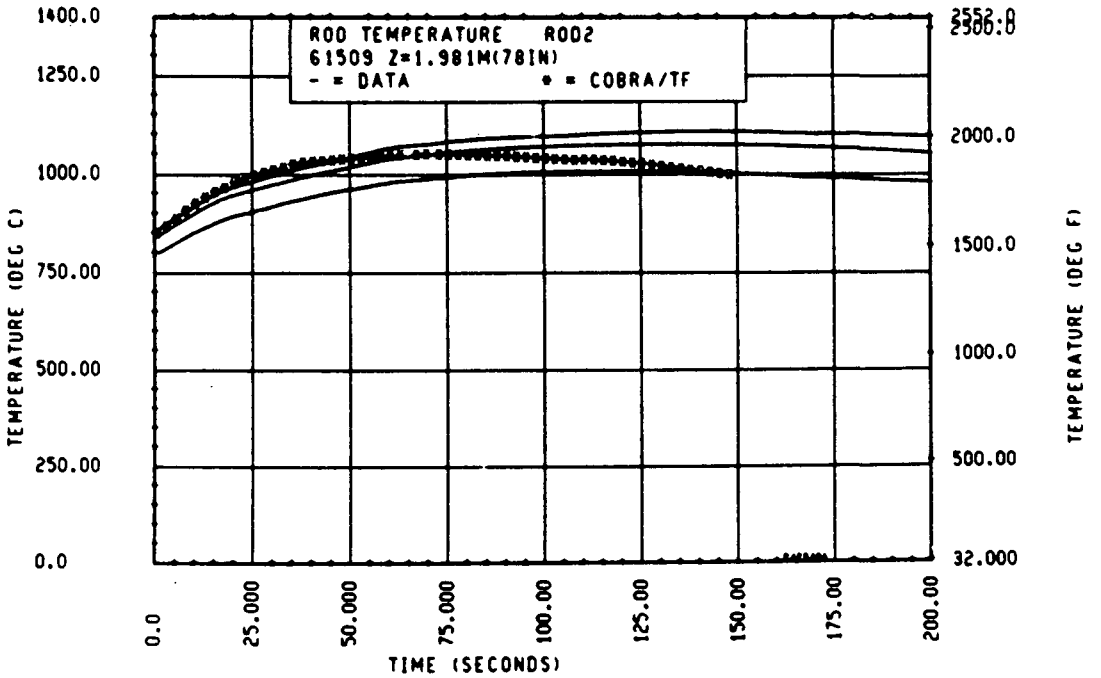

Figure 5-112. Comparison of COBRA-TF-Calculated Heater Rod Temperature Versus Time With FLECHT SEASET 163-Rod Data, Test 61509, 1.98 m (78 in.) Elevation, Rod 2

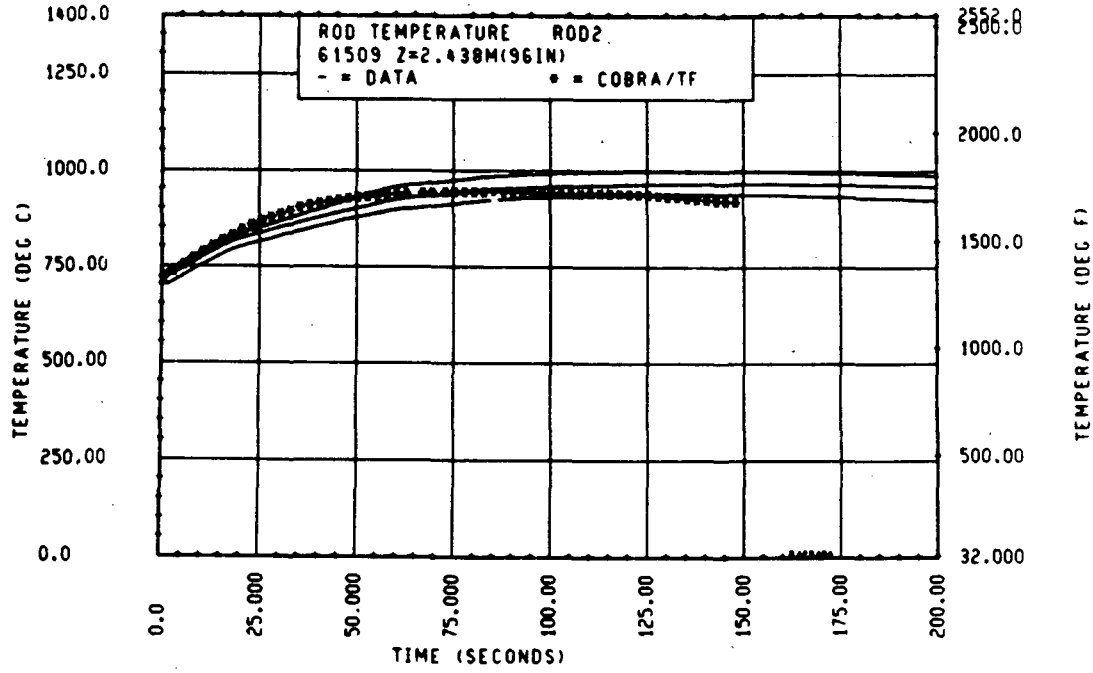

Figure 5-113. Comparison of COBRA-TF-Calculated Heater Rod Temperature Versus Time With FLECHT SEASET 163-Rod Data, Test 61509, 2.44 m (96 in.) Elevation, Rod 2

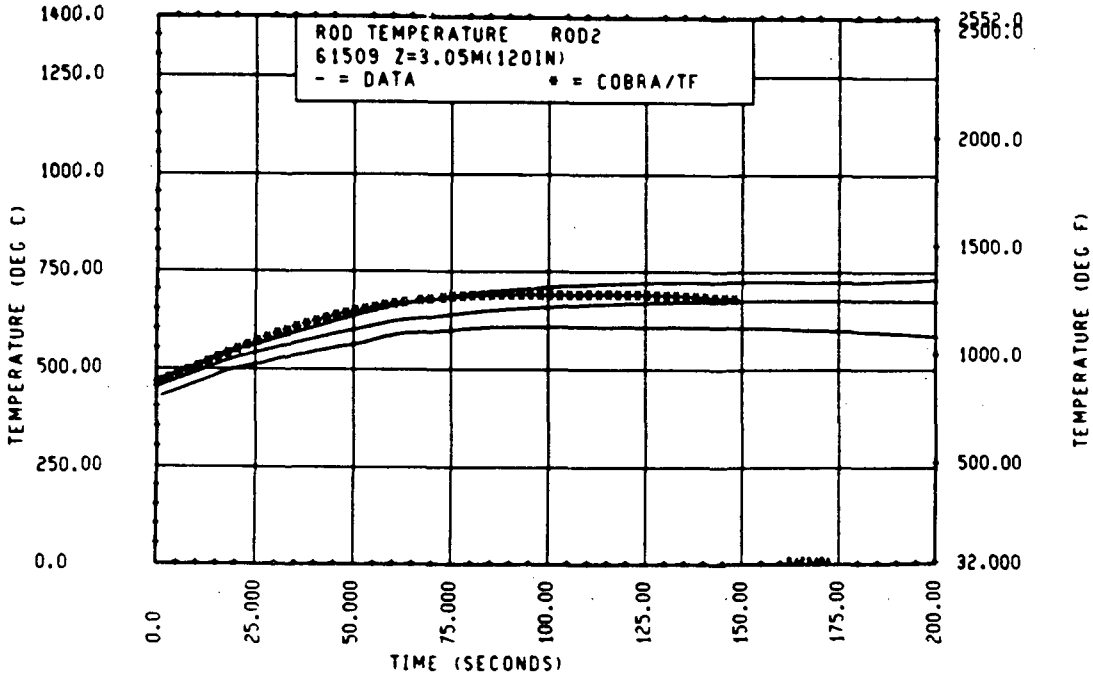

Figure 5-114. Comparison of COBRA-TF-Calculated Heater Rod Temperature Versus Time With FLECHT SEASET 163-Rod Data, Test 61509, 3.05 m (120 in.) Elevation, Rod 2

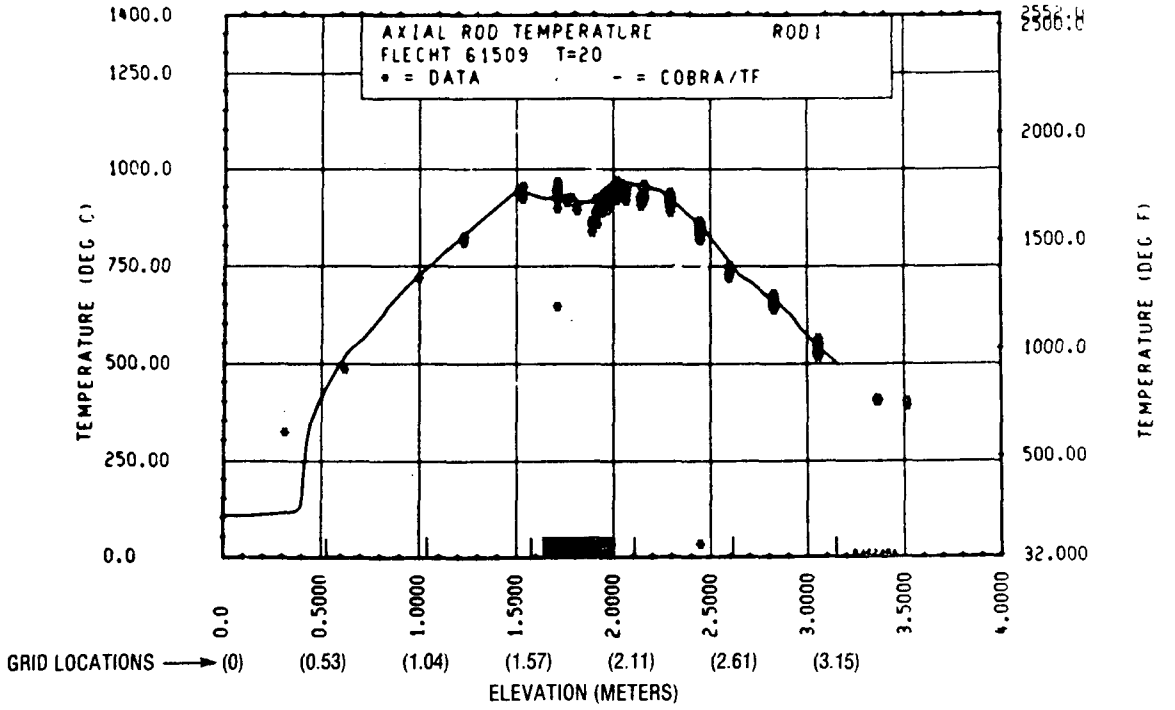

Figure 5-115. Comparison of COBRA-TF-Calculated Axial Rod Temperature Versus Elevation With FLECHT SEASET 163-Rod Data, Test 61509, t = 20 Seconds, Rod 1

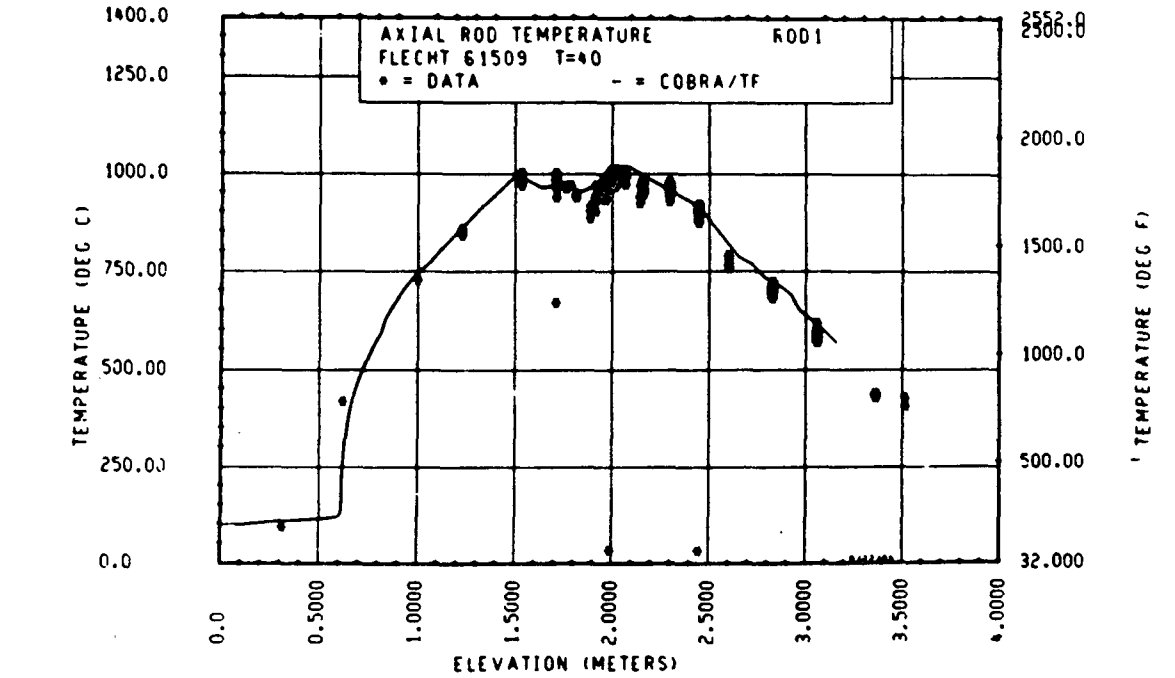

Figure 5-116. Comparison of COBRA-TF-Calculated Axial Rod Temperature Versus Elevation With FLECHT SEASET 163-Rod Data, Test 61509, t = 40 Seconds, Rod 1

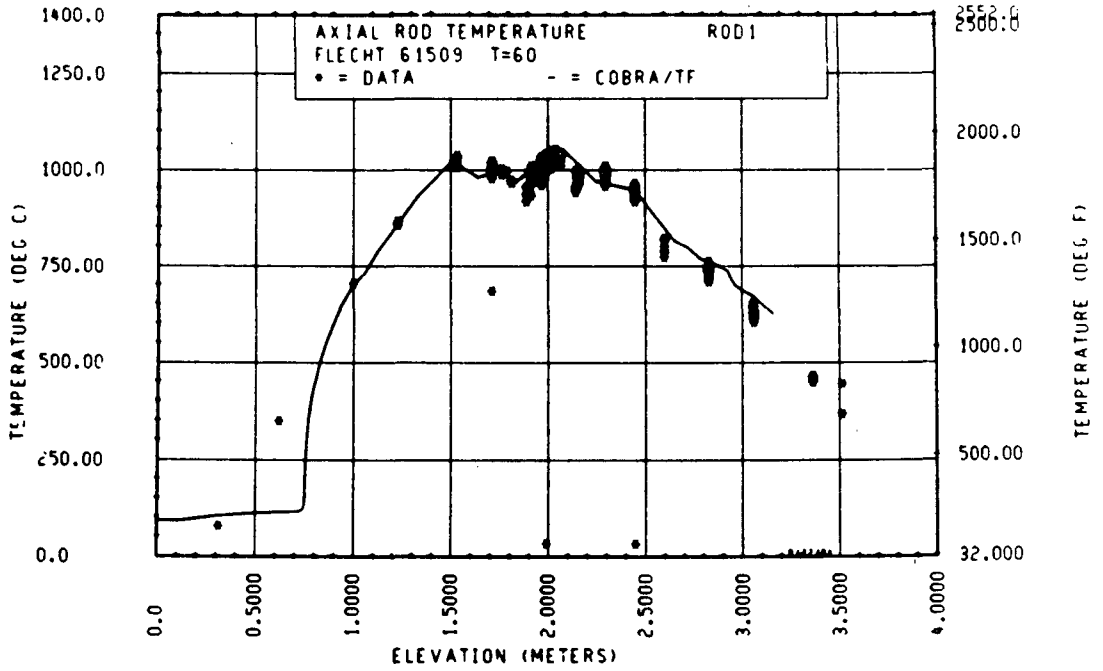

Figure 5-117. Comparison of COBRA-TF-Calculated Axial Rod Temperature Versus Elevation With FLECHT SEASET 163-Rod Data, Test 61509, t = 60 Seconds, Rod 1

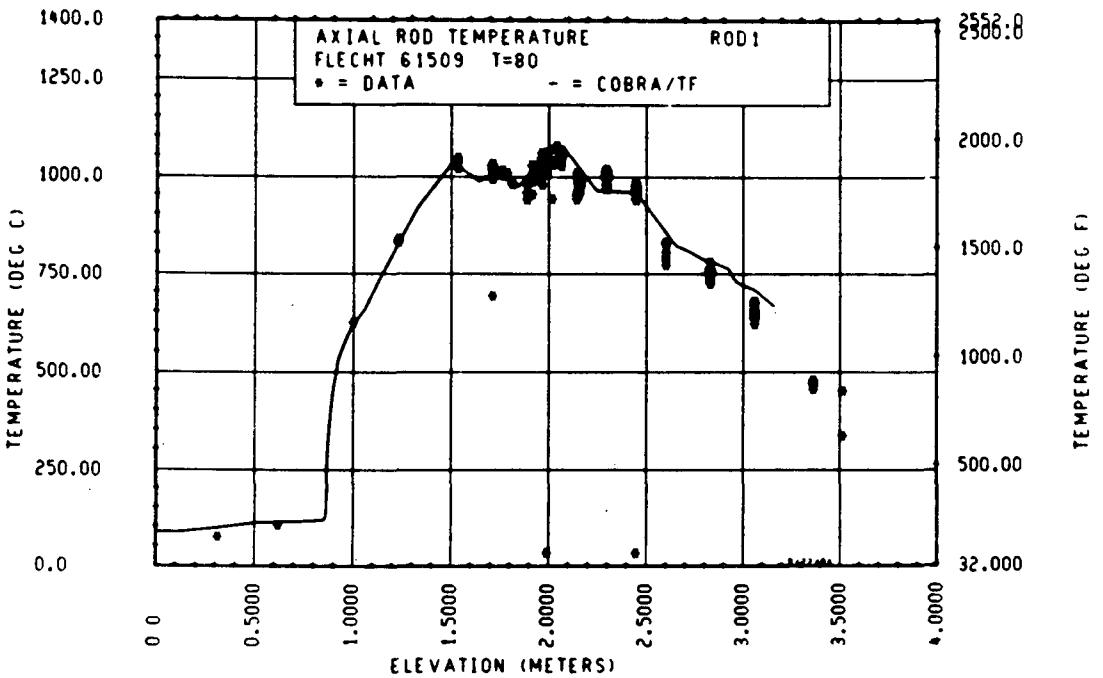

Figure 5-118. Comparison of COBRA-TF-Calculated Axial Rod Temperature Versus Elevation With FLECHT SEASET 163-Rod Data, Test 61509, t = 80 Seconds, Rod 1

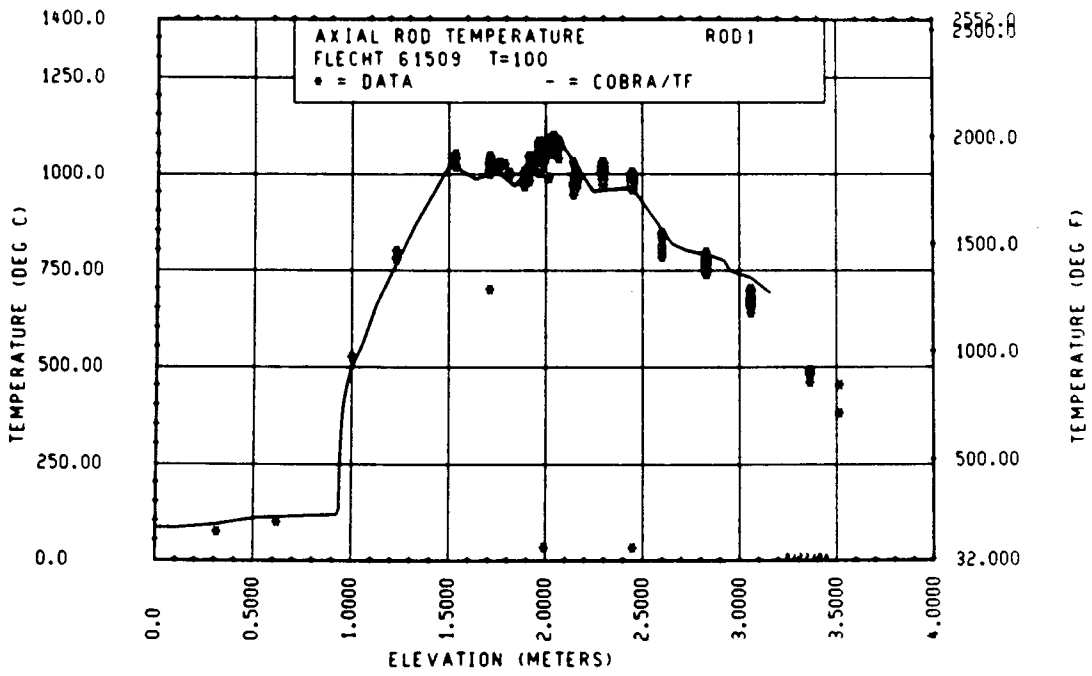

Figure 5-119. Comparison of COBRA-TF-Calculated Axial Rod Temperature Versus Elevation With FLECHT SEASET 163-Rod Data, Test 61509, t = 100 Seconds, Rod 1

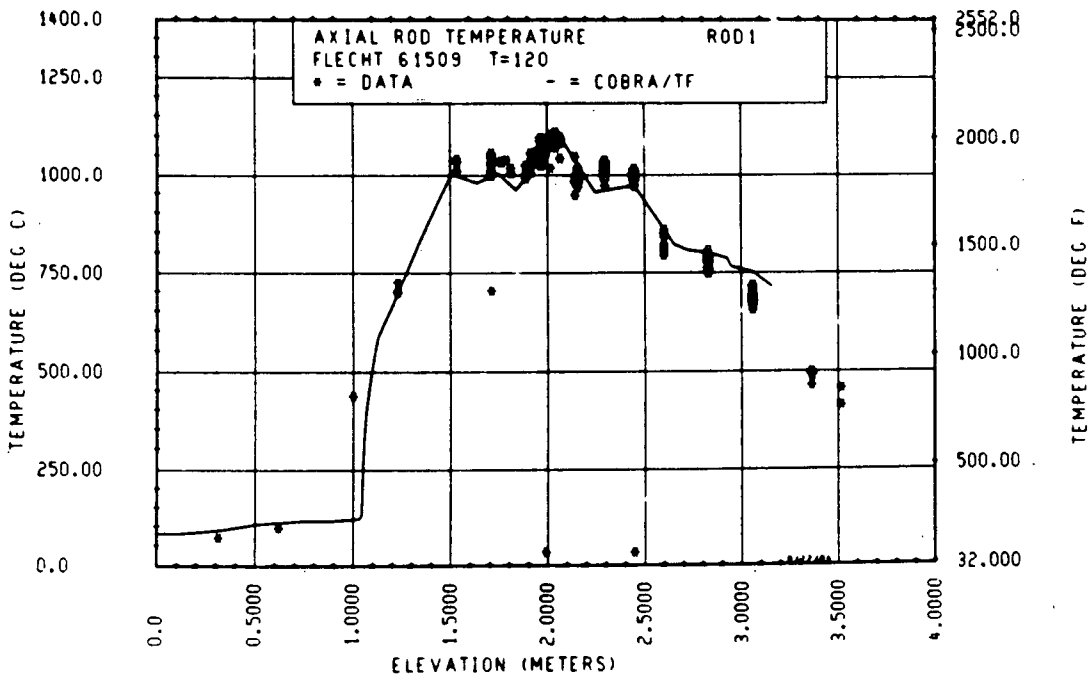

Figure 5-120. Comparison of COBRA-TF-Calculated Axial Rod Temperature Versus Elevation With FLECHT SEASET 163-Rod Data, Test 61509, t = 120 Seconds, Rod 1

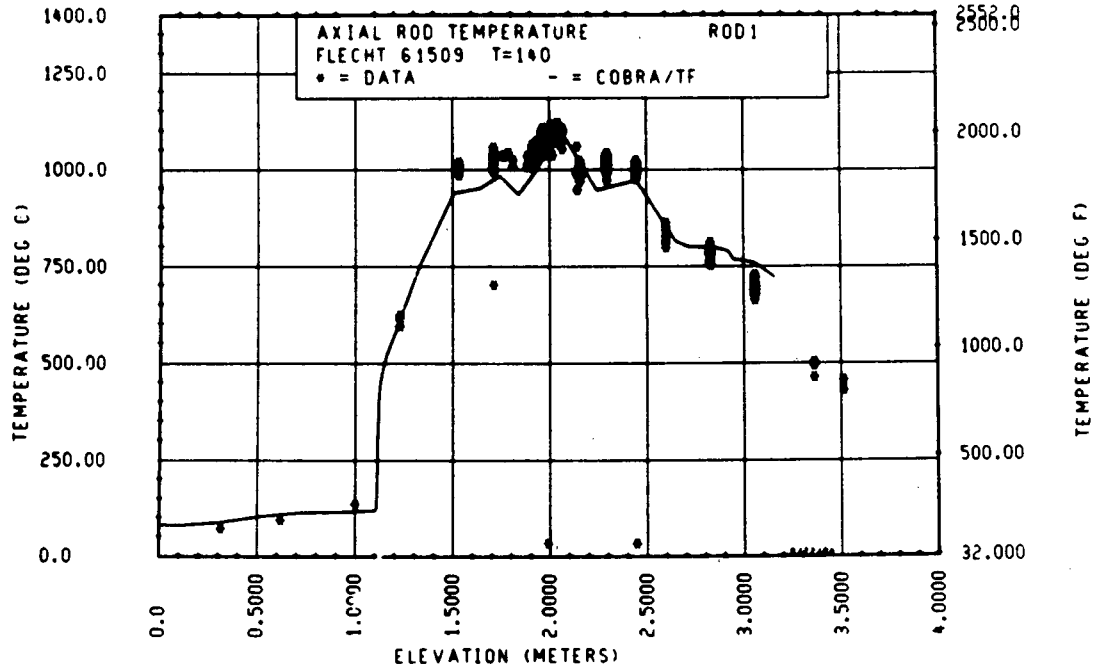

Figure 5-121. Comparison of COBRA-TF-Calculated Axial Rod Temperature Versus Elevation With FLECHT SEASET 163-Rod Data, Test 61509, t = 140 Seconds, Rod 1

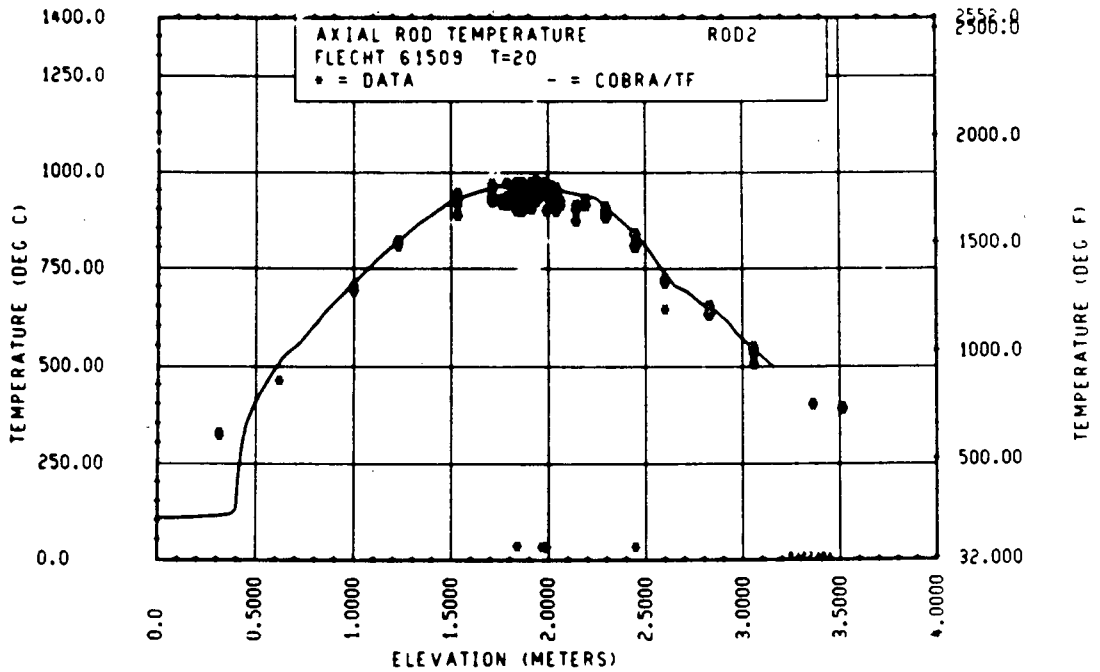

Figure 5-122. Comparison of COBRA-TF-Calculated Axial Rod Temperature Versus Elevation With FLECHT SEASET 163-Rod Data, Test 61509, t = 20 Seconds, Rod 2

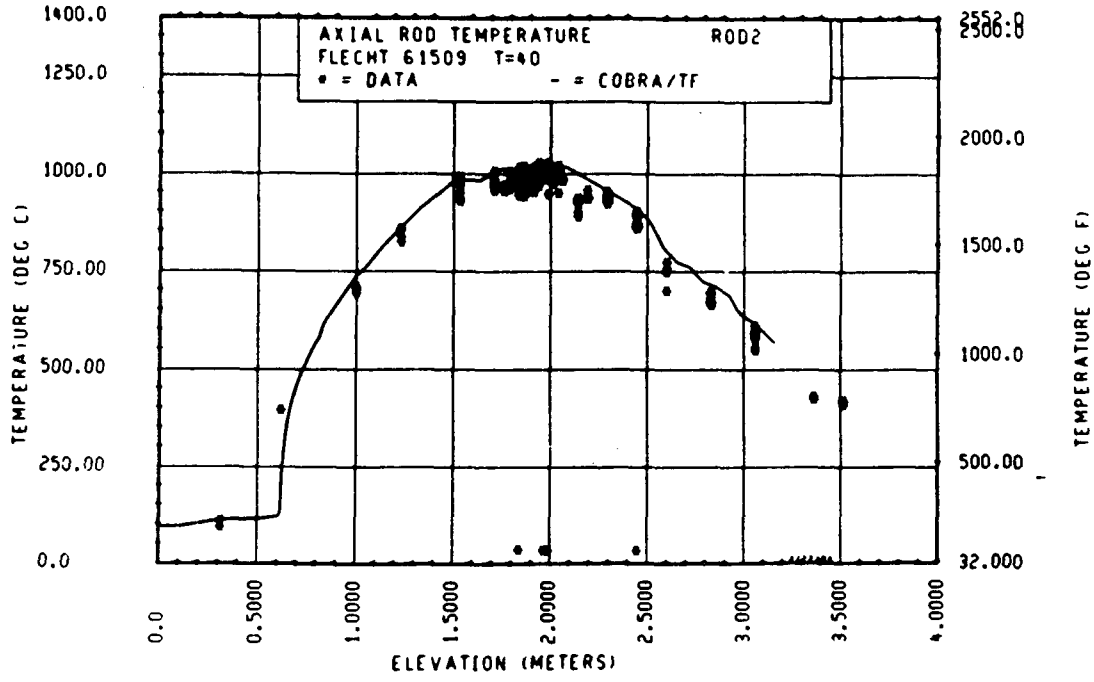

Figure 5-123. Comparison of COBRA-TF-Calculated Axial Rod Temperature Versus Elevation With FLECHT SEASET 163-Rod Data, Test 61509, t = 40 Seconds, Rod 2

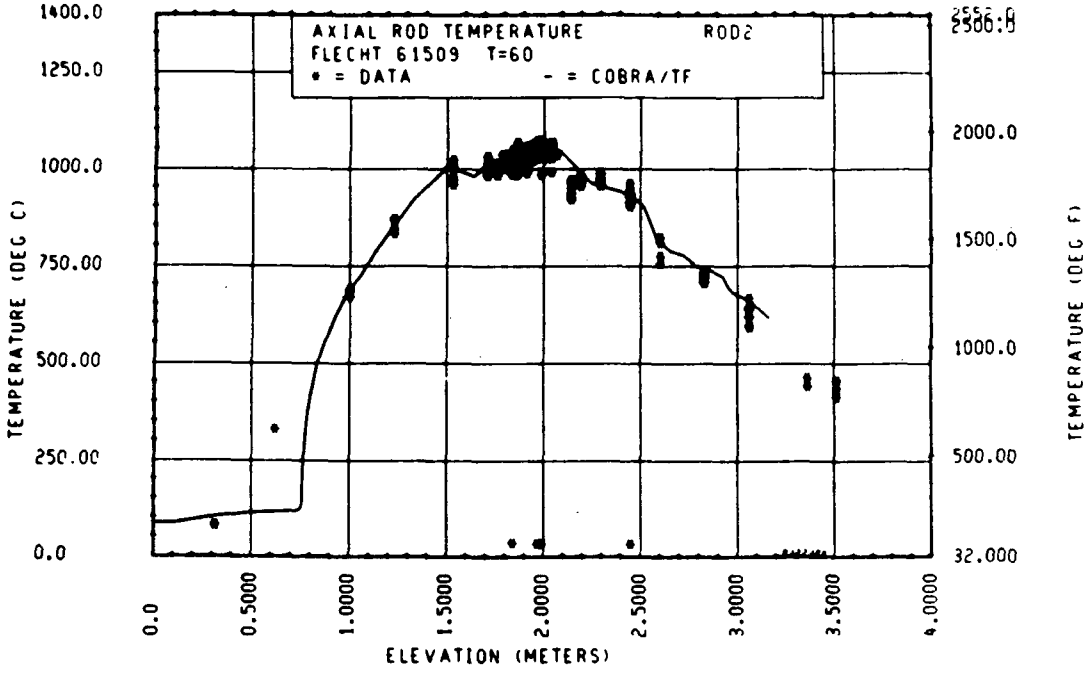

Figure 5-124. Comparison of COBRA-TF-Calculated Axial Rod Temperature Versus Elevation With FLECHT SEASET 163-Rod Data, Test 61509, t = 60 Seconds, Rod 2

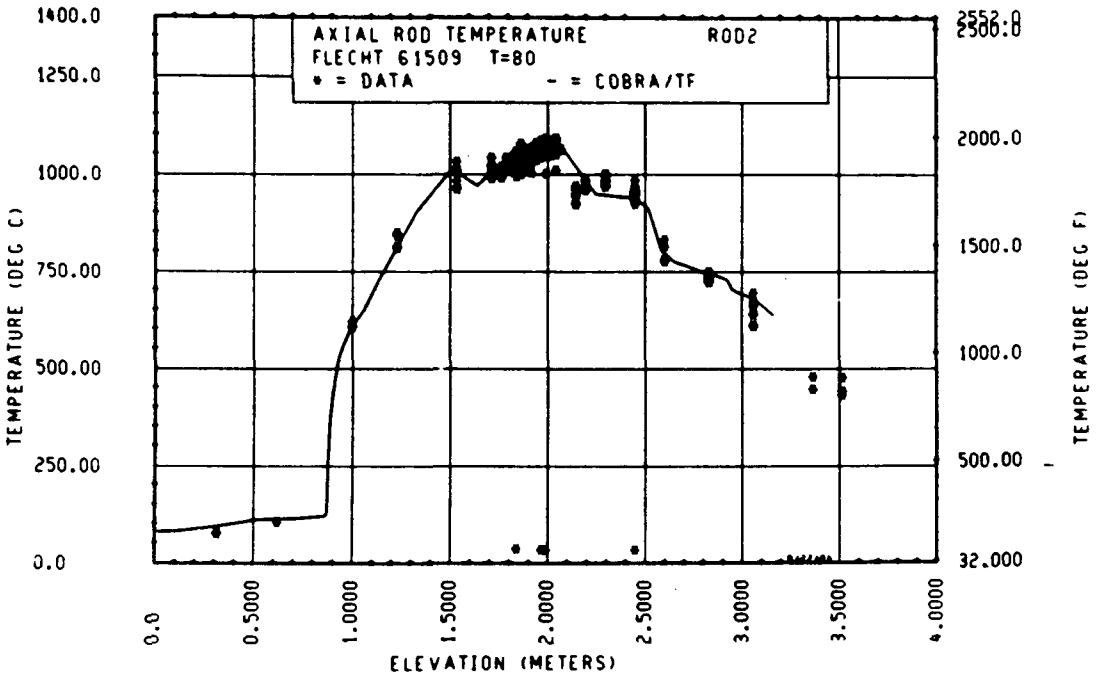

Figure 5-125. Comparison of COBRA-TF-Calculated Axial Rod Temperature Versus Elevation With FLECHT SEASET 163-Rod Data, Test 61509, t = 80 Seconds, Rod 2

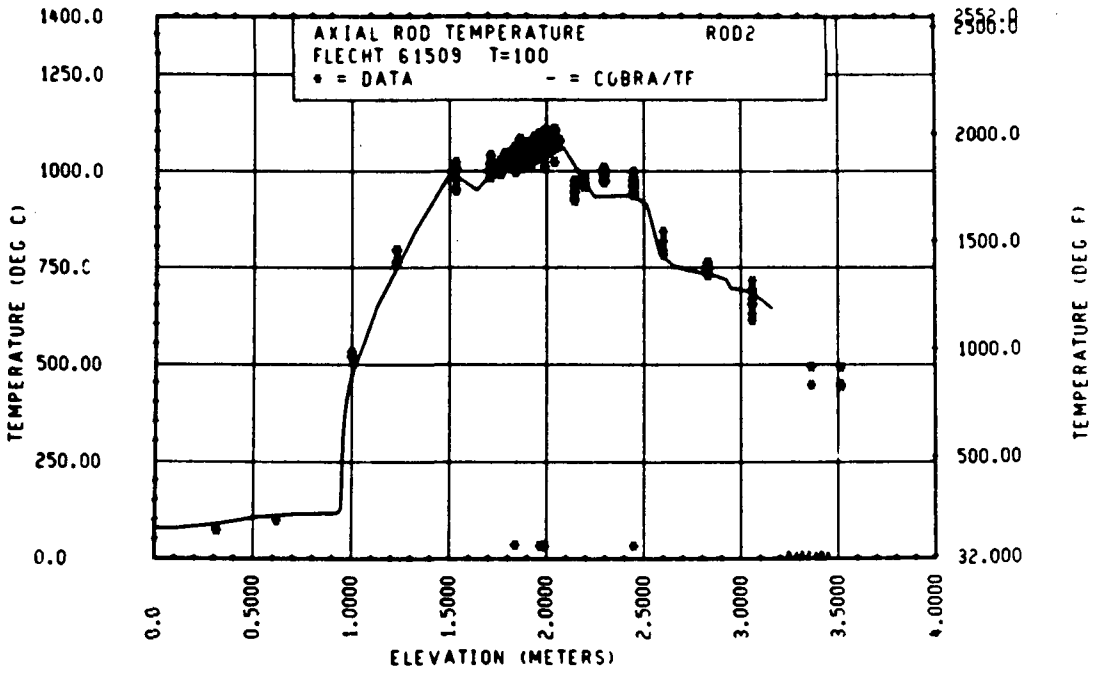

Figure 5-126. Comparison of COBRA-TF-Calculated Axial Rod Temperature Versus Elevation With FLECHT SEASET 163-Rod Data, Test 61509, t = 100 Seconds, Rod 2

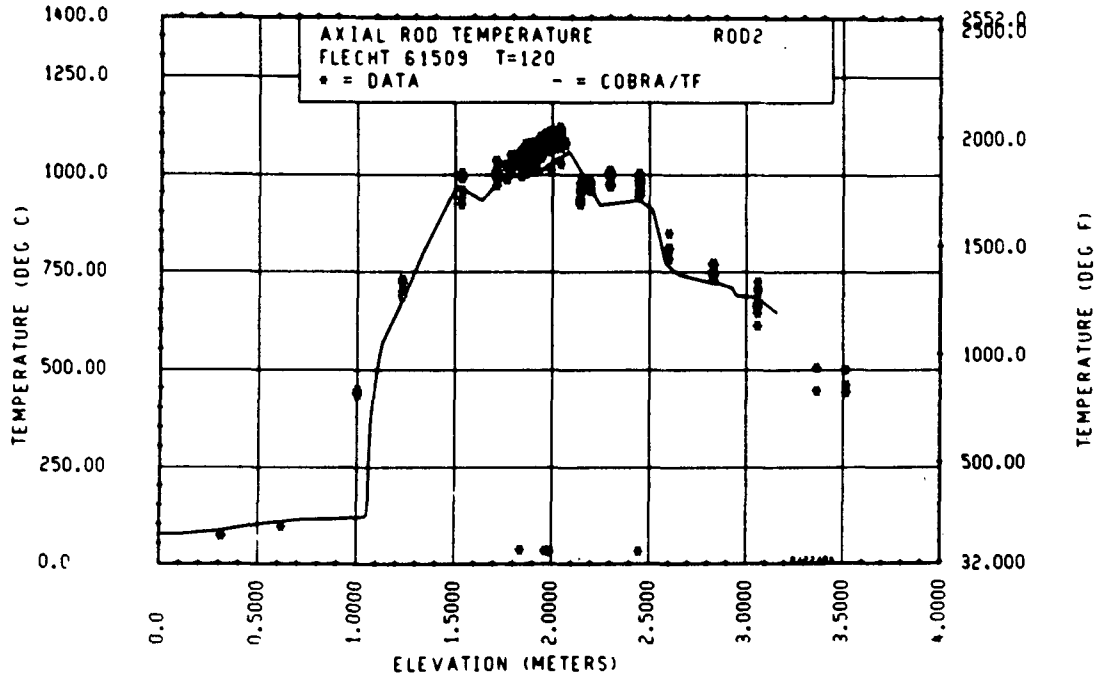

Figure 5-127. Comparison of COBRA-TF-Calculated Axial Rod Temperature Versus Elevation With FLECHT SEASET 163-Rod Data, Test 61509, t = 120 Seconds, Rod 2

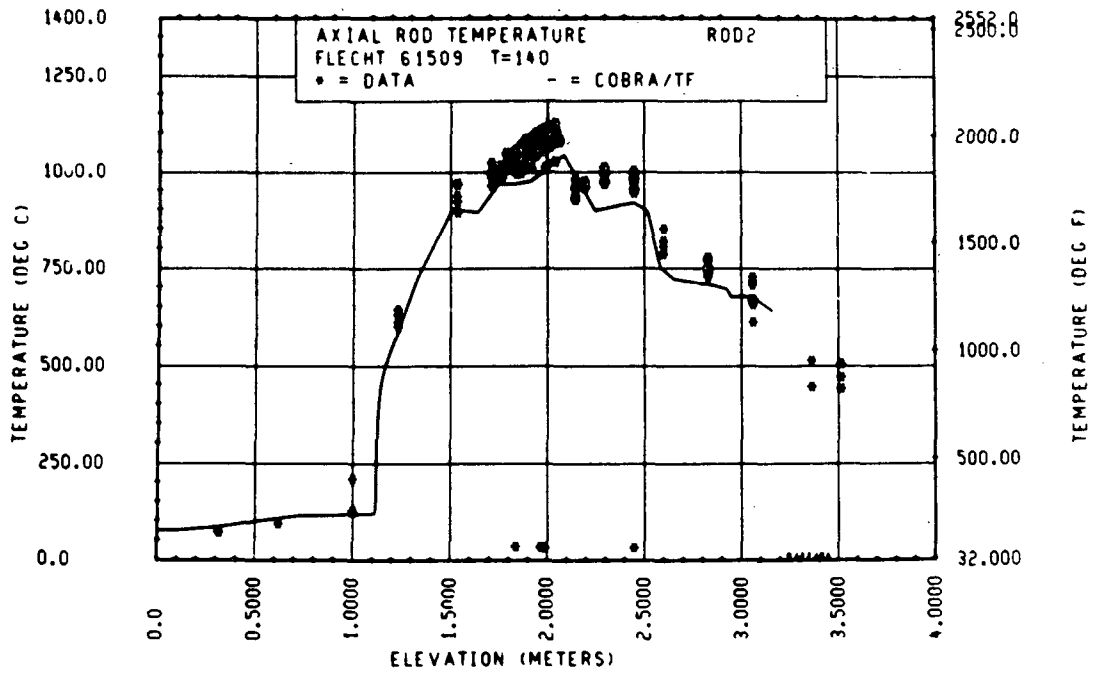

Figure 5-128. Comparison of COBRA-TF-Calculated Axial Rod Temperature Versus Elevation With FLECHT SEASET 163-Rod Data, Test 61509, t = 140 Seconds, Rod 2

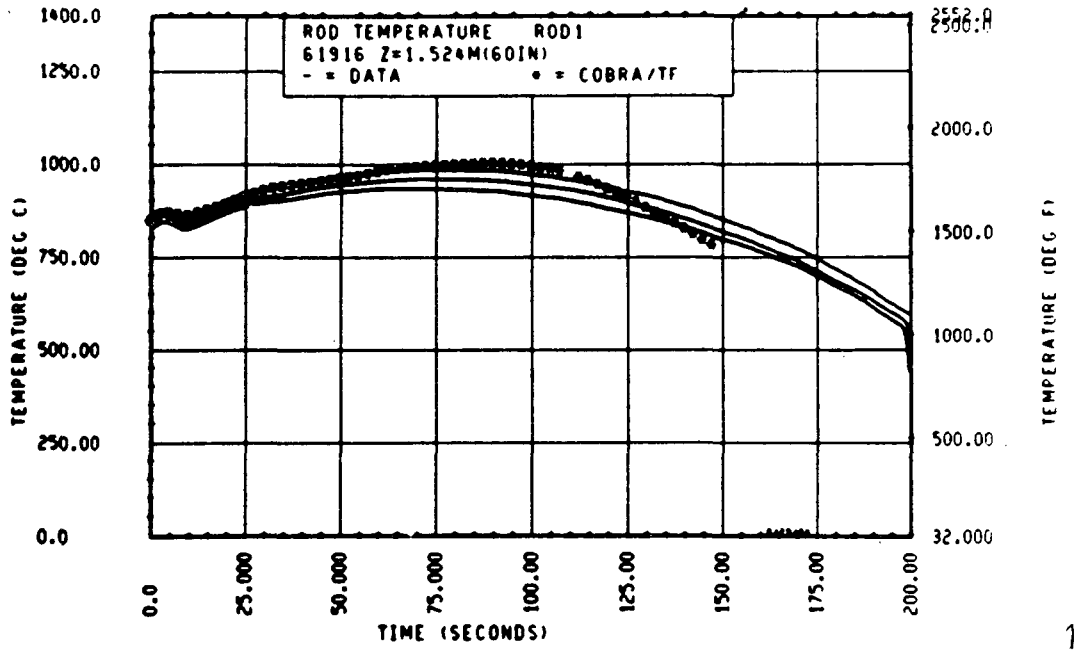

Figure 5-129. Comparison of COBRA-TF-Calculated Heater Rod Temperature Versus Time With FLECHT SEASET 163-Rod Data, Test 25916, 1.52 m (60 in.) Elevation, Rod 1

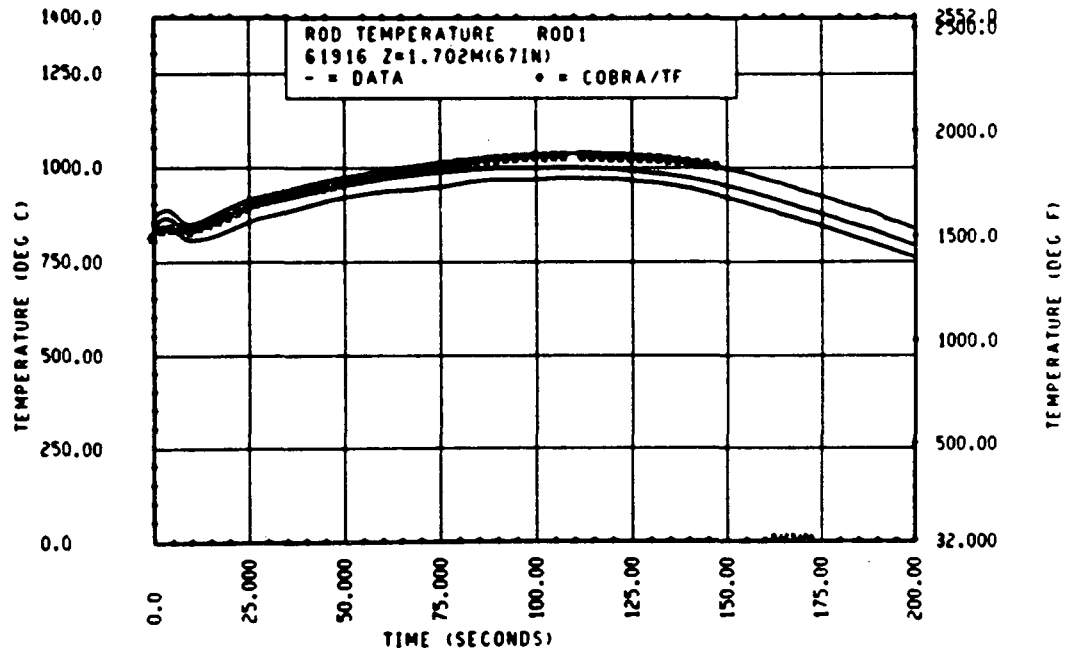

Figure 5-130. Comparison of COBRA-TF-Calculated Heater Rod Temperature Versus Time With FLECHT SEASET 163-Rod Data, Test 61916, 1.70 m (67 in.) Elevation, Rod 1

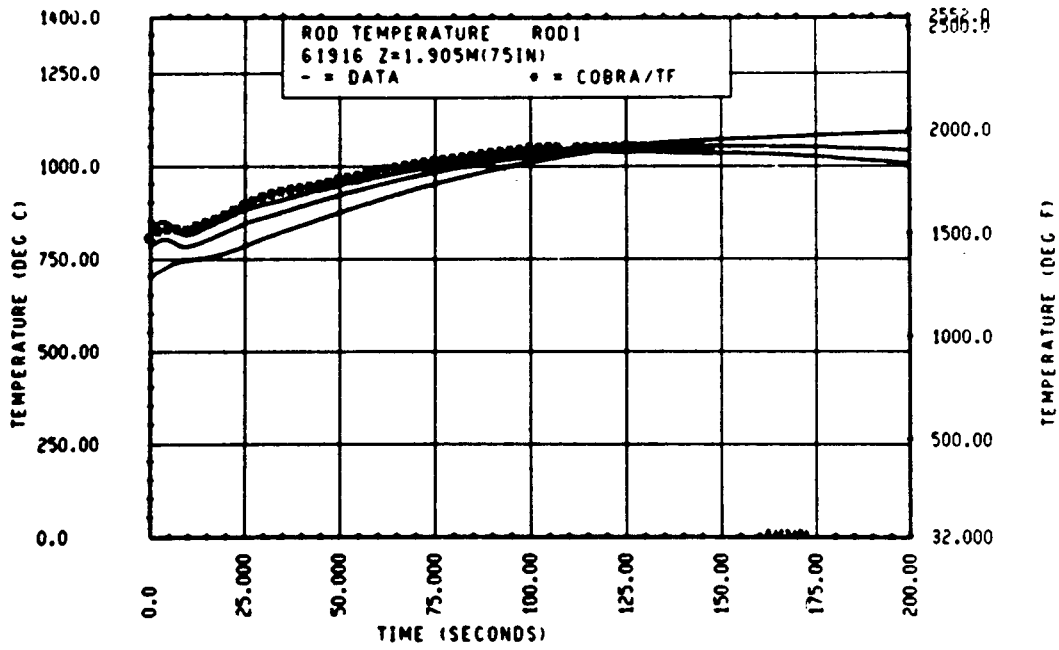

Figure 5-131. Comparison of COBRA-TF-Calculated Heater Rod Temperature Versus Time With FLECHT SEASET 163-Rod Data, Test 61916, 1.90 m (75 in.) Elevation, Rod 1

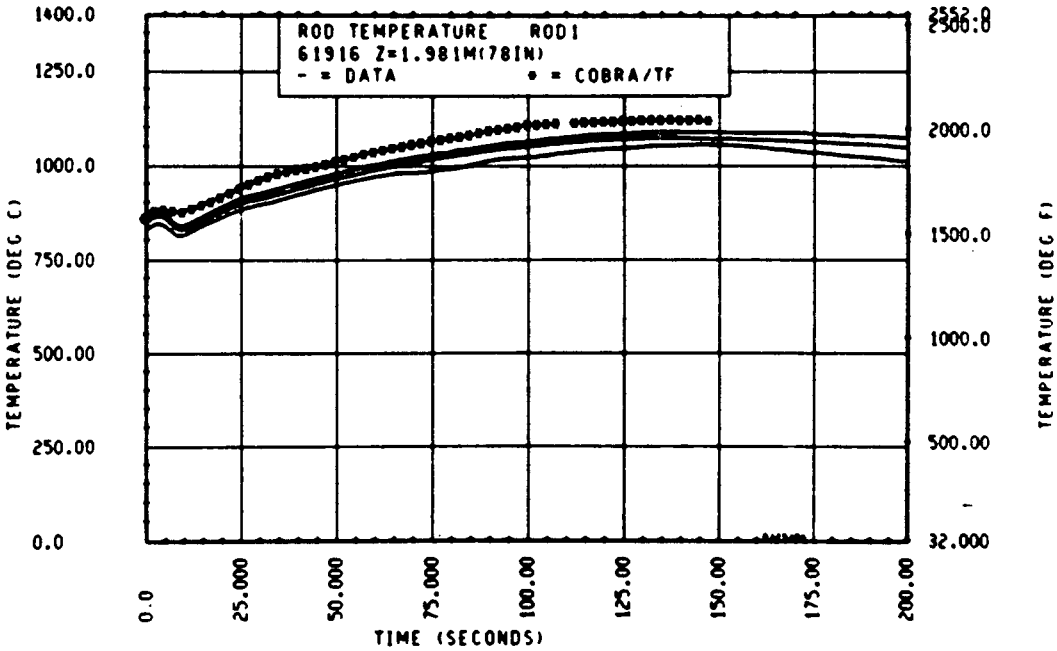

Figure 5-132. Comparison of COBRA-TF-Calculated Heater Rod Temperature Versus Time With FLECHT SEASET 163-Rod Data, Test 61916, 1.98 m (78 in.) Elevation, Rod 1

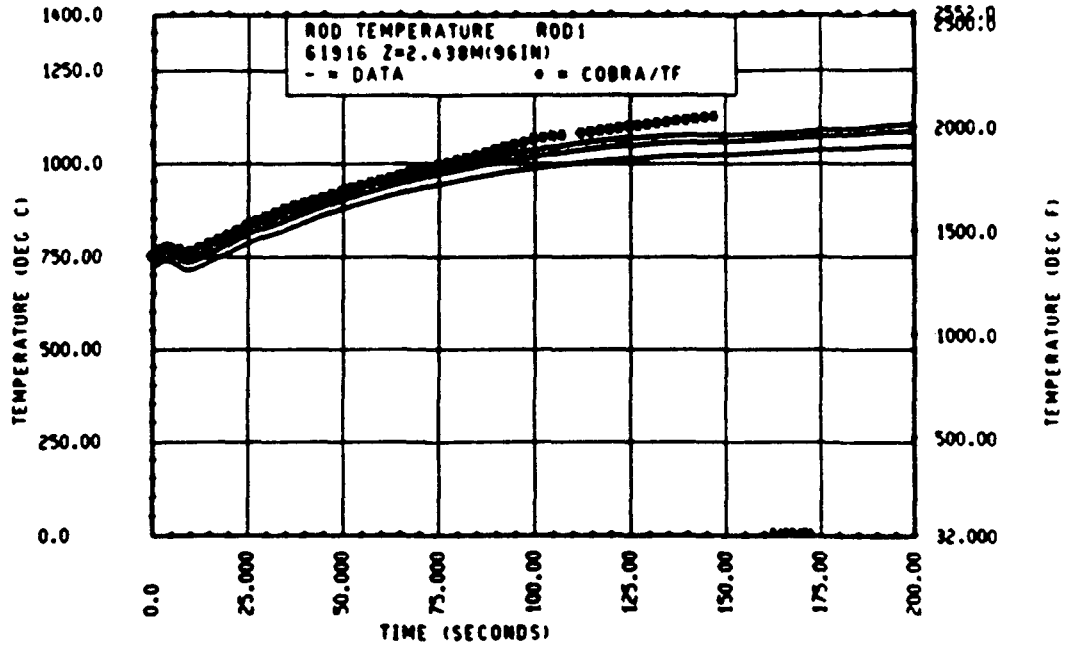

Figure 5-133. Comparison of COBRA-TF-Calculated Heater Rod Temperature Versus Time With FLECHT SEASET 163-Rod Data, Test 61916, 2.44 m (96 in.) Elevation, Rod 1

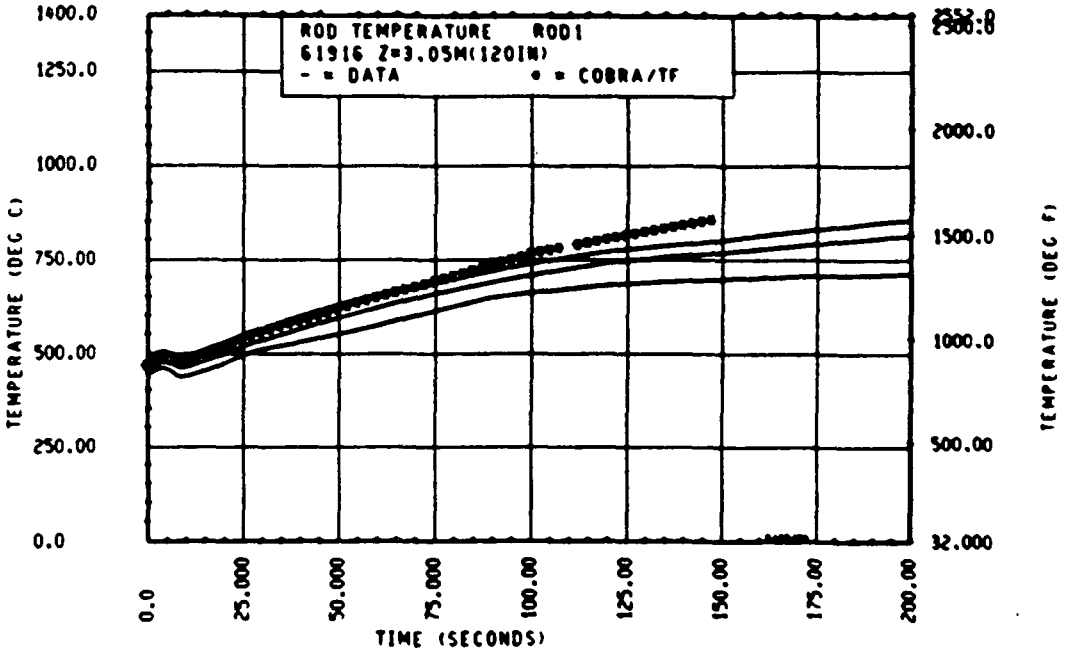

Figure 5-134. Comparison of COBRA-TF-Calculated Heater Rod Temperature Versus Time With FLECHT SEASET 163-Rod Data, Test 61916, 3.05 m (120 in.) Elevation, Rod 1

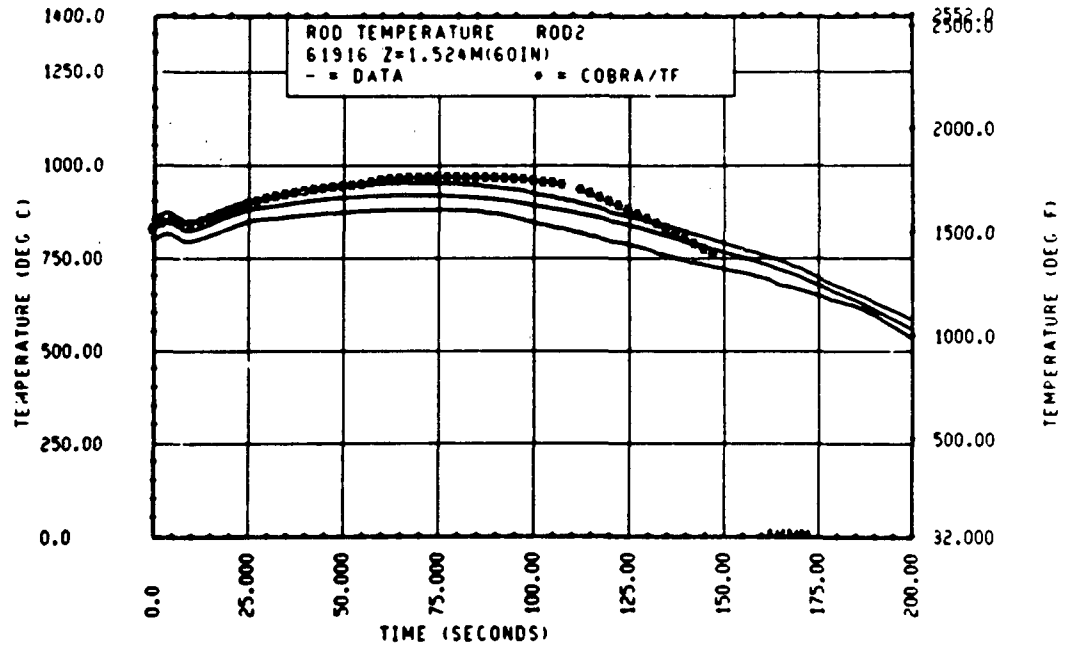

Figure 5-135. Comparison of COBRA-TF-Calculated Heater Rod Temperature Versus Time With FLECHT SEASET 163-Rod Data, Test 61916, 1.52 m (60 in.) Elevation, Rod 2

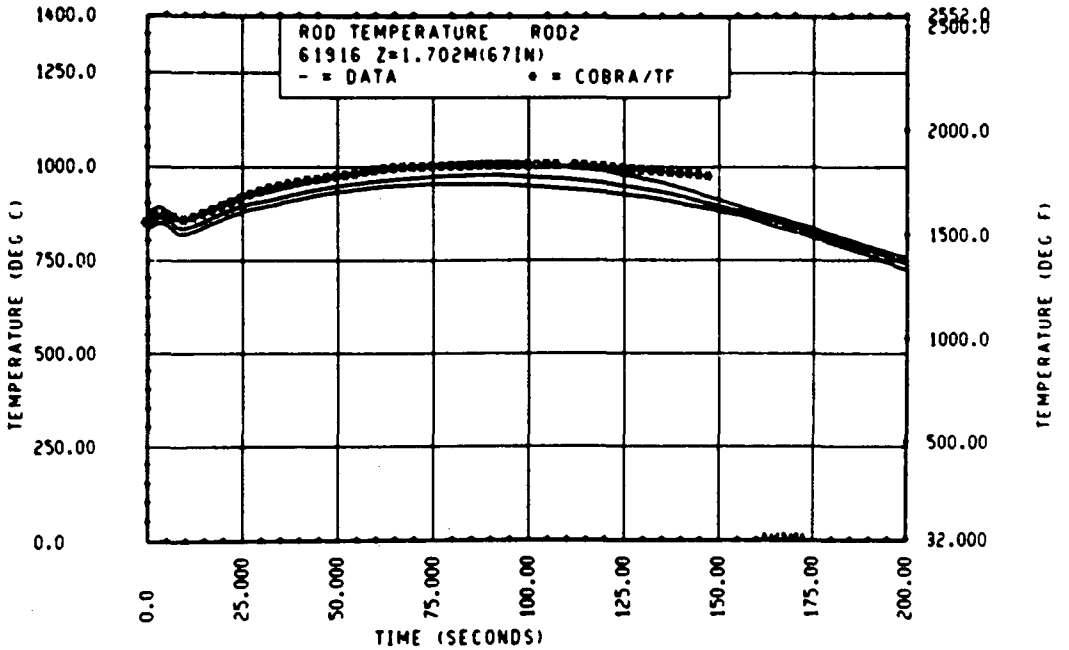

Figure 5-136. Comparison of COBRA-TF-Calculated Heater Rod Temperature Versus Time With FLECHT SEASET 163-Rod Data, Test 61916, 1.70 m (67 in.) Elevation, Rod 2

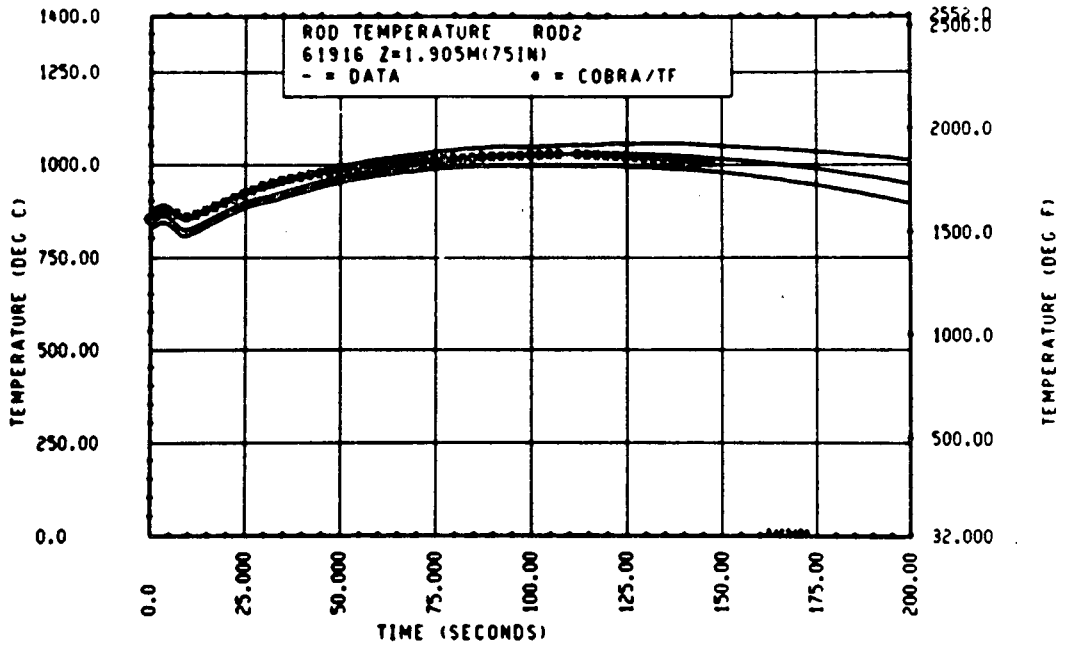

Figure 5-137. Comparison of COBRA-TF-Calculated Heater Rod Temperature Versus Time With FLECHT SEASET 163-Rod Data, Test 61916, 1.90 m (75 in.) Elevation, Rod 2

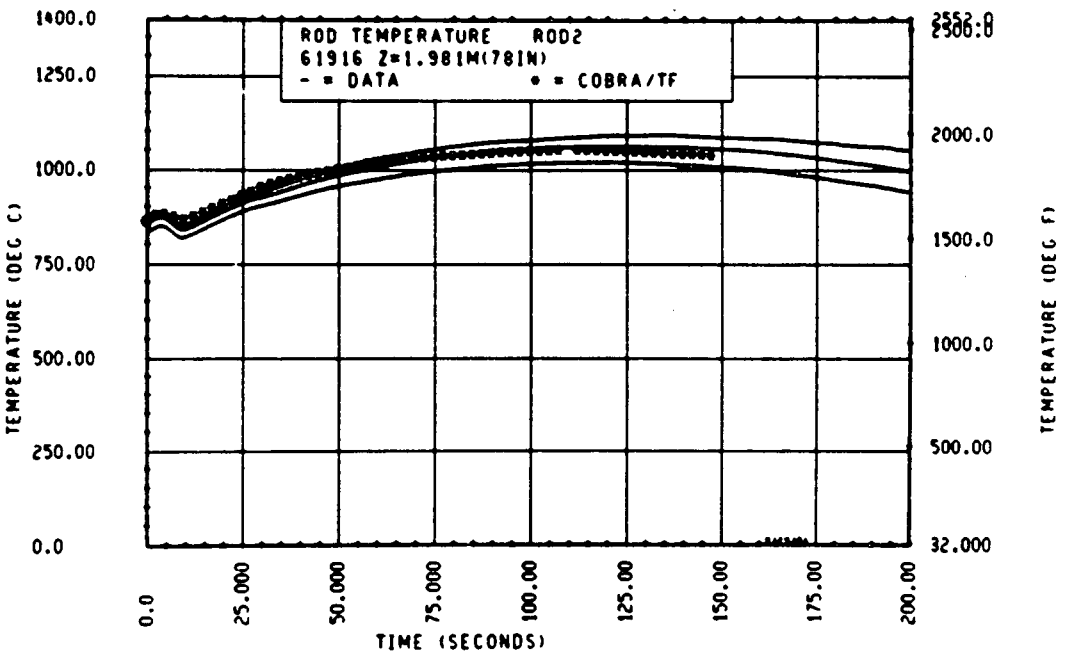

Figure 5-138. Comparison of COBRA-TF-Calculated Heater Rod Temperature Versus Time With FLECHT SEASET 163-Rod Data, Test 61916, 1.98 m (78 in.) Elevation, Rod 2

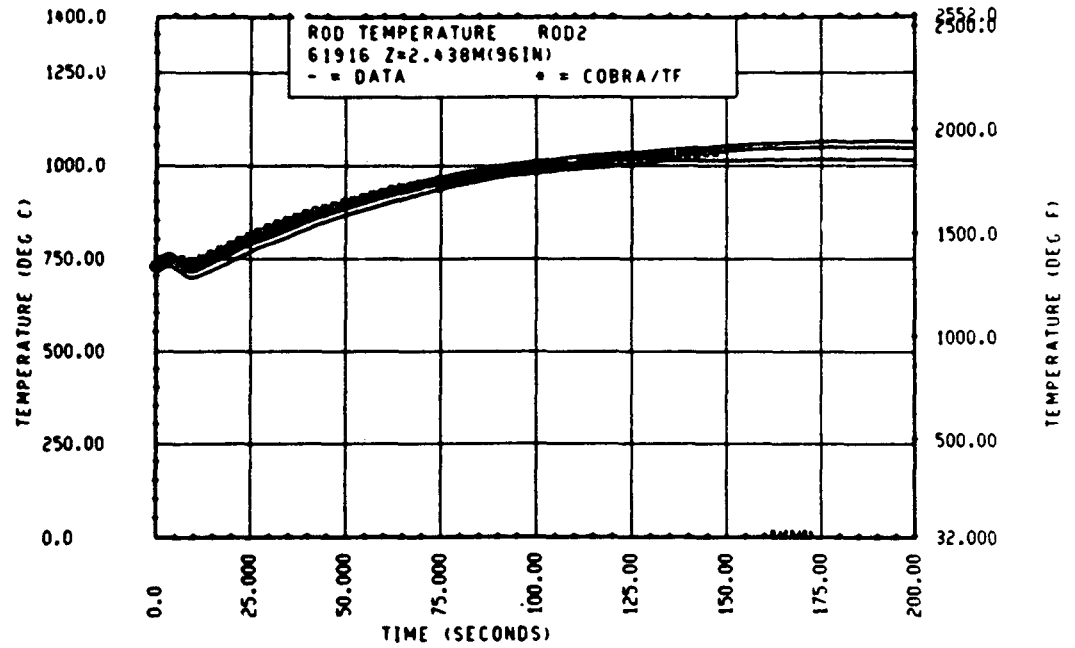

Figure 5-139. Comparison of COBRA-TF-Calculated Heater Rod Temperature Versus Time With FLECHT SEASET 163-Rod Data, Test 61916, 2.44 m (96 in.) Elevation, Rod 2

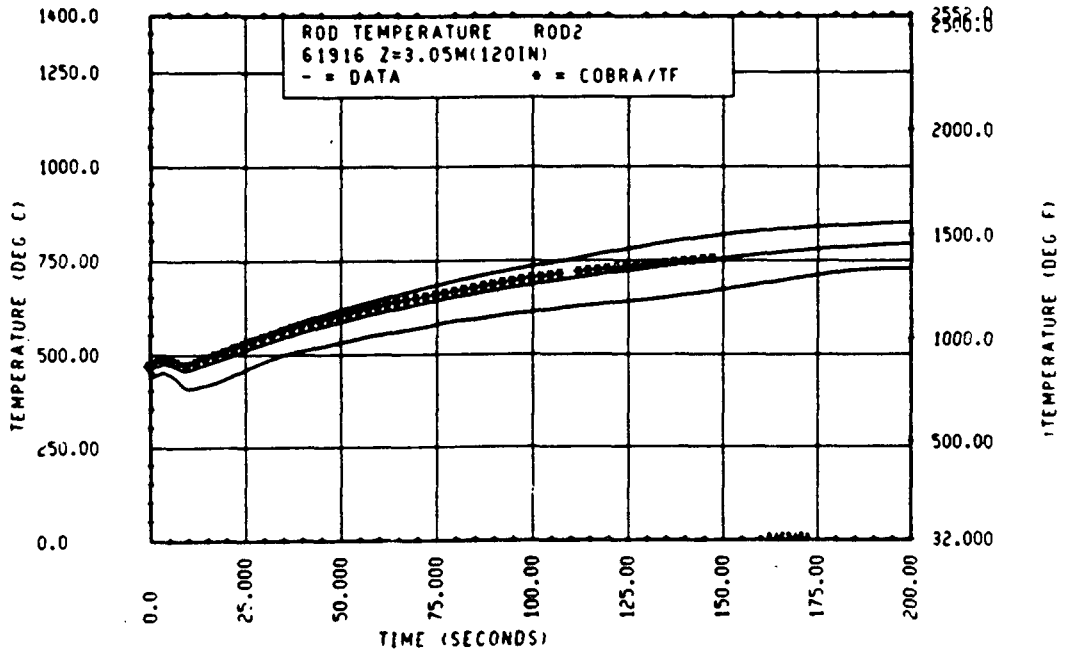

Figure 5-140. Comparison of COBRA-TF-Calculated Heater Rod Temperature Versus Time With FLECHT SEASET 163-Rod Data, Test 61916, 3.05 m (120 in.) Elevation, Rod 2

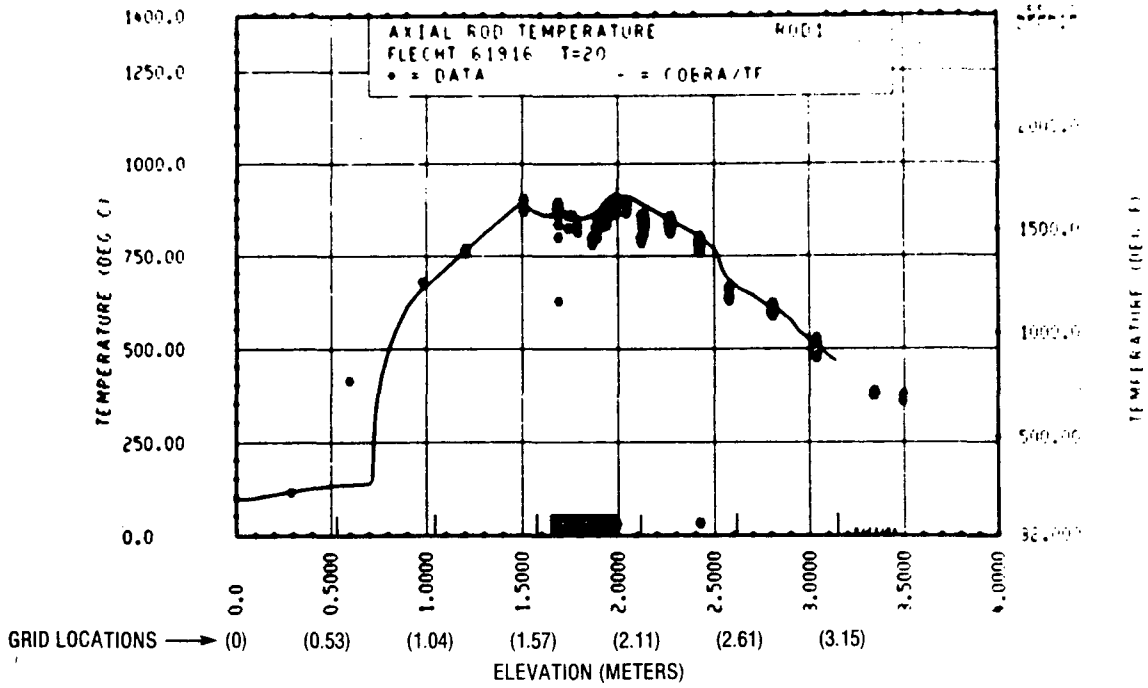

Figure 5-141. Comparison of COBRA-TF-Calculated Axial Rod Temperature Versus Elevation With FLECHT SEASET 163-Rod Data, Test 61916, t = 20 Seconds, Rod 1

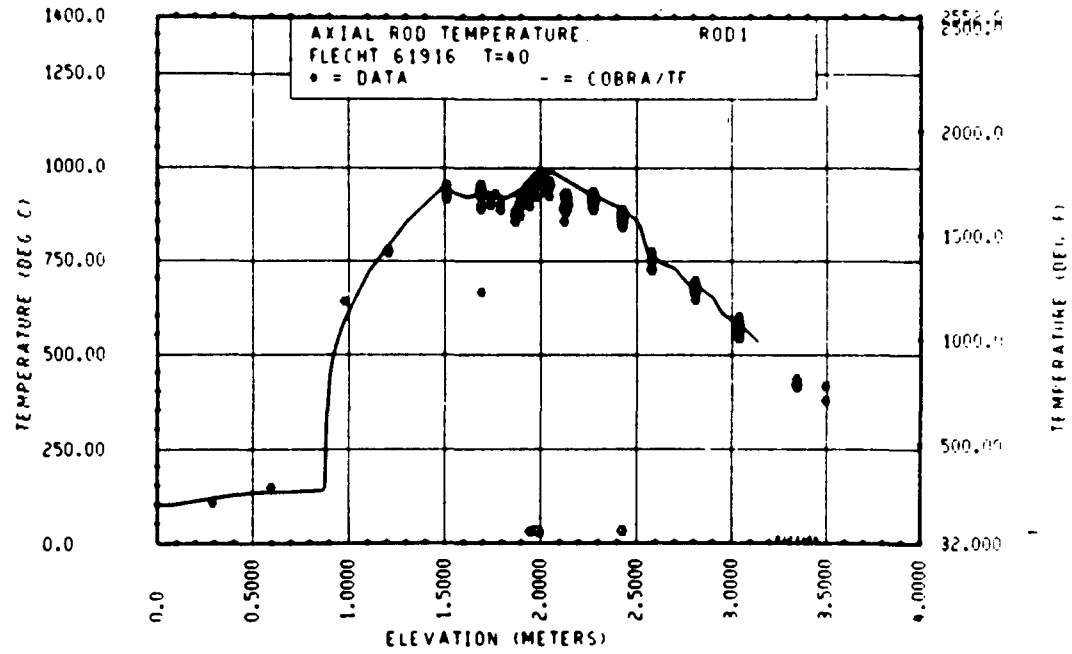

Figure 5-142. Comparison of COBRA-TF-Calculated Axial Rod Temperature Versus Elevation With FLECHT SEASET 163-Rod Data, Test 61916, t = 40 Seconds, Rod 1

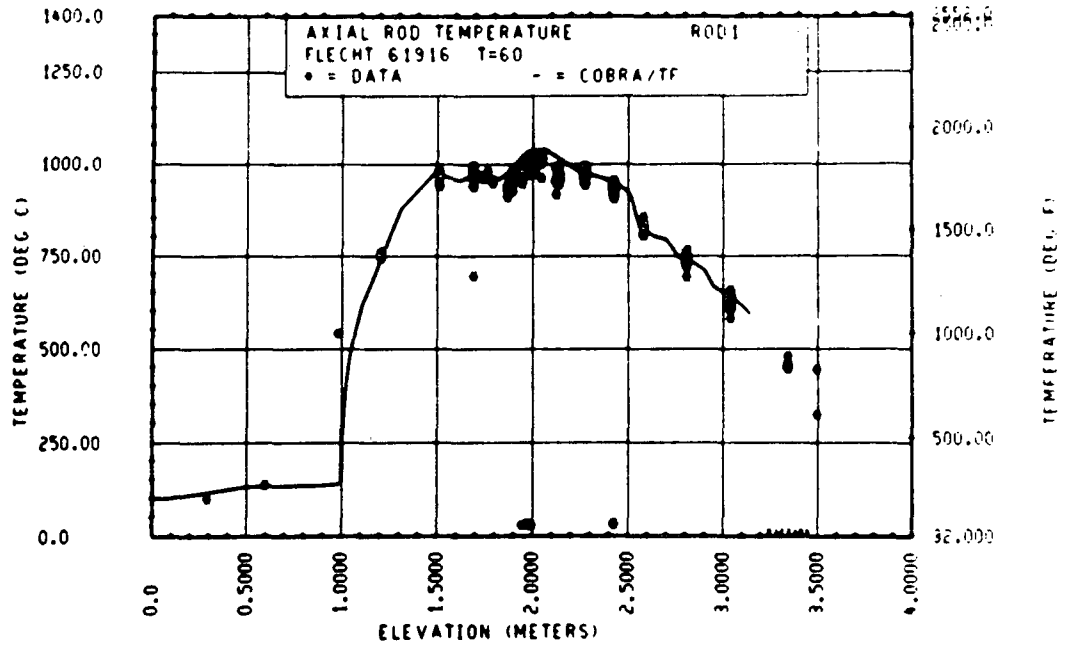

Figure 5-143. Comparison of COBRA-TF-Calculated Axial Rod Temperature Versus Elevation With FLECHT SEASET 163-Rod Data, Test 61916, t = 60 Seconds, Rod 1

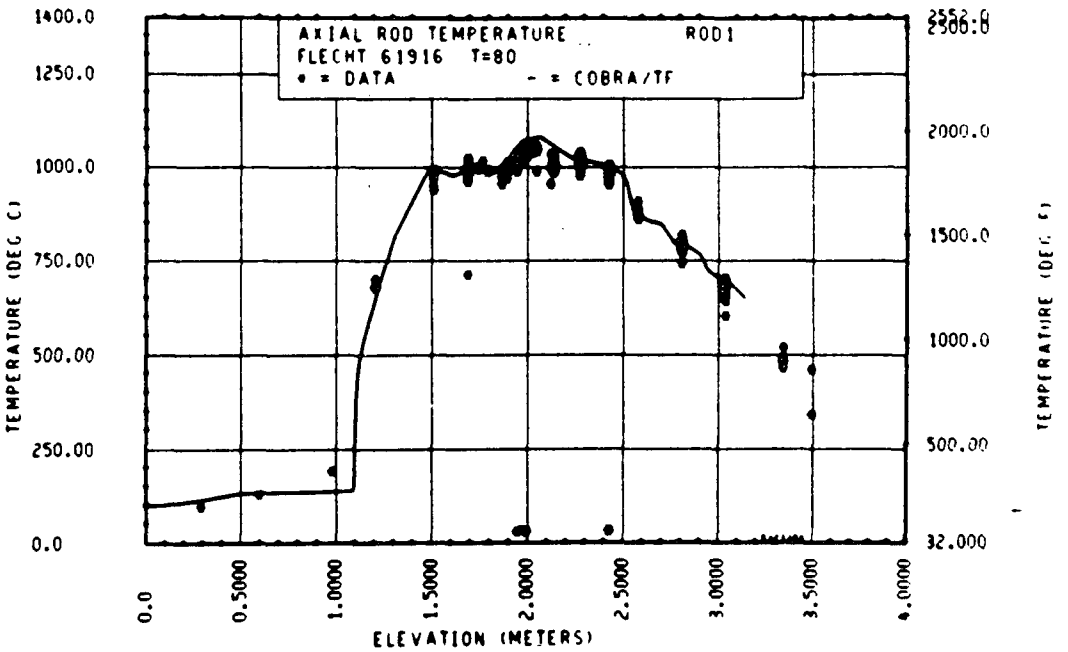

Figure 5-144. Comparison of COBRA-TF-Calculated Axial Rod Temperature Versus Elevation With FLECHT SEASET 163-Rod Data, Test 61916, t = 80 Seconds, Rod 1

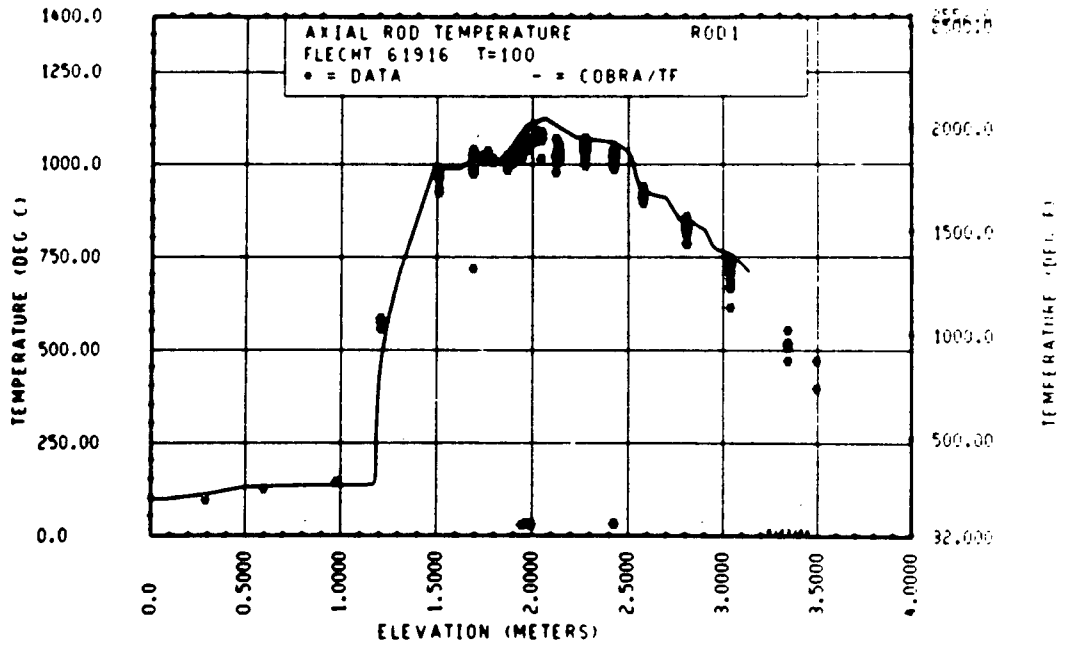

Figure 5-145. Comparison of COBRA-TF-Calculated Axial Rod Temperature Versus Elevation With FLECHT SEASET 163-Rod Data, Test 61916, t = 100 Seconds, Rod 1

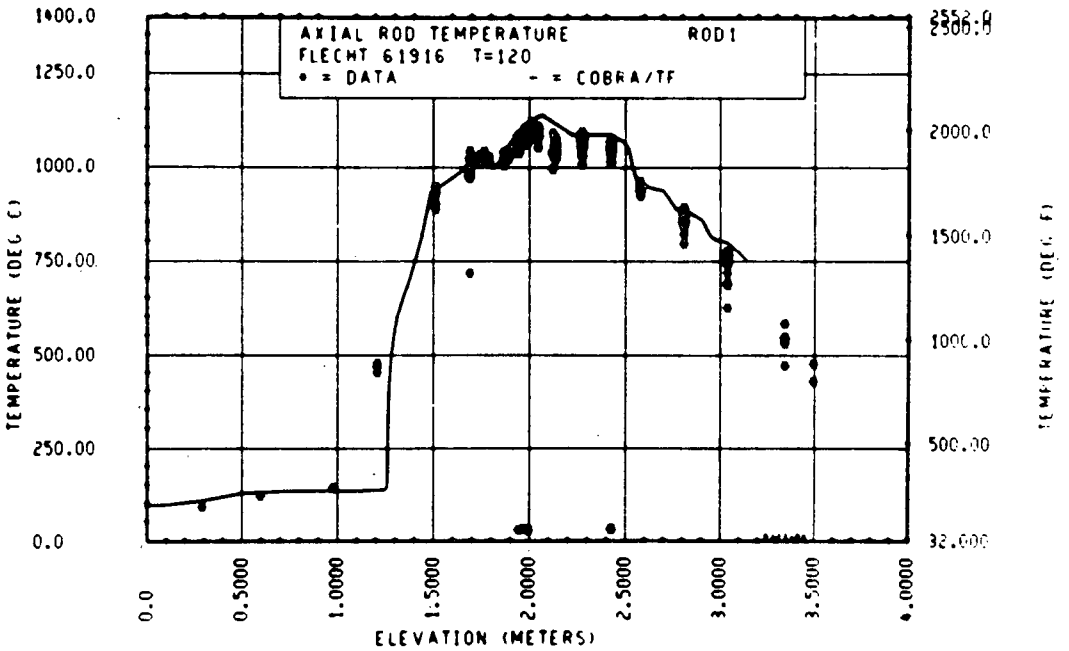

Figure 5-146. Comparison of COBRA-TF-Calculated Axial Rod Temperature Versus Elevation With FLECHT SEASET 163-Rod Data, Test 61916, t = 120 Seconds, Rod 1

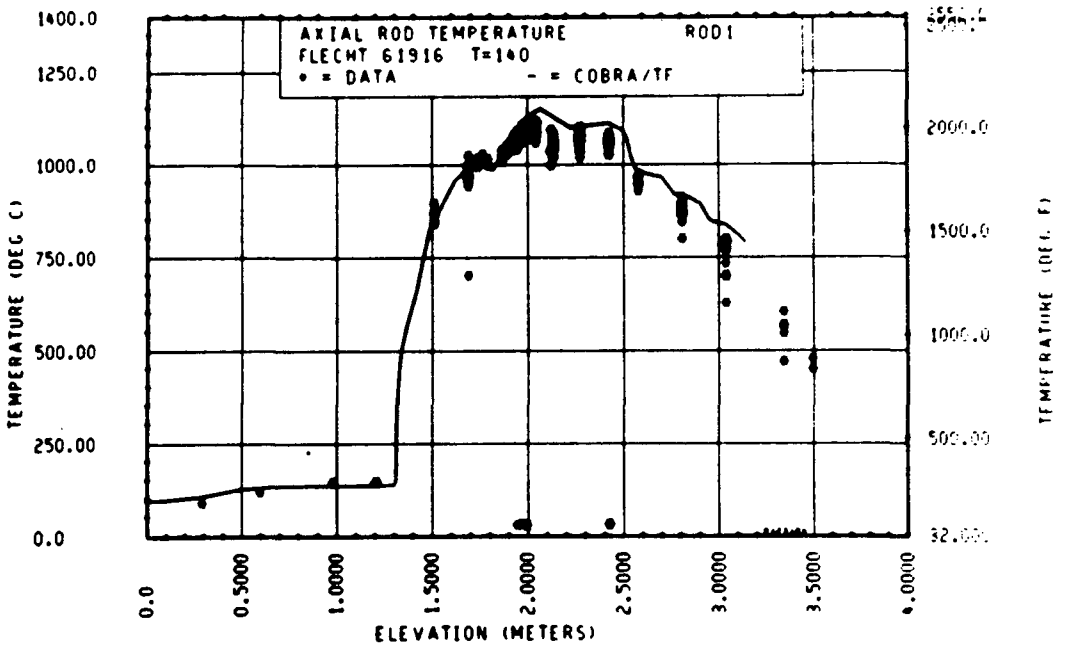

Figure 5-147. Comparison of COBRA-TF-Calculated Axial Rod Temperature Versus Elevation With FLECHT SEASET 163-Rod Data, Test 61916, t = 140 Seconds, Rod 1

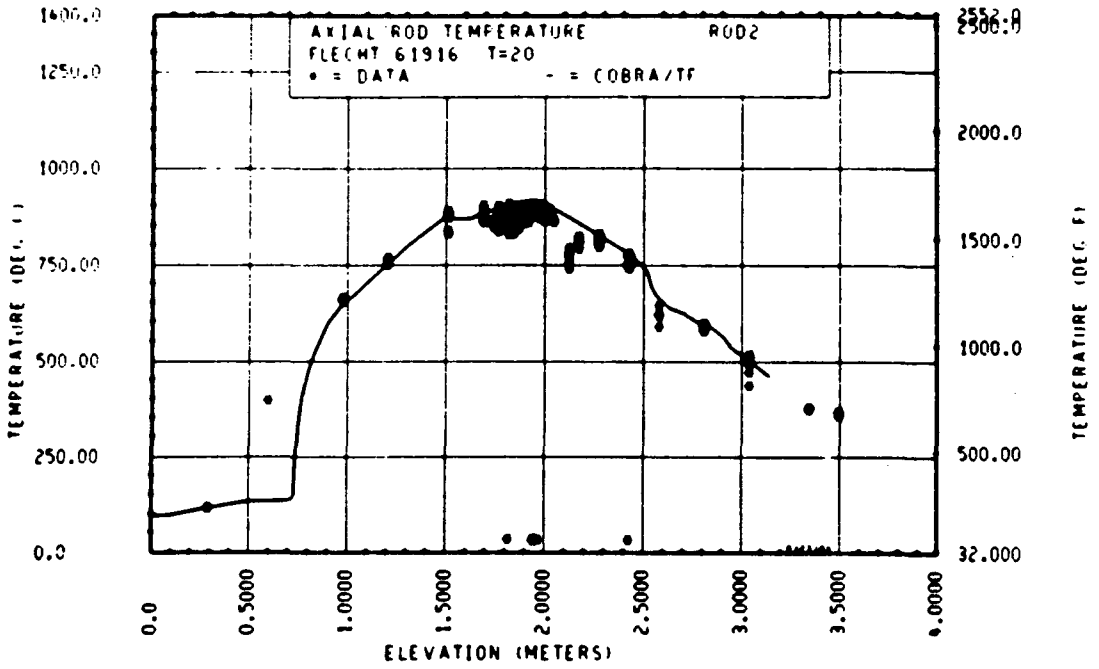

Figure 5-148. Comparison of COBRA-TF-Calculated Axial Rod Temperature Versus Elevation With FLECHT SEASET 163-Rod Data, Test 61916, t = 20 Seconds, Rod 2

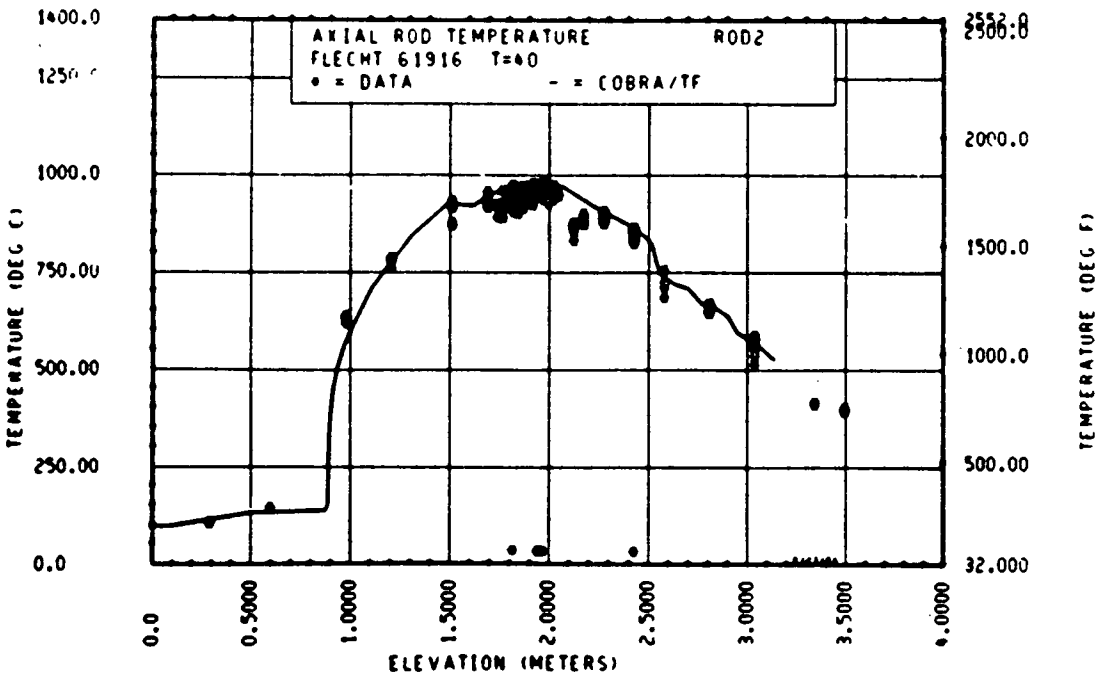

Figure 5-149. Comparison of COBRA-TF-Calculated Axial Rod Temperature Versus Elevation With FLECHT SEASET 163-Rod Data, Test 61916, t = 40 Seconds, Rod 2

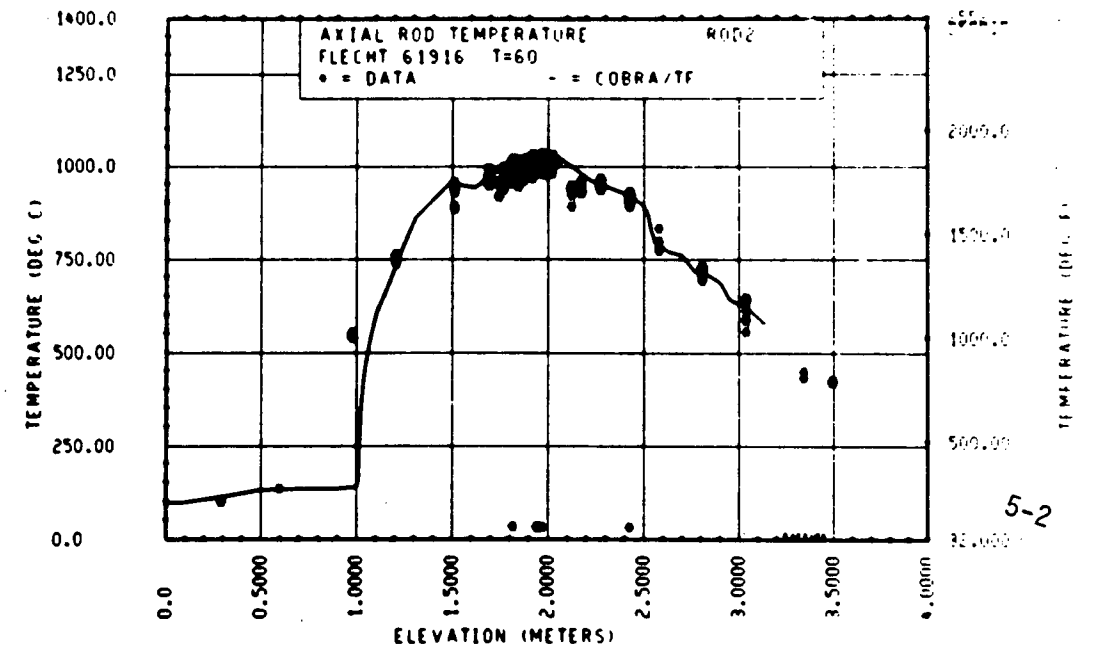

Figure 5-150. Comparison of COBRA-TF-Calculated Axial Rod Temperature Versus Elevation With FLECHT SEASET 163-Rod Data, Test 61916, t = 60 Seconds, Rod 2

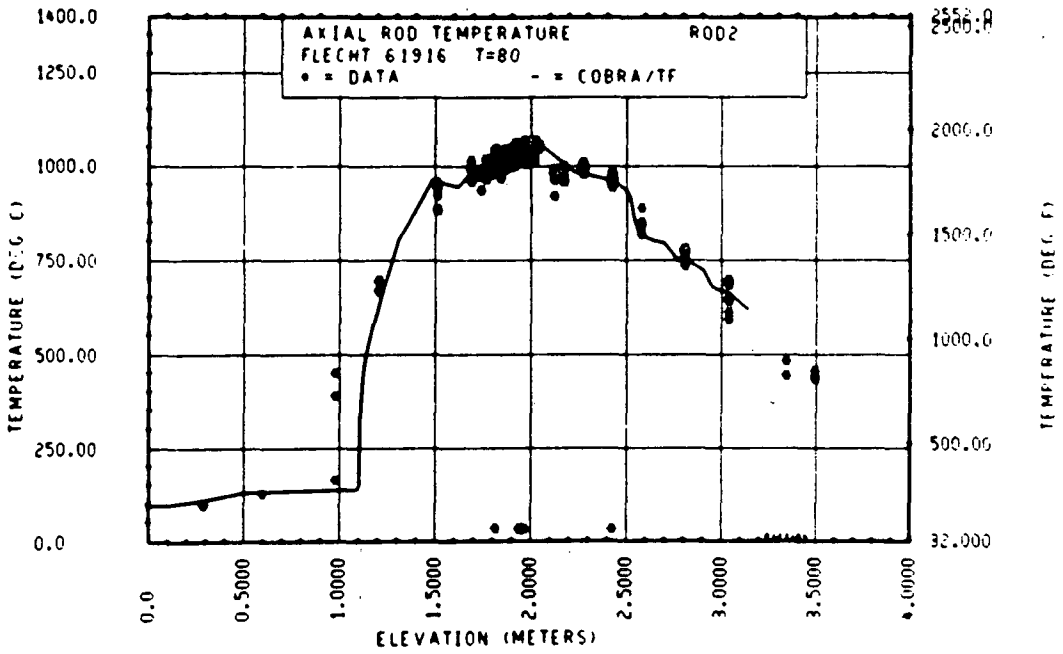

Figure 5-151. Comparison of COBRA-TF-Calculated Axial Rod Temperature Versus Elevation With FLECHT SEASET 163-Rod Data, Test 61916, t = 80 Seconds, Rod 2

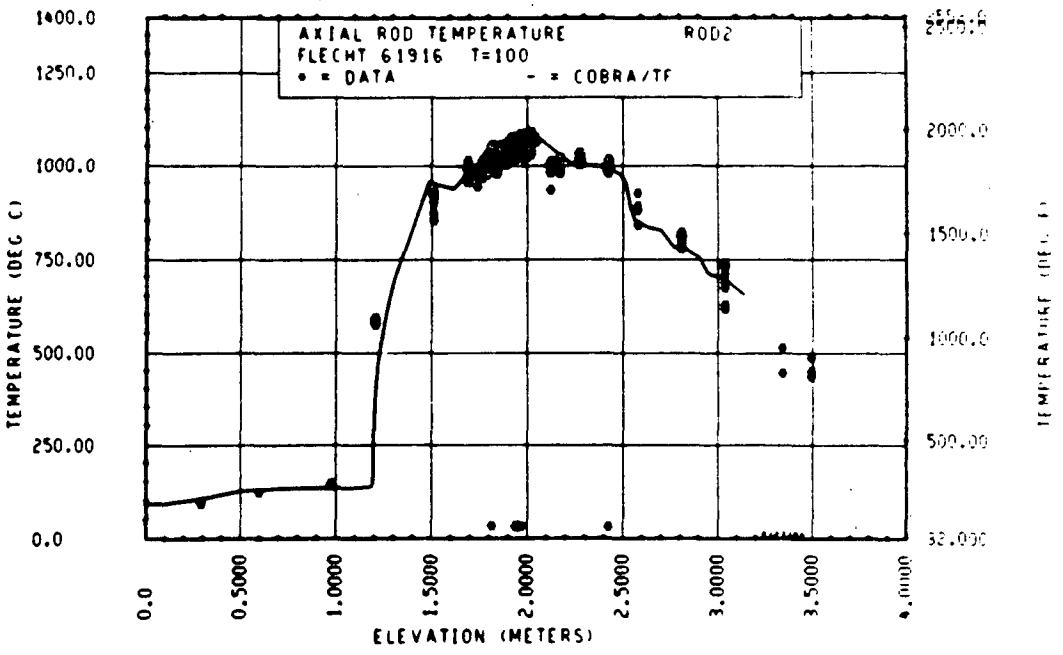

Figure 5-152. Comparison of COBRA-TF-Calculated Axial Rod Temperature Versus Elevation With FLECHT SEASET 163-Rod Data, Test 61916, t = 100 Seconds, Rod 2

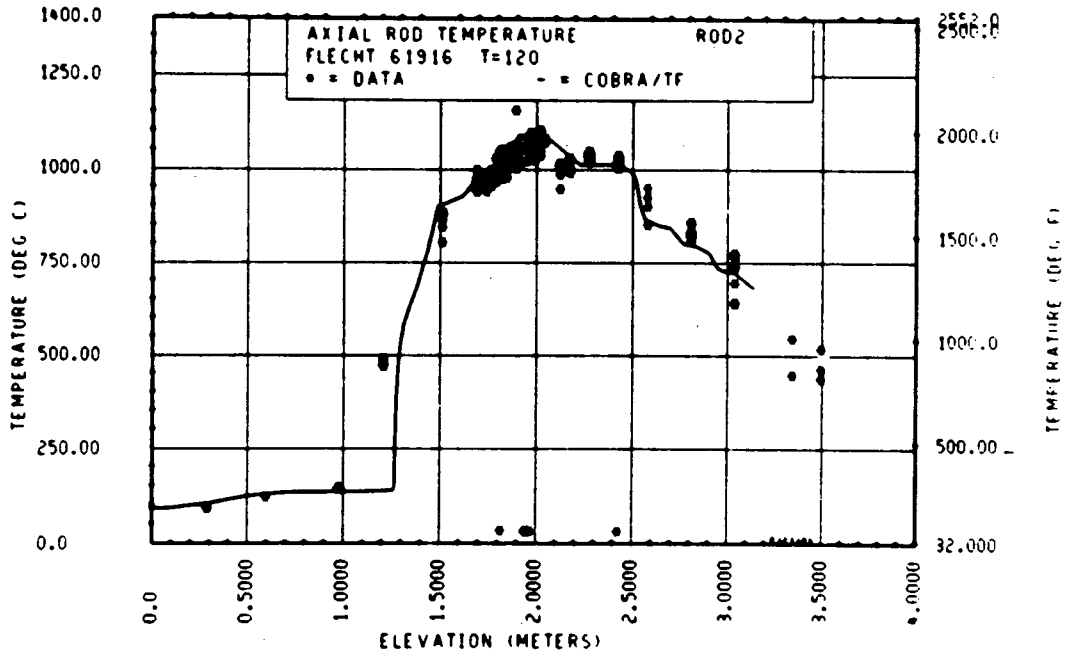

Figure 5-153. Comparison of COBRA-TF-Calculated Axial Rod Temperature Versus Elevation With FLECHT SEASET 163-Rod Data, Test 61916, t = 120 Seconds, Rod 2

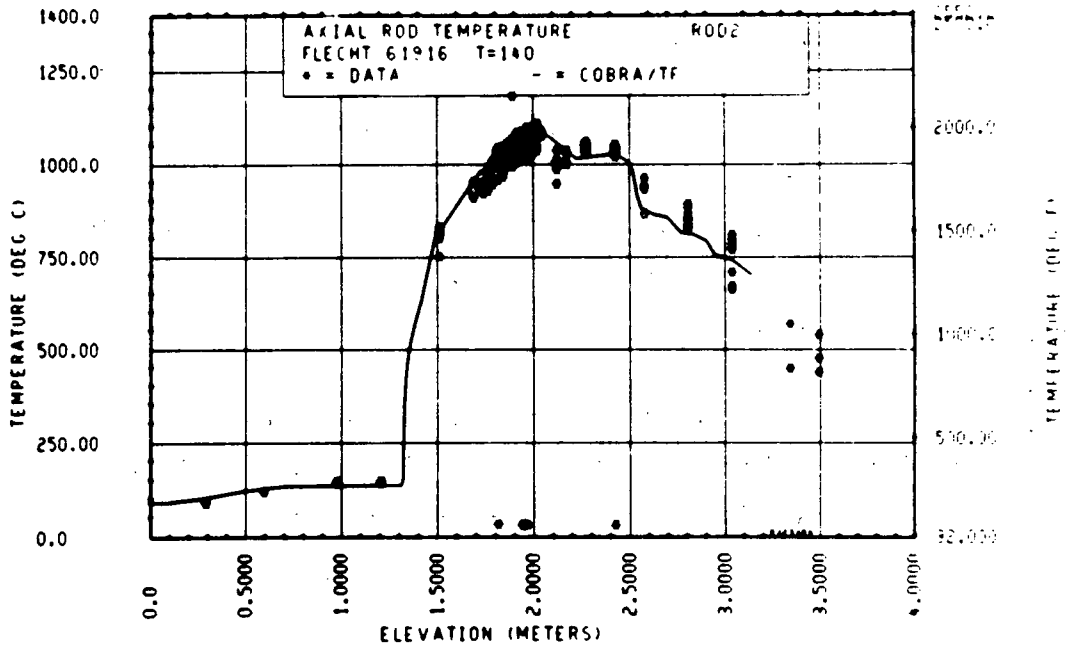

Figure 5-154. Comparison of COBRA-TF-Calculated Axial Rod Temperature Versus Elevation With FLECHT SEASET 163-Rod Data, Test 61916, t = 140 Seconds, Rod 2

5-141 shows the axial location of the spacer grids and the blockage zone.) The rod 1 comparisons are quite good, but do show a small overprediction of the heater rod temperatures at the upper elevations. This is also apparent on the axial heater rod temperature plots. For this test, the grid effect at the 1.57 m (62 in.) elevation appears correct, but the blockage heat transfer effects appear stronger in the data than in the COBRA-TF predictions. The rod 2 comparisons are quite good.

5-5. DISCUSSION OF COBRA-TF RESULTS FOR FLECHT SEASET 163-ROD BLOCKED BUNDLE

The blockage models used to compare the 163-rod blocked bundle data in paragraph 5-4 were identical to the models used to analyze the FEBA data and the 21-rod bundle FLECHT SEASET data. No models were changed to represent the 163-rod blocked bundle tests. Therefore, the 163-rod bundle tests provide independent verification of the COBRA-TF code and blockage models.

A comparison of the calculated temperature differences in the blocked region with and without the blockage models is shown in figures 5-155 through 5-161. The calculated axial temperature for rod 1 (node 1), the blockage island, is plotted against elevation for different times. The difference between the two sets of data is that one calculation (curve A) uses the blockage heat transfer models and the other (curve B) does not. (Both calculations model the blockage effect of flow bypass.) As these figures show, there is very little difference until the entrainment becomes developed and significant droplet breakup is occurring. Once the droplet breakup occurs, the temperature calculated with the blockage models is approximately 50° C (90° F) lower than that calculated without the blockage models. This is consistent with the results obtained in section 4, which showed that droplet breakup was one of the dominant heat transfer effects.

A measure of how well the models predict the 163-rod bundle data is shown in figures 5-162 through 5-165 as bias plots similar to those presented for the 21-rod bundle and FEBA data. The delta temperature is the measured blockage

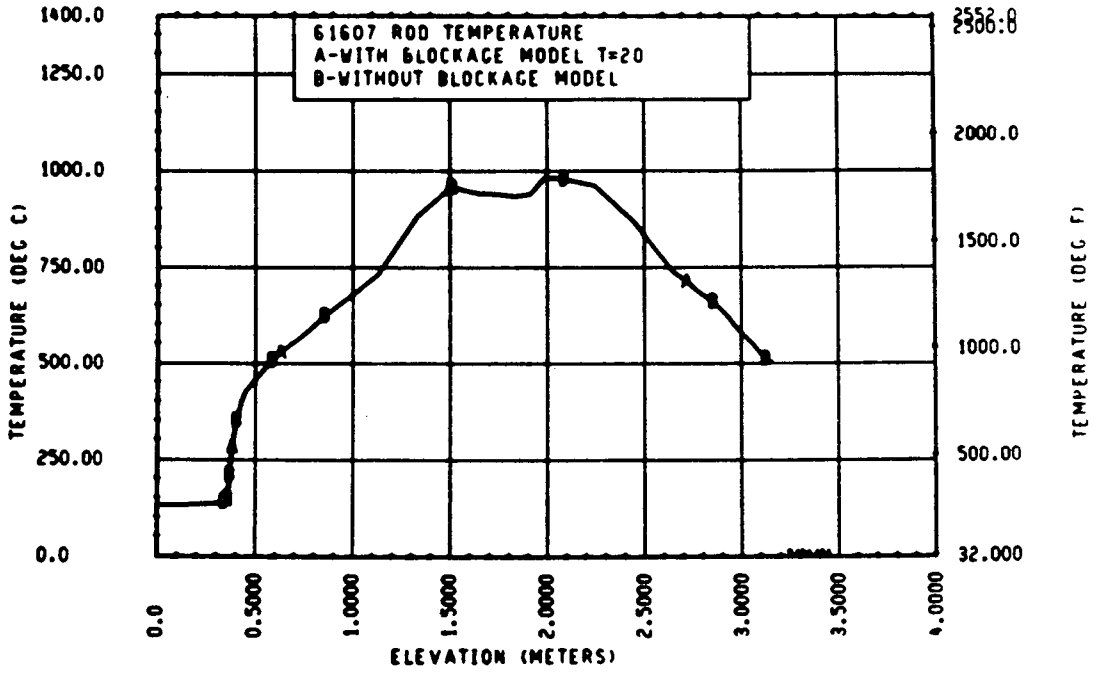

Figure 5-155. Effect of Blockage Models on Calculated Rod Temperature Differences, FLECHT SEASET Test 61607, t = 20 Seconds

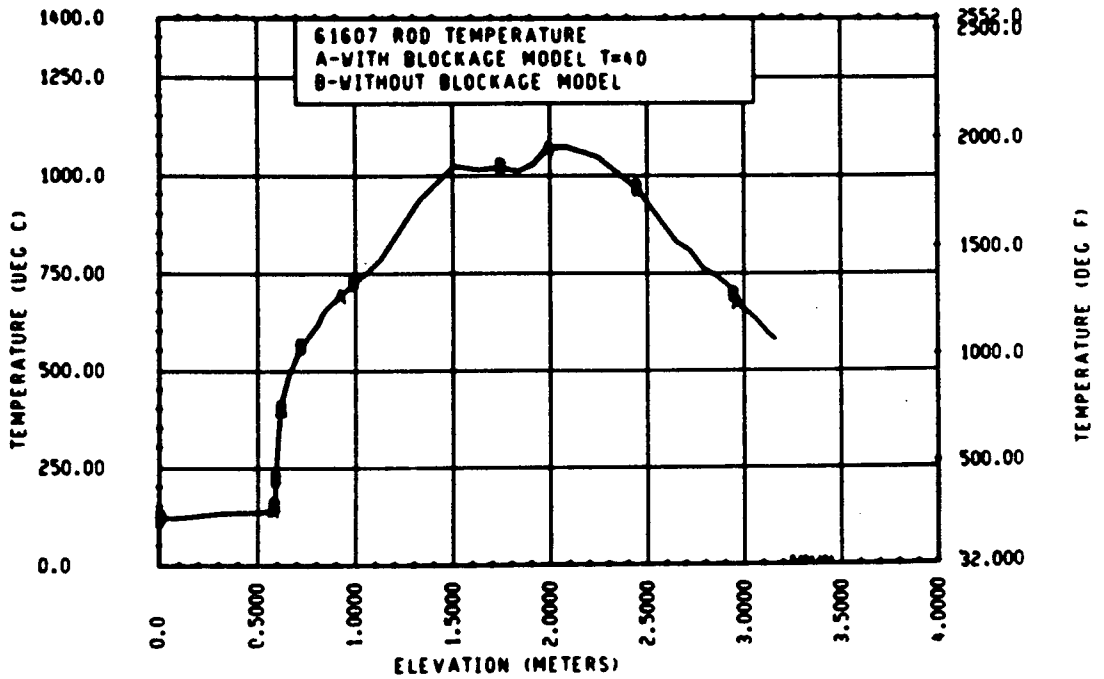

Figure 5-156. Effect of Blockage Models on Calculated Rod Temperature Differences, FLECHT SEASET Test 61607, t = 40 Seconds

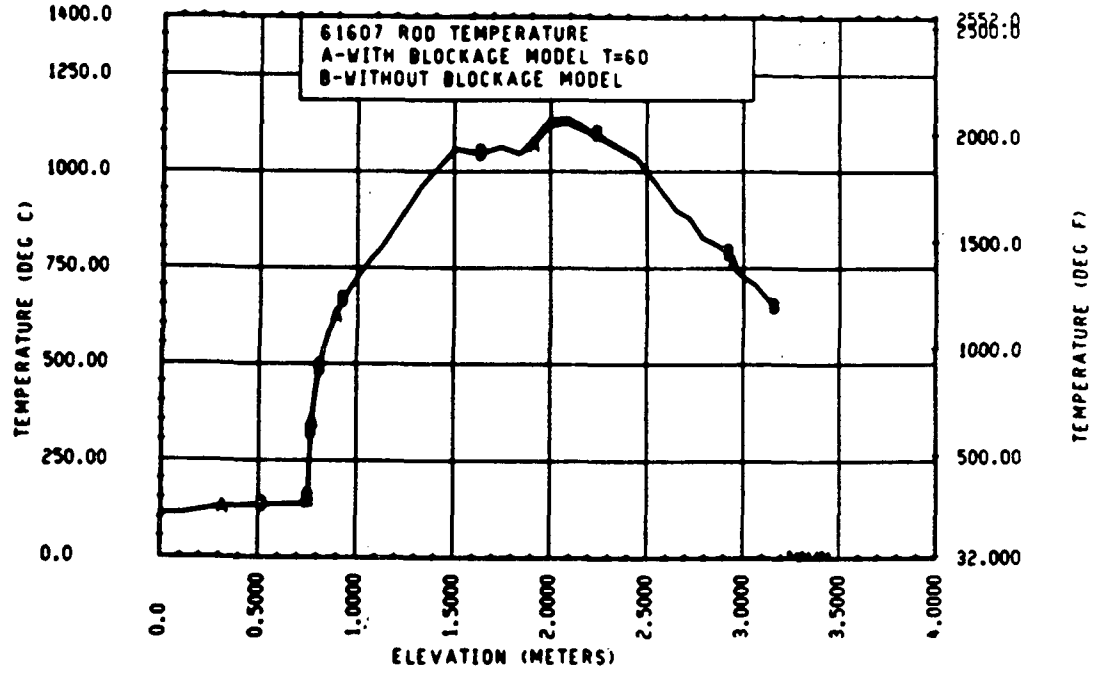

Figure 5-157. Effect of Blockage Models on Calculated Rod Temperature Differences, FLECHT SEASET Test 61607, t = 60 Seconds

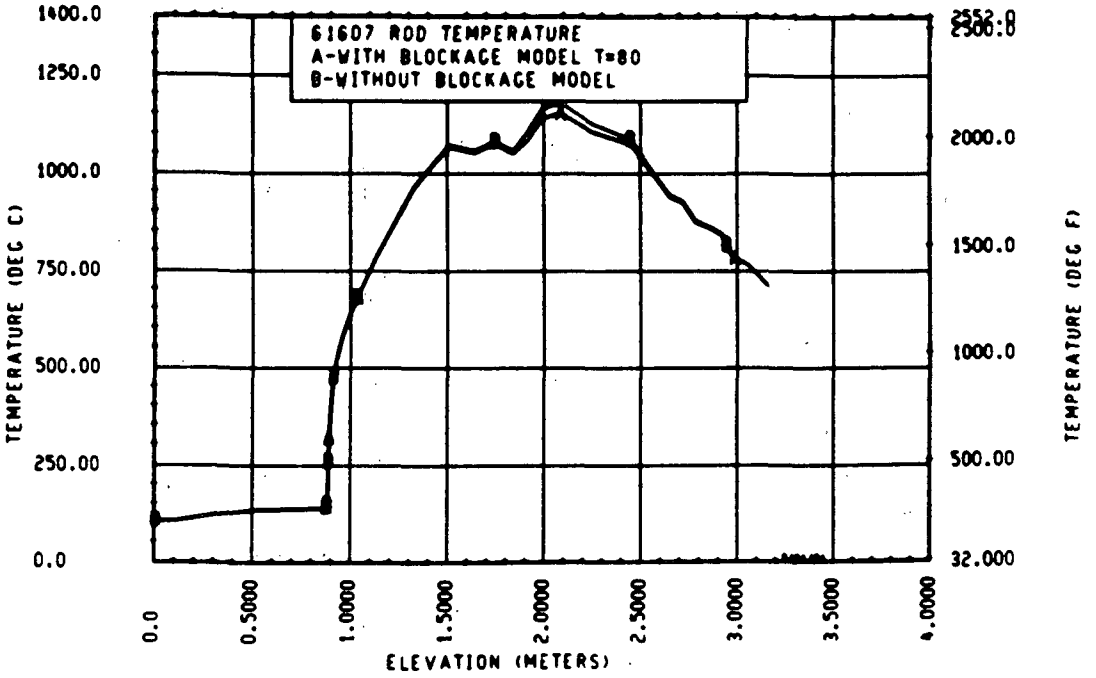

Figure 5-158. Effect of Blockage Models on Calculated Rod Temperature Differences, FLECHT SEASET Test 61607, t = 80 Seconds

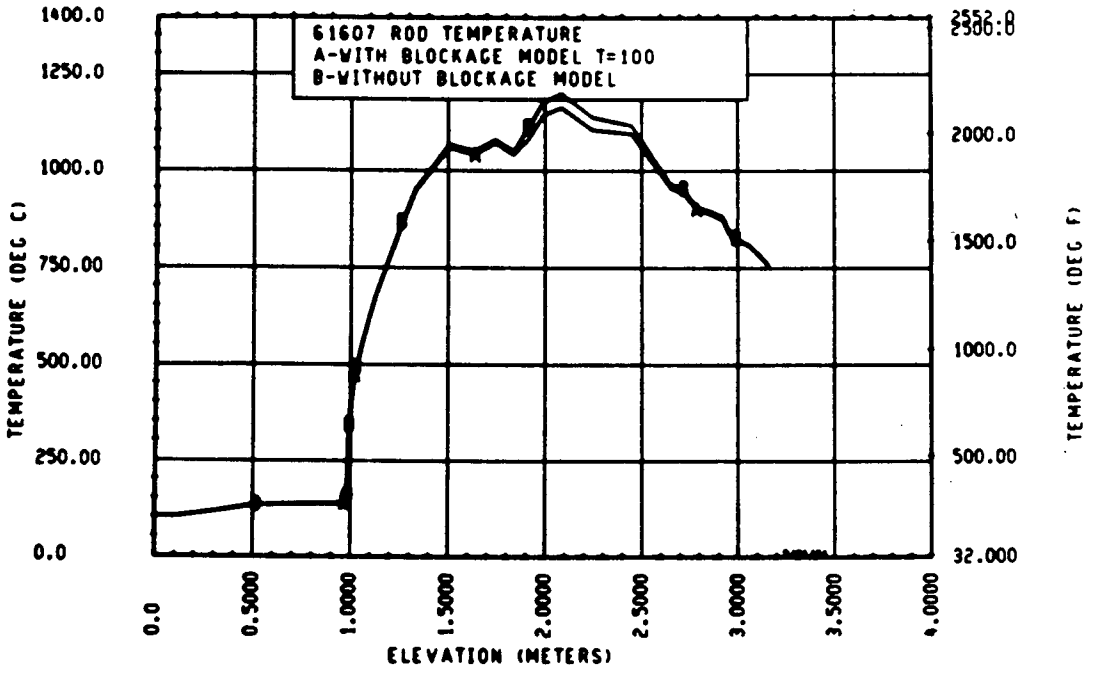

Figure 5-159. Effect of Blockage Models on Calculated Rod Temperature Differences, FLECHT SEASET Test 61607, t = 100 Seconds

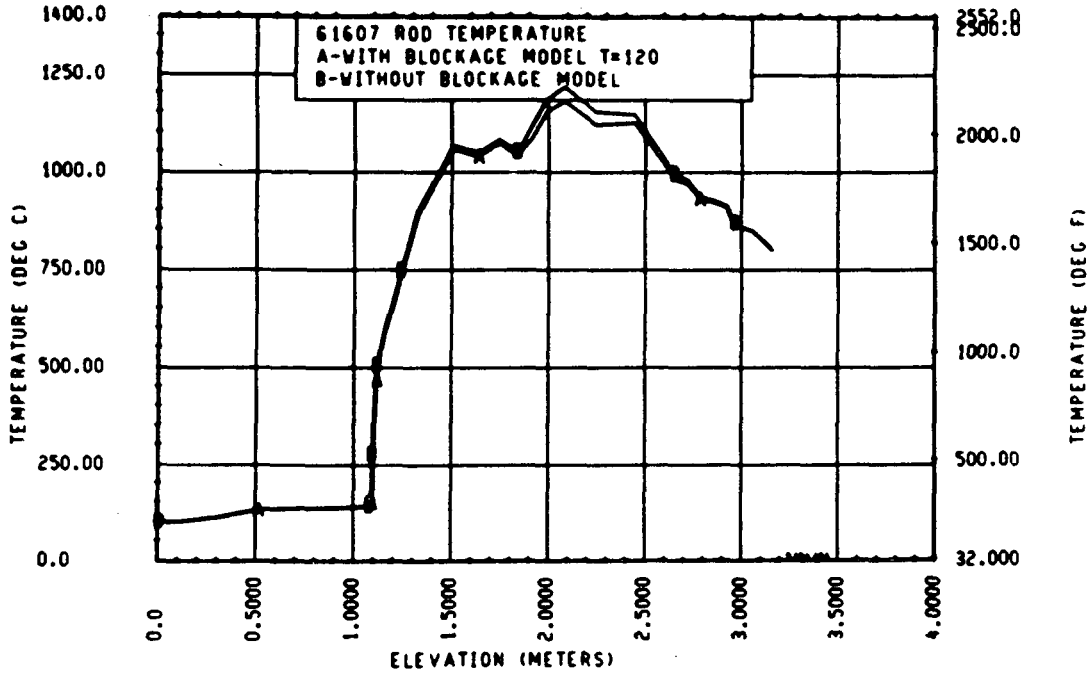

Figure 5-160. Effect of Blockage Models on Calculated Rod Temperature Differences, FLECHT SEASET Test 61607, t = 120 Seconds

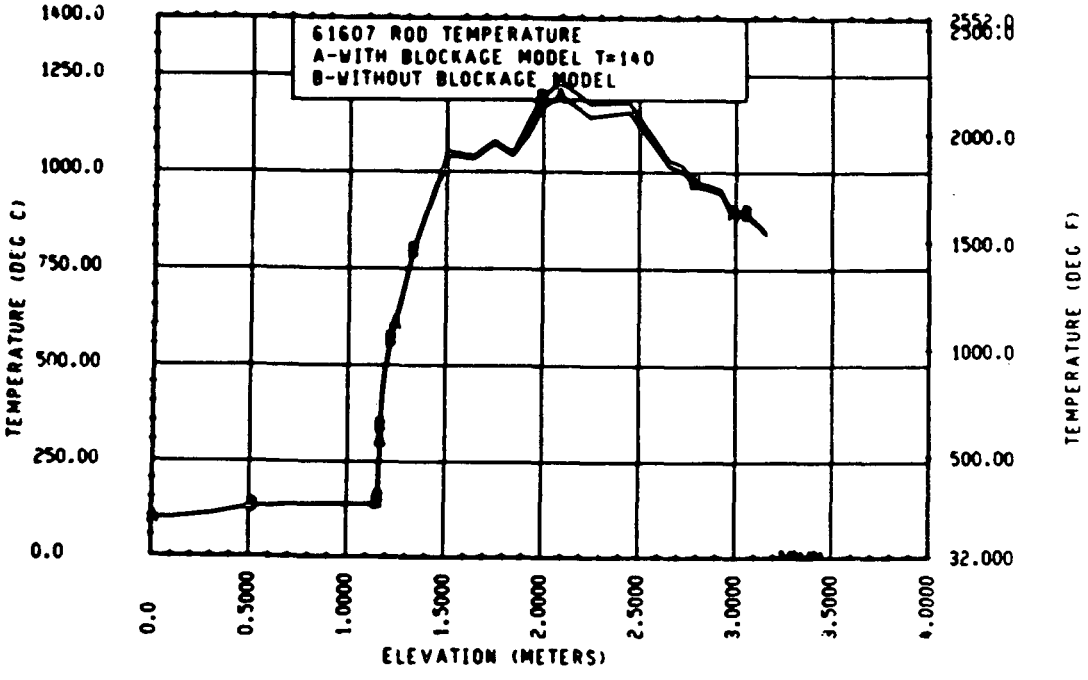

Figure 5-161. Effect of Blockage Models on Calculated Rod Temperature Differences, FLECHT SEASET Test 61607, t = 140 Seconds

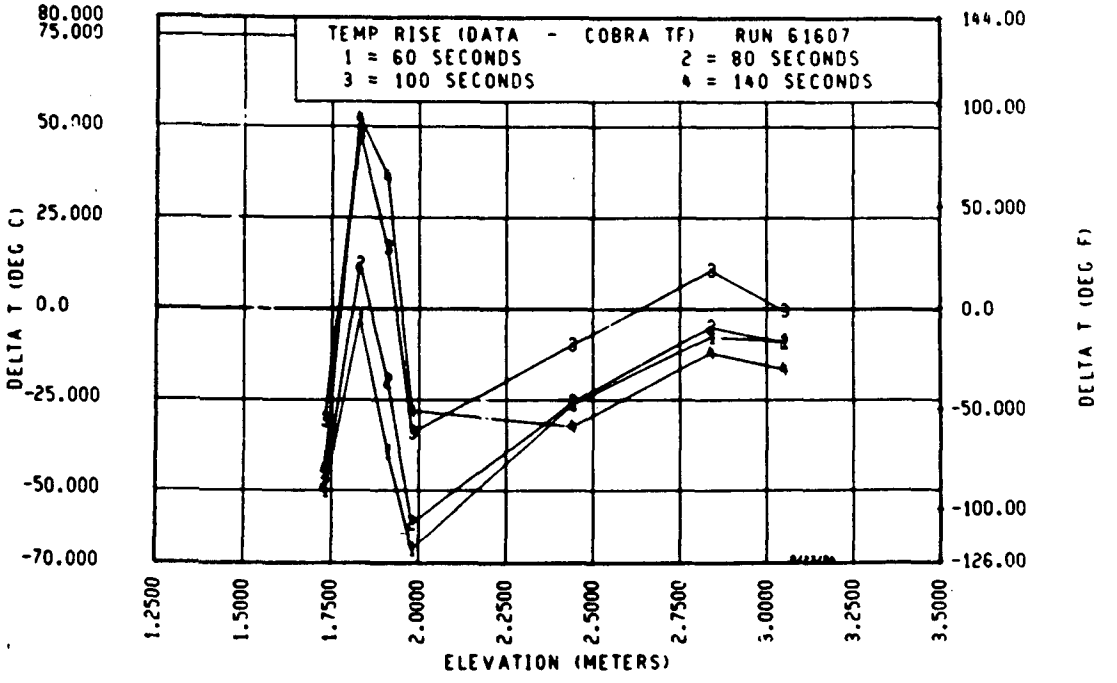

Figure 5-162. Temperature Rise Versus Elevation, FLECHT SEASET Test 61607

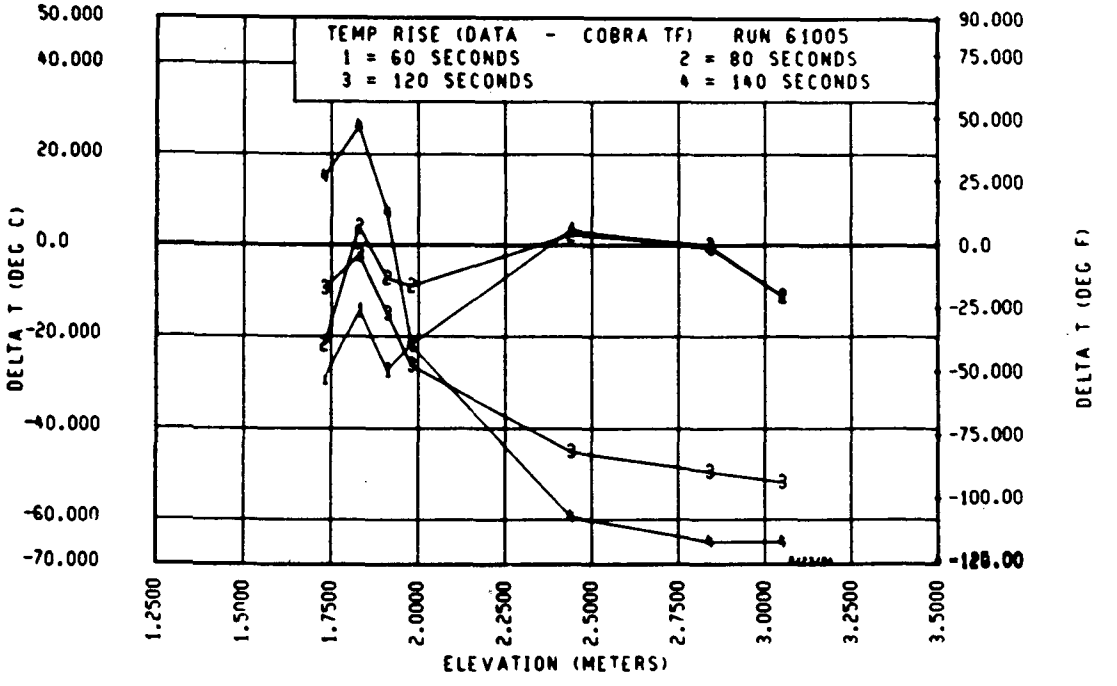

Figure 5-163. Temperature Rise Versus Elevation, FLECHT SEASET Test 61005

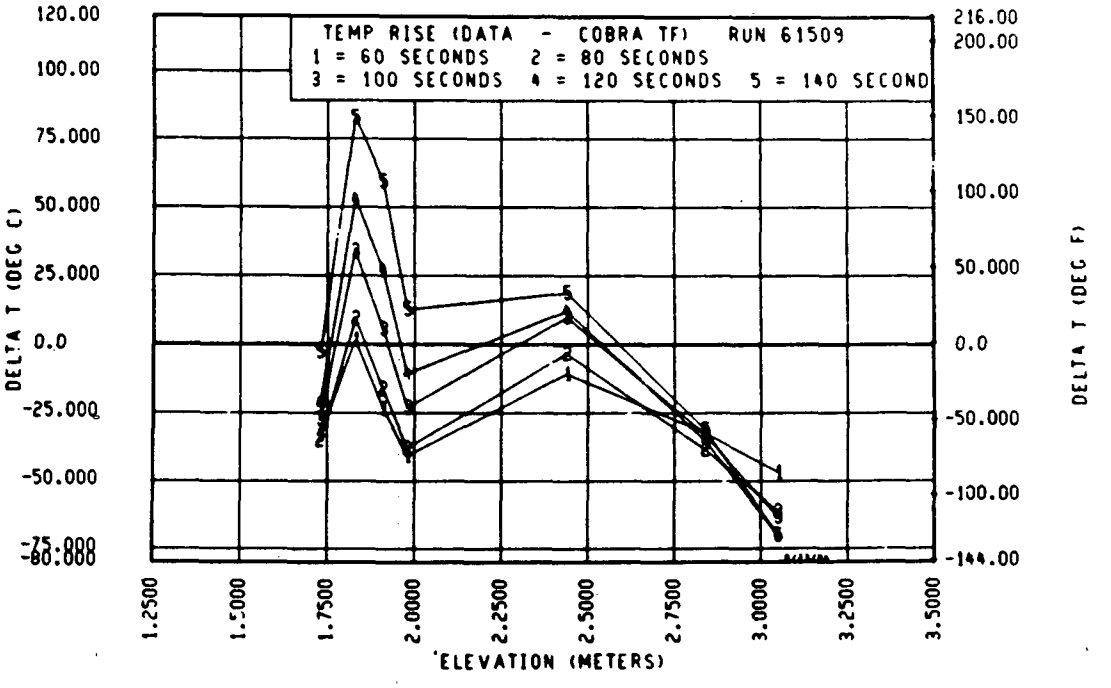

Figure 5-164. Temperature Rise Versus Elevation, FLECHT SEASET Test 61509

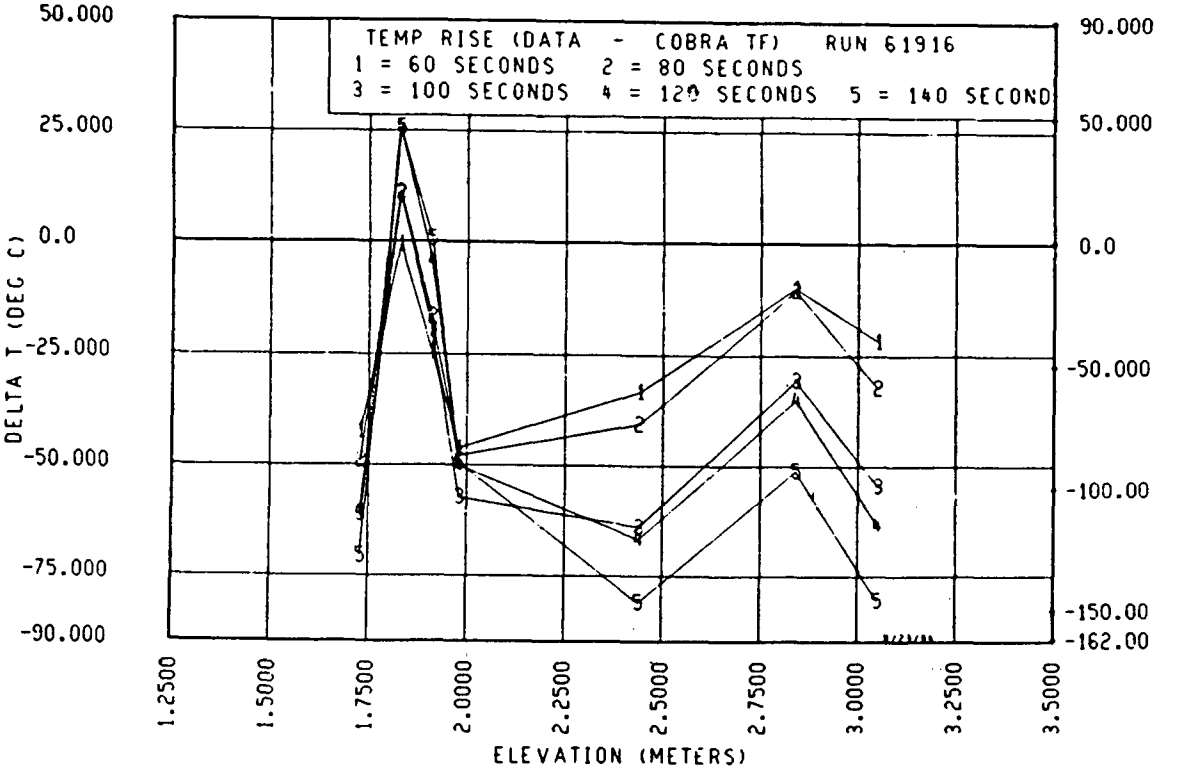

Figure 5-165. Temperature Rise Versus Elevation, FLECHT SEASET Test 61916

island temperature rise (T_{max} - $T_{initial}$) minus the calculated temperature rise from the COBRA-TF predictions. The delta temperature rise is plotted against elevation up the bundle for different times. Figures 5-162 through 5-165 indicate two specific trends:

- The heat transfer in the blockage zone is overpredicted in some cases (the data temperature rise is higher than that predicted by the code).
- The heat transfer downstream of the blockage is underpredicted, since the COBRA-TF temperature rise is larger than the data.

The shapes of all the bias curves are similar, and shift relative to a delta of zero (perfect agreement) as a function of test conditions. As shown in previous bias plots, the low pressure test (61509) shows smaller deltas than the other experiments. This is consistent with the other low pressure test bias plots, since there are lower predicted temperature rise values.

The data in figures 5-162 through 5-165 are presented numerically and averaged over time in table 5-2. The agreement is reasonable, but there is a bias toward underpredicting the blockage heat transfer effects downstream of the blockage.

TABLE 5-2

COMPARISON OF COBRA-TF AND 163-ROD BLOCKED BUNDLE

TIME-AVERAGED TEMPERATURE RISE VALUES

Elevation [m (in.)]	$(\Delta T \text{ rise})_{data} - (\Delta T \text{ rise})_{COBRA-TF}$ for Indicated Test [°C (°F)]			
	61005	61509	61607	61916
1.75 (69)	-8.87 (-15.97)	-21.75 (-39.15)	-45.00 (-81.00)	-55.25 (-99.45)
1.95 (77)	-0.25 (-0.45)	-19.25 (-34.65)	-50.33 (-90.60)	-47.50 (-85.50)
2.40 (94)	-24.25 (-43.65)	3.25 (5.85)	-27.00 (-48.60)	-55.25 (-99.45)
2.85 (112)	-28.50 (-51.30)	-33.75 (-60.75)	-8.33 (-15.00)	-27.00 (-48.60)
3.05 (120)	-34.25 (-61.65)	-54.00 (-97.20)	-10.33 (-18.60)	49.50 (89.10)
Elevation-averaged	-19.22 (-34.60)	-25.10 (-45.18)	-28.20 (-50.76)	-46.90 (-84.42)

SECTION 6
CONCLUSIONS AND RECOMMENDATIONS

6-1. CONCLUSIONS

The objective of the FLECHT SEASET program was to assess the heat transfer effects of rod bundle blockages caused by fuel rod swelling, and to develop models which could represent these effects. This objective has been achieved. The experimental data from both the FLECHT SEASET 21-rod bundle program and the Karlsruhe FEBA program have provided a valid data base with which to develop blockage models to represent the heat transfer effects of flow blockage. The models which have been developed in this program are basic and sufficiently mechanistic that they should be capable of extrapolation to different blockage geometries with reasonable certainty. The models developed, however, do require that the calculation be performed with a state-of-the-art two-phase computer code like COBRA-TF.

The blockage models developed from the smaller-scale blockage bundle tests (21-rod bundle, FEBA), the literature, and single-tube data have been validated against the larger 163-rod blocked bundle data without any changes. The comparison with the larger rod bundle data also factored in the flow bypass effects that would be expected to occur in a PWR if single fuel bundles or portions of fuel bundles were blocked. The agreement between the 163-rod bundle data and the COBRA-TF calculations was quite good, particularly in light of the complexity of the heat transfer processes that were occurring.

A significant effort was spent to improve the base-case COBRA-TF calculation scheme before any attempt was made to included the effects of blockage. The first series of COBRA-TF calculations and comparisons with the unblocked FLECHT SEASET data indicated that the basic models in the code could not agree with the data with sufficient accuracy that effects like grids or blockages would be correctly modeled. Therefore, effort was spent to examine the basic code models to improve the agreement with the unblocked data. Three main areas were significantly improved upon, to the extent that the final results were acceptable.

The first area was that of calculating the entrained liquid above the froth front such that the froth front, vapor superheating, and resulting droplet heat transfer would be properly calculated. This required modifying the vapor velocity that was used within the node to calculate the entrainment and the viscosity of the vapor phase, consideration of heated and wetted perimeters for different size cells, and the use of finer axial mesh cells.

The second area of code improvement was smoothing the transitions and numerical oscillations that occurred as a front (quench, froth, or two-phase) crossed from one axial node to another. Although the calculated rod temperature profile could show some unrealistic spikes, other calculated parameters such as mass entrainment, vapor velocity, vapor superheat, and total flow out would vary significantly. Since the blockage and grid models depended on the amount of entrainment, numerical oscillations in the calculated entrainment could cause significant temperature swings. A method of smoothing the transitions between nodes was developed and used. In addition, finer axial noding was used lower in the bundle.

The third major base-case code improvement was the inclusion of a rod-to-rod, rod-to-surface radiation heat transfer model, which was particularly important for small bundles and to model the effect of guide tube thimbles (which are radiation heat sinks).

Inclusion of these models and code modifications, along with the models for spacer grid heat transfer, significantly improved the agreement between the code predictions and the unblocked bundle data, and reduced code uncertainty. The additional complexity of the flow blockage effects can be modeled and their effects are not be lost in the overall code uncertainty.

In retrospect, it is believed that the approach used to develop and validate the COBRA-TF code was correct and the results are acceptable.

6-2. RECOMMENDATIONS

The models presented in this report have been validated against extensive but still somewhat limited data. Continued efforts to verify COBRA-TF and the

blockage and grid models are recommended, so that the models and code will be more universally accepted.

As indicated in paragraph 6-1, accurate calculation of entrainment is a requirement if reflood is to be modeled correctly. What is needed is improved small-scale experiments in this area, along with further improved two-phase modeling of the complex entrainment process. Current NRC-funded work at Argonne National Laboratory should help to resolve this problem. However, it is believed that some additional small-scale experiments are still necessary.

The models developed in this report resolve only part of the total flow blockage heat transfer problem. Fuel rod swelling, straining, and the resulting blockage shape constitute a complex and coupled mechanical/thermal-hydraulic problem. This particular version of COBRA-TF should be combined with the latest version of the FRAP-T materials code to solve the coupled mechanical and thermal-hydraulics problem. The resulting total model could then be compared with in-pile and out-of-pile experimental data.

The result would provide the NRC with a mechanistic calculational tool with which to assess the results of fuel rod swelling and blockages for a LOCA, such that margins can be identified and regulations in this area can be relaxed.

APPENDIX A
COBRA-TF MODELS OF FLECHT SEASET AND FEBA

This appendix documents the noding schemes employed for the COBRA-TF analyses performed as part of the FLECHT SEASET flow blockage model development effort. The COBRA-TF input description and a listing of the input for the 163-rod model is presented in appendix F.

A-1. FLECHT SEASET 161-ROD BUNDLE MODEL

To minimize computer run time, the noding schemes were designed to be as coarse as possible and yet adequately represent the physical characteristics of the bundle. For the 161-rod bundle, a simple two-channel model was chosen (figure A-1). It was necessary to model the near wall region separately from the bundle interior because of the large temperature gradient between the internal rods and the housing wall.

The channel boundary was selected to give two channels of approximately equal flow area. Flow areas for each channel were calculated as follows:

- Central region -- Nominal dimensions for the rod pitch [12.6 mm (0.496 in.)], rod diameter [9.5 mm (0.374 in.)], and thimble diameter [12.04 mm (0.474 in.)] were employed to calculate a flow area of 7.606×10^{-3} m^2 (11.79 in.^{2}).
- Peripheral channel -- The calculated flow area for the central channel was subtracted from the measured[1] average bundle flow area (1.632×10^{-2} m^2 (25.29 in.^{2}), to give a flow area of 8.716×10^{-3} m^2 (13.51 in.^{2}). Hence, all the bundle excess flow area was assumed to reside in the outside channel.

The axial noding scheme (figure A-2) was designed to match node centers (where rod and vapor temperatures are calculated) with thermocouple locations, and to match node boundaries (where flows are calculated) with grid spacer locations.

---

1. Loftus, M. J., et al., "PWR FLECHT SEASET Unblocked Bundle, Forced and Gravity Reflood Task Data Report," NRC/EPRI/ Westinghouse-7, June 1980.

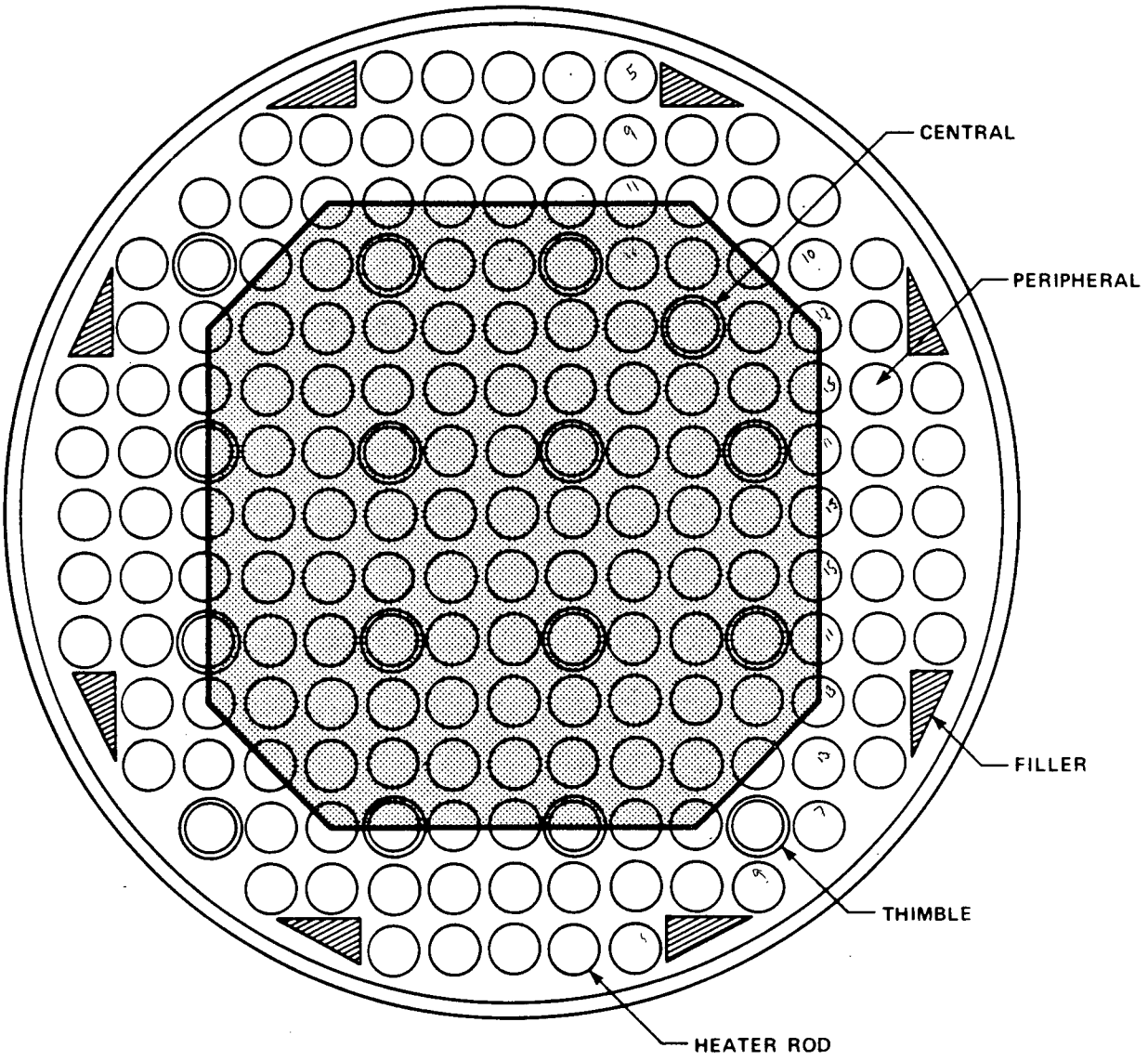

Figure A-1. Channel Layout for FLECHT SEASET 161-Rod Bundle

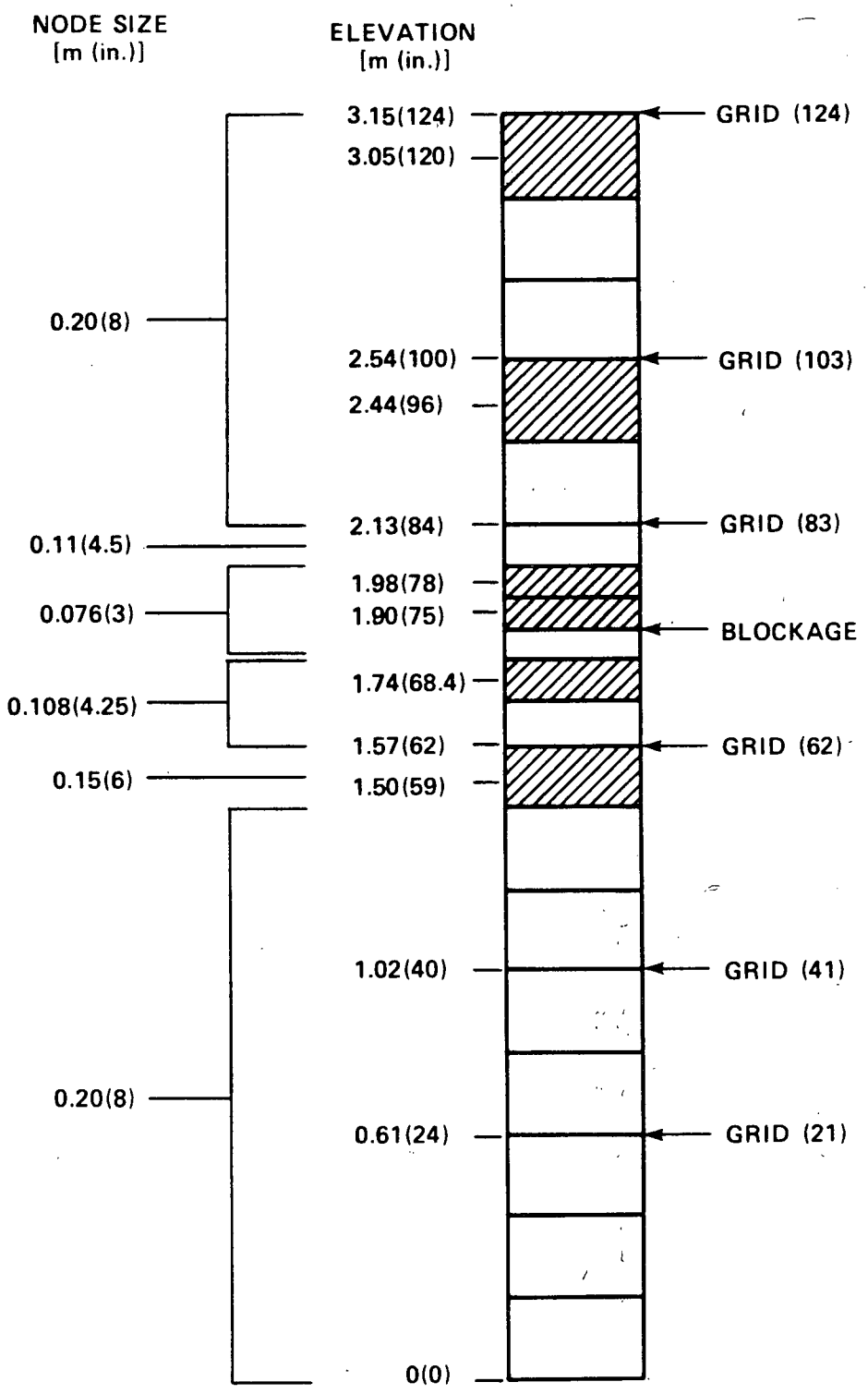

Figure A-2. FLECHT SEASET 161-Rod Bundle Axial Noding Scheme

In addition, it was desirable to employ the same axial noding for all the FLECHT SEASET simulations. For the blocked bundles (21-rod configurations C and F, and the 163-rod bundle), it was necessary to provide several fine nodes in the blockage region to define the channel flow area restriction. To accomplish this, three 0.076 m (3 in.) nodes were used. A restriction imposed by the finite difference form of the momentum flux terms requires that adjacent nodes change in length by a factor of less than two. Consequently, a gradual transition is made from the more coarse 0.20 m (8 in.) nodes to the relatively fine nodes. Unfortunately, the presence of the fine nodes results in a severe Courant time step limitation. To reduce the total number of nodes, the top 0.51 m (20 in.) of the heated length was not modeled.

The use of two fluid channels requires that at least two heater rods be simulated, one for each channel. Since the temperature and heat release characteristics of the triangular fillers are expected to be similar to that of the housing, one cylindrical heat slab is used to model them both. Both the metal mass and perimeter are specified as equal to the sum of the housing and fillers, except that the perimeter between the filler and the housing is not included. Also, the thimbles in the central channel are modeled by one tube conductor. The calculated surface heat flux for each rod is multiplied by the area and appropriate number of rods for the channel to which it is connected.

A separate thermal radiation model is employed for each fluid channel, to determine the radiation heat transfer between rods and to the steam and drops. For the 161-rod bundle, the central channel is considered to be far enough away from the housing that no significant radiative heat loss to the housing is expected. Therefore, no attempt was made to model radiation between the central and peripheral channels.

The radiation enclosure for the central channel (figure A-3) consists of two subchannels, one normal subchannel and one thimble subchannel. In this model, the radiation heat flux for the central channel heater rod (numbered 1 in the figure) is represented by the average of the seven rod surfaces. Similarly,

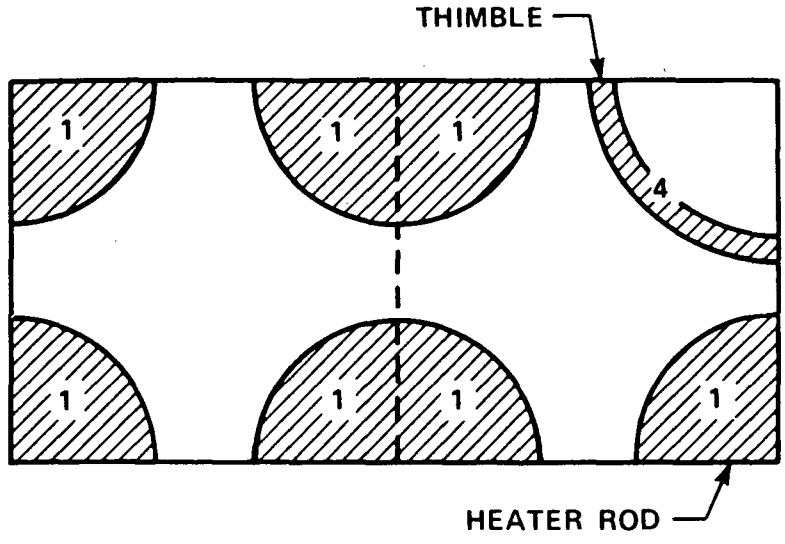

Figure A-3. Radiation Enclosure for Central Channel of FLECHT SEASET 161-Rod Model

the radiation for the thimble (numbered 4) is given by that of the thimble surface. Radiative heat flow to the fluid is calculated for each of these subchannels and multiplied by a factor of 45 (approximately the number of subchannel pairs in the central channel).

Figure A-4 illustrates the radiation enclosure for the peripheral channel. Radiation heat fluxes are calculated for 11 surfaces: 10 one-fourth heater rods and the housing. As before, the radiation heat flux for the peripheral heater rod (numbered 2) is taken as the average of the 10 surfaces. A multiplication factor of 32 is employed to convert the fluid heat inputs for the peripheral channel.

Grid spacers are modeled at six axial elevations (figure A-2). Blockage factors of 0.2952 and 0.21 were calculated for the central and peripheral channels, respectively. Grid spacer loss coefficients are computed from the Rehme model:[1]

$$K_G = C \cdot f(Re) \cdot \left(\frac{A_G}{A_C}\right)^2$$

where

K_G = grid loss coefficient
C = multiplier for grid shape
f = friction factor
$\frac{A_G}{A_C}$ = grid blockage fraction

The recommended value of 1.4[2] is used for the grid shape factor.

---

1. Rehme, K., "Pressure Drop of Spacer Grids in Smooth and Roughened Rod Bundles," Nuclear Technology 31, 1977, 314-317.

2. Loftus, M. J., et al., "PWR FLECHT SEASET 21-Rod Rundle Flow Blockage Task Data and Analysis Report," NRC/EPRI/ Westinghouse-11, September 1982.

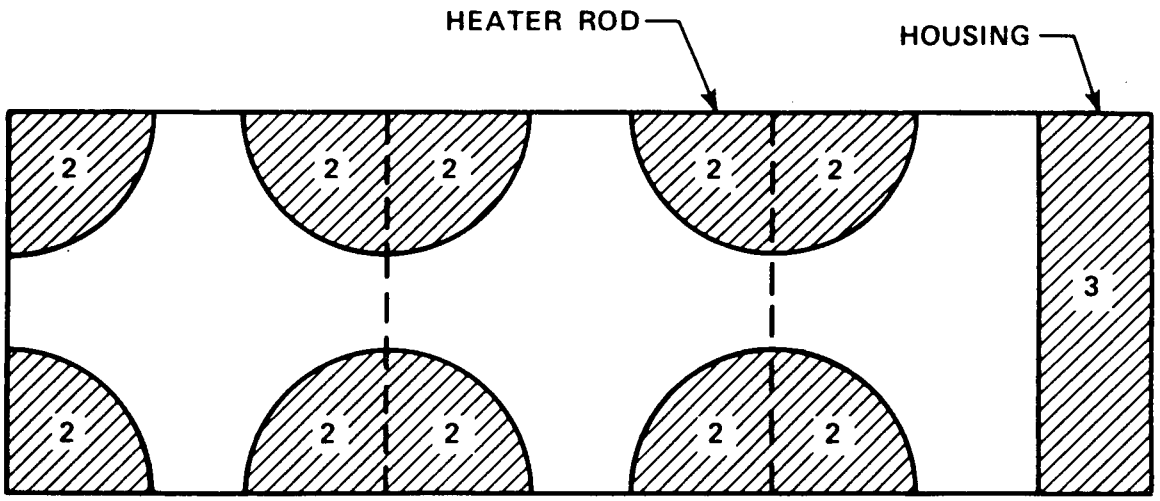

Figure A-4. Radiation Enclosure for Peripheral Channel of FLECHT SEASET 161-Rod Model

The FLECHT chopped cosine axial power profile (peak/average = 1.66) is input to COBRA-TF. However, since the nodes do not align with the power steps, the profile is integrated over each node. The resulting power profile is compared to the FLECHT profile in figure A-5. The experimental power decay curve is input and employed in a straightforward manner.

Tables of temperature versus elevation are input for the initial temperatures of the heater rods, thimble, and housing. COBRA-TF performs a linear interpolation on these tables to find the temperature at the node centers. The tables are generated by averaging the measured temperatures for the heater rods that lie within the region coincident with the fluid channel.

Flow and enthalpy boundary conditions are specified at the bundle inlet. Initially, the inlet water is assumed to be saturated at the bottom of the heated length. The fluid enthalpy is ramped over time (figure A-6) to the measured value. (The fluid thermocouple is located approximately 0.2 m (8 in.) below the heated length.) The applied time delay is approximated by dividing the above distance by the flooding velocity. A pressure boundary condition is applied at the bundle exit.

A-2. FLECHT SEASET 21-ROD BUNDLE MODEL

The following paragraphs describe the COBRA-TF models for the FLECHT SEASET 21-rod bundle, configurations A (unblocked), C (concentric, coplanar), and F (nonconcentric, noncoplanar). Only input models that are different from those of the 161-rod bundle are described below.

A-3. 21-Rod Bundle, Configuration A

A two-channel model of a one-eighth symmetry section (figure A-7) was selected for the unblocked bundle. As before, the flow area for the central channel was calculated from nominal dimensions to be 1.318×10^{-4} m^2 (0.2043 $in.^2$).

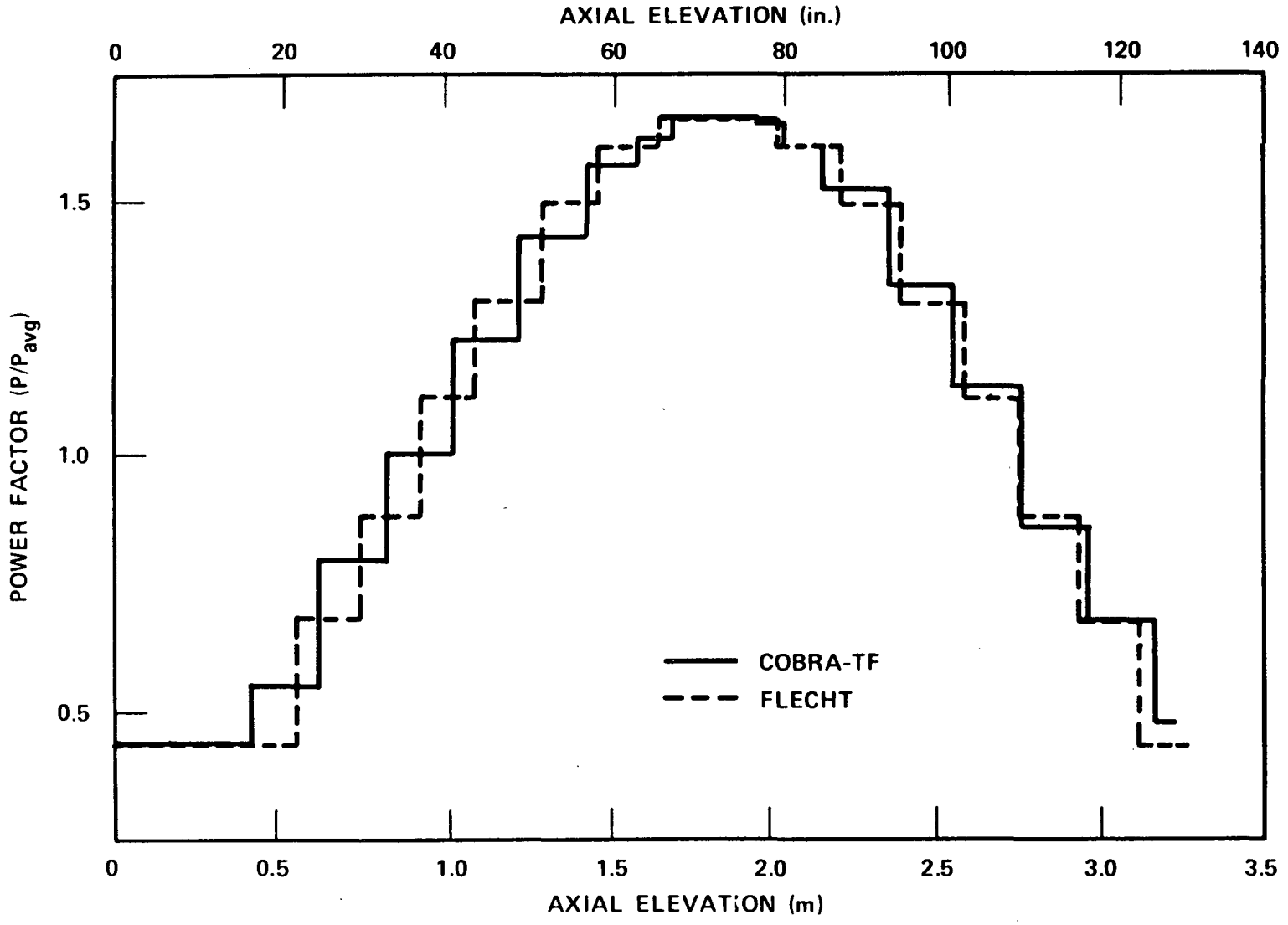

Figure A-5. Axial Power Profile Comparison

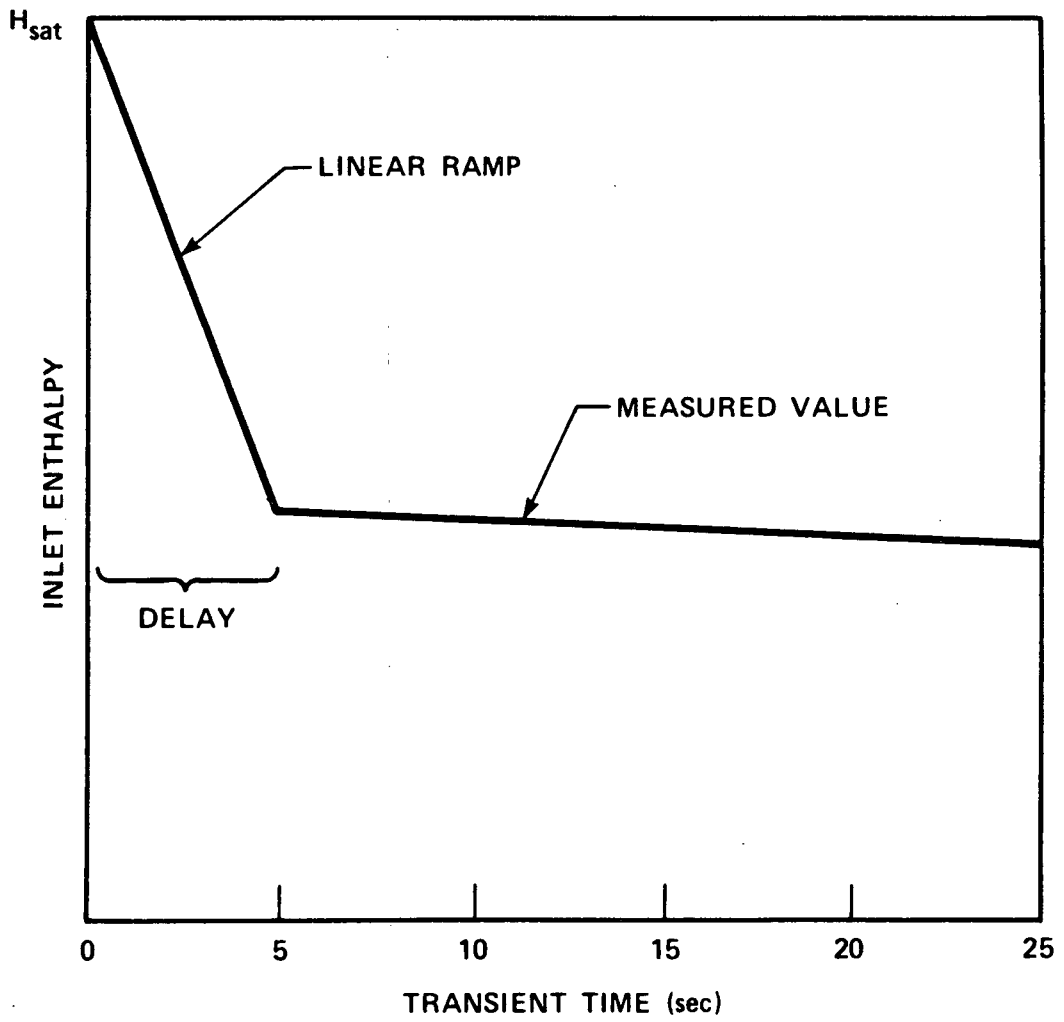

Figure A-6. Input Inlet Enthalpy Versus Time

The measured average bundle flow area [2.08 x 10^{-3} m^2 (3.224 $in.^2$)[1]] was used to compute the area of the peripheral channel [1.281 x 10^{-4} m^2 (0.1985 $in.^2$).

Because of the potentially severe radial temperature gradient from the center of the bundle to the housing, a total of four heat transfer surfaces were modeled. Two heater rods were simulated in the central channel and one heater rod was simulated in the peripheral channel (figure A-7). The housing and filler were lumped together as the fourth heat transfer surface.

The small bundle size [the housing inside diameter was only 0.0682 m (2.69 in.)] necessitated a more complex radiation model than the 161-rod bundle. Five radiation subchannels were employed to calculate the radiative heat transfer (figure A-8). Two normal subchannels model the central channel; all the surfaces in each subchannel are either rod 1 or rod 2. Thus, rod 1 radiates to the fluid and, through a gap, to rod 2. Rod 2, in turn "sees" the fluid, the peripheral heater rod (rod 3), and the housing. Three special subchannels model the radiation in the outside channel.

To qualify this radiation model for the 21-rod bundle,[1] a heatup simulation was performed. In this test, the heater rods and housing are postulated to be initially at saturation temperature in a steam environment. The power is turned on [1.3 kw/m (0.4 kw/ft) peak] and the rods heat up until a temperature of 870° C (1600° F) is reached (in about 87 seconds). Figures A-9 and A-10 compare the COBRA-TF predictions with measured data for the central heater rod and the housing. Both centerline temperatures are overpredicted, indicating that the actual bundle heat loss to the ambient was not correctly accounted for. However, the temperature difference across the bundle (rod 1 -- housing) was within 8 percent of the measured value.

---

1. Loftus, M. J., et al., "PWR FLECHT SEASET 21-Rod Rundle Flow Blockage Task Data and Analysis Report," NRC/EPRI/ Westinghouse-11, September 1982.

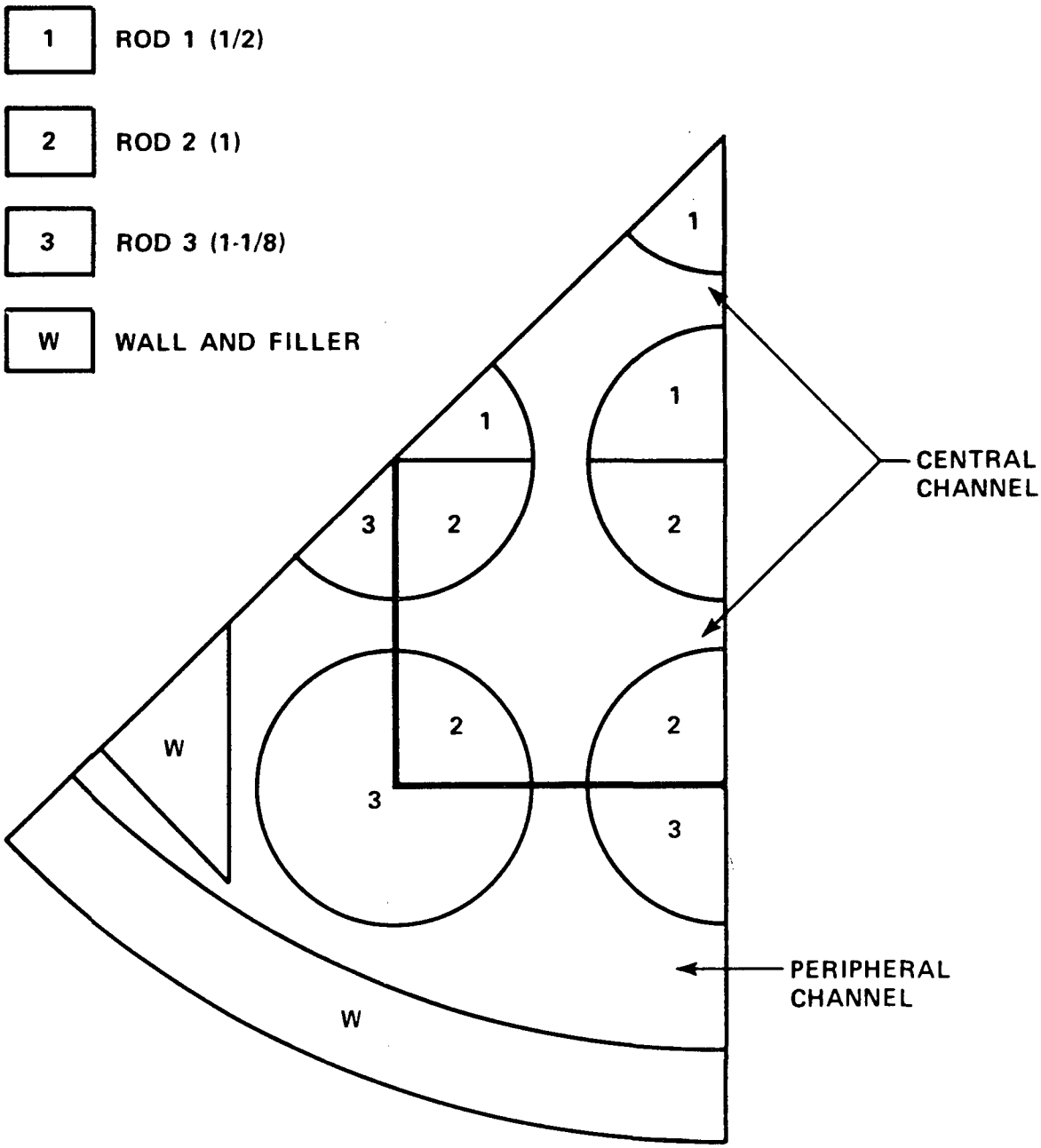

Figure A-7. FLECHT SEASET 21-Rod Bundle Radial Noding, Bundles A and C

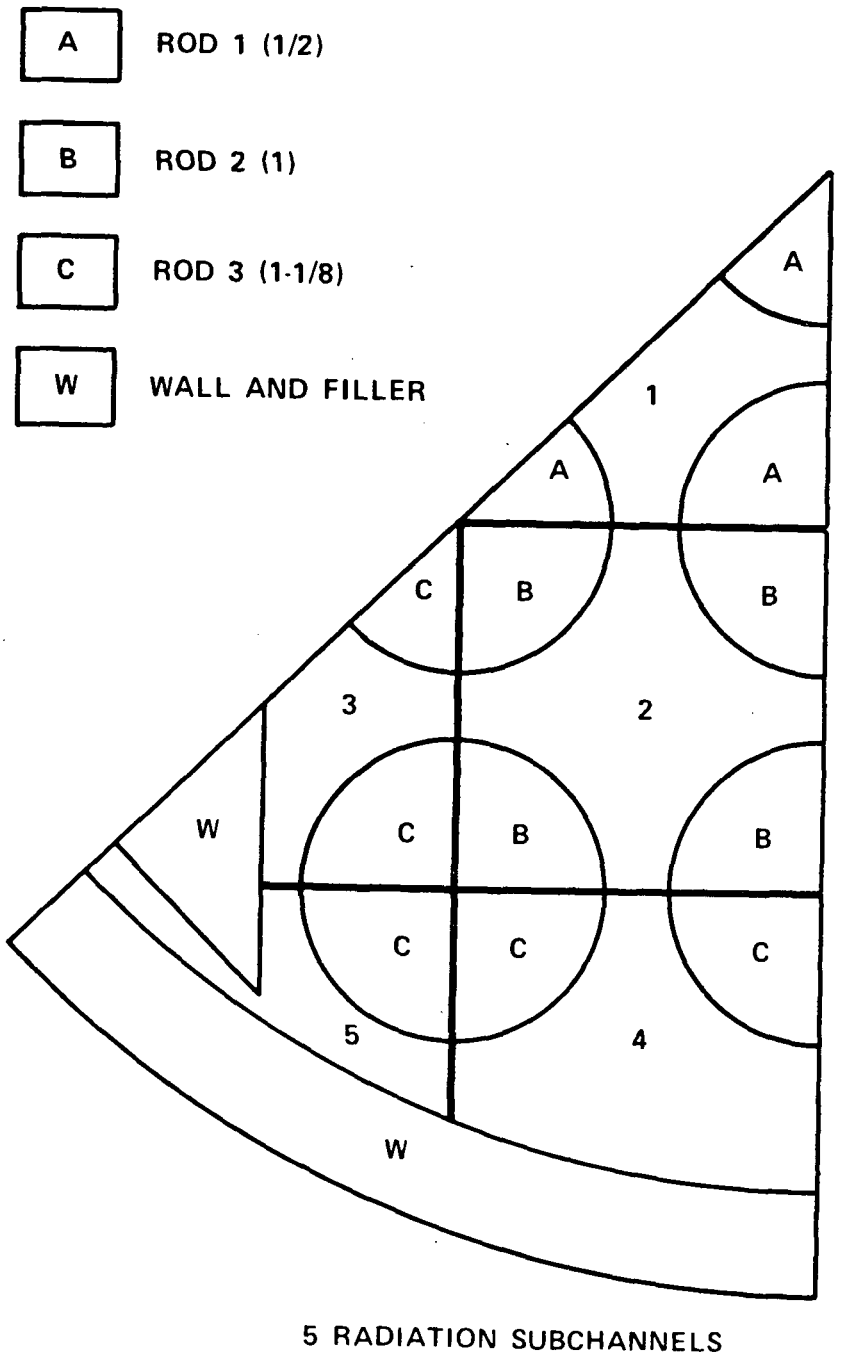

Figure A-8. FLECHT SEASET 21-Rod Bundle Radiation Model Noding

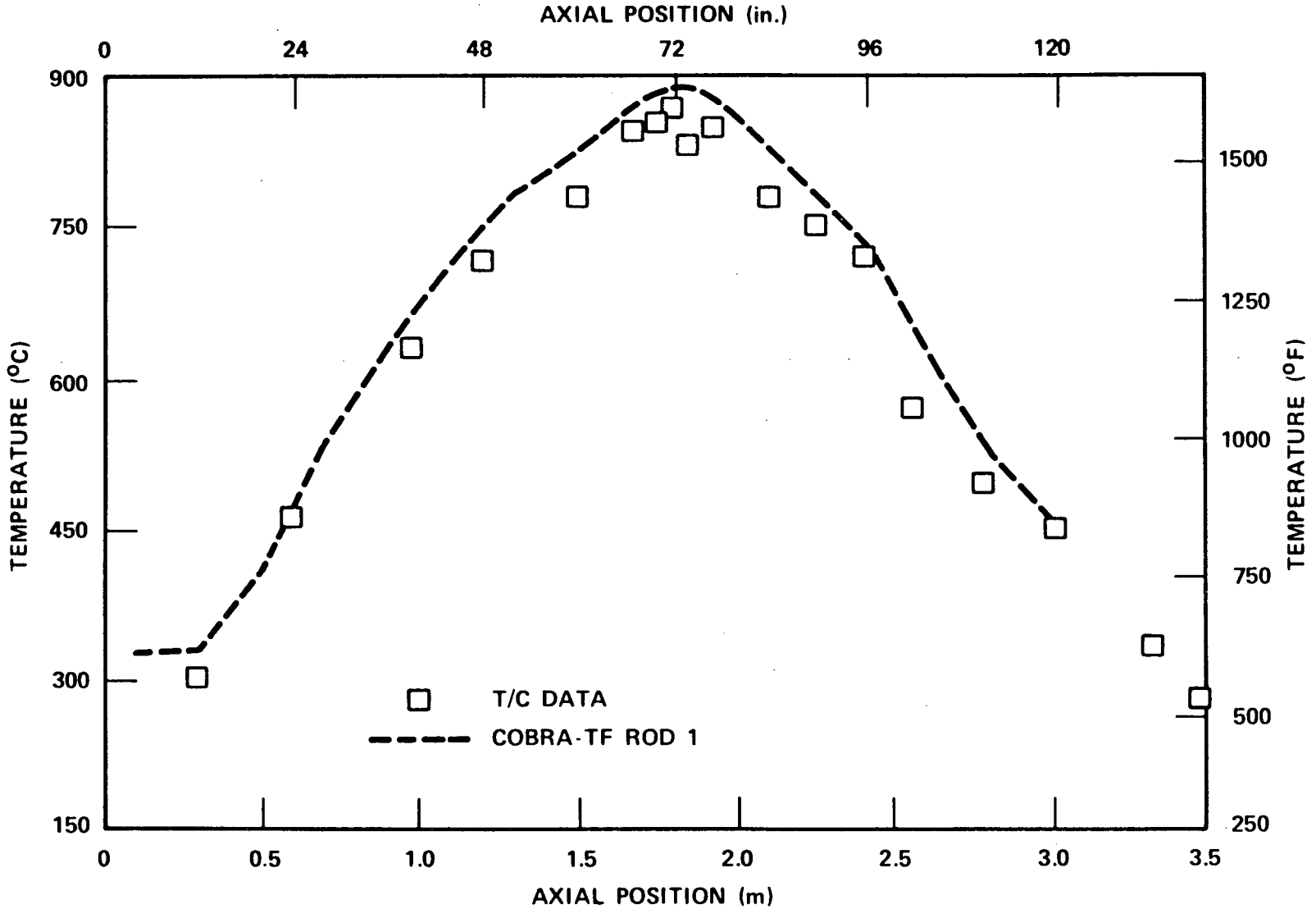

Figure A-9. FLECHT SEASET 21-Rod Bundle Heatup Test Rod Group 1 Axial Temperature Profile

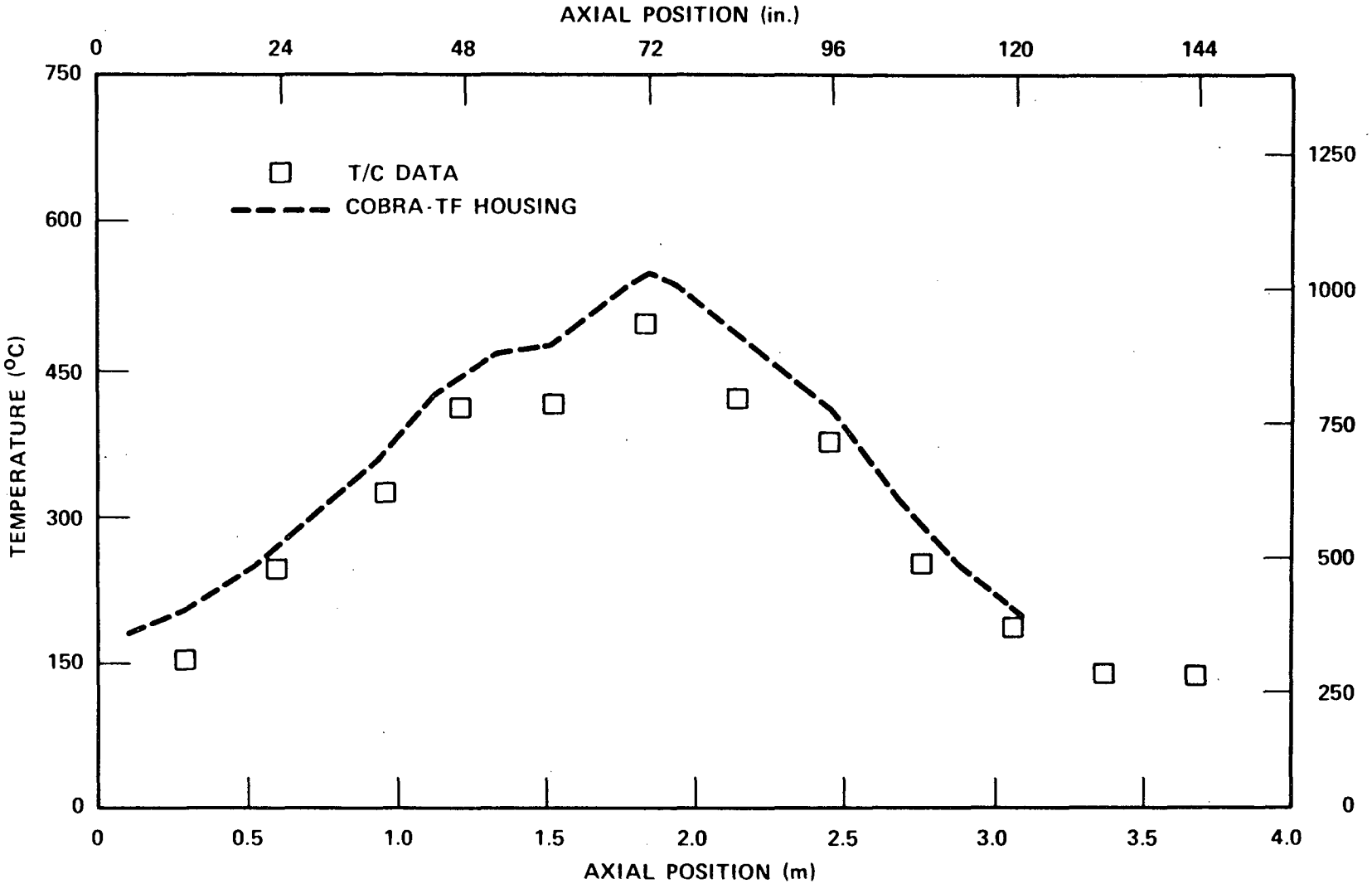

Figure A-10. FLECHT SEASET 21-Rod Bundle Heatup Test Axial Profile of Shroud Temperature

Blockage factors of 0.2673 and 0.1544 were calculated for the grid spacers in the central and peripheral channels, respectively. For the 21-rod bundle, the steam probes (which are attached to the grids in the central region of the bundle) significantly affected the grid blockage ratio and pressure drop. Consequently, the grid blockage factors and shape coefficients were different for each elevation. These coefficients were determined through simulations of the configuration A hydraulic characteristics test series.

Since no steam probes were located at the 0.53 m (21 in.) elevation, the pressure drop data for this elevation were used to set the shape coefficient for a bare grid (C = 1.63). This bare grid shape factor was then applied at every elevation for the peripheral channel, which contains no steam probes. Then the pressure drop data were used to adjust the shape coefficient for the center channel. Table A-1 lists the grid blockage factors and coefficients for the central channel. Figure A-11 presents the computed bundle pressure drop and table A-2 gives the individual pressure drop results for each grid.

A-4. 21-Rod Bundle, Configuration C

Configuration C contains a coplanar flow blockage consisting of the short concentric sleeves with no flow bypass (as shown in section 4). The COBRA-TF input is identical to that of configuration A except for the blockage information, which is detailed below.

Figure A-12 illustrates the placement of the flow blockage upon the axial noding scheme. The momentum area (flow area at cell boundary), continuity area (cell volume/height), wetted perimeter, and gap flow area factors are given in table A-3. The geometry factors of table A-3 are defined relative to the nominal values in the unblocked regions of the bundle.

TABLE A-1
GRID BLOCKAGE AND SHAPE FACTORS,
FLECHT SEASET 21-ROD BUNDLE, CONFIGURATION A

Axial Elevation (in.)	Steam Probe Blockage (A_P/A_C)	Total Grid Blockage [$(A_G+A_P)/A_C$]	Grid Loss Shape Factor
21	0	0.2673	1.63
42	0.014	0.2813	1.879
62	0.0977	0.3650	1.641
83	0.131	0.3983	1.807
104	0.066	0.3333	1.756
124	0.042	0.3093	1.772

TABLE A-2
GRID PRESSURE DROP RESULTS, FLECHT SEASET
21-ROD BUNDLE, CONFIGURATION A

Grid Elevation [m (in.)]	$(\Delta P)_{calc}/(\Delta P)_{meas}$ at Indicated Reynolds Number					Average Error (%)
	2645	5431	8518	11464	16287	
0.53 (21)	1.118	1.024	0.983	0.967	0.977	4.3
1.07 (42)	0.932	0.940	0.986	0.948	0.979	4.5
1.57 (62)	0.819	0.929	0.987	0.976	1.029	6.4
2.11 (83)	0.883	0.957	0.947	0.965	1.122	7.5
2.46 (104)	0.975	0.967	0.962	0.933	0.966	3.9
3.15 (124)	0.913	0.982	0.957	0.971	1.006	3.7

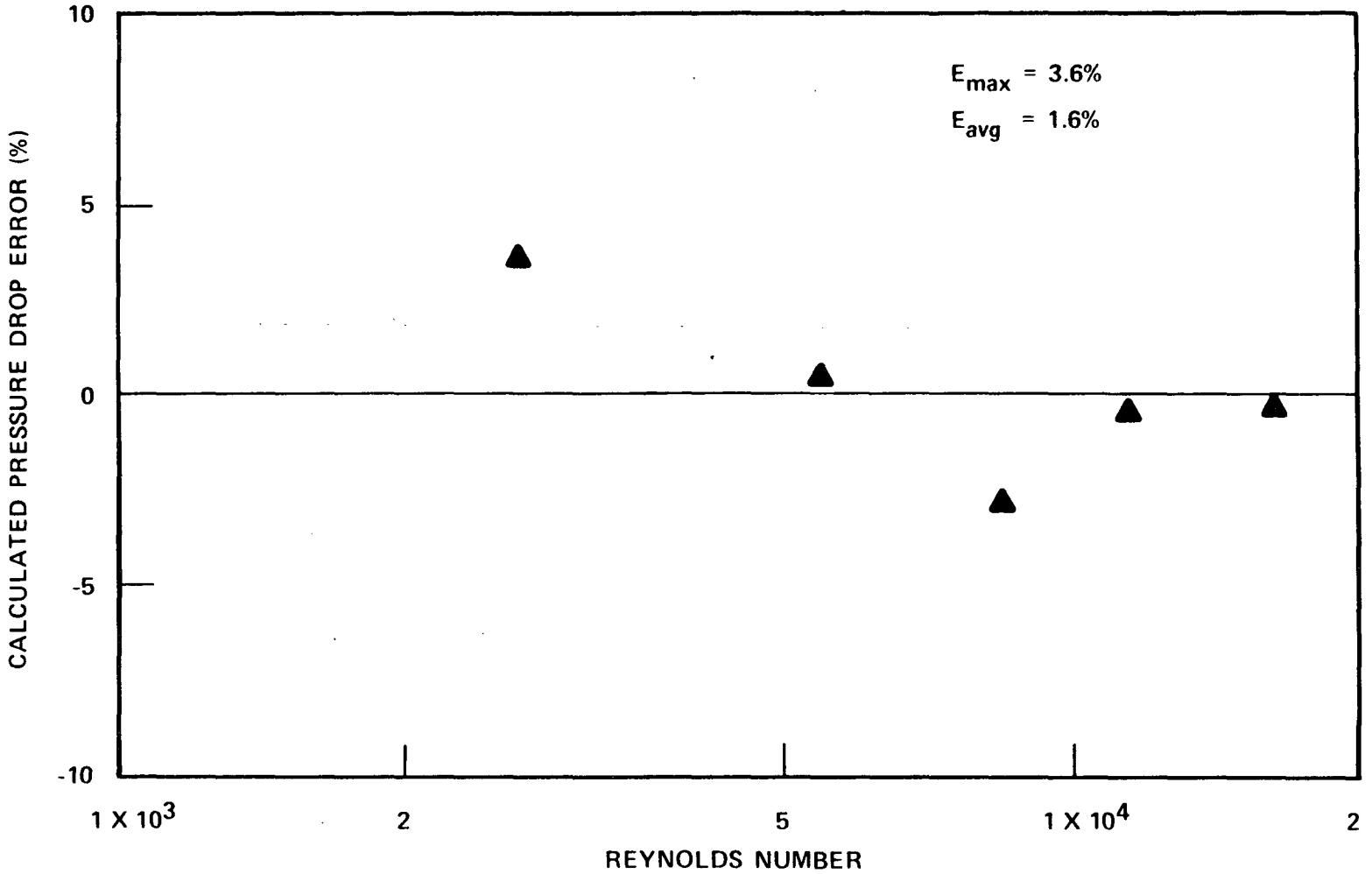

Figure A-11. FLECHT SEASET 21-Rod Bundle Pressure Drop Results

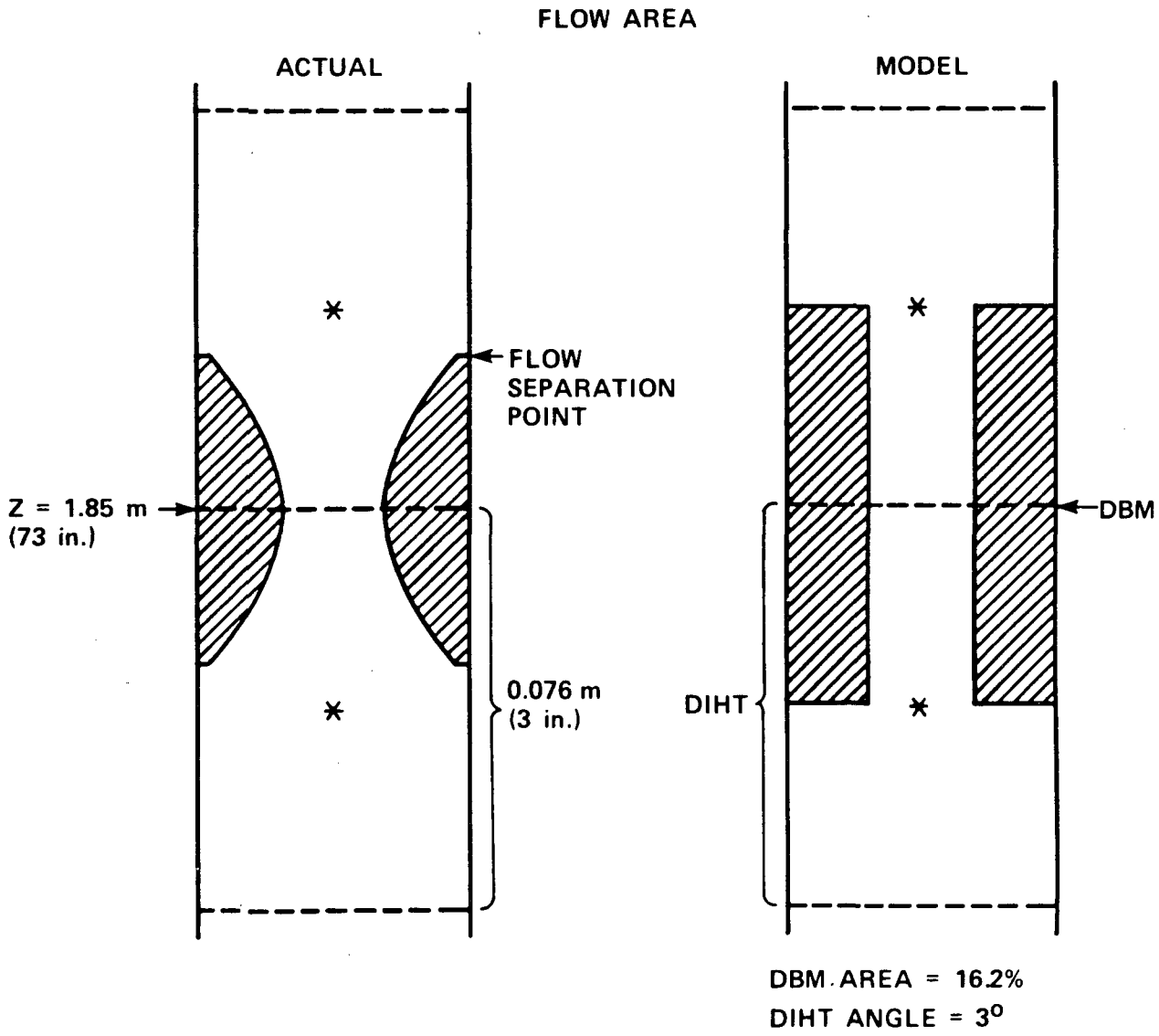

Figure A-12. FLECHT SEASET 21-Rod Bundle Concentric/Coplanar Blockage Geometry, Configurations B and C

TABLE A-3
BLOCKAGE GEOMETRY, FLECHT SEASET 21-ROD BUNDLE,
CONFIGURATION C

Factor	Value	
	Channel 1	Channel 2
Momentum area (node 12)	0.3878	0.6716
Continuity area (nodes 12 and 13)	0.8507	0.9147
Wetted perimeter (node 12)	1.326	1.142
Gap area (nodes 12 and 13)	0.7503	

A blockage loss coefficient formula, similar to that of the grids, is built into COBRA-TF. The user is required to specify the blockage area fraction and a shape factor. To determine the appropriate value for this shape factor, a hydraulic characteristics test was simulated for configuration C. The calculated pressure drop due to the increased skin friction and momentum losses (flow diverts since the blockage in channel 1 is less than that in channel 2) was sufficient to model the blockage losses; no additional loss coefficient was specified. For example, at a Reynolds number of 9525, the measured bundle pressure drop was 9.425 Pa (1.367 psi) and the calculated pressure drop was 9.598 Pa (1.392 psi), an error of less than 2 percent.

The blockage heat transfer model parameters for convective enhancement, droplet breakup, and drop impact heat transfer were calculated (paragraphs 4-9 through 4-16); they are listed in table A-4.

A-5. 21-Rod Bundle, Configuration F

Configuration F had a nonconcentric sleeve placed on every rod in a noncoplanar distribution. Since the blockage fraction for the center four subchannels is significantly different from that of the next row of subchannels (because

TABLE A-4
BLOCKAGE HEAT TRANSFER MODEL PARAMETERS, FLECHT SEASET
21-ROD BUNDLE, CONFIGURATION C

Parameter	Value	
	Channel 1	Channel 2
Convective enhancement		
Separation point [m (in.)]	1.8833 (74.145)	1.8833 (74.145)
Diameter at separation point [m (in.)]	0.01053 (0.4146)	0.01053 (0.4146)
Maximum enhancement	1.88	1.88
Droplet breakup		
Area fraction (%)	16.2	2.8
Drop impact heat transfer		
Impact area/rod [m^2 ($in.^2$)]	5.38×10^{-5} (0.0834)	5.38×10^{-5} (0.0834)
Impact angle (sleeve) (°)	3	3

of bulge orientation, shown in figure A-13), the central channel of the COBRA-TF model was split into two channels. This resulted in a three-channel model (figure A-14), with the following flow areas:

- Channel 1 -- 4.39×10^{-5} m^2 (6.71×10^{-2} $in.^2$)
- Channel 2 -- 8.79×10^{-5} m^2 (1.34×10^{-1} $in.^2$)
- Channel 3 -- 1.28×10^{-5} m^2 (1.96×10^{-1} $in.^2$)

Figure A-15 is a plot of the actual flow area restrictions for each of the COBRA-TF channels. These curves were calculated by averaging the individual subchannel flow blockages over the subchannels represented by the COBRA-TF subchannel. Figure A-16 illustrates the placement of the blockage upon the axial noding scheme. The geometry factors for each channel are given in table A-5.

NODE LENGTH: 2.5 cm (1 in.)
LOCAL TEMPERATURE STANDARD DEVIATION: 7°C (12°F)
MEAN TEMPERATURE: LOCTA RESULTS

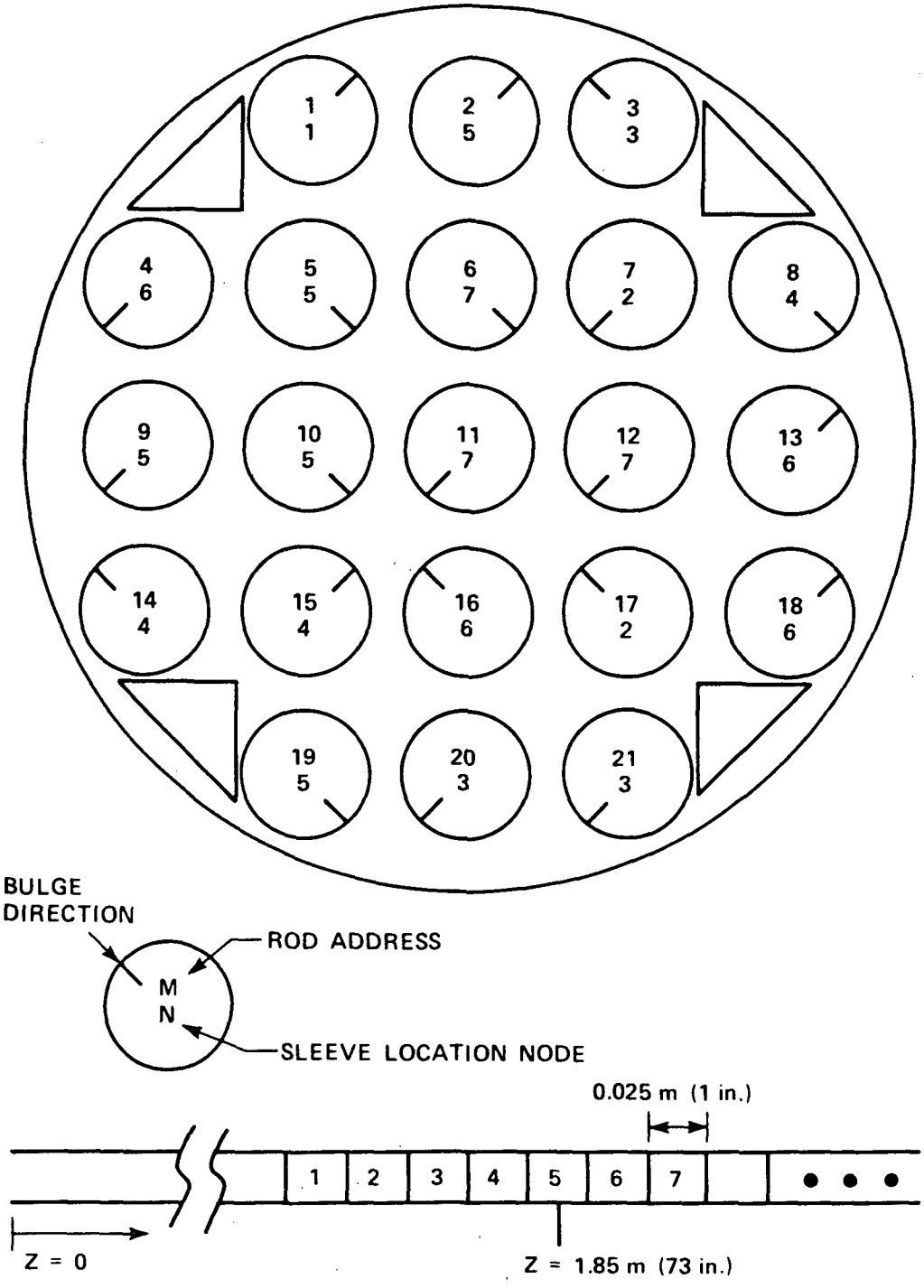

Figure A-13. FLECHT SEASET 21-Rod Bundle Noncoplanar Sleeve Distribution and Bulge Direction for Nonconcentric Sleeves

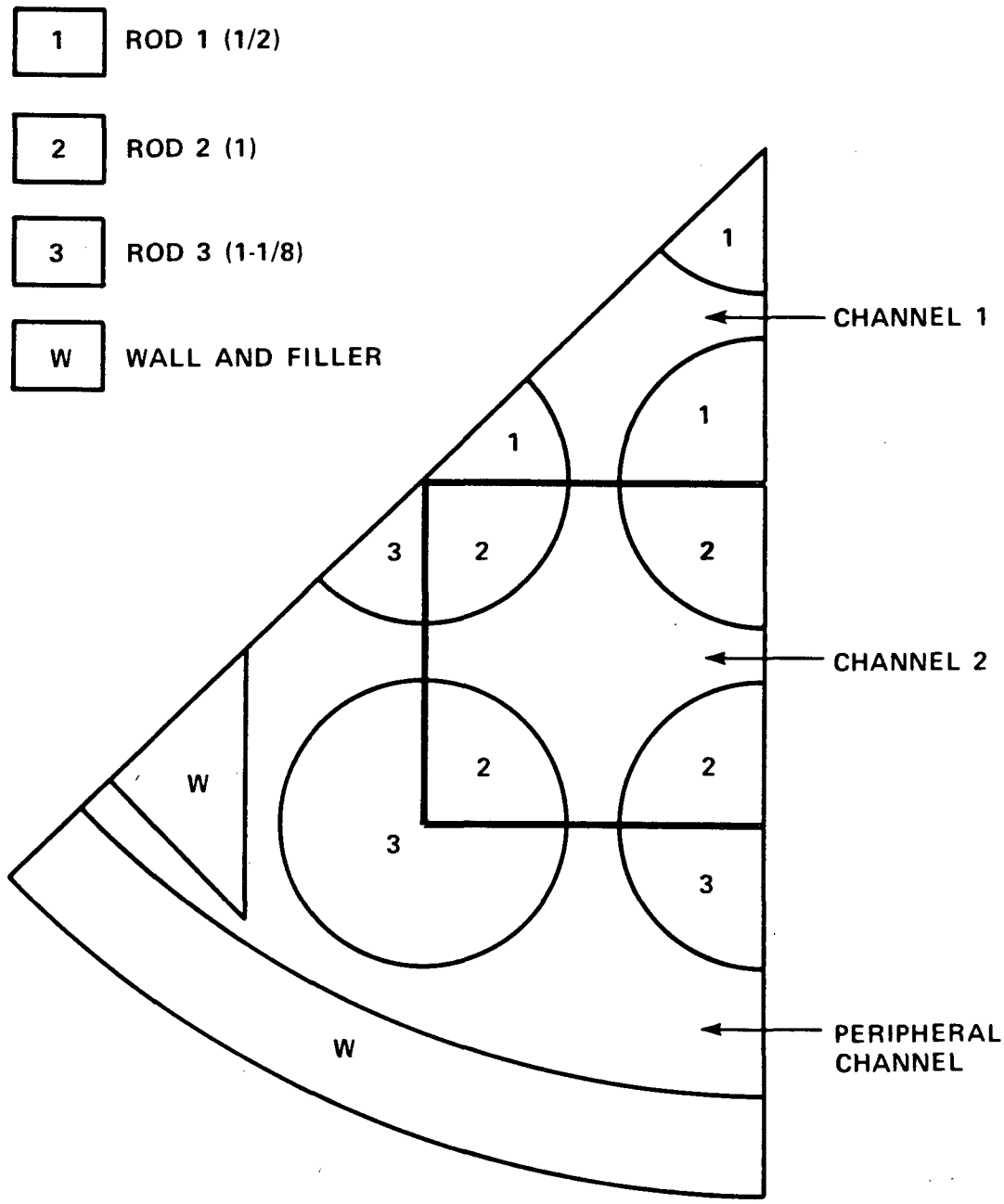

Figure A-14. FLECHT SEASET 21-Rod Bundle Radial Noding, Bundles B and F

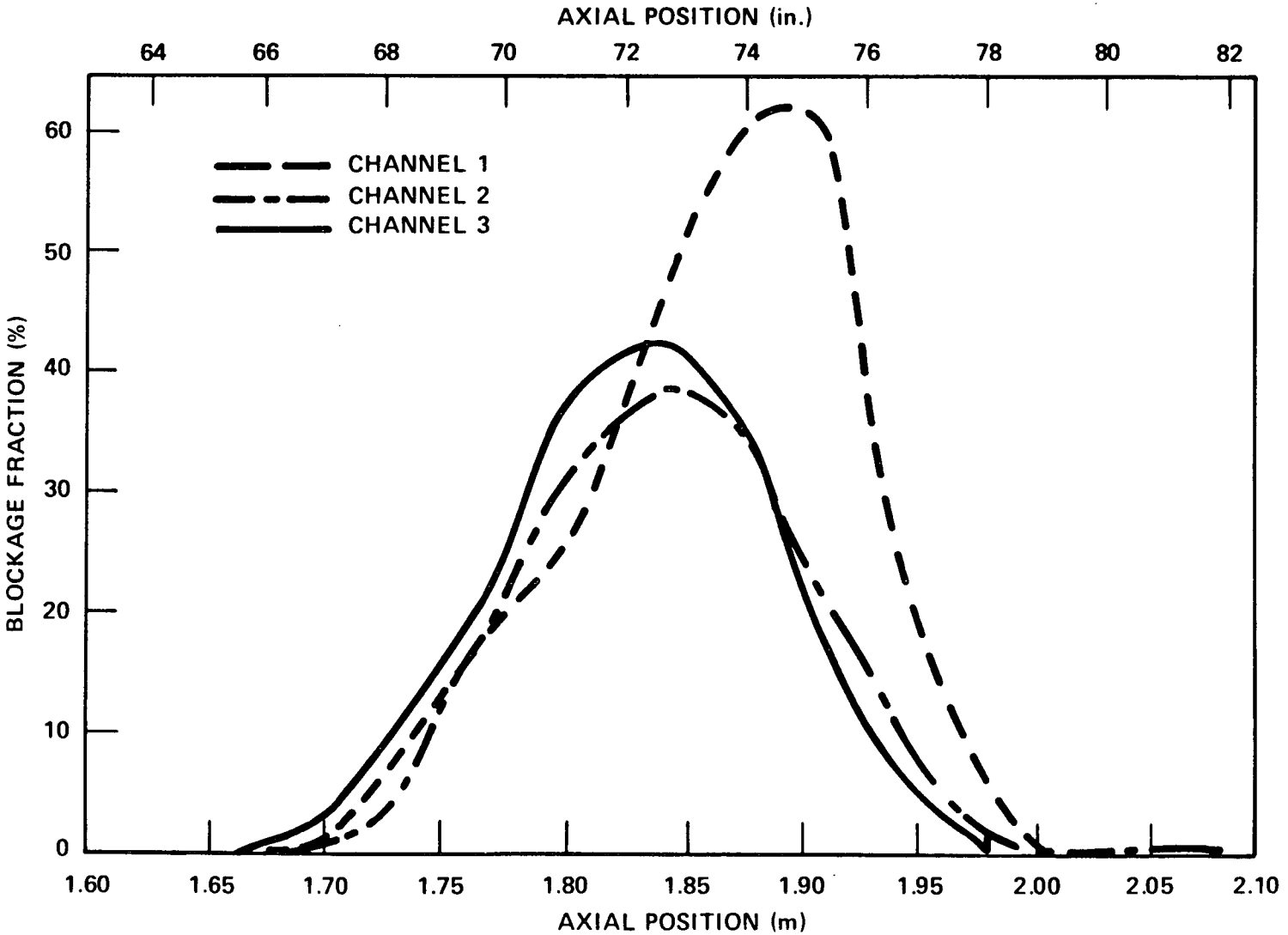

Figure A-15. FLECHT SEASET Configuration F Flow Area Restrictions

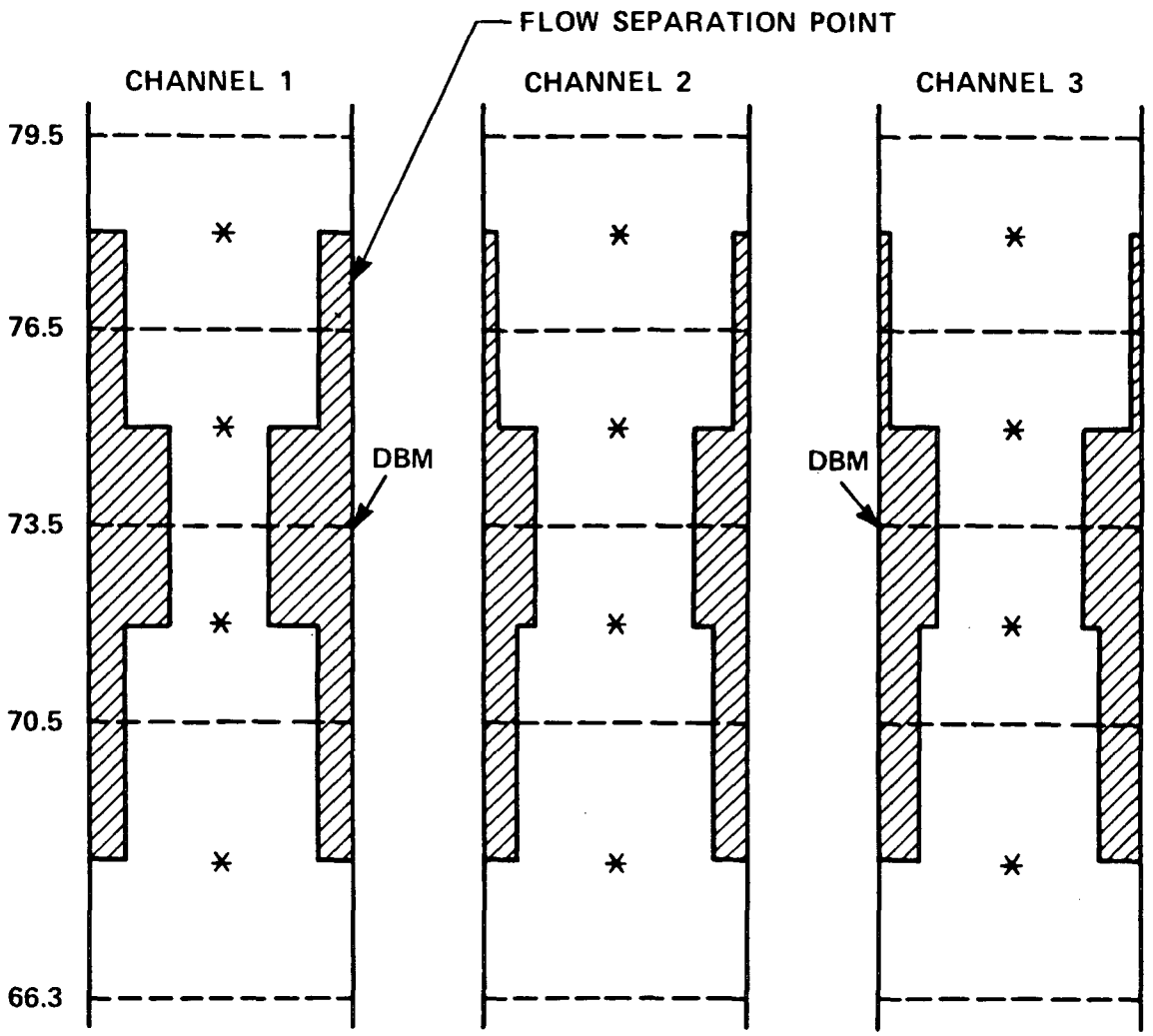

	CHANNEL 1	CHANNEL 2	CHANNEL 3
MAXIMUM BLOCKAGE	62.0%	39.0%	42.0%
DBM AREA	31.3%	0%	13.3%
FLOW SEPARATION POINT	1.96 m (77.4")	–	–

Figure A-16. FLECHT SEASET 21-Rod Bundle Nonconcentric/ Noncoplanar Blockage Geometry, Configuration F

TABLE A-5
BLOCKAGE GEOMETRY, FLECHT SEASET 21-ROD BUNDLE,
CONFIGURATION F

Factor	Value		
	Channel 1	Channel 2	Channel 3
Momentum area			
Node 11	0.755	0.748	0.688
Node 12	0.380	0.615	0.576
Node 13	0.740	0.893	0.927
Continuity area			
Node 11	0.9082	0.9302	0.8721
Node 12	0.6145	0.6544	0.6039
Node 13	0.4808	0.7575	0.7786
Node 14	0.9179	0.9717	0.9823
Wetted perimeter			
Node 11	1.142	1.146	1.078
Node 12	1.326	1.216	1.103
Node 13	1.12	1.064	1.019
Gap area			
Node 11	0.8222	0.7701	
Node 12	0.4698	0.3671	
Node 13	0.5634	0.6731	
Node 14	0.9239	0.9831	

A hydraulic characteristics test (Re = 14598) was simulated for configuration F. With no additional (grid-type) loss coefficient specified for the blockage, the bundle pressure drop was overestimated by 6 percent. Therefore, no additional losses were modeled.

The blockage heat transfer model parameters for configuration F are listed in table A-6. Using the methods of appendix D, flow separation was calculated to occur in channel 1 only, and zero droplet breakup was estimated for channel 2 (all of the sleeve bulges point away from channel 2).

To examine the convective enhancement model, a steam cooling test (41002F) was simulated. Figure A-17 shows the results of this calculation. The individual data points represent the measured enhancement values for the nine center heater rods, the dashed line is the enhancement calculated using the values in table A-6 and integrating equation (4-7) over the nodes downstream of the separation point, and the solid line presents the results of the COBRA-TF calculation. Enhancement due to flow acceleration and cross flow is evident upstream of the separation point and approximates the data. However, the enhancement immediately downstream of the separation point is significantly underpredicted. Consequently, the overall blockage enhancement effect just downstream of the blockage should be underestimated during reflood transients.

A-6. FLECHT SEASET 163-ROD BUNDLE MODEL

The 163-rod bundle is identical to the 161-rod bundle with the following exceptions:

- Two blockage "islands" of the same geometry as configuration F are included.
- Two thimbles (rod positions F-7 and I-10, the center of each island) are replaced by heater rods.

To model the blockage island, assuming one-half symmetry, with as much detail as used for the configuration F model would require a model of at least five channels. Because of this requirement, and since the 163-rod bundle data do not indicate large rod-to-rod differences in the blockage zone, it was decided

TABLE A-6
BLOCKAGE HEAT TRANSFER MODEL PARAMETERS, FLECHT SEASET
21-ROD BUNDLE, CONFIGURATION F

Parameter	Value Channel 1	Channel 2	Channel 3
Convective enhancement			
Separation point [m (in.)]	1.967 (77.43)	--	--
Diameter at separation point [m (in.)]	0.009898 (0.3897)	--	--
Maximum enhancement	1.96	--	--
Droplet breakup			
Area fraction (%)	31.3		13.3
Drop impact heat transfer			
Impact area/rod [m^2 ($in.^2$)]	5.44×10^{-5} (0.0844)	3.38×10^{-5} (0.0524)	3.72×10^{-5} (0.0578)
Impact angle (sleeve) (°)	2.7	2.7	2.7

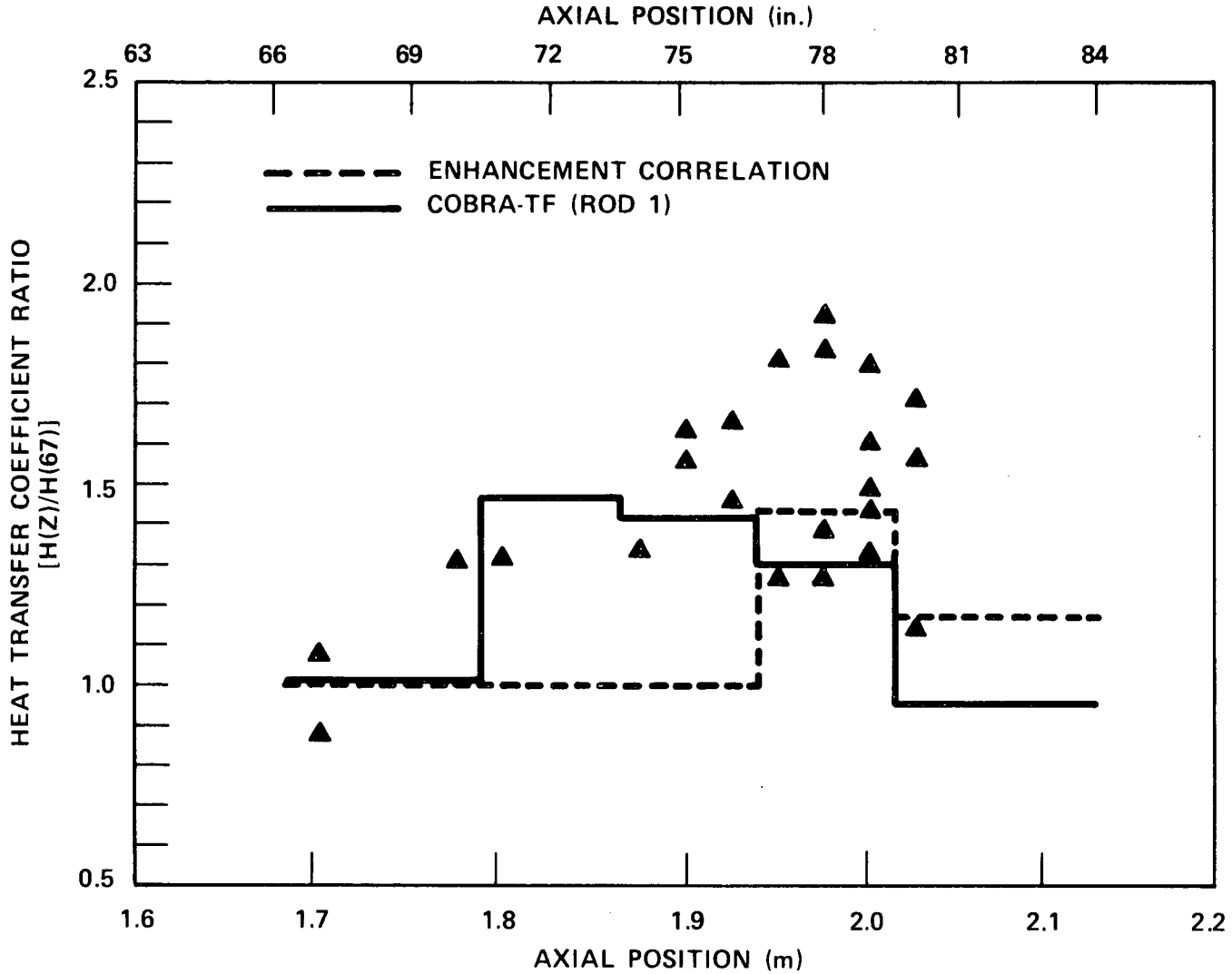

Figure A-17. FLECHT SEASET 21-Rod Bundle Heat Transfer Coefficient Enhancement

to lump the blockage region into one channel. Therefore, a three-channel model (figure A-18) was employed.

Flow areas for channels 1 (blockage) and 2 (bypass) were calculated from the nominal dimensions. The measured bundle flow area, minus the areas of channels 1 and 2, is used for the peripheral channel (channel 3). The flow areas and number of heater rods for each channel are as follows:

Channel	Flow Area [m^2 ($in.^2$)]	Number of Rods Modeled
1	1.362×10^{-3} (2.111)	15.5
2	3.607×10^{-3} (5.591)	38
3	2.929×10^{-3} (4.540)	28

A total of four heat transfer surfaces are employed to model the heater rods and housing. The heater rods contained within each channel are modeled by one average rod and the housing and filler are lumped together into the fourth surface.

Since there are no thimbles in the blockage zone, rod-to-rod radiation is neglected and a simple rod-fluid model is employed for channel 1. Although thimbles are present in the bypass region, the simple rod-fluid model was also used for channel 2. For the peripheral channel, it was necessary to model the radiative heat transfer from the rods to the housing. A radiation enclosure consisting of one normal and one edge subchannel (similar to that shown in figure A-4) is used to compute the radiation for channel 3.

The number of steam probes in the 163-rod bundle is small relative to the flow area. Also, the steam probes are not concentrated in the center of the blockage island (as they are in the 21-rod bundle). Therefore, it was not necessary to model different grid blockage areas and loss coefficient factors for each elevation. The grid blockage factors are 0.2952 (channels 1 and 2) and 0.21 (channel 3). A loss coefficient scale factor of 1.4, the same as for the 161-rod bundle, was used.

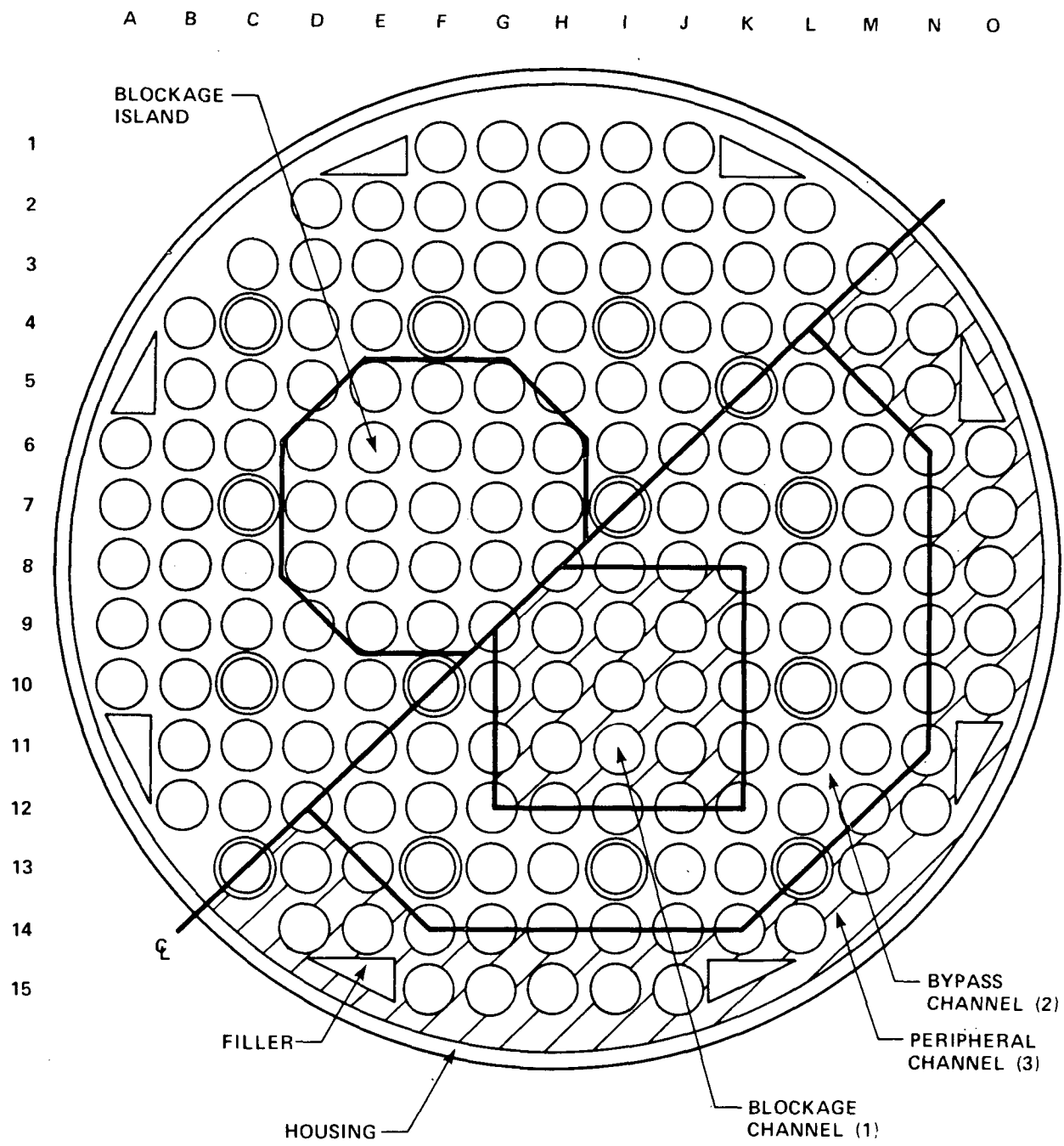

Figure A-18. FLECHT SEASET 163-Rod Bundle Noding Scheme

The flow blockage of each subchannel contained in the blockage region was averaged to determine the blockage geometry for channel 1. This calculation yielded a maximum blockage of 48 percent. Table A-7 lists the geometry factors that affect the hydrodynamic solution. As in the configuration F model, no additional loss coefficients were specified for the blockage.

The flow blockage heat transfer model parameters (table A-8) were calculated by the methods presented in appendixes C and D. This method results in no flow separation, and hence no convective enhancement, for the blockage channel. Flow separation probably does occur (there were no 163-rod steam cooling tests) and the blockage effect should be underestimated just downstream of the blockage.

The droplet breakup fraction for channel 1 was determined by averaging the breakup fraction for each individual subchannel. Therefore, although the average maximum blockage is 48 percent (which would give a DBM area of zero in figure C-2), some of the channels are much more severely blocked; the result is a calculated average DBM area fraction of 8.1 percent.

A-7. FEBA 5x5 BUNDLE MODEL

A total of eight different bundles were tested in the FEBA test series. Four of these were simulated with COBRA-TF to assess the grid spacer and flow blockage models. The COBRA-TF models for these four bundles, series I, II, VII, and VIII, are detailed below.

A-8. FEBA Series I

Series I simulated bottom reflood in an unblocked 25-rod bundle with the rod pitch and diameter of a KWU fuel bundle. Similar to the FLECHT SEASET 21-rod bundle model, a one-eighth symmetry, two-channel model (figure A-19) was selected. The flow areas were calculated from the nominal dimensions to be 2.27×10^{-4} m^2 (0.352 $in.^2$) and 2.59×10^{-4} m^2 (0.401 $in.^2$) for the central and peripheral channels, respectively.

The usual compromises between matching node boundaries with grid (or blockage) locations and node centers with thermocouple locations resulted in the axial

TABLE A-7
BLOCKAGE GEOMETRY, FLECHT SEASET 163-ROD BUNDLE

Factor	Value at Indicated Node			
	11	12	13	14
Momentum area	0.728	0.521	0.877	--
Continuity area	0.883	0.608	0.708	0.963
Wetted perimeter	1.576	1.261	1.072	--
Gap area	0.770	0.3671	0.673	0.983

TABLE A-8
BLOCKAGE HEAT TRANSFER MODEL PARAMETERS, FLECHT SEASET 163-ROD BUNDLE, CONFIGURATION C

Parameter	Value
Convective enhancement	None
Droplet breakup	
Area fraction (%)	8
Droplet impact heat transfer	
Impact area/rod [m^2 ($in.^2$)]	4.21×10^{-5} (0.0652)
Impact angle (sleeve) (°)	2.7

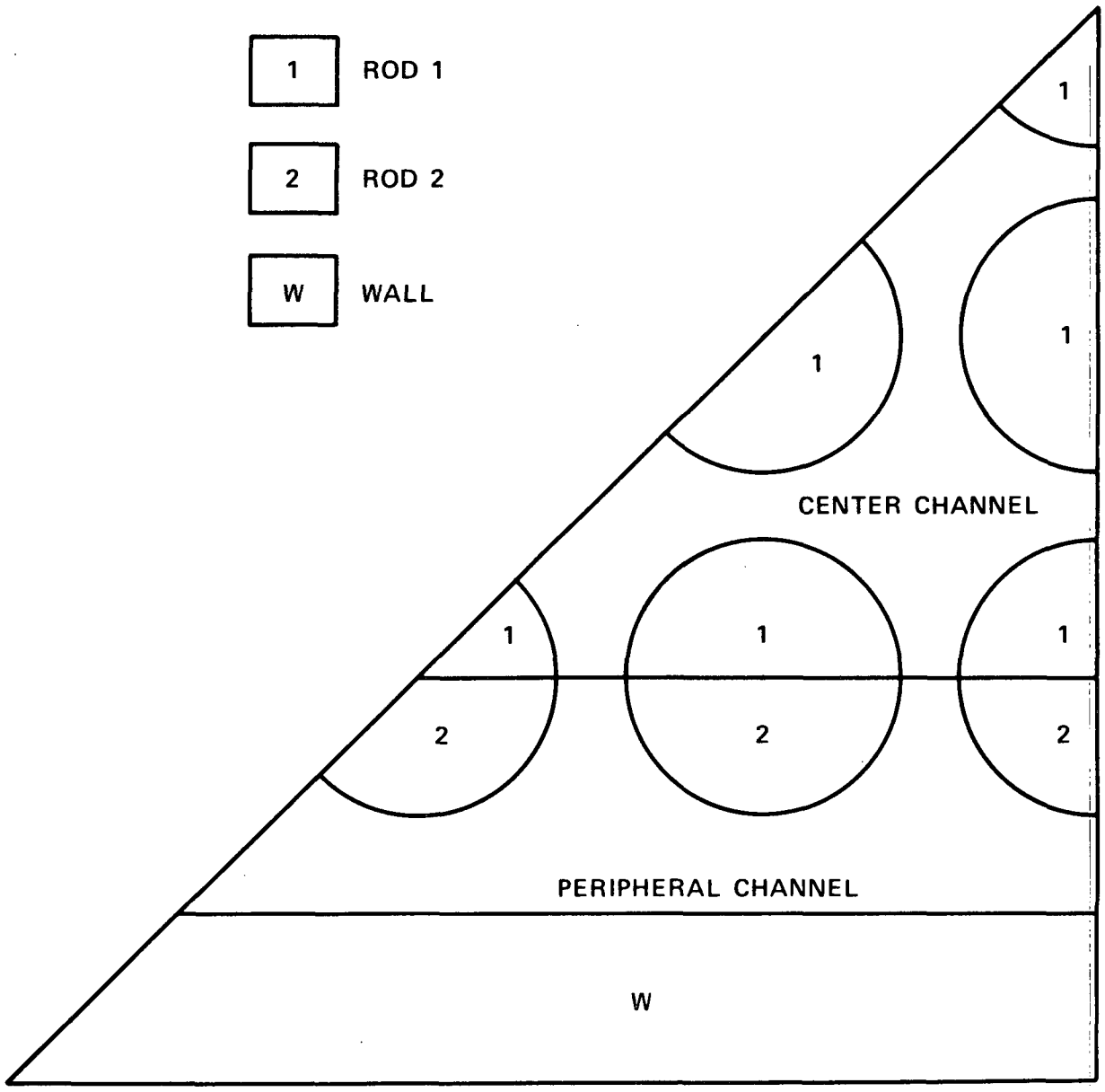

Figure A-19. FEBA 5x5 Bundle Radial Noding

noding scheme of figure A-20. A series of fine nodes [0.1 m (4 in.)] are placed near the bundle midplane [1.95 m (77 in.) from the bottom] to resolve the grid or blockage effect. This noding scheme is used for all the FEBA simulations.

Three heat transfer surfaces are modeled, one for the heater rods in each coolant channel, and one for the housing. Modeling the conduction in the FEBA heater rods (figure A-21) is straightforward with two exceptions. Each material region is modeled separately, specifying the number of nodes and material type (as is done for the FLECHT SEASET rods). However, the density of the ceramic insulator (MgO), which can vary greatly from one facility to another, is critical in determining the bundle heatup rate. After conferring with the KFK investigators, a value of 3150 kg/m^3 (196.7 lb/ft^3) was chosen.

Another modeling consideration is the presence of a thin gap between the MgO and the Inconel cladding. The contact "conductance" across this gap was estimated by the experimenters to be approximately 440 Btu/hr-ft-°F (761 w/m-°C). To model this conductance, a thin one-node region is employed with the material conductivity set so that the conductance equals that of the gap. It is important to specify reasonable values for the density and specific heat (for instance, $\rho Cp \simeq 3800$ J/m^3-°C (60 Btu/ft^3-°F) so that the explicit axial conduction solution does not become limiting.

Thermal radiation between the heater rods and the housing is of less importance in FEBA than in the FLECHT SEASET 21-rod bundle for two reasons:

- The difference between rod and housing initial temperature is much smaller (a 2-hour low-power heatup is used).
- The absolute temperature levels, both initially and at turnaround, are lower [1200° K (1700° F) versus 1400° K (2100° F).

For the above reasons, a simple, more approximate radiation enclosure was assumed. Figure A-22 illustrates this simple two-channel (one normal and one edge subchannel) radiation model.

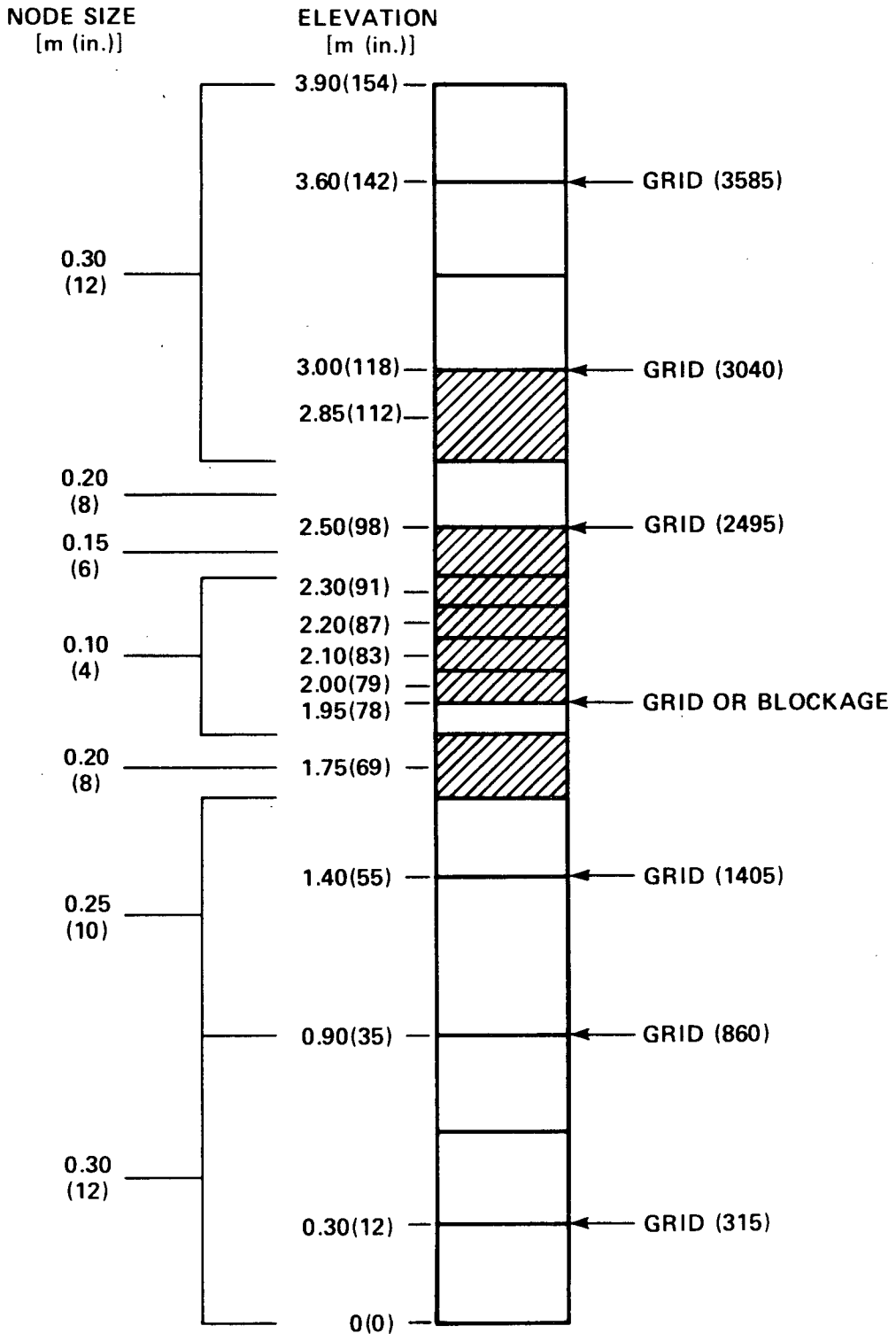

Figure A-20. FEBA 5x5 Bundle Axial Noding Scheme

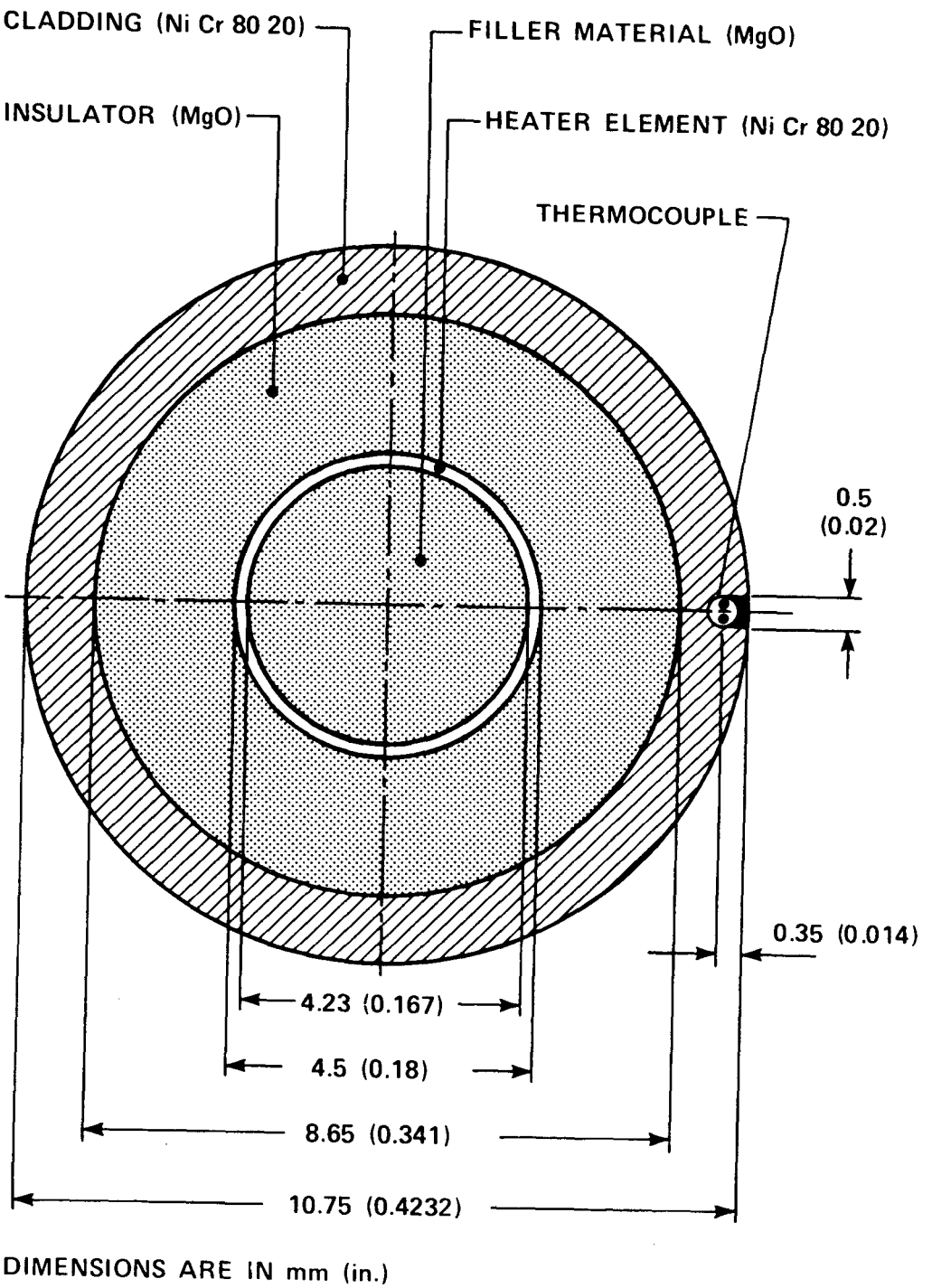

Figure A-21. Cross Section of FEBA Heater Rod

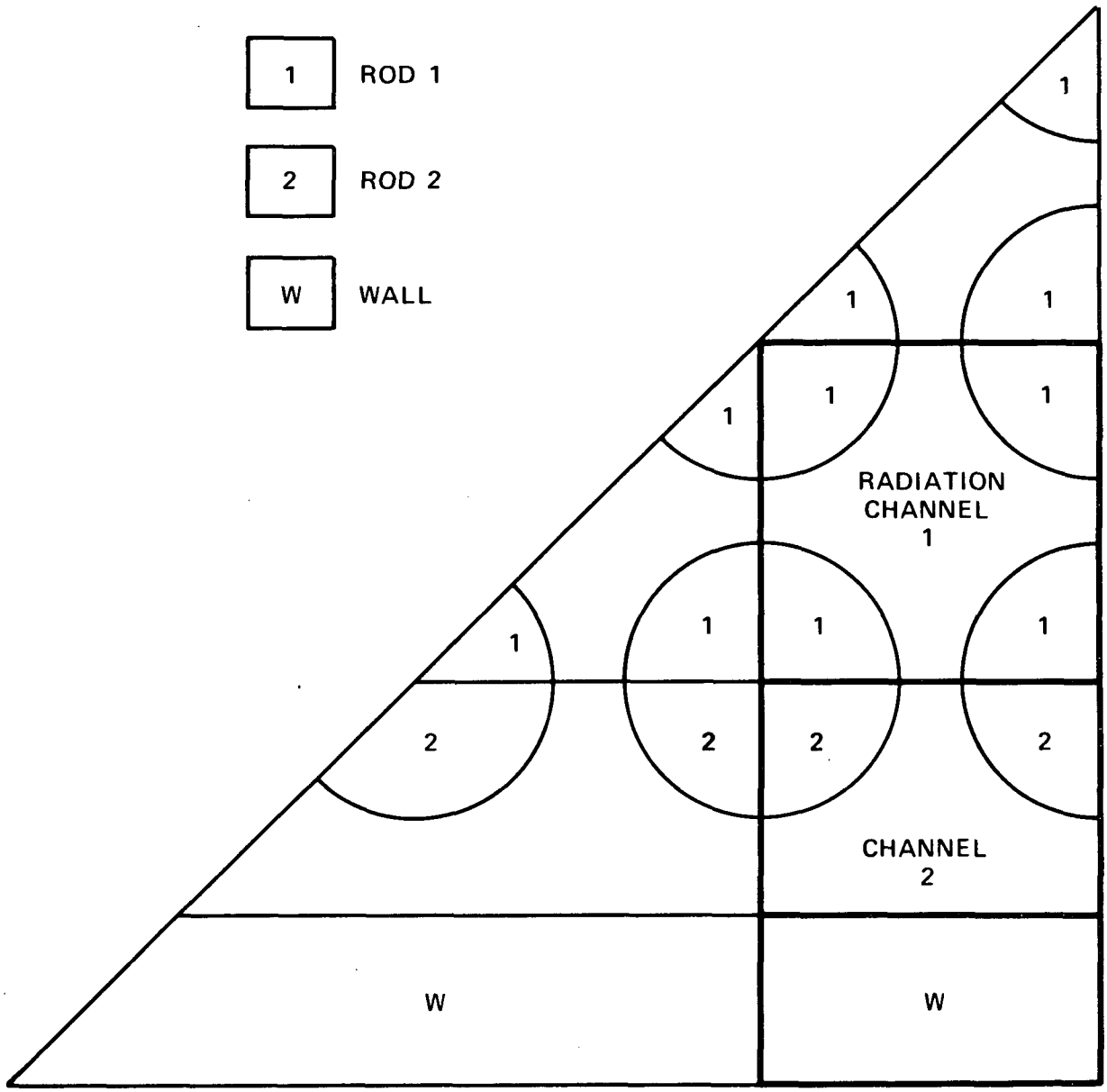

Figure A-22. FEBA Radiation Model

Grid blockage factors of 0.2365 and 0.2052 were calculated for the spacers in the central and peripheral channels, respectively. Grids are located at seven axial positions (figure A-20). Loss coefficients were calculated using the Rehme model with a grid shape multiplier of 1.4.

The specified axial power shape, peak-to-average = 1.10, was input directly and integrated over the axial node lengths to yield an average value for each node. The temporal forcing function on power was input from the measured bundle power versus time. The power level at time zero should be set to the power used during the bundle heatup (usually about 3 percent). During initialization of the rod temperatures, a steady-state conduction equation is solved for the temperature distribution within the rod. The power at time zero and rod surface temperature are used as the boundary conditions. As in the FLECHT SEASET simulations, the initial rod surface temperatures are generated by averaging the measured values over regions coincident with the radial noding scheme.

Flow and enthalpy boundary conditions were specified at the inlet (beginning of heated length and pressure at the outlet. Initially, the inlet water is assumed to be saturated and is ramped over time to the measured value. This accounts for the distance of approximately 0.2 m (8 in.) from the heated length to the bottom of the channel box (were the fluid is assumed to be equal to that of the lower plenum).

A-9. FEBA Series II

The geometry is exactly that of FEBA series I with the exception that the midplane spacer grid [at 1.95 m (77 in.)] is removed. Replicate tests for series I and II were used to determine the grid efficiency factor.

A-10. FEBA Series VII

The FEBA series VII tests used the bundle geometry of series II with a 62-percent coplanar flow blockage located at the bundle midplane. All 25 rods

and the housing had sleeves, so that all subchannels have the blockage factor. The COBRA-TF input is identical to that of series II except for the blockage input detailed below.

Figure A-23 illustrates the placement of the flow blockage upon the axial noding scheme. The flow area reduction is specified for three axial node boundaries (locations where the fluid velocity is calculated). This scheme makes the blockage appear somewhat longer than actual; it was employed so that the blockage noding schemes for series VII and VIII would be the same (see paragraph A-11). The blockage geometry factors given in table A-9 are the same for both channels.

The wetted perimeter factor, which gives the correct value of hydraulic diameter in the blockage throat, is 1.365. At the node boundaries above and below the midplane (nodes 8 and 10), the wetted perimeter factor is set to 0.3859 (same as the flow area factor) to preserve the nominal hydraulic diameter at these nodes, so that the blockage pressure drop will not be overpredicted. For continuity nodes 9 and 10, the gaps are completely blocked. Rather than input gap area factos of zero, the cross flows at these elevations are set to zero (see card group 13 input, appendix F). As in the FLECHT SEASET simulations, no additional blockage loss coefficient was specified.

The blockage heat transfer model parameters are listed in table A-10.

A-11. FEBA Series VIII

The FEBA series VIII tests used the same bundle geometry as series VII with a 90-percent coplanar blockage. Figure A-24 illustrates the placement of the flow blockage upon the axial noding scheme.

The momentum flux terms in COBRA-TF place a limit on the flow area variation that can occur over one node. For stability, the flow area should not vary by more than a factor of about three. Consequently, two nodes are required to reduce the flow area by a factor of 10 (90-percent blockage). Table A-11 lists the blockage geometry factors.

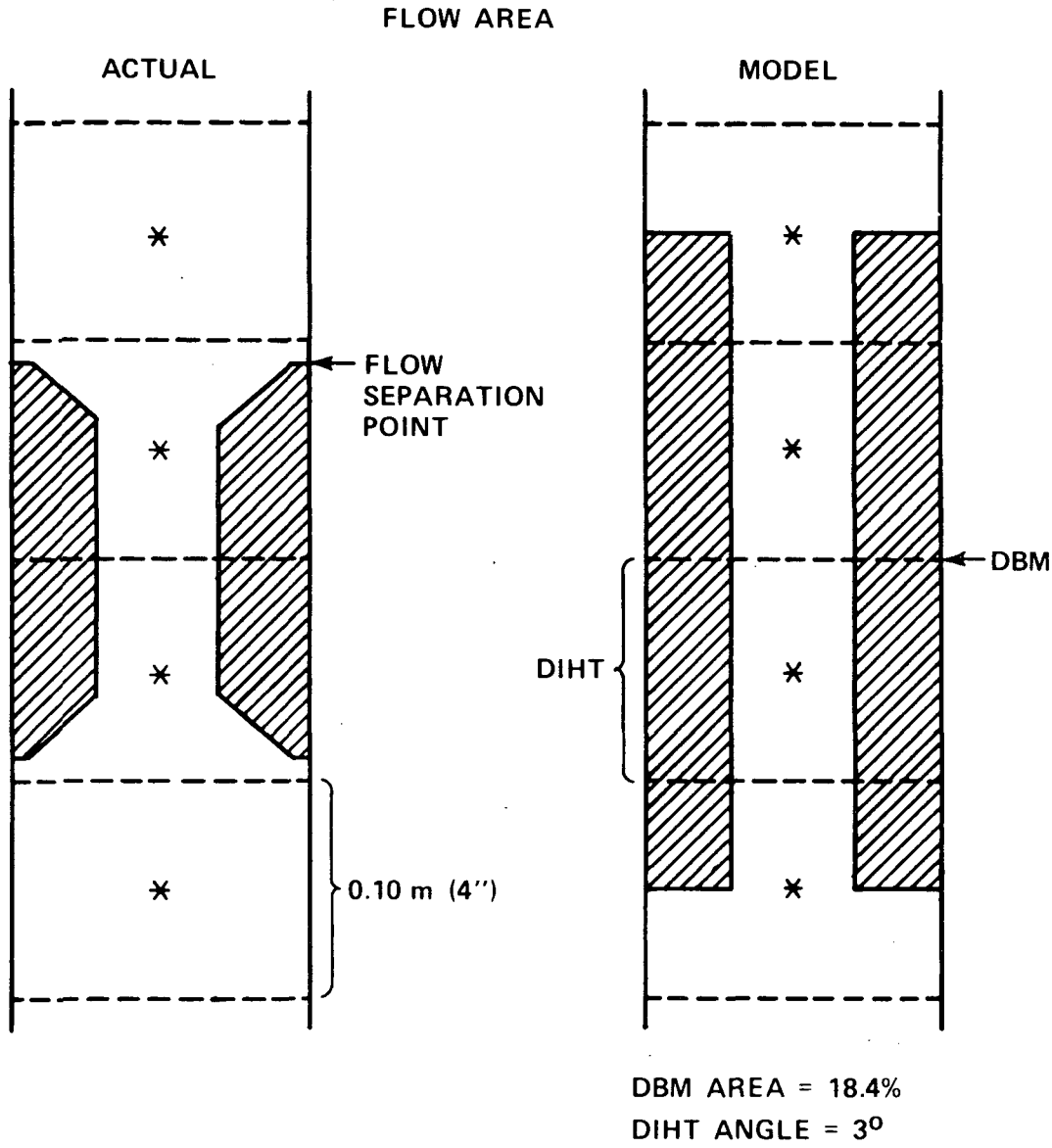

Figure A-23. FEBA 62-Percent Blockage Geometry

TABLE A-9
BLOCKAGE GEOMETRY, FEBA SERIES VII

Factor	Value at Indicated Node		
	8	9	10
Momentum area	0.3859	0.3859	0.3859
Continuity area	--	0.5317	0.5317
Wetted perimeter	0.3859	1.365	0.3859
Gap area	--	0.0	0.0

TABLE A-10
FEBA BLOCKAGE HEAT TRANSFER MODEL PARAMETERS

Parameter	Value	
	Series VII	Series VIII
Convective enhancement		
Separation point [m (in.)]	2.04 (80)	2.01 (79)
Diameter at separation point [m (in.)]	0.01140 (0.4489)	0.007475 (0.2943)
Maximum enhancement	1.94	2.58
Droplet breakup		
Area fraction (%)	18.4	62.8
Droplet impact heat transfer		
Impact area/rod [m^2 ($in.^2$)]	1.719×10^{-4} (0.1083)	1.023×10^{-4} (0.1587)
Impact angle (sleeve) (°)	3	3

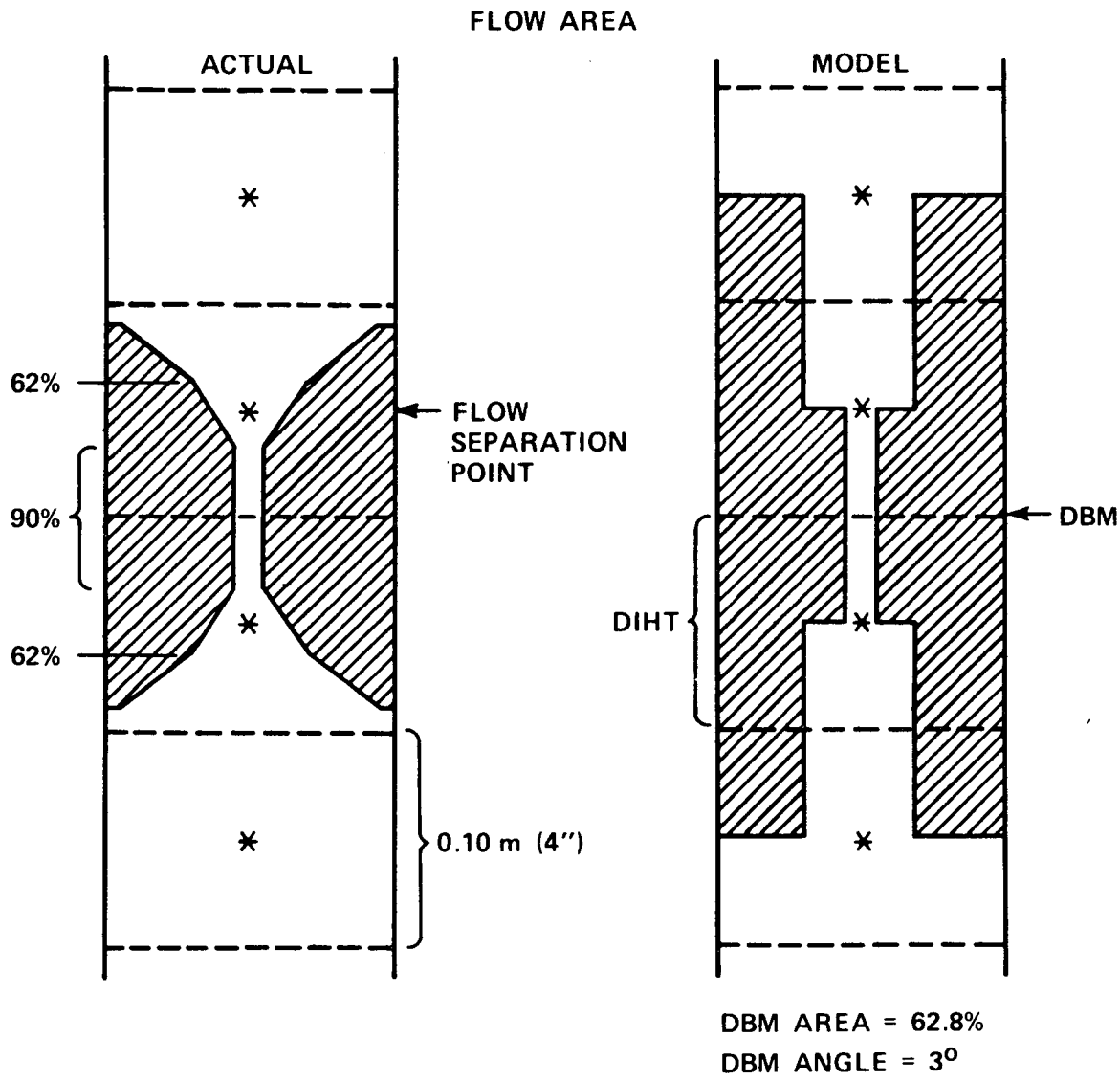

Figure A-24. FEBA 90-Percent Blockage Geometry

The blockage heat transfer model parameters are given in table A-10.

A-12. ROD BUNDLE SCALING FACTORS

In modeling all of the above geometries, lumped channels consisting of ideal subchannels, thimble subchannels, edge subchannels, corners, and the like have been employed. It was necessary to include a rod bundle scaling factor (RBSF) to relate these geometries to an ideal subchannel for which the COBRA-TF reflood entrainment model was derived. The entrainment rate for a node is given by

$$S_E = (\text{constant}) \cdot \left(RBSF \cdot \frac{V_v}{V_{crit}} \right)^2 \cdot \dot{m}_v$$

The scaling factor is calculated from

$$RBSF = \frac{A_F}{N_R \cdot A_{SC}}$$

where

A_F = bundle flow area
A_{SC} = subchannel flow area
N_R = equivalent number of rods

N_R is calculated from the total heated perimeter divided by the heater rod perimeter. The total heated perimeter includes that of all heater rods and any other surface that can be considered to be in inverted annular film boiling. Therefore, do not include the perimeter of either cold surfaces or of elements which do not have a significant amount of stored energy. For example, thick housings should be included in the perimeter and thimbles should not. The values of RBSF are given in table A-12.

TABLE A-11
BLOCKAGE GEOMETRY, FEBA SERIES VII

Factor	Value at Indicated Node		
	8	9	10
Momentum area	0.3859	0.1	0.3859
Continuity area	--	0.3959	0.3959
Wetted perimeter	0.3859	0.4507	0.3859
Gap area	--	0.0	0.0

TABLE A-12
ROD BUNDLE SCALING FACTORS

Case	RBSF
FLECHT SEASET 161-rod bundle	0.9764
FLECHT SEASET 21-rod bundle	0.8153
FLECHT SEASET 163-rod bundle	0.9711
FEBA	0.9979
Ideal subchannel	1.0

APPENDIX B
NODING SENSITIVITY STUDIES USING COBRA-TF

A series of noding sensitivity studies were performed using COBRA-TF to determine whether there would be an observable effect of noding size on the calculated results. Both axial and radial noding variations were studied. FLECHT SEASET test 31805 was used to perform the sensitivity study.

Figure B-1 shows the effects of varying the node size from 0.15 to 0.30 m (6 to 12 in.). Curve A in these plots is the intermediate point between the noding represented by curves B and C. The fact that curve A usually lies between curves B and C indicates that averaging the results from curves B and C would yield curve A.

Figure B-2 shows the effects of comparing 0.15 m (6 in.) axial nodes to 0.46 m (18 in.) nodes, such that the center of the 0.46 m (18 in.) node is at the interface of the three 0.15 m (6 in.) nodes. Therefore, curves A and C should agree very well if there are no noding effects. The agreement shown by the plots of figure B-2 is excellent.

Comparisons of axial temperature plots are shown in figure B-3 for three different axial nodings; again, the agreement is very good. The biggest differences occur with the 0.46 m (18 in.) nodes with straight lines connected between the nodes.

Radial noding was also investigated using two and five radial nodes for the 161-rod bundle. The inner three nodes of the five-node model correspond to the same area as the inner node of the two-node model. The inner node of the two-node model is curve A in figure B-4; the inner nodes of the five-node model are curves B, C, and D. Again, the agreement is quite good with curve A (shown by the larger inner node) being the average of the other curves, which have more radial detail.

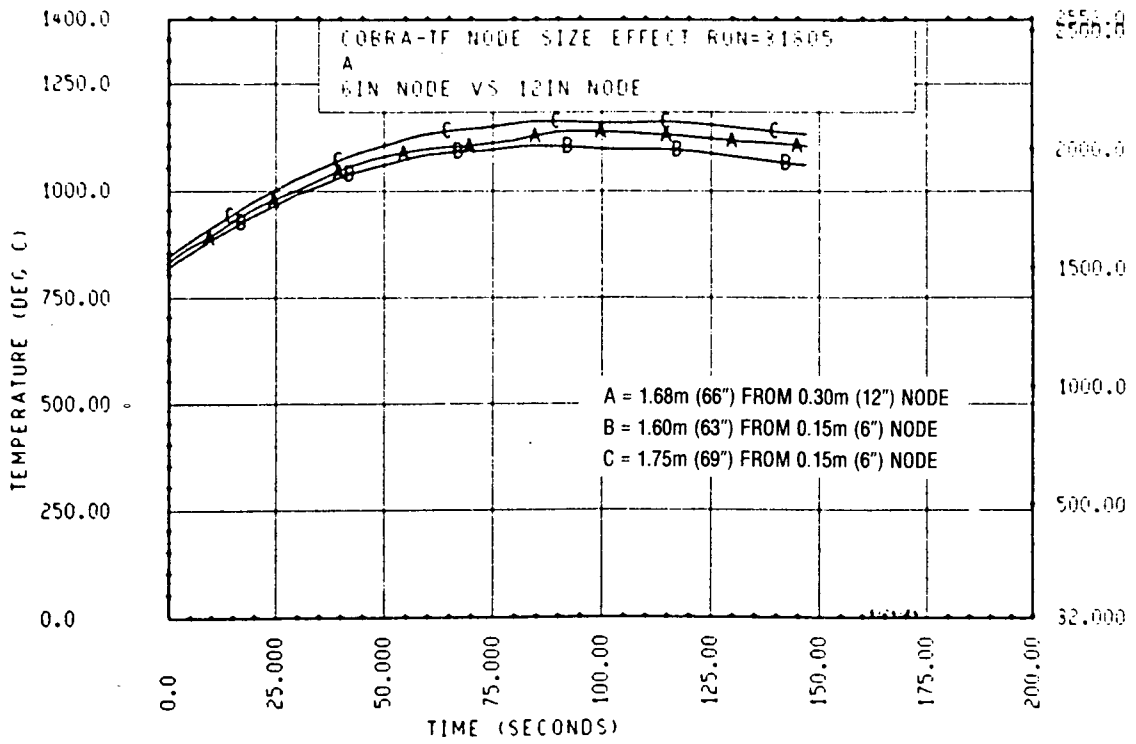

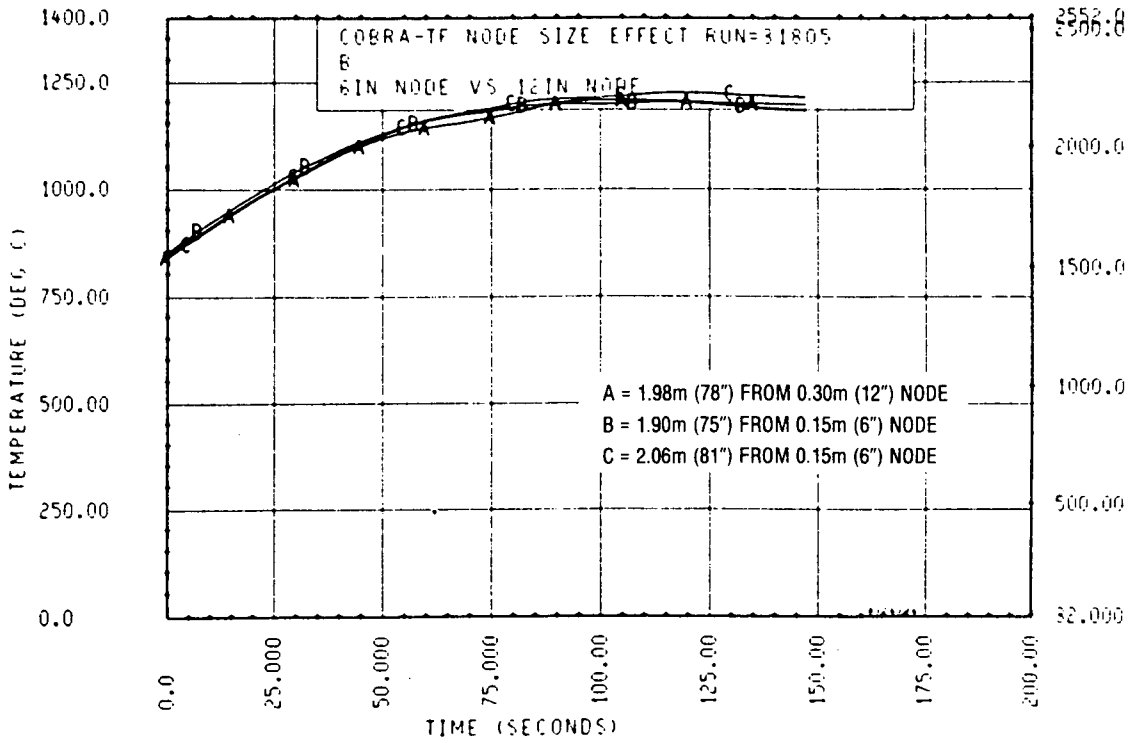

Figure B-1. COBRA-TF Results (Temperature Versus Time) With 0.15 and 0.30 m (6 and 12 in.) Axial Node Sizes (sheet 1 of 2)

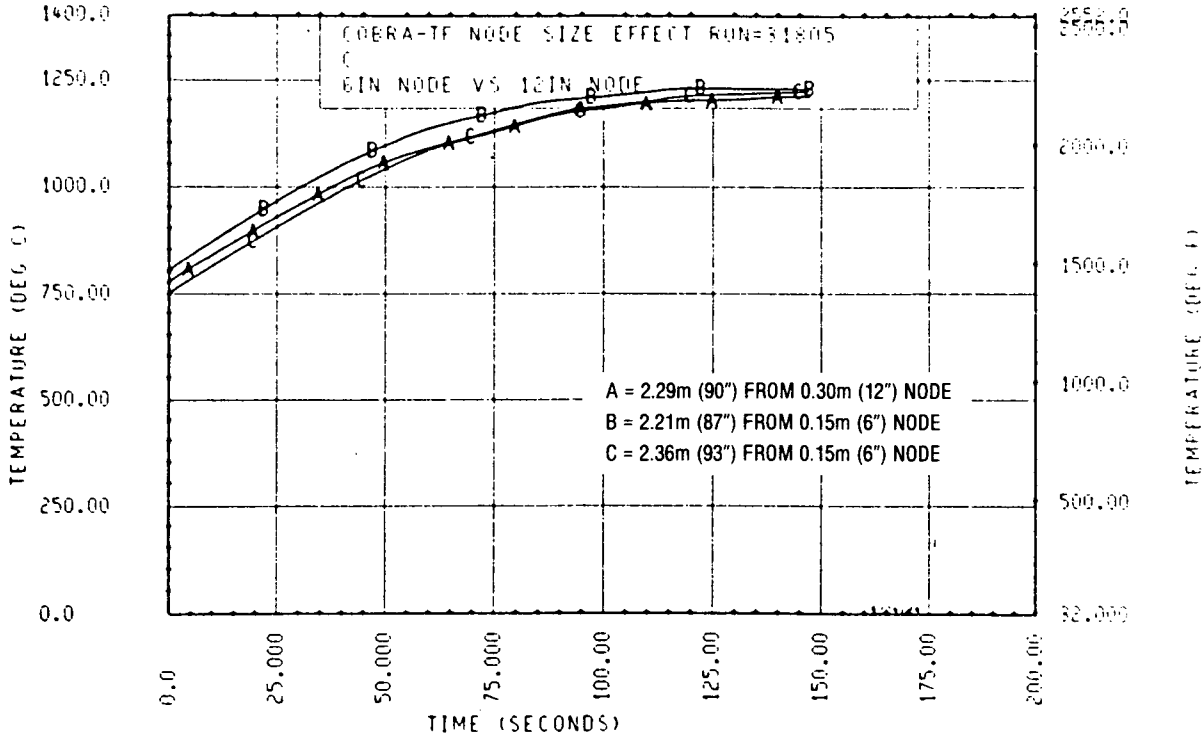

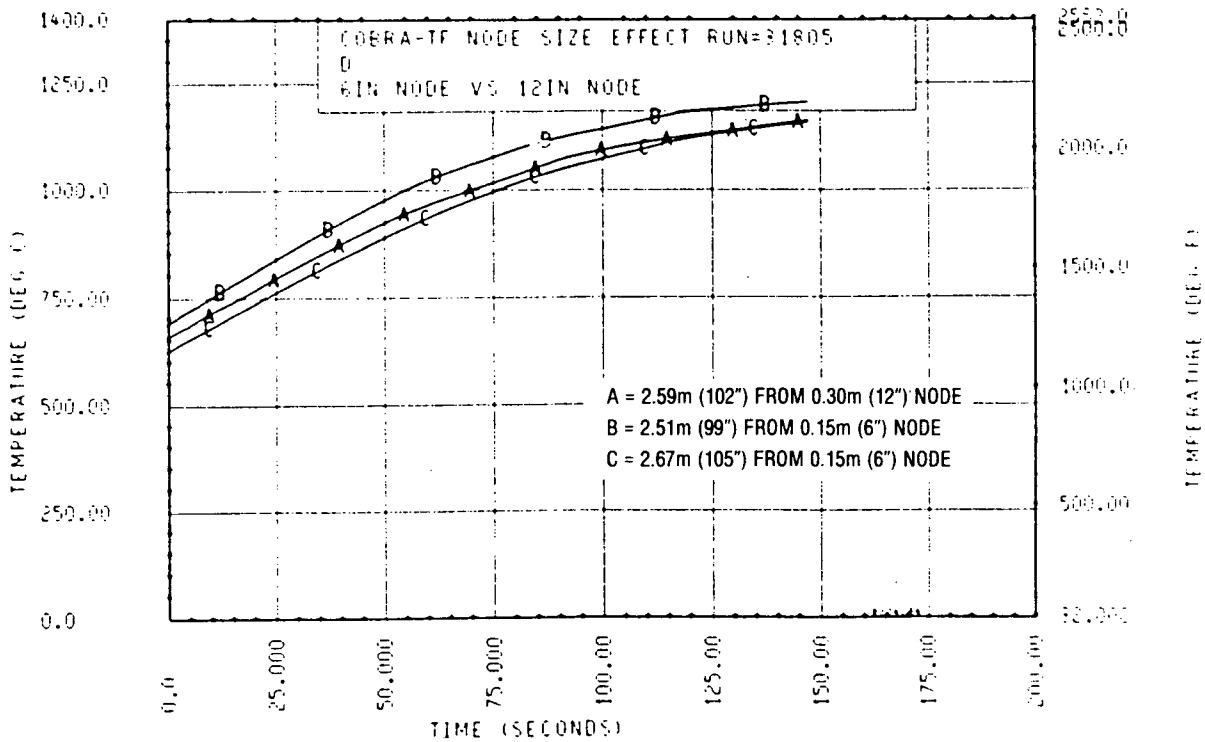

Figure B-1. COBRA-TF Results (Temperature Versus Time) With 0.15 and 0.30 m (6 and 12 in.) Axial Node Sizes (sheet 2 of 2)

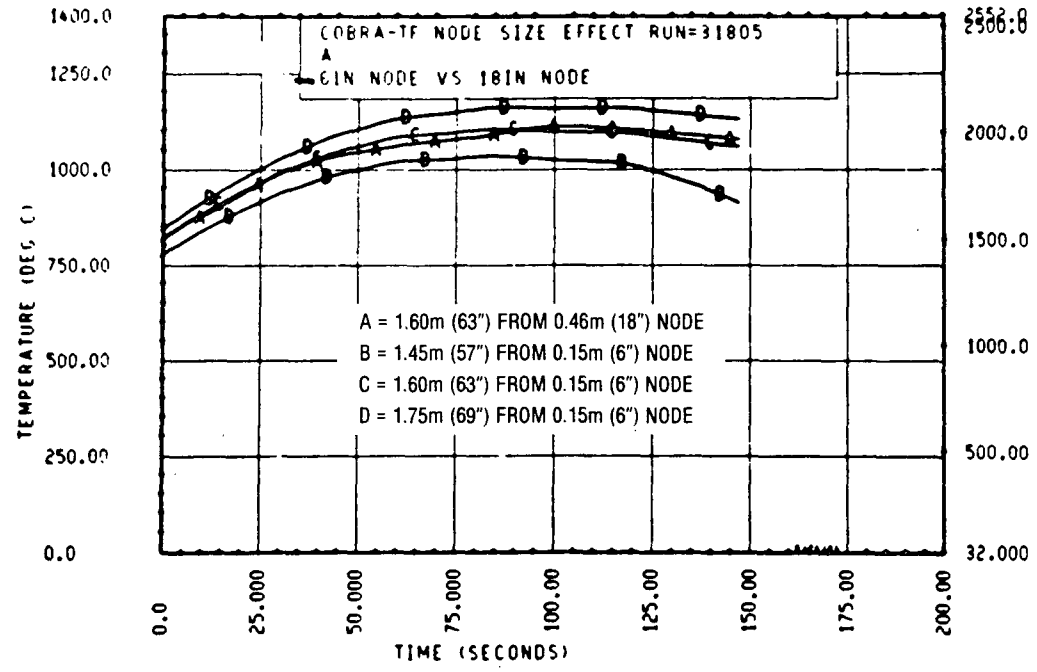

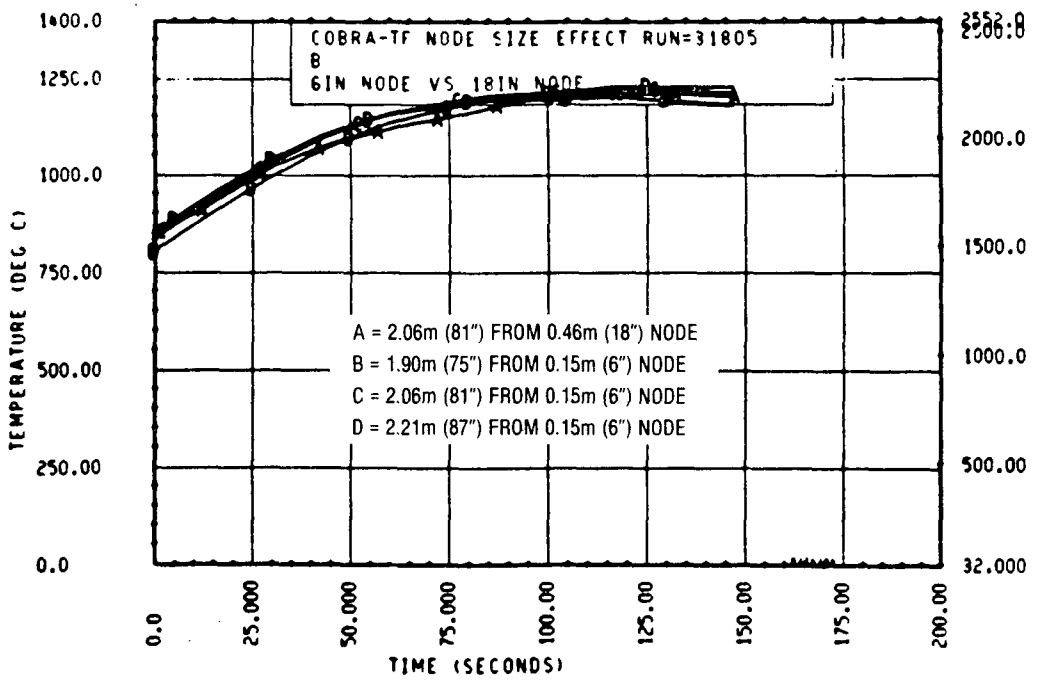

Figure B-2. COBRA-TF Results (Temperature Versus Time) With 0.15 and 0.46 m (6 and 18 in.) Axial Node Sizes (sheet 1 of 2)

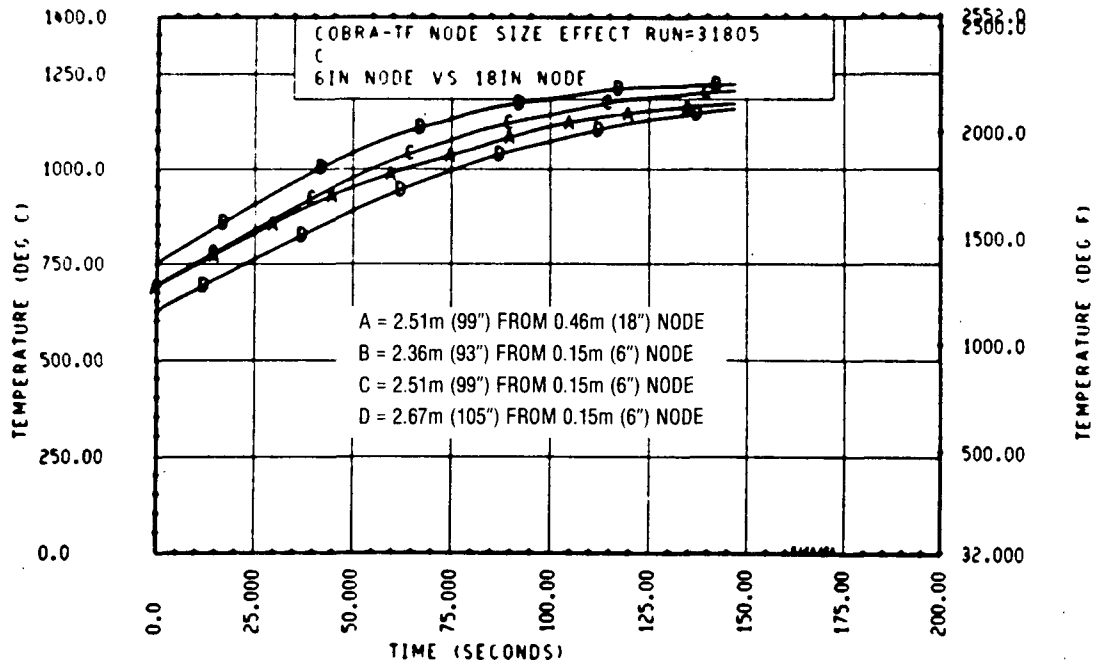

Figure B-2. COBRA-TF Results (Temperature Versus Time) With 0.15 and 0.46 m (6 and 18 in.) Axial Node Sizes (sheet 2 of 2)

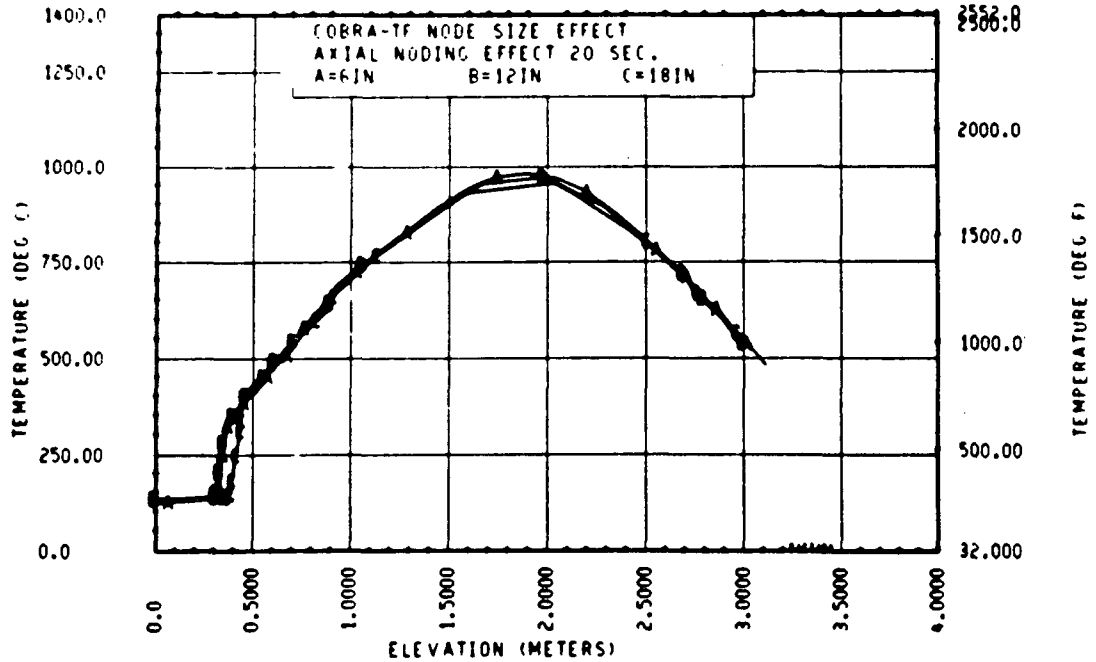

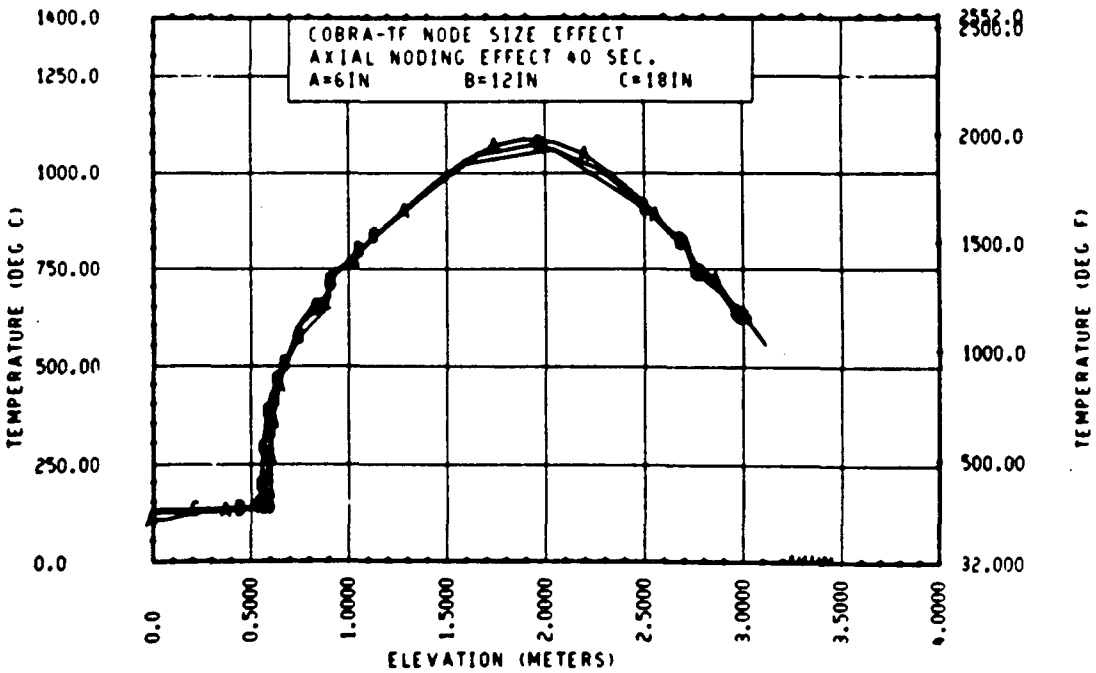

Figure B-3. COBRA-TF Results (Temperature Versus Elevation) With 0.15, 0.30, and 0.46 m (6, 12, and 18 in.) Axial Node Sizes (sheet 1 of 4)

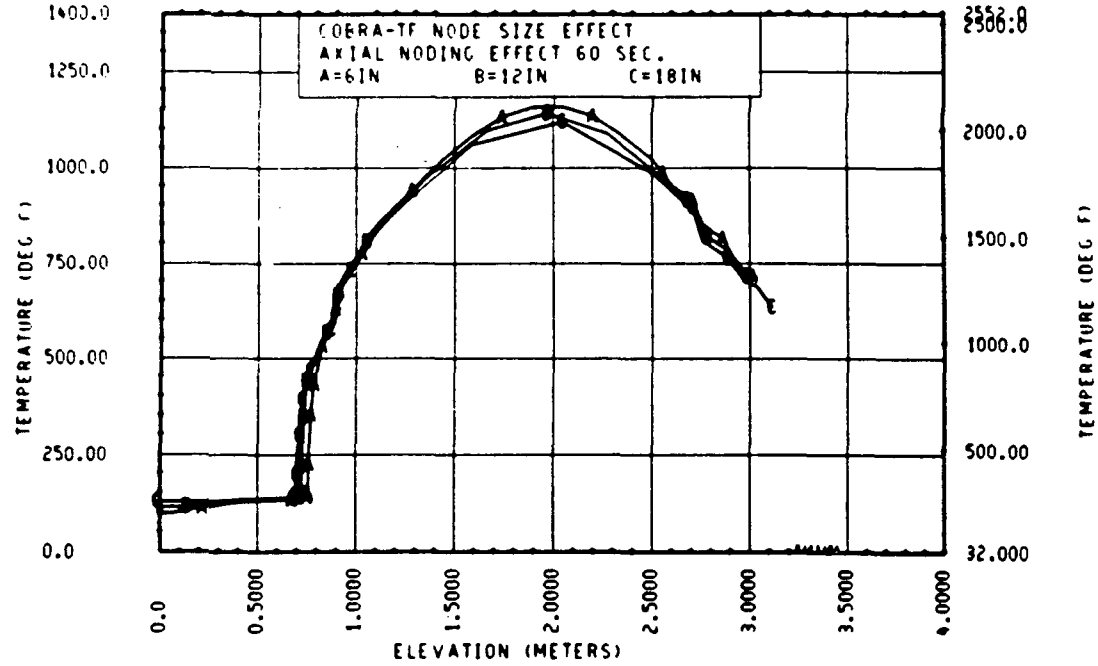

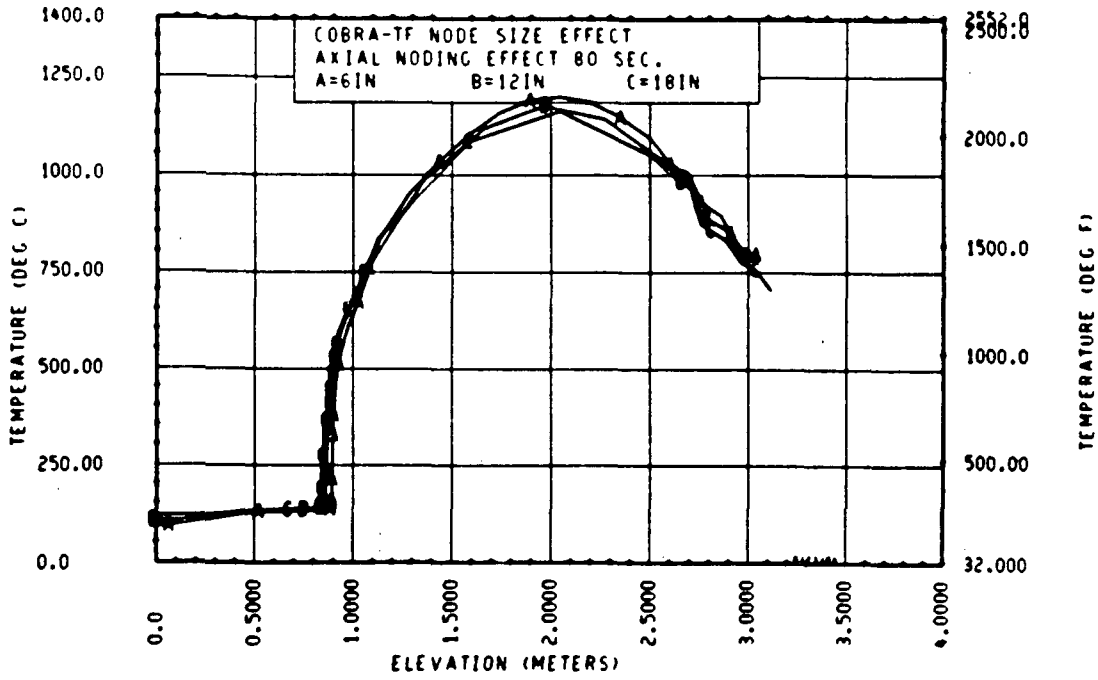

Figure B-3. COBRA-TF Results (Temperature Versus Elevation) With 0.15, 0.30, and 0.46 m (6, 12, and 18 in.) Axial Node Sizes (sheet 2 of 4)

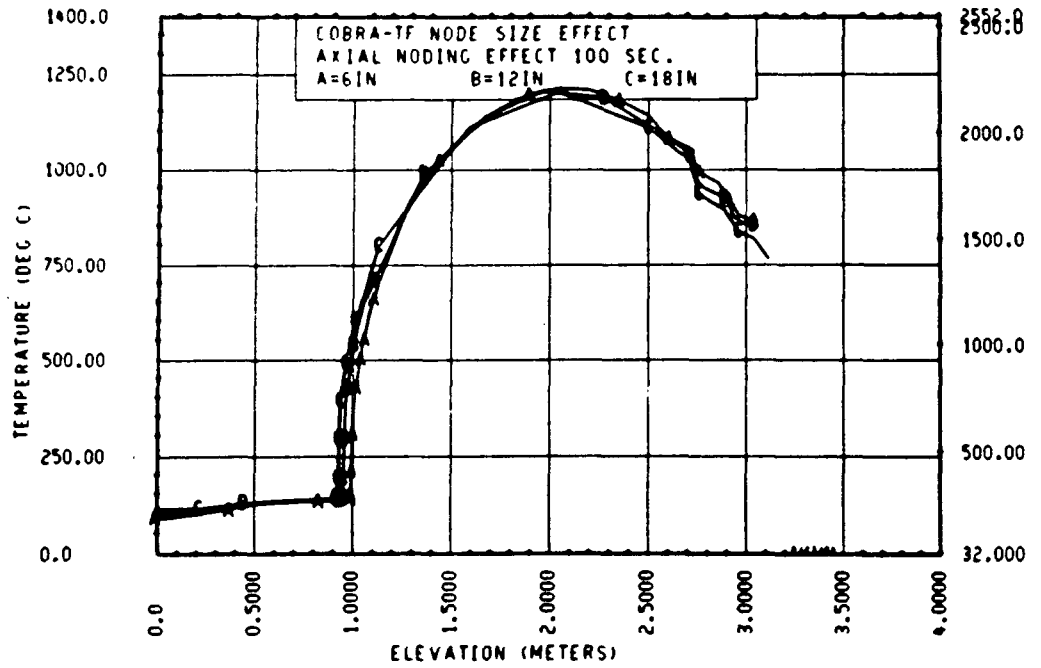

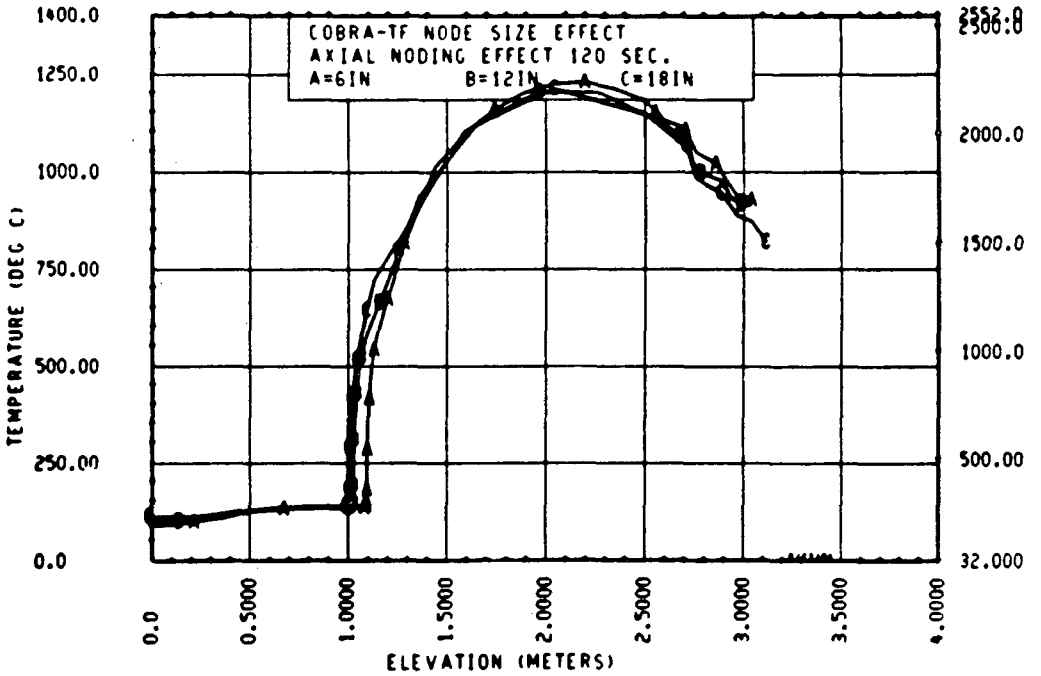

Figure B-3. COBRA-TF Results (Temperature Versus Elevation) With 0.15, 0.30, and 0.46 m (6, 12, and 18 in.) Axial Node Sizes (sheet 3 of 4)

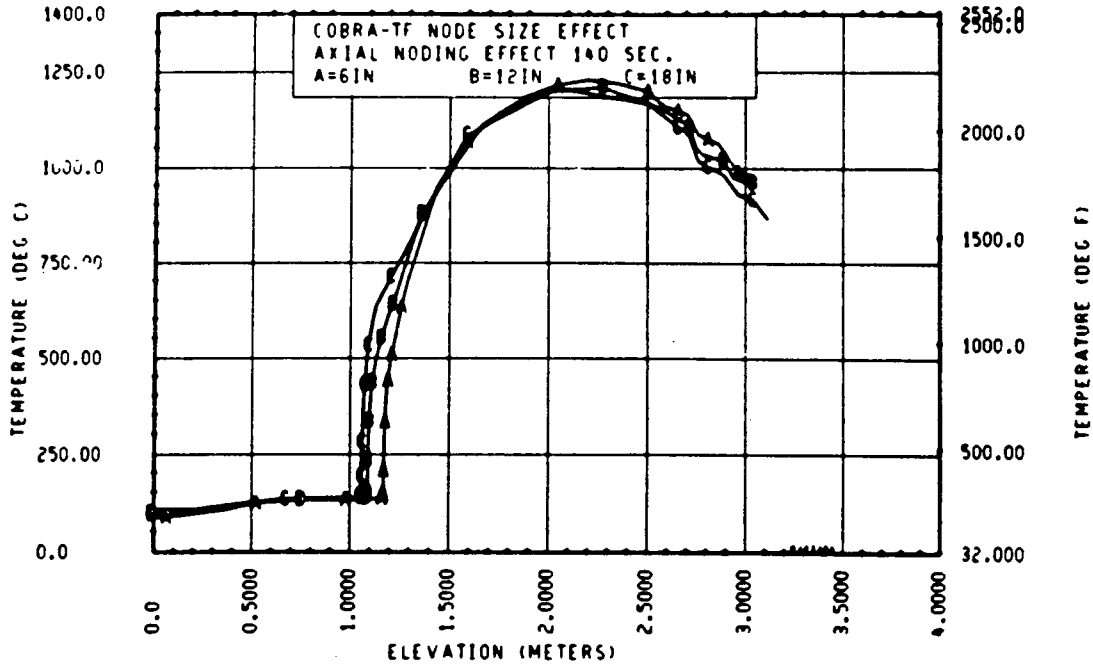

Figure B-3. COBRA-TF Results (Temperature Versus Elevation) With 0.15, 0.30, and 0.46 m (6, 12, and 18 in.) Axial Node Sizes (sheet 4 of 4)

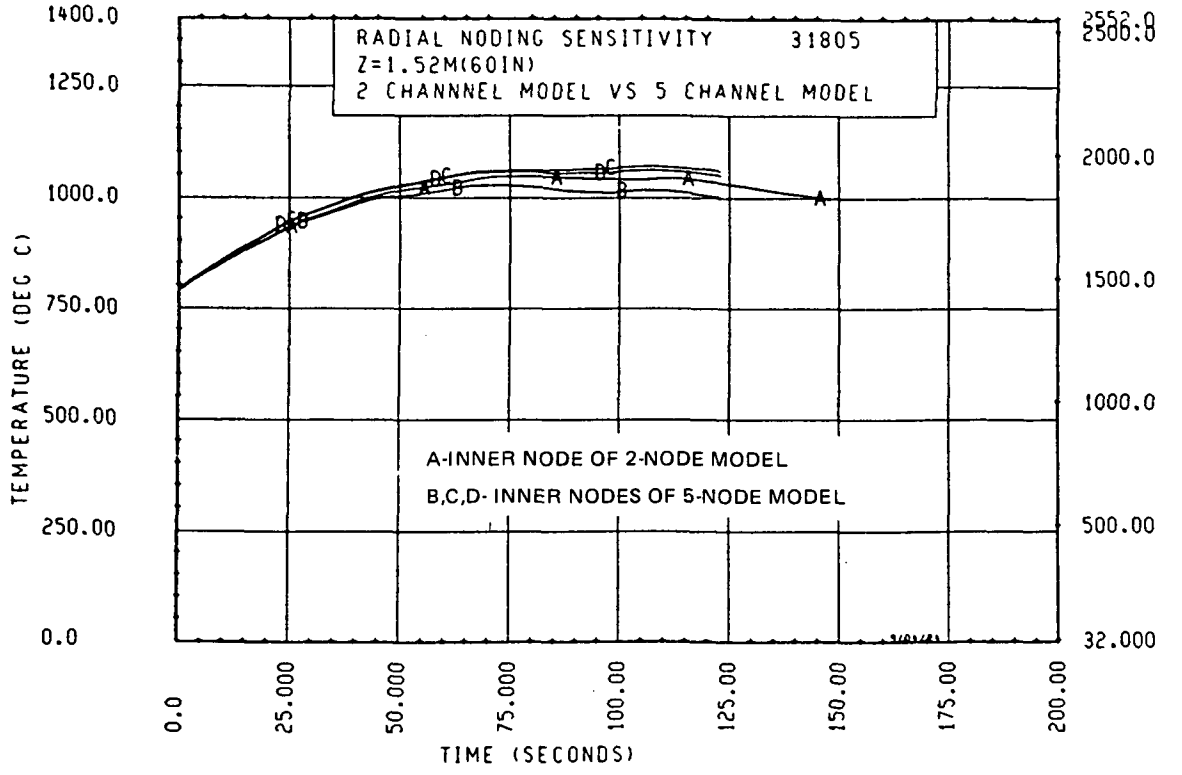

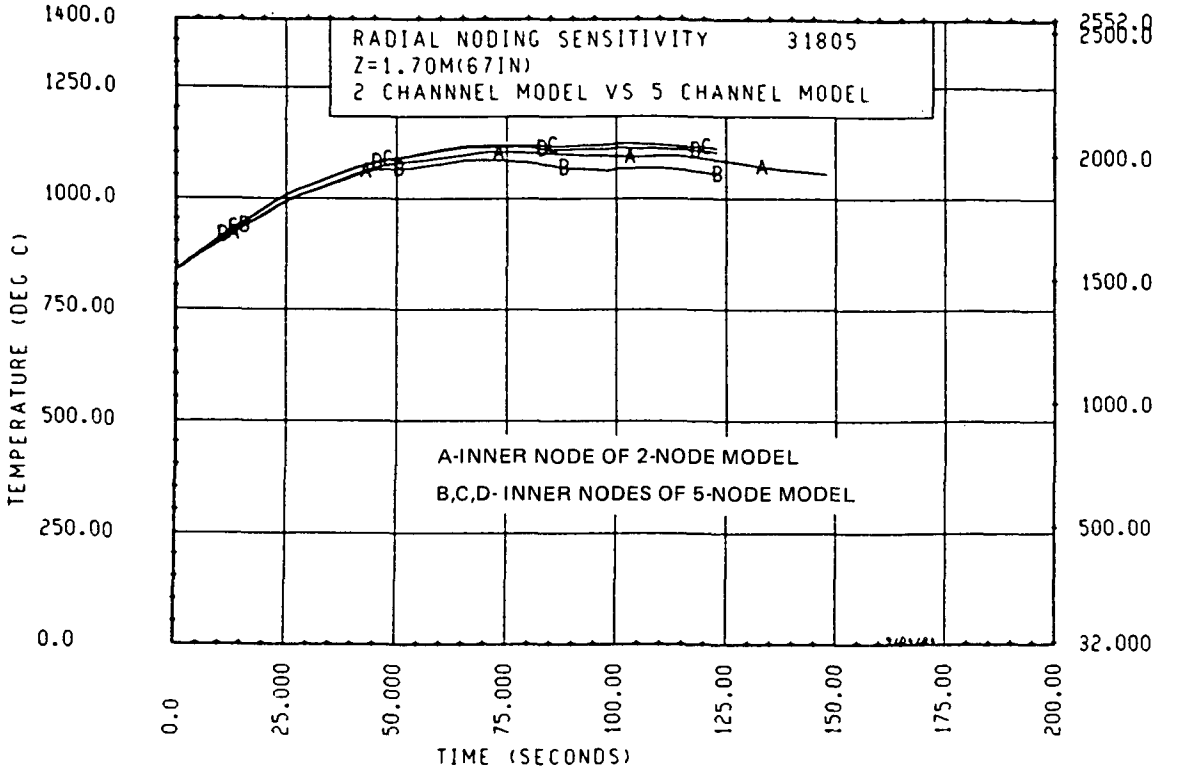

Figure B-4. COBRA-TF Results (Temperature Versus Time) With Two and Five Radial Nodes (sheet 1 of 3)

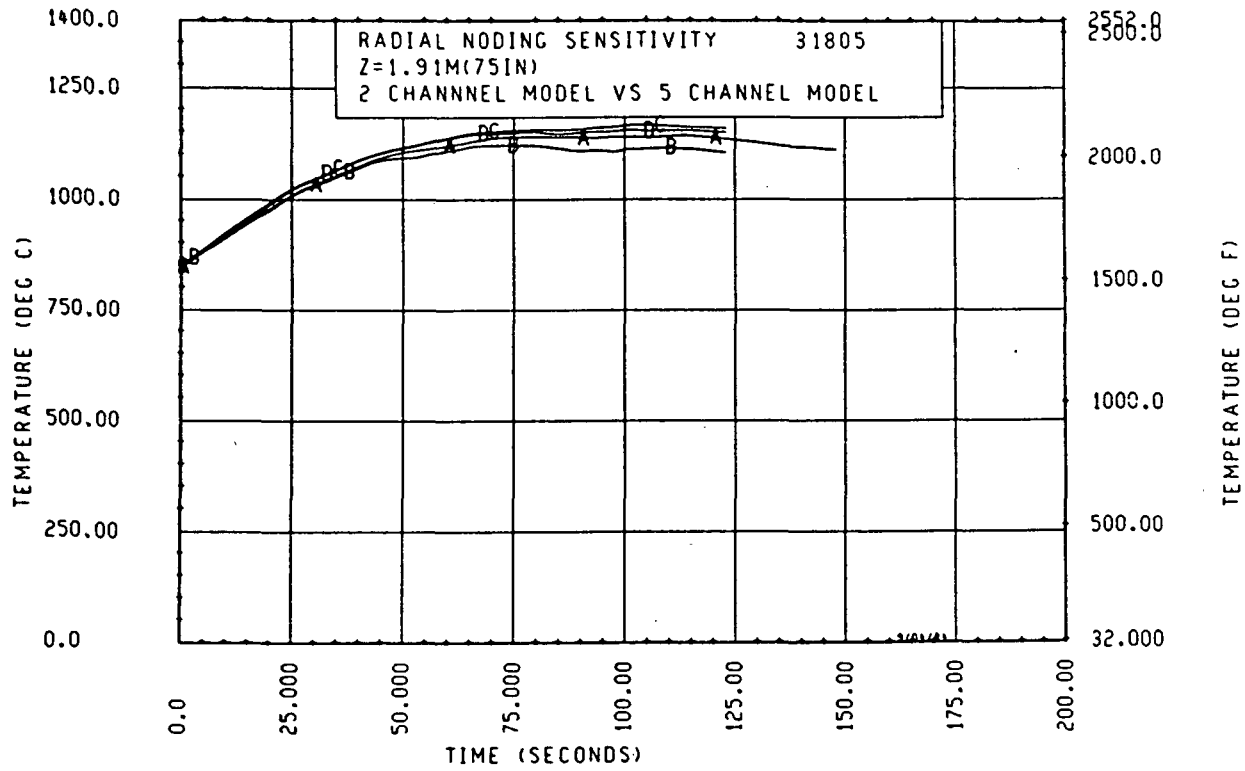

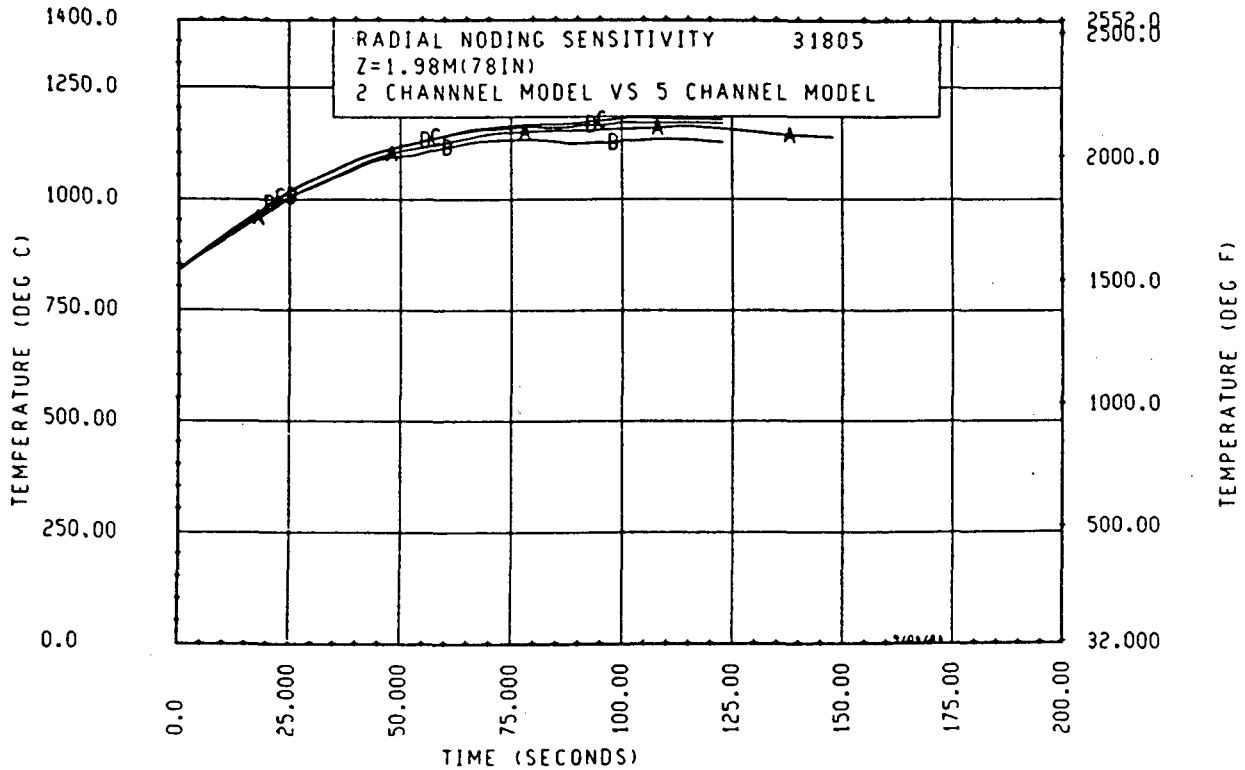

Figure B-4. COBRA-TF Results (Temperature Versus Time) With Two and Five Radial Nodes (sheet 2 of 3)

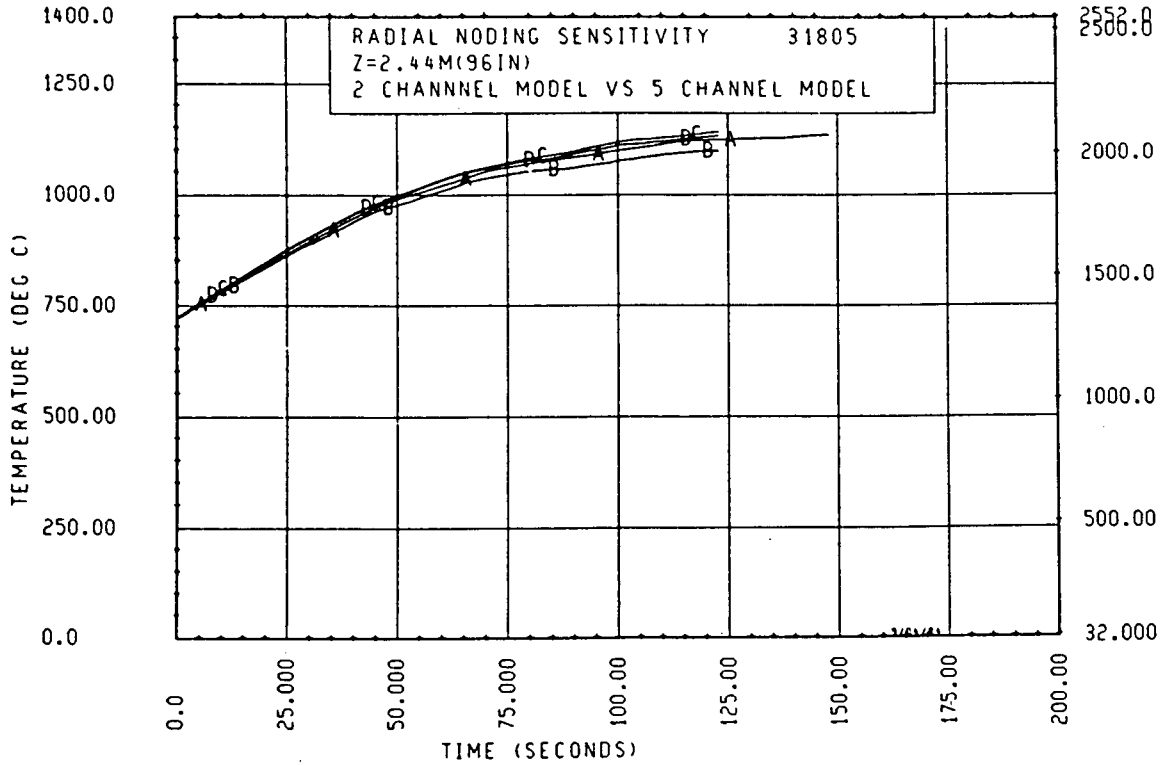

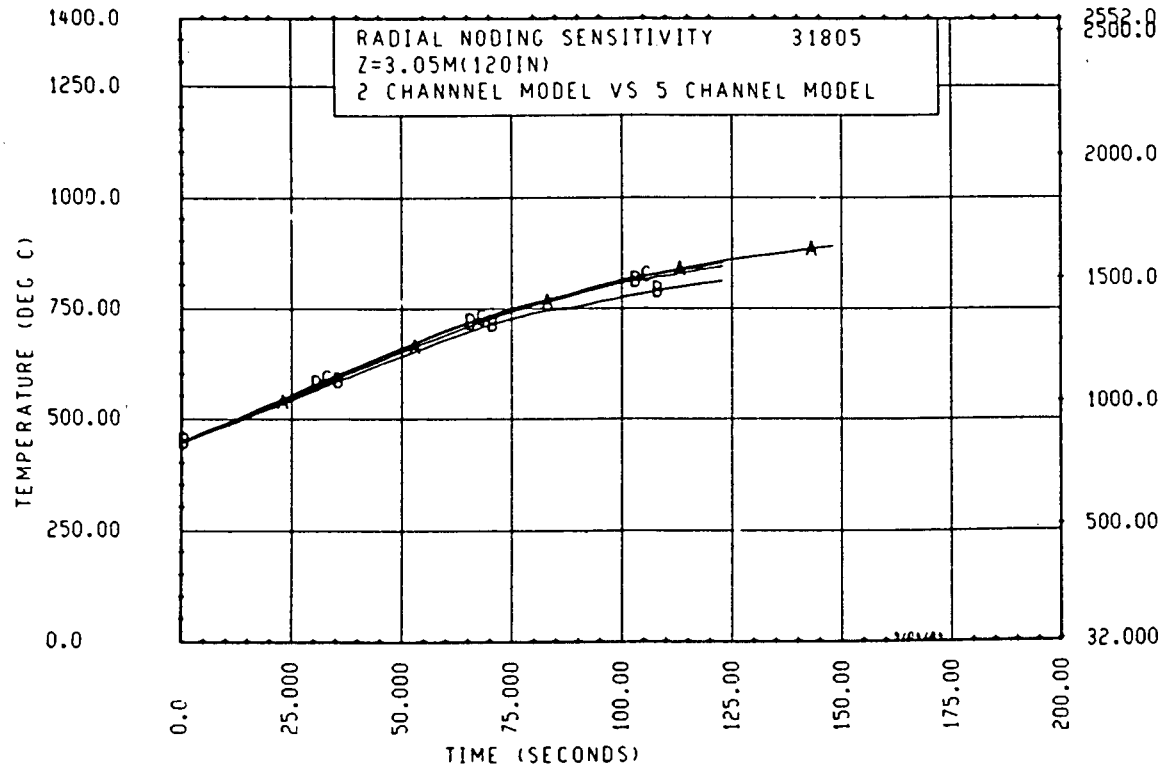

Figure B-4. COBRA-TF Results (Temperature Versus Time) With Two and Five Radial Nodes (sheet 3 of 3)

APPENDIX C
CALCULATON OF DROPLET BREAKUP AREA FOR CONCENTRIC COPLANAR BLOCKAGE

The droplet breakup area for a concentric coplanar blockage is defined as the shaded area in figure C-1, using the following assumptions:

- o A droplet has only vertical component velocity before impacting the blockage sleeve.

- o When the gap distance is greater than a certain distance (x in figure C-1), a droplet can pass through without breakup.

Droplets impacting on a flat plate heated above the Leidenfrost point undergo a process of deformation, flattening, and reformulation.[1] As the drop velocity normal to the plate increases, the droplet spreads into a liquid sheet so that the surface tension faces cannot reform the drop and shattering occurs. For droplet shattering to occur, the impact Weber number, We_D, must be greater than 30.

The concentric sleeve geometries employed in the FLECHT SEASET AND FEBA tests have an incident angle of approximately 3 degrees in the converging section of the blockage. Clearly, unrealistically high drop axial velocities would be required to exceed the impact Weber number shattering criteria [$\sin(3°) = 0.052$]. However, an examination of the converging sections reveals an area in the gap region where incident drops would be "captured" and constrained to lose most of their axial momentum. In effect, this small region (the shaded area of figure C-1) would appear to be a flat plate normal to the droplet flow.

---

1. Wachters, L. H. J., and Westerling, N. A. J., "The Heat Transfer From a Hot Wall to Impinging Water Drops in a Spheroidal State," Chem. Engr. Sci.21, 1966, 1047-1056.

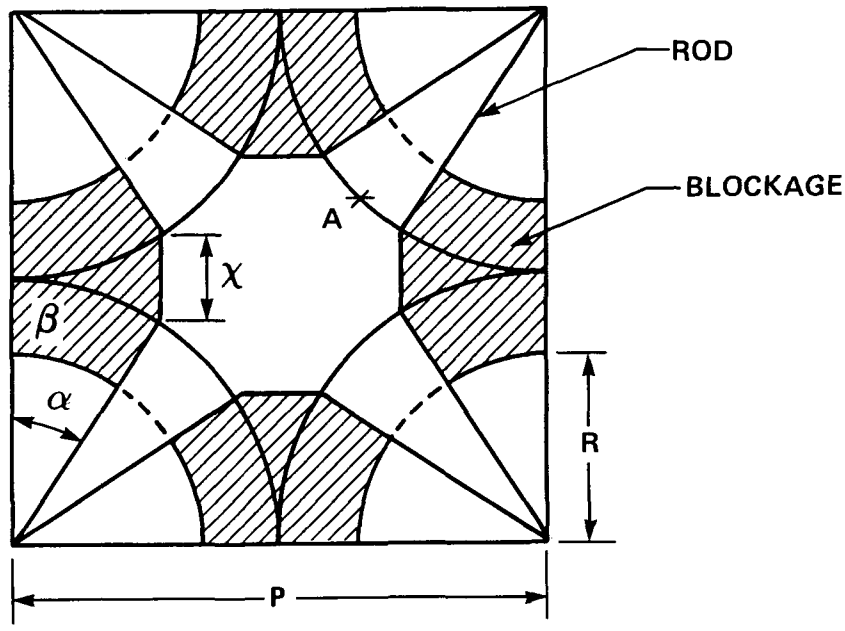

P = PITCH

R = RADIUS OF HEATER ROD

η = BLOCKAGE RATIO, PROJECTED BLOCKAGE AREA/ NORMAL SUBCHANNEL FLOW AREA

ψ = BREAKUP AREA RATIO, BREAKUP AREA/ NORMAL FLOW AREA

α , β IN DEGREES

Figure C-1. Blocked Subchannel

A breakup area ratio, Ψ, can be calculated using the above assumptions for a general concentric coplanar blockage.

The projected blockage area in figure C-1 is described by

$$4\left[\frac{P}{2}\cdot\frac{P}{2}\tan\alpha+\pi\left(\frac{\frac{P}{2}}{\cos\alpha}\right)^2\left(\frac{90-2\alpha}{360}\right)-\frac{\pi}{4}R^2\right]$$

Then,

$$\eta=\frac{P^2\tan\alpha+\pi\left(\frac{P}{\cos\alpha}\right)2\left(\frac{90-2\alpha}{360}\right)-\pi R^2}{P^2-\pi R^2}$$

$$\eta=\frac{\tan\alpha+\left(\frac{\pi}{\cos^2\alpha}\right)\left(\frac{90-2\alpha}{360}\right)-\pi\left(\frac{R}{P}\right)^2}{1-\pi\left(\frac{R}{P}\right)^2}$$

$$\text{Breakup area}=4\left(\frac{(X+P)}{2}\right)\cdot\left(\frac{P}{2}\right)\cdot\left(\frac{1}{\cos\alpha}\right)\cdot\sin\beta-\pi R^2\cdot\frac{2\beta}{360}$$

Then,

$$\Psi=\frac{(X+P)\,P\left(\frac{1}{\cos\alpha}\right)\cos\beta-4\pi R^2\left(\frac{2\beta}{360}\right)}{P^2-\pi R^2}$$

where $x=P\left(1-\frac{\cos\beta}{\cos\alpha}\right)$

For a given geometry and blockage shape, x or β is the only unknown parameter. The gap distance, x, should be smaller than a droplet diameter; otherwise, the droplet may pass through the shaded area without breakup. To determine an appropriate value for x, a droplet breakup area ratio was calculated for a FLECHT SEASET 21-rod bundle with 62-percent coplanar blockage at 0.28 MPa (40 psia) with various values of x. It was assumed that x is dependent on a large droplet diameter.

At 0.28 MPa (40 psia), D (droplet diameter) $\approx$ 1.27 mm (0.0500 in.) and,

- If x = 1/2 D = 6.35 mm (0.025 in.), Ψ (breakup area ratio) = 0.2672
- If x = 1/3 D = 4.24 mm (0.0167), Ψ = 0.2128
- If x = 1/4 D = 3.17 mm (0.0125), Ψ = 0.1797
- If x = 1/5 D = 2.54 mm (0.010), Ψ = 0.1617

A study of 21-rod configuration C data indicates that the blockage heat transfer effect is less than that of a grid which has a breakup area ratio of about 25 percent. Another important factor is that, should a droplet pass through a point at which the gap distance is x, the maximum diameter of the shattered small droplets will be at most x. Thus, the x = 1/5 D criterion was chosen as a starting point.

Based on the 1/5 D criterion, a curve of the droplet breakup area ratio versus blockage area ratio was constructed (figure C-2). When the minimum gap distance between two blockages is greater than 1/5 D, there is no droplet breakup. The droplet breakup diameter relationship was also fixed and an empirical efficiency factor adjusted to produce a total effect that is approximately correct.

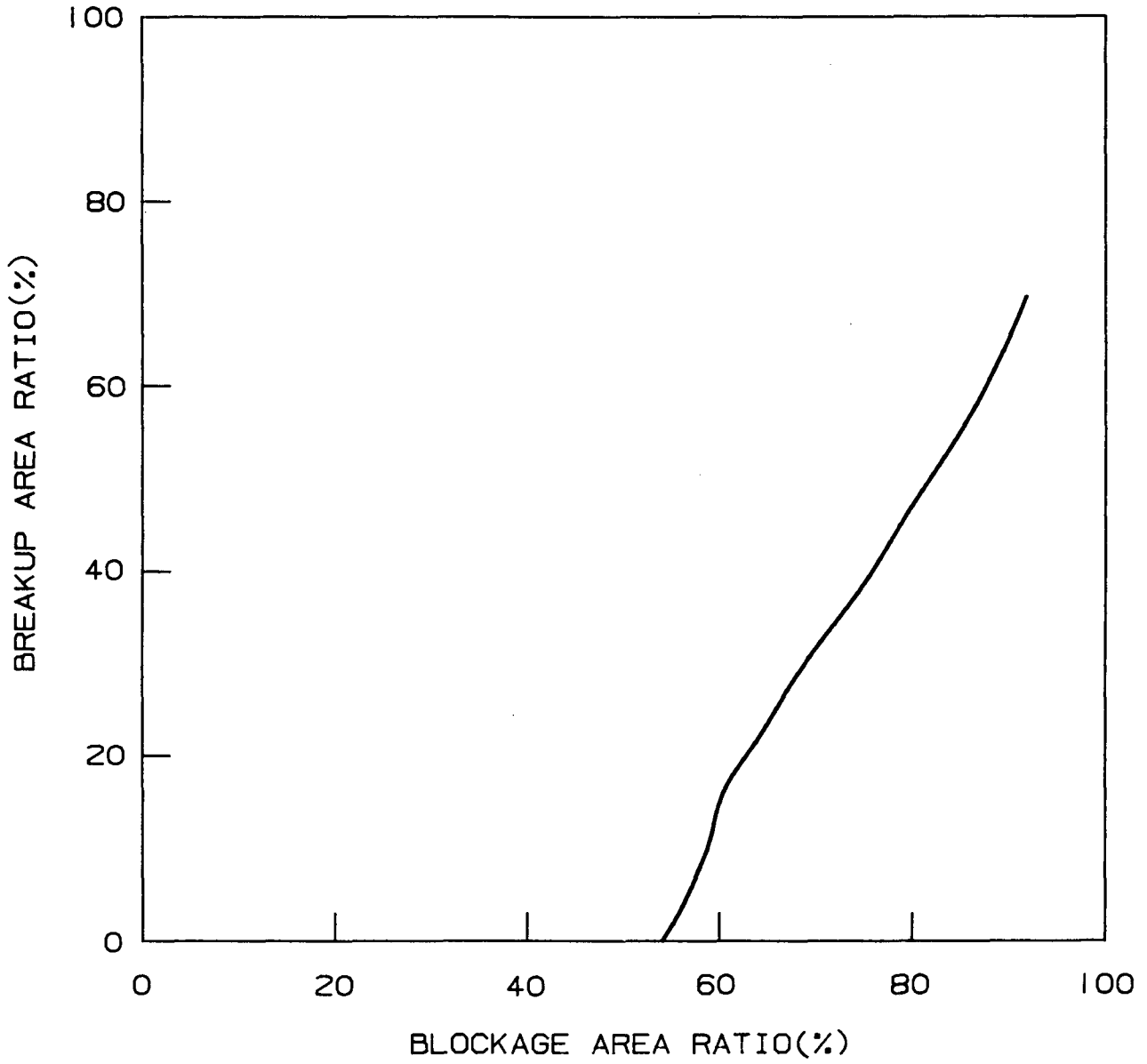

Figure C-2. Breakup Area Ratio as a Function of Blockage Area Ratio

APPENDIX D
MODELING A NONCOPLANAR BLOCKAGE AS A COPLANAR BLOCKAGE

A simple method, detailed below, was used to transform a noncoplanar blockage into an equivalent blockage for the COBRA-TF blockage model.

D-1. CALCULATION OF CONTINUITY AREA

The selection of the flow channels in COBRA-TF for the 21-rod nonconcentric, noncoplanar blocked bundle was based on the following criteria. First, the internal "hot" rods should be separated from the outside "cold" rods and housing. Second, the most severely blocked channel should be modeled.

The continuity area for each COBRA-TF flow channel was calculated by averaging the flow area of the subchannels within that region. For example, channel 1 consists of the four center subchannels and channel 2 the eight adjacent subchannels. The blocked area fraction was integrated axially for each flow channel and averaged for each axial node. Also, the gap width between COBRA-TF flow channels was calculated from each subchannel's gap width at the flow channel boundary. Thus, for each flow channel, the blockage was treated in a coplanar manner.

D-2. CALCULATION OF SEPARATION POINT

The separation point was determined using the criterion published by ESDU.[1] This criterion, which is a function of two nondimensional quantities, outlet area/inlet area and diffuser length/inlet radius, is applicable to constant-angle diffusing sections and fully turbulent flow. This criterion was simplified to the following equation:

---

1. "Performance of Conical Diffusers in Incompressive Flow," ESDU Item No. 73204, Engineering Sciences Data Unit, London, pp. 251-259.

$$\log y = 0.114 \text{ to } 0.203 \log x + 0.04614 (\log x)^2 - 0.01995 (\log x)^2 \quad \text{(D-1)}$$

where $x = Lx/R_1$ = nondimensional distance from diffuser inlet.

The following iterative procedure is employed to determine if and where the flow separates:

- Choose downstream location Lx.
- Determine local flow area, Ax, at Lx.
- Calculate y [equation (D-1)].
- If $(Ax/A_1) \geq y$, where (Ax/A_1) = local flow area/diffuser inlet area for separation to occur, separation occurs.
- Iterate until $(Ax/A_1) = y$. The current value of Lx is the separation point.

The method of blockage modeling is shown in figure D-1. The example calculations were done for COBRA-TF flow channel 1 for the 21-rod bundle configuration F. The most blocked point for channel 1 is 1.89 m (74.4 in.). This point becomes the diffuser inlet point. Then,

$$\pi R_i^2 = (1 - 0.62)[4 \cdot (0.496^2 - \pi/4 (0.374)^2)] = A$$

$$R_i = 0.2566 \text{ in.}$$

The iterative calculations were performed and the following table was created.

Lx	Lx/R_i	Ax/A_i	y
0	0	1	
0.828	3.22	1.145	1.68
1.587	6.185	1.64	1.966
2.415	9.41	2.11	2.1725
2.829	11.025	2.245	2.225
3.243	12.6	2.365	2.326

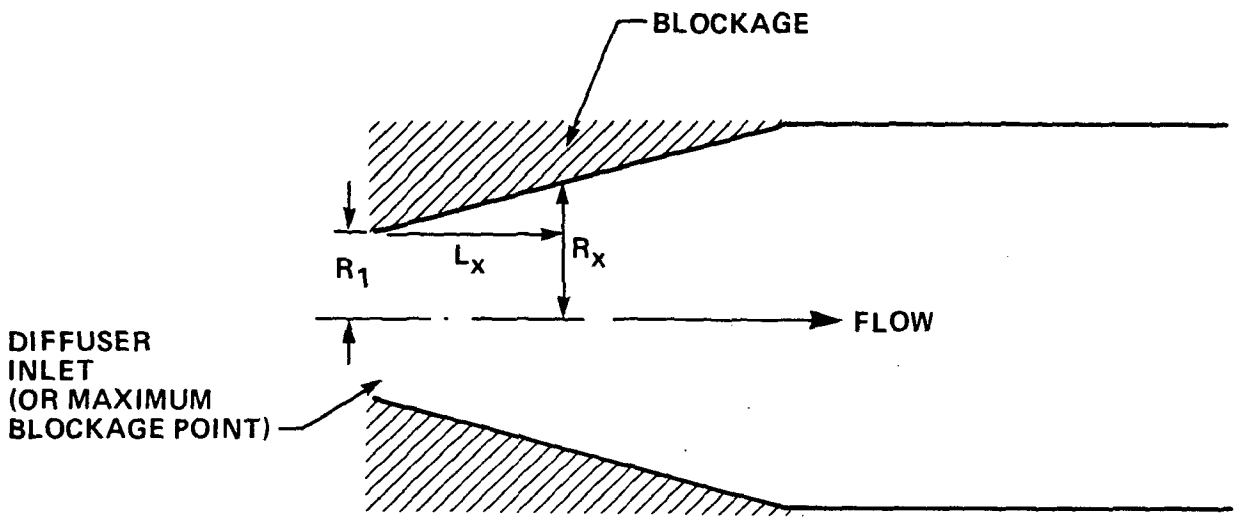

Figure D-1. Single Diffuser Blockage Model

When Lx = 3.243, Ax/A_i > y; separation occurs. Interpolating between the last two values yields

Lx = 3.046 Ax/A_i = y

Therefore, the separation point is

Z = 74.4 + 3.046 = 77.446 in. or 1.97 m

Likewise, the separation points for channels 2 and 3 can be calculated.

D-3. DROPLET BREAKUP AREA FOR NONCONCENTRIC NONCOPLANAR BLOCKAGE

The droplet breakup area for concentric coplanar blockage was discussed and calculated as a function of the blockage ratio in appendix C. The droplet breakup area for nonconcentric noncoplanar blockage was defined as a function of blockage only, and independent of blockage shape. Then, the curve in figure D-2 was used to calculate the droplet breakup area.

To calculate the droplet breakup area fraction for the COBRA-TF flow channel, the maximum blockage area ratio for each actual subchannel was identified, and the corresponding breakup area obtained from figure D-2. These droplet breakup area ratios for each subchannel were averaged for the COBRA-TF flow channels:

Channel 1 -- 0.3125
Channel 2 -- 0
Channel 3 -- 0.13255

Models not discussed here were incorporated in the same way as a coplanar blockage.

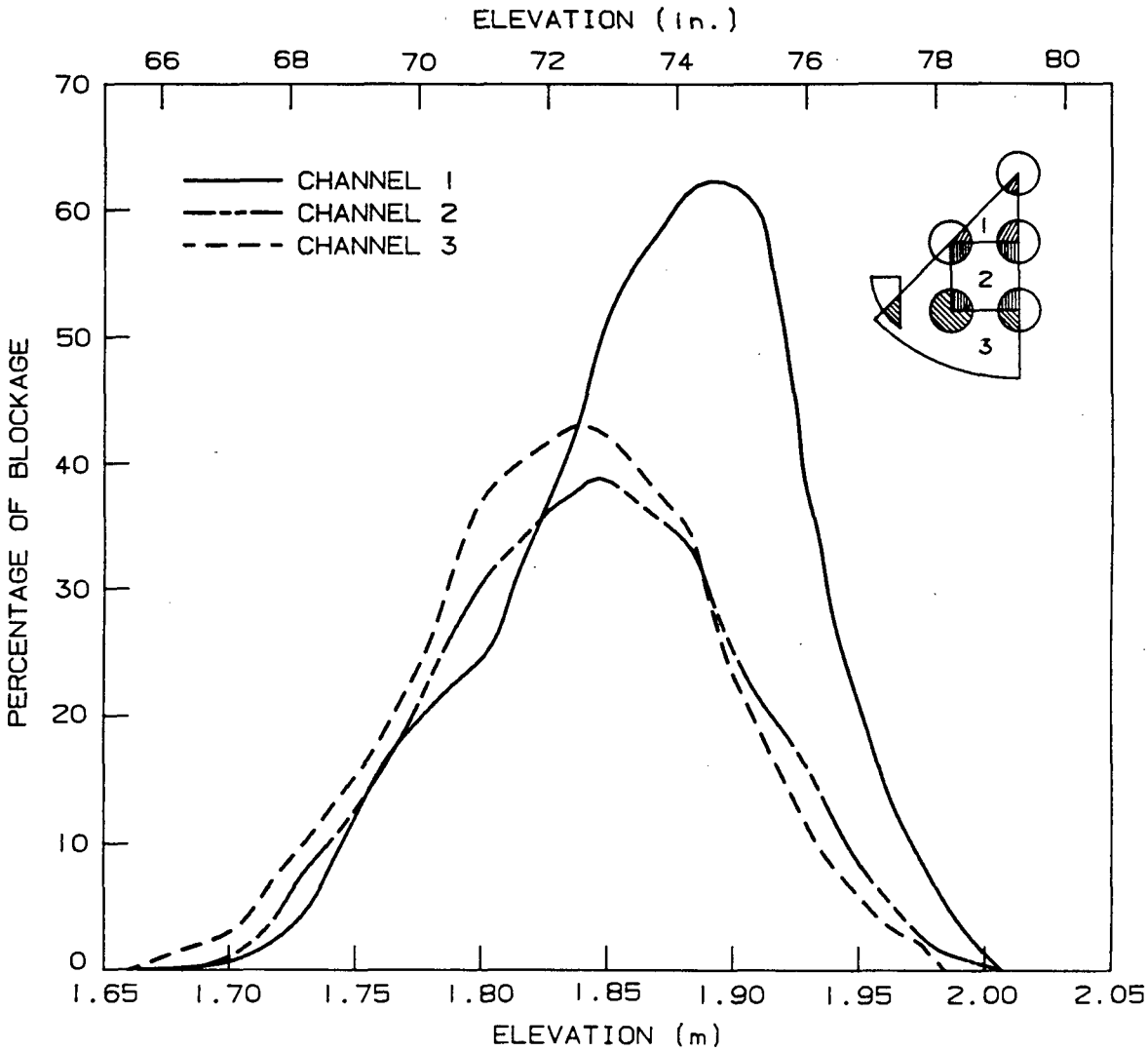

Figure D-2. Blockage Area Ratio for COBRA-TF Flow Channel, Configuration F

APPENDIX E
VAPOR TEMPERATURE MEASUREMENT LOCATIONS IN THE FLECHT SEASET 163-ROD BUNDLE

Vapor measurements were made with three types of instruments in the FLECHT SEASET 163-rod bundle:

- Bare thermocouples placed in the subchannels and supported from the spacer grids
- Self-aspirating steam probes which had a radiation shield and were supported from the spacer grids
- Guide tube thimbles (aspirated) with thermocouples inside

The construction details of each of these vapor temperature measurement instruments are described in NRC/EPRI/Westinghouse Report No. 13.[1] The placement of each type of vapor instrumentation is shown in figures E-1 through E-12 for each elevation in the 163-rod blocked bundle. Also shown are the radial nodes used in the COBRA-TF simulation of the 163-rod blocked bundle tests.

1. Loftus, M. J., et al., "PWR FLECHT SEASET 163-Rod Bundle Flow Blockage Task Data Report," NRC/EPRI/Westinghouse-13, September 1983.

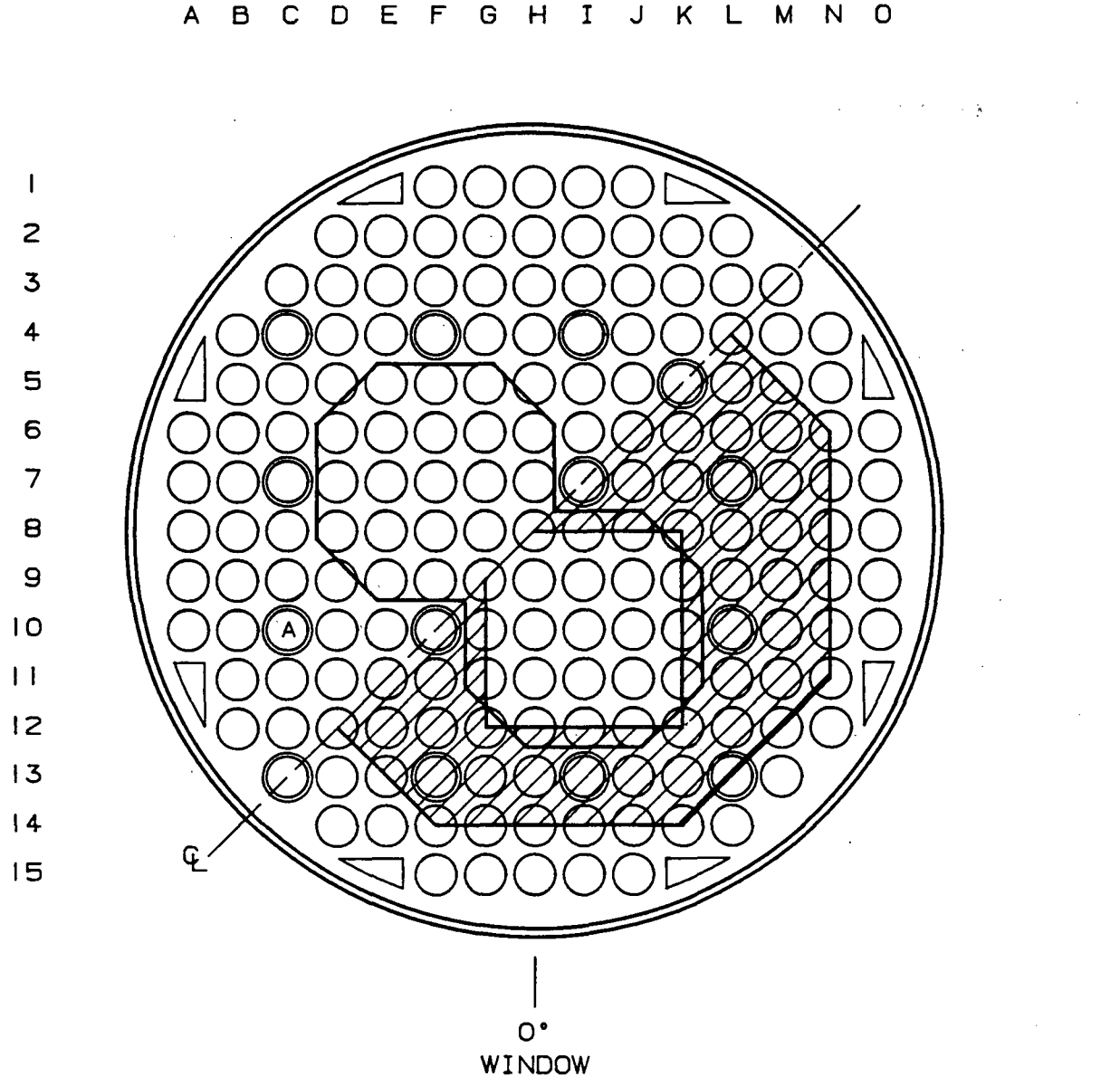

Figure E-1. 163-Rod Blocked Bundle Vapor Temperature Instrumentation, 0.99 m (39 in.) Elevation

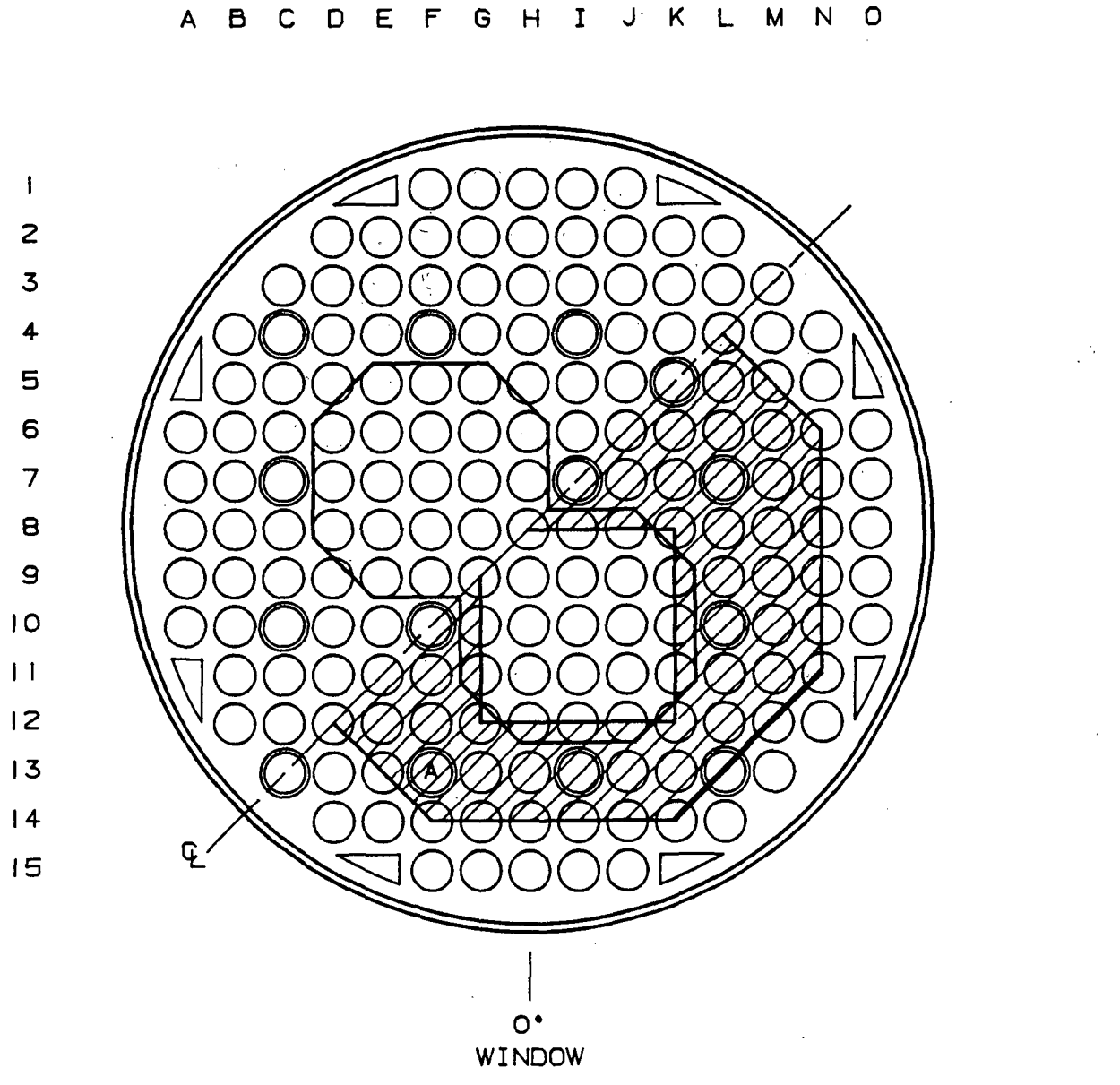

Figure E-2. 163-Rod Blocked Bundle Vapor Temperature Instrumentation, 1.22 m (48 in.) Elevation

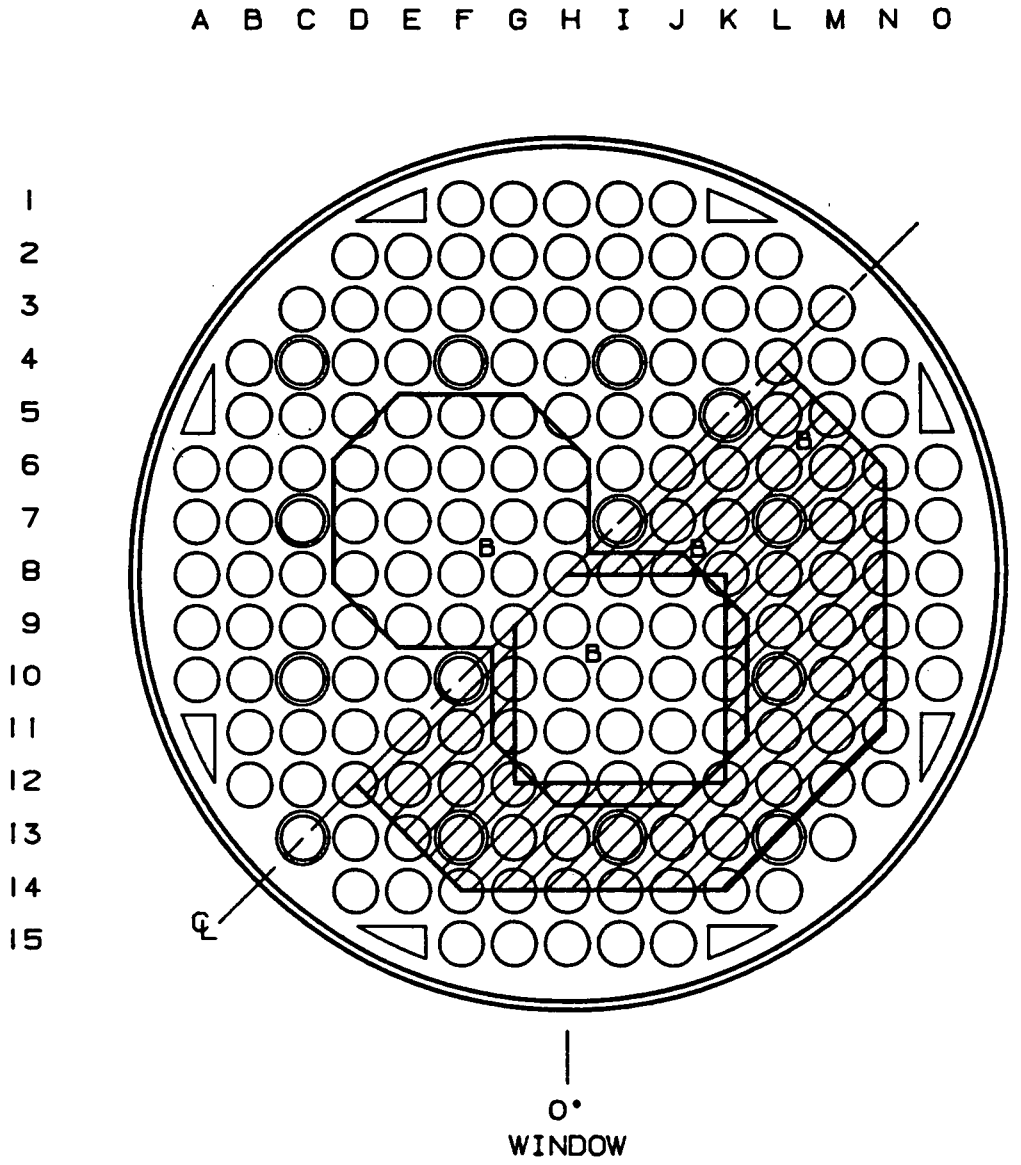

Figure E-3. 163-Rod Blocked Bundle Vapor Temperature Instrumentation, 1.47 m (58 in.) Elevation

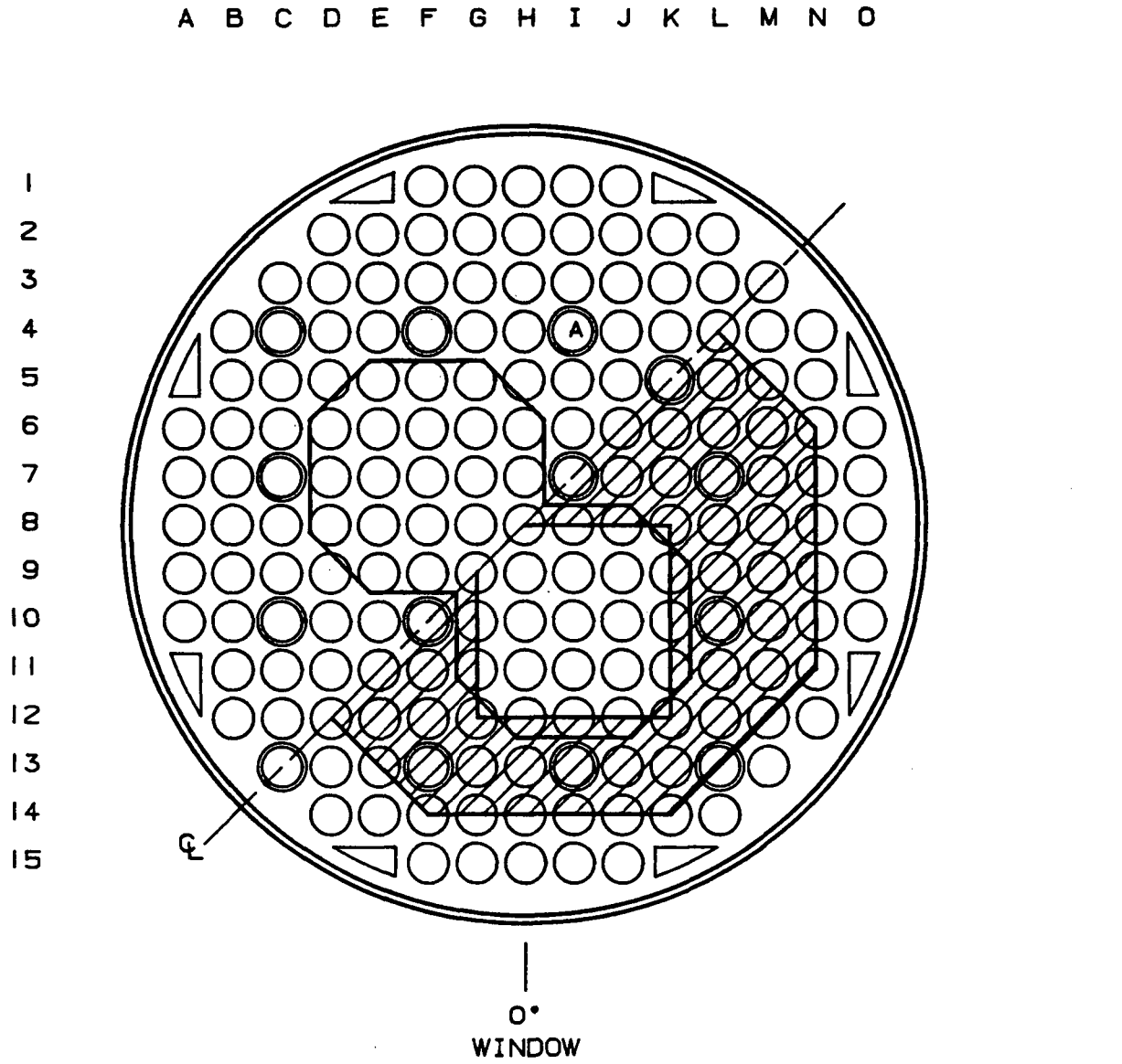

Figure E-4. 163-Rod Blocked Bundle Vapor Temperature Instrumentation, 1.52 m (60 in.) Elevation

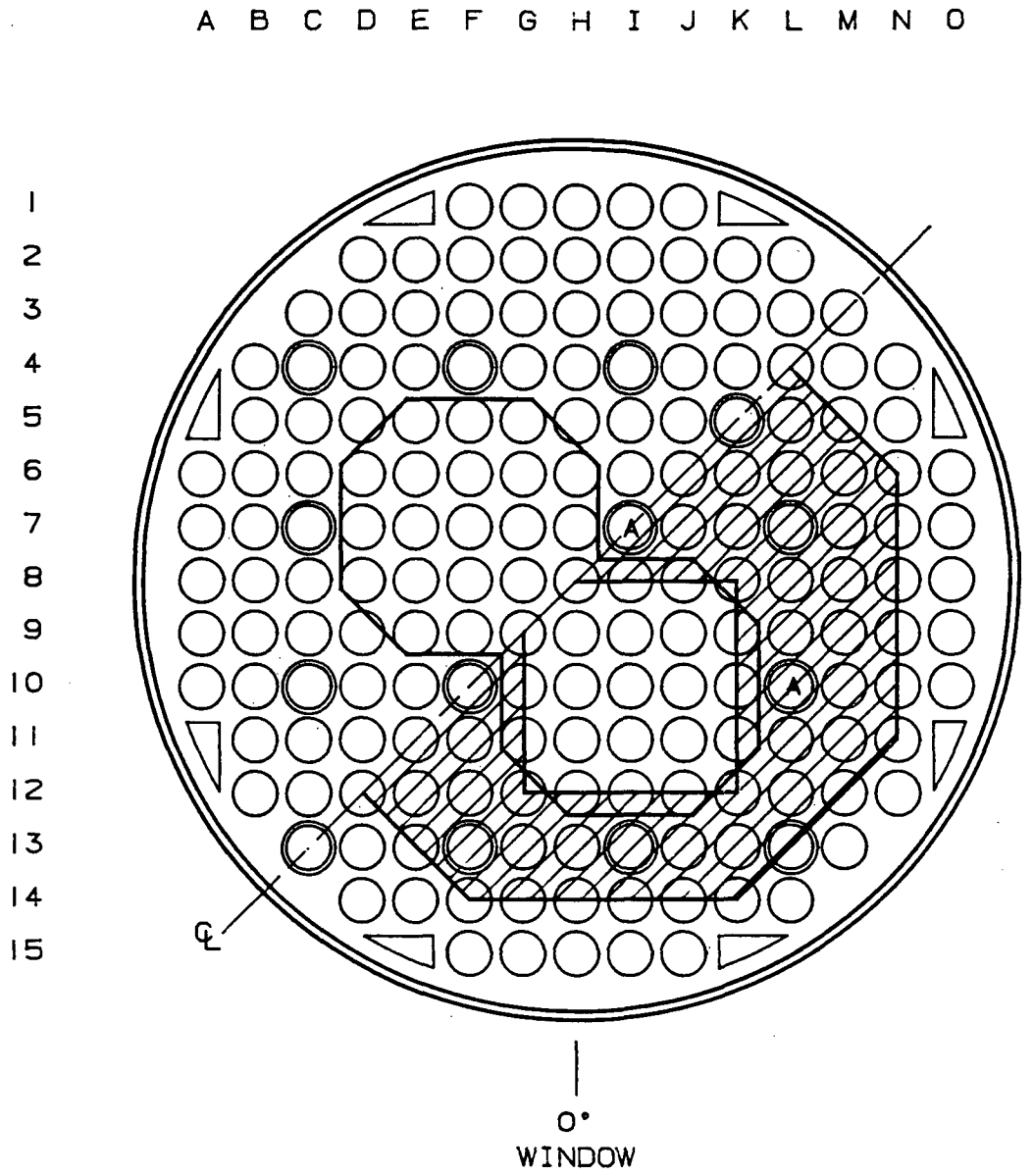

Figure E-5. 163-Rod Blocked Bundle Vapor Temperature Instrumentation, 1.83 m (72 in.) Elevation

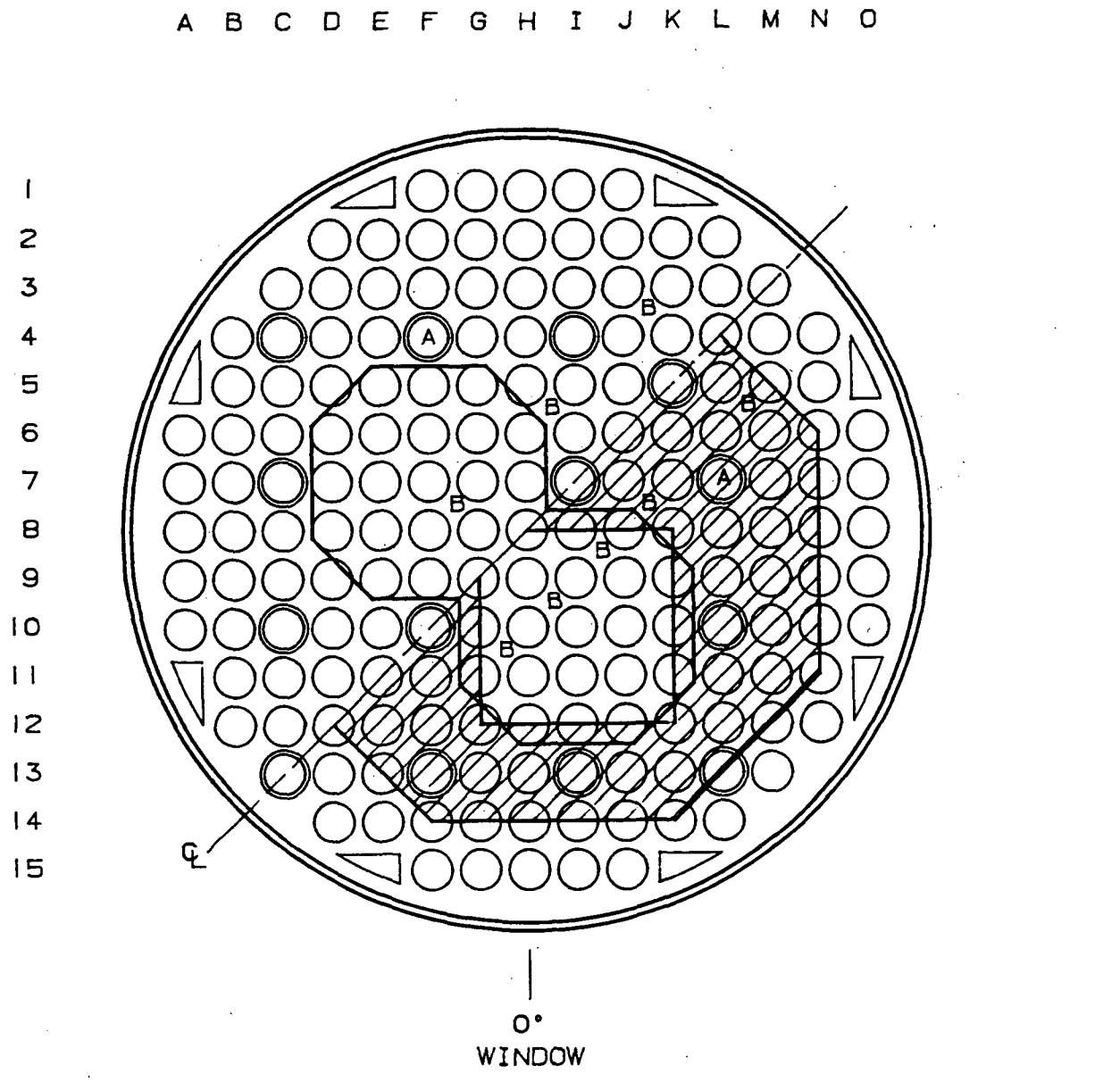

Figure E-6. 163-Rod Blocked Bundle Vapor Temperature Instrumentation, 1.98 m (78 in.) Elevation

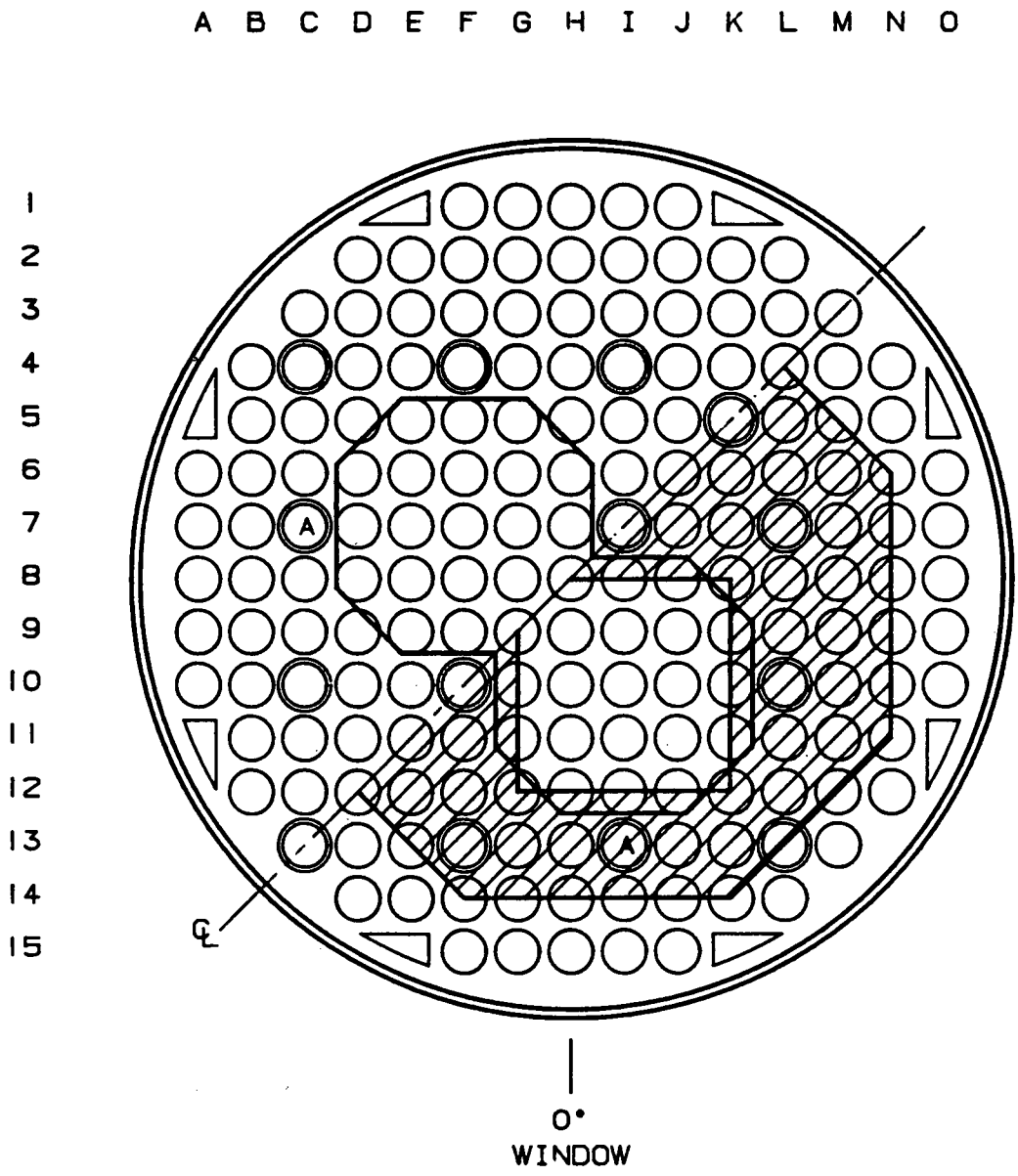

Figure E-7. 163-Rod Blocked Bundle Vapor Temperature Instrumentation, 2.29 m (90 in.) Elevation

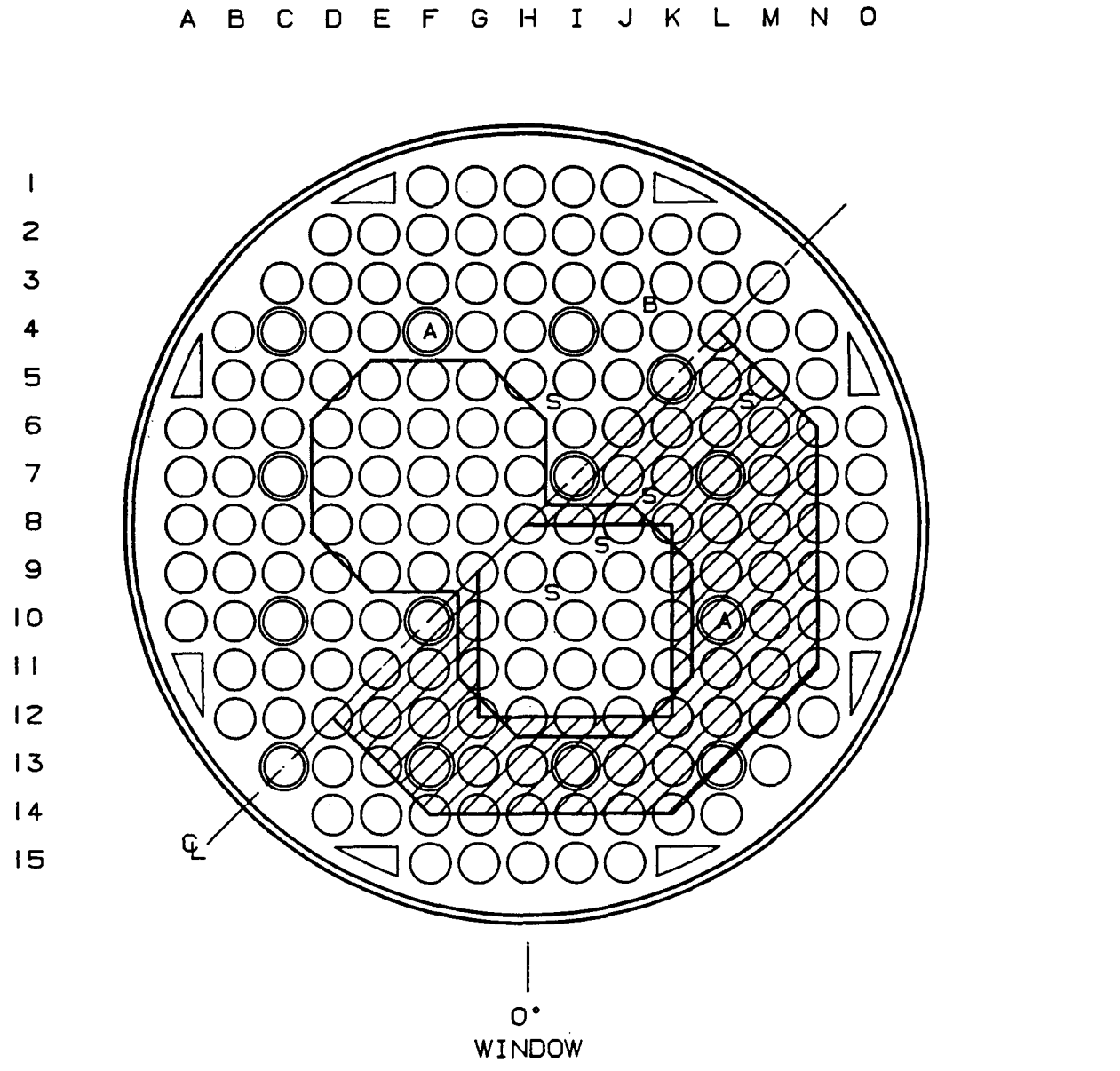

Figure E-8. 163-Rod Blocked Bundle Vapor Temperature Instrumentation, 2.44 m (96 in.) Elevation

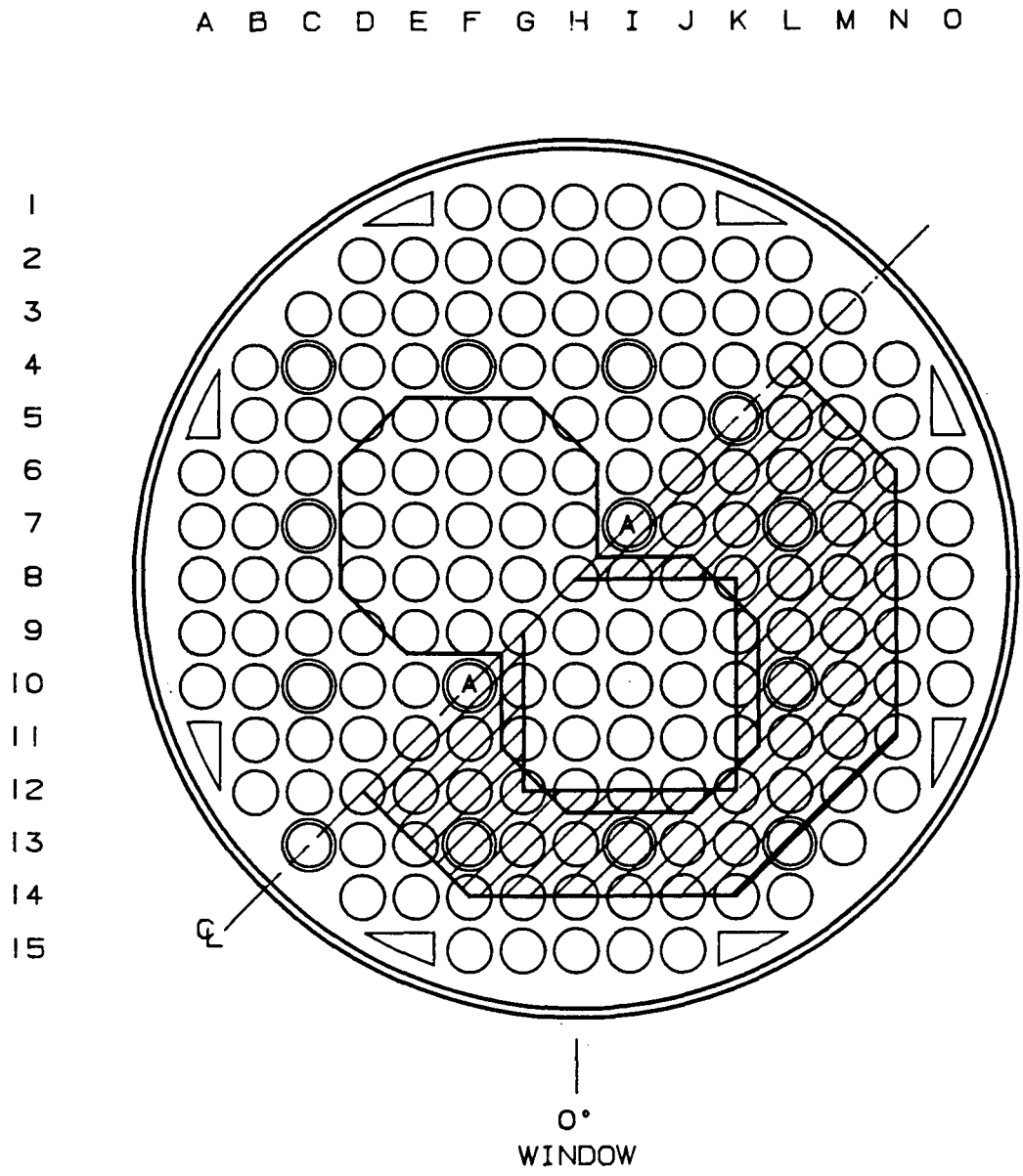

Figure E-9. 163-Rod Blocked Bundle Vapor Temperature Instrumentation, 2.82 m (111 in.) Elevation

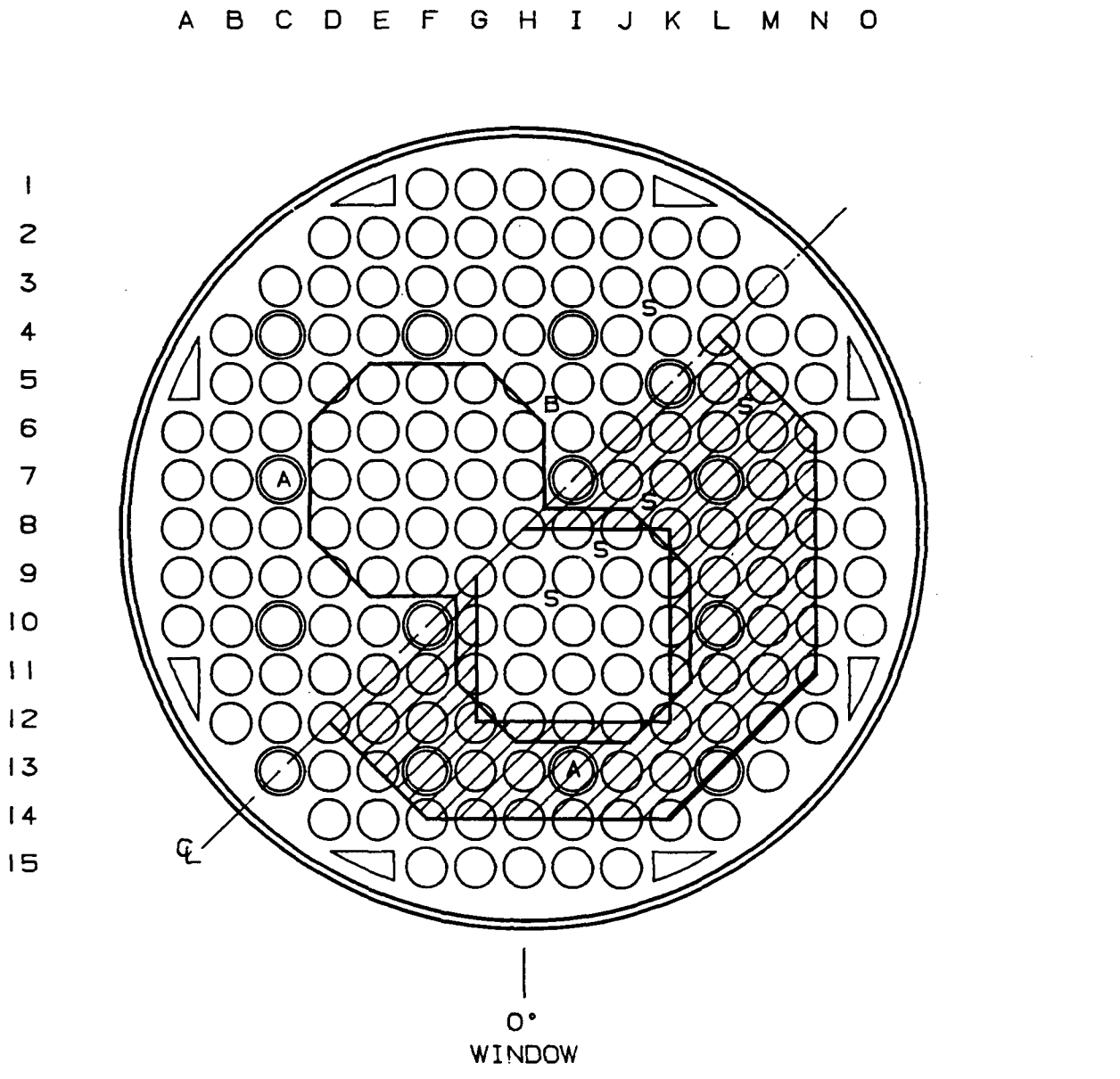

Figure E-10. 163-Rod Blocked Bundle Vapor Temperature Instrumentation, 3.05 m (120 in.) Elevation

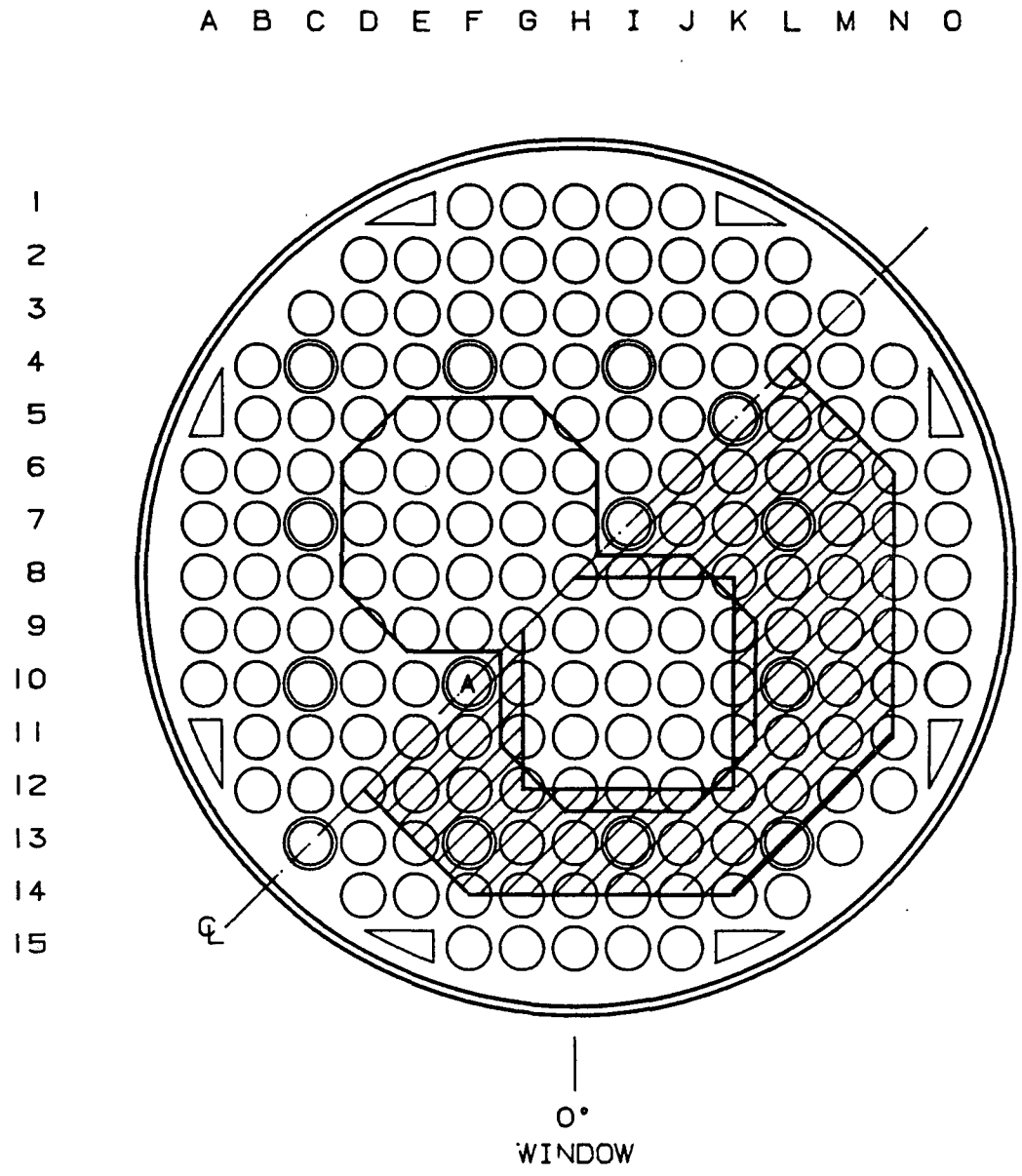

Figure E-11. 163-Rod Blocked Bundle Vapor Temperature Instrumentation, 3.35 m (132 in.) Elevation

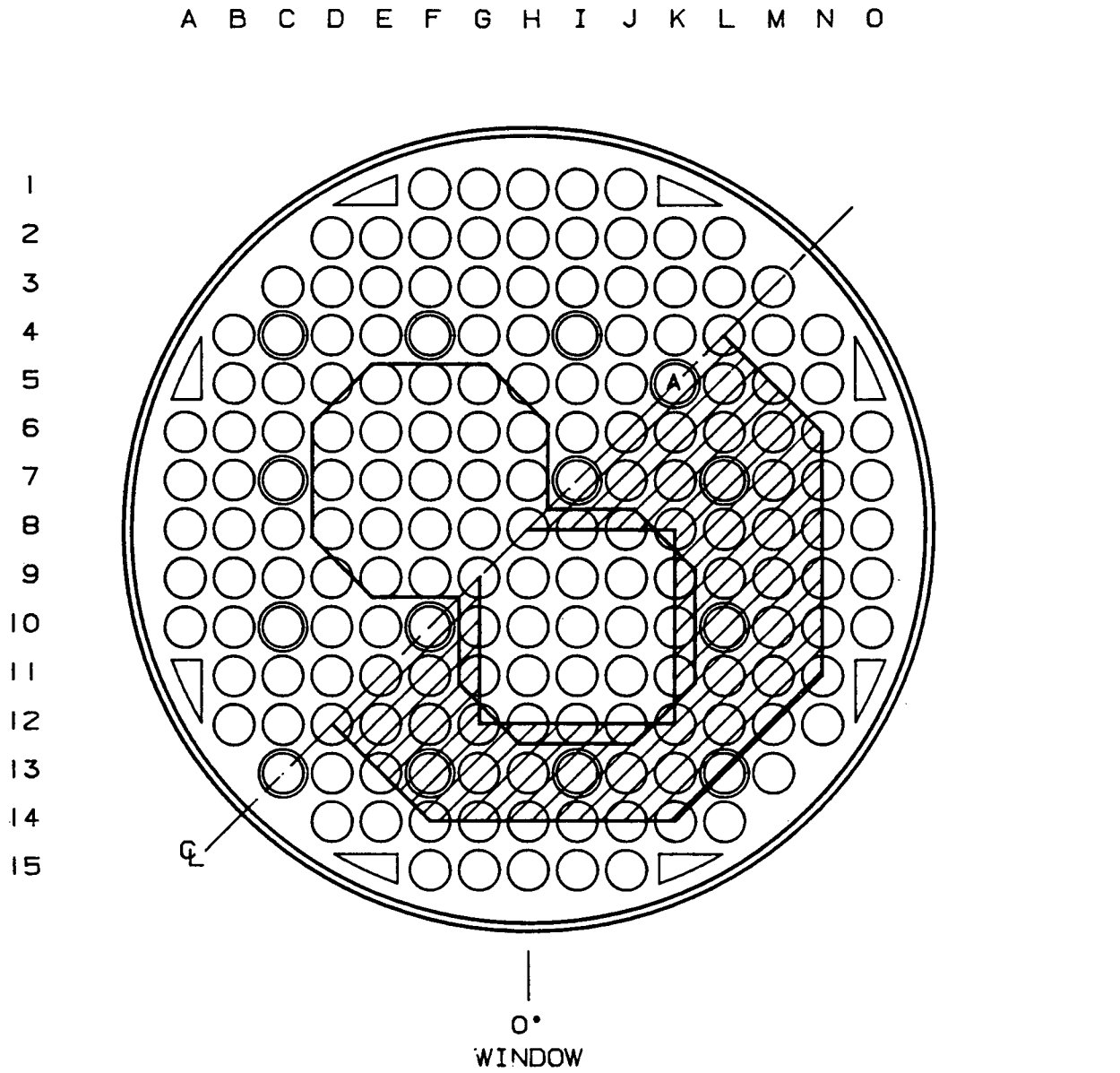

Figure E-12. 163-Rod Blocked Bundle Vapor Temperature Instrumentation, 3.51 m (138 in.) Elevation

APPENDIX F
COBRA-TF INPUT INSTRUCTIONS AND FLECHT SEASET EXAMPLE

COBRA-TF input instructions and a sample calculation for FLECHT SEASET (test 61607) are reproduced on the following pages.

MAIN PROBLEM CONTROL- DATA, read by subroutine INPUT

INPUT.1: ICOBRA FORMAT(I14)

Columns	Variable	Description
1-14	ICOBRA	Enter vessel input units option: 0 = Use English units (default). 1 = Use metric units; code will convert the data to English units.

Restart Data:

INPUT.2: DSTEP, TIMET FORMAT(I14,E14.0)

Columns	Variable	Description
1-14	DSTEP	Enter the time step number of the dump to be used for restarting. Enter zero (0) if this is not a restart.
15-28	TIMET	Enter the restart time for the problem. Enter zero (0.0) if this is not a restart.

Iteration Control:

INPUT.3: EPSO,OITMAX,IITMAX FORMAT(E14.0,2I14)

Columns	Variable	Description
1-14	EPSO	Enter the outer iteration convergence criterion; suggested value = 0.001.
15-28	OITMAX	Enter the maximum number of outer iterations; suggested value = 5.
29-42	IITMAX	Enter the maximum number of vessel iterations; suggested value = 40.

Title Card, read by subroutine COBRAI

COBRA.1 INIT, TEXT FORMAT(2I5,17A4)

Columns	Variable	Description
6-10	INIT	Enter the vessel initialization option. Valid entries are: 1 = initial start 4 = fill vessel arrays with data obtained from a restart file
11-80	TEXT	Enter alphanumeric information to identify the simulation.

VESSEL Group 1: Calculation Variables and Initial Conditions, read by subroutine SETIN

VESSEL1.1. NGROUP,NDX FORMAT(2I5)

Columns	Variable	Description
1-5	NGROUP	Enter one (1).
6-10	NGAS	Number of noncondensible gases (minimum of one)

VESSEL1.2 PREF,HIN,GIN,AFLUX,GHIN,VFRAC(1),VFRAC(2) FORMAT(8F10.0)

Columns	Variable	Description
1-10	PREF	Enter the initial vessel operating pressure, in psi (if ICOBRA = 0) or N/m^2 (if ICOBRA = 1).
11-20	HIN	Enter the enthalpy for fluid initialization, in Btu/lbm (if ICOBRA = 0) or J/kg (if ICOBRA = 1).
21-30	GIN	Not used.
31-40	AFLUX	Enter the average linear heat rate per active rod i kw/ft (if ICOBRA = 0) or kw/m (if ICOBRA = 1).

41-50	GHIN	Enthalpy of noncondensible gas mixture
51-60	VFRAC(1)	Volume fraction of liquid
61-70	VFRAC(2)	Volume fraction of vapor in gas mixture
71-80	RBSF	Rod bundle scaling factor. Enter 1.0 for ideal subchannel; see paragraph A-12.

VESSEL1.3 (GTYPE(I),VFRAC(I+2),I=1,NGAS) FORMAT(4(8A,2X,F10.))

Columns	Variable	Description
1-8, 21-28...	GTYPE(I)	Name of gas (left justified) Examples: air, argon, helium, hydro, kryto, nitro, oxyge, xneno.
10-20, 30-40...	VFRAC(I+2)	Volume fraction of gas (I) in mixture.

VESSEL Group 2: Channel Description, read by subroutine SETIN

VESSEL2.1 NGROUP,NCHANL FORMAT(2I5)

Columns	Variable	Description
1-5	NGROUP	Enter two (2).
6-10	NCHANL	Enter the number of channels in the problem.

Cards VESSEL2.2 and VESSEL2.3 are read in pairs, NCHANL times.

VESSEL2.2 I,AN(I),PW(I),ABOT(I),ATOP(I),NAMGAP FORMAT(I5,4F5.0,I5)

Columns	Variable	Description
1-5	I	Enter the channel identification number. (Note: Channel index numbers must be unique, but they do not have to be sequential. Skipping numbers is permitted, so long as exactly NCHANL channels are identified.)
6-10	AN(I)	Enter the nominal channel area, in $in.^2$ (if ICOBRA = 0) or m^2 (if ICOBRA = 1). (Do not enter zero.)

11-15	PW(I)	Enter the channel wetted perimeter, in inches (if ICOBRA = 0) or meters (if ICOBRA = 1). (Do not enter zero.)
16-20	ABOT(I)	Enter the area of the bottom of the channel for use in the momentum equation. Units are $in.^2$ (if ICOBRA = 0) or m^2 (if ICOBRA = 1). If ABOT(I) is entered as zero (0.0), it is set to AN(I).
21-25	ATOP(I)	Enter the area on the top of the channel for use in the momentum equation. Units are $in.^2$ (if ICOBRA = 0) or m^2 (if ICOBRA = 1). If ATOP(I) is entered as zero (0), it is set to AN(I).
26-30	NAMGAP	Enter the number of gaps for which the vertical velocity of channel I convects transverse momentum between sections.

VESSEL2.3 (INODE(I,N),KGAPB(I,N),KGAPA(I,N),N=1,NAMGAP) FORMAT(15I5)
Read only if NAMGAP > 0 for channel I.

NOTE: Omit this card if NAMGAP is zero (0) for channel I.

Columns	Variable	Description
1-5, 16-20, 31-23, 46-50, 61-65	INODE(I,N)	Enter the index number of the node where the vertical velocity of channel I convects transverse momentum across a section boundary. (Note: INODE will be either at the bottom of the channel (INODE(I,N)=1), or the top of the channel, (INODE(I,N)=NONODE+1), where NONODE is the number of axial levels in the section containing channel I. INODE is defined in the section where the vertical momentum equation is solved.

6-10, 21-25, 36-40, 51-55, 66-70	KGAPB(I,N)	Enter the index number of the gap below the section boundary. Enter zero if there is no gap below the section boundary. (Note: If KGAPB is not zero, the positive velocity of channel I at INODE(I,N) convects transverse momentum out of KGAPB into KGAPA. The negative velocity of channel I at INODE(I,N) convects transverse momentum from KGAPA into KGAPB; but if KGAPB is zero, this momentum is dissipated.)
11-15, 26-30, 41-45, 56-60, 71-75	KGAPA(I,N)	Enter the index number of the gap above the section boundary. Enter zero if there is no gap above the section boundary. Note: If KGAPA is not zero, the positive velocity of channel I at INODE(I,N) convects transverse momentum from KGAPB (if KGAPB ≠ 0) into KGAPA. (If KGAPA is zero, this momentum is dissipated.) The negative velocity of channel I at INODE(I,N) convects transverse momentum from KGAPA to KGAPB, (if KGAPB ≠ 0; if KGAPB is zero, this momentum is dissipated.)

VESSEL Group 3: Transverse Channel Connection (Gap) Data, read by subroutine SETIN

This group is omitted if there are no transverse connections between channels.

VESSEL 3.1 NGROUP,NK FORMAT(2I5)

Columns	Variable	Description
1-5	NGROUP	Enter three (3).
6-10	NK	Enter the number of transverse connections (gaps).

Cards VESSEL3.2 and VESSEL3.3 are read in pairs NK times.

VESSEL3.2 K,IK(K),JK(K),GAPN(K),LENGTH(K),WKR(K),FWALL(K),IGAPB(K),
IGAPA(K),FACTOR(K),(IGAP(K,N),JGAP(K,N),N=1,3)
FORMAT(3I5,4F5.0,2I5,F5.0,6I5)

Columns	Variable	Description
1-5	K	Enter the gap identification number. (Note: Gap numbers must be unique but they do not have to be sequential. NK gaps must be input.)
6-10	IK(K)	Enter the identification number of the lower-numbered channel of the pair that connects through gap K.
11-15	JK(K)	Enter the identification number of the higher-numbered channel of the pair that connects through gap K.
16-20	GAPN(K)	Enter the nominal gap width, in inches (if ICOBRA = 0) or meters (if ICOBRA = 1).
21-25	LENGTH(K)	Enter the distance between the center of channel IK(K) and the center of channel JK(K), in inches (if ICOBRA = 0) or meters (if ICOBRA = 1).
26-30	WKR(K)	Enter the loss coefficient (velocity head) for gap K.
31-35	FWALL(K)	Enter the wall friction factor for the gap. Valid entries are: 0.0 = no walls 0.5 = one wall 1.0 = two walls
36-40	IGAPB(K)	Enter the index number of the gap below gap K. Enter zero if there is no gap below gap K. (The velocity of IGAPB(K) convects vertical momentum at node 1 into (or out of) channel IK(K) out of (or into) JK(K).)

41-45	IGAPA(K)	Enter the index number of the gap above gap K. (The velocity of IGAPA(K) convects vertical momentum at the top node of the section into (or out of) channel IK(K) out of (or into) JK(K).) Enter zero if there is no gap above gap K.
46-50	FACTOR(K)	Enter 1.0 if gap positive flow (from channel IK(K) to channel JK(K)) is in the same direction as positive flow for the global coordinate system. Enter -1.0 if gap positive flow is opposite to positive flow for the global coordinate system. (Default = 1.0).
51-55 61-65 71-75	IGAP(K,N)	Enter the index numbers of gaps facing the IK(K) side of gap K. If the gap faces a wall, enter -1. If the gap faces a vessel connection to a one-dimensional component, enter -2.
56-60 66-70 76-80	JGAP(K,N)	Enter the gap numbers facing the JK(K) side of gap K. If the gap faces a wall, enter -1. If the gap faces a vessel connection to a one-dimensional component, enter -2. Up to three (3) sets of (IGAP,JGAP) may be entered.

Note: The input for FACTOR, IGAP and JGAP is required only if the three-dimensional form of the transverse momentum equation is desired.

VESSEL3.3 GMULT(K),ETANR(K) FORMAT(2F5.0)

Columns	Variable	Description
1-5	GMULT(K)	Enter the number of actual gaps modeled by gap K.

6-10	ETANR(K)	Enter the crossflow deentrainment fraction.

VESSEL3.4 NLMGAP FORMAT(I5)

Columns	Variable	Description
1-5	NLMGAP	Enter the number of gaps that convect orthogonal transverse momentum. (This is required only for the three-dimensional form of the transverse momentum equation.) Enter zero if the three-dimensional form of the transverse momentum equation is not desired.

Card VESSEL3.5 is read NLMGAP times.

VESSEL3.5 (KGAP1(N), KGAP2(N),KGAP3(N),N=1,NLMGAP) Read only if NLMGAP > 0. FORMAT(12I5)

Columns	Variable	Description
1-5, 16-20, 31-35, 46-50	KGAP1(N)	Enter the index number of a gap whose velocity transports transverse momentum from one gap to another.
6-10, 21-25, 36-40, 51-55	KGAP2(N)	Enter the index number of the gap that receives the transverse momentum convected by the positive velocity of gap KGAP1. A nonzero value must be entered.
11-15, 26-30, 41-45, 56-60	KGAP3(N)	Enter the index number of the gap that the positive velocity of KGAP1 transports transverse momentum out of. (The positive velocity of KGAP1 transports momentum from KGAP3 to KGAP2. Note: The negative velocity of KGAP1 will transport transverse momentum in the opposite direction; i.e., from KGAP2 into KGAP3.) A nonzero number must be entered.

Up to four sets of (KGAP1, KGAP2, KGAP3) entries are specified per card. If NLMGAP > 4, repeat this card until all NLMGAP sets have been entered.

VESSEL Group 4: Vertical Channel Connection Data, read by subroutine SETIN

VESSEL4.1 NGROUP,NSECTS,NSIM,IREBAL FORMAT(4I5)

Columns	Variable	Description
1-5	NGROUP	Enter four (4).
6-10	NSECTS	Enter the number of sections in this problem.
11-15	NSIM	Enter the number of simultaneous solution groups.
16-20	IREBAL	Enter the rebalancing option. Valid entries are: 1 = rebalance 0 = no rebalancing

Cards VESSEL4.2 and VESSEL4.3 are read in a group NSECTS times.

VESSEL4.2 ISEC,NCHN,NONODE,DXS(ISEC,1),IVARDX FORMAT(3I5,F10.0,I5)

Columns	Variable	Description
1-5	ISEC	Enter the section number. Begin with section number 1 on the bottom of the vessel and proceed toward the top, incrementing ISEC by 1.
6-10	NCHN	Enter the number of channels in section ISEC.
11-15	NONODE	Enter the number of vertical levels in section ISEC.
16-25	DXS(ISEC,1)	Enter the vertical node length in this section, in inches (if ICOBRA = 0) or meters (if ICOBRA = 1).
26-30	IVARDX	Flag for variable node length in this section. For constant node length, IVARDX=0 (default). If IVARDX>0, read IVARDX pairs in variable ΔX table.

Card VESSEL4.3 is read only if IVARDX > 0.

VESSEL4.3 (JLEV(I), VARDX(I),I=1,IVARDX) FORMAT(5,(I5,F10)

Columns	Variable	Description
1-5, 16-20...	JLEV(I)	Last axial level in section to have a node length of VARDX(I). JLEV(IVARDX) must be greater than or equal to NONODE+1.
6-15, 21-30...	VARDX(I)	Axial node length, in inches (ICOBRA=0) or meters (ICOBRA=1)

Card VESSEL4.4 is read NCHN times for each section.

VESSEL4.4 I,(KCHANA(I,J),J=2,7),(KCHANB(I,J),J=2,7) FORMAT(13I5)

Columns	Variable	Description
1-5	I	Enter the identification number of a channel in section ISEC.
6-10, 11-15, etc.	KCHANA(I,J)	Enter the indices of channels in the section above ISEC that connect to channel I. If channel I does not connect to any channels above, enter I in KCHANA(I,2).
36-40 41-45, etc.	KCHANB(I,J)	Enter the indices of channels in the section below ISEC that connect to channel I. If channel I does not connect to any channels below, enter I in KCHANB(I,2).

VESSEL4.5 IWIDE FORMAT(I5)

Columns	Variable	Description
1-5	IWIDE	Enter the maximum difference between the index numbers of adjacent cells in a simultaneous solution group.

VESSEL4.6 (MSIM(I),I=1,NSIM) FORMAT(12I5)

Columns	Variable	Description
1-5	MSIM(I)	Enter the last cell number in each simultaneous solution group. (Note that this input asks for cell number, not vertical level number.

Twelve values are entered per card. If NSIM is greater than 12, repeat card VESSEL4.6 until NSIM values have been entered.

VESSEL Group 5: Geometry Variation Data, read by subroutine SETIN

The input for this group allows the user to specify vertical variations in the continuity area, momentum area, or wetted perimeter for channels, and in the transverse width for gaps. It can be omitted if such variations are not needed.

VESSEL5.1 NGROUP,NAFACT FORMAT(2I5)

Columns	Variable	Description
1-5	NGROUP	Enter five (5).
6-10	NAFACT	Enter the number of geometry variation tables to be entered.
	NAXLDIM	Maximum number OF ENTRIES IN VERTICAL VARIATION TABLE

Cards VESSEL5.2 and VESSEL5.3 are read in a group NAFACT times.

VESSEL5.2 NAXL(I) FORMAT(I5)

Columns	Variable	Description
1-5	NAXL(I)	Enter the number of points in this variation table.

VESSEL5.3 (JAXL(I,N),AFACT(I,N),N=1,NAXL(I)) FORMAT(8(I5,F5.0)

Columns	Variable	Description
1-5,11-15, 21-25,31-35 41-45,51-55	JAXL(I,N)	Enter the node number at which to apply the area variation factor for table I, point N.
6-10,16-20, 26-30,36-40 46-50,56-60	AFACT(I,N)	Enter the variation factor for table I, point N. Area = AFACT(I,N)*AN(I), or Gap width = AFACT(I,N)*GAPN(K)

Eight pairs of (JAXL,AFACT) are entered per card. Repeat card VESSEL5.3 until NAXL pairs have been entered. The tables are numbered sequentially in the code, in the order they are read in on cards VESSEL5.2 and VESSEL5.3.

VESSEL Group 6: Channels and Gaps Affected by Variation Tables, read by subroutine SETIN

This group is read only if vertical variation tables have been specified in group 5.

VESSEL6.1 NGROUP,N1 FORMAT(2I5)

Columns	Variable	Description
1-5	NGROUP	Enter six (6).
6-10	N1	Enter the total number of channel and gap variation table cards to be read.

Card VESSEL6.2 is read N1 times.

VESSEL6.2 IACT,IAMT,IPWT,(ICRG(M),M=1,12) FORMAT(16I5)

Columns	Variable	Description
1-5	IACT	Enter a positive integer corresponding to a variation table number, for channel continuity area variation.

		Enter a negative integer, whose absolute value corresponds to a variation table number, for gap width variation.
6-10	IAMT	Enter a variation table number for channel momentum area variation. Enter zero (0) if IACT is negative.
11-15	IPWT	Enter a variation table number for wetted perimeter variation. Enter zero (0) if IACT is negative.
16-20	ICRG(M)	Enter the index numbers of the channels (or gaps if IACT is negative) that the tables identified in IACT, IAMT and IPWT are to be applied to. (Up to 13 channels or gaps may be specified per card.)

VESSEL Group 7: Local Loss Coefficient and Grid Spacer Data, read by subroutine SETIN

VESSEL7.1 NGROUP,NCD,NGT,IFGQF,IFSDRP,IFESPV,IFTPE,DUM1,DUM2,NFBS FORMAT(10I5)

Columns	Variable	Description
1-5	NGROUP	Enter seven (7).
6-10	NCD	Enter the number of loss coefficient specifications to be read. (These include vertical momentum losses only. Transverse losses are specified in group 3.)
11-15	NGT	Number of grid types to be read.
16-20	IFGQF	Flag for grid quench front model (1=on, 0=off).
21-25	IFSDRP	Flag for small drop model (1=on, 0=off).
26-30	IFESPV	Flag for grid convective enhancement (1=on, 0=off).
31-35	IFTPE	Flag for two-phase enhancement of dispersed flow heat transfer (1=on, 0=off).
36-45	Not Used	
46-50	NFBS	Number of flow blockages

Card VESSEL7.2 is read NCD times.

VESSEL7.2 CDL,J,(ICDUM(I),I=1,12) FORMAT(F5.0,13I5)

Columns	Variable	Description
1-5	CDL	Enter the loss coefficient (velocity head).
6-10	J	Enter the node number where the loss coefficient is applied. (NOTE: The vertical node number is relative to the beginning of the section containing the channel(s) listed in ICDUM(I).)
11-15	ICDUM(I)	Enter the index number(s) of channel(s) the loss coefficient will be applied to at node J. (Up to twelve channels may use the specified loss coefficient CDL at vertical node J.)

Cards VESSEL7.3 through VESSEL7.5 are read NGT times.

VESSEL7.3

ING,NGAL(NG),NGCL(NG),IGMAT(NG),GLOSS(NG),GABLOC(NG),GLONG(NG),GPERIM(NG)
FORMAT(4I5,4F10.0)

Columns	Variable	Description
1-5	ING	Grid type number (must be sequential starting with 1)
6-10	NGAL(NG)	Number of axial locations for grid type ING (maximum = 16)
11-15	NGCL(NG)	Number of channels containing grid ING at levels NGAL
16-20	IGMAT(NG)	Grid material type index corresponding to material types in card group 10
21-30	GLOSS(NG)	Loss coefficient multiplier (suggest 1.0 for round edge grids; 1.4 for square edge grids)

31-40	GABLOC(NG)	Fraction of channel area blocked by grid
41-50	GLONG(NG)	Grid length, in inches (if ICOBRA=0) or meters (if ICOBRA=1)
51-60	GPERIM(NG)	Grid perimeter, in inches (if ICOBRA=0) or meters (if ICOBRA=1)

VESSEL7.4 (NNGL(NG,NN), NN=1,NGAL) FORMAT(16I5)

Columns	Variable	Description
1-5, 6-10, 15-20,... 76-80	NNGL(NG,NN)	Axial node number of momentum cells containing grid type ING

VESSEL7.5 NCNGL(NG,M),GMULT(NG,M)(NGROD(NG,M,L),NGSURF(NG,M,L)L=1.6) FORMAT(I5,F10.0,12I5)

Columns	Variable	Description
1-5	NCNGL(NG,M)	Channel ID number with grid type ING at axial levels NNGL(NG,NN) (specified above)
6-15	GMULT(NG,M)	Number of grids contained in channel NCNGL(NG,M)
16-20, 26-30, 36-40,... 66-70	NGROD(NG,M,L)	Whole rod number with surface surrounding grid (maximum of six)
21-25, 31-35, 41-45,...	NGSURF(NG,M,L)	Rod surface index of whole rod NGROD(NG,M,L) surrounding grid ING. (Note: average temperature of all surfaces surrounding grid is used to transport heat between grid and heater rods.)
71-75		

Repeat Card 7.5 NGCL(NG) times.

Repeat Cards 7.3, 7.4, and 7.5 NGT times.

VESSEL7.6

I,IFB(I),JSFB(I),NRFB(I),SPOINT(I),DSEP(I),THROAT(I),AFLBLK(I),CDFB(I),ABLOCK(I)

FORMAT(4I5,6F10.0)

I - flow blockage index number

IFB - channel index number

JSFB - axial node index number

NRFB - number of rods that block this channel

SPOINT - axial position of the flow separation point (in.)

DSEP - channel diameter at separation point ($in.^2$), ($D = \sqrt{\frac{4}{\pi}A}$)

THROAT - diffuser diameter at exit

AFLBLK - area for DBM (fraction of channel) x 0.25

CDFB - loss coefficient (Rehme multiplier)

ABLOCK - blockage area ratio

VESSEL7.7

NRODFB(I,N),KRODFB(I,N),ANGIHT(I,N),ARAIHT( )

NRODFB - index number of rod

KRODFB - surface number

ANGIHT - angle for impact heat transfer (°)

ARAIHT - area for impact heat transfer ($in.^2$/per rod)

VESSEL Group 8: Rod and Unheated Conductor Data, read by subroutine SETIN

VESSEL 8.1 NGROUP,NROD,NSROD,NC,NRTAB,NRAD,NLTYP,NSRAD,NXF FORMAT(9I5)

Columns	Variable	Description
1-5	NGROUP	Enter eight (8).
6-10	~~NROD~~ NRROD	Enter number of rods.
11-15	NSROD	Enter number of unheated conductors.
16-20	NC	Conduction model flag; (1) for radial conduction only. (2) for radial and axial conduction. (3) for radial, axial, and aximuthal conduction.
21-25	NRTAB	Enter number of temperature initialization tables to be read.
26-30	NRAD	Enter number of radiation channels.
31-35	NLTYP	Enter number of location types.
36-40	~~NSRAD~~ NSTATE	~~Enter total number of rod or slab surfaces with radiation:~~ SS rod calcs at beginning of heating if >0
41-45	NXF	Enter number of time steps between radiation calculations (Default = 1.0).

NCAN — Yamanouchi canister quench model

RADFLG — Rad calc only! if Radflg = 2 then exclude fluid

ROD GEOMETRY DATA

This card is read to define the geometry of structures that generate heat, including nuclear fuel rods. It is read NROD times.

VESSEL8.2

N,IFTYP(N),IAXP(N),NRENODE(N),DAXMIN(N),RMULT(N),RADIAL(N),HGAP(N),ISECR(N), HTAMB(N),TAMB(N) FORMAT(4I5,4F10.0,I5,2F5.0) Read only if NROD > 0.

Columns	Variable	Description
1-5	N	Enter rod identification number. (Note: Rod index numbers must be entered sequentially, from 1 to NROD. Skipping numbers is not permitted.)

6-10	IFTYP(N)	Enter geometry type identification number. (Refer to group 9 for geometry type input data.)
11-15	IAXP(N)	Enter axial power profile table identification number. (Refer to group 11 for axial power profile input data.)
16-20	NRENODE(N)	Enter renoding flag for heat transfer solution for rod N = 0; no fine mesh renoding > 0; renoding every NRENODE(N) time steps < 0; renoding every |NRENODE(N)| time steps, based on inside surface temperatures
21-30	DAXMIN(N)	Enter minimum axial node size, in inches (if ICOBRA = 0) or meters (if ICOBRA = 1). (This is used only if fine mesh renoding is used.)
31-40	RMULT(N)	Enter rod multiplication factor (number of rods modeled by rod N). (This number can contain fractional parts.)
41-50	RADIAL(N)	Enter radial power factor (normalized to average power).
51-60	HGAP(N)	Enter constant gap conductance, in Btu/hr-ft^2-°F (if ICOBRA = 0) or W/m^2-°C (if ICOBRA = 1). (This parameter is used only for nuclear fuel rods that do not have the dynamic gap conductance model specified by their geometry type.) Enter zero if rod N does not model a nuclear fuel rod.
61-65	ISECR(N)	Number of sections containing rod N
66-70	HTAMB(N)	Heat transfer coefficient for heat loss to ambient from surface not connected to a channel (Btu/hr-ft^2-°F) or (W/m^2-°C)
71-75	TAMB(N)	Sink temperature for ambient heat loss, (°F) or (°K)

VESSEL8.3 (NSCHC(K),PIE(N,K),K=1,8) FORMAT(8(I5,F5.0))

Columns	Variable	Description
1-5, 11-15, 21-25...	NSCHC(K)	Channel number with thermal connections to rod N
6-10, 16-20, 26-30...	PIE(N,K)	Fraction of rod N thermally connected to channel NSCHC(K)

VESSEL8.4 (NISCHC(N,K),K=1,8) Format (8(I5,5X)). Omit if no inside surfaces exist for rod N.

Columns	Variable	Description
1-5, 11-15, 21-26...	NISCHC(N,K)	Negative of channel number connected to the inside of fraction K of rod N

UNHEATED CONDUCTOR DATA

This card is read for each of the NSROD conductor rods (also called heat slabs).

VESSEL8.5 N,ISTYP(N),HPERIM(N),HPERIMI(N),RMULS(N),HTAMBS(N),TAMBS(N)
Read only if NSROD > 0. FORMAT(2I5,5F10.0)

Columns	Variable	Description
1-5	N	Enter unheated conductor identification number. (Note: Unheated conductor index numbers must be entered sequentially, from 1 to NSROD. Skipping numbers is not permitted.)
6-10	ISTYP(N)	Enter geometry type identification number. (Refer to group 9 for geometry type input data.)

11-20	HPERIM(N)	Enter wetted perimeter on outside surface, in inches (if ICOBRA = 0) or meters (if ICOBRA = 1).
21-30	HPERIMI(N)	Enter wetted perimeter on inside surface, in inches (if ICOBRA = 0) or meters (if ICOBRA = 1). (Enter zero for a solid cylinder.)
31-40	RMULS(N)	Enter multiplication factor (number of elements modeled by unheated conductor N). (This number can contain fractional parts.)
40-45	NSLCHC(N)	Channel number on inside of slab.
46-50	NDSLCH(N)	Negative of channel number on outside of slab.
51-60	HTAMBS(N)	Heat transfer coefficient for heat loss to the ambient (Btu/hr-ft^2-°F) or W/m^2-°C)
61-70	TAMBS(N)	Sink temperature for ambient heat loss (°F) or (°K)

ROD TEMPERATURE INITIALIZATION TABLES

Cards VESSEL8.6 through VESSEL8.9 are read to specify which temperature tables apply to which rods and unheated conductors. The sequence is repeated NRTAB times, and all rods and conductors must be accounted for.

VESSEL8.6 I,NRT1,NST1,NRAX1 FORMAT(4I5)

Columns	Variable	Description
1-5	I	Enter identification number of temperature table.
6-10	NRT1	Enter number of rods using table I.
11-15	NST1	Enter number of unheated conductors using Table I.
16-20	NRAX1	Enter number of pairs of elements in table I.

VESSEL8.7 (IRTAB(I,L),L=1,NRT1) FORMAT(12I5) Read only if NRT1 > 0.

Columns	Variable	Description
1-5	IRTAB(I,L)	Enter identification numbers of rods using table I for temperature initialization. Enter the negative of the rod identification number if the temperature boundary is to be applied to the inside surface of the rod.

Note: The steady-state conduction equation is solved for these rods using the temperatures from table I as a boundary condition on the rod surface.

VESSEL8.8 (ISTAB(I,L),L=1,NST1) FORMAT(12I5) Read only if NST1 > 0.

Columns	Variable	Description
1-5	ISTAB(I,L)	Enter identification numbers of unheated conductors using table I for temperature initialization.

Note: A flat radial temperature profile is assumed initially in unheated conductors.

VESSEL8.9 (AXIALT(I,L),TRINIT(I,L),L=1,NRAX1) FORMAT(8F10.0) Power Shape Temp Shape

Columns	Variable	Description
1-10	AXIALT(I,L)	Enter the vertical position relative to the
21-30		bottom of the VESSEL, in inches (if
		ICOBRA = 0) or meters (if ICOBRA = 1).
41-50		
61-70		
11-20	TRINIT(I,L)	Enter the temperature to be applied at
31-40		AXIALT(I,L), in °F (if ICOBRA = 0) or °K (if
51-60		ICOBRA = 1).
71-80		

Note: The vertical locations of the bottom and top of each rod or unheated conductor using table I must be contained within the range AXIALT(I,1) to AXIALT(I,NRAX1).

Radiation Initialization Tables

Cards VESSEL8.10 through VESSEL8.11.5 are read in to specify orientation and which location type tables apply to which fluid channels, rods, and unheated conductors.

Channel Orientation and Location Type Card

VESSEL8.10 (IDCRAD(IRAD),NSIDR(IRAD),LOCATE(IRAD),NRRAD(IRAD), NSYMF(IRAD),MLTF(1,IRAD),MLTF(2,IRAD),MLTF(3,IRAD), MLTF(4,IRAD),VDMLT(IRAD),IRAD=1,NRAD) FORMAT(9I5,F5.0)
Read only if NRAD>0. (MLTF(I,IRAD),I=1,4) are real numbers)

Columns	Variable	Description
1-5	IDCRAD(IRAD)	Radiation channel ID number
6-10	NSIDR(IRAD)	Number of fluid channel which contains IDCRAD(IRAD)
11-15	LOCATE(IRAD)	Location type for radiation channel IDCRAD(IRAD): <0 contains no unheated conductors. >0 has both rods and unheated conductors.
16-20	NRRAD(IRAD)	Number of contributing radiation surfaces for IDCRAD(IRAD): = 20 location types 1,2,3,7,8 = 16 location types 4,5 = 8/0 location type 6 = 14 location type 9
21-25	NSYMF(IRAD)	Enter flag for fluid channel or rod lumping. = 0 no lumping = 1 lumped fluid channels

26-35	MLTF(1,IRAD)	Enter surface lumping factor for surface position 1. Ratio of total calculated to actually modeled surface areas of this rod type contained in location type 1DCRAD(IRAD) times the ratio of total surface areas in all channels of this rod type to this surface area (Default=1.0).
36-45	MLTF(2,IRAD)	Enter surface lumping factor for surface position 2. Ratio of total calculated to actually modeled surface areas of this rod type contained in location type IDCRAD(IRAD) times the ratio of total surface areas in all channels of this rod type to this surface area (Default=1.0).
46-55	MLTF(3,IRAD)	Enter surface lumping factor for surface position 3. Ratio of total calculated to actually modeled surface areas of this rod type contained in location type IDCRAD(IRAD) times the ratio of total surface areas in all channels of this rod type to this surface area (Default=1.0).
56-65	MLTF(4,IRAD)	Enter surface lumping factor for surface position 4. Ratio of total calculated to actually modeled surface areas of this rod type contained in location type IDCRAD(IRAD) times the ratio of total surface areas in all channels of this rod type to this surface area (Default=1.0).
66-75	VDMLT(IRAD)	Vapor/droplet multiplication factor. Total number of radiation channels being modeled by this location type (Default=1.0).

Radiation Channel Orientation Array

VESSEL8.10.1 (LRAD(IRAD,J),J=1,NRRAD(IRAD)) FORMAT(16I5)

Columns	Variable	Description
1-5	LRAD(IRAD,J)	Rod number in position "J" for appropriate
6-10		radiation channel IDCRAD(IRAD). Negative for
11-15...		inside surface.

*Note: See text for proper rod orientation.

Repeat VESSEL8.10 and VESSEL8.10.1 until all radiation channels have been input.

Radiation Location Type Information

VESSEL8.11 (IDTYP(I),I=1,NLTYP) FORMAT(I5)

Columns	Variable	Description
1-5	IDTYP(I)	Location type to be input
		> 0 manual input to follow.
		< 0 auto view factor routine to be used.

Manual Location Type Input If IDTYP(I) < 0 skip VESSEL8.11.1 to 8.11.4

Area Input

VESSEL8.11.1 (ARAD(J),J=1,JTOT)) FORMAT(8F10.0) JTOT=total number surfaces for location type IDTYP(I)

Columns	Variable	Description
1-10	ARAD(J)	Surface area of position "J" for location type
11-20		IDTYP(I) in inches (if ICOBRA=0) or centimeters
21-30...		(if ICOBRA=1)

Emissivity Input

VESSEL8.11.2 (ERAD(J)J=1,JTOT) FORMAT(8F10.0) JTOT=Total number of surfaces for location type IDTYP(I)

Columns	Variable	Description
1-10	ERAD(J)	Enter the emissivity of position "J" for
11-20		location type IDTYP(I).
21-30...		

View Factor Input

VESSEL8.11.3 ((FRAD(J,K),J=1,JL),K=J,JL) FORMAT(8F10.0)
JL=Total number of radiant surfaces in location type IDTYP(I).

Columns	Variable	Description
Card Set 1		
1-10	FRAD(1,K)	Enter radiation view factor between surface 1
11-20		and surface "K".
21-30...		
Card Set 2		
1-10	FRAD(2,K)	Enter radiation view factor between surface 2
11-20		and surface "K".
21-30...		
Card Set "J"		
1-10	FRAD(J,K)	Enter radiation view factor between surface "J"
11-20		and surface "K", where "J" > "K".
21-30...		

Continue until all "J" surfaces have been input, starting each "J" surface group with a new card set.

Beam Length Input

VESSEL 8.11.4 ((DRAD(J,K),J=1,JL),K=J,JL) FORMAT(8F10.0)
JL=Total number of radiant surfaces in location type IDTYP(I)

Columns	Variable	Description
Card Set 1		
1-10	DRAD(1,K)	Enter beam length between surface 1 and surface
11-20		"K" in inches (if ICOBRA=0) or centimeters (if
21-30...		ICOBRA=1).
Card Set 2		
1-10	DRAD(2,K)	Enter beam length between surface 2 and surface
11-20		"K" in inches (if ICOBRA=0) or centimeters (if
21-30...		ICOBRA=1).
Card Set "J"		
1-10	DRAD(J,K)	Enter beam length between surface "J"
11-20		and surface "K" in inches (if ICOBRA=0) or
21-30...		centimeters (if ICOBRA=1) where "J" > "K".

Continue until all "J" surfaces have been input, starting each "J" surface group with a new card set.

Repeat VESSEL8.11 and VESSEL8.11.4 until all IDTYP(I)s are input for IDTYP(I)>0.

Auto View Factor Input

Omit if IDTYP(I)>0.

VESSEL8.11.5 (APAR(1II),III=1,7) FORMAT(7F10.0)

Columns	Variable	Description
1-10	APAR(1)	Enter first parameter for auto view factor input according to location type. Enter nominal rod diameter in inches (if ICOBRA=0)

	d	or centimeters (if ICOBRA=1).
11-20	APAR(2)	Enter second parameter for auto view factor input according to location type. If location type
	d1	=1,2,3,7 enter rod diameter of rod in oversized rod location.
	p	=4,5,8 enter pitch of rods
	g	=6,9 enter gap width between rod and wall in inches (if ICOBRA=0) or centimeters (if ICOBRA=1.
21-30	APAR(3)	Enter third parameter for auto view factor input. If location type
	p	=1,2,3,7 enter pitch of rods
	g	=4,5,8 enter gap width between rod
	and	wall
	em1	=6,9 enter emissivity of rod in inches (if ICOBRA=0) or centimeters (if ICOBRA=1).
31-40	APAR(4)	Enter fourth auto view factor input parameter. If location type
	em1	=1,2,3,7,8 enter emissivity of rods
	rad	=4,5,9 enter radius of curvature of the wall
	em2	=6 enter the emissivity of the wall in inches (if ICOBRA=0) or in centimeters (if ICOBRA=1).
41-50	APAR(5)	Enter fifth auto view factor input parameter. If location type
	rad	=2,3,6,7 enter radius of curvature of wall
	disc	=4,5 enter displacement from centerline axis to rod position 1 in inches (if ICOBRA=0) or centimeters (if ICOBRA=1).

51-60	APAR(6)	Enter sixth auto view factor input parameter. If location type
	em2	=2,3,7 enter emissivity of the wall
	em1	=4,5 enter emissivity of the rods
61-70	APAR(7)	Enter seventh auto view factor input parameter. If location type
	em2	=4,5 enter emissivity of wall

VESSEL Group 9: Conductor Geometry Description, read by subroutine SETIN

The geometry types are read in this group. The geometry types are numbered sequentially in the order they are read in. Nuclear rod geometry types are read using cards-VESSEL9.2 through VESSEL9.5. All other geometry types are read using cards VESSEL9.6-- and VESSEL9.7.

VESSEL9.1 NGROUP,NFUELT,IRELF,ICONF,IMWR FORMAT(5I5)

Columns	Variable	Description
1-5	NGROUP	Enter nine (9).
6-10	NFUELT	Enter number of geometry types to be read in. Note: A geometry type may be used by both rods and unheated conductors, but for the unheated conductor, any heat generation specified for the type will be ignored.
11-15	IRELF	Fuel relocation flag (1=on, 0=off) (This is used only for nuclear fuel rods using the dynamic gap conductance model).
16-20	ICONF	Fuel degradation flag (1=on,0=off) (NOTE: if IRELF=1, then ICONF=1.)
21-25	IMWR	Flag for metal-water reaction (zirconium dioxide only) =0, off =1, Cathcart (for best-estimate analysis) =2, Baker-Just (for evaluation model analysis)

NUCLEAR FUEL GEOMETRY TYPES

These data are read only for nuclear fuel geometry types. If FTYPE(I) is not entered as NUCL, the geometry data is interpreted by line VESSEL9.6.

VESSEL9.2 I,FTYPE(I),DROD,DFUEL(I),NFUEL,IMATF,IMATC,IMATOX(I),DCORE,TCLAD, FTDENS(I),IGPC(I),IGFORC,IRADP (Read only for nuclear geometry types.) FORMAT(I5,1X,A4,2F10.0,4I5,3F5.0,3I5)

Columns	Variable	Description
1-5	I	Enter the geometry type identification number. (Note: Geometry type index numbers must be entered sequentially, from 1 to NFUELT. Skipping numbers is not permitted.)
7-10	FTYPE(I)	Enter NUCL.
11-20	DROD	Enter rod outside diameter, in inches (if ICOBRA = 0) or meters (if ICOBRA = 1).
21-30	DFUEL(I)	Enter fuel pellet diameter, in inches (if ICOBRA = 0) or meters (if ICOBRA = 1).
31-35	NFUEL	Enter number of radial nodes in fuel pellet.
36-40	IMATF	Fuel material properties flag: Enter zero (0) for built-in UO_2 properties. Enter a positive integer corresponding to the identification number of a material properties tables for user-input properties. (Refer to group 10 for material properties input data.)
41-45	IMATC	Clad material properties flag: Enter zero (0) for built-in zirconium properties.

		Enter a positive integer corresponding to the identification number of a material properties table for user-input properties. (Refer to group 10 for material properties input data.)
46-50	IMATOX(I)	Clad oxide property flag: Enter zero (0) for built-in zirconium dioxide properties. Enter a positive integer corresponding to the identification number of a material properties table for user-input properties (see group 10).
51-55	DCORE	Enter diameter of central void for cored fuel, in inches (if ICOBRA = 0) or meters (if ICOBRA = 1). Enter zero for uncored fuel.
56-60	TCLAD	Enter clad thickness, in inches (if ICOBRA = 0) or meters (if ICOBRA = 1).
61-65	FTDENS(I)	Enter fuel theoretical density as a fraction (used only if built-in UO_2 properties have been flagged; i.e., if IMATF = 0). (Note: Do not enter zero.)
66-70	IGPC(I)	Gap conductance option flag; Enter zero (0) for constant gap conductance (as specified by HGAP(N) on card VESSEL8.2). Enter a positive integer for user-specified nonuniform gap conductance (entered on card VESSEL9.4 in a table of IGPC(I) elements). Enter a negative integer for the dynamic gap conductance model. (|IGPC(I)| is the number of entries in the cold gap width vs axial location table, read on card VESSEL9.4.)

71-75	IGFORC	Flag for temporal forcing function on gap conductance (valid only if IGPC(I) > 0: Enter zero (0) for constant gap conductance. Enter a positive integer for a temporal forcing function with IGFORC table entries.
76-80	IRADP	Enter number of entries in radial power profile table for the fuel pellet. Enter zero (0) for a uniform radial power profile.

VESSEL9.3 PGAS(I),VPLEN(I),ROUFF(I),ROUFC(I),(GSFRAC(L),L=1,6), OXIDET
Read only if FTYPE(I) = NUCL and IGPC(I) < 0.
FORMAT(4F10.0,6F5.,F10.0)

Columns	Variable	Description
1-10	PGAS(I)	Enter cold pin gas pressure for nuclear fuel rod geometry type 1, in psia (if ICOBRA = 0) or N/m2 (if ICOBRA = 1).
11-20	VPLEN(1)	Enter gas plenum volume, in in^3 (if ICOBRA = 0) or m^3 (if ICOBRA = 1).
21-30	ROUFF(I)	Enter fuel pellet surface roughness in inches (if ICOBRA = 0) or meters (if ICOBRA = 1).
31-40	ROUFC(I)	Enter surface roughness of clad inner surface, in inches (if ICOBRA = 0) or meters (if ICOBRA = 1). (Note: Fuel and clad surface roughness should correspond to those used in FRAPCON-2 since the correlation is empirical.) Fuel surface ROUFF = 0.000085 inches Clad surface ROUFC = 0.000045 inches
41-45	GSFRAC(1)	Enter molar fraction of helium gas present.
46-50	GSFRAC(2)	Enter molar fraction of xenon gas present.
51-55	GSFRAC(3)	Enter molar fraction of argon gas present.
56-60	GSFRAC(4)	Enter molar fraction of krypton gas present.
61-65	GSFRAC(5)	Enter molar fraction of hydrogen gas present.

66-70	GSFRAC(6)	Enter molar fraction of nitrogen gas present. Note: $\sum_{L=1}^{6}$ GSFRAC(L) = 1.0
71-80	OX1DET	Enter initial oxide thickness for the zircaloy metal-water reaction rate equation in inches (if ICOBRA = 0) or meters (if ICOBRA = 1). (Used only if IMWR > 0.)

VESSEL9.4 (AXJ(I,L),AGFACT(I,L),L=1,|IGPC(I)|) Read only if FTYPE(I) = NUCL and |IGPC(I)| > 0. FORMAT(8F10.0).

Columns	Variable	Description
1-10 21-30 41-50 61-70	AXJ(I,L)	Enter topmost vertical position, measured from the bottom of the rod, at which the cold gap width (or gap conductance) AGFACT(I,L) is applied. (All vertical levels below AXJ(I,L) and above AXJ(I,L-1) will have AGFACT(I,L) for gap width or gap conductance.) Units on AXJ(I,L) are inches (if ICOBRA = 0) or meters (if ICOBRA = 1).
11-20 31-40 51-60 71-80	AGFACT(I,L)	Enter cold gap width if IGPC(I) is negative. Units are inches (if ICOBRA = 0) or meters (if ICOBRA = 1). Enter gap conductance if IGPC(I) is positive. Units are Btu/hr-ft^2-°F (if ICOBRA = 0) or W/m^2-°C (if ICOBRA = 1).

VESSEL9.5 (RODP(L),POWR(L),L=IRADP) Read only if FTYPE(I) = NUCL and IRADP > 0. FORMAT(8F10.0)

Columns	Variable	Description
1-10 21-30 41-50	RADP(L)	Enter the relative radial location (r/r_o) where corresponding power factor (POWR(L)) is applied.

61-70	$\frac{r}{r_o} = \frac{(\text{radius} - \text{DCORE}/2)}{\frac{1}{2}(\text{DFUEL(I)} - \text{DCORE})}$	
11-20 31-40 51-60 71-80	POWR(L)	Enter the relative power factor (i.e., the ratio of local power at location RADP(L) to total rod power).

NONNUCLEAR GEOMETRY TYPES

These data are read for all geometry types that do not describe nuclear fuel.

VESSEL9.6 I,FTYPE(I),DROD,DIN,NFUEL,IMATOX(I),IMATIX(I) Read only if FTYPE(I)≠ NUCL FORMAT(I5,1X,A4,2F10.0,3I5)

Columns	Variable	Description
1-5	I	Enter geometry type identification number.
7-10	FTYPE(I)	Enter four-character alphanumeric geometry type flag: HROD = solid cylinder TUBE = hollow tube WALL = flat plate
11-20	DROD	Enter outside diameter for HROD or TUBE geometries, in inches (if ICOBRA = 0) or meters (if ICOBRA = 1). Enter the wetted perimeter for WALL geometries, in inches (if ICOBRA = 0) or meters (if ICOBRA = 1).
21-30	DIN	Enter inside diameter for TUBE geometries, in inches (if ICOBRA = 0) or meters (if ICOBRA = 1).

		Enter thickness for WALL geometries, in inches (if ICOBRA = 0) or meters (if ICOBRA = 1). Enter zero (0.0) for (HROD) solid cylinder geometries.
31-35	NFUEL	Enter the number of regions within the conductor. (Each region has a uniform power profile and consists of one material.)
36-40	IMATOX(I)	Enter material property table identification number for oxide on outside surface. (Default is zirconium oxide; IMATOX(I) = 0). Enter the index number of the material property table for material in region NFUEL if there is no oxide present.
41-45	IMATIX(I)	Enter material property table identification number for oxide on inside surface (Default is zirconium oxide; (IMATIX(I) = 0); applies only to TUBEs or WALLs.) Enter the index number of the material property table for material in region 1 if there is no oxide present.

Data sets for the NFUEL regions of geometry type I are entered starting at the centerline for HROD types and at the inside surface for TUBE and WALL types. Data sets are entered in sequence moving radially toward the outside surface.

VESSEL9.7 (NODER(L),MATR(L),TREG(L),QREG(L),L=1,NFUEL) Read only if FTYPE(I) ≠ NUCL. FORMAT(4(2I5,2F5.0))

Columns	Variable	Description
1-5 21-25 41-45 61-65	NODER(L)	Enter the number of radial heat transfer nodes in region L.

6-10 26-30 46-50 66-70	MATR(L)	Enter the material property table identification number for region L.
11-15 31-35 51-55 71-75	TREG(L)	Enter the thickness of region L, in inches (if ICOBRA = 0) or meters (if ICOBRA = 1). Note: For TUBE and HROD geometry types, $\sum_{L=1}^{NFUEL} TREG(L) = 0.5\ (DROD - DIN)$
16-20 36-40 56-60 76-80	QREG(L)	Enter radial power factor for region L. (This profile is automatically normalized to unity.)

VESSEL Group 10: Material Properties Tables, read by subroutine SETIN

This input group is required only if user-supplied material properties were flagged by input in group 9 (i.e., with nonzero values for IMATF, IMATC, IMATOX(I), IMATIX(I) or MATR(L) for any geometry type).. If only default material properties are used, (i.e, zircaloy and UO2), this group is omitted.

VESSEL10.1 NGROUP,NMAT FORMAT(2I5)

Columns	Variable	Description
1-5	NGROUP	Enter ten (10).
6-10	NMAT	Enter number of material properties tables to be read in.

Cards VESSEL10.2 and VESSEL10.3 are read in pairs NMAT times.

VESSEL10.2 N,NNTDP,RCOLD(N),IMATAN(N) FORMAT(2I5,F10.0,20X,A10)

Columns	Variable	Description
1-5	N	Enter the material property table identification number.

6-10	NNTDP	Enter the number of entries in material properties table N.
11-20	RCOLD(N)	Enter the cold density in lbm/ft^3 (if ICOBRA = 0), or kg/m^3 (if ICOBRA = 1) for material N. (This value is used to define the mass in the heat transfer nodes composed of material type N.)
41-50	IMATAN(N)	Alphanumeric label for material (e.g., stainless)

VESSEL10.3 (TPROP(I,N),CPF1(I,N),THCF(I,N) 1=1,NNTDP) FORMAT(6F10.0)

Columns	Variable	Description
1-10 31-40	TPROP(I,N)	Enter the temperature for entry I in material property table N. Units are °F (if ICOBRA = 0) or °K (if ICOBRA = 1).
11-20 41-50	CPF1(I,N)	Enter the specific heat for entry I in material property table N. Units are Btu/lb-°F (if ICOBRA = 0) or J/kg-°C (if ICOBRA = 1).
21-30 51-60	THCF(I,N)	Enter the thermal conductivity for entry I in material property table N. Units are Btu/hr-ft-°F (if ICOBRA = 0) or W/m-°C (if ICOBRA = 1).

VESSEL Group 11: Axial Power Tables and Forcing Functions, read by subroutine SETIN

VESSEL11.1 NGROUP,NAXP,NQ,NGPFF FORMAT(4I5)

Columns	Variable	Description
1-5	NGROUP	Enter eleven (11).
6-10	NAXP	Enter number of axial power profile tables to be read. (Minimum of one.)
11-15	NQ	Enter number of pairs of elements in the power forcing function table.

		Enter zero (0) if power is constant.
16-20	NGPFF	Enter number of pairs of elements in gap conductance forcing function table. Enter zero (0) if there is no forcing function on gap conductance.

Axial Power Tables

Cards VESSEL11.2 and VESSEL11.3 are read in pairs NAXP times.

VESSEL11.2 I,NAXN(I) FORMAT(2I5)

Columns	Variable	Description
1-5	I	Enter axial power profile table identification number.
6-10	NAXN(I)	Enter number of pairs of elements in axial power profile table I.

VESSEL11.3 (Y(I,N),AXIAL(I,N),N=1,NAXN(I)) FORMAT(8F10.0)

Columns	Variable	Description
1-10	Y(I,N)	Enter vertical location, relative to bottom of
21-30		the VESSEL, where axial power factor AXIAL(I,N)
41-50		is applied. Use inches (if ICOBRA = 0) or
61-70		meters (if ICOBRA = 1).
11-20	AXIAL(I,N)	Enter relative power factor (the ratio of local
31-40		power to average power) at vertical location
51-60		Y(I,N).
71-80		

All rods using the same table should start and end at the same vertical locations. In the table, Y(I,1) must be the vertical location of the beginning of the rods, and Y(I,NAXN(I)) must be the vertical location of the end of the rods.

Power Forcing Function

VESSEL11.4 (YQ(N),FQ(N),N=1,NQ) FORMAT(8F10.0) Read only if NQ > 0.

Columns	Variable	Description
1-10	YQ(N)	Enter transient time (seconds).
21-30		
41-50		
61-70		
11-20	FQ(N)	Enter the power factor:
31-40		
51-60		FQ(N) = Power at time YQ(N) / initial power
71-80		

Gap Conductance Forcing Function

VESSEL11.5 (YGPFF(N),FGPFF(N),N=1,NGPFF) FORMAT(8F10.0) Read only if NGPFF > 0.

Columns	Variable	Description
1-10	YGPFF(N)	Enter transient time (in seconds).
21-30		
41-50		
61-70		
11-20	FGPFF(N)	Enter conductance factor:
31-40		
51-60		FGPFF(N) = Power at time YQ(N) / initial power
71-80		

VESSEL Group 12: Turbulent Mixing Data, read by subroutine SETIN

VESSEL12.1 NGROUP,N1 FORMAT(2I5)

Columns	Variable	Description
1-5	NGROUP	Enter twelve (12).

6-10	N1	Enter number of sections in which turbulence will be applied.

Card VESSEL12.2 is read N1 times.

VESSEL12.2 I,BETA(I,AAAK(I) FORMAT(I5,2F5.0)

Columns	Variable	Description
1-5	I	Section index number.
6-10	BETA(I)	Mixing coefficient ($\beta = w'/G \cdot S$)
11-16	AAAK(I)	Equilibrium distribution weighting factor in void drift model. Suggested value=1.0.

VESSEL Group 13: Boundary Condition Data, read by subroutine SETIN

VESSEL13.1 NGROUP,NIBND,NKBND,NFUNCT,NGBND FORMAT(5I5)

Columns	Variable	Description
1-5	NGROUP	Enter thirteen (13).
6-10	NIBND	Enter the total number of vertical mesh cell boundary conditions.
11-15	NKBND	Enter the total number of transverse momentum cells for which crossflow will be set to zero.
16-20	NFUNCT	Enter the number of forcing functions for the boundary conditions.
21-25	NGBND	Enter the number of groups of contiguous transverse momentum cells for which crossflows will be set to zero.

NBCD1P
NBCRD

VESSEL13.2 (NPTS(K),K=1,NFUNCT) FORMAT(16I5) Read only if NFUNCT > 0.

Columns	Variable	Description
1-5,...	NPTS(K)	Enter the number of points (pairs of values) in forcing function table K.

Sixteen values are entered per card. Repeat card VESSEL13.2 until NFUNCT values have been entered.

Card VESSEL13.3 is read NFUNCT times.

VESSEL13.3 ((ABSCIS(K,I),ORDINT(K,I),I=1,NPTS(K)),K=1,NFUNCT) Read only if NFUNCT > 0. FORMAT(5(F5.0,F10.0))

Columns	Variable	Description
1-5,16-20, 31-35,46-50, 61-65	ABSCIS(K,I)	Enter the time, in seconds, the factor is applied.
6-15,21-30, 36-45,51-60, 66-75	ORDINT(K,I)	Enter the forcing function factor to be applied at time ABSCIS(K,I).

Five pairs of (ABSCIS,ORDINT) are entered per card. Repeat card VESSEL13.3 until NPTS(K) points have been entered for forcing function table K. Continue entering data until NFUNCT tables have been specified.

Card VESSEL13.4 is read NIBND times.

VESSEL13.4
(IBOUND(L,M),L=1,2),ISPEC(M),NPFN(M),NHFN(M),PVALUE(M),HVALUE(M),XVALUE(M)
FORMAT(5I5,3F10.0) Read only if NIBND > 0.

Columns	Variable	Description
1-5	IBOUND(1,M)	Enter the index number of the channel boundary condition M applies to.
6-10	IBOUND(2,M)	Enter the vertical node number at which

		boundary condition M is applied. (NOTE: The node number is referenced to the beginning of the section that the channel identified in IBOUND(1,M) resides in.)
11-15	ISPEC(M)	Enter the boundary condition type. Valid options are: 1 = pressure and enthalpy boundary condition 2 = flow and enthalpy 3 = flow only 4 = mass source (flow rate and enthalpy) 5 = pressure sink and enthalpy
16-20	NPFN(M)	Enter the index number of the forcing function table by which the first parameter of the boundary condition will be varied. (NOTE: The forcing function tables are numbered sequentially in the order they are read in on card VESSEL13.3.) For example: If ISPEC(M) = 1 and NPFN(M) = 3, the specified pressure will be adjusted according to the third forcing function entered on VESSEL13.3. Enter zero if the boundary condition is constant.
21-25	NHFN(M)	Enter the index number of the forcing function table by which the second parameter of the boundary condition will be varied. (For example: If ISPEC(M) = 1 and NHFN(M) = 6, the specified enthalpy will be adjusted according to the 6th forcing function specified on VESSEL13.3.) Enter zero if the boundary condition is constant.
26-35	PVALUE(M)	Enter the first boundary value. If ISPEC(M) = 1 or 5, enter pressure, in psia (if ICOBRA = 0) or N/m^2 (if ICOBRA = 1).

		If ISPEC(M) = 2, 3 or 4, enter flow rate, in lbm/sec (if ICOBRA = 0) or kg/sec (if ICOBRA = 1).
36-45	HVALUE(M)	Enter enthalpy in Btu/lbm (if ICOBRA = 0) or J/kg (if ICOBRA = 1). Enter zero (0) if ISPEC(M) = 3.
46-55	XVALUE(M)	Pressure (psia) must be input for ISPEC(M)=2,3 or 4.

VESSEL13.5 HMGA(N),(GVALUE(NGA,N),NGA=1,NGASP2) (read only if ISPEC(N)≠3) FORMAT(16F5.0)

Columns	Variable	Description
1-5	HMGA(N)	Enthalpy of noncondensible gas mixture
6-10	GVALUE(NGA,N)	Volume fraction of gas in vapor-gas mixture
11-15...		(read in same order as in card group 1)

VESSEL13.6 NHMFN(N),(NGFN(NGA,N),NGA=1,NGASP2) FORMAT(12I5)

Columns	Variable	Description
1-5	NHMFN(N)	Index number of forcing function applied to gas mixture enthalpy
6-10, 11-15...	NGFN(NGA,N)	Index number of forcing function applied to volume fraction of each gas

Card VESSEL13.7 is read after cards VESSEL13.4 and VESSEL13.6 have been read NIBND times, and only if some ISPEC(M) has been specified as 5 (i.e., a pressure sink boundary condition). Card VESSEL13.7 is read once for each pressure sink, in the same order they are specified in the input for card

VESSEL13.7 ASINK(K),SINKK(K),DXSINK(K) FORMAT(3F5.0) Read only if some ISPEC(M) = 5.

Columns	Variable	Description
1-5	ASINK(K)	Enter the flow area of the pressure sink, in $in.^2$ (if ICOBRA = 0) or m^2 (if ICOBRA = 1).
6-10	SINKK(K)	Enter the loss coefficient (velocity head) of the pressure sink.
11-15	DXSINK(K)	Enter the length of the momentum control volume for the sink, in inches (if ICOBRA = 0) or meters (if ICOBRA = 1).

Card VESSEL13.8 is read NGBND times.

Card VESSEL13.8 is read only if some ISPEC(M) has been specified as 4 (i.e., a mass injection boundary condition). Card VESSEL13.8 is read once for each mass injection boundary condition, in the same order they are specified in the input for card VESSEL13.4.

VESSEL13.8 AINJT(K) FORMAT(F5.0) Read only if some ISPEC(M) = 4.

Columns	Variable	Description
1-5	AINJT(K)	Enter the flow area of the mass injection in $in.^2$ (if ICOBRA = 0) or m^2 if (ICOBRA = 1).

VESSEL13.9 K,JSTART,JEND FORMAT(3I5) Read only if NGBND > 0.

Columns	Variable	Description
1-5	K	Enter the gap number to which a zero (0.0) crossflow is to be applied.
6-10	JSTART	Enter the continuity cell number at which to start applying the zero crossflow.
11-15	JEND	Enter the continuity cell number at which to stop applying the zero crossflow.

(Note: The crossflow will be set to zero for gap K between nodes JSTART and JEND. The node numbers are given relative to the beginning of the section containing gap K.)

This card may be repeated as many times as necessary for a given gap K, to identify all axial levels that have zero crossflow. The total number of transverse momentum cells with zero crossflow boundary conditions specified by card VESSEL13.8 must sum to NKBND.

VESSEL Group 14: Output Options, read by subroutine SETIN

VESSEL14.1 NGROUP,N1,NOUT1,NOUT2,NOUT3,NOUT4,IPROPP,IOPT FORMAT(8I5)

Columns	Variable	Description
1-5	NGROUP	Enter fourteen (14).
6-10	N1	Enter the general vessel output option. Valid entries are: 1 = print channels only 2 = print channels and gaps only 3 = print rods and unheated conductors only 4 = print rods, unheated conductors, and channels only 5 = print channels, gaps, rods, and unheated conductors
11-15	NOUT1	Enter the number of channels to be printed (used if N1 = 1, 2, 4, or 5). If NOUT1 = 0, all channels will be printed. If NOUT1 > 0, an array of NOUT1 channel numbers. must be entered on card VESSEL14.2.
16-20	NOUT2	Enter the number of rods to be printed (used if N1 > 2). If NOUT2 = 0, all rods will be printed.

		If NOUT2 > 0, an array of NOUT2 rod numbers must be entered on card VESSEL14.4.
21-25	NOUT3	Enter the number of gaps to be printed (used if N1 = 2 or 5). If NOUT3 = 0, all gaps will be printed. If NOUT3 > 0, an array of NOUT3 gap numbers must be entered on card VESSEL14.3.
26-30	NOUT4	Enter the number of unheated conductors to be printed (used if N1 > 2). If NOUT4 = 0, all unheated conductors will be printed. If NOUT4 > 0, an array of NOUT4 unheated conductor numbers must be entered on card VESSEL14.5.
31-35	IPROPP	Enter the property table print option. Valid entries are: 0 = do not print the property table 1 = print the property table
36-40	IOPT	Enter the debug print option. Valid entries are: 0 = normal printout only 2 = debug printout (print extra data for channels, rods and gaps)
41-45	IREWR	0 = NO rewind of .run 1 = rewind of .run

VESSEL14.2 (PRINTC(I),I=1,NOUT1) FORMAT(16I5) Read only if N1 ≠ 3 and NOUT1 > 0.

Columns	Variable	Description
1-5,...	PRINTC(I)	Enter the index numbers of channels to be printed. Sixteen values are entered per card. Repeat this card until NOUT1 values have been entered.

VESSEL14.3 (PRINTG(I),I=1,NOUT3) FORMAT(16I5) Read only if N1 = 2 or 5 and NOUT3 > 0.

Columns	Variable	Description
1-5,...	PRINTG(I)	Enter the index numbers of gaps to be printed. Sixteen values are entered per card. Repeat this card until NOUT3 values have been entered.

VESSEL14.4 (PRINTR(I),I=1,NOUT2) FORMAT(16I5) Read only if N1 > 2 and NOUT2 > 0.

Columns	Variable	Description
1-5,...	PRINTR(I)	Enter the index numbers of rods to be printed. Sixteen values are entered per card. Repeat this card until NOUT2 values have been entered.

VESSEL14.5 (PRINTS(I),I=1,NOUT4) FORMAT(16I5) Read only if NOUT4 > 0.

Columns	Variable	Description
1-5,...	PRINTS(I)	Enter the index numbers of unheated conductors to be printed. Sixteen values are entered per card. Repeat this card until NOUT4 values have been entered.

VESSEL14.6 NDUMEND FORMAT(I5)

Columns	Variable	Description
1-5	NDUMEND	Enter zero (0) to terminate VESSEL group control card input.

Graphics Options, read by subroutine IGRAF

GRAF.1 MOVIE,TMOVIE FORMAT(I5,F10.2)

Columns	Variable	Description
1-5	MOVIE	Enter the movie process option. Valid entries are: 0 = no movie (recommended option) 1 = save data for particle tracker movie. Note: The COBRA/TRAC code has the capability to dump data that can be used to make particle-tracker movies of simulations. However, the software to actually make the particle-tracker movies is not part of the COBRA/TRAC package, and will be released and documented separately.
6-15	TMOVIE	Enter the time interval at which to save data for the movie. Valid only if MOVIE = 1.

Note: Movie option currently disabled. Enter a blank card.

GRAF.2 MXGDMP,IGRFOP,NLLR FORMAT(4I5)

Columns	Variable	Description
1-5	MXGDMP	Enter the maximum number of time steps for which graphics data will be saved. Absolute maximum is MI (RESPEC parameter). (Note: This cannot be changed on a restart.)
6-10	IGRFOP	Enter the vessel graphics option, as follows: 0 for normal vessel dump (all variables saved for all vessel computational cells) N, where N is the number of user-selected vessel variables to be saved for graphics

11-15	NLLR	Enter the number of liquid level calculations. (Number of GRAF.3 cards.) (Valid only if IGRFOP > 0.)

16-20

Card GRAF.3. is read once for a liquid level calculation in channels that are all in the same section. If a liquid level calculation includes channels in different sections, GRAF.3 is read once for each section involved. Card GRAF.3 is read a total of NLLR times.

GRAF.3 (NCHLL(N),JSLL(N),JCELL(N),(ICLL(I,N),I=1,NCHLL(N)) Read only if NLLR > 0. FORMAT(16I5)

Columns	Variable	Description
1-5	NCHLL(N)	Enter the number of channels in a section to be used for liquid level calculation N.
6-10	JSLL(N)	Enter the starting axial node number for the liquid level calculation. This value should be negative if continuing input from previous sections of a liquid level calculation that crosses section boundaries.
11-15	JELL(N)	Enter the ending axial node number (in the section containing channels ICLL(I,N)) to be included in the liquid level calculation.
16-20	ICLL(I,N)	Enter the index numbers of NCHLL(N) channels to use in the liquid level calculation.
21-25		(Enter up to 13 values on the first line. If
...		NCHLL(N) > 13, continue on the next line, entering values in the 16I5 format.)

GRAF.4 ((IGRF(I,J),J=1,2),GRFN(I),I=1,IGRFOP) Read only if IGRFOP > 0.
FORMAT(5(2I5,F5.0)

Columns	Variable	Description
1-5	IGRF(I,1)	Enter a number signifying the vessel variable to be saved. Valid entries are:
16-20		
31-35		
46-50		
61-65		

Channel variables--

1 = pressure
2 = void fraction
3 = entrained liquid fraction
4 = liquid fraction
5 = liquid temperature
6 = vapor temperature
7 = liquid density
8 = vapor density
9 = vapor flow
10 = liquid flow
11 = entrained liquid flow
12 = vapor generation rate
13 = heat transfer rate to liquid
14 = heat transfer rate to vapor
15 = drop mass entrainment rate
16 = drop mass deentrainment rate
17 = drop interfacial area density
18 = ETAENP
19 = HASHL
20 = HASCL
21 = HASHV
22 = flow regime
23 = boundary condition type
24 = interfacial drag coefficient (XK)
25 = interfacial drag coefficient (XKGE)
37 = mixture density; $(\alpha\rho_v+(1-\alpha)\rho_\ell)$

		Gap variables-- 26 = vapor crossflow 27 = liquid crossflow 28 = entrained liquid crossflow Rod variables-- 29 = heat transfer mode 30 = liquid temperature (seen by rod IGRF(I,2)) 31 = vapor temperature (seen by rod IGRF(I,2)) 32 = heat transfer coefficient to liquid 33 = heat transfer coefficient to vapor 34 = heat flux 35 = rod surface temperature 36 = peak temperature on rod identified in IGRF(I,2) at axial node GRFN(I) Slab variables-- 38 = slab surface temperature
6-10 21-25 36-40 51-55 66-70	IGRF(I,2)	Enter channel, rod, or gap number for which selected variable will be saved. Parameters 1-25 and 37 are channel variables; 26-28 are gap variables; 29-36 are rod variables. If IGRF(I,1) = 35 or 36 and the <u>inside</u> surface temperature is desired, enter the <u>negative</u> of the rod number. (When any rod is divided into two or more azimuthal surfaces, IGRF(I,2) must be the rod surface number rather than the whole rod number. The surface number is determined by counting the number of rod fractions in the order read on card 8.3).
11-15 26-30	GRFN(I)	Enter the vertical node number for which the selected variable will be saved.

41-45	For rod variables, enter the vertical elevation in inches. (Must be within 1 inch of a
56-60	vertical node location.)
71-75	For IGRF(I,1)=36, enter the radial node index. (Node 1 is on the inside of the rod.)

TIME DOMAIN DATA, read by subroutine TIMSTP

After all component data have been entered, the user must define the time domain for the simulation. The total time can be divided into several domains of specified duration. Each time domain can have different minimum and maximum time step sizes and different edit intervals. To terminate the calculation, a time domain with a negative time step size is entered. Two cards are required to specify the data for each time domain.

TIME.1 DTMIN,DTMAX,TEND,RTWFP,TMAX FORMAT(5E14.6)

Columns	Variable	Description
1-14	DTMIN	Enter the minimum time step allowed for this domain, in seconds. Enter a negative value to terminate the calculation.
15-28	DTMAX	Enter the maximum time step allowed for this domain, in seconds.
29-42	TEND	Enter the end of this time domain, in seconds.
43-56	RTWFP	Enter the ratio of conduction solution and fluid solution time step sizes. (Used to obtain steady-state conditions. The conduction solution can generally take time steps greater than the fluid solution. For transient calculations, RTWFP should be one.)
57-70	TMAX	Enter the maximum CPU time allowed for this run. If this CPU limit is reached during this simulation time domain, the run will terminate. (Dump files will be written, so the calculation can be restarted.)

TIME.2 EDINT,GFINT,DMPINT,SEDINT,TCKLEND FORMAT(5E14.6)

Columns	Variable	Description
1-14	EDINT	Enter the print interval for this time domain. Output will be printed every EDINT seconds.
15-28	GFINT	Enter the graphics interval for this time domain. Data for graphics will be saved every GFINT seconds.
29-42	DMPINT	Enter the restart dump interval. Data for restarts will be saved every DMPINT seconds. (NOTE: For larger problems, the restart dumps create relatively large files, and can become unmanageable if too many dumps are written during a simulation. Regardless of the value for input DMPINT, the dump logic automatically writes dumps at the beginning of a calculation, at the end of a calculation, and after every 60 minutes of CPU time during the calculation. This is usually quite sufficient, and DMPINT can be set to a large value.)
43-56	SEDINT	Enter the "short edit" interval for this time domain. (A "short edit" is an abbreviated print.) Short edits will be performed every SEDINT seconds.
57-70	TCLKEND	Enter the wall clock time (decimal, 24-hour clock) at which to stop the calculation and create a restart dump and edit. (This is useful for running the calculation during particular shifts; for example, TCLKEND can be entered as 7.5 to stop the calculation at 7:30 am. Enter zero if this feature is not used.

Repeat cards TIME.1 and TIME.2 for each time domain desired. A final time domain with a negative value for DTMIN must be entered to terminate the calculation.

```
          0
          0     0.0
       1.0e-3            10            40
        1     *****  flecht-seaset test 61607 - 0.8 in/sec reflood  *****
    1    1
 40.1      1170.      0.0        .4219     673.0       1.0e-08  .9999    .9711
air         0.0001
    2    3
    12.11118.21
    25.59154.25
    34.54052.81               45.88
    3    2
    1    1    21.7081.488.8478 0.0     0    0 1.0     0    0
 14.  0.0
    2    2    32.9281.31461.01 0.0     0    0 1.0     0    0
 24.  0.0
    0
    4    1    2    1
    1    3   19        8.0    6
    8        8.0    9        6.0   11 4.25        14 3.0         15 4.5
   20 8.00
    1    1                                 1
    2    2                                 2
    3    3                                 3
    3
   30   57
    5    7
    4
   10 .993   11 .728   12 .521   13 .877
    4
   11.8833   12.6076   13.7078   14.9632
    3
   111.157   121.261   131.072
    3
   11 .945   12 .911   13 .993
    3
   11.9814   12.9202   13.9576
    3
   111.033   121.052   131.004
    4
   11.7701   12.3671   13.6731   14.9831
    6    3
    2    1    3    1
    5    4    6    2
   -7    0    0    1
    7    0    2    1    1    1    1    0    0    2
```

```
1    5    2    4 1.4       0.2952    1.75      1.984
4    6    9   15   17
1 15.5            1    1
2 44.5            2    1
2    5    1    4 1.4       0.2100    1.75      1.984
4    6    9   15   17
3 24.0            3    1
1    1   12    1 0.0       .4164     .4164     .0202     0.0       .4790
1    1 2.70       0.0652
2    2   12    1 0.0       .4164     .4164     .0032     0.0       .0890
2    1 2.70       0.0131
8    4    0    2    4    4    3         1
1    1    1    2        .05      15.5        1.0      5000.    1
1 1.0
2    1    1    2        .05      38.0        1.0      5000.    1
2 1.0
3    1    1    2        .05      28.0        1.0      5000.    1
3 1.0
4    2    0   -2        .05       0.5        0.0      5000.    10.55  70.
0 1.0
-3
1    1    1   20
1
0.0        270.       12.       686.       24.       898.       49.       1245.
48.        1377.      60.       1570.      67.       1459.      70.       1518.
71.        1477.      75.       1475.      78.0      1565.      81.       1557.
86.        1565.      90.       1515.      96.       1380.      102.      1179.
111.       1080.      120.      872.       132.      696.       138.      673.
2    1        20
2
0.0        270.       12.       686.       24.       867.       39.       1199.
48.        1367.      60.       1526.      67.       1568.      70.       1549.
71.        1538.      75.       1565.      78.0      1574.      81.       1511.
86.        1524.      90.       1471.      96.       1333.      102.      1121.
111.       1056.      120.      875.       132.      692.       138.      664.
3    1        20
3
0.0        270.       12.       687.       24.       868.       39.       1199.
48.        1364.      60.       1526.      67.       1571.      70.       1578.
71.        1533.      75.       1581.      78.0      1608.      81.       1547.
86.        1527.      90.       1476.      96.       1338.      102.      1146.
111.       1056.      120.      902.       132.      692.       138.      643.
4    1        10
4
0.0        270.       24.       290.       48.       339.       60.       370.0
72.        377.0      84.       339.0      96.       339.0      108.      350.0
120.       289.0      132.      278.0
1    1    1   20    1       4.0       4.0       4.0       4.0      15.5
1    1    1    1    1    1    1    1    1    1    1    1    1    1    1    1
1    1    1    1
2    2    1   20    1 4.0       4.0       4.0       4.0       38.
2    2    2    2    2    2    2    2    2    2    2    2    2    2    2    2
2    2    2    2
3    3   -2   19    1  6.       6.        6.        6.       18.667
3    3    3    3    3    3    3    3    3    3    3    3    3    3   -4    3
3    3    3
4    3   -4   13    1 6.0       6.0       1.293     0.0      18.667
3    3   -4    3    3    3    3    3   -4    3    3    3   -4
-1
   .374     0.7       .374      .496
```

rod.

thimbles

```
 -2
0.374     0.7       2.976     .496      3.811     0.0       0.7       .374

 -4
   .374      0.7     3.472     0.496     3.811     0.0       0.7

  9    2
  1 hrod      .374          4    1    1
  1    2  .02          2    3.0675  1.0    3    2.0745          2    1 .025
  2 tube    11.308      8.288    2    .5    1
  4    1.2101  0.0     2    5 1.30    0.0
 10    5
  1    4      501.
     0.0      0.107     7.550     200.0     0.114     9.14
  1200.0      0.142     13.34     2400.     0.174     18.54
  2   10      124.8
     0.0      .1484     14.78      500.     .3131     14.33
   1000.      .3964     13.89     1200.     .4168     13.71
   1400.      .4323     13.53     1600.     .4441     13.36
   1800.      .4532     13.18     2000.     .4600     13.00
   2200.      .4652     12.82     2400.     .4692     12.64
  3    8     211.7
0.0         .1325     13.404    200.      .1669     13.507
600.        .2262     13.713    1000.     .2662     13.919
1400.       .3455     14.125    1800.     .2977     14.331
2200.       .3056     14.537    2400.     .3090     14.64
  4    9     525.
32.         0.2       10.11     400.      .116      10.11
600.        .121      11.10     800.      .126      12.1
1000.       .132      13.2      1200.     .14       14.3
1400.       .145      15.5      1600.     .149      16.7
2500.       .167      22.1
  5    1  6.0
     0.0        0.3    0.0166
 11    1   23
  1   32     144.
     0.0        .43      21.6       .43      21.61      .68      28.8       .68
   28.81        .88      36.0       .88      36.01     1.11      43.2      1.11
   43.21       1.3       50.4      1.3       50.41     1.49      57.6      1.49
   57.61       1.6       64.8      1.6       64.81     1.66      79.2      1.66
   79.21       1.6       86.4      1.6       86.41     1.49      93.6      1.49
   93.61       1.3      100.8      1.3      100.81     1.11      108.      1.11
  108.01        .88     115.2       .88     115.21      .68     122.4       .68
  122.41        .43     144.0       .43     144.01      0.0     168.0       0.
     0.0      .5710       1.0     .9962       2.5     .9884      5.0      .9752
     10.      .9493       15.     .9306       20.     .9110      25.      .8963
     30.      .8817       40.     .8590       50.     .8376      60.      .8201
     75.      .7860      100.     .7484      125.     .7383      150.     .7040
    175.      .6835      200.     .6665      250.     .6362      300.     .6116
    400.      .5756      600.     .5255      800.     .4912
 12    1
  1 .01 1.0
 13    6    0    2    0    0
  3    3
0.0  0.0        0.2   0.7057   300. .70570
0.0  2.4877     9.26 1.0        500.  1.0
   1    1    2    1    2   0.08620      94.98  40.1
673.  1.0 .9999.0001

   2    1    2    1    2   0.22838      94.98  40.1
673.  1.0 .9999.0001

   3    1    2    1    2   0.18540      94.98  40.1
673.  1.0 .9999.0001

   1   21    1    0    0  40.1       1200.     40.1
673.  1.0 .9999.0001

   2   21    1    0    0  40.1       1200.     40.1
673.  1.0 .9999.0001

   3   21    1    0    0  40.1       1200.     40.1
673.  1.0 .9999.0001

  14    5                   0    0    2


 300    0    0
        .0002          .015          200.0          1.0     14400.00
          20.          2.50           800.        800.0
        -.001         0.005            5.0          1.0         200.0
        10.0          10.0            500.         500.
```

FORM 335 (6-83) U.S. NUCLEAR REGULATORY COMMISSION

BIBLIOGRAPHIC DATA SHEET

1. REPORT NUMBER (Assigned by TIDC, add Vol. No., if any)
NUREG/CR-4166
EPRI NP-4111
WCAP-10375

2. Leave blank

3. TITLE AND SUBTITLE
nalysis of FLECHT-SEASET 163-Rod Blocked Bundle Data using COBRA-TF

4. RECIPIENT'S ACCESSION NUMBER

5. DATE REPORT COMPLETED
MONTH: August YEAR: 1985

6. AUTHOR(S)
C.Y. Paik, L.E. Hochreiter/Westinghouse Electric Corp.
J.M. Kelly, R.J. Kohrt/Battelle Northwest Laboratory

7. DATE REPORT ISSUED
MONTH: October YEAR: 1985

8. PERFORMING ORGANIZATION NAME AND MAILING ADDRESS (Include Zip Code)
estinghouse Electric Corporation
uclear Energy Systems
Post Office Box 355
Pittsburgh, Pennsylvania 15230

9. PROJECT/TASK/WORK UNIT NUMBER

10. FIN NUMBER
B6204

SPONSORING ORGANIZATION NAME AND MAILING ADDRESS (Include Zip Code)
Division of Radiation Programs and Earth Sciences
U.S. Nuclear Regulatory Commission
Office of Nuclear Regulatory Research
Washington, D. C. 20555

Electric Power Research Institute
3412 Hillview Avenue
Palo Alto, CA 94303

12a. TYPE OF REPORT
Technical

12b. PERIOD COVERED (Inclusive dates)
September 1982-December 1984

SUPPLEMENTARY NOTES

ABSTRACT (200 words or less)

low blockage and spacer grid heat transfer models for rod bundle arrays have been developed for a two-phase flow situation characteristic of a PWR reflood. These models have been incorporated into COBRA-TF, which is a three-dimensional, three-field, two-fluid mechanistic two-phase flow subchannel computer code. Comparison of the predicted flow blockage heat transfer in large rod bundle arrays with test data indicates that the blockage and grid heat transfer models used with the COBRA-TF code agree quite well with the measured data. Bias plots of the predicted and measured temperature rises from different tests indicate that, in general, the computer code calculations tend to underpredict the heat transfer improvement observed to have been caused by grids and blockage in the experiments. The principal reason for heat transfer improvement due to blockage and grids is the breakup of the entrained liquid droplets in the superheated steam flow above the quench front. The breakup of these entrained drops results in a population of much smaller drops, which are more easily evaporated in the superheated vapor. The enhanced heat transfer observed in and downstream of blockages and grids is also attribute to increased turbulence caused by the droplets in the steam flow. The resulting computer models and methods of modeling both grids and blockages, which are described in this report, are believed to be applicable to PWR saefty analysis. Application of such models is expected to significantly reduce or eliminate the calculated peak clad temperature penalty due to flow blockage for a hypothetical PWR LOCA, using the Appendix K criteria.

15a. KEY WORDS AND DOCUMENT ANALYSIS

15b. DESCRIPTORS

FLECHT SEASET
Rod Blockage Heat Transfer
COBRA-TF
Spacer Grid Heat Transfer

16. AVAILABILITY STATEMENT
Unlimited

17. SECURITY CLASSIFICATION (This report)
Unclassified

18. NUMBER OF PAGES

19. SECURITY CLASSIFICATION (This page)
Unclassified

20. PRICE
$